JCTC Journal of Chemical Theory and Computation

Special Issue in Honor of John P. Perdew for His 65th Birthday

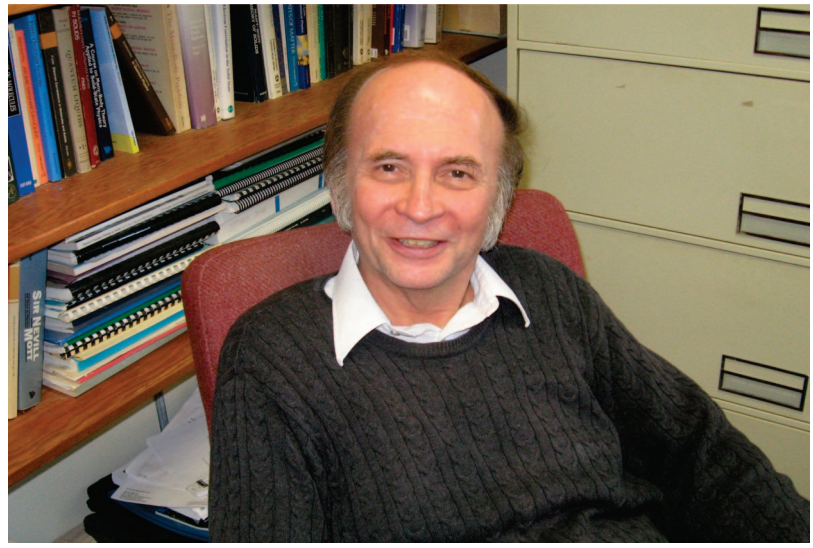

Short Biography: From a Conversation with John Perdew

John Perdew was born August 30, 1943, in the Appalachian mountain region of western Maryland. He grew up in the small city of Cumberland, where his parents, Paul Perdew and Elma Carr Perdew, were both teachers. At Allegany High School, good mathematics courses convinced him that some things could be proved. A National Merit Scholarship brought him to Gettysburg College in Pennsylvania, where Professor Richard Mara's elegant introductory lectures left no doubt in John's mind that mathematical clarity and physical intuition could come together in one science: physics.

John was a graduate student of physics at Cornell 1965−1971, a turbulent time for many and a time of challenge for him—first to get through the graduate courses and then to find (over a period of several frustrating years) a successful approach to his dissertation problem. There his thesis advisor John Wilkins and his teachers Neil Ashcroft and David Mermin got him started on solid state theory. After the completion of his dissertation, he got his first taste of theoretical chemistry when Wilkins asked him to try to explain the cooperativity effect in the oxygenation of hemoglobin. But his freshman chemistry course had not prepared him to deal with such a large and complicated system.

At that time, electronic structure calculations for solids, when they were done at all, were still typically based on the Hartree approximation. Some physicists and chemists were exploring the local density or Slater $X\alpha$ approximations, but that information did not trickle down to John. The density functional theory of Kohn and Sham 1965 was first presented to him when he was a postdoc with Sy Vosko at Toronto 1971−1974. A second postdoc fellowship with David Langreth at Rutgers 1974−1977 convinced him that this theory was a sound foundation on which to build both improved approximations and successful applications.

The late 1970s were a hard time to find a job in physics. In his later postdoc years, John sent out hundreds of applications per year, usually without getting an interview. He even applied for an experimental faculty position at Tulane University in New Orleans and was hired there in 1977 (since experimentalists were too expensive!). John has spent more than 30 happy years there, exploring the exact density functional theory and constructing/testing its needed approximations, never tiring of this deep and practically important subject, enjoying the good company of more faculty colleagues, postdocs, and students than can be named here.

John's first collaboration with Mel Levy of Tulane Chemistry was "In Defense of the Hohenberg-Kohn Theorem and Density Functional Theory", *Int. J. Quantum Chem.* **1982**, *21*, 511. This article was officially labeled a "polemic" in an editorial in the same issue. Kieron Burke, now at UC Irvine, Chemistry, joined his group as a postdoc in 1993.

10.1021/ct900098q CCC: $40.75
Published on Web 03/16/2009

My research collaboration with John commenced in August of 2002 after a Sandia Workshop in Albuquerque on density functionals. At the time, it was increasingly clear that *local* hybrids (or hyper-GGAs in John's "Jacob's Ladder" hierarchy of functionals) were the way forward. In Fall 2005, with Hurricane Katrina seriously devastating New Orleans, John spent a forced sabbatical in my group at Rice University in Houston. He endured the near miss of another big category 4 storm (Rita) that same Fall. Twenty-two papers and several functionals later, our joint scientific adventure still continues.

Gus Scuseria
Rice University

Early Days at Tulane

It gives me pleasure to recall the early days at Tulane, where I often interacted and collaborated with John.

I arrived at Tulane a year before John began his faculty appointment. Prophetically for DFT, Walter Kohn visited and reviewed the Physics Department during that year, thus anticipating (or perhaps causing) John's appearance. I first met John in 1977 at his job interview lecture, which took place in the planetarium, an appropriate venue in which to discuss the universal functional.

I came to Tulane with the intent of concentrating on DFT. Wonderful for me was the coincidence that John was hired. The odds were close to zero in those days that two people, in two relatively small departments, would work on the fundamentals of DFT and would happen to have offices about 50 feet apart on the same floor.

The semiofficial Quantum Theory Group was formed in 1977, composed of faculty members from physics, chemistry, and mathematics. For years we regularly held spirited informal seminars on our research. Members of the group attended John's lively and lucid DFT course during his first or second year at Tulane.

Driven by our addiction to the subject and also somewhat, perhaps, by the fact that we were junior faculty members, at odd times we were the only people working on the fifth floor of Stern Hall. Indeed, I remember this to be quite clearly the case 30 years ago, between the Fall and Spring semesters of the 1978−1979 academic year, when I walked a few steps to John's office to show him some observations that eventually resulted in my first real DFT publication at Tulane. He was always there to share the excitement and make insightful suggestions. He was also very generous with his ideas.

Several years after the famous Perdew−Zunger self-interaction correction paper [*Phys. Rev. B* **1981**, *23*, 5048], John excitedly came to me and said that he arrived at something very promising, a real-space cutoff of the gradient expansion for the exchange hole [*Phys. Rev. Lett*. **1985**, *55*, 1665]. He said the numbers looked really good. I quote: "They have to be, given the quality of the theory." The work corrected the divergence problem of the second-order gradient expansion approximation (GEA). A correlation energy paper followed closely [*Phys. Rev. B* **1986**, *33*, 8822]. These two papers marked John's entrance into research on the GGA, a term that I believe he coined. We now know the delightful consequences of all this.

John and I have, of course, published a number of articles together. After our collaboration on the "polemical" *Int. J. Quantum Chem*. paper, our next joint venture was the PPLB article containing surprising results concerning fractional particle number and derivative discontinuities of the energy [*Phys. Rev. Lett*. **1982**, *49*, 1691]. My family spent part of the summer of 1982 in Newton, MA. It was then that drafts of the manuscript were transported between Tulane, Newton, and Chapel Hill, where Bob Parr was and still is located. John suggested that we use Federal Express: "Let's get it out fast.". This was my first exposure to FedEx, and as a result I still feel excitement when I walk into one of their offices. Anyway, our band gap paper followed soon after [*Phys. Rev. Lett*. **1983**, *51*, 1884]. In the mid 1980s we collaborated on our counterintuitive coordinate scaling results and virial theorems in DFT [*Phys. Rev. A* **1985**, *32*, 2010]. It was, as usual, much fun.

In those early days, there was always a feeling of anticipation that something wonderful was eventually going to happen with DFT. There was this mysterious functional, and all one had to do was crack its code.

Mel Levy
Guest Editor
Duke University (Visiting Professor)
Tulane University (Professor Emeritus)

On the Border

In September 1993, I arrived at Tulane as John's new postdoc. For condensed matter theory, times were even rougher than in the early 1970s. I had already been a postdoc for four years and looked headed for academia's dustbin. Although I had never worked in DFT, John took a big chance on hiring me, giving me an opportunity for which I will always be grateful.

John had one or two graduate students back then, but I was his first postdoc for a long time. He was toiling away at the (now standard) DFT-developer tasks: constructing new functionals, finding new exact conditions, explaining failures, publishing errata, etc. Because the group was small, he had time to meet me every day, usually for lunch and coffee afterward. Every day, I would ask really dumb questions, often for the third or fourth time. Every day, he would explain things to me, never running out of patience, and always appearing to enjoy it. After about 3 months, I kind of got my bearings, the questions improved, and the answers were fascinating.

Up to about that time, DFT was an obscure subject studied by a handful of devotees. Every year, there would be one DFT session at the APS March meeting, which would be standing room only. But that was because users were hoping for a new functional and usually left empty-handed. The DFT die-hards would go have supper together that night, often fitting around a single table, and talk endlessly about all their favorite DFT exotica. Funding was always scarce, and many had paid their own way to the meeting.

John had recently created a generalized gradient approximation (GGA) called PW91, but it was largely being

rejected by the unwashed masses of condensed matter physics. This was because that community had become so used to the local density approximation (LDA or S-VWN5) that most of their codes were constructed to function only at that level of accuracy. During the first APS meeting after I began with John, I could not move from one room to another without someone stopping me to explain why GGAs do not work.[1] Since my first project was to check and help publish the PW91 derivation, this career move did not look too promising.

Meanwhile, there was a revolution taking place in chemistry, because it had just been shown that GGAs and hybrids were sufficiently accurate for many chemical purposes, and suddenly real chemists (not just theoretical ones) were using DFT. Barriers were coming down between the two disciplines, and John was getting invited to lots of chemistry meetings. We were writing up more and more material. Because there was so much stored in John's brain and published in obscure manuscripts without figures, whenever we could simply figure out how to calculate something inside the theory for a model system, we would see new things in the figures we had made or find a new molecular context for the work. I recall that after Matthias Ernzerhof joined us, we submitted our first article to the *Journal of Chemical Physics*, which naturally was roundly rejected by the referees. (It was later accepted, once we had done a better job of explaining what we were trying to do and had taken most of the DFT out.)

As time went on, we wrote and published a lot. One of the most pleasurable aspects was our joint love of the English language, and our constant attempts to run jokes past the editors. In particular, John always loved coming up with catchy titles to the papers. One of our favorites, "GGAs: A Glance under the Hood", was rejected by an ACS publisher, because chemists searching abstracts would assume we were working on fume hoods. We also fought a losing battle against acronyms (at least, those not beginning with a P).

Our most well-known work from that period was the GGA called PBE. This was really the triumphant culmination of two decades of John's work on GGAs but was also catalyzed by several key events. One was the refusal of *Physical Review B* to publish the complete derivation of PW91, on the basis that some of the material had already appeared.[2] Another was my observation that, when parametrizing the results of the numerical construction of the GGA exchange-correlation hole into the PW91 energy density, John had accidentally (and ever so slightly) screwed up an exact condition. That really stuck in his craw. The last I will mention is that, in order to satisfy as many constraints as possible, John had inserted some very small terms that do not kick-in except at very small gradients, ensuring restoration of the original gradient expansion. This would sometimes lead to nasty wiggles in the potential, unnecessarily raising lots of cut-offs in plane-wave codes.

Thus, John was inspired to produce a final GGA that would contain only those elements needed for calculations, and that could be explained by relatively transparent physical arguments. In fact, PBE is very similar to PW91, but somehow it was the right functional at the right time for condensed matter physics.[3] Weitao Yang was the first in a long line to revise PBE, so we enjoyed pointing out his Procrustean dilemma. A quick second was the Danish RPBE of Hammer and Norskov, who asked the important question, PBE or not PBE. This was followed by so many more that John himself finally got into the game with the balefully named PBEsol.

At my last APS meeting as John's postdoc, I had the pleasure of watching Don Hamann[2] explain to a huge audience on a huge screen that PBE was giving the right answer for the right reasons for a pressure-induced phase transition in quartz, and I never had to defend PBE to physicists again. Thus, given its motivations, PBE is really just one more John Perdew erratum, correcting a few last functional typos in PW91 and pulling one more fast one on the editors of *Physical Review Letters*.

In all, I spent 3 years at Tulane, and those were the most research-productive years of my life. John and I wrote over 30 papers in that time, with many great collaborators. These years were also the most fun, because John made them so, with his relaxed informal approach to everything and his allowance for independence.[4] Not only did I learn all I needed about DFT to make a career from it, I also learned vital skills for writing papers, explaining ideas, and surviving in academia. These served me well in finally getting a faculty position at a small (but wonderful) chemistry department, something I never managed to do in physics, and a step I have never regretted.

A few years later, I was happy to return to Tulane for a mini-meeting with John and Mel and Hardly Gross, just 2 weeks after Walter Kohn shared a Nobel Prize in Chemistry.[5] We were all very happy but had no idea just how big, broad, and exciting the field would subsequently become. Much of the physics underlying that award came from the exceptionally deep and patient work of John, so his work truly lies on the border between chemistry and physics.

I am very happy to have helped contribute to both John's scientific enterprise as well as to this special celebratory issue. We on the border salute you, John, and look forward to many more functionals and fun article titles.

Kieron Burke
Guest Editor
University of California, Irvine

References

(1) There are still a few die-hards in condensed matter that prefer LDA, which gets the lattice constant of bulk silicon almost exactly right. Even PBEsol did not beat that.

(2) Don Hamann is an extremely distinguished solid-state theorist who spent much of his career at Bell Labs. He mentioned that it took him 2 weeks of hard work in the library at the Aspen Center for Physics to find and read all the bits of the PW91 derivation, scattered as they were over many papers and years. In summer 2001, he also pointed out to us that PBE gets the ground-state energy of the hydrogen atom right to about 4 digits and wondered if we had done some surreptitious fitting. This was news to us

and either just dumb luck or some fundamental consistency in the universe.

(3) Of course all good chemists know that PBE is woefully inadequate for many dissociation energies and that you really need a hybrid, such as PBE0, a.k.a. PBE1PBE.

(4) Another bonus that came with being at Tulane was the chance to interact and collaborate with Mel Levy who was in the chemistry department. He famously wrote in his research proposal when he applied for a faculty position there that he would find the exact XC functional (which, in a sense, he did with his constrained search approach). This was a brilliant move, as he spent his entire career at Tulane working on that original proposal, and he is still not finished!

(5) This was when Hardy Gross (a.k.a. E.K.U.) first asked me about how to calculate conductances through single molecules, a project he and I have happily worked away at for a decade now. Hmm, sounds quite like Mel's original proposal.

CT900098Q

JCTC Journal of Chemical Theory and Computation

Evaluation of Density Functionals and Basis Sets for Carbohydrates

Gábor I. Csonka,*,† Alfred D. French,‡ Glenn P. Johnson,‡ and Carlos A. Stortz§

Department of Inorganic and Analytical Chemistry, Budapest University of Technology, Szent Gellért tér 4, Budapest, H-1521 Hungary, Southern Regional Research Center, U.S. Department of Agriculture, 1100 Robert E. Lee Boulevard, New Orleans, Louisiana 70124, and Departamento de Química Orgánica-CIHIDECAR, Universidad de Buenos Aires, Ciudad Universitaria, 1428 Buenos Aires, Argentina

Received October 20, 2008

Abstract: Correlated ab initio wave function calculations using MP2/aug-cc-pVTZ model chemistry have been performed for three test sets of gas phase saccharide conformations to provide reference values for their relative energies. The test sets consist of 15 conformers of α- and β-D-allopyranose, 15 of 3,6-anhydro-4-*O*-methyl-D-galactitol, and four of β-D-glucopyranose. For each set, conformational energies varied by about 7 kcal/mol. Results obtained with the Hartree−Fock method, with pure density functional approximations (DFAs) like LSDA, PBEsol, PBE, and TPSS and with hybrid DFAs like B3PW91, B3LYP, PBEh, and M05-2X, were then compared to the reference and local MP2 relative energies. Basis sets included 6−31G*, 6−31G**, 6−31+G*, 6−31+G**, 6−311+G**, 6−311++G**, cc-pVTZ(-*f*), cc-pVTZ, and aug-cc-pVTZ(-*f*). The smallest basis set that gives good DFA relative energies is 6−31+G**, and more converged results can be obtained with 6−311+G**. The optimized geometries obtained from a smaller basis set, 6−31+G*, were useful for subsequent single point energy calculations with larger basis sets. The best agreement with MP2 was shown by M05-2X, but only when using a dense DFT grid. The popular B3LYP functional is not the best for saccharide conformational studies. The B3PW91 functional gives systematically better results, but other hybrid functionals like PBEh or TPSSh are even better. Overall, the nonempirical PBE GGA and TPSS meta-GGA functionals also performed better than B3LYP.

1. Introduction

Nature combines sugars in an almost infinite array of compounds that are each involved in very specific interactions. These interactions do not depend on elemental composition alone but on the shape or conformation of the carbohydrate as well. A major difficulty in understanding such interactions is that the conformational space of carbohydrates is, at least potentially, very large. Even for monosaccharides, variations in ring shape and exocyclic group orientations can combine in many different ways.[1] Combining monosaccharides into oligo- or polysaccharides results in exponentially larger numbers of potential geometries to consider. Thus, computational studies of the conformational space of carbohydrates must be fast enough to evaluate many different structures. At the same time, reliable selection of the important conformers requires highly accurate methods that have a firm theoretical foundation.

For the past 20 years, energies of carbohydrate conformers have mostly been calculated with empirical force fields, but there has been little agreement among the proponents of the various molecular mechanics methods.[2−4] In addition, most empirical methods do not handle chemical reactivity, and

* To whom correspondence should be addressed. E-mail: csonkagi@gmail.com.
† Budapest University of Technology.
‡ U.S. Department of Agriculture.
§ Universidad de Buenos Aires.

10.1021/ct8004479 CCC: $40.75
Published on Web 03/04/2009

subtle dependencies on variable electronic structure are usually lost. Therefore, a number of workers have used electronic structure theory despite its much slower (and far more computationally expensive) arrival at an optimized geometry and minimized energy.

Three major categories of methods are based on electronic structure theory. The first category, semiempirical quantum mechanics, is easily the fastest but should not be used for work that demands accuracy. The MNDO, AM1, and PM3 semiempirical methods fail to provide accurate relative energies for carbohydrates,[5,6] despite attempts to improve their performance.[7] The second category, ab initio quantum mechanics or wave function (WFN) methods, such as Hartree−Fock (HF) theory, shows systematic errors caused by the lack of Coulomb-type electron correlation. For typical problems with carbohydrates, errors from the lack of correlation are often canceled by basis set errors. For example, split-valence 6−31G* and cc-pVDZ basis sets give fairly good relative energies for carbohydrate conformers with HF theory.[8] However, those good results are based on unreliable error compensation. Attempts to improve the results by using the larger cc-pVTZ or cc-pVQZ basis sets, under-stabilize the $^1C_4$ β-D-glucose conformers resulting from HF error.[8,9] Post-HF or correlated methods like MP2, MP3, MP4, and CCSD(T) with noniterative triples explicitly treat Coulomb correlation. These methods might give reliable equilibrium geometries and relative energies by MP2 complete basis set (CBS) extrapolations using aug-cc-pVTZ, aug-cc-pVQZ, or aug-cc-pV5Z basis sets (noted as MP2/CBS[4,5]). It was found that relative energies of molecules with localized bonds can be reasonably approximated (typical accuracy is around 0.2 kcal/mol) by the MP2/aug-cc-pVTZ model chemistry.[10] Thus, the conventional canonical MP2 method can be suitable for calculating reference energies. However, these calculations would be very expensive for thorough surveys of the conformational space of monosaccharides (cf., $O(N^5)$ scaling of computer time with the size N). The pseudospectral local MP2 (LMP2) approximation[11,12] is considerably faster than canonical MP2 and approaches linear scaling for large systems but neglects dispersion-relevant terms. In addition, a consistent domain selection is critically important for different conformers. There is little knowledge about the effect of this LMP2 approximation for carbohydrates, and so we shall compare the MP2 and LMP2 results.

The third category comprises methods based on Kohn−Sham (KS) Density Functional Theory (DFT).[13] These methods treat electron correlation much more efficiently than post-HF methods. The simplest approximation is the nonempirical local spin density approximation (LSDA), the second level is the generalized gradient approximation (GGA, e.g., PBE[14]), and the third level is the meta-GGA (e.g., TPSS[15]). The hybrid functionals at the fourth level are fully nonlocal and semiempirical. (Although called semiempirical, these functionals are entirely different from the unreliable classical semiempirical WFN methods such as MNDO, AM1 and PM3.)

Because of its efficiency, DFT is widely used, having been applied to many types of chemical problems, as well as to condensed matter physics. The most popular GGA functionals are PBE,[14] BLYP,[16,17] and PW91,[18] and their hybrid variants: PBEh,[14,19,20] B3LYP,[21] and B3PW91.[18,22] The functional used most often for studies of carbohydrate conformations[5,9,23−42] has been B3LYP. Its wide acceptance is based, in part, on excellent calculated molecular geometries, molecular atomization energies, and enthalpies of formation of the molecules in the G2/97 test set.[43] More recent studies,[44] however, showed that B3LYP fails seriously for larger molecules of the G3/99 test set. The increase in B3LYP error with molecular size is evident from comparison of the errors for the series of *n*-alkanes: methane, ethane, etc., up to octane.[44] In Grimme's work,[45] B3LYP gave an error only slightly smaller than HF theory (10.3 and 13.4 kcal/mol, respectively) for the difference in energy between *n*-octane and its isomer, 2,2,3,3-tetramethylbutane. Depending on the test set, B3PW91 performs better than B3LYP or vice versa.[43,46,47] One important difference between the B3LYP and B3PW91 functionals is that the former does not respect the uniform electron gas limit while the latter does (see discussion in the Methods section). It is suspected that this error contributes to the deteriorating performance of B3LYP for large molecules and metals,[48] while other functionals perform considerably better for larger molecules or even for bulk solids.[48] There is growing evidence that B3LYP is not the best hybrid GGA method for conformational space studies of larger molecules.[13,49−51]

Some authors have reported that a large basis set (6−311++G**) with diffuse functions also on the hydrogen atoms is necessary for B3LYP relative energies of carbohydrate conformers.[25,26,30,31,33,36,38,40,42] This contradicts an earlier paper of Csonka,[9] who suggested that the 6−31+G* basis set is sufficient for geometry calculations and 6−31+G** or 6−311+G** suffice for relative energy calculations, whereas the 6−311++G** basis set is unnecessarily large.

In this paper, the performance of hybrid and nonempirical pure functionals (see section 2, Methods) is tested on a set of 15 allopyranose conformers, on a set of 15 conformers of the five-membered ring 3,6-anhydro-4-*O*-methyl-D-galactitol,[52] a conformationally flexible system, and on a set of four conformers of D-glucose[8,9,23] using various basis sets[40] (Figure 1). The MP2 method is used for reference because it includes to some extent the long-range correlation effects that are missing from the popular DFT functionals. Recent work shows that medium range correlation[53−55] can be reproduced by nonempirical functionals like PBE and PBEsol.[54] Our focus here is on the relative energies calculated from the total energies. If those values are good, then reliable enthalpy and free energy values can be calculated through established methods.

2. Methods

We used the following methods for the present study: canonical MP2, pseudospectral LMP2,[11,12] HF, KS-DFT approximations like hybrid HF/DFT: B3LYP, B3PW91, PBEh, and M05-2X,[56,57] and pure nonempirical DFT of increasing complexity: LSDA, PBE, PBEsol, and TPSS. The exchange-correlation (xc) energy E_{xc}^{hybrid} of recent hybrid functionals like PBEh is defined as

$$E_{xc}^{hybrid} = aE_x^{HF} + (1 - a)E_x^{DFA} + E_c^{DFA} \quad (1)$$

where a is a mixing factor of E_x^{HF} Hatree-Fock and E_x^{DFA} density functional approximation (local functionals like GGA or meta-GGA) exchange energies, and E_c^{DFA} is a density functional approximation correlation energy. The value of a cannot be fixed universally. Good thermochemistry can be obtained[15] by setting $0.1 < a < 0.25$. To obtain good reaction energy barriers, values of $a > 0.5$ are usually required (cf., M05-2X).[56,57]

The first successful and popular hybrid B3PW91 xc energy was defined by Becke as

$$E_{xc}^{B3PW91} = aE_x^{HF} + (1 - a)E_x^{LDA} + b\Delta E_x^{B} + E_c^{LDA} + c\Delta E_c^{PW91} \quad (2)$$

where E_x^{LDA} and ΔE_x^{B} are the LDA exchange energy and Becke 88 exchange energy correction to the LDA, respectively. E_c^{LDA} and ΔE_c^{PW91} are the LDA correlation energy and Perdew−Wang correlation energy correction to the LDA, respectively. The a, b, and c constants were optimized for good thermochemistry on the G2 test set ($a = 0.2$, $b = 0.72$, $c = 0.81$). It was noted that the b and c parameters may cancel each other's effect (e.g., the effect of increasing the value of b can be compensated by the effect of decreasing c and vice versa); thus different parameter sets can give practically the same result.[58]

The popular hybrid B3LYP xc energy was defined somewhat differently

$$E_{xc}^{B3LYP} = aE_x^{HF} + (1 - a)E_x^{LDA} + b\Delta E_x^{B} + (1 - c)E_c^{VWN3} + cE_c^{LYP} \quad (3)$$

where E_c^{VWN3} and E_c^{LYP} are the Vosko−Wilk−Nussair parametrization[59] to random phase approximation (thus not to the exact LDA correlation) and the Lee−Yang−Parr correlation energies, respectively. Becke's values for a, b, and c were used. Neither E_c^{VWN3} nor E_c^{LYP} reproduce the known exact correlation energy of the homogeneous electron gas. It has been shown that the short-range correlations are described well by the LYP functional, but important long-range correlations are missing.[60]

The methods were combined with standard Gaussian basis sets from 6−31G* up to 6−311++G** and some correlation consistent basis sets: cc-pVTZ(-*f*) (without *f* functions on heavy atoms and *d* functions on hydrogen atoms), cc-pVTZ, and aug-cc-pVTZ.[61] Because the diffuse functions on the hydrogen atoms have negligible effect on the relative energies (vide infra), we suggest eliminating these functions from the aug-cc-pVTZ basis set. The resulting basis set is denoted as a-cc-pVTZ.

The present calculations were carried out with Gaussian 03,[62] Jaguar 6.0107, or 7.0213[63] on a 32-node Linux cluster, or on a Windows-based computer. We observed numerical instabilities for pseudospectral LMP2/cc-pVQZ calculations and thus did not use this model chemistry. Note that the domains generated by the procedure applied in the Jaguar computer program are sensitive to the basis set and this might lead to erratic basis set convergence, which we did experience in this work. A similar observation was made by Kaminsky et al.[10]

When using the Jaguar implementation of M05-2X with the standard DFT grid, we found that many conformer minimizations had large numerical errors in the gradient calculations. This would lead the minimizations out of the proper minimum to a completely different geometry. Indicators of this situation were a large number of optimization steps and increasing energy. In most of these cases, the final geometry was fairly different from the geometry obtained with the higher density DFT grid. It was therefore essential to use the dense DFT grid with M05-2X in Jaguar (the computer time increased 54−75%). No similar problem was observed for the B3LYP, B3PW91, or PBEh functionals. For the B3LYP functional, the difference of the total energies calculated with standard and dense numerical integration grids is in the range of −0.07 and +0.04 kcal/mol for the conformers studied in this paper. For relative energies (vide infra), this translates to 0.02 kcal/mol mean absolute deviation (MAD) in the range of −0.06 and +0.06 kcal/mol. This is the inherent error of the numerical integration grid.

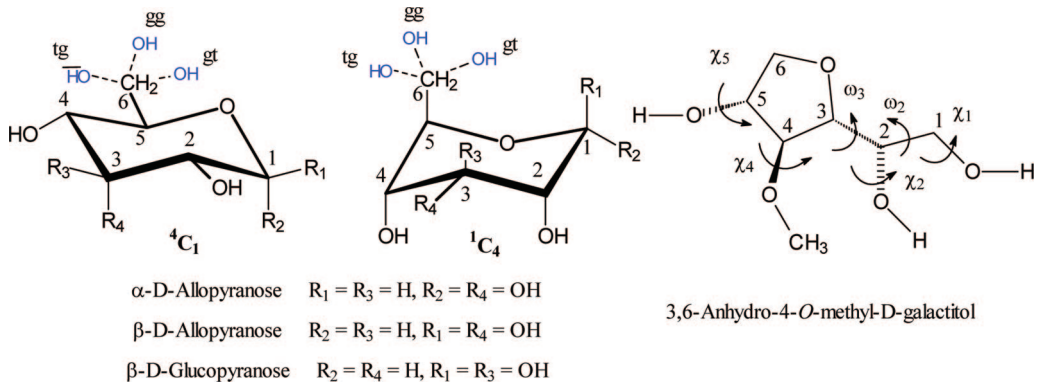

Figure 1. Schematic representations of the α,β-D-allopyranose and glucopyranose rings and the torsion angles in the 3,6-anhydro-4-*O*-methyl-D-galactitol. The ring carbon atoms are numbered according to the standard. For the O(5)−C(5)−C(6)−O(6) torsion angle of pyranoses tg, gg, and gt denotes that O(6) is in the anti position to O(5) and the gauche position to C(4), O(6) is in the gauche position to O(5) and to C(4), and O(6) is in the gauche position to O(5) and the anti position to C(4), respectively.

The geometries were fully relaxed and optimized unless single point calculations were mentioned. The puckering parameters were obtained according to Cremer and Pople.[64] The Boltzmann population of a particular conformer j within the set of n conformers was calculated as ($T = 298$ K)

$$P_j = \frac{e^{-E_j/RT}}{\sum_{i=1}^{n} e^{-E_i/RT}} \quad (4)$$

where P_j is the ratio of the conformer j, E_j is the energy of the conformer j, R is the gas constant, and T is the temperature in K. P_j is expressed as % or ppm, by multiplying by 100 or 10^6, respectively. The P_j ratios are useful for characterizing the various conformer distributions and show the practical implications for the predicted equilibria that are caused by using the various model chemistries (method and basis set).

We use the following definitions of the relative energies:

$$\Delta E_{\text{model}}(\text{conf}_i, \text{conf}_{\text{ref}}) = E_{\text{model}}(\text{conf}_i) - E_{\text{model}}(\text{conf}_{\text{ref}}) \quad (5)$$

is the difference between the energy of the ith conformer, conf_i and the energy of a reference conformer, conf_{ref} using the given model chemistry.

$$\Delta\Delta E_{\text{model A}-\text{model B}}(\text{conf}_i, \text{conf}_{\text{ref}}) = \Delta E_{\text{model A}}(\text{conf}_i, \text{conf}_{\text{ref}}) - \Delta E_{\text{model B}}(\text{conf}_i, \text{conf}_{\text{ref}}) \quad (6)$$

is the difference between the relative energies of the ith conformer calculated with two different model chemistries.

$$\Delta\Delta E_{\text{corrMP2}}(\text{conf}_i, \text{conf}_{\text{ref}}) = \Delta E_{\text{MP2}}(\text{conf}_i, \text{conf}_{\text{ref}}) - \Delta E_{\text{HF}}(\text{conf}_i, \text{conf}_{\text{ref}}) \quad (7)$$

is the relative (MP2) correlation energy difference of the ith conformer. Note that $E_{\text{corrMP2}}(\text{conf}_i) = E_{\text{MP2}}(\text{conf}_i) - E_{\text{HF}}(\text{conf}_i)$, and thus the relative (MP2) correlation energy difference equals $\Delta E_{\text{corrMP2}}(\text{conf}_i, \text{conf}_{\text{ref}})$.

The model and reference conformer dependent mean deviation (MD) is defined as

$$\text{MD}_{\text{model A}-\text{model B}}(\text{conf}_{\text{ref}}) = \frac{1}{n-1}\sum_{i=1}^{n} \Delta\Delta E_{\text{model A}-\text{model B}}(\text{conf}_i, \text{conf}_{\text{ref}}) \quad (8)$$

and the model and reference conformer dependent mean absolute deviation (MAD) is defined as

$$\text{MAD}_{\text{model A}-\text{model B}}(\text{conf}_{\text{ref}}) = \frac{1}{n-1}\sum_{i=1}^{n} |\Delta\Delta E_{\text{model A}-\text{model B}}(\text{conf}_i,\text{conf}_{\text{ref}})| \quad (9)$$

Note that within a given test set of conformers the MD and MAD between the two compared models (model A and model B) depend on the choice of the reference conformers. If we compare several tested model chemistries to the MP2 reference using eqs 6 and 9, the evaluation of the performance of the tested models might depend on the choice of the reference conformer. One way to eliminate this problem is to compare the range of $\Delta\Delta E_{\text{modelA}-\text{modelB}}(\text{conf}_i, \text{conf}_{\text{ref}})$ values of eq 7. We note this as the range of the relative difference, $RRD = \max \Delta\Delta E - \min \Delta\Delta E$.

3. Results and Discussion

3.1. D-Allopyranose Conformers. Schnupf et al.[40] recently performed B3LYP/6−311++G** geometry optimizations on α- and β-D-allopyranose, with chair, boat, and skew ring shapes, and various exocyclic group orientations. We selected fifteen of their 102 structures for the current work, including 13 $^4C_1$ conformers (8 α- and 5 β-anomers, with gg, gt, and tg hydroxymethyl rotamers, see Figure 1), one α- and one β- $^1C_4$ conformer (the ALL15 test set; six of the selected conformers are shown in Figure 2). The range of the B3LYP/6−31+G** relative energies is 5.51 kcal/mol. The Cartesian coordinates (Å), total energies (a.u.), and $\Delta E_{\text{model}}(\text{conf}_i, 1)$ (kcal/mol) of the tested conformers are in the Supporting Information. The first low-energy reference conformer is the $^4C_1$ α-D-allopyranose with torsion angles O(5)−C(5)−C(6)−O(6) ≅180° and C(5)−C(6)−O(6)−H ≅ −60°, noted as tg and g^-, respectively (see, conformer 1 in Figure 2).

First we compare the MP2/cc-pVTZ(-*f*), MP2/a-cc-pVTZ(-*f*) and LMP2/cc-pVTZ(-*f*) relative energies from eq. 5 using the optimized B3LYP/6−31+G* geometries (to exclude geometry effects). The MP2 and LMP2 relative energy differences calculated from eq 6 and the relative correlation energy differences calculated from eq 7 show considerable deviations with the same cc-pVTZ(-*f*) basis set

$$\Delta\Delta E_{\text{corrLMP2}}(\text{conf}_i, 1) = 0.8\Delta\Delta E_{\text{corrMP2}}(\text{conf}_i, 1) - 0.21(\text{kcal/mol}) \quad (10)$$

with $R^2 = 0.989$. This shows that the missing correlation energy has a considerable influence on the relative energy differences calculated using eq 6. Note that the LMP2 approximation also neglects part of the dispersion-relevant double excitations and might show slower basis set convergence[10] than MP2. The intramolecular effect of this LMP2 approximation is not clear. Detailed analysis for the ALL15 test set shows that the LMP2 correlation energy is less negative, thus part of the MP2 correlation energy (about 2.4% or 32 kcal/mol) is lost. However, LMP2/cc-pVTZ(-*f*) and MP2/a-cc-pVTZ(-*f*) relative energies show a good agreement (RRD = 0.48, and MAD =0.10 kcal/mol). We have also performed MP2/cc-pVQZ(-*g*) calculations and CBS[3,4] extrapolation for the first five conformers and obtained good agreement with the MP2/a-cc-pVTZ(-*f*) results (RRD = 0.2 kcal/mol). This shows that the use of the diffuse *s*, *p*, and *d* functions is advantageous for MP2 relative energy calculations. At the MP2 level we found that the a-cc-pVTZ(-*f*) basis set represents a good compromise between accuracy and speed in agreement with Kaminsky et al.[10] Table 1 shows the good agreement between our reference MP2 and LMP2 results for β and $^1C_4$ ratios.

Smaller groups of conformers can be found in the test set for which the $\Delta\Delta E_{\text{corrLMP2}}(\text{conf}_i)$ and $\Delta\Delta E_{\text{corrMP2}}(\text{conf}_i)$ (eq 7) are within ± 0.2 kcal/mol (like conformers {1, 8, 15} shown in Figure 3a or {2, 6, 13} or {5, 7, 9, 10, 12}). Within

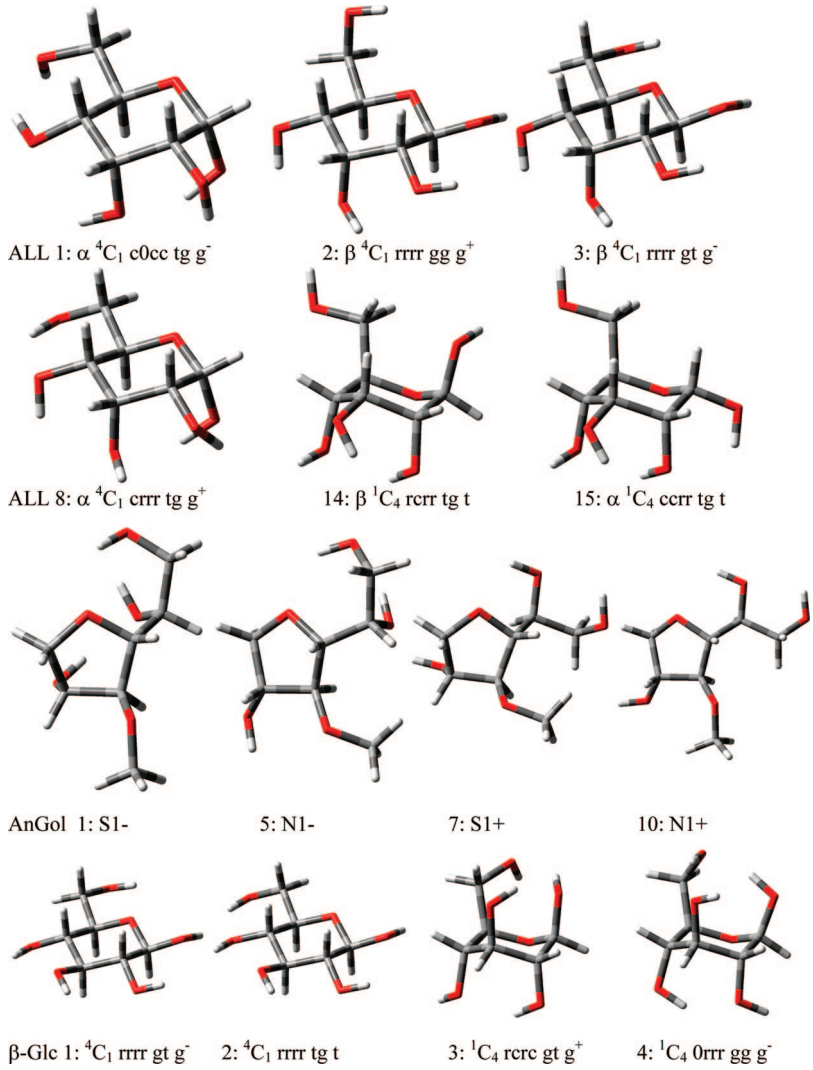

Figure 2. Geometries of some of the selected α,β-D-allopyranose, 3,6-anhydro-4-*O*-methyl-D-galactitol, and β-D-glucopyranose conformers of the ALL15, AnGol15 and Glc4 test sets are shown, respectively. α and β denote the anomeric configurations, $^4C_1$ and $^1C_4$ denote the ring shapes. r denotes the counterclockwise, c the clockwise, 0 the neutral OH directions. tg, gt, and gg show the hydroxymethyl orientation (cf. Figure 1), and g-, g+ and t the O(6)H orientation.

these groups, the HF, MP2, and LMP2 relative energies (eq 5) agree with MAD < 0.2 and RRD < 0.35 kcal/mol. These relative energies are almost converged because the HF energies converge considerably faster to the basis set limit than the MP2 energies and the correlation contributions to the relative energies are negligible. Thus, within these groups of conformers the HF method gives reliable relative energies at a much lower cost than the very expensive MP2/CBS extrapolations. These reliable relative energies are suitable for testing density functional methods. Note that $\Delta\Delta E_{corrMP2}(conf_i, 1)$s between α and β anomers are large positive values, 2.9−3.9 kcal/mol (inclusion of the MP2 correlation energy destabilizes the β anomers), and these relative energies are less converged with respect to the basis set.

Figure 3b shows the performance of the hybrid functionals and the effect of using B3PW91 (eq 2) instead of B3LYP (eq 3).[16−18] The conventional hybrid functionals show similar agreement with the MP2 results ($RRD_{B3LYP-MP2}$ = 1.19, $RRD_{PBEh-MP2}$ = 1.12 $RRD_{B3PW91-MP2}$ = 1.09 kcal/mol). The M05-2X hybrid results agree best with the MP2 results ($RRD_{M05-2X-MP2}$ = 0.90 kcal/mol). M05-2X has shown considerably better performance than B3LYP for main-group thermochemistry, kinetics, and noncovalent interactions.[56,57] The M05-2X functional does model some of the medium range correlation effect that is missing from the B3LYP functional. This could be the origin of better agreement between M05-2X and MP2 results.

Figure 3c shows quite good agreement between the nonempirical PBE, TPSS and MP2 results. PBE and TPSS functionals show the second and third best performances after the M05-2X functional ($RRD_{PBE-MP2}$ = 0.97 and $RRD_{TPSS-MP2}$ = 1.09 kcal/mol). As M05-2X, PBE and TPSS functionals treat medium range correlation correctly,[53] this could be the origin of the good agreement with the MP2 results. LDA shows a large error compared to MP2, and this error is the opposite of the HF error (cf., Figures 3a and c and $RRD_{LSDA-MP2}$ = 3.39 kcal/mol).

Table 1 shows how HF results deteriorate (with serious overestimation of the β-anomer and underestimation of the $^1C_4$ conformer ratios) as the basis set quality increases to near the basis set limit, in agreement with earlier observa-

Table 1. Boltzmann Populations Calculated (at 25 °C) for the ALL15 Test Set, for β-Anomers (of $^4C_1$ Conformers), and of Total $^1C_4$ Conformers, Calculated by Different Methods[a]

method	β-anomers (%)	$^1C_4$ (ppm)
reference method: MP2/a-cc-pVTZ(−*f*)[b]	**23.0**	**280**
LMP2/cc-pVTZ(−*f*)[b]	**27.6**	**339**
MP2/cc-pVTZ(−*f*)[b]	11.1	**254**
B3LYP/6−311++G**	40.4	88
B3LYP/6−311+G**	40.5	86
B3LYP/6−311+G**//B3LYP/6−31+G**	41.1	83
B3LYP/6−311+G**[b]	41.2	82
B3LYP/6−31+G**	39.4	95
B3LYP/6−31+G**[b]	39.3	94
B3LYP/6−31+G*	30.7	101
B3PW91/6−311+G**	29.2	96
B3PW91/6−311+G**//B3PW91/6−31+G*	28.1	93
B3PW91/6−31+G**	28.7	99
B3PW91/6−31+G//**B3PW91/6−31+G*	**26.7**	104
B3PW91/6−31+G*	19.8	110
PBEh/6−311+G**	**27.1**	92
M05-2X/6−311+G**	**18.6**	92
M05-2X/6−311+G**//M05-2X/6−31+G**	**18.7**	92
M05-2X/6−311+G**//M05-2X/6−31+G*	**18.8**	90
M05-2X/6−31+G**	18.0	135
M05-2X/6−31+G**//M05-2X/6−31+G*	18.2	134
M05-2X/6−31+G*	11.6	132
LSDA/6−311+G**	1.0	31
PBE/6−311+G**	12.1	**138**
TPSS/6−311+G**	7.9	**141**
HF/6−31G*	68.5	41
HF/cc-pVTZ(-*f*)//B3LYP/6−31+G*	92.1	19

[a] The best agreements with the MP2 reference are shown in bold. [b] Geometry optimized at the B3LYP/6−31+G* level.

tions.[9] The large basis set HF results give reliable relative energies only within a few groups of conformers as discussed earlier. Figure 3a shows the effect of the electron correlation at the MP2 level (cf., MP2 and HF curves, $RRD_{HF\text{-}MP2}$ = 3.42 kcal/mol).

The Boltzmann populations in Table 1 show that B3LYP gives too large of a β-anomer ratio (cf., conformers 2, 3, 6, 11, and 13, in Figure 3) and too small of a $^1C_4$ conformer ratio. The $^1C_4$ ratios obtained by PBE and TPSS are closer to the MP2 results than any hybrid functional result (cf., Table 1). Note that B3LYP/6−31+G* results deviate considerably from the results obtained with the larger basis sets, as 6−31+G* basis set is poor for relative energy calculations. However, the single-point calculations that use this geometry and a better basis set (e.g., 6−31+G** or larger) give sufficiently converged relative energies (see discussion below).

Next we focus on determining the optimal basis set, that is, one that gives converged results for density functionals. Schnupf et al.[40] claimed that the minimal and optimal basis set for B3LYP conformational energy studies of the allopyranose conformations is 6−311++G**, contradicting the recommendations of one of the present authors (GIC).[9] However, Schnupf et al. did not present results for the recommended 6−31+G** and 6−311+G** basis sets. The relative energy differences (eq 6) in Figure 4 show that the B3LYP/6−311+G** relative energies are indistinguishable from the B3LYP/6−311++G** relative energies at the scale of the figure. Thus, eliminating the diffuse functions on the H-atoms (using + instead of ++) has a negligible effect on relative energies,[9] although there is a very slight influence on the total energies (not shown). (Diffuse functions are important for H-atoms if they have negative partial charges.) The model dependent MAD (cf., eq 7, where model B is B3LYP/6−311++G** and model A is B3LYP/6−311+G**) is equal to 0.03 kcal/mol (comparable to the 0.02 kcal/mol grid error discussed in the Methods section). Even the B3LYP/6−31+G** results show quite small deviations from the more expensive B3LYP/6−311++G** results (MAD = 0.15 kcal/mol). Removing the *p* polarization functions from the H-atoms (cf. 6−31+G* basis set, results in Figure 3a), more than doubles the MAD (0.32 kcal/mol). Consequently, the 6−31+G* basis set should not be used for relative energy calculations, in agreement with previous suggestions.[9,40] Table 1 also shows that simplifying the basis set systematically decreases the proportion of β-anomers.

Finally, we consider whether single point calculations based on geometries determined with smaller basis sets can be used safely. Table 1 and Figure 4 show that the most expensive, fully optimized B3LYP/6−311++G** results and single point B3LYP/6−31+G**//B3LYP/6−31+G* or B3LYP/6−311+G**//B3LYP/6−31+G* results are very similar (MAD =0.15 and 0.02 kcal/mol, cf. eq 7). Calculations carried out with B3PW91 yield a similar conclusion (Table 1, Figure 4b). Thus, the basis set dependence of B3LYP and B3PW91 geometries is small, and these small geometry changes do not influence the relative energies for the allose test set. For geometry optimization, the 6−31+G* basis set is sufficient. The basis set and geometry errors are considerably smaller than the error of the B3LYP functional. For allose, these model chemistries require about 50% and 20% less computer time, respectively, compared to full geometry optimization with the 6−311++G** basis set. Note that a large number of diffuse functions makes the convergence of the SCF and the geometry optimization cycles more difficult, so using more diffuse functions than necessary can lead to convergence problems or no convergence at all in some cases.

In summary, for the ALL15 test set the nonempirical GGA and meta-GGA and empirical M05-2X functionals show good agreement with the reference MP2/a-cc-pVTZ(−*f*) results. The order of the methods against this reference is the following: LMP2 ≫ M05-2X > PBE > TPSS > B3PW91 > PBEh > B3LYP ≫LSDA ≅ HF (basis set limit).

3.2. 3,6-Anhydro-4-O-methyl-D-galactitol Conformers. Navarro and Stortz recently studied[52] the conformational space of 3,6-anhydro-4-*O*-methyl-D-galactitol (AnGol) by molecular mechanics and quantum mechanical methods (B3LYP and MP2). AnGol has a flexible five-membered ring and six exocyclic torsion angles (cf., Figures 1 and 2), all of them with a large influence on the energy. The two main stable conformations of the five-membered ring were identified as North (N), around E_4, ^5E, and E_6 (Cremer−Pople puckering parameter $\phi \approx 250-320°$), and South (S), around $^6T_5$ ($\phi \approx 120°$). Fifteen conformers derived from the four most stable conformations in each of the ring regions and of its main side chain were used.[52] The conformers 1−15 were designated as S1−, S2−, S4−, S3−, N1−, N2−, S1+, S2+, N3−, N1+, S4+, S3+, N3+, N2+, and N4+, respectively,

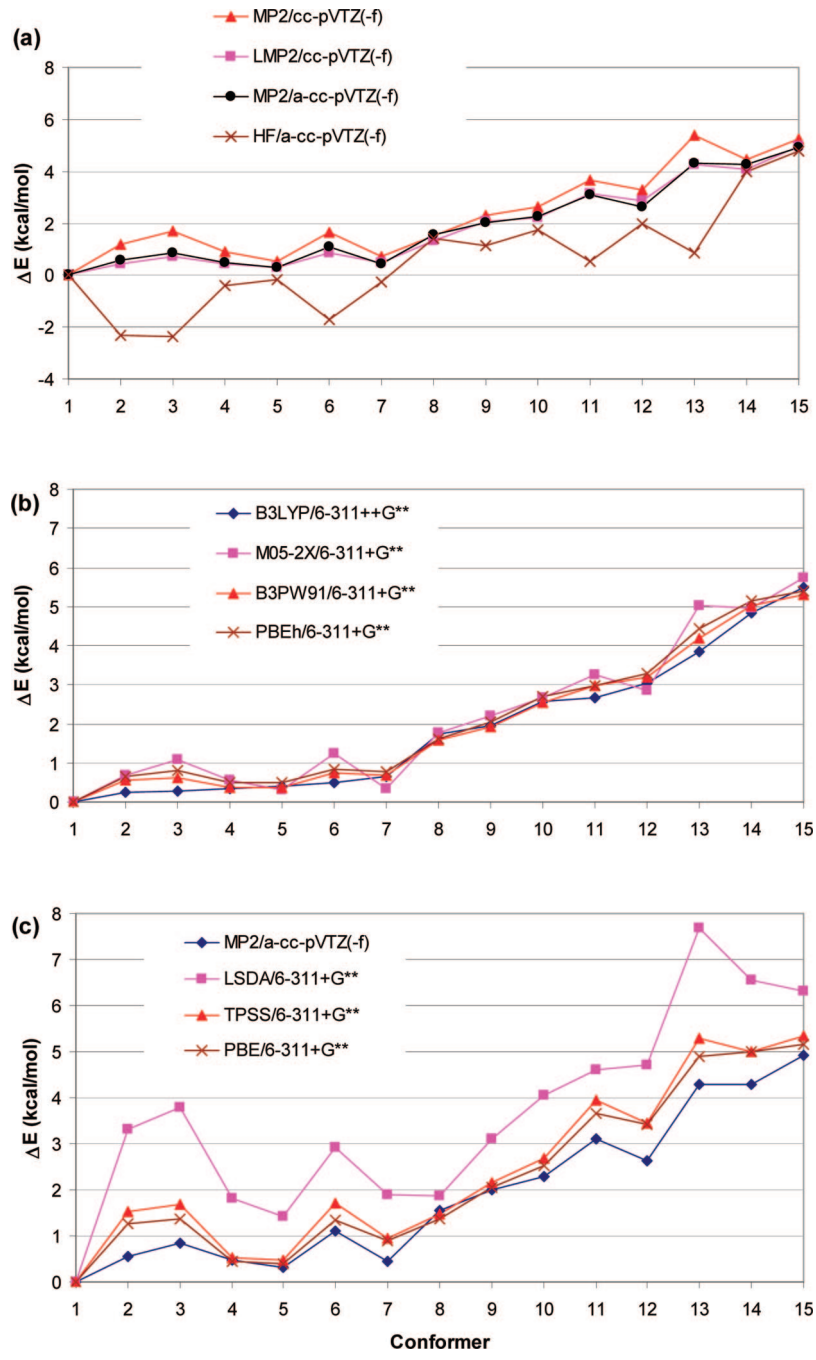

Figure 3. Relative energies of the ALL15 conformers (with respect to conformer 1), $\Delta E_{model}(conf_i,1)$ (see, eq. 5) optimized by various model chemistries as shown in the legends. The single point MP2, LMP2, and HF energies were calculated with B3LYP/6−31+G* geometry.

in ref 52 and constitute the current AnGol15 test set (conformers 1, 5, 7, and 10 are shown in Figure 2). The range of the B3LYP/6−31+G** relative energies is 6.18 kcal/mol.[52] The MP2/6−311+G**//B3LYP/6−31+G** results for the 15 conformers in Figure 5a and Table 2 were obtained from the previous study.[52]

The conformational space of the 3,6-anhydro-4-*O*-methyl-D-galactitol is quite different from the conformational space of the D-allopyranose (cf., Figure 1). It is an interesting question whether the observations on model chemistries for allose are valid for this more flexible compound.

Earlier studies for compounds like 2-hydroxytetrahydropyran and 2-methoxytetrahydropyran showed[62] that MP2/6−311++G** overestimates the absolute values of relative energies compared to MP2/CBS extrapolation results.[65] It was also shown that CCSD(T) contributions are quite small (0.02−0.1 kcal/mol), so MP2/CBS results are quite well converged for correlation energy differences. Gould et al. found a considerable difference between the relative energies of the MP2 and LMP2 methods, and proposed the latter method for benchmark calculations for di- and trisaccharides because of the smaller basis set error.[66]

Our results in Table 2 show that the single point LMP2/aug-cc-pVTZ and cc-pVTZ(−*f*) results agree very well (MAD = 0.18 kcal/mol) for the proportion of N (0.07−0.09%) and ω_3 = g+ (0.22%) conformers. The LMP2/aug-cc-pVTZ

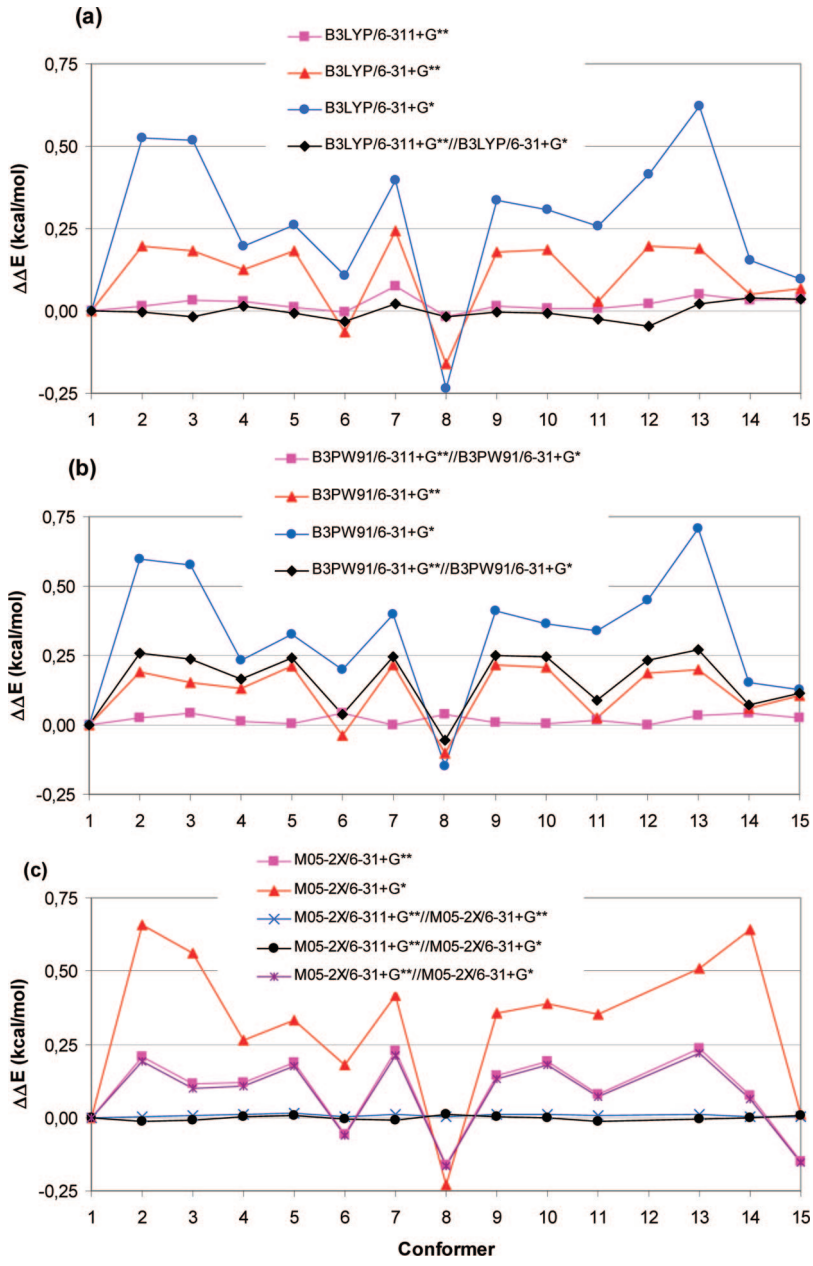

Figure 4. Differences in relative energies for the ALL15 allose conformers (with respect to conformer 1), $\Delta\Delta E_{\text{modelA}-\text{modelB}}(\text{conf}_i, 1)$ of eq 7. Model A is shown in the legends and (a) model B = B3LYP/6−311++G**, (b) model B =B3PW91/6−311+G**, and (c) model B = M05-2X/6−311+G**.

relative energies are somewhat different (MAD = 0.30 kcal/mol) and give lower ratios for the minor conformers. The MP2/6−311+G** and MP2/a-cc-pVTZ(-*f*) results agree quite well (MAD = 0.15, RRD = 0.75 kcal/mol). This is considerably better agreement than the agreement between MP2/cc-pVTZ(-*f*) and MP2/a-cc-pVTZ(-*f*) results (MAD = 0.52, RRD = 0.99 kcal/mol). This shows the importance of the inclusion of the diffuse functions into the basis set for MP2 calculations. The agreement between LMP2 and MP2 results is considerably worse for the AnGol15 test set than for the ALL15 test set (cf., Figure 5a). The differences between the LMP2 and MP2 limits can be attributed to the intramolecular effect of the missing dispersion-relevant double excitations from the LMP2 approximation. The CBS extrapolation is beyond the scope of the current study as it requires very expensive calculations with quadruple-ζ basis sets. We can select again smaller groups of conformers for which the $\Delta\Delta E_{\text{corrMP2}}(\text{conf}_i)$ (eq 7) are within ± 0.2 kcal/mol (like conformers {1, 2}, {3, 4}, {5,6,11,12,15}, {7,8}, and {9,10}). Within these groups the HF, MP2 and LMP2 relative energies agree with MAD < 0.2 kcal/mol. The effect of the electron correlation is shown in Figure 5a (cf., HF and MP2 curves). It is larger for the Angol15 test set than for the ALL15 test set (RRD = 4.83 and MAD = 3.18 kcal/mol).

Figure 5b shows the very good agreement between M05-2X and MP2/a-cc-pVTZ(-*f*) results (MD = 0.2 and MAD = 0.3 kcal/mol), while other functionals show considerably poorer performance. The M05-2X functional shows particularly good performance for the smaller group of conformers where the relative energies are known with higher precision (MAD < 0.1 and RRD < 0.1−0.4 kcal/mol). Similar

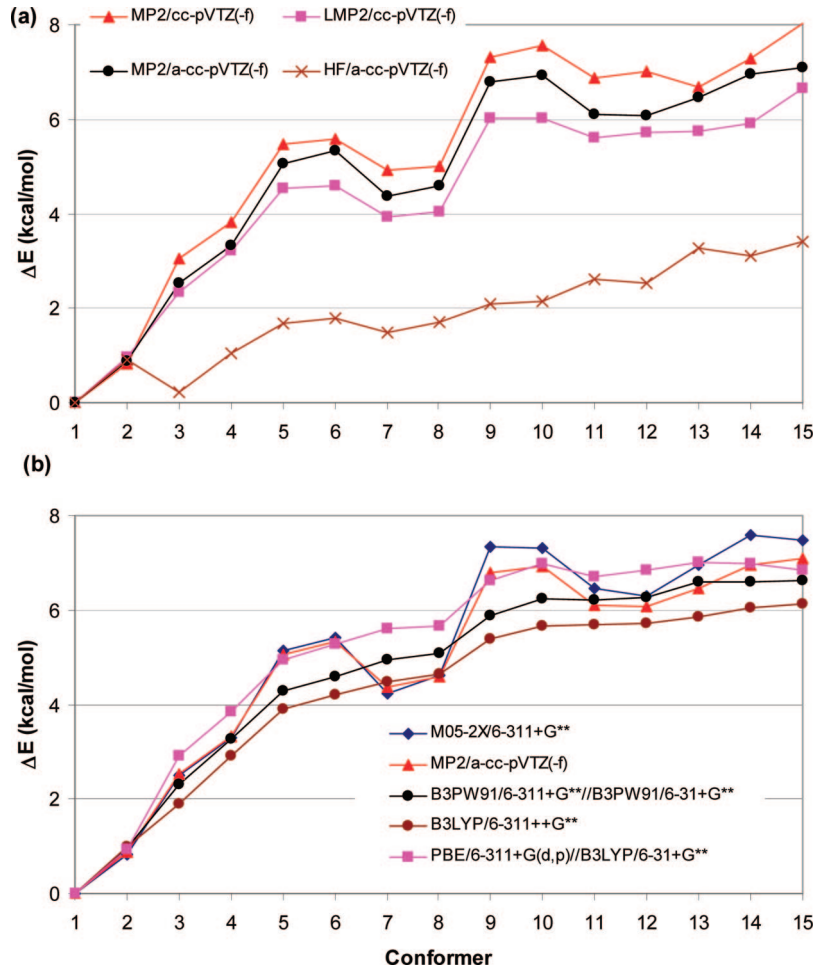

Figure 5. Relative energies of the AnGol15 conformers (with respect to conformer 1), $\Delta E_{model}(conf_i,1)$ (cf., eq 5) optimized by various model chemistries as shown in the legends. The single point MP2, LMP2, and HF energies were calculated with B3LYP/6−31+G* geometry.

agreement between MP2 and M05-2X results was observed earlier.[55] The MP2 and B3LYP results are similar for Southern conformers (1−4, 7, 8 11, 12), but the B3LYP functional underestimates the relative energies for Northern conformers (5, 6, 9, 10, and 13−15). The B3PW91 functional shows considerably better performance than B3LYP (cf. MAD = 0.42 and 0.68 kcal/mol, respectively). The PBE and TPSS (not shown) functionals show an opposite error, that is, they give correct Northern conformer relative energies (eq 5), but systematically overestimate the relative energies for Southern conformers.

The LSDA method shows very serious underestimation of the ratio of N and ω_3 = g+ conformers (cf., Table 2). The HF/6−31G* model chemistry performs relatively well, as usual, but increasing the basis set quality to the basis set limit leads to serious errors and gives erroneously high populations of the minor conformers (cf., Table 2 and Figure 4b). Similar to the ALL15 test set, the HF and the LSDA functional yields the opposite error. The results in Table 2 show that the relative energies and geometries calculated by M05-2X are even less basis set dependent (0.11 kcal/mol < MAD) than those of B3LYP or B3PW91 (MAD < 0.16 kcal/mol), when comparing 6−311+G** or 6−31+G** calculations. All calculations using the 6−31+G* basis set give poor relative energies (cf. MAD = 0.54−0.62 kcal/mol).

Next, we investigate the consistency of the optimized geometries. We noted for the ALL15 and AnGol15 test sets that B3CF/6−311+G**//B3CF/6−31+G* (CF = LYP or PW91) relative energies approximate very well the relative energies of the B3CF/6−311++G** fully optimized structures. The results in Table 3 show that the geometries given by the B3LYP method with the 6−31+G*, 6−31+G**, and 6−311++G** basis sets agree very well. The small differences in Table 3 do not result in substantial changes in the relative energies (note that around the geometry minimum the energy surface is flat as the gradients are zero). Consequently, the 6−31+G* geometry can be used for single point energy calculations, and this gives a considerable efficiency compared to the geometry optimization with the 6−311++G** basis set suggested by many papers (approximately one-third of the computational time is needed). Table 3 also shows that the B3LYP optimized geometries are quite similar to those of B3PW91 (slightly different exocyclic torsions, and somewhat larger puckering), while those obtained by LSDA are very different. Minimization with the HF/6−31G* model chemistry leads to very similar geometries to those obtained by B3LYP calculations (cf. Table 3): puckering is almost identical, and small differences in the exocyclic angles can be observed. The M05-2X geometries are different from the B3LYP and HF/6−31G*

Table 2. Boltzmann Populations Calculated (at 25 °C) for the AnGol15 Test Set, for the Northern (N) Conformers, and of Conformers Carrying the Larger Side Chain Torsion, ω_3 (Defined by Atoms H3−C3−C2−C1) with a g+ Value Calculated by Different Methods[a]

Method	N conformers (%)	ω_3 = g + (ppm)
reference method: MP2/a-cc-pVTZ(−*f*)[b]	**0.090**	**2200**
LMP2/cc-pVTZ(−*f*)[c]	0.071	**2208**
LMP2/cc-pVTZ[c]	**0.092**	**2196**
LMP2/aug-cc-pVTZ[c]	0.078	**2200**
MP2/6−311+G**[b]	0.027	1135
MP2/cc-pVTZ(−*f*)[b]	0.017	388
B3LYP/6−311++G**	0.197	**992**
B3LYP/6−311+G**//B3LYP/6−31+G*	0.199	824
B3LYP/6−31+G**	0.143	721
B3LYP/6−31+G*	0.073	265
B3PW91/6−311+G//B3PW91/6−31+G****	**0.103**	444
B3PW91/6−31+G**	0.076	325
M05-2X/6−311+G**	0.025	**983**
M05-2X/6−311+G**//M05-2X/6−31+G**	0.025	958
M05-2X/6−311+G**//M05-2X/6−31+G*	0.025	958
M05-2X/6−31+G**	0.023	752
M05-2X/6−31+G**//M05-2X/6−31+G*	0.021	805
M05-2X/6−31+G*	0.010	233
LSDA/6−311+G**//LSDA/6−31+G**	0.000	0
LSDA/6−31+G**	0.000	0
PBE/6−311+G**[b]	0.034	166
TPSS/6−311+G**[b]	0.031	132
HF/6−31G*	0.432	3818
HF/aug-cc-pVTZ[c]	7.275	96256
HF/cc-pVTZ[c]	3.962	48594
HF/cc-pVTZ(-*f*)[c]	4.486	46311
HF/6−311+G**[b]	3.965	49896

[a] The best agreements with the MP2 reference are shown in bold. [b] Geometry optimized at the B3LYP/6−31+G** level. [c] Geometry optimized at the B3LYP/6−311+G** level.

geometries (cf. the difference in the puckering parameters in Table 3). Thus, the differences between the M05-2X and the B3LYP geometries can be attributed to the medium range correlation effects being better described by the M05-2X functional.

The relative time scale for single point calculations LSDA/6−311+G**, B3LYP/6−311+G**, LMP2/cc-pVTZ(-*f*), LMP2/cc-pVTZ, and LMP2/aug-cc-pVTZ is 1, 1.6, 4.2, 10, and 50, respectively. Note that the time requirement of pure GGA functionals like PBE is similar to that of the LSDA.

In summary, for the AnGol15 test the M05-2X functional shows a good agreement with the reference MP2/a-cc-pVTZ(-*f*) results. The order of the functionals, LMP2 and HF is the following: M05-2X > LMP2 > TPSS ≅ PBE > B3PW91 > B3LYP ≫ HF (basis set limit) > LSDA.

3.3. β-D-Glucopyranose Conformers. The GLC4 test set is composed of two low-energy $^4C_1$ conformers (1 and 2) and two $^1C_4$ conformers (3 and 4) of β-D-glucopyranose. These four conformers were used for testing KS-DFT functionals before[9,23] and a composite energy is available[8] for the relative energies of these structures (cf., Table 4). This composite energy is based on the MP2/cc-pVTZ//MP2/cc-pVDZ model chemistry, with basis set correction at the HF level up to cc-pVQZ and correlation correction using MP2 and CCSD/6−31G*. Such estimations of the basis set limit and the correlation contribution are possibly unreliable, and the composite energies might be imprecise for conformers 3 and 4. Note that for conformers 3 and 4 the relative energies obtained with the MP2/cc-pVTZ//MP2/cc-pVDZ model chemistry are far from the composite energies;[8,23] thus the basis set and correlation corrections are large, 2.3 and 3.3 kcal/mol, respectively.

In the present work, we use the MP2/a-cc-pVTZ(-*f*)//B3LYP/6−31+G* model chemistry as a new alternative reference (cf., Table 4). These, and the LMP2/cc-pVTZ(-*f*)//B3LYP/6−31+G* results agree within 0.5 kcal/mol. We have also performed an MP2/CBS[3,4] estimation for the relative energies[67] using separate HF extrapolation and MP2 correlation contribution extrapolations of the cc-pVTZ and cc-pVQZ relative energies.[68] These results agree again within 0.5 kcal/mol error with the MP2/a-cc-pVTZ(-*f*) results. However, as Table 1 shows, the previous composite calculation[8] gave poor relative energy for conformer **4** (∼1.5 kcal/mol error). More precise determination of the relative energy of conformer **4** of the GLC4 set requires a considerably larger computational effort, one that is beyond the scope of the current paper.

The current results in Table 4 show the good performance of the PBE, TPSSh, PBEh, and B3PW91 functionals (MAD = 0.12, 0.28, 0.32, 0.41 kcal/mol, respectively). In addition, the single point calculations deliver quite good results showing that even the geometries obtained with the smallest basis set applied in this paper (6−31G*) are useful. The B3LYP functional again performs slightly worse, MAD = 0.69 kcal/mol) than the B3PW91, PBEh or M05-2X functionals (MAD = 0.64 kcal/mol, because of overestimation of the stability of the conformers **3** and **4**, see Table 4). The HF/cc-pVDZ model chemistry performs reasonably well but the HF/cc-pVTZ//HF/cc-pVDZ model chemistry performs poorly (with serious underestimation of the hydrogen bond (H-bond strength), cf. results for the ALL15 and AnGol15 test sets). The PBEsol/6−311+G** model chemistry, using the new pure GGA functional, performs similar to TPSS, and M05-2X, with MAD = 0.65 kcal/mol despite the fact that PBEsol was successfully applied to isomerization problems.[55] The smaller enhancement factor for the large reduced gradient gives too strong H-bonds (like the LSDA). A change to the large gradient behavior of the exchange functional leads to improved results for saccharides as our preliminary results show. The details will be published elsewhere.

Notice the poor performance of the MP2/cc-pVTZ//MP2/cc-pVDZ, MP2/cc-pVDZ, MP2/6−31-G*, and CCSD/6−31G*//MP2/6−31G* model chemistries (MAD =1.12, 3.88, and 2.61 kcal/mol, respectively) used for the composite energies. The relative energies calculated by the DFT/6−31G* model chemistry are also very poor (MD < −5 kcal/mol; MAD > 5 kcal/mol), and show serious overestimation of intramolecular H-bond strength because of the basis set error. The minimal basis set required for reasonable energy is 6−31+G**. The 6−311+G** basis set gives converged results as observed for the previous test sets.

These results show that the GLC4 test set is particularly sensitive to the correct description of the intramolecular H-bond. So this leads to a somewhat different conclusion than the results from the larger ALL15 and AnGol15 test sets. These results shows clearly that the good HF/DZ results

Table 3. Average of the Absolute Values of Geometric Deviations (Six exo-Cyclic Torsions and Puckering parameters Q and ϕ) between Optimized Geometries (1 and 2) Obtained by Different Methods and Basis Sets for the 15 Selected 3,6-Anhydro-4-*O*-methylgalactose Conformers (AnGol15 Test Set)

optimized geometry 1	optimized geometry 2	exocyclic torsions (deg)	Q (Å)	ϕ (deg)
B3LYP/6−31+G**	B3LYP/6−311++G**	0.4	0.002	0.7
B3LYP/6−31+G*	B3LYP/6−311++G**	0.5	0.002	0.7
B3LYP/6−31+G*	B3LYP/6−31+G**	0.3	0.001	0.5
B3PW91/6−31+G**	B3LYP/6−311++G**	0.8	0.007	1.6
LSDA/6−31+G**	B3LYP/6−311++G**	5.0	0.026	5.4
M05-2X/6−311+G**	B3LYP/6−311++G**	1.3	0.024	5.4
M05-2X/6−31+G**	B3LYP/6−311++G**	1.3	0.025	5.8
M05-2X/6−31+G**	M05-2X/6−311+G**	0.6	0.002	1.2
M05-2X/6−31+G*	M05-2X/6−31+G**	0.3	0.001	0.6
HF/6−31G*	B3LYP/6−311++G**	2.0	0.002	0.9
HF/6−31G*	M05-2X/6−311+G**	2.7	0.022	9.7

Table 4. Relative Energies of Conformers 2, 3, and 4 of the GLC4 Test Set with Respect to Conformer 1 (Eq *5*) and Boltzmann Populations Calculated (at 25 °C) for the $^1C_4$ Conformers, Calculated by Different Methods[a]

method	ref	**2**	**3**	**4**	% $^1C_4$
MP2/a-cc-pVTZ(-f)//B3LYP/6−31+G*	this work	**0.38**	**5.76**	**5.10**	**0.0158**
MP2/CBS[3,4]//B3LYP/6−31+G*	67		**6.25**	**5.43**	
LMP2/cc-pVTZ(-f)//B3LYP/6−31+G*	this work	**0.29**	**5.92**	**5.63**	**0.0074**
composite	8	0.27	6.41	6.99	0.0017
MP2/cc-pVTZ//MP2/cc-pVDZ	8	0.07	4.13	3.65	0.1607
MP2/6−31G*	8	−0.45	0.66	−0.60	31.4
CCSD/6−31G*//MP2/6−31G*	8	−0.34	2.07	1.68	3.1
HF/6−31G*	8	−0.15	6.73	6.76	0.0010
HF/cc-pVDZ	8	−0.09	**6.23**	**6.34**	0.0023
HF/cc-pVTZ// B3LYP/6−31+G*	this work	0.49	11.11	10.96	0.0000
HF/cc-pVQZ// B3LYP/6−31+G*	this work	0.66	12.15	11.95	0.0000
HF/CBS[3,4]//B3LYP/6−31+G*	67	0.70	12.43	12.22	0.0000
B3LYP/6−31+G*	9	−0.12	6.92	4.93	0.0113
B3LYP/6−31+G**	this work	0.06	7.22	5.40	0.0060
B3LYP/6−31+G**//B3LYP/6−31+G*	this work	0.07	7.27	5.41	0.0059
B3LYP/6−311+G**	this work	0.16	7.24	5.59	0.0048
B3LYP/6−311+G**//B3LYP/6−31+G*	this work	0.16	7.36	5.64	0.0044
B3PW91/6−31+G**	this work	0.09	6.63	5.02	0.0120
B3PW91/6−311+G**	this work	**0.19**	**6.67**	5.22	0.0093
PBEh/6−31+G**	this work	−0.02	5.98	4.48	0.0271
PBEh/6−311+G**	this work	**0.09**	**6.14**	**4.80**	**0.0178**
TPSSh/6−311+G//TPSSh/6−31G***	this work	**0.18**	**5.24**	**5.23**	**0.0166**
M05-2X/6−31+G**	this work	0.03	4.69	4.37	0.0508
M05-2X/6−311+G**	this work	0.10	4.64	4.58	0.0449
PBE/6−311+G//PBE/6−31G***	this work	**0.16**	**5.78**	**4.98**	**0.0158**
PBEsol/6−31+G**	this work	0.03	5.46	3.39	0.1708
PBEsol/6−311+G**	this work	0.13	5.54	3.62	0.1274
TPSS/6−311+G**//TPSS/6−31G*	this work	0.18	4.74	4.36	0.0558
PBE/6−31G*	this work	−0.73	−1.05	−4.83	99.9
TPSS/6−31G*	this work	−0.60	−1.23	−4.18	99.7
TPSSh/6−31G*	this work	−0.59	−0.29	−2.64	96.0

[a] All energies are indicated in kcal/mol. The best agreements with the MP2 reference are shown in bold.

are coming from basis set error, and basis set limit HF results are very poor due to serious underestimation of the intramolecular H-bond. Small basis sets overestimate the intramolecular H-bond strength. The success of the nonempirical PBE functional shows that it is particularly good for intramolecular H-bonds. Adding some exact exchange (PBEh) weakens the H-bond, and reducing the exchange-correlation gradient enhancement factor (PBEsol), strengthens the H-bond. The TPSS meta-GGA functional that was derived to mimic the large gradient behavior of PBE GGA also shows good performance, but for this special test set it is not as good as PBE.

In summary, for the GLC4 test the PBE functional shows a good agreement with the reference MP2/a-cc-pVTZ(-*f*) results. The order of the functionals, LMP2 and HF is the following: PBE > LMP2 > TPSSh ≅ PBEh > B3PW91 > B3LYP ≅ TPSS ≅ PBEsol ≅ M05-2X ≫ HF (basis set limit).

4. Conclusions

The aim of this paper is to establish a protocol that can be used successfully and efficiently for modeling carbohydrates. In this paper, we have tested various DFT model chemistries on three sets of carbohydrate conformations. The ALL15 test set contains 13 $^4C_1$ structures (8 α- and 5 β-anomers, with gg, gt, and tg hydroxymethyl rotamers), and two $^1C_4$ conformers of α- and β-D-allopyranose. The AnGol15 test set included 15 conformers of 3,6-anhydro-4-*O*-methyl-D-galactitol, whereas the GLC4 contains two low energy $^4C_1$

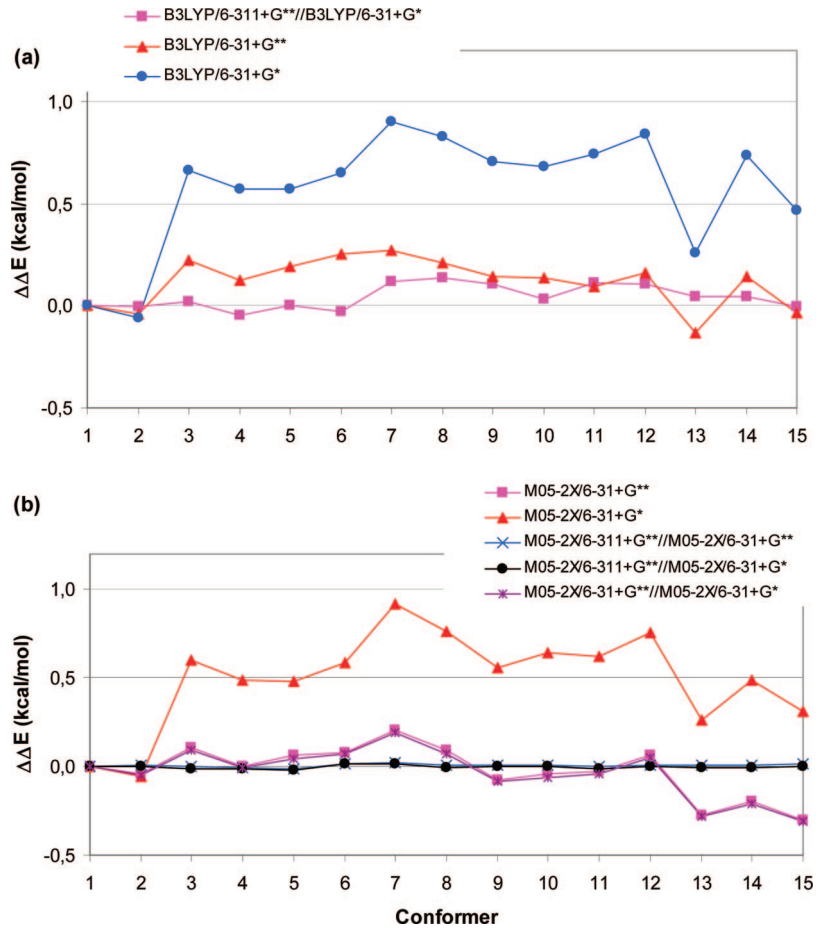

Figure 6. Differences in relative energies for the AnGol15 conformers (with respect to conformer 1), $\Delta\Delta E_{\text{modelA}-\text{modelB}}(\text{conf}_i, 1)$ of eq 7 optimized by various model chemistries. Model A is shown in the legends and (a) model B = B3LYP/6−311++G** and (b) model B = M05-2X/6−311+G**.

chair and two higher energy $^1C_4$ chair forms of β-D-glucopyranose. These test sets sample the lowest 6−7 kcal/mol energy range of conformation space. We have tested nonempirical functionals such as local spin density approximation (LSDA), generalized gradient approximation GGA (e.g., PBE, PBEsol), and meta-GGA (e.g., TPSS). We have also tested semiempirical hybrid functionals like PBEh, B3LYP, B3PW91, and a many fit-parameter empirical hybrid functional, M05-2X. Empirical functionals often perform very well on the test set used for fitting, and even outside the fitting set. However, the fitting set for M05-2X contains many small molecules, and there is no guarantee of good results on larger sugar molecules. We have chosen the MP2/a-cc-pVTZ(-*f*) model chemistry as reference and checked that by several MP2/CBS[3,4] calculations. The following conclusions can be drawn from our results:

1. The LMP2/cc-pVTZ(-*f*) and LMP2/aug-cc-pVTZ model chemistries give similar relative energies for the conformers in our test sets and those relative energies are in a reasonable (0.3 kcal/mol) agreement with MP2/a-cc-pVTZ(−*f*) and several MP2/CBS[3,4] results. The composite energies suggested earlier for the GLC4 test set show large 1.5 kcal/mol error compared to our new reference.
2. For B3CF (where CF = LYP or PW91) type hybrid functionals, the diffuse functions on hydrogen atoms are not needed, but diffuse functions on heavy atoms and polarization functions on all atoms are essential for good relative energies. For geometry optimization, the 6−31+G* basis set is sufficient; thus, the B3CF/6−311+G**//B3CF/6−31+G* model chemistry gives converged relative energies with a mean absolute deviation of about 0.3 kcal/mol compared to MP2 reference results.
3. The B3CF/6−31+G**//B3CF/6−31+G* model chemistry gives relative energies with an error that is about half of the error of the functional. The quickest model chemistry that delivers useful results is B3CF/6−31+G**//B3CF/6−31G*.
4. Calculations with B3PW91 or PBEh give results similar to those with B3LYP, although β-anomers appear to be less stabilized.
5. For the ALL15 test set, the nonempirical GGA and meta-GGA and empirical M05-2X functionals show good agreement with the reference MP2 results. The order of the quality of the functionals, LMP2 and HF methods is the following: LMP2 ≫ M05-2X > PBE > TPSS > B3PW91 > PBEh > B3LYP ≫LSDA ≅ HF (basis set limit).
6. For the AnGol15 test set, M05-2X functionals shows a good agreement with the reference MP2 results. The order of the quality of the functionals, LMP2, and HF

methods is the following: M05-2X > LMP2 > TPSS ≅ PBE > B3PW91 > B3LYP ≫ HF (basis set limit) > LSDA.

7. For the GLC4 test the order of the quality of the functionals, LMP2 and HF methods is the following: PBE > LMP2 > TPSSh ≅ PBEh > B3PW91 > B3LYP ≅ TPSS ≅ PBEsol ≅ M05-2X ≫ HF (basis set limit).
8. Calculations with HF give reasonable results with double-ζ basis sets (6−31G* and cc-pVDZ), but the HF limit (aug-cc-pVTZ) relative energies are clearly wrong, leading to serious underestimation of the stabilities of the β-anomers, $^1C_4$ chair conformations, and intramolecular H-bond strength. This result is in agreement with earlier observations.
9. Calculations with the M05-2X hybrid meta-GGA require a dense DFT grid for reliable results. The M05-2X results are better for the ALL15 and AnGol15 test sets than the results obtained by popular DFT functionals (B3LYP, B3PW91, or PBEh). For the GLC4 test set the PBE functional gives better results. Our preliminary results show that the M06-2X functional performs similarly to M05-2X for sugars, and it also requires a dense numerical integration grid for reliable results.
10. The GLC4 test set is particularly suitable for testing DFT methods because the relative energies are very sensitive to the correct description of the intramolecular H-bonds. Interestingly, non empirical functionals (particularly PBE) perform better on this test set than the empirical hybrid ones. The H-bond overestimation is decreasing in the following order: TPSS ≅ PBEsol ≅ M05-2X > TPSSh > PBE where PBE is just right. The underestimation is increasing in the following order: PBEh < B3PW91 < B3LYP ≪ HF (basis set limit). The results on this test set also show that small 6−31G* basis set overestimates intramolecular H-bonds with any method.
11. The popular B3LYP functional is not the best for saccharide conformational studies. The B3PW91 functional gives systematically better results, but all other hybrid functionals are even better. The M05-2X functional gives the best results.
12. We suggest to use M05-2X/6−311+G**//M05-2X/6−31+G* model chemistry for carbohydrate conformational space studies except for energy differences between $^1C_4$ and $^4C_1$ conformers where PBE/6−31+G** model chemistry performs better.
13. The nonempirical PBE GGA and TPSS meta-GGA functionals show a better overall performance than B3LYP.

Because the LMP2/cc-pVTZ and MP2/a-cc-pVTZ(-*f*) results do not always give consensus relative energies for the conformational space of the monosaccharides studied here, higher level calculations are needed for benchmarking DFT for the conformational space of carbohydrates. These infinite basis set extrapolation calculations are in progress.

Acknowledgment. Dedicated to John Paul Perdew on the occasion of his 65th birthday. This work was supported by grants from UBA and CONICET (C.A.S.), and normal research funds from the Agricultural Research Service of the US Department of Agriculture (ADF and G.P.J.). C.A.S. is Research Member of the National Research Council of Argentina (CONICET).

Supporting Information Available: Geometries and/or total energies of ALL15, AnGol15, and Glc4 test sets. This material is available free of charge via the Internet at http://pubs.acs.org.

References

(1) French, A. D.; Brady, J. W. *ACS Symp. Ser.* **1990**, *430*, 1–19.

(2) Pérez, S.; Imberty, A.; Engelsen, S. B.; Gruza, J.; Mazeau, K.; Jiménez-Barbero, J.; Poveda, A.; Espinosa, J. F.; van Eyck, B. P.; Johnson, G.; French, A. D.; Kouwijzer, M. L. C. E.; Grootenius, P. D. J.; Bernardi, A.; Raimondi, L.; Senderowitz, H.; Durier, V.; Vergoten, G.; Rasmussen, K. *Carbohydr. Res.* **1998**, *314*, 141–155.

(3) Imberty, A.; Pérez, S. *Chem. Rev.* **2000**, *100*, 4567–4588.

(4) Kirschner, K. N.; Yongye, A. B.; Tschampel, S. M.; González-Outeiriño, J.; Daniels, C. R.; Foley, B. L.; Woods, R. J. *J. Comput. Chem.* **2008**, *29*, 622–655.

(5) Csonka, G. I.; Éliás, K.; Csizmadia, I. G. *J. Comput. Chem.* **1997**, *18*, 330–342.

(6) Csonka, G. I.; Angyán, J. G. *J. Mol. Struct. (THEOCHEM)* **1997**, *393*, 31–38.

(7) McNamara, J. P.; Muslim, A-M.; Abdel-Aal, H.; Wang, H.; Mohr, M.; Hillier, I. H.; Bryce, R. A. *Chem. Phys. Lett.* **2004**, *394*, 429–436.

(8) Barrows, S. E.; Dulles, F. J.; Cramer, C. J.; French, A. D.; Truhlar, D. G. *Carbohydr. Res.* **1995**, *276*, 219–251.

(9) Csonka, G. I. *J. Mol. Struct. (THEOCHEM)* **2002**, *584*, 1–4.

(10) Kaminsky, J.; Mata, R. A.; Werner, H. J.; Jensen, F. *Mol. Phys.* **2008**, *106*, 1899–1906.

(11) Pulay, P.; Saebo, S. *Theor. Chim. Acta* **1986**, *69*, 357–368.

(12) Murphy, R. B.; Beachy, M. D.; Friesner, R. A.; Ringnalda, M. N. *J. Chem. Phys.* **1995**, *103*, 1481–1490.

(13) Kohn, W.; Becke, A. D.; Parr, R. G. *J. Phys. Chem.* **1996**, *100*, 12974–12980.

(14) Perdew, J. P.; Burke, K.; Ernzerhof, M. *Phys. Rev. Lett.* **1996**, *77*, 3865–3868.

(15) Tao, J.; Perdew, J. P.; Staroverov, V. N.; Scuseria, G. E. *Phys. Rev. Lett.* **2003**, *91*, 146401/1–146401/4.

(16) Becke, A. D. *Phys. Rev. A* **1988**, *38*, 3098–3100.

(17) Lee, C.; Yang, W.; Parr, R. G. *Phys. Rev. B* **1988**, *37*, 785–789.

(18) Perdew, J. P.; Chevary, J. A.; Vosko, S. H.; Kackson, K. A.; Pederson, M. A.; Singh, D. J.; Fiolhais, C. *Phys. Rev. B* **1992**, *46*, 6671–6687.

(19) Adamo, C.; Barone, V. *J. Chem. Phys.* **1999**, *110*, 6158–6170.

(20) Ernzerhof, M.; Scuseria, G. E. *J. Chem. Phys.* **1999**, *110*, 5029–5036.

(21) Stephens, P. J.; Devlin, F. J.; Chabalowski, C. F.; Frisch, M. J. *J. Phys. Chem.* **1994**, *98*, 11623–11627.

(22) Becke, A. D. *J. Chem. Phys.* **1993**, *98*, 5648–5652.

(23) Csonka, G. I.; Elias, K.; Csizmadia, I. G. *Chem. Phys. Lett.* **1996**, *257*, 49–60.

(24) Lii, J.-H.; Ma, B.; Allinger, N. L. *J. Comput. Chem.* **1999**, *20*, 1593–1603.

(25) Momany, F. A.; Willett, J. L. *J. Comput. Chem.* **2000**, *21*, 1204–1219.

(26) Strati, G. L.; Willett, J. L.; Momany, F. A. *Carbohydr. Res.* **2002**, *337*, 1833–1849.

(27) Appell, M.; Strati, G.; Willett, J. L.; Momany, F. A. *Carbohydr. Res.* **2004**, *339*, 537–551.

(28) French, A. D.; Jonhson, G. P. *Cellulose* **2004**, *11*, 449–462.

(29) Hemmingsen, L.; Madsen, D. E.; Esbensen, A. L.; Olsen, L.; Engelsen, S. B. *Carbohydr. Res.* **2004**, *339*, 937–948.

(30) Momany, F. A.; Appell, M.; Strati, G.; Willett, J. L. *Carbohydr. Res.* **2004**, *339*, 553–567.

(31) Appell, M.; Willett, J. L.; Momany, F. A. *Carbohydr. Res.* **2005**, *340*, 459–468.

(32) French, A. D.; Jonhson, G. P.; Kelterer, A-M.; Csonka, G. I. *Tetrahedron: Asymm.* **2005**, *16*, 577–586.

(33) Momany, F. A.; Appell, M.; Willett, J. L.; Bosma, W. B. *Carbohydr. Res.* **2005**, *340*, 1638–1655.

(34) Stortz, C. A. *J. Comput. Chem.* **2005**, *26*, 471–483.

(35) French, A. D.; Jonhson, G. P. *Can. J. Chem.* **2006**, *84*, 603–612.

(36) Hricovini, M. *Carbohydr. Res.* **2006**, *341*, 2575–2580.

(37) Kurihara, Y.; Ueda, K. *Carbohydr. Res.* **2006**, *341*, 2565–2574.

(38) Momany, F. A.; Appell, M.; Willett, J. L.; Schnupf, U.; Bosma, W. B. *Carbohydr. Res.* **2006**, *341*, 525–537.

(39) Bagno, A.; Rastrelli, F.; Saielli, F. *J. Org. Chem.* **2007**, *72*, 7373–7381.

(40) Schnupf, U.; Willett, J. L.; Bosma, W. B.; Momany, F. A. *Carbohydr. Res.* **2007**, *342*, 196–216.

(41) Bohn, M. L.; Colombo, M. I.; Rúveda, E. A.; Stortz, C. A. *Org. Biomol. Chem.* **2008**, *6*, 554–561.

(42) Schnupf, U.; Willett, J. L.; Bosma, W. B.; Momany, F. A. *J. Comput. Chem.* **2008**, *29*, 1103–1112.

(43) Curtiss, L. A.; Raghavachari, K.; Redfern, P. C.; Pople, J. A. *J. Chem. Phys.* **1997**, *106*, 1063–1079.

(44) Curtiss, L. A.; Raghavachari, K.; Redfern, P. C.; Pople, J. A. *J. Chem. Phys.* **2000**, *112*, 7374–7383.

(45) Grimme, S. *Angew. Chem., Int. Ed.* **2006**, *45*, 4460–4464.

(46) Staroverov, V. N.; Scuseria, G. E.; Tao, J. M.; Perdew, J. P. *J. Chem. Phys.* **2003**, *119*, 12129–12137.

(47) Csonka, G. I.; Ruzsinszky, A.; Tao, J. M.; Perdew, J. P. *Int. J. Quantum Chem.* **2005**, *101*, 506–511.

(48) Paier, J.; Marsman, M.; Kresse, G. *J. Chem. Phys.* **2007**, *127*, 024103.

(49) Wodrich, M. D.; Corminboeuf, C.; Schleyer, P. V. *Org. Lett.* **2006**, *8*, 3631–3634.

(50) Grimme, S.; Steinmetz, M.; Korth, M. J. *Chem. Theory Comput.* **2007**, *3*, 42–45.

(51) Schreiner, P. R.; Fokin, A. A.; Pascal, R. A.; de Meijere, A. *Org. Lett.* **2006**, *8*, 3635–3638.

(52) Navarro, D. A.; Stortz, C. A. *Carbohydr. Res.* **2008**, *343*, 2292–2298.

(53) Ruzsinszky, A.; Csonka, G. I.; Perdew, J. P. *J. Phys. Chem. A.* **2005**, *109*, 11015–11021.

(54) Perdew, J. P.; Ruzsinszky, A.; Csonka, G. I.; Vydrov, O. A.; Scuseria, G. E.; Constantin, L.; Zhou, X.; Burke, K. *Phys. Rev. Lett.* **2008**, *100*, 136406.

(55) Csonka, G. I.; Ruzsinszky, A.; Perdew, J. P.; Grimme, S. J. *Chem. Theory Comput.* **2008**, *4*, 888–891.

(56) Zhao, Y.; Truhlar, D. G. *Org. Lett.* **2006**, *8*, 5753–5755.

(57) Zhao, Y.; Schultz, N. E.; Truhlar, D. G. *J. Chem. Theory Comput.* **2006**, *2*, 364–382.

(58) Csonka, G. I.; Nguyen, N. A.; Kolossváry, I. *J. Comput. Chem.* **1997**, *18*, 1534–1545.

(59) Vosko, S. H.; Wilk, L.; Nusair, M. *Can. J. Phys.* **1980**, *58*, 1200–1211.

(60) Tao, J.; Gori-Giorgi, P.; Perdew, J. P.; McWeeny, R. *Phys. Rev. A* **2001**, *63*, 325131–325135.

(61) For standard basis sets see http://www.emsl.pnl.gov/forms/basisform.html (accessed Aug 19, 2008).

(62) Frisch, M. J.; Trucks, G. W.; Schlegel, H. B.; Scuseria, G. E.; Robb, M. A.; Cheeseman, J. R.; Montgomery, Jr., J. A.; Vreven, T.; Kudin, K. N.; Burant, J. C.; Millam, J. M.; Iyengar, S. S.; Tomasi, J.; Barone, V.; Mennucci, B.; Cossi, M.; Scalmani, G.; Rega, N.; Petersson, G. A.; Nakatsuji, H.; Hada, M.; Ehara, M.; Toyota, K.; Fukuda, R.; Hasegawa, J.; Ishida, M.; Nakajima, T.; Honda, Y.; Kitao, O.; Nakai, H.; Klene, M.; Li, X.; Knox, J. E.; Hratchian, H. P.; Cross, J. B.; Bakken, V.; Adamo, C.; Jaramillo, J.; Gomperts, R.; Stratmann, R. E.; Yazyev, O.; Austin, A. J.; Cammi, R.; Pomelli, C.; Ochterski, J. W.; Ayala, P. Y.; Morokuma, K.; Voth, G. A.; Salvador, P.; Dannenberg, J. J.; Zakrzewski, V. G.; Dapprich, S.; Daniels, A. D.; Strain, M. C.; Farkas, O.; Malick, D. K.; Rabuck, A. D.; Raghavachari, K.; Foresman, J. B.; Ortiz, J. V.; Cui, Q.; Baboul, A. G.; Clifford, S.; Cioslowski, J.; Stefanov, B. B.; Liu, G.; Liashenko, A.; Piskorz, P.; Komaromi, I.; Martin, R. L.; Fox, D. J.; Keith, T.; Al-Laham, M. A.; Peng, C. Y.; Nanayakkara, A.; Challacombe, M.; Gill, P. M. W.; Johnson, B.; Chen, W.; Wong, M. W.; Gonzalez, C.; Pople, J. A.; *Gaussian 03*, revision C.02, Gaussian, Inc., Wallingford CT, 2004.

(63) *Jaguar 6.0*, release 107; Schrodinger, LLC: Portland, OR, 2005.

(64) Cremer, D.; Pople, J. A. *J. Am. Chem. Soc.* **1975**, *97*, 1354–1358.

(65) Weldon, A. J.; Vickrey, T. L.; Tschumper, G. S. *J. Phys. Chem. A* **2005**, *109*, 11073–11079.

(66) Gould, I. R.; Bettley, H. A-A.; Bryce, R. A. *J. Comput. Chem.* **2007**, *28*, 1965–1973.

(67) Grimme, S.; Csonka, G. I. For CBS[3,4] extrapolation of HF relative energies, we used the HF/cc-pVnZ// B3LYP/6−31+G* ΔE values from Table 4, where n = T,Q. For MP2 correlation correction we used−6.81 and−6.45 kcal/mol for conformer 3, and−7.08 and−6.79 kcal/mol for conformer 4. Then we used $\Delta E[\infty] \approx \Delta E[Q] + c_{ext}(\Delta E[Q]-\Delta E[T])$, where for HF $c_{ext} = 0.27$; for MP2 $c_{ext} = 0.730 = 1/((4/3)^3-1)$.

(68) Helgaker, T.; Klopper, W.; Koch, H.; Noga, J. *J. Chem. Phys.* **1997**, *106*, 9639–9646.

CT8004479

JCTC Journal of Chemical Theory and Computation

Dependence of Response Functions and Orbital Functionals on Occupation Numbers

S. Kurth,*,† C. R. Proetto,‡ and K. Capelle§

Institut für Theoretische Physik, Freie Universität Berlin, Arnimallee 14, D-14195 Berlin, Germany

Received November 27, 2008

Abstract: Explicitly orbital-dependent approximations to the exchange-correlation energy functional of density functional theory typically not only depend on the single-particle Kohn−Sham orbitals but also on their occupation numbers in the ground-state Slater determinant. The variational calculation of the corresponding exchange-correlation potentials with the optimized effective potential (OEP) method therefore also requires a variation of the occupation numbers with respect to a variation in the effective single-particle potential, which is usually not taken into account. Here it is shown under which circumstances this procedure is justified.

1. Introduction

The central quantity of density functional theory,[1,2] the exchange-correlation energy E_{xc}, is a unique (though unknown) functional of the electron density. Popular approximations such as the local density approximation (LDA) and generalized gradient approximations (GGA's) express E_{xc} as an *explicit* functional of the density.

Recently, another class of approximations has attracted increasing interest: *implicit* density functionals, expressing E_{xc} as explicit functionals of the Kohn−Sham single particle orbitals and energies and therefore only as implicit functionals of the density.[3,4] Members of this class of functionals are the exact exchange functional (EXX), the popular hybrid functionals which mix generalized gradient approximation (GGA) exchange with a fraction of exact exchange,[5−8] the Perdew−Zunger self-interaction correction,[9] and meta-GGA functionals[10−12] which include the orbital kinetic energy density as a key ingredient.

At zero temperature, the orbital functionals mentioned above depend on the occupied orbitals only. Other functionals, such as the second-order correlation energy of Görling−Levy perturbation theory,[13] in addition depend explicitly on the unoccupied orbitals and the orbital energies. Moreover, all these orbital functionals are not only explicit functionals of the orbitals but also explicit functionals of the occupation numbers which, in turn, depend on the single-particle orbital energies. This additional energy dependence is ignored in common implementations of orbital- or energy-dependent functionals.

In order to calculate the single-particle Kohn−Sham potential corresponding to a given orbital functional, the so-called optimized effective potential (OEP) method is used.[3,4,14] The OEP method is a variational method which aims to find that local potential whose orbitals minimize the given total energy expression. In principle, when performing the variation of the local potential, one not only should vary the orbitals but also the orbital energies and occupation numbers. Typically, however, the variation with respect to the occupation numbers is not explicitly performed. In this work, we will investigate when and why this is justified.

2. Density Response Function

In this section, we analyze the problem of the eigenvalue dependence of the occupation numbers in the density and the noninteracting static linear density response function for various situations. We consider the case of zero temperature

* E-mail: stefan_kurth@ehu.es.

† Permanent address: Nano-Bio Spectroscopy Group and European Theoretical Spectroscopy Facility (ETSF), Dpto. de Física de Materiales, Universidad del País Vasco UPV/EHU, Centro Mixto CSIC-UPV/EHU, Av. Tolosa 72, E-20018 San Sebastián, Spain.

‡ Permanent address: Centro Atómico Bariloche and Instituto Balseiro, 8400 S. C. de Bariloche, Río Negro, Argentina.

§ Permanent address: Departamento de Física e Informática, Instituto de Física de São Carlos, Universidade de São Paulo, Caixa Postal 369, 13560-970 São Carlos, São Paulo, Brazil.

10.1021/ct800512m CCC: $40.75
Published on Web 02/20/2009

and distinguish between variations at fixed and variable particle number, i.e., for the canonical and grand-canonical ensemble.

2.1. Fixed Particle Number. The density of N noninteracting electrons (at zero temperature) moving in some electrostatic potential $v_s(\mathbf{r})$ is given by

$$n(\mathbf{r}) = \sum_i^{\text{occ}} |\varphi_i(\mathbf{r})|^2 \tag{1}$$

where the single-particle orbitals are solutions of the Schrödinger equation

$$\left(-\frac{\nabla^2}{2} + v_s(\mathbf{r})\right)\varphi_i(\mathbf{r}) = \varepsilon_i \varphi_i(\mathbf{r}) \tag{2}$$

and the sum in eq 1 runs over the N occupied orbitals of the N-electron Slater determinant. For the ground-state density, one can rewrite eq 1 as

$$n(\mathbf{r}) = \sum_i \theta(\varepsilon_F - \varepsilon_i)|\varphi_i(\mathbf{r})|^2 = \sum_i f_i |\varphi_i(\mathbf{r})|^2 \tag{3}$$

where the sum now runs over *all* orbitals. ε_F is the Fermi energy, $\theta(x)$ is the Heavyside step function, and $f_i = \theta(\varepsilon_F - \varepsilon_i)$ is the occupation number of orbital $\varphi_i(\mathbf{r})$. It is evident from eq 3 that the density not only depends on the (occupied) orbitals $\varphi_i(\mathbf{r})$ but also on the orbital energies ε_i, since the very specification of which orbitals are occupied and which unoccupied depends on their energies.

Through eq 2, both of these quantities are functionals of the potential $v_s(\mathbf{r})$, i.e., $\varphi_i(\mathbf{r}) = \varphi_i[v_s](\mathbf{r})$, $\varepsilon_i = \varepsilon_i[v_s]$. The static density response function, which is the functional derivative of n with respect to v_s, is therefore given as

$$\tilde{\chi}(\mathbf{r}, \mathbf{r}') = \frac{\delta n(\mathbf{r})}{\delta v_s(\mathbf{r}')} = \sum_i \frac{\delta f_i}{\delta v_s(\mathbf{r}')}|\varphi_i(\mathbf{r})|^2 + \chi(\mathbf{r}, \mathbf{r}') \tag{4}$$

with

$$\begin{aligned}\chi(\mathbf{r}, \mathbf{r}') &= \sum_i f_i \left(\frac{\delta \varphi_i(\mathbf{r})}{\delta v_s(\mathbf{r}')}\varphi_i^*(\mathbf{r}) + \text{c.c.}\right) \\ &= \sum_{\substack{i,k \\ i\neq k}} f_i \left(\frac{\varphi_k^*(\mathbf{r})\varphi_k(\mathbf{r}')\varphi_i(\mathbf{r})\varphi_i^*(\mathbf{r}')}{\varepsilon_i - \varepsilon_k} + \text{c.c.}\right)\end{aligned} \tag{5}$$

The last step follows from first order perturbation theory, which can be used to obtain

$$\frac{\delta \varphi_i(\mathbf{r})}{\delta v_s(\mathbf{r}')} = \sum_{\substack{k \\ k\neq i}} \frac{\varphi_k(\mathbf{r})\varphi_k^*(\mathbf{r}')\varphi_i(\mathbf{r}')}{\varepsilon_i - \varepsilon_k} \tag{6}$$

For simplicity, we have assumed a nondegenerate single-particle spectrum.

Usually, $\chi(\mathbf{r}, \mathbf{r}')$ of eq 5 is taken as the static density response function instead of $\tilde{\chi}$. Both expressions differ by the first term on the right-hand side of eq 4, becoming identical only if this term vanishes. In order to see when and how this happens we consider two cases.

Case 1 comprises systems for which the single-particle spectrum has a finite gap between the highest occupied orbital (eigenvalue ε_N) and the lowest unoccupied orbital (eigenvalue ε_{N+1}). Then, the Fermi energy ε_F lies strictly between these two orbital energies, $\varepsilon_N < \varepsilon_F < \varepsilon_{N+1}$. Within the single-particle gap, the position of ε_F is arbitrary (at zero temperature). The important point now is that upon (infinitesimal) variation of the potential v_s, ε_F remains fixed and does not need to be varied. The reason is that the variation $\delta\varepsilon_N$ of ε_N due to the variation of v_s is infinitesimal as well and ε_F can be chosen such that $\varepsilon_F > \varepsilon_N + \delta\varepsilon_N$, thus leaving the particle number unchanged. Then the functional derivative of the occupation number with respect to v_s becomes

$$\frac{\delta f_i}{\delta v_s(\mathbf{r})} = \frac{\partial \theta(\varepsilon_F - \varepsilon_i)}{\partial \varepsilon_i}\frac{\delta \varepsilon_i}{\delta v_s(\mathbf{r})} = -\delta(\varepsilon_F - \varepsilon_i)|\varphi_i(\mathbf{r})|^2 \tag{7}$$

where $\delta(x)$ is the Dirac delta function, and we used the relation

$$\frac{\delta \varepsilon_i}{\delta v_s(\mathbf{r})} = |\varphi_i(\mathbf{r})|^2 \tag{8}$$

which can be obtained from first-order perturbation theory. In the present case, the Fermi energy (which is in the single-particle gap) is not equal to any of the single-particle energies, the delta function in eq 7 vanishes, and $\tilde{\chi}(\mathbf{r}, \mathbf{r}')$ of eq 4 coincides with the usual form of the static density response function of eq 5.

Case 2 is the case of a vanishing single-particle gap, i.e., the case of an open-shell or metallic system. For notational simplicity, in the following discussion, we still work with the assumption of a nondegenerate single-particle spectrum. Of course, particularly for open-shell systems, this assumption is inappropriate. The more general case including degenerate single-particle orbitals is discussed in the Appendix.

The crucial difference to case 1 is that an infinitesimal variation of the potential v_s now not only leads to a variation $\delta\varepsilon_i$ of the single-particle energies but also to a variation $\delta\varepsilon_F$ of the Fermi energy. This latter variation has to be taken into account in order for the particle number to be conserved (i.e., the infinitesimal variation δN of the particle number upon variation of the potential strictly has to vanish, $\delta N = 0$). Then, the functional derivative of the occupation number with respect to the potential consists of two terms and reads

$$\begin{aligned}\frac{\delta f_i}{\delta v_s(\mathbf{r})} &= \frac{\partial \theta(\varepsilon_F - \varepsilon_i)}{\partial \varepsilon_F}\frac{\delta \varepsilon_F}{\delta v_s(\mathbf{r})} + \frac{\partial \theta(\varepsilon_F - \varepsilon_i)}{\partial \varepsilon_i}\frac{\delta \varepsilon_i}{\delta v_s(\mathbf{r})} \\ &= \delta(\varepsilon_F - \varepsilon_i)(|\varphi_F(\mathbf{r})|^2 - |\varphi_i(\mathbf{r})|^2)\end{aligned} \tag{9}$$

where φ_F is the highest occupied orbital with orbital energy equal to the Fermi energy. Due to the delta function, the right-hand side (rhs) of eq 9 vanishes and again $\tilde{\chi}(\mathbf{r}, \mathbf{r}')$ of eq 4 coincides with the static density response function $\chi(\mathbf{r}, \mathbf{r}')$ of the form given in eq 5.

From eq 4, the linear change in the density due to the perturbation $\delta v_s(\mathbf{r})$ is $\delta n(\mathbf{r}) = \int d^3r' \tilde{\chi}(\mathbf{r}, \mathbf{r}')\delta v_s(\mathbf{r}')$. One can then check explicitly that the result $\tilde{\chi}(\mathbf{r}, \mathbf{r}') = \chi(\mathbf{r}, \mathbf{r}')$ obtained here is fully consistent with a fixed number of particles:

$$\begin{aligned}\delta N &= \int d^3r\, \delta n(\mathbf{r}) = \int d^3\mathbf{r}'\, \delta v_s(\mathbf{r}') \int d^3r\, \tilde{\chi}(\mathbf{r}, \mathbf{r}') \\ &= \int d^3\mathbf{r}'\, \delta v_s(\mathbf{r}') \int d^3r\, \chi(\mathbf{r}, \mathbf{r}') = 0\end{aligned} \tag{10}$$

where the last equality follows from the orthonormality of the single-particle orbitals.

We note that the problem we are discussing here involves the response function $(\delta n[v_s])/(\delta v_s)$ itself and is thus conceptually distinct from the question of invertibility of this response function, which appears when the single-particle potentials are not uniquely determined by the densities.[15]

2.2. Grand Canonical Ensemble. The analysis is slightly altered if the system of noninteracting electrons is connected to a particle bath, i.e., for the grand canonical ensemble characterized by a chemical potential μ. The density (at zero temperature) is then given by

$$n(\mathbf{r}) = \sum_i \theta(\mu - \varepsilon_i)|\varphi_i(\mathbf{r})|^2 = \sum_i f_i|\varphi_i(\mathbf{r})|^2 \quad (11)$$

where the occupation number now is given by $f_i = \theta(\mu - \varepsilon_i)$ and the sum again runs over all single-particle orbitals. When varying the occupation numbers with respect to variations of the potential, the chemical potential remains constant, independent of the single-particle spectrum having a finite or vanishing gap at μ. The variation of f_i then is obtained similarly to case 1 of the previous subsection as

$$\frac{\delta f_i}{\delta v_s(\mathbf{r})} = \frac{\partial \theta(\mu - \varepsilon_i)}{\partial \varepsilon_i}\frac{\delta \varepsilon_i}{\delta v_s(\mathbf{r})} = -\delta(\mu - \varepsilon_i)|\varphi_i(\mathbf{r})|^2 \quad (12)$$

This term does not vanish if the chemical potential is aligned with one of the single-particle energies, and the static density response function for the grand-canonical ensemble reads

$$\tilde{\chi}(\mathbf{r}, \mathbf{r}') = \chi(\mathbf{r}, \mathbf{r}') - \sum_i \delta(\mu - \varepsilon_i)|\varphi_i(\mathbf{r})|^2|\varphi_i(\mathbf{r}')|^2 \quad (13)$$

It is worth noting that now, due to the second term on the rhs of eq 13, δN (eq 10) is different from zero which is of course consistent with the fact that here we are dealing with an open system.

3. Implications for the Optimized Effective Potential

The central idea of density functional theory is to write the ground-state energy E_{tot} of N interacting electrons moving in an external potential $v_0(\mathbf{r})$ as a functional of the ground-state density. This energy functional may then be split into various pieces as

$$E_{tot} = T_s[n] + \int d^3r\, v_0(\mathbf{r})n(\mathbf{r}) + U[n] + E_{xc}[n] \quad (14)$$

where $T_s[n]$ is the kinetic energy functional of *noninteracting* electrons,

$$U[n] = \frac{1}{2}\int d^3r \int d^3r' \frac{n(\mathbf{r})n(\mathbf{r}')}{|\mathbf{r} - \mathbf{r}'|} \quad (15)$$

is the classical electrostatic energy, and E_{xc} is the exchange-correlation energy functional which incorporates all complicated many-body effects and in practice has to be approximated. Minimization of eq 14 with respect to the density leads to an effective single-particle equation of the form of eq 2 where the effective potential is

$$v_s(\mathbf{r}) = v_0(\mathbf{r}) + \int d^3r' \frac{n(\mathbf{r}')}{|\mathbf{r} - \mathbf{r}'|} + v_{xc}(\mathbf{r}) \quad (16)$$

with the exchange-correlation potential

$$v_{xc}(\mathbf{r}) = \frac{\delta E_{xc}}{\delta n(\mathbf{r})} \quad (17)$$

While the most popular approximations to the exchange-correlation energy E_{xc} are explicit functionals of the density, there has been increasing interest in another class of approximations which are are only *implicit* functionals of the density. These functionals instead depend explicitly on the Kohn−Sham single-particle orbitals as well as on the Kohn−Sham orbital energies. One example for such a functional is the exact exchange energy given as

$$E_x^{EXX} = -\frac{1}{4}\int d^3r \int d^3r' \frac{|\gamma(\mathbf{r}, \mathbf{r}')|^2}{|\mathbf{r} - \mathbf{r}'|} \quad (18)$$

where

$$\gamma(\mathbf{r}, \mathbf{r}') = \sum_i f_i\varphi_i(\mathbf{r})\varphi_i^*(\mathbf{r}') \quad (19)$$

is the single-particle density matrix. As one can see, E_x^{EXX} depends on the single-particle energies through the occupation numbers f_i. Other functionals such as, e.g., the correlation energy functional of second-order Görling−Levy perturbation theory,[13] depend on the orbital energies also in other ways (see below).

In order to distinguish a genuine dependence on orbital energies from a dependence on occupation numbers, we write for a general exchange-correlation energy functional $E_{xc} = E_{xc}[\{\varphi_i\}, \{\varepsilon_i\}, \{f_i\}]$. The exchange-correlation potential of such a functional can be computed by using the chain rule of functional differentiation as

$$v_{xc}(\mathbf{r}) = \frac{\delta E_{xc}}{\delta n(\mathbf{r})} = \int d^3\mathbf{r}' \frac{\delta E_{xc}}{\delta v_s(\mathbf{r}')}\frac{\delta v_s(\mathbf{r}')}{\delta n(\mathbf{r})} \quad (20)$$

Acting with the density response operator (eq 4) on both sides of this equation, one arrives at

$$\begin{aligned}\int d^3\mathbf{r}'\, v_{xc}(\mathbf{r}')\tilde{\chi}(\mathbf{r}', \mathbf{r}) &= \frac{\delta E_{xc}}{\delta v_s(\mathbf{r})} \\ &= \sum_i \int d^3\mathbf{r}' \left(\left(\frac{\delta E_{xc}}{\delta \varphi_i(\mathbf{r}')}\Big|_{\{\varepsilon_k\},\{f_k\}}\frac{\delta \varphi_i(\mathbf{r}')}{\delta v_s(\mathbf{r})} + \text{c.c.}\right) + \right. \\ &\left. \frac{\partial E_{xc}}{\partial \varepsilon_i}\Big|_{\{\varphi_k\},\{f_k\}}\frac{\delta \varepsilon_i}{\delta v_s(\mathbf{r})} + \frac{\partial E_{xc}}{\partial f_i}\Big|_{\{\varphi_k\},\{\varepsilon_k\}}\frac{\delta f_i}{\delta v_s(\mathbf{r})}\right) \quad (21)\end{aligned}$$

In the last step, we have used the chain rule once again and we also emphasize in the notation that when varying with respect to one set of variables (orbitals, orbital energies, or occupation numbers) the other variables remain fixed.

Equation 21 is the OEP integral equation in its general form. For a given approximate E_{xc}, this equation *defines* the corresponding $v_{xc}(\mathbf{r})$ and has to be solved in a self-consistent way together with the Kohn−Sham equations (eq 2). It differs in three ways from the form most commonly found in the literature (see, e.g., refs 3 and 4 and references therein). One, the explicit energy dependence is handled in a similar way as is the orbital dependence, via the chain rule. The other two arise from the implicit energy dependence of the occupation numbers and are our main concern here. Similar

to the discussion in the previous section, we will again distinguish between the two cases of fixed particle number and systems in contact with a particle bath and discuss the role of these extra terms in both cases.

3.1. Fixed Particle Number. As we have seen in section 2, for the case of fixed particle number at zero temperature, the functional derivative $\delta f_i/\delta v_s(\mathbf{r})$ vanishes both for systems with a finite and vanishing HOMO−LUMO gap. This has two consequences for eq 21: first, we can replace the response function $\tilde{\chi}$ by the function χ of eq 5, and second, the last term on the rhs of eq 21 drops out. Therefore, the OEP equation reads

$$\int d^3r'\, v_{xc}(\mathbf{r}')\chi(\mathbf{r}',\mathbf{r}) = \sum_i \left[\int d^3r' \left(\frac{\delta E_{xc}}{\delta \varphi_i(\mathbf{r}')}\bigg|_{\{\varepsilon_k\},\{f_k\}} \frac{\delta \varphi_i(\mathbf{r}')}{\delta v_s(\mathbf{r})} + \text{c.c.} \right) + \frac{\partial E_{xc}}{\partial \varepsilon_i}\bigg|_{\{\varphi_k\},\{f_k\}} \frac{\delta \varepsilon_i}{\delta v_s(\mathbf{r})} \right] \quad (22)$$

This equation shows that despite the dependence of E_{xc} on the occupation numbers (which, in turn, depend on the orbital energies), the variation with respect to these occupation numbers may be omitted for the calculation of the OEP integral equation for the exchange-correlation potential. This is, of course, what has been done in the vast majority of cases discussed in the literature.

We note in passing that integrating eq 22 over all space and using the orthornormality of the Kohn−Sham orbitals one can deduce the sum rule[16]

$$\sum_i \frac{\partial E_{xc}}{\partial \varepsilon_i}\bigg|_{\{\varphi_k\},\{f_k\}} = 0 \quad (23)$$

On quite general grounds, one expects that for an isolated system with a fixed number of particles, $v_{xc}(\mathbf{r})$ is only defined up to a constant. To check if eq 22 meets this condition, we need an explicit expression for E_{xc}. As a nontrivial example, we use

$$E_{xc} \approx E_x^{EXX} + E_c^{(2)} \quad (24)$$

where E_x^{EXX} is the exact exchange energy of eq 18 and $E_c^{(2)}$ is the second-order correlation energy of Görling−Levy perturbation theory[13,17,18] defined by

$$E_c^{(2)} = E_{c,1} + E_{c,2} \quad (25)$$

where

$$E_{c,1} = \sum_{i,j} \frac{f_i(1-f_j)}{(\varepsilon_i - \varepsilon_j)} \left| \langle i|v_x|j\rangle + \sum_k f_k (ik||kj) \right|^2 \quad (26)$$

and

$$E_{c,2} = \frac{1}{2} \sum_{i,j,k,l} \frac{f_i f_j (1-f_k)(1-f_l)}{(\varepsilon_i + \varepsilon_j - \varepsilon_k - \varepsilon_l)} (ij||kl)[(kl||ij) - (kl||ji)] \quad (27)$$

In the equations above, we have used the notations

$$(ij||kl) = \int d^3r \int d^3r' \, \frac{\varphi_i^*(\mathbf{r})\varphi_k(\mathbf{r})\varphi_j^*(\mathbf{r}')\varphi_l(\mathbf{r}')}{|\mathbf{r}-\mathbf{r}'|} \quad (28)$$

and

$$\langle i|v_x|j\rangle = \int d^3r\, \varphi_i^*(\mathbf{r}) v_x(\mathbf{r}) \varphi_j(\mathbf{r}) \quad (29)$$

Suppose now that we introduce a rigid shift $v_s(\mathbf{r}) \rightarrow v_s(\mathbf{r}) + C$ in the effective single particle potential of eq 2. As a result, if $\{\varphi_i\}$, $\{\varepsilon_i\}$, $\{f_i\}$ are a set of solutions for $v_s(\mathbf{r})$, the solutions for $v_s(\mathbf{r}) + C$ are $\{\varphi_i\}$, $\{\varepsilon_i + C\}$, $\{f_i\}$. This holds provided that eq 22 determines $v_{xc}(\mathbf{r})$ only up to a constant. Inspection of eq 18 confirms that this is the case: the left-hand side (lhs) is invariant under a rigid shift of $v_{xc}(\mathbf{r})$, and eqs 18 and 25 are invariant under the change $\{\varepsilon_i\} \rightarrow \{\varepsilon_i + C\}$.

3.2. Grand Canonical Ensemble. The situation is different if the system is in contact with a particle bath. Since in this case $\delta f_i/\delta v_s(\mathbf{r})$ does not vanish one has to use the full OEP eq 21. Here, the dependence of both the density and the exchange-correlation energy on the occupation numbers has to be taken into account explicitly when performing the variations and the two extra terms resulting from this variation cannot be neglected. Applications of this OEP formalism for open systems have been reported for quasi-two-dimensional electron gases (2DEG) in *n*-doped semiconductor quantum wells where the *n*-doped regions act as particle reservoirs.[19−21] A qualitative discussion of the importance of the extra terms for the particular case of 2DEG can be found in the discussion of eqs 6−8 of ref 21.

As another consequence of the extra terms, integration of eq 21 over all space leads to the modified sum rule

$$-\sum_i \delta(\mu - \varepsilon_i)\bar{v}_{xc,i} = \sum_i \left(\frac{\partial E_{xc}}{\partial \varepsilon_i}\bigg|_{\{\varphi_k\},\{f_k\}} - \frac{\partial E_{xc}}{\partial f_i}\bigg|_{\{\varphi_k\},\{\varepsilon_k\}} \delta(\mu - \varepsilon_i) \right) \quad (30)$$

where

$$\bar{v}_{xc,i} = \int d^3r\, v_{xc}(\mathbf{r})|\varphi_i(\mathbf{r})|^2 \quad (31)$$

We take the exact exchange functional (eq 18) as an example for a functional which does not explicitly depend on the single-particle energies. In this case, the first term on the rhs of eq 30 vanishes. If there exists a single-particle state whose energy equals the chemical potential, $\varepsilon_N = \mu$, we then obtain

$$\bar{v}_{x,N}^{EXX} = \frac{\partial E_x^{EXX}}{\partial f_N} \quad (32)$$

This relation is the complete analogue for the grand canonical ensemble of a well-known relation for fixed particle number which reads[22−24]

$$\bar{v}_{x,N}^{EXX} = \bar{u}_{x,N}^{EXX} \quad (33)$$

where

$$\bar{u}_{x,N}^{EXX} = \frac{1}{f_N} \int d^3r\, \varphi_N(\mathbf{r}) \frac{\delta E_x^{EXX}}{\delta \varphi_N(\mathbf{r})} \quad (34)$$

For open 2DEG's, this relation has been obtained previously by studying the asymptotic behavior of the exact-exchange potential.[20]

For the grand-canonical ensemble, $v_{xc}(\mathbf{r})$ is *fully determined* by eq 21 since this equation is *not* invariant under a rigid shift of the potential: the lhs is not invariant due to the

extra term in $\tilde{\chi}(\mathbf{r}, \mathbf{r}')$ in eq 13. The rhs is not invariant because E_{xc} changes under the transformation $\{\varepsilon_i\} \rightarrow \{\varepsilon_i + C\}$. This is due to the fact that the chemical potential μ (which is determined by the particle reservoirs) remains fixed in the grand canonical ensemble and the above transformation leads to a change in the set of occupation numbers and self-consistent KS orbitals, $\{f_i\}$ and $\{\varphi_i\}$, respectively. This is consistent with the result of Argaman and Makov[25] who showed that in a grand-canonical ensemble the single-particle potentials are uniquely determined by the densities.

4. Conclusions

In this work, we have addressed the question why and when one can ignore the explicit dependence on the orbital occupation numbers (which in turn depend explicitly on the orbital energies) when calculating both the static linear density response function and the effective single-particle potential corresponding to an orbital-dependent exchange-correlation energy functional. We have shown that the variation of the occupation numbers may safely be neglected for systems with fixed particle number. For systems connected to a particle bath, however, this variation leads to nonvanishing contributions and needs to be taken into account.

Acknowledgment. S.K. acknowledges support through the Ikerbasque foundation. C.R.P. was supported by the European Community through a Marie Curie Incoming International Fellowship (MIF1-CT-2006-040222) and CONICET of Argentina through PIP 5254. K.C. was supported by FAPESP and CNPq. We thank Stefano Pittalis, Hardy Gross, Angel Rubio, and Santiago Rigamonti for useful discussions.

Appendix: Degenerate Single-Particle Spectrum

In general, the single-particle spectrum will have eigenvalues which may be degenerate. In particular, in the case of open-shell systems, the energy of the highest occupied orbital is degenerate and the arguments of case 2 discussed in section 2.1 need to be modified.

As degeneracy is in almost all cases related to symmetry, we will use the language of group theory. In particular, the single-particle orbitals will be labeled by a complete set of quantum numbers $\{n, l, m\}$ where n is the principal quantum number (which is not related to symmetry), l is a label denoting the irreducible representation of the symmetry group $\mathcal{G}$ of the single-particle potential $v_s(\mathbf{r})$, and m labels a partner within that representation. The single-particle equation now reads

$$\left(-\frac{\nabla^2}{2} + v_s(\mathbf{r})\right)\varphi_{nlm}(\mathbf{r}) = \varepsilon_{nl}\varphi_{nlm}(\mathbf{r}) \tag{35}$$

and it should be noted that the eigenvalue ε_{nl} is independent of the partner label m. Furthermore, writing the energy eigenvalue as a functional of the potential, $\varepsilon_{nl}[v_s]$, one has to keep in mind that this functional is only well defined for potentials which are invariant under the transformations of the symmetry group $\mathcal{G}$ because l refers to an irreducible representation of that group. Therefore, we calculate the variation of the orbital energies, $\delta\varepsilon_{nl} = \varepsilon_{nl}[v_s + \delta v_s] - \varepsilon_{nl}[v_s]$ resulting from a variation $\delta v_s(\mathbf{r})$ which preserves the symmetry of $v_s(\mathbf{r})$. Replacing $v_s \rightarrow v_s + \delta v_s$, $\varphi_{nlm} \rightarrow \varphi_{nlm} + \delta\varphi_{nlm}$, in eq 35, one finds that the first-order change in the energy eigenvalue is given by

$$\delta\varepsilon_{nl} = \int \mathrm{d}^3 r\, |\varphi_{nlm}(\mathbf{r})|^2 \delta v_s(\mathbf{r}) \tag{36}$$

Summing this equation over the partner label m one obtains

$$d_{nl}\delta\varepsilon_{nl} = \int \mathrm{d}^3 r \sum_m |\varphi_{nlm}(\mathbf{r})|^2 \delta v_s(\mathbf{r}) \tag{37}$$

where d_{nl} is the degeneracy of ε_{nl}. Now, we note that the single-particle orbitals $\varphi_{nlm}(\mathbf{r})$ may be written as

$$\varphi_{nlm}(\mathbf{r}) = R_{nl}(\mathbf{r})X_{lm}(\mathbf{r}) \tag{38}$$

where $R_{nl}(\mathbf{r})$ is a totally symmetric function which is invariant under all symmetry transformations T of the group $\mathcal{G}$ and $X_{lm}(\mathbf{r})$ is a function which transforms according to the irreducible representation l of $\mathcal{G}$, i.e.,

$$X_{lm}(R^{-1}(T)\mathbf{r}) = \sum_{m'} \Gamma^{(l)}(T)_{m'm} X_{lm'}(\mathbf{r}) \tag{39}$$

Here, $R(T)$ is a 3×3 matrix describing the symmetry operation $T \in \mathcal{G}$ in three-dimensional space and $\Gamma^{(l)}(T)$ is the representation matrix of group element T in the irreducible representation l of $\mathcal{G}$. Noting now that $\sum_m |X_{lm}(\mathbf{r})|^2$ is a totally symmetric function, we find for the functional derivative

$$\frac{\delta\varepsilon_{nl}}{\delta v_s(\mathbf{r})} = |\tilde{R}_{nl}(\mathbf{r})|^2 \tag{40}$$

where we have defined

$$\tilde{R}_{nl}(\mathbf{r}) = \frac{1}{\sqrt{d_{nl}}} R_{nl}(\mathbf{r}) \sqrt{\sum_m |X_{lm}(\mathbf{r})|^2} \tag{41}$$

which is again invariant under all symmetry transformations of the group $\mathcal{G}$.

Equation 40 will shortly be used to repeat the arguments of section 2.1 for the degenerate, open-shell case. Before we do so, we point out that the definition of the density of eq 3 needs to be modified because not all orbitals with energy ε_F are (fully) occupied. This can be achieved, e.g., by writing the density as

$$n(\mathbf{r}) = \sum_{n,l,m} f_{nlm} |\varphi_{nlm}(\mathbf{r})|^2 \tag{42}$$

and occupying all degenerate orbitals of the partially filled subshell with the same fractional number of electrons, i.e., by defining the occupation number of the partially filled subshell by $f_{nlm} = f_{nl} = (n_{nl}/d_{nl})\theta(\varepsilon_F - \varepsilon_{nl})$ where n_{nl} is the number of electrons in the open subshell. With this definition, the static density response function reads

$$\tilde{\chi}(\mathbf{r}, \mathbf{r}') = \chi(\mathbf{r}, \mathbf{r}') + \sum_{n,l,m} \frac{\delta f_{nl}}{\delta v_s(\mathbf{r})} |\varphi_{nlm}(\mathbf{r})|^2 \tag{43}$$

with

$$\chi(\mathbf{r},\mathbf{r}') = \sum_{\substack{n,l,m \\ n',l',m' \\ \varepsilon_{nl}\neq\varepsilon_{n'l'}}} f_{nl}\left(\frac{\varphi^*_{n'l'm'}(\mathbf{r})\varphi_{n'l'm'}(\mathbf{r}')\varphi_{nlm}(\mathbf{r})\varphi^*_{nlm}(\mathbf{r}')}{\varepsilon_{nl}-\varepsilon_{n'l'}} + \text{c.c.}\right) \tag{44}$$

and

$$\frac{\delta f_{nl}}{\delta v_s(\mathbf{r})} = \frac{n_{nl}}{d_{nl}}\delta(\varepsilon_F - \varepsilon_{nl})(|\tilde{R}_F(\mathbf{r})|^2 - |\tilde{R}_{nl}(\mathbf{r})|^2) = 0 \tag{45}$$

where the last equality follows because the total symmetric part of degenerate orbitals is identical. Therefore, just as in the nondegenerate case at fixed particle number, the functional derivative with respect to the occupation numbers may be neglected both in the calculation of the density response function as well as in the derivation of the OEP equation.

References

(1) Hohenberg, P.; Kohn, W. Inhomogeneous Electron Gas. *Phys. Rev.* **1964**, *136*, B864.

(2) Kohn, W.; Sham, L. J. Self-consistent equations including exchange and correlation. *Phys. Rev.* **1965**, *140*, A1133.

(3) Grabo, T.; Kreibich, T.; Kurth, S.; Gross, E. K. U., Orbital functionals in density functional theory: the optimized effective potential method. In *Strong Coulomb Correlations in Electronic Structure Calculations: Beyond Local Density Approximations*; Anisimov, V. I., Ed.; Gordon and Breach: Amsterdam, The Netherlands, 2000; pp 203−311.

(4) Kümmel, S.; Kronik, L. Orbital-dependent density functionals: Theory and applications. *Rev. Mod. Phys.* **2008**, *80*, 3.

(5) Becke, A. D. A new mixing of Hartree-Fock and local density-functional theories. *J. Chem. Phys.* **1993**, *98*, 1372.

(6) Becke, A. D. Density-functional thermochemistry: III. The role of exact exchange. *J. Chem. Phys.* **1993**, *98*, 5648.

(7) Becke, A. D. Density-functional thermochemistry: IV. A new dynamical correlation functional and implications for exact-exchange mixing. *J. Chem. Phys.* **1996**, *104*, 1040.

(8) Adamo, C.; Barone, V. Toward reliable density functional methods without adjustable parameters: The PBE0 model. *J. Chem. Phys.* **1999**, *110*, 6158.

(9) Perdew, J. P.; Zunger, A. Self-Interaction correction to density-functional approximations for many-electron systems. *Phys. Rev. B* **1981**, *23*, 5048.

(10) (a) Perdew, J. P.; Kurth, S.; Zupan, A.; Blaha, P. Accurate Density Functional with Correct Formal Properties: A Step Beyond the Generalized Gradient Approximation. *Phys. Rev. Lett.* **1999**, *82*, 2544. (b) Perdew, J. P.; Kurth, S.; Zupan, A.; Blaha, P. *Phys. Rev. Lett.* **1999**, *82*, 5179.

(11) Kurth, S.; Perdew, J. P.; Blaha, P. Molecular and Solid State Tests of Density Functional Approximations: LSD, GGA's, and Meta-GGA's. *Int. J. Quantum Chem.* **1999**, *75*, 889.

(12) Tao, J.; Perdew, J. P.; Staroverov, V. N.; Scuseria, G. E. Climbing the Density Functional Ladder: Nonempirical Meta-Generalized Gradient Approximation Designed for Molecules and Solids. *Phys. Rev. Lett.* **2003**, *91*, 146401.

(13) Görling, A.; Levy, M. Correlation-energy functional and its high-density limit obtained from a coupling-constant perturbation expansion. *Phys. Rev. B* **1993**, *47*, 13105.

(14) Talman, J. D.; Shadwick, W. F. Optimized effective atomic central potential. *Phys. Rev. A* **1976**, *14*, 36.

(15) Capelle, K.; Vignale, G. Nonuniqueness of the Potentials of Spin-Density-Functional Theory. *Phys. Rev. Lett.* **2001**, *86*, 5546.

(16) Engel, E.; Jiang, H. Orbital-Dependent Representation of the Correlation Energy Functional: Properties of Second-Order Kohn-Sham Perturbation Expansion. *Int. J. Quantum Chem.* **2006**, *106*, 3242.

(17) Engel, E.; Jiang, H.; Facco Bonetti, A. Solubility of the optimized-potential-method integral equation for finite systems. *Phys. Rev. A* **2005**, *72*, 052503.

(18) Rigamonti, S.; Proetto, C. R. Correlation Kohn-Sham potential for quasi-two-dimensional electron gases. *Phys. Rev. B* **2006**, *73*, 235319.

(19) Rigamonti, S.; Reboredo, F. A.; Proetto, C. R. Exact-exchange density-functional theory applied to a strongly inhomogeneous electron gas. *Phys. Rev. B* **2003**, *68*, 235309.

(20) Rigamonti, S.; Proetto, C. R.; Reboredo, F. A. Novel properties of the Kohn-Sham exchange potential for open systems: Application to the two-dimensional electron gas. *Europhys. Lett.* **2005**, *70*, 116.

(21) Rigamonti, S.; Proetto, C. R. Signatures of Discontinuity in the Exchange-Correlation Energy Functional Derived from the Subband Electronic Structure of Semiconductor Quantum Wells. *Phys. Rev. Lett.* **2007**, *98*, 066806.

(22) Krieger, J. B.; Li, Y.; Iafrate, G. J. Construction and application of an accurate local spin-polarized Kohn-Sham potential with integer discontinuity: Exchange-only. *Phys. Rev. A* **1992**, *45*, 101.

(23) Levy, M.; Görling, A. Density-functional exchange identity from coordinate scaling. *Phys. Rev. A* **1996**, *53*, 3140.

(24) Kreibich, T.; Kurth, S.; Grabo, T.; Gross, E. K. U. Asymptotic Properties of the Optimized Effective Potential. *Adv. Quantum Chem.* **1999**, *33*, 31.

(25) Argaman, N.; Makov, G. Thermodynamics as an alternative foundation for zero-temperature density-functional theory and spin-density-functional theory. *Phys. Rev. B* **2002**, *66*, 052413.

CT800512M

JCTC Journal of Chemical Theory and Computation

Reconstruction of Density Functionals from Kohn−Sham Potentials by Integration along Density Scaling Paths

Alex P. Gaiduk, Sergey K. Chulkov, and Viktor N. Staroverov*

Department of Chemistry, The University of Western Ontario, London, Ontario N6A 5B7, Canada

Received November 30, 2008

Abstract: We demonstrate by specific examples that if a Kohn−Sham exchange-correlation potential is given explicitly in terms of the electron density and its derivatives, then one can easily reconstruct the parent density functional by evaluating analytically (or numerically with one-dimensional quadratures) the van Leeuwen−Baerends line integral (*Phys. Rev. A* **1995**, *51*, 170−178) along a path of (coordinate)-scaled densities. The choice of a density scaling path amounts to defining the gauge of the resultant exchange-correlation energy density. The well-known Levy−Perdew virial relation for exchange potentials can be viewed as an analytical line integral along the electron-number-conserving uniform density scaling path. Energies obtained from model exchange-correlation potentials should be interpreted with caution because the reconstructed density functional is unique (up to a gauge transformation) only if the model Kohn−Sham potential is a functional derivative.

1. Introduction

The exchange-correlation (xc) potential of Kohn−Sham density functional theory[1−3] is formally defined as the functional derivative of the exchange-correlation energy functional $E_{xc}[\rho]$, that is

$$v_{xc}([\rho];\mathbf{r}) = \frac{\delta E_{xc}[\rho]}{\delta \rho(\mathbf{r})} \tag{1}$$

where $\rho(\mathbf{r})$ is the electron density found from Kohn−Sham orbitals as $\rho(\mathbf{r}) = 2\Sigma_i^{occ.}|\phi_i(\mathbf{r})|^2$. For simplicity, we will write all equations here for spin-compensated closed-shell systems, so that ϕ_i are the occupied Kohn−Sham orbitals of either one spin. The notation $v_{xc}([\rho]; \mathbf{r})$ emphasizes that v_{xc} is also a functional of ρ at each $\mathbf{r}$.

A functional $E_{xc}[\rho]$ that can be written in the form

$$E_{xc}[\rho] = \int \mathrm{d}^3 r\, f_{xc}(\mathbf{r}, \rho, \nabla\rho, \nabla^2\rho, ...) \tag{2}$$

where $\mathrm{d}^3 r \equiv \mathrm{d}x\,\mathrm{d}y\,\mathrm{d}z$, is said to be an *explicit* density functional. The functional derivative of explicit functionals can be found directly by using a standard formula of the calculus of variations[2,4] and cast in the form

$$v_{xc}([\rho];\mathbf{r}) = \frac{\partial f_{xc}}{\partial \rho} - \nabla\cdot\left(\frac{\partial f_{xc}}{\partial \nabla\rho}\right) + \nabla^2\left(\frac{\partial f_{xc}}{\partial \nabla^2\rho}\right) - ... \tag{3}$$

in which $\partial f_{xc}/\partial\nabla\rho$ is a shorthand for a vector with three components $\partial f_{xc}/\partial\rho'_\alpha$, where $\rho'_\alpha \equiv \partial\rho/\partial\alpha$ and $\alpha = x, y, z$. A functional of Kohn−Sham orbitals that cannot be reduced to the form of eq 2 is said to be *implicit* or orbital-dependent.[5] The functional derivative of an implicit functional can be found indirectly as a solution of the optimized effective potential equation.[5−7] Thus, given a density functional $E_{xc}[\rho]$, it is always possible to find the corresponding functional derivative $v_{xc}([\rho]; \mathbf{r})$.

An interesting and practically important question is whether it is possible to invert functional differentiation, that is, to reconstruct an exchange-correlation functional from a given Kohn−Sham potential. Clearly, the solution to the inverse problem is not unique because exchange-correlation energy density $f_{xc}(\mathbf{r})$ of eq 2 is defined only up to an arbitrary function that integrates to zero.[8−13] Therefore, we will qualify the question: Given a functional derivative $v_{xc}([\rho]; \mathbf{r})$, is it possible to reconstruct its parent functional up to a gauge transformation of the energy density?

It is well-known that for exchange-only functionals, the functional differentiation can be inverted by the Levy−Perdew virial relation[14,15]

* Corresponding author e-mail: vstarove@uwo.ca.

10.1021/ct800514z CCC: $40.75
Published on Web 03/10/2009

$$E_x[\rho] = -\int d^3r\, \rho(\mathbf{r})\mathbf{r}\cdot\nabla v_x([\rho];\mathbf{r}) \quad (4)$$

Less known is the fact that it is also possible to recover the entire exchange-correlation functional from the corresponding Kohn−Sham potential by the line-integral method of van Leeuwen and Baerends[16−19]

$$E_{xc}[\rho] = \int_0^1 dt \int d^3r\, v_{xc}([\rho_t];\mathbf{r})\frac{\partial \rho_t(\mathbf{r})}{\partial t} \quad (5)$$

where $\rho_t(\mathbf{r})$ is a continuously parametrized density such that $E_{xc}[\rho_0] = 0$ and $\rho_1(\mathbf{r}) = \rho(\mathbf{r})$. Unlike exchange-only functionals, an exchange-correlation functional cannot be reconstructed from $v_{xc}([\rho];\mathbf{r})$ at density $\rho(\mathbf{r})$ alone: eq 5 requires knowing the Kohn−Sham potential along a whole *path* of densities. It is essential, however, that the mapping from $\rho_t(\mathbf{r})$ to $v_{xc}([\rho_t];\mathbf{r})$ does not have to be variational and that the resulting value of $E_{xc}[\rho]$ is path-independent.

The purpose of this work is to draw attention to the fact that if the exchange-correlation potential is given analytically in terms of $\rho(\mathbf{r})$, then the knowledge of the potential for all intermediate densities $\rho_t(\mathbf{r})$ is implicitly included. In such cases, the line integration in eq 5 can be carried out numerically or even analytically. We will demonstrate this by evaluating line integrals for several explicit exchange and correlation potentials along alternative density transformation paths to recover the corresponding parent functionals, often in unrecognizable disguise. We will also discuss what happens when one attempts to reconstruct a density functional from a potential $v_{xc}([\rho];\mathbf{r})$ that is not a functional derivative.

2. Integration of Functional Derivatives

On the basis of eq 3, it is obvious that for any *local* exchange-correlation potential (that is, a potential that depends only on $\mathbf{r}$ and ρ but not on $\nabla\rho$ or higher derivatives), the exchange-correlation energy density of the parent functional can be found simply as an indefinite integral (antiderivative) of v_{xc} with respect to ρ. This implies that any local $v_{xc}([\rho];\mathbf{r})$ is a functional derivative of some $E_{xc}[\rho]$. For gradient-dependent potentials, a more general method is required, such as eq 5.

Let us derive the van Leeuwen−Baerends formula. Consider an arbitrary exchange-correlation functional $E_{xc}[\rho]$. Following van Leeuwen and Baerends,[16] we introduce a parametrized density $\rho_t(\mathbf{r})$, where t is a parameter varying in the range $A \le t \le B$. If $E_{xc}[\rho_t]$ is a continuous function of t in this interval, then we can write

$$E_{xc}[\rho_B] - E_{xc}[\rho_A] = \int_A^B dt\, \frac{dE_{xc}[\rho_t]}{dt} \quad (6)$$

As shown in the Appendix, the derivative in eq 6 can be rewritten as

$$\frac{dE_{xc}[\rho_t]}{dt} = \int d^3r \frac{\delta E_{xc}[\rho_t]}{\delta \rho_t(\mathbf{r})}\frac{\partial \rho_t(\mathbf{r})}{\partial t} \quad (7)$$

where the integral is over the entire real-space domain of the density $\rho_t(\mathbf{r})$. The functional derivative appearing in eq 7 is the Kohn−Sham potential written in terms of the parametrized density

$$\frac{\delta E_{xc}[\rho_t]}{\delta \rho_t(\mathbf{r})} \equiv v_{xc}([\rho_t];\mathbf{r}) = v_{xc}([\rho];\mathbf{r})\Big|_{\rho=\rho_t} \quad (8)$$

Combining eqs 6−8 we obtain

$$E_{xc}[\rho_B] - E_{xc}[\rho_A] = \int_A^B dt \int d^3r\, v_{xc}([\rho_t];\mathbf{r})\frac{\partial \rho_t(\mathbf{r})}{\partial t} \quad (9)$$

which holds for an arbitrary path connecting ρ_A and ρ_B.[16] Equation 9 is the most general form of the van Leeuwen−Baerends line integral. In particular, if $\rho_t(\mathbf{r})$ is parametrized in the range $0 \le t \le 1$ in such a way that $E_{xc}[\rho_0] = 0$ and $\rho_1(\mathbf{r}) = \rho(\mathbf{r})$, then eq 9 reduces to eq 5.

The standard interpretation[16] of the van Leeuwen−Baerends formula is that it provides an "energy expression" for obtaining the value of $E_{xc}[\rho_B]$ when the value of $E_{xc}[\rho_A]$ is known (for numerical examples, see refs 20−22). Here we adopt a somewhat different view according to which eq 5 is a solution to the inverse problem of functional differentiation. To emphasize this, we will call an expression for $E_{xc}[\rho]$ obtained by eq 5 a *reconstruction* of the density functional. The fact that the integration path in eq 5 is arbitrary (except for the end points) suggests that there are many equivalent reconstructions from a given functional derivative.

3. Density Scaling Paths

In this work, we are concerned with reconstruction of density functionals from exchange-correlation potentials that are *explicit* functionals of the density. For such potentials, it is convenient to take $\rho_t(\mathbf{r})$ as a magnitude- or coordinate-scaled density. This allows one to have $v_{xc}([\rho_t];\mathbf{r})$ in a closed form at any point along the integration path. We will employ the following three density scaling transformations:

(a) Linear scaling[16,23−25]

$$\rho_q(\mathbf{r}) = q\rho(\mathbf{r}) \quad (10)$$

which we will call here the q-scaling. A line of q-scaled densities from $q = 0$ to $q = 1$ will be referred to as a Q-path.

(b) Uniform number-conserving coordinate scaling studied extensively by Levy[26]

$$\rho_\lambda(\mathbf{r}) = \lambda^3\rho(\lambda\mathbf{r}) \quad (11)$$

or the λ-scaling. A line of λ-scaled densities from $\lambda = 0$ to $\lambda = 1$ will be called a Λ-path.

(c) Thomas−Fermi-inspired scaling introduced by Perdew and co-workers[27]

$$\rho_\zeta(\mathbf{r}) = \zeta^2\rho(\zeta^{1/3}\mathbf{r}) \quad (12)$$

which we will call the ζ-scaling. A line of ζ-scaled densities from $\zeta = 0$ to $\zeta = 1$ is termed a Z-path.

Among these paths, only the Λ-path conserves the electron number. The number of electrons along the Q- and Z-paths changes as qN and ζN, respectively, where N is the electron number at $\rho_1(\mathbf{r})$. Note that the condition $E_{xc}[\rho_0] = 0$ is trivially satisfied for the Q-path. For the Λ-path, $\rho_\lambda(\mathbf{r})$

becomes infinitely dilute (vanishes locally) as $\lambda \to 0$, so that $\lim_{\lambda\to 0} E_{xc}[\rho_\lambda] = 0$.[17,26,28] For the Z-path, both $\rho_\zeta(\mathbf{r})$ and $E_{xc}[\rho_\zeta]$ vanish in the $\zeta \to 0$ limit.

Partial derivatives of these scaled densities with respect to their scaling parameters are readily obtained by applying the chain rule of differentiation. For future reference, we write out the results

$$\frac{\partial \rho_q(\mathbf{r})}{\partial q} = \rho(\mathbf{r}) \tag{13}$$

$$\frac{\partial \rho_\lambda(\mathbf{r})}{\partial \lambda} = \lambda^2[3\rho(\lambda\mathbf{r}) + (\lambda\mathbf{r})\cdot\nabla_{\lambda\mathbf{r}}\rho(\lambda\mathbf{r})] \tag{14}$$

$$\frac{\partial \rho_\zeta(\mathbf{r})}{\partial \zeta} = \zeta\left[2\rho(\zeta^{1/3}\mathbf{r}) + \frac{\zeta^{1/3}\mathbf{r}}{3}\cdot\nabla_{\zeta^{1/3}\mathbf{r}}\rho(\zeta^{1/3}\mathbf{r})\right] \tag{15}$$

If $v_{xc}([\rho_t];\mathbf{r})$ and $\partial\rho_t(\mathbf{r})/\partial t$ in eq 5 are piecewise-continuous functions of $\mathbf{r}$ and t and if the real-space integral exists for every t, as can be expected for physical exchange-correlation potentials and reasonable scaling transformations of the density, then by Fubini's theorem[29] the order of integration over t and $\mathbf{r}$ in eq 5 can be interchanged. We will exploit this property repeatedly in sections 4−6.

4. Levy−Perdew Virial Relation

The Levy−Perdew virial relation is a special case of the generalized virial theorem derived by Ghosh and Parr[15] based on universal scaling properties of homogeneous density functionals. Here we would like to emphasize an even deeper generalization,[16] according to which the Levy−Perdew relation is a special case of the line integral (eq 5) taken along the Λ-path. To see this, recall that the functional derivative of any valid exchange functional is homogeneous of degree one with respect to the uniform density scaling[30,31]

$$v_x([\rho_\lambda];\mathbf{r}) = \lambda v_x([\rho];\lambda\mathbf{r}) \tag{16}$$

Using eqs 5, 14, and 16 we have

$$E_x[\rho] = \int_0^1 d\lambda \int d^3r \lambda v_x([\rho];\lambda\mathbf{r}) \times \lambda^2[3\rho(\lambda\mathbf{r}) + (\lambda\mathbf{r})\cdot\nabla_{\lambda\mathbf{r}}\rho(\lambda\mathbf{r})] \tag{17}$$

The parameter λ in the second integral can be eliminated by the variable change $\lambda\mathbf{r} \to \mathbf{r}'$. The result is

$$E_x[\rho] = \int_0^1 d\lambda \int d^3r' v_x([\rho];\mathbf{r}')[3\rho(\mathbf{r}') + \mathbf{r}'\cdot\nabla_{\mathbf{r}'}\rho(\mathbf{r}')] \tag{18}$$

where $d^3r' = d^3(\lambda r) \equiv d(\lambda x)d(\lambda y)d(\lambda z)$. Switching back to $\mathbf{r}$ and noting that the integral over λ is simply 1, we obtain

$$E_x[\rho] = \int d^3r v_x([\rho];\mathbf{r})[3\rho(\mathbf{r}) + \mathbf{r}\cdot\nabla\rho(\mathbf{r})] \tag{19}$$

An additional integration by parts in the last equation gives eq 4. The two forms of the Levy−Perdew reconstruction given by eqs 4 and 19 differ only by a gauge transformation of the energy density.

5. Examples

We will now illustrate how eq 5 can be used to reconstruct exchange and correlation density functionals from the corresponding functional derivatives. For verification purposes, our examples deliberately employ potentials whose parent functionals are known from the outset. Of course, in real-life applications of the line integral method, parent functionals would be normally unknown *a priori*.

5.1. Local Density Approximation for Exchange. Consider the local density approximation (LDA) for exchange

$$E_x^{LDA}[\rho] = -C_x \int d^3r \rho^{4/3}(\mathbf{r}) \tag{20}$$

where $C_x = (3/4)(3/\pi)^{1/3}$. The functional derivative of the LDA functional is

$$v_x^{LDA}([\rho];\mathbf{r}) = -\frac{4}{3}C_x\rho^{1/3}(\mathbf{r}) \tag{21}$$

Suppose we did *not* know what functional generated this potential. Let us employ the line integral method to reconstruct this "unknown" functional.

Under the q-scaling of the density, the LDA exchange potential transforms as

$$v_x^{LDA}([\rho_q];\mathbf{r}) = q^{1/3}v_x^{LDA}([\rho];\mathbf{r}) \tag{22}$$

Multiplying this potential by $\partial\rho_q(\mathbf{r})/\partial q = \rho(\mathbf{r})$ and integrating over q we obtain the Q-reconstruction

$$E_{x,Q}^{LDA}[\rho] = \frac{3}{4}\int d^3r \rho(\mathbf{r})v_x^{LDA}([\rho];\mathbf{r}) \tag{23}$$

which, in view of eq 21, is identical with $E_x^{LDA}[\rho]$.

Under the uniform density scaling, the LDA exchange potential transforms as

$$v_x^{LDA}([\rho_\lambda];\mathbf{r}) = \lambda v_x^{LDA}([\rho];\lambda\mathbf{r}) \tag{24}$$

Inserting the λ-scaled LDA potential into eq 5 (or directly into eq 19) we obtain the Λ-reconstruction

$$E_{x,\Lambda}^{LDA}[\rho] = \int d^3r v_x^{LDA}([\rho];\mathbf{r})[3\rho(\mathbf{r}) + \mathbf{r}\cdot\nabla\rho(\mathbf{r})] \tag{25}$$

which is just the Levy−Perdew relation. It is not obvious, but can be proven by invoking the divergence theorem, that the value of $E_{x,\Lambda}^{LDA}[\rho]$ is equal to $E_{x,Q}^{LDA}[\rho]$ for any ρ vanishing at infinity. Numerical evaluation of the integrals of eqs 23 and 25 for test densities also confirms their equivalence.

The Q- and Λ-reconstructions of the LDA for exchange are well-known results. In fact, eqs 23 and 25 are special cases of the scaling identities for strictly local functionals derived by Parr et al.[32] using the density functional expansion method.

Consider now the ζ-scaling of the LDA exchange potential

$$v_x^{LDA}([\rho_\zeta];\mathbf{r}) = \zeta^{2/3}v_x^{LDA}([\rho];\zeta^{1/3}\mathbf{r}) \tag{26}$$

Substitution of the ζ-scaled LDA exchange potential into the line integral formula yields

$$E_{x,Z}^{LDA}[\rho] = \int_0^1 d\zeta \int d^3r\, \zeta^{2/3} v_x^{LDA}([\rho];\zeta^{1/3}\mathbf{r}) \times \zeta\left[2\rho(\zeta^{1/3}\mathbf{r}) + \frac{\zeta^{1/3}\mathbf{r}}{3}\cdot\nabla_{\zeta^{1/3}\mathbf{r}}\rho(\zeta^{1/3}\mathbf{r})\right] \quad (27)$$

After the substitution $\zeta^{1/3}\mathbf{r}\rightarrow\mathbf{r}$ and integration over ζ we obtain the Z-reconstruction of the LDA

$$E_{x,Z}^{LDA}[\rho] = \frac{3}{5}\int d^3r\, v_x^{LDA}([\rho];\mathbf{r})\left[2\rho(\mathbf{r}) + \frac{\mathbf{r}}{3}\cdot\nabla\rho(\mathbf{r})\right] \quad (28)$$

This functional is actually a linear combination of the Q- and Λ-reconstructions, namely, $^4/_5E_{x,Q}^{LDA}[\rho] + {}^1/_5E_{x,\Lambda}^{LDA}[\rho]$, as can be seen by combining eqs 23 and 25. Since each of the Q- and Λ-reconstructions is numerically equivalent to $E_x^{LDA}[\rho]$, the value of $E_{x,Z}^{LDA}[\rho]$ is also equal to $E_x^{LDA}[\rho]$. Thus, eqs 23, 25, and 28 are different but equivalent representations of the same functional.

5.2. Generalized Gradient Approximation for Exchange. To illustrate how the line integral formalism works for gradient-dependent Kohn−Sham potentials, we will reconstruct the exchange functional of Gill[33]

$$E_x^{G96}[\rho] = E_x^{LDA}[\rho] - \int d^3r\,\beta\rho^{4/3}(\mathbf{r})s^{3/2}(\mathbf{r}) \quad (29)$$

where s is a dimensionless reduced gradient defined as

$$s = \frac{|\nabla\rho|}{\rho^{4/3}} \quad (30)$$

and $\beta = 2^{1/6}/137$ is a constant. The functional derivative of the Gill exchange can be written as

$$v_x^{G96}([\rho];\mathbf{r}) = v_x^{LDA}([\rho];\mathbf{r}) + w_x^{G96}([\rho];\mathbf{r}) \quad (31)$$

where the first term is given by eq 21 and

$$w_x^{G96}([\rho];\mathbf{r}) = \frac{2\beta}{3}\rho^{1/3}s^{3/2} + \nabla\cdot\left(\frac{3\beta}{2\rho^{4/3}s^{1/2}}\nabla\rho\right) \quad (32)$$

The last expression was obtained with the help of eq 3 and by using the identity $\partial s/\partial\nabla\rho = \rho^{-8/3}s^{-1}\nabla\rho$.

Under the q-scaling, $s_q(\mathbf{r}) = q^{-1/3}s(\mathbf{r})$, so the Gill potential becomes

$$v_x^{G96}([\rho_q];\mathbf{r}) = q^{1/3}v_x^{LDA}([\rho];\mathbf{r}) + q^{-1/6}w_x^{G96}([\rho];\mathbf{r}) \quad (33)$$

The line integral of this potential along the Q-path is

$$E_{x,Q}^{G96}[\rho] = E_x^{LDA}[\rho] + \frac{6}{5}\int d^3r\,\rho(\mathbf{r})w_x^{G96}([\rho];\mathbf{r}) \quad (34)$$

where we have utilized eq 23. The integral in eq 34 can be simplified through integration by parts to give

$$\int d^3r\,\rho(\mathbf{r})w_x^{G96}([\rho];\mathbf{r}) = -\frac{5}{6}\int d^3r\,\beta\rho^{4/3}s^{3/2} \quad (35)$$

Inserting this result into eq 34 we obtain the right-hand side of eq 29. Thus, the line integral of the Gill exchange potential along the Q-path recovers the energy density of the parent functional in the original gauge.

Under the λ-scaling, the Gill exchange potential transforms just like any other exchange potential

$$v_x^{G96}([\rho_\lambda];\mathbf{r}) = \lambda v_x^{G96}([\rho];\lambda\mathbf{r}) \quad (36)$$

so the line integral along the Λ-path is simply the Levy−Perdew reconstruction

$$E_{x,\Lambda}^{G96}[\rho] = E_x^{LDA}[\rho] + \int d^3r\, w_x^{G96}([\rho];\mathbf{r})[3\rho(\mathbf{r}) + \mathbf{r}\cdot\nabla\rho(\mathbf{r})] \quad (37)$$

Finally, under the ζ-scaling, $s_\zeta(\mathbf{r}) = \zeta^{-1/3}s(\zeta^{1/3}\mathbf{r})$, so

$$v_x^{G96}([\rho_\zeta];\mathbf{r}) = \zeta^{2/3}v_x^{LDA}([\rho];\zeta^{1/3}\mathbf{r}) + \zeta^{1/6}w_x^{G96}([\rho];\zeta^{1/3}\mathbf{r}) \quad (38)$$

The line integral along the Z-path is then

$$E_{x,Z}^{G96}[\rho] = E_x^{LDA}[\rho] + \frac{6}{7}\int d^3r\, w_x^{G96}([\rho];\mathbf{r})\left[2\rho(\mathbf{r}) + \frac{\mathbf{r}}{3}\cdot\nabla\rho(\mathbf{r})\right] \quad (39)$$

This functional is a linear combination of the Q- and Λ-reconstructions $E_{x,Q}^{G96}[\rho]$ and $E_{x,\Lambda}^{G96}[\rho]$ with the weights $^5/_7$ and $^2/_7$, respectively. Therefore, $E_{x,Z}^{G96}[\rho]$ is also numerically equivalent to the original $E_x^{G96}[\rho]$ up to a gauge transformation of the energy density.

It would be straightforward, although tedious, to carry out similar reconstructions for gradient-dependent exchange potentials derived from more complicated functionals such as Becke's 1988 exchange.[34] However, when the parent functional is known *a priori* in some gauge, such reconstructions are of interest only as ways of generating gauge-transformed energy densities.

5.3. Local Density Approximation for Correlation. Consider now the Wigner correlation functional[35]

$$E_c^W[\rho] = -\int d^3r\,\frac{a\rho}{b + r_s} \quad (40)$$

where $r_s = (3/4\pi\rho)^{1/3}$ and $a = 0.44$ and $b = 7.8$ are constants. The functional derivative of $E_c^W[\rho]$ is

$$v_c^W([\rho];\mathbf{r}) = -a\frac{b + (4/3)r_s(\mathbf{r})}{[b + r_s(\mathbf{r})]^2} \quad (41)$$

where we have used the fact that $dr_s/d\rho = -r_s/3\rho$. Let us reconstruct the Wigner correlation functional from $v_c^W([\rho];\mathbf{r})$ by using eq 5 and integrating the potential along three distinct density scaling paths.

The q-scaled Wigner correlation potential is

$$v_c^W([\rho_q];\mathbf{r}) = -a\frac{b + (4/3)q^{-1/3}r_s(\mathbf{r})}{[b + q^{-1/3}r_s(\mathbf{r})]^2} \quad (42)$$

The Q-reconstruction is, therefore

$$E_{c,Q}^W[\rho] = -a\int d^3r\,\rho(\mathbf{r})\int_0^1 dq\,\frac{b + (4/3)q^{-1/3}r_s}{(b + q^{-1/3}r_s)^2} = -\int d^3r\,\frac{a\rho(\mathbf{r})}{b + r_s(\mathbf{r})} \quad (43)$$

which is precisely the original functional $E_c^W[\rho]$.

Under the uniform density scaling, the Wigner correlation potential transforms as

$$v_c^W([\rho_\lambda];\mathbf{r}) = -a\frac{b + (4/3)\lambda^{-1}r_s(\lambda\mathbf{r})}{[b + \lambda^{-1}r_s(\lambda\mathbf{r})]^2} \quad (44)$$

The line integral along the Λ-path can be written as

$$E_{c,\Lambda}^W[\rho] = -a\int_0^1 d\lambda \int \frac{d^3(\lambda r)}{\lambda}\frac{b + (4/3)\lambda^{-1}r_s(\lambda\mathbf{r})}{[b + \lambda^{-1}r_s(\lambda\mathbf{r})]^2} \times [3\rho(\lambda\mathbf{r}) + (\lambda\mathbf{r})\cdot\nabla_{\lambda\mathbf{r}}\rho(\lambda\mathbf{r})] \quad (45)$$

Changing the real-space integration variable $\lambda\mathbf{r}\rightarrow\mathbf{r}$ and integrating over λ we obtain the Λ-reconstruction of the Wigner functional

$$E_{c,\Lambda}^W[\rho] = -a\int d^3r[3\rho(\mathbf{r}) + \mathbf{r}\cdot\nabla\rho(\mathbf{r})] \times \left[\frac{1}{b}\ln\frac{b + r_s}{r_s} + \frac{1}{3(b + r_s)}\right] \quad (46)$$

Similarly, we have derived the Z-reconstruction

$$E_{c,Z}^W[\rho] = -a\int d^3r\left[2\rho(\mathbf{r}) + \frac{\mathbf{r}}{3}\cdot\nabla\rho(\mathbf{r})\right] \times \left[\frac{1 - r_s/b - (3/2)(r_s/b)^2}{b + r_s} + \frac{3r_s^{3/2}\tan^{-1}\sqrt{b/r_s}}{2b^{5/2}}\right] \quad (47)$$

which, unlike the exchange functionals above, does not appear to be a linear combination of the Q- and Λ-reconstructions.

We have implemented the functionals $E_{c,\Lambda}^W[\rho]$ and $E_{c,Z}^W[\rho]$ in a development version of the Gaussian program[36] and evaluated them numerically for a number of atoms and molecules using several Gaussian basis sets and large real-space grids. Our calculations confirm that, within submicrohartree errors of the real-space integration, the correlation energies obtained by eqs 46 and 47 are exactly the same as those obtained by eq 40.

5.4. Generalized Gradient Approximation for Correlation. Consider the gradient-dependent Wilson−Levy correlation functional for spin-compensated systems[37]

$$E_c^{WL}[\rho] = \int d^3r\frac{(a_0 + a_1 s)\rho}{b_0 + b_1 s + r_s} \quad (48)$$

where s is the dimensionless reduced density gradient given by eq 30 and $a_0 = -0.74860$, $a_1 = 0.06001$, $b_0 = 3.60073$, and $b_1 = 2^{4/3}b_1'$, where $b_1' = 0.90000$ are constants. The functional derivative of this approximation can be written as

$$v_c^{WL}([\rho];\mathbf{r}) = \frac{\partial f_c^{WL}}{\partial\rho} - \nabla\cdot\left(\frac{\partial f_c^{WL}}{\partial\nabla\rho}\right) \quad (49)$$

where

$$f_c^{WL} = \frac{(a_0 + a_1 s)\rho}{b_0 + b_1 s + r_s} \quad (50)$$

is the correlation energy density in the initial gauge and

$$\frac{\partial f_c^{WL}}{\partial\rho} = \frac{a_0 - a_1 s/3}{b_0 + b_1 s + r_s} - \frac{1}{3}\frac{(r_s - 4b_1 s)(a_0 + a_1 s)}{(b_0 + b_1 s + r_s)^2} \quad (51)$$

$$\frac{\partial f_c^{WL}}{\partial\nabla\rho} = \left[\frac{a_1 s\rho^{-5/3}}{b_0 + b_1 s + r_s} - \frac{(a_0 + a_1 s)b_1\rho^{-8/3}}{(b_0 + b_1 s + r_s)^2}\right]\nabla\rho \quad (52)$$

Rewriting eq 49 in terms of ρ_q and substituting the result into eq 5 we obtain for the Q-reconstruction

$$E_{c,Q}^{WL}[\rho] = \int d^3r\rho(\mathbf{r})\tilde{v}_{c,Q}^{WL}([\rho];\mathbf{r}) \quad (53)$$

where $\tilde{v}_{c,Q}^{WL}$ is the *hypercorrelated*[9] potential defined by

$$\tilde{v}_{c,Q}^{WL}([\rho];\mathbf{r}) = \int_0^1 dq\, v_c^{WL}([\rho_q];\mathbf{r}) \quad (54)$$

which can be evaluated analytically. Alternatively, one can first simplify the Hessian-dependent term in eq 53 through integration by parts and then integrate the result over q. In the latter case, the Q-reconstructed energy density is identical with the f_c^{WL} of eq 50.

Before proceeding further, we point out that analytical integration over the density scaling parameter can be too complicated to be worth pursuing. In such cases, it is much more efficient to evaluate the line integral *numerically* for each real-space grid point $\mathbf{r}$ using a one-dimensional Gauss−Legendre quadrature[38] with a sufficient number of nodes. After the numerical integration over the density scaling parameter at each $\mathbf{r}$ is completed, the real-space integration is performed as usual using standard three-dimensional quadratures. The overhead cost associated with the numerical integration over a density scaling parameter is actually quite small. As a test, we have implemented a 64-point Gauss−Legendre quadrature over q in eq 53 (after it was simplified by real-space integration by parts) and used it for a number of atomic and molecular densities. The agreement between the total correlation energies obtained by analytical and numerical integration over q is excellent.

We have also implemented a Λ-path reconstruction of the Wilson−Levy correlation functional using 16-, 32-, and 64-node Gauss−Legendre quadratures for the integral over λ. Provided that a large basis set is used (e.g., the universal Gaussian basis set of ref 39), the agreement between the Λ-reconstruction of the Wilson−Levy functional and its conventional implementation can be made better than 1 microhartree.

We have not evaluated the line integral of the Wilson−Levy correlation potential along the Z-path, but it would not be difficult to do so using numerical quadratures.

5.5. Functionals Other Than Exchange-Correlation. So far, we have dealt exclusively with exchange-correlation functionals and potentials. However, the line integration technique is very general in that it applies to functionals of any other type. We shall illustrate this with examples involving the Coulomb repulsion and the von Weizsäcker kinetic energy functionals.

The Coulomb repulsion functional is

$$J[\rho] = \frac{1}{2}\int \mathrm{d}^3r \int \mathrm{d}^3r' \, \frac{\rho(\mathbf{r})\rho(\mathbf{r}')}{|\mathbf{r}-\mathbf{r}'|} \tag{55}$$

and has the following functional derivative

$$v_J([\rho];\mathbf{r}) = \int \mathrm{d}^3r' \, \frac{\rho(\mathbf{r}')}{|\mathbf{r}-\mathbf{r}'|} \tag{56}$$

The q-scaled Coulomb potential is

$$v_J([\rho_q];\mathbf{r}) = q v_J([\rho];\mathbf{r}) \tag{57}$$

The line integral along the Q-path recovers the Coulomb energy density in the original gauge

$$J_{\mathrm{Q}}[\rho] = \frac{1}{2}\int \mathrm{d}^3r \rho(\mathbf{r}) v_J([\rho];\mathbf{r}) = J[\rho] \tag{58}$$

In contrast, line integrals of the Coulomb potential along the Λ- and Z-paths result in gauge-transformed Coulomb energy densities. Specifically, under the λ-scaling

$$v_J([\rho_\lambda];\mathbf{r}) = \lambda v_J([\rho];\lambda\mathbf{r}) \tag{59}$$

so the line integral is

$$J_{\Lambda}[\rho] = \int \mathrm{d}^3r \, v_J([\rho];\mathbf{r})[3\rho(\mathbf{r}) + \mathbf{r}\cdot\nabla\rho(\mathbf{r})] \tag{60}$$

This functional is numerically equivalent to $J[\rho]$ because it has the same value for an arbitrary density (which can be verified numerically). Similarly, under the ζ-scaling

$$v_J([\rho_\zeta];\mathbf{r}) = \zeta^{4/3} v_J([\rho];\zeta^{1/3}\mathbf{r}) \tag{61}$$

so the Z-reconstruction of the Coulomb repulsion is

$$J_{\mathrm{Z}}[\rho] = \frac{3}{7}\int \mathrm{d}^3r \, v_J([\rho];\mathbf{r})\left[2\rho(\mathbf{r}) + \frac{\mathbf{r}}{3}\cdot\nabla\rho(\mathbf{r})\right] \tag{62}$$

This functional is a linear combination of the functionals $J_{\mathrm{Q}}[\rho]$ and $J_{\Lambda}[\rho]$ with coefficients $^6/_7$ and $^1/_7$, respectively. Therefore, $J_{\mathrm{Z}}[\rho] = J[\rho]$ for an arbitrary ρ.

Next consider the von Weizsäcker kinetic energy functional which is defined by

$$T_W[\rho] = \int \mathrm{d}^3r t_W(\mathbf{r}) = \int \mathrm{d}^3r \, \frac{1}{8}\frac{|\nabla\rho(\mathbf{r})|^2}{\rho(\mathbf{r})} \tag{63}$$

Using eq 3, we obtain the functional derivative

$$v_W([\rho];\mathbf{r}) = \frac{t_W}{\rho} - \frac{1}{4}\frac{\nabla^2\rho}{\rho} \tag{64}$$

Under the q-scaling

$$v_W([\rho_q];\mathbf{r}) = \frac{t_W(\mathbf{r})}{\rho(\mathbf{r})} - \frac{1}{4}\frac{\nabla^2\rho(\mathbf{r})}{\rho(\mathbf{r})} = v_W([\rho];\mathbf{r}) \tag{65}$$

so the Q-path reconstruction yields

$$\begin{aligned} T_W^{\mathrm{Q}}[\rho] &= \int \mathrm{d}^3r \, v_W([\rho];\mathbf{r})\rho(\mathbf{r}) \\ &= \int \mathrm{d}^3r\left[t_W(\mathbf{r}) - \frac{1}{4}\nabla^2\rho(\mathbf{r})\right] \end{aligned} \tag{66}$$

which equals $T_W[\rho]$ because the Laplacian of $\rho(\mathbf{r})$ integrates to zero.

Under the uniform density scaling

$$v_W([\rho_\lambda];\mathbf{r}) = \lambda^2 v_W([\rho];\lambda\mathbf{r}) \tag{67}$$

so the line integral along the Λ-path is

$$T_W^{\Lambda}[\rho] = \frac{1}{2}\int \mathrm{d}^3r \, v_W([\rho];\mathbf{r})[3\rho(\mathbf{r}) + \mathbf{r}\cdot\nabla\rho(\mathbf{r})] \tag{68}$$

Finally, under the ζ-scaling we have

$$v_W([\rho_\zeta];\mathbf{r}) = \zeta^{2/3} v_W([\rho];\zeta^{1/3}\mathbf{r}) \tag{69}$$

and the line integral along the Z-path yields

$$T_W^{\mathrm{Z}}[\rho] = \frac{3}{5}\int \mathrm{d}^3r \, v_W([\rho];\mathbf{r})\left[2\rho(\mathbf{r}) + \frac{\mathbf{r}}{3}\cdot\nabla\rho(\mathbf{r})\right] \tag{70}$$

This functional is the sum of $^3/_5 T_W^{\mathrm{Q}}[\rho]$ and $^2/_5 T_W^{\Lambda}[\rho]$. Hence, $T_W^{\mathrm{Z}}[\rho] = T_{\mathrm{W}}[\rho]$.

An example of a reconstruction of the noninteracting kinetic energy functional $T_s[\rho]$ from the exact kinetic potential via the generalized Ghosh−Parr virial relation[15] has been given by King and Handy.[40] We remark here that their method is equivalent to performing a Λ-reconstruction of the $T_s[\rho]$ functional.

6. Potentials That Are Not Functional Derivatives

Not every analytical expression constructed from $\rho(\mathbf{r})$, $\nabla\rho(\mathbf{r})$, and $\nabla^2\rho(\mathbf{r})$ is a functional derivative of some generalized gradient approximation with respect to $\rho(\mathbf{r})$. In order for a model potential $v_M([\rho];\mathbf{r})$ to be a functional derivative of some density functional, it must satisfy the condition[16,31]

$$\frac{\delta v_M([\rho];\mathbf{r})}{\delta\rho(\mathbf{r}')} = \frac{\delta v_M([\rho];\mathbf{r}')}{\delta\rho(\mathbf{r})} \tag{71}$$

A model potential $v_M([\rho];\mathbf{r})$ that does not have a parent density functional from which it can be derived by eq 1 will be called here a *stray* potential. Existence of stray potentials adds an interesting dimension to the density functional reconstruction problem because the line integral evaluated for a stray potential is path-dependent.[16] This principle can be used as a test for stray potentials.

Consider, for example, the following problem:[41] Does there exist a density functional for which the expression

$$v_M([\rho];\mathbf{r}) = \frac{|\nabla\rho(\mathbf{r})|}{\rho(\mathbf{r})} \tag{72}$$

is a functional derivative? We will show that the answer to this question is negative.

Under the q-scaling, this "potential" is unchanged

$$v_M([\rho_q];\mathbf{r}) = \frac{|\nabla\rho_q|}{\rho_q} = v_M([\rho];\mathbf{r}) \tag{73}$$

Therefore, the line integral along the Q-path is

$$I_{\mathrm{Q}} = \int_0^1 \mathrm{d}q \int \mathrm{d}^3r \, v_M([\rho_q];\mathbf{r})\frac{\partial\rho_q(\mathbf{r})}{\partial q} = \int \mathrm{d}^3r |\nabla\rho(\mathbf{r})| \tag{74}$$

Under the uniform density scaling

$$v_M([\rho_\lambda];\mathbf{r}) = \frac{|\nabla\rho_\lambda|}{\rho_\lambda} = \lambda v_M([\rho];\lambda\mathbf{r}) \tag{75}$$

so the line integral along the Λ-path is

$$I_\Lambda = \int_0^1 \mathrm{d}\lambda \int \mathrm{d}^3 r\, v_M([\rho_\lambda];\mathbf{r}) \frac{\partial \rho_\lambda(\mathbf{r})}{\partial \lambda} = \int \mathrm{d}^3 r \frac{|\nabla \rho(\mathbf{r})|}{\rho(\mathbf{r})} [3\rho(\mathbf{r}) + \mathbf{r}\cdot\nabla\rho(\mathbf{r})] \quad (76)$$

Finally, under the ζ-scaling

$$v_M([\rho_\zeta];\mathbf{r}) = \frac{|\nabla \rho_\zeta(\mathbf{r})|}{\rho_\zeta(\mathbf{r})} = \zeta^{1/3} v_M([\rho];\zeta^{1/3}\mathbf{r}) \quad (77)$$

and the line integral along the Z-path is

$$I_Z = \int_0^1 \mathrm{d}\zeta \int \mathrm{d}^3 r\, v_M([\rho_\zeta];\mathbf{r}) \frac{\partial \rho_\zeta(\mathbf{r})}{\partial \zeta} = \frac{3}{4} \int \mathrm{d}^3 r \frac{|\nabla \rho(\mathbf{r})|}{\rho(\mathbf{r})} \left[2\rho(\mathbf{r}) + \frac{\mathbf{r}}{3}\cdot\nabla\rho(\mathbf{r})\right] \quad (78)$$

It is easy to see that the three reconstructions are related to each other by the equation $I_Z = {}^3/_4 I_Q + {}^1/_4 I_\Lambda$.

We have evaluated numerically the three integrals given by eqs 74, 76, and 78 for a number of atoms and molecules and, for each system, obtained three different values. For example, using the Hartree−Fock densities of the Ne atom obtained in the universal Gaussian basis set of ref 39, we found (in atomic units) $I_Q = 62.227$, $I_\Lambda = 22.424$, and $I_Z = 52.276$. Therefore, the quantity defined by eq 72 is not a functional derivative of any density functional with respect to $\rho(\mathbf{r})$.

Many of the model Kohn−Sham potentials for exact exchange proposed in the literature[42−51] are probably stray. For example, Levy−Perdew virial energies obtained from several such approximations deviate by up to a few hartrees from the correct exact-exchange values.[52]

7. Discussion

The significance of the van Leeuwen−Baerends method for computational density functional theory is not difficult to appreciate. Since line integrals of analytical potentials can be evaluated efficiently, one can turn the Kohn−Sham scheme inside out and model the Kohn−Sham exchange-correlation potential directly[42−51] instead of approximating the density functional. This is possible because only the potential is required in principle to solve the Kohn−Sham equations, while the energy is an add-on that can be evaluated only when needed (e.g., to distinguish the true solution from false minima).

Generally, when a model Kohn−Sham potential has a simple behavior under some scaling transformation of the density, it is possible to evaluate the line integral analytically to obtain a closed-form expression that relates the unscaled potential directly to the energy. The Levy−Perdew−Ghosh−Parr virial relation can be viewed as a special case of line integrals for potentials that are homogeneous under uniform density scaling. Exchange, Coulomb repulsion, and noninteracting kinetic energy functionals all fall into this category. By contrast, the exact correlation potential and realistic approximations to it are not homogeneous with respect to any simple density scaling transformation.

It is pertinent to note that the exact and even some approximate exchange-correlation potentials jump by a constant when the electron number in a partially filled electronic shell or subshell crosses an integer.[53−55] Discontinuous changes of $v_{xc}([\rho_t];\mathbf{r})$ along a number-nonconserving integration path would certainly complicate the line integral method.[16,17] Fortunately, no discontinuities arise at any point of the number-nonconserving Q- and Z-paths for the local and semilocal approximations considered in this work, not least because the q-scaling and ζ-scaling are very different from the consecutive (Aufbau) filling of Kohn−Sham orbitals.

We have seen that the line integral method generally recovers the parent density functional $E_{xc}[\rho]$ from a functional derivative $v_{xc}([\rho_t];\mathbf{r})$ only up to a gauge transformation of the energy density. Drawing on the idea of Burke and co-workers,[8−11] we can define the hypercorrelated exchange-correlation energy density

$$\tilde{f}_{xc}(\mathbf{r}) = \int_0^1 \mathrm{d}t\, v_{xc}([\rho_t];\mathbf{r}) \frac{\partial \rho_t(\mathbf{r})}{\partial t} \quad (79)$$

Then a choice of the density scaling path in eq 79 amounts to defining a gauge transformation for the exchange-correlation energy density. In particular, integration along the Λ-path yields the virial energy density of refs 16 and 8−11

$$\tilde{f}_{xc}^{\Lambda}(\mathbf{r}) = \int_0^1 \frac{\mathrm{d}\lambda}{\lambda} v_{xc}\left([\rho_\lambda];\frac{\mathbf{r}}{\lambda}\right)[3\rho(\mathbf{r}) + \mathbf{r}\cdot\nabla\rho(\mathbf{r})] \quad (80)$$

where we have made the substitution $\lambda\mathbf{r}\rightarrow\mathbf{r}$ to avoid the appearance of λ on the left-hand side. The line integral along the Q-path formally defines the energy density

$$\tilde{f}_{xc}^{Q}(\mathbf{r}) = \rho(\mathbf{r}) \int_0^1 \mathrm{d}q\, v_{xc}([\rho_q];\mathbf{r}) \quad (81)$$

which, in contrast to the virial energy density of eq 80, does not depend on the choice of origin and is constant within a finite volume of a uniform electron gas. For purely local approximations, where $v_{xc}([\rho];\mathbf{r}) = \partial f_{xc}/\partial\rho$, one can show that $\tilde{f}_{xc}^{Q}(\mathbf{r}) = f_{xc}(\mathbf{r})$, which explains the coincidences noted after eqs 23 and 43. Integration along the Z-path gives a third energy density

$$\tilde{f}_{xc}^{Z}(\mathbf{r}) = \int_0^1 \mathrm{d}\zeta\, v_{xc}\left([\rho_\zeta];\frac{\mathbf{r}}{\zeta^{1/3}}\right)\left[2\rho(\mathbf{r}) + \frac{\mathbf{r}}{3}\cdot\nabla\rho(\mathbf{r})\right] \quad (82)$$

where we have made the replacement $\zeta^{1/3}\mathbf{r}\rightarrow\mathbf{r}$.

When $v_{xc}([\rho];\mathbf{r})$ is a functional derivative, the total exchange-correlation energies obtained by integrating the energy densities of eqs 80−82 may not coincide exactly in finite basis sets, but these discrepancies disappear in the complete basis set limit.

8. Conclusions

We have demonstrated that it is relatively easy to reconstruct an exchange-correlation density functional from the corresponding functional derivative $v_{xc}([\rho];\mathbf{r})$ if the latter is

known explicitly in terms of the density. This requires evaluating the van Leeuwen−Baerends line integral along some path of parametrized densities. The linear density scaling path (Q-path) and the uniform density scaling path (Λ-path) are two convenient choices. When $v_{xc}([\rho]; \mathbf{r})$ is homogeneous with respect to the chosen density scaling, the line integration can be completed analytically to give a closed-form expression similar to the generalized Ghosh−Parr virial relation. The choice of the density transformation path determines the gauge of the reconstructed exchange-correlation energy density.

If the potential $v_{xc}([\rho]; \mathbf{r})$ is stray, that is, not a functional derivative of some density functional, then a) the line integral is path-dependent and b) the Kohn−Sham equations do not represent a solution to a variational energy minimization problem. This implies that exchange-correlation energies assigned to stray potentials are somewhat arbitrary and, hence, should be interpreted with caution. Most semilocal exchange-correlation potentials modeled from Kohn−Sham orbitals are probably stray because an arbitrary combination of $\rho(\mathbf{r})$ and its derivatives is very unlikely to be a functional derivative of some density functional.[56] Nevertheless, a line integral energy expression obtained for a stray potential may still be used to *define* a new density functional approximation.

We conclude by reiterating Mel Levy's yet unfulfilled prediction[19] that the line integral method will play an increasingly prominent role in future developments of density functional theory.

Acknowledgment. This work is dedicated to Professor John P. Perdew on the occasion of his 65th birthday. Financial support was provided by the Natural Sciences and Engineering Research Council of Canada (NSERC) through the Discovery Grants Program.

Appendix: Differentiation of a Functional with Respect to Parameter of the Function

The chain rule for differentiation of a functional of a parametrized density with respect to the parameter (eq 7) follows directly from eq A.33 of ref 2. Here we will give an alternative derivation of this formula. As in ref 2, we will consider the case of a one-dimensional density $\rho(x)$ and a functional that depends on x, $\rho(x)$, and $\rho'(x) \equiv \mathrm{d}\rho/\mathrm{d}x$ only. Generalizations of the following proof to three dimensions and higher derivatives are straightforward.

Consider a general density functional of the form

$$E[\rho_t] = \int_{-\infty}^{\infty} f(x, \rho_t, \rho_t')\,\mathrm{d}x \tag{83}$$

where $\rho_t(x)$ is a parametrized density and $\rho_t' \equiv \mathrm{d}\rho_t(x)/\mathrm{d}x$. Let us treat the scaling parameter t as an argument of ρ, that is, $\rho_t(x) \equiv \rho(x, t)$. Then $\rho_t' = \partial\rho(x, t)/\partial x$. Differentiation of eq 83 with respect to t gives

$$\frac{\mathrm{d}E[\rho_t]}{\mathrm{d}t} = \int_{-\infty}^{\infty}\left(\frac{\partial f}{\partial \rho_t}\frac{\partial \rho_t}{\partial t} + \frac{\partial f}{\partial \rho_t'}\frac{\partial \rho_t'}{\partial t}\right)\mathrm{d}x \tag{84}$$

Since $\partial\rho_t'/\partial t = \partial^2\rho(x, t)/\partial x\partial t$, we can integrate the second term in the parentheses by parts. Assuming that the product $(\partial f/\partial\rho_t')\partial\rho(x, t)/\partial t$ vanishes as $x \to \pm\infty$ (as it should in any finite system), we obtain

$$\begin{aligned}\int_{-\infty}^{\infty}\frac{\partial f}{\partial \rho_t'}\frac{\partial \rho_t'}{\partial t}\,\mathrm{d}x &= \int_{-\infty}^{\infty}\frac{\partial f}{\partial \rho_t'}\frac{\partial^2\rho(x, t)}{\partial x\partial t}\,\mathrm{d}x \\ &= -\int_{-\infty}^{\infty}\left(\frac{\mathrm{d}}{\mathrm{d}x}\frac{\partial f}{\partial \rho_t'}\right)\frac{\partial\rho(x, t)}{\partial t}\,\mathrm{d}x\end{aligned} \tag{85}$$

Substitution of this result into eq 84 yields

$$\frac{\mathrm{d}E[\rho_t]}{\mathrm{d}t} = \int_{-\infty}^{\infty}\left(\frac{\partial f}{\partial \rho_t} - \frac{\mathrm{d}}{\mathrm{d}x}\frac{\partial f}{\partial \rho_t'}\right)\frac{\partial \rho_t}{\partial t}\,\mathrm{d}x \tag{86}$$

The expression in parentheses is the functional derivative of $E[\rho_t]$ with respect to ρ_t.[4] Thus, we can write

$$\frac{\mathrm{d}E[\rho_t]}{\mathrm{d}t} = \int_{-\infty}^{\infty}\frac{\delta E[\rho_t]}{\delta \rho_t}\frac{\partial \rho_t}{\partial t}\,\mathrm{d}x \tag{87}$$

which completes the proof.

References

(1) Kohn, W.; Sham, L. J. *Phys. Rev.* **1965**, *140*, A1133.

(2) Parr, R. G.; Yang, W. *Density-Functional Theory of Atoms and Molecules*; Oxford University Press: New York, 1989.

(3) Dreizler, R. M.; Gross, E. K. U. *Density Functional Theory*; Springer: Berlin, 1990.

(4) Arfken, G. B.; Weber, H. J. *Mathematical Methods for Physicists*, 4th ed.; Academic Press: San Diego, 1995; pp 952−991.

(5) Kümmel, S.; Kronik, L. *Rev. Mod. Phys.* **2008**, *80*, 3.

(6) Grabo, T.; Kreibich, T.; Kurth, S.; Gross, E. K. U. In *Strong Coulomb Correlations in Electronic Structure Calculations*; Anisimov, V. I., Ed.; Gordon and Breach: Amsterdam, 2000; pp 203−311.

(7) Engel, E. In *A Primer in Density Functional Theory*; Fiolhais, C., Nogueira, F., Marques, M., Eds.; Springer: Berlin, 2003; pp 56−122.

(8) Lam, K.-C.; Cruz, F. G.; Burke, K. *Int. J. Quantum Chem.* **1998**, *69*, 533.

(9) Cruz, F. G.; Lam, K.-C.; Burke, K. *J. Phys. Chem. A* **1998**, *102*, 4911.

(10) Burke, K.; Cruz, F. G.; Lam, K.-C. *J. Chem. Phys.* **1998**, *109*, 8161.

(11) Burke, K.; Cruz, F. G.; Lam, K.-C. *Int. J. Quantum Chem.* **1998**, *70*, 583.

(12) Springborg, M.; Dahl, J. P. *J. Chem. Phys.* **1999**, *110*, 9360.

(13) Tao, J.; Staroverov, V. N.; Scuseria, G. E.; Perdew, J. P. *Phys. Rev. A* **2008**, *77*, 012509.

(14) Levy, M.; Perdew, J. P. *Phys. Rev. A* **1985**, *32*, 2010.

(15) Ghosh, S. K.; Parr, R. G. *J. Chem. Phys.* **1985**, *82*, 3307.

(16) van Leeuwen, R.; Baerends, E. J. *Phys. Rev. A* **1995**, *51*, 170.

(17) van Leeuwen, R.; Gritsenko, O. V.; Baerends, E. J. *Top. Curr. Chem.* **1996**, *180*, 107.

(18) van Leeuwen, R. Ph.D. Thesis, Vrije Universiteit Amsterdam, 1994.

(19) Levy, M. In *Recent Development and Applications of Modern Density Functional Theory*; Seminario, J. M., Ed.; Elsevier: Amsterdam, 1996; pp 3−24.

(20) Parr, R. G.; Ghosh, S. K. *Phys. Rev. A* **1995**, *51*, 3564.

(21) Karasiev, V.; López-Boada, R. *Phys. Rev. A* **1998**, *58*, 1954.

(22) Karasiev, V. V.; Ludeña, E. V.; Valderrama, E. In *Recent Advances in Density Functional Methods, Part III*; Barone, V., Bencini, A., Fantucci, P., Eds.; World Scientific: Singapore, 2002; pp 224−233.

(23) Liu, S.; Parr, R. G. *Phys. Rev. A* **1996**, *53*, 2211.

(24) Chan, G. K.-L.; Handy, N. C. *Phys. Rev. A* **1999**, *59*, 2670.

(25) Nagy, Á. *J. Chem. Phys.* **2005**, *123*, 044105.

(26) Levy, M. In *Density Functional Theory*; Gross, E. K. U., Dreizler, R. M., Eds.; Plenum: New York, 1995; pp 11−31.

(27) Perdew, J. P.; Constantin, L. A.; Sagvolden, E.; Burke, K. *Phys. Rev. Lett.* **2006**, *97*, 223002.

(28) Levy, M. *Phys. Rev. A* **1991**, *43*, 4637.

(29) Korn, G. A.; Korn, T. M. *Mathematical Handbook for Scientists and Engineers: Definitions, Theorems, and Formulas for Reference and Review*, 2nd ed.; McGraw-Hill: New York, 1968; p 108.

(30) Ou-Yang, H.; Levy, M. *Phys. Rev. Lett.* **1990**, *65*, 1036.

(31) Ou-Yang, H.; Levy, M. *Phys. Rev. A* **1991**, *44*, 54.

(32) Parr, R. G.; Liu, S.; Kugler, A. A.; Nagy, Á. *Phys. Rev. A* **1995**, *52*, 969.

(33) Gill, P. M. W. *Mol. Phys.* **1996**, *89*, 433.

(34) Becke, A. D. *Phys. Rev. A* **1988**, *38*, 3098.

(35) Pines, D. In *Solid State Physics*; Seitz, F., Turnbull, D., Eds.; Academic Press: New York, 1955; Vol. 1, p 375.

(36) Frisch, M. J.; Trucks, G. W.; Schlegel, H. B.; Scuseria, G. E.; Robb, M. A.; Cheeseman, J. R.; Montgomery, J. A., Jr.; Vreven, T.; Scalmani, G.; Mennucci, B.; Barone, V.; Petersson, G. A.; Caricato, M.; Nakatsuji, H.; Hada, M.; Ehara, M.; Toyota, K.; Fukuda, R.; Hasegawa, J.; Ishida, M.; Nakajima, T.; Honda, Y., Kitao, O.; Nakai, H.; Li, X.; Hratchian, H. P.; Peralta, J. E.; Izmaylov, A. F.; Kudin, K. N.; Heyd, J. J.; Brothers, E.; Staroverov, V. N.; Zheng, G.; Kobayashi, R.; Normand, J.; Sonnenberg, J. L.; Iyengar, S. S.; Tomasi, J.; Cossi, M.; Rega, N.; Burant, J. C.; Millam, J. M.; Klene, M.; Knox, J. E.; Cross, J. B.; Bakken, V.; Adamo, C.; Jaramillo, J.; Gomperts, R.; Stratmann, R. E.; Yazyev, O.; Austin, A. J.; Cammi, R.; Pomelli, C.; Ochterski, J. W.; Ayala, P. Y.; Morokuma, K.; Voth, G. A.; Salvador, P.; Dannenberg, J. J.; Zakrzewski, V. G.; Dapprich, S.; Daniels, A. D.; Strain, M. C.; Farkas, O.; Malick, D. K.; Rabuck, A. D.; Raghavachari, K.; Foresman, J. B.; Ortiz, J. V.; Cui, Q.; Baboul, A. G.; Clifford, S.; Cioslowski, J.; Stefanov, B. B.; Liu, G.; Liashenko, A.; Piskorz, P.; Komaromi, I.; Martin, R. L.; Fox, D. J.; Keith, T.; Al-Laham, M. A.; Peng, C. Y.; Nanayakkara, A.; Challacombe, M.; Chen, W.; Wong, M. W.; Pople, J. A. *Gaussian Development Version, Revision F.02*; Gaussian, Inc.: Wallingford, CT, 2006.

(37) Wilson, L. C.; Levy, M. *Phys. Rev. B* **1990**, *41*, 12930.

(38) Press, W. H.; Teukolsky, S. A.; Vetterling, W. T.; Flannery, B. P. *Numerical Recipes in Fortran 77: The Art of Scientific Computing*, 2nd ed.; Cambridge University Press: Cambridge, 1992; pp 140−155.

(39) de Castro, E. V. R.; Jorge, F. E. *J. Chem. Phys.* **1998**, *108*, 5225.

(40) King, R. A.; Handy, N. C. *Phys. Chem. Chem. Phys.* **2000**, *2*, 5049.

(41) Savin, A. Private communication.

(42) van Leeuwen, R.; Baerends, E. J. *Phys. Rev. A* **1994**, *49*, 2421.

(43) Lembarki, A.; Rogemond, F.; Chermette, H. *Phys. Rev. A* **1995**, *52*, 3704.

(44) Gritsenko, O.; van Leeuwen, R.; van Lenthe, E.; Baerends, E. J. *Phys. Rev. A* **1995**, *51*, 1944.

(45) Gritsenko, O. V.; van Leeuwen, R.; Baerends, E. J. *Int. J. Quantum Chem.* **1997**, *61*, 231.

(46) Gritsenko, O. V.; Schipper, P. R. T.; Baerends, E. J. *Int. J. Quantum Chem.* **2000**, *76*, 407.

(47) Harbola, M. K.; Sen, K. D. *Int. J. Quantum Chem.* **2002**, *90*, 327.

(48) Harbola, M. K.; Sen, K. D. *Bull. Mater. Sci.* **2003**, *26*, 69.

(49) Umezawa, N. *Phys. Rev. A* **2006**, *74*, 032505.

(50) Becke, A. D.; Johnson, E. R. *J. Chem. Phys.* **2006**, *124*, 221101.

(51) Staroverov, V. N. *J. Chem. Phys.* **2008**, *129*, 134103.

(52) Gaiduk, A. P.; Staroverov, V. N. *J. Chem. Phys.* **2008**, *128*, 204101.

(53) Perdew, J. P.; Parr, R. G.; Levy, M.; Balduz, J. L., Jr. *Phys. Rev. Lett.* **1982**, *49*, 1691.

(54) Perdew, J. P. In *Density Functional Methods in Physics*; Dreizler, R. M., da Providência, J., Eds.; Plenum: New York, 1985; pp 265−308.

(55) Armiento, R.; Kümmel, S.; Körzdörfer, T. *Phys. Rev. B* **2008**, *77*, 165106.

(56) Perdew, J. P. Private communication.

CT800514Z

JCTC Journal of Chemical Theory and Computation

Extension to Negative Values of the Coupling Constant of Adiabatic Connection for Interaction-Strength Interpolation

Jianwei Sun*

Department of Physics and Quantum Theory Group, Tulane University, New Orleans, Louisiana 70118

Received November 30, 2008

Abstract: A new exchange and correlation functional, called ISIN here, of the fifth rung of Jacob's ladder is presented. It is based on the explicit approximation of W_λ, the integrand in the adiabatic connection (AC) with λ representing the coupling constant. Besides utilizing the two leading terms of each asymptotic expansion of W_λ at $\lambda = 0$ and ∞, the ISIN extends the coupling constant λ to negative values (i.e., to attractive electron−electron interactions). For the simple system of two electrons on the surface of a sphere (2ESS), the correlation energies yielded by the ISIN are in excellent agreement with the exact values. However, the ISIN seriously fails to approximate W_λ when W_0, the slope at $\lambda = 0$, goes to $-\infty$, which leads to much more negative correlation energies for real systems.

1. Introduction

In recent years, density-functional theory (DFT)[1,2] has become one of the most frequently applied methods in many-body theory, largely due to the fact that the basic variable in DFT is the simple, non-negative particle density $n(\mathbf{r})$, instead of the complicated (correlated) N-particle wave function ψ. In principle, the exact ground-state energy of the interacting N-electron system, including the correlation energy missed in the Hartree−Fock (HF) theory, can be obtained by solving the Kohn−Sham (KS) single-particle equations of the auxiliary noninteracting system, given the exact density functional $E_{xc}[n]$ for the exchange-correlation energy. In practice, however, $E_{xc}[n]$ must be approximated, and the accuracy of the approximation therefore determines the success of KS DFT. Significant insight into this quantity is obtained from the adiabatic connection (AC),[3−10] which smoothly connects the KS noninteracting system to the interacting physical system.

With the aid of the adiabatic connection, $E_{xc}[n]$ is represented by the coupling-constant integral[3,4]

$$E_{xc}[n] = \int_0^1 d\lambda W_\lambda[n] \tag{1}$$

$$W_\lambda[n] = \langle \psi^\lambda | \hat{V}_{ee} | \psi^\lambda \rangle - U[n] \tag{2}$$

Here, $U[n]$ is the classical coulomb energy of a continuous charge distribution with density $n(\mathbf{r})$

$$U[n] = \frac{1}{2} \int d^3r \int d^3r' \frac{n(\mathbf{r})n(\mathbf{r}')}{|\mathbf{r} - \mathbf{r}'|} \tag{3}$$

$\hat{V}_{ee} = ((e^2)/2)\sum_{i=1}^{N}\sum_{j(i\neq j)=1}^{N}|\hat{\mathbf{r}}_i - \hat{\mathbf{r}}_j|^{-1}$ is the two-particle Coulomb interaction operator for electrons. $\psi^\lambda[n]$ is that wave function which minimizes the expectation value $\langle \hat{T} + \lambda \hat{V}_{ee} \rangle$ for a fictive electron system with the kinetic-energy operator $\hat{T}$ and the interaction $\lambda \hat{V}_{ee}$, subject to the constraint that it has the ground-state density $n(\mathbf{r})$ of the real system with interaction $\hat{V}_{ee}(\lambda = 1)$.

When $\lambda = 0$, the wave function is the noninteracting Kohn−Sham single determinant $\psi^0[n]$, so $W_0[n] = \langle \psi^0[n] | \hat{V}_{ee} | \psi^0[n] \rangle - U[n] = E_x[n]$, where $E_x[n]$ is the exact orbital exchange energy evaluated using Kohn−Sham orbitals. The exact slope of W'_λ at $\lambda = 0$ is known exactly to be twice the second-order correlation energy from Goerling-Levy density functional perturbation theory (GL2),[11,12] $W'_0[n] = 2E_c^{GL2}[n]$. Therefore, in the weak interaction limit, we have

$$W_\lambda = W_0 + W'_0\lambda \quad \lambda \to 0 \tag{4}$$

When $\lambda = 1$, the wave function is the exact wave function of the interacting physical system, $\psi^1[n]$, so

* Corresponding author e-mail: jsun@tulane.edu.

10.1021/ct800515w CCC: $40.75
Published on Web 02/24/2009

$$W_1[n] = \langle \psi^1[n] | \hat{V}_{ee} | \psi^1[n] \rangle - U[n] = V_{ee} - U[n] \quad (5)$$

which is the difference between the total electron−electron repulsion energy V_{ee} of the interacting physical system and the Coulomb energy.

There have been a number of attempts to construct exchange-correlation functionals by explicitly approximating W_λ. By linearly interpolating W_0 and W_1, where the latter is approximated by the local spin-density approximation (LSDA), Becke first introduced the so-called hybrid exchange-correlation functional.[13] With different assumptions for the λ dependence in the range of [0, 1] and local or semilocal exchange-correlation functionals to approximate W_1, many other constructions have been proposed, including nonempirical PBE0,[6] the [1/1]-Pade-based form of Ernzerhof,[14] the two-legged representation of Burke et al.,[15] and the MCY proposed by Mori-Sanchez, Cohen, and Yang.[16] The MCY also adds the information of W'_0, approximated by a modified Tao-Perdew-Staroverov-Scuseria[17] (TPSS) slope to avoid the computational expense of W'_0. Instead of W_1, Seidl et al.[18,19] used information from the strong interaction limit $\lambda \to \infty$, where W_λ approaches asymptotically a finite value W_∞

$$W_\lambda = W_\infty + W'_\infty \lambda^{-1/2} \quad \lambda \to \infty \quad (6)$$

The so-called interaction strength interpolation (ISI) functional interpolates the weak and strong interaction limits with W_∞ and W'_∞ approximated in the point-charge-plus-continuum (PC) model. Due to their nonlinearity in terms of $W_0[n]$, $W'_0[n]$, $W_\infty[n]$, and $W'_\infty[n]$, the [1/1]-Pade-based form of Ernzerhof,[14] the MCY,[16] and the ISI[18,19] are not size consistent, which is an important property of the exact $E_{xc}[n]$: $E_{xc}[n_1 + n_2] = E_{xc}[n_1] + E_{xc}[n_2]$ for two well separated densities n_1 and n_2.

Despite these attempts, the exact dependence W_λ is known only for the uniform electron gas (UEG) and for some relatively simple systems.[15,20,21] One of these systems is two electrons on the surface of a sphere (2ESS), which recently has been solved numerically for $\lambda \in [-\infty,\infty]$ by Seidl.[21] The extension of λ to negative values for this simple system then naturally brings up questions: does W_λ with negative λ exist for every system? If so, what is the asymptotical form as $\lambda \to -\infty$? Although the exchange-correlation energy is only an integral over $\lambda \in [0,1]$, the asymptotical form at limit $\lambda \to \infty$ still provides much information concerning W_λ, especially as a function of λ. On the contrary, at $\lambda = 1$, there is not an exact general form available for W_λ. Furthermore, with such information built in, the ISI[18,19] obtains accuracy comparable to the [1/1]-Pade-based form of Ernzerhof[14] and the MCY,[16] much better than the GL2 where only the weak interaction ($\lambda \to 0$) limit is used. Therefore, it is suspected that the construction of an exchange-correlation functional might benefit from the information at $\lambda \to -\infty$ too, to the extent that this limit is known.

In this paper, it is assumed that for every system W_λ exists for negative λ. An exchange-correlation functional triggered almost by the solution of 2ESS is then proposed in section 2 by approximating W_λ with λ extending to negative values. Results for 2ESS and some simple atoms are presented in section 3, followed by conclusions and future work discussed in section 4.

2. Interaction Strength Interpolation Extended to Negative λ (ISIN)

In ref 21, Seidl introduced an extra term to the ISI to recover the third leading term in the weak ($\lambda \to 0$) and strong ($\lambda \to \infty$) interaction limit, respectively, which led to a new functional, ISI3, and increased the accuracy of the correlation energy for 2ESS. However, this improvement was bought at a high price since the third leading term in the weak ($\lambda \to 0$) interaction limit, W''_∞, is the third-order of the GL perturbation expansion, although the third leading term in the strong ($\lambda \to \infty$) interaction limit, W''_∞, is 0.[18]

By extending to negative λ and using two leading terms in the weak ($\lambda \to 0$) and strong ($\lambda \to \infty$) interaction limit, respectively, I propose

$$W_\lambda^{ISIN} = a + b\lambda \, arcctg(c\lambda) + \frac{d}{(1 + e^2\lambda^2)^{1/4}} \quad (7)$$

where $a = W_0 - f(W_0 - W_\infty)$, $b = (2)/(\pi)W'_0$, $c = (2)/(\pi)(W'_0)/((W_\infty - W_0)(1 - f))$, $d = f(W_0 - W_\infty)$, and $e = ((f(W_0 - W_\infty))/(W'_\infty))^2$.

With f chosen to be 0.5 without fitting to any data, surprisingly, it gives remarkably good results for 2ESS as shown in Figure 1 and Table 1. Actually, the value for f is between 0.5 and 0.51 if we vary f to search for the most nearly exact energy of 2ESS at $R = 1$. And the variation of the energy is negligible with f from 0.5 to 0.51. $f = 0.5$ is used in this article. It is not guaranteed that, for all cases, W_λ^{ISIN} is a monotonically decreasing function over $\lambda \in [-\infty,\infty]$, as shown in eq 9 later. However, it is indeed so guaranteed for $\lambda \geq 0$. As $\lambda \to -\infty$, W_λ^{ISIN} is linearly dependent on λ, which matches the exact solution of 2ESS although the coefficients at this limit are different.[21] Note that the constraint of W''_∞ being 0 is fulfilled automatically in ISIN.

The exchange-correlation energy of ISIN is obtained by analytical integration, according to eq 1, of eq 7

$$E_{xc}^{ISIN} = a + \frac{b}{2c^2}[(1 + c^2) arcctg(c) + c - \pi/2] + \frac{2d}{(1 + e^2)^{1/4}} + \frac{\sqrt{2}d}{e}\left[F\left(\alpha, \frac{1}{\sqrt{2}}\right) - 2E\left(\alpha, \frac{1}{\sqrt{2}}\right)\right] \quad (8)$$

where $\alpha = \arccos[(1 + e^2)^{-1/4}]$. $F(\alpha,k)$ and $E(\alpha,k)$ are the first- and second-kind incomplete elliptic integrals with the modulus $k = 1/\sqrt{2}$. An interesting point is that eq 8 gives the exact value for the H atom, where $W_0 = W_\infty = -0.3125$ Ha and $W'_0 = W'_\infty = 0$. Even if we use the PC model value of $W_\infty^{PC} = -0.313$ Ha and $W'^{PC}_\infty = 0.043$ Ha for the H atom, the correlation energy is still negligible, about 0.5×10^{-10} Ha.

Because the inputs $W_0[n]$, $W'_0[n]$, $W_\infty[n]$, *and* $W'_\infty[n]$ are size consistent, so is $W_\lambda^{ISIN}[n]$ in the weak- and strong-interaction limits. However, due to its nonlinearity, $E_c^{ISIN}[n]$ is not generally size consistent.

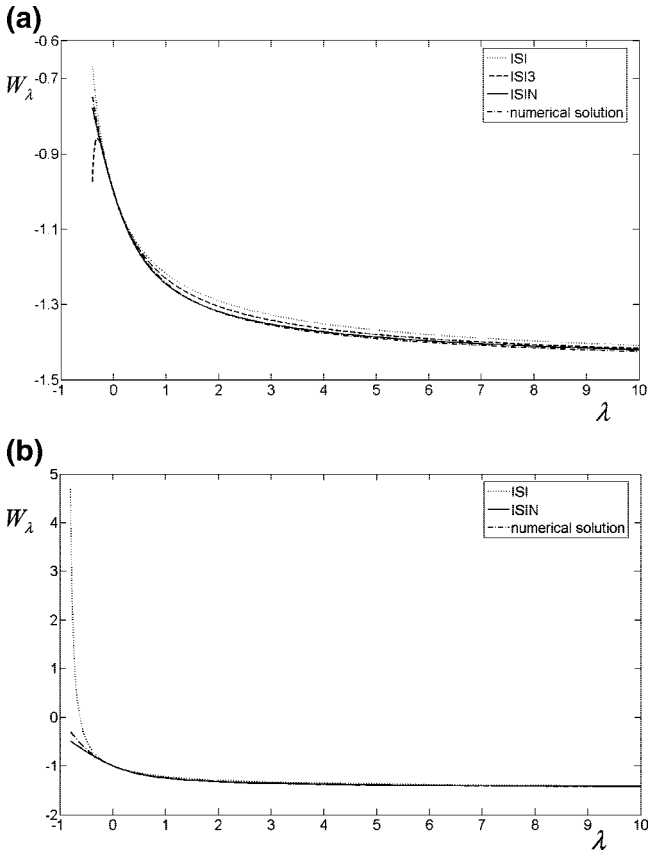

Figure 1. The coupling constant integrand W_λ of different approximations compared to the numerical solution for the singlet system of 2ESS. (a) $\lambda \in (-0.4,10)$; (b) $\lambda \in (-0.8,10)$, ISI3 is not shown in this figure since it has a singularity in this range. Here 2ESS means two electrons on the surface of a sphere of radius $R = 1$ Bohr.

Table 1. Correlation Energies $E_c[R]$ of the Singlet System of 2ESS[a]

R	ISI[b]	ISI3[b]	ISIN	exact[b]
0.1	−0.2118	−0.2157	−0.2183	−0.2175
0.2	−0.1985	−0.2045	−0.2094	−0.2064
0.5	−0.1679	−0.176	−0.1844	−0.1796
1	−0.1349	−0.1426	−0.1511	−0.1473
2	−0.0984	−0.104	−0.1098	−0.1081
5	−0.0562	−0.0587	−0.0608	−0.0605
10	−0.0337	−0.0348	−0.0355	−0.0355
M.E	0.007643	0.002657	−0.00206	
M.A.E	0.007643	0.002657	0.00206	

[a] The unit is Hartree. Here 2ESS means two electrons on the surface of a sphere of radius R =1 bohr. [b] Values are from ref 21.

3. Results and Discussions

In the 2ESS system, the electrons, distributing uniformly, are confined to the 2D surface of a sphere with radius R, variation of which can result in different density of the charge. The limit of $R \to \infty$ ($R \to 0$) corresponds to the low density (high density), i.e. the strong interaction (weak interaction). With W_0, W'_0, W_∞, and W'_∞ given in eqs 38 and 39 in ref 21 for the singlet system of 2ESS, Figure 1(a) plots W_λ vs λ with $\lambda \in [-0.4,10]$ for $R = 1$ Bohr. By recovering the additional third leading term in the strong and weak interaction limit, respectively, ISI3 shows significant improvement over ISI, while ISIN, by extending to negative λ with correct linear dependence as $\lambda \to -\infty$ (although the coefficient for this limit is not recovered) and recovering W'_∞ automatically, is slightly closer to the numerical solution. This observation is corroborated by Table 1, the correlation energies $E_c[R]$ for different R, where the mean absolute error drops from 0.007643 Ha of ISI largely to 0.002657 Ha of ISI3, then slightly to 0.00206 Ha of ISIN. Figure 1(b) shows that W_λ^{ISIN} deviates from the numerical solution very much for $\lambda < -0.5$ due to the inconsistency of the coefficient at $\lambda \to -\infty$, which is, however, still better than the other two, namely ISI and ISI3, obviously.

Table 2. Correlation Energies E_c of Atoms[a]

system	ISI[b]	ISIN	exact[b]
He	−0.041	−0.044	−0.042
Exp.	−0.034	−0.038	−0.037
Be	−0.1	−0.112	−0.096
Ne	−0.405	−0.439	−0.394

[a] Exp. is the two-electron system with exponential density $n(\mathbf{r}) = 2\exp(-2r)/\pi$. W_∞ and W'_∞, evaluated in the PC model, along with W_0 and W'_0, are given in Table 3 of ref 18. The unit is Hartree. [b] Values are from ref 18.

Table 3. Atomization Energies of 18 Molecules (in Units of 1 kcal/mol), in Second-Order Goerling-Levy Perturbation Theory (GL2),[14] in ISI,[18,19] in ISIN, and from Experiment (as in ref 22)

mol.	GL2[c]	ISI[c]	ISIN	expt
H2	114	107.3	109.2	109.5
LiH	70	58.8	61.4	57.8
Li2	39	22.5	24.6	24.4
LiF	193	142.7	157.9	138.9
Be2	22	5.7	8.6	3
CH4	454	423.4	433.3	419.3
NH3	340	300.9	313.2	297.4
OH	128	108.6	114.5	106.4
H2O	274	235.7	248.4	232.2
HF	173	143.7	153.2	140.8
B2	190	68.1	88.4	71
CN	335	188.1	220.5	178.5
CO	355	265.9	292.1	259.3
N2	342	234.6	262	228.5
NO	265	157.9	184.2	152.9
O2	230	123.6	149.6	120.5
O3	407	136.8	187.1	148.2
F2	134	34	51.2	38.5
ME	74	1.7	18.5	
MAE	74	4.3	18.5	

[c] Values are from ref 19.

Although ISIN works well in this simple 2ESS model, it turns out that it is inferior to ISI when applied to the real system, as shown in Table 2. The inferiority might be due to the fact that, while ISI does not break down completely for metals and systems with large static correlation, W_λ^{ISIN} does when $W'_0 \to -\infty$

$$\lim_{W'_0 \to -\infty} W_\lambda^{ISIN} = W_\infty + \frac{d}{(1 + e^2\lambda^2)^{1/4}} \tag{9}$$

As $W'_0 \to -\infty$, the second term in the right-hand side of eq 7 becomes discontinuous at $\lambda = 0$, jumping from 0 to b/c, which then leads to $\lim_{\lambda \to 0^+} \lim_{W'_0 \to -\infty} W_\lambda^{ISIN} = (W_0 + W_\infty)/2$, more negative to the supposed W_0. This discontinuity implies that W_λ^{ISIN} biases toward W_∞ and thus results in more

negative correlation energies, as shown in Tables 1 and 2. This is also corroborated by the calculation of the atomization energies of 18 small molecules, using the idea and data given in refs 14, 18, and 19. In Table 3, ISIN overbinds these molecules with the mean absolute error (MAE) of 18.5 kcal/mol, compared to 4.3 kcal/mol of ISI, due to the fact that the molecules have much larger W_0' because of static correlation, therefore, much more spurious negative correlation energies, than their component atoms. However, ISIN is still better than GL2, which gave a MAE of 74 kcal/mol.[14]

4. Conclusion and Future Work

With the coupling constant λ extending to negative values, the ISIN explicitly approximates W_λ, covering the two leading terms of the asymptotic expansion of W_λ at $\lambda = 0$ and ∞, respectively. For the simple system of 2ESS, ISIN works well, even better than ISI3. The mean absolute error of the correlation energies $E_c[R]$ for different R yielded by the ISIN is 0.00206 Ha, slightly better than 0.002657 Ha by ISI3 and much better than 0.007643 Ha by ISI. However, due to the discontinuity of W_λ^{ISIN} at $\lambda = 0$ as $W_\lambda' \to -\infty$, W_λ^{ISIN} breaks down completely with W_λ^{ISIN} biasing toward W_∞, resulting in much more negative correlation energies and overbinding of molecules for real systems.

Although the ISIN proposed in this article fails to give accurate correlation energies for real systems, the future work on this subject might be to find one which recovers the behavior of ISI as $W_0' \to -\infty$, meanwhile extending λ to negative values.

Acknowledgment. Helpful discussion with Professor John P. Perdew is acknowledged.

References

(1) Perdew, J. P.; Schmidt, K. In *Density Functional Theory and Its Applications to Materials*; Van-Doren, V., Alsenoy, C. V., Geerlings., P., Eds.; American Institute of Physics: New York, 2001; p 1.

(2) Parr, R. G.; Yang, W. *Density-Functional Theory of Atoms and Molecules*; Oxford University Press: Oxford Press, 1989. (a) Dreizler, R. M.; Gross, E. K. U. *Density Functional Theory*; Springer: Berlin, 1990.

(3) Langreth, D. C.; Perdew, J. P. *Solid State Commun.* **1975**, *17*, 1425.

(4) Gunnarsson, O.; Lundqvist, B. I. *Phys. Rev. B* **1976**, *13*, 4274.

(5) Langreth, D. C.; Perdew, J. P. *Phys. Rev. B* **1977**, *15*, 2884.

(6) Perdew, J. P.; Ernzerhof, M.; Burke, K. *J. Chem. Phys.* **1996**, *105*, 9982.

(7) Levy, M. *Phys. Rev. A* **1991**, *43*, 4637.

(8) Joubert, D. P.; Srivastava, G. P. *J. Chem. Phys.* **1998**, *109*, 5212.

(9) Colonna, F.; Savin, A. *J. Chem. Phys.* **1999**, *110*, 2828.

(10) Frydel, D.; Terilla, W. M.; Burke, K. *J. Chem. Phys.* **2000**, *112*, 5292.

(11) Goerling, A.; Levy, M. *Phys. Rev. B* **1993**, *47*, 13105.

(12) Goerling, A.; Levy, M. *Phys. Rev. A* **1995**, *52*, 4493.

(13) Becke, A. D. *J. Chem. Phys.* **1993**, *98*, 1372.

(14) Ernzerhof, M. *Chem. Phys. Lett.* **1996**, *263*, 499.

(15) Burke, K.; Ernzerhof, M.; Perdew, J. P. *Chem. Phys. Lett.* **1997**, *265*, 115.

(16) Mori-Sanchez, P.; Cohen, A. J.; Yang, W. *J. Chem. Phys.* **2006**, *124*, 091102.

(17) Tao, J.; Perdew, J. P.; Staroverov, V. N.; Scuseria, G. E. *Phys. Rev. Lett.* **2003**, *91*, 146401.

(18) Seidl, M.; Perdew, J. P.; Kurth, S. *Phys. Rev. B* **2000**, *62*, 0125022005, 72, 029904(E).

(19) Seidl, M.; Perdew, J. P.; Kurth, S. *Phys. Rev. Lett.* **2000**, *84*, 5070.

(20) Peach, M. J. G.; Teale, A. M.; Tozer, D. J. *J. Chem. Phys.* **2007**, *126*, 244104.

(21) Seidl, M. *Phys. Rev. A* **2007**, *75*, 062506.

(22) Perdew, J. P.; Kurth, S.; Zupan, A.; Blaha, P. *Phys. Rev. Lett.* **1999**, *82*, 2544; **1999**, *82*, 5179(E) and references therein.

CT800515W

JCTC Journal of Chemical Theory and Computation

Polarizabilities of Polyacetylene from a Field-Counteracting Semilocal Functional

A. Karolewski, R. Armiento, and S. Kümmel*

Physics Institute, University of Bayreuth, D-95445 Bayreuth, Germany

Received December 1, 2008

Abstract: Predicting the polarizabilities of extended conjugated molecules with semilocal functionals has been a long-standing problem in density functional theory. These difficulties are due to the absence of a term in the typical semilocal Kohn−Sham exchange potentials that has been named "ultranonlocal". Such a term should develop in extended systems when an external electric field is applied, and it should counteract the field. We calculate the polarizabilities of polyacetylene molecules using the recently developed extended Becke−Johnson functional. Our results show that this functional predicts the polarizabilities with much better accuracy than typical semilocal functionals. Thus, the field-counteracting term in this functional, which is semilocal in the Kohn−Sham orbitals, can realistically describe real molecules. We discuss approaches of constructing an energy functional that corresponds to this potential functional, for example, via the Levy−Perdew virial relation.

1. Introduction: Step Structures in the Kohn−Sham Potential

The enormous success of density functional theory (DFT) in solid-state physics and molecular chemistry to a considerable extent has been due to the remarkable balance between accuracy and computational cost which (semi)local functionals like the local density approximation and generalized gradient approximations provide. Yet, the developers of some of the most reliable semilocal functionals themselves pointed out[1] a feature of the exact exchange-correlation potential of Kohn−Sham density functional theory that none of the standard semilocal functionals has: the exact potential is discontinuous as a function of the particle number. This "derivative discontinuity" feature of Kohn−Sham theory has found considerable attention over the years, with refs 2–5 being just a few examples from a body of literature that is far too vast to cite in completeness. The derivative discontinuity of ground-state density functional theory in the solid-state context is prominently related to the band gap question, see, for example, refs 2 and 6–8. In molecular physics, it is related to at least two frequently encountered problems.

As was already pointed out in ref 1, it is only due to the derivative discontinuity that Kohn−Sham theory can lead to neutral fragments when a molecule dissociates. The spatial features which the exact Kohn−Sham exchange-correlation potential develops in order to enforce this "principle of integer preference"[9] are schematically depicted in Figure 1. When two different atoms, A and B, with A having a larger electronegativity than B, are considered as being rigorously disconnected, the highest occupied eigenvalue of A is more negative than the one of B. When the same two atoms are close to each other and form a diatomic molecule, the

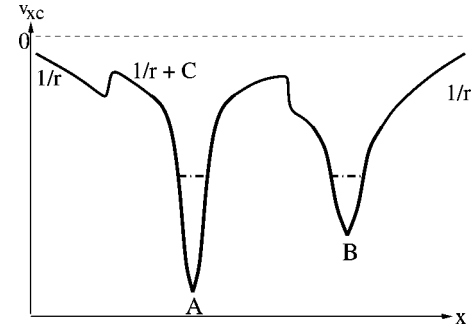

Figure 1. Schematic depiction of the exact v_{xc} for a system of two different atoms at a very large separation (arbitrary units). The dashed−dotted lines indicate the energies of the Kohn−Sham eigenvalues discussed in the main text. To the left of A, the potential first tends to a positive constant C and then steps down to fall off to 0 like 1/*r*.

* Corresponding author e-mail: Stephan.Kuemmel@uni-bayreuth.de.

10.1021/ct8005198 CCC: $40.75
Published on Web 03/20/2009

eigenvalues of the molecule in general will be different from the eigenvalues of the separate atoms, reflecting the charge redistribution that is associated with the electronic bond. However, now consider the situation that the distance between the two atoms forming the molecule is steadily increased to large values, that is, one is looking at a stretched diatomic molecule A−B. If the interatomic distance is extremely large, for example, on the scale of meters, then this "extremely stretched diatomic molecule" will show the same physical properties as two separate neutral atoms. Therefore, one may be tempted to think that the Kohn−Sham eigenvalues one finds for the stretched diatomic molecule are the same as the ones for the two isolated atoms. But this is not the case for the ultimate, exact density functional: When the two atoms, A and B, are considered as one very extended system, a steplike structure develops in ν_{xc}, and due to this step, the Kohn−Sham potential of the stretched molecule is not simply the sum of the two Kohn−Sham potentials of two isolated atoms. In the stretched molecule, the step in ν_{xc} "lifts up" the potential well of A, nearly aligning the eigenvalues which would be the highest occupied eigenvalues of A and B if the atoms were rigorously isolated. At any very large but finite separation, one eigenvalue in the stretched diatomic will be infinitesimally higher in energy than the other, and its corresponding orbital will be mostly localized around atom B. When the interatomic distance tends to infinity, the eigenvalues become degenerate.

The exact ν_{xc} of the very stretched diatomic molecule is schematically depicted in Figure 1, with the dashed−dotted lines indicating the energies of the just discussed two eigenvalues. The eigenvalue difference becomes smaller as the distance between A and B becomes larger. Also, with increasing distance, the steps in ν_{xc} become sharper, and the down-step of ν_{xc} to the left of A, which occurs in the region of space where the density starts to be dominated by the highest occupied orbital, moves farther to the left. Potentials that are reconstructed from accurate densities show features similar to the ones just described.[10,11] But the ν_{xc} of a standard semilocal density functional does not at all show the step structure. Therefore, such functionals typically lead to fractionally charged dissociation fragments.[12]

To date, step structures in the correlation potential are not incorporated in any of the typical density functional approximations. Functionals showing them have been constructed[13] but are involved to compute and typically rely on reconstructions from ensemble densities.[11,14] For exchange, however, the situation is more transparent. Due to the fact that the expression for the Kohn−Sham exchange functional is known in terms of the Kohn−Sham orbitals, the step structure in the Kohn−Sham exchange potential can be understood analytically. It has been discussed in detail, for example, by Krieger et al.,[3,15] with the exchange potential "step structure" being closely related to orbital overlap or occupation of a new orbital upon the addition of an extra electron.[6,16,8] Several approximations showing such steps have been developed.[3,17–19,32]

The step structure features of ν_{xc} are related to a second nontrivial problem. Long-range charge transfer is not well described by standard semilocal functionals.[20] This issue manifests very prominently in the well-known fact that the static electric polarizabilities of extended molecular systems are seriously overestimated by semilocal functionals.[21] This failure is due to the fact that the exact exchange potential of an extended molecular system develops a term which counteracts an externally applied electric field that polarizes the system,[22] but this term is missing in the semilocal approximations.

The problem of correctly describing the electrical response of conjugated polymers is of great practical interest because of the widespread use that these materials find in optoelectronic applications. So far, the only density functionals that yield a proper field-counteracting term were exact-exchange,[22–24] range-separated[25,26] or other[27] functionals using exact exchange, or self-interaction corrected functionals.[28–30] Compared to semilocal approaches, these functionals are associated with a considerably increased computational burden stemming from having to evaluate many Coulomb integrals on the one hand and having to solve the optimized effective potential (OEP) equation on the other. (The latter statement applies to those approaches staying in the Kohn−Sham realm). Therefore, a computationally cheaper approach yielding a comparable accuracy is highly desirable.

Recently, Becke and Johnson[31] showed that a simple expression which is semilocal in the Kohn−Sham orbitals quite accurately reproduces the "step-structure features" of the exact exchange Kohn−Sham potential. Yet more recently, the expression proposed by Becke and Johnson has been extended to yield proper asymptotic behavior and behave consistently for systems in an external electric field.[32] The extended Becke−Johnson (BJ) expression for the exchange potential of a system in an external electric field Fz is

$$\nu_x^{eBJ}(\mathbf{r}) = \nu_x^{h}(\mathbf{r}) + \nu_x^{corr}(\mathbf{r}) \quad (1)$$

where we have dropped the spin index for ease of notation. Here, $\nu_x^{h}(\mathbf{r})$ is interpreted as an effective potential due to the exchange hole. Presently, the Slater potential is employed, but other, simpler choices can be made without a significant loss of accuray.[31] The second term, $\nu_x^{corr}(\mathbf{r})$, is a correction modeling the response part of the exact exchange potential. The steplike structures in the extended BJ expression are exclusively due to $\nu_x^{corr}(\mathbf{r})$. Explicitly, this term reads

$$\nu_x^{corr}(\mathbf{r}) = \frac{1}{\pi}\sqrt{\frac{5}{12}}\left(\sqrt{\frac{2\tau}{n}} - \sqrt{-2\epsilon_{max}} - \frac{Fz}{\sqrt{-2\epsilon_{max}}}\right) \quad (2)$$

(in Hartree atomic units), where $\tau = (1/2)\Sigma_{i_{occ}}|\nabla\varphi_i|^2$ is the noninteracting kinetic energy density computed from the occupied Kohn−Sham orbitals φ_i, n is the density, and ε_{max} denotes the highest-occupied Kohn−Sham eigenvalue.

It was shown[32] that this potential shows a step structure which, as discussed in the context of Figure 1, is closely connected to the derivative discontinuity. It was also shown that it yields polarizabilities of small hydrogen chains with an accuracy comparable to that of exact exchange methods. These results showed that constructing approximations for ν_{xc} directly (instead of approximations for E_{xc}) is an attractive idea that may lead to an elegant and efficient solution of the

field-counteracting term problem. However, two important questions regarding this approach have remained open so far: First, how reliable are the conclusions that were drawn from the hydrogen chain results; that is, does the approach also work for real, existing conjugated molecules? In other words, did the simplicity of the hydrogen chain model lead to artificially good results? Second, can one construct an energy corresponding to this potential functional, for example, via the exchange virial relation?[33] The latter question is interesting also from the point of view of recent work which shed additional light on the BJ approach by showing that it is one of a whole class of potential approximations and used the exchange virial relation to construct energy expressions.[34]

We address both of these questions in the following. In section 2, we report static electric dipole polarizabilities of acetylene oligomers. Our results show that the extended BJ expression yields polarizabilities that compare favorably with previously calculated exact exchange values. They also show that the extended BJ potential can lead to nonvanishing asymptotic constants, a feature known from the exact Kohn−Sham exchange potential. These findings solidify the relevance of the extended BJ potential and the idea of developing exchange-correlation *potential* functionals. In section 3, we demonstrate the problems of defining an energy corresponding to the model potential. We show that straightforwardly using the exchange virial relation is problematic, and we give ideas of how this problem may be addressed in future work.

2. Electric Response of Polyacetylene and the Effect of Orbital Nodal Surfaces

Polyacetylene has been the paradigm conjugated polymer of molecular electronics research efforts. As well, it has become the paradigm system for the failure of semilocal functionals to describe the electrical response of extended conjugated molecules. Therefore, calculating the static electric polarizabilities of polyacetylene units is an ideal test for the practical usefulness of the extended BJ potential functional. To the best of our knowledge, it is the first test for real conjugated systems and therefore important. The only previous test that we know of was for hydrogen chains.[32] This previous test may thus not completely account for the complexity of a real molecule's electronic structure.

Our calculations are based on a fully numerical solution of the Kohn−Sham equations on a real space grid.[32,35] We thus avoid possible problems due to basis set limitations in the polarizability calculations. The polarizabilities are obtained by a finite-field, finite-difference approach; that is, we calculate the electrical dipole moment along the molecular axis, μ, for several values of the applied electric field, F, and obtain $\alpha = d\mu/dF$ from finite differences. A general and more detailed description of this type of approach can be found, for example, in ref 36. The molecular geometry that we based our calculations on is the Hartree−Fock geometry schematically depicted in Figure 2. Our aim here is to assess the validity of a theoretical approach by comparison to reference work. Therefore, we chose the geometry that was used in earlier works.[21,38–40]

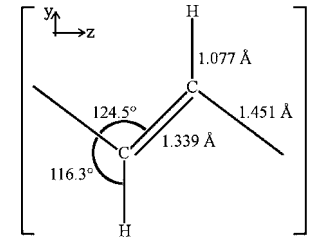

Figure 2. Sketch of the geometry that the polyacetylene calculations were based on. See main text for discussion.

Table 1. Longitudinal Static Electric Dipole Polarizabilities (in a_0^3) for Polyacetylene Units As Obtained from LDA, the Extended Becke−Johnson Functional, Hartree−Fock,[38] and Perturbation Theory (MP2) Calculations[39]

	C_4H_6	C_6H_8	C_8H_{10}	$C_{10}H_{12}$	$C_{12}H_{14}$	$C_{14}H_{16}$
LDA	88	174	296	457	661	915
ext. BJ	70	134	224	338	480	649
HF	75	142	229	332	448	575
MP2	64	112	187	267	357	455

Table 1 compares the values for the longitudinal static electric polarizability that are obtained in the local density approximation[37] (LDA), the extended Becke−Johnson (ext. BJ) approach,[32] unrestricted Hartree−Fock (HF),[38] and second-order Møller−Plesset perturbation theory (MP2).[39] Typical values obtained with generalized gradient approximation functionals are similar to LDA and therefore not given separately. Comparing the LDA polarizabilities (first row of Table 1) to the HF and MP2 ones (bottom rows) exemplifies the known serious overestimation of the response of conjugated systems that is obtained with semilocal density functionals.

So far, the standard interpretation of the BJ potential has been that it is an approximation to the exact Kohn−Sham exchange potential. In this spirit and in view of previous results indicating that Kohn−Sham exact exchange and HF exchange lead to very similar polarizabilities,[24] a reasonable comparison to make is the one between the extended BJ and the HF results. Looking at C_4H_6 to $C_{10}H_{12}$ in rows two and three of Table 1 gives a very positive impression in this respect. The values from the extended BJ functional are within roughly 5% of the HF values, slightly underestimating the HF result for the smallest systems and slightly overestimating for the large ones. This is a substantial improvement over the huge overestimation that one finds with LDA. For the two largest molecules that we studied, $C_{12}H_{14}$ and $C_{14}H_{16}$, the extended BJ potential still yields a substantial improvement over LDA, but the difference with respect to the HF results increases to 7% and 13%, respectively. Thus, the extended BJ potential in this respect behaves similarly[24] to the Krieger−Li−Iafrate (KLI) approximation.[3] In view of the fact that the decisive ingredient in the BJ potential is a semilocal quantity,[31] this quality, although not perfect, is without doubt an encouraging result.

A natural question is whether the reasonable polarizabilities of polyacetylene that one finds in the extended BJ approach can be traced back to a field-counteracting term like in the case of hydrogen chains and exact-exchange methods. In order to investigate this question, we have

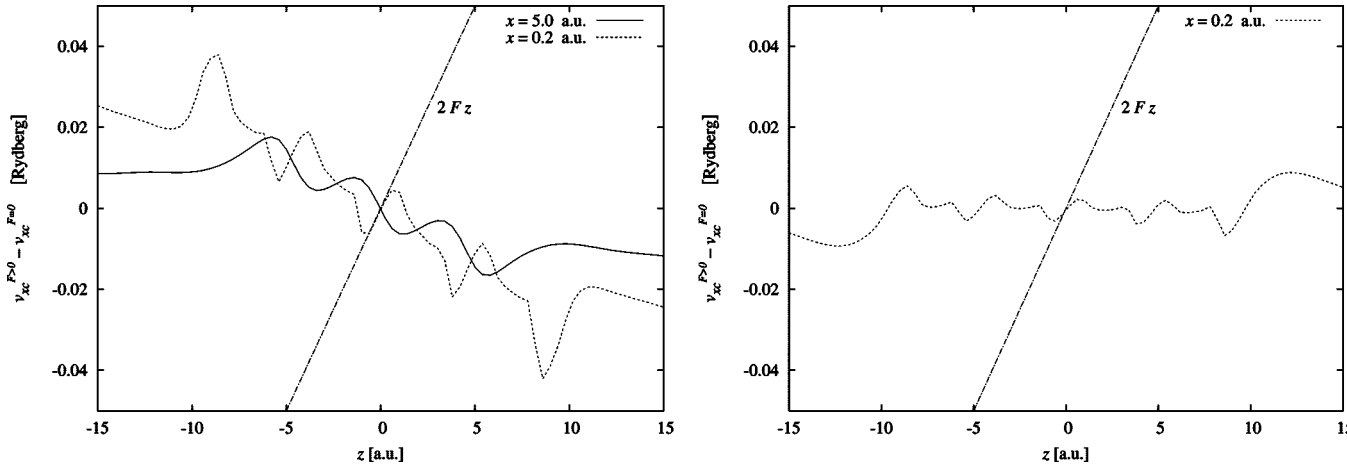

Figure 3. The difference between the exchange-correlation potentials with and without an externally applied electric field for C_8H_{10} (in atomic units). The molecule lies in the (y,z) plane. Left half: The full curve shows the ν_{xc} difference along the line (x = 5, y = 0, z). The dashed curve shows the ν_{xc} difference along the line (x = 0.2, y = 0, z), which is the z line closest to the molecular plane that lies exactly on our numerical grid. The straight dashed−dotted line indicates the external electric field. Note that the extended BJ potential counteracts the external field, as it should. Also note that the asymptotic behavior of the BJ ν_{xc} difference depends on the distance to the molecular plane. Right half: The same difference shown for LDA along the line (x = 0.2, y = 0, z). Note that the overall trend of LDA is with the external field.

followed the practice introduced in ref 22 and plotted the difference between the ν_{xc} one finds along the molecular axis with an external electric field applied and the ν_{xc} one finds without external field. The left half of Figure 3 shows this potential difference for the extended BJ approach, the right half for LDA. For the extended BJ potential, we show two plots. Each one is along a line running parallel to the molecular axis, which in our case lies in the z direction, compare Figure 2. The full curve shows the potential difference one finds at a distance of 5 au above the molecular plane. This curve looks reassuringly similar to what was found for the hydrogen chains in ref 32 and to what one may expect on the basis of earlier exact-exchange calculations: the exchange-correlation potential slopes against the external electric field (straight dashed−dotted line).

However, looking at the plot in the immediate vicinity of the molecular plane (dashed curve, $x = 0.2$ au) reveals two noticeable differences. First, the plot shows considerably more structure in the region of space where the density is appreciable. This is understandable, as one is looking at the potential closer to the nuclear cores, and thus, greater variations in the density and potential are plausible. However, the second and striking discrepancy is that the potential difference does not seem to level off outside the region of space where the valence electron density is appreciable. On first sight, this looks like a serious problem since the extended BJ potential was derived by enforcing that ν_{xc} should fall off to zero. This condition seems to be violated here. In the following, we explain this observation, showing that it is a natural consequence of a feature of the BJ construction which, to the best of our knowledge, had not been revealed so far.

First, consider a system without an external dipole field, that is, $F = 0$ in eq 2. In ref 32, it was argued that subtracting the term $\sqrt{(-2\varepsilon_{max})}$ ensures that $v_x^{eBJ}(\mathbf{r})$ falls off to zero as $r \rightarrow \infty$. This argument assumed that the density is dominated by the highest occupied orbital as $r \rightarrow \infty$. This condition appears to be a very natural one and is fulfilled almost everywhere in space—but not necessarily on nodal surfaces of the highest-occupied Kohn−Sham orbital. Therefore, the extended BJ expression can go to a nonvanishing asymptotic constant on nodal surfaces of the highest-occupied Kohn−Sham orbital that extend to infinity. We have checked this explicitly for the example of the Carbon atom and indeed find that the extended BJ expression goes to a nonvanishing constant on the nodal line. Although this feature may appear spurious on first sight, it is in fact a good one because it is shared by the exact Kohn−Sham exchange potential! The latter is also known to exhibit nonvanishing asymptotic constants on nodal surfaces of the highest occupied orbital.[41,42]

The surprising asymptotics seen for the potential difference at $x = 0.2$ au in Figure 3 have a similar origin. In ref 32, the term $-Fz/\sqrt{(-2\varepsilon_{max})}$, compare eq 2, was introduced to enforce the condition that ν_x falls off to 0 asymptotically also for a system in an external dipole field. The derivation was based on the argument that asymptotically, the density is dominated by the highest occupied orbital. However, the polyacetylene segments which we study here have a highest occupied orbital for which the molecular plane is a nodal surface. Thus, similar to the no-field case discussed in the previous paragraph, the field-counteracting term involving the highest occupied eigenvalue will enforce the proper boundary condition $\nu_{xc}(\mathbf{r} \rightarrow \infty) \rightarrow 0$ everywhere except for points lying on nodal surfaces of the highest occupied orbital extending to infinity. When one is not exactly on but quite close to a nodal surface, ν_{xc} will fall off to 0 eventually. However, the closer one is to the nodal surface, the farther away from the molecule one has to go in order to see this falloff. In practical calculations, this region can be so far out that it is not on the numerical grid. This is the explanation for the surprising behavior of the $x = 0.2$ au curve in the left half of Figure 3.

Finally, we address a technical question. Our real-space grid technique requires us to use pseudopotentials to

eliminate the nuclear singularity. Therefore, one may ask how far this influences the results for the polarizability. For the hydrogen atom, the pseudopotential does not model core electrons but simply "smoothes" the nuclear divergence. Thus, the pseudopotential approximation is particularly harmless for H, and we have found that it makes practically no difference for the polarizability calculation whether one uses a norm-conserving pseudopotential[43] or a local one.[44] But even for carbon, the influence of the pseudopotential on the polarizability is small. Switching from a standard LDA norm-conserving pseudopotential[43] to a self-consistently constructed exact-exchange pseudopotential[45] has a small but visible influence on the plots in Figure 3 due to the changed eigenvalues, but changes in the polarizability are less than 1%, that is, on a scale that is irrelevant for the purposes of our work.[46]

3. The Becke−Johnson Expression and the Exchange Virial Relation

Having seen that the extended BJ approach may offer a chance to solve the static charge-transfer problem on the basis of only semilocal functional ingredients, it is a natural next step to investigate how the BJ approach can be turned into a generally usable density functional. To this end, one needs to find an energy functional corresponding to the extended BJ potential.

One possible way of defining an energy functional corresponding to a given exchange potential v_x is to employ the Levy−Perdew exchange virial relation[33]

$$E_x = -\int n(\mathbf{r})\mathbf{r}\cdot\nabla v_x(\mathbf{r})\,d^3r \qquad (3)$$

In the case that $v_x(\mathbf{r})$ is a functional derivative, the virial relation will yield the correct value of the energy functional of which $v_x(\mathbf{r})$ is the functional derivative. The problem is, however, that eq 3 will also yield some energy value if $v_x(\mathbf{r})$ is not a functional derivative. Whether that value has physical meaning is not clear.

In the context of polarizability calculations, a simple test of E_x-v_x correspondence is given by comparing the polarizability one obtains from the first derivative of the dipole moment (as described above) to the one obtained from the second derivative of the energy with respect to the applied field. The former is the value which directly reflects the potential and is thus the right one to look at when investigating potential approximations. The latter reflects the energy expression. When the employed potential is the one that minimizes the employed energy expression, the two values one obtains for α should match. In this case, discrepancies are only an indication for possible limitations of the numerical quality of the calculation. However, if the rigorous connection between energy functional and potential is severed, this inconsistency manifests in noticeable differences between the results obtained by the two ways of calculating the polarizability. This has previously been discussed and tested[36] for the KLI approximation[3] to the exchange-only OEP. There, the polarizabilities obtained from μ and E differed noticeably, although the KLI exchange ground-state energy is typically very close to the OEP exchange energy.

Table 2. Differences in Percentage between the Longitudinal Polarizabilities for Polyacetylene Units as Obtained by Taking the Second Derivative with Respect to the Field of the Energy and the First Derivative of the Dipole Moment[a]

	C_4H_6	C_6H_8	C_8H_{10}	$C_{10}H_{12}$	$C_{12}H_{14}$	$C_{14}H_{16}$
LDA	<1	<1	<1	<1	1	2
ext. BJ	42	51	56	64	85	101

[a] cf. Table 1. For the extended BJ functional, the virial energy of eq 3 was used.

Performing this test for whether using the virial expression directly can be a reasonable way of defining an energy functional corresponding to the BJ potential, we have calculated the polarizabilities also from the energy. With respect to polarizabilities obtained from the dipole moment reported in Table 1, we find pronounced differences. They are reported in Table 2. The comparison with LDA, also given in Table 2, shows that this is not a problem of numerical accuracy. This finding is in line with calculations that reported considerable discrepancies for virial energies.[49] Following the above logic, we have to conclude that the extended BJ potential is not a functional derivative. This seems highly plausible in view of the conjecture that the Slater potential is not a functional derivative[47] and that quite generally it is a nontrivial requirement that a given function be a functional derivative.[48] Therefore, simply using the virial expression with the BJ potential is not a rigorous way of defining a consistent energy-potential pair.

One might adopt an alternative point of view and look at the BJ potential in a way similar to the one adopted for the KLI and other[8] approximate potential expressions. In this way of thinking, the proper energy expression is the Fock exchange energy, and the BJ potential is an approximation to the exchange-only OEP. However, trying to "discuss away" the problem of energy-potential consistency in this manner in our opinion is not a long-term solution either. Ultimately, the extended BJ approach should show its true strengths and capabilities in time-dependent DFT, because a time-dependent extension of the BJ approach (or some other semilocal construction sharing its main features) may solve the problem of long-range charge-transfer excitations in a computationally easy way. But without being a proper functional derivative, the potential most likely will suffer from the same problems that were observed for, for example, the time-dependent KLI potential.[50]

One possible way of obtaining a consistent E_x-v_x pair having the important features of the BJ expression is to use eq 3 in a different way. One may take the point of view that plugging the BJ expression into the right-hand side of eq 3 defines an energy functional. The potential corresponding to this energy expression must then be obtained by taking the functional derivative of this energy with respect to the density. One may hope that, in this way, one can derive a potential that is "as close as possible" to the BJ potential, but at the same time being a functional derivative. Having tried this approach in practice does not make it look very promising, though. Considering just one part of the BJ potential for simplicity, for example, the Slater potential for a system with N occupied orbitals

$$v_x^{\text{Slater}}(\mathbf{r}) = -\frac{1}{n}\int \frac{|\sum_{i=1}^{N}\varphi_i^*(\mathbf{r})\varphi_i(\mathbf{r}')|^2}{|\mathbf{r}-\mathbf{r}'|}\,d^3r' \qquad (4)$$

plugging this into the right-hand side of eq 3 and taking the functional derivative $\delta/\delta n$ after some lengthy algebra leads to the potential

$$\begin{aligned} v_x^{\text{intSlater}}(\mathbf{r}) = {} & \frac{2}{n(\mathbf{r})}\int \frac{\sum_{i=1}^{N}\varphi_i^*(\mathbf{r})\,\varphi_i(\mathbf{r}')}{|\mathbf{r}-\mathbf{r}'|} \times \\ & [\sum_{i=1}^{N}\varphi_i^*(\mathbf{r}')\,(\mathbf{r}\cdot\nabla)\,\varphi_i(\mathbf{r})]\,d^3r' - \\ & \frac{1}{n(\mathbf{r})}\int \frac{(\sum_{i=1}^{N}\varphi_i^*(\mathbf{r})\,\varphi_i(\mathbf{r}'))^2}{|\mathbf{r}-\mathbf{r}'|}[\mathbf{r}(\mathbf{r}-\mathbf{r}')]\,d^3r' - \\ & \frac{1}{n(\mathbf{r})}\left[3+2\frac{(\mathbf{r}\cdot\nabla)\,n(\mathbf{r})}{n(\mathbf{r})}\right]v_x^{\text{Slater}}(\mathbf{r}) + \\ & \int d^3r' \int d^3r'' \int d^3r'''\,[3n(\mathbf{r}') + (r'\cdot\nabla')\,n(\mathbf{r}')]\times \\ & \frac{1}{n(\mathbf{r}')}\sum_{i=1}^{N}2\chi_{\text{KS}}^{-1}(\mathbf{r},\mathbf{r}''')\frac{\sum_{k=1}^{N}\varphi_k^*(\mathbf{r}')\,\varphi_k(\mathbf{r}'')}{|\mathbf{r}'-\mathbf{r}''|}\times \\ & \left[\frac{\delta\varphi_i(\mathbf{r}')}{\delta v_{\text{KS}}(\mathbf{r}''')}\varphi_i(\mathbf{r}'') + \frac{\delta\varphi_i(\mathbf{r}'')}{\delta v_{\text{KS}}(\mathbf{r}''')}\varphi_i(\mathbf{r}')\right] \qquad (5) \end{aligned}$$

with $v_{\text{KS}}(\mathbf{r})$ denoting the Kohn−Sham potential and $\chi_{\text{KS}}{}^{-1}$ the inverse of the Kohn−Sham response function. This is not a pleasant equation. Similarly, having to take the functional derivative of v_x^{corr} with respect to the density quickly becomes involved as the functional chain rule must be invoked to calculate the functional derivatives of the Kohn−Sham orbitals. Thus, this approach, as far as we can tell, leads to expressions that are more complicated than the exact exchange OEP equation itself. The beauty of the BJ expression, which to a considerable extent lies in its simplicity, is thus lost.

From a pragmatic point of view and for certain applications, it may be possible to define an energy via one of the routes discussed above. But one has to face the fact that presently there is no rigorous or conceptually satisfying way of defining an energy corresponding to the BJ potential. On the other hand, being able to construct an easy-to-evaluate semilocal functional that will capture the essence of the charge-transfer physics is such a tempting idea that we believe it is a worthwhile task to continue working on.

In this manuscript, we demonstrated the capabilities of such "potential functionals" by showing that the extended BJ potential leads to much better polarizabilities of polyacetylene molecules than typical semilocal functionals. We further showed that there is a yet closer similarity between the BJ expression and the exact exchange potential than previously discussed, as both lead to nonvanishing asymptotic constants on nodal surfaces of the highest occupied orbital that extend to infinity. We demonstrated that, for the systems studied here, the BJ potential can be used in combination with pseudopotentials without a relevant loss of accuracy. Finally, we critically discussed ways of how a consistent energy- and potential-functional pair may be found.

Future work will focus on three aspects. First, it appears quite feasible to eliminate the Slater potential. This was already discussed by Becke and Johnson in their original work,[31] and this step will not only make the functional computationally yet more attractive, it will also ameliorate the problem of making the potential a functional derivative. Second, it may be possible to replace v_x^{corr} by a different orbital expression,[51] or possibly even by an expression which does not depend on the Kohn−Sham orbitals explictly. Again, this will not only improve computational efficiency but may also allow for writing the potential in such a way that eq 3 can be used for a proper "functional integration". Third, extending the BJ approach to the time domain[51] may be a way of constructing an exchange-correlation functional that can handle dynamical long-range charge transfer. Thus, semilocal functionals may still offer greater possibilities than what one typically expects from them.

Acknowledgment. We acknowledge stimulating discussions with T. Körzdörfer and financial support by the German−Israeli foundation and the Deutscher Akademischer Austauschdienst. This article is dedicated to John Perdew, as one of us (S.K.) gratefully acknowledges numerous discussions with him on topics touched upon in this article: the strengths and weaknesses of semilocal functionals, the importance of the concept of the derivative discontinuity, and the exchange virial relation.

References

(1) Perdew, J. P.; Parr, R. G.; Levy, M.; Balduz, J. L., Jr. *Phys. Rev. Lett.* **1982**, *49*, 1691.

(2) Godby, R. W.; Schlüter, M.; Sham, L. J. *Phys. Rev. B: Condens. Matter Mater. Phys.* **1988**, *37*, 10159.

(3) Krieger, J. B.; Li, Y.; Iafrate, G. J. *Phys. Rev. A: At., Mol., Opt. Phys.* **1992**, *45*, 101.

(4) Mundt, M.; Kümmel, S. *Phys. Rev. Lett.* **2005**, *95*, 203004.

(5) Teale, A. M.; De Proft, F.; Tozer, D. J. *J. Chem. Phys.* **2008**, *129*, 044110.

(6) Perdew, J. P.; Levy, M. *Phys. Rev. Lett.* **1983**, *51*, 1884.

(7) Dreizler, R. M.; Gross, E. K. U. *Density Functional Theory*; Springer: Berlin, 1990; pp 145−147.

(8) Kümmel, S.; Kronik, L. *Rev. Mod. Phys.* **2008**, *80*, 3.

(9) Perdew, J. P. *Adv. Quantum Chem.* **1990**, *21*, 113.

(10) Gritsenko, O. V.; Baerends, E. J. *Phys. Rev. A: At., Mol., Opt. Phys.* **1996**, *54*, 1957.

(11) Lein, M.; Kümmel, S. *Phys. Rev. Lett.* **2005**, *94*, 143003.

(12) This has recently been discussed in detail in, e.g.: Ruzsinszky, A.; Perdew, J. P.; Csonka, G. I.; Vydrov, O. A.; Scuseria, G. E. *J. Chem. Phys.* **2006**, *125*, 194112.

(13) de Wijn, A. S.; Lein, M.; Kümmel, S. *Europhys. Lett.* **2008**, *84*, 43001.

(14) Sagvolden, E.; Perdew, J. P. *Phys. Rev. A: At., Mol., Opt. Phys.* **2008**, *77*, 012517.

(15) Krieger, J. B.; Li, Y.; Iafrate, G. J. *Phys. Lett. A* **1990**, *146*, 256.

(16) van Leeuwen, R.; Gritsenko, O. V.; Baerends, E. J. *Z. Phys. D* **1995**, *33*, 229.

(17) Gritsenko, O. V.; van Leeuwen, R.; van Lenthe, E.; Baerends, E. J. *Phys. Rev. A: At., Mol., Opt. Phys.* **1995**, *51*, 1944.

(18) Gritsenko, O. V.; Baerends, E. J. *Phys. Rev. A: At., Mol., Opt. Phys.* **2001**, *64*, 042506.

(19) Della Sala, F.; Görling, A. *J. Chem. Phys.* **2001**, *115*, 5718.

(20) Tozer, D. J. *J. Chem. Phys.* **2003**, *119*, 12697.

(21) Champagne, B.; et al. *J. Chem. Phys.* **1998**, *109*, 10489.

(22) van Gisbergen, S. J. A.; et al. *Phys. Rev. Lett.* **1999**, *83*, 694.

(23) Mori-Sánchez, P.; Wu, Q.; Yang, W. *J. Chem. Phys.* **2003**, *119*, 11001.

(24) Kümmel, S.; Kronik, L.; Perdew, J. P. *Phys. Rev. Lett.* **2004**, *93*, 213002.

(25) Iikura, H.; Tsuneda, T.; Hirao, K. *J. Chem. Phys.* **2001**, *115*, 3540.

(26) Sekino, H.; Maeda, Y.; Kamiya, M. *Mol. Phys.* **2005**, *103*, 2183.

(27) Varsano, D.; Marini, A.; Rubio, A. *Phys. Rev. Lett.* **2008**, *100*, 133002.

(28) Körzdörfer, T.; Mundt, M.; Kümmel, S. *Phys. Rev. Lett.* **2008**, *100*, 133004.

(29) Pemmaraju, C. D.; Sanvito, S.; Burke, K. *Phys. Rev. B: Condens. Matter Mater. Phys.* **2008**, *77*, 121204 (R).

(30) Ruzsinszky, A.; Perdew, J. P.; Csonka, G. I.; Scuseria, G. E.; Vydrov, O. A. *Phys. Rev. A: At., Mol., Opt. Phys.* **2008**, *77*, 060502 (R) .

(31) Becke, A. D.; Johnson, E. R. *J. Chem. Phys.* **2006**, *124*, 221101.

(32) Armiento, R.; Kümmel, S.; Körzdörfer, T. *Phys. Rev. B: Condens. Matter Mater. Phys.* **2008**, *77*, 165106.

(33) Levy, M.; Perdew, J. P. *Phys. Rev. A: At., Mol., Opt. Phys.* **1985**, *32*, 2010.

(34) Staroverov, V. N. *J. Chem. Phys.* **2008**, *129*, 134103.

(35) Kronik, L.; Makmal, A.; Tiago, M. L.; Alemany, M. M. G.; Jain, M.; Huang, X.; Saad, Y.; Chelikowsky, J. R. *Phys. Status Solidi B* **2006**, *243*, 1063.

(36) Kümmel, S.; Kronik, L. *Comput. Mater. Sci.* **2006**, *35*, 321.

(37) Perdew, J. P.; Wang, Y. *Phys. Rev. B: Condens. Matter Mater. Phys.* **1992**, *45*, 13244.

(38) Kirtman, B.; Toto, J. L.; Robins, K. A.; Hasan, M. *J. Chem. Phys.* **1995**, *102*, 5350.

(39) Toto, T. T. *Chem. Phys. Lett.* **1995**, *244*, 59.

(40) Van Faassen, M.; de Boeij, P. L.; van Leeuwen, R.; Berger, J. A.; Snijders, J. G. *Phys. Rev. Lett.* **2002**, *88*, 186401.

(41) Della Sala, F.; Görling, A. *J. Chem. Phys.* **2002**, *116*, 5374; *Phys. Rev. Lett.* **2002**, *89*, 033003.

(42) Kümmel, S.; Perdew, J. P. *Phys. Rev. B: Condens. Matter Mater. Phys.* **2003**, *68*, 035103.

(43) Troullier, N.; Martins, J. L. *Phys. Rev. B: Condens. Matter Mater. Phys.* **1991**, *43*, 1993. For C, we used the core radii (2s) 1.60 and (2p) 1.60 a.u., for H 1.39.

(44) Gygi, F. *Phys. Rev. B: Condens. Matter Mater. Phys.* **1993**, *48*, 11692.

(45) Engel, E.; Höck, A.; Schmid, R. N.; Dreizler, R. M.; Chetty, N. *Phys. Rev. B: Condens. Matter Mater. Phys.* **2001**, *64*, 125111.

(46) We are aware of other systems and observables where differences can be larger: Makmal, A.; Armiento, R.; Engel, E.; Kronik, L.; Kümmel, S. Work in progress.

(47) Ou-Yang, H.; Levy, M. *Phys. Rev. Lett.* **1990**, *65*, 1036.

(48) van Leeuwen, R.; Baerends, E. J. *Phys. Rev. A: At., Mol., Opt. Phys.* **1995**, *51*, 170.

(49) Gaiduk, A. P.; Staroverov, V. N. *J. Chem. Phys.* **2008**, *128*, 204101.

(50) Mundt, M.; Kümmel, S.; van Leeuwen, R.; Reinhard, P.-G. *Phys. Rev. A: At., Mol., Opt. Phys.* **2007**, *75*, 050501.

(51) Armiento, R.; Karolewski, A.; Kümmel, S. Work in progress.

CT8005198

JCTC Journal of Chemical Theory and Computation

Van der Waals Interactions in Density-Functional Theory: Rare-Gas Diatomics

Felix O. Kannemann and Axel D. Becke*

Department of Chemistry, Dalhousie University, Halifax, Nova Scotia, Canada B3H 4J3

Received December 1, 2008

Abstract: The application of conventional GGA and meta-GGA density functionals to van der Waals interactions is fraught with difficulties. Conventional functionals do not contain the physics of the dispersion interaction. To make matters worse, the exchange part alone can yield anything from severe overbinding to severe over-repulsion depending on the choice of functional. We have assessed a variety of exchange GGAs for their ability to reproduce exact Hartree−Fock repulsion energies in rare-gas systems, and we find that PW86 [*Phys. Rev. B* 1986, *33*, 8800] performs remarkably well. The addition of a dynamical correlation GGA and the nonempirical dispersion model of Becke and Johnson [*J. Chem. Phys.* 2007, *127*, 154108] to PW86 gives a simple GGA plus dispersion theory yielding excellent rare-gas interaction curves for pairs involving He through Kr, with only two adjustable parameters for damping of the dispersion terms.

1. Introduction

Density functional theory (DFT) is a successful and accurate method for electronic structure calculations of atoms, molecules, and solids. Its application to soft matter and weakly bound systems, including intermolecular complexes, biomolecules, molecular crystals, and polymers, depends on a realistic description of van der Waals (vdW) interactions including the London dispersion force. Dispersion arises from correlated motions of electrons on well-separated systems and is an inherently nonlocal electron correlation effect. Density functionals based on the local density approximation (LDA) or the semilocal generalized gradient approximation (GGA) do not account for such long-range correlations and, consequently, fail to reproduce the attractive R^{-6} behavior of the interatomic potential between closed-shell atoms at large separation R.[1]

Problems with LDA and GGA functionals in vdW interactions arise not only in the asymptotic region, however. At the equilibrium separation of typical dispersion-bound van der Waals complexes, such as rare-gas diatomics or stacked aromatic rings, there is a weak wave function overlap leading to considerable Hartree−Fock (HF) repulsion between the monomers. Lacks and Gordon[2] found that LDA and GGA exchange functionals applied to the helium and neon dimers give widely varying interaction energies, from too repulsive (B88)[3] to spurious binding (LDA, PW91[4,5]), when compared to exact Hartree−Fock repulsion.

A DFT treatment of vdW interactions should address both issues, the erratic behavior of approximate exchange functionals near equilibrium separations, as well as the missing long-range attraction caused by dispersion.[6] Many different approaches have been used in the literature and only a superficial overview is given here. For more complete discussions, see refs 1 and 6−8.

The van der Waals density functional (vdW-DF) approach of Langreth et al.[9,10] uses an approximate nonlocal correlation functional derived from response theory to account for long-range dispersion interactions. It is combined with revPBE[11] exchange and LDA correlation to give a seamless functional valid at all interatomic distances. The revPBE GGA was chosen for exchange as it does not produce artificial binding in vdW complexes.[12,13] The original vdW-DF method consistently overestimated the separation in vdW complexes, which was ascribed to the overestimation of Hartree−Fock repulsion by revPBE.[10] The substitution of revPBE by HF exchange indeed improves the separations and establishes the correct relative stability of different benzene dimer conformations but leads to significant overestimation of

* To whom correspondence should be addressed. E-mail: axel.becke@dal.ca.

10.1021/ct800522r CCC: $40.75
Published on Web 03/23/2009

binding energies,[14−16] suggesting that the nonlocal correlation part in vdW-DF is not fully compatible with HF exchange.

Other nonempirical approaches circumvent the problems associated with approximate exchange functionals by using a separation of the electron−electron interaction into a long-range part treated exactly and a short-range part described by an exchange GGA. The method of Hirao et al.[17,18] combines long-range HF with short-range B88[3] exchange. Short-range correlation is treated by the OP[19] functional, while the long-range correlation comes from the nonlocal Andersson−Langreth−Lundqvist[20] (ALL) vdW functional multiplied by a damping function depending on empirical atomic radii. The range-separated hybrid (RSH+MP2) method of Ángyán et al.[6,21] employs the LDA for short-range exchange and correlation, HF for long-range exchange, and second-order perturbation theory (MP2) to account for the dispersion interaction in a seamless manner.

The three methods mentioned so far have in common that long-range dispersion is treated by explicitly nonlocal correlation functionals of the vdW-DF, ALL, or MP2 type. These are inherently more computationally demanding than the (semi)local functionals of conventional DFT. To retain the computational efficiency of DFT, empirical dispersion terms of the form $-C_6/R^6$ have been added to conventional density functionals to give methods collectively known as DFT-D.[8,22−24] The C_6 coefficients are empirical parameters derived from fits, atomic calculations, or approximate formulas. In addition, the dispersion term must be attenuated at small separations R by damping functions depending on empirical vdW radii. Some DFT-D methods use additional global scaling factors that depend on the underlying density functional to account for differences in the description of Hartree−Fock repulsion[8,24] and may include reparametrization.[24]

Another approach involves modifying standard DFT functionals to give a good description of van der Waals interactions without an explicit dispersion or nonlocal correlation correction. This is done by refitting the exchange-correlation functional while including van der Waals complexes in the training set.[25−29] An exception is the Wilson−Levy correlation functional[30] combined with HF exchange, which gives good results for various vdW complexes near their equilibrium distances without adjustment, although lacking theoretical justification.[31]

In summary, previous attempts to make DFT applicable to van der Waals complexes either (a) include explicitly nonlocal correlation which is computationally demanding, (b) introduce highly empirical dispersion corrections, or (c) refit functionals that are fundamentally unable to account for dispersion interactions to van der Waals data nevertheless.

The nonempirical dispersion model of Becke and Johnson[32−37] has previously been used in conjunction with exact Hartree−Fock exchange[38,39] to give an accurate treatment of vdW interactions. In this work, we replace Hartree−Fock exchange with an exchange GGA that well reproduces Hartree−Fock repulsion in rare-gas diatomics. This functional is then combined with various correlation GGAs and the Becke−Johnson dispersion model. The method is calibrated on all pair interactions between the atoms He, Ne, Ar, and Kr and yields excellent equilibrium separations, binding energies, and interatomic potential energy curves.

2. Hartree−Fock Repulsion in Rare-Gas Diatomics

Hartree−Fock theory gives (in the complete basis set limit) repulsive potentials for rare-gas diatomics. Exchange functionals should accurately reproduce this Hartree−Fock repulsion if DFT is to be applied to vdW interactions.

The only systematic benchmark study of the ability of exchange functionals to reproduce Hartree−Fock repulsion in rare-gas diatomics is by Lacks and Gordon.[2] They showed that most exchange functionals give large errors, over 100%, for the exchange-only interaction energy in He_2 and Ne_2, even though total atomic exchange energies are within 1%. Some functionals such as B88 are too repulsive, others such as PW91 or the LDA give an artifactual *attractive* interaction.

The broad range of exchange-only interaction energies obtained from approximate functionals is illustrated in Figure 1 for the neon dimer. The interaction energy of two Ne atoms is plotted as a function of interatomic separation for exact HF exchange, the exchange-only LDA (xLDA), and the GGA exchange functionals B86,[40] B86b,[41] B88,[3] PW86,[42] PW91,[4,5] PBE,[43,44] and revPBE.[11] The HF and xLDA curves are self-consistent. The GGA curves are evaluated using the xLDA orbitals (i.e., post-xLDA). All calculations are performed with the fully numerical, basis-set-free Numol program of Becke and Dickson.[45,46]

Van der Waals interaction curves are extremely sensitive to the choice of GGA exchange functional.[47−50] We obtain in Figure 1 everything from massive "binding" of ∼500 μH (xLDA and PW91) to repulsion of ∼800 μH (B88) compared to the exact Hartree−Fock repulsion energy of ∼100 μH at the experimental equilibrium separation of Ne_2.[51] The curves can be ordered according to the behavior of the exchange GGA at large reduced density gradient χ

$$\chi(\mathbf{r}) = \frac{|\nabla p(\mathbf{r})|}{p(\mathbf{r})^{4/3}} \tag{1}$$

GGA exchange functionals can be expressed in the form

$$E_X^{GGA} = \int e_X^{LDA}(\mathbf{r}) F[\chi(\mathbf{r})] \tag{2}$$

where e_X^{LDA} is the LDA exchange energy density, and $F[\chi(\mathbf{r})]$ is the "exchange enhancement factor". Standard exchange GGAs, such as those in Figure 1, all have similar behavior for small χ. However, they behave very differently at large χ (see Figure 1 in ref 47), corresponding in real space to the region very far from nuclei (i.e., the asymptotic tail density). The functionals displaying artifactual binding in Figure 1 are those with relatively small enhancement factor at large χ; those being overly repulsive have relatively large enhancement factor at large χ. Inspection of Figure 1 suggests that PW86 best reproduces the exact Hartree−Fock repulsion curve in Ne_2, especially near the equilibrium separation.

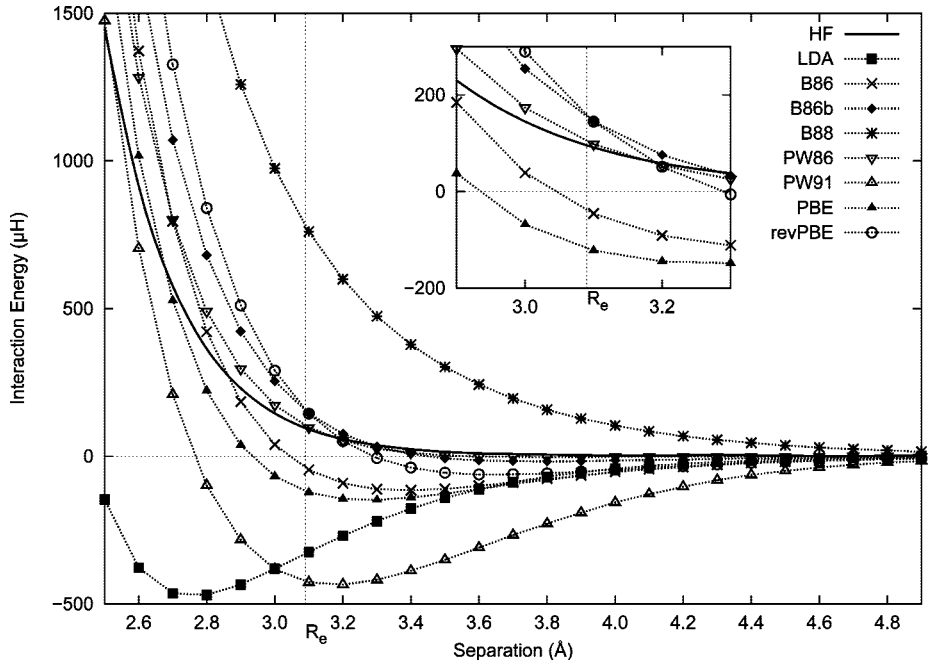

Figure 1. Hartree−Fock repulsion, xLDA, and exchange-only GGA interaction energies of Ne_2.

Table 1. Hartree−Fock Repulsion Energies (μH) for Rare-Gas Diatomics at Tang−Toennies Reference Equilibrium Separations r_{ref}^{TT} (Å)

	r_{ref}^{TT}[51]	ΔE^{HF}
He_2	2.97	28
He−Ne	3.05	47
He−Ar	3.50	85
He−Kr	3.69	103
Ne_2	3.09	96
Ne−Ar	3.48	190
Ne−Kr	3.65	227
Ar_2	3.76	435
Ar−Kr	3.89	538
Kr_2	4.01	674

Table 2. Hartree−Fock Repulsion Energy Errors (%) of Exchange GGAs at Reference Equilibrium Separations r_{ref}^{TT} (Post-HF)

	B86	B86b	B88	PW86	PW91	PBE	revPBE
MPE	−76	32	374	34	−337	−106	2
MAPE	85	34	374	34	337	106	60
MaxAPE	239	57	679	53	832	259	153

Table 3. Hartree−Fock Repulsion Energy Errors (%) of Exchange GGAs at Reference Equilibrium Separations r_{ref}^{TT} (Post-xLDA)

	B86	B86b	B88	PW86	PW91	PBE	revPBE
MPE	−96	53	542	20	−418	−158	51
MAPE	111	53	542	22	418	158	75
MaxAPE	309	72	1126	82	1133	381	124

Lacks and Gordon concluded that PW86 and B86b best reproduced Hartree−Fock repulsion in He_2 and Ne_2 on the basis of post-HF calculations with the xLDA, PW86, PW91, B86, B86b, B88, and DK87[52] functionals.

We have extended their assessment to all pair interactions between the rare-gas atoms He, Ne, Ar, and Kr, using both

Table 4. Exact (Hartree−Fock) and PW86 Repulsion Energies (μH) for Rare-Gas Diatomics at Equilibrium Separations. Worst Cases (MaxAPE) in Bold

	ΔE^{HF} SCF, numerical	ΔE^{PW86} post-xLDA, numerical	ΔE^{PW86} SCF, aug-cc-pV5Z (aug-cc-pV6Z, aug-pc-4) CP
He_2	28	**51**	29 (30, 30)
He−Ne	47	64	52 (50, 51)
He−Ar	85	107	87 (89, 88)
He−Kr	103	116	98
Ne_2	96	104	**117** (**113**, **115**
Ne−Ar	190	189	198 (197, 198)
Ne−Kr	227	201	219
Ar_2	435	505	503 (507, 512)
Ar−Kr	538	611	626
Kr_2	674	764	796
MPE		20	8 (6, 6)
MAPE		22	10 (6, 6)
MaxAPE		82	22 (18, 20)

Hartree−Fock and xLDA orbitals, and including the exchange functionals PBE[43,44] and revPBE.[11] Table 1 shows exact Hartree−Fock repulsion energies ΔE^{HF} computed with Numol at the reference equilibrium separations of Tang and Toennies.[51] Table 2 gives the mean percent error (MPE), mean absolute percent error (MAPE) and maximum absolute percent error (MaxAPE) of GGA exchange functionals with respect to ΔE^{HF}, evaluated using Hartree−Fock orbitals (i.e., post-HF). In agreement with Lacks and Gordon, B86b and PW86 best reproduce Hartree−Fock repulsion. With xLDA orbitals however, we find that PW86 is superior to all other functionals tested (Table 3). Self-consistent GGA calculations are currently not possible with Numol.

We then used Gaussian03[53] to obtain fully self-consistent interaction energies with the PW86 functional using the keyword iop(3/74=800). A numerical integration grid of 400 radial shells and 590 angular points per atom was used, the SCF convergence criterion was set to 10^{-8} with full integral accuracy during the SCF cycles. We used the aug-cc-pV5Z[54−57]

basis set throughout as well as aug-cc-pV6Z[58,59] and aug-pc-4[60] for the subset of systems containing only He, Ne, and Ar atoms because these basis sets are not available for Kr. Basis sets were obtained from the EMSL basis-set library.[61,62] The counterpoise (CP)[63] procedure was used to correct for basis set superposition error, which was found to be up to 5% of ΔE^{PW86} for He−Ne and Ne_2 with the aug-cc-pV5Z basis set. The resulting PW86/aug-cc-pV5Z-CP interaction energies are given in Table 4, with results for aug-cc-pV6Z and aug-pc-4 in parentheses. The self-consistent PW86 interaction energies are even more accurate than the post-HF and post-xLDA results. In particular, the overestimation of Hartree−Fock repulsion in He_2 is significantly improved.

PW86 is a remarkably accurate exchange GGA for reproducing Hartree−Fock repulsion energies in rare-gas diatomics. Compared to more sophisticated approaches to correct for deficiencies in approximate exchange functionals when applied to van der Waals complexes, such as the use of long-range Hartree−Fock exchange[6,17,18,21] or exact-exchange-based functionals themselves,[31,36,37] it has the obvious benefit of computational efficiency.

PW86 is also appealing because of its simple functional form and the absence of any empirical parameters.[42] As with any typical GGA, it gives atomic exchange energies accurate to within 1%,[2,42] and is therefore of similar utility for general quantum chemistry as the more popular functionals B88, PW91, or PBE (see section 5).

3. Dynamical Correlation and Dispersion Corrections

Having found a suitable exchange GGA for use with van der Waals interactions, we now consider the correlation functional. Typical semilocal correlation functionals account for short-range dynamical correlation arising from interelectronic cusp conditions.[64] Semilocal functionals are inherently unable to describe the long-range electron correlations between *nonoverlapping* fragments that give rise to the asymptotic dispersion interaction.[1,6,12,65] The application of GGAs to van der Waals interactions therefore requires an explicit long-range dispersion correction. Empirical corrections have been used successfully but suffer from limited applicability and transferability.[7,8,22−24,66−68] The recent dispersion model of Becke and Johnson,[35] however, is nonempirical.

The Becke−Johnson model employs the dipole moment of an electron and its associated exchange hole (as an approximation to the full exchange-correlation hole) as the source of position-dependent multipole moments leading to the dispersion interaction.[32,35,69] System-dependent interatomic dispersion coefficients $C_{6,ij}$, $C_{8,ij}$, and $C_{10,ij}$ are thus obtained from the exchange-hole dipole moment, effective atomic polarizabilities, and second-order perturbation theory. The dispersion model has two variants, an exact-exchange version where the dipole moment of the exchange hole and its reference electron is calculated using occupied orbitals (XX), and a density-functional version based on the Becke−Roussel model of the exchange hole (BR).[70]

The asymptotic dispersion terms need to be damped at small separations R. The Becke−Johnson scheme[37] uses

$$E_{\mathrm{disp}} = -\frac{1}{2}\sum_{i\neq j}\left(\frac{C_{6,ij}}{R_{\mathrm{vdW},ij}^{6}+R_{ij}^{6}} + \frac{C_{8,ij}}{R_{\mathrm{vdW},ij}^{8}+R_{ij}^{8}} + \frac{C_{10,ij}}{R_{\mathrm{vdW},ij}^{10}+R_{ij}^{10}}\right) \quad (3)$$

where the sum is over all pairs of atoms i and j, and the effective interatomic van der Waals separation $R_{\mathrm{vdW},ij}$ is related to a "critical" interatomic separation $R_{\mathrm{c},ij}$ by

$$R_{\mathrm{vdW},ij} = a_1 R_{c,ij} + a_2 \quad (4)$$

The critical separation $R_{c,ij}$ is given by the average value of the ratios $(C_{8,ij}/C_{6,ij})^{1/2}$, $(C_{10,ij}/C_{6,ij})^{1/4}$, and $(C_{10,ij}/C_{8,ij})^{1/2}$, and corresponds to the separation where the three asymptotic dispersion terms are approximately equal in magnitude

$$\frac{C_{6,ij}}{R_{ij}^{6}} \approx \frac{C_{8,ij}}{R_{ij}^{8}} \approx \frac{C_{10,ij}}{R_{ij}^{10}} \quad (5)$$

This is where the asymptotic series expansion is expected to break down. The two coefficients a_1 and a_2 in eq 4 are empirical parameters assumed to be universal and determined as described below.

We combine the PW86 exchange functional with various GGA functionals for dynamical correlation $E_{\mathrm{C}}^{\mathrm{GGA}}$ and the Becke−Johnson dispersion model as follows:

$$E_{\mathrm{XC}} = E_{\mathrm{X}}^{\mathrm{PW86}} + E_{\mathrm{C}}^{\mathrm{GGA}} + E_{\mathrm{disp}}^{\mathrm{BJ}} \quad (6)$$

We use the standard correlation GGAs P86,[71,72] PW91,[4,5] and PBE.[43,44] All following calculations were performed with the Numol program using LDA orbitals and the Perdew−Wang uniform-gas exchange-correlation parametrization[73] (i.e., post-xcLDA). We used numerical grids of 302 angular points per atom, and 80, 120, 160, and 200 radial shells for the He, Ne, Ar, and Kr atoms, respectively.

The coefficients a_1 and a_2 in eq 4 were determined by minimizing the root-mean-square percent error (RMSPE) for the interaction energies of the ten rare-gas pairs involving He, Ne, Ar, and Kr with respect to reference binding energies at the experimental equilibrium separations of Table 1. We chose the rare-gas reference data of Tang and Toennies (TT)[51] following the suggestion by Gerber and Ángyán.[6]

Results of our fits are shown in Table 5. The exact-exchange version (XX) of the dispersion model gives somewhat better fits than the density-functional version (BR) for all correlation GGAs. The PW91 and PBE correlation

Table 5. Best-Fit Dispersion Damping Parameters and Interaction-Energy RMS Percent Errors for Various Combinations of Correlation GGA and Becke−Johnson Dispersion

	a_1	a_2/Å	RMSPE
P86-XX	1.80	−1.16	20.5
P86-BR	1.54	−0.53	28.7
PW91-XX	0.96	0.87	8.1
PW91-BR	0.76	1.35	12.5
PBE-XX	0.95	0.87	7.8
PBE-BR	0.75	1.25	12.0

functionals give almost identical results, not surprising given that PBE generally behaves very much like PW91.[43] P86, however, yields errors more than twice as large compared to PW91 and PBE. We therefore omit P86 from further consideration.

4. Binding Energy Curves

We have calculated binding energy curves using PW86x and PBEc and the dispersion damping parameters in Table 5. These are shown for the homonuclear dimers of He, Ne, Ar, and Kr in Figures 2−5, together with the TT reference potentials. The PW91c curves are essentially identical to the PBEc binding energy curves. For clarity, we also omit the curves for the BR version of the Becke−Johnson dispersion model. They are qualitatively similar to the XX-based curves and only slightly inferior. PW86xPBEc+disp gives binding energy curves that closely reproduce the reference curves. The largest deviations are observed for the heavier diatomics Ne−Kr, Ar−Ar, Ar−Kr, and Kr−Kr.

Equilibrium separations were found by potential-energy scans in steps of 0.01 Å and are shown in Table 6, together with the TT reference values (Å). Our results are reported as reduced quantities, defined as equilibrium separation divided by the reference value. The methods using either

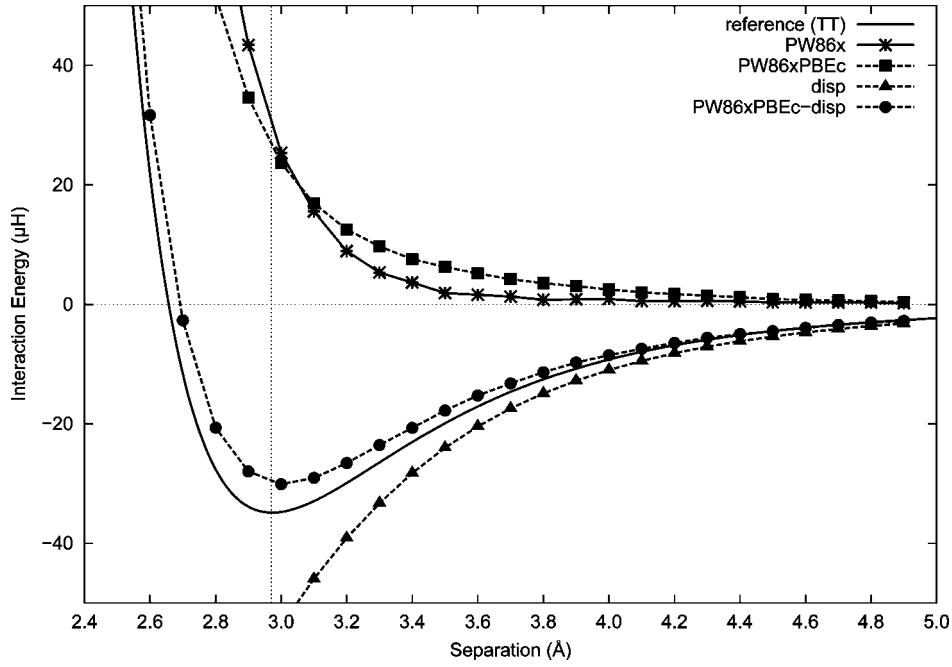

Figure 2. He_2 binding energy curves.

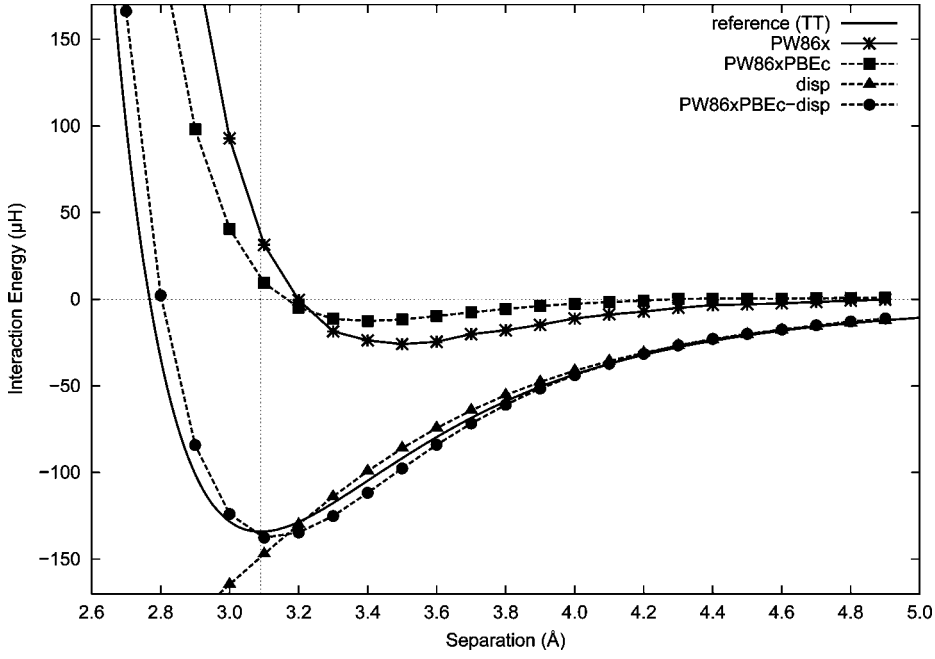

Figure 3. Ne_2 binding energy curves.

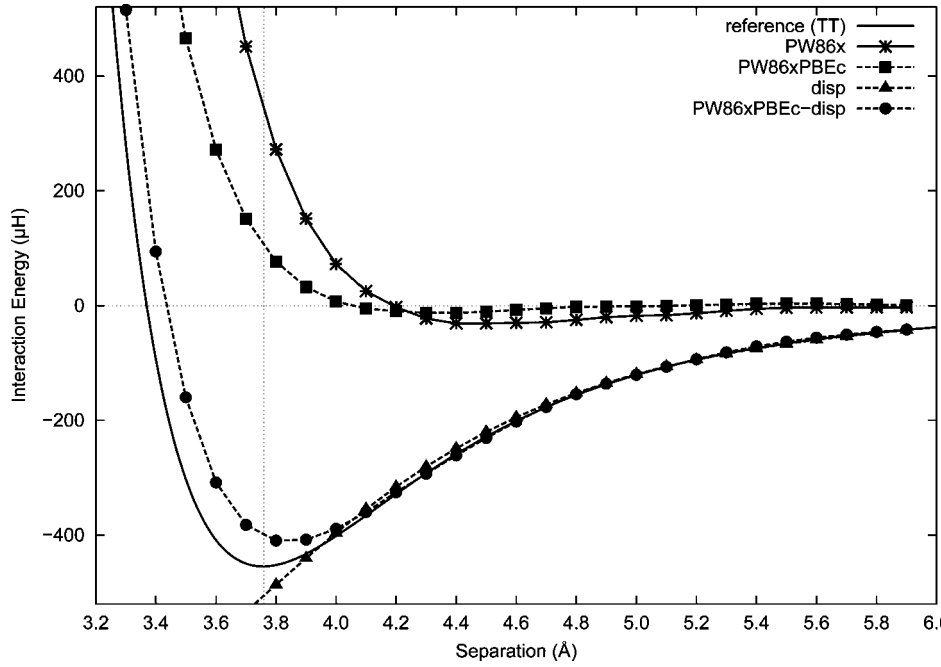

Figure 4. Ar_2 binding energy curves.

Table 6. Reference Equilibrium Separations (Å) and Calculated Reduced Equilibrium Separations for Various Combinations of Correlation GGA and Becke−Johnson Dispersion

	reference (TT)[51]	PW91-XX	PW91-BR	PBE-XX	PBE-BR
He_2	2.97	1.009	1.019	1.012	1.022
He−Ne	3.05	0.994	0.994	0.997	0.997
He−Ar	3.50	0.995	0.998	0.998	1.001
He−Kr	3.69	0.988	0.991	0.994	0.996
Ne_2	3.09	1.006	1.000	1.010	1.003
Ne−Ar	3.48	1.007	0.998	1.010	1.004
Ne−Kr	3.65	0.993	0.990	0.996	0.993
Ar_2	3.76	1.019	1.014	1.022	1.017
Ar−Kr	3.89	1.018	1.010	1.018	1.013
Kr_2	4.01	1.012	1.007	1.015	1.010
MPE		0.4	0.2	0.7	0.6
MAPE		1.0	0.8	1.0	0.8
MaxAPE		1.9	1.9	2.2	2.2

PW91 or PBE dynamical correlation are very accurate, with mean absolute and maximum errors of about 1% and 2%, respectively.

Binding energies obtained at the equilibrium separations are given in Table 7 as reduced quantities, along with the TT reference values (μH). For comparison, we also include CCSD(T),[6] DFT+CCSD(T),[74] and RSH+MP2[6] results. We obtain excellent binding energies with the dispersion-corrected GGA functionals, surpassing even CCSD(T) in accuracy, though our results are admittedly *fits* to the reference data.

5. Conclusions

Standard semilocal density functionals without an explicitly nonlocal correlation part or an asymptotic dispersion correction are unable to describe van der Waals interactions. Not only do they miss the attractive R^{-6} behavior at long-range but those that give vdW binding at shorter separations do so as a result of artifactual binding in their exchange parts. We have examined a variety of exchange GGAs for their ability to reproduce exact Hartree−Fock repulsion in rare-gas diatomics. While the selected functionals gave widely differing results, the PW86 exchange functional was found to be the most accurate.

PW86x was then combined with dynamical correlation functionals P86, PW91, and PBE and the nonempirical dispersion model of Becke and Johnson to give binding energy curves for the diatomics of the rare-gas atoms He, Ne, Ar, and Kr. The P86 correlation functional yielded poor results in these systems. The PW91 and PBE correlation functionals gave binding energy curves of excellent quality. Our scheme contains only two empirical parameters in the dispersion damping function. In future work, the method will be tested on vdW complexes beyond rare-gas diatomics.

We expect that functionals like eq 6, containing PW86 for exchange, will have wide applicability beyond van der Waals systems. PW86x has not been extensively benchmarked in the past but should perform similar to other exchange GGAs. The results of atomization-energy calculations on the 222 molecules of the G3/99 benchmark set of Curtiss et al.[75] are presented in Table 8. The computations are done post-xcLDA with the Numol program. We compare mean errors (ME), mean absolute errors (MAE), and maximum absolute errors (MaxAE) for the functional

$$E_{XC} = E_X^{GGA} + E_C^{PBE} + E_{disp}^{BJ} \quad (7)$$

using the exchange GGAs B86, B86b, B88, PW86, and PBE. We use the exact-exchange version of the Becke−Johnson dispersion model (XX) with the optimized damping parameters from Table 5, $a_1 = 0.95$ and $a_2 = 0.87$ Å.

All exchange GGAs perform similarly with the exception of PBE, which gives noticeably larger atomization energy

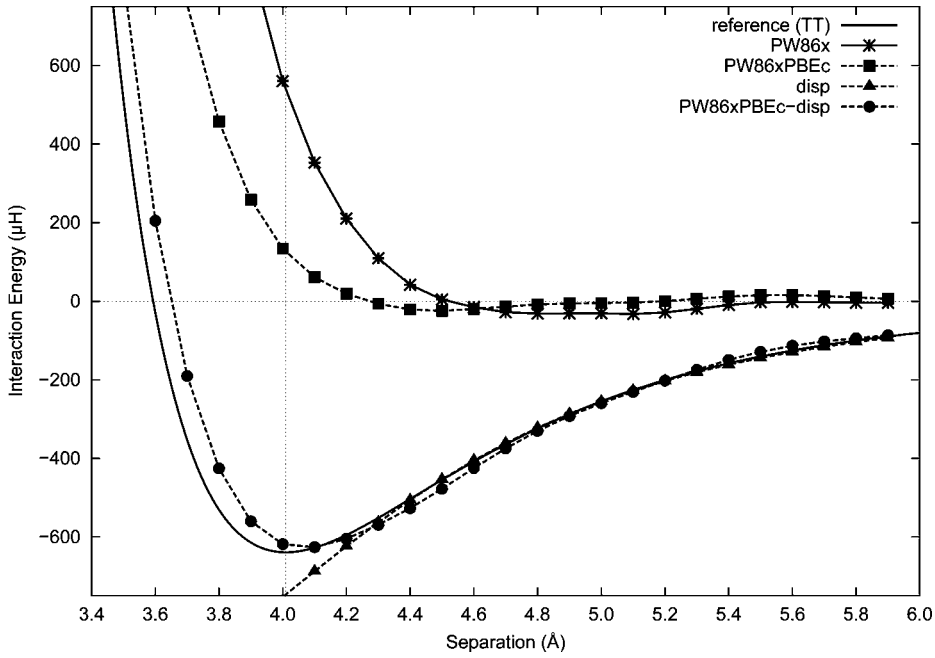

Figure 5. Kr_2 binding energy curves.

Table 7. Reference Binding Energies (μH) and Calculated Reduced Equilibrium Binding Energies for Various Combinations of Correlation GGA and Becke−Johnson Dispersion

	reference (TT)[51]	CCSD(T)[6]	DFT + CCSD(T)[74]	RSH + MP2[6]	PW91-XX	PW91-BR	PBE-XX	PBE-BR
He_2	34.8	0.85	0.62	0.58	0.86	0.77	0.87	0.78
He−Ne	66	0.85	0.75	0.68	1.09	1.11	1.08	1.10
He−Ar	93.7	0.86	0.84	0.85	1.03	0.97	1.02	0.96
He−Kr	99.6	0.85	0.82	0.85	1.04	0.94	1.02	0.93
Ne_2	134	0.79	0.86	0.73	1.05	1.19	1.03	1.17
Ne−Ar	211	0.81	0.97	0.87	1.04	1.09	1.02	1.07
Ne−Kr	224	0.81	1.02	0.89	1.15	1.16	1.13	1.14
Ar_2	454	0.83	1.00	1.00	0.92	0.93	0.91	0.92
Ar−Kr	531	0.84	1.02	1.00	0.97	0.96	0.95	0.95
Kr_2	638	0.83	1.04	1.00	0.99	0.98	0.98	0.96
MPE		−16.8	−10.5	−15.5	1.3	0.9	0.1	−0.3
MAPE		16.8	12.3	15.6	6.5	10.1	5.9	10.0
MaxAPE		21.1	37.8	41.9	14.6	23.2	13.4	22.4

Table 8. Atomization-Energy Errors (kcal/mol) for the Exchange-Correlation Functional of eq *7*

E_X^{GGA}	ME	MAE	MaxAE
B86	6.8	9.2	37.4
B86b	11.1	12.2	50.5
B88	6.9	9.5	37.4
PW86	7.1	10.0	41.8
PBE	23.3	23.7	87.0

errors compared to the other functionals. These results are consistent with previous atomization energy benchmarks for plain GGAs without a dispersion correction.[76] We conclude that PW86 exchange, combined with a dynamical correlation GGA and the Becke−Johnson dispersion model, yields excellent results for vdW interactions in rare-gas diatomics, and its performance for atomization energies is comparable to other standard GGAs.

Acknowledgment. This work is supported by the Natural Sciences and Engineering Research Council of Canada (NSERC) and the Killam Trust of Dalhousie University. Computational facilities are provided by ACEnet, the Atlantic Computational Excellence network.

References

(1) Dobson, J. F.; McLennan, K.; Rubio, A.; Wang, J.; Gould, T.; Le, H. M.; Dinte, B. P. *Aust. J. Chem.* **2001**, *54*, 513.

(2) Lacks, D. J.; Gordon, R. G. *Phys. Rev. A* **1993**, *47*, 4681.

(3) Becke, A. D. *Phys. Rev. A* **1988**, *38*, 3098.

(4) Perdew, J. P. In *Electronic Structure of Solids*; Ziesche, P., Eschrig, H., Eds.; Akademie Verlag: Berlin, 1991; p 11.

(5) Perdew, J. P.; Chevary, J. A.; Vosko, S. H.; Jackson, K. A.; Pederson, M. R.; Singh, D. J.; Fiolhais, C. *Phys. Rev. B* **1992**, *46*, 6671.

(6) Gerber, I. C.; Ángyán, J. G. *J. Chem. Phys.* **2007**, *126*, 044103.

(7) Grimme, S.; Antony, J.; Schwabe, T.; Mück-Lichtenfeld, C. *Org. Biomol. Chem.* **2007**, *5*, 741.

(8) Jurecka, P.; Cerný, J.; Hobza, P.; Salahub, D. R. *J. Comput. Chem.* **2007**, *28*, 555.

(9) Dion, M.; Rydberg, H.; Schröder, E.; Langreth, D. C.; Lundqvist, B. I. *Phys. Rev. Lett.* **2004**, *92*, 246401 .

(10) Thonhauser, T.; Cooper, V. R.; Li, S.; Puzder, A.; Hyldgaard, P.; Langreth, D. C. *Phys. Rev. B* **2007**, *76*, 125112.

(11) Zhang, Y.; Yang, W. *Phys. Rev. Lett.* **1998**, *80*, 890.

(12) Rydberg, H.; Dion, M.; Jacobson, N.; Schröder, E.; Hyldgaard, P.; Simak, S. I.; Langreth, D. C.; Lundqvist, B. I. *Phys. Rev. Lett.* **2003**, *91*, 126402.

(13) Langreth, D. C.; Dion, M.; Rydberg, H.; Schröder, E.; Hyldgaard, P.; Lundqvist, B. I. *Int. J. Quantum Chem.* **2005**, *101*, 599.

(14) Puzder, A.; Dion, M.; Langreth, D. C. *J. Chem. Phys.* **2006**, *124*, 164105.

(15) Thonhauser, T.; Puzder, A.; Langreth, D. C. *J. Chem. Phys.* **2006**, *124*, 164106.

(16) Vydrov, O. A.; Wu, Q.; Van Voorhis, T. *J. Chem. Phys.* **2008**, *129*, 014106.

(17) Kamiya, M.; Tsuneda, T.; Hirao, K. *J. Chem. Phys.* **2002**, *117*, 6010.

(18) Sato, T.; Tsuneda, T.; Hirao, K. *J. Chem. Phys.* **2007**, *126*, 234114.

(19) Tsuneda, T.; Suzumura, T.; Hirao, K. *J. Chem. Phys.* **1999**, *110*, 10664.

(20) Andersson, Y.; Langreth, D. C.; Lundqvist, B. I. *Phys. Rev. Lett.* **1996**, *76*, 102.

(21) Ángyán, J. G.; Gerber, I. C.; Savin, A.; Toulouse, J. *Phys. Rev. A* **2005**, *72*, 012510.

(22) Wu, X.; Vargas, M. C.; Nayak, S.; Lotrich, V.; Scoles, G. *J. Chem. Phys.* **2001**, *115*, 8748.

(23) Wu, Q.; Yang, W. *J. Chem. Phys.* **2002**, *116*, 515.

(24) Grimme, S. *J. Comput. Chem.* **2006**, *27*, 1787.

(25) Kurita, N.; Sekino, H. *Chem. Phys. Lett.* **2001**, *348*, 139.

(26) Xu, X.; Goddard, W. A. *Proc. Natl. Acad. Sci. U. S. A.* **2004**, *101*, 2673.

(27) Zhao, Y.; Truhlar, D. G. *J. Phys. Chem. A* **2005**, *109*, 5656.

(28) Zhao, Y.; Truhlar, D. *J. Phys. Chem. A* **2006**, *110*, 5121.

(29) Zhang, Y.; Vela, A.; Salahub, D. *Theor. Chem. Acc.* **2007**, *118*, 693.

(30) Wilson, L. C.; Levy, M. *Phys. Rev. B* **1990**, *41*, 12930.

(31) Walsh, T. R. *Phys. Chem. Chem. Phys.* **2005**, *7*, 443.

(32) Becke, A. D.; Johnson, E. R. *J. Chem. Phys.* **2005**, *122*, 154104.

(33) Becke, A. D.; Johnson, E. R. *J. Chem. Phys.* **2005**, *123*, 154101.

(34) Becke, A. D.; Johnson, E. R. *J. Chem. Phys.* **2006**, *124*, 014104.

(35) Becke, A. D.; Johnson, E. R. *J. Chem. Phys.* **2007**, *127*, 154108.

(36) Johnson, E. R.; Becke, A. D. *J. Chem. Phys.* **2005**, *123*, 024101.

(37) Johnson, E. R.; Becke, A. D. *J. Chem. Phys.* **2006**, *124*, 174104.

(38) Johnson, E. R.; Becke, A. D. *Chem. Phys. Lett.* **2006**, *432*, 600.

(39) Becke, A. D.; Johnson, E. R. *J. Chem. Phys.* **2007**, *127*, 124108.

(40) Becke, A. D. *J. Chem. Phys.* **1986**, *84*, 4524.

(41) Becke, A. D. *J. Chem. Phys.* **1986**, *85*, 7184.

(42) Perdew, J. P.; Yue, W. *Phys. Rev. B* **1986**, *33*, 8800.

(43) Perdew, J. P.; Burke, K.; Ernzerhof, M. *Phys. Rev. Lett.* **1996**, *77*, 3865.

(44) Perdew, J. P.; Burke, K.; Ernzerhof, M. *Phys. Rev. Lett.* **1997**, *78*, 1396.

(45) Becke, A. D.; Dickson, R. M. *J. Chem. Phys.* **1988**, *89*, 2993.

(46) Becke, A. D.; Dickson, R. M. *J. Chem. Phys.* **1990**, *92*, 3610.

(47) Zhang, Y.; Pan, W.; Yang, W. *J. Chem. Phys.* **1997**, *107*, 7921.

(48) Wesolowski, T.; Parisel, O.; Ellinger, Y.; Weber, J. *J. Phys. Chem. A* **1997**, *101*, 7818.

(49) van Mourik, T.; Gdanitz, R. J. *J. Chem. Phys.* **2002**, *116*, 9620.

(50) Ruzsinszky, A.; Perdew, J. P.; Csonka, G. I. *J. Phys. Chem. A* **2005**, *109*, 11015.

(51) Tang, K. T.; Toennies, J. P. *J. Chem. Phys.* **2003**, *118*, 4976.

(52) DePristo, A. E.; Kress, J. D. *J. Chem. Phys.* **1987**, *86*, 1425.

(53) Frisch, M. J.; Trucks, G. W.; Schlegel, H. B.; Scuseria, G. E.; Robb, M. A.; Cheeseman, J. R.; Montgomery, Jr., J. A.; Vreven, T.; Kudin, K. N.; Burant, J. C.; Millam, J. M.; Iyengar, S. S.; Tomasi, J.; Barone, V.; Mennucci, B.; Cossi, M.; Scalmani, G.; Rega, N.; Petersson, G. A.; Nakatsuji, H.; Hada, M.; Ehara, M.; Toyota, K.; Fukuda, R.; Hasegawa, J.; Ishida, M.; Nakajima, T.; Honda, Y.; Kitao, O.; Nakai, H.; Klene, M.; Li, X.; Knox, J. E.; Hratchian, H. P.; Cross, J. B.; Bakken, V.; Adamo, C.; Jaramillo, J.; Gomperts, R.; Stratmann, R. E.; Yazyev, O. ; Austin, A. J. ; Cammi, R. ; Pomelli, C. ; Ochterski, J. W. ; Ayala, P. Y.; Morokuma, K.; Voth, G. A.; Salvador, P.; Dannenberg, J. J.; Zakrzewski, V. G.; Dapprich, S.; Daniels, A. D.; Strain, M. C.; Farkas, O.; Malick, D. K.; Rabuck, A. D.; Raghavachari, K.; Foresman, J. B.; Ortiz, J. V.; Cui, Q.; Baboul, A. G.; Clifford, S.; Cioslowski, J.; Stefanov, B. B.; Liu, G.; Liashenko, A.; Piskorz, P.; Komaromi, I.; Martin, R. L.; Fox, D. J.; Keith, T.; Al-Laham, M. A.; Peng, C. Y.; Nanayakkara, A.; Challacombe, M.; Gill, P. M. W.; Johnson, B.; Chen, W.; Wong, M. W.; Gonzalez, C.; Pople, J. A. *Gaussian 03*, revision 05; Gaussian, Inc.: Wallingford, CT, 2004.

(54) Dunning, T. H. *J. Chem. Phys.* **1989**, *90*, 1007.

(55) Wilson, A. K.; Woon, D. E.; Peterson, K. A.; Dunning, T. H. *J. Chem. Phys.* **1999**, *110*, 7667.

(56) Woon, D. E.; Dunning, T. H. *J. Chem. Phys.* **1993**, *98*, 1358.

(57) Woon, D. E.; Dunning, T. H. *J. Chem. Phys.* **1994**, *100*, 2975.

(58) van Mourik, T.; Wilson, A. K.; Dunning, T. H *Mol. Phys.* **1999**, *96*, 529.

(59) van Mourik, T.; Dunning, T. H. *Int. J. Quantum Chem.* **2000**, *76*, 205.

(60) Jensen, F. *J. Phys. Chem. A* **2007**, *111*, 11198.

(61) Feller, D. *J. Comput. Chem.* **1996**, *17*, 1571.

(62) Schuchardt, K. L.; Didier, B. T.; Elsethagen, T.; Sun, L.; Gurumoorthi, V.; Chase, J.; Li, J.; Windus, T. L. *J. Chem. Inf. Model.* **2007**, *47*, 1045.

(63) Boys, S. F.; Bernardi, F. *Mol. Phys.* **1970**, *19*, 553.

(64) Becke, A. D. *J. Chem. Phys.* **1988**, *88*, 1053.

(65) Kristyán, S.; Pulay, P. *Chem. Phys. Lett.* **1994**, *229*, 175.

(66) Grimme, S. *J. Comput. Chem.* **2004**, *25*, 1463.

(67) Antony, J.; Grimme, S. *Phys. Chem. Chem. Phys.* **2006**, *8*, 5287.

(68) Ortmann, F.; Bechstedt, F.; Schmidt, W. G. *Phys. Rev. B* **2006**, *73*, 205101.

(69) Ángyán, J. G. *J. Chem. Phys.* **2007**, *127*, 024108.

(70) Becke, A. D.; Roussel, M. R. *Phys. Rev. A* **1989**, *39*, 3761.

(71) Perdew, J. P. *Phys. Rev. B* **1986**, *33*, 8822.

(72) Perdew, J. P. *Phys. Rev. B* **1986**, *34*, 7406.

(73) Perdew, J. P.; Wang, Y. *Phys. Rev. B* **1992**, *45*, 13244.

(74) Goll, E.; Werner, H.-J.; Stoll, H. *Phys. Chem. Chem. Phys.* **2005**, *7*, 3917.

(75) Curtiss, L. A.; Raghavachari, K.; Redfern, P. C.; Pople, J. A. *J. Chem. Phys.* **2000**, *112*, 7374.

(76) Staroverov, V. N.; Scuseria, G. E.; Tao, J.; Perdew, J. P. *J. Chem. Phys.* **2003**, *119*, 12129.

CT800522R

JCTC Journal of Chemical Theory and Computation

Modified Ehrenfest Formalism for Efficient Large-Scale ab initio Molecular Dynamics

Xavier Andrade,*,† Alberto Castro,‡ David Zueco,§ J. L. Alonso,¶ Pablo Echenique,¶ Fernando Falceto,|| and Ángel Rubio*,†

Nano-bio Spectroscopy Group and European Theoretical Spectroscopy Facility (ETSF), Departamento de Física de Materiales, Universidad del País Vasco UPV/EHU, Centro Mixto CSIC-UPV, and DIPC, Edificio Korta, Av. Tolosa 72, E-20018 San Sebastián, Spain, Institut für Theoretisch Physik, Freie Universität Berlin, Arnimallee, 14, Berlin 14195, Deutschland, Institut für Physik, Universität Augsburg, Universitätsstraβe 1, D-86135 Augsburg, Germany, Instituto de Biocomputación y Física de Sistemas Complejos (BIFI), Universidad de Zaragoza, Spain, and Departamento de Física Teórica, Universidad de Zaragoza, Pedro Cerbuna 12, E-50009 Zaragoza, Spain

Received December 1, 2008

Abstract: We present in detail the recently derived ab initio molecular dynamics (AIMD) formalism [Alonso et al. *Phys. Rev. Lett.* **2008**, *101*, 096403], which due to its numerical properties, is ideal for simulating the dynamics of systems containing thousands of atoms. A major drawback of traditional AIMD methods is the necessity to enforce the orthogonalization of the wave functions, which can become the bottleneck for very large systems. Alternatively, one can handle the electron−ion dynamics within the Ehrenfest scheme where no explicit orthogonalization is necessary, however the time step is too small for practical applications. Here we preserve the desirable properties of Ehrenfest in a new scheme that allows for a considerable increase of the time step while keeping the system close to the Born−Oppenheimer surface. We show that the automatically enforced orthogonalization is of fundamental importance for large systems because not only it improves the scaling of the approach with the system size but it also allows for an additional very efficient parallelization level. In this work, we provide the formal details of the new method, describe its implementation, and present some applications to some test systems. Comparisons with the widely used Car−Parrinello molecular dynamics method are made, showing that the new approach is advantageous above a certain number of atoms in the system. The method is not tied to a particular wave function representation, making it suitable for inclusion in any AIMD software package.

1. Introduction

In the last decades, the concept of theoretical atomistic simulations of complex structures in different fields of research (from materials science, in general, to biology) has emerged as a third discipline between theory and experiment. Computational science is now an essential adjunct to laboratory experiments; it provides high-resolution simulations that can guide research and serve as tools for discovery. Today, computer simulations unifying electronic structure and ion dynamics have come of age, although important challenges remain to be solved. This "virtual lab" can provide valuable information about complex materials with refined resolution in space and time, allowing researchers to gain

* E-mail: xavier@tddft.org (X.A.); angel.rubio@ehu.es (Á.R.).
† Universidad del País Vasco.
‡ Freie Universität Berlin.
§ Universität Augsburg.
¶ BIFI.
|| Universidad de Zaragoza.

10.1021/ct800518j CCC: $40.75
Published on Web 03/20/2009

understanding about the microscopic and physical origins of materials behavior: from low-dimensional nanostructures to geology, atmospheric science, renewable energy, (nano)-electronic devices, (supra)molecular chemistry, etc. Since the numerical approaches to handle those problems require "large-scale calculations" the success of this avenue of research was only possible due to the development of high-performance computers.[1] The present work addresses our recent developments in the field of first-principles molecular dynamics simulations. Before getting into the details, we would like to frame properly the work from a historical perspective.

Molecular dynamics (MD)[2] consists of "following the dynamics of a system of atoms or molecules governed by some interaction potential; in order to do so, one could at any instant calculate the force on each particle by considering the influence of each of its neighbors. The trajectories could then be traced by allowing the particles to move under a constant force for a short-time interval and then by recalculating a new force to apply for the next short-time interval, and so on." This description was given in 1959 by Alder and Wainwright[3] in one the first reports of such a computer-aided calculation,[4] though the first MD simulation was probably done by Fermi et al.[5] for a one-dimensional model solid. We can still use this description to broadly define the scope of MD, although many variants and ground-breaking developments have appeared during these fifty years, addressing mainly two key issues: the limitation in the number of particles and the time ranges that can be addressed, and the accuracy of the interaction potential.

The first issue was already properly stated by Alder and Wainwright: "The essential limitations of the method are due to the relatively small number of particles that can be handled. The size of the system of molecules is limited by the memory capacity of the computing machines." This statement is not obsolete, although the expression "small number of particles" has today of course a very different meaning—linked as it is to the exponentially growing capacities of computers.

The second issue—the manner in which the atomic interaction potential is described—has also developed significantly over the years. Alder and Wainwright used solid impenetrable spheres in the place of atoms; nowadays, in the realm of the so-called "classical" MD, one makes use of *force fields*: simple mathematical formulas are used to describe atomic interactions. The expressions are parametrized by fitting either to reference first-principles calculations or experimental data. These models have become extremely sophisticated and successful, although they are ultimately bound by a number of limitations. For example, it is difficult to tackle electronic polarization effects and one needs to make use of polarizable models, whose transferability is very questionable but are widely used with success in many situations. Likewise, the force field models are constructed assuming a predetermined bond arrangement, disabling the option of chemical reactions—some techniques exist that attempt to overcome this restriction,[6] but they are also difficult to transfer and must be carefully adapted to each particular system.

The road toward precise, nonempirical interatomic potentials reached its destination when the possibility of performing ab initio MD (AIMD) was realized.[7,8] In this approach, the potential is not modeled a priori via some parametrized expression, but rather generated "on the fly" by performing accurate first-principles electronic structure calculations. The accuracy of the calculation is therefore limited by the level of theory used to obtain the electronic structure—although one must not forget that underlying all MD simulations is the electronic−nuclear separation *ansatz* and the classical limit for the nuclei. The use of very accurate first principles methods for the electrons implies very large computational times, and therefore, it is not surprising that AIMD was not really born until density-functional theory (DFT) became mature—since it provides the necessary balance between accuracy and computational feasibility.[9] Of fundamental importance was the development of gradient generalized exchange and correlation functionals, like the ones proposed by John Perdew,[10−12] that can reproduce experimental results better than the local density approximation.[13−15] In fact, the whole field of AIMD was initiated by Car and Parrinello in 1985,[16] in a ground-breaking work that unified DFT and MD and introduced a very ingenious acceleration scheme based on fake electronic dynamics. As a consequence, the term AIMD in most occasions refers exclusively to this technique proposed by Car and Parrinello. However, it can be understood in a more general sense, including more possibilities that have developed thereafter—and in the present work, we will in fact discuss one of them. The new scheme proposed below will benefit from all the algorithm developments and progress being done in the CP framework.

As a matter of fact, the most obvious way to perform AIMD would be to compute the forces on the nuclei by performing electronic structure calculations on the ground-state Born−Oppenheimer potential energy surface. This we can call ground-state Born−Oppenheimer MD (gsBOMD). It implies a demanding electronic minimization at each step, and schemes using time-reversible integrators have been recently developed.[17] The Car−Parrinello (CP) technique is a scheme that allows to propagate the Kohn−Sham (KS) orbitals with a fictitious dynamics that nevertheless mimics gsBOMD—bypassing the need for the expensive minimization. This idea has produced an enormous impact, allowing for successful applications in a surprisingly wide range of areas (see the special number in ref 18 and references therein). Still, it implies a substantial cost, and many interesting potential applications have been frustrated due to the impossibility of attaining the necessary system size or simulation time length. There have been several efforts to refine or redefine the CP scheme in order to enhance its power: linear scaling methods[19] attempt to speed-up in general any electronic structure calculation; the use of a localized orbital representation (instead of the much more common plane-waves utilized by CP practitioners) has also been proposed;[20] recently, Kühne and co-workers[21] have proposed an approach which is based on CP, but which allows for sizable gains in efficiency. In any case, the cost associated with the orbital orthonormalization that is required

in any CP-like procedure is a potential bottleneck that hinders its application to very large-scale simulations.

Another possible AIMD strategy is Ehrenfest MD, to be presented in the following section. In this case, the electron-nuclei separation *ansatz* and the Wentzel−Kramers−Brillouin[22] (WKB) classical limit are also considered; however, the electronic subsystem is not assumed to evolve on only one of the electronic adiabatic states—typically the ground-state one. Instead the electrons are allowed to evolve on an arbitrary wave function that corresponds to a combinations of adiabatic states. As a drawback, the time-step required for a simulation in this scheme is determined by the maximum electronic frequencies, which means about 3 orders of magnitude less than the time step required to follow the nuclei in a BOMD.

If one wants to do Ehrenfest MD, the traditional "ground-state" DFT is not enough, and one must rely on time-dependent density functional theory (TDDFT).[23] Coupling TDDFT to Ehrenfest MD provides with an orthogonalization-free alternative to CP AIMD—plus it allows for excited-states AIMD. If the system is such that the gap between the ground-state and the excited states is large, Ehrenfest MD tends to gsBOMD. The advantage provided by the lack of need of orthogonalization is unfortunately offset by the smallness of the required time step.[7,13] Recently, some of the authors of the present article have presented a formalism for large-scale AIMD based on Ehrenfest and TDDFT, that borrows some of the ideas of CP in order to increase this time step and make TDDFT-Ehrenfest competitive with CP.[24]

This article intends to provide a more detailed description of this proposed methodology: we start, in section 2 by revisiting the mathematical route that leads from the full many-particle electronic and nuclear Schrödinger equation to the Ehrenfest MD model. Next, we clear up some confusions sometimes found in the literature related to the application of the Hellmann−Feynman theorem, and we discuss the integration of Ehrenfest dynamics in the TDDFT framework. Section 4 presents in detail the aforementioned novel formalism, along with a discussion regarding symmetries and conservation laws. Sections 5 and 6 are dedicated to the numerical technicalities, including several application examples.

2. Ehrenfest Dynamics: Fundaments and Implications for First Principles Simulations

The starting point is the time-dependent Schrödinger equation (atomic units[25] are used throughout this paper) for a molecular system described by the wave function $\Phi(\{x_j\}_{j=1}^n,\{X_J\}_{J=1}^N, t)$:

$$i\dot{\Phi}(\{x_j\}_{j=1}^n, \{X_J\}_{J=1}^N, t) = \hat{H}\Phi(\{x_j\}_{j=1}^n, \{X_J\}_{J=1}^N, t) \quad (1)$$

where the dot indicates the time derivative and we denote as $\mathbf{r}_j$, σ_j, and $\mathbf{R}_J$, Σ_J the Euclidean coordinates and the spin of the jth electron and the Jth nuclei, respectively, with $j = 1,..., n$, and $J = 1,..., N$. We also define $x_j := (\mathbf{r}_j,\sigma_j)$ and $X_J := (\mathbf{R}_J,\Sigma_J)$, and we shall denote the whole sets $r := \{\mathbf{r}_j\}_{j=1}^n$, $R := \{\mathbf{R}_J\}_{J=1}^N$, $x := \{x_j\}_{j=1}^n$, and $X := \{X_J\}_{J=1}^N$, using single letters in order to simplify the expressions.

The nonrelativistic molecular Hamiltonian operator is defined as

$$\begin{aligned}\hat{H} &:= -\sum_J \frac{1}{2M_J}\nabla_J^2 - \sum_j \frac{1}{2}\nabla_j^2 + \sum_{J<K}\frac{Z_J Z_K}{|\mathbf{R}_J - \mathbf{R}_K|} + \\ &\quad \sum_{j<k}\frac{1}{|\mathbf{r}_j - \mathbf{r}_k|} - \sum_{Jj}\frac{Z_J}{|\mathbf{R}_J - \mathbf{r}_j|} \\ &:= -\sum_J \frac{1}{2M_J}\nabla_J^2 - \sum_j \frac{1}{2}\nabla_j^2 + \hat{V}_{\text{n-e}}(r,R) \\ &:= -\sum_J \frac{1}{2M_J}\nabla_J^2 + \hat{H}_{\text{e}}(r,R)\end{aligned} \quad (2)$$

where all sums must be understood as running over the whole natural set for each index, unless otherwise specified. M_J is the mass of the Jth nucleus in units of the electron mass, and Z_J is the charge of the Jth nucleus in units of (minus) the electron charge. Also note that we have defined the nuclei-electrons potential $\hat{V}_{\text{n-e}}(r,R)$ and the electronic Hamiltonian $\hat{H}_{\text{e}}(r,R)$ operators.

The initial conditions of eq 1 are given by

$$\Phi^0 := \Phi(x, X, 0) \quad (3)$$

and we assume that $\Phi(x,X,t)$ vanishes at infinity $\forall t$.

Now, in order to derive the quantum-classical molecular dynamics (QCMD) known as Ehrenfest molecular dynamics from the above setup, one starts with a separation ansatz for the wave function $\Phi(x,X,t)$ between the electrons and the nuclei,[26] leading to the so-called time-dependent self-consistent-field (TDSCF) equations.[7,27] The next step is to approximate the nuclei as classical point particles via short wave asymptotics or WKB approximation.[7,22,27] The resultant Ehrenfest MD scheme is contained in the following system of coupled differential equations:[27]

$$i\dot{\psi}(x,t) = \hat{H}_{\text{e}}(r, R(t))\psi(x,t) \quad (4a)$$

$$M_J\ddot{\mathbf{R}}_J(t) = -\int \mathrm{d}x\, \psi^*(x,t)[\nabla_J \hat{H}_{\text{e}}(r;R(t))]\psi(x,t), \quad J = 1,...,N \quad (4b)$$

where $\psi(x,t)$ is the wave function of the electrons, $\mathbf{R}_J(t)$ are the nuclear trajectories, and we have used $\mathrm{d}x$ to indicate integration over all spatial electronic coordinates and summation over all electronic spin degrees of freedom. Also, a semicolon has been used to separate the r from the $R(t)$ in the electronic Hamiltonian, in order to stress that only the latter are actual time-dependent degrees of freedom the system.

The initial conditions in Ehrenfest MD are given by

$$\psi^0 := \psi(x, 0) \quad (5a)$$

$$\mathbf{R}_J^0 := \mathbf{R}_J(0), \quad \dot{\mathbf{R}}_J^0 := \dot{\mathbf{R}}_J(0), \quad J = 1,...,N \quad (5b)$$

and we assume that $\psi(x,t)$ vanishes at infinity $\forall t$.

Also note that, since in this scheme $\{\mathbf{R}_J,\psi\}$ is a set of independent variables, we can rewrite eqs 4b as

$$M_J\ddot{\mathbf{R}}_J(t) = -\nabla_J \int \mathrm{d}x\, \psi^*(x,t)\hat{H}_{\text{e}}(r;R(t))\psi(x,t), \quad J = 1,...,N \quad (6)$$

a fact which is similar in form, but unrelated to the Hellmann−Feynman theorem.[28] As pointed out by Tully,[29] it is likely that the confusion about whether eqs 6 should be used to define the Ehrenfest MD, or the gradient must be applied to the electronic Hamiltonian inside the integral, as in (4b), has arisen from applications in which $\psi(x,t)$ is expressed as a finite expansion in the set of adiabatic basis functions, $\eta_a(x;R)$, defined as the eigenfunctions[30] of $\hat{H}_e(r;R)$:

$$\hat{H}_e(r;R(t))\eta_a(x;R(t)) = E_a(R(t))\eta_a(x;R(t)) \tag{7}$$

The use of a precise notation, such as the one introduced in this section, helps to avoid this kind of confusions. An example of a misleading notation in this context would consist in writing $\psi(r,R,t)$ for the electronic wave function,[29,31] when, as we have emphasized, there exists no explicit dependence of ψ on the nuclear positions R.

In Ehrenfest MD, transitions between electronic adiabatic states are included. This can be made evident by performing the following change of coordinates from $\{\psi,R\}$ to $\{c,R'\}$ (with $c := \{c_a\}_{a=1}^{\infty}$):

$$\psi(x,t) = \sum_a c_a(t)\eta_a(x;R'(t)) \tag{8a}$$

$$R_J(t) = R'_J(t), \quad J = 1, ..., N \tag{8b}$$

where $\eta_a(x;R)$ are known functions given by (7) and, even if the transformation between the R and the R' is trivial, we have used the prime to emphasize that there are two distinct sets of independent variables: $\{\psi,R\}$ and $\{c,R'\}$. This is very important if one needs to take partial derivatives, since a partial derivative with respect to a given variable is only well defined when the independent set to which that variable belongs is specified.[32] For example, a possible mistake is to assume that, since c_a "is independent of" $\mathbf{R}'_J$, and $\mathbf{R}_J = \mathbf{R}'_J$, then c_a "is also independent" of $\mathbf{R}_J$ and, therefore, the unprimed partial derivative $\nabla_J c_a$ is zero. The flaw in this reasoning is that the unprimed partial derivative ∇_J is defined to be performed at constant ψ and not at constant c, since the relevant set of independent variables is $\{\psi,R\}$. In fact, if we write the inverse transformation

$$c_a(t) = \int dx\, \psi^*(x,t)\eta_a(x;R(t)), \quad a = 1, ...,\infty \tag{9a}$$

$$\mathbf{R}'_J(t) = \mathbf{R}_J(t), \quad J = 1, ..., N \tag{9b}$$

we can clearly appreciate that, even if it is independent from R' by construction, c_a is neither independent from ψ nor from R.[33] On the other hand, if we truncated the sum in (8a), then there would appear an explicit dependence of ψ on R and the state of affairs would be different, since $\{\psi,R\}$ would no longer be a set of independent variables. However, in the context of an exact (infinite) expansion in (8a), the right-hand sides of eqs 4b and 6 are equal, as we mentioned before, and we do not have to worry about which one is more appropriate. It is in this infinite-adiabatic basis situation that we will now use eq 4b and the expansion in (8a) to illustrate the nonadiabatic character of Ehrenfest MD.

If we perform the change of variables described in eqs 8a to the Ehrenfest MD eqs 4a and we use that

$$\nabla_J \hat{H}_e(r;R) = \nabla'_J \hat{H}_e(r;R') \tag{10}$$

we see that we will have to calculate terms of the form

$$\int dx\, \eta_a^*(x;R'(t))\nabla'_j \hat{H}_e(r;R'(t))\eta_b(x;R'(t)) \tag{11}$$

which can be easily extracted from the relation

$$\nabla'_J \int dx\, \eta_a^*(x;R'(t))\hat{H}_e(r;R'(t))\eta_b(x;R'(t)) = \nabla'_J E_a(R'(t))\delta_{ab} \tag{12}$$

In this way, we obtain for the nuclear Ehrenfest MD equation

$$M_J \ddot{\mathbf{R}}'_J(t) = -\sum_a \left|c_a(t)\right|^2 \nabla'_J E_a(R'(t)) - \sum_{a,b} c_a^*(t)c_b(t)[E_a(R'(t)) - E_b(R'(t))]\mathbf{d}_J^{ab}(R'(t)), \quad J = 1, ..., N \tag{13}$$

where the nonadiabatic couplings (NACs) are defined as

$$\mathbf{d}_J^{ab}(R'(t)) := \int dx\, \eta_a^*(x;R'(t))\nabla'_J \eta_b(x;R'(t)) \tag{14}$$

To obtain the new electronic Ehrenfest MD equation, we perform the change of variables to (4a) and we then multiply the resulting expression by $\eta_b^*(x;R'(t))$ and integrate over the electronic coordinates x. Proceeding in this way, we arrive at

$$i\hbar \dot{c}_a(t) = E_a(R'(t))c_a(t) - i\hbar \sum_b c_b(t)[\sum_J \dot{\mathbf{R}}'_J(t)\cdot\mathbf{d}_J^{ab}(R'(t))] \tag{15}$$

In the nuclear eqs 13, we can see that the term depending on the moduli $|c_a(t)|^2$ directly couples the population of the adiabatic states to the nuclei trajectories, whereas interferences between these states are included via the $c_a^*(t)c_{b\neq a}(t)$ contributions. Analogously, in the electronic equations above, the first term represents the typical evolution of the coefficient of an eigenstate of a Hamiltonian, but differently from the full quantum case, in Ehrenfest MD, the second term couples the evolution of all states with each other's through the velocity of the classical nuclei and the NACs.

Moreover, Ehrenfest MD is fully (quantum) coherent, since the complex coefficients $c_a(t)$, are the ones corresponding to the quantum superposition in the electronic wave function. A proper theory that treats realistically the electronic process of coherence and decoherence is of fundamental importance to properly interpret transition rates and to have control over processes happening at the attosecond/femtosecond time scales, such as the description of the optimal-pulse laser (in optimal control theory) that enhances a given channel in a chemical reaction, the manipulation of qbits in quantum computing devices, the generation of soft X-rays by high-harmonic generation, or the energy transfer processes in photosynthetic units.[34]

At finite temperature, it is known that Ehrenfest MD cannot account for the Boltzmann equilibrium population of the quantum subsystem.[35,36] The underlying reason of this failure is the mean field approximation in eq 4b which

neglects the nuclei response to the microscopic fluctuations in the electronic charge density.

In order to address this point, it is important to distinguish between two different physical situations considered in the literature for studying equilibrium within Ehrenfest: In ref 35, a mixed quantum−classical system is coupled, only via the classical degrees of freedom, to a classical bath. The dissipative dynamics is integrated using a Nosé thermostat, while the mixed quantum−classical one is integrated using Ehrenfest. In ref 36, on the other hand, the classical degrees of freedom are the bath to which the quantum system is coupled, i.e., the thermalization of a quantum system due to its "Ehrenfest-like" coupling to a bath or solvent, is discussed. Only the first of these two approaches corresponds to the physical problem we want to deal with, namely, the thermalization of a mixed quantum−classical molecule in a bath.

Once the aforementioned drawback has been recognized, some authors have proposed several *patches* to ensure the Boltzmann population equilibrium for the quantum subsystem: In Tully's surface hopping (SH) method,[37] the quantum degrees of freedom also follow eq 4a; however, instead of the mean-field dynamics (4b), the classical degrees of freedom follow a stochasticlike equation describing jumps between adiabatic states. Unfortunately, this method does not give in general the desired equilibrium averages either,[38] and it looses the physical meaning of time during propagation.

Another new method by Bastida and collaborators,[39] proposes an ad-hoc modification of the Ehrenfest equations in order to obtain the correct equilibrium distribution of a quantum system coupled to a classical bath, i.e., the classical degrees of freedom are the solvent for the quantum system. Their idea can be summarized as follows: Expressing in (15) the complex coefficients in polar form ($c_a = \rho_a \exp\{i\theta_a\}$) and writing the equations for the moduli, one obtains $\dot{\rho}_a = -\sum_b \rho_b \cos(\theta_a - \theta_b) D_{ab}$, where we have used the compact notation: $D_{ab} = \sum_J \dot{\mathbf{R}}_J(t) \cdot \mathbf{d}_J^{ab}(R'(t))$, cf. eq 15. Analogous equations are derived for the phases θ_a. Written like this, the equations are formally similar to balancelike equations for the diagonal elements of the density matrix of the quantum system in the adiabatic basis. These kinetic equations have been extensively studied in relaxation processes, and it is known that, to ensure equilibrium, the coefficients, D_{ab}, must fulfill the detailed-balance condition, i.e., $D_{ab} = \exp\{-\beta\Delta_{ba}\} D_{ba}$, with Δ_{ba} being the energy difference between the b and a states.[40] The proposal by Bastida et al.[39] proceeds by defining some modified transition coefficients $\tilde{D}_{ab}$, such that detailed balance is enforced, thus approaching the Boltzmann equilibrium population for the quantum system.

Coming back to the situation discussed in ref 35, i.e., where the classical subsystem is not a bath but a part of the mixed quantum−classical system coupled to a reservoir, one can go beyond Ehrenfest and make use of the formalism developed in refs 41−43. The description in these works is not mean-field and the quantum−classical dynamics is treated *exactly*. Although its practical implementation seems cumbersome, it is a path to explore, with possible modifications, in the near future.

Finally we should mention ref 44, where the complementary situation to ref 35 is studied, coupling the quantum system directly to the bath, while the classical degrees of freedom are not coupled directly to any reservoir. A study of the deviations from equilibrium in this case is still missing.

3. Ehrenfest-TDDFT

TDDFT offers a natural framework on which to implement Ehrenfest MD. In fact, starting by an extension[45] of the Runge−Gross theorem[46] to arbitrary multicomponent systems, one can develop a TDDFT[47] for the combined system of electrons and nuclei described by (1). Then, after imposing a classical treatment of nuclear motion, one arrives to an Ehrenfest-TDDFT dynamics. This scheme can also be generated from the following Lagrangian:[24,47,48]

$$L[\varphi(t), \varphi(t), R(t), \dot{R}(t)] := \frac{i}{2} \sum_A \int d\mathbf{r} (\varphi_A^*(\mathbf{r}, t) \dot{\varphi}_A(\mathbf{r}, t) - \dot{\varphi}_A^*(\mathbf{r}, t) \varphi_A(\mathbf{r}, t)) + \sum_J \frac{M_J}{2} \dot{\mathbf{R}}_J(t) \cdot \dot{\mathbf{R}}_J(t) - E_{\mathrm{KS}}[\varphi(t), R(t)] \quad (16)$$

where we have denoted by $\varphi := \{\varphi_A\}_{A=1}^{n/2}$, the whole set of Kohn−Sham (KS) orbitals of a closed-shell molecule, and $E_{\mathrm{KS}}[\varphi,R]$ is the KS energy:

$$E_{\mathrm{KS}}[\varphi, R] := 2 \sum_A \int d\mathbf{r}\, \varphi_A^*(\mathbf{r}, t) \left(-\frac{\nabla^2}{2}\right) \varphi_A(\mathbf{r}, t) - \int d\mathbf{r} \sum_J \left(\frac{Z_J}{|\mathbf{R}_J(t) - \mathbf{r}|}\right) \rho(\mathbf{r}, t) + \frac{1}{2} \int d\mathbf{r}\, d\mathbf{r}' \frac{\rho(\mathbf{r}, t) \rho(\mathbf{r}', t)}{|\mathbf{r} - \mathbf{r}'|} + E_{\mathrm{XC}}[\rho(\mathbf{r}, t)] + \sum_{J<K} \frac{Z_J Z_K}{|\mathbf{R}_J(t) - \mathbf{R}_K(t)|} \quad (17)$$

where $E_{\mathrm{XC}}[\rho(r)]$ is the exchange-correlation energy and the time-dependent electronic density is defined as

$$\rho(\mathbf{r}, t) := 2 \sum_A \left|\varphi_A(\mathbf{r}, t)\right|^2 \quad (18)$$

In the following section, we introduce a modification of the Ehrenfest-TDDFT dynamics obtained from (16) aimed to the study of situations in which the contribution of the electronic excited states to the nuclei dynamics is negligible, i.e., situations in which one is interested in performing ground-state Born−Oppenheimer molecular dynamics (gs-BOMD).[7]

4. Modified Ehrenfest-TDDFT Formalism

4.1. Lagrangian and Equations of Motion. We now introduce the basic concepts and approximations that define the new fast Ehrenfest-TDDFT dynamics framework that some of the authors introduced in ref 24. The new scheme can be obtained from the following Lagrangian

$$L[\varphi,\dot{\varphi},R,\dot{R}] := \mu\frac{i}{2}\sum_A \int \mathrm{d}\mathbf{r}\,[\varphi_A^*(\mathbf{r},t)\dot{\varphi}_A(\mathbf{r},t) - \dot{\varphi}_A^*(\mathbf{r},t)\varphi_A(\mathbf{r},t)] + \sum_J \frac{M_J}{2}\dot{\mathbf{R}}_J\cdot\dot{\mathbf{R}}_J - E_{\mathrm{KS}}[\varphi,R] \quad (19)$$

Note that the major modification with respect to the Ehrenfest-TDDFT Lagrangian in eq 16 is the presence of a parameter μ that introduces a rescaling of the electronic velocities (Ehrenfest-TDDFT is recovered when $\mu = 1$). The equations of motion of the new Lagrangian, eq 19, are the following:

$$i\mu\dot{\varphi}_A(\mathbf{r},t) = \frac{\delta E_{\mathrm{KS}}[\varphi,R]}{\delta\dot{\varphi}_A^*} = -\frac{1}{2}\nabla^2\varphi_A(\mathbf{r},t) + v_{\mathrm{eff}}[\varphi,R]\varphi_A(\mathbf{r},t), \quad A = 1,...,\frac{n}{2} \quad (20a)$$

$$M_J\ddot{\mathbf{R}}_J = -\nabla_J E_{\mathrm{KS}}[\varphi,R], \qquad J = 1,...,N \quad (20b)$$

where v_{eff} is the time-dependent KS effective potential. As we are interested in the adiabatic regime, we will restrict the exchange and correlation potential to depend only on the instantaneous density (in general the exchange correlation potential in TDDFT depends on the density of all previous times, although for practical calculation this same adiabatic approximation is done).

Compare with the gsBOMD Lagrangian

$$L_{\mathrm{BO}}[\varphi,R,\dot{R}] := \sum_J \frac{M_J}{2}\dot{\mathbf{R}}_J\cdot\dot{\mathbf{R}}_J - E_{\mathrm{KS}}[\varphi,R] + \sum_{AB}\Lambda_{AB}^{\mathrm{BO}}\left(\int \mathrm{d}\mathbf{r}\,\varphi_A^*(\mathbf{r},t)\varphi_B(\mathbf{r},t) - \delta_{AB}\right) \quad (21)$$

and the corresponding equations of motion:

$$-\frac{1}{2}\nabla^2\varphi_A(\mathbf{r},t) + v_{\mathrm{eff}}[\varphi,R]\varphi_A(\mathbf{r},t) = \sum_B \Lambda_{AB}^{\mathrm{BO}}\varphi_B(\mathbf{r},t), \quad A = 1,...,\frac{n}{2} \quad (22a)$$

$$\int \mathrm{d}\mathbf{r}\,\varphi_A^*(\mathbf{r},t)\varphi_B(\mathbf{r},t) = \delta_{AB}, \qquad A,B = 1,...,\frac{n}{2} \quad (22b)$$

$$M_J\ddot{\mathbf{R}}_J = -\nabla_J E_{\mathrm{KS}}[\varphi,R], \qquad J = 1,...,N \quad (22c)$$

where $\Lambda^{\mathrm{BO}} := (\Lambda_{AB}^{\mathrm{BO}})$ is a Hermitian matrix of time-dependent Lagrange multipliers that ensure that the orbitals φ form an orthonormal set at each instant of time. The Euler−Lagrange equations corresponding to $\Lambda_{AB}^{\mathrm{BO}}$ in (22b) are exactly these orthonormality constraints, and, together with eq 22a, constitute the time-independent KS equations. Therefore, assuming no metastability issues in the optimization problem, the orbitals φ are completely determined[49] by the nuclear coordinates R, being in fact the BO ground state (gs), $\varphi = \varphi^{\mathrm{gs}}(R)$, which allows us to write the equations of motion for gsBOMD in a much more compact and familiar form:

$$M_J\ddot{\mathbf{R}}_J = -\nabla_J E_{\mathrm{KS}}[\varphi^{\mathrm{gs}}(R),R], \quad J = 1,...,N \quad (23)$$

We can also compare the dynamics introduced in eqs 20a with CPMD, whose Lagrangian reads

$$L_{\mathrm{CP}}[\varphi,\dot{\varphi},R,\dot{R}] := \frac{1}{2}\mu_{\mathrm{CP}}\sum_A \int \mathrm{d}\mathbf{r}\,|\dot{\varphi}_A(\mathbf{r},t)|^2 + \sum_J \frac{M_J}{2}\dot{\mathbf{R}}_J\cdot\dot{\mathbf{R}}_J - E_{\mathrm{KS}}[\varphi,R] + \sum_{AB}\Lambda_{AB}^{\mathrm{CP}}\left(\int \mathrm{d}\mathbf{r}\,\varphi_A^*(\mathbf{r},t)\varphi_B(\mathbf{r},t) - \delta_{AB}\right) \quad (24)$$

and the corresponding equations of motion are

$$\mu_{\mathrm{CP}}\ddot{\varphi}_A(\mathbf{r},t) = -\frac{1}{2}\nabla^2\varphi_A(\mathbf{r},t) + v_{\mathrm{eff}}[\varphi,R] + \sum_B \Lambda_{AB}^{\mathrm{CP}}\varphi_B(r,t), \quad A = 1,...,\frac{n}{2} \quad (25a)$$

$$\int \mathrm{d}\mathbf{r}\,\varphi_A^*(\mathbf{r},t)\varphi_B(\mathbf{r},t) = \delta_{AB}, \qquad A,B = 1,...,\frac{n}{2} \quad (25b)$$

$$M_J\ddot{\mathbf{R}}_J = -\nabla_J E_{\mathrm{KS}}[\varphi,R], \qquad J = 1,...,N \quad (25c)$$

where $\Lambda^{\mathrm{CP}} := (\Lambda_{AB}^{\mathrm{CP}})$ is again a Hermitian matrix of time-dependent Lagrange multipliers that ensure the orthonormality of the orbitals φ, and μ_{CP} is a fictitious electrons "mass" which plays a similar role to the parameter μ in our new dynamics.

Before discussing in details the main concepts of the present dynamics, it is worthwhile to state its main advantages and deficiencies (that will be the topic of discussion in the next sections). When applied to perform gsBOMD, the method can gain a large speed-up over Ehrenfest MD; it preserves exactly the total energy and the wave function orthogonality and allows for a very efficient parallelization scheme that requires low communication. However, the speed-up comes at a cost as it increases the nonadiabatic effects. Also, the method as discussed above will not work properly for metals and small-gap systems.[50]

4.2. Symmetries and Conserved Quantities. In the following we will study the conserved quantities associated to the global symmetries of the Lagrangian in eq 19 and we shall compare them with those of gsBOMD and CPMD. We will also be interested in a gauge symmetry that is the key to understand the behavior of eq 19 in the limit $\mu \to 0$ and its relation with gsBOMD.

The first symmetry we want to discuss is the time translation invariance of (19). This is easily recognized as L does not depend explicitly on time. Associated to this invariance there is a conserved "energy". Namely, using the Noether theorem, we have that

$$E = \sum_A \int \mathrm{d}\mathbf{r}\left[\frac{\delta L}{\delta\dot{\varphi}_A(\mathbf{r},t)}\dot{\varphi}_A(\mathbf{r},t) + \frac{\delta L}{\delta\dot{\varphi}_A^*(\mathbf{r},t)}\dot{\varphi}_A^*(\mathbf{r},t)\right] + \sum_{J,p}\frac{\partial L}{\partial\dot{R}_J^p}\dot{R}_J^p - L = \sum_J \frac{1}{2}M_J\dot{R}_J^2 + E_{\mathrm{KS}}[\varphi,R] \quad (26)$$

is constant under the dynamics given by eq 20a, where $p = 1, 2, 3$ indexes the Euclidean coordinates of vectors $\dot{\mathbf{R}}_J$ (and $\mathbf{R}_J$ if needed).

Notice that E does not depend on the unphysical parameter μ and actually coincides with the exact energy that is conserved in gsBOMD. The situation is different in CPMD.

There, we also have time translation invariance, but the constant of motion reads

$$E_{\mathrm{CP}} = \int \mathrm{d}\mathbf{r} \sum_A \frac{1}{2}\mu_{\mathrm{CP}}\dot{\varphi}_A^*(\mathbf{r},t)\dot{\varphi}_A(\mathbf{r},t) + E \qquad (27)$$

which depends directly on the unphysical mass of the electrons, μ_{CP}, and its conservation implies that the physical energy E varies in time. Still, this drawback has a minor effect, since it has been shown that the CP physical energy follows closely the exact gsBOMD energy curve.

The second global symmetry we want to consider is the change of orthonormal basis of the space spanned by $\{\varphi_A\}_{A=1}^{n/2}$. Namely, given a Hermitian matrix S_{AB} ($S^+ = S$), we define the following transformation:

$$\varphi'_A = \sum_B (\mathrm{e}^{-iS})_{AB}\varphi_B \qquad (28)$$

The Lagrangian in (19) depends on φ only through $\rho = 2\sum_A|\varphi_A|^2$ and $\sum_A\varphi_A^*\dot{\varphi}_A$. Provided the matrix S is Hermitian and constant in time, both expressions are left unchanged by the transformation. Hence, we can invoke again Noether theorem to obtain a new conserved quantity that reads

$$-i\sum_{A,B}\int \mathrm{d}\mathbf{r}\left[\frac{\delta L}{\delta\dot{\varphi}_A(\mathbf{r},t)}S_{AB}\varphi_B(\mathbf{r},t) - \frac{\delta L}{\delta\dot{\varphi}_A^*(\mathbf{r},t)}S_{AB}\varphi_B^*(\mathbf{r},t)\right] = \mu\sum_{A,B}\int \mathrm{d}\mathbf{r}\,\varphi_A^*(\mathbf{r},t)S_{AB}\varphi_B(\mathbf{r},t) \qquad (29)$$

Observe that we have a constant of motion for any Hermitian matrix S. This permits us to combine different choices of S in order to obtain that

$$\int \mathrm{d}\mathbf{r}\,\varphi_A^*(\mathbf{r},t)\varphi_B(\mathbf{r},t) = \mathrm{const}, \quad \forall A,B = 1,...,\frac{n}{2} \qquad (30)$$

In other words, if we start with an orthonormal set of wave functions φ and we let evolve the system according to eqs 20a and 20b, the family of wave functions maintains its orthonormal character along time, i.e. the operator preserves the inner product of the wave functions that define the Ehrenfest trajectory.

We would like to mention here that the above property is sometimes substantiated on a supposed unitarity of the evolution operator.[7,48,51] Simply noticing that the evolution of φ is not linear as both (20a) and (20b) are nonlinear equations and that unitary evolution requires linearity,[52] one can discard from the start the unitarity argument.

There is however a delicate point here that is worth discussing. The issue is that the $\mu \to 0$ limit of our dynamics should correspond to gsBOMD in eqs 22a (which includes Lagrange multipliers to keep orthonormalization), but the Lagrangian in (19) does not contain any multipliers and in fact they are unnecessary, as our evolution preserves the orthonormalization. This may rise some doubts on the equivalence between gsBOMD and the limit of vanishing μ of our dynamics.

To settle the issue, we introduce the additional dynamical fields $\Lambda := (\Lambda_{AB})$, corresponding to Lagrange multipliers, in our Lagrangian in eq 19, i.e.,

$$\tilde{L}[\varphi,\dot{\varphi},R,\dot{R},\Lambda] = L[\varphi,\dot{\varphi},R,\dot{R}] + \sum_{AB}\Lambda_{AB}\left(\int \mathrm{d}\mathbf{r}\,\varphi_A^*(\mathbf{r},t)\varphi_B(\mathbf{r},t) - \delta_{AB}\right) \qquad (31)$$

This modification has an important consequence: the global symmetry in (28) becomes a gauge one with time-dependent matrix elements. Actually one can easily verify that $\tilde{L}$ is invariant under

$$\varphi' = \mathrm{e}^{-iS}\varphi \qquad (32a)$$

$$\Lambda' = \mathrm{e}^{-iS}\Lambda\mathrm{e}^{iS} - i\mu\mathrm{e}^{-iS}\frac{\mathrm{d}}{\mathrm{d}t}\mathrm{e}^{iS} \qquad (32b)$$

This implies that, for $\mu \neq 0$, the fields Λ_{AB} can be transformed to any desired value by suitably choosing the gauge parameters $S_{AB}(t)$. Their value is therefore irrelevant and one could equally well take $\Lambda = 0$, as in (19), or $\Lambda = \Lambda^{\mathrm{BO}}$ (the value it has in gsBOMD) without affecting any physical observable. This solves the puzzle and shows that the $\mu \to 0$ limit of the dynamics of eq 20a is in fact the exact gsBOMD.

4.2.1. Physical Interpretation. If we take eq 20a and write the left-hand side as

$$\mu\frac{\mathrm{d}\varphi}{\mathrm{d}t} = \frac{\mathrm{d}\varphi}{\mathrm{d}t_{\mathrm{e}}} \qquad (33)$$

the resulting equation can be seen as the standard Ehrenfest method in terms of a fictitious time t_{e}. Two important properties can be obtained from this transformation.

On the one hand, it is easy to see that the effect of μ is to scale the TDDFT ($\mu = 1$) excitation energies by a $1/\mu$ factor. So for $\mu > 1$, the gap of the artificial system is decreased with respect to the real one, while for small values of μ, the excited states are pushed up in energy forcing the system to stay in the adiabatic regime. This gives a physical explanation to the $\mu \to 0$ limit shown before.

On the other hand, given the time step for standard Ehrenfest dynamics, $\Delta t(\mu = 1)$, from (33), we can obtain that the time step as a function of μ is

$$\Delta t(\mu) = \mu\Delta t(\mu = 1) \qquad (34)$$

so, for $\mu > 1$ propagation will be μ times faster than Ehrenfest.

By taking into account these two results we can see that there is a tradeoff in the value of μ: low values will give physical accuracy while large values will produce a faster propagation. The optimum value, that we will call $\mu_{\max}$, is the maximum value of μ that still keeps the system near the adiabatic regime. It is reasonable to expect that this value will be given by the ratio between the electronic gap and the highest vibrational frequency in the system. For many systems, like some molecules or insulators, this ratio is large and we can expect large improvements with respect to standard Ehrenfest MD. For other systems, like metals, this ratio is small or zero and our method will not work well

without modifications (that are presently being worked on). We note that a similar problem appears in the application of CP to these systems.

4.3. Numerical Properties. From the numerical point of view, our method inherits the main advantage of Ehrenfest dynamics: since propagation preserves the orthogonality of the wave function, it needs not be imposed and the numerical cost is proportional to $N_W N_C$ (with N_W as the number of orbitals and N_C as the number of grid points or basis set coefficients). For CP, a reorthogonalization has to be done each time step, so the cost is proportional to $N_W^2 N_C$. From these scaling properties, we can predict that for large enough systems our method will be less costly than CP. As we will show below this, crossing can occur for around 1000 atoms for our implementation and the systems we have considered.

Due to the complex nature of the propagator, Ehrenfest dynamics has to be performed using complex wave functions. In CP, real wave functions can be used if the system is finite (without a magnetic field) or if the system is a supercell using only the gamma point. However, with respect to CP, the actual number of degrees of freedom to be treated is the same, since CP equations are second order a second field has to be stored, either the artificial "velocity" of the wave functions or the wave function of the previous step.

An important point of comparison between Ehrenfest and CP is the dependency of the maximum time step with the simulation parameters: μ, μ_{CP}, and the cutoff energy (E_{cut}). While for our modified Ehrenfest scheme, it will scale like

$$\Delta t_{\max} \propto \frac{\mu}{E_{\mathrm{cut}}} \tag{35}$$

For CP dynamics, we have that[7]

$$\Delta t_{max}^{\mathrm{CP}} \propto \sqrt{\frac{\mu_{\mathrm{CP}}}{E_{\mathrm{cut}}}} \tag{36}$$

Since μ and μ_{CP} are different quantities, we cannot infer anything without knowing the effect of their value in the results, but as we will see from our calculations, even though in the new scheme the time step increases linearly with μ, the separation from the BO surface is also more sensitive to its value. On the other hand, the dependence with the cutoff energy is one of the major drawbacks of Ehrenfest dynamics, and probably it can explain why, as we will see, it is slower than CP for small systems. However in most cases, this cutoff energy is independent from the size of the system and will only represent a difference in the prefactor in the scaling of both methods, so its effect should be compensated for large systems.

5. Methods

The scheme described above was implemented in the Octopus code.[53,54] Octopus is a general purpose code to handle equilibrium and nonequilibrium phenomena using (TD)DFT. It can be used to simulate atoms, molecules, low dimensional systems, and periodic structures under the presence of arbitrary electromagnetic fields. The code is distributed under a free software license, and many new features are incorporated regularly. Octopus uses a real-space grid representation combined with the finite differences approximation for the calculation of derivatives.[55,56] The nuclei−electron interaction is replaced by norm-conserving Troullier Martins pseudopotentials. Unless stated otherwise, the Perdew−Zunger[57] parametrization of the local density approximation (LDA) is used for the exchange and correlation functional. The Poisson equation is solved using the interpolating scaling functions method.[58]

5.1. Time-Propagation. Given an initial condition $\phi(t = 0)$ and $R(t = 0)$, we want to calculate $\phi(t)$ and $R(t)$ for a time $t > 0$ from (20). For the ionic part, eq 20b, once the forces are computed,[59] the Newton equations can be handled easily by the standard velocity Verlet algorithm.

For the electronic part, eq 20a, the transformation in eq 33 allows us to use the standard Ehrenfest propagation methods, making our scheme trivial to implement in an existing real-time Ehrenfest code. The key part for the real-time solution of equation 20a is to approximate the propagation operator

$$\varphi(t + \Delta t) = \hat{U}(t + \Delta t, t)\varphi(t) \tag{37}$$

in an efficient and stable way. From the several methods available (see ref for a review), in this work, we have chosen the *approximated enforced time-reversal symmetry* (AETRS) method. For a Hamiltonian $\hat{H}(t)$, in AETRS, the propagator is approximated by the explicitly time-reversible expression

$$\hat{U}(t + \Delta t, t) = \exp\left\{-i\frac{\Delta t}{2}\hat{H}(t + \Delta t)\right\} \exp\left\{-i\frac{\Delta t}{2}\hat{H}(t)\right\} \tag{38}$$

with $\hat{H}(t + \Delta t)$ obtained from an interpolation from previous steps. For the calculation of the exponential in eq 38, a simple fourth-order Taylor expansion is used. Note that the truncation to any order of the Taylor expansion for the exponential operator implies that the norm of the vector is no longer conserved. This theoretical error must be kept below an acceptable threshold in order to ensure the preservation of the orthonormality of the orbitals. In any case, a small inevitable error will always lead to a slight change in the norm. If the norm is reduced, the method is said to be "contractive"—this property is desirable since it leads to stable propagations, as opposed to the case in which the norm increases: in this latter case, the propagation becomes unstable. The choice for a fourth order truncation is advantageous because it is, for a very wide range of time-steps, a contractive approximation to the exponential.

Moreover, the careful preservation of time reversibility is crucial to avoid unphysical drifts in the total energy. We have found (for the cases presented in this work and for our particular numerical implementation) the combination of the AETRS approximation to the propagator together with the Taylor expansion representation of the exponential, to be the most efficient approach. Our tests show that numerically the error in orthonormality, measured as the dot product between orbitals, has an oscillatory behavior and it is typically of the order of 10^{-10} but for some pairs of orbitals it can increase to 10^{-8}.

We also implemented the Car−Parrinello scheme to compare it with our approach. In this case, the electronic part is integrated by the RATTLE/Velocity Verlet algorithm as described in ref 61.

5.2. Parallelization Strategy. The challenge of AIMD of going toward very large systems and large simulation times is clearly linked to implementations that run efficiently in parallel architectures. This is the case of CP methods, that are known to perform very well in this kind of system;[62] the parallelization is usually based on domain decomposition (known as parallelization over Fourier coefficients in plane-wave codes) and K-points. However, good scalability can only be obtained if the system is large enough to have a favorable computation−communication ratio with respect to the latency of the interconnection.

This type of parallelization is also applicable to the present Ehrenfest dynamics, and *on top* of that, the new scheme can add a different level of parallelization: since the propagation step is independent for each orbital, it is natural to parallelize the problem by distributing the Kohn−Sham states among processors. Communication is only required once per time step to calculate quantities that depend on a sum over states: the time dependent densities and the forces over the ions. This type of sum of a quantity over several nodes is known as a reduction and the communication cost grows logarithmically with the number of nodes.

The main limitation to the parallel scalability in our real space implementation was observed to come from the parts of the code that do not depend on the states (global quantities), mainly the regeneration of the ionic potential

$$V^{\text{ion}} = \sum_J \hat{V}_J^{\text{local}}(\mathbf{r} - \mathbf{R}_J) \tag{39}$$

and the calculation of the forces due to the local part of the ionic potential

$$F_J^{\text{local}} = \int \mathrm{d}\mathbf{r}\, \frac{\mathrm{d}\rho(\mathbf{r})}{\mathrm{d}\mathbf{r}}\, \hat{V}_J^{\text{local}}(\mathbf{r} - \mathbf{R}_J) \tag{40}$$

As these expressions depend on the atoms index J, a complementary parallelization in atoms is used to speed-up these code sections. For example, to generate the ionic potential, each processor generates the potential for a subset of the atoms and then a reduction operation is performed to obtain the total ionic potential.

Once this auxiliary parallelization over atoms is taken into account, it results in a very efficient scheme, similar to K-point parallelization for periodic systems, where, as long as there are enough states to distribute, the scaling is linear even with slow interconnections (as a rule of thumb, for our implementation 10−15 orbitals per processor are required for a good efficiency). In the case of CP, due to orthogonalization between states the evolution is not independent, so this parallelization scheme is more complex to implement and requires more communication, making it much less practical.

In our implementation, we have combined this parallelization over states with real space domain decomposition (see ref 54 for details). This dual parallelization strategy also has the advantage that allows us to decompose the two levels of complexity, the size of the region of space simulated and the number of orbitals, that increase when we move to study larger systems.

Below we address the relative gain in performance of the code once this second level of parallelization is used. To avoid as much as possible issues related to different software packages, we decided to implement the two schemes, CP and Ehrenfest, in the same code. Although this might not be the best parallel implementation of CP that is available in the community, it allows a direct assessment of the impact of this extra level of parallelization. Given the simplicity and the high level nature of parallelization over states, it is expected that this gain will be transferable to other implementations.

6. Applications: Model and Realistic Systems

6.1. Two Band Model. To illustrate the properties of the new scheme, and also to compare it to CP in a complementary manner to the calculations in the rest of the manuscript, we apply it to a model system. The simple toy model we use is based on the one used in the work by Pastore et al. to test CP.[63] Its equations of motion are produced by the Lagrangian

$$L_{\text{toy}} = \frac{\mu}{2}(\dot{\theta}_1\theta_2 - \dot{\theta}_2\theta_1) + \frac{1}{2}M_R\dot{R}^2 + \frac{1}{2}M_G\dot{G}^2 - \frac{1}{2}K_R(R - R_0)^2 - \frac{1}{2}K_G(G - G_0)^2 + \frac{G}{2}[\cos(\theta_1 - R) + \cos(\theta_2 - R)] \tag{41}$$

where θ_1 and θ_2 correspond to electronic degrees of freedom, R corresponds to the nuclear motion, and G mimicks the gap. The parameters M_R, K_R, R_0, and G_0 have been taken from the experimental values for the N_2 molecule (interpreting R as the length of the N−N bond).

The dynamics produced by (41) has been then compared to the analogous CP one [obtained by simply changing the θ-kinetic energy by $(\mu_{\text{CP}}/2)(\dot{\theta}_1^2 + \dot{\theta}_2^2)$] and to the gsBO reference [defined by setting $\mu = 0$, and θ_1 and θ_2 to the values that minimize the potential energy in (41), $\theta_1 = \theta_2 = R$]. In all simulations, the initial conditions of R and G have been increased a 10% from their equilibrium values R_0 and G_0, we have set $\dot{R}(0) = \dot{G}(0) = 0$, and the initial electronic coordinates have been placed at the gsBO minimum (for CP, $\dot{\theta}_1(0) = \dot{\theta}_2(0) = 0$).

To compare the approximate nuclear trajectory $R(t)$ to the gsBO one $R_{\text{BO}}(t)$, we define $d_R := 100/\Delta R\{(1/T)\int_0^T[R(t) - R_{\text{BO}}(t)]^2\,\mathrm{d}t\}^{1/2}$, where ΔR is the maximum variation of R in the gsBO case. In Figure 1a, we show that this distance smoothly decreases to zero as $\mu \to 0$ for our model. In Figure 1b, in turn, we compare the gsBO force on R to the one obtained from the new method averaging over a intermediate time between those associated to the electronic and nuclear motions. The distance d_F between these forces (defined analogously to d_R), also goes to zero when $\mu \to 0$.

Now, we estimate the relation between the maximum time step allowed by the fourth order Runge−Kutta numerical integration of the equations of motion and the error, given

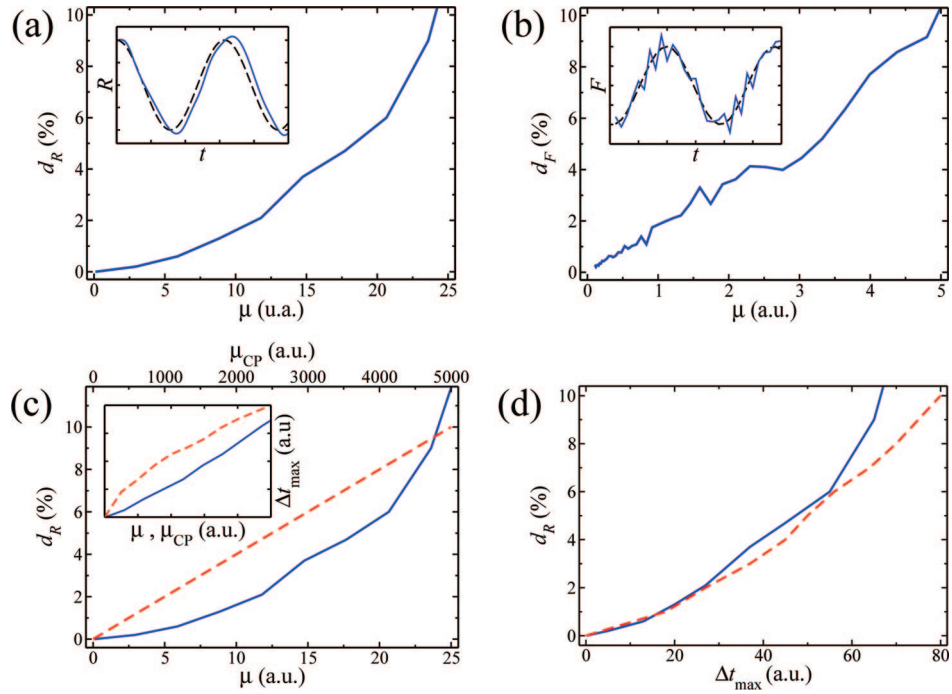

Figure 1. (a) Distance d_R from the R-dynamics produced by (41) to the gsBO one as a function of μ. (inset) gsBO R-trajectory [broken (black) line] and the approximate one for $d_R = 10\%$ [solid (blue) line]. (b) Distance between the averaged force on R produced by (41) and the gsBO one. (inset) gsBO force [broken (black) line] and the approximate one for $d_F = 10\%$ [solid (blue) line]. (c) Dependence on μ (and μ_{CP}) of the distance d_R and of the maximum time Δt_{max} step (inset) for both the new scheme [solid (blue) line] and CP [broken (red) line]. (d) Error/time step profile for both the new dynamics and CP [same colors as in part b].

by d_R. The first, denoted by Δt_{max}, has been defined as the largest time step that produced trajectories for all the dynamical variables of the system with a distance less than 0.1% to the "exact" trajectories. In Figure 1c, we can see that, although Δt_{max} grows more slowly in our method than in CP (as expected from the discussion in section 4.3), the behavior of the error (d_R) is better for the new dynamics introduced here. These two effects approximately balance each other yielding the error/time step relations depicted in Figure 1d, where the new scheme is shown to behave similarly to CPMD for a significant range of values of d_R. We stress however that, to actually compare the relative performance of both methods the numerical work required in each time step would have to be considered. In this sense, the more realistic simulations in the next sections are more representative.

6.2. Nitrogen Molecule. For the Nitrogen molecule (N_2), we calculate the trajectories for different values of μ, using the same initial conditions as in the toy model. A time step of $\mu \times 0.0012$ fs is used, and the system is propagated by 242 fs. In Figure 2, we plot the potential energy as a function of the interatomic distance during the trajectory for each run; in the inset, we also give the vibrational frequency for the different values of μ, obtained as the position of the peak in the Fourier transform of the velocity autocorrelation function. It is possible to see that for $\mu = 20$ the simulation remains steadily close to the BO potential energy surface and there is only a 3.4% deviation of the vibrational frequency. For $\mu = 30$, the system starts to strongly separate from the gsBO surface as we start to get strong mixing of the ground-state BO surfaces with higher energy BO surfaces. This behavior

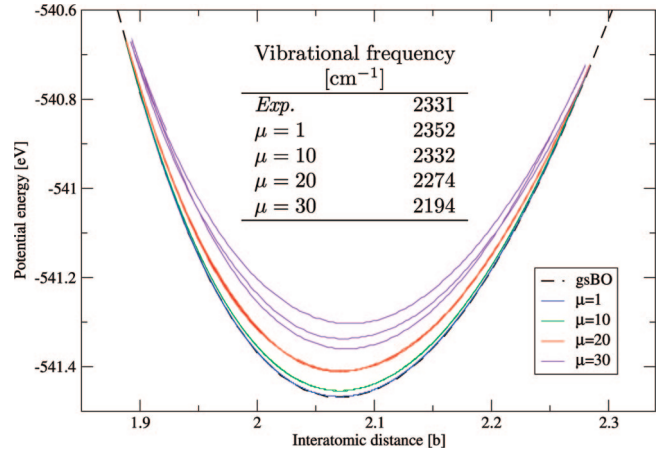

Figure 2. KS potential energy $E_{KS}[\varphi,R]$ as a function of the internuclear distance R in N_2 molecule simulations: (bottom to top) gsBO result [broken (black) line] and $\mu = 1$ [solid (blue) line], 10 [solid (green) line], 20 [solid (red) line], and 30 [solid (violet) line]. (inset) Vibrational frequencies from experiment[64] and calculated from the trajectory using different values of μ and a spacing of 0.35 b and a box of radius 7.6 b around each atom.

is consistent with the physical interpretation given in section 4.2.1 as for this system $\mu_{max} \approx 27$.

6.3. Benzene. Next, we applied the method to the Benzene molecule. We set up the atoms in the equilibrium geometry with a random Maxwell−Boltzmann distribution for 300 K. Each run was propagated for a period of time of ~400 fs with a time step of $\mu \times 0.001$ fs (that provide a reasonable convergence in the spectra). Vibrational frequencies were

Table 1. Selected Vibrational Frequencies (cm^{-1}) for the Benzene Molecule, Obtained Using Different Values of μ and a Spacing of 0.35 b and a Box of Radius 7.6 b around Each Atom

$\mu = 1$	398	961	1209	1623	3058
$\mu = 5$	396	958	1204	1620	3040
$\mu = 10$	391	928	1185	1611	2969
$\mu = 15$	381	938	1181	1597	2862

obtained from the Fourier transform of the velocity autocorrelation function. In Table 1, we show some low, medium, and high frequencies of benzene as a function of μ. The general trend is a red-shift of the frequencies with a maximum deviation of 7% for $\mu = 15$. Still, to make a direct comparison with experiment, we computed the infrared spectra as the Fourier transform of the electronic dipole operator. In Figure 3, we show how the spectra changes with μ. For large μ, besides the red-shift, spurious peaks appear above the higher vibrational frequency (not shown), this is probably due to a nonadiabatic effect as $\mu_{max} \approx 14$ if we consider the first virtual TDDFT excitation energy. We performed equivalent CP calculations for different values of μ_{CP} and found that, as shown in Figure 3, it is possible to relate the physical error induced in both methods and establish and a relation between μ and μ_{CP}.

Having established the link between μ and μ_{CP}, we address the numerical performance of our new method compared to CP. As explained in section 4.3, the maximum time step has a different behavior with the cutoff energy, or equivalently, in this case, the grid spacing (the spacing is proportional to $(1/E_{cut})^{1/2}$). This can be seen in Figure 4, where we plot the maximum time step both Ehrenfest and CP as a function of the grid spacing. This is important since, in order to be able to do a comparison for large number of atoms, we use a larger spacing (0.6 b or 14 Ha) than that required for the converged results previously shown (0.35 b or 40 Ha). So for the small spacing case, Ehrenfest results should be scaled by a 1.7 factor; these two values gives us a range of

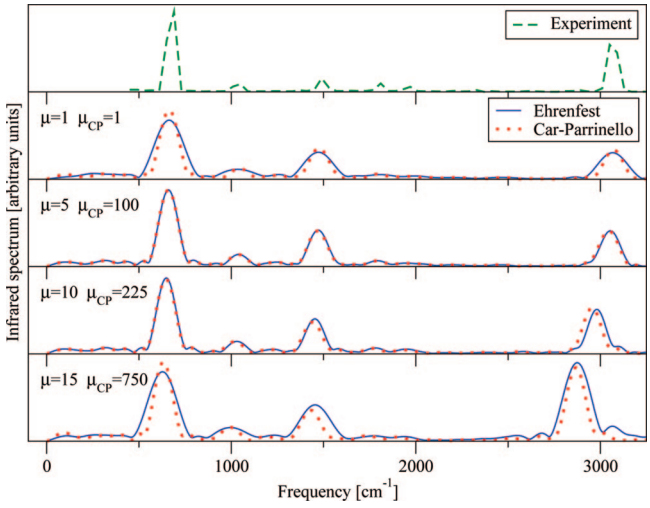

Figure 3. Calculated infrared spectrum for benzene for different values of μ, compared to CP dynamics and to an experiment from ref 65. A spacing of 0.35 b and a box of radius 7.6 b around each atom were used.

comparison, since most calculations are performed in this range of precision (14−80 Ha).

To compare in terms of system size, we simulated several Benzene molecules in a cell. For the new scheme, a value of $\mu = 15$ is used while for CP $\mu_{CP} = 750$, (values that yield a similar deviation from the BO surface, according to Figure 3). The time steps used are 3.15 and 7.26 a.u., respectively. The computational cost is measured as the simulation time required to propagate one atomic unit of time; this is an objective measure to compare different MD schemes. We performed the comparison both for serial and parallel calculations; the results are shown in Figure 5. In the serial case, CP is 3.5 times faster for the smaller system, but the difference reduces to only 1.7 times faster for the larger one. Extrapolating the results, we predict that the new dynamics will become less demanding than CP for around 1100 atoms, if we consider the small spacing the crossover point moves to 2000 atoms. In the parallel case, the performance difference is reduced, being CP only 2 times faster than our method for small systems and with a crossing point below 750 atoms (1150 atoms with the smaller spacing). This is due to the better scalability of the Ehrenfest approach, as seen in Figure 5c. Moreover, in our implementation, memory requirements are lower than those for CP: in the case of 480 atoms, the ground-state calculation requires a maximum of 3.5 Gb, whereas in the molecular dynamics, Ehrenfest requires 5.6 Gb while CP needs 10.5 Gb. The scaling of the memory requirements is the same for both methods, and we expect this differences to remain proportional for all system sizes.

6.4. Fullerene Molecule: C_{60}. To end the computational assessment of the new formalism, we illustrate out method for the calculation of the infrared spectrum of a prototype molecule, C_{60}. This time we switch to the PBE[12] exchange and correlation functional since it should give slightly better vibrational properties than LDA.[15] For the simulation shown below, we use a value of $\mu = 5$ that provides a reasonable convergence in the spectra. The calculated IR spectra are in very good agreement with the experiment (see Figure 6) for low and high energy peaks (the ones more sensitive to the values of μ as seen in Figure 3). The result is robust and independent of the initial condition of the simulation. The low energy splitting of IR spectrum starts to be resolved for simulations longer than 2 ps.

7. Conclusions

First principles molecular dynamics is usually performed in the framework of ground-state Born−Oppenheimer calculations or Car−Parrinello schemes. A major drawback of both methods is the necessity to enforce the orthogonalization of the wave functions, which can become the bottleneck for very large systems. Alternatively, one can handle the electron−ion dynamics within the Ehrenfest scheme where no explicit orthogonalization is necessary. However, in Ehrenfest, the time step needs to be much smaller than in both the Born−Oppenheimer and the Car−Parrinello schemes. In this work, we have presented a new approach to AIMD based on a generalization of Ehrenfest-TDDFT dynamics. This approach, we recall, relies on the electron−nuclei

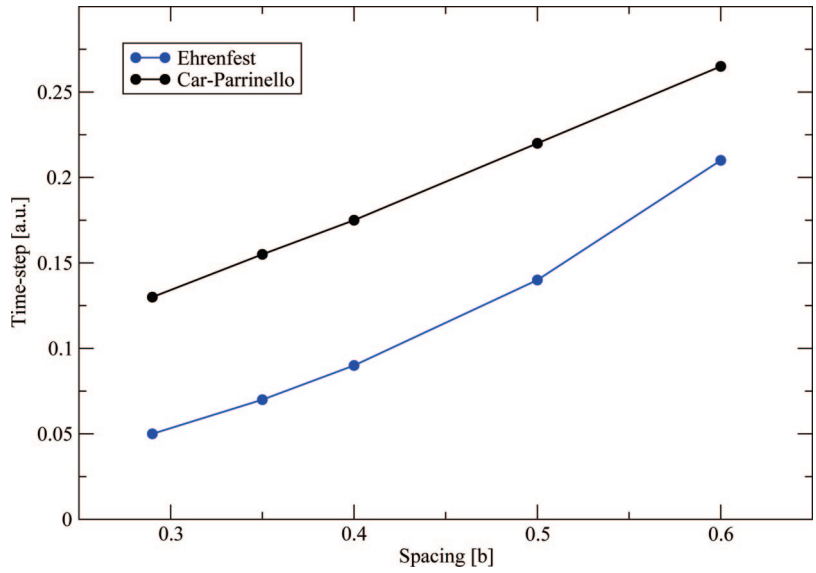

Figure 4. Comparison of the dependence of the time step in terms of the spacing. In the case of Ehrenfest, the time step dependence is quadratic, while for CP, it is linear.

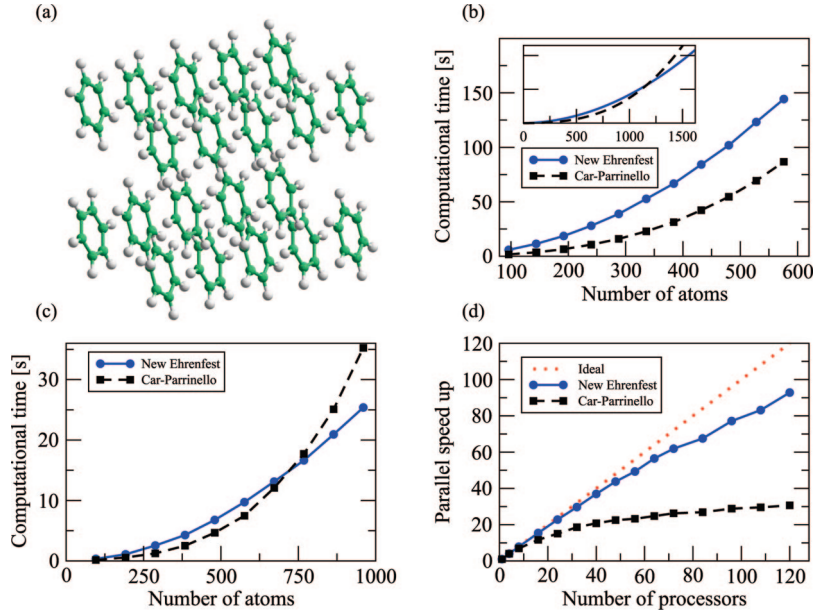

Figure 5. Computational performance comparisons of our method, with $\mu = 15$ and CP, with $\mu_{CP} = 750$ for an array of benzene molecules with finite boundary conditions, a spacing of 0.6 b, and a box of radius 7.6 b around each atom. Performance is measured as the computational time required to propagate one atomic unit of time. (a) Scheme of the benzene molecule array. (b) Single processor computational cost for different system sizes. (inset) Polynomial extrapolation for larger systems. This simulation was performed on one core of an Intel Xeon E5435 processor. (c) Parallel computational cost for different system sizes. This simulation was performed on 32 Intel Itanium 2 (1.66 GHz) processor cores of a SGI Altix. (d) Parallel scaling with respect to the number of processor for a system of 480 atoms in a SGI Altix system. In both cases, a mixed states−domain parallelization is used to maximize the performance.

separation ansatz, plus the classical limit for the nuclei taken through short-wave asymptotics. Then, the electronic subsystem is handled with time-dependent density functional theory. The resulting model consists of two coupled sets of equations: the time-dependent Kohn−Sham equations for the electrons and a set of Newtonian equations for the nuclei, in which the expression for the forces resembles, but is in fact unrelated to, the Güttinger−Hellmann−Feynman form. We have stressed the relevance of notational precision, in order to avoid this and other possible common misunderstandings.

We have shown how the new scheme preserves the desirable properties of Ehrenfest allowing for a considerable increase of the time step while keeping the system close to the Born−Oppenheimer surface. The automatically enforced orthogonalization is of fundamental importance for large systems because it reduces the scaling of the numerical cost with the number of particles and, in addition, allows for a very efficient parallelization, hence giving the method tremendous potential for applications in computational science. Specially if the method is integrated into codes that have other levels of parallelization, enabling them to scale

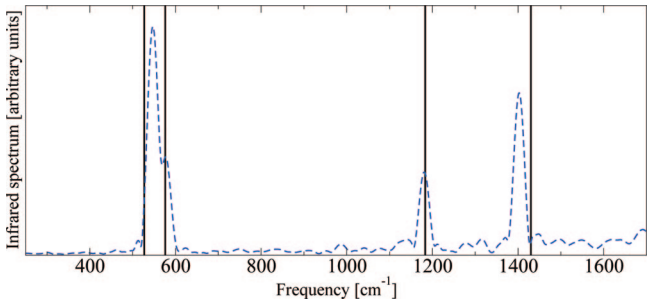

Figure 6. Infrared spectrum of C_{60}. The (blue) dashed line corresponds to the calculated one ($\mu = 5$ and 2 ps of time) while the black bars are the experimental values from ref 66.

to even more processors or to keeping the same level of parallel performance while treating smaller systems.

Our approach introduces a parameter μ that for particular values recovers either Ehrenfest dynamics or Born−Oppenheimer dynamics. In general μ controls the tradeoff between the closeness of the simulation to the BO surface and the numerical cost of the calculation (analogously to the role of the fictitious electronic mass in CP). We have shown that for a certain range of values of μ, the dynamics of the fictitious system is close enough to the Born−Oppenheimer surface while allowing for a good numerical performance. We have made direct comparisons of the numerical performance with CP, and, while quantitatively our results are system- and implementation-dependent, they prove that our method can outperform CP for some relevant systems. Namely, large-scale systems that are of interest in several research areas and that can only be studied from first principles MD in massively parallel computers. To increase its applicability, it would be important to study if the improvements developed to optimize CP can be combined with our approach,[67] in particular techniques to treat small gap or metallic systems.[68]

Note that the introduction of the parameter μ comes at a cost, as we change the time scale of the movements of the electrons with respect to the Ehrenfest case, which implies a shift in the electronic excitation energies. This must be taken into account to extend the applicability of our method for nonadiabatic MD and MD under electromagnetic fields, in particular for the case of Raman spectroscopy, general resonant vibrational spectroscopy as well as laser induced molecular bond rearrangement. In this respect, we stress that in the examples presented in this work, we have utilized the new model to perform Ehrenfest dynamics in the limit where this model tends to ground state, adiabatic MD. In this case, as it became clear with these examples, the attempt to gain computational performance by enlarging the value of the parameter μ must be done carefully, since the nonadiabatic influence of the higher lying electronic states states increases with increasing μ. We believe, however, that there are a number of avenues to be explored that could reduce this undesired effect; we are currently exploring the manner in which the "acceleration" parameter μ can be introduced while keeping the electronic system more isolated from the excited states.

Nevertheless, Ehrenfest dynamics incorporates in principle the possibility of electronic excitations and nonadiabaticity. The proper incorporation of the electronic response is crucial for describing a host of dynamical processes, including laser-induced chemistry, dynamics at metal or semiconductor surfaces, or electron transfer in molecular, biological, interfacial, or electrochemical systems. The two most widely used approaches to account for nonadiabatic effects are the surface-hopping method and the Ehrenfest method implemented here. The surface-hopping approach extends the Born−Oppenheimer framework to the nonadiabatic regime by allowing stochastic transitions subject to a time- and momenta-dependent hopping probability. On the other hand, Ehrenfest successfully adds some nonadiabatic features to molecular dynamics but is rather incomplete. This approximation can fail either when the nuclei have to be treated as quantum particles (e.g., tunnelling) or when the nuclei respond to the microscopic fluctuations in the electron charge density (heating)[69] not reproducing the correct thermal equilibrium between electrons and nuclei (which constitutes a fundamental failure when simulating the vibrational relaxation of biomolecules in solution). We have briefly addressed these issues in section 2; as mentioned there, there have been some proposals in the literature to modify Ehrenfest in order to fulfill Boltzmann equilibrium.[37,39] Currently we are also investigating related extensions to Ehrenfest to obtain the correct equilibrium in our simulations.

Acknowledgment. We would like to thank A. Bastida, G. Ciccotti, and E. K. U. Gross for illuminating discussions. This work has been supported by the research projects DGA (Aragón Government, Spain) E24/3, and MEC (Spain). P.E. is supported by a MEC/MICINN (Spain) postdoctoral contract. X.A and Á.R. acknowledge funding by the Spanish MEC (FIS2007-65702-C02-01), "Grupos Consolidados UPV/EHU del Gobierno Vasco" (IT-319-07), and the European Community through NoE Nanoquanta (NMP4-CT-2004-500198), e-I3 ETSF (INFRA-2007-1.2.2: Grant Agreement Number 211956), NANO-ERA Chemistry, DNA-NANODEVICES (IST-2006-029192), and SANES (NMP4-CT-2006-017310) projects. Computational resources were provided by the Barcelona Supercomputing Center, the Basque Country University UPV/EHU (SGIker Arina) and ETSF.

References

(1) As stated by Dirac in 1929, "The fundamental laws necessary for the mathematical treatment of a large part of physics and the whole of chemistry are thus completely known, and the difficulties lies only in the fact that application of these laws leads to equations that are too complex to be solved".

(2) Ciccotti, G.; Frenkel, D.; McDonald, I. *Simulations of liquids and solids: molecular dynamics and montecarlo methods in statistical mechanics*; North-Holand: Amsterdam, 1987; pp 1−25.

(3) Alder, B. J.; Wainwright, T. E. *J. Chem. Phys.* **1959**, *31*, 459–466.

(4) Computer simulations of the dynamics of systems of interacting molecules based on the Monte Carlo methods were presented some years before.[70] Also, before the work of Alder and Wainwright, some previous "computations" were reported

that did not utilize modern computers, but rather real physical models of the system, i.e. rubber balls linked by rods.[71] The rapid improvement of digital computer machines discouraged this cumbersome, yet entertaining, methodology.

(5) (a) Fermi, E.; Pasta, J.; Ulam, S.; Tsingou, M. *Studies of nonlinear problems I*, Los Alamos Scientific Laboratory Report No. LA-1940, **1955**. As discussed by(b) Ford, J. *Phys. Rep.* **1992**, *213*, 271–310.

(6) Warshel, A.; M., W. R. *J. Chem. Phys.* **1980**, *102*, 6218–6226.

(7) Marx, D.; Hutter, J. Ab initio molecular dynamics: Theory and implementation. *Modern Methods and Algorithms of Quantum Chemistry*; John von Neumann Institut für Computing: Jülich, 2000; pp 329−477.

(8) Tuckerman, M. E. *J. Phys.: Condens. Matter* **2002**, *14*, R1297–R1355.

(9) (a) *A Primer in Density Functional Theory*; Fiolhais, C., Nogueira, F., Marques, M., Eds.; Lecture Notes in Physics; Springer-Verlag: Berlin, Heidelberg, 2003; pp 1−51. (b) Hohenberg, P.; Kohn, W. *Phys. Rev.* **1964**, *136*, B864−B871. (c) Kohn, W.; Sham, L. J. *Phys. Rev.* **1965**, *140*, A1133−A1138. (d) Kohn, W. *Rev. Mod. Phys.* **1999**, *71*, 1253–1266.

(10) Perdew, J. P.; Wang, Y. *Phys. Rev. B* **1986**, *33*, 8800–8802.

(11) Perdew, J. P. *Phys. Rev. B* **1986**, *33*, 8822–8824.

(12) Perdew, J. P.; Burke, K.; Ernzerhof, M. *Phys. Rev. Lett.* **1996**, *77*, 3865–3868.

(13) Car, R. In *Monte Carlo and Molecular Dynamics of Condensed Matter Systems*; Binder, K., Ciccotti, G., Eds.; Italian Phyisical Society SIF: Bologna, 1996; Chapter 23.

(14) Laasonen, K.; Sprik, M.; Parrinello, M.; Car, R. *J. Chem. Phys.* **1993**, *99*, 9080–9089.

(15) Favot, F.; Dal Corso, A. *Phys. Rev. B* **1999**, *60*, 11427–11431.

(16) Car, R.; Parrinello, M. *Phys. Rev. Lett.* **1985**, *55*, 2471–2474.

(17) (a) Niklasson, A. M. N. *Phys. Rev. Lett.* **2008**, *100*, 123004. (b) Niklasson, A. M. N.; Tymczak, C. J.; Challacombe, M. *Phys. Rev. Lett.* **2006**, *97*, 123001.

(18) Andreoni, W.; Marx, D.; Sprik, M. *ChemPhysChem* **2005**, *6*, 1671–1676.

(19) Goedecker, S. *Rev. Mod. Phys.* **1999**, *71*, 1085–1123.

(20) Schlegel, H. B.; Millam, J. M.; Iyengar, S. S.; Voth, G. A.; Daniels, A. D.; Scuseria, G. E.; Frisch, M. J. *J. Chem. Phys.* **2001**, *114*, 9758–9763.

(21) Kühne, T. D.; Krack, M.; Mohamed, F. R.; Parrinello, M. *Phys. Rev. Lett.* **2007**, *98*, 066401.

(22) (a) Wentzel, G. *Z. Phys.* **1926**, *38*, 518. (b) Kramers, H. A. *Z. Phys.* **1926**, *39*, 828. (c) Brillouin, L. *Chem. Rev.* **1926**, *183*, 24.

(23) (a) *Time-dependent density-functional theory*; Marques, M. A. L., Ullrich, C. A., Nogueira, F., Rubio, A., Burke, K., Gross, E. K. U., Eds.; Springer-Verlag: Berlin, Heidelberg, 2006; Vol. 706, pp 1−12. (b) Runge, E.; Gross, E. K. U. *Phys. Rev. Lett.* **1984**, *706*, 997–1000.

(24) Alonso, J. L.; Andrade, X.; Echenique, P.; Falceto, F.; Prada-Gracia, D.; Rubio, A. *Phys. Rev. Lett.* **2008**, *101*, 096403.

(25) Echenique, P.; Alonso, J. L. *Mol. Phys.* **2007**, *105*, 3057–3098.

(26) (a) Gerber, R. B.; Buch, V.; Ratner, M. A. *J. Chem. Phys.* **1982**, *77*, 3022–3030. (b) Gerber, R. B.; Ratner, M. A. *Adv. Chem. Phys.* **1988**, *70*, 97–132.

(27) (a) Bornemann, F. A.; Nettesheim, P.; Schütte, C. *J. Chem. Phys.* **1996**, *105*, 1074–1085. (b) Bornemann, F. A.; Nettesheim, P.; Schütte, C. *Quantum-classical molecular dynamics as an approximation to full quantum dynamics*, Preprint SC 95-26, Konrad-Zuse-Zentrum für Informationstechnik: Berlin, 1995.

(28) Perhaps the first detailed derivation of the so-called Hellmann−Feynman theorem was given in the work of Güttinger [*Z. Phys.* **1931**, *73*, 169−184]. The theorem had nevertheless been used before that date.[72] The derivations of Hellmann[73] and Feynman,[74] who named the theorem, came a few years afterwards.

(29) Tully, J. L. Mixed quantum-classical dynamics: Mean-field and surface-hopping. In *Classical and Quantum Dynamics in Condensed Phase Simulation*; Berne, B. J., Ciccotti, G., Coker, D. F., Eds.; World Scientific: Singapore, 1998; pp 489−515.

(30) In general, $\{\eta_a(x;R)\}$ may contain a discrete and a continuous part. However, in this manuscript, we will forget the continuous part in order to simplify the mathematics.

(31) Grochowski, P.; Lesyng, B. *J. Chem. Phys.* **2003**, *119*, 11541–11555.

(32) In the development of the classical formalism of thermodynamics, this point is crucial.

(33) This mistake is made, for example, in ref 31 when going from their expression 8 to their expression 9. Having not realized the existence of the two distinct sets of independent variables, $\{\psi,R\}$ and $\{c,R'\}$, they treat the $|c_a|^2$ as constants when taking the partial derivative with respect to q (our R) at the right hand side of (8), thus arriving at (9), where the crossterms $\int dx\, \eta_a^*(x;R'(t))\nabla_j' \hat{H}_e(r;R'(t))\eta_b(x;R'(t))$, with $b \neq a$, are incorrectly missing (see the correct derivation of EMD in the adiabatic basis below).

(34) Lee, H.; Cheng, Y.-C.; Fleming, G. R. *Science* **2007**, *316*, 1462–1465.

(35) Mauri, F.; Car, R.; Tosatti, E. *Europhys. Lett.* **1993**, *24*, 431.

(36) (a) Käb, G. *J. Chem. Phys.* **2004**, *108*, 8866. (b) Parandekar, P. V.; Tully, J. C. *J. Chem. Phys.* **2005**, *122*, 094102.

(37) Tully, J. *J. Chem. Phys.* **1990**, *93*, 1061.

(38) Schmidt, J. R.; Parandekar, P. V.; Tully, J. C. *J. Chem. Phys.* **2008**, *129*, 044104.

(39) (a) Bastida, A.; Cruz, C.; Zúñiga, J.; Requena, A.; Miguel, B. *Chem. Phys. Lett.* **2006**, *417*, 53–57. (b) Bastida, A.; Cruz, C.; Zúñiga, J.; Requena, A.; Miguel, B. *J. Chem. Phys.* **2007**, *126*, 014503.

(40) Blum, K. *Density Matrix Theory and Applications*, 2nd ed.; Springer: New York, 1996; p 274.

(41) Kapral, R.; Ciccotti, G. *J. Chem. Phys.* **1999**, *110*, 8919–8929.

(42) Nielsen, S.; Kapral, R.; Ciccotti, G. *J. Chem. Phys.* **2001**, *115*, 5805–5815.

(43) Kapral, R. *Annu. Phys. Chem* **2006**, *57*, 129.

(44) Prezhdo, O. V. *J. Chem. Phys.* **1999**, *111*, 8366–8377.

(45) Li, T.-C.; Tong, P. *Phys. Rev. A* **1986**, *34*, 529–532.

(46) Runge, E.; Gross, E. K. U. *Phys. Rev. Lett.* **1984**, *52*, 997–1000.

(47) Gross, E. K. U.; Dobson, J. F.; Petersilka, M. Density-functional theory of time-dependent phenomena. In *Density Functional Theory*; Nalewajski, Ed.; Springer-Verlag: Berlin, Heidelberg, 1996; Vol. 181, pp 81−172.

(48) Theilhaber, J. *Phys. Rev. B* **1992**, *46*, 12990–13003.

(49) This fact is not in contradiction with the above discussion about coordinates' independence. The difference between Ehrenfest MD and gsBOMD is that in the Lagrangian for the latter, the orbital "velocities" $\dot{\varphi}$ do not appear, thus generating eqs 22a and 22b, which can be regarded as *constraints* between the φ and the R.

(50) We are exploring how to overcome this limitation by mapping the real Hamiltonian into another one that produces the same dynamics but not having contributions from the empty states.

(51) Kalia, R. K.; Vashishta, P.; Yang, L. H.; Dech, F. W.; Rowlan, J. *Int. J. Supercomp. Appl.* **1990**, *4*, 22–33.

(52) For a one to one transformation U, we may define unitarity as the property of preserving the scalar product, i.e. given two arbitrary vectors f and g, we have $\langle f,g\rangle = \langle Uf, Ug\rangle$. One can easily see that any reversible transformation U that enjoys the previous property is necessarily linear:

$$\begin{aligned}\langle U(f_1 + f_2), Ug\rangle &= \langle f_1 + f_2, g\rangle \\ &= \langle f_1, g\rangle + \langle f_2, g\rangle \\ &= \langle Uf_1, Ug\rangle + \langle Uf_2, Ug\rangle \\ &= \langle Uf_1 + Uf_2, Ug\rangle\end{aligned}$$

As U is reversible, Ug is an arbitrary vector, and therefore, we must have

$$U(f_1 + f_2) = Uf_1 + Uf_2$$

Hence as the equations of motion (20a) and (20b) are clearly nonlinear, the evolution is nonlinear too, and consequently, it cannot be a unitary transformation as defined above. If we fix the value of the density for all times, then the operator will become linear and it will be unitary.

(53) Marques, M. A. L.; Castro, A.; Bertsch, G. F.; Rubio, A. *Comput. Phys. Commun.* **2003**, *151*, 60–78.

(54) Castro, A.; Marques, M. A. L.; Appel, H.; Oliveira, M.; Rozzi, C. A.; Andrade, X.; Lorenzen, F.; Gross, E. K. U.; Rubio, A. *Phys. Status Solidi B* **2006**, *243*, 2465–2488.

(55) Chelikowsky, J. R.; Troullier, N.; Saad, Y. *Phys. Rev. Lett.* **1994**, *72*, 1240–1243.

(56) Hirose, K.; Ono, T.; Fujimoto, Y.; Tsukamoto, S. *First-Principles Calculations in Real-Space formalism*; Imperial College Press: London, 2005; pp 12−14.

(57) Perdew, J. P.; Zunger, A. *Phys. Rev. B* **1981**, *23*, 5048–5079.

(58) Genovese, L.; Deutsch, T.; Neelov, A.; Goedecker, S.; Beylkin, G. *J. Chem. Phys.* **2006**, *125*, 074105.

(59) In principle the forces acting over the ions are given by eq 20b; however, due to the derivatives of the ionic potential (that can have very high Fourier components), this expression is difficult to calculate accurately on real-space grids. Fortunately, an alternative expression in terms of the gradient of the wave functions can be obtained for both the local and nonlocal parts of the pseudopotential.[56]

(60) Castro, A.; Marques, M. A. L.; Rubio, A. *J. Chem. Phys.* **2004**, *121*, 3425–3433.

(61) Tuckerman, M. E.; Parrinello, M. *J. Chem. Phys.* **1994**, *101*, 1316–1329.

(62) (a) Hutter, J.; Curioni, A. *Parallel Comput.* **2005**, *31*, 1–17. (b) Cavazzoni, C.; Chiarotti, G. L. *Comput. Phys. Commun.* **1999**, *123*, 56–76.

(63) Pastore, G.; Smargiassi, E.; Buda, F. *Phys. Rev. A* **1991**, *44*, 6334–6347.

(64) Crawford, M. F.; Welsh, H. L.; Locke, J. L. *Phys. Rev.* **1949**, *75*, 1607.

(65) Director NIST Mass Spec Data Center, S. S. Mass Spectra. In *NIST Chemistry WebBook, NIST Standard Reference Database Number 69*; Linstrom, P. J., Mallard, W. G., Eds.; National Institute of Standards and Technology: Gaithersburg, MD, 2005.

(66) Cabioc'h, T.; Kharbach, A.; Le Roy, A.; Riviere, J. P. *Chem. Phys. Lett.* **1998**, *285*, 216–220.

(67) Kuhne, T. D.; Krack, M.; Mohamed, F. R.; Parrinello, M. *Phys. Rev. Lett.* **2007**, *98*, 066401.

(68) Marzari, N.; Vanderbilt, D.; Payne, M. C. *Phys. Rev. Lett.* **1997**, *79*, 1337–1340.

(69) Horsfield, A. P.; Bowler, D. R.; Ness, H.; Sánchez, C. G.; Todorov, T. N.; Fisher, A. J. *Rep. Prog. Phys.* **2006**, *69*, 1195–1234.

(70) Metropolis, N.; Rosenbluth, A. W.; Rosenbluth, M. N.; Teller, A. H.; Teller, E. *J. Chem. Phys.* **1953**, *21*, 1087–1092.

(71) Bernal, J. D. *Nature* **1959**, *183*, 141–147.

(72) Wallace, D. B. An Introduction to the Hellmann-Feynman theory. M.Sc. thesis, University of Central Florida: Orlando, FL, 2005.

(73) Hellmann, H. *Einführung in die Quantenchemie*; Frank Deuticke: Leipzig, 1937; p 285.

(74) Feynman, R. P. *Phys. Rev.* **1939**, *56*, 340–343.

CT800518J

JCTC Journal of Chemical Theory and Computation

Electronic Zero-Point Oscillations in the Strong-Interaction Limit of Density Functional Theory

Paola Gori-Giorgi,*[,†,‡] Giovanni Vignale,[§] and Michael Seidl[||]

Laboratoire de Chimie Théorique, CNRS, Université Pierre et Marie Curie, 4 Place Jussieu, 75252 Paris, France, Afdeling Theoretische Chemie, Vrije Universiteit, De Boelelaan 1083, 1081 HV Amsterdam, The Netherlands, Department of Physics and Astronomy, University of Missouri, Columbia, Missouri 65211, and Institute of Theoretical Physics, University of Regensburg, 93040 Regensburg, Germany

Received December 2, 2008

Abstract: The exchange-correlation energy in Kohn−Sham density functional theory can be expressed exactly in terms of the change in the expectation of the electron−electron repulsion operator when, in the many-electron Hamiltonian, this same operator is multiplied by a real parameter λ varying between 0 (Kohn−Sham system) and 1 (physical system). In this process, usually called adiabatic connection, the one-electron density is kept fixed by a suitable local one-body potential. The strong-interaction limit of density functional theory, defined as the limit $\lambda\rightarrow\infty$, turns out to be like the opposite noninteracting Kohn−Sham limit ($\lambda\rightarrow 0$) mathematically simpler than the physical ($\lambda = 1$) case and can be used to build an approximate interpolation formula between $\lambda\rightarrow 0$ and $\lambda\rightarrow\infty$ for the exchange-correlation energy. Here we extend the systematic treatment of the $\lambda\rightarrow\infty$ limit [*Phys. Rev. A* **2007**, *75*, 042511] to the next leading term, describing zero-point oscillations of strictly correlated electrons, with numerical examples for small spherical atoms. We also propose an improved approximate functional for the zero-point term and a revised interpolation formula for the exchange-correlation energy satisfying more exact constraints.

1. Introduction

Kohn−Sham (KS) density functional theory (DFT)[1−3] is a very successful method for electronic structure calculations thanks to its unique combination of low computational cost and remarkable accuracy. In the Kohn−Sham formalism, the ground-state energy of a many-electron system in a given external potential $\hat{V}_{\rm ext} = \sum_{i=1}^{N} v_{\rm ext}(\mathbf{r}_i)$ is rewritten as a functional of the one-electron density $\rho(\mathbf{r})$

$$E[\rho] = F[\rho] + \int d^3r \rho(\mathbf{r}) v_{\rm ext}(\mathbf{r}) \tag{1}$$

where

$$F[\rho] = \min_{\Psi\rightarrow\rho} \langle \Psi | \hat{T} + \hat{V}_{\rm ee} | \Psi \rangle \tag{2}$$

with the operators (in Hartree atomic units $e = m = \hbar = a_0 = 1$ used throughout)

$$\hat{T} = -\frac{1}{2}\sum_{i=1}^{N} \nabla_i^2 \tag{3}$$

$$\hat{V}_{\rm ee} = \frac{1}{2}\sum_{i,j=1}^{N} \frac{1-\delta_{ij}}{|\mathbf{r}_i - \mathbf{r}_j|} \tag{4}$$

In eq (2) the minimum search is carried over all antisymmetric wave functions yielding a given density ρ.[4] The universal functional $F[\rho]$ of eq (2) is further divided into

$$F[\rho] = T_s[\rho] + U[\rho] + E_{\rm xc}[\rho] \tag{5}$$

where the noninteracting kinetic energy functional $T_s[\rho]$ is obtained by replacing $\hat{V}_{\rm ee}$ with zero in eq (2)

* Corresponding author e-mail: gori@lct.jussieu.fr.
† CNRS, Université Pierre et Marie Curie.
‡ Vrije Universiteit.
§ University of Missouri.
|| University of Regensburg.

10.1021/ct8005248 CCC: $40.75
Published on Web 03/23/2009

$$T_s[\rho] = \min_{\psi \to \rho} \langle \psi | \hat{T} | \psi \rangle \tag{6}$$

and the Hartree functional $U[\rho]$ is the classical electrostatic repulsion energy

$$U[\rho] = \frac{1}{2} \int d^3r \int d^3r' \frac{\rho(\mathbf{r})\rho(\mathbf{r}')}{|\mathbf{r} - \mathbf{r}'|} \tag{7}$$

The only quantity that needs to be approximated is the functional for the exchange-correlation energy, $E_{xc}[\rho]$, defined as the quantity needed to make eq (5) exact. The great success of KS DFT in solid state physics stems from the fact that even the simplest approximation for $E_{xc}[\rho]$, the local-density approximation (LDA), already gives remarkable results for basic properties of simple solids. A fundamental step forward to improve the solid-state physics results, and to spread the use of KS DFT into the quantum chemistry world, has been the advent of generalized gradient approximations (GGA), which are, to a large amount, due to the work of John P. Perdew and his co-workers.[5−7]

Despite its success in scientific areas now ranging from material science to biology, KS-DFT is far from being perfect, and a huge effort is put forth nowadays in trying to improve the approximations for $E_{xc}[\rho]$ (for recent reviews see, e.g., refs 8 and 9). The focus of a large part of the scientific community working in this area has shifted from seeking explicit functionals of the density (like the GGAs) to implicit density functionals that construct the exchange-correlation energy from the KS orbitals. For example, predicted atomization energies of molecules have been improved by meta-GGAs (MGGA)[10,11] which make use of the orbital kinetic energy density, by hybrid functionals (see, e.g., refs 12 and 13) which mix a fraction of exact exchange with GGA exchange and correlation, and by range-separated hybrids, in which only long- or short-range exact exchange is used (see, e.g., refs 14−18).

The next step[19] toward higher accuracy could be fully nonlocal functionals, which use 100% of exact exchange (for a recent review, see ref 20). Despite several attempts and the increasing understanding of the crucial problems,[21] the construction of a fully nonlocal correlation energy functional compatible with exact exchange is still an issue. A possible way to address this problem is to use the information contained in the strong-interaction limit of DFT.[22] To explain this strategy, we have first to recall an exact formula[23−25] for $E_{xc}[\rho]$

$$E_{xc}[\rho] = \int_0^1 d\lambda W_\lambda[\rho] \tag{8}$$

The integrand $W_\lambda[\rho]$ is given by

$$W_\lambda[\rho] = \langle \Psi_\lambda[\rho] | \hat{V}_{ee} | \Psi_\lambda[\rho] \rangle - U[\rho] \tag{9}$$

where $\Psi_\lambda[\rho]$, for a given value of $\lambda \geq 0$, is the wave function that minimizes $\langle \Psi | \hat{T} + \lambda \hat{V}_{ee} | \Psi \rangle$ and yields the density ρ. If ρ is v-representable for all $\lambda \geq 0$, $\Psi_\lambda[\rho]$ is the ground-state of a fictitious N-electron system with the Hamiltonian

$$\hat{H}_\lambda[\rho] = \hat{T} + \lambda \hat{V}_{ee} + \hat{V}^\lambda_{ext}[\rho] \tag{10}$$

where the λ-dependent external potential

$$\hat{V}^\lambda_{ext}[\rho] = \sum_{i=1}^{N} v^\lambda_{ext}([\rho];\mathbf{r}_i) \tag{11}$$

ensures that $\hat{H}_\lambda[\rho]$ have the same given ($\lambda = 1$) ground-state density $\rho(\mathbf{r})$ for all λ. When $\lambda = 0$, the Hamiltonian of eq (10) becomes the KS Hamiltonian, and $v^{\lambda=0}_{ext}([\rho];\mathbf{r}) = v_{KS}(\mathbf{r})$, the familiar KS potential, while for $\lambda = 1$ we recover the Hamiltonian of the physical system.

We can use perturbation theory to obtain an expansion of $W_\lambda[\rho]$ in powers of λ starting from $\lambda = 0$

$$W_\lambda[\rho] = E_x[\rho] + 2\lambda E_c^{GL2}[\rho] + O(\lambda^2) \tag{12}$$

where $E_x[\rho]$ is the exchange energy, and $E_c^{GL2}[\rho]$ is the second-order correlation energy in Görling-Levy[26] perturbation theory. However, like in the Møller−Plesset case,[27] this perturbation series expansion seems to have a finite radius of convergence which for many atoms and molecules is less than 1.[22] Moreover, evaluating terms of ever higher order becomes impracticably expensive. Nevertheless, the exact lowest-order terms $E_x[\rho]$ and $E_c^{GL2}[\rho]$ can be used for an alternative approach,[22] called interaction-strength interpolation (ISI), to approximate the integrand in eq (8). The basic idea of ISI is to combine the $\lambda \to 0$ limit of eq (12) with the information from the opposite strong-interaction limit, $\lambda \to \infty$, to construct an interpolation formula for $W_\lambda[\rho]$. This way, the information on the physical system at $\lambda = 1$ is extracted from an interpolation between $\lambda \to 0$ and $\lambda \to \infty$. ISI is based on previous ideas and attempts to construct approximate formulas for $W_\lambda[\rho]$ when $0 \leq \lambda \leq 1$.[12,13,28,29] Its novelty is the introduction of the strong-interaction limit, thus extending the construction of $W_\lambda[\rho]$ to the whole domain $\lambda \in [0,\infty]$.

In the strong-interaction limit, $\lambda \to \infty$, we will show in the next sections that $W_\lambda[\rho]$ has the asymptotic expansion

$$W_\lambda[\rho] = W_\infty[\rho] + \frac{W'_\infty[\rho]}{\sqrt{\lambda}} + O(\lambda^{-p}) \tag{13}$$

where $p \geq 5/4$. The expansion (13) was justified from physical arguments in refs 30 and 31, and a simple approximation for the two functionals $W_\infty[\rho]$ and $W'_\infty[\rho]$, the point-charge plus continuum (PC) model,[32] has been used for the ISI, yielding atomization energies with errors within 4.3 kcal/mol.[22] In a recent paper,[33] the functional $W_\infty[\rho]$ of eq (13) has been constructed exactly. The main object of the present work is the extension of the systematic treatment of ref 33 to the next term, $W'_\infty[\rho]$.

The paper is organized as follows. In the next section 2, we briefly review the results of ref 33, recalling that the strong-interaction limit of DFT reduces to a $3N$-dimension classical equilibrium problem whose minimum is degenerate over a three-dimensional subspace. In sections 3 and 4 we define local curvilinear coordinates based on the local normal modes around the degenerate minimum. These local curvilinear coordinates will be used, in section 5, to expand the Hamiltonian of eq (10) for $\lambda \to \infty$, up to the order $\lambda^{1/4}$. The corresponding expansion of $\Psi_\lambda[\rho]$ is carried out in section 6, and the exact expression for $W'_\infty[\rho]$ is obtained in section

7, where we also report numerical results for small spherical atoms, and we propose an improved PC functional for $W'_\infty[\rho]$. In section 8 we revise the interpolation formula for the ISI functional in order to satisfy the exact expansion of eq (13) up to $O(\lambda^{-1})$. The last section 9 is devoted to conclusions and perspectives. More details of the derivation of our expansion are given in Appendix A, and a fully analytic example is reported in Appendix B.

2. Strictly Correlated Electrons (SCE)

In the $\lambda\rightarrow\infty$ limit it has been shown[30,33] that, in order to keep the N electrons in the given density ρ, the external potential in eq (10) must compensate the infinitely strong interelectronic repulsion, thus becoming proportional to λ

$$\lim_{\lambda\rightarrow\infty}\frac{v_{\mathrm{ext}}^{\lambda}([\rho],\mathbf{r})}{\lambda}=v_{\mathrm{SCE}}([\rho],\mathbf{r}) \tag{14}$$

with a smooth finite function $v_{\mathrm{SCE}}([\rho],\mathbf{r})$. (For brevity, the argument $[\rho]$ will be often dropped in the following).

The leading term in eq (10) when $\lambda\rightarrow\infty$ is then a purely multiplicative potential-energy operator

$$\hat{H}_{\lambda\rightarrow\infty}[\rho]=\lambda(\hat{V}_{ee}+\hat{V}_{SCE})+O(\sqrt{\lambda}) \tag{15}$$

The square $|\Psi_{\lambda\rightarrow\infty}[\rho]|^2$ of the corresponding wave function is a distribution that is zero everywhere except for electronic configurations for which $\hat{V}_{\mathrm{ee}}+\hat{V}_{\mathrm{SCE}}$ has its global minimum. In order to guarantee a given *smooth* density $\rho(\mathbf{r})$ in such a "classical" state, this global minimum must be degenerate over a three-dimensional subspace of $\mathbb{R}^{3N}$[33] (otherwise, the density would be a sum of delta peaks centered in the equilibrium positions of the N electrons). We call this classical state with a smooth density "strictly correlated electrons" (SCE). The square of the SCE wave function $|\Psi_{\mathrm{SCE}}[\rho]|^2=|\lim_{\lambda\rightarrow\infty}\Psi_\lambda[\rho]|^2$ reads

$$|\Psi_{\mathrm{SCE}}(\mathbf{r}_1,...,\mathbf{r}_N)|^2=\frac{1}{N!}\sum_P\int ds\frac{\rho(\mathbf{s})}{N}\delta(\mathbf{r}_1-f_{P(1)}(\mathbf{s}))\delta(\mathbf{r}_2-f_{P(2)}(\mathbf{s}))...\delta(\mathbf{r}_N-\mathbf{f}_{P(N)}(\mathbf{s})) \tag{16}$$

where $\mathbf{f}_1,..,\mathbf{f}_N$ are "comotion functions", with $\mathbf{f}_1(\mathbf{r})=\mathbf{r}$, and P denotes a permutation of $\{1,...N\}$. This means that the N points $\mathbf{r}_1,...,\mathbf{r}_N$ in 3D space found upon simultaneous measurement of the N electronic positions in the SCE state always obey the $N-1$ relations

$$\mathbf{r}_i=\mathbf{f}_i(\mathbf{r}_1)\quad(i=2,...,N) \tag{17}$$

If the $N-1$ comotion functions $\mathbf{f}_i(\mathbf{s})$ satisfy the differential equation

$$\rho(\mathbf{f}_i(\mathbf{r}))d^3f_i(\mathbf{r})=\rho(\mathbf{r})d^3r \tag{18}$$

together with special transformation properties[33] (see also ref 34), the SCE wave function of eq (16) yields the given density $\rho(\mathbf{r})$. One has then to find the initial conditions for the integration of eq (18) that minimize the expectation of $\hat{V}_{\mathrm{ee}}$. The leading coefficient $W_\infty[\rho]$ in eq (13) has a simple analytic expression in terms of the $\mathbf{f}_i(\mathbf{s})$ [see eq (80)] and has been evaluated for spherical atoms with up to $N=10$ electrons.[33]

In order to treat the next leading term, $W'_\infty[\rho]$ of eq (13), we have to consider the next terms in the $\lambda\rightarrow\infty$ expansion of the Hamiltonian of eq (10), i.e., the kinetic energy $\hat{T}$ and the next orders of $\hat{V}_{\mathrm{ext}}^{\lambda}$. Physically, we expect that $W'_\infty[\rho]$ is determined by zero-point oscillations around the degenerate SCE minimum. In the following, we give a formal justification to this physical argument.

3. The SCE Potential-Energy Minimum

Writing $\underline{r}\equiv(\mathbf{r}_1,...,\mathbf{r}_N)\in\mathbb{R}^{3N}\equiv\Omega$, we consider the asymptotic potential-energy function ($\Omega\rightarrow\mathbb{R}$)

$$E_{\mathrm{pot}}(\underline{r}):=\lim_{\lambda\rightarrow\infty}\frac{\hat{H}_\lambda[\rho]}{\lambda}=\frac{1}{2}\sum_{i,j=1}^{N}\frac{1-\delta_{ij}}{|\mathbf{r}_i-\mathbf{r}_j|}+\sum_{i=1}^{N}v_{\mathrm{SCE}}(\mathbf{r}_i)=\hat{V}_{\mathrm{ee}}+\hat{V}_{\mathrm{SCE}} \tag{19}$$

As said, the SCE external potential $v_{\mathrm{SCE}}(\mathbf{r})$ has the very special property that the function $E_{\mathrm{pot}}(\underline{r})$ has a degenerate minimum E_{SCE} on the 3D subset

$$\Omega_0=\{\underline{f}(\mathbf{s})|\mathbf{s}\in\mathbb{R}^3\}\subset\Omega \tag{20}$$

where $\underline{f}(\mathbf{s})=(\mathbf{s},\mathbf{f}_2(\mathbf{s}),...,\mathbf{f}_N(\mathbf{s}))$, with the $\mathbb{R}^3\rightarrow\mathbb{R}^3$ comotion functions $\mathbf{f}_i(\mathbf{s})$. In other words, for all $\underline{r}\in\Omega_0$, the function $E_{\mathrm{pot}}(\underline{r})$ assumes the same constant value

$$E_{\mathrm{SCE}}=W_\infty[\rho]+U[\rho]+\sum_{i=1}^{N}v_{\mathrm{SCE}}(\mathbf{f}_i(\mathbf{s})) \tag{21}$$

which, in particular, is its global minimum within Ω. For illustration, see the analytical example of eq (108) in Appendix B.

In the very limit $\lambda\rightarrow\infty$, when $\hat{H}_\lambda[\rho]\rightarrow\lambda E_{\mathrm{pot}}(\underline{r})+O(\sqrt{\lambda})$, the square of the wave function $|\Psi_\lambda[\rho]|^2$ becomes the distribution $|\Psi_{\mathrm{SCE}}[\rho]|^2$ of eq (16), which is strictly zero everywhere in Ω except for the 3D subset Ω_0 where $E_{\mathrm{pot}}(\underline{r})$ is minimum[33]

$$\Psi_{\mathrm{SCE}}([\rho],\underline{r})\equiv 0\quad\forall\underline{r}\in\Omega\backslash\Omega_0 \tag{22}$$

For large, but finite $\lambda\gg 1$, the electrons are expected to perform small zero-point oscillations about the SCE configurations $\underline{r}\in\Omega_0$, within a narrow $3N$-D "envelope" Ω_ε (with a small width $\varepsilon>0$) of the 3D subset $\Omega_0\subset\Omega$

$$\Omega_\varepsilon=\{\underline{r}\in\Omega|d(\underline{r},\Omega_0)<\varepsilon\} \tag{23}$$

Here, for a given $\underline{r}\in\Omega$, the quantity

$$d(\underline{r},\Omega_0):=\min_{\mathbf{s}\in\mathbb{R}^3}|\underline{r}-\underline{f}(\mathbf{s})| \tag{24}$$

is the minimum $3N$-D distance between $\underline{r}$ and any $\underline{f}(\mathbf{s})\in\Omega_0$. Notice that $\Omega_0\subset\Omega_\varepsilon\subset\Omega$ and $\Omega_0=\lim_{\varepsilon\rightarrow 0}\Omega_\varepsilon$.

For $\underline{r}\in\Omega_\varepsilon$, $E_{\mathrm{pot}}(\underline{r})$ may be expanded about $\underline{f}(\mathbf{s})\in\Omega_0$

$$E_{\rm pot}(\underline{r}) = E_{\rm SCE} + \frac{1}{2}\sum_{\mu,\nu=1}^{3N} M_{\mu\nu}(\mathbf{s})(r_\mu - f_\mu(\mathbf{s}))(r_\nu - f_\nu(\mathbf{s})) + ... \quad (25)$$

Since $E_{\rm pot}(\underline{r})$ is minimum at $\underline{r} = \underline{f}(\mathbf{s})$, there are no first-order terms. [The dots represent the terms of third and higher orders.] For any given $\mathbf{s} \in \mathbb{R}^3$, the Hessian matrix $M_{\mu\nu}(\mathbf{s})$ in the second-order term has $3N$ non-negative eigenvalues $\omega_\mu(\mathbf{s})^2$ which can be labeled such that

$$\omega_\mu(\mathbf{s})^2 = 0 \ (\mu = 1, 2, 3)$$
$$\omega_\mu(\mathbf{s})^2 > 0 \ (\mu = 4, ..., 3N) \quad (26)$$

The corresponding $3N$-D normalized eigenvectors $\underline{e}^\mu(\mathbf{s})$, with components $e^\mu_\sigma(\mathbf{s})$ ($\sigma = 1,..., 3N$), are pairwise orthogonal

$$\underline{e}^\mu(s) \cdot \underline{e}^\nu(\mathbf{s}) \equiv \sum_{\sigma=1}^{3N} e^\mu_\sigma(\mathbf{s}) e^\nu_\sigma(\mathbf{s}) = \delta_{\mu\nu} \quad (27)$$

The first three eigenvectors, with zero eigenvalues, lie in the space "tangential" to Ω_0, and the remaining $3N - 3$ eigenvectors are "orthogonal" to Ω_0

$$\underline{e}^\mu(\mathbf{s}) \cdot \frac{\partial \underline{f}(\mathbf{s})}{\partial s_\alpha} = 0 \quad (\mu = 4, ..., 3N, \quad \alpha = 1, 2, 3) \quad (28)$$

where $\alpha = 1, 2, 3$ denotes the three Cartesian components (x, y, z) of $\mathbf{s}$.

4. Local Normal Modes

For sufficiently small $\varepsilon > 0$, we use these eigenvectors to introduce a set of $3N$ curvilinear coordinates in Ω_ε. A given point $\underline{r} = (r_{11}, r_{12}, r_{13},..., r_{N1}, r_{N2}, r_{N3}) \in \Omega_\varepsilon$ is written in terms of these local curvilinear coordinates as follows. The first three curvilinear coordinates are the Cartesian coordinates s_1, s_2, s_3 of the minimizing vector $\mathbf{s}$ in eq (24), fixed by the condition that the $3N$-D vector $\underline{r} - \underline{f}(\mathbf{s})$ in Ω is orthogonal to Ω_0 in the point $\underline{f}(\mathbf{s})$

$$(\underline{r} - \underline{f}(\mathbf{s})) \cdot \frac{\partial \underline{f}(\mathbf{s})}{\partial s_\alpha} = 0 \quad (\alpha = 1, 2, 3) \quad (29)$$

The remaining $3N - 3$ coordinates are the projections q_4,..., q_{3N} of $\underline{r} - \underline{f}(\mathbf{s})$ onto the local eigenvectors $\underline{e}^4(\mathbf{s})$,..., $\underline{e}^{3N}(\mathbf{s})$

$$\underline{r} - \underline{f}(\mathbf{s}) = \sum_{\mu=4}^{3N} q_\mu \underline{e}^\mu(\mathbf{s}) \quad (30)$$

The first three eigenvectors $\underline{e}^{1,2,3}(\mathbf{s})$ are not needed, since they are tangential to Ω_0 at the point $\underline{f}(\mathbf{s})$ and therefore orthogonal to $\underline{r} - \underline{f}(\mathbf{s})$. Inverting eq (30) yields

$$q_\mu = \underline{e}^\mu \cdot (\underline{r} - \underline{f}(\mathbf{s})) \quad (\mu = 4, ..., 3N) \quad (31)$$

For these new curvilinear coordinates, we also write

$$(s_1, s_2, s_3, q_4, ..., q_{3N}) = (\mathbf{s}, \underline{q}) \quad (32)$$

Notice that $\underline{r}$ has $3N$ components, while $\underline{q}$ has only $3N - 3$ ones. In this notation, eq (30) reads

$$r_\nu = f_\nu(\mathbf{s}) + \sum_{\mu=4}^{3N} e^\mu_\nu(\mathbf{s}) q_\mu \ (\nu = 1, ..., 3N) \quad (33)$$

This is the transformation formula between the Cartesian coordinates $\underline{r}$ and the "local normal modes" $(\mathbf{s}, \underline{q})$ in the $3N$-D configuration space Ω.

In terms of the q_μ, the second-order contribution in the Taylor expansion (25) becomes diagonal

$$\tilde{E}_{\rm pot}(\mathbf{s}, \underline{q}) = E_{\rm SCE} + \frac{1}{2}\sum_{\mu=4}^{3N} \omega_\mu(\mathbf{s})^2 q_\mu^2 + \frac{1}{3!}\sum_{\mu,\nu,\sigma=4}^{3N} E^{(3)}_{\mu\nu\sigma}(\mathbf{s}) q_\mu q_\nu q_\sigma + ... \quad (34)$$

Here, the third-order term is derived from the corresponding term in eq (25) (in the present notation)

$$\frac{1}{3!}\sum_{\xi,\eta,\zeta=1}^{3N} \left.\frac{\partial^3 E_{\rm pot}(\underline{r})}{\partial r_\xi \partial r_\eta \partial r_\zeta}\right|_{\underline{r}=\underline{f}(\mathbf{s})} (r_\xi - f_\xi(\mathbf{s}))(r_\eta - f_\eta(\mathbf{s}))(r_\zeta - f_\zeta(\mathbf{s})) \quad (35)$$

Using here eq (33) for $r_\nu - f_\nu(\mathbf{s})$, we find

$$E^{(3)}_{\mu\nu\sigma}(\mathbf{s}) = \sum_{\xi,\eta,\zeta=1}^{3N} \left.\frac{\partial^3 E_{\rm pot}(\underline{r})}{\partial r_\xi \partial r_\eta \partial r_\zeta}\right|_{\underline{r}=\underline{f}(\mathbf{s})} e^\mu_\xi(\mathbf{s}) e^\nu_\eta(\mathbf{s}) e^\sigma_\zeta(\mathbf{s}) \quad (36)$$

Substituting eq (33) for $\underline{r}$ in the wave function $\Psi_\lambda(\underline{r})$ that represents the state $\Psi_\lambda[\rho]$ yields the transformed wave function $\tilde{\Psi}_\lambda(\mathbf{s}, \underline{q})$. While the original wave function obeys

$$\int d^3 r_1 ... \int d^3 r_N |\Psi_\lambda(\underline{r})|^2 \equiv \int d\underline{r} |\Psi_\lambda(\underline{r})|^2 = 1 \quad (37)$$

the transformed one is normalized according to

$$\int d^3 s \int d\underline{q} J(\mathbf{s}, \underline{q}) |\tilde{\Psi}_\lambda(\mathbf{s}, \underline{q})|^2 = 1 \quad (38)$$

where $J(\mathbf{s}, \underline{q})$ is the Jacobian associated with the coordinate transformation (33), see eq (101) in Appendix A.

For sufficiently large $\lambda \gg 1$, the wave function $\Psi_\lambda(\mathbf{s}, \underline{q})$ strongly suppresses all configurations $\underline{r} \in \Omega$ except for the ones inside the narrow envelope Ω_ε of the 3D subset Ω_0. This means that $\tilde{\Psi}_\lambda(\mathbf{s}, \underline{q})$ is essentially different from zero only for $(q_4^2 + ... + q_{3N}^2)^{1/2} < \varepsilon$, where ε decreases with growing $\lambda \gg 1$ and goes to zero in the limit $\lambda \to \infty$.

More precisely, since the quadratic term in eq (34) is multiplied by λ in the Hamiltonian (10), the scale of the quantum fluctuation is $\varepsilon \sim \lambda^{-1/4} \equiv \alpha$ for $\lambda \to \infty$. Therefore, it will be useful to switch for a given value of $\lambda \gg 1$ from the present curvilinear coordinates $(\mathbf{s}, \underline{q})$ to scaled coordinates $(\mathbf{s}, \underline{u})$ where

$$\underline{u} = \lambda^{1/4} \underline{q} \Leftrightarrow \underline{q} = \alpha \underline{u} \quad (\alpha = \lambda^{-1/4}) \quad (39)$$

This second transformation yields the wave function

$$\Psi_\alpha(\mathbf{s}, \underline{u}) = \tilde{\Psi}_\lambda(\mathbf{s}, \alpha \underline{u}) \quad (40)$$

According to eq (38), we now have

$$\int d^3 s \int d\underline{u} K_\alpha(\mathbf{s}, \underline{u}) |\Psi_\alpha(\mathbf{s}, \underline{u})|^2 = 1 \quad (41)$$

with the scaled Jacobian

$$K_\alpha(\mathbf{s}, \underline{u}) = \alpha^{3N-3} J(\mathbf{s}, \alpha\underline{u}) \tag{42}$$

Later on, we shall make use of the expansion

$$J(\mathbf{s}, \underline{q}) = J(\mathbf{s}, \underline{0}) + \sum_{\mu=4}^{3N} J_\mu^{(1)}(\mathbf{s}) q_\mu + O(q_\nu^2) \tag{43}$$

whose derivation is reported in Appendix A.

5. Expansion of the Hamiltonian

To obtain an expansion for large $\lambda \gg 1$ (or, equivalently, for small $\alpha \equiv \lambda^{-1/4} \ll 1$), we must express the Hamiltonian $\hat{H}_\lambda[\rho]$ of eq (10) in terms of the scaled coordinates $(\mathbf{s}, \underline{u})$. To this end, we split $\hat{H}_\lambda[\rho]$ into three pieces

$$\hat{H}_\lambda[\rho] = \hat{T} + \lambda E_{\text{pot}}(\underline{r}) + (\hat{V}_{\text{ext}}^{\lambda} - \lambda \hat{V}_{\text{SCE}}) \tag{44}$$

and treat these separately now.

5.1. Kinetic Energy (First Term). For the kinetic-energy operator $\hat{T}$, the $3N$-D Laplacian is obtained in Appendix A in terms of the curvilinear coordinates q_μ from the general transformation rule

$$\sum_{i=1}^{3} \nabla_i^2 \equiv \sum_{\mu=1}^{3N} \frac{\partial^2}{\partial r_\mu^2} = \sum_{\mu,\nu=1}^{3N} \frac{1}{\sqrt{G}} \frac{\partial}{\partial q_\mu} \left(\sqrt{G} G^{\mu\nu} \frac{\partial}{\partial q_\nu} \right) \tag{45}$$

(To simplify the notation, we write $s_\mu \equiv q_\mu$ for $\mu = 1, 2, 3$ in this subsection.) Here, the matrix $G^{\mu\nu}$ is the inverse of the metric tensor $G_{\mu\nu}$, defined by

$$G_{\mu\nu} = \sum_{\xi=1}^{3N} \frac{\partial r_\xi}{\partial q_\mu} \frac{\partial r_\xi}{\partial q_\nu} \equiv \frac{\partial \underline{r}}{\partial q_\mu} \cdot \frac{\partial \underline{r}}{\partial q_\nu} \tag{46}$$

and G is its determinant, $G = \det(G_{\mu\nu})$. Switching in a second step from the q_μ to the scaled coordinates u_μ yields the expansion (see Appendix A)

$$\hat{T} = \sqrt{\lambda}[\hat{T}^{(0)} + \alpha \hat{T}^{(1)} + \alpha^2 \hat{T}^{(2)} + O(\alpha^3)] \tag{47}$$

The operators $\hat{T}^{(n)}$ are independent of λ (or $\alpha \equiv \lambda^{-1/4}$)

$$\hat{T}^{(0)} = \frac{-1}{2} \sum_{\mu=4}^{3N} \frac{\partial^2}{\partial u_\mu^2} \tag{48}$$

$$\hat{T}^{(1)} = \frac{-1}{2} \sum_{\mu=4}^{3N} X_\mu(\mathbf{s}) \frac{\partial}{\partial u_\mu} \tag{49}$$

where $X_\mu(\mathbf{s})$ is reported in Appendix A. Notice that the α^2 term is constant, since $\alpha^2\sqrt{\lambda} = 1$.

5.2. SCE Potential Energy (Second Term). For the second term in eq (44), we use the Taylor expansion (34), with $q_\mu = \alpha u_\mu$, to find

$$\lambda E_{\text{pot}}(\underline{r}) = \lambda \Bigg[E_{\text{SCE}} + \frac{\alpha^2}{2} \sum_{\mu=4}^{3N} \omega_\mu(\mathbf{s})^2 u_\mu^2 + \frac{\alpha^3}{3!} \sum_{\mu,\nu,\sigma=4}^{3N} E_{\mu\nu\sigma}^{(3)}(\mathbf{s}) u_\mu u_\nu u_\sigma + \frac{\alpha^4}{4!} \sum_{\mu,\nu,\sigma,\tau=4}^{3N} E_{\mu\nu\sigma\tau}^{(4)}(\mathbf{s}) u_\mu u_\nu u_\sigma u_\tau + O(\alpha^5) \Bigg] \tag{50}$$

5.3. The Remaining External Potential (Third Term). For the last term in eq (44), we make an ansatz that will later on turn out to be consistent

$$\hat{V}_{\text{ext}}^{\lambda} - \lambda \hat{V}_{\text{SCE}} = \sqrt{\lambda} \sum_{n=0}^{\infty} \alpha^n V^{(n)}(\underline{r}) \tag{51}$$

Using eq (30) for $\underline{r}$ and $q_\mu = \alpha u_\mu$, we may expand

$$\begin{aligned} V^{(n)}(\underline{r}) &\equiv V^{(n)}(\underline{f}(\mathbf{s}) + \alpha \sum_{\mu=4}^{3N} \underline{e}^{\mu}(\mathbf{s}) u_\mu) \\ &= V^{(n)}(\underline{f}(\mathbf{s})) + \alpha \sum_{\sigma=1}^{3N} V_\sigma^{(n)}(\underline{f}(\mathbf{s})) \sum_{\mu=4}^{3N} e_\sigma^\mu(\mathbf{s}) u_\mu + \\ &\quad + \frac{\alpha^2}{2} \sum_{\sigma,\tau=1}^{3N} V_{\sigma\tau}^{(n)}(\underline{f}(\mathbf{s})) \sum_{\mu,\nu=4}^{3N} e_\sigma^\mu(\mathbf{s}) e_\tau^\nu(\mathbf{s}) u_\mu u_\nu + \\ &\quad + O(\alpha^3) \end{aligned} \tag{52}$$

Here, the coefficients $V_\sigma^{(n)}$, $V_{\sigma\tau}^{(n)}$, etc. denote the partial derivatives of $V^{(n)}(\underline{r})$ at $\underline{r} = \underline{f}(\mathbf{s})$

$$V_{\sigma\tau}^{(n)}(\underline{f}(\mathbf{s})) = \left. \frac{\partial^2 V^{(n)}(\underline{r})}{\partial r_\sigma \partial r_\tau} \right|_{\underline{r}=\underline{f}(\mathbf{s})} \text{ etc.} \tag{53}$$

Now, eq (51) yields the expansion

$$\hat{V}_{\text{ext}}^{\lambda} - \lambda \hat{V}_{\text{SCE}} = \sqrt{\lambda}[\hat{V}^{(0)} + \alpha \hat{V}^{(1)} + \alpha^2 \hat{V}^{(2)} + O(\alpha^3)] \tag{54}$$

with α-independent (multiplicative) operators

$$\hat{V}^{(0)} = V^{(0)}(\underline{f}(\mathbf{s})) \tag{55}$$

$$\hat{V}^{(1)} = V^{(1)}(\underline{f}(\mathbf{s})) + \sum_{\sigma=1}^{3N} V_\sigma^{(0)}(\underline{f}(\mathbf{s})) \sum_{\mu=4}^{3N} e_\sigma^\mu(\mathbf{s}) u_\mu \tag{56}$$

$$V^{(2)} = V^{(2)}(\underline{f}(\mathbf{s})) + \sum_{\sigma=1}^{3N} V_\sigma^{(1)}(\underline{f}(\mathbf{s})) \sum_{\mu=4}^{3N} e_\sigma^\mu(\mathbf{s}) u_\mu + \frac{1}{2} \sum_{\sigma,\tau=1}^{3N} V_{\sigma\tau}^{(0)}(\underline{f}(\mathbf{s})) \sum_{\mu,\nu=4}^{3N} e_\sigma^\mu(\mathbf{s}) e_\tau^\nu(\mathbf{s}) u_\mu u_\nu \tag{57}$$

5.4. Full Hamiltonian. Eventually, combining eqs (47), (50), and (54), we obtain the expansion (recall that $\alpha = \lambda^{-1/4}$)

$$\hat{H}_\lambda[\rho] = \lambda E_{\text{SCE}} + \sqrt{\lambda}[\hat{H}^{(0)} + \alpha \hat{H}^{(1)} + \alpha^2 \hat{H}^{(2)} + O(\alpha^3)] \tag{58}$$

with α-independent operators $\hat{H}^{(n)}$. The first two terms read

$$\hat{H}^{(0)} = -\frac{1}{2}\sum_{\mu=4}^{3N}\frac{\partial^2}{\partial u_\mu^2} + V^{(0)}(\underline{f}(\mathbf{s})) + \frac{1}{2}\sum_{\mu=4}^{3N}\omega_\mu(\mathbf{s})^2 u_\mu^2 \quad (59)$$

$$\hat{H}^{(1)} = -\frac{1}{2}\sum_{\mu=4}^{3N} X_\mu(\mathbf{s})\frac{\partial}{\partial u_\mu} + V^{(1)}(\underline{f}(\mathbf{s})) + \sum_{\sigma=1}^{3N} V_\sigma^{(0)}(\underline{f}(\mathbf{s}))\sum_{\mu=4}^{3N} e_\sigma^\mu(\mathbf{s})u_\mu + \frac{1}{3!}\sum_{\mu,\nu,\sigma=4}^{3N} E^{(3)}_{\mu\nu\sigma}(\mathbf{s})u_\mu u_\nu u_\sigma \quad (60)$$

6. Expansion of the Ground State

Due to eq (58), the lowest eigenvalue $E_\lambda[\rho]$ of $\hat{H}_\lambda[\rho]$ (i. e., its ground-state energy) has the expansion

$$E_\lambda[\rho] = \lambda E_{\mathrm{SCE}} + \sqrt{\lambda}[E^{(0)} + \alpha E^{(1)} + \alpha^2 E^{(2)} + O(\alpha^3)] \quad (61)$$

We define $E'_\alpha[\rho] = E^{(0)} + \alpha E^{(1)} + \alpha^2 E^{(2)} + O(\alpha^3)$ as the lowest eigenvalue of the operator

$$\hat{H}'_\alpha[\rho] = \hat{H}^{(0)} + \alpha\hat{H}^{(1)} + \alpha^2\hat{H}^{(2)} + O(\alpha^3) \quad (62)$$

Since E_{SCE} is a constant, $\hat{H}_\lambda[\rho]$ and $\hat{H}'_\alpha[\rho]$, with $\alpha = \lambda^{-1/4}$, have the same ground state

$$\bar{\Psi}_\alpha(\mathbf{s},\underline{u}) = \frac{\Psi^{(0)} + \alpha\Psi^{(1)} + \alpha^2\Psi^{(2)} + O(\alpha^3)}{\sqrt{\mathcal{N}_\alpha}} \quad (63)$$

For the α-dependent normalization constant

$$\mathcal{N}_\alpha = \int d^3s \int d\underline{u} K_\alpha(\mathbf{s},\underline{u})|\Psi^{(0)}(\mathbf{s},\underline{u}) + O(\alpha)|^2 \quad (64)$$

we obtain

$$\mathcal{N}_\alpha = \alpha^{3N-3}[1 + O(\alpha)] \quad (65)$$

when $\Psi^{(0)}$ is normalized according to

$$\int d^3s \int d\underline{u} J(\mathbf{s},\underline{0})|\Psi^{(0)}(\mathbf{s},\underline{u})|^2 = 1 \quad (66)$$

Collecting terms of equal orders $O(\alpha^n)$ in the eigenvalue equation $\hat{H}'_\alpha[\rho]\bar{\Psi}_\alpha = E'_\alpha[\rho]\bar{\Psi}_\alpha$ yields a hierarchy of equations. The leading one is $\hat{H}^{(0)}\Psi^{(0)} = E^{(0)}\Psi^{(0)}$, where $\hat{H}^{(0)}$ is given by eq (59). For a given fixed $\mathbf{s} \in \mathbb{R}^3$, the Hamiltonian $\hat{H}^{(0)}$ describes an uncoupled set of $3N - 3$ harmonic oscillators in 1D. To be more precise, these oscillators are coupled via the dynamical variable $\mathbf{s}$, but the dynamics of $\mathbf{s}$ is much slower, only appearing at orders $O(\lambda^0)$. Consequently, the leading term in the wave function factorizes into a product of Gaussians $\Phi_\omega(u) = (\omega/\pi)^{1/4}e^{-\omega u^2/2}$, with $\int_{-\infty}^{\infty} du|\Phi_\omega(u)|^2 = 1$

$$\Psi^{(0)}(\mathbf{s},\underline{u}) = C^{(0)}(\mathbf{s})\prod_{\mu=4}^{3N}\Phi_{\omega_\mu(\mathbf{s})}(u_\mu) \quad (67)$$

Since $V^{(0)}(\underline{f}(\mathbf{s}))$ is a pure multiplicative operator, the resulting eigenvalue of $\hat{H}^{(0)}$ is, for a given $\mathbf{s}$

$$E^{(0)}(\mathbf{s}) = V^{(0)}(\underline{f}(\mathbf{s})) + \sum_{\mu=4}^{3N}\frac{\omega_\mu(\mathbf{s})}{2} \quad (68)$$

Due to eq (61), this expression cannot depend on the variable $\mathbf{s}$, implying a condition on the $n = 0$ coefficient $V^{(0)}(\underline{r})$ in our ansatz (51)

$$V^{(0)}(\underline{f}(\mathbf{s})) = -\sum_{\mu=4}^{3N}\frac{\omega_\mu(\mathbf{s})}{2} + \mathrm{const} \quad \forall \mathbf{s} \in \mathbb{R}^3 \quad (69)$$

The role of the external potential at the order $\sqrt{\lambda}$ in eq (10) is thus to keep the degeneracy of the SCE minimum (found at the order λ) through the order $\sqrt{\lambda}$. This is necessary in order to keep the given smooth density $\rho(\mathbf{r})$: if one of the SCE configurations (i.e., a given particular $\mathbf{s}_0$) had a lower energy than the others, the SCE wave function would collapse in that particular $\mathbf{s}_0$, and the density would become a sum of delta peaks centered in $\mathbf{f}_i(\mathbf{s}_0)$ (with $i = 1,..., N$).

The degeneracy with respect to $\mathbf{s}$ allows us to weight each configuration with the density $\rho(\mathbf{s})$ and to write

$$E^{(0)} = \int d^3s \frac{\rho(\mathbf{s})}{N}\left[V^{(0)}(\underline{f}(\mathbf{s})) + \sum_{\mu=4}^{3N}\frac{\omega_\mu(\mathbf{s})}{2}\right] \quad (70)$$

This expression for $E^{(0)}$ is consistent with the wave function of eq (67), as we we will now discuss. In order to determine the prefactor $C^{(0)}(\mathbf{s})$ of the wave function we observe that in the wave function $\tilde{\Psi}_\lambda(\mathbf{s}, \underline{q})$, the coordinate $\mathbf{s} \in \mathbb{R}^3$ has the probability distribution

$$\rho_\lambda(\mathbf{s}) = \int d\underline{q} J(\mathbf{s},\underline{q})|\tilde{\Psi}_\lambda(\mathbf{s},\underline{q})|^2 = \int d\underline{q} J(\mathbf{s},\underline{q})|\bar{\Psi}_\alpha(\mathbf{s},\lambda^{1/4}\underline{q})|^2 \quad (71)$$

where $\alpha = \lambda^{-1/4}$. Using eqs (63) and (65), we find

$$\rho_\lambda(\mathbf{s}) = \int d\underline{q} J(\mathbf{s},\underline{q})\frac{|\Psi^{(0)}(\mathbf{s},\lambda^{1/4}\underline{q})|^2}{\alpha^{3N-3}}[1 + O(\alpha)] \quad (72)$$

In the limit $\lambda\rightarrow\infty$ when $\rho_\lambda(\mathbf{s})$ must become rigorously proportional to the electron density $\rho(\mathbf{s})$

$$\lim_{\lambda\rightarrow\infty}\rho_\lambda(\mathbf{s}) = \frac{\rho(\mathbf{s})}{N} \quad (73)$$

the terms $O(\alpha)$ in eq (72) can be dropped and eq (67) yields

$$\frac{\rho(\mathbf{s})}{N} = \lim_{\lambda\rightarrow\infty}|C^{(0)}(\mathbf{s})|^2\int d\underline{q} J(\mathbf{s},q) \times \prod_{\mu=4}^{3N}\lambda^{1/4}|\Phi_{\varpi\mu(\mathbf{s})}(\lambda^{1/4}q_\mu)|^2 \quad (74)$$

Since $\Phi_\omega(u)$ is a normalized Gaussian, the μ-th factor of the product in eq (74) approaches the δ-function $\delta(q_\mu)$ as $\lambda\rightarrow\infty$. Therefore, the right-hand side of eq (74) equals $|C^{(0)}(\mathbf{s})|^2 J(\mathbf{s}, \underline{0})$, implying the result

$$|C^{(0)}(\mathbf{s})|^2 = \frac{1}{N}\frac{\rho(\mathbf{s})}{J(\mathbf{s},\underline{0})} \quad (75)$$

Notice that the uncoupled oscillator wave function of eq (67) has the correct density to the order $\lambda^{-1/2}$ targeted here. Corrections to the density (and the coupling between the oscillators) enter $W_\lambda[\rho]$ at higher orders.

The next order in the perturbative treatment of the ground-state energy of eq (62) leads to

$$E^{(1)} = \langle \Psi^{(0)} | \hat{H}^{(1)} | \Psi^{(0)} \rangle = V^{(1)}(\underline{f}(\mathbf{s})) \tag{76}$$

The same argument used for eq (69) yields

$$V^{(1)}(\underline{f}(\mathbf{s})) = \text{const.} \tag{77}$$

independent of $\mathbf{s}$. The important point here is that the terms coming from $\hat{T}$ and $\hat{V}_{ee}$ in the Hamiltonian $\hat{H}^{(1)}$ of eq (60) have zero expectation on the ground-state of the harmonic oscillator, so that there is no contribution to this order to the large-λ expansion of $W_\lambda[\rho]$. As we shall see in the next section 7, the order $\sqrt{\lambda}\alpha = \lambda^{1/4}$ in $E_\lambda[\rho]$ of eq (61) corresponds to the order $\lambda^{-3/4}$ in the large-λ expansion of $W_\lambda[\rho]$.

Notice that, in our treatment of the strong-interaction limit of DFT, we did not consider the effect on the energy of the spin state or, more generally, of the statistics. This is because the electrons are always localized in different regions of space well separated from each other. The effect on the energy of the spin state or of statistics in the $\lambda \to \infty$ limit can be estimated as being of the order $O(e^{-\lambda^{1/4}})$, which is the order of magnitude of the overlap between two different gaussians of eq (67).

7. The Functional $W'_\infty[\rho]$

From the expansion of $E_\lambda[\rho]$ of the previous section 6, we can easily compute $W_\lambda[\rho]$ using the Hellmann−Feynmann theorem

$$W_\lambda[\rho] + U[\rho] = \frac{\partial E_\lambda[\rho]}{\partial \lambda} - \int \rho(\mathbf{r}) \frac{\partial v_{\text{ext}}^\lambda(\mathbf{r})}{\partial \lambda} d^3r \tag{78}$$

From section 6, we obtain, in the $\lambda \to \infty$ limit

$$E_\lambda[\rho] - \int \rho(\mathbf{r}) v_{\text{ext}}^\lambda(\mathbf{r}) d^3r = \lambda \langle \Psi_{\text{SCE}} | \hat{V}_{ee} | \Psi_{\text{SCE}} \rangle + \\ + \sqrt{\lambda} \int d^3s \frac{\rho(\mathbf{s})}{N} \sum_{\mu=4}^{3N} \frac{\omega_\mu(\mathbf{s})}{2} + O(\lambda^0) \tag{79}$$

By differentiating both sides with respect to λ, from eq (78) we obtain the expansion for $W_\lambda[\rho]$ of eq (13) with

$$W_\infty[\rho] = \int d^3s \frac{\rho(\mathbf{s})}{N} \sum_{i=1}^{N} \sum_{j>i}^{N} \frac{1}{|\mathbf{f}_i(\mathbf{s}) - \mathbf{f}_j(\mathbf{s})|} - U[\rho] \tag{80}$$

in agreement with the results of ref 33, and the exact expression for the next leading term

$$W'_\infty[\rho] = \frac{1}{2} \int d^3s \frac{\rho(\mathbf{s})}{N} \sum_{\mu=4}^{3N} \frac{\omega_\mu(\mathbf{s})}{2} \tag{81}$$

This result generalizes (and proves) eq (35) of ref 30 for spherical two-electron densities. As shown by eq (76), there is no $\lambda^{-3/4}$ term in $W_{\lambda\to\infty}[\rho]$. There is also no term $\propto \lambda^{-1}$, which would imply a term $\propto \log(\lambda)$ in $E_\lambda[\rho]$ and thus in the kinetic energy $\langle \Psi_\lambda | \hat{T} | \Psi_\lambda \rangle$. Such a term would violate the known high-density scaling of $\langle \Psi_\lambda | \hat{T} | \Psi_\lambda \rangle$[35] (see also the erratum).[36]

Table 1. Comparison of the Values $W'_\infty[\rho]$ in Hartree Atomic Units Obtained with the SCE Construction and with the PC Model[32a]

	SCE (H)	PC (H)	error (mH)
He	0.62084	0.729	108
Li	1.38	1.622	240
Be	2.59	2.928	334
B	4.2	4.702	502
C	6.3	7.089	840
Ne	22	24.423	2423

[a] The absolute errors of the PC model are also reported.

As an example of application, we have computed $W'_\infty[\rho]$ for the same set of spherical (or sphericalized) atomic densities used in ref 33 to evaluate $W_\infty[\rho]$. For each point $(\mathbf{f}_1(\mathbf{s}),..., \mathbf{f}_N(\mathbf{s}))$ on the degenerate SCE minimum constructed in ref 33, we have evaluated the Hessian matrix, the corresponding eigenvalues $\omega_\mu^2(\mathbf{s})$, and thus $W'_\infty[\rho]$ of eq (81). In Table 1 we compare our results with the approximate PC functional[32]

$$W'^{PC}_\infty[\rho] = \int d^3r \left[C\rho(\mathbf{r})^{3/2} + D \frac{|\nabla \rho(\mathbf{r})|^2}{\rho(\mathbf{r})^{7/6}} \right] \tag{82}$$

where $C = 1.535$ and $D = -0.02558$.

As explained in ref 33, the SCE minimum for spherical densities is constructed from a set of radial comotion functions and the angular minimization is done numerically. When one of the electrons is close to the nucleus, the numerical minimization displays instabilities in the smallest (but nonzero) eigenvalues of the Hessian. However, as shown by eq 81, such configurations are weighted by the density (in the spherically symmetric case by $4\pi s^2 \rho(s)$) so that the error they introduce is relatively small. This error, however, increases with the number of electrons. The number of digits in our results of Table 1 is determined by this numerical error. Notice, however, that Table 1 shows that the discrepancy of the PC model with respect to our results is much larger than our estimated numerical errors on the SCE values.

While the PC model for the coefficient $W_\infty[\rho]$ makes errors of the order of 60 mH,[33] we see from Table 1 that the functional $W'_\infty[\rho]$ is much more seriously overestimated. We can reduce these errors by recalling that in the PC model for $W'_\infty[\rho]$ the coefficient D of eq (82) was fixed by the condition that the PC value for the He atom be equal to the one obtained from the MGGA functional of ref 10. Now that we have exact values, it seems natural to change D in order to make the PC model equal to the SCE result for the He atom. This gives $D = -0.028957$. The values for the other atoms obtained with the revised PC model are reported in Table 2: we see that the error is now substantially reduced.

8. Revised ISI

In refs 22 and 32 an expression for $W_\lambda[\rho]$ that interpolates between the two limits of eqs (12) and (13) has been

Table 2. Comparison of the Values $W'_\infty[\rho]$ in Hartree Atomic Units Obtained with the SCE Construction and with the Revised PC Model of Section 7[a]

	SCE (H)	revPC (H)	error (mH)
Li	1.38	1.4066	26
Be	2.59	2.579	11
B	4.2	4.207	7
C	6.3	6.43	130
Ne	22	22.96	960

[a] The absolute errors of the revised PC model are also reported.

proposed and tested using the PC approximation for the functionals $W_\infty[\rho]$ and $W'_\infty[\rho]$. The interaction-strength interpolation (ISI) formula for $W_\lambda[\rho]$ of refs 22 and 32, however, contains a spurious term $\propto \lambda^{-1}$ in its $\lambda\rightarrow\infty$ expansion,[32] which, as explained after eq (81), has the wrong scaling behavior in the high-density limit. Here we propose a revised ISI functional which does not have this problem.

Instead of modeling $W_\lambda[\rho]$, we use the same ISI interpolation formula of ref 22 directly for the integral $E_{\rm xc}^\lambda[\rho]$

$$E_{\rm xc}^\lambda[\rho] = \int_0^\lambda d\lambda' W_{\lambda'}[\rho] \tag{83}$$

satisfying the exact $\lambda\rightarrow 0$ and $\lambda\rightarrow\infty$ asymptotic behaviors

$$E_{\rm xc}^{\lambda,{\rm revISI}}[\rho] = a[\rho]\lambda + \frac{b[\rho]\lambda}{\sqrt{1 + c[\rho]\lambda} + d[\rho]} \tag{84}$$

The four functionals $a[\rho]$, $b[\rho]$, $c[\rho]$, and $d[\rho]$ are determined by imposing the $\lambda\rightarrow 0$ expansion of eq (12) and the $\lambda\rightarrow\infty$ expansion of eq (13), and they are thus determined by the two weak-interaction limit functionals $E_x[\rho]$ and $E_c^{\rm GL2}[\rho]$ and the two strong-interaction limit functionals $W_\infty[\rho]$ and $W'_\infty[\rho]$

$$a[\rho] = W_\infty[\rho] \tag{85}$$

$$b[\rho] = -\frac{8E_c^{\rm GL2}[\rho]W'_\infty[\rho]^2}{(E_x[\rho] - W_\infty[\rho])^2} \tag{86}$$

$$c[\rho] = \frac{16E_c^{\rm GL2}[\rho]^2W'_\infty[\rho]^2}{(E_x[\rho] - W_\infty[\rho])^4} \tag{87}$$

$$d[\rho] = -1 - \frac{8E_c^{\rm GL2}[\rho]W'_\infty[\rho]^2}{(E_x[\rho] - W_\infty[\rho])^3} \tag{88}$$

The final formula for the revised ISI functional is obtained by putting $\lambda = 1$ in eq (84)

$$E_{\rm xc}^{\rm revISI}[\rho] = a[\rho] + \frac{b[\rho]}{\sqrt{1 + c[\rho]} + d[\rho]} \tag{89}$$

For the correlation energy of the neutral atoms considered here, this revised ISI gives essentially the same results of the original ISI of ref 22. This is probably due to the fact that neutral atoms are much more similar to the $\lambda = 0$ wave function than to the infinitely strongly interacting system (for an illustration from the pair-density point of view, see ref 37). We can expect to observe more sensitivity on how the $\lambda\rightarrow\infty$ limit is treated when studying more correlated systems, like stretched bonds or low-density quantum dots. Such studies will be the object of future work.

9. Conclusions and Perspectives

We have presented a systematic treatment of the strong-interaction limit of density functional theory up to the second leading term, describing zero-point oscillations of strictly correlated electrons. We have evaluated numerically this zero-point contribution for small atoms, and we have used our results to improve a previous approximate functional for this term. A new interpolation formula for the exchange-correlation energy, satisfying more exact constraints, has been proposed, and will be tested elsewhere.

Besides the possibility of constructing an interpolation formula for $E_{\rm xc}[\rho]$, the two functionals $W_\infty[\rho]$ of ref 33 and $W'_\infty[\rho]$ evaluated in this work, are of valuable interest for the development of Kohn−Sham DFT. They are an example of exact implicit density functionals for systems in which the electron−electron repulsion largely dominates over the kinetic energy. They can be used to test properties of the exact exchange-correlation functional like the Lieb-Oxford bound[38,39] and to test how approximate functionals perform in this limit.[40,41]

Several issues still need to be addressed and will be the object of future work. The main problem of the ISI functional is the lack of size consistency. A possible remedy is to perform the interpolation of eq (84) locally, using energy densities all defined in the same gauge (this is, at least, the standard way in which approximate DFT addresses size consistency, even if it is not always a solution in the presence of degeneracy).[42,43] A first step in our future work, thus, will be the analysis of exact energy densities for the functionals $W_\infty[\rho]$ and $W_\infty'[\rho]$ (see also ref 37) and the construction of corresponding approximations. Another important problem is the development of a reliable algorithm to solve the SCE problem for a given nonspherical density. Other promising research lines are the study of the next leading term, which is of purely kinetic origin, and the construction of approximations to describe the effect of the spin state on the energy.

Acknowledgment. We thank Mel Levy, Kieron Burke, and Andreas Savin for stimulating discussions. P.G.-G. was supported by ANR (07-BLAN-0272), and G.V. was supported by DOE under Grant No. DE-FG02-05ER46203.

A. Transformation of the Laplacian

In order to write down the components of the metric tensor G_{ik} of our local curvilinear coordinate transformation, we define the indices as follows: α, β, γ,.. denote the Cartesian components 1, 2, 3 $\equiv x, y, z$ of $\mathbf{s}$, the indices μ, ν, σ, τ,... denote the normal-mode components q_μ, and the Latin indices i, k,... denote general components, either α,.. or μ,.... We then have to distinguish three blocks in the metric tensor G_{ik}: $\alpha\beta$, $\mu\nu$, and $\alpha\mu$

$$G_{\beta\gamma} = g_{\beta\gamma}(\mathbf{s}) - 2\sum_{\mu=4}^{3N} q_\mu \frac{\partial^2 \underline{f}(\mathbf{s})}{\partial s_\gamma \partial s_\beta} \cdot \underline{e}^\mu(\mathbf{s}) + \sum_{\mu,\nu=4}^{3N} \frac{\partial \underline{e}^\mu(\mathbf{s})}{\partial s_\beta} \cdot \frac{\partial \underline{e}^\nu(\mathbf{s})}{\partial s_\gamma} q_\mu q_\nu \quad (90)$$

$$G_{\beta\nu} = \sum_{\mu=4}^{3N} q_\mu \frac{\partial \underline{e}^\mu(\mathbf{s})}{\partial s_\beta} \cdot \underline{e}^\nu(\mathbf{s}) \quad (91)$$

$$G_{\mu\nu} = \delta_{\mu\nu} \quad (92)$$

where in eq (90) we have defined the 3×3 metric tensor $g_{\alpha\beta}(\mathbf{s})$ which only concerns the coordinates s_1, s_2, and s_3

$$g_{\alpha\beta}(\mathbf{s}) = \frac{\partial \underline{f}(\mathbf{s})}{\partial s_\alpha} \cdot \frac{\partial \underline{f}(\mathbf{s})}{\partial s_\beta} \quad (93)$$

When $\lambda \to \infty$, our wave function is zero everywhere except very close to Ω_0, i.e., for very small $q_\mu \propto \lambda^{-1/4}$. Introducing the scaled coordinates $u_\mu = \lambda^{1/4} q_\mu$, we see that the metric tensor G_{ik} has the λ-dependence

$$G_{ik} = G_{ik}^{(0)} + \frac{1}{\lambda^{1/4}} \sum_{\mu=4}^{3N} u_\mu \Delta_{ik}^\mu + \frac{1}{\lambda^{1/2}} \sum_{\mu,\nu=4}^{3N} u_\mu u_\nu Z_{ik}^{\mu\nu} \quad (94)$$

where Δ^μ and $Z^{\mu\nu}$ are tensors of elements

$$\Delta_{\gamma\beta}^\mu = -2 \frac{\partial^2 \underline{f}(\mathbf{s})}{\partial s_\gamma \partial s_\beta} \cdot \underline{e}^\mu(\mathbf{s}) \quad (95)$$

$$\Delta_{\beta\nu}^\mu = \frac{\partial \underline{e}^\mu(\mathbf{s})}{\partial s_\beta} \cdot \underline{e}^\nu(\mathbf{s}) \quad (96)$$

$$\Delta_{\nu\tau}^\mu = 0 \quad (97)$$

and

$$Z_{\beta\gamma}^{\mu\nu} = \frac{\partial \underline{e}^\mu(\mathbf{s})}{\partial s_\beta} \cdot \frac{\partial \underline{e}^\nu(\mathbf{s})}{\partial s_\gamma} \quad (98)$$

$$Z_{\beta\tau}^{\mu\nu} = 0 \quad (99)$$

$$Z_{\tau\sigma}^{\mu\nu} = 0 \quad (100)$$

and $G_{ik}^{(0)}$ has elements $G_{\alpha\beta}^{(0)} = g_{\alpha\beta}$ and $G_{\mu\nu}^{(0)} = \delta_{\mu\nu}$ and all the off-diagonal components equal to zero. In order to compute the large-λ expansion of eq (45), we have to expand the determinant G, and the components G^{ik} of the inverse metric tensor. Using standard formulas, we obtain

$$\sqrt{G} = \sqrt{g}\left(1 + \frac{1}{2\lambda^{1/4}} \sum_{\mu=4}^{3N} u_\mu \sum_{\alpha\beta} g^{\alpha\beta} \Delta_{\alpha\beta}^\mu\right) + O(\lambda^{-1/2}) \quad (101)$$

where g is the determinant of $g_{\alpha\beta}$, and $g^{\alpha\beta}$ are the components of its inverse. The tensor $\mathbf{G}^{-1}$ of components G^{ik} has the large-λ expansion, up to orders $\lambda^{-1/2}$

$$\mathbf{G}^{-1} = \mathbf{G}^{(0)^{-1}} - \frac{1}{\lambda^{1/4}} \sum_{\mu=4}^{3N} u_\mu \mathbf{G}^{(0)-1} \Delta^\mu \mathbf{G}^{(0)^{-1}} \quad (102)$$

Inserting these expansions into eq (45) we obtain eqs (48) and (49) with

$$X^\mu(\mathbf{s}) = \frac{1}{2} \sum_{\alpha\beta} g^{\alpha\beta}(\mathbf{s}) \Delta_{\alpha\beta}^\mu(\mathbf{s}) \quad (103)$$

Finally, the Jacobian of our change of coordinates is simply equal to $\sqrt{G}$ of eq (101).

B. Analytic Example

As an illustration, we consider a system of two electrons in 1D space (i.e., on the x-axis) with a given ground-state density $\rho(x)$

$$\int_{-\infty}^{\infty} dx \rho(x) = 2 \quad (104)$$

In this case, eq (17) reads $x_2 = f_2(x_1)$, with the single comotion function $f_2(s) \equiv f(s)$ which, according to ref 33, obeys the differential equation $\rho(f(s))f'(s) = \rho(s)$. For the Lorentzian density, $f(s)$ is found analytically

$$\rho(x) = \frac{2}{\pi} \frac{1}{1 + x^2} \Rightarrow f(s) = -\frac{1}{s} \quad (105)$$

In this case, the SCE external potential, fixed by the conditions $(d/dx)v_{\mathrm{SCE}}(x) = \mathrm{sgn}(x)|x - f(x)|^{-2}$ and $v_{\mathrm{SCE}}(x) \to 0$ for $x \to \pm\infty$, is given by

$$v_{\mathrm{SCE}}(x) = \left|\arctan(x) - \frac{x}{1 + x^2}\right| - \frac{\pi}{2} \quad (106)$$

In terms of $\underline{f}(s) \equiv (s, f(s))$, eq 20 now yields a 1D subset of $\Omega = \mathbb{R}^2$

$$\Omega_0 = \{\underline{f}(s) | s \in \mathbb{R}\} \subset \Omega \quad (107)$$

In the example (105), Ω_0 is given by the two branches of the hyperbola $x_2 = f(x_1) \equiv -1/x_1$ in the x_1x_2-plane Ω. In the following, we focus on the branch Ω_0^+ with $x_1 > 0$ and $x_2 < 0$, $\Omega_0^+ = \{\underline{f}(s) | s \in \mathbb{R}^+\}$.

The asymptotic potential-energy function, cf. eq (19)

$$E_{\mathrm{pot}}(\underline{x}) = \frac{1}{x_1 - x_2} + v_{\mathrm{SCE}}(x_1) + v_{\mathrm{SCE}}(x_2) \quad (108)$$

assumes its highly degenerate minimum for all $\underline{x} \in \Omega_0$. Consequently, the first partial derivatives

$$\frac{\partial E_{\text{pot}}(\underline{x})}{\partial x_1} = -\frac{1}{(x_1 - x_2)^2} + \frac{x_1^2}{(1 + x_1^2)^2}$$
$$\frac{\partial E_{\text{pot}}(\underline{x})}{\partial x_2} = +\frac{1}{(x_1 - x_2)^2} - \frac{x_2^2}{(1 + x_2^2)^2} \quad (109)$$

are vanishing for $\underline{x} = \underline{f}(s)$ when the Hessian matrix of $E_{\text{pot}}(\underline{x})$ becomes

$$M(s) = \frac{2s}{(1 + s^2)^3}\begin{pmatrix} 1 & -s^2 \\ -s^2 & s^4 \end{pmatrix} \quad (110)$$

It has the two eigenvalues

$$\omega_1(s)^2 = 0, \quad \omega_2(s)^2 = \frac{2s}{(1 + s^2)^3}(1 + s^4) > 0 \quad (111)$$

The corresponding normalized eigenvectors are

$$\underline{e}^1(s) = \frac{1}{\sqrt{1 + s^4}}\begin{pmatrix} s^2 \\ 1 \end{pmatrix}, \quad \underline{e}^2(s) = \frac{1}{\sqrt{1 + s^4}}\begin{pmatrix} 1 \\ -s^2 \end{pmatrix} \quad (112)$$

While $e^1(s)$ is tangential, $\underline{e}^2(s)$ is orthogonal to Ω_0^+ at $\underline{f}(s) \in \Omega_0^+$ and generally given by

$$\underline{e}^2(s) = \frac{1}{\sqrt{1 + f'(s)^2}}\begin{pmatrix} f'(s) \\ -1 \end{pmatrix} \equiv \underline{e}(s) \quad (113)$$

For a point $\underline{x} = (x_1, x_2) \in \Omega_\varepsilon$, close to Ω_0^+, the curvilinear coordinates (s, q) are defined by eq (30)

$$\underline{x} = \underline{f}(s) + \underline{e}(s)q \quad (114)$$

where s is fixed by the condition that the vector $\underline{e}(s)$ in the x_1x_2-plane is orthogonal to Ω_0^+ at $\underline{f}(s) \in \Omega_0^+$.

In terms of the partial derivatives of eq (114), the metric tensor is given by the (2×2)-matrix

$$(G_{\mu\nu}) = \begin{pmatrix} \frac{\partial \underline{x}}{\partial s} \cdot \frac{\partial \underline{x}}{\partial s} & \frac{\partial \underline{x}}{\partial s} \cdot \frac{\partial \underline{x}}{\partial q} \\ \frac{\partial \underline{x}}{\partial q} \cdot \frac{\partial \underline{x}}{\partial s} & \frac{\partial \underline{x}}{\partial q} \cdot \frac{\partial \underline{x}}{\partial q} \end{pmatrix} \quad (115)$$

Using eqs (113) and (114), we obtain

$$\frac{\partial \underline{x}}{\partial s} = \underline{f}'(s) + q\underline{e}'(s)$$
$$= \begin{pmatrix} 1 \\ f'(s) \end{pmatrix}\left[1 + q\frac{f''(s)}{[1 + f'(s)^2]^{3/2}}\right]$$
$$\frac{\partial \underline{x}}{\partial q} = \underline{e}(s) \quad (116)$$

and thus

$$(G_{\mu\nu}) = \begin{pmatrix} g(s,q) & 0 \\ 0 & 1 \end{pmatrix} \quad (117)$$

where $g(s, q) = J(s, q)^2$, with the Jacobian

$$J(s,q) = \left[1 + q\frac{f''(s)}{[1 + f'(s)^2]^{3/2}}\right]\sqrt{1 + f'(s)^2} \quad (118)$$

In the particular case of the density (105), we have

$$J(s,q) = \frac{\sqrt{1 + s^4}}{s^2} - q\frac{2s}{1 + s^4} \quad (119)$$

and the coefficients of eq (13) are given by

$$W_\infty[\rho] + U[\rho] \equiv 2\int_0^\infty ds \frac{\rho(s)}{2}\frac{1}{s - f(s)} = \frac{1}{\pi}\int_0^\infty \frac{ds 2s}{(1 + s^2)^2} = \frac{1}{\pi} = 0.31831 \quad (120)$$

$$W'_\infty[\rho] \equiv 2\int_0^\infty ds \frac{\rho(s)}{2}\omega_2(s) = \frac{2}{\pi}\int_0^\infty \frac{ds}{(1 + s^2)^2}\sqrt{2s\frac{1 + s^4}{1 + s^2}} = 0.633902 \quad (121)$$

References

(1) Hohenberg, P.; Kohn, W. *Phys. Rev.* **1964**, *136*, B 864.

(2) Kohn, W.; Sham, L. J. *Phys. Rev. A* **1965**, *140*, 1133.

(3) Kohn, W. *Rev. Mod. Phys.* **1999**, *71*, 1253.

(4) Levy, M. *Proc. Natl. Acad. Sci. U.S.A.* **1979**, *76*, 6062.

(5) Perdew, J. P. In *Electronic Structure of Solids, 91*; Ziesche, P., Eschrig, H., Eds.; Akademie Verlag: Berlin, 1991.

(6) Perdew, J. P.; Chevary, J. A.; Vosko, S. H.; Jackson, K. A.; Pederson, M. R.; Singh, D. J.; Fiolhais, C. *Phys. Rev. B* **1992**, *46*, 6671.

(7) Perdew, J. P.; Burke, K.; Ernzerhof, M. *Phys. Rev. Lett.* **1996**, *77*, 3865.

(8) Mattsson, A. E. *Science* **2002**, *298*, 759.

(9) Perdew, J. P.; Ruzsinszky, A.; Tao, J.; Staroverov, V. N.; Scuseria, G. E.; Csonka, G. I. *J. Chem. Phys.* **2005**, *123*, 062201.

(10) Perdew, J. P.; Kurth, S.; Zupan, A.; Blaha, P. *Phys. Rev. Lett.* **1999**, *82*, 2544.

(11) Tao, J.; Perdew, J. P.; Staroverov, V. N.; Scuseria, G. E. *Phys. Rev. Lett.* **2003**, *91*, 146401.

(12) Becke, A. D. *J. Chem. Phys.* **1993**, *98*, 1372.

(13) Becke, A. D. *J. Chem. Phys.* **1993**, *98*, 5648.

(14) Iikura, H.; Tsuneda, T.; Yanai, T.; Hirao, K. *J. Chem. Phys.* **2001**, *115*, 3540.

(15) Heyd, J.; Scuseria, G. E.; Ernzerhof, M. *J. Chem. Phys.* **2003**, *118*, 8207.

(16) Vydrov, O. A.; Heyd, J.; Krukau, A. V.; Scuseria, G. E. *J. Chem. Phys.* **2006**, *125*, 074106.

(17) Vydrov, O. A.; Scuseria, G. E. *J. Chem. Phys.* **2006**, *125*, 234109.

(18) Henderson, T. M.; Izmaylov, A. F.; Scuseria, G. E.; Savin, A. *J. Chem. Phys.* **2007**, *127*, 221103.

(19) Perdew, J. P.; Schmidt, K. In *Density Functional Theory and Its Application to Materials*; Van Doren, V. et al., Eds.; AIP Press: Melville, NY, 2001.

(20) Kümmel, S.; Kronik, L. *Rev. Mod. Phys.* **2008**, *80*, 3.

(21) Perdew, J. P.; Ruzsinszky, A.; Csonka, G. I.; Vydrov, O. A.; Scuseria, G. E.; Staroverov, V. N.; Tao, J. *Phys. Rev. A* **2007**, *76*, 040501.

(22) Seidl, M.; Perdew, J. P.; Kurth, S. *Phys. Rev. Lett.* **2000**, *84*, 5070.

(23) Harris, J.; Jones, R. *J. Phys. F* **1974**, *4*, 1170.

(24) Langreth, D. C.; Perdew, J. P. *Solid State Commun.* **1975**, *17*, 1425.

(25) Gunnarsson, O.; Lundqvist, B. I. *Phys. Rev. B* **1976**, *13*, 4274.

(26) Görling, A.; Levy, M. *Phys. Rev. A* **1994**, *50*, 196.

(27) Olsen, J.; Christiansen, O.; Koch, H.; Jorgensen, P. *J. Chem. Phys.* **1996**, *105*, 5082.

(28) Ernzerhof, M. *Chem. Phys. Lett.* **1996**, *263*, 499.

(29) Burke, K.; Ernzerhof, M.; Perdew, J. P. *Chem. Phys. Lett.* **1997**, *265*, 115.

(30) Seidl, M. *Phys. Rev. A* **1999**, *60*, 4387.

(31) Seidl, M.; Perdew, J. P.; Levy, M. *Phys. Rev. A* **1999**, *59*, 51.

(32) Seidl, M.; Perdew, J. P.; Kurth, S. *Phys. Rev. A* **2000**, *62*, 012502.

(33) Seidl, M.; Gori-Giorgi, P.; Savin, A. *Phys. Rev. A* **2007**, *75*, 042511.

(34) Liu, B. Ph. D. Thesis, New York University, 2006.

(35) Levy, M.; Perdew, J. P. *Phys. Rev. A* **1985**, *32*, 2010.

(36) Seidl, M.; Perdew, J. P.; Kurth, S. *Phys. Rev. A* **2005**, *72*, 029904(E) .

(37) Gori-Giorgi, P.; Seidl, M.; Savin, A. *Phys. Chem. Chem. Phys.* **2008**, *10*, 3440.

(38) Lieb, E. H.; Oxford, S. *Int. J. Quantum Chem.* **1981**, *19*, 427.

(39) Chan, G. K.-L.; Handy, N. C. *Phys. Rev. A* **1999**, *59*, 3075.

(40) Staroverov, V. N.; Scuseria, G. E.; Tao, J.; Perdew, J. P. *Phys. Rev. B* **2004**, *69*, 075102.

(41) Jung, J.; Garcia-Gonzalez, P.; Alvarellos, J. E.; Godby, R. W. *Phys. Rev. A* **2004**, *69*, 052501.

(42) Gori-Giorgi, P.; Savin, A. *J. Phys.: Conf. Ser.* **2008**, *117*, 012017.

(43) Savin, A. *Chem. Phys*. **2009**, *356*, 91.

CT8005248

JCTC Journal of Chemical Theory and Computation

Long-Range-Corrected Hybrids Based on a New Model Exchange Hole

Elon Weintraub,† Thomas M. Henderson,* and Gustavo E. Scuseria

Department of Chemistry, Rice University, 6100 Main Street, Houston, Texas 77005-1892

Received December 3, 2008

Abstract: By admixing a fraction of exact Hartree−Fock-type exchange with conventional semilocal functionals, global hybrids greatly improve the accuracy of Kohn−Sham density functional theory. However, because global hybrids exhibit incorrect asymptotic decay of the exchange-correlation potential, they can have large errors for diverse quantities such as reaction barrier heights, nonlinear optical properties, and Rydberg and charge-transfer excitation energies. These errors can be removed by using a long-range-corrected hybrid, which uses exact exchange in the long range. Evaluating the long-range-corrected exchange energy requires a model for the semilocal exchange hole, and such models are scarce. Recently, two of us introduced one such model (*J. Chem. Phys.* **2008**, *128*, 194105). This model obeys several exact constraints and was designed specifically for use in long-range-corrected hybrids. Here, we give sample results for three long-range-corrected hybrids based upon our exchange hole model and show how the model can easily be applied to any generalized gradient approximation (GGA) for the exchange energy to create a long-range-corrected GGA.

1. Introduction

Due to its remarkable combination of accuracy and computational simplicity, Kohn−Sham (KS) density functional theory (DFT)[1,2] has become the predominant method in electronic structure calculations for molecules and solids.[3] The key ingredient in KS-DFT is the exchange-correlation functional, which accounts for many-body effects in a simple single-particle picture. Unfortunately, while many properties of the exact exchange-correlation functional are known, and (through the constrained search formalism)[4,5] even the precise form is available, a computationally tractable form is not.

Simple semilocal functionals, in which the exchange-correlation energy density at a point $\boldsymbol{r}$ depends only the density, its derivatives, and possibly the KS orbitals and their derivatives at $\boldsymbol{r}$, have been reasonably successful. The simplest (semi)local functional is the local density approximation (LDA), which takes the exchange-correlation energy density at a point with density n to be the exchange-correlation energy density of a homogeneous electron gas (HEG) with density n. More sophisticated generalized gradient approximations[6−10] (GGAs) and meta-GGAs[11−14] improve upon this basic form by adding information about the local density gradient (GGAs) and the local kinetic energy density or local density laplacian (meta-GGAs).

To reach the accuracy expected in molecular calculations, however, it is generally necessary to incorporate some fraction of nonlocal Hartree−Fock-type exchange. Usually, this is done by means of a global hybrid functional,[15−19] in which the exchange-correlation energy is written as

$$E_{\mathrm{xc}}^{\mathrm{GH}} = E_{\mathrm{xc}}^{\mathrm{DFA}} + c\left(E_{\mathrm{x}}^{\mathrm{HF}} - E_{\mathrm{x}}^{\mathrm{DFA}}\right) \tag{1}$$

Here, $E_{\mathrm{xc}}^{\mathrm{DFA}}$, $E_{\mathrm{x}}^{\mathrm{DFA}}$, and $E_{\mathrm{x}}^{\mathrm{HF}}$ are respectively some semilocal density functional approximation (DFA) to the exchange-correlation energy, a semilocal approximation to the exchange energy, and nonlocal Hartree−Fock (HF) exchange. The constant c controls the fraction of exact exchange included and usually varies between about 1/5 and 1/2. But while the simple global hybrid form is the most commonly used way of including some amount of HF-type exchange, much progress has been made over the past decade in

* Corresponding author e-mail: Thomas.Henderson@rice.edu.
† Permanent address: Rutgers University, New Brunswick, NJ 08901.

10.1021/ct800530u CCC: $40.75
Published on Web 03/20/2009

functionals with more flexible admixtures. One promising route is to use a range-separated fraction of exact exchange.[20−22] (Note that these works propose also to use a range-separated fraction of wave function correlation, which we here prefer to avoid.)

In a range-separated hybrid, the interelectronic Coulomb operator is generally decomposed into a long-range (LR) and a short-range (SR) part, typically as

$$\frac{1}{r_{12}} = \underbrace{\frac{\mathrm{erfc}(\omega r_{12})}{r_{12}}}_{\mathrm{SR}} + \underbrace{\frac{\mathrm{erf}(\omega r_{12})}{r_{12}}}_{\mathrm{LR}} \tag{2}$$

Different fractions of exact exchange are used in the two ranges. That is, the exchange-correlation energy of a range-separated hybrid can be written as

$$E_{\mathrm{xc}}^{\mathrm{RSH}} = E_{\mathrm{xc}}^{\mathrm{DFA}} + c_{\mathrm{SR}}(E_{\mathrm{x}}^{\mathrm{SR\text{-}HF}} - E_{\mathrm{x}}^{\mathrm{SR\text{-}DFA}}) + c_{\mathrm{LR}}(E_{\mathrm{x}}^{\mathrm{LR\text{-}HF}} - E_{\mathrm{x}}^{\mathrm{LR\text{-}DFA}}) \tag{3}$$

For applications to solids, in which the long-range HF-type exchange is both computationally and formally problematic,[23] we use a screened exchange which sets $c_{\mathrm{LR}} = 0$.[24−27] In finite systems, long-range HF-type exchange is the exact long-range exchange-correlation functional, unless long-range correlations (such as might be found, for instance, in dissociation on the symmetry-restricted surface) are present. It is therefore common in finite systems to set $c_{\mathrm{LR}} = 1$ and $c_{\mathrm{SR}} = 0$.[28−33] Functionals which use 100% long-range HF-type exchange are termed long-range-corrected hybrids. Long-range-corrected hybrids dramatically improve upon global hybrids in the description of charge transfer and Rydberg excitations,[29,34] nonlinear optical properties,[28,35] reaction barrier heights,[30−32] and so on. The two limits of screened and long-range-corrected functionals can be reconciled by using exact exchange in the *middle* range, as in the recently proposed functional of Henderson et al.[36,37]

To define the long-range or short-range semilocal exchange energy, we require a semilocal model for the exchange hole. While many semilocal functionals are constructed from such a model, many others are not. Most range-separated hybrids of GGAs have used one of two models: the LDA-based model of Iikura and co-workers[28] (ITYH) or the model of Ernzerhof and Perdew[38] (EP). The ITYH model is quite flexible and can readily be applied to any GGA or meta-GGA. The EP model was parametrized to reproduce the GGA of Perdew et al.[9] (PBE), and while it could be reparameterized to fit other GGAs, this has not, to the best of our knowledge, been done.

Recently, two of us proposed a new GGA model, based on that of EP, but constructed specifically for use in range-separated hybrids.[39] This new exchange hole model (here denoted HJS) follows the EP model in satisfying more exact constraints than does the model of ITYH, but differs from the EP model in that the range-separated exchange energy density can be evaluated analytically.

In this work, we examine the performance of three long-range-corrected hybrid functionals based on our newer exchange hole model. Let us be clear at the outset that our intention is not to provide a thorough benchmarking of new long-range-corrected hybrids. Rather, it is to show how, by modifying a few parameters in the HJS hole model, one can construct long-range-corrected hybrids of various GGAs, affording much (but not all) of the flexibility inherent in the approach of ITYH while avoiding some of its weaknesses (see ref 39).

Section 2 of this paper briefly describes the HJS model exchange hole, while in section 3 we remind the reader of the form of the exchange functionals considered here. Section 4 presents the results of long-range-corrected hybrids based on those GGAs, and general conclusions are drawn in section 5. Appendix A provides a numerically stable expression for the short-range exchange energy coming from the HJS model exchange hole.

2. HJS Model Exchange Hole

The HJS model exchange hole is given by

$$\mathscr{T}(s,y) = \left[\left(\frac{9}{4}\frac{\mathscr{A}}{y^2} + \mathscr{B} + \mathscr{C}\mathscr{F}(s)y^2 + \mathscr{E}\mathscr{G}(s)y^4\right)\mathrm{e}^{-\mathscr{D}y^2} - \frac{9}{4y^4}(1 - \mathrm{e}^{-\mathscr{A}y^2})\right]\mathrm{e}^{-s^2\mathscr{H}(s)y^2} \tag{4}$$

where

$$y = k_{\mathrm{F}} r_{12} \tag{5a}$$

$$s = \frac{|\nabla n|}{2k_{\mathrm{F}} n} \tag{5b}$$

$$k_{\mathrm{F}} = (3\pi^2 n)^{1/3} \tag{5c}$$

The exchange hole for σ-spin electrons can readily be obtained by replacing the total density n with the density of σ-spin electrons n_σ, and writing $k_{\mathrm{F},\sigma} = (6\pi^2 n_\sigma)^{1/3}$.

The parameters $\mathscr{A}$, $\mathscr{B}$, $\mathscr{C}$, $\mathscr{D}$, and $\mathscr{E}$ are chosen so that, at $s = 0$, the HJS model exchange hole reduces to a nonoscillating approximation to the LDA exchange hole, with proper value and curvature at $y = 0$, proper energy and normalization, and minimal oscillation. Numerical values to six digits are $\mathscr{A} = 0.757211$, $\mathscr{B} = -0.106364$, $\mathscr{C} = -0.118649$, $\mathscr{D} = 0.609650$, and $\mathscr{E} = -0.0477963$. (Note that $\mathscr{B}$, $\mathscr{C}$, and $\mathscr{E}$ are defined in terms of $\mathscr{A}$ and $\mathscr{D}$, and so are defined to more decimal places; see ref 39 for the equations relating the various parameters.)

The function $\mathscr{G}(s)$ is chosen to enforce normalization for nonzero gradients, while $\mathscr{F}(s)$ enforces proper curvature at $y = 0$ for small gradients, and is restricted such that it remains bounded. These functions take the form

$$\mathscr{F}(s) = 1 - \frac{1}{27\mathscr{C}}\frac{s^2}{1 + s^2/s_0^2} - \frac{1}{2\mathscr{C}}s^2\mathscr{H}(s) \tag{6a}$$

$$\mathscr{E}\mathscr{G}(s) = -\frac{2}{5}\mathscr{C}\mathscr{F}(s)\lambda - \frac{4}{15}\mathscr{B}\lambda^2 - \frac{6}{5}\mathscr{A}\lambda^3 - \frac{4}{5}\sqrt{\pi}\lambda^{7/2} - \frac{12}{5}\lambda^{7/2}(\sqrt{\zeta} - \sqrt{\eta}) \tag{6b}$$

where $s_0 = 2$, and where we have defined

$$\zeta = s^2\mathscr{H}(s) \tag{7a}$$

$$\eta = \mathscr{A} + s^2\mathscr{H}(s) = \mathscr{A} + \zeta \tag{7b}$$

$$\lambda = \mathscr{D} + s^2\mathscr{H}(s) = \mathscr{D} + \zeta \tag{7c}$$

Finally, the function $\mathscr{H}(s)$ is chosen so that the HJS model exchange hole gives the desired exchange energy. The ratio of the GGA exchange energy density to the LDA exchange energy density is termed the enhancement factor:

$$F_x = \frac{\epsilon_x^{GGA}}{\epsilon_x^{LDA}} \tag{8}$$

For a GGA, F_x depends only the reduced gradient s. In terms of the model exchange hole, it is given by

$$F_x(s) = -\frac{8}{9}\int_0^\infty dy\, y\mathscr{T}(s,y) \tag{9a}$$

$$= \mathscr{A} - \frac{4}{9}\frac{\mathscr{B}}{\lambda} - \frac{4}{9}\frac{\mathscr{C}\mathscr{T}(s)}{\lambda^2} - \frac{8}{9}\frac{\mathscr{E}\mathscr{G}(s)}{\lambda^3} + \zeta\ln\left(\frac{\zeta}{\lambda}\right) - \eta\ln\left(\frac{\eta}{\lambda}\right) \tag{9b}$$

Given a GGA (and thus an enhancement factor), we solve the foregoing equation numerically for $\mathscr{H}(s)$ over a range of values of s and fit the resulting curve to

$$\mathscr{H}(s) = (a_2s^2 + a_3s^3 + a_4s^4 + a_5s^5 + a_6s^6 + a_7s^7)/(1 + b_1s + b_2s^2 + b_3s^3 + b_4s^4 + b_5s^5 + b_6s^6 + b_7s^7 + b_8s^8 + b_9s^9) \tag{10}$$

constraining this rational function to have the correct small s and large s expansion when possible. [Usually, this means fixing a_2 to give the second-order gradient expansion coefficient from the target enhancement factor, setting $a_3 = a_2b_1$ to eliminate the third-order gradient expansion coefficient, and writing $a_7 = ab_9$, $a_6 = ab_8$, and $a_5 = ab_7 + bb_9$, where a is chosen so that the $s\rightarrow\infty$ limit of the enhancement factor is the correct constant, and b is chosen so that the next term in the asymptotic expansion of $F_x(s)$ is also correct.]

Once we have defined $\mathscr{H}(s)$, we use our model exchange hole to define the range-separated enhancement factor. Most commonly, we use

$$V_{ee}^{SR} = \frac{\mathrm{erfc}(\omega r_{12})}{r_{12}} \tag{11}$$

in which case the range-separated enhancement factor is given by

$$F_x^{SR}(s,\nu) = -\frac{8}{9}\int_0^\infty dy\, y^2\frac{\mathrm{erfc}(\nu y)}{y}\mathscr{T}(s,y) \tag{12}$$

where $\nu = \omega/k_F$. This integral can be evaluated explicitly, and the result is

$$F_x^{SR}(s,\nu) = \mathscr{A} - \frac{4}{9}\frac{\mathscr{B}}{\lambda}(1-\chi) - \frac{4}{9}\frac{\mathscr{C}\mathscr{T}(s)}{\lambda^2}\left(1 - \frac{3}{2}\chi + \frac{1}{2}\chi^3\right) - \frac{8}{9}\frac{\mathscr{E}\mathscr{G}(s)}{\lambda^3}\left(1 - \frac{15}{8}\chi + \frac{5}{4}\chi^3 - \frac{3}{8}\chi^5\right) + 2\nu\left(\sqrt{\zeta+\nu^2} - \sqrt{\eta+\nu^2}\right) + 2\zeta\ln\left(\frac{\nu+\sqrt{\zeta+\nu^2}}{\nu+\sqrt{\lambda+\nu^2}}\right) - 2\eta\ln\left(\frac{\nu+\sqrt{\eta+\nu^2}}{\nu+\sqrt{\lambda+\nu^2}}\right) \tag{13}$$

where

$$\chi = \frac{\nu}{\sqrt{\lambda+\nu^2}} \tag{14}$$

Evaluating this expression for large ν is fraught with numerical problems; see Appendix A for an analytic simplification which allows more robust evaluation of the enhancement factor.

3. Three Prototype Exchange Functionals

We do not wish here to provide an exhaustive survey of long-range-corrected hybrids based on various combinations of semilocal exchange and semilocal correlation functionals. Instead, we wish to consider three functionals in particular: the PBE GGA of Perdew, Burke, and Ernzerhof,[9] the PBEsol functional of Perdew and co-workers,[10] and the BLYP combination of Becke's 1988 exchange functional[6] and the correlation functional of Lee, Yang, and Parr.[7] While PBE provides a reasonably balanced description of finite systems and solids, PBEsol is geared principally for applications to solids, and BLYP is more successful for atoms and molecules. The three functionals thus provide prototype cases for us. The parameters defining $\mathscr{H}(s)$ for each are listed in Table 1. Note that we show the coefficients of powers of $s_\sigma = |\nabla n_\sigma|/(2(6\pi^2)^{1/3}n_\sigma^{4/3})$.

3.1. PBE and PBEsol. The PBE exchange enhancement factor can be written as

$$F_x^{PBE} = 1 + \kappa\frac{\mu s^2}{\kappa + \mu s^2} \tag{15}$$

where $\kappa = 0.804$ enforces the local Lieb−Oxford bound, and $\mu \approx 0.2195$ controls the small gradient behavior, which for the foregoing functional form is

$$F_x^{PBE} = 1 + \mu s^2 + ... \tag{16}$$

The exact small gradient expansion turns out to be[40]

$$F_x = 1 + \frac{10}{81}s^2 + ... \approx 1 + 0.1235s^2 + ... \tag{17}$$

so PBE responds too strongly to small fluctuations in the density. This is intentional—the gradient expansion of the PBE *correlation* functional is correct, and the exact gradient response of the PBE exchange functional is sacrificed so that the linear response of the PBE exchange-correlation functional is the same as that of the LSDA.

Unfortunately, the overly large value of the second-order gradient coefficient in F_x causes problems in solids, in which

Table 1. Parameters in the Rational Functions Defining $H(s)$ for Various GGAs

	PBE	PBEsol	B88
a_2	0.015 9941	0.004 7333	0.025 3933
a_3	0.085 2995	0.040 3304	−0.067 3075
a_4	−0.160 368	−0.057 4615	0.089 1476
a_5	0.152 645	0.043 5395	−0.045 4168
a_6	−0.097 1263	−0.021 6251	−0.007 6581
a_7	0.042 2061	0.006 3721	0.014 2506
b_1	5.333 19	8.520 56	−2.650 60
b_2	−12.478 0	−13.988 5	3.911 08
b_3	11.098 8	9.285 83	−3.315 09
b_4	−5.110 13	−3.272 87	1.544 85
b_5	1.714 68	0.843 499	−0.198 386
b_6	−0.610 380	−0.235 543	−0.136 112
b_7	0.307 555	0.084 7074	0.064 7862
b_8	−0.077 0547	−0.017 1561	0.015 9586
b_9	0.033 4840	0.005 0552	$-2.450\,66 \times 10^{-4}$

for many properties, PBE offers little improvement over LDA. To remedy this, PBEsol takes the PBE form, but enforces the exact gradient expansion for exchange instead of for correlation. Accordingly, the PBEsol exchange enhancement factor is

$$F_{\mathrm{x}}^{\mathrm{PBEsol}} = 1 + \kappa\frac{\bar{\mu}s^2}{\kappa + \bar{\mu}s^2} \tag{18}$$

with $\bar{\mu} = 10/81$. The corresponding PBEsol correlation functional sacrifices the exact gradient expansion for correlation, and is chosen to provide a best fit to jellium surface energies (really, to jellium surface energies as predicted by the TPSS meta-GGA). The resulting functional performs more like LDA than does PBE, and performance improves for solids but degrades for molecules.

3.2. BLYP. In finite systems, the exchange energy density should asymptotically behave as $-\rho/r$, essentially so that the self-Coulomb repulsion of electrons in density tails can cancel with their self-exchange. Neither PBE nor PBEsol satisfies this constraint. It can, however, be enforced in the GGA framework. The B88 exchange functional does so by writing the enhancement factor for σ-spin electrons as

$$F_{\mathrm{x}}^{\mathrm{B88}} = 1 + \frac{1}{C_{\mathrm{x}}}\frac{\beta {x_\sigma}^2}{1 + 6\beta x_\sigma \sinh^{-1}(x_\sigma)} \tag{19}$$

Here, we have defined

$$x_\sigma = \frac{|\nabla n_\sigma|}{n_\sigma^{4/3}} = 2(6\pi^2)^{1/3}s_\sigma \tag{20a}$$

$$C_{\mathrm{x}} = \frac{3}{4\pi}(6\pi^2)^{1/3} \tag{20b}$$

$$\beta = 0.0042 \tag{20c}$$

The functional form of eq 19 guarantees the proper decay of the exchange energy density (but not the exchange potential) for exponentially decaying densities, though for large gradients the enhancement factor is not bounded.

Because the B88 enhancement factor is unbounded, the functional form we have chosen for $\mathscr{H}(s)$ is not asymptotically correct. We note from eq 10 that $s^2\mathscr{H}(s)$ goes to a finite limiting value as s goes to infinity. With bounded $s^2\mathscr{H}(s)$, we have bounded $\mathscr{F}(s)$, hence bounded $\mathscr{G}(s)$, and hence a bounded enhancement factor, $F_{\mathrm{x}}(s)$. In fact, near $s = 70$, our best fit to $\mathscr{H}(s)$ has a pole, and, for larger s, $\mathscr{H}(s)$ is negative and the enhancement factor acquires an imaginary part.

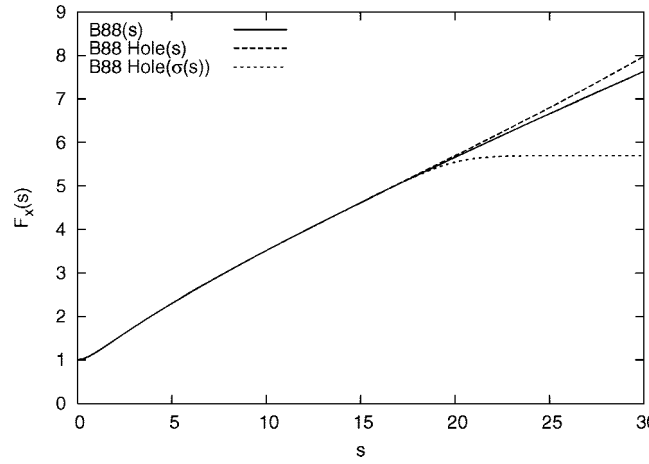

Figure 1. Exchange enhancement factors for the B88 functional, our exchange hole model to it, and the exchange hole model incorporating $\sigma(s)$.

Since we do not wish to change the functional form of $\mathscr{H}(s)$ in our model exchange hole, we are forced to do something about the large s behavior. We choose to modify the dimensionless density gradient, replacing s with $\sigma(s)$ in our code for the B88 exchange hole, with

$$\sigma(s) = -\ln\left(\frac{\mathrm{e}^{-s} + \xi}{1 + \xi}\right) \tag{21}$$

$$\xi = \frac{1}{\mathrm{e}^{20} - 1} \tag{22}$$

For small s, $\sigma(s) \approx s$, while, for large s, $\sigma(s)$ approaches 20. In doing so, we keep a reasonable fit to the exact B88 enhancement factor for $s \lesssim 20$, but the enhancement factor from our exchange hole model is bounded as s goes to infinity. Since the discrepancies between the B88 enhancement factor and that from our exchange hole model occur only at quite large s, we do not anticipate any significant energetic effects. Figure 1 shows the B88 enhancement factor, the enhancement factor from our exchange hole model, and the enhancement factor from our exchange hole model with $\sigma(s)$ used in place of s. As we shall see shortly, the energetic effects of cutting off the reduced gradient at $s = 20$ are negligible.

Note that we have reparametrized $\mathscr{H}(s)$ for our B88 hole model to improve agreement with the B88 enhancement factor for small gradients.

4. Results

In this section, we show results for long-range-corrected hybrids of the GGAs listed earlier. We also include a long-range-corrected LDA based on the $s = 0$ limit of the HJS exchange hole. For each functional considered, we optimize the parameter ω of eq 2 against the AE6 set of heats of

Table 2. Mean and Mean Absolute Errors for the AE6 Set of Atomization Energies, BH6 Set of Barrier Heights, and the Total Atomic Energies of H−Ar, Comparing GGAs (PBE, PBEsol, and BLYP) to Functionals Obtained from GGA Hole Models (EP PBE Hole, HJS PBE Hole, PBEsol Hole, and BLYP Hole)[a]

	AE6		BH6		atoms	
method	ME	MAE	ME	MAE	ME	MAE
LDA	76.96	76.96	−18.05	18.05	67.78	67.78
LDA hole	76.96	76.96	−18.05	18.05	67.78	67.78
PBEsol	35.40	35.40	−12.99	12.99	40.09	40.09
PBEsol hole	35.39	35.39	−12.99	12.99	40.09	40.09
PBE	11.89	15.14	−9.57	9.57	8.55	8.55
HJS PBE hole	11.88	15.13	−9.57	9.57	8.55	8.55
EP PBE hole	9.75	13.23	−9.41	9.41	7.21	7.24
BLYP	−1.96	6.88	−8.03	8.03	−0.56	1.21
BLYP hole	−1.94	6.88	−8.04	8.04	−0.56	1.21

[a] Results are in kilocalories per mole (AE6, BH6) or mH/electron (atomic total energies). We include LDA and the LDA limit of our hole model for comparison. Results are reported to two decimal places because it is only at this level that discrepancies between our exchange hole models and their parent semilocal functionals can be seen.

formation[41] and the BH6 set of barrier heights.[41] We then examine errors for the G1,[42,43] G2,[44] and G3[45] sets of heats of formation, the HTBH38[46] and NHTBH38[47] sets of reaction barriers, and the total atomic energies of H−Ar.[48] Throughout this work, we use the 6-311++G(3df,3pd) basis set and define errors as theory − experiment.

Before we examine long-range-corrected hybrids, however, we validate our parametrizations of the exchange holes by comparing, for several test sets, the results from the GGAs we consider to the results from our exchange holes. Table 2 shows the mean errors (ME) and mean absolute errors (MAE) for the AE6 set, the BH6 set, and the total atomic energies of H−Ar. We also include LDA and the results from the PBE hole model of Ernzerhof and Perdew.

As Table 2 makes clear, the PBE hole model of Ernzerhof and Perdew does not quite reproduce the PBE exchange energy, but actually gives results superior to those of PBE. This may explain some small portion of the accuracy of range-separated hybrids based upon it (because the values for very large or very small ω are more accurate than are those from PBE itself). The HJS version of the PBE hole more precisely reproduces the PBE results, and thus its thermochemical performance is slightly worse than that of the EP hole model. This can be expected to carry over to range-separated hybrids as well.

Table 2 also verifies that, as expected, PBEsol is intermediate in quality between LDA and PBE. Finally, we see that BLYP significantly outperforms the other two GGAs for thermochemistry and that cutting off the reduced gradient at $s = 20$ indeed has no significant effect.

4.1. Optimizing ω for Long-Range-Corrected Hybrids. To optimize the value of ω for the long-range-corrected hybrids under consideration, we minimize the mean absolute error in the AE6 set of atomization energies and the BH6 set of barrier heights. Since, for the very successful long-range-corrected LC-ωPBE hybrid of Vydrov and Scuseria,[31] the errors in atomization energies are roughly three times as large as the errors in barrier heights, we weight barrier heights as three times as important as atomization energies in choosing ω. We use LC-ωPBE orbitals in this portion of the work; our experience shows that self-consistency makes only a small difference. Figures 2−4 show the MAE in kilocalories per mole for the AE6 and BH6 sets as a function of ω, as well as the MAE in milliHartree per electron for the total energies of H−Ar. Note the significant difference in scale on the three figures. All three figures include results for "PBE", which signifies what we shall term LC-ωPBE08 and by which we mean a version of LC-ωPBE based on the HJS exchange hole.

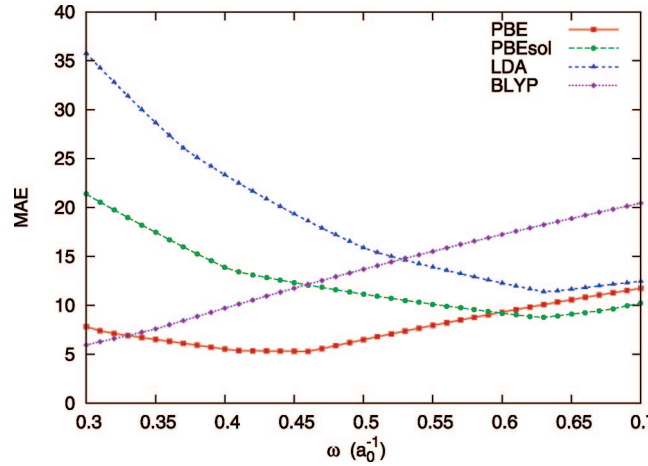

Figure 2. Mean absolute errors in the AE6 set (kcal/mol) from the LC-ωPBE08, LC-ωPBEsol, LC-ωLDA, and LC-ωBLYP functionals as a function of ω.

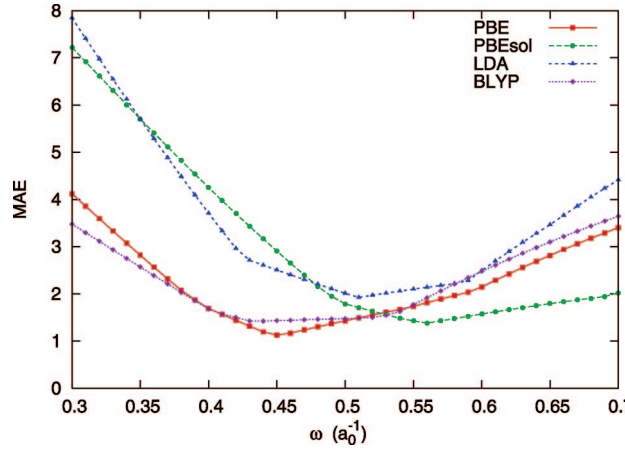

Figure 3. Mean absolute errors in the BH6 set (kcal/mol) from the LC-ωPBE08, LC-ωPBEsol, LC-ωLDA, and LC-ωBLYP functionals as a function of ω.

We begin with a few general comments before turning to the individual GGAs. Performance for thermochemistry is very strongly functional-dependent. Indeed, while LC-ωLDA, LC-ωPBEsol, and LC-ωPBE08 show a minimum in the error as a function of ω, LC-ωBLYP does not, at least in the range considered here. The optimal value of ω appears to increase as the functional becomes more like LDA. Note in this context that even the best results for LC-ωPBEsol and LC-ωLDA yield errors on the order of 10−15 kcal/mol. Barrier heights, by contrast, all show minima in the range of ω considered, and over a fairly narrow range at that. Note also that the best results for barrier heights are consistently

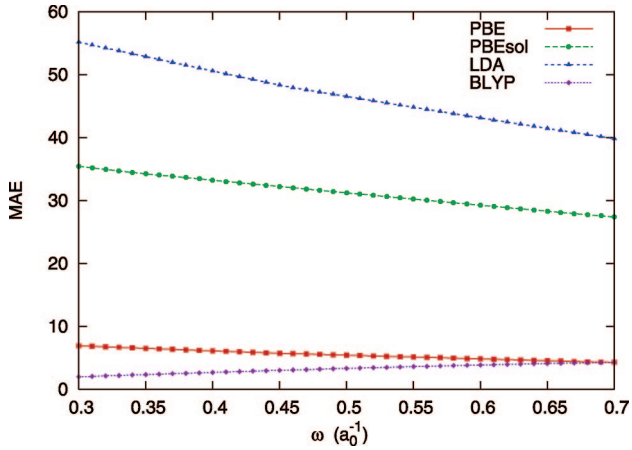

Figure 4. Mean absolute errors in the atomic total energies of H−Ar (mH/electron) from the LC-ωPBE08, LC-ωPBEsol, LC-ωLDA, and LC-ωBLYP functionals as a function of ω.

in the range of 1−3 kcal/mol. We are less interested in atomic total energies but wish to remind the reader of the characteristically large errors in LDA-based hybrids and to point out that these errors are also observed in LC-ωLDA and LC-ωPBEsol.

We now turn to the selection of ω for the various long-range-corrected hybrids under consideration, beginning with PBE. Since the differences between the EP and HJS hole models for PBE are rather small, we do not expect significant differences between LC-ωPBE and what we shall term LC-ωPBE08. We also expect the value of ω in LC-ωPBE08 to be similar to the value used in LC-ωPBE ($\omega = 0.40a_0^{-1}$, where a_0 is the Bohr radius). In fact, the optimal value for LC-ωPBE08 is, by our criterion, $\omega = 0.45a_0^{-1}$. As can be seen from Figures 2 and 3, this value essentially optimizes the barrier heights, as errors in atomization energy are rather flat near this value.

Before considering PBEsol, we turn to LC-ωLDA. We should emphasize here that, by LC-ωLDA, we mean a long-range-corrected functional based on the zero-gradient limit of the HJS exchange hole (which is a nonoscillating approximation to the true LDA exchange hole). Results are thus expected to be similar to, but not identical to, previous results using a long-range-corrected LDA. Figures 2 and 3 show that, unlike with LC-ωPBE08, the minima for the AE6 and BH6 sets as a function of ω do not overlap particularly well. While barrier heights are optimized with $\omega \approx 0.5a_0^{-1}$, atomization energies prefer $\omega \approx 0.6a_0^{-1} - 0.65a_0^{-1}$. This is in qualitative agreement with the results of ref 49, which finds that the optimal value of ω for long-range-corrected LDA is smaller for barrier heights than it is for thermochemistry. Our criterion selects $\omega = 0.60a_0^{-1}$, essentially because barrier heights are rather less sensitive to the precise value of ω than are atomization energies, at least in the range under consideration.

Since PBEsol is intermediate between PBE and LDA, we expect the value of ω to be between that used in LC-ωPBE and the optimal value in a long-range-corrected LDA. From Figure 2, it is clear that LC-ωPBEsol does not perform as well for thermochemistry as does LC-ωPBE, and the thermochemically optimal ω is essentially the same as for LC-ωLDA. But LC-ωPBEsol performs almost as well as does LC-ωPBE for barrier heights, though the value of ω needed is rather larger. We select $\omega = 0.60a_0^{-1}$ for the functional, though any value between $0.55a_0^{-1}$ and $0.65a_0^{-1}$ would do.

Table 3. Errors in Thermochemistry for Several Long-Range-Corrected GGAs and for Their Parent GGAs[a]

	G1		G2		G3		atoms	
model	ME	MAE	ME	MAE	ME	MAE	ME	MAE
LDA	−36.2	36.2	−83.3	83.3	−121.5	121.5	67.8	67.8
PBEsol	−16.9	17.2	−40.7	40.9	−58.7	58.8	40.1	40.1
PBE	−6.7	8.2	−16.1	16.9	−21.7	22.2	8.6	8.6
BLYP	−2.9	4.8	−0.6	7.3	3.8	9.5	−0.6	1.2
LC-ωLDA	−2.3	8.4	−6.2	12.0	−8.4	14.6	39.9	42.9
LC-ωPBEsol	1.5	5.5	−5.1	9.5	−9.9	13.6	28.5	29.2
LC-ωPBE	2.1	3.5	−0.4	3.7	−0.9	4.2	4.4	5.0
LC-ωPBE08	2.8	3.9	0.0	3.9	−1.1	4.7	5.0	5.7
LC-ωBLYP	3.1	4.5	7.8	8.3	13.1	13.5	−2.6	2.7

[a] We show mean errors (ME) and mean absolute errors (MAE) in kilocalories per mole for the G1, G2, and G3 sets of heats of formation, and in mH/electron for the total atomic energies of H−Ar.

Finally, since B88 is in some sense "farther" from LDA than is PBE, we might expect the optimal value of ω for LC-ωBLYP to be somewhat lower than the $0.45a_0^{-1}$ used in LC-ωPBE08. As Figures 2 and 3 establish, this is indeed the case. While there is a broad minimum in the error for barrier heights, the error for atomization energies strictly increases as a function of ω in the region considered. We choose $\omega = 0.40a_0^{-1}$ as a compromise between accuracy for reaction barriers and that for atomization energies, though a slightly smaller value would also suffice.

With these optimized values for ω, we use self-consistent orbitals in what follows. Note that optimization using self-consistent orbitals and larger test sets could lead to slightly different choices of ω, as could weighting atomization energies differently relative to barrier heights. Throughout, we use the procedures described in ref 50.

4.2. Thermochemistry. Performance for thermochemistry can be examined somewhat more thoroughly by calculating the heats of formation for the molecules in the G1, G2, and G3 sets. Because the G2 (G3) set is a superset of the G1 (G2) set which primarily adds larger molecules, we can identify size-dependent errors by examining the relative performance for the three sets. Results are shown in Table 3. We also include results for total atomic energies, since it is known that, by adjusting the atomic energies, one can dramatically improve heats of formation.[51]

As might be expected, LC-ωPBE08 does not perform much differently than does LC-ωPBE. Since we have already seen that the EP PBE hole model gives slightly better thermochemistry than does PBE, it is not terribly surprising that LC-ωPBE08 is slightly inferior to LC-ωPBE. Nonetheless, results from LC-ωPBE08 are quite reasonable, and it is reassuring to note that the small differences between the EP and HJS model exchange holes have only small effects on the accuracy of long-range-corrected hybrids.

The success of LC-ωPBE is already well-documented, and it is not our intent to belabor the point, even with a slightly different hole model. But we do wish to point out that there

Table 4. Errors in Barrier Heights for Several Long-Range-Corrected GGAs and for Their Parent GGAs[a]

	HTBH38		NHTBH38	
model	ME	MAE	ME	MAE
LDA	−17.9	17.9	−12.4	12.7
PBEsol	−13.1	13.1	−9.9	10.1
PBE	−9.7	9.7	−8.5	8.6
BLYP	−7.8	7.8	−8.7	8.7
LC-ωLDA	3.7	4.2	5.6	5.8
LC-ωPBEsol	1.3	2.1	4.1	4.4
LC-ωPBE	−0.5	1.3	1.4	2.4
LC-ωPBE08	0.4	1.4	2.5	2.9
LC-ωBLYP	0.0	2.2	0.5	1.8

[a] We show mean errors (ME) and mean absolute errors (MAE) in kcal/mol for the HTBH38 and NHTBH38 sets of reaction barriers.

is something rather special about the PBE GGA; other long-range-corrected hybrids based on the same hole model but parametrized to reproduce different GGAs are noticeably inferior. That LC-ωPBEsol is not as accurate for thermochemistry as is LC-ωPBE is unsurprising, since LC-ωLDA is less accurate than is LC-ωPBE. We see large size-dependent errors in LC-ωPBEsol and LC-ωLDA, which is not terribly surprising since the atomic total energies are very poor. Interestingly, the size effects in LC-ωLDA are noticeably weaker than are those in LC-ωPBEsol.

Surprisingly, LC-ωBLYP fares little better in this regard than does LC-ωPBEsol or LC-ωLDA. While atomic energies are much better than they are for the other long-range-corrected hybrids investigated (but worse than those from BLYP itself), the heats of formation predicted by LC-ωBLYP are disappointingly poor. Additionally, unlike in BLYP, there is a large size-dependent error.

4.3. Barrier Heights. To more thoroughly assess performance for reaction barriers, we consider the HTBH38 set of 38 hydrogen-transfer barriers, and the NHTBH38 set of 38 non-hydrogen-transfer barriers. Results are presented in Table 4. Here, we see that, in all cases, semilocal functionals struggle to accurately describe reaction barriers, while the long-range-corrected hybrids are uniformly accurate. Part of this accuracy, admittedly, is due to ω being chosen with barrier heights emphasized, but a glance at Figure 3 shows that the range of ω over which long-range-corrected hybrids give reasonable barrier heights is rather broad. We note also that the errors in barrier heights are somewhat increased with LC-ωPBEsol and particularly with LC-ωLDA.

4.4. Ionization Potentials and Electron Affinites. We have thus far avoided any consideration of charged species. Since ions do play important roles in chemistry, it is worth considering performance of long-range-corrected hybrids for these cases. To assess performance of our long-range-corrected hybrids for charged species, we examine the G2 ion test set,[52] excluding N_2^+ and H_2S^+, which do not converge at the GGA level.[52] Our test set thus includes 86 ionization potentials (IPs) and 58 electron affinities (EAs). Results are calculated as the difference between the self-consistent energies of the neutral and charged species (in other words, these are "Δ-SCF" calculations). We report them in Table 5.

Table 5. Errors in Ionization Potentials (eV) and Electron Affinites (eV) for Several Long-Range-Corrected GGAs and for Their Parent GGAs[a]

	IP		EA	
model	ME	MAE	ME	MAE
LDA	0.05	0.23	0.23	0.24
PBEsol	−0.15	0.24	−0.08	0.21
PBE	−0.11	0.23	0.06	0.12
BLYP	−0.19	0.29	0.01	0.12
LC-ωLDA	0.64	0.64	0.46	0.46
LC-ωPBEsol	0.28	0.31	0.14	0.22
LC-ωPBE	0.07	0.19	0.02	0.18
LC-ωPBE08	0.11	0.20	0.02	0.19
LC-ωBLYP	−0.02	0.20	−0.03	0.18

[a] We show mean errors (ME) and mean absolute errors (MAE) for the 86 ionization potentials and 58 electron affinites of the G2 ion test set.

The principle result to which we should draw attention is that for neither IPs nor EAs does the long-range-correction improve upon the parent semilocal functional. That the semilocal functionals perform so well for electron affinites may be somewhat surprising, though it is documented in the literature. (See, for example, ref 50; note, however, that because we do not include plane waves in our basis set, these results may be somewhat artifactual.[53]) It is also perhaps somewhat surprising that LC-ωLDA fares so poorly for these compounds, even though the LSDA itself is not significantly worse than the GGAs we have examined. We note that while having the correct asymptotic decay of the exchange potential is critical if the ionization potential is to be evaluated from the highest occupied orbital energy, it is less important for ionization potentials evaluated in the Δ-SCF approach. We can of course evaluate the electron affinity from the ionization potential of the negatively charged species, and the same consideration would apply there.

5. Conclusions

Long-range-corrected hybrids offer some significant advantages, provided that they can be constructed. We feel that in constructing such a hybrid, one should make every effort to satisfy as many exact constraints as possible. By using the recently proposed GGA exchange hole model of ref 39, we can construct long-range-corrected hybrids from an exchange hole that obeys numerous exact constraints. Various GGAs differ only in the parameters used to define the function $\mathscr{H}(s)$, and once those parameters are determined for one's GGA of choice, the same code can be used for any long-range-corrected hybrid. Of course, which GGAs yield accurate long-range-corrected hybrids within this scheme is not known, but we can draw a few tentative conclusions. First, it does not seem to be particularly important which GGA is used in treating barrier heights of chemical reactions, though LC-ωLDA is notably poorer in this regard. The choice of GGA matters significantly more for atomic energies and for thermochemistry. Naturally, the proper range-separation parameter ω depends on the functional, and while we can draw no firm conclusions here, for the functionals we have considered, the optimal ω decreases as the gradient-dependence increases.

Acknowledgment. This work was supported by the National Science Foundation (Grant CHE-0807194) and the Welch Foundation (Grant C-0036). E.W. acknowledges additional support from the National Science Foundation and the U.S. Department of Defense (PHY-0755008).

Appendix A: Analytic Simplifications of the Range-Separated Enhancement Factor

We can identify several areas where numerical difficulties in evaluating the range-separated enhancement factor of eq 13 are likely to occur as ν becomes large. The polynomials in χ multiplying $\mathscr{B}/\lambda$, $\mathscr{CF}(s)/\lambda^2$, and $\mathscr{EG}(s)/\lambda^3$ all go to zero as ν goes to infinity. The logarithms vanish, and the remaining terms cancel up to order $1/\nu^2$. Here, we simplify the result in such a way as to be more numerically stable.

To simplify the polynomials in χ, we observe that

$$1-\chi=\frac{1-\chi^2}{1+\chi}=\frac{1}{1+\chi}\frac{\lambda}{\lambda+\nu^2}=\frac{\lambda}{\Lambda} \tag{23}$$

where this serves to define Λ. We note that, as $\nu\rightarrow 0$, $\Lambda\rightarrow\lambda$, while, as $\nu\rightarrow\infty$, $\Lambda\rightarrow 2\nu^2$.

To simplify the logarithms, we use, for example,

$$\begin{aligned}\frac{\nu+\sqrt{\zeta+\nu^2}}{\nu+\sqrt{\lambda+\nu^2}}&=1+\frac{\sqrt{\zeta+\nu^2}-\sqrt{\lambda+\nu^2}}{\nu+\sqrt{\lambda+\nu^2}}\\&=1+\frac{1}{\nu+\sqrt{\lambda+\nu^2}}\frac{\zeta-\lambda}{\sqrt{\zeta+\nu^2}+\sqrt{\lambda+\nu^2}}\end{aligned} \tag{24}$$

For large ν, this is $1+\mathscr{O}(1/\nu^2)$, and we can expand the logarithm in a power series.

We can simplify the remaining terms by noting that

$$\begin{aligned}2\nu\left(\sqrt{\zeta+\nu^2}-\sqrt{\eta+\nu^2}\right)&=\frac{2\nu(\zeta-\eta)}{\sqrt{\zeta+\nu^2}+\sqrt{\eta+\nu^2}}\\&=-\frac{2\nu\mathscr{A}}{\sqrt{\zeta+\nu^2}+\sqrt{\eta+\nu^2}}\end{aligned} \tag{25}$$

We thus have

$$\mathscr{A}+2\nu\left(\sqrt{\zeta+\nu^2}-\sqrt{\eta+\nu^2}\right)=\mathscr{A}\left(1-\frac{2\nu}{\sqrt{\zeta+\nu^2}+\sqrt{\eta+\nu^2}}\right) \tag{26a}$$

$$=\mathscr{A}\left(\frac{\zeta}{\left(\sqrt{\zeta+\nu^2}+\sqrt{\eta+\nu^2}\right)\left(\sqrt{\zeta+\nu^2}+\nu\right)}+\frac{\eta}{\left(\sqrt{\zeta+\nu^2}+\sqrt{\eta+\nu^2}\right)\left(\sqrt{\eta+\nu^2}+\nu\right)}\right) \tag{26b}$$

Putting it all together, a numerically more robust expression for the range-separated GGA enhancement factor is

$$\begin{aligned}F_{\mathrm{x}}^{\mathrm{SB}}(s,\nu)=\mathscr{A}&\left(\frac{\zeta}{\left(\sqrt{\zeta+\nu^2}+\sqrt{\eta+\nu^2}\right)\left(\sqrt{\zeta+\nu^2}+\nu\right)}+\frac{\eta}{\left(\sqrt{\zeta+\nu^2}+\sqrt{\eta+\nu^2}\right)\left(\sqrt{\eta+\nu^2}+\nu\right)}\right)-\frac{4}{9}\frac{\mathscr{B}}{\Lambda}-\\&\frac{4}{9}\frac{\mathscr{CF}(s)}{\Lambda^2}\left(1+\frac{1}{2}\chi\right)-\frac{8}{9}\frac{\mathscr{EG}(s)}{\Lambda^3}\left(1+\frac{9}{8}\chi+\frac{3}{8}\chi^2\right)+\\&2\zeta\ln\left(1-\frac{1}{\nu+\sqrt{\lambda+\nu^2}}\frac{\lambda-\zeta}{\sqrt{\lambda+\nu^2}+\sqrt{\zeta+\nu^2}}\right)-\\&2\eta\ln\left(1-\frac{1}{\nu+\sqrt{\lambda+\nu^2}}\frac{\lambda-\eta}{\sqrt{\lambda+\nu^2}+\sqrt{\eta+\nu^2}}\right)\end{aligned} \tag{27}$$

References

(1) Parr, R. G.; Yang, W. *Density Functional Theory of Atoms and Molecules*; Oxford University Press: New York, 1989.

(2) Dreizler, R. M.; Gross, E. K. U. *Density Functional Theory*; Plenum Press: New York, 1995.

(3) Scuseria, G. E.; Staroverov, V. N. Progress in the development of exchange-correlation functionals. In *Theory and Applications of Computational Chemistry: The First 40 Years*; Dykstra, C. E., Frenking, G., Kim, K. S., Scuseria, G. E., Eds.; Elsevier: Amsterdam, 2005.

(4) Levy, M. *Phys. Rev. A* **1982**, *26*, 1200.

(5) Lieb, E. H *Int. J. Quantum Chem.* **1983**, *24*, 243.

(6) Becke, A. D. *Phys. Rev. A* **1988**, *38*, 3098.

(7) Lee, C.; Yang, W.; Parr, R. G. *Phys. Rev. B* **1987**, *37*, 785.

(8) Perdew, J. P. In *Electronic Structure of Solids '91*; Ziesche, P., Eschrig, H., Eds.; Akademie Verlag: Berlin, 1991.

(9) Perdew, J. P.; Burke, K.; Ernzerhof, M. *Phys. Rev. Lett.* **1996**, *77*, 3865; **1997**, *E78*, 1396.

(10) Perdew, J. P.; Ruzsinszky, A.; Csonka, G. I.; Vydrov, O. A.; Scuseria, G. E.; Constantin, L. A.; Zhou, X.; Burke, K. *Phys. Rev. Lett.* **2008**, *100*, 136406.

(11) Voorhis, T. V.; Scuseria, G. E. *J. Chem. Phys.* **1998**, *109*, 400.

(12) Perdew, J. P.; Kurth, S.; Zupan, A.; Blaha, P. *Phys. Rev. Lett.* **1998**, *82*, 2544.

(13) Tao, J.; Perdew, J. P.; Staroverov, V. N.; Scuseria, G. E. *Phys. Rev. Lett.* **2003**, *91*, 146401.

(14) Zhao, Y.; Truhlar, D. G. *J. Chem. Phys.* **2006**, *125*, 194101.

(15) Becke, A. D. *J. Chem. Phys.* **1993**, *98*, 1372.

(16) Becke, A. D. *J. Chem. Phys.* **1993**, *98*, 5648.

(17) Stephens, P. J.; Devlin, F. J.; Chabalowski, C. F.; Frisch, M. J. *J. Phys. Chem.* **1994**, *98*, 11623.

(18) Ernzerhof, M.; Scuseria, G. E. *J. Chem. Phys.* **1999**, *110*, 5029.

(19) Adamo, C.; Barone, V. *J. Chem. Phys.* **1999**, *110*, 6158.

(20) Savin, A.; Flad, H.-J *Int. J. Quantum Chem.* **1995**, *56*, 327.

(21) Savin, A. On degeneracy, near-degenaracy and density functional theory In *Recent Developments and Applications of Modern Density Functional Theory*; Seminario, J. M., Ed.; Elsevier: Amsterdam, 1996.

(22) Leininger, T.; Stoll, H.; Werner, H.-J.; Savin, A. *Chem. Phys. Lett.* **1997**, *275*, 151.

(23) Monkhorst, H. J. *Phys. Rev. B* **1979**, *20*, 1504.

(24) Heyd, J.; Scuseria, G. E.; Ernzerhof, M. *J. Chem. Phys.* **2003**, *118*, 8207.

(25) Heyd, J.; Scuseria, G. E. *J. Chem. Phys.* **2004**, *120*, 7274.

(26) Heyd, J.; Scuseria, G. E. *J. Chem. Phys.* **2004**, *121*, 1187.

(27) Heyd, J.; Scuseria, G. E.; Ernzerhof, M. *J. Chem. Phys.* **2006**, *124*, 219906.

(28) Iikura, H.; Tsuneda, T.; Yanai, T.; Hirao, K. *J. Chem. Phys.* **2001**, *115*, 3540.

(29) Tawada, Y.; Tsuneda, T.; Yanagisawa, S.; Yanai, T.; Hirao, K. *J. Chem. Phys.* **2004**, *120*, 8425.

(30) Gerber, I. C.; Ángyán, J. G. *Chem. Phys. Lett.* **2005**, *415*, 100.

(31) Vydrov, O. A.; Scuseria, G. E. *J. Chem. Phys.* **2006**, *125*, 234109.

(32) Song, J.-W.; Hirosawa, T.; Tsuneda, T.; Hirao, K. *J. Chem. Phys.* **2007**, *126*, 154105.

(33) Chai, J.-D.; Head-Gordon, M. *J, Chem. Phys.* **2008**, *128*, 084106.

(34) Rohrdanz, M. A.; Herbert, J. M. *J. Chem. Phys.* **2008**, *129*, 034107.

(35) Sekino, H.; Maeda, Y.; Kamiya, M. *Mol. Phys.* **2005**, *103*, 2183.

(36) Henderson, T. M.; Izmaylov, A. F.; Scuseria, G. E.; Savin, A. *J. Chem. Phys.* **2007**, *127*, 221103.

(37) Henderson, T. M.; Izmaylov, A. F.; Scuseria, G. E.; Savin, A. *J. Chem. Theory. Comput.* **2008**, *4*, 1254.

(38) Ernzerhof, M.; Perdew, J. P. *J. Chem. Phys.* **1998**, *109*, 3313.

(39) Henderson, T. M.; Janesko, B. G.; Scuseria, G. E. *J. Chem. Phys.* **2008**, *128*, 194105.

(40) Antoniewicz, P. R.; Kleinman, L. *Phys. Rev. B* **1985**, *31*, 6779.

(41) Lynch, B. J.; Truhlar, D. G. *J. Phys. Chem. A* **2003**, *107*, 8996; **2004**, *E108*, 1460.

(42) Pople, J. A.; Head-Gordon, M.; Fox, D. J.; Raghavachari, K.; Curtiss, L. A. *J. Chem. Phys.* **1989**, *90*, 5622.

(43) Curtiss, L. A.; Jones, C.; Trucks, G. W.; Raghavachari, K.; Pople, J. A. *J. Chem. Phys.* **1990**, *93*, 2537.

(44) Curtiss, L. A.; Raghavachari, K.; Redfern, P. C.; Pople, J. A. *J. Chem. Phys.* **1997**, *106*, 1063.

(45) Curtiss, L. A.; Raghavachari, K.; Redfern, P. C.; Pople, J. A. *J. Chem. Phys.* **2000**, *112*, 7374.

(46) Zhao, Y.; Lynch, B. J.; Truhlar, D. G. *Phys. Chem. Chem. Phys.* **2004**, *7*, 43.

(47) Zhao, Y.; González-García, N.; Truhlar, D. G. *J. Phys. Chem. A* **2005**, *109*, 2012; **2006**, *110*, 4942(E).

(48) Chakravorty, S. J.; Gwaltney, S. R.; Davidson, E. R.; Parpia, F. A.; Fischer, C. F. *Phys. Rev. A* **1993**, *47*, 3649.

(49) Vydrov, O. A.; Heyd, J.; Krukau, A. V.; Scuseria, G. E. *J. Chem. Phys.* **2006**, *125*, 074106.

(50) Staroverov, V. N.; Scuseria, G. E.; Tao, J.; Perdew, J. P. *J. Chem. Phys.* **2003**, *119*, 12129.

(51) Brothers, E. N.; Scuseria, G. E. *J. Chem. Theory Comput.* **2006**, *4*, 1045.

(52) Curtiss, L. A.; Redfern, P. C.; Raghavachari, K.; Pople, J. A. *J. Chem. Phys.* **1998**, *109*, 42.

(53) Rösch, N.; Trickey, S. B. *J. Chem. Phys.* **1996**, *106*, 8940.

CT800530U

JCTC Journal of Chemical Theory and Computation

Regularized Gradient Expansion for Atoms, Molecules, and Solids

Adrienn Ruzsinszky,*,† Gábor I. Csonka,‡ and Gustavo E. Scuseria§

Department of Physics and Quantum Theory Group, Tulane University, New Orleans, Louisiana 70118, Department of Inorganic and Analytical Chemistry, Budapest University of Technology and Economics, H-1521 Budapest, Hungary, and Department of Chemistry, Rice University, Houston, Texas 77005

Received December 4, 2008

Abstract: A new, regularized gradient expansion (RGE) approximation density functional (i.e., a generalized gradient approximation or GGA that recovers the second-order gradient expansion for exchange in the slowly varying limit) was designed in an attempt to obtain good solid-state and molecular properties at the same time from a single GGA. We assess the performance of this functional for molecular atomization energies, solid lattice constants, and jellium surface energies. We compare the performance of this functional to the modified Perdew-Burke-Ernzerhof generalized gradient approximation (PBEsol GGA), the original PBE GGA, and the Tao-Perdew-Staroverov-Scuseria (TPSS) meta-GGA.

I. Introduction

Kohn−Sham spin density functional theory[1,2] is now the most widely used method to calculate the ground-state energies of atoms, molecules, solids, surfaces, and more complex systems. In Kohn−Sham theory, the exchange-correlation energy is a functional of the electron spin densities and is the only quantity that must be approximated. The development of increasingly accurate but universal approximations, for use throughout condensed matter physics and quantum chemistry, is the aim of this work. This development relies upon physical insights, paradigm examples, and exact constraints on the exchange-correlation energy, plus minimal empiricism where necessary.

The popular density functionals can be assigned to the rungs of a Jacob's ladder[3] according to their number and kind of ingredients. The local ingredients include the electron density, the gradient and Laplacian of the density, and other quantities that are indirectly determined by the density, constructed from the Kohn−Sham orbitals. The more sophisticated density functionals[4−7] include the kinetic energy density as well. Climbing up to the ladder, the accuracy of the density functionals increases, and the high-level approximations are expected to achieve the goal of functional development: to achieve high accuracy for a wide range of systems from solids to atoms.

The lowest rung of the ladder, the LSDA (local spin density approximation),[1] uses the electron density only, is exact for the uniform electron gas, and reaches moderate accuracy for systems with slowly varying density. The nonempirical GGA (generalized gradient approximation)[8] density functionals rely on the correct features of the LSDA while improving the atomization energies which are seriously overestimated by the LSDA. Although some semiempirical GGAs are more accurate for molecules, they all fail to provide good lattice constants and surface energies. The generally useful nonempirical PBE-GGA[9] satisfies two constraints relevant to solids, the uniform-density limit and the good linear response of the LSDA.

It was shown in ref 10 that the exchange energy of neutral atoms is well approximated by an asymmetric expansion in the atomic number Z: $E_x = -2.208Z^{5/3} - 0.196Z + ...$ The first term is determined by the LSDA, while the second term arises from the gradient expansion of a GGA approximation. In order to be asymptotically exact for large Z, and accurate for most finite Z, the functional must account for both the slowly varying term and the cusp correction. No GGA can get both effects right individually. The exchange gradient

* Corresponding author e-mail: aruzsinszky@gmail.com.
† Tulane University.
‡ Budapest University of Technology and Economics.
§ Rice University.

10.1021/ct8005369 CCC: $40.75
Published on Web 02/25/2009

expansion coefficient (μ) of the popular GGAs was set to obtain good atomic and atomization energies and good thermochemistry. This coefficient, however, is about twice as large as the exact slowly varying gradient expansion coefficient for exchange ($\mu_{GGA} = 0.22-25$ vs $\mu_{GEA} = 10/81$).

Results for molecular atomization energies support the conclusion that PBE is a generally useful nonempirical GGA. The PBE form satisfies two constraints for solids, and thus it can be a reasonable starting point for further development. Unfortunately, the surface energy of jellium in the PBE approximation is less accurate than that of LSDA.[11]

On the other hand, the GGA is a very limited functional form that must necessarily be somewhat biased toward either atoms and small molecules or toward solids and surfaces. The derivation of the PBE GGA by constraint satisfaction[9] had to choose two out of three constraints on the small-gradient behavior, since a single GGA cannot satisfy all three together. And it had to choose a particular way of satisfying these constraints. These choices were influenced by the prior GGA construction from the sharp real-space cutoff of the spurious long-range parts of the gradient expansions[8] for the exchange and correlation hole densities. The employed sharp or step-function cutoffs are parameter-free but are more appropriate to atoms and small molecules (where the electron density cuts off exponentially) than to solids (where the holes can be more diffuse).

Reference 10 concluded that while the second-order gradient expansion is relevant to solids, those real systems are much closer to the limit of validity of the expansion for exchange than they are for correlation. If we are interested only in solids, it makes more sense to use the first principles gradient coefficient for exchange μ=0.123 and choose β=0.037 to recover the good LSDA linear response. Greater accuracy requires us to make a fission and led us recently to develop the successful PBEsol[12] for solids while keeping the successful PBE for atoms.

By incorporating more complex ingredients and exact properties into the exchange-correlation energy, a higher-rung functional can simultaneously recover the good LSD linear response and the correct second-order gradient expansion for both exchange and correlation. Meta-GGAs improve upon the GGAs by the satisfaction of one paradigm for condensed matter and another for quantum chemistry. The paradigm for condensed matter physics is the slowly varying limit,[13] and that for quantum chemistry is the one and two-electron density.[14] The kinetic energy density is an ingredient which permits recovery of the slowly varying limit through higher-orders in the ∇ operator.

Since meta-GGAs are not widely available in solid state codes, there has been a great need to develop simple low-level functionals that are accurate for restricted classes of systems (e.g., solids). The semilocal functionals of the first three rungs are computationally efficient in self-consistent calculations.

Predicting lattice constants more accurately than LSDA remains a challenge, even for state-of-the-art meta-GGAs; the TPSS meta-GGA only achieves a moderate improvement upon the Perdew-Burke-Ernzerhof (PBE) GGA.[15] We built the correct physics for solids into the new PBEsol generalized gradient approximation,[12] and we have cast it in a form that makes it extremely easy for solid-state calculators to test and apply. On the other hand the PBE is more successful in chemistry than PBEsol, because it more radically reduces the LSD overestimate of molecular atomization energies. This situation motivated us to try to develop GGAs without being biased toward either atoms and small molecules on the one hand or toward solids and surfaces on the other, combining all the favorable properties of different GGAs. For recent developments building on the PBEsol concept see ref 16.

II. Regularized Gradient Expansion

A universally useful GGA is approached in this work by adding a higher-order term to the denominator of the PBEsol GGA enhancement factor. We recall the exchange enhancement factor $F_x^{PBE}(s)$ for PBE GGA, which gives the enhancement over LSDA exchange as a function of the reduced density gradient s (defined below). The parameter μ controls the approach of F_x^{PBE} to its slowly varying or $s \rightarrow 0$ *and* rapidly varying or $s \rightarrow \infty$ limits (1 and $1 + \kappa$, respectively), while the parameter $\kappa = 0.804$ sets the large-gradient limit. (Satisfaction of the Lieb-Oxford bound[17] on E_x for all possible densities requires $\kappa \leq 0.804$, and $\kappa = 0$ recovers LSDA exchange.)

PBEsol is a first (RGE1) regularized gradient expansion (RGE) approximation, because it removes the spurious divergence of the second-order gradient expansion. A second RGE or RGE2 exchange energy also has the form

$$E_x^{RGE2}[n] = \int d^3r n \cdot \varepsilon_x^{unif}(n) \cdot F_x^{RGE2}(s) \qquad (1)$$

where $\varepsilon_x^{unif}(n) = -3(3\pi^2 n)^{1/3}/4\pi$ is the exchange energy per electron for the uniform electron gas of density n, and $s = |\nabla n|/[4(3\pi^2 n)^{1/3} n]$ is the dimensionless density gradient. The form of eq 1 satisfies the uniform density scaling property of the exchange energy.

For the second-order gradient coefficient for exchange, valid for the slowly varying limit, we use the first-principles $\mu = 10/81$ as justified in ref 12

$$F_x^{RGE2}(s) = 1 + \kappa - \frac{\kappa}{1 + \frac{\mu s^2}{\kappa} + \left(\frac{\mu s^2}{\kappa}\right)^2} \qquad (2)$$

Note that $F_x(s) = 1 + \mu s^2 + \ldots$ as $s \rightarrow 0$ and that the s^4 term of this expansion is designed to vanish for RGE2. In other words, RGE2 is designed to recover the second-order gradient expansion for exchange over a wide range of s. In the large- gradient limit

$$\lim_{s \rightarrow \infty} F_x \rightarrow 1 + \kappa \qquad (3)$$

In this work we restore the slowly varying limit over a wide range of s. This choice can give more accurate lattice constants and surface energies than PBE.[12] But with the successful PBEsol functional for solids we encountered a dilemma: no functional achieved high accuracy for solid

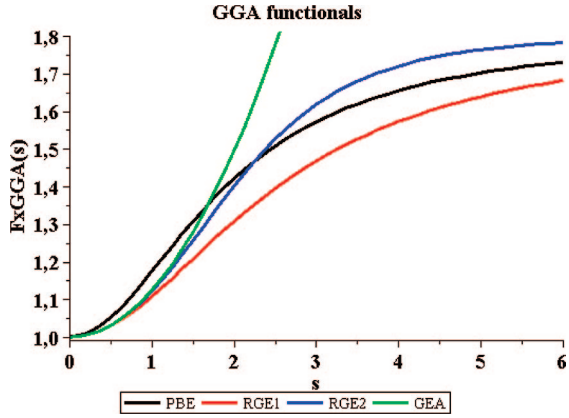

Figure 1. Comparison of the PBE, RGE1 (PBEsol), RGE2, and GEA ($1 + 10/81\ s^2$) exchange enhancement factors for reduced exchange gradient s ($0 \le s \le 6$).

properties and atomic energies at the same time. With the selection of $\mu = 10/81$ we cannot ensure good quality atomization energies within the limited frame of the PBEsol GGA, since GGAs cannot use other inputs than the electron density and its gradient. At the higher meta-GGA level, the parameter μ is determined by recovering the PBE-GGA large gradient limit, and the functional can be exact to fourth-order in the slowly varying limit. We miss this flexibility at the GGA level and have to find a reasonable interpolation between the large gradient and small gradient limits. In other words we have to find the way to resolve this inconsistency of the GGAs without climbing up to the meta-GGA level.

With this formulation of the denominator of F_x in the RGE2, we try to restore the approach of F_x to the large gradient limit at the GGA level, keeping μ at its exact value justified in the successful PBEsol functional. This form gives better atomic exchange energies that the PBEsol (RGE1) form. The RGE1 functional is defined as PBEsol exchange combined with the standard PBE correlation. Our RGE2 formula satisfies the Lieb-Oxford bound like PBE,[9] and, since the spin-polarized F_x increases with s to a maximum value of $F_x \le 1.804$, the Lieb-Oxford bound is satisfied as well.

The nonlocality of F_x is displayed in Figure 1, where we also compare F_x of the RGE2 and RGE1 (PBEsol) functionals over the range of interest for real systems. The range $0 \le s \le 3$ is the important region for most properties of real systems, while $0 \le s \le 1$ is relevant for the valence-electron regions of densely packed solids. For a universally useful functional, the nonlocality must be enhanced for $s \ge 2$, compared to the RGE1 functional. The approach of F_x to the large-gradient limit seems to be relevant for free atoms.[12] The RGE2 F_x agrees well with the RGE1 in the valence region of densely packed solids and increases over the PBE-GGA in the relevant large gradient region for the free atoms.

The increase with s has been discussed in the context of the atomization energies.[18] Other works on atomization energies and isodesmic stabilization energies[19] confirm that real systems can be split into two groups: solids and molecules.[20] These groups represent two different universality classes for the gradient expansion; in the solids the electrons live in the classically allowed region, while in the molecules they spend considerable time in classically forbidden regions.

Our universally useful RGE2 is expected to respect both classes, and in addition an earlier work by us[19] confirmed that the diminished gradient makes the semilocal functionals better not only for solids but also for single-bonded hydrocarbons.

It has been known for a long time that the PBE-GGA overestimates the atomization energies. This overbinding is attributed to an inconsistency of the atomic and molecular energies at the GGA level of approximation.[18] The overestimation is increased with the reduced gradient expansion PBEsol and arises from the worsened total energies of the free atoms. The RGE2 is expected to improve the bad-quality atomization energies of the PBEsol GGA due to increased F_x values in the large-s region. Accurate total energies of free atoms call for an increased F_x in the region of $s \ge 2$ relevant to free atoms, although an overenhanced exchange might spoil the energies of molecules leading to overestimation of atomization energies.

For a slowly varying density, the correlation energy has a second-order gradient expansion

$$E_c[n] = \int dr^3 n[\varepsilon_c^{unif}(n) + \beta t^2] \tag{4}$$

where

$$t = \frac{|\nabla n|}{\left[2\sqrt{4(3\pi^2 n)^{\frac{1}{3}}/\pi}\right]n} \tag{5}$$

is the reduced correlation gradient on the scale of the Thomas-Fermi screening wave vector instead of the Fermi wave vector used in the exchange. The value of the correlation gradient expansion coefficient β respects the expansion from the work of Langreth and Perdew, which implies the Ma-Brueckner high-density limit for the gradient coefficient for correlation.[21,22]

Once again, as in our PBEsol work, the role of correlation should be revisited. Since the convergence conditions are more severe for the second-order gradient expansion in the case of correlation than they are in the case of exchange, it may not be so important in practice to recover the correct Langreth-Vosko gradient expansion for correlation, even in solids.[23]

Another condition relevant to solids is the linear response of the uniform electron gas to a weak perturbing potential. For small density variations of the uniform gas, the LSD is an accurate approximation, while the second-order gradient expansion is not. For such small density variations, s and t will be small, and a GGA will have the expansions (1) and (4). A good description which recovers the LSD requires a cancelation between the second-order gradient terms

$$\mu = \frac{\pi^2}{3}\beta \tag{6}$$

We have shown in the PBEsol construction that the GGA form is too limited to allow for a perfect description of all small density variations, so a choice must be made among the constraints. We can keep the original PBE form but

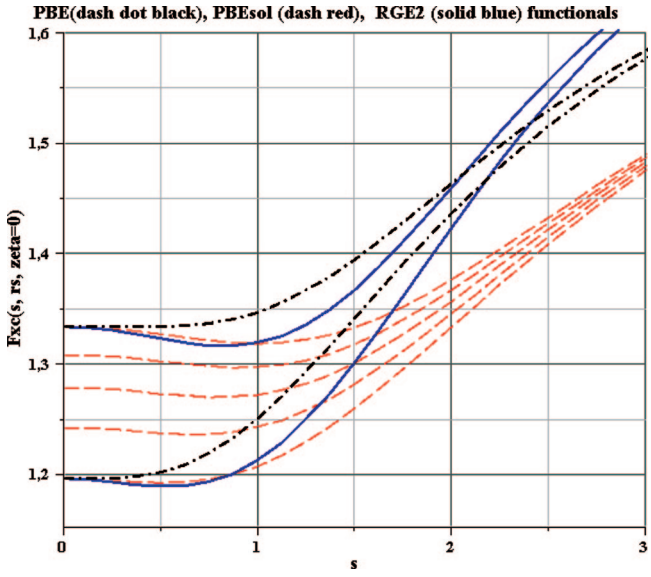

Figure 2. Exchange-correlation gradient enhancement factors, $F_{xc}(s,r_s,\zeta=0)$ vs the reduced density gradient s in the range $0 \le s \le 3$ for the generalized gradient approximations PBE (dash dot black), PBEsol (dash red), and RGE2 (solid blue) for $r_s = 2$, 3, 4, 5, and 6 (PBEsol) and $r_s = 2$, and 6 (PBE and RGE2). r_s denotes the Wigner-Seitz radius, and ζ denotes the relative spin polarization. $r_s = 2$ and 6 are the smallest and largest enhancement curves, respectively. In LDA $F_{xc}(s,r_s,\zeta=0) = F_{xc}(s=0,r_s,\zeta=0)$.

change the second-order gradient coefficients for exchange and correlation to satisfy solidlike constraints. The expansion of the correlation has proven to be less relevant, and eq 6 can be respected by a reduced gradient coefficient for correlation. With this choice we could keep the constraint of the linear response in our RGE2 as well, but we decided to follow the way we chose for the PBEsol functional and sacrifice the constraint of the linear response for the sake of good surface energies. The correlation gradient expansion coefficient $\beta = 0.053$ of the RGE2 correlation was set to obtain TPSS jellium surface exchange-correlation energies in the same way as in PBEsol (see discussion later). Figure 2 shows the comparison between the PBE, PBEsol, and RGE2 exchange-correlation enhancement factors $F_{xc}(s,r_s,\zeta = 0)$ for the spin-unpolarized density, where r_s is the Wigner-Seitz radius and $\zeta = (n_\uparrow - n_\downarrow)/n$ is the relative spin polarization (here $\zeta = 0$) and

$$E_{xc}^{RGE2}[n] = \int d^3r n \cdot \varepsilon_x^{unif}(n) \cdot F_{xc}^{RGE2}(s, r_s, \zeta) \qquad (7)$$

For small s, the PBEsol and RGE2 functionals are quite similar for electron densities around $2 < r_s < 6$ (typical for valence region of the metals studied in this paper). However, for large s values, the two functionals behave quite differently, as shown in Figure 2.

The exchange-correlation (xc) energy E_{xc}^{hybid} of the hybrid functionals is defined as

$$E_{xc}^{hybid} = a \cdot E_x^{HF} + (1 - a) \cdot E_x^{DFA} + E_c^{DFA} \qquad (8)$$

where a is a mixing factor of E_x^{HF} Hartree−Fock, and E_x^{DFA} density functional approximation (local GGA or meta-GGA functionals) exchange energies, and E_c^{DFA} is a density functional approximation correlation energy. The value of a cannot be fixed universally. Good thermochemistry can be obtained by setting $0.1 < a < 0.25$ (cf. PBEh and TPSSh in Table 1). To obtain good reaction energy barriers usually $a > 0.5$ values are required. The amount of HF exchange was controlled via Iop(3/76) of the GAUSSIAN program.[30]

III. Results and Discussion

In an assessment of a universal density functional, the performance has to be tested on a test of atomization energies and bulk solids. We used a triple-ζ-quality basis set. The AE6 test set of Lynch and Truhlar[24] provides a quick but representative evaluation for the atomization energies of diverse molecular systems: the AE6 set of atomization energies includes six molecules: SiH_4, S_2, SiO, C_3H_4, C_2H_2O, and C_4H_8.

This test set is small, however quite diverse, and was constructed to reproduce the error of larger sets. For the AE6 data set, we show two sets of results coming from different correlation parameters β of eq 4. $\beta = 0.066725$ reproduces the original PBE correlation, while the selection of $\beta = 0.053$ sacrifices the good linear response in favor of better surface energies (*vide infra*) and comes from a fitting to meta-GGA (TPSS) quality surface energies.

The results in Table 1 show that the value of the parameter β influences the results, and $\beta = 0.066725$ gives better agreement with experiment. Both version of the RGE2/6−311G(3*df*,2*p*) improve the atomization energies considerably compared to the PBEsol/6−311G(3*df*,2*p*) results. This shows clearly the importance of the larger enhancement factor F_x for the large gradient limit for better atomization energy. For functionals that show overbinding tendency, like PBE, PBEsol, and RGE2, applying a smaller basis set (e.g., 6−311G(d,p)) improves the agreement with the experimental results, as shown in ref 18. We constructed hybrids from the PBEsol and RGE2 functionals, denoted as PBEsolh and RGE2h in Table 1 (cf. eq 8). To obtain best agreement with experiment for the AE6 test set, we mix 37% exact exchange with the RGE2 GGA exchange. This gives almost as good a result as that of the quite good TPSSh functional. It is expected that the large exact exchange ratio in RGE2h would help to obtain improved barrier heights for chemical reactions. (This will be studied elsewhere.) To obtain good atomization energies, the PBEsol hybrid functional requires more than 50% exact exchange. However, PBEsol was constructed for solids, and we do not detail the optimization of the PBEsol hybrid in this paper.

The test set of 18 solids[15] was distributed over simple metals, semiconductors, ionic solids, and transition metals, and for this test set PBEsol showed essentially 0% error in the lattice constant, when compared to experimental values extrapolated to absolute zero temperature and corrected for zero-point anharmonic expansion.[15] The experimental low temperature (5 K) lattice constants values are from refs 25 (Li), 26 (Na, K), 27 (Al, Pb, Cu, Rh, Pd, and Ag), and 28 (NaCl). The rest are based on room temperature values from refs 29 (C, Si, SiC, Ge, GaAs, NaF, LiF) and from 26 (LiCl), corrected to the $T = 0$ limit using thermal expansion

Table 1. Errors (kcal/mol) of the Atomization Energies of the AE6 Test Set Calculated with PBE, PBEsol, RGE2, and TPSSh Functionals Using the 6-311G(3*df*,2*p*) Basis Set[b]

	PBE	PBEsol	PBEsolh	RGE2[a]	RGE2	RGE2h	RGE2h	RGE2h	RGE2h	TPSSh	expt
μ	0.21951	0.12346	0.12346	0.12346	0.12346	0.12346	0.12346	0.12346	0.12346	–	
β	0.0667	0.0460	0.0460	0.0667	0.0530	0.0530	0.0530	0.0530	0.0530	–	
a	0.00	0.00	0.25	0.00	0.00	0.25	0.30	0.37	0.40	0.10	
SiH_4	−9.2	1.3	1.5	−8.8	−4.8	−3.1	−2.7	−2.1	−1.8	10.7	322.4
SiO	3.6	12.9	−3.0	2.9	4.3	−8.7	−11.2	−14.4	−16.1	−11.0	192.1
S_2	13.1	21.9	10.5	16.5	16.2	7.2	5.5	3.2	2.1	3.4	101.7
C_3H_4	16.4	45.1	26.0	18.9	22.4	8.8	6.2	2.7	1.0	0.0	704.8
$C_2H_2O_2$	31.8	64.7	28.0	35.9	38.5	10.2	4.7	−2.4	−6.0	−7.0	633.4
C_4H_8	18.7	69.5	47.7	27.7	33.4	20.5	18.1	14.9	13.3	5.3	1149.0
ME	12.4	35.9	18.4	15.5	18.3	5.8	3.4	0.3	−1.2	0.2	
MAE	15.5	35.9	19.5	18.5	20.0	9.8	8.1	6.6	6.7	6.2	
rms	17.8	44.1	25.4	21.5	23.8	11.1	9.6	8.7	8.9	7.3	
StDev	14.0	28.2	19.1	16.3	16.7	10.4	9.8	9.6	9.7	8.0	
Min	−9.2	1.3	−3.0	−8.8	−4.8	−8.7	−11.2	−14.4	−16.1	−11.0	
Max	31.8	69.5	47.7	35.9	38.5	20.5	18.1	14.9	13.3	10.7	

[a] RGE2 exchange + PBE correlation with $\beta = 0.066725$. This choice of β results in slightly too large surface energies, and has negligible influence on the lattice constants compared to the choice of $\beta = 0.0530$. [b] The values of the exchange (μ) and correlation (β) gradient expansion coefficients are shown. The weight of the exact exchange (*a*) is also shown for the hybrid functionals (cf. eq 8).

corrections from ref 27 (Note that a linear extrapolation of the lattice constant from 300 K to 0 K is neither accurate nor used here.) Note that in ref 15 the ZPAE corrections for C, Si, SiC, Ge, GaAs, NaCl, NaF, LiCl, LiF, and MgO are incorrectly given; those values should be multiplied by 2, as corrected in the erratum of ref 12. This small test set is not representative, but a recent study shows[32] that the extension of the test set does not radically change the overall statistics.

Our original calculations for solids were made with the periodic-boundary-condition version of the Gaussian[30] code. The RGE2 functional is implemented self-consistently into the developmental version of Gaussian, and the lattice constants are computed with optimized geometry. We use the same Gaussian-type orbital (GTO) basis sets as in our earlier work.[12] In order to make the calculations efficient, the small-exponent functions have to be removed from the molecular GTOs and the exponents of the remaining valence functions reoptimized. For details see refs 15 and 31. It was observed that the GTO basis set used in this study makes the lattice constants slightly larger (by 0.01 Å on average) compared to solid state codes like BAND or VASP.[32]

The valence electron densities of the 18 solids we have studied have reduced density gradients in the range $0 < s < 2.2$.[32] To make the GGA recover the second-order gradient expansion for exchange over a wide range of solid-state-like densities, we have to enhance the gradient expansion beyond the one used in the PBEsol functional. This enhancement is achieved by adding the higher-order term to the denominator of the enhancement factor.

In Table 2 we compare the new RGE2 results with the PBE-GGA, PBEsol, and TPSS lattice constants. The PBEsol is very accurate and produces a mean error (ME) of 0.02 Å for these 18 solids, as noted earlier.[12,32] The TPSS lattice constants are somewhat too long and cannot compete in accuracy with the PBEsol values. Notice that the TPSS and RGE2 lattice constants are quite similar for simple metals and semiconductors. The RGE2 shows a good performance for transition metals in this test set (actually better than PBEsol). The lesson we take from our PBEsol work is that

Table 2. Strukturbericht Symbols (Str.), Equilibrium Lattice Constants (Å), and Statistical Data of 18 Test Solids Calculated with the GAUSSIAN Program[e]

	Strukt.	LSDA	PBEsol	RGE2	PBE	TPSS	Expt.
μ		0.000	0.1235	0.123	0.21951		
β		0.000	0.0460	0.053	0.06673		
Li	A2	3.383	**3.453**	3.501	3.453	3.475	3.449
Na	A2	4.049	4.159	4.239	**4.199**	4.233	4.210
K	A2	5.093	**5.232**	5.354	5.296	5.362	5.212
Al	A1	4.008	**4.038**	4.052	4.060	**4.035**	4.020
ME[a]		-0.089	**-0.002**	0.064	0.029	0.054	
MAE[b]		0.089	**0.023**	0.064	0.035	0.054	
Cu	A1	3.530	3.578	**3.597**	3.635	3.593	3.596
Rh	A1	**3.791**	3.819	3.830	3.871	3.846	3.793
Pd	A1	3.851	**3.888**	3.897	3.950	3.917	3.877
Ag	A1	3.997	4.045	**4.061**	4.129	4.076	4.064
ME[a]		-0.040	**0.000**	**0.014**	0.064	0.025	
MAE[b]		0.040	**0.019**	**0.015**	0.064	0.027	
C	A4	**3.537**	3.562	3.573	3.579	3.579	3.543
Si	A4	**5.410**	5.442	5.460	5.479	5.466	5.416
SiC	B3	**4.355**	4.381	4.395	4.404	4.394	4.342
Ge	A4	**5.634**	5.693	5.727	5.776	5.744	5.640
GaAs	B3	**5.626**	5.687	5.723	5.772	5.745	5.638
ME[a]		**-0.003**	0.037	0.060	0.086	0.070	
MAE[b]		**0.009**	0.037	0.060	0.086	0.070	
NaCl	B1	5.471	**5.611**	5.731	5.696	5.696	5.565
NaF	B1	4.505	**4.633**	4.733	4.700	4.706	4.579
LiCl	B1	4.968	**5.072**	5.152	5.146	5.113	5.074
LiF	B1	3.904	**4.002**	4.082	4.063	4.026	3.964
MgO	B1	**4.178**	4.229	4.266	4.270	4.247	4.184
ME[a]		-0.068	**0.036**	0.119	0.102	0.084	
MAE[b]		0.068	**0.037**	0.119	0.102	0.084	
TME[c]		-0.049	**0.020**	0.067	0.073	0.060	
TMAE[d]		0.050	**0.030**	0.067	0.074	0.061	

[a] Mean error. [b] Mean absolute error. [c] Total mean error. [d] Total mean absolute error. [e] μ and β are the parameters of the exchange and correlation enhancement factors in eqs 2 and 4. The Strukturbericht symbols are used for the structure as follows: A1, fcc; A2, bcc; A4, diamond; B1, rock salt; B3, zinc blend. The experimental (5−50 K) lattice constants values are from refs 25 (Li), 26 (Na, K), 27 (Al, Cu, Rh, Pd, Ag), and 28 (NaCl). The rest are based on room temperature values from refs 29 (C, Si, SiC, Ge, GaAs NaF, LiF, MgO) and 26 (LiCl), corrected to the $T = 0$ limit using the thermal expansion from ref 27. An estimate of the zero-point anharmonic expansion is subtracted out from the experimental values.[32] The best theoretical values are in boldface.

Table 3. Jellium Surface Exchange σ_x and Exchange-Correlation Energies σ_{xc} (erg cm^{-2}) for LSDA, PBE, PBEsol ($\kappa = 0.804$, $\mu = 0.1234568$, $\beta = 0.046$), RGE2 ($\kappa = 0.804$, $\mu = 0.1234568$, $\beta = 0.053$), TPSS, Exact, Diffusion Monte Carlo (DMC), and Corrected Random Phase Approximation (RPA+)[f]

		r_s			
method	σ	2	3	4	6
LSDA[a]	x	3037	669	222	43.0
PBE[a]	x	2438	468	128	11.8
PBEsol	**x**	**2666**	**540**	**162**	**22.9**
RGE2	**x**	**2622**	**523**	**153**	**19.5**
TPSS[a]	x	2553	498	141	15.4
exact[b]	**x**	**2624**	**526**	**157**	**22**
LSDA[a]	xc	3354	764	261	53
PBE[a]	xc	3265	743	252	52
PBEsol	**xc**	**3374**	**774**	**267**	**56**
RGE2	**xc**	**3373**	**771**	**265**	**55**
TPSS[a]	xc	3380	772	266	55
DMC[c]	xc	3392	768	261	52.5
RPA+[d]	xc	3413	781	268	54
RGE2xPBEc[e]	xc	3449	797	278	59.5

[a] Reference 15. [b] Reference 35. [c] Diffusion Monte Carlo.[36] [d] Corrected random phase approximation.[37] [e] RGE2 exchange + PBE correlation with $\beta = 0.066725$. This choice of β results in slightly too large surface energies and has negligible influence on the lattice constants but improves atomization energies (cf. Table 1 compared to the choice of $\beta = 0.0530$. [f] r_s is the Wigner-Seitz radius. (1 au = 1.557 10^6 erg cm^{-2}).

good lattice constants can be achieved when the correct Antoniewicz-Kleinman[33]second-order gradient expansion for exchange is recovered *over a wider range of solid-state-like densities than it is in TPSS*. The TPSS meta-GGA already recovers this expansion, but only for solid-like densities that are very slowly varying over space. This observation applies especially for ionic solids, for which TPSS and RGE2 seriously overestimate the lattice constants.[15] A similar observation has been made recently[32] for the Armiento-Mattsson 2005 GGA.[34]

Overall, the performance of our RGE2 functional lies between PBE and TPSS. Transition metals have very slowly varying densities, with a maximum reduced gradient of less than one, while ionic crystals have a maximum reduced gradient around two (2.2).[32] To achieve accurate atomization energies, we have to enhance the nonlocality of our functional, but this comes at the price of reduced accuracy for lattice constants of ionic solids at the GGA level.

The surface energies of different approximations were tested on jellium, a model for simple metals in which the electrons are distributed in a positive background truncated at a plane. The density of the bulk region is characterized by the Wigner-Seitz radius, r_s, which stems from the density of the positive background. The exact value of the exchange component of the jellium surface energy is known.[35] There is a significant improvement in the exchange energy of a slowly varying density when we pass from PBE to TPSS, and thus the inner part of the surface density profile is better treated as shown in Table 3. The excellent performance of the RGE2 exchange functional is apparent from Table 3. Note that the RGE2 exchange functional has no empirical parameter, and it is better than the similarly nonempirical PBEsol exchange. For the surface exchange-correlation energy, the

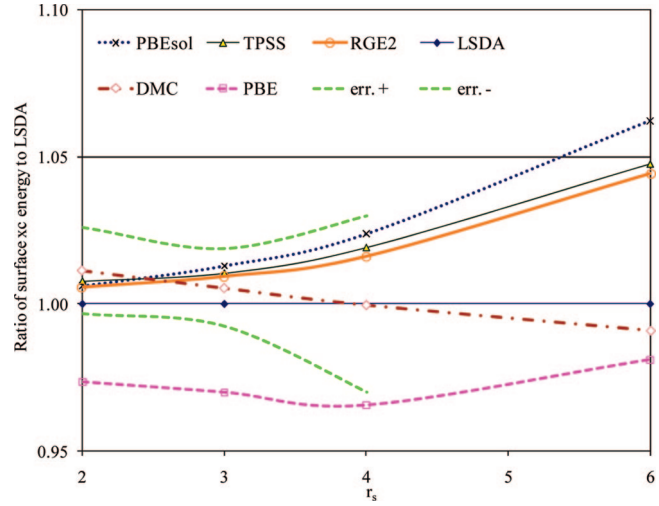

Figure 3. Ratio of calculated surface exchange-correlation energy to that of LSDA, as a function of r_s for various approximations. The upper and lower error bars of the diffusion Monte Carlo (DMC) surface exchange-correlation energy (ref 36), err + and err −, are also shown for $r_s < 4$.

RGE2 results were fitted to the TPSS functional, and they show an excellent agreement with the TPSS functional for whole r_s range in Figure 3. The diffusion Monte Carlo[36] and the most precise surface exchange-correlation energy results coming from the random phase approximation (RPA+) with short-range correction[37] are also shown in Table 3. Comparison of the results in Tables 2 and 3 shows that the excellent RGE results for jellium surface energies do not guarantee good lattice constants, for a wide range of solids.

IV. Conclusions

We designed a new generalized gradient expansion or GGA, a regularized gradient expansion or RGE2 that recovers the second-order gradient expansion for exchange in the slowly varying limit, in an attempt to obtain good solid-state and molecular properties at the same time from a single GGA. The performance of this functional for molecular atomization energies is better than the performance of PBEsol but worse than that of PBE. For the AE6 atomization test set, we constructed an optimized RGE2 hybrid, with 37% exact exchange and 63% RGE2 exchange. This RGE2h gives reasonable molecular atomization energies with mean absolute error (MAE) of 6.6 kcal/mol (while the quite good nonempirical TPSSh functional has MAE = 6.2 kcal/mol). For lattice constants of solids, the RGE2 functional is worse than the PBEsol functional except for transition metals. Interestingly the overall performance of the RGE2 for solids is similar to TPSS. However this test set of 18 solids is not representative, and thus tests on larger test sets are planned. The correlation gradient expansion coefficient β of the RGE2 correlation was set to obtain TPSS jellium surface exchange-correlation energies in the same way as in PBEsol, but the RGE2 agrees somewhat better with TPSS than PBEsol. Our results show that the excellent RGE2 jellium surface energies do not guarantee good lattice constants, for a wide range of solids.

Acknowledgment. Support is acknowledged from NSF-MTA (98).

References

(1) Kohn, W.; Sham, L. J. *Phys. Rev.* **1965**, *140*, A1133.

(2) *A Primer in Density Functional Theory*; Fiolhais, C., Nogueira, F., Marques, M., Eds.; Springer-Verlag: Berlin, 2003.

(3) Perdew, J. P.; Schmidt, K. In *Density Functional Theory and Its Applications to Materials*; Van Doren, V. E., Van Alsenoy, K., Geerlings, P., Eds.; American Institute of Physics: Melville, NY, 2001.

(4) Van Voorhis, T.; Scuseria, G. E. *J. Chem. Phys.* **1998**, *109*, 400.

(5) Adamo, C.; Ernzerhof, M.; Scuseria, G. E. *J. Chem. Phys.* **2000**, *112*, 2643.

(6) Perdew, J. P.; Kurth, S.; Zupan, A.; Blaha, P. *Phys. Rev. Lett.* **1999**, *82*, 2544.

(7) Tao, J.; Perdew, J. P.; Staroverov, V. N.; Scuseria, G. E. *Phys. Rev. Lett.* **2003**, *9*, 1–146401.

(8) (a) Perdew, J. P. *Phys. Rev. Lett.* **1985**, *55*, 1665. (b) Perdew, J. P.; Wang, Y. *Phys. Rev. B* **1986**, *33*, 8800(R.

(9) Perdew, J. P.; Burke, K.; Ernzerhof, M. *Phys. Rev. Lett.* **1996**, *77*, 3865. *Phys. Rev. Lett.* **1997**, *78*, 1396 (E). For other GGAs, see references therein.

(10) Perdew, J. P.; Constantin, L. A.; Sagvolden, E.; Burke, K. *Phys. Rev. Lett.* **2006**, *97*, 223002.

(11) Constantin, L. A.; Perdew, J. P.; Tao, J. *Phys. Rev. B* **2006**, *73*, 205104, and references therein.

(12) Perdew, J. P.; Ruzsinszky, A.; Csonka, G. I.; Vydrov, O. A.; Scuseria, G. E.; Constantin, L.; Zhou, X.; Burke, K. *Phys. Rev. Lett.* **2008**, *100*, 136406. Erratum submitted.

(13) Svendsen, P. S.; von Barth, U. *Phys. Rev. B* **1996**, *54*, 17402.

(14) Tao, J.; Perdew, J. P.; Staroverov, V. N.; Scuseria, G. E. *Phys. Rev. Lett.* **2003**, *91*, 146401. For other meta-GGAs, see references therein.

(15) Staroverov, V. N.; Scuseria, G. E.; Tao, J.; Perdew, J. P. *Phys. Rev. B* **2004**, *69*, 075102. Erratum submitted.

(16) Zhao, Y.; Truhlar, D. G. *J. Chem. Phys.* **2008**, *128*, 184109.

(17) Lieb, E. H.; Oxford, S. *Int. J. Quantum Chem.* **1981**, *19*, 427.

(18) Csonka, G. I.; Ruzsinszky, A.; Tao, J.; Perdew, J. P. *Int. J. Quantum Chem.* **2005**, *101*, 506.

(19) Csonka, G. I.; Perdew, J. P.; Ruzsinszky, A.; Grimme, S. *J. Chem. Theory Comput.* **2008**, *4*, 888.

(20) Csonka, G. I.; Vydrov, O. A.; Scuseria, G. E.; Ruzsinszky, A.; Perdew, J. P. *J. Chem. Phys.* **2007**, *126*, 244107.

(21) Langreth, D. C.; Perdew, J. P. *Phys. Rev. B* **1980**, *21*, 5469.

(22) Langreth, D. C.; Mehl, M. J. *Phys. Rev. B* **1983**, *28*, 1809.

(23) Langreth, D. C.; Vosko, S. H. *Adv. Quantum Chem.* **1990**, *21*, 175.

(24) Lynch, B. J.; Truhlar, D. G. *J. Phys. Chem. A* **2003**, *107*, 8996; **2004**, *108*, 1460(E).

(25) Young, D. A. *Phase Diagrams of the Elements*; University of California Press: Berkeley, 1991.

(26) Wyckoff, R. W. G. *Crystal Structures*; John Wiley & Sons: New York, London, 1963.

(27) (a) Touloukian, Y. S.; Kirby, R. K.; Taylor, R. E.; Desai, P. D. *Thermal Expansion-Metallic Elements and Alloys, Thermophysical Properties of Matter*; IFI/Plenum: New York, 2002; Vol. 12. (b) Touloukian, Y. S.; Kirby, R. K.; Taylor, R. E.; Lee, T. Y. R. *Thermal Expansion-Nonmetallic Solids, Thermophysical Properties of Matter*; IFI/Plenum: New York, 2002; Vol. 13.

(28) Wang, K.; Reeber, R. R. *Phys. Chem. Miner.* **1996**, *23*, 354360.

(29) *Landolt-Börnstein, New Series, Group III*; Hellwege, K.-H., Ed.; Springer: Berlin, 1966.

(30) Frisch, M. J.; Trucks, G. W.; Schlegel, H. B.; Scuseria, G. E.; Robb, M. A.; Cheeseman, J. R.; Montgomery, J. A., Jr.; Vreven, T.; Kudin, K. N.; Burant, J. C.; Millam, J. M.; Iyengar, S. S.; Tomasi, J.; Barone, V.; Mennucci, B.; Cossi, M.; Scalmani, G.; Rega, N.; Petersson, G. A.; Nakatsuji, H.; Hada, M.; Ehara, M.; Toyota, K.; Fukuda, R.; Hasegawa, J.; Ishida, M.; Nakajima, T.; Honda, Y.; Kitao, O.; Nakai, H.; Klene, M.; Li, X.; Knox, J. E.; Hratchian, H. P.; Cross, J. B.; Bakken, V.; Adamo, C.; Jaramillo, J.; Gomperts, R.; Stratmann, R. E.; Yazyev, O.; Austin, A. J.; Cammi, R.; Pomelli, C.; Ochterski, J. W.; Ayala, P. Y.; Morokuma, K.; Voth, G. A.; Salvador, P.; Dannenberg, J. J.; Zakrzewski, V. G.; Dapprich, S.; Daniels, A. D.; Strain, M. C.; Farkas, O.; Malick, D. K.; Rabuck, A. D.; Raghavachari, K.; Foresman, J. B.; Ortiz, J. V.; Cui, Q.; Baboul, A. G.; Clifford, S.; Cioslowski, J.; Stefanov, B. B.; Liu, G.; Liashenko, A.; Piskorz, P.; Komaromi, I.; Martin, R. L.; Fox, D. J.; Keith, T.; Al-Laham, M. A.; Peng, C. Y.; Nanayakkara, A.; Challacombe, M.; Gill, P. M. W.; Johnson, B.; Chen, W.; Wong, M. W.; Gonzalez, C.; Pople, J. A. Gaussian Development Version, Revision D.02; Gaussian, Inc.: Pittsburgh, PA, 2005.

(31) Heyd, J.; Peralta, J. E.; Scuseria, G. E.; Martin, R. L. *J. Chem. Phys.* **2005**, *123*, 174101.

(32) Csonka, G. I.; Perdew, J. P.; Ruzsinszky, A.; Philipsen, P. H. T.; Lebègue, S; Paier, J.; Vydrov, O. A.; Ángyán, J. G. 2008, submitted.

(33) Antoniewicz, P. R.; Kleinman, L. *Phys. Rev. B* **1985**, *31*, 6779.

(34) Armiento, R.; Mattsson, A. E. *Phys. Rev. B* **2005**, *72*, 085108.

(35) Pitarke, J. M.; Eguiluz, A. G. *Phys. Rev. B* **2001**, *63*, 045116.

(36) Wood, B.; Hine, N. D. H.; Foulkes, W. M. C.; García-González, P. *Phys. Rev. B* **2007**, *76*, 035403.

(37) Yan, Z.; Perdew, J. P.; Kurth, S. *Phys. Rev. B* **2000**, *61*, 16430.

CT8005369

JCTC Journal of Chemical Theory and Computation

Revisiting Molecular Dissociation in Density Functional Theory: A Simple Model

David G. Tempel,[§,†] Todd J. Martínez,[‡] and Neepa T. Maitra*[,†]

Department of Physics and Astronomy, Hunter College and City University of New York, 695 Park Avenue, New York, New York 10065, and Department of Chemistry and The Beckman Institute, University of Illinois, Urbana, Illinois 61801

Received December 4, 2008

Abstract: A two-electron one-dimensional model of a heteroatomic molecule composed of two open-shell atoms is considered. Including only two electrons isolates and examines the effect that the highest occupied molecular orbital has on the Kohn−Sham potential as the molecule dissociates. We reproduce the characteristic step and peak that previous high-level wave function methods have shown to exist for real molecules in the low-density internuclear region. The simplicity of our model enables us to investigate in detail their development as a function of bond-length, with little computational effort, and derive properties of their features in the dissociation limit. We show that the onset of the step is coincident with the internuclear separation at which an avoided crossing between the ground-state and lowest charge-transfer excited-state is approached. Although the step and peak features have little effect on the ground-state energetics, we discuss their important consequences for dynamics and response.

I. Introduction

The unprecedented balance between accuracy and efficiency of density functional theory (DFT)[1−5] is in large part the result of the discoveries of John Perdew. The mapping of the true system of interacting electrons to a fictitious one in which the electrons do not interact, yet reproduce the true electron density, requires accurate approximations for the exchange-correlation (xc) potential, which remained elusive until the developments in the 1980's of Perdew and co-workers. Understanding and incorporating exact conditions and physical principles underlie the robustness and reliability of Perdew's functionals. In this spirit, we study here the structure of the exact xc potential as a molecule dissociates, whose landscape of steps and peaks Perdew was one of the first to explore.

In DFT, one solves self-consistently the Kohn−Sham (KS) single-particle equations

$$\left(-\frac{1}{2}\nabla^2 + v_S[\rho](\mathbf{r})\right)\phi_i(\mathbf{r}) = \epsilon_i\phi_i(\mathbf{r}) \tag{1}$$

where $v_S[\rho](\mathbf{r})$ is the KS potential, a functional of the ground-state electronic density, ρ. (Atomic units, $e^2 = \hbar = m_e = 1$, are used throughout this paper). It is usually written as the sum $v_S[\rho](\mathbf{r}) = v_{ext}[\rho](\mathbf{r}) + v_H[\rho](\mathbf{r}) + v_{XC}[\rho](\mathbf{r})$, where $v_{ext}(\mathbf{r})$ is the potential due to the nuclei, $v_H(\mathbf{r}) = \int d^3\mathbf{r}'\rho(\mathbf{r}')/|\mathbf{r} - \mathbf{r}'|$ is the classical Hartree potential and $v_{XC}(\mathbf{r})$ is the exchange-correlation (xc) potential, incorporating the remaining many-body effects in a one-body potential. The KS orbitals ϕ_i yield the true density according to

$$\rho(\mathbf{r}) = \sum_{i=1}^{N}\phi_i(\mathbf{r})^2 \tag{2}$$

In principle, the ground-state density and all static properties of the true interacting system are exactly recovered, but in practice approximations are needed for the unknown xc potential $v_{xc}[\rho]$ as a functional of the density. Typically, semilocal functionals, such as GGA's[6] and meta-GGA's[7,8] give good energies and structural properties at equilibrium

* To whom correspondence should be addressed. E-mail: nmaitra@hunter.cuny.edu

† Department of Physics and Astronomy, Hunter College and City University of New York.

‡ Department of Chemistry and The Beckman Institute, University of Illinois.

§ Present address: Department of Physics, Harvard University, 17 Oxford Street, Cambridge, MA 02138.

10.1021/ct800535c CCC: $40.75
Published on Web 03/17/2009

molecular geometries; the nonempirical constructions of Perdew and co-workers impart a reliability to the description of diverse systems and properties. However, GGA's do not perform so well for weakly coupled subsystems. Notably, recent work has been very successful in describing van der Waal's forces using sophisticated nonlocal approximations in DFT.[9−11] For molecules dissociating into open-shells, the failure of semilocal approximations becomes drastic, yielding unphysical fractional charges on the separated species.[12−15] This problem was first highlighted by Perdew,[13,14] motivated by the observation of Slater[12] that his "$X\alpha$" method yields a similar result.

Figure 7 of ref 14 shows that the exact xc potential develops a "region of positive constant" around the atom with the "tighter density distribution", in the limit of infinite separation, using a simple one-dimensional model. More generally, the effect of molecular dissociation on the ground-state xc potential for the case of real diatomic closed-shell molecules consisting of open shell atoms has been studied systematically, by Baerends, Gritsenko, and co-workers, in a series of papers.[16−21] In ref 16, the simplest case of this, the two-electron H_2 molecule was studied. The absence of long-range left-right correlation in Hartree−Fock, renders its potential overly repulsive near the nuclei, leading to an overly diffuse density. A highly accurate xc potential was constructed from correlated CISD first- and second- order density matrices in ref. 16, and the resulting correlation potential was shown to considerably reduce the repulsion at the nuclei. It was also shown that the xc potential develops a sharp maximum (peak) at the bond midpoint. A very thorough analysis of the KS potential in stretched H_2 was performed later in ref 21, where the effect of different approximate constructions for the KS orbital was investigated and explained in detail (see also section IVB). Using an iterative method introduced in ref 22, the authors of ref 17 were the first to construct molecular KS potentials for more than two electrons from correlated densities. They studied LiH (and H_2) and found significant differences with the local density approximation (LDA) at large separations. The authors of ref 19 calculated the xc potential for the monohydrides XH (X = Li, B, F), analyzing its structure via a decomposition or "partitioning" of v_{XC} into various "energy" and "response" components related to the electronic structure.[16,18,20] It was shown that left-right correlation leads to a build-up in the xc potential around the H atom (a "step", as was observed in the simple model of ref 14). The peak present in the bond midpoint of H_2 was found, in the case of the monohydrides, to shift toward the H atom while becoming significantly smaller because of the presence of core electrons softening the left-right correlation effects. The partitioning scheme (reviewed in section II), which had earlier been used to examine atomic xc potentials,[18,20] proved to be a particularly useful tool in the analysis, providing insight into the origin of the peak and step structures.

Molecular dissociation in DFT is particularly relevant when considering time-dependent processes and nuclear dynamics on potential energy surfaces. The advent of time-dependent density functional theory (TDDFT)[23−25] allows for a density-functional description of full electron dynamics and here accurate long-range potentials are an important ingredient for many applications, for example, photodissociation dynamics, excitations in large molecules, including charge-transfer, and molecular transport. A recent paper[26] discussed promising aspects, as well as challenges, in getting accurate excited energy surfaces from TDDFT; certainly it is important to get the ground-state potential energy surface correct.

In the present paper, we study the xc potential of a dissociating closed-shell heteroatomic molecule consisting of two open-shell atoms by analyzing a simple one-dimensional model of two different "one-electron atoms". The two "electrons" and two "nuclei" interact via soft-Coulomb interactions with the softening parameters chosen to approximate certain properties of the real LiH molecule. This simple model allows numerically exact solution at a wide range of separations with little computational effort, while reproducing the essential features, from the point of view of molecular dissociation, of the xc potential for real three-dimensional molecules. It allows some analytic treatment of these features that yields further insight into the "step" and "peak" structures mentioned above; for example, predicting the asymptotic height and position of the peak and an explanation of why such a structure, that hardly affects the energetics, must be there. A detailed examination of the stretched bond-length where the step begins to appear, reveals a correlation with the position of the avoided crossing between the ground-state and lowest charge-transfer states. We explain why.

A two-electron model isolates the effects caused by the valence electrons, which play the major role in dissociative processes, without additional potential-features arising from core electrons. In the KS description of dissociation, the major role is played by the KS HOMO, which in the case of open-shell fragments, is delocalized across the molecule. By including only the HOMO in our model, we isolate and examine effects on the dissociating potential energy surface caused solely by this most important orbital. The model is presented in section III, while section IV contains the numerical and analytic results.

We may draw conclusions from this simple model about real three-dimensional molecules composed of open-shell fragments of general odd electron-number, but with a little caution: we find quantitative differences resulting from the lack of core electrons in our model and the much longer effective range of the soft-Coulomb interaction in 1D compared to the true 3D Coulomb interaction. The soft-Coulomb interaction is used in many interesting investigations of strong-field dynamics[27−32] and, recently, in the context of TDDFT:[33,34] these models capture the essence of phenomena such as nonsequential double-ionization, and laser-induced electron-recollision. The peak and step are challenging features for approximations to capture and are lacking in almost all functionals used today. Being in a low-density region, the peak structure has negligible energetic consequence; however it does play a role when response or full dynamics is considered: for example, it reduces the (hyper-)polarizability of long-chain systems.[35] Because they represent barriers to electron transport, the work here is also

relevant to one-dimensional transport calculations in molecular wires,[36] although this fact has not been discussed before, so perhaps not yet been fully appreciated. The step structure, essential to avoid the fractional charge problem, has severe consequences for the structure of the TDDFT xc kernel as we discuss in section V.

II. Decomposition of the xc Potential

The partitioning of the xc potential[16−20] was motivated by first decomposing the xc energy components into "potential" and "kinetic" terms of the form:

$$\begin{aligned} E_{xc}[\rho] &= W_{xc}[\rho] + T_c[\rho] \quad \text{where} \\ W_{xc}[\rho] &= \frac{1}{2}\int \rho(\mathbf{r}) v_{xc}^{hole}[\rho](\mathbf{r}) d^3r \quad \text{and} \\ T_c[\rho] &= \int \rho(\mathbf{r}) v_c^{kin}[\rho](\mathbf{r}) \end{aligned} \tag{3}$$

implicitly define hole and correlation kinetic potentials, v_{xc}^{hole} and v_c^{kin}. The total xc potential is then partitioned into three components

$$v_{xc}[\rho](\mathbf{r}) = v_{xc}^{hole}[\rho](\mathbf{r}) + v_{c,kin}[\rho](\mathbf{r}) + v_{resp}[\rho](\mathbf{r}) \tag{4}$$

$v_{xc}^{hole}[\rho](\mathbf{r})$ is the Coulomb potential of the xc hole

$$v_{xc}^{hole}(\mathbf{r}) = \int \frac{\rho_{xc}(\mathbf{r}, \mathbf{r}_2)}{|\mathbf{r} - \mathbf{r}_2|} d^3\mathbf{r}_2 \tag{5}$$

where the xc hole $\rho_{xc}(\mathbf{r}_1, \mathbf{r}_2)$ is defined through the pair density $P(\mathbf{r}_1, \mathbf{r}_2)$ (joint probability of finding an electron at $\mathbf{r}_1$ while another is at $\mathbf{r}_2$), via $P(\mathbf{r}_1, \mathbf{r}_2) = \rho(\mathbf{r}_1)(\rho(\mathbf{r}_2) + \rho_{xc}(\mathbf{r}_1, \mathbf{r}_2))$. When added to the Hartree potential, $v_{xc}^{hole}(\mathbf{r}) + v_H(\mathbf{r})$ represents the average repulsion an electron at position $\mathbf{r}$ experiences caused by the other (N-1) electrons in the system. In terms of the conditional probability amplitude, whose square gives the probability of finding the other (N-1) electrons in the system with space-spin coordinates $\mathbf{x}_2$, $\mathbf{x}_3$,..., $\mathbf{x}_N$ when an electron is known to be at position $\mathbf{r}_1$

$$\Phi(s_1, \mathbf{x}_2, ..., \mathbf{x}_N|\mathbf{r}_1) = \frac{\Psi(\mathbf{x}_1, \mathbf{x}_2, ..., \mathbf{x}_N)}{\sqrt{\frac{\rho(\mathbf{r}_1)}{N}}} \tag{6}$$

where $\Psi(\mathbf{x}_1, \mathbf{x}_2, ..., \mathbf{x}_N)$ is the interacting many-electron wave function, we have

$$v_{xc}^{hole}(\mathbf{r}) + v_H(\mathbf{r}) = \int \Phi^*(s_1, \mathbf{x}_2, ..., \mathbf{x}_N|\mathbf{r}) \times \left[\sum_{i=2}^{N} \frac{1}{|\mathbf{r} - \mathbf{r}_i|}\right] \Phi(s, \mathbf{x}_2, ..., \mathbf{x}_N|\mathbf{r}) ds_1 d\mathbf{x}_2 ... d\mathbf{x}_N \tag{7}$$

The second term in eq 4, $v_{c,kin}[\rho](\mathbf{r})$, is the correlation contribution to the kinetic component of the xc potential. It is the difference of the kinetic components of the interacting and noninteracting KS systems

$$v_{c,kin}(\mathbf{r}) = v_{kin}(\mathbf{r}) - v_{s,kin}(\mathbf{r}) \tag{8}$$

where the kinetic components may be written in terms of the conditional probability amplitude

$$\begin{aligned} v_{kin}(\mathbf{r}_1) &= \frac{1}{2}\int |\nabla_1 \Phi(s_1, \mathbf{x}_2, ..., \mathbf{x}_N|\mathbf{r}_1)|^2 ds_1 d\mathbf{x}_2 ... d\mathbf{x}_N \\ &= \frac{\nabla_1' \nabla_1 \rho(\mathbf{r}_1', \mathbf{r}_1)^2\Big|_{r_1 = r_1'}}{\rho(\mathbf{r}_1)} - \frac{[\nabla\rho(\mathbf{r}_1)]^2}{8\rho(\mathbf{r}_1)^2} \end{aligned} \tag{9}$$

and

$$\begin{aligned} v_{s,kin}(\mathbf{r}_1) &= \frac{1}{2}\int |\nabla_1 \Phi_s(s_1, \mathbf{x}_2, ..., \mathbf{x}_N|\mathbf{r}_1)|^2 ds_1 d\mathbf{x}_2 ... d\mathbf{x}_N \\ &= \frac{1}{2}\sum_{i=1}^{N} \left|\nabla_1 \frac{\phi_i(\mathbf{r}_1)}{\rho^{1/2}(\mathbf{r}_1)}\right|^2 \end{aligned} \tag{10}$$

In eq 9, $\rho(\mathbf{r}_1', \mathbf{r}_1)$ is the first-order spin-summed reduced density-matrix, and in eq 10, $\Phi_s(s_1, \mathbf{x}_2, ..., \mathbf{x}_N|\mathbf{r}_1)$ is the conditional probability amplitude of the KS system, which is defined as in eq 6 but with the KS single Slater determinant, whose orbitals are $\phi_i(\mathbf{r})$, replacing the full many-electron wave function.

The final term in eq 4 is the so-called response potential. It may be further partitioned into terms representing the response of the xc hole and the response of the correlation kinetic potential,[18,19] but we will not pursue this further decomposition here.

For two electrons in a spin-singlet, many of these expressions simplify considerably, as the KS single-Slater determinant consists of one doubly occupied spatial orbital, $\phi_0(\mathbf{r})$, which is equal to square root of half the density

$$\phi_0(\mathbf{r}) = \sqrt{\frac{\rho(\mathbf{r})}{2}} \tag{11}$$

Substituting into eq 1, we can solve explicitly for the KS potential as a functional of the density

$$v_S[\rho](\mathbf{r}) = \frac{\nabla^2\sqrt{\rho(\mathbf{r})}}{2\sqrt{\rho(\mathbf{r})}} - I \tag{12}$$

where I is the first ionization potential of the system. From eq 10, $v_{s,kin}(\mathbf{r}) = 0$ and eq 8 reduces to

$$v_{c,kin}(\mathbf{r}) = v_{kin}(\mathbf{r}) \tag{13}$$

Also, for two electrons, $v_x(\mathbf{r}) = v_x^{hole}(\mathbf{r}) = -(1/2)v_H(\mathbf{r})$. The exchange component to the response potential, v_{resp} is zero. We may therefore write

$$v_x(\mathbf{r}) = -v_H(\mathbf{r})/2 = v_x^{hole}(\mathbf{r}) \tag{14}$$

$$v_c(\mathbf{r}) = v_c^{hole}(\mathbf{r}) + v_{c,kin}(\mathbf{r}) + v_{c,resp}(\mathbf{r}) \tag{15}$$

As was found in refs 18 and 19, as a heteroatomic molecule dissociates, a step structure in the low-density bond midpoint region arises in the response component, v_{resp}, accompanied by a peak structure in the kinetic component $v_{c,kin}$ of the xc potential (see also Figures 3 and 4).

Consider now a simplified description of the molecule that has includes just one electron on each atom. As explained in ref 16 and reflected in eq 9, $v_{kin}(\mathbf{r})$ depends on the gradient of the conditional probability amplitude, so describes how

strongly the motion of an electron at reference position **r** is correlated with the other electrons in the system. For **r** near one of the nuclei, the reference electron moves in a potential dominated by the nuclear potential, the conditional amplitude Φ reduces to the atomic HOMO of the other atom, and does not change for small changes around **r**; hence $v_{\rm kin}$ goes to zero. But in the internuclear region, the motion of the two electrons becomes correlated: as the reference position moves from one nucleus to the other, the conditional probability of finding the other switches from being toward one atom to the other, and so $v_{\rm kin}$ peaks.

The origin of the step structure was also analyzed extensively in ref 19 and shown to arise in the correlation component of the response potential, $v_c^{\rm resp}$. It was discovered earlier,[14,39] in relation to the derivative discontinuity,[13,14,39,40] that the correlation potential for a long-range molecule composed of two open-shell atoms must have a step in the midpoint region, whose size is such that the atomic HOMO orbital energies realign. From Koopman's theorem, the HOMO energy equals the ionization potential; therefore the step has a size $\Delta I = I_2 - I_1$, where $I_{2,1}$ is the larger(smaller) ionization potential of the two atoms, raising the potential of the more tightly bound atom. Far away from the molecule the potential near this atom steps back down to zero. A simple way to understand the origin of the step is to realize that had the step not been there, then one could lower the ground-state energy of the long-range molecule by transferring a fraction of charge from the atom with the higher ionization potential to that with the lower, leading to the molecule dissociating into fractionally charged species. Because this cannot happen, the KS potential develops a step in the bonding region, which realigns the atomic HOMOs, so preventing any bias. Another way to put this is that the chemical potential must be the same throughout the long-range molecule and equal to the molecular HOMO orbital energy. Since the chemical potential of the true system is the smallest ionization potential in the system at infinite separation, the KS potential near the atom with the larger atomic ionization potential must be uniformly raised by ΔI to bring it to the ionization potential of the other atom, while asymptotically stepping back down to zero.

We shall now introduce our two-electron model to study these features further and how they develop as a function of bond-length.

III. A One-Dimensional Two-Electron Model of LiH

A simple one-dimensional, two-electron model of lithium hydride can be used to illustrate several important features of heteroatomic dissociation. Much of the essential physics of the dissociation process may be captured by focusing on the chemically important valence electrons, while representing the effect of the core electrons by an average effective potential, such as a pseudopotential or frozen-core approximation. In the case of LiH, the two core electrons are localized in the Li 1s shell, while the two valence electrons are delocalized across the molecule. Our goal is to analyze the effect of bond breaking and formation on the various xc components (eq 4), which in a real molecule will be partially obscured by shell structure and other many-electron effects from the electrons in the Li 1s core. Our two-electron model enables us to circumvent this complication, by focusing solely on the electrons involved in the bond, and their effect on the Kohn−Sham characteristics. As further simplication, it is reasonable to use a one-dimensional model, where the coordinate is taken to be along the bond axis, for cylindrically symmetric systems such as a diatomic molecule.

As is often done in one-dimensional models, the Coulomb potential $\pm 1/|\mathbf{r} - \mathbf{r}'|$ is replaced by a soft-Coulomb potential, $\pm 1/[a + (x - x')^2]^{1/2}$. For a model of LiH at interatomic separation R, we write the electron−nuclear potential as

$$v_{\rm ext}(x) = -\frac{1}{\sqrt{a + (x - R/2)^2}} - \frac{1}{\sqrt{b + (x + R/2)^2}} \quad (16)$$

The "softening parameters" a and b are directly related to the ionization potentials of the individual atoms (see shortly). Similarly, the electron−electron repulsion is represented by a soft-Coulomb form

$$v_{\rm ee}(x_1, x_2) = \frac{1}{\sqrt{c + (x_1 - x_2)^2}} \quad (17)$$

We place Li at $-R/2$ and H at $R/2$, and choose the parameters $a = 0.7$, $b = 2.25$, and $c = 0.6$, for reasons explained in the following. With $a = 0.7$, the ionization potential of hydrogen in our model comes out to be 0.776H as compared with 0.5H for the real atom. Taking $b = 2.25$ yields that of Li in our model as 0.476H as compared with 0.198H for the real lithium atom. The correct difference in ionization potentials of the atoms $\Delta I = I_{\rm H} - I_{\rm Li} = 0.3$H is however exactly reproduced by our parameters; ΔI is a key quantity in our analysis of the KS potential at large interatomic separations. Because of the long-range nature of the soft-Coulomb interaction, we choose the atomic ionization potentials be larger than in the true 3D case to prevent the atomic densities of the individual atoms from being too diffuse. Other factors considered were the equilibrium bond length (model 1.6 au, true 3.0 au), dissociation energy (model 0.068H, true 0.092H) and molecular first ionization potential (model 0.51H, true 0.29H), where the nuclear−nuclear interaction is modeled by

$$v_{\rm nn}(R) = \frac{1}{\sqrt{(a + b - c) + R^2}} \quad (18)$$

In Figure 1, the dissociation curve for our model is plotted for comparison with that of 3D LiH.[41]

IV. Numerical Solution and Results

We use a standard Runge−Kutta differential equation solver, as implemented in the octopus code,[42−44] to numerically solve for the ground-state wave function $\Psi(x, x')$ of the Hamiltonian:

$$H = -\frac{1}{2}\frac{d^2}{dx_1^2} - \frac{1}{2}\frac{d^2}{dx_2^2} + v_{\rm ext}(x_1) + v_{\rm ext}(x_2) + v_{\rm ee}(x_1 - x_2) \quad (19)$$

where $v_{ext}(x)$ and $v_{ee}(x_1 - x_2)$ are defined in eqs 16 and 17. The above two particle Hamiltonian is mathematically equivalent to that of one particle moving in the two-dimensional potential[42−44]

$$v_{ext}(x) + v_{ext}(y) + v_{ee}(x - y) \tag{20}$$

We solve the equivalent one-particle Schrödinger equation on a rectangular two-dimensional 25 by 25 au real space grid. The grid points are separated by a distance of 0.04 au.

The density is obtained from the wave function through $\rho(x) = 2\int dx' |\Psi(x, x')|^2$ and then substituted into eq 12 to yield the exact KS potential. The xc potential can be isolated from subtracting the external potential eq 16 and the Hartree potential, $v_H(x) = \int \rho(x) v_{ee}(x - x')dx'$ (using v_{ee} from eq 17). Because $v_X(x) = -v_H(x)/2$, we may also extract the correlation potential alone $v_c(x)$. From the conditional probability amplitude 6, we construct $v_{xc}^{hole}(x)$ according to eq 7.

The exact KS potential is plotted at several different internuclear distances in Figure.(2) alongside the external potential and the density. As the molecule dissociates, steplike and peaklike features clearly develop in the KS potential. There is a build-up in the KS potential around the more electronegative atom that, at each R, eventually returns to zero on the right-hand side of the atom (one sees the beginning of the return to zero at the smaller separations shown, but at separation $R = 10.0$, this occurs beyond the region plotted).

These features occur in the response and kinetic components of the correlation potential, as is evident in Figure 3. Here, we plot the xc potential (solid), which is the sum of the xc-hole potential (dotted) and the response components $v_{c,\,kin} + v_{resp}$ (dashed). At equilibrium bond-length ($R = 1.6$ au), the xc potential is dominated by the potential of the xc hole. As the molecule dissociates the $v_{c,\,kin} + v_{resp}$ components become large giving rise to clear peak and step structures. At large separation, the local variation of the total xc potential around each atom is almost entirely caused by the xc hole: at $R = 6.0$ au and 10.0 au, v_{xc} and v_{xc}^{hole} exactly coincide near Li, while near H they have the same shape, but the well in v_{xc} is translated upward by exactly 3.0 au relative to v_{xc}^{hole}, which is the magnitude of the step ΔI (see section II). At $R = 6.0$ au, the step has reached its asymptotic value of $I_H - I_{Li} = 3.0$ au. As the molecule is pulled apart further, the step does not increase in size, but becomes flatter and larger in spatial extent. In section IVA, we show that the bond-length at which the step begins to develop is related to the position of the avoided crossing between the ground-state and the state that eventually becomes the lowest charge-transfer state.

A sharp peak near the rise of the step is evident in the xc potential (Figure 3); this occurs in the kinetic component to the correlation potential, $v_{c,kin}$, as discussed in section II. We return to an analysis of its magnitude and location in the widely separated limit and an explanation of its role in achieving the exact density of the interacting system in section IVB.

In Figure 4, we plot the potentials for the separation $R = 10.0$. This is the largest separation for which we could converge our numerical method. In the limit of very large separation, we expect that the KS potential reduces simply

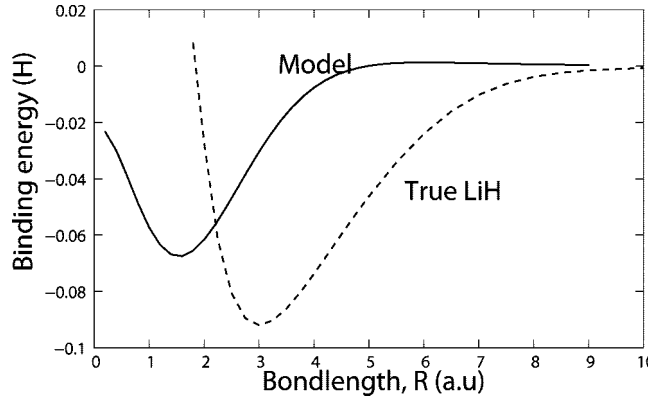

Figure 1. Binding energy for (1) model 1D LiH and (2) true 3D LiH.

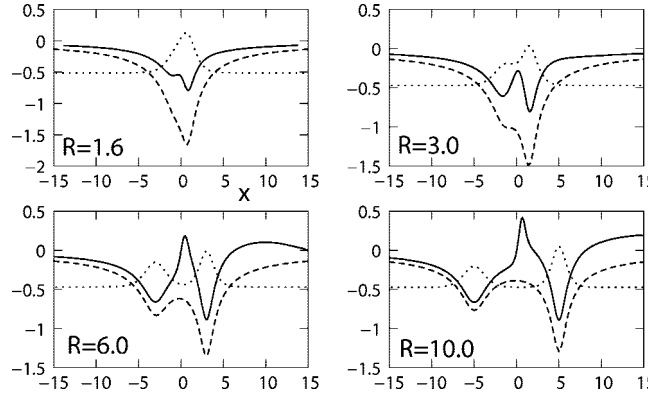

Figure 2. v_S (solid curves), v_{ext} (dashed), and the density (dotted curves) plotted at the internuclear separations indicated.

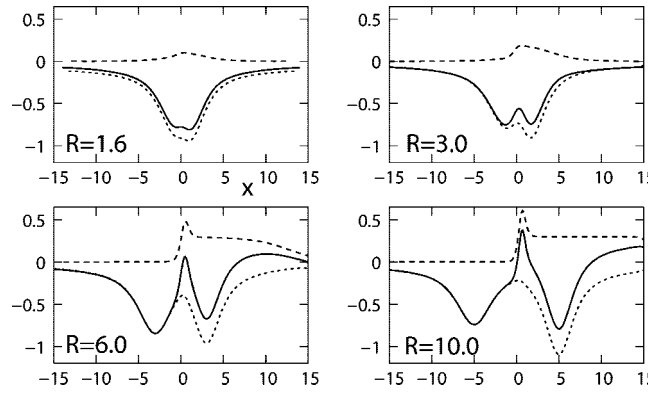

Figure 3. Total xc potential v_{xc} (solid curves), $v_{c,kin} + v_{resp}$ (dashed curves), v_{xc}^{hole} (dotted curves) at various internuclear separations.

to the external potential in the region of the nuclei because it would be a one-electron system around each nucleus. There may be a possible shift up or down relative to the external potential because constants in potentials have no physical relevance. That is, we expect the Hartree-plus-xc potential becomes flat in the atomic regions. We notice in our model at $R = 10.0$, that this is approximately true: there is however a gentle slope in v_{Hxc}, upward around the left nucleus, and downward on the right, and this is largely the result of a Hartree effect. Compared to the atomic densities in true Coulomb-interacting systems, the soft-Coulomb densities in

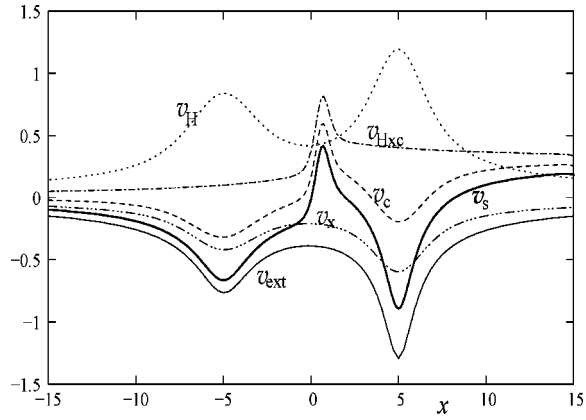

Figure 4. Components of the potentials for $R = 10.0$.

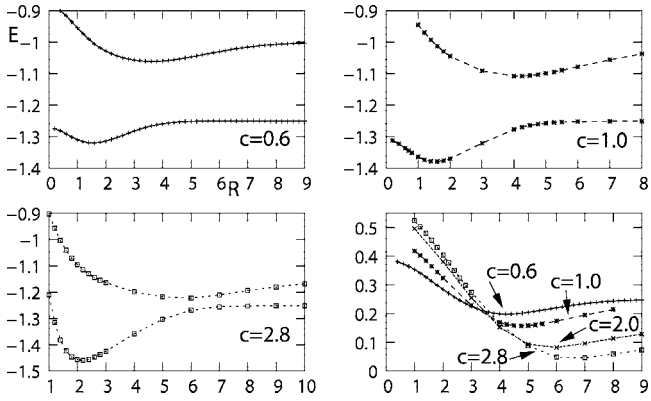

Figure 5. Ground-state and first-excited state (charge-transfer) potential energy surfaces for our model with $c = 0.6$ (top left), $c = 1.0$ (top right), $c = 2.8$ (bottom left). The energy differences between the surfaces are shown in the bottom right figure; their minimum lies at the avoided crossing.

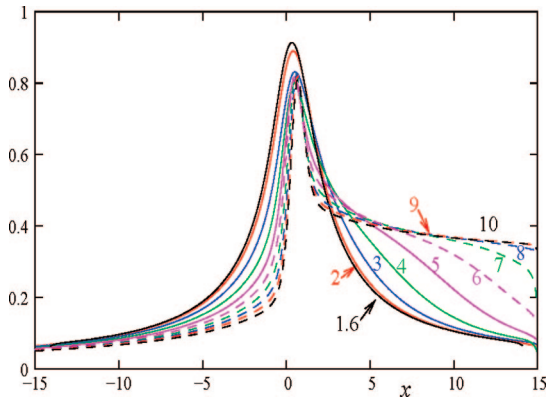

Figure 6. Hartree-exchange-correlation potential, $v_{Hxc}(x)$ for our LiH model ($c = 0.6$); the values of interatomic separation R are indicated.

one-dimension fall off much slower away from their nuclei, resulting in a longer-ranged Hartree and xc potential than in the true 3D counterpart. It is clear from the graph that the Hartree potential is still significant in the interatomic region. In addition to long-ranged correlation effects from the density on the "other" atom (i.e., the peak and step), the xc potential must cancel the local Hartree potential: the exchange potential takes care of half of this cancelation (eq 14), but the correlation potential must also contribute a well of half

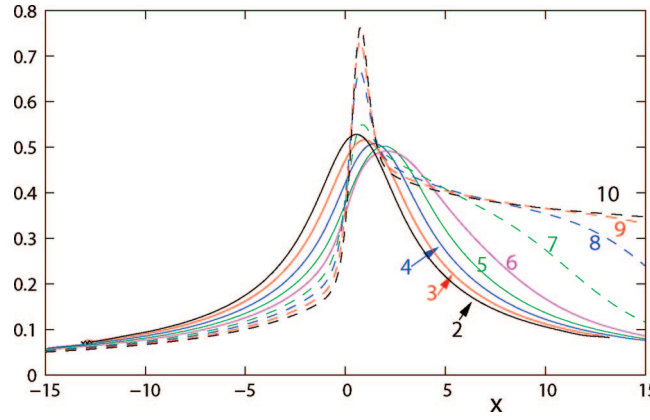

Figure 7. Hartree-exchange-correlation potential, $v_{Hxc}(x)$ for our LiH model ($c = 2.8$); the values of interatomic separation R are indicated.

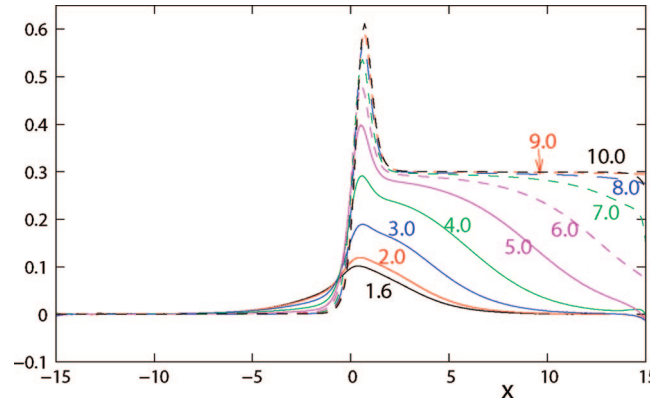

Figure 8. Kinetic and response components of the correlation potential $v_{c,kin} + v_{c,resp}$ for our model with $c = 0.6$; the values of interatomic separation R are indicated.

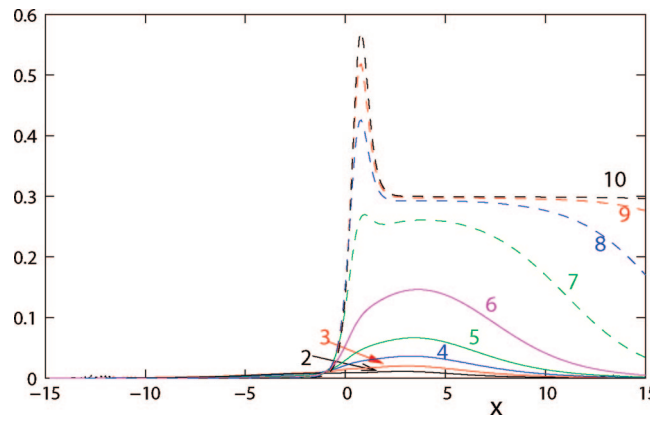

Figure 9. Kinetic and response components of the correlation potential $v_{c,kin} + v_{c,resp}$ for our model with $c = 2.8$.

the size of the Hartree, as is evident in the graph. Despite the long-rangedness of the Hartree potential, $R = 10.0$ can still be viewed as "asymptotic" from the point of view of the peak and step structures in the correlation potential: the graph shows clearly that the potential on the hydrogen nucleus on the right is raised by ΔI, and the peak has a height of about 0.76 (see last section).

A. Onset of the Step: Relation to Potential Energy Surface Crossings. We now show that the bond-length at which the step begins to significantly develop is correlated

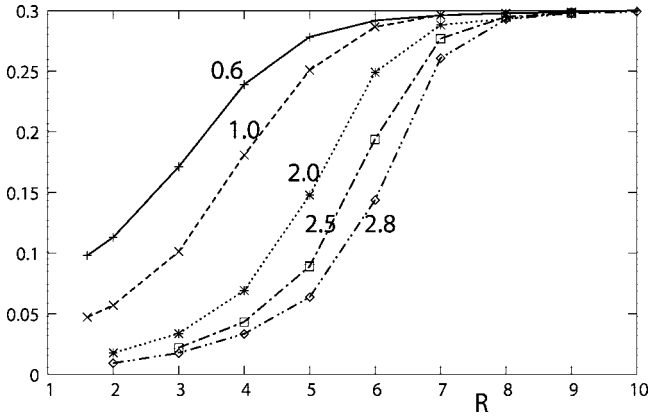

Figure 10. Value of $v_{c\,kin} + v_{resp}$ at the location of the H atom in our model, as a function of the internuclear separation R, and with c-values as indicated.

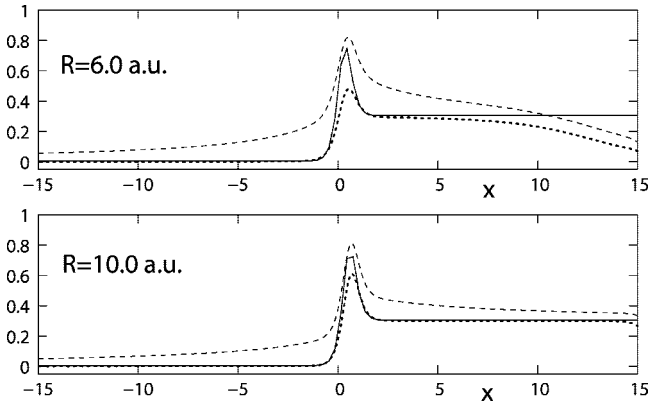

Figure 11. Asymptotic expression for v_{Hxc} (solid curve) in the interatomic region compared to v_{Hxc} in our model (dashed curve), and $v_{kin} + v_{resp}$ (dotted line) in our model at separations indicated.

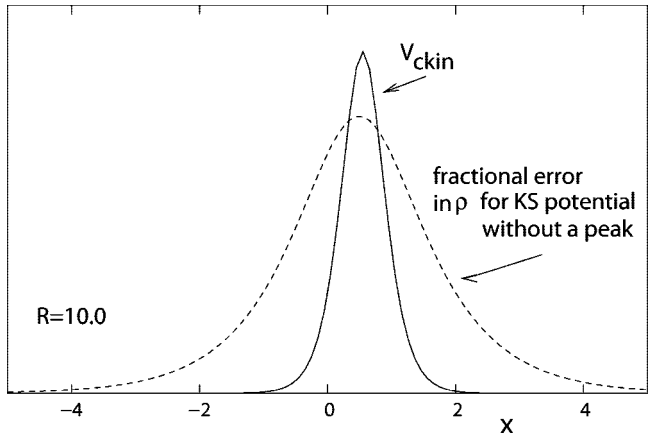

Figure 12. Peak in $v_{c\,kin}(x)$ and that in the fractional density-error of the KS orbital solution to the KS potential with the peak taken out, $\sqrt{(\rho_H\rho_{Li})}/(\rho_H + \rho_{Li})$, (see text) have the same location.

with the position of the avoided crossing in the potential energy surfaces associated with the ground-state and the lowest excited charge transfer state. In a diabatic picture, ionic and covalent curves cross at an internuclear distance, R_C, which is approximately equal to $1/(I_D - A_A)$, where I_D is the ionization energy of the donor and A_A the electron affinity of the acceptor, in the lowest charge-transfer state of the long-range molecule.[45] When one considers the adiabatic potential energy surfaces, the crossing becomes an avoided one, whose splitting exponentially decreases as a function of R_C.[45]

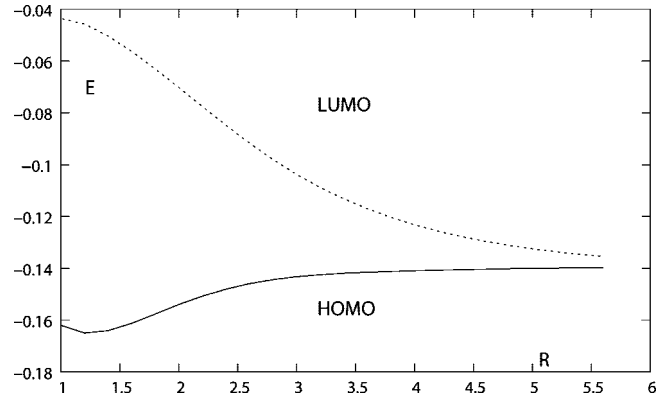

Figure 13. LSD KS eigenvalues for LiH become near-degenerate as a function of internuclear separation R.

What has not been previously pointed out, however, is that the step structure in the KS potential begins to develop in the vicinity of the avoided crossing. Why this must be so lies in the fact that the step is an asymptotic feature, that arises once the two atoms are independent systems, and its shift of the eigenvalues of the more tightly bound atom ensures that the ground-state solution of the KS potential has exactly half the density (i.e., one electron) on either side of the midpoint (see section II). The development of the step must therefore track the independence of the two atomic systems (measured, for example, by their indifference to a perturbation on the other atom). The avoided crossing marks the point at which the molecule transitions (moving from short bond distances to longer ones) from a single system to two independent systems. The width of this transition tracks the magnitude of the ground-excited energy gap at the avoided crossing, that is, it should be wider when the avoided crossing is at small bond distances and sharper when the avoided crossing occurs at large distances.

Our model demonstrates this explicitly. Figure 5 presents the ground- and first excited-state potential energy surfaces for three different values of the electron−electron soft-Coulomb parameter, c. As c increases, the avoided crossing moves out and becomes sharper; the lowest-energy gap therefore decreases, indicating that the transition from ionic to covalent character occurs more abruptly.

In Figure 6, we plot the Hartree plus xc potential, $v_{Hxc}(x) = v_H(x) + v_{xc}(x)$ for a range of internuclear separations R, for $c = 0.6$. Because this is the net potential that gets added to the external potential, we expect that in the limit of wide separation, it becomes flat around each nucleus because it should describe essentially two one-electron systems. We see this in the graph, where a definite step is visible from $R = 5.0$ and higher. We see that it is indeed in the approach to the avoided crossing, at about $R = 4.0$, that a shoulder first becomes clearly visible around the atom with the higher IP; this develops fully into a step of size ΔI, as the molecule dissociates.

In Figure 7, we plot v_{Hxc} for $c = 2.8$. The step begins to develop at larger R, corresponding to the larger R_C where the avoided crossing occurs. Also, as the avoided crossing becomes sharper, the onset of the step happens more rapidly.

The long-rangedness of the density in soft-Coulomb systems means that the Hartree and exchange terms decay slower than in the usual Coulomb case. To clarify the step and peak structures, we plot just the kinetic plus response term in Figure 8 for our LiH model of $c = 0.6$ and in Figure 9 for $c = 2.8$. The relation between the R at which the step develops and the avoided crossing discussed above is seen more clearly in these figures. Finally, in Figure 10, we plot the value of $v_{c,kin} + v_{resp}$ at the location of the atom with the larger IP (the H atom in our model), as a function of internuclear separation R, for various different c-values. This graph shows quite clearly that the development of the step tracks the location and sharpness of the avoided crossing: the larger the separation at which the avoided crossing occurs (i.e., larger c-value), the consequently larger R the step is onset and that the step develops more sharply, corresponding to the sharper avoided crossing at larger distances.

B. Asymptotic Separation Limit, and the Significance of the Peak. Analytic expressions for the xc potential and its components in our two-electron model can be found in the separated-atom limit, by adopting the Heitler−London form for the wave function

$$\Phi_{HL}(x,x') = \frac{\phi_H(x)\phi_{Li}(x') + \phi_{Li}(x)\phi_H(x')}{\sqrt{2(1 + S_{H,Li}^2)}} \tag{21}$$

where $S_{H,Li}$ is the overlap integral

$$S_{H,Li} = \int \phi_H(x)\phi_{Li}(x)dx \tag{22}$$

We will focus on the interatomic region, far from either nuclei, in this limit. To lowest order in the separation R, the orbitals $\phi_{Li}(x)$ and $\phi_H(x)$ in this region may be written

$$\begin{aligned} \phi_H(x) &= \sqrt{\alpha_H} e^{\alpha_H(x-\frac{R}{2})} \\ \phi_{Li}(x) &= \sqrt{\alpha_{Li}} e^{-\alpha_{Li}(x+\frac{R}{2})} \end{aligned} \tag{23}$$

where $\alpha = \sqrt{(2I)}$, with I being the first ionization potential of the atom. Similar expressions hold for the three-dimensional case, with Coulomb interaction; the only differences being that instead the orbitals have asymptotic dependence according to

$$\phi(x) = \alpha^{3/2} e^{-\alpha[(x \pm (R/2))^2 + y^2 + z^2]^{1/2}} \tag{24}$$

(where the x-axis is taken to be the bond axis).

It is a simple exercise to construct the first-order density-matrix and the density using these orbitals. Substituting into eqs 12 and 9 yields the large-separation limit of the KS potential and $v_{kin}(r)$.

In the limit of large interatomic separation, the Hartree potential vanishes as the inverse distance from the nuclei in the interatomic region. Also, in this limit, the second-order density matrix factorizes into a product of densities and it follows from eq 5 that $v_{xc}^{hole}(r)$ also falls off as the inverse distance from the nuclei in the interatomic region. The KS potential is then dominated by contributions from $v_{kin}(r)$ and $v_{resp}(r)$. Explicitly, in one dimension, this is given by

$$\begin{aligned} v_S = &\frac{1}{2}\frac{|\phi'_H|^2 + |\phi'_{Li}|^2 + 2\sqrt{\epsilon}(\phi'_H)(\phi'_{Li})}{|\phi_H|^2 + |\phi_{Li}|^2 + 2\sqrt{\epsilon}\phi_H\phi_{Li}} + \\ &\frac{1}{2}\frac{\phi_H\phi''_H + \phi_{Li}\phi''_{Li} + \sqrt{\epsilon}(\phi_{Li}\phi''_H + \phi_H\phi''_{Li})}{|\phi_H|^2 + |\phi_{Li}|^2 + 2\sqrt{\epsilon}\phi_H\phi_{Li}} - \\ &\frac{1}{4}\frac{(\phi_H\phi'_H + \phi_{Li}\phi'_{Li} + \sqrt{\epsilon}(\phi_{Li}\phi'_H + \phi_H\phi'_{Li})^2}{(|\phi_H|^2 + |\phi_{Li}|^2 + 2\sqrt{\epsilon}\phi_H\phi_{Li})^2} - I_{Li} \end{aligned} \tag{25}$$

In the above expression, ϕ' and ϕ'' denote the first and second spatial derivatives of the orbital, and ε is the square of the overlap integral at interatomic separation R

$$\epsilon = \frac{\alpha_H\alpha_{Li}}{(\alpha_H - \alpha_{Li})^2}(e^{-R\alpha_{Li}} - e^{-R\alpha_H})^2 \tag{26}$$

In Figure 11), the asymptotic expression for $v_{Hxc}(= v_S - v_{ext})$ using the orbitals of eq 23 is plotted for comparison with the $v_{c,kin}(r) + v_{resp}(r)$ component of the numerical solution using the soft-Coulomb potentials. (As noted earlier, the soft-Coulomb orbitals are longer-ranged than their 3D Coulomb counterparts, so v_{Hxc} achieves its asymptotic form only at larger distances.) We see that the step reaches its asymptotic limit more quickly than the peak. For instance, at $R = 10.0$ au the peak for the numerical solution is somewhat smaller than that of the analytic expression, although the step has already reached its asymptotic value of 3.0H.

We next derive asymptotic expressions for the location and magnitude of the peak and step structures as functions of the internuclear separation. Defining the location of the peak from the condition $(d/dx)v_{c,kin}|_{x_{peak}} = 0$, we obtain

$$x_{peak} = \frac{R}{2}\frac{\left(1 - \sqrt{\frac{I_{Li}}{I_H}}\right)}{\left(1 + \sqrt{\frac{I_{Li}}{I_H}}\right)} + \frac{1}{\sqrt{32}}\frac{\ln\frac{I_{Li}}{I_H}}{\sqrt{I_{Li}} + \sqrt{I_H}} \tag{27}$$

where I_{Li} and I_H are the ionization potentials of Li and H, respectively. For the 3D case, the second term on the right is modified to be

$$\frac{3}{\sqrt{32}}\frac{\ln\frac{I_{Li}}{I_H}}{\sqrt{I_{Li}} + \sqrt{I_H}} \tag{28}$$

Defining the location of the step by its inflection point, that is, from the condition $(d^2/dx^2)v_{resp} = 0$, one obtains the same result, that is,

$$x_{step} = x_{peak} \tag{29}$$

Therefore, in the asymptotic limit, our two-electron model shows that the location of the peak and step coincide. The second term in eq 27 is negative, but in general small

compared to the first term for large interatomic separation R. Therefore, the peak and step structures are located closer to the hydrogen atom, more generally, closer to the more electronegative atom of a diatomic molecule. On the other hand, the minimum of the density

$$x_{\min(n)} = \frac{R}{2}\frac{\left(1 - \sqrt{\frac{I_{\mathrm{Li}}}{I_{\mathrm{H}}}}\right)}{\left(1 + \sqrt{\frac{I_{\mathrm{Li}}}{I_{\mathrm{H}}}}\right)} + \frac{1}{\sqrt{32}}\frac{\ln\frac{I_{\mathrm{Li}}^2}{I_{\mathrm{H}}^2}}{\sqrt{I_{\mathrm{Li}}} + \sqrt{I_{\mathrm{H}}}} \qquad (30)$$

lies closer to Li than the peak/step location, but still on the side of the bond midpoint closer to H: The first term of eq 30 is identical to eq 27, while the second term contains the logarithm of the ratio $I_{\mathrm{Li}}^2/I_{\mathrm{H}}^2$ instead of the ratio $I_{\mathrm{Li}}/I_{\mathrm{H}}$, which is smaller than one.

Our simple two-electron model thus explains the earlier observations in real molecules:[19] In the general many-electron heteroatomic case, given that the peak and step structures arise from the delocalized HOMO, our analysis can predict their positions. The location of the step was seen to coincide with the peak in the true LiH molecule, with both lying closer to the H atom, at least for the largest interatomic distances that those calculations were able to perform. For the homoatomic case, our results (eqs 27 and 30) predict that $x_{\mathrm{peak}} = x_{\min(n)} = 0$, and so, the minimum of the density and peak location coincide at the bond midpoint; also borne out by the examples in the literature.

We next turn to the magnitudes of the structures. Using the density matrix constructed from the orbitals in eq 23, one can show that the magnitude of the peak structure in $v_{\mathrm{kin}}(r)$, in the limit that the overlap integral vanishes, is given by the expression

$$v_{\mathrm{c,kin}}^{\max} = \frac{1}{4}\left(\sqrt{I_{\mathrm{H}}} + \sqrt{I_{\mathrm{Li}}}\right)^2 \qquad (31)$$

For our two-electron model of LiH, this gives a value of 0.616 au. Adding the value of the step in v_{resp} at its inflection point ($\Delta I/2 = 0.15$ au), gives 0.7672 au, which is indeed the peak to which our numerical solution asymptotes. For the homoatomic case, the above expression gives a value of $V_{\mathrm{peak}} = 0.5$ au, agreeing with the results of ref 19 and16 for the true homoatomic two electron system H_2. However, in ref 19, the magnitude of the peak for *true* LiH, was significantly smaller than this prediction. This discrepancy is due to the effect of the localized core electrons in the Li 1s shell, which lead to a dramatic decrease in the magnitude of the gradient of the conditional probability amplitude eq 6 in the interatomic region, and hence by eq 9, a decrease in the magnitude of the peak.

As discussed in section II, the peak emerges out of analyzing the change in the conditional probability. We now give a different argument for why the peak must be there, even though it has negligible effect on the ground-state energetics. The peak occurs when one takes the "nonbonding" orbital as the KS orbital

$$\phi = \sqrt{(\rho_{\mathrm{H}} + \rho_{\mathrm{Li}})/2} \qquad (32)$$

(Here ρ_{H} is the atomic density of the H atom and ρ_{Li} that of the Li atom, that is, the squares of the orbitals in eq 23). This is the exact doubly occupied KS orbital, since twice its square yields the exact density in the limit of infinite separation, $\rho = 2|\phi|^2 = \rho_{\mathrm{H}} + \rho_{\mathrm{Li}}$.

If one instead takes the "bonding orbital"

$$\phi_{\mathrm{bond}} = \left(\sqrt{\rho_{\mathrm{H}}/2} + \sqrt{\rho_{\mathrm{Li}}/2}\right) \qquad (33)$$

and finds the KS potential corresponding to this, there is *no* peak structure (but there is still the step). That is, if one asks what is the KS orbital for the KS potential with the peak structure sliced out, the KS orbital would instead be ϕ_{bond}. Now the density corresponding to ϕ_{bond} is

$$\rho_{\mathrm{bond}} = 2|\phi_{\mathrm{bond}}|^2 = \rho_{\mathrm{H}} + \rho_{\mathrm{Li}} + 2\sqrt{\rho_{\mathrm{H}}\rho_{\mathrm{Li}}} \qquad (34)$$

that is, is equal to the sum of the atomic densities *plus* a term $2\sqrt{(\rho_{\mathrm{H}}\rho_{\mathrm{Li}})}$. This term is indeed very small, but taken as a fraction of the total density, $(\rho_{\mathrm{H}}\rho_{\mathrm{Li}})^{1/2}/(\rho_{\mathrm{H}} + \rho_{Li})$, displays a peak at the exact same location as the peak in the *exact* KS potential, eq 27 (Figure 12). The shape of the peak is different but its maximum coincides in the limit of infinite separation. This suggests an interpretation of the peak in $v_{\mathrm{c,kin}}$ (in the exact KS potential), as a barrier that pushes back to the atomic regions the extraneous density $2\sqrt{(\rho_{\mathrm{H}}\rho_{\mathrm{Li}})}$ that would be in the bonding region if the peak was absent. Since the KS system by definition must get the density correct the peak must be there.

The interpretation here is closely related to the analysis of ref 21 of homoatomic molecules, where it was shown that the kinetic energy density for the exact KS orbital develops a well in the bond midpoint region, that must be compensated by a peak in the KS potential to keep the constant value of the KS orbital energy. An LCAO approximation to the orbital (analogous to ϕ_{bond} above) does not display the well.

V. Discussion and Implications

Using a simple one-dimensional model of a two-electron heteroatomic molecule, we studied features of the exact KS potential that arise for real 3D heteroatomic molecules. In particular, we examined the characteristic step and peak structure in the internuclear region, which develop as the molecule dissociates. These unusual features are a peculiarity of the noninteracting KS description: on the one hand, as a molecule dissociates, the interaction between the electrons on one atom and those on the other vanishes, so why, fundamentally, do such stark structures appear in the KS potential? The answer ultimately lies in the single-Slater-determinant description in the KS system: although this is indeed how the exact KS system describes the state, it is far from the true wave function which needs, even qualitatively, two Slater determinants. In the two-electron model, the KS system consists of a doubly occupied spatial orbital, blatently far from the true two-orbital interacting system. Mathematically, the structures can be understood by considering the response and kinetic components of the correlation potential,

as explained in earlier works and in Section II of the present paper. Physically, a KS potential that lacks the step leads to dissociation into fractional charges; a KS potential that lacks the peak leads to a KS orbital that yields an incorrect (albeit exponentially small) density in the internuclear region. The former point is well-recognized in the literature, while the latter point elaborates on an earlier interpretation[21] (section IVB).

Because of the simplicity of our two-electron model, we are able to investigate in much more detail than in the earlier literature, the development of these structures and their asymptotic properties. Several of these features carry over to the true many-electron 3D case, since they arise from the HOMO orbital. We showed that the step begins to develop at the internuclear separation, where the avoided crossing in the ground and lowest charge-transfer state is approached, and explained why. We gave an exact formula for the location of the step and peak, in the limit of large separation, finding that the two structures are located at the same place, and closer to the atom with the larger IP, consistent with the few calculations done on real molecules in the literature.

Because they are in a region of very low electron-density, these features, in themselves, have little energetic consequences for the ground states of these systems. However they have dramatic consequences for time-dependent processes, excitations, and response. For example, it has been shown that the related peaks that appear in the interatomic regions of a hydrogen chain significantly (and correctly) reduce the polarizability of the chain and that local and semilocal approximations which lack the peak, consequently significantly underestimate the (hyper-)polarizability.[35] As TDDFT begins to be utilized in molecular transport calculations, we anticipate the peaks will act as barriers decreasing the current.

The step in the KS potential ultimately imposes a rather complicated structure on the exact xc kernel of TDDFT.[37,38] Because of the realignment of the atomic HOMOs, the molecular HOMO and LUMO are symmetric and antisymmetric combinations of the atomic HOMO's, separated in energy merely by the tunnelling factor, that vanishes as exp ($-$ const R) as the molecule dissociates. Therefore three KS determinants become near-degenerate: the doubly occupied HOMO, a single-excitation to the LUMO, and a double-excitation to the LUMO. That is, the step introduces *static correlation* in the KS system that is not present in the true interacting system. It is the job of the TDDFT xc kernel to "undo" this static correlation, in order to yield good excitation energies in the true system. This has a dramatic effect on the structure of the xc kernel for charge-transfer excitations in molecules composed of open-shell fragments;[37,38] in particular, the double-excitation induces a strong-frequency-dependence on the kernel.

Almost all the approximations in use today do not capture the step and peak structure in the potential. Carefully constructed orbital functionals for the correlation potential may display these structures, as has been explicitly shown in ref 46. Interestingly, static correlation in the KS system is nonetheless not escaped in the usual (semi)local approximations. Delocalized orbitals underlie the fractional charge problem, and the HOMO and LUMO become near-degenerate as the molecule dissociates. Figure 13 demonstrates this for the LiH molecule within LSD; a similar merging of the HOMO and LUMO is also seen in GGA.

Acknowledgment. This work is financially supported by the National Science Foundation NSF CHE-0547913 (N.T.M. and D.G.T.), NSF CHE-07-19291 (T.J.M.), a Research Corporation Cottrell Scholar Award (N.T.M.), and the Hunter Gender Equity Project (N.T.M. and D.G.T.).

References

(1) Hohenberg, P.; Kohn, W. *Phys. Rev.* **1964**, *136*, B 864.

(2) Kohn, W.; Sham, L. J. *Phys. Rev.* **1965**, *140*, A 1133.

(3) Kohn, W. *Rev. Mod. Phys.* **1999**, *71*, 1253.

(4) Perdew, J. P.; Kurth, S. Density Functionals for Non-Relativistic Coulomb Systems in the New Century. In *A Primer in Density Functional Theory*; Fiolhais, C., Nogueira, F., Marques, M., Eds.; Springer: Berlin, Heidelberg, New York, 2003; Vol. 620, pp 1−55.

(5) *A Primer in Density Functional Theory*; Springer Lecture Notes in Physics 620; Fiolhais, C., Nogueira, F., Marques, M., Eds.; Springer: Berlin, Heidelberg, New York, 2003.

(6) Perdew, J. P.; Burke, K.; Ernzerhof, M. *Phys. Rev. Lett.* **1996**, *77*, 3865.

(7) Staroverov, V. N.; Scuseria, G. E.; Tao, J.; Perdew, J. P. *J. Chem. Phys.* **2003**, *119*, 12129.

(8) Staroverov, V. N.; Scuseria, G. E.; Tao, J.; Perdew, J. P. *J. Chem. Phys.* **2004**, *121*, 11507(E).

(9) Rydberg, H.; Dion, M.; Jacobson, N.; Schroder, E.; Hyldgaard, P.; Simak, S. I.; Langreth, D. C.; Lundqvist, B. I. *Phys. Rev. Lett.* **2003**, *91*, 126402.

(10) Cooper, V. R.; Thonhausr, T.; Langreth, D. C. *J. Chem. Phys.* **2008**, *128*, 204102.

(11) Vydrov, O. A.; Wu, Q.; van Voorhis, T. *J. Chem. Phys.* **2008**, *129*, 014106.

(12) Slater, J. C. *The Self-Consistent Field for Molecules and Solids*; McGraw-Hill: New York, 1974.

(13) Perdew, J. P.; Parr, R. G.; Levy, M.; Balduz, J. L. *Phys. Rev. Lett.* **1982**, *49*, 1691.

(14) Perdew, J. P. What do the Kohn-Sham orbitals mean? How do atoms dissociate? In *Density Functional Methods in Physics*; Dreizler, R. M., da Providencia, J., Eds.; Plenum: New York, 1985; p 265.

(15) Ruzsinszky, A.; Perdew, J. P.; Csonka, G. I.; Vydrov, O. A.; Scuseria, G. E. *J. Chem. Phys.* **2006**, *125*, 194112.

(16) Buijse, M. A.; Baerends, E. J.; Snijders, J. G. *Phys.Rev. A.* **1989**, *40*, 4190.

(17) Gritsenko, O. V.; van Leeuwen, R.; Baerends, E. J. *Phys.Rev. A.* **1995**, *52*, 1870.

(18) Gritsenko, O. V.; van Leeuwen, R.; Baerends, E. J. *J. Chem. Phys.* **1996**, *104*, 8535.

(19) Gritsenko, O. V.; Baerends, E. J. *Phys.Rev. A.* **1996**, *54*, 1957.

(20) Gritsenko, O. V.; van Leeuwen, R.; Baerends, E. J. *J. Chem. Phys.* **1994**, *101*, 8955.

(21) Gritsenko, O. V.; Baerends, E. J. *Theor. Chem. Acc.* **1997**, *96*, 44.

(22) van Leeuwen, R.; Baerends, E. J. *Phys. Rev. A.* **1994**, *49*, 2421.

(23) Runge, E.; Gross, E. K. U. *Phys. Rev. Lett.* **1984**, *52*, 997.

(24) Petersilka, M.; Gossmann, U. J.; Gross, E. K. U. *Phys. Rev. Lett.* **1996**, *76*, 1212.

(25) *Time-Dependent Density Functional Theory*; Marques, M. A. L., Ulrich, C. A., Nogueira, F., Rubio, A., Burke, K., Gross, E. K. U., Eds.; Springer: Berlin, 2006.

(26) Levine, B. G.; Ko, C.; Quenneville, J.; Martinez, T. J. *Mol. Phys.* **2006**, *104*, 1039.

(27) Javanainen, J.; Eberly, J.; Su, Q. *Phys. Rev. A.* **1988**, *38*, 3430.

(28) Eberly, J.; Grobe, R.; Law, C.; Su, Q. In *Atoms in Intense Laser Fields*; Gavrila, M., Ed.; Academic Press: Boston, 1992.

(29) Villeneuve, D. M.; Ivanov, M. Y.; Corkum, P. B. *Phys. Rev. A.* **1996**, *54*, 736.

(30) Bandrauk, A.; Ngyuen, H. *Phys. Rev. A.* **2002**, *66*, 031401(R).

(31) Bandrauk, A.; Lu, H. *Phys. Rev. A.* **2005**, *72*, 023408.

(32) Lein, M.; Gross, E. K. U.; Engel, V. *Phys. Rev. Lett.* **2002**, *85*, 4707.

(33) Ngyuen, H.; Bandrauk, A. *Phys. Rev. A.* **2006**, *73*, 032708.

(34) Lein, M.; Kümmel, S. *Phys. Rev. Lett.* **2005**, *94*, 143003.

(35) Kümmel, S.; Kronik, L.; Perdew, J. P. *Phys. Rev. Lett.* **2004**, *93*, 213002.

(36) Koentopp, M.; Chang, C.; Burke, K.; Car, R. J. *Phys. Cond. Matt.* **2008**, *20*, 083203.

(37) Maitra, N. T. *J. Chem. Phys.* **2005**, *122*, 234104.

(38) Maitra, N. T.; Tempel, D. G. *J. Chem. Phys.* **2006**, *125*, 184111.

(39) Almbladh, C. O.; von Barth, U. *Phys. Rev. B.* **1985**, *31*, 3231.

(40) Perdew, J. P.; Levy, M. *Phys. Rev. B.* **1997**, *56*, 16021.

(41) Boutalib, A.; Gadea, F. X. *J. Chem. Phys.* **1992**, *97*, 1144.

(42) Castro, A.; Appel, H.; Oliveira, M.; Rozzi, C. A.; Andrade, X.; Lorenzen, F.; Marques, M. A. L.; Gross, E. K. U.; Rubio, *A. Phys. Status Solidi B* **2006**, *243*, 2465–2488.

(43) Marques, M. A. L.; Castro, A.; Bertsch, G. F.; Rubio, A. *Comput. Phys. Commun.* **2003**, *151*, 60–2003.

(44) http://www.tddft.org/programs/octopus/wiki/index.php/MainPage (accessed 2008).

(45) Grice, R.; Herschbach, D. R. *Mol. Phys.* **1972**, *27*, 159.

(46) Gritsenko, O. V.; Baerends, E. J. *Int. J. Quantum Chem.* **2006**, *106*, 3167.

CT800535C

JCTC Journal of Chemical Theory and Computation

Qualitatively Correct Charge-Transfer Excitation Energies in HeH^+ by Time-Dependent Density-Functional Theory Due to Exact Exchange Kohn−Sham Eigenvalue Differences

Tino Gimon,* Andrey Ipatov, Andreas Heßelmann, and Andreas Görling

Lehrstuhl für Theoretische Chemie, Universität Erlangen-Nürnberg, Egerlandstr. 3, D-91058 Erlangen, Germany

Received December 5, 2008

Abstract: Time-dependent density-functional theory in the response regime is shown to yield qualitatively correct charge-transfer excitation energies in the system HeH^+ if the exact Kohn−Sham exchange potential is employed to determine the Kohn−Sham orbitals and eigenvalues entering the time-dependent density-functional calculation. The employed exact-exchange kernel is frequency-independent and, like conventional kernels in the local density approximation or in generalized gradient approximations, does not contribute to the charge-transfer excitation energy. This shows that it can be that not the exchange-correlation kernel, as generally believed, but the exchange-correlation potential plays the crucial role in the description of charge-transfer excitations.

One of the presently most widely used approaches to calculate electronic excitation energies of molecules or clusters is time-dependent density-functional theory (TDDFT) in the response regime.[1−8] Besides excitation energies, oscillator strengths and thus UV/vis spectra are also accessible. Furthermore, circular dichroism spectra can be calculated.

While current density-functional response methods,[9−17] that is, methods based on TDDFT in the response regime, are often very successful, they also exhibit a number of serious shortcomings due to the necessary approximations in the required exchange-correlation functionals. Excitations into states with Rydberg character are poorly described.[18] This problem can be solved by determining the Kohn−Sham (KS) orbitals and eigenvalues that enter a density-functional response calculation with asymptotically corrected exchange-correlation potentials[19−26] or more fundamentally[27] with an exact-exchange (EXX) KS method,[28−31] that is, a KS method that employs the exact local KS exchange potential. For other failures of current density-functional response methods, no convincing, generally applicable remedies are available at present. Excitation energies of molecules with long conjugated systems of π electrons[32−36] are systematically underestimated, and the description of two-electron excitations is problematic.[37]

The perhaps most important deficiency of density-functional response methods employing presently available approximations for the exchange-correlation functionals is their incapability to correctly describe charge-transfer (CT) excitations.[16,40−44] Excitations with significant CT can be underestimated by several electron volts, and the behavior of CT excitations between two separated units with the distance of the units is described qualitatively wrong. CT excitation energies between neutral fragments, in particular, excitations from the highest occupied molecular orbital (HOMO) of one fragment to the lowest unoccupied molecular orbital (LUMO) of the other, should approach $(I - A) - 1/R$, with I denoting the ionization energy of the donor, A denoting the electron affinity of the acceptor, and R standing for the distance of the units. Present density-functional response methods do not yield this $-1/R$ behavior. Instead, the CT excitation energies, at relatively small distances R approach a constant given by the difference between the KS eigenvalues of the LUMO of the acceptor and those of the HOMO of the donor. HOMO−LUMO CT excitations from a neutral to a cationic unit, on the other hand, approach

* Corresponding author e-mail: tino.gimon@chemie.uni-erlangen.de.

10.1021/ct800539a CCC: $40.75
Published on Web 03/11/2009

$(I - A)$ at small distances R, while current density-functional response methods exhibit an erroneous $1/R$ behavior. In the limit of an infinite distance R, the current density-functional response methods yield CT excitation energies that equal the eigenvalue difference between the LUMO and the HOMO. This eigenvalue difference, however, in general, does not equal the CT excitation energy given by $(I - A)$ in this limit. While the negative of the HOMO eigenvalue equals the ionization energy I[45,46] in the exact formalism and represents a well-defined approximation for I in practice, the negative of the LUMO eigenvalue differs from the electron affinity A by the derivative discontinuity of the exchange-correlation energy at integer electron numbers[47,48,51] and therefore cannot serve as an approximation for A.

The failure of current density-functional response methods to describe CT excitations usually is attributed to shortcomings in the employed approximations for the exchange-correlation kernel, the frequency-dependent functional derivative of the exchange-correlation potential with respect to the electron density. In particular, the neglect of the frequency dependency of the kernel, the adiabatic approximation, is made responsible for the failure to describe CT excitations. Here, we show that in certain cases problems in describing CT exitations are caused by shortcomings of the approximations of the exchange-correlation potential, not the kernel.

For the simple test system HeH^+,[49,50] we here show that a density-functional response method that employs the EXX KS potential and kernel and neglects correlation yields a qualitative correct behavior with the HeH^+ distance R for the energy of the CT excitation from the He 1s orbital to the H^+ 1s orbital. To our knowlewdge, this is the first time that a density-functional response method has correctly described the distance behavior of a CT excitation without the introduction of special correction terms to enforce the correct behavior.[41,51] Even more important is the finding that the EXX kernel employed in the density-functional response calculation turns out to be not responsible for the correct distance behavior of the CT excitation. Indeed, in the system HeH^+, the exchange kernel does not contribute at all to the excitation energy at large distances R. The CT excitation energy like in conventional TDDFT methods using functionals within the local density-approximation (LDA) or generalized gradient approximations (GGA) equals the difference between the KS eigenvalue of the LUMO of the acceptor, the H^+ 1s orbital, and the HOMO of the donor, the He 1s orbital. However, in contrast to LDA or GGA eigenvalue differences, the EXX eigenvalue difference does not exhibit an unphysical $1/R$ behavior but correctly approaches a constant already at small distances, R. This means that, for HeH^+, the adiabatic approximation or, generally, approximations to the exchange-correlation kernel, in contrast to what is generally believed, are not responsible for the failure of conventional TDDFT methods, that is, density-functional response methods employing the LDA or GGAs, to describe CT excitations.

Most density-functional response methods for excitation energies are based on the nonlinear eigenvalue equation

$$[\varepsilon^2 - 4\varepsilon^{1/2}\mathbf{K}(\omega)\varepsilon^{1/2}]\,\mathbf{z}(\omega) = \omega^2\,\mathbf{z}(\omega) \tag{1}$$

introduced by Casida.[5,13,52] The dimension of eq 1 is given by the product of the number of occupied KS orbitals times the number of unoccupied KS orbitals. In eq 1, the eigenvalue ω^2 equals the square of the excitation frequency or energy ω. The eigenvector $\mathbf{z}(\omega)$ determines the transition density $\rho(\omega,\mathbf{r})$ of the excitation via

$$\rho(\omega, \mathbf{r}) = \sum_{i}^{\text{occ}} \sum_{a}^{\text{unocc}} z_{ia}(\omega)\, \varepsilon_{ia}^{(-1/2)}\, \phi_i(\mathbf{r})\, \phi_a(\mathbf{r}) \tag{2}$$

in terms of products of occupied KS orbitals times unoccupied KS orbitals, φ_i and φ_a, respectively, with $\varepsilon_{ia} = \varepsilon_a - \varepsilon_i$ denoting the difference of the corresponding KS eigenvalues ε_a and ε_i. The elements $K_{ia,jb}(\omega)$ of the matrix $\mathbf{K}(\omega)$ are given by

$$K_{ia,jb}(\omega) = \int \mathrm{d}\mathbf{r}\, \mathrm{d}\mathbf{r}'\, \phi_i(\mathbf{r})\, \phi_a(\mathbf{r})\, f_{\text{uxc}}(\omega, \mathbf{r}, \mathbf{r}')\, \phi_j(\mathbf{r}')\, \phi_b(\mathbf{r}') \tag{3}$$

and the elements $\varepsilon_{ia,jb}$ of the diagonal matrix ε are given by $\varepsilon_{ia,jb} = \delta_{ia,jb}(\varepsilon_a - \varepsilon_i)$. The indices ia and jb are superindices labeling the products of occupied times unoccupied KS orbitals. The sum of the Coulomb kernel $1/|\mathbf{r} - \mathbf{r}'|$ and the exchange-correlation kernel is denoted by f_{uxc}. In practice, almost always the frequency dependence of the matrix $\mathbf{K}$ is neglected. That is, the adiabatic approximation is made, and the nonlinear eigenvalue, eq 1, turns into a linear one.

We now consider an intermolecular CT excitation that can be described as an excitation from an occupied orbital, φ_i, of one molecule into an unoccupied orbital, φ_a, of another molecule. At large intermolecular distances R, the spatial overlap of the two orbitals vanishes, and the product $\varphi_i\varphi_a$ approaches zero everywhere. As a result, one row and one column of $\mathbf{K}$ approach zero, and one eigenvector of eq 1 is a unit vector with an entry of one at the position ia. The corresponding eigenvalue is given by ε_{ia}^2. This means that the CT excitation energy obtained with a conventional density-functional response method equals the corresponding KS eigenvalue difference $\varepsilon_a - \varepsilon_i$. The only way to obtain a CT excitation energy that differs from the corresponding KS eigenvalue difference seems to be seen when the kernel f_{uxc} approaches infinity in such a way that the matrix elements $K_{ia,jb}(\omega)$, eq 3, containing the vanishing product $\varphi_i\varphi_a$ approach finite values. This represents a complicated demand on the kernel that is believed to be intimately related to the frequency dependence of the kernel. Adiabatic LDA or GGA kernels are finite and clearly cannot exhibit the required behavior. Therefore, all density-functional response methods employing LDA or GGA kernels yield CT excitation energies that equal the corresponding KS eigenvalue differences.

For the special case of a nonspin-polarized two-electron system, the exact local KS exchange potential is known. It equals simply the negative of half of the Coulomb potential. For a nonspin-polarized two-electron system, the exchange kernel is also known exactly.[54] It equals the negative of half of the Coulomb kernel; that is, it is given by $-1/(2|\mathbf{r} - \mathbf{r}'|)$. Thus, in this special case, the exchange kernel is frequency-independent, does not approach infinity except at $\mathbf{r} = \mathbf{r}'$,

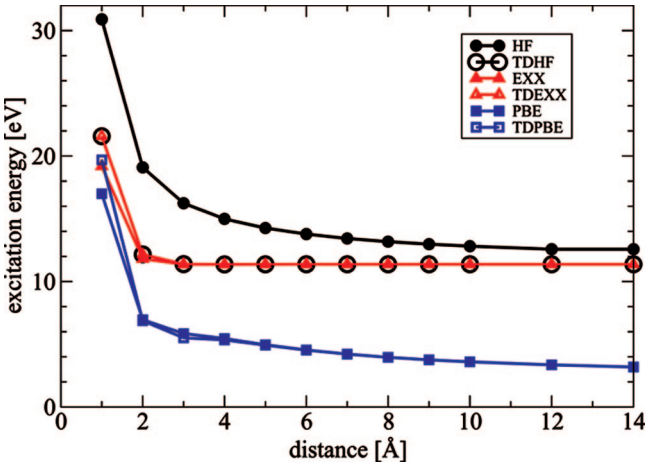

Figure 1. Charge-transfer excitation energies in HeH^+ (He 1s → H^+ 1s) for varying HeH^+ distances as obtained by TDPBE, TDHF, and TDEXX and corresponding eigenvalue differences (PBE, HF, and EXX). The EXX and TDEXX curves as well as the PBE and TDPBE curves in most regions cannot be distinguished from each other.

and thus does lead to vanishing matrix elements $K_{ia,jb}(\omega)$ in eqs 1 and 3 for indices *ia* or *jb* referring to a CT excitation. Therefore, time-dependent exact-exchange (TDEXX) calculations have to yield CT excitation energies that equal the corresponding KS eigenvalue difference for nonspin-polarized two-electron systems.

For a nonspin-polarized two-electron system, it is straightforward to turn any Hartree−Fock (HF) and any time-dependent Hartree−Fock (TDHF) method into an EXX KS and a TDEXX density-functional response method, respectively. It is merely necessary to multiply the terms originating from exchange in the HF and TDHF method by zero, that is, to neglect them, and to multiply the terms originating from the Coulomb potential and Coulomb kernel by one-half. We carried out such a modification in the program package TURBOMOLE[55] and then performed HF/TDHF, EXX/TDEXX, LDA/TDLDA (LDA and time-dependent LDA), and PBE/TDPBE (GGA and time-dependent GGA with the exchange-correlation potential and kernel attributable to Perdew, Burke, and Ernzerhof)[53] calculations for HeH^+ and the CT excitation from the He 1s orbital to the H^+ 1s orbital.

Five different basis sets, the aug-cc-pVXZ basis sets of Dunning[56,57] with X = D, T, Q, 5, and 6, were employed in the calculations. In Figure 1, results for the aug-cc-pV6Z basis set are shown, which are fully converged with respect to the basis set size. The TDHF energy for the considered CT excitation differs strongly from the corresponding HF eigenvalue difference. As expected, the TDHF CT energy exhibits a qualitative correct behavior with the HeH^+ distance *R*. TDHF considers the response of the first-order density matrix not the response of the density, like TDDFT. A representation of the response of the first-order density matrix in terms of products $\varphi_i(\mathbf{r})\,\varphi_a(\mathbf{r}')$ of occupied times unoccupied orbitals does not vanish in CT cases due to the occurrence of the two different variables, $\mathbf{r}$ and $\mathbf{r}'$, in the products. Therefore, TDHF describes charge-transfer excitations qualitatively correctly.

Figure 1 shows that the TDPBE as well as the TDEXX energies for the considered CT excitation equal the corresponding KS eigenvalue differences, as could be expected from the discussion above. However, while the TDPBE CT excitation energies exhibit a qualitatively wrong $1/R$ behavior with the HeH^+ distance *R*, TDEXX CT excitation energies exhibit the qualitative correct behavior. Indeed, the TDEXX results are identical to the TDHF ones. LDA/TDLDA results, which are not displayed here, show the same behavior as the PBE and TDPBE results.

The differences between LDA and PBE eigenvalue differences, on the one hand, and the TDEXX eigenvalues, on the other, can be explained as follows. For a HeH^+ distance *R* that is large compared to the spatial extent of the 1s orbitals of He and H^+, the effective KS potential around the He atom equals that of an isolated He atom plus the constant $-1/R$, the constant being the term originating to leading order in the HeH^+ distance *R* from the electrostatic potential of the H^+, that is, of a proton. The He 1s orbital eigenvalue therefore, to leading order in *R*, equals the eigenvalue of the 1s orbital of an isolated He atom minus $1/R$. This holds true for the LDA and the PBE as well as the EXX eigenvalues of the He 1s orbital. The eigenvalue of the H^+ 1s orbital in the LDA and the PBE cases, to leading order in *R*, equals that of an isolated proton, that is, that of atomic hydrogen, for large *R* values. The reason is that the effective KS potential of He is short-range because the LDA and PBE exchange-correlation potentials erroneously are short-range and because the Hartree potential and the electrostatic potential of the He nucleus cancel each other asymptotically. This means that the eigenvalue of the H^+ 1s orbital in the LDA and the PBE cases is constant for large distances *R*. The difference between the H^+ 1s eigenvalue and the He 1s eigenvalue therefore exhibits the erroneous $1/R$ behavior for large distances *R*.

In the EXX case, the effective KS potential of He, on the other hand, is long-range and correctly approaches $-1/r$ for large distances *r*, from the He nucleus because the exact-exchange KS potential exhibits such a $-1/r$ behavior. As a result, the He atom contributes, to leading order in *R*, a constant $-1/R$ to the effective KS potential around the H^+. Therefore, the H^+ 1s eigenvalue like the He 1s eigenvalue equals the eigenvalue of an isolated H^+ minus $1/R$. In the difference between the H^+ 1s and the He 1s eigenvalue, the $1/R$ terms cancel, and the eigenvalue difference at large distances *R* is constant, as it should be. The wrong behavior of the LDA and PBE eigenvalue difference thus has its origin in the qualitatively wrong asymptotic behavior of LDA and PBE exchange potentials that are caused by unphysical Coulomb self-interations of each electron that are not canceled completely by the approximate LDA and PBE exchange functionals. The fact that the LDA and PBE exchange-correlation potential and not the kernel causes the qualitatively wrong CT excitation energies is confirmed by carrying out density-functional response calculations employing the LDA or GGA kernel but EXX orbitals and eigenvalues. Such calculations yield de facto identical results as the EXX/TDEXX calculations.

Of course, other GGA functionals than the PBE lead to the same qualitatively wrong results for the considered CT excitation in HeH^+. Moreover, CT excitation energies from neutral to positively charged units in other systems than HeH^+, including systems with more than two electrons, are also described in the same way wrongly with LDA and GGA functionals in density-functional response methods.

The simple two-electron example of HeH^+ certainly is a special case. Not only are the exchange potential and kernel exactly known in terms of the electron density in this case, but, moreover, in this special case, the negative of the eigenvalue of the LUMO, the 1s orbital of H^+, exactly equals the electron affinity for large He H^+ distances. This is not the case in general, and therefore EXX eigenvalue differences in general are not sufficient to describe CT excitations qualitativly correctly. Nevertheless, this special case does point to a new aspect of the CT problem of TDDFT, namely, that the KS eigenvalue differences at least in special cases may be essential for the behavior of excitation energies with the distance *R*. Indeed, in the special case of HeH^+, the KS eigenvalue differences exclusively determine this behavior, while the exchange-correlation kernel does not contribute to it at all. This means for the CT problem that not only the exchange-correlation kernel is of importance but also the exchange-correlation potential in the KS calculation determining the KS eigenvalues, and their differences may be crucial.

Acknowledgment. The authors gratefully acknowledge the funding of the German Research Council (DFG), which, within the framework of its "Excellence Initiative", supports the Cluster of Excellence "Engineering of Advanced Materials" (www.eam.uni-erlangen.de) at the University of Erlangen−Nuremberg. Furthermore, support from the DFG priority program 1145 is acknowledged.

References

(1) Stott, M. J.; Zaremba, E. *Phys. Rev. A: At., Mol., Opt. Phys.* **1980**, *21*, 12.

(2) Zangwill, A.; Soven, P. *Phys. Rev. Lett.* **1980**, *45*, 204.

(3) Mahan, G. D. *Phys. Rev. A: At., Mol., Opt. Phys.* **1980**, *22*, 1780.

(4) Runge, E.; Gross, E. K. U. *Phys. Rev. Lett.* **1984**, *52*, 997.

(5) Casida, M. E. Time-Dependent Density Functional Response Theory for Molecules. In *Recent Advances in Density Functional Methods*, 1st ed.; Chong, D. P., Ed.; World Scientific Publishing Co. Pte. Ltd.: Singapore, 1995; *Part I*, pp 155−192.

(6) Gross, E. K. U.; Dobson, J. F.; Petersilka, M. Density Functional Theory IIM. In *Topics in Current Chemistry*, 1st ed.; Nalewajski, R. F. Ed.; Springer: Berlin, Germany, 1996; Vol. 181, pp 81−172, and reference therein.

(7) Görling, A. *Int. J. Quantum Chem.* **1988**, *69*, 265.

(8) Marques, M. A. L. Time-Dependent Density Functional Theory. In *Lecture Notes in Physics*, 1st ed.; Marques, M. A. L., Ullrich, C. A., Nogueira, F., Rubio, A., Burke, K., Gross, E. K. U., Eds.; Springer: Berlin, Germany, 2006; Vol. 706.

(9) van Gisbergen, S. J. A.; Snijders, J. G.; Baerends, E. J. *J. Chem. Phys.* **1995**, *103*, 9347.

(10) Jamorski, C.; Casida, M. E.; Salahub, D. R. *J. Chem. Phys.* **1996**, *104*, 5134.

(11) Bauernschmitt, R.; Ahlrichs, R. *Chem. Phys. Lett.* **1996**, *256*, 454.

(12) Stratmann, R. E.; Scuseria, G. E.; Frisch, M. J. *J. Chem. Phys.* **1998**, *109*, 8218.

(13) Görling, A.; Heinze, H. H.; Ruzankin, S. P.; Staufer, M.; Rösch, N. *J. Chem. Phys.* **1999**, *110*, 2785.

(14) Heinze, H. H.; Görling, A.; Rösch, N. *J. Chem. Phys.* **2000**, *113*, 2088.

(15) Hirata, S.; Head-Gordon, M. *Chem. Phys. Lett.* **1999**, *302*, 375.

(16) Tozer, D. J.; Amos, R. D; Handy, N. C.; Roos, B. O.; Serrano-Andrés, L *Mol. Phys.* **1999**, *97*, 859.

(17) Yabana, K.; Bertsch, G. F. *Int. J. Quantum Chem.* **1999**, *75*, 55.

(18) Casida, M. E.; Jamorski, C.; Casida, K. C.; Salahub, D. R. *J. Chem. Phys.* **1998**, *108*, 4439.

(19) van Leeuwen, R.; Baerends, E. J. *Phys. Rev. A: At., Mol., Opt. Phys.* **1994**, *49*, 2421.

(20) Gritsenko, O. V.; Schipper, P. R. T.; Baerends, E. J. *Chem. Phys. Lett.* **1999**, *302*, 199.

(21) Schipper, P. R. T.; Gritsenko, O. V.; van Gisbergen, S. J. A.; Baerends, E. J. *J. Chem. Phys.* **2000**, *112*, 1344.

(22) Grüning, M.; Gritsenko, O. V.; van Gisbergen, S. J. A.; Baerends, E. J. *J. Chem. Phys.* **2001**, *114*, 652.

(23) Tozer, D. J.; Handy, N. C. *J. Chem. Phys.* **1998**, *109*, 10180.

(24) Allen, M. J.; Tozer, D. J. *J. Chem. Phys.* **2000**, *113*, 5185.

(25) Casida, M. E.; Casida, K. C.; Salahub, D. R. *Int. J. Quantum Chem.* **1998**, *70*, 933.

(26) Casida, M. E.; Salahub, D. R. *J. Chem. Phys.* **2000**, *113*, 8918; *Int. J. Quantum Chem.* **1999**, *75*, 55.

(27) Della Sala, F.; Görling, A. *Int. J. Quantum Chem.* **2003**, *91*, 131.

(28) Görling, A. *Phys. Rev. Lett.* **1999**, *83*, 5459.

(29) Ivanov, S.; Hirata, S.; Bartlett, R. J. *Phys. Rev. Lett.* **1999**, *83*, 5455.

(30) Yang, W.; Wu, Q. *Phys. Rev. Lett.* **2002**, *89*, 143002.

(31) He*β*elmann, A.; Götz, A. W.; Della Sala, F.; Görling, A. *J. Chem. Phys.* **2007**, *127*, 054102.

(32) Champagne, B.; et al. *J. Chem. Phys.* **1998**, *109*, 10489.

(33) van Gisbergen, S. J. A.; et al. *Phys. Rev. Lett.* **1999**, *83*, 694.

(34) Cai, Z. L.; Sendt, K.; Reimers, J. R. *J. Chem. Phys.* **2002**, *117*, 5543.

(35) Grimme, S.; Parac, M. *Chem. Phys. Chem.* **2003**, *4*, 292.

(36) Weimer, M.; Hieringer, W.; Della Sala, F.; Görling, A. *Chem. Phys.* **2005**, *309*, 77.

(37) An approach to treat the special case of an admixture of a two-electron excitation into a one-electron excitation separated, that is, not strongly interacting, with other excitations was recently introduced and applied in refs 38 and 39.

(38) Maitra, N. T.; Zhang, F.; Cave, R. J.; Burke, K. *J. Chem. Phys.* **2004**, *120*, 5932.

(39) Mazur, G.; Wlodarczyk, R. *J. Comput. Chem.* In press.

(40) Dreuw, A.; Fleming, G. R.; Head-Gordon, M. *J. Phys. Chem. B* **2003**, *107*, 6500.

(41) Dreuw, A.; Weisman, J. L.; Head-Gordon, M. *J. Chem. Phys.* **2003**, *119*, 2943.

(42) Sobolewski, A. L.; Domcke, W. *Chem. Phys.* **2003**, *294*, 73.

(43) Hieringer, W.; Görling, A. *Chem. Phys. Lett.* **2006**, *419*, 557.

(44) Hieringer, W.; Görling, A. *Chem. Phys. Lett.* **2006**, *426*, 234.

(45) Perdew, J. P.; Parr, R. G.; Levy, M.; Balduz, J. L. *Phys. Rev. Lett.* **1982**, *49*, 1691.

(46) Almbladh, C. O.; von Barth, U. *Phys. Rev. B: Condens. Matter Mater. Phys.* **1985**, *31*, 3231.

(47) Perdew, J. P.; Levy, M. *Phys. Rev. Lett.* **1983**, *51*, 1884.

(48) Sham, L. J.; Schlüter, M. *Phys. Rev. Lett.* **1983**, *51*, 1888.

(49) In ref 50, the system HeH^+ was considered within time-dependent density-matrix-functional theory.

(50) Giesbertz, K. J. H.; Baerends, E. J.; Gritsenko, O. V. *Phys. Rev. Lett.* **2008**, *101*, 033004.

(51) Gritsenko, O. V.; Baerends, E. J. *J. Chem. Phys.* **2004**, *121*, 655.

(52) Furche, F. *J. Chem. Phys.* **2001**, *114*, 5982.

(53) Perdew, J. P.; Burke, K.; Ernzerhof, M. *Phys. Rev. Lett.* **1996**, *77*, 3865.

(54) Petersilka, M.; Gross, E. K. U.; Burke, K. *Int. J. Quantum Chem.* **2000**, *80*, 534.

(55) Ahlrichs, R.; Bär, M.; Häser, M.; Horn, H.; Kölmel, C. *Chem. Phys. Lett.* **1989**, *162*, 165.

(56) Dunning, T. H., Jr. *J. Chem. Phys.* **1989**, *90*, 1007.

(57) Woon, D. E.; Dunning, T. H., Jr. *J. Chem. Phys.* **1994**, *100*, 2975.

CT800539A

JCTC Journal of Chemical Theory and Computation

Second-Order Perturbation Theory with Fractional Charges and Fractional Spins

Aron J. Cohen, Paula Mori-Sánchez, and Weitao Yang*

Department of Chemistry, Duke University, Durham, North Carolina 27708

Received December 5, 2008

Abstract: In this work the behavior of MP2 for fractional occupations is investigated. The consideration of fractional charge behavior gives a simple derivation of an expression for the chemical potential (or the derivative of energy with respect to the number of electrons) of MP2. A generalized optimized effective potential formalism (OEP) has been developed in which the OEP is a nonlocal potential, which can be applied to explicit functionals of the orbitals and eigenvalues and also facilitates the evaluation of the chemical potential. The MP2 derivative improves upon the corresponding Koopmans' theorem in Hartree−Fock theory for the ionization energy and also gives a good estimate of the electron affinity. In strongly correlated systems with degeneracies and fractional spins, MP2 diverges, and another corrected second-order perturbative method ameliorates this failure for the energy but still does not recapture the correct behavior for the energy derivatives that yield the gap. Overall we present a view of wave function based methods and their behavior for fractional charges and spins that offers insight into the application of these methods to challenging chemical problems.

Introduction

Recent work[1−3] has highlighted exact conditions for the energy of systems with fractional charges and fractional spins. These conditions are massively violated by currently used approximations in density functional theory (DFT). The exact energy for fractional charges is a straight line interpolation between the integer points.[4] Density functional approximations for the exchange-correlation energy (DFAs) such as LDA, GGA,[5−7] and conventional hybrid functionals[8] violate this exact condition and have a convex error for the energy of fractional systems. This led to the concept of many-electron self-interaction[9−11] and a delocalization error[1] that affects the calculation of many differing types of species and properties. Many of the well-known problems of DFAs can be related to this error for fractional charges such as overestimation of molecular polarizabilities, overestimation of molecular conductance, underestimation of charge-transfer excitation energies, underestimation of hydrogen transfer reaction barriers, and underestimation of the band gap in solids. Hartree−Fock (HF) shows the opposite concave behavior[11,12] for fractional charges and hence an error toward localization in larger systems. It has also been shown that the exact energy for fractional spins should be constant and at the same energy as the corresponding integer spin pure states. For example the dissociation limit of the H_2 molecule gives two separated atoms each with half an α electron and half a β electron that should be degenerate in energy with the normal H atom. Again HF and DFAs violate this constancy condition and display massive errors for these fractional spin systems that give rise to a large static correlation error. Furthermore, the combination and extension of both fractional charges and fraction spin conditions to consider any general fractional occupations has recently revealed[13] a much more stringent condition for the energy functional: it has a flat plane behavior, linear along the fractional charge coordinate and constant along the fractional spin coordinate, with a clear line of discontinuity at integer numbers of electrons. Violation of this condition by approximate functionals is important because it leads to qualitative failures to describe, for example, the gap of strongly correlated systems.

With these perspectives we would like to investigate some wave function methods beyond DFT to see if they violate the same exact conditions, by examining simple systems with

* Corresponding author e-mail: weitao.yang@duke.edu.

10.1021/ct8005419 CCC: $40.75
Published on Web 03/18/2009

fractional occupations. This may give insight into the relative performance of DFAs and wave function-based methods in challenging situations that are related to delocalization error and static correlation error.

In this work we focus on second-order Møller-Plesset perturbation theory (MP2). MP2 has developed a long standing reputation in the quantum chemistry community and is still a very widely used method with many applications and active development. It reliably alleviates the lack of correlation in HF to give much improved results for many energetic and geometric properties.

Systems with Fractional Charges and Fractional Spins

We explain here how to carry out DFT calculations with fractional charge and fractional spins. The key feature of DFT calculations is the use of a noninteracting reference system to represent the physical electron density and the noninteracting kinetic energy. The noninteracting reference system can have a local one-electron potential, as in the common Kohn−Sham approach (KS), or a nonlocal one-electron potential, as in the generalized Kohn−Sham approach.

In a usual DFT calculation the specification of the charge and the multiplicity of the system are sufficient to give the number of electrons of each spin and hence the set of occupation numbers for the orbitals, $\{n_i\}$. The lowest set of orbitals of each spin (as determined by the energy of the orbital, $\{\varepsilon_i\}$) are occupied ($n_i = 1$), and the higher energy orbitals are unoccupied $n_a = 0$

$$\varepsilon_i \leq \varepsilon_f : n_i = 1 \tag{1}$$

$$\varepsilon_a > \varepsilon_f : n_a = 0 \tag{2}$$

Systems with fractional charge or fractional spins are not themselves physical systems, but they come from the dissociation limits of physical systems,[13,14] making these fractional systems critical for analyzing the performance of DFAs.

Fractional charge systems can also come from the grand canonical ensemble at zero temperature,[4] and so do fractional spin systems.[3] However, an ensemble calculation with any DFA would clearly give the total energies satisfying the linearity condition for fractional charge and also the constancy condition for fractional spins, making error only at the integer points, even though the DFAs can have massive delocalization and static correlation errors. Therefore such ensemble calculations are not useful for investigating the origins of errors in DFAs. As a system dissociates, such as H_2^+, the bonding highest occupied molecular orbital (HOMO) becomes delocalized over two centers, and each center sees only part of the HOMO. In other words, the HOMO of each center appears as half-occupied. This is why calculations with fractional orbital occupations in KS or generalized KS are the relevant and important approach for studying DFAs.

Fractional charges and fractional spins are given in practical calculations by a simple change of the occupation numbers, that not all these occupations have to be either one or zero even at zero temperature. For example if we consider a hypothetical system with fractional charges, then the only way this can appear is with fractional occupation of one orbital, the frontier orbital. For a $J + \delta$ system with J integer and $0 < \delta < 1$ then

$$\varepsilon_i < \varepsilon_f : n_i = 1 \tag{3}$$

$$\varepsilon_f = \varepsilon_f : n_f = \delta \tag{4}$$

$$\varepsilon_a > \varepsilon_f : n_a = 0 \tag{5}$$

In a system with degeneracy it is also possible to get fractional occupations of orbitals, this time even with integer number of electrons, for example a g-fold degeneracy can give

$$\varepsilon_i < \varepsilon_f : n_i = 1 \tag{6}$$

$$\varepsilon_f = \varepsilon_f : \sum_g n_f^g = 1 \tag{7}$$

$$\varepsilon_a > \varepsilon_f : n_a = 0 \tag{8}$$

the n_f^g do not have to be integer. A simple example of this is a hydrogen atom where the α and β orbitals are degenerate leading to the scenario of fractional spins.

To make this point clear, let us consider a simple fractional charge system, for example a hydrogen atom with half an electron, $H^{1/2+}$. There are two possible ways to view this system: (1) An ensemble average perspective, that requires two calculations on the hydrogen atom, with zero electrons and with one electron, and then taking the appropriate linear combination of the two; and (2) the fractional occupation perspective, where a hydrogen atom with half an electron is explicitly calculated. For the exact energy functional these two views give identical results. However for DFAs the difference between the two is striking: (1) always gives a reasonable answer, as all methods perform well for H and H^+, and it is only (2) which reveals the failures of the approximate methods, e.g. a too low energy for $H^{1/2+}$ with LDA, for example. And even more importantly, it is only (2) which corresponds to the energy of stretched H_2^+, a real integer system.

Thus, for this fractional hydrogen with half an electron, LDA gives a very bad energy, and a better LDA energy could be obtained by the linear combination of the energies of H and H^+. However, we are not really interested in the best energy of $H^{1/2+}$ but only in the one that would be obtained if $H^{1/2+}$ was found in a real system, such as stretched H_2^+. Thus, we focus on dissociating real systems and understanding the methods, and here is where the fractional occupation approach is very insightful. The power of the fractional occupation perspective relies on the fact that fractional charges and fractional spins do arise naturally in the limit of dissociation of systems with integer occupations and reveal spectacular failures of many currently used methods. Also, as the exact conditions for the energy functional are known for fractional charges and spins, these failures can be understood and better methods developed.

MP2 with Fractional Occupations

We now extend the MP2 expression for fractional occupations, involving unoccupied orbitals, beyond the previous

results of HF and other DFAs containing only occupied orbitals.[11] In canonical MP2 from a HF reference Hamiltonian, the correlation energy is given by

$$E_c^{\mathrm{MP2}} = \frac{1}{4}\sum_{ij}^{occ}\sum_{ab}^{virt}\frac{\langle ij||ab\rangle^2}{\varepsilon_i + \varepsilon_j - \varepsilon_a - \varepsilon_b} \tag{9}$$

where standard notation is used for the two electron integrals, $\langle ij||ab\rangle = \langle ij|ab\rangle - \langle ij|ba\rangle$ and $\langle ij|ab\rangle = \int\int \varphi_i(\mathbf{x})\varphi_a(\mathbf{x})(1/(|\mathbf{r} - \mathbf{r}'|)\varphi_j(\mathbf{x}')\varphi_b(\mathbf{x}')d\mathbf{x}d\mathbf{x}'$, where $\mathbf{x}$ and $\mathbf{x}'$ are combined spatial and spin coordinates. In this equation i and j denote occupied orbitals and a and b denote virtual orbitals. All orbitals are canonical HF orbitals, and ε_p represents HF single particle energies (eigenvalues).

This expression can be generalized to include occupation numbers, n_p, by considering the finite temperature grand-canonical ensemble,[15] also see Casida[26]

$$E_c^{\mathrm{MP2}} = \frac{1}{4}\sum_{ij}^{all}\sum_{ab}^{all} n_i n_j \frac{\langle ij||ab\rangle^2}{\varepsilon_i + \varepsilon_j - \varepsilon_a - \varepsilon_b}(1 - n_a)(1 - n_b) \tag{10}$$

Note that with the inclusion of occupation numbers the summations now run over all orbitals, and there is no separation into occupied and virtual orbitals.

It is now possible to investigate the behavior of the total MP2 energy expression with fractional occupation of the orbitals in an external potential $v(\mathbf{r})$

$$E_v^{\mathrm{MP2}} = \sum_i^{all} n_i\langle\varphi_i|-\frac{1}{2}\nabla^2|\varphi_i\rangle + \int v(\mathbf{r})\rho(\mathbf{r})d\mathbf{r} + \sum_{i\geq j}^{all} n_i n_j\langle ij||ij\rangle + \frac{1}{4}\sum_{ijab}^{all} n_i n_j \frac{\langle ij||ab\rangle^2}{\varepsilon_i + \varepsilon_j - \varepsilon_a - \varepsilon_b}(1 - n_a)(1 - n_b) \tag{11}$$

where the occupation numbers, $0 \leq n_i \leq 1$, sum up to give the total number of electrons, $\Sigma_i^{all} n_i = N$, and give the electron density, $\rho(\mathbf{r}) = \Sigma_i^{all} n_i \varphi_i^2(\mathbf{r})$. In this case the number of electrons, N, does not have to be an integer.

The original finite temperature grand-canonical ensemble[4] and in the specific case of MP2[15] would give for fractional charge a linear interpolation of energies between the two nearby integers. This is not very interesting, because it does not tell us how the approximate energy functional will behave in physical systems with integer number of electrons but with fractional charge character.[1] Instead, we extend the functional to fractional charges following what has been done for normal KS or HF functionals.[11,12] Thus, at fractional charges, we carry out the fractional-charge self-consistent HF calculation, and we add the MP2 correlation energy as a perturbation using the HF orbitals obtained for the same fractional charge. We could also carry out the fully self-consistent optimization including the MP2 correlation energy,[16,17] but we do not do that.

As in previous studies we consider the behavior of the energy expression as we fractionally add or subtract an electron from a zero-temperature ground-state system, $n_i = 1$ for $i < f$, $n_f = \delta$, $n_a = 0$ for $a > f$, where f denotes a frontier orbital, either the highest occupied molecular orbital (HOMO) or the lowest unoccupied molecular orbital (LUMO).

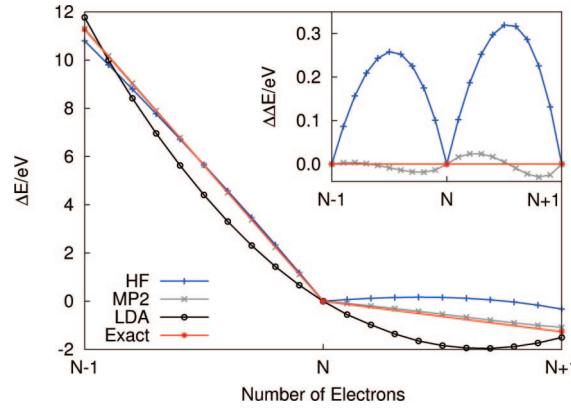

Figure 1. Behavior of the energy of the carbon atom with fractional numbers of electron electrons for HF, MP2, LDA, and exact. The inset shows the deviation of HF and MP2 from their corresponding linear interpolations. All calculations are unrestricted, and no symmetry constraints have been applied.

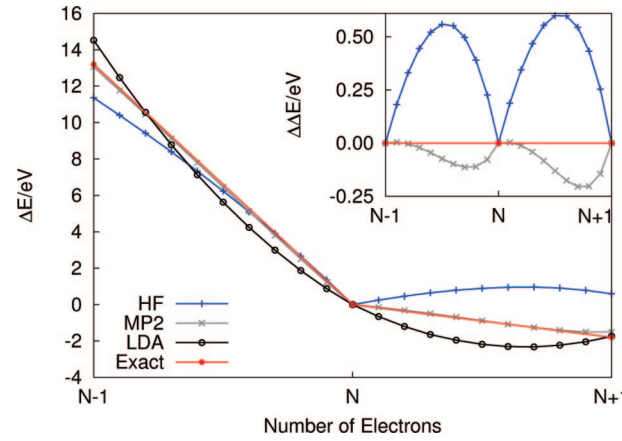

Figure 2. The same as Figure 1 for the OH molecule.

Figure 1 shows MP2 calculations with fractional numbers of electrons (E *vs* N curve) for the carbon atom with five to seven electrons. HF and LDA results are also included for comparison. Calculations have been carried out with a cc-pVQZ basis set in a modified version of NWChem.[18] LDA and HF calculations are self-consistent with fixed occupation numbers, and the MP2 energy is given by eq (11) with these fractionally occupied self-consistent HF orbitals. The exact energy for fractional numbers of electrons is a set of straight lines connecting integer points.[4] For the carbon atom ($N = 6$), the straight line to the left is the ionization energy (experimental value of $I = 11.27$ eV), and the straight line to the right is the negative of the electron affinity (experimental value of $A = 1.27$ eV) as shown in Figure 1. Also shown in the inset is the deviation from the straight line. Another E *vs* N curve is shown in Figure 2 for the OH molecule which has experimental values of $I = 13.2$ eV and $A = 1.8$ eV.

Previous work[1] has related many important errors of DFAs to the nature of their E *vs* N curves: concavity giving localization error and convexity giving delocalization error. HF has a large localization error in this respect, and fur-

thermore the integer points are a long way from the exact values of I and A, due to the lack of correlation in HF. MP2 corrects both of these errors of HF for the carbon atom, with a much better prediction of I and A and also importantly a much straighter interpolation between the integers. For OH the MP2 curve is not as straight, and in general the behavior could be checked for any system of interest.

It is clear that HF does not have the correct straight line behavior between the integers, and the concave behavior is best understood as being due to the lack of electron correlation. This is quite different in essence to the behavior of DFAs, as seen for LDA, which have a convex interpolation and delocalization error. For these DFAs as the system size increases to the bulk limit, many-electron self-interaction error decreases causing the E *vs* N lines to get straighter, however there is a corresponding increase in the delocalization error because the orbitals spread out too much. For HF as the system size increases there is just a growing lack of correlation. Overall, the fact that MP2 and HF do not have this systematic convex behavior means that they will perform differently to DFAs in situations where the delocalization error is important. As MP2 can be closer to the correct straight line behavior and does not in general seem to have an inherent energetic bias for fractional charges, it should have the possibility to have an improved performance in problems related to self-interaction.

Derivatives of the Energy with Respect to *N*

We now explore the partial derivative of the energy with respect to the total number of electrons, keeping the external potential fixed. This is the chemical potential, and its discontinuity is directly related to the energy gap (band gap in solids). We have recently developed the expressions for evaluating the derivative for calculations with an explicit functional of the electron density or the KS orbitals and eigenvalues.[19] The latter functional can be calculated through the optimized effective potential or through the generalized KS method. Specifically, for a variational method such as LDA, the derivative of the energy with respect to the number of electrons is given by the derivative with respect to the frontier orbital occupation number, $dE_v/dN = (\partial E/\partial n_f)_{v_s} = \varepsilon_f$, where v_s is the minimizing local KS potential and ε_f is the KS frontier eigenvalue; this result has been obtained from the derivation of ref 19 in combination with the Janak theorem.[20] Variational methods that include HF can be treated within a generalized KS equation (where the energy is minimized with respect to the orbitals), and the derivatives of the energy are again given by the frontier eigenvalues as discussed in ref 19.

We now extend the formalism of ref 19 to consider a generalized OEP framework where the energy is minimized with respect to a generalized KS potential $v_s^{NL}(\mathbf{r},\mathbf{r}')$. In this case the minimizing potential $v_s^{NL,gs}(\mathbf{r},\mathbf{r}')$ is a nonlocal potential and hence differs from the usual OEP minimizing potential, which is local. This is a simple extension of the potential functional formalism to nonlocal reference potentials for the noninteracting systems.[21]

We consider the potential as the basic variable such that the ground-state energy as a functional of v_s^{NL} and N is given by

$$E_v^{gs} = \min_{v_s^{NL}} E_v[v_s^{NL}, N] = E_v[v_s^{NL,gs}, N] \tag{12}$$

The derivatives with respect to N can be obtained using the chain rule and are simply given by

$$\frac{\partial E_v}{\partial N} = \frac{\partial E_v[v_s^{NL}, N]}{\partial N} \tag{13}$$

$$= \left(\frac{\partial E_v}{\partial N}\right)_{v_s^{NL}} + \int d\mathbf{r}d\mathbf{r}' \frac{\delta E_v}{\delta v_s^{NL}(\mathbf{r},\mathbf{r}')} \cdot \frac{\partial v_s^{NL}(\mathbf{r},\mathbf{r}')}{\partial N} \tag{14}$$

At the minimizing $v_s^{NL} = v_s^{NL,gs}$, the second term disappears because the functional is stationary, and we have

$$\frac{\partial E_v}{\partial N} = \left(\frac{\partial E_v}{\partial N}\right)_{v_s^{NL}} \tag{15}$$

Furthermore, at a constant v_s^{NL}, the total number of electron change can only vary the frontier orbital occupation number n_f, and we have

$$\left(\frac{\partial E_v}{\partial N}\right)_{v_s^{NL}} = \left(\frac{\partial E_v}{\partial n_f}\right)_{v_s^{NL}} \tag{16}$$

which is analogous to what we obtained for the usual OEP when the reference potential is local.[19]

An example of $E_v[v_s^{NL},N]$ is the HF energy functional, and its minimizer is just the one-electron nonlocal potential consisting of the Coulomb and exchange operators. The chemical potential for a HF calculation is just given by eq 16. More generally, the generalized OEP formulation of eq 12 allows one to perform DFT calculations for any explicit functional of the orbitals and eigenvalues, such as MP2. This offers an approach to self-consistent DFT, alternative to the local potential OEP.[16,17]

MP2 is not carried out in a variational fashion but utilizes the minimizing HF potential, $v_s^{NL,HF}$, namely

$$E_v^{\mathrm{MP2}} = E_v^{\mathrm{MP2}}[v_s^{NL,HF}, N] \tag{17}$$

An approximate derivative can be obtained using eq (16)

$$\frac{\partial E_v^{\mathrm{MP2}}}{\partial N} \approx \left(\frac{\partial E[v_s^{NL,HF}, N]}{\partial n_f}\right)_{v_s^{NL,HF}} \tag{18}$$

Applying this expression (eq 18) to the MP2 energy of eq 11 gives an equation for the derivative of the energy with respect to any orbital occupation number

$$\left(\frac{\partial E_v^{\mathrm{MP2}}}{\partial n_p}\right)_{v_s^{NL,HF}} = \langle\varphi_p| - \frac{1}{2}\nabla^2 + v|\varphi_p\rangle + \sum_i 2n_i(\langle ip|ip\rangle - \langle ip|pi\rangle) + \frac{1}{2}\left[\sum_{jab} n_j(1-n_a)(1-n_b)\frac{\langle pj||ab\rangle^2}{\varepsilon_p + \varepsilon_j - \varepsilon_a - \varepsilon_b} - \sum_{ijb} n_i n_j(1-n_b)\frac{\langle ij||pb\rangle^2}{\varepsilon_i + \varepsilon_j - \varepsilon_p - \varepsilon_b}\right] \tag{19}$$

When evaluated for a zero temperate ground state, with integer occupations, it gives expressions for the derivatives

Table 1. Comparison, in eV, of ε_{homo} with $-I$, ε_{lumo} with $-A$, and the $\varepsilon_{lumo} - \varepsilon_{homo}$ with $I - A$ for HF and MP2[a]

mol	ε_{HF}	$\partial E_v^{MP2}/\partial n_f$	$I-A$	ε_{HF}	$\partial E_v^{MP2}/\partial n_f$	I	ε_{HF}	$\partial E_v^{MP2}/\partial n_f$	A
Li	5.63	5.14	4.8	5.34	5.37	5.4	−0.29	0.23	0.6
Be	9.60	9.69	9.0	8.41	8.98	9.4	−1.19	−0.71	0.4
B	9.76	8.58	8.0	8.67	8.45	8.3	−1.09	−0.13	0.3
C	12.72	10.51	10.00	11.94	11.33	11.27	−0.78	0.82	1.27
N	18.89	15.81	14.46	15.52	14.44	14.53	−3.37	−1.37	0.07
O	16.83	12.77	12.16	14.19	13.17	13.62	−2.64	0.40	1.46
F	20.01	13.71	14.02	18.47	16.41	17.42	−1.54	2.70	3.40
F_2	20.50	13.39	14.4	18.13	13.70	15.7	−2.37	0.31	1.3
OH	16.56	10.95	11.4	13.95	12.12	13.2	−2.61	1.17	1.8
NH_2	15.49	11.32	10.6	12.60	11.46	11.4	−2.89	0.14	0.8
CH_3	13.30	10.42	9.8	10.47	9.64	9.9	−2.83	−0.78	0.1
CN	13.29	10.80	10.2	14.14	14.54	14.0	0.85	3.74	3.8
O_2	17.98	11.57	11.8	15.18	11.06	12.2	−2.80	−0.51	0.4
MAE	3.84	0.66		0.98	0.56		3.02	0.78	
	From finite difference using $\Delta n = 0.001$								
MAE	3.84	0.79		0.98	0.75		3.02	0.70	

[a] Calculations are unrestricted with a cc-pVQZ basis set and with no symmetry constraints. MAE the mean absolute error and the MAE for finite difference derivatives of HF and MP2, with a change of the occupation number of 0.001, are also shown.

with respect to frontier occupations and, using eq 18, approximate derivatives of the energy with respect to the number of electrons

$$\left.\frac{\partial E_v^{MP2}}{\partial N}\right|_{\pm} \approx \left(\frac{\partial E_v^{MP2}}{\partial n_f}\right)_{v_s^{NL,HF}} = \langle f|-\frac{1}{2}\nabla^2 + v|f\rangle + \sum_i^{occ} 2(\langle if|if\rangle - \langle if|fi\rangle) + \frac{1}{2}\left[\sum_j^{occ}\sum_{ab}^{virt}\frac{\langle fj||ab\rangle^2}{\varepsilon_f+\varepsilon_j-\varepsilon_a-\varepsilon_b} - \sum_{ij}^{occ}\sum_b^{virt}\frac{\langle ij||fb\rangle^2}{\varepsilon_i+\varepsilon_j-\varepsilon_f-\varepsilon_b}\right] = \varepsilon_f^{MP2} \quad (20)$$

For MP2 the single-particle energy of eq 20 does not exactly agree with the full derivative. However the difference is relatively small as can be seen from the comparison with the finite difference calculation of the derivative. For example, for the carbon atom, the finite difference derivative with $\Delta n = 0.001$ gives $\Delta E/\Delta n_{homo} = -11.103$ *eV* and $\Delta E/\Delta n_{lumo} = -0.881$ *eV*, and eq 20 gives $\partial E/\partial n_{homo} = -11.334$ *eV* and $\partial E/\partial n_{lumo} = -0.824$ *eV*. The slight difference between the two results is due to the fact that the potential has been fixed, and therefore the second term in eq 14 has been ignored. Fixing the potential at $v_s^{NL,HF}$ is equivalent to freezing the orbitals and the eigenvalues upon varying the occupation numbers, which is different than just fixing the orbitals. The orbital relaxation can be evaluated using coupled-perturbed HF, but this correction would not be needed if the energy is minimized with respect to the orbitals, as previously done within DFT.[16,17] Furthermore, the eigenvalues on the bottom of eq 10 can also vary with the occupation number and hence they also contribute. If an expression for the full derivatives of eq 11 with respect to the number of electrons is needed, then these orbital and eigenvalue contributions must be included as dictated by eq 14.

The results in Table 1 compare the HOMO and LUMO single-particle energies from HF and MP2 with the corresponding I and A experimental values of a set of small atoms and molecules. Koopmans' theorem, which equates the HF frontier single-particle energies with $-I$ and $-A$, is improved upon by the second-order MP2 frontier single-particle energies. The MP2 LUMO energy gives a reasonable approximation to $-A$, whereas the HF LUMO energy seems almost meaningless. The difference between the derivative to the left, I, and the derivative to the right, A, gives the gap which is much improved with MP2 for these small systems. Also the overall mean absolute error calculated with finite difference, which is obviously the same for HF due to its variational nature, shows that the neglected parts of the derivative for MP2 do not lead to any qualitative differences for this set of molecules. The MP2 approximation to I and A and the gap can be obtained at almost no extra cost while doing a normal MP2 calculation.

The expression for the MP2 single-particle energy eq 20 can also be obtained from the second-order self-energy in propagator theory[22] and has been used to calculate the quasiparticle band gap of solids.[23,24] In the present work it is derived in a very simple manner and with a clear connection to the behavior for fractional numbers of electrons. This idea can also be easily extended to other wave function based methods (e.g., coupled cluster) if the method can be generalized to finite temperature to include occupation numbers. Then the behavior for fractional numbers of electrons could be investigated, and the straightness of the *E vs N* curve will give an indication of the quality of the frontier orbital eigenvalues and more generally on performance of problems related to the delocalization error.

MP2 for Fractional Spins

Next we would like to investigate MP2 for fractional spins to understand its performance on static correlation problems. However, there is very little to explore as the energy for any system with more than one fractional occupation within a degenerate set in eq 10 diverges. This is clearest for the stretched H_2 molecule where the restricted MP2 energy goes to $-\infty$ as shown in Figure 3. Another example is a calculation on the spherical boron atom (with occupation of 1/3 for each of the α p orbitals) where the MP2 energy also diverges. In other words, MP2 fails for systems with strong correlations which is well-known in chemistry as exemplified by the poor performance on transition metal compounds. This failure in degenerate situations can be attempted to be corrected by different techniques, and one of the simplest such methods

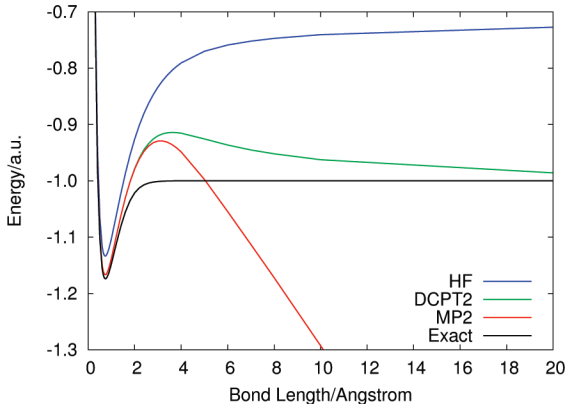

Figure 3. The energy of the H_2 molecule as it is stretched, calculated with a cc-pVQZ basis set with HF, MP2, DCPT2, and exact. It should be noted that the DCPT2 energy goes slightly below −1.0 au at larger distances, e.g. at 10000 Angstrom it is −1.0125 au.

in the literature is the degenerate corrected perturbation theory (DCPT2) of Assfeld et al.[25]

The DCPT2 correlation energy is given by

$$E_c^{DCPT2} = \frac{1}{8}\sum_{ij}^{occ}\sum_{ab}^{virt} D_{abij} - \sqrt{(D_{abij})^2 + 4\langle ij||ab\rangle^2} \quad (21)$$

where $D_{abij} = \varepsilon_a + \varepsilon_b - \varepsilon_i - \varepsilon_j$. The inclusion of fractional occupations in a analogous way to MP2 gives

$$E_c^{DCPT2} = \frac{1}{8}\sum_{ijab}^{all} D_{abij} - \sqrt{(D_{abij})^2 + 4n_i n_j\langle ij||ab\rangle^2(1-n_a)(1-n_b)} \quad (22)$$

The total energy of DCPT2 is given by eq 11 replacing the MP2 part with eq 22.

Figure 4 shows the behavior for fractional charge and spin combined for the H atom from zero to two electrons with spin-up occupation $0 \le n_\alpha \le 1$ and spin-down occupation $0 \le n_\beta \le 1$, as studied previously.[13] The consideration of this figure and the energy at $[n_\alpha,n_\beta]$ has been critical for understanding the performance of DFT methods and goes beyond the separate consideration of fractional charges, which can be seen along the edges (connecting [0,0] to [1,0] to [1,1] and conversely [0,0] to [0,1] to [1,1]), and the pure fractional spins, which can be seen across the middle (connecting 1,0] with [0,1]). The problem of a Mott insulator is highlighted by the point at [1/2,1/2] and its gap from the line [0,0] to [1/2,1/2] to [1,1].

The exact energy of H $[n_\alpha,n_\beta]$ is plotted in Figure 4a and shows a flat plane behavior with a discontinuous derivative at all points along the constancy line at $N = n_\alpha + n_\beta = 1$. Figure 4b illustrates the behavior of the MP2 energy, which diverges to $-\infty$ except along the pure fractional charge line, seen along the edges of the plot and corresponding to Figure 1. Figure 4c shows the DCPT2 energy of eq 22, which has a very similar behavior to MP2 along the fractional charge line but corrects for the divergence of the MP2 energy expression for fractional spins. There is some slight strange behavior due to the nonanalyticity of the square-root function,

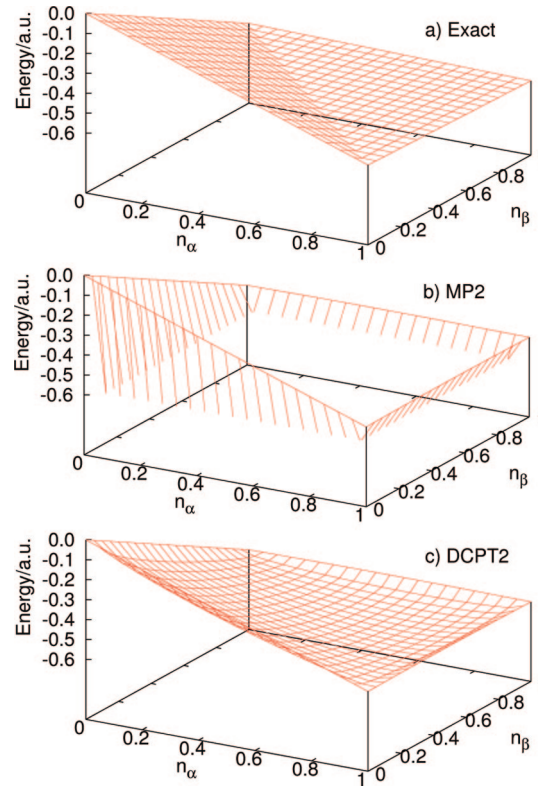

Figure 4. The energy of the hydrogen atom with fractional charges and fractional spins combined for exact, MP2, and DCPT2. All calculations use a cc-pVQZ basis set.

but it only affects points next to the fractional charge line. For the middle point of the plot, an H atom with $n_\alpha = n_\beta = 1/2$ which is the prototype of a strongly correlated system, DCPT2 gives a reasonable energy that exactly corresponds to the dissociation limit of H_2 presented in Figure 3.

It is extremely interesting to see that at the key middle point with $n_\alpha = n_\beta = 1/2$, the slope to the left and the right, $\partial E_v^{DCPT2}/\partial N|_\pm$, are the same, and therefore there is no discontinuous behavior and a zero gap. This illustrates the possibility for a method to give the energy of a strongly correlated system correctly but still fail to even qualitatively give its gap.

Conclusion

In conclusion, in the spirit of DFT, we have investigated the MP2 method for fractional charges and fractional spins. We find that it gives a reasonable straight line behavior for fractional charges between the integers. A generalized OEP formalism has been developed for nonlocal KS potentials, which can be used to perform DFT calculations for any explicit functional of the orbitals and eigenvalues. It also facilitates the calculation of the chemical potential. Thus, the MP2 single-particle energies can be obtained by differentiating the MP2 energy expression with respect to the frontier occupation numbers at fixed KS potential and give HOMO and LUMO single-particle energies that are in good agreement with experimental $-I$ and $-A$. For fractional spin systems with exact degeneracies MP2 unphysically diverges to give an energy of $-\infty$. Degenerate-corrected perturbation theory alleviates this divergence but still qualitatively fails

for the scenario of combined fractional charge and fractional spins, as it misses the key derivative discontinuity necessary to give the gap.

Overall the understanding of a wave function based method such as MP2 can be enlightened by considering its performance for exact conditions of the energy that can be explored in extremely simple tests.

Acknowledgment. We dedicate this article to Professor John Perdew to wish him a happy 65th birthday and to thank him for his inspiring and pioneering work. The authors also acknowledge the support of funding from the National Science Foundation.

References

(1) Mori-Sánchez, P.; Cohen, A. J.; Yang, W. *Phys. Rev. Lett.* **2008**, *100*, 146401-1–146401-4.

(2) Cohen, A. J.; Mori-Sánchez, P.; Yang, W. *Science* **2008**, *321*, 792–784.

(3) Cohen, A. J.; Mori-Sánchez, P.; Yang, W. *J. Chem. Phys.* **2008**, *129*, 121104.

(4) Perdew, J. P.; Parr, R. G.; Levy, M.; Balduz, J. L., Jr. *Phys. Rev. Lett.* **1982**, *49*, 1691–1694.

(5) Perdew, J. P.; Burke, K.; Ernzerhof, M. *Phys. Rev. Lett.* **1996**, *77*, 3865.

(6) Becke, A. D. *Phys. Rev. A* **1988**, *38*, 3098–3100.

(7) Lee, C.; Yang, W.; Parr, R. G. *Phys. Rev. B* **1988**, *37*, 785–789.

(8) Becke, A. D. *J. Chem. Phys.* **1993**, *98*, 5648–5652.

(9) Ruzsinszky, A.; Perdew, J. P.; Csonka, G. I.; Vydrov, O. A.; Scuseria, G. E. *J. Chem. Phys.* **2006**, *125*, 194112-1–194112-8.

(10) Ruzsinszky, A.; Perdew, J. P.; Csonka, G. I.; Vydrov, O. A.; Scuseria, G. E. *J. Chem. Phys.* **2007**, *126*, 104102-1–104102-8.

(11) Mori-Sánchez, P.; Cohen, A. J.; Yang, W. *J. Chem. Phys.* **2006**, *125*, 201102-1–201102-4.

(12) Perdew, J. P.; Ruzsinszky, A.; Csonka, G. I.; Vydrov, O. A.; Scuseria, G. E.; Staroverov, V. N.; Tao, J. *Phys. Rev. A* **2007**, *76*, 040501(R).

(13) Mori-Sánchez, P.; Cohen, A. J.; Yang, W. *Phys. Rev. Lett.* **2009**, *102*, 066403-1−066403-4.

(14) Yang, W.; Zhang, Y.; Ayers, P. W. *Phys. Rev. Lett.* **2000**, *84*, 5172–5175.

(15) Blaizot, J.-P.; Ripka, G. *Quantum Theory of Finite Systems*; The MIT Press: 1986; p 437.

(16) Mori-Sanchez, P.; Wu, Q.; Yang, W. *J. Chem. Phys.* **2005**, *123*, 062204-1−062204-14.

(17) Bartlett, R. J.; Lotrich, V. F.; Schweigert, I. V. *J. Chem. Phys.* **2005**, *123*, 062205.

(18) High Performance Computational Chemistry Group. Pacific Northwest National Laboratory, Richland, Washington 99352, U.S.A., 2002.

(19) Cohen, A. J.; Mori-Sánchez, P.; Yang, W. *Phys. Rev. B* **2008**, *77*, 115123-1–115123-6.

(20) Janak, J. F. *Phys. Rev. B* **1978**, *18*, 7165–7168.

(21) Yang, W.; Ayers, P. W.; Wu, Q. *Phys. Rev. Lett.* **2004**, *92*, 146404-1–146404-4.

(22) Linderberg, J.; Öhrn, Y. *Propagators in Quantum Chemistry*; John Wiley & Sons: New York, 1973.

(23) Pino, R.; Scuseria, G. E. *J. Chem. Phys.* **2004**, *121*, 2553–2557.

(24) Ayala, P. Y.; Kudin, K. N.; Scuseria, G. E. *J. Chem. Phys.* **2001**, *115*, 9698–9707.

(25) Assfeld, X.; Almlöf, J. E.; Truhlar, D. G. *Chem. Phys. Lett.* **1995**, *241*, 438–444.

(26) Casida, M. *Phys. Rev. B* **1999**, *59*, 4694–4698.

CT8005419

JCTC Journal of Chemical Theory and Computation

Validity of the Extended Koopmans' Theorem

Matthias Ernzerhof*

Département de Chimie, Université de Montréal C.P. 6128 Succursale A, Montréal, Québec H3C 3J7, Canada

Received December 12, 2008

Abstract: The generalized Koopmans' theorem (EKT) yields an estimate of ionization potentials (IPs) of an *N*-electron system. This estimate (IP^{EKT}) is obtained as an eigenvalue of a generalized eigenvalue problem. Katriel and Davidson provided a proof [Katriel, J.; Davidson, E. R. *Proc. Natl. Acad. Sci. U.S.A.*, **1980**, *77*, 1403.] that the EKT predicts the exact lowest IP for ground states of Coulomb systems. However, subsequently, several articles have been published challenging the exactness of the EKT and providing disproofs. This apparent contradiction is resolved by demonstrating that the lowest eigenvalue of the generalized Koopmans' procedure does, in general, not exist. This explains why contradictory results are obtained about the lowest IP^{EKT} since its existence has implicitly been assumed. Nonetheless, it will also be shown here that the generalized Koopmans' approach gives IPs that are arbitrarily close to the exact lowest ionization energy. The eigenvalues obtained according to the EKT have an accumulation point given by the exact lowest IP.

1. Introduction

Koopmans' theorem[1] is widely used to estimate ionization energies on the basis of Hartree−Fock calculations. In view of the usefulness of this theorem, considerable efforts have been made to generalize Koopmans' theorem by broadening its Hartree−Fock framework. An extended Koopmans' theorem (EKT), based on correlated wave functions, has been developed by Day, Smith, and Garrod[2,3] and Morrell, Parr, and Levy.[4] The EKT is presently employed on a regular basis as witnessed by several recent publications including.[5−8] The EKT makes use of an extended Fock operator $F(1,1')$ constructed from the one- and two-particle density matrix of a correlated wave function. i (e.g., 1 or $1'$) stands for the spatial and spin coordinates ($\mathbf{r}_i$, σ_i) indexed with i. An approximation (IP^{EKT}) to the lowest ionization potential (IP) of the N-particle ground state (ψ) is then obtained as the lowest eigenvalue of the generalized eigenvalue problem[2,4] (implicitly assuming that the lowest eigenvalue does exist)

$$\int d1' F(1,1')\varphi(1') = \mathrm{IP}^{\mathrm{EKT}} \int d1' \gamma(1,1')\varphi(1'), \quad (1)$$

where

$$F(1,1') = h(1)\gamma(1,1') + \int d2 \frac{\Gamma(1,2;1',2)}{|\mathbf{r}_1 - \mathbf{r}_2|} \quad (2)$$

$h(1) = -1/2\Delta_{r_1} + v(1)$ is the one-particle Hamiltonian. v denotes a local external potential. $\gamma(1,1')$ and $\Gamma(1,2;1',2')$ are given by

$$\gamma(1,1') = \langle\psi|\hat{\Psi}^\dagger(1')\hat{\Psi}(1)|\psi\rangle \quad (3)$$

and

$$\Gamma(1,2;1',2') = \langle\psi|\hat{\Psi}^\dagger(1')\hat{\Psi}^\dagger(2')\hat{\Psi}(2)\hat{\Psi}(1)|\psi\rangle \quad (4)$$

respectively. $\hat{\Psi}(1)$ stands for a field operator,[9] which annihilates an electron in the state corresponding to the argument of the operator. The fact that only the one- and two- particle density matrices are needed to construct $F(1,1')$ has contributed to the popularity of the extended Koopmans' procedure because these quantities are available in many quantum chemistry program codes.

Morrell, Parr, and Levy[4] have shown that the "lowest" eigenvalue (implicitly assuming it exists) of the generalized eigenvalue problem eq 1 is given by the asymptotic, exponential decay length of the electron density, that is, $\lim_{r\to\infty}\rho(r) \propto \exp(-2(2\mathrm{IP}^{\mathrm{EKT}})^{1/2}r)$. They also conjectured that the decay length of the density is equal to the exact lowest

* E-mail: Matthias.Ernzerhof@UMontreal.ca.

10.1021/ct800552k CCC: $40.75
Published on Web 03/24/2009

ionization energy. This conjecture was supported by Ahlrichs,[10] Levy and Parr,[11] and Katriel and Davidson.[12] The question whether the lowest ionization energy obtained from the EK procedure is exact has been discussed extensively in the literature. Up to, now no completely satisfying answer has been found. Katriel and Davidson[12] argued that IP^{EKT} is equal to the exact ionization energy. Their argument is based on the asymptotic behavior of the wave function as one electron wanders away from the finite system. Doubts about the exactness of the EK procedure have been raised by Smith and Öhrn.[13] Pickup[14] and Pickup and Snijders[15] analyzed the EK procedure using the perturbation expansion of the ionization energy. They showed that in general certain second-order contributions of the expansion of the exact IP are missing in the perturbation expansion of IP^{EKT}. Andersen and Simons arrived at the same conclusion.[16] Olsen and Sundholm[17] presented a numerical investigation of the perturbation expansion and concluded that the missing terms in the EKT perturbation expansion are zero and that the IP^{EKT} is exact. More recently, a sufficient condition for the validity of the EKT has been derived[18] that is difficult to verify in practical calculations, however. Despite these attempts to resolve the paradox concerning the exactness of IP^{EKT}, a satisfying solution has not been found in the sense that the shortcomings of either the proof, the disproof, or of both have not been discovered.

Numerical studies have been undertaken[19−28] to obtain a better understanding of the accuracy of the EK procedure. Without going into details, we state the main results of these investigations. Comparison of the lowest ionization energy, as obtained from Full-CI calculations,[22,24−28] with IP^{EKT} obtained employing the Full-CI density matrices shows that there is strong numerical evidence that these two quantities converge toward the same number upon increasing the size of the one-particle basis set. We want to stress that it is of course not possible to resolve the paradox, apparent in the formal investigations of the EKT, via numerical calculations. However, the accuracy of the numerical results underlines the usefulness of the EK procedure.

In the present work, we will shown that a careful interpretation of the results of Katriel and Davidson and the findings of Pickup and Snijders,[14,15] and Andersen and Simons[16] removes the incompatibilities. We argue that the question whether the lowest eigenvalue of the EK procedure gives the exact lowest IP or not is not the right question to ask since the lowest eigenvalue of the EKT eigenvalue problem does, in general, not exist. However, all proofs and disproofs given previously implicitly assume that a lowest eigenvalue does exist.

To close the introduction we provide an outline of the article. In section 2, the working equations of the EKT for the lowest IP are derived. In section 3, the argument by Katriel and Davidson is examined, it is shown that their findings do not support the conclusion that IP^{EKT} is exact. The asymptotic behavior of the wave function in then used in section 4 to show that no eigenvalue of the EK procedure can yield the exact lowest IP. In the last section (section 5), we show that it is however possible to find eigenvalues of eq 1, which are arbitrarily close (but not equal) to the exact, lowest ionization energy, that is, the eigenvalues of the EKT eigenvalue problem have an accumulation point at the exact, lowest IP.

2. Working Equations of the Extended Koopmans' Theorem

Following,[2,3] we summarize the extended Koopmans' procedure as far as it is relevant for the present work. We start from the ansatz

$$|\psi^{N-1}\rangle = \mathcal{N}^{-1/2} \int d1 \varphi(1) \hat{\Psi}(1) |\psi\rangle \tag{5}$$

for the $(N-1)$-particle wave function. $\mathcal{N}$ denotes an appropriate normalization constant. The linear combination of $\hat{\Psi}(1)$ operators in eq 5 annihilates an electron in the orbital $\varphi(1)$ in $|\psi\rangle$. The amplitude $\varphi(1)$ constitutes the actual variational parameter in eq 5. Using this trial function in the Raleigh−Ritz quotient and varying the energy with respect to the amplitude $\varphi(1)$ leads to an eigenvalue equation for $\varphi(1)$

$$\int d1' \{\langle\psi|\hat{\Psi}^\dagger(1)\hat{H}\hat{\Psi}(1')|\psi\rangle - E^{(N-1)}\langle\psi|\hat{\Psi}^\dagger(1)\hat{\Psi}(1')|\psi\rangle\}\varphi(1') = 0 \tag{6}$$

where we assume, as throughout the paper, that all wave functions and orbitals are real. Since we are interested in the difference between the energy E^{N-1} of the approximate $(N-1)$-particle wave function and the energy E of the N-particle system, we add $0 = d1'\{-\langle\psi|\hat{\Psi}^\dagger(1)\hat{\Psi}(1')\hat{H}|\psi\rangle + E\langle\psi|\hat{\Psi}^\dagger(1)\hat{\Psi}(1')|\psi\rangle\}\varphi(1')$ to eq 6. Furthermore, we make use of the definition of the one-particle density matrix, $\gamma(1,1') = \langle\psi|\hat{\Psi}^\dagger(1)\hat{\Psi}(1')|\psi\rangle$, to obtain

$$\begin{aligned}\int d1' \{&\langle\psi|\hat{\Psi}^\dagger(1)\hat{H}\hat{\Psi}(1')|\psi\rangle - \langle\psi|\hat{\Psi}^\dagger(1)\hat{\Psi}(1')\hat{H}|\psi\rangle + \\ &(E - E^{(N-1)})\langle\psi|\hat{\Psi}^\dagger(1)\hat{\Psi}(1')|\psi\rangle\}\varphi(1') = 0 \Leftrightarrow \\ \int d1' \{&-\langle\psi|\hat{\Psi}^\dagger(1)[\hat{\Psi}(1'), \hat{H}]|\psi\rangle - IP^{EKT}\gamma(1,1')\}\varphi(1') = 0\end{aligned} \tag{7}$$

The eigenvalues of the this generalized eigenvalue problem are obviously bound from below by the exact, lowest ionization energy of the N-particle system. We define the extended Fock operator $F(1,1')$ by

$$F(1,1') = -\langle\psi|\hat{\Psi}^\dagger(1)[\hat{\Psi}(1'), \hat{H}]|\psi\rangle \tag{8}$$

and recast eq 7 to yield extended Hartree−Fock equation

$$\int d1' F(1,1')\varphi(1') = IP^{EKT} \int d1' \gamma(1,1')\varphi(1') \tag{9}$$

Analogous to Hartree−Fock orbitals, the eigenfunctions φ_i of this generalized eigenvalue problem do not only have a well defined energy but also a well defined occupation number since the φ_i are orthogonal in the metric given by the one-particle density matrix

$$\int d1 d1' \varphi_i(1)\gamma(1,1')\varphi_i(1') = 0 \text{ for } i \neq j \tag{10}$$

The eigenvalues of the metric $\gamma(1,1')$ vary in the interval [0,1]. Note that orbitals with a vanishing norm in the metric

$\gamma(1,1')$ do not represent eigenfunctions of the EKT eigenvalue problem. We do not expect to find the smallest, nonzero eigenvalue of $\gamma(1,1')$ in a Coulomb system, and we will also show that it is not possible to find a φ_i with the lowest energy eigenvalue (i.e., lowest IP^{EKT}).

An explicit expression for $F(1,1')$ is obtained by evaluating the commutator in eq 7. This leads to the representation of $F(1,1')$ given in the introduction. Replacing the exact one-particle density matrix and two-particle density matrix of the N-particle system in eq 9 by the corresponding quantities in the Hartree−Fock approximation leads back to the well-known Hartree−Fock equations.

3. Revisiting the Proof of the Exactness of IP^{EKT}

The proof of the exactness of the EK procedure[12] is based on the behavior[12,29,30] of the ground-state wave function of a Coulomb system as the Nth electron wanders away from the others ($r_N \gg r_1,..., r_{N-1}$, where $r_i = |\mathbf{r}_i|$). The earlier literature[12,29] does not completely describe the asymptotic behavior in the case where the $(N-1)$-electron system is degenerate (for a detailed discussion see ref 30). However, the basic idea presented here does not depend on whether the $(N-1)$-particle ground-state is degenerate or not, and for the sake of simplicity we focus on the case where the $(N-1)$-particle state is nondegenerate and where the results of Katriel and Davidson[12] and others[29] concerning the asymptotic behavior of the ground-state wave function are complete. To summarize these results, we focus on the coordinate of the Nth electron and take the limit $r_N \rightarrow \infty$. The N-particle wave function as a function of the coordinates of the remaining $(N-1)$-electrons collapses toward the energetically lowest accessible[29] $(N-1)$-particle state $\psi^{N-1}(1,..., N-1)$. Accessible $(N-1)$-particle states are states which can be reached from the N-particle state by removing one electron, without violating symmetry restrictions.[29] The detailed derivation shows that[12,29,30]

$$\lim_{r_N\rightarrow\infty} \psi(1,...,N) = N^{-1/2}\rho^{1/2}(N)\psi^{N-1}(1,...,N-1) \quad (11)$$

$\rho(N)$ denotes the spin density. The wave function of the $(N-1)$-particle system is entirely contained in the wave function of the N-particle system in the sense of the limiting procedure of eq 11. In general, however, we do not expect that the N-electron system collapses toward the exact $(N-1)$-particle system for any *finite distance* between the Nth-electron and the $(N-1)$-particle system.

To make the relation of eq 11 to the ansatz eq 5 for the $(N-1)$-particle wave function more explicit we note that eq 11 is equivalent to

$$\lim_{r_N\rightarrow\infty} \hat{\Psi}(N)|\psi\rangle = \rho^{1/2}(N)|\psi^{N-1}\rangle \Rightarrow$$
$$|\psi^{N-1}\rangle = \lim_{r_N\rightarrow\infty} \rho^{-1/2}(N)\hat{\Psi}(N)|\psi\rangle \quad (12)$$

In their argument in favor of the exactness of the EKT, Katriel and Davidson discussed a slightly different representation of eq 12, which we now introduce. To express eq 12 in terms of the natural spin orbitals (NSO's) $n_i(l)$ of ψ, we expand $\hat{\Psi}(N)$ in terms of the NSO's (including the NSO's with zero occupation number)

$$\begin{aligned}\hat{\Psi}(N) &= \sum_I n_i(N)\int dN' n_i(N')\hat{\Psi}(N') \\ &= \sum_i n_i(N)\hat{a}_{n_i}\end{aligned} \quad (13)$$

so that

$$|\psi^{N-1}\rangle = \lim_{r_N\rightarrow\infty} \rho^{-1/2}(N)\sum_i n_i(N)\hat{a}_{n_i}|\psi\rangle \quad (14)$$

$\hat{a}_{n_i}$ denotes the destruction operator corresponding to the orbital n_i. Equation 14 appears to indicate[12] that the lowest ionization energy, obtained according to the EK procedure, is exact since the $(N-1)$-particle wave function can be obtained from ψ by annihilation of an electron. This would imply that there exists an orbital, say $\varphi(N)$, such that

$$\begin{aligned}\int dN\varphi(N)\hat{\Psi}(N)|\psi\rangle &= \hat{a}_\varphi|\psi\rangle \\ &\propto |\psi^{N-1}\rangle\end{aligned} \quad (15)$$

However, all eq 14 (or equivalently eq 12) is saying is that there exists a *sequence* of orbitals

$$\varphi_{r_N}(\mathbf{r})\sigma_N = \rho^{-1/2}(\mathbf{r}_N)\sqrt{\delta(\mathbf{r}-\mathbf{r}_N)}\sigma_N \quad (16)$$

such that we obtain the lowest accessible $(N-1)$-electron state if $\varphi_{\mathbf{r}_N}(\mathbf{r})\sigma_N$ is annihilated in ψ and if we take the limit $r_N \rightarrow \infty$. This does not mean that taking the limit $r_N \rightarrow \infty$, before annihilating the orbital $\varphi_{\mathbf{r}_N}(\mathbf{r})\sigma_N$, defines an orbital φ with the property $\hat{a}_\varphi|\psi\rangle \propto |\psi^{N-1}\rangle$. Taking $r_N \rightarrow \infty$ before applying $\hat{a}_{\varphi_{\mathbf{r}_N}\sigma_N}$ to ψ would (according to eq 12) mean that we destroy a particle at infinite separation from the finite system and multiply the result by $\infty = \lim_{\mathbf{r}_N\rightarrow\infty}\rho^{-1/2}(\mathbf{r}_N)$, an operation which is meaningless.

4. Disproof of the Exactness of IP^{EKT}

In the preceding section we have shown that the argument given by Katriel and Davidson does not imply that the lowest ionization energy can be obtained as the lowest eigenvalue of the EK procedure. Now we provide a proof that no eigenvalue of the generalized EKT eigenvalue equation (eq 9) can be equal to the lowest IP of the N-particle system. This result is intuitively clear since the eigenfunction of the extended Fock operator will be nonzero for finite distances to the $(N-1)$-particle system so that the $(N-1)$-particle system gets polarized by the Nth-electron and this in turn raises the energy compared to the exact $(N-1)$-particle ground state.

The asymptotic collapse of the wave function of a finite system (i.e., $\lim_{r_N\rightarrow\infty}\psi(1,..., N) = N^{-1/2}\rho^{1/2}(N)\psi^{N-1}(1,..., N-1)$) leads to conditions on the two-particle density matrix of a finite system. We get for instance

$$\lim_{r_1\to\infty}\Gamma(1,2;1,2') = N(N-1)\lim_{r_1\to\infty}\int d3,...dN\psi(1,2',3,...N)\psi(1,2,3,...N) = \rho(1)(N-1)\int d3,...dN\psi^{N-1}(2',3,...N)\psi^{N-1}(2,3,...N) = \rho(1)\gamma^{N-1}(2,2') \quad (17)$$

Now we assume that the EK procedure predicts the exact, lowest ionization energy, that is, that there exist a φ such that

$$|\psi^{N-1}\rangle = \gamma_{\varphi\varphi}^{-1/2}a_\varphi|\psi\rangle \quad (18)$$

The normalization factor $\gamma_{\varphi\varphi}$ is given by $\gamma_{\varphi\varphi} = \langle\psi|a_\varphi^\dagger a_\varphi|\psi\rangle$. We use eq 18 to evaluate a certain two-particle density matrix element, namely

$$\int d2d2'\varphi(2)\varphi(2')\Gamma(1,2;1,2') = \langle\psi|a_\varphi^\dagger\hat{\Psi}^\dagger(1)\hat{\Psi}(1)a_\varphi|\psi\rangle = \gamma_{\varphi,\varphi}\rho^{N-1}(1) \quad (19)$$

In the limit $r_1 \to \infty$, eq 19 is incompatible with eq 17 because the density matrix element falls off like $\rho^{N-1}(1)$ instead of showing the correct $\rho(1)$ behavior. The exponential decay of the electron density of a system is given by $\exp(-2(2I)^{1/2}r)$, and since in all examples of interacting Coulomb systems known to us $I^N < I^{N-1}$, we see that ρ^{N-1} becomes exponentially small compared to ρ as $r_1 \to \infty$. These considerations show that the asymptotic behavior of the wave function as $r_N \to \infty$ leads to the conclusion that the EK procedure does not have an eigenvalue which is equal to the exact ionization energy.

5. Discussion and Conclusion

We have shown that no eigenvalue of the extended Hartree−Fock equation (eq 1) yields the exact, lowest IP. On the other hand, it can readily be verified that the EK procedure has the potential to give an arbitrarily good approximation to the lowest IP. It is always possible to find an orbital ϕ, with the corresponding energy $\epsilon = \langle\psi|a_\phi^\dagger a_\phi|\psi\rangle^{-1}\cdot\int d1d1'\phi(1)F(1,1')\phi(1')$, satisfying the inequality

$$\epsilon < \frac{\langle\psi|\hat{\Psi}^\dagger(1)(H-E)\hat{\Psi}(1)|\psi\rangle}{\langle\psi|\hat{\Psi}^\dagger(1)\hat{\Psi}(1)|\psi\rangle} \quad (20)$$

for any given $\mathbf{r}_1$. For the spatial part of ϕ, we could for instance choose $\phi(\mathbf{r}) = \sqrt{[\delta(\mathbf{r}-\mathbf{R})]}$, with $|\mathbf{R}| \gg r_1$. This shows that the lowest IP can be approximated by the EK procedure with any desired accuracy, since $\hat{\Psi}(1)|\psi\rangle$ asymptotically collapses toward $|\psi^{N-1}\rangle$ as r_1 increases.

Our discussion implies that the eigenfunctions of the extended Hartree−Fock equation, which are close in energy to the lowest ionization energy, have a rather counterintuitive character; they minimize the interaction with the $(N-1)$-particle system, and not much can be learned from them about the N-particle system. This has important implications for the choice of basis sets for the EK approach. It is necessary to add basis functions which make it possible for an electron to travel far away from the remaining electrons. On the other hand, the corresponding eigenfunctions will have a very small occupation number so that the generalized eigenvalue problem eq 1 might become ill-conditioned.[27]

Our findings are compatible with the perturbation theoretical disproofs of the exactness of the EK procedure.[14−16] In these disproofs, EKT eigenvalues are shown to be different from the exact, lowest ionization energy. However, it is not shown that it is impossible to find EK eigenvalues which are arbitrarily close to the exact, lowest ionization energy.

Acknowledgment. Most of the work reported here was performed some time ago during a stay at Tulane University with John Perdew. This period was very defining for my scientific career and numerous ideas that we discussed throughout this time still occupy me today. John's optimistic and perseverant approach to science continues to be a great inspiration. Financial support provided by NSERC is gratefully acknowledged.

References

(1) Koopmans, T. A. *Physica* **1934**, *1*, 104.

(2) Day, O. W.; Smith, D. W.; Garrod, C. *Int. J. Quantum Chem. Symp.* **1974**, *8*, 501.

(3) Smith, D. W.; Day, O. W. *J. Chem. Phys.* **1975**, *62*, 113.

(4) Morrell, M. M.; Parr, R. G.; Levy, M. *J. Chem. Phys.* **1975**, *62*, 549.

(5) Piris, M.; Matxain, J. M.; Ugalde, J. M. *J. Chem. Phys.* **2008**, *129*, 014108.

(6) Vetere, V.; Monari, A.; Bendazzoli, G. L.; Evangelisti, S.; Paulus, B. *J. Chem. Phys.* **2008**, *128*, 024701.

(7) Angelotti, W. F. D.; Streit, L.; Fonseca, A. L. D.; Custodio, R. *Int. J. Quantum Chem.* **2008**, *108*, 2459.

(8) Ayers, P. W.; Melin, J. *Theor. Chem. Acc.* **2007**, *117*, 371.

(9) Fetter, A. L.; Walecka, J. D. *Quantum Theory of Many-Particle Systems*; McGraw-Hill: New York, 1971, pp 12−21.

(10) Ahlrichs, R. *J. Chem. Phys.* **1976**, *64*, 2706.

(11) Levy, M.; Parr, R. G. *J. Chem. Phys.* **1976**, *64*, 2707.

(12) Katriel, J.; Davidson, E. R. *Proc. Natl. Acad. Sci. U.S.A.* **1980**, *77*, 4403.

(13) Smith, H. V.; Öhrn, Y. On a formula for electron binding energies In *Reduced Density Operators with Applications to Physical and Chemical Systems II*; Erdahl, R. M., Ed.; Queens' University: Kingston, Ontario, 1974, p 193.

(14) Pickup, B. T. *Chem. Phys. Lett.* **1975**, *33*, 422.

(15) Pickup, B. T.; Snijders, J. G. *Chem. Phys. Lett.* **1988**, *153*, 69.

(16) Andersen, E.; Simons, J. *J. Chem. Phys.* **1977**, *66*, 1067.

(17) Olsen, J.; Sundholm, D. *Chem. Phys. Lett.* **1998**, *288*, 282.

(18) Pernal, K.; Cioslowski, J. *J. Chem. Phys.* **2001**, *114*, 4359.

(19) Day, O. W.; Smith, D. W.; Morrison, R. C. *J. Chem. Phys.* **1975**, *62*, 115.

(20) Ellenbogen, J. C.; Day, O. W.; Smith, D. W.; Morrison, R. C. *J. Chem. Phys.* **1977**, *66*, 4795.

(21) Morrison, R. C. *Chem. Phys. Lett.* **1979**, *62*, 131.

(22) Morrison, R. C. *J. Chem. Phys.* **1992**, *96*, 3718.

(23) Morrison, R. C.; Liu, G. *Int. J. Quantum Chem.* **1992**, *13*, 1004.

(24) Sundholm, D.; Olsen, J. *J. Chem. Phys.* **1993**, *98*, 3999.

(25) Morrison, R. C. *J. Chem. Phys.* **1993**, *99*, 6221.

(26) Sundholm, D.; Olsen, J. *J. Chem. Phys.* **1993**, *99*, 6222.

(27) Morrison, R. C.; Dixon, C. M.; Mizell, J. R. *Int. J. Quantum Chem. Symp.* **1994**, *28*, 309.

(28) Morrison, R. C. *Int. J. Quantum Chem.* **1994**, *49*, 649.

(29) Levy, M.; Perdew, J. P.; Sahni, V. *Phys. Rev. A* **1984**, *30*, 2745.

(30) Ernzerhof, M.; Burke, K.; Perdew, J. P. *J. Chem. Phys.* **1996**, *105*, 2798.

CT800552K

JCTC Journal of Chemical Theory and Computation

Tightened Lieb–Oxford Bound for Systems of Fixed Particle Number

Mariana M. Odashima and K. Capelle

Departamento de Física e Informática, Instituto de Física de São Carlos, Universidade de São Paulo, Caixa Postal 369, São Carlos, 13560-970 SP, Brazil

S. B. Trickey*

Quantum Theory Project, Departments of Physics and Chemistry, University of Florida, Gainesville, Florida 32611

Received December 18, 2008

Abstract: The Lieb–Oxford bound is a constraint upon approximate exchange-correlation functionals. We explore a nonempirical tightening of that bound in both universal and electron number-dependent form. The test functional is PBE. Regarding both atomization energies (slightly worsened) and bond lengths (slightly improved), we find the PBE functional to be remarkably insensitive to the value of the Lieb–Oxford bound. This both rationalizes the use of the original Lieb–Oxford constant in PBE and suggests that enhancement factors more sensitive to sharpened constraints await discovery.

I. Background

Construction of approximate exchange-correlation (XC) functionals in DFT without reliance on empirical data is an important task, both conceptually and practically. Perhaps the most widely used constraint-based approximate XC functional today is the extremely popular Perdew–Burke–Ernzerhof (PBE) generalized gradient approximation (GGA).[3] One of the constraints on which the PBE GGA X functional (and some others also) is based is the Lieb–Oxford bound.[5] In the DFT literature, this bound commonly is expressed as

$$\frac{E_{\mathrm{xc}}[n]}{E_{\mathrm{x}}^{\mathrm{LDA}}[n]} \leq \lambda_{\mathrm{LO}} \tag{1}$$

where

$$E_{\mathrm{x}}^{\mathrm{LDA}}[n] = -\frac{3}{4}\left(\frac{3}{\pi}\right)^{1/3} \int d^3 r n^{4/3}(\mathbf{r}) \tag{2}$$

The LO value for the constant is

$$\lambda_{\mathrm{LO}} = 2.273 \tag{3}$$

The possibility of tightening this bound has been the subject of recurrent interest in DFT. A slightly tighter value $\lambda_{\mathrm{CH}} = 2.215$ was found by Chan and Handy.[6] Vela[7] later reported that using a spatially varying implementation of the LO bound, which always is tighter than λ_{LO}, improved the results for a test set of light inorganic and organic molecules calculated using constraint-based GGAs.

Shortly thereafter and independently, two of us (OC hereafter)[8,9] gave numerical evidence from exact and near-exact calculations on atoms, small molecules, and model systems that the true bound is much tighter. That analysis proceeded by defining the *functional* $\lambda[n]$

$$\lambda[n] = \frac{E_{\mathrm{xc}}[n]}{E_{\mathrm{x}}^{\mathrm{LDA}}[n]} \tag{4}$$

with both numerator and denominator evaluated on the actual density of each system. In general, this functional cannot be evaluated exactly, because neither E_{xc} nor the density is known exactly. However, it can be evaluated to high accuracy for systems for which near-exact XC energies and system densities are known from configuration interaction or quantum Monte Carlo calculations. The result[8,9] is that

* Corresponding author e-mail: trickey@qtp.ufl.edu.

10.1021/ct8005634 CCC: $40.75
Published on Web 03/10/2009

real systems typically have $\lambda[n] \in (1.1 \ldots 1.3)$. The higher end of the interval typically corresponds to more rarefied, diffuse density distributions, while the lower end corresponds to more compact densities. Values above 1.3 were only found for extreme low-density limits of model Hamiltonians: the $k \rightarrow 0$ limit of Hooke's atom has $\lambda[k \rightarrow 0] = 1.489$, and the $r_s \rightarrow \infty$ limit of the homogeneous electron gas has $\lambda[r_s \rightarrow \infty] = 1.9555 := \lambda_{HEG}$.

On the basis of these results, OC conjectured[8,9] that further tightening of the LO bound, beyond that obtained by Chan and Handy, can be achieved and suggested that for real systems (excluding unphysical limits of model Hamiltonians) $\lambda_{OC1} = 1.35$ may provide the tightest upper limit, whereas for arbitrary systems $\lambda_{OC2} = 2.00 \approx \lambda_{HEG}$ is the upper limit.

OC also speculated that system-specific upper limits could be found, thereby providing upper limits for all systems sharing some common properties. Earlier, there was other evidence for system-specific limits. Novikov et al.[10] used a reduced κ parameter (defined below) in the PBE XC functional to some benefit. This reduction (see our discussion below) is equivalent to a reduced LO bound. The numerical rationalization for this was published somewhat later by Peltzer y Blanca et al.[11] Translating to effective values of λ, broadly they found that 3d metals do better with $\lambda \approx \lambda_{LO}$, 4d metals benefit from $\lambda \approx 1.81 \rightarrow 1.94$, and 5d metals benefit from $\lambda \approx 1.69 \rightarrow 1.84$. The notable exception was Fe, where the effective λ was 2.8, an illustration of the fact that all the limitations of a specified XC form cannot be corrected by a single parameter fix. (Recently, there has also been a study of reduced κ in the PBE functional but the reduction is done in such a way as to respect the original Lieb−Oxford bound,[12] and is not directly related to the issue at hand.)

Other than this one empirical example, the available data did not allow any general characterization of λ-value classes. Here, we propose and explore a generally applicable, entirely nonempirical way to characterize classes of systems with a common maximum value of $\lambda[n]$. This characterization is based on a rarely mentioned part of the original Lieb−Oxford article, in which they show that tighter estimates of the upper limit on $\lambda[n]$ can be achieved by restricting the λ functional to densities that integrate to a specified particle number N. We therefore introduce the *function* $\lambda(N)$, which for a given value of N provides a universal upper limit upon $\lambda[n]$ valid for all systems such that $\int d^3rn(\mathbf{r}) = N$. The maximum value of $\lambda(N)$, attained for $N \rightarrow \infty$, is the value λ_{LO} used in common density functionals. The function $\lambda(N)$ assigns to each class of systems of common particle number an upper limit $\lambda(N) \leq \lambda_{LO}$.

In construction of constraint-based functionals, the fact that the upper limit can be tightened universally (from λ_{LO} to λ_{CH} and perhaps on to λ_{OC2}) or in a system-specific way (e.g., using $\lambda(N)$) has not been taken into account, and the consequences of a replacement of λ_{LO} by one of the lower values in currently popular functionals are unknown. We study some of those consequences here.

II. Construction of a Particle-Number-Dependent Bound

To explore the system-specific bound provided by the function $\lambda(N)$ requires facing the problem that, while Lieb and Oxford proved the existence of this function and deduced some of its properties, they did not obtain a closed analytical expression for all N. We thus propose a simple approximation to $\lambda(N)$, compatible with all known information on the universal LO bound. The following facts are known about $\lambda(N)$:[5,8,9]

(i) Its value at $N = 1$ is $\lambda(N = 1) = 1.48 := \lambda_1$.

(ii) Its value at $N = 2$ is not known, but is above $\lambda_{min}(N = 2) = 1.67$.

(iii) The function $\lambda(N)$ is monotonic, that is, $\lambda(N + 1) \geq \lambda(N)$.

(iv) Its value at $N = \infty$ is not known, but must be less than or equal to $\lambda_{max}(N \rightarrow \infty) := \lambda_\infty$. Different proposals for the value of λ_∞ are $\lambda_{LO} = 2.273$, $\lambda_{CH} = 2.215$, and $\lambda_{OC2} = 2.00 \approx \lambda_{HEG}$.

(v) The largest value of $\lambda[n]$ found for any system studied specifically is that for the extreme low-density limit of the homogeneous electron gas $\lambda_{HEG}(r_s \rightarrow \infty) = 1.9555$. For real physical systems, $\lambda[n]$ typically ≤ 1.3. These values provide empirical lower bounds on the function $\lambda(N)$.

Note that standard density functionals either do not make use of the Lieb−Oxford bound at all (and some can violate it)[13−16] or exploit only property (iv), normally with the weakest value for λ_∞, namely λ_{LO}. To construct a model for the function $\lambda(N)$, we exploit properties (i) (value at $N = 1$), (iii) (monotonicity), and (iv) (value at $N \rightarrow \infty$). We use properties (ii) (theoretical lower limit at $N = 2$) and (v) ($\lambda[n]$ for model and real systems) as consistency tests for the construction. With all this in mind, we propose the simple interpolation:

$$\lambda(N) = \left(1 - \frac{1}{N}\right)\lambda_\infty + \frac{\lambda_1}{N} \tag{5}$$

where λ_∞ is λ_{LO}, λ_{CH}, or λ_{OC2}. By construction this interpolation obeys properties (i), (iii), and (iv). Direct inspection shows that it also respects properties (ii) and (v).

Figure 1 illustrates this function for the three different choices of λ_∞ and compares it to the known value at $N = 1$, the lower limit at $N = 2$, and some representative data for atoms, molecules, and the homogeneous electron gas.

We note that the function $\lambda(N)$ is a global multiplicative factor and as such can be applied in the context of both the global and the local LO bound. As PBE makes use of the local form,[16] we here explore consequences of the N-dependence of λ in this context, but as a matter of principle, the issue of tightening the bound and/or making it N-dependent applies to the global bound as well.

III. Implementation and Computational Protocols

A. Modification of PBE GGA. To explore these ideas, we implemented the various possible replacements of λ_{LO} in the PBE GGA. At the outset, we remark that, on the basis

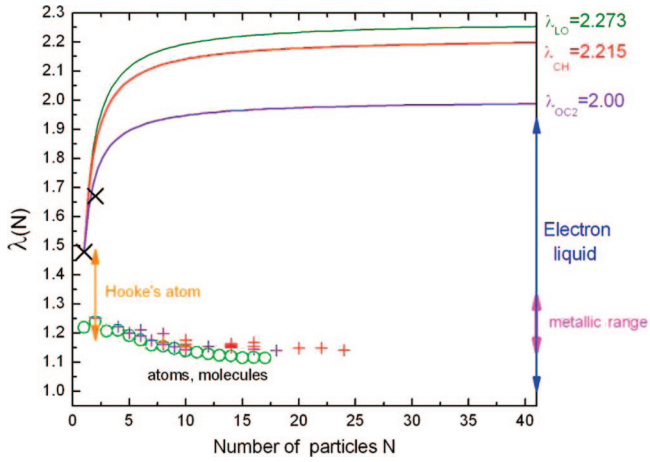

Figure 1. Interpolation function $\lambda(N)$ for three different choices of λ_∞, compared to known theoretical results and empirical data. Black crosses represent the exact value at $N = 1$ and the lower bound at $N = 2$. Values at $N \rightarrow \infty$ are indicated on the right vertical axis. The three continuous curves are our interpolation (eq 5) using the three alternative choices for λ_∞. All other data represent ranges or values for selected real systems, providing empirical lower bounds.

of previous experience with the revPBE functional,[16] we expect that lowering λ in PBE will have a detrimental effect on atomic total energies. (In revPBE, an *increase* of λ was shown to improve atomic total energies and molecular atomization energies, at the expense of worsened bond lengths.)

Since the actual values of $\lambda[n]$ for physical systems are known to fall far below λ_{LO}, and the theoretical information available from the CH numerical tightening and from the function $\lambda(N)$ both indicate that lower values of λ are appropriate, this detrimental effect must be considered a severe shortcoming of the GGA. An important issue of energetics, therefore, is whether the atomization energies are improved when tightened LO bounds are used in a GGA. Further investigation is needed to see if meta-GGA functionals[4] suffer from the same problem, but that is beyond the scope of this study. Because the quality of predicted equilibrium energies and system geometries is the first prerequisite for any generally useful approximate XC functional, the effects of tightening the LO bound upon Kohn−Sham orbitals (e.g., their utility as frontier orbitals) and eigenvalues also will be considered separately.

In any event, there are five possibilities for tightening, pertaining to two categories. Category I is a simple replacement of the constant value λ_{LO} by the alternative lower constants λ_{CH} or λ_{OC2}. Category II replaces the constant by the function $\lambda(N)$, with the three possible choices for λ_∞. The resulting five choices are to be compared to the original choice λ_{LO}, made in the construction of PBE.

In the original PBE GGA, the LO bound is enforced locally (but not pointwise) through the choice of the parameter κ in the exchange enhancement factor:

$$F_x^{\mathrm{PBE}} := 1 + \kappa - \frac{\kappa}{1 + \mu s^2/\kappa} \tag{6}$$

with the dimensionless reduced gradient given by:

$$s(\mathbf{r}) = \frac{1}{2(3\pi^2)^{1/3}} \frac{|\nabla n(\mathbf{r})|}{n(\mathbf{r})^{4/3}} \tag{7}$$

Taking spin-polarization into account, satisfaction of eq 2 by the enhancement factor in eq 6 for all densities (a sufficient condition) is equivalent to

$$F_x[n, s] \leq \frac{\lambda_{LO}}{2^{1/3}} = 1.804 \tag{8}$$

Since $\lim_{s\rightarrow\infty} F_x[n, s] = 1 + \kappa$, the result is

$$\kappa_{\mathrm{PBE}} = 0.804 \tag{9}$$

Of course, the simple choice of a different universal bound leads to

$$\kappa(\lambda_\infty) = \frac{\lambda_\infty}{2^{1/3}} - 1 \tag{10}$$

The equivalent modification to include the N-dependent LO bound (eq 5) is

$$\kappa(N, \lambda_\infty) = \frac{\lambda(N, \lambda_\infty)}{2^{1/3}} - 1 \tag{11}$$

The result of considering such altered LO bounds is five variants of the PBE exchange functional:

PBE(λ_{CH}): PBE96 exchange but with $\lambda_\infty = \lambda_{CH} = 2.215$.

PBE(λ_{OC2}): PBE96 exchange but with $\lambda_\infty = \lambda_{OC2} = 2.00$.

PBE($\lambda_{LO}(N)$): PBE96 exchange but with $\lambda(N, \lambda_\infty)$ and $\lambda_\infty = \lambda_{LO} = 2.273$.

PBE($\lambda_{CH}(N)$): PBE96 exchange but with $\lambda(N, \lambda_\infty)$ and $\lambda_\infty = \lambda_{CH} = 2.215$.

PBE($\lambda_{OC2}(N)$): PBE96 exchange but with $\lambda(N, \lambda_\infty)$ and $\lambda_\infty = \lambda_{OC2} = 2.00$.

The first two, along with the original PBE = PBE(λ_{LO}), comprise category I, the latter three, category II. We denote the six variants collectively as PBE(λ) in what follows.

It is important for clarity of interpretation of our results to note that the five new variants alter *only* the value of the LO bound that is enforced and *not* the way in which the bound is enforced. In both original PBE and our variations, the bound is enforced locally as a sufficient condition. Whether global enforcement is better is a distinct question not considered here. Note also that, just as with original PBE, while the enforcement is local it is not pointwise (we do not have $\lambda(\mathbf{r})$).

B. Protocols. All five variants were introduced in the code deMon2k, development version 2.4.2,[17] by systematic modification of the exchange-correlation modules. Subsequently, the implementation was validated by comparison of atomic calculations done with hard-coded modifications of the code soatom.f.[18] Throughout, we used the full PBE correlation functional, not the deMon cutoff version (i.e., we used the deMon2k "PBESSF" option), for all PBE(λ). Because deMon2k uses variational Coulombic fitting, there is a choice of density fitting (auxiliary) basis sets and of the method for evaluating XC matrix elements. Initially, we used the so-called A2 density fitting basis (deMon2k option "AUXIS(2)") and the option to do the numerical integrals for the XC

Table 1. Comparison of Effects of Various Lieb−Oxford Bounds in the PBE Exchange Functional for the Li_2 Molecule[a]

functional	E_{atom}	E_{Li_2}	ΔE	R_e
PBE(λ_{LO})	−7.460992748	−14.953949056	20.06	2.7236
PBE(λ_{CH})	−7.457436406	−14.946932892	20.01	2.7218
PBE(λ_{OC2})	−7.441633876	−14.915640294	20.31	2.7155
PBE($\lambda_{LO}(N)$)	−7.442385785	−14.937217688	32.91	2.7196
PBE($\lambda_{CH}(N)$)	−7.439006265	−14.930264047	32.79	2.7181
PBE($\lambda_{OC2}(N)$)	−7.424518016	−14.899876726	31.90	2.7131

[a] See text for notation about functionals. E_{atom} and E_{Li_2} are total energies in hartrees. ΔE is the total atomization energy in kilocalories per mole, and R_e is the equilibrium bond length in angstroms.

Table 2. Values of the PBE Exchange Functional Parameter $\kappa(N, \lambda_\infty)$ for the PBE(λ) Functionals for $N = 3$ (Li Atom) and $N = 6$ (Li_2 Molecule)

functional	$\kappa(3, \lambda_\infty)$	$\kappa(6, \lambda_\infty)$
PBE(λ_{LO})	0.804319	0.804319
PBE(λ_{CH})	0.757967	0.757967
PBE(λ_{OC2})	0.587401	0.587401
PBE($\lambda_{LO}(N)$)	0.594439	0.699379
PBE($\lambda_{CH}(N)$)	0.563537	0.660752
PBE($\lambda_{OC2}(N)$)	0.449826	0.518614

quantities using the fitted (auxiliary) density (deMon2k "AUXIS" option). We return to these options below.

For development of a suitable protocol (Kohn−Sham basis, fitting basis) we first studied the Li_2 molecule in a triple-ζ-plus-polarization (TZVP) KS basis. The results are in Table 1. Note that ΔE is the total atomization energy, $2E_{Li,atom} - E_{Li_2}$ (not the cohesive energy per atom). Regarding the quality of the calculation, observe that for the unmodified PBE functional, our results are almost identical with those given by Ernzerhof and Scuseria,[19] $\Delta E = 20$ kcal/mol, $R_e = 2.727$ Å. (For reference, they quote experimental values as 26 kcal/mol and 2.673 Å.)

As would be expected from naïve use of a particle-number-dependent model, the results in Table 1 show a clear size-inconsistency problem, signaled by the big shift in ΔE between the N-independent models, PBE(λ), and the N-dependent models, PBE($\lambda(N)$). The fact that there is no such shift in the R_e values is a clear sign that the problem is in the comparison with the isolated atom. Equation 11 illustrates the point. In a naïve application of the N-dependent models, the Li atom has $\lambda(3, \lambda_\infty)$ while the Li_2 molecule has $\lambda(6, \lambda_\infty)$ (with the three choices of λ_∞). The result is a separated atom limit of the diatomic molecule which is not the same as the isolated atom. Table 2 shows the very substantial difference in the PBE parameter κ for these two situations.

Table 4. O and O_2 (Triplet) Total Energies (E_H), Molecular Atomization Energy (kcal/mol), and Equilibrium Bond Length (Å) for the Ordinary PBE XC Functional As Calculated in deMon2k, TZVP Basis ("deMon-TZVP"); Gaussian 03, 6311+G(3df,2p) Basis (Ref 19 "ES"); ACES-II, aug-cc-PVTZ (Ref 25 "AP"); and deMon2k, aug-cc-PVTZ Basis ("deMon-aug")

calcd	$E_{tot,O}$	E_{tot,O_2}	ΔE	R_e
deMon-TZVP	−75.00612438	−150.23282532	138.4	1.23491
ES			143	1.217
AP	−75.00773627	−150.24372619	143.2	1.21996
deMon-aug	−75.00781596	−150.24387554	143.2	1.22008

Table 3 shows how a size-consistent set of parameters, here for $N = 6$, resolves the problem. (For clarity, note that we made the common choice throughout all these calculations and ignored the DFT spin-symmetry problem. Thus, the separated atoms are spin-polarized even though the molecule has multiplicity of one.) Throughout this study, we used this same size-consistent procedure, namely applying to the separated atoms the modified LO constants proper for the value of N of the aggregated system (molecule) in question. For heteronuclear molecules, especially hydrides, this protocol results in a rather disparate enforcement of the LO bound for atoms of substantially different N, a matter for later study and refinement. (We note that the use of the original PBE functional implies the most disparate enforcement of all, as it amounts to using the largest $N \rightarrow \infty$ value of λ for all finite N.)

Table 3 also compares the effect of the two different options in deMon2k for evaluation of the XC matrix elements. First is the deMon A2 density fitting basis (deMon2k option "AUXIS(2)") and the aforementioned deMon2k option ("AUXIS") for evaluation of XC quantities

Table 3. Comparison of Effects of Various Lieb−Oxford Bounds in the PBE Exchange Functional for the Li_2 Molecule[a]

functional	E_{atom}	E_{Li_2}	ΔE	R_e
PBE(λ_{LO})	−7.460992748	−14.953949056	20.06	2.7236
PBE(λ_{CH})	−7.457436406	−14.946932892	20.01	2.7218
PBE(λ_{OC2})	−7.441633876	−14.915640294	20.31	2.7155
PBE($\lambda_{LO}(N)$)	−7.452520577	−14.937217688	20.19	2.7196
PBE($\lambda_{CH}(N)$)	−7.449007723	−14.930264047	20.24	2.7181
PBE($\lambda_{OC2}(N)$)	−7.433703689	−14.899876726	20.37	2.7131
PBE(λ_{LO})	−7.460613173	−14.953310471	20.13	2.7304
PBE(λ_{CH})	−7.457076546	−14.946319641	20.18	2.7277
PBE(λ_{OC2})	−7.441303732	−14.915029100	20.34	2.7181
PBE($\lambda_{LO}(N)$)	−7.452179554	−14.936623118	20.25	2.7244
PBE($\lambda_{CH}(N)$)	−7.448674591	−14.929672255	20.28	2.7222
PBE($\lambda_{OC2}(N)$)	−7.433359029	−14.899212818	20.39	2.7143
reference values[20−23]	−7.47806	−14.9938	26	2.673

[a] N-dependent functionals done with $N = 6$ size-consistent parameters. TZVP KS basis. Upper set is the A2 fitting basis with AUXIS XC evaluation option, lower set is GEN-A2 and BASIS option. See text for details as well as notation for functionals. E_{atom} and E_{Li_2} are total energies in hartrees. ΔE is the total atomization energy in kilocalories per mole. R_e is the equilibrium bond length in angstroms.

Table 5. As in Table *3* but for Triplet O_2 and for Two Different Basis Sets TZVP/GEN-A2 (Upper Set), aug-cc-PVTZ/GEN-A2* (Lower Set)

functional	E_{atom}	E_{O_2}	ΔE	R_e
PBE(λ_{LO})	−75.00612438	−150.23282532	138.4	1.2349
PBE(λ_{CH})	−74.99689680	−150.21624772	139.6	1.2343
PBE(λ_{OC2})	−74.95432779	−150.13915494	144.6	1.2315
PBE($\lambda_{LO}(N)$)	−74.99835094	−150.21886346	139.4	1.2344
PBE($\lambda_{CH}(N)$)	−74.98900193	−150.20202494	140.6	1.2338
PBE($\lambda_{OC2}(N)$)	−74.94639261	−150.12467907	145.5	1.2310
PBE(λ_{LO})	−75.00781596	−150.24387554	143.2	1.2201
PBE(λ_{CH})	−74.99853463	−150.22722985	144.4	1.2195
PBE(λ_{OC2})	−74.95571887	−150.14986185	149.6	1.2167
PBE($\lambda_{LO}(N)$)	−74.99998015	−150.22985618	144.3	1.2196
PBE($\lambda_{CH}(N)$)	−74.99059055	−150.21295118	145.4	1.2189
PBE($\lambda_{OC2}(N)$)	−74.94774275	−150.13534295	150.5	1.2162
reference values[20–23]	−75.0674	−150.2770	118	1.208

Table 6. Comparison of Effects of Various Lieb−Oxford Bounds in the PBE Exchange Functional upon the Atomization Energies (kcal/mol) of Various Small Molecules

species	$2S+1$	PBE(λ_{LO})	PBE(λ_{CH})	PBE(λ_{OC2})	PBE($\lambda_{LO}(N)$)	PBE($\lambda_{CH}(N)$)	PBE($\lambda_{OC2}(N)$)	expt[22]
Li_2	1	20.13	20.18	20.34	20.25	20.28	20.39	26
Be_2	1	9.71	9.95	10.94	10.12	10.35	11.28	2.3
B_2	3	76.7	77.3	80.1	77.6	78.2	80.8	71.3
C_2	1	142.3	143.4	147.9	143.6	144.6	148.9	146
N_2	1	235.5	236.7	241.7	236.7	237.9	242.6	227
O_2	3	138.4	139.6	144.6	139.4	140.6	145.5	118
F_2	1	51.56	52.46	56.30	52.23	53.12	56.90	38
Ne_2	1	0.1279	0.1438	0.2236	0.1385	0.1549	0.2369	0.0839
Ar_2	1	0.1377	0.1631	0.2998	0.1462	0.1732	0.3122	0.2846
HF	1	142.645	143.161	145.401	143.356	143.864	146.037	142
LiH	1	54.53	54.54	54.57	54.57	54.57	54.54	58
OH	2	110.361	110.762	112.458	110.976	111.365	112.981	107
NH	3	88.95	89.18	90.07	89.34	89.55	90.36	88
NiH	2	74.05	75.05	76.63	74.86	75.21	76.79	58.8
H_2O	1	235.9	236.8	240.5	237.1	237.9	241.5	235
NH_3	1	305.686	306.664	310.761	307.029	307.976	311.882	297
CH_4	1	427.184	428.245	432.736	428.641	429.673	433.983	420
C_6H_6	1	1423.74	1430.39	1458.48	1425.84	1432.45	1460.30	1362

using the fitted (auxiliary) density on a numerical grid. Second is the richer GEN-A2 fitting basis and evaluation of the XC quantities from the density formed straightforwardly from the KS orbitals also on the numerical grid ("BASIS" option). In principle, the latter procedure is the more accurate and is the one we adopted. Nevertheless, the trends in the PBE(λ) series are essentially the same in the less-accurate procedure.

Our other exploratory test was the O_2 molecule, a triplet ground-state system. The TZVP PBE atomization energy (see the first two lines of Table 4) is about 3% off from the published result of Ernzerhof and Scuseria,[19] who used the substantially richer basis 6311+G(3df,2p). An ACES-II[24] calculation using another rich basis (aug-cc-PVTZ) matched the deMon2k results with that same KS basis and the richer density-fitting basis ("GEN-A2*" option). These results, in the third and fourth lines of Table 4, calibrate the effects of basis set differences. Results for the PBE(λ) series in the aug-cc-PVTZ/GEN-A2* basis sets also are in Table 5. The relative shifts among the six PBE variants are the same irrespective of basis sets, but the richer basis sets make the atomization energies larger and bond lengths slightly shorter. Ernzerhof and Scuseria[19] quote the experimental data as $\Delta E = 118$ kcal/mol and $R_e = 1.208$ Å. Thus, all six PBE variants (original plus five new) give too deep a binding energy at slightly elongated bond lengths.

The preceding discussion makes clear that systematic comparison of the six PBE variants generally does not require a fully saturated basis set. Rare gas dimers, discussed below, are an exception. Therefore, except for rare gas dimers, we adopted the following protocol: (i) use TZVP for the KS basis, (ii) use GEN-A2 or GEN-A3 algorithms to generate the fitting-function basis (and thereby minimize the effect of the variational Coulombic fitting, which gives a lower bound to the Coulombic repulsion that can be deceptive with a poorly chosen fitting basis), and (iii) use the deMon2k BASIS option for evaluation of the XC matrix elements. This protocol combines a reasonably rich KS basis with an abundance of caution in treating the XC quantities.

For the rare gas dimers, test calculations on Ar_2 with both a DZVP and a 6-311++G(3df,3pd) KS basis set demonstrated that these do not reproduce known, large-basis PBE results for this dimer.[26,27] Since those two calculations were completely independent and gave essentially identical values, $\Delta E = 0.138$ kcal/mol, $R_e = 4.00$ Å, it is essential to reproduce them. Therefore, we shifted to the aug-cc-pVTZ KS basis,[28] as used by Zhao and Truhlar, and the deMon2k GEN-A3 fitting function basis. This combination gives the

Table 7. Comparison of Effects of Various Lieb−Oxford Bounds in the PBE Exchange Functional upon the Bond Lengths (Å) and Bond Angles (deg) of Various Small Molecules[a]

species	PBE(λ_{LO})	PBE(λ_{CH})	PBE(λ_{OC2})	PBE($\lambda_{LO}(N)$)	PBE($\lambda_{CH}(N)$)	PBE($\lambda_{OC2}(N)$)	expt[23]
Li_2	2.7304	2.7277	2.7181	2.7244	2.7222	2.7143	2.673
Be_2	2.4409	2.4379	2.4259	2.4355	2.4328	2.4218	2.45
B_2	1.6208	1.6198	1.6159	1.6194	1.6185	1.6148	1.590
C_2	1.2595	1.2590	1.2567	1.2590	1.2584	1.2562	1.243
N_2	1.1112	1.1108	1.1091	1.1108	1.1104	1.1087	1.098
O_2	1.2349	1.2343	1.2315	1.2344	1.2338	1.2310	1.208
F_2	1.4301	1.4290	1.4242	1.4293	1.4282	1.4235	1.412
Ne_2	3.0808	3.0418	2.8709	3.0546	3.0162	2.8550	3.091
Ar_2	3.99907	3.9124	3.6964	3.9469	3.8929	3.6841	3.7565
HF	0.9385	0.9385	0.9385	0.9385	0.9385	0.9385	0.917
LiH	1.6065	1.6058	1.6029	1.6039	1.6033	1.6012	1.595
OH	0.9899	0.9899	0.9898	0.9899	0.9899	0.9897	0.971
NH	1.0549	1.0549	1.0548	1.0549	1.0549	1.0548	1.036
NiH	1.4580	1.4594	1.4553	1.4599	1.4590	1.4549	1.477
H_2O, R	0.9750	0.9749	0.9747	0.9749	0.9749	0.9746	0.959
H_2O, θ	104.21	104.24	104.39	104.25	104.29	104.43	103.9
NH_3, R	1.0252	1.0252	1.0245	1.0250	1.0249	1.0244	1.012
NH_3, θ	106.40	106.44	106.62	106.45	106.49	106.67	106.7
CH_4	1.0990	1.0989	1.0984	1.0988	1.0987	1.0982	1.086
C_6H_6, R_{CC}	1.3995	1.3990	1.3965	1.3994	1.3988	1.3963	1.397
C_6H_6, R_{CH}	1.0947	1.0946	1.0943	1.0947	1.0946	1.0943	1.084

[a] The NH_3 bond angle is θ_{HNH}. See text for notation about functionals. CH_4 was done with T_d symmetry enforced.

same PBE results as the foregoing two references. We treated Ne_2 with the corresponding aug-cc-pVTZ KS basis and GEN-A3 fitting function basis.

IV. Results and Discussion

For PBE(λ), Table 6 gives the atomization energies for 18 light molecules, while Table 7 gives bond lengths and bond angles for those same systems. (As a technical aside, note that NiH is a difficult system to treat.) Absolute relative errors in the atomization energy are shown in Figure 2, and the corresponding bond length data are in Figure 3.

Several features stand out from these results. With a few exceptions, the general pattern is that both atomization energies and bond lengths are remarkably insensitive to changes in the enforcement of the LO bound. This outcome is consistent with what one might have inferred from Figure 1. The $\lambda(N)$ that we are justified in using (in the sense that our interpolation respects the known constraints) is substantially larger than the λ values imputed for actual molecules. Thus, one might conclude that a more refined way of implementing the LO bound in a GGA is needed.

However, two systems, Ne_2 and Ar_2, are notably sensitive to the value of λ in the atomization energies. Be_2 is somewhat similar in sensitivity. A coherent interpretation by classes of molecules is possible: unlike the other atoms, Ne and Ar are closed-shell atoms and the Be atom is similar in having $l = 0$ symmetry. Thus, we may suspect that the well-known peculiarities of closed-shell interactions are the source of the distinct behavior. (We do not venture any remarks on the validity and limitations of GGA XC functionals for such molecules.) For the equilibrium bond lengths, Ne_2 and Ar_2 still stand out from all other systems by being most sensitive to changes in λ (Figure 3). However, the classification of Be_2 with Ne_2 and Ar_2 is at least consistent in that the Be_2 bond-length variation is at odds with all the other open-shell systems. The behavior of Be_2 does not seem to be traceable to being from the rapidly varying part of the $\lambda(N)$ function, since Li_2 is in that region also and it is insensitive in both bond length and atomization energy.

To display the effects of imposition of the size-consistent molecular N values on the LO bounds in atoms, we also calculated some isolated atom total energies at their intrinsic $N = Z$ values. For H, C, N, O, and F, Table 8 displays the results for the intrinsic value versus the results for the highest N molecule in which each element was used in the present study. As would be expected from the interpolation in eq 5 and the constraints on which it is based, the total energy of the H atom exhibits the largest percentage variation between intrinsic and molecular values for the three N-dependent variants PBE($\lambda(N)$).

V. Concluding Remarks

Our results show that PBE is rather insensitive to changes in λ for covalently and ionically bound small molecules when measured by atomization energies and bond lengths. The total energies are notably more sensitive, presumably because of the large s contributions from the density tails. Overall, a reduced, and thus, in principle, better, value of λ produces slightly worsened energies and slightly improved bond lengths. This insensitivity explains why PBE can be successful even though it uses the λ_∞ value even for small N. In this sense, the present study provides additional insight into the success of PBE for small systems. On the other hand, a suitably designed, constraint-based functional should give improved results when the constraints it incorporates are sharpened. The failure of PBE to meet this expectation must be considered a limitation of the PBE functional form.

In the case of the closed-shell systems, we find a more pronounced λ dependence than in the covalent and ionic systems. Because of the delicate nature of binding in these systems, more detailed investigation would be needed to make conclusive statements. In the spirit of the preceding paragraph, it would appear to be more productive to focus

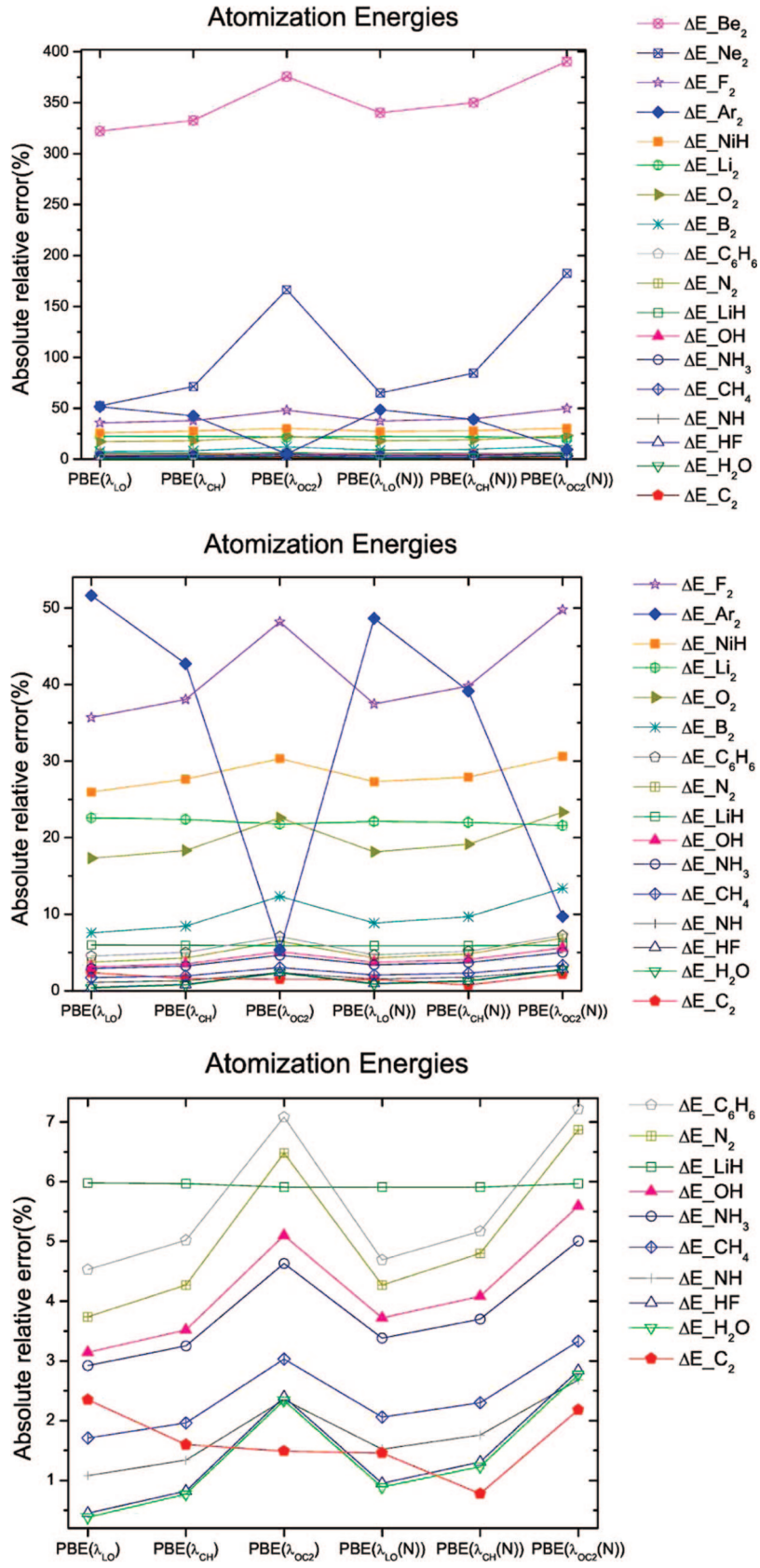

Figure 2. Top panel: Absolute relative errors in atomization energies for all 18 molecules for original PBE and the five variants. Middle panel: As in the upper panel but with the worst two cases (Be_2, Ne_2) removed to allow a finer scale. Bottom panel: As in the middle panel but with the worst six cases of that panel (F_2, Ar_2, NiH, Li_2, O_2, B_2) removed to allow a finer scale.

on developing enhancement factors that are more sensitive to sharpening of constraints.

An appealing thought is that the insensitivity found here may also have to do with the way that the LO bound is

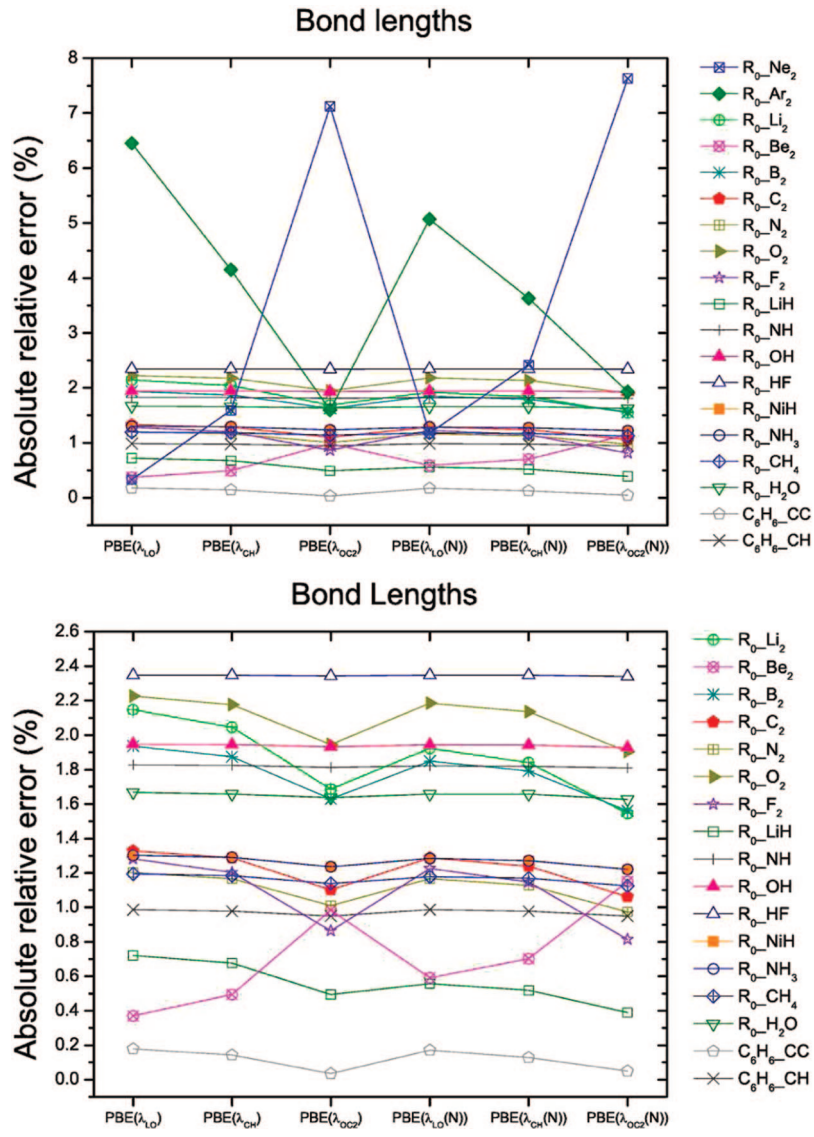

Figure 3. Upper panel: Absolute relative errors in bond lengths for all 18 molecules for the original PBE and the five variants. Lower panel: As in the upper panel but with the two most sensitive cases (Ar_2, Ne_2) removed to allow a finer scale.

Table 8. Total Energies (Hartree au) for Five Chemically Important Atoms from Various Lieb−Oxford Bounds in the PBE Exchange Functional[a]

XC	H	C	N	O	F
PBE(λ_{LO})	−0.498147969	−37.794851185	−54.530389203	−75.006124382	−99.664580137
PBE(λ_{CH})	−0.497515476	−37.787528107	−54.522145702	−74.996896796	−99.654626939
PBE(λ_{OC2})	−0.494726517	−37.754129975	−54.484419695	−74.954327792	−99.608420218
PBE($\lambda_{LO}(N)$) (intrinsic N)	−0.481206885	−37.777286824	−54.513676785	−74.989918352	−99.649171204
PBE($\lambda_{LO}(N)$) (highest N)	−0.497950959	−37.792580522	−54.52240237	−74.99835094	−99.65716700
PBE($\lambda_{CH}(N)$) (intrinsic N)	−0.481206885	−37.769885027	−54.505322010	−74.980521867	−99.639010126
PBE($\lambda_{CH}(N)$) (highest N)	−0.497316032	−37.785199634	−54.51406717	−74.98900193	−99.64707222
PBE($\lambda_{OC2}(N)$) (intrinsic N)	−0.481206885	−37.736869483	−54.467831152	−74.937949507	−99.592621018
PBE($\lambda_{OC2}(N)$) (highest N)	−0.494539297	−37.751826019	−54.47640949	−74.94639261	−99.60074422
exact[20]	−0.5	−37.8450	−54.5893	−75.0674	−99.7341

[a] Results for the N-dependent functionals are given both for the values of N intrinsic to the specific atom and for the highest molecular N used: 42 for H, 42 for C, 14 for N, 16 for O, 18 for F.

implemented in DFT in general. The original LO bound is for the Coulombic exchange and correlation energy W_{xc} and does not include the correlation kinetic energy, $T_c = T - T_s \geq 0$, which contributes to E_{xc}. As a result, $E_{xc} \geq W_{xc}$ and

the functional $\lambda[n] = E_{xc}[n]/E_x^{LDA}[n]$ which was evaluated in refs 8 and 9 is smaller than the functional

$$\lambda_W[n] := \frac{W_{xc}[n]}{E_x^{LDA}[n]} \tag{12}$$

If the effect of T_c were large enough, it might explain at least part of the large difference between the values of $\lambda[n]$ and $\lambda(N)$ in Figure 1. What limited numerical evidence we have, however, suggests that $\lambda_W[n]$ is only about 10% larger than $\lambda[n]$, a very modest shift compared to the difference in Figure 1.

The more general point, however, that the LO bound is a constraint on exchange *and* correlation together, seems to be sustained by our findings, in that the PBE form enforces the bound purely on exchange. One speculation is that the insensitivity found here is in part a consequence of that restricted use of the LO bound.

Finally, we consider aspects of *N*-dependence and chemical classification for enforcement of the LO bound. The first insight is that, in retrospect, *N*-dependent satisfaction of the LO bound actually arose very early in DFT, before the LO proof. In Slater's Xα model, E_{xc} is modeled by scaling E_x^{LDA}. (From a modern perspective, Xα is a one-parameter XC model that gains simplicity at the cost of violating correct scaling for C.) The α-parameter is *N*-dependent[29] and exhibits very clear shell structure.[30,31] For Xα, the LO functional $\lambda[n]$ of eq 4 is just $3\alpha/2$. With typical values of α,[30,31] this gives $\lambda[n] = 1.0745$ for H ($N = 1$) to 1.0387 for Rn ($N = 86$). Comparison with Figure 1 shows that these values are slightly smaller than the highly accurate empirical values found in refs 8 and 9.

The importance of shell-dependent classification was evident in the modern work of refs 8 and 9. The numerical results of this study also leave a strong suggestion that such classification would be helpful. An advantage of the present classification of λ with respect to *N* alone is that it can be done in an entirely nonempirical way, as it relies only upon exact properties of the function $\lambda(N)$. (This is a clear distinction from all parametrized approaches.) Of course, the choice of interpolating function is not unique, but the fact that the upper limit on λ depends on *N* is completely general, as are the properties of $\lambda(N)$ used in the construction of our interpolation. What this means is that whatever shell-dependent classification might be invented, it must somehow be an addition to (or incorporate) classification by particle number, not supplant it. Because that classification will have to avoid size inconsistency, we suspect that the formulation will require additional insight, including additional constraints.

Dedication. John Perdew has contributed major insights to both fundamental and computational aspects of density functional theory. A consistent feature of his work is to prove relationships and apply them as rigorous constraints in the construction of approximate functionals. For those general reasons as well as a particular one, we are pleased to present this article in celebration of John's work and his contributions as part of this birthday festschrift. The particular reason is that the constraint we consider here was introduced to DFT by John,[1] further analyzed by him in collaboration with Mel Levy,[2] and incorporated in John's GGA[3] and meta-GGA[4] functionals.

Acknowledgment. S.B.T. thanks Ajith Perera for the ACES-II calculations on O_2 and Andreas Köster, Gerald Geudtner, and Patrizia Calaminici (Cinvestav, México DF) for technical advice on the use of deMon2k. M.M.O. was supported by FAPESP. K.C. was supported by FAPESP and CNPq. S.B.T. was supported in part by the U.S. National Science Foundation under DMR-0325553 (ITR).

References

(1) Perdew, J. P. Unified Theory of Exchange and Correlation beyond the Local Density Approximation. In *Electronic Structure of Solids*; Ziesche, P., Eschrig, H., Eds.; Akademie Verlag: Berlin, 1991; pp 11−20.

(2) Perdew, J. P.; Levy, M. *Phys. Rev. B* **1993**, *48*, 11638.

(3) Perdew, J. P.; Burke, K.; Ernzerhof, M. *Phys. Rev. Lett.* **1996**, *77*, 3865; Erratum *Phys. Rev. Lett.* **1997**, *78*, 1396.

(4) Perdew, J. P.; Tao, J.; Staroverov, V. N.; Scuseria, G. E. *J. Chem. Phys.* **2004**, *120*, 6898.

(5) (a) Lieb, E. H.; Oxford, S. *Int. J. Quantum Chem.* **1981**, *19*, 427. (b) Lieb, E. H. *Phys. Lett.* **1979**, *70A*, 444.

(6) Chan, G. K.-L.; Handy, N. C. *Phys. Rev. A* **1999**, *59*, 3075.

(7) Vela, A. The Lieb-Oxford Bound and the Large Gradient Correction in the Exchange Energy. In *Symposium 19, XV International Materials Research Congress*; Academia Mexicana de Ciencia de Materiales: Cancún, México, 2006.

(8) Odashima, M. M.; Capelle, K. *J. Chem. Phys.* **2007**, *127*, 054106.

(9) Odashima, M. M.; Capelle, K. *Int. J. Quantum Chem.* **2008**, *108*, 2428.

(10) Novikov, D. L.; Freeman, A. J.; Christensen, N. E.; Svane, A.; Rodriguez, C. O. *Phys. Rev. B* **1997**, *56*, 7206.

(11) Peltzer y Blancá, E. L.; Rodriguez, C. O.; Shitu, J.; Novikov, D. L. *J. Phys.: Condens. Matter* **2001**, *13*, 9463.

(12) Csonka, G. I.; Vydrov, O. A.; Scuseria, G. E.; Ruzsinszky, A.; Perdew, J. P. *J. Chem. Phys.* **2007**, *126*, 244107.

(13) (a) Perdew, J. P.; Wang, Y. *Phys. Rev. B* **1986**, *33*, 8800; **1989**, *40*, 3399. (b) Perdew, J. P. *Phys. Rev. B* **1986**, *33*, 8822; **1986**, *34*, 7406.

(14) (a) Becke, A. D. *Phys. Rev. A* **1988**, *38*, 3098. (b) Lee, C.; Yang, W.; Parr, R. G. *Phys. Rev. B* **1988**, *37*, 785.

(15) Wilson, L. C.; Levy, M. *Phys. Rev. B* **1990**, *41*, 12930.

(16) (a) Zhang, Y.; Yang, W. *Phys. Rev. Lett.* **1998**, *80*, 890. (b) Perdew, J. P.; Burke, K.; Ernzerhof, M. *Phys. Rev. Lett.* **1998**, *80*, 891.

(17) Köster, A. M.; Calaminici P.; Casida, M. E.; Flores-Moreno, R.; Geudtner, G.; Goursot, A.; Heine, T.; Ipatova, A.; Janetzco, F.; Martin del Campo, J.; Patchkovskii, S.; Reveles, J. U.; Salahub, D. R.; Vela, A. deMon2K; Cinvestav: Mexico City, Mexico, 2006.

(18) (a) Trickey, S. B.; Alford, J. A.; Boettger, J. C. In *Computational Materials Science*; Leszczynski, J., Ed.; Theoretical and Computational Chemistry 15; Elsevier: Amsterdam, 2004; p 171. (b) Boettger, J. C. *Phys. Rev. B* **2000**, *62*, 7809. (c) Birkenheuer, U.; Boettger, J. C.; Rösch, N. *J. Chem. Phys.* **1994**, *100*, 6826. (d) Boettger, J. C. *Int. J. Quantum Chem.* **1993**, *S27*, 147. (e) Mintmire, J. W.; Sabin, J. R.; Trickey, S. B. *Phys. Rev. B* **1982**, *26*, 1743.

(19) Ernzerhof, M.; Scuseria, G. E. *J. Chem. Phys.* **1999**, *110*, 5029.

(20) (a) Total atomic energies from Davidson, E. R.; Hagstrom, S. A.; Chakravorty, S. J.; Umar, V. M.; Froese Fischer, C. *Phys. Rev. A* **1991**, *44*, 7071. (b) Chakravorty, S. J.; Davidson, E. R. *J. Phys. Chem.* **1996**, *100*, 6167.

(21) (a) Diffusion Monte Carlo total energies for Li_2, Be_2, B_2, C_2, N_2, O_2, and F_2 from Filippi, C.; Umrigar, C. J. *J. Chem. Phys.* **1996**, *105*, 213. (b) For LiH, NH, OH, and HF, from Lüchow, A.; Anderson, J. B. *J. Chem. Phys.* **1996**, *105*, 7573. (c) For H_2O, NH_3, and CH_4, from Manten, S.; Lüchow, A. *J. Chem. Phys.* **2001**, *115*, 5362. (d) For C_6H_6, from Casula, M.; Attaccalite, C.; Sorella, S. *J. Chem. Phys.* **2004**, *121*, 7110.

(22) (a) Experimental atomization energies for Li_2, N_2, O_2, F_2, LiH, NH, OH, HF, H_2O, NH_3, CH_4, and C_6H_6 from ref 19. For Be_2, from Bondybey, V. E. *Chem. Phys. Lett.* **1984**, *109*, 436. (b) For B_2, from Carrol, M. T.; Bader, R. F. W.; Vosko, S. H. *J. Phys. B: At. Mol. Opt. Phys.* **1987**, *20*, 3599. (c) For C_2, from Goursot, A.; Malrieu, J. P.; Salahub, D. R. *Theor. Chim. Acta* **1995**, *91*, 225. (d) For Ne_2 and Ar_2, from Ogilvie, J. F.; Wang, F. Y. H. *Exp. J. Mol. Struct.* **1992**, *273*, 277. (e) For NiH, from Diaconu, C. V.; Cho, A. E.; Doll, J. D.; Freeman, D. L. *J. Chem. Phys.* **2004**, *121*, 10026.

(23) (a) Experimental bond lengths for Li_2, N_2, O_2, F_2, LiH, NH, OH, and HF from ref 19. For Be_2, from ref 22a. (b) For B_2, from Staroverov, V. N.; Scuseria, G. E.; Tao, J.; Perdew, J. P. *J. Chem. Phys.* **2003**, *119*, 12129. (c) For C_2, from ref 22c. (d) For H_2O, NH_3, and CH_4, from DeFrees, D. J.; Levi, B. A.; Pollack, S. K.; Hehre, W. J.; Binkley, J. S.; Pople, J. A. *J. Am. Chem. Soc.* **1979**, *101*, 4085. (e) For C_6H_6, from Swensona, D. W. H.; Jaegera, H. M.; Dykstra, C. E. *Chem. Phys.* **2006**, *326*, 329. (f) For Ne_2 and Ar_2, from ref 22d. (g) For NiH, from ref 22e.

(24) Stanton, J. F.; Gauss, J.; Perera, S. A.; Watts, J. D.; Nooijen, M.; Yau, A.; Oliphant, N.; Szalay, P. G.; Lauderdale, W. J.; Gwaltney, S. R.; Beck, S.; Balková, A.; Bernholdt, D. E.; Baeck, K.-K.; Rozyczko, P.; Sekino, H.; Huber, C.; Pittner, J.; Bartlett, R. J. ACES-II, a program product of the Quantum Theory Project; University of Florida. Integral packages included are VMOL (Almlöf, J.; Taylor, P. R.); VPROPS (Taylor, P. R.); and ABACUS (Helgaker, T.; Jensen, H. J. Aa.; Jørgensen, O.; Olsen, J.; Taylor, P. R.).

(25) Perera, S. A. University of Florida. Personal communication with S.B.T., May 2008.

(26) Patton, D. C.; Pederson, M. R. *Phys. Rev. A* **1997**, *56*, R2495; Erratum *Phys. Rev. A* **2005**, *71*, 019906(E).

(27) Zhao, Y.; Truhlar, D. G. *J. Phys. Chem. A* **2006**, *110*, 5121.

(28) Extensible Computational Chemistry Environment basis set database, version 1.0, as developed and distributed by the Molecular Science Computing Facility, Environmental and Molecular Sciences Laboratory, which is part of the Pacific Northwest Laboratory, P.O. Box 999, Richland, Washington 99352, and funded by the U.S. Department of Energy. The Pacific Northwest Laboratory is a multiprogram laboratory operated by Battelle Memorial Institute for the U.S. Department of Energy under Contract DE-AC06-76RLO 1830.

(29) Slater, J. C. *Adv. Quantum Chem.* **1972**, *6*, 1.

(30) Schwarz, K. *Phys. Rev. B* **1972**, *5*, 2466.

(31) Schwarz, K. *Theor. Chim. Acta* **1974**, *34*, 225.

CT8005634

JCTC Journal of Chemical Theory and Computation

The DBH24/08 Database and Its Use to Assess Electronic Structure Model Chemistries for Chemical Reaction Barrier Heights

Jingjing Zheng, Yan Zhao, and Donald G. Truhlar*

Received December 19, 2008

Abstract: The diverse barrier height database DBH24 is updated by using W4 and W3.2 data (Karton, A.; Tarnopolsky, A.; Lamère, J.-F.; Schatz, G. C.; Martin, J. M. L. *J. Phys. Chem. A* **2008**, *112*, 12868) to replace previous W1 values; we call the new database DBH24/08. We used the new database to assess 348 model chemistries, each consisting of a combination of a wave function theory level or a density functional approximation with a one-electron basis set. All assessments are made by simultaneous consideration of accuracy and cost. The assessment includes several electronic structure methods and basis sets that have not previously been systematically tested for barrier heights. Some conclusions drawn in our previous work (Zheng, J.; Zhao, Y.; Truhlar, D. G. *J. Chem. Theory Comput.* **2007**, *3*, 569) are still valid when using this improved database and including more model chemistries. For example, BMC-CCSD is again found to be the best method whose cost scales as N^6, and its cost is an order of magnitude smaller than the N^7 method with best performance-to-cost ratio, G3SX(MP3), although the mean unsigned error is only marginally higher, namely 0.70 kcal/mol vs 0.57 kcal/mol. Other conclusions are now broader in scope. For example, among single-reference N^6 methods (that is, excluding MRMP2), we now conclude not only that doubly hybrid density functionals and multicoefficient extrapolated density functional methods perform better than second-order Møller−Plesset-type perturbation theory (MP2) but also that they perform better than any correlation-energy-scaled MP2 method. The most recommended hybrid density functionals, if functionals are judged only on the basis of barrier heights, are M08-SO, M06-2X, M08-HX, BB1K, BMK, PWB6K, MPW1K, BHandHLYP, and TPSS25B95. MOHLYP and HCTH are found to be the best performing local density functionals for barrier heights. The basis set cc-pVTZ+ is more efficient than aug-cc-pVTZ with similar accuracy, especially for density functional theory. The basis sets cc-pVDZ+, 6−31+G(d,p), 6−31B(d,p), 6−31B(d), MIDIY+, MIDIX+, and MIDI! are recommended for double-ζ-quality density functional calculations on large systems for their good balance between accuracy and cost, and the basis sets cc-pVTZ+, MG3S, MG3SXP, and aug-cc-pVDZ are recommended for density functional calculations when larger basis sets are affordable. The best performance of any methods tested is attained by CCSD(T)(full)/aug-cc-pCV(T+d)Z with a mean unsigned error of 0.46 kcal/mol; however, this is several orders of magnitude more expensive than M08-SO/cc-pVTZ+, which has a mean unsigned error of only 0.90 kcal/mol.

1. Introduction

We recently developed a representative database for thermochemical kinetics, called DBH24,[1,2] based on the full database NHTBH38/04[3] and 44 hydrogen transfer reactions in Database/3.[4] The databases, NHTBH38/04 and Database/3, have 38 barrier heights for non-hydrogen-transfer reactions and 44 barrier heights for hydrogen-transfer reactions. The DBH24 database is a statistically representative subset of

* Corresponding author e-mail: truhlar@umn.edu.

10.1021/ct800568m CCC: $40.75
Published on Web 03/23/2009

NHTBH38/04 and the hydrogen-transfer reactions in Database/3. It contains 6 barrier heights each for heavy-atom transfer, nucleophilic substitution, unimolecular and association reactions, and hydrogen-transfer reactions, respectively. This representative database can adequately reproduce the mean signed errors (MSEs), mean unsigned errors (MUEs), and root-mean-square errors (RMSEs) of the entire database. Because the representative database is much smaller than the entire databases, it significantly reduces the computational costs and makes testing of high-level model chemistries more affordable.

A single-level model chemistry is a combination of a level of electronic structure wave function theory or density functional approximation and a basis set; a multilevel model chemistry is a way to combine such combinations to extrapolate to a more accurate result. A model chemistry is also called a "method". In our previous work,[1] we assessed 205 model chemistries for chemical reaction barrier heights using the entire database or the representative DBH24 database. The model chemistries tested included various levels of single-level wave function theory, multicoefficient correlation methods, local and hybrid density functional approximations, and semiempirical molecular orbital methods. In the present article we retest these methods against an improved database, and we add 143 additional methods to the comparison.

The best estimates of barrier heights in the DBH24 database are from either high-level theoretical calculations, e.g., the Weizmann-1[5] (W1) or the multireference configuration interaction method[6] (MRCI), or they are values derived from experimental data. Recently, Karton et al.[7] carried out calculations with the Weizmann-4 (W4) and Weizmann-3.2 (W3.2) model chemistries[8] for these 24 barrier heights. These W4 and W3.2 calculations are more reliable than the W1 values[3] used in the original DBH24 database. This motivated us to update the DBH24 database, and in the present article we present the updated database called DBH24/08.

After the publication of our first comprehensive assessment of model chemistries for barrier heights in 2007,[1] a number of new density functionals, wave function methods, and basis sets became available, and it also became apparent that more of the previously available methods needed testing. Here we make our assessment more complete by adding additional model chemistries not covered in our previous papers[1,9] to our benchmark data set.

2. DBH24/08 Database

Table 1 lists the new best estimates of barrier height that constitute the DBH24/08 database. We updated 14 barrier heights calculated at W1 values in the original DBH24 database by the new[7] W4 or W3.2 values. Those values of barrier heights based on other theoretical calculations than W1 and values derived from experimental rate constants are still considered to be the best estimates for those cases. Below is a brief review of the methods used for the best estimates of barrier height in the DBH24/08 database that are not taken as W4 or W3.2 values.

Table 1. Best Estimates of Barrier Height (in kcal/mol) in the DBH24/08 Database

reactions	forward/reverse BH	method
Heavy-Atom Transfer		
$H + N_2O \leftrightarrow OH + N_2$	17.13/82.47	W4
$H + ClH \leftrightarrow HCl + H$	18.00/18.00	CAS+1+2+QC/CBS plus core-valence correlation
$CH_3 + FCl \leftrightarrow CH_3F + Cl$	6.75/60.00	W3.2
Nucleophilic Substitution		
$Cl^-\cdots CH_3Cl \leftrightarrow ClCH_3\cdots Cl^-$	13.41/13.41	W3.2
$F^-\cdots CH_3Cl \leftrightarrow FCH_3\cdots Cl^-$	3.44/29.42	W3.2
$OH^- + CH_3F \leftrightarrow HOCH_3 + F^-$	−2.44/17.66	W3.2
Unimolecular and Association		
$H + N_2 \leftrightarrow HN_2$	14.36/10.61	W4
$H + C_2H_4 \leftrightarrow CH_3CH_2$	1.72/41.75	VSEC
$HCN \leftrightarrow HNC$	48.07/32.82	W4
Hydrogen Transfer		
$OH + CH_4 \leftrightarrow CH_3 + H_2O$	6.7/19.6	experiment
$H + OH \leftrightarrow O + H_2$	10.7/13.1	CAS+1+2+QC/CBS plus core-valence correlation
$H + H_2S \leftrightarrow H_2 + HS$	3.6/17.3	experiment

Barrier heights for the reactions $H + ClH \leftrightarrow HCl + H$ and $H + OH \leftrightarrow O + H_2$ were calculated using the CAS+1+2+QC method at the complete basis set limit including core-valence correlation by Peterson and Dunning.[10] Here CAS+1+2 denotes MRCI with single and double excitations from a complete active space self-consistent field (CASSCF) reference, and +QC denotes a Davidson correction for higher excitations. The active space used in the CASSCF and MRCI calculations is the full valence space plus two additional orbitals of π_x and π_y symmetry. The best estimates of barrier heights of $H + C_2H_4 \leftrightarrow CH_3CH_2$ are based on the variable scaled external correlation (VSEC) method.[11] The VSEC method[12] adjusts the dynamical correlation energy along the reaction path to reproduce the high-pressure limit experimental rate constants for the addition and the unimolecular corrections[13] (VTST/MT). Therefore, this barrier height based on the VSEC method can be considered to have the quality of experimental data. The best estimated barrier heights for the $OH + CH_4 \leftrightarrow CH_3 + H_2O$ and $H + H_2S \leftrightarrow H_2 + HS$ reactions were made by comparing the best available theoretical calculation and best experiment for the reaction rate constants at 600 K.[14] For $OH + CH_4$ the theoretical rate constant[15] was calculated by using VTST/MT, and the experimental data were taken from ref 16. Peng et al. performed experiments and calculations using conventional TST and an Eckart correction for quantum mechanical tunneling for the rate constant of the $H + H_2S$ reaction.[17] Since we used rate constants at 600 K at which the tunneling contribution is moderate, the one-dimensional Eckart correction for tunneling is considered to be acceptable for this case. For these reactions, the best estimate of forward barrier height is determined by $V^{\ddagger}$(best estimate) = $V^{\ddagger}$(theory) + $\Delta V^{\ddagger}$. The adjustment to the barrier height is calculated using the equation $\Delta V^{\ddagger} = RT\ln(k_{theory}(T)/k_{experiment}(T))$, where k_{theory} and $k_{experiment}$ are respectively the theoretical and experimental reaction rate constants at 600 K, and R is the molar gas constant. The reverse barrier height is calculated by adding

the reaction exoergicity to the best estimate of the forward barrier height. The exoergicity is calculated from experimental total atomization energies.[18]

3. Computational Details

Details for the calculations not mentioned here can be found in the previous papers.[1,9,19]

3.1. Electronic Structure Levels. We carried out calculations employing a diverse array of density functionals, electronic structure wave function levels, basis sets, and multilevel methods for the 24 barrier heights, and we assessed their accuracy statistically against the DBH24/08 database. Some of the calculations were available from previous studies,[1,9,19] and others are new. The added multilevel methods are BMC-CCSD-C,[20] BMC-QCISD,[20] G2,[21] G3,[22] G3/3,[4] G3S,[23] G3S/3,[4] G3SX(MP2),[24] G4,[25] G4(MP2),[26] SCS-MP2,[27] and SOS-MP2.[28,29] We also added one single-level model chemistry based on the CEPA[30] version 1 approximation. We also added calculations with multireference perturbation theory, in particular MRMP2/nom-CPO/MG3S from ref 19. The added density functionals are B2-PLYP,[31] B2GP-PLYP,[7] B2K-PLYP,[32] B2T-PLYP,[32] mPW2-PLYP,[33] mPW2K-PLYP,[32] B3PW91,[34−36] B3P86,[34,35,37] M06,[38] M06-2X,[38] M08-HX,[39] M08-SO,[39] MOHLYP,[40] mPW1KK,[41] mPW25B95,[42] PBEsol,[43] SOGGA,[44] TPSS-20B95,[42] and TPSS25B95.[42] Note that some of the multilevel methods may also be considered to be single-level methods with adjusted coefficients, and other multilevel methods involving both wave function correlation and density functional correlation may be considered to be fifth rung density functional approximations. Calculations involving both Hartree−Fock exchange and density functional exchange (generalized Kohn-sham theory) are, as usual, considered to be a hybrid-type of density functional approximation. In single-level wave function methods, core electrons are uncorrelated except where indicated "(full)". In density functional calculations all electrons are explicit, and all are correlated.

3.2. Basis Sets. The additional basis sets used in this work are 3−21G,[45] 6−31B(d,p),[20] cc-pVDZ+,[46] cc-pVTZ+,[46] cc-pV(T+d)Z+,[46] G3LargeXP,[25] G3MP2LargeXP,[25] G45Z,[25] G4QZ,[25] G4MP2QZ,[26] G4MP2TZ,[26] MG3SXP,[39] MIDIX+,[47] MIDIY+,[47] STO-2G,[48] STO-3G,[48] and STO-3G+.[48,49] The MG3SXP (where XP denotes "extra polarization") basis differs from the MG3S[4] one in the same way that G3LargeXP[25] differs from G3Large,[22] in particular, the 2df polarization functions of G3Large on Li−Ne are replaced by a 3df set, and the 3d2f polarization functions on Al−Ar are replaced by 4d2f, where the polarization functions are those recommended by Curtiss et al.[25] The basis set cc-pVTZ+[46] is cc-pVTZ[50] for H and cc-pVTZ plus the Pople-style diffuse s and p functions[49] for non-hydrogenic atoms, while cc-pV(T+d)Z+ is the cc-pV(T+d)Z[51] basis set plus the same diffuse functions as in the cc-pVTZ+. The cc-pVDZ+ basis is constructed in the same way as the cc-pVTZ+ basis. The basis 6−31B(d,p) is 6−31+B(d,p)[20] without diffuse functions. MIDIX+ and MIDIY+ basis sets are obtained by adding diffuse function on all elements with nuclear charges of 3 or larger to MIDIX[52] (also called MIDI!) and MIDIY[47] basis sets. The MIDIY basis set is the same as MIDIX (or MIDI!) but with a polarization function added to hydrogen. STO-3G+ is STO-3G plus the Pople-style diffuse s and p functions[49] for non-hydrogenic atoms.

3.3. Software. The additional calculations mentioned above were carried out using the *Gaussian 03* package[53] and *MN-GFM 4.1* module[54] except that CCSD(T)[55] and CEPA calculations were done by the *Molpro* program.[56]

3.4. Relativistic Effects. The effect of spin−orbit coupling was added to the energies of the Cl, O, OH, and HS radicals, which lower their energies by 0.84, 0.22, 0.20, and 0.54 kcal/mol, respectively.[57] Scalar relativistic effects[58] were neglected, which is not a serious approximation since the heaviest element involved in DBH24/08 is Cl.

3.5. Geometries. Most calculations in this work used structures optimized using the QCISD/MG3 method with the spin-restricted formalism for closed-shell and the spin-unrestricted formalism for open-shell systems. Note that we also use the QCISD/MG3 geometries for those multilevel methods, e.g., G*n* (n = 2, 3, 4) and CBS, which were originally defined to use a lower-level geometry. The only exception is MRMP2, for which calculations were carried out at consistently optimized geometries. We also tested a few methods for fully optimized calculations.

3.6. Vibrational Contributions. The barrier heights calculated in this work are all zero-point exclusive. No vibrational, rotational, or translational contributions are included in DBH24/08 or in any of the calculations in this paper.

3.6. Timings. The computational "cost" of a given method is assessed as the single-processor CPU time for calculating an energy gradient of the molecule phosphinomethanol divided by the time for an MP2/6−31+G(d,p) energy gradient calculation with the same computer program on the same computer. We use gradient calculations to illustrate computational cost because gradients are important for geometry optimization and dynamics calculations. Analytic gradients were always used unless they are not available in the computer program that we used, in which case we used numerical gradients. In *Gaussian 03* a numerical gradient of phophinomethanol uses 49 single-point energies, whereas in *Molpro* it uses 19 single-point energies for phophinomethanol. For local DFT methods, we calculated two costs corresponding to carrying out the calculation with and without density fitting,[59] and the table gives the smaller of the two. The timings for CR-CC(2,3) were not run directly but were estimated as 1.5 times the cost of CCSD(T) with the same basis set.

In a few cases the timings were run more than once under different computer load conditions, and the results were averaged. The SOS-MP2 timings were run with the *Q-Chem* program, and all other timings were run using the software specified in Section 3.3 or refs 1, 9, and 19. Although some multilevel wave function methods, e.g., G*n* (n = 2, 3, 4) and CBS, are usually defined to use a lower-level geometry and are not normally employed in gradient calculations, we include gradient timing for them here so that the reader can judge their approximate cost on the same grounds as the other methods.

4. Results and Discussion

In the present article, we employed 348 model chemistries to calculate the 24 barrier heights in the DBH24/08 database. We selected the electronic structure methods that are often used in the literature or that are new but tend to give promising results. When we run a calculation with a multilevel method, we also can get the results for each single-level method in the multilevel components simultaneously. Therefore we also listed these single-level methods' results in Table 2, so that one can see how much the multilevel method improves the accuracy over each of its components. Most density functionals are run with MG3S basis sets at first. If a density functional gives good results, we also run this density functional with more basis sets so that we can assess the methods with a greater variety of performance-to-cost ratios.

All electronic structure methods will be assessed based on a combination of accuracy against DBH24/08, the scaling power σ, and the "cost". The scaling power is defined such that the number of arithmetic operations in the calculation increases as N^σ in the limit of large N, where N is the number of atoms, and the scaling refers to increasing N with a given number of basis functions on each atom. The scaling would be different if one increased the number of basis functions with N fixed.[60] Furthermore, one does not reach the large-N limit with respect to system size until very large systems (much larger than those considered here) are considered. So one must be cautious in using σ to categorize methods. One must be even more cautious in using the cost values. One cannot stress too much the somewhat arbitrary character of the timings. We tried to minimize this by computing every cost as the relative cost of two calculations with the same software on the same computer where the denominator is a method (MP2/6−31+G(d,p)) that is available in almost all software packages. Nevertheless the timings do depend on the software. Timing differences less than a factor of 2 are not meaningful except when one is comparing similar methods, and timings of inexpensive methods are inevitably contaminated by overhead. Thus all timings greater than 1.0 are rounded to two significant figures, and those less than 1.0 are rounded to one significant figure. Another disadvantage of using timings as costs is that the true cost also involves components of memory and disk usage, software cost, and human time.

An example showing the vagaries of timings is a comparison the timings for SOS-MP2/MG3S and SOS-MP2/cc-pVTZ. Our standard method of assessing cost gives 17 and 15, respectively (see Table 2). If the former calculation had the same number of iterations as the latter, the timing would be only 11. Such an effect is partly noise, but it may also be due in part to the fact that calculations involving diffuse functions often require more iterations. Furthermore, unlike cc-VTZ, the MG3S basis set has the same exponents for *s* and *p* functions; this gives a cost savings in *Gaussian* but not in most other computer programs.

Despite all these complex considerations, no evaluation of methods that does not consider cost can serve as a guide to practical work, so we must consider cost. Therefore, after consideration of various cost estimates, we selected the simple relative timings explained above, which has the advantage of being systematic, easy to understand, and easy for a reader to apply to new methods when he or she has a new method to assess in comparison to those considered here. To avoid tediousness, we will not repeat the cautionary notes about timings, but the reader should keep them in mind as we proceed with discussion.

4.1. Calculations at Standard Geometries. Table 2 lists, for calculations at geometries optimized with the QCISD/MG3 method (and for consistently optimized MRMP2/MG3S), the mean signed errors and mean unsigned errors for the DBH24/08 database as well as the errors for its components: heavy-atom transfer (HATBH6), nucleophilic substitution (NSBH6), unimolecular and association (UABH6), and hydrogen-transfer (HTBH6) reactions. All methods are listed in order of increasing MUE for the DBH24/08 database and are listed in separation sections for each scaling order σ. Table 2 also gives references[3,4,7,14,19,21−44,55,61−111] for the electronic structure methods, which should be useful since some of the acronyms are more familiar than others.

To systematically create a list of recommended methods, we started with the best N^7 method, (where "best" is defined as lowest MUE), then added the best N^7 method that has a lower cost, and then added the best N^7 method that has a lower cost than both of these, etc., until we got to the bottom of the N^7 list. Then we did the same for the N^6, N^5, N^4, and N^3 methods. When adding methods to the recommended list, we also checked the scaling. For example, if there is an N^4 method that has both lower cost and lower MUE than an N^5 method on the list, then that N^5 method is removed from the list. This created a list based on the performance for the overall DBH24/08 database. MUEs that remain on the list when the process is complete are in bold in Table 2. This process was then repeated for each of the four smaller databases. The MUEs of the five resulting lists are all in bold in Table 2. When searching for an affordable method for a specific application, the bold entries in Table 2 provide a short list of methods that should be considered. Any method that earned at least one bold MUE is also in bold with its timing in bold, in order to make the table easier to read.

The most accurate method overall is CCSD(T) with all electrons correlated and a triple-ζ core-valence correlated basis set, which can achieve accuracy better than 0.5 kcal/mol. But the cost of this accuracy is that this method is 2 orders of magnitude higher than for any other method listed in Table 2. G3SX(MP3) has the best cost-adjusted performance; it has the same accuracy as the CCSD(T)/aug-cc-pV(T+d)Z method, but it is about 18 times more efficient.

CCSD(T)-KS denotes a CCSD(T) calculation based on reference orbitals from a density functional calculation (using a spin-restricted calculation with the BLYP functional here); otherwise oribtals were obtained from a restricted Hartree−Fock calculation. Comparison of the results for CCSD(T)-KS/aug-cc-pVTZ and CCSD(T)/aug-cc-pVTZ calculations shows that the choice of orbitals makes only a very small difference in the MUE for the representative barrier height calculations and using Kohn−Sham orbitals actually raises the MUE by 0.03 kcal/mol.

Table 2. Mean Signed Errors (MSEs) and Mean Unsigned Errors (MUEs) (in kcal/mol) for the DBH24/08 Database Calculated at QCISD/MG3 Geometries[a]

			HATBH6		NSBH6		UABH6		HTBH6		DBH24	
methods	type	theory ref	MSE	MUE	MSE	MUE	MSE	MUE	MSE	MUE	MUE	cost
					N^7 Methods							
CCSD(T)(full)/aug-cc-pCV(T+d)Z	WFT	55	0.52	0.63	−0.34	0.36	0.14	0.28	0.08	0.58	**0.46**	**25000**
CCSD(T)(full)/aug-cc-pCVTZ	WFT	55	0.54	0.67	−0.37	0.38	0.14	0.28	0.08	0.58	0.47	32000
CCSD(T)(full)/aug-cc-pVTZ	WFT	55	−0.14	0.59	−0.63	0.63	0.31	0.33	−0.60	0.60	**0.54**	**14000**
CCSD(T)/aug-cc-pV(T+d)Z	WFT	55	0.45	**0.63**	−0.63	0.63	0.07	0.33	0.06	0.67	0.57	**2200**
G3SX(MP3)	ML	24	−0.34	**0.76**	−0.11	0.43	−0.02	0.41	0.57	0.68	**0.57**	**120**
G3SX	ML	24	−0.38	**0.74**	−0.64	0.64	0.08	0.31	0.39	0.60	0.57	**890**
G4	ML	25	0.34	0.81	−0.34	0.56	0.07	**0.24**	0.72	0.72	0.58	**7700**
G4(MP2)	ML	26	0.25	**0.33**	0.50	0.57	−0.26	0.44	1.04	1.04	0.59	**3100**
CR-CC(2,3)(full)A/aug-cc-pCVTZ	WFT	65	1.13	1.13	−0.06	0.17	0.37	0.45	0.27	0.66	0.60	48000
CR-CC(2,3)A/aug-cc-pV(T+d)Z	WFT	65	1.02	1.03	−0.34	0.34	0.30	0.45	0.26	0.73	0.64	3300
CR-CC(2,3)(full)D/aug-cc-pCVTZ	WFT	65	1.00	1.00	−0.32	0.42	0.36	0.48	0.24	0.68	0.64	48000
CR-CC(2,3)(full)C/aug-cc-pCVTZ	WFT	65	0.99	0.99	−0.32	0.43	0.36	0.48	0.24	0.68	0.64	48000
CR-CC(2,3)B/aug-cc-pV(T+d)Z	WFT	65	1.24	1.24	−0.16	**0.16**	0.33	0.49	0.33	0.76	0.66	**3300**
CR-CC(2,3)(full)B/aug-cc-pCVTZ	WFT	65	1.35	1.35	0.13	0.17	0.40	0.48	0.34	0.69	0.67	48000
CR-CC(2,3)C/aug-cc-pV(T+d)Z	WFT	65	0.87	0.87	−0.64	0.64	0.29	0.49	0.21	0.74	0.69	3300
MCG3-MPW	ML	64	−0.67	1.09	−0.61	0.61	−0.13	0.61	−0.07	**0.44**	0.69	**100**
CR-CC(2,3)D/aug-cc-pV(T+d)Z	WFT	65	0.88	0.88	−0.64	0.64	0.29	0.49	0.21	0.74	0.69	3300
CCSD(T)/aug-cc-pVTZ	WFT	55	0.59	0.95	−0.78	0.78	0.07	0.33	0.09	0.70	0.69	4700
CCSD(T)-KS/aug-cc-pVTZ	WFT	55	0.47	0.91	−0.92	0.92	0.06	0.31	0.03	0.76	0.72	3900
MCG3-MPWB	ML	64	−0.67	1.05	−0.36	0.62	−0.15	0.62	−0.31	0.59	0.72	100
G3	ML	22	0.62	0.75	−1.10	1.10	0.22	0.39	0.68	0.68	0.73	1500
G3S/3	ML	4	−0.86	1.08	−0.85	0.85	−0.09	0.42	0.25	0.58	0.73	1500
G3S	ML	23	−0.38	1.00	−0.93	0.93	0.09	0.35	0.42	0.69	0.74	1500
MCG3-TS	ML	64	−0.50	**0.86**	−1.09	1.09	0.11	0.53	−0.22	0.55	0.76	**100**
CR-CC(2,3)A/aug-cc-pVTZ	WFT	65	1.16	1.35	−0.49	0.49	0.30	0.45	0.28	0.75	0.76	7100
CR-CC(2,3)B/aug-cc-pVTZ	WFT	65	1.37	1.49	−0.31	0.31	0.33	0.49	0.35	0.78	0.77	7100
CR-CC(2,3)C/aug-cc-pVTZ	WFT	65	1.03	1.14	−0.81	0.81	0.29	0.49	0.23	0.77	0.80	7100
CR-CC(2,3)D/aug-cc-pVTZ	WFT	65	1.04	1.15	−0.81	0.81	0.29	0.49	0.23	0.76	0.80	7100
G3/3	ML	4	0.91	1.04	−0.98	0.98	0.26	0.40	0.87	0.87	0.82	1500
MCG3/3	ML	4	−0.52	1.25	−0.53	0.69	−0.30	0.58	−0.33	0.86	0.84	90
CCSD(T)/cc-pV(T+d)Z+	WFT	55	1.51	1.51	−0.18	0.75	0.34	0.55	0.72	0.97	0.94	540
CCSD(T)/cc-pVTZ+	WFT	55	1.65	1.65	−0.33	0.81	0.34	0.55	0.75	0.99	1.00	870
G2	ML	21	1.18	1.43	−0.48	0.75	0.41	0.53	1.33	1.33	1.01	2300
CCSD(T)(full)/MG3S	WFT	55	1.50	1.57	−0.11	0.91	0.83	0.83	1.06	1.16	1.12	1000
CR-CC(2,3)(full)C/MG3S	WFT	65	1.73	1.73	0.00	0.79	0.96	0.96	1.11	1.16	1.16	1500
CR-CC(2,3)(full)D/MG3S	WFT	65	1.74	1.74	0.00	0.80	0.95	0.95	1.11	1.16	1.16	1500
CCSD(T)/MG3S	WFT	55	1.63	1.71	−0.35	1.12	0.67	0.67	1.16	1.22	1.18	300
QCISD(T)/MG3S	WFT	66	1.58	1.65	−0.69	1.31	0.65	0.65	1.10	1.20	1.20	5100
CR-CC(2,3)C/MG3S	WFT	65	1.85	1.85	−0.28	1.00	0.79	0.79	1.21	1.22	1.22	450
CR-CC(2,3)D/MG3S	WFT	65	1.86	1.86	−0.28	1.00	0.79	0.79	1.21	1.22	1.22	450
CR-CC(2,3)(full)A/MG3S	WFT	65	2.07	2.07	0.17	0.82	1.06	1.06	1.25	1.27	1.31	1500
CR-CC(2,3)A/MG3S	WFT	65	2.20	2.20	−0.08	0.92	0.90	0.90	1.36	1.36	1.34	450
G3SX(MP2)	ML	24	0.44	1.69	−0.20	0.69	−0.52	1.06	1.87	1.90	1.34	150
CR-CC(2,3)(full)B/MG3S	WFT	65	2.29	2.29	0.36	0.82	1.10	1.10	1.32	1.32	1.38	1500
CR-CC(2,3)B/MG3S	WFT	65	2.42	2.42	0.12	0.85	0.93	0.93	1.42	1.42	1.41	450
CCSD(T)/aug-cc-pVDZ	WFT	55	1.00	2.27	−1.99	1.99	−0.33	0.68	0.03	0.76	1.42	140
CBS-QB3	ML	67,68	−0.62	1.68	−0.96	1.07	−2.07	2.42	−1.22	1.32	1.62	360
CBS-Q	ML	69	−1.88	1.91	−1.60	1.63	−2.47	2.53	−0.68	0.86	1.73	370
CEPA(1)/MG3S	WFT	30	−2.05	4.19	0.53	0.86	0.94	1.10	1.78	1.81	1.99	90
CCSD(T)/MG3SXP	WFT	55	3.09	4.13	1.03	2.01	0.31	0.86	1.12	1.18	2.04	280
CBS-Lq	ML	70	−1.31	2.31	0.06	1.52	−3.12	3.55	−0.80	1.20	2.14	180
CCSD(T)/cc-pV(T+d)Z	WFT	55	1.76	1.76	−3.01	5.10	0.32	0.47	0.87	1.38	2.18	670
CCSD(T)/cc-pVTZ	WFT	55	1.90	1.90	−3.15	5.27	0.32	0.47	0.89	1.41	2.26	630
CBS-4M	ML	68,69	1.14	3.51	2.50	2.98	−2.24	2.71	−0.20	0.55	2.44	170
CCSD(T)/6−311G(2df,2p)	WFT	55	1.88	2.20	−3.92	8.15	0.57	0.76	1.35	1.85	3.24	380
QCISD(T)/6−311G(2df,2p)	WFT	66	1.77	2.28	−4.23	8.37	0.56	0.75	1.16	1.62	3.25	2300
MP4/MG3S	WFT	62	7.81	7.81	−1.34	1.42	3.23	3.62	2.40	2.40	3.81	2900
QCISD(T)/6−31G(d)	WFT	66	4.25	4.93	−2.73	8.19	1.45	3.04	4.76	5.61	5.44	63
CCSD(T)/6−31G(d)	WFT	55	4.56	5.18	−2.53	8.15	1.53	3.09	4.80	5.62	5.51	8.1
MP4/6−311G(2df,2p)	WFT	62	8.00	8.00	−4.58	8.64	3.20	3.82	2.35	2.35	5.70	1600
MP4/6−31+G(d)	WFT	62	10.07	10.07	−0.47	2.28	3.97	4.88	5.64	5.64	5.72	82
MP4/6−311G(2d,p)	WFT	62	9.13	9.13	−5.00	8.88	3.08	4.02	2.98	3.36	6.35	460
MP4/6−31G(2df,p)	WFT	62	8.22	8.22	−4.34	9.31	4.22	4.48	4.09	4.26	6.57	610
MP4/6−31G(d)	WFT	62	10.73	10.73	−2.88	8.58	4.22	5.40	6.02	6.45	7.79	37
					N^6 Methods							
BMC-CCSD	ML	20	0.52	1.28	−0.02	0.54	−0.24	0.37	0.19	0.63	**0.70**	**17**
BMC-CCSD-C	ML	20	0.50	1.37	0.07	0.53	−0.37	0.37	0.26	0.64	0.73	17
BMC-QCISD	ML	20	1.35	1.50	0.08	0.56	0.10	**0.30**	0.55	0.77	0.78	**16**

Table 2. Continued

methods	type	theory ref	HATBH6 MSE	HATBH6 MUE	NSBH6 MSE	NSBH6 MUE	UABH6 MSE	UABH6 MUE	HTBH6 MSE	HTBH6 MUE	DBH24 MUE	cost
MCQCISD-MPWB	ML	64	−0.49	**0.94**	−0.08	0.65	−0.09	0.89	−0.53	0.63	0.78	**29**
MCQCISD-MPW	ML	64	−0.72	1.19	−0.34	0.55	−0.14	0.94	−0.42	0.52	0.80	27
MC-QCISD/3	ML	4	1.48	1.53	−0.20	**0.21**	0.49	0.66	0.89	0.98	0.84	**16**
MCQCISD-TS	ML	64	−0.80	1.00	−1.12	1.12	0.06	0.69	−0.65	0.79	0.90	29
MCUT-MPWB	ML	64	1.53	1.53	−0.22	0.59	1.09	1.52	−0.52	0.56	1.05	28
MCUT-MPW	ML	64	1.38	1.81	−0.90	0.90	1.17	1.54	−0.54	0.54	1.20	26
MCUT-TS	ML	64	1.18	1.61	−1.56	1.56	1.27	1.32	−0.59	0.68	1.29	28
CCSD(full)/aug-cc-pVTZ	WFT	71	3.43	3.43	1.72	1.72	1.42	1.42	1.18	1.18	1.94	3200
CCSD/aug-cc-pVTZ	WFT	71	4.11	4.11	1.56	1.56	1.17	1.22	1.84	1.84	2.18	2400
CCSD/aug-cc-pV(T+d)Z	WFT	71	3.98	3.98	1.72	1.72	1.17	1.22	1.82	1.82	2.18	2500
CCSD(full)/aug-cc-pCVTZ	WFT	71	4.19	4.19	2.01	2.01	1.26	1.26	1.88	1.88	2.34	6800
QCISD/MG3S	WFT	66	4.41	4.41	1.18	1.28	1.30	1.30	2.37	2.37	2.34	150
CCSD(full)/aug-cc-pV(T+d)Z	WFT	71	4.18	4.18	2.04	2.04	1.26	1.26	1.89	1.89	2.34	3500
CCSD/cc-pVTZ+	WFT	71	5.00	5.00	1.95	1.95	1.42	1.47	2.39	2.39	2.70	320
CCSD/MG3S	WFT	71	5.00	5.00	1.92	1.92	1.72	1.72	2.75	2.75	2.85	240
CCSD(full)/MG3S	WFT	71	4.93	4.93	2.18	2.18	1.90	1.90	2.68	2.68	2.92	380
MC-UT/3	ML	4	7.02	7.02	0.25	**0.35**	3.12	3.12	2.33	2.33	3.21	**15**
CCSD/MG3SXP	WFT	71	6.09	6.31	2.96	3.04	1.41	1.60	2.63	2.63	3.40	350
CCSD/cc-pV(T+d)Z+	WFT	71	4.87	4.87	2.11	2.11	1.42	1.47	6.35	6.35	3.70	350
MP4SDQ/MG3S	WFT	62	8.95	8.95	1.40	1.42	3.38	3.38	3.56	3.56	4.33	95
QCISD/6−31B(d)	WFT	66	6.40	9.04	−0.72	**5.20**	2.26	**2.41**	4.86	5.06	5.43	**1.5**
CCSD/6−31B(d)	WFT	71	6.74	9.17	0.32	5.45	2.57	2.68	4.99	5.08	5.59	2.3
MP3/MG3S	WFT	62	10.70	10.70	3.33	3.33	4.44	4.44	4.29	4.29	5.69	71
QCISD/6−31G(d)	WFT	66	6.18	6.26	−1.75	8.09	1.98	2.71	5.44	5.89	5.74	19
CCSD/6−31G(d)	WFT	71	6.44	6.50	−1.04	7.95	2.19	2.83	5.56	5.91	5.80	2.4
MP4SDQ/6−31+G(d)	WFT	62	10.69	10.69	1.53	2.38	4.15	4.57	6.30	6.30	5.98	1.6
MP4SDQ/6−31G(2df,p)	WFT	62	9.05	9.05	−2.12	8.23	4.32	4.32	4.96	4.96	6.64	14
MP3/6−31+G(d)	WFT	62	12.36	12.36	3.65	3.65	5.22	5.22	7.13	7.13	7.09	1.4
MP3/6−31G(2df,p)	WFT	62	10.77	10.77	−0.39	7.57	5.38	5.38	5.54	5.54	7.32	2.8
MP4SDQ/6−31G(d)	WFT	62	11.17	11.17	−1.29	8.21	4.38	**5.06**	6.02	6.45	7.72	**0.9**
MP4DQ/6−31B(d)	WFT	62	12.84	12.84	1.85	**6.18**	5.62	5.62	6.90	6.90	7.89	**0.8**
MP3/6−31G(d)	WFT	62	12.85	12.85	0.51	**7.60**	5.43	5.64	7.34	7.34	8.36	**0.7**
					N^5 Methods							
MRMP2/nom-CPO/MG3S	WFT	19, 72	−1.38	1.88	0.84	0.89	−0.40	1.06	1.28	1.58	0.90	540
B2GP-PLYP/MG3S	DFT	7	0.42	1.37	−1.28	1.28	1.26	1.26	−0.34	0.55	1.12	21
mPW2K-PLYP/MG3S	DFT	32	1.80	1.80	−0.77	1.02	1.79	1.79	0.22	**0.32**	1.23	**21**
B2T-PLYP/MG3S	DFT	32	−0.58	1.27	−1.67	1.67	0.89	0.98	−0.87	1.04	1.24	21
MC3BB	ML	63	1.69	2.31	0.42	**0.60**	1.60	1.60	−0.43	0.63	1.28	**13**
B2K-PLYP/MG3S	DFT	32	2.12	2.12	−0.58	0.87	1.85	1.85	0.52	0.52	1.34	21
MC3MPWB	ML	64	1.78	2.46	0.14	**0.59**	1.71	1.71	−0.53	0.75	1.38	**14**
MCCO-MPWB	ML	64	1.10	1.65	0.98	1.38	1.11	1.27	−1.27	1.27	1.39	26
MC3MPW	ML	63	1.91	**2.49**	0.06	**0.72**	2.19	2.19	−0.46	**0.61**	1.50	**12**
MC3TS	ML	64	2.02	2.31	−0.90	0.90	2.28	2.28	−0.22	**0.52**	1.50	**14**
MCCO-TS	ML	64	1.16	2.10	−1.15	1.45	1.63	1.63	−0.92	0.92	1.53	27
mPW2-PLYP/MG3S	DFT	33	−1.81	1.87	−2.17	2.17	0.49	0.98	−1.75	1.75	1.69	21
MCCO-MPW	ML	64	2.16	2.64	0.28	1.54	1.90	1.90	−0.65	1.09	1.79	24
B2-PLYP/MG3S	DFT	31	−2.29	2.40	−2.52	2.52	0.33	**0.78**	−1.79	1.84	1.88	**21**
MC-CO/3	ML	4	9.44	9.44	−0.11	1.19	4.80	4.80	2.66	2.66	4.52	13
MP2/aug-cc-pVTZ	WFT	73	10.69	10.69	0.34	0.67	4.70	5.53	3.06	3.20	5.02	120
MP2/G3MP2LargeXP	WFT	73	11.18	11.18	0.99	0.99	4.99	5.84	3.94	3.94	5.49	31
MP2(full)/G3LargeXP	WFT	73	11.04	11.04	1.25	1.25	5.07	5.92	3.81	3.81	5.50	56
MP2/MG3	WFT	73	11.38	11.38	0.62	0.93	5.16	6.06	3.96	3.96	5.58	14
MP2/MG3S	WFT	73	10.70	10.70	3.33	3.33	4.44	4.44	3.99	3.99	5.62	14
SAC-MP2/6−31+G(d,2p)	ML	4	11.17	**11.17**	0.52	3.04	5.49	6.25	2.81	2.81	5.82	**1.5**
MP2/6−31+G(d,2p)	WFT	73	12.08	12.08	1.17	**2.46**	5.28	5.66	4.06	4.06	6.07	**1.5**
MP2/cc-pVTZ	WFT	73	11.74	11.74	−2.22	4.83	4.91	5.87	3.51	3.51	6.49	18
SAC-MP2/6−31+G(d,p)	ML	4	11.99	**11.99**	0.65	3.04	6.27	7.09	4.32	4.32	6.61	**1.0**
MP2/6−31++G(d,p)	WFT	73	12.51	12.51	1.36	2.48	5.67	6.32	5.50	5.50	6.70	1.1
MP2/6−31+G(d,p)	WFT	73	12.93	12.93	1.39	**2.48**	5.94	6.40	5.57	5.57	6.85	**1.0**
SCS-MP2/MG3S	ML	27	14.23	14.23	1.46	1.46	6.01	6.47	5.57	5.57	6.93	14
MP2/aug-cc-pV(D+d)Z	WFT	73	12.09	12.09	−2.42	7.64	4.57	6.01	3.76	3.76	7.37	4.3
SCS-MP2/cc-pVTZ	ML	27	14.36	14.36	−1.48	4.68	5.70	6.24	5.06	5.06	7.58	18
MP2/6−31+G(d)	WFT	73	13.34	13.34	1.38	**2.67**	6.01	7.45	6.71	6.71	7.54	**0.6**
MP2(full)/6−31G(2df,p)	WFT	73	11.30	11.30	−2.61	8.68	6.23	7.08	4.82	4.82	7.97	3.6
MP2/6−31B(d)	WFT	73	13.11	**13.11**	−1.04	**5.22**	6.33	7.50	6.22	6.22	**8.01**	**0.4**
MP2/6−31G(2df,p)	WFT	73	11.51	11.51	−2.88	8.60	6.04	6.90	5.06	5.06	8.02	3.0
MP2/6−31G(d)	WFT	73	13.86	13.86	−1.59	8.62	6.19	7.93	6.89	6.89	9.33	0.4
					N^4 Methods							
M08-SO/cc-pVTZ+	DFT	39	−0.42	0.95	0.41	**0.45**	0.14	1.32	−0.82	0.89	**0.90**	**21**

Table 2. Continued

			HATBH6		NSBH6		UABH6		HTBH6		DBH24	
methods	type	theory ref	MSE	MUE	MSE	MUE	MSE	MUE	MSE	MUE	MUE	cost
M06-2X/aug-cc-pVTZ	DFT	38	−0.27	**0.67**	0.54	0.66	0.06	1.10	−0.58	1.30	0.93	**60**
M06-2X/MG3S	DFT	38	−0.06	**0.73**	0.60	0.85	0.36	1.09	−0.50	1.25	**0.98**	**16**
M06-2X/cc-pVTZ+	DFT	38	−0.06	0.77	0.38	0.76	0.18	1.13	−0.50	1.30	0.99	22
M08-SO/MG3SXP	DFT	39	−0.43	1.06	0.41	**0.64**	0.09	1.39	−0.87	1.09	**1.04**	**15**
M06-2X/MG3SXP	DFT	38	−0.02	0.85	0.73	0.99	0.23	1.12	−0.49	1.28	1.06	20
M08-SO/MG3S	DFT	39	−0.53	1.09	0.19	**0.67**	0.23	1.43	−0.86	1.05	**1.06**	**14**
M08-HX/cc-pVTZ+	DFT	39	0.20	1.27	0.69	1.28	0.49	1.29	−0.48	**0.65**	1.12	**21**
M08-HX/MG3SXP	DFT	39	0.12	1.09	0.88	1.43	0.51	1.26	−0.45	0.71	1.12	15
M08-HX/MG3S	DFT	39	0.02	1.18	0.73	1.35	0.72	1.29	−0.50	**0.71**	1.14	**14**
BB1K/MG3S	DFT	34, 74, 75	0.04	1.07	0.96	1.10	0.55	1.56	−0.95	1.06	**1.20**	**11**
M06-2X/MG3	DFT	38	−0.52	0.81	0.57	0.88	0.66	1.93	−0.51	1.27	1.22	18
BMK/MG3S	DFT	76	−0.94	**0.94**	0.62	**0.77**	0.98	2.06	−1.12	1.12	1.22	**13**
MPWB1K//MG3S	DFT	75, 77, 78	−0.05	1.08	0.91	1.01	0.60	1.63	−1.24	1.24	1.24	12
BB1K/cc-pVTZ+	DFT	34, 74, 75	0.10	1.00	1.03	1.35	0.37	1.57	−0.98	1.08	1.25	19
BB1K/MG3SXP	DFT	34, 74, 75	0.06	1.15	1.09	1.23	0.43	1.57	−0.94	**1.04**	1.25	**13**
MPWB1K/cc-pVTZ+	DFT	75, 77, 78	0.03	1.00	0.99	1.18	0.41	1.64	−1.26	1.26	1.27	20
PWB6K/MG3S	DFT	79	0.58	1.33	0.85	0.94	0.85	1.59	−0.91	1.23	1.27	12
MPWB1K/MG3SXP	DFT	75, 77, 78	−0.02	1.16	1.03	1.13	0.47	1.63	−1.17	1.20	1.28	14
PWB6K/cc-pVTZ+	DFT	79	0.65	1.33	0.92	1.10	0.67	1.60	−0.93	1.08	1.28	20
M06-2X/aug-cc-pVDZ	DFT	38	−0.75	1.46	−0.01	1.25	−0.37	1.35	−1.27	1.27	**1.33**	**4.0**
MPWB1K/aug-pc2	DFT	75, 77, 78	−0.29	0.95	1.47	1.51	0.42	1.61	−1.29	1.40	1.37	58
M06-2X/6−31+G(d,p)	DFT	38	−0.86	**1.38**	0.51	1.36	0.44	1.52	−0.83	1.64	**1.48**	**3.0**
MPW1K/MG3S	DFT	14	−0.15	**1.07**	0.81	1.10	0.95	2.42	−1.06	1.34	1.48	**11**
M06-2X/cc-pVDZ+	DFT	38	−0.71	1.90	0.48	1.34	−0.31	1.24	−1.44	1.53	1.50	2.6
MPWB1K/MG3	DFT	75, 77, 78	−0.51	1.26	0.86	0.95	0.92	2.45	−1.26	1.37	1.51	13
MPW1K/MG3SXP	DFT	14	−0.13	1.21	0.93	1.14	0.82	2.46	−0.98	1.29	1.53	11
MPW1K/cc-pVTZ+	DFT	14	−0.06	1.07	0.89	1.42	0.76	2.47	−1.07	1.35	1.58	16
M08-SO/aug-cc-pVDZ	DFT	39	−1.69	1.69	−0.49	0.96	−0.35	1.99	−1.94	1.94	1.64	5.2
BB1K/6−31+G(d, p)	DFT	34, 74, 75	−0.31	1.62	0.81	**1.32**	0.84	2.19	−0.95	1.53	**1.66**	**2.0**
M08-SO/6−31+G(d,p)	DFT	39	−1.37	1.71	−0.01	**0.83**	0.57	2.51	−1.03	1.62	1.67	**2.1**
M08-HX/6−31+G(d,p)	DFT	39	−0.76	1.84	0.60	1.62	0.92	2.21	−0.79	**1.05**	1.68	**2.1**
MPWB1K/6−31+G(d,p)	DFT	75, 77, 78	−0.41	1.69	0.75	1.33	0.88	2.36	−1.25	1.45	1.71	2.0
M08-SO/cc-pVDZ+	DFT	39	−1.64	1.78	−0.03	1.13	−0.32	1.92	−2.11	2.11	1.74	2.2
M05-2X/MG3S	DFT	80	1.36	2.31	−1.05	1.65	1.38	1.76	−0.28	1.29	1.75	14
M05-2X/MG3	DFT	80	0.98	1.93	−1.07	1.67	1.64	2.24	−0.28	1.31	1.79	13
BB1K/cc-pVDZ+	DFT	34, 74, 75	−0.44	2.09	0.71	1.36	0.02	1.73	−2.01	2.01	1.79	23
PWB6K/6−31+G(d,p)	DFT	79	0.19	2.12	0.69	1.38	1.13	2.29	−0.94	1.40	**1.80**	**1.9**
B97-3/MG3S	DFT	81	−2.29	2.50	−0.49	0.98	0.71	1.63	−2.14	2.19	1.82	11
MPWB1K/aug-pc1	DFT	75, 77, 78	−0.63	2.30	0.26	1.37	−0.18	1.82	−2.09	2.09	1.90	4.0
MPW1K/6−31+G(d,p)	DFT	14	−0.50	**1.40**	0.50	**1.56**	1.29	3.21	−0.97	**1.42**	1.90	**1.4**
M05-2X/6−31+G(d,p)	DFT	80	0.72	2.56	−0.90	1.87	1.46	1.90	−0.56	1.49	1.95	2.1
MPW1K/cc-pVDZ+	DFT	14	−0.66	1.62	0.42	1.63	0.50	2.55	−1.96	2.04	**1.96**	**1.4**
BB1K/6−31+B(d,p)	DFT	34, 74, 75	−1.49	3.42	0.03	1.68	1.04	2.22	−1.21	1.21	2.13	2.3
MPWKCIS1K/MG3S	DFT	3, 75, 82	−1.29	1.90	1.38	1.38	0.95	3.35	−1.89	2.01	2.16	13
BHandHLYP/MG3S	DFT	34, 83, 84	1.70	2.87	0.71	1.45	1.02	2.37	0.18	2.09	2.19	10
M08-SO/MIDIY+	DFT	39	−1.57	3.07	−2.94	2.94	1.05	1.43	−1.41	1.41	2.21	1.7
BB1K/MIDIY+	DFT	34, 74, 75	−2.03	2.19	−2.55	2.55	1.69	2.35	−1.80	1.84	2.23	1.7
B1B95/MG3S	DFT	34, 75	−3.81	3.81	−1.23	1.23	−0.55	1.09	−3.06	3.06	2.30	11
M06/MG3S	DFT	38	−3.61	4.05	−1.62	1.65	0.54	1.91	−1.57	1.68	2.32	16
M06-2X/MIDIY+	DFT	38	−2.06	2.67	−2.91	2.91	1.30	1.70	−1.35	2.06	2.34	1.9
MPW1B95/MG3S	DFT	75, 77, 78	−3.73	3.73	−0.67	1.18	−0.44	1.23	−3.30	3.30	2.36	12
M05/MG3S	DFT	80	−3.25	4.79	0.02	0.94	1.00	2.48	−0.68	1.54	2.43	14
BHandHLYP/cc-pVDZ+	DFT	34, 83, 84	1.04	3.62	0.26	**1.82**	0.43	2.44	−0.92	2.09	**2.49**	**1.2**
M06-HF/MG3S	DFT	85	4.33	4.41	−0.89	1.86	1.11	1.80	1.49	2.03	2.53	16
M06-HF/6−31+G(d,p)	DFT	85	3.57	4.79	−0.20	1.54	1.39	1.66	0.90	2.42	2.60	3.0
MPW1K/MIDIY+	DFT	14	−2.32	2.32	−2.68	2.68	2.09	3.58	−1.85	2.03	2.65	1.2
M08-SO/MIDIX+	DFT	39	−2.66	3.60	−2.51	2.51	0.75	2.06	−2.39	2.48	2.66	1.6
BB1K/MIDIX+	DFT	34, 74, 75	−3.01	3.31	−2.30	2.30	1.41	2.20	−2.68	2.93	2.69	1.6
B97-2/MG3S	DFT	86	−3.04	4.16	−1.74	1.74	0.92	1.81	−2.80	3.11	2.71	11
PW6B95/MG3S	DFT	79	−4.28	4.28	−2.19	2.19	−0.54	1.17	−3.38	3.38	2.76	12
M05/6−31+G(d,p)	DFT	80	−3.73	4.95	−0.58	1.00	0.88	3.23	−0.82	1.98	2.79	2.1
M06-2X/MIDIX+	DFT	38	−2.88	3.40	−2.69	2.69	1.06	2.03	−2.21	3.08	2.80	1.9
M06-2X/6−31B(d,p)	DFT	38	−1.16	3.49	−2.11	5.18	0.79	1.26	−1.28	**1.33**	2.81	**1.8**
BHandHLYP/6−31+G(d,p)	DFT	34, 83, 84	1.17	3.46	0.37	**1.74**	1.23	3.20	0.05	2.97	2.84	**1.3**
TPSS25B95/MG3S	DFT	42	−4.39	4.39	−3.55	3.55	−0.47	**0.88**	−2.95	2.95	2.94	**7.8**
MPW1KK/MG3S	DFT	41	4.32	4.32	3.20	3.20	2.12	2.96	1.41	1.41	2.97	10
MPW1K/MIDIX+	DFT	14	−3.22	3.22	−2.40	2.40	1.85	3.15	−2.65	3.14	**2.98**	**1.0**
BB1K/6−31B(d,p)	DFT	34, 74, 75	−0.57	3.68	−1.95	4.97	1.13	2.31	−1.39	**1.44**	3.10	**1.3**
MPWB1K/MG3T	DFT	75, 77, 78	−0.88	1.39	−3.78	7.26	0.83	2.26	−1.56	1.68	3.15	8.8
BHandHLYP/MIDIX+	DFT	34, 83, 84	−1.55	2.52	−2.65	2.65	1.73	3.16	−1.73	4.32	**3.16**	0.9

Table 2. Continued

			HATBH6		NSBH6		UABH6		HTBH6		DBH24	
methods	type	theory ref	MSE	MUE	MSE	MUE	MSE	MUE	MSE	MUE	MUE	cost
BHandHLYP/MIDIY+	DFT	34, 83, 84	−0.54	3.53	−3.00	3.00	2.08	3.56	−0.72	2.61	3.18	1.1
M06-2X/6−31B(d)	DFT	38	−0.75	4.81	−2.21	5.22	1.05	**1.05**	−0.70	1.84	3.23	**1.7**
mPW1PW/MG3S	DFT	36, 78	−5.09	5.09	−2.10	2.10	−0.39	1.93	−3.87	3.87	3.25	11
MPWB1K/6−31B(d,p)	DFT	75, 77, 78	−0.67	3.69	−1.96	5.22	1.19	2.48	−1.69	1.69	3.27	1.3
MPW25B95/MG3S	DFT	42	−5.51	5.51	−2.21	2.21	−0.94	1.17	−4.32	4.32	3.30	12
MPW1K/6−31B(d,p)	DFT	14	−0.75	3.32	−2.08	4.83	1.63	3.63	−1.48	**1.65**	3.36	**1.0**
M05-2X/6−31B(d,p)	DFT	80	0.53	4.91	−3.43	5.47	1.82	1.89	−0.91	**1.36**	3.41	**1.5**
PWB6K/6−31B(d,p)	DFT	79	−0.01	4.36	−1.94	5.32	1.44	2.50	−1.36	1.47	3.41	1.4
B98/MG3S	DFT	87	−4.75	4.75	−3.16	3.16	0.09	1.84	−3.92	3.92	3.42	11
B97−1/MG3S	DFT	86	−4.81	4.81	−3.31	3.31	0.19	1.67	−4.06	4.06	3.46	11
M08-SO/6−31B(d,p)	DFT	39	−1.92	4.36	−2.58	5.48	1.00	2.31	−1.61	1.68	3.46	2.0
M08-SO/6−31B(d)	DFT	39	−1.67	5.33	−2.63	5.47	1.12	1.90	−1.09	1.35	3.51	1.8
M05-2X/MG3T	DFT	80	0.64	1.87	−5.66	8.69	1.54	2.04	−0.46	1.49	3.52	11
PBE1PBE/MG3S	DFT	92, 111	−5.81	5.81	−2.09	2.09	−0.63	1.93	−4.54	4.54	3.59	10
BB1K/6−31B(d)	DFT	34, 74, 75	−0.27	5.23	−2.08	4.97	1.24	1.92	−0.83	2.27	3.60	1.3
mPW1PW/6−31+G(d,p)	DFT	36, 78	−5.56	5.56	−2.27	2.27	−0.17	2.76	−3.86	3.86	3.61	1.4
M08-HX/6−31B(d)	DFT	39	−0.81	5.61	−2.04	5.55	1.46	**1.69**	−1.09	1.69	3.64	**1.4**
MPW1K/6−31B(d)	DFT	14	−0.32	4.56	−2.22	4.83	1.77	3.24	−0.84	**2.07**	**3.67**	**0.8**
M08-HX/6−31G(d,p)	DFT	39	−0.90	1.95	−3.83	9.51	1.01	1.85	−0.99	1.55	3.72	1.6
B3PW91/MG3S	DFT	34−36	−6.19	6.19	−2.60	2.60	−0.79	1.87	−4.34	4.34	3.75	9.1
TPSS20B95/MG3S	DFT	42	−5.80	5.80	−4.49	4.49	−0.86	1.05	−3.67	3.67	3.75	7.8
M06-2X/6−31G(d,p)	DFT	38	−1.12	1.58	−4.10	10.25	0.48	1.23	−1.00	2.06	3.78	1.8
B1LYP/6−31+G(d,p)	DFT	34, 83, 110	−5.64	5.64	−3.14	3.14	−0.78	2.48	−3.71	4.07	3.83	1.4
MPWB1K/6−31G(d,p)	DFT	75, 77, 78	−0.68	**1.98**	−3.74	9.52	0.84	2.12	−1.47	2.18	3.95	**1.3**
PBE1PBE/6−31+G(d,p)	DFT	92, 111	−6.26	6.26	−2.26	2.26	−0.39	2.75	−4.53	4.53	3.95	1.4
BHandH/MG3S	DFT	34, 83, 84	−4.82	5.16	−0.19	1.25	−0.51	3.32	−6.30	6.30	4.01	10
BHandHLYP/6−31B(d,p)	DFT	34, 83, 84	1.03	5.37	−2.08	4.81	1.55	3.75	−0.45	2.21	4.03	0.8
X3LYP/MG3S	DFT	34, 36, 83, 89	−6.72	6.72	−2.96	2.96	−1.20	1.75	−4.83	4.83	4.07	11
MPWB1K/cc-pVDZ	DFT	75, 77, 78	−1.29	3.01	−5.18	9.03	−0.17	**1.48**	−2.76	2.76	4.07	**1.6**
B3PW91/6−31+G(d,p)	DFT	34−36	−6.67	6.67	−2.76	2.76	−0.59	2.69	−4.36	4.36	4.12	1.5
B3LYP/MG3S	DFT	34, 35, 83	−6.74	6.74	−3.55	3.55	−1.21	1.69	−4.65	4.65	4.15	9.4
BHandHLYP/6−31B(d)	DFT	34, 83, 84	1.35	**5.31**	−2.20	4.81	1.66	3.34	0.03	**3.53**	**4.25**	**0.7**
M05-2X/6−31G(d,p)	DFT	80	0.43	2.34	−5.44	11.05	1.52	1.77	−0.70	1.98	4.28	1.5
MPW1K/6−31G(d)	DFT	14	−0.60	**2.04**	−3.65	9.28	1.64	**3.13**	−0.59	2.76	4.30	**0.8**
τ-HCTHh/MG3S	DFT	86, 90	−6.24	6.24	−4.69	4.69	0.05	1.84	−4.78	4.78	4.39	11
B3LYP*/6−31+G(d,p)	DFT	91	−5.88	5.88	−2.55	2.84	1.86	4.87	−3.73	4.11	4.42	1.3
PBE1KCIS/MG3S	DFT	82, 88, 92, 93	−7.57	7.57	−2.01	2.01	−0.87	2.80	−5.62	5.62	4.50	12
M06/6−31+G(d,p)	DFT	38	−4.02	4.40	−2.19	2.25	0.50	2.62	−8.51	9.22	4.62	3.0
M05-2X/6−31G(d)	DFT	80	0.62	2.86	−5.36	11.01	1.91	1.91	−0.20	2.75	4.63	1.5
M06/6−31B(d,p)	DFT	38	−4.97	7.10	−5.24	6.77	0.64	2.51	−2.27	2.27	4.66	1.8
B97-3/6−31G(d)	DFT	81	−2.89	4.13	−5.62	10.46	1.22	**1.92**	−2.14	2.19	4.67	**0.9**
M05/6−31B(d,p)	DFT	80	−3.96	8.01	−3.29	5.84	1.09	3.03	−1.26	1.91	4.70	1.5
O3LYP/MG3S	DFT	83, 94, 95	−7.34	7.34	3.31	5.02	−1.29	2.09	−4.37	4.37	4.70	11
B3LYP/6−31+G(d, p)	DFT	34, 35, 83	−7.44	7.44	−3.84	3.84	−1.17	2.59	−4.91	5.12	4.75	1.4
MPW3LYP/MG3S	DFT	77, 78, 83	−7.53	7.53	−4.66	4.66	−1.34	1.80	−5.19	5.19	4.80	11
mPW1PW/6−31B(d,p)	DFT	36, 78	−5.74	6.14	−5.24	6.04	0.11	2.87	−4.32	4.32	4.84	1.0
TPSS1KCIS/MG3S	DFT	64, 82, 96	−7.81	7.81	−5.06	5.06	−1.16	1.59	−4.91	4.91	4.84	13
B3P86/MG3S	DFT	34, 35, 37	−8.13	8.13	−3.28	3.28	−1.34	2.78	−5.95	5.95	5.04	9.1
PBE1PBE/6−31B(d,p)	DFT	92, 111	−6.33	6.59	−5.27	6.17	−0.10	2.73	−4.93	4.93	5.10	1.0
B3P86/6−31+G(d,p)	DFT	34, 35, 37	−8.63	8.63	−3.43	3.43	−1.17	3.58	−5.99	5.99	5.41	1.4
MPW1KCIS/MG3S	DFT	3, 75, 82	−8.81	8.81	−4.54	4.54	−1.24	2.61	−6.28	6.28	5.56	13
B97-2/6−31G(d)	DFT	86	−3.63	5.96	−6.81	11.19	1.39	2.07	−2.32	3.19	5.60	0.9
B3LYP/6−31B(d,p)	DFT	34, 35, 83	−7.52	7.52	−6.96	7.66	−0.97	2.71	−5.33	5.33	5.80	0.9
TPSSh/MG3S	DFT	96	−10.11	10.11	−5.92	5.92	−2.81	2.86	−6.64	6.64	6.38	13
HFLYP/MG3S	DFT	97	11.81	11.81	5.18	5.18	3.64	4.24	5.52	5.52	6.69	9.4
HFLYP/6−31+G(d,p)	DFT	97	11.66	11.66	4.52	4.52	4.11	5.17	5.66	5.67	6.76	1.4
HFTPSS/6−31+G(d,p)	DFT	96	10.34	10.34	6.73	6.73	3.12	6.33	4.40	5.32	7.18	2.0
BB1K/6−31B(d)	DFT	34, 74, 75	−0.27	5.23	−16.92	19.82	1.24	1.92	−0.83	2.27	7.31	1.2
SOS-MP2/MG3S	ML	28, 29	15.35	15.35	1.51	1.51	6.60	6.96	5.89	5.89	7.43	17
MPW1K/3−21G+	DFT	14	−4.57	6.90	−9.15	9.15	5.91	8.50	−3.42	6.11	7.67	0.8
M05-2X/MIDI!	DFT	80	−5.16	5.92	−12.44	18.31	1.40	2.75	−3.36	3.83	7.70	1.2
M06-2X/MIDI!	DFT	38	−6.63	6.82	−11.76	17.91	0.15	2.23	−3.52	4.24	7.80	1.5
BB1K/MIDI!	DFT	34, 74, 75	−6.71	7.21	−11.17	16.86	0.55	2.24	−3.99	5.01	7.83	1.2
BHandHLYP/MIDI!	DFT	34, 83, 84	−5.54	5.54	−10.85	17.01	0.70	**3.29**	−3.23	**5.64**	**7.87**	**0.6**
MPW1K/MIDI!	DFT	14	−6.80	6.99	−11.19	16.41	1.04	**3.25**	−3.84	4.96	7.90	**0.7**
M08-SO/MIDI!	DFT	39	−7.02	7.37	−11.47	18.00	−0.34	2.31	−4.07	4.74	8.11	1.2
SOS-MP2/cc-pVTZ	ML	28, 29	15.67	15.67	−1.11	4.60	6.09	6.43	5.83	5.83	8.13	15
HF/MIDIX+	WFT	98	15.61	15.61	3.03	**3.19**	4.59	5.32	10.54	10.54	**8.66**	**0.2**
HF/MIDI!	WFT	98	11.74	11.74	−2.25	**10.46**	3.53	**4.94**	8.98	**9.65**	**9.20**	**0.1**
HF/MIDIY+	WFT	98	16.78	16.78	2.45	3.26	5.07	5.07	11.87	11.87	9.24	0.3

Table 2. Continued

methods	type	theory ref	HATBH6 MSE	HATBH6 MUE	NSBH6 MSE	NSBH6 MUE	UABH6 MSE	UABH6 MUE	HTBH6 MSE	HTBH6 MUE	DBH24 MUE	cost
HF/6−31+G(d,2p)	WFT	98	18.10	18.10	5.47	5.56	3.83	4.02	12.29	12.29	9.99	1.0
HF/6−31+G(d,p)	WFT	98	18.14	18.14	5.52	5.63	4.10	4.10	12.50	12.50	10.09	0.7
HF/6−31+G(d)	WFT	98	18.01	18.01	5.49	5.60	4.39	4.39	12.47	12.47	10.12	0.3
HF/G4MP2TZ	WFT	98	18.01	18.01	6.65	6.65	3.35	3.53	12.29	12.29	10.12	5.1
HF/G3Large	WFT	98	18.14	18.14	6.31	6.31	3.61	3.68	12.41	12.41	10.14	13
HF/6−31G(d)	WFT	98	17.62	17.62	2.67	6.36	**4.31**	4.31	12.28	12.28	10.14	**0.2**
HF/MG3S	WFT	98	18.29	18.29	6.28	6.28	3.66	3.72	12.43	12.43	10.18	9.2
HF/G3MP2LargeXP	WFT	98	18.20	18.20	6.37	6.37	3.49	3.69	12.45	12.45	10.18	10
HF/G3LargeXP	WFT	98	18.21	18.21	6.40	6.40	3.49	3.69	12.45	12.45	10.19	17
HF/G4MP2QZ	WFT	98	18.07	18.07	6.69	6.69	3.42	3.63	12.46	12.46	10.21	47
HF/G3HFQZ	WFT	98	18.13	18.13	6.59	6.59	3.42	3.63	12.47	12.47	10.21	39
HF/G4HF5Z	WFT	98	18.08	18.08	6.74	6.74	3.41	3.64	12.50	12.50	10.24	350
MPW1K/STO-3G+	DFT	14	−7.80	11.57	1.23	**2.06**	4.05	15.15	−0.377	12.86	10.41	**0.4**
HF/6−31B(d,p)	WFT	98	18.27	18.67	3.81	6.81	4.64	4.64	11.95	11.95	10.51	0.2
HF/6−31B(d)	WFT	98	18.44	18.79	3.59	6.69	4.63	4.63	12.08	12.08	10.55	0.2
MPW1K/3−21G	DFT	14	−5.48	**5.48**	−15.96	23.87	6.16	9.16	−4.52	**7.71**	11.56	**0.5**
HF/STO-3G+	WFT	98	10.62	21.03	8.83	8.83	8.63	14.23	10.51	16.75	15.21	0.09
MPW1K/STO-3G	DFT	14	−6.11	**6.79**	−17.18	37..83	11.09	16.82	−7.11	16.77	19.55	**0.4**
HF/STO-3G	WFT	98	8.14	17.93	7.31	35.94	13.92	16.72	5.90	21.30	22.97	0.08
HF/STO-2G	WFT	98	6.68	15.50	6.96	46.63	14.73	17.61	6.21	19.09	24.71	0.06
					N^3 Methods							
MOHLYP/MG3SXP	DFT	40	−1.40	**2.94**	−0.70	2.92	−0.77	1.94	2.72	4.20	**3.00**	**4.2**
MOHLYP/MG3S	DFT	40	−1.45	**3.02**	−0.80	3.12	−0.64	1.83	2.68	4.21	**3.05**	**4.0**
MOHLYP/cc-pVTZ+	DFT	40	−1.33	**2.78**	−0.91	3.26	−0.92	2.04	2.65	4.18	3.07	**5.1**
MOHLYP/6−31+G(d,p)	DFT	40	−1.88	3.21	−1.34	3.21	−0.59	1.55	2.46	4.48	**3.11**	**1.4**
MOHLYP/cc-pVDZ+	DFT	40	−1.84	**4.10**	−1.16	**3.02**	−1.25	2.45	0.98	**2.99**	**3.14**	**1.3**
MOHLYP/aug-cc-pVTZ	DFT	40	−1.51	**2.65**	−0.02	3.78	−1.05	2.17	2.62	4.12	3.18	**7.6**
MOHLYP/MIDIY+	DFT	40	−4.01	**4.73**	−5.30	5.30	0.15	1.84	1.36	**3.87**	**3.93**	**1.2**
M06-L/aug-cc-pVTZ	DFT	99	−6.11	6.85	−3.18	3.18	0.27	1.57	−4.22	4.22	3.95	13
M06-L/MG3S	DFT	99	−6.08	6.91	−3.35	3.35	0.92	2.58	−2.92	3.05	3.98	5.7
M06-L/cc-pVTZ+	DFT	99	−6.10	6.99	−3.28	3.28	0.32	1.59	−4.27	4.27	4.03	7.5
M06-L/MG3SXP	DFT	99	−5.97	6.90	−3.29	3.29	0.37	1.77	−4.06	4.16	4.03	7.3
MOHLYP/6−31B(d,p)	DFT	40	−1.67	**5.97**	−5.01	5.39	−0.36	**1.17**	2.27	**4.24**	**4.19**	**0.9**
M06-L/6−31+G(d,p)	DFT	99	−6.26	7.19	−4.24	4.24	0.43	2.32	−4.01	4.01	4.44	2.1
VSXC/MG3S	DFT	100	−6.89	6.89	−5.01	5.01	−0.05	1.49	−4.90	4.90	4.57	5.2
HCTH/MG3S	DFT	86	−8.82	8.82	−2.88	**2.88**	−0.66	1.64	−5.17	5.17	4.63	**3.9**
VSXC/6−31+G(d,p)	DFT	100	−7.42	7.42	−4.63	4.63	0.01	2.16	−4.97	4.97	4.79	2.0
M06-L/cc-pVDZ+	DFT	99	−6.44	7.88	−4.41	4.41	−0.18	2.56	−4.89	4.89	4.94	2.4
MOHLYP/MIDIX+	DFT	40	−4.89	5.97	−5.06	5.06	−0.20	3.31	0.62	5.90	5.06	1.0
MOHLYP/6−31B(d)	DFT	40	−1.19	**7.45**	−5.03	5.47	−0.26	**1.49**	3.05	6.05	5.11	**0.8**
OLYP/MG3S	DFT	83, 94	−10.17	10.17	−3.20	3.20	−2.21	2.21	−5.80	5.80	5.34	3.7
M06-L/MIDIY+	DFT	99	−7.15	8.74	−6.74	6.74	1.44	2.83	−4.75	4.75	5.65	2.0
τ-HCTH/MG3S	DFT	90	−9.19	9.19	−6.12	6.12	−0.57	1.99	−6.13	6.13	5.86	5.4
M06-L/MIDIX+	DFT	99	−8.10	9.87	−6.21	6.21	1.26	2.79	−5.14	5.14	6.00	1.8
M06-L/6−31B(d,p)	DFT	99	−7.37	9.13	−7.31	7.78	0.68	2.37	−4.77	4.77	6.01	1.7
M06-L/6−31B(d)	DFT	99	−6.90	10.55	−7.18	7.71	0.76	1.95	−3.83	3.83	6.01	1.5
VSXC/6−31B(d.p)	DFT	100	−7.68	9.75	−7.79	8.30	0.22	2.18	−5.29	5.29	6.38	1.3
M06-L/6−31G(d)	DFT	99	−6.31	8.56	−8.52	12.01	0.71	1.79	−3.13	3.20	6.39	1.6
G96LYP/MG3S	DFT	83, 101	−10.93	10.93	−6.35	6.35	−2.75	2.75	−6.52	6.52	6.64	3.9
TPSSKCIS/MG3S	DFT	82, 96	−11.63	11.63	−7.67	7.67	−2.22	2.22	−7.00	7.00	7.13	5.7
mPWKCIS/MG3S	DFT	75, 82	−11.98	11.98	−6.80	6.80	−2.46	2.46	−7.48	7.48	7.18	6.1
BB95/MG3S	DFT	75	−12.57	12.57	−6.60	6.60	−3.06	3.06	−7.94	7.94	7.54	5.4
mPWPW91/MG3S	DFT	36, 78	−12.71	12.71	−7.42	7.42	−2.59	2.59	−8.39	8.39	7.78	3.8
BLYP/MG3S	DFT	34, 83	−12.37	12.37	−8.74	8.74	−3.06	3.06	−7.75	7.75	7.98	3.7
BLYP/6−31+G(d, p)	DFT	34, 83	−13.24	13.24	−7.64	7.64	−3.18	3.18	−8.18	8.18	8.06	1.3
TPSS/MG3S	DFT	96	−13.03	13.03	−7.53	7.53	−3.62	3.62	−8.22	8.22	8.10	5.5
PBE/MG3S	DFT	88	−13.61	13.61	−7.01	7.01	−2.88	2.88	−9.25	9.25	8.19	3.7
PBEsol/6−31+G(d,p)	DFT	43	−14.25	14.25	−7.06	7.06	−2.81	2.83	−9.41	9.41	8.39	1.4
mPWLYP/MG3S	DFT	78, 83	−13.45	13.45	−8.19	8.19	−3.24	3.24	−8.77	8.77	8.41	3.7
BP86/MG3S	DFT	34, 37	−14.00	14.00	−7.13	7.13	−3.40	3.40	−9.21	9.21	8.43	3.9
BLYP/6−31B(d,p)	DFT	34, 83	−13.26	13.26	−11.31	11.31	−3.08	3.08	−8.49	8.49	9.04	1.0
MOHLYP/MIDI!	DFT	40	−9.26	**9.96**	−16.57	19.50	−1.37	**3.99**	−1.11	6.84	**10.07**	**0.7**
M06-L/MIDI!	DFT	99	−11.24	12.77	−16.57	18.98	0.76	2.86	−6.12	6.12	10.18	1.4
SOGGA/MG3S	DFT	44	−17.46	17.46	−7.14	7.14	−3.93	3.93	−12.96	12.96	10.38	3.7
SOGGA/cc-pVTZ+	DFT	44	−17.34	17.34	−7.09	7.09	−4.13	4.13	−12.96	12.96	10.38	4.7
SOGGA/MG3SXP	DFT	44	−17.50	17.50	−7.03	7.03	−4.07	4.07	−12.95	12.95	10.39	4.1
SOGGA/6−31+G(d,p)	DFT	44	−17.98	17.98	−7.07	7.07	−3.76	3.79	−12.90	12.90	10.44	1.4
PM3	SEMO	102	−12.88	16.51	13.82	**14.56**	6.10	13.94	−3.44	5.64	**12.67**	**5 × 10^{-5}**
AM1	SEMO	103	−8.51	**11.82**	10.43	15.62	13.19	18.90	−0.02	**5.13**	12.87	**5 × 10^{-5}**
SPL/MG3S	DFT	104	−22.41	22.41	−8.44	8.44	−5.07	5.07	−17.67	17.67	13.40	2.5

Table 2. Continued

			HATBH6		NSBH6		UABH6		HTBH6		DBH24	
methods	type	theory ref	MSE	MUE	MSE	MUE	MSE	MUE	MSE	MUE	MUE	cost
SPWL/MG3S	DFT	105	−22.52	22.52	−8.36	8.36	−5.21	5.21	−17.89	17.89	13.49	3.5
PM6	SEMO	106	−21.07	22.38	−0.90	**4.19**	14.10	22.07	−8.03	14.09	15.68	$\mathbf{1 \times 10^{-4}}$
RM1	SEMO	107	−19.47	20.59	0.17	15.41	10.61	19.86	−5.60	7.15	15.75	5×10^{-5}
PDDG/PM3	SEMO	108	−16.32	17.97	15.46	15.46	5.38	**13.57**	−8.91	17.55	16.14	$\mathbf{5 \times 10^{-5}}$
SCC-DFTB[b]	SEMO	109	9.69	**11.54**			1.10	**9.77**	−30.34	30.34	17.22	$\mathbf{4 \times 10^{-4}}$

[a] WFT denotes wave function theory; ML denotes multilevel method; DFT denotes density functional theory; SEMO denotes semiempirical molecular orbital method. [b] For this method, the value for the HAT category includes only the reaction $H + N_2O \rightarrow OH + N_2$ and its reverse.

In CCSD(T) calculations, using the cc-pVTZ+ basis set instead of the cc-pVTZ basis set improves the MUE from 2.26 to 1.00 kcal/mol, but it only increases the cost by 40%. For S_N2 reactions, cc-pVTZ+ has a significantly lower MUE (0.81 kcal/mol) than cc-pVTZ. Although the aug-cc-pVTZ basis set further improves the MUE to 0.69 kcal/mol, the cost of aug-cc-pVTZ is about 7.5 times larger than that of cc-pVTZ for CCSD(T) calculations. In DFT calculations, cc-pVTZ+ is almost as good as the aug-cc-pVTZ basis set. The latter has *s*, *p*, *d*, and *f* diffuse functions for all elements except H and has *s*, *p*, and *d* diffuse functions on H, whereas the only diffuse function in cc-pVTZ+ are diffuse *s* and *p* functions on non-hydrogenic atoms. As compared with the aug-cc-pVTZ and cc-pVTZ basis sets, the basis cc-pVTZ+ has a very good balance between computational cost and accuracy.

In the methods that scale as N^6, BMC-CCSD outperforms all the other methods. It even has almost the same accuracy as the CCSD(T)/aug-cc-pVTZ method, but it is about 280 time more efficient. The MUE is only 23% higher than that of G3SX(MP3), but the computational cost is about 6 times smaller than that of G3SX(MP3). Furthermore, BMC-CCSD scales as N^6, whereas G3SX(MP3) and CCSD(T) scale as N^7. The other variants, BMC-QCISD and BMC-CCSD-C, have similar performance to BMC-CCSD, but BMC-CCSD is the most recommended. All single-level coupled cluster calculations only with single and double excitations (CCSD) have MUEs of 1.94 kcal/mol or higher.

In the methods that scale as N^5, the MUEs for DBH24 have a large gap between 1.9 and 4.5 kcal/mol. The methods with MUEs smaller than 1.9 kcal/mol are doubly hybrid density functionals or MRMP2, while the methods with MUEs larger than 4.5 kcal/mol are MP2 or correlation-energy-scaled MP2 methods. Some of the doubly hybrid density functionals, MC3BB,[63] MC3MPW,[63] MC3MPWB,[64] MC3TS,[64] MCG3-MPW, -MPB, and -TS,[64] and MCCO-MPW, -MPWB and -TS,[64] are sometimes called multicoefficient extrapolated DFT methods. In these models, HF orbitals are used for the occupied and unoccupied orbitals to calculate the second-order Møller−Plesset-type perturbation theory correction, although in unpublished past original studies it was checked that similar results are obtained with Kohn−Sham orbitals. The B2P-LYP, B2GP-PLYP, B2K-PLYP, and mPW2-PLYP density functionals employ the Kohn−Sham occupied and unoccupied orbitals. Our calculations show that spin-component scaled (SCS) MP2 and scaled opposite-spin (SOS) MP2 methods (which scales as N^4) consistently overestimate the barrier heights and degrade the MP2 accuracy for barrier height calculations, which was also pointed out by Jung et al. in a previous paper.[28] Methods that involve scaling all correlation (SAC) with MP2 have better performance than SCS-MP2 even with smaller basis sets. In unpublished work, we tried to reparameterize the scaling coefficients in SCS-MP2 using the DBH24/08 database and found that the accuracy cannot be improved significantly, with errors that are always larger than 5.0 kcal/mol. This study and the large gap in the N^5 methods shown in Table 2 imply that it is difficult to achieve accuracy better than 4.0 kcal/mol for calculating barrier height only by using the correlation energy or scaled correlation energy calculated by single-reference second-order perturbation theory. The accuracy for barrier height calculations can be improved dramatically by mixing density functional correlation energy and MP2 correlation energy.

As listed in bold in Table 2, the most recommended hybrid density functionals for barrier heights are M08-SO, M06-2X, M08-HX, BB1K, BMK, PWB6K, MPW1K, BHandH-LYP, and TPSS25B95. The newly developed M06-2X, M08-HX, and M08-SO density functional have the best performance among the fourth-rung hybrid density functionals (even including fifth-rung doubly hybrid density functionals), and they can achieve accuracy better than 1.2 kcal/mol with a reasonable triple-ζ basis set, e.g., cc-pVTZ+, MG3S, and MG3SXP. The density functionals M06-2X, BB1K, PWB6K, and MPW1K can achieve accuracy better than 2.0 kcal/mol with a double-ζ basis set, 6−31+G(d,p).

The recommended cost-effective basis sets as shown in Table 2 are MIDIX+, 6−31B(d), and MIDI!. The relative costs of these basis sets are below 1.0 when using the BHandHLYP and MPW1K density functionals. Actually, MIDIY+ has better performance than MIDIX+ and has similar or a little bit higher cost than MIDIX+ because MIDY+ has a *p* set of polarization functions on each hydrogen. The basis set 6−31B(d,p) was tested by using a number of density functionals; this basis set has the same size as the Pople's 6−31G(d,p), but it is more diffuse without using diffuse functions. A few density functional calculations, in particular, M06-2X, M05-2X, and MPWB1K, give smaller MUEs with 6−31B(d,p) than 6−31G(d,p) by 0.7−1.0 kcal/mol. Although 6−31B(d,p) rather than 6−31G(d,p) is more diffuse, it still cannot be as accurate as the 6−31+G(d,p) basis set. This shows the importance of diffuse functions to calculate barrier heights with density functional theory, as was already pointed out by Lynch et al.[112] The MG3SXP basis set includes more polarization functions than MG3S, but it dose not improve MG3S systematically for the tested

Table 3. Comparison of Mean Signed Errors (MSEs) and Mean Unsigned Errors (MUEs) (in kcal/mol) Calculated at Different Geometries

	HATBH6		NSBH6		UABH6		HTBH6		DBH24
methods	MSE	MUE	MSE	MUE	MSE	MUE	MSE	MUE	MUE
CCSD/MG3S//QCISD/MG3	5.00	5.00	1.92	1.92	1.72	1.72	2.75	2.75	2.85
CCSD/MG3S	4.70	4.70	1.92	1.92	1.50	1.50	2.58	2.58	2.67
MP2/MG3S//QCISD/MG3	11.59	11.59	0.69	0.86	5.25	6.10	0.14	2.88	5.63
MP2/MG3S	9.87	9.87	0.61	0.79	5.51	5.75	4.40	4.40	5.20
B3LYP/MG3S//QCISD/MG3	−6.74	6.74	−3.55	3.55	−1.21	1.69	−4.65	4.65	4.15
B3LYP/MG3S	−6.16	6.16	−3.64	3.64	−0.83	1.70	−4.34	4.36	3.97
M05-2X/MG3S//QCISD/MG3	1.36	2.31	−1.05	1.65	1.38	1.76	−0.28	1.29	1.75
M05-2X/MG3S	1.59	2.46	−1.02	1.65	1.64	1.99	0.03	1.36	1.87
M06-2X/MG3S//QCISD/MG3	−0.06	0.73	0.60	0.85	0.36	1.09	−0.50	1.25	0.98
M06-2X/MG3S	0.03	0.72	0.58	0.90	0.46	1.07	−0.36	1.19	0.97

density functionals (e.g., M06-2X, M08-HX, M08-SO, and SOGGA) and wave function methods (e.g., CCSD(T) and CCSD).

It is very interesting that MOHLYP and HCTH are the only local density functionals in the bold recommended combinations of local density functional and basis set on the cost-to-performance basis used to make entries bold in Table 2. The MOHLYP density functional was originally designed for inorganometallic and organometallic chemistry. It has MUEs for HAT reactions about 3.0 kcal/mol, while the other local density functionals have MUEs for HAT reactions around 7.0 kcal/mol or above. M06-L which has a better performance over broader test sets has a similar performance to MOHLYP for barrier heights of all types of reactions except HAT reactions.

A word of caution is in order in interpreting the bold entries in Table 2. In presenting these bold entries in Table 2 we considered only barrier heights. Even for thermochemical kinetics one wants a method that accounts for energies of reaction as well as barrier heights, and in other cases one might also want to consider other properties such as ionization potential, dipole moments, or noncovalent interactions in selecting a method for a given application. We know, for example, that MPW1K and MPWB1K are better overall methods than BHandHLYP, and M06-L is a better overall method than MOHLYP. Nevertheless the selection of bold entries in Table 2 emerges from a rigorous impartial screening, and the boldface methods deserve consideration whenever we consider barrier heights.

4.2. Effect of Consistent Geometry Optimization. Table 3 lists mean signed errors and mean unsigned errors for the CCSD, MP2, B3LYP, M05-2X, and M06-2X methods with the MG3S basis set calculated at QCISD/MG3 geometries and at the geometries optimized with the corresponding methods.[19] The deviations between the two sets of MUEs for DBH24/08 are around 0.4 kcal/mol or smaller for all the tested methods. M06-2X/MG3S gives the smallest deviation between the MUEs at QCISD/MG3 geometries and at the consistently optimized geometries; these deviations of MUEs for each type of reactions in the DBH24/08 database are smaller than 0.06 kcal/mol. We conclude that using either QCISD/MG3 geometries or consistently optimized geometries gives similar results for the more accurate methods listed in Table 2.

5. Conclusions

In this paper, we updated our DBH24 database by using W4 and W3.2 data to replace previous W1 values; we call the new database DBH24/08. We assessed 348 model chemistries, each containing of a combination of wave function theory level or density functional approximation with a one-electron basis set. There are too many methods in the table to comment explicitly on all the interesting pairwise comparisons, but a few key issues will be summarized here to conclude the paper. Some conclusions drawn in our previous work[1] are reconfirmed by using this improved database and including more methods. For example, BMC-CCSD is still the best model chemistry whose cost scales as N^6 and its cost is an order of magnitude smaller than the N^7 method with the best cost-adjusted performance, G3SX(MP3), although the mean unsigned error is only marginally higher, namely 0.70 kcal/mol vs 0.57 kcal/mol. Other conclusions are now broader in scope. For example, among the N^5 methods except MRMP2 we now conclude not only that doubly hybrid density functionals and multicoefficient extrapolated density functional methods perform better than MP2 but also that they perform better than any correlation-energy-scaled MP2 method. The most recommended hybrid density functionals, judged entirely on the basis of barrier height calculations, are M08-SO, M06-2X, M08-HX, BB1K, BMK, PWB6K, MPW1K, BHandHLYP, and TPSS25B95. MOHLYP, M06-L, VSXC, and HCTH are found to be the best performing local density functionals for barrier heights. The basis set MG3S and 6−31+G(d,p) are the most recommended triple-ζ and double-ζ basis sets for calculations using density functional theory according performance-for-cost considerations. The basis set cc-pVTZ+ is more efficient than aug-cc-pVTZ with similar accuracy, especially for density functional theory. The basis sets cc-pVDZ+, 6−31+G(d,p), 6−31B(d,p), 6−31B(d), MIDIY+, MIDIX+, and MIDI! are recommended for density functional calculations on large systems for their good balance between accuracy and cost, and the basis sets cc-pVTZ+, MG3S, MG3SXP, and aug-cc-pVDZ are recommended for density functional calculations when larger basis sets are affordable. The best performance of any methods tested is attained by CCSD(T)(full)/aug-cc-pCV(T+d)Z with a mean unsigned error of 0.46 kcal/mol; however, this is several orders of

magnitude more expensive than M08-SO/cc-pVTZ+ with a mean unsigned error of 0.90 kcal/mol.

Acknowledgment. This work was supported by the U.S. Department of Energy, Office of Basic Energy Sciences under Grant No. DE-FG02-86ER13579 and by the Air Force Office of Scientific Research under Grant No. FA9550-08-1-018.

References

(1) Zheng, J.; Zhao, Y.; Truhlar, D. G. *J. Chem. Theory Comput.* **2007**, *3*, 569.

(2) Lynch, B. J.; Truhlar, D. G. *J. Phys. Chem. A* **2003**, *107*, 8996.

(3) Zhao, Y.; Gonzalez-Garcia, N.; Truhlar, D. G. *J. Phys. Chem. A* **2005**, *109*, 2012.

(4) Lynch, B. J.; Truhlar, D. G. *J. Phys. Chem. A* **2003**, *107*, 3898.

(5) Martin, J. M. L.; de Oliveira, G. *J. Chem. Phys.* **1999**, *111*, 1843.

(6) (a) Brown, F. B.; Shavitt, I.; Shepard, R. *Chem. Phys. Lett.* **1984**, *105*, 363. (b) Werner, H.-J. *Adv. Chem. Phys.* **1987**, *69*, 1.

(7) Karton, A.; Tarnopolsky, A.; Jean-François, L.; Schatz, G. C.; Martin, J. M. L. *J. Phys. Chem. A* **2008**, *112*, 12868.

(8) Karton, A.; Rabinovich, E.; Martin, J. M. L.; Ruscic, B. *J. Chem. Phys.* **2006**, *125*, 144108.

(9) Zheng, J.; Gour, J. R.; Lutz, J. J.; Wloch, M.; Piecuch, P.; Truhlar, D. G. *J. Chem. Phys.* **2008**, *128*, 044108.

(10) Peterson, K. A.; Dunning, T. H. *J. Phys. Chem. A* **1997**, *101*, 6280.

(11) Villa, J.; Corchado, J. C.; Gonzalez-Lafont, A.; Lluch, J. M.; Truhlar, D. G. *J. Phys. Chem. A* **1999**, *103*, 5061.

(12) Villa, J.; Gonzalez-Lafont, A.; Lluch, J. M.; Truhlar, D. G. *J. Am. Chem. Soc.* **1998**, *120*, 5559. Brown, F. B.; Truhlar, D. G. *Chem. Phys. Lett.* **1985**, *117*, 307.

(13) Fernandez-Ramos, A.; Ellingson, B. A.; Garrett, B. C.; Truhlar, D. G. Variational Transition State Theory with Multidimensional Tunneling. In *Reviews in Computational Chemistry*; Cundari, T. R., Lipkowitz, K. B., Eds.; Wiley-VCH: Hoboken, NJ, 2007; Vol. 23, pp 125.

(14) Lynch, B. J.; Fast, P. L.; Harris, M.; Truhlar, D. G. *J. Phys. Chem. A* **2000**, *104*, 4811.

(15) Melissas, V. S.; Truhlar, D. G. *J. Chem. Phys.* **1993**, *99*, 3542.

(16) Atkins, R. *J. Phys. Chem. Ref. Data Monograph* **1989**, *1*, 18.

(17) Peng, J.; Hu, X.; Marshall, P. *J. Phys. Chem. A* **1999**, *103*, 5307.

(18) Tratz, C. M.; Fast, P. L.; Truhlar, D. G. *PhysChemComm* **1999**, *2*, 70.

(19) Tishchenko, O.; Zheng, J.; Truhlar, D. G. *J. Chem. Theory Comput.* **2008**, *4*, 1208.

(20) Lynch, B. J.; Zhao, Y.; Truhlar, D. G. *J. Phys. Chem. A* **2005**, *109*, 1643.

(21) Curtiss, L. A.; Raghavachari, K.; Trucks, G. W.; Pople, J. A. *J. Chem. Phys.* **1991**, *94*, 7221.

(22) Curtiss, L. A.; Raghavachari, K.; Redfern, P. C.; Rassolov, V.; Pople, J. A. *J. Chem. Phys.* **1998**, *109*, 7764.

(23) Curtiss, L. A.; Raghavachari, K.; Redfern, P. C.; Pople, J. A. *J. Chem. Phys.* **2000**, *112*, 1125.

(24) Curtiss, L. A.; Redfern, P. C.; Raghavachari, K.; Pople, J. A. *J. Chem. Phys.* **2001**, *114*, 108.

(25) Curtiss, L. A.; Redfern, P. C.; Raghavachari, K. *J. Chem. Phys.* **2007**, *126*, 084108.

(26) Curtiss, L. A.; Redfern, P. C.; Raghavachari, K. *J. Chem. Phys.* **2007**, *127*, 124105.

(27) Grimme, S. *J. Chem. Phys.* **2003**, *118*, 9095. Grimme, S. *J. Comput. Chem.* **2003**, *24*, 1529.

(28) Jung, Y.; Lochan, R. C.; Dutoi, A. D.; Head-Gordon, M. *J. Chem. Phys.* **2004**, *121*, 9793.

(29) Jung, Y.; Head-Gordon, M. *Phys. Chem. Chem. Phys.* **2006**, *8*, 2831.

(30) Meyer, W. *J. Chem. Phys.* **1973**, *58*, 1017.

(31) Grimme, S. *J. Chem. Phys.* **2006**, *124*, 034108.

(32) Tarnopolsky, A.; Karton, A.; Sertchook, R.; Vuzman, D.; Martin, J. M. L. *J. Phys. Chem. A* **2008**, *112*, 3.

(33) Schwabe, T.; Grimme, S. *Phys. Chem. Chem. Phys.* **2006**, *8*, 4398.

(34) Becke, A. D. *Phys. Rev. A* **1988**, *38*, 3098.

(35) Stephens, P. J.; Devlin, F. J.; Chabalowski, C. F.; Frisch, M. J. *J. Phys. Chem.* **1994**, *98*, 11623.

(36) Perdew, J. P. In *Electronic Structure of Solids'91*; Ziesche, P., Eschrig, H., Eds.; Akademie Verlag: Berlin, 1991.

(37) Perdew, J. P. *Phys. Rev. B* **1986**, *33*, 8822.

(38) Zhao, Y.; Truhlar, D. G. *Theor. Chem. Acc.* **2008**, *120*, 215.

(39) Zhao, Y.; Truhlar, D. G. *J. Chem. Theory Comput.* **2008**, *4*, 1849.

(40) Schultz, N. E.; Zhao, Y.; Truhlar, D. G. *J. Phys. Chem. A* **2005**, *109*, 11127.

(41) Thompson, J. D.; Cramer, C. J.; Truhlar, D. G. *Theor. Chem. Acc.* **2005**, *113*, 107.

(42) Quintal, M. M.; Karton, A.; Iron, M. A.; Boese, A. D.; Martin, J. M. L. *J. Phys. Chem. A* **2006**, *110*, 709.

(43) Perdew, J. P.; Ruzsinszky, A.; Csonka, G. I.; Vydrov, O. A.; Scuseria, G. E.; Constantin, L. A.; Zhou, X.; Burke, K. *Phys. Rev. Lett.* **2008**, *100*, 136406.

(44) Zhao, Y.; Truhlar, D. G. *J. Chem. Phys.* **2008**, *128*, 184109.

(45) Binkley, J. S.; Pople, J. A.; Hehre, W. J. *J. Am. Chem. Soc.* **1980**, *102*, 939. Gordon, M. S.; Binkley, J. S.; Pople, J. A.; Pietro, W. J.; Hehre, W. J. *J. Am. Chem. Soc.* **1982**, *104*, 2797.

(46) Papajak, E.; Leverentz, H.; Zheng, J.; Truhlar, D. G. *J. Chem. Theory Comput.*, in press.

(47) Lynch, B. J.; Truhlar, D. G. *Theor. Chem. Acc.* **2004**, *111*, 335.

(48) Hehre, W. J.; Ditchfield, R.; Stewart, R. F.; Pople, J. A. *J. Chem. Phys.* **1970**, *52*, 2769. Hehre, W. J.; Stewart, R. F.; Pople, J. A. *J. Chem. Phys.* **1969**, *51*, 2657.

(49) Clark, T.; Chandrasekhar, J.; Spitznagel, G. W.; Schleyer, P. V. *J. Comput. Chem.* **1983**, *4*, 294.

(50) Dunning, T. H. *J. Chem. Phys.* **1989**, *90*, 1007. Woon, D. E.; Dunning, T. H. *J. Chem. Phys.* **1993**, *98*, 1358.

(51) Dunning, T. H.; Peterson, K. A.; Wilson, A. K. *J. Chem. Phys.* **2001**, *114*, 9244.

(52) Thompson, J. D.; Winget, P.; Truhlar, D. G. *PhysChemComm* **2001**, 6.

(53) Frisch, M. J.; Trucks, G. W.; Schlegel, H. B.; Scuseria, G. E.; Robb, M. A.; Cheeseman, J. R.; Zakrzewski, V. G.; Montgomery, J. A., Jr.; Stratmann, R. E.; Burant, J. C.; Dapprich, S.; Millam, J. M.; Daniels, A. D.; Kudin, K. N.; Strain, M. C.; Farkas, O.; Tomasi, J.; Barone, V.; Cossi, M.; Cammi, R.; Mennucci, B.; Pomelli, C.; Adamo, C.; Clifford, S.; Ochterski, J.; Petersson, G. A.; Ayala, P. Y.; Cui, Q.; Morokuma, K.; Malick, D. K.; Rabuck, A. D.; Raghavachari, K.; Foresman, J. B.; Cioslowski, J.; Ortiz, J. V.; Baboul, A. G.; Stefanov, B. B.; Liu, G.; Liashenko, A.; Piskorz, P.; Komaromi, I.; Gomperts, R.; Martin, R. L.; Fox, D. J.; Keith, T.; Al-Laham, M. A.; Peng, C. Y.; Nanayakkara, A.; Challacombe, M.; Gill, P. M. W.; Johnson, B. G.; Chen, W.; Wong, M. W.; Andres, J. L.; Gonzalez, C.; Head-Gordon, M.; Replogle, E. S.; Pople, J. A. *Gaussian03; Revision E.01 ed.*; Gaussian, Inc.: Pittsburgh, PA, 2003.

(54) Zhao, Y.; Truhlar, D. G. *MN-GFM: Minnesota Gaussian Functional Module; version 4.1 ed.*; University of Minnesota: Minneapolis, 2009.

(55) Raghavachari, K.; Trucks, G. W.; Pople, J. A.; Head-Gordon, M. *Chem. Phys. Lett.* **1989**, *157*, 479.

(56) Werner, H.-J.; Knowles, P. J.; Amos, R. D.; Bernhardsson, A.; Berning, A.; Celani, P.; Cooper, D. L.; Deegan, M. J. O.; Dobbyn, A. J.; Eckert, F.; Hampel, C.; Hetzer, G.; Korona, T.; Lindh, R.; Lloyd, A. W.; McNicholas, S. J.; Manby, F. R.; Meyer, W.; Mura, M. E.; Nicklass, A.; Palmieri, P.; Pitzer, R.; Rauhut, G.; Schtuz, M.; Schumann, U.; Stoll, H.; Stone, A. J.; Tarroni, R.; Thorsteinsson, T. *MOLPRO; 2006.1 ed.*; University of Birmingham: Birmingham, 2006.

(57) Moore, C. E. Atomic Energy Levels;Natl. Bur. Stand. (US) Circ. , 1949.

(58) Martin, J. M. L.; Sundermann, A.; Fast, P. L.; Truhlar, D. G. *J. Chem. Phys.* **2000**, *113*, 1348.

(59) Eichkorn, K.; Treutler, O.; Öhm, H.; Häser, M.; Ahlrichs, R. *Chem. Phys. Lett.* **1995**, *240*, 283. Dunlap, B. I. *J. Mol. Struct. (Theochem)* **2000**, 37.

(60) Raghavachari, K.; Anderson, J. B. *J. Phys. Chem.* **1996**, *100*, 12960.

(61) Curtiss, L. A.; Redfern, P. C.; Raghavachari, K.; Rassolov, V.; Pople, J. A. *J. Chem. Phys.* **1999**, *110*, 4703.

(62) Hehre, W. J.; Radom, L.; Schleyer, P. v. R.; Pople, J. A. *Ab Initio Molecular Orbital Theory*; Wiley: New York, 1986.

(63) Zhao, Y.; Lynch, B. J.; Truhlar, D. G. *J. Phys. Chem. A* **2004**, *108*, 4786.

(64) Zhao, Y.; Lynch, B. J.; Truhlar, D. G. *Phys. Chem. Chem. Phys.* **2005**, *7*, 43.

(65) Piecuch, P.; Wloch, M. *J. Chem. Phys.* **2005**, *123*, 224105. Piecuch, P.; Wloch, M.; Gour, J. R.; Kinal, A. *Chem. Phys. Lett.* **2006**, *418*, 467. Wloch, M.; Lodriguito, M. D.; Piecuch, P.; Gour, J. R. *Mol. Phys.* **2006**, *104*, 2149.

(66) Pople, J. A.; Head-Gordon, M.; Raghavachari, K. *J. Chem. Phys.* **1987**, *87*, 5968.

(67) Montgomery, J. J. A.; Frisch, M. J.; Ochterski, J. W.; Petersson, G. A. *J. Chem. Phys.* **1999**, *110*, 2822.

(68) Montgomery, J. J. A.; Frisch, M. J.; Ochterski, J. W.; Petersson, G. A. *J. Chem. Phys.* **2000**, *112*, 6532.

(69) Ochterski, J. W.; Petersson, G. A.; Montgomery, J. J. A. *J. Chem. Phys.* **1996**, *104*, 2598.

(70) Petersson, G. A.; Tensfeldt, T. G.; Montgomery, J. J. A. *J. Chem. Phys.* **1991**, *94*, 6091.

(71) Purvis III, G. D.; Bartlett, R. J. *J. Chem. Phys.* **1982**, *76*, 1910.

(72) Hirao, K. Quantum Chem. *Int. J.* **1992**, 517. Hirao, K *Chem. Phys. Lett.* **1992**, *196*, 397.

(73) Møller, C.; Plesset, M. S. *Phys. Rev.* **1934**, *46*, 618.

(74) Zhao, Y.; Lynch, B. J.; Truhlar, D. G. *J. Phys. Chem. A* **2004**, *108*, 2715.

(75) Becke, A. D. *J. Chem. Phys.* **1996**, *104*, 1040.

(76) Boese, A. D.; Martin, J. M. L. *J. Chem. Phys.* **2004**, *121*, 3405.

(77) Zhao, Y.; Truhlar, D. G. *J. Phys. Chem. A* **2004**, *108*, 6908.

(78) Adamo, C.; Barone, V. *J. Chem. Phys.* **1998**, *108*, 664.

(79) Zhao, Y.; Truhlar, D. G. *J. Phys. Chem. A* **2005**, *109*, 5656.

(80) Zhao, Y.; Schultz, N. E.; Truhlar, D. G. *J. Chem. Theory Comput.* **2006**, *2*, 364.

(81) Keal, T. W.; Tozer, D. J. *J. Chem. Phys.* **2005**, *123*, 121103.

(82) Krieger, J. B.; Chen, J.; Iafrate, G. J.; Savin, A. *Electron Correlations and Materials Properties*; Gonis, A.; , Kioussis, N., Eds.; Plenum: New York, 1999; p 463. Rey, J.; Savin, A. *Int. J. Quantum Chem.* **1998**, *69*, 581. Toulouse, J.; Savin, A.; Adamo, C. *J. Chem. Phys.* **2002**, *117*, 10465.

(83) Lee, C. T.; Yang, W. T.; Parr, R. G. *Phys. Rev. B* **1988**, *37*, 785.

(84) Becke, A. D. *J. Chem. Phys.* **1993**, *98*, 1372.

(85) Zhao, Y.; Truhlar, D. G. *J. Phys. Chem. A* **2006**, *110*, 13126.

(86) Hamprecht, F. A.; Cohen, A. J.; Tozer, D. J.; Handy, N. C. *J. Chem. Phys.* **1998**, *109*, 6264.

(87) Schmider, H. L.; Becke, A. D. *J. Chem. Phys.* **1998**, *108*, 9624.

(88) Perdew, J. P.; Burke, K.; Ernzerhof, M. *Phys. Rev. Lett.* **1996**, *77*, 3865.

(89) Xu, X.; Goddard, W. A. *Proc. Natl. Acad. Sci. U.S.A.* **2004**, *101*, 2673.

(90) Boese, A. D.; Handy, N. C. *J. Chem. Phys.* **2002**, *116*, 9559.

(91) Reiher, M.; Salomon, O.; Hess, B. A. *Theor. Chem. Acc.* **2001**, *107*, 48.

(92) Adamo, C.; Barone, V. *J. Chem. Phys.* **1999**, *110*, 6158.

(93) Zhao, Y.; Truhlar, D. G. *J. Chem. Theory Comput.* **2005**, *1*, 415.

(94) Handy, N. C.; Cohen, A. J. *Mol. Phys.* **2001**, *99*, 403.

(95) Hoe, W. M.; Cohen, A. J.; Handy, N. C. *Chem. Phys. Lett.* **2001**, *341*, 319.

(96) Staroverov, V. N.; Scuseria, G. E.; Tao, J. M.; Perdew, J. P. *J. Chem. Phys.* **2003**, *119*, 12129. Tao, J. M.; Perdew, J. P.; Staroverov, V. N.; Scuseria, G. E. *Phys. Rev. Lett.* **2003**, *91*, 146401.

(97) Di Valentin, C.; Pacchioni, G.; Bredow, T.; Dominguez-Ariza, D.; Illas, F. *J. Chem. Phys.* **2002**, *117*, 2299.

(98) Roothaan, C. C. J. *Rev. Mod. Phys.* **1951**, *23*, 69.

(99) Zhao, Y.; Truhlar, D. G. *J. Chem. Phys.* **2006**, *125*, 194101.

(100) Van Voorhis, T.; Scuseria, G. E. *J. Chem. Phys.* **1998**, *109*, 400.

(101) Gill, P. M. W. *Mol. Phys.* **1996**, *89*, 433.

(102) Stewart, J. J. P. *J. Comput. Chem.* **1989**, *10*, 209.

(103) Dewar, M. J. S.; Zoebisch, E. G.; Healy, E. F.; Stewart, J. J. P. *J. Am. Chem. Soc.* **1985**, *107*, 3902.

(104) Seidl, M.; Perdew, J. P.; Levy, M. *Phsy. Rev. A* **1999**, *59*, 51.

(105) Perdew, J. P.; Wang, Y. *Phys. Rev. B* **1992**, *45*, 13244.

(106) Stewart, J. J. P. *J. Mol. Model.* **2007**, *13*, 1173.

(107) Rocha, G. B.; Freire, R. O.; Simas, A. M.; Stewart, J. J. P. *J. Comput. Chem.* **2006**, *27*, 1101.

(108) Jorgensen, W. L.; Tubert-Brohman, I.; Guimaraes, C. R. W. *Improved semiempirical MO methods: PDDG/PM3*; Abstracts of Papers of the American Chemical Society, 2004. Repasky, M. P.; Chandrasekhar, J.; Jorgensen, W. L. *J. Comput. Chem.* **2002**, *23*, 1601. Tubert-Brohman, I.; Guimaraes, C. R. W.; Jorgensen, W. L. *J. Chem. Theory Comput.* **2005**, *1*, 817. Tubert-Brohman, I.; Guimaraes, C. R. W.; Repasky, M. P.; Jorgensen, W. L. *J. Comput. Chem.* **2004**, *25*, 138.

(109) Elstner, M.; Porezag, D.; Jungnickel, G.; Elsner, J.; Haugk, M.; Frauenheim, T.; Suhai, S.; Seifert, G. *Phys. Rev. B* **1998**, *58*, 7260.

(110) Adamo, C.; Barone, V. *Chem. Phys. Lett.* **1997**, *274,* 242.

(111) Ernzerhof, M.; Scuseria, G. E. *J. Chem. Phys.* **1999**, *110*, 5029.

(112) Lynch, B. J.; Zhao, Y.; Truhlar, D. G. *J. Phys. Chem. A* **2003**, *107*, 1384.

CT800568M

JCTC Journal of Chemical Theory and Computation

Potential-Driven Adiabatic Connection in Density Functional Theory

Andreas Savin*

Laboratoire de Chimie Théorique, UMR 7616, CNRS and Université Pierre et Marie, Curie—Paris VI, 4, place Jussieu, F-75252 Paris Cedex 5, France

Received December 30, 2008

Abstract: As density functional theory conventionally assumes that the density of a chosen model system (e.g., the Kohn−Sham system) is the same as the exact one, one might expect that approximations to the exact density introduce supplementary errors by falsifying the density. In fact, this is not true: by modeling the exchange-correlation holes for all densities, density functional approximations avoid this problem. The technique used to show it is a potential-driven adiabatic connection which hopefully will also permit constructing new approximations in the spirit of DFT.

Introduction

DFT. In density functional theory (DFT), the Schrödinger equation is solved for model systems where the interaction between particles is fictitious, that is, not the physical, Coulomb one. In the Kohn−Sham model,[1] for example, the interaction is reduced to its simplest form: it is set to zero. The energy of the model is, of course, different from that of the physical system. Insight into the nature of this difference, which is needed for obtaining the energy, can be obtained by considering an "adiabatic connection", a process in which the interaction is progressively modified from that of the model to that of the physical system.[2−5] The evolution between the model and the physical system can be characterized by a parameter, λ, which varies between λ_0, characterizing the model, and λ_1, characterizing the physical system.

In its most widespread formulation, the expression of the correction to the model energy, needed to obtain the exact energy, contains the evolution of the pair density, $P_2(r_1,r_2)$ along the adiabatic connection. Modeling $P_2(r_1,r_2)$ was not only successfully used for constructing many of the density functional approximations (see, e.g., refs 6−12) but is also explicitly used in methods like the random phase approximation (see, e.g., refs 13 and 14). In its most widespread variant, although P_2 is a function of λ, the one-particle density $n(r)$ does not vary along the adiabatic connection.[3,4]

Model Densities May Not Be Exact. With a density functional approximation (DFA), the model does not yield the exact density; in general, $n^{\lambda_0} \neq n^{\lambda_1}$. In the following, a simple example will be given. It can be considered exaggerated, but it has the advantage that accurate numbers are known for it.[15] The system of two noninteracting particles in the potential $-\zeta/r$ will be assumed to be an approximation of the exact Kohn−Sham system which yields the density of the He atom. The choice of $\zeta = 1.344$ yields the exact asymptotic decay of the density of the He atom. This model system thus reproduces exactly only a given property of the physical density, not the physical density itself. One can numerically construct a system in which the interaction between electrons is of the Coulomb type but has the density of this model, $n^{\lambda_0} = 2(\zeta^3/\pi)\exp(-\zeta r)$,[15] and calculate the ground-state energy of the fully interacting system having this density, in the external potential of the He atom. Keeping the density constant produces a very large error in the total energy ($\approx$0.13 hartree). Not surprisingly, the largest error comes from the electrostatic part of the electron−electron interaction, $\approx$0.37 hartree, and the difference in the one-particle part of the energy is on the same order of magnitude, $\approx$0.3 hartree. If one concentrates, however, on the parts which are modeled in DFT, the situation is better: the correlation energy obtained for the physically interacting system with n^{λ_0} is −0.043 hartree, reasonably close to that of the He atom (see, e.g., ref 16), −0.042 hartree. However, the exchange energy differs considerably; it is −0.840 hartree[15] for the system with n^{λ_0}, versus −1.025 for the He atom (see, e.g., ref 16).

* Author e-mail: andreas.savin@lct.jussieu.fr.

10.1021/ct8005776 CCC: $40.75
Published on Web 03/19/2009

This example seems to support the idea that one should take into account the change of the density between the model and the physical system.

Objective. The objective of this paper is to show that, with a slightly modified adiabatic connection, the problem of variable density is in fact avoided by DFAs. The key idea is that one has to take into account that DFAs provide models for all densities. Furthermore, it will be argued that the modified adiabatic connection allows going beyond DFAs in a systematic way. Of course, like in all methods of quantum chemistry, this last step has to be payed with more computational effort.

The Modified Adiabatic Connection

Family of Hamiltonians. Let us consider a family of model Hamiltonians, $\lambda_0 \leq \lambda \leq \lambda_1$:

$$H^\lambda \equiv H(v^\lambda, w^\lambda) = T + V^\lambda + W^\lambda \quad (1)$$

where

$$V^\lambda = \sum_{i=1,N} v^\lambda(r_i) \quad (2)$$

is a local one-particle potential,

$$V_{ne} = \sum_{i=1,N} v_{ne}(r_i) \quad (3)$$

is the physical, local one-particle potential ($v^{\lambda_1} \equiv v_{ne}$), and

$$W^\lambda = \sum_{i<j} w(r_i, r_j) \quad (4)$$

is an operator which describes a fictitious two-particle interaction, which becomes, for $\lambda = \lambda_1$, the physical two-particle interaction

$$V_{ee} = \sum_{i<j} v_{ee}(r_i, r_j) \quad (5)$$

where $v_{ee}(r,r') = 1/|r - r'|$, in hartree atomic units.

In order to compare with DFT, v^λ is further decomposed:

$$v^\lambda(r) = v_{ne}(r) + v_h(r;n, v_{ee} - w^\lambda) + v_{xc}{}^\lambda(r) \quad (6)$$

where

$$v_h(r;n,w) \equiv \int d^3 r' n(r') w(r, r') \quad (7)$$

and $v_{xc}{}^\lambda$ is defined by eq 6. Below, for analyzing approximations, we will proceed in a different way: we will choose some $v_{xc}{}^\lambda(r)$ and use eq 6 to define v^λ; $v_{xc}{}^\lambda$ will be chosen to vanish as $\lambda \to \lambda_1$, to ensure that $v^{\lambda_1} \to v_{ne}$.

Energy Expression. To obtain the total energy, we will write, also in analogy to DFT,

$$E = \langle \Psi^\lambda | T + V_{ne} + W^\lambda | \Psi^\lambda \rangle + U[n^\lambda; v_{ee} - w^\lambda] + E_{xc}[v^\lambda, w^\lambda] \quad (8)$$

where Ψ is an antisymmetric wave function; Ψ^λ will be used as a notation for a minimizing Ψ. Ψ^λ yields the one-particle density $n^\lambda(r)$. Furthermore,

$$U[n;w] \equiv \frac{1}{2} \iint n(r)\, n(r')\, w(r, r') \quad (9)$$

is a Hartree (i.e., electrostatic) term, and E_{xc} is defined by eq 8.

Please notice that the last two terms on the right-hand side of eq 8 vanish when $\lambda = \lambda_1$.

Variation with λ. In order to study the change with respect to λ, after taking the derivative of eq 8 with respect to λ, we get

$$0 = \langle \Psi^\lambda | \partial_\lambda W^\lambda | \Psi^\lambda \rangle - U[n^\lambda; \partial_\lambda w^\lambda] - \int v_{xc}{}^\lambda \partial_\lambda n^\lambda + \partial_\lambda E_{xc}[v^\lambda, w^\lambda] \quad (10)$$

To obtain eq 10, we have used the variational character of Ψ^λ for H^λ,

$$\partial_\lambda \langle \Psi^\lambda | T + V_{ne} + W^\lambda | \Psi^\lambda \rangle = \partial_\lambda \langle \Psi^\lambda | T + V^\lambda + W^\lambda | \Psi^\lambda \rangle + \partial_\lambda \int d^3 r\, (v_{ne} - v^\lambda)\, n^\lambda = \langle \Psi^\lambda | \partial_\lambda V^\lambda + \partial_\lambda W^\lambda | \Psi^\lambda \rangle - \int d^3 r\, n^\lambda\, \partial_\lambda v^\lambda + \int d^3 r\, (v_{ne} - v^\lambda)\, \partial_\lambda n^\lambda = \langle \Psi^\lambda | \partial_\lambda W^\lambda | \Psi^\lambda \rangle + \int d^3 r\, (v_{ne} - v^\lambda)\, \partial_\lambda n^\lambda \quad (11)$$

and

$$\partial_\lambda U[n^\lambda; v_{ee} - w^\lambda] = \int d^3 r\, v_h(r; n^\lambda, v_{ee} - w) \partial_\lambda n^\lambda - \frac{1}{2} \iint d^3 r\, d^3 r'\, n(r)\, n(r')\, \partial_\lambda w^\lambda \quad (12)$$

as well as eq 6.

Integrated Formulas. Equation 10 can be integrated over λ, between λ_0 and λ_1, to yield

$$E_{xc}[v^{\lambda_0}, w^{\lambda_0}] = \int_{\lambda_0}^{\lambda_1} d\lambda (\langle \Psi^\lambda | \partial_\lambda W^\lambda | \Psi^\lambda \rangle - U[n^\lambda; \partial_\lambda w^\lambda] - \int v_{xc}(r; n^\lambda, v_{ee} - v^\lambda)\, \partial_\lambda n^\lambda) \quad (13)$$

One can also use the exchange-correlation part of the pair density produced by Ψ^λ, $P_2(r_1,r_2;\Psi^\lambda)$,

$$P_{xc}(r_1, r_2; \Psi^\lambda) = P_2(r_1, r_1; \Psi^\lambda) - n^\lambda(r_1)\, n^\lambda(r_2) \quad (14)$$

to rewrite eq 13 as

$$E_{xc}[v^{\lambda_0}, w^{\lambda_0}] = \int_{\lambda_0}^{\lambda_1} d\lambda\, \frac{1}{2} \iint d^3 r\, d^3 r'\, P_{xc}(r_1, r_2; \Psi^\lambda)\, \partial_\lambda w^\lambda(r, r') - \int_{\lambda_0}^{\lambda_1} d\lambda \int v_{xc}^\lambda(r)\, \partial_\lambda n^\lambda(r) \quad (15)$$

Hamiltonian-Driven Adiabatic Connections. In the derivation of the formulas above, the adiabatic connection was driven by the change in the Hamiltonian, in particular, by the change of the one- and two-body potential: it was potential-driven. One can also produce model Hamiltonians by changing the kinetic energy operator. For example, one can keep the two-body operator equal to v_{ee} for all λ's (cf., e.g., ref 17). With such a one-body-operator-driven adiabatic connection, one can produce expressions for the correlation

energy which depend on the one-body density matrix along the adiabatic connection, $\gamma(r,r';\Psi^\lambda)$.

This type of adiabatic connection will not be discussed here, as it is only seldom used to produce approximations to the universal correlation energy functional.

Relationship to DFT

Relationship to Exact DFT. The adiabatic connection formula of DFT is well-known.[3] The resulting equation has the same form as eq 15 without the last term on the right-hand side, as n does not vary with λ. One should keep in mind that in DFT E_{xc} is not determined by v^{λ_0} and w^{λ_0}, but by n and w^{λ_0},

$$E_{xc}[n,w^{\lambda_0}] = \int_{\lambda_0}^{\lambda_1} d\lambda \frac{1}{2} \iint d^3r\, d^3r'\, P_{xc}(r,r';\Psi^\lambda)\, \partial_\lambda w^\lambda(r,r') \tag{16}$$

and that v^λ is constructed by using in eq 6:

$$v_{xc}{}^\lambda(r) = \delta E_{xc}[n,w^{\lambda_0}]/\delta n(r) \tag{17}$$

Density Functional Approximations. In practice, DFAs are made to define the model systems: E_{xc} is in general replaced by some approximation, $\tilde{E}_{xc}$:

$$\tilde{E}_{xc}[\tilde{n}^{\lambda_0},\lambda_0] = \int_{\lambda_0}^{\lambda_1} d\lambda \frac{1}{2} \iint d^3r\, d^3r'\, \tilde{P}_{xc}(r,r';\tilde{n}^{\lambda_0}(r))\, \partial_\lambda w^\lambda(r,r') \tag{18}$$

$\tilde{P}_{xc}$ is some model for P_{xc}; in LDA, for example, it is that of the uniform electron gas with density $\tilde{n}^{\lambda_0}(r)$. $\tilde{n}^{\lambda_0}$ is the density obtained from $\tilde{\Psi}^{\lambda_0}$, which in turn depends on w^{λ_0} and v^{λ_0}. For the latter, eq 6 is used, and

$$\tilde{v}_{xc}{}^{\lambda_0}(r;n,w) \equiv \delta \tilde{E}_{xc}[n,\lambda_0]\, \delta n(r) \tag{19}$$

at $n = n^{\lambda_0}$.

Comparing the equation of DFT, eq 16, with that of DFAs, eq 18, one can notice two differences: (i) the latter uses of a model, and (ii) the model uses n^{λ_0} instead of n^λ. The latter point arises because the DFT assumption was made in the derivation, namely, n was assumed not to change with λ. (When a calculation at λ_0 is done, only n^{λ_0} is known, so that the information about $n^{\lambda(>\lambda_0)}$ is missing.)

Derivative of $\tilde{E}_{xc}$ with Respect to λ. Notice that $\tilde{E}_{xc}$ depends on λ implicitly, via the λ dependence of n^λ, and explicitly, for a given λ, as the functional will change for the same density, as the interaction w^λ changes with λ:

$$\partial_\lambda \tilde{E}_{xc}[n^\lambda,\lambda] = \partial_\lambda \tilde{E}_{xc}[n^\lambda,\tilde{\lambda}]|_{\tilde{\lambda}=\lambda} + \partial_\lambda \tilde{E}_{xc}[n,\lambda]|_{n=n^\lambda} \tag{20}$$

The first term on the right-hand side is the derivative of $\tilde{E}_{xc}$ at fixed λ, which by the chain rule is

$$\partial_\lambda \tilde{E}_{xc}[n^\lambda,\tilde{\lambda}]|_{\tilde{\lambda}=\lambda} = \int \tilde{v}_{xc}(r;n^\lambda,w^\lambda)\, \partial_\lambda n^\lambda(r) \tag{21}$$

while the last term on the right-hand side of eq 20, the derivative at fixed n, is, by using eq 18,

$$\partial_\lambda \tilde{E}_{xc}[n,\lambda]|_{n=n^\lambda} = -\frac{1}{2} \iint d^3r\, d^3r' \tilde{P}_{xc}(r,r';n^\lambda(r))\, \partial_\lambda w^\lambda(r,r') \tag{22}$$

Special Choice for $v_{xc}{}^\lambda$. We now go back to the adiabatic connection in which the density is allowed to vary but specify now a potential which, until now, was arbitrary. We choose

$$v_{xc}{}^\lambda(r) = \tilde{v}_{xc}(r;n^\lambda,w^\lambda) \tag{23}$$

By this choice,

$$\begin{aligned} \Psi^\lambda &= \tilde{\Psi}^\lambda \\ n^\lambda &= \tilde{n}^\lambda \end{aligned} \tag{24}$$

Adiabatic Connection for the Special Choice of $v_{xc}{}^\lambda$. We can use eq 23 in eq 15; next, we use eq 21, followed by eq 20, and finally use eq 22:

$$\begin{aligned} E_{xc}[v^{\lambda_0},w^{\lambda_0}] = {} & \int_{\lambda_0}^{\lambda_1} d\lambda \frac{1}{2} \iint d^3r\, d^3r'\, P_{xc}(r_1,r_2;\Psi^\lambda) \times \\ & \partial_\lambda w^\lambda(r,r') - \int_{\lambda_2}^{\lambda_1} d\lambda \int \tilde{v}_{xc}(r;n^\lambda,w^\lambda)\, \partial_\lambda n^\lambda(r) = \\ & \int_{\lambda_0}^{\lambda_1} d\lambda \frac{1}{2} \iint d^3r\, d^3r'\, P_{xc}(r_1,r_2;\Psi^\lambda)\, \partial_\lambda w^\lambda(r,r') - \\ & \int_{\lambda_2}^{\lambda_1} d\lambda (\partial_\lambda \tilde{E}_{xc}[n^\lambda,\tilde{\lambda}]|_{\tilde{\lambda}=\lambda}) = \\ & \int_{\lambda_0}^{\lambda_1} d\lambda \frac{1}{2} \iint d^3r\, d^3r'\, P_{xc}(r_1,r_2;\Psi^\lambda)\, \partial_\lambda w^\lambda(r,r') - \\ & \int_{\lambda_2}^{\lambda_1} d\lambda (\partial_\lambda \tilde{E}_{xc}[n^\lambda,\lambda] - \partial_\lambda \tilde{E}_{xc}[n,\lambda]|_{n=n^\lambda}) = \\ & \int_{\lambda_0}^{\lambda_1} d\lambda \frac{1}{2} \iint d^3r\, d^3r'\, P_{xc}(r_1,r_2;\Psi^\lambda)\, \partial_\lambda w^\lambda(r,r') - \\ & \int_{\lambda_2}^{\lambda_1} d\lambda (\partial_\lambda \tilde{E}_{xc}[n^\lambda,\lambda]) - \\ & \int_{\lambda_2}^{\lambda_1} d\lambda \frac{1}{2} \iint d^3r\, d^3r'\, \tilde{P}_{xc}(r,r';n^\lambda(r))\, \partial_\lambda w^\lambda(r,r') \end{aligned}$$

so that, with $\tilde{E}_{xc}[n^{\lambda_0},\lambda_1] = 0$,

$$\begin{aligned} & E_{xc}[v^{\lambda_0},w^{\lambda_0}] - \tilde{E}_{xc}[n^{\lambda_0},\lambda_0] = \\ & \int_{\lambda_0}^{\lambda_1} d\lambda \frac{1}{2} \iint d^3r\, d^3r' (P_{xc}(r_1,r_2;\Psi^\lambda) - \\ & \tilde{P}_{xc}(r,r';n^\lambda(r)))\, \partial_\lambda w^\lambda(r,r') \end{aligned} \tag{26}$$

Interpretation. Equation 26 shows that the error of the model is due to the difference between $P_{xc}(\Psi^\lambda)$ and the model $\tilde{P}_{xc}(n^\lambda)$. As in DFA, the models are defined to work for all densities (as one does not know beforehand what density is of interest); they also work for n^λ. Thus, from the perspective of eq 26 (and that of the modified adiabatic connection), there is no need for any supplementary correction due to density changes.

Relevance for DFAs. When the ground-state energy is computed, eq 26 tells us that we can comfortably ignore the fact that the density of the model is not the exact one—as long as the DFA is based upon a hole model. Most of the existing approximations used (the local density approximation, LDA; most of the generalized gradient approximations, GGAs; etc.) are based on hole models.

Notice also that in "density functional calculations", sometimes potentials are used which are not derivatives of a functional of the density. They show up, for example, when optimized effective potentials are used, or when making approximations for time-depenent DFT, for example, for

correcting the asymptotic behavior of the approximate Kohn−Sham potential. In such situations, one leaves the standard frame of DFT, but not that of the present approach.

Perspectives

Losses and Gains. A Hamiltonian-driven adiabatic connection is identical to the adiabatic connection in DFT when the density is kept constant. When the density is not kept fixed, it loses the pure beauty of DFT. However, the added flexibility might not only bring theory closer to what is done in practice in DFAs but also might give some hints about how to improve approximations. Finally, many of the successful DFAs were constructed from hole models, and they can continue to be used in the potential-driven adiabatic connection.

Choosing v^λ. Analysis of v^λ was used over the years to understand DFAs, which are normally constructed by using an ansatz of the form

$$\tilde{E}_{xc}[n,\lambda_0] = \int d^3r n(r)\, \partial_\lambda \tilde{\varepsilon}_{xc}{}^\lambda(n(r),|\nabla n(r)|^2,...) \quad (27)$$

Unfortunately, the equality does not suffice to define $\tilde{\varepsilon}_{xc}$: the left-hand side is a number, while $\tilde{\varepsilon}_{xc}$ is a function. (In other words, any function which multiplied with n integrates to zero can be added to $\tilde{\varepsilon}_{xc}$ without changing the value of the integral.) However, in DFT, one can compare safely, for a given system, the accurate $v_{xc}{}^\lambda$, eq 17, with that obtained from approximations. Thus, one can also use the knowledge gained in the past years for constructing accurate $v_{xc}{}^\lambda$'s in DFT and for constructing v^λ for the potential-driven adiabatic connection.

Because of the requirement of using model systems having as the ground-state density the exact one, DFT ensures that the model system is in most cases sufficiently close to the exact one, for example, has the exact electrostatic energy. In practice, however, as the exact density is unknown, DFAs produce only "reasonable" densities. Thus, to have similar performance in the potential-driven adiabatic connection, the v^λ should yield "reasonable" densities, and thus be sufficiently "close" to the v^λ which keeps the density constant. As the terms "reasonable" and "close" are not well-defined, the choice of v^λ is left to further exploration. It is possible to perform calculations in the spirit of DFT without the constraint of using potentials which are derivatives of some density functional. To start the explorations, however, one can imagine using forms of v^λ similar to those existing in DFAs; a few parameters in v^λ could be determined "on the fly", that is, made system-specific, for example, by using perturbation theory, see below.

State Following. In the potential-driven adiabatic connection, the model system does not have to be in its ground state. (Of course, the model for the pair density will have to show some dependence on the state chosen, e.g., by a dependence on the depth of the exchange-correlation hole, cf. refs 18−20.) Because of convenient choices of v^λ, it should not only be possible to follow a given state along the adiabatic connection but also to avoid some of the surprises produced in model systems keeping the ground-state density constant (the change of the nature of the ground state, artificial degeneracies, missing degeneracies, jumps, etc.). As the potential-driven adiabatic connection has more flexibility, size-consistency problems such as those presented in ref 21 might also be avoided.

Perturbation Series for Improving $E_{xc}{}^\lambda$. The idea to use perturbation theory to improve density functionals (see, e.g., ref 22) can also be borrowed for the present context. Considering the system at λ_0, defined by the Hamiltonian H^{λ_0}, one can recover information about the system at H^λ by using perturbation series where the perturbation operator is $H^\lambda - H^{\lambda_0}$. Obtaining the first-order correction to the energy might be not very expensive, as only the wave function (or the reduced density matrices) at λ_0 are needed. The "slope of the correction", being now known, can be used for improving "on the fly" E_{xc}, for example, by readjusting the depth of the exchange-correlation hole.

Such an approach to correct E_{xc} was already used with a different adiabatic connection, where the one-electron part of the Hamiltonian is modified.[17]

By a change of viewpoint, one can see the perturbation series as resulting from taking derivatives with respect to λ. Taking the first derivative with respect to λ in eq 8 is equivalent to considering the first-order perturbation term. Higher derivatives are related to higher orders in perturbation theory. One can consider that, as when deriving eq 10, the total physical energy, E, is independent of λ. This method yields further equations which can be used to constrain E_{xc} using information specific to the system.

The adiabatic connection, eq 13 or eq 15, amounts to replacing the perturbation expansion at one point with first-order perturbation corrections at all points between λ_0 and λ_1. This suggests that one could repeat the calculation at a new λ_0, say λ_0', and use both the information at λ_0 and λ_0' to improve an existing ansatz for an approximation of the exchange-correlation term. This could be useful, for instance, if we either wanted to avoid the effort of higher-order perturbation calculations or we do not trust the perturbation expansion to higher order.

Still another way to exploit the adiabatic connection is to use different potentials and to compute different corrections to it, starting at the same λ_0. Of course, in principle, the physical energy, E, is independent of the path chosen. This constraint may be a path to further improve the approximations for E_{xc}.

Acknowledgment. Stimulating discussions with Paul Ayers (McMaster University, Hamilton, Canada), Paola Gori-Giorgi (CNRS, Paris, France), and Julien Toulouse (Université Pierre et Marie Curie - Paris VI, Paris, France) are gratefully acknowledged. Financial support was granted by the ANR-07-BLAN-0272-03. It is a pleasure to dedicate this paper to John Perdew who with his work, deep understanding, and infinite patience has helped so many of us to enjoy DFT.

References

(1) Kohn, W.; Sham, L. J. *Phys. Rev.* **1965**, *140*, A 1133.

(2) Harris, J.; Jones, R. O. *J. Phys. F: Metal Phys.* **1974**, *4*, 1170.

(3) Langreth, D.; Perdew, J. P. *J. Solid State Commun.* **1975**, *17*, 1425.

(4) Gunnarsson, O.; Lundqvist, B. I. *Phys. Rev.* **1976**, *13*, 4274.

(5) Yang, W. *J. Chem. Phys.* **1998**, *109*, 10107.

(6) Ziegler, T.; Rauk, A.; Baerends, E. J. *Theor. Chim. Acta.* **1977**, *43*, 261.

(7) Becke, A. D. *Int. J. Quantum Chem.* **1983**, *23*, 1915.

(8) Perdew, J. P. *Phys. Rev. Lett.* **1985**, *55*, 1665.

(9) Perdew, J. P.; Chevary, J. A.; Vosko, S. H.; Jackson, K. A.; Pederson, M. R.; Singh, D. J.; Fiolhais, C. *Phys. Rev. B: Condens. Matter Mater. Phys.* **1992**, *46*, 6671.

(10) Ernzerhof, M.; Perdew, J. P. *J. Chem. Phys.* **1998**, *109*, 3313.

(11) Gori-Giorgi, P.; Perdew, J. P. *Phys. Rev. B: Condens. Matter Mater. Phys.* **2002**, *66*, 165118.

(12) Heyd, J.; Scuseria, G. E.; Ernzerhof, M. *J. Chem. Phys.* **2006**, *66*, 165118; erratum, *124*, 219906.

(13) Kohn, W.; Meir, Y.; Makarov, D. E. *Phys. Rev. Lett.* **1998**, *80*, 4153.

(14) Furche, F. *Phys. Rev. B: Condens. Matter Mater. Phys.* **2001**, *64*, 195120.

(15) Colonna, F.; Savin, A. *J. Chem. Phys.* **1999**, *110*, 2828.

(16) Umrigar, C. J.; Gonze, X. *Phys. Rev. A: At., Mol., Opt. Phys.* **1994**, *50*, 3827.

(17) Gutlé, C.; Savin, A. *Phys. Rev. A: At., Mol., Opt. Phys.* **2007**, *75*, 032519.

(18) Becke, A. D.; Savin, A.; Stoll, H. *Theor. Chim. Acta* **1995**, *91*, 147.

(19) Perdew, J. P.; Savin, A.; Burke, K. *Phys. Rev. A: At., Mol., Opt. Phys.* **1995**, *51*, 4531.

(20) Perdew, J. P.; Ernzerhof, M.; Burke, K.; Savin, A. *Int. J. Quantum Chem.* **1997**, *61*, 197.

(21) Savin, A. *Chem. Phys.* **2009**, *356*, 91.

(22) Seidl, M.; Perdew, J. P.; Levy, M. *Phys. Rev. A: At., Mol., Opt. Phys.* **1999**, *59*, 51.

CT8005776

JCTC Journal of Chemical Theory and Computation

Density Functional Partition Theory with Fractional Occupations

Peter Elliott,*,† Morrel H. Cohen,‡ Adam Wasserman,§ and Kieron Burke†,||

Department of Physics and Astronomy, University of California, Irvine, California 92697, Department of Physics and Astronomy, Rutgers University, 136 Frelinghuysen Road, Piscataway, New Jersey 08854, Department of Chemistry, Princeton University, Washington Road, Princeton, New Jersey 08544, Department of Chemistry, Purdue University, West Lafayette, Indiana 47907, and Department of Chemistry, University of California, Irvine, California 92697

Received January 7, 2009

Abstract: Partition theory (PT) is a formally exact methodology for calculating the density of any molecule or solid via separate calculations on individual fragments. Just as Kohn−Sham density functional theory (DFT) introduces noninteracting fermions in an effective potential that is defined to yield the exact density of the interacting problem, in PT a global effective potential is found that ensures that the sum of the fragment densities is that of the full system. By combining the two, density functional partition theory (DFPT) produces a DFT scheme that yields the (in principle) exact molecular density and energy via Kohn−Sham calculations on fragments. We give the full formalism and illustrate DFPT in the general case of noninteger fragment occupations.

1. Introduction

In the world of electronic structure, molecules and solids are typically considered in one of two distinct ways. In the first, the system is treated as a whole, and molecular orbitals (or bloch wave functions for bulk crystals) are calculated. These are solutions of some effective potential theory, such as Kohn−Sham density functional theory[1,2] or Hartree−Fock,[3,4] and often describe the system well near equilibrium geometries. The major difficulty is then finding usefully accurate approximations to the total energy. In the second view, one considers isolated atoms as the starting point, and then relatively weak interactions between such units. This view appears necessary for strongly correlated solids such as NiO, strongly correlated molecules such as Cr_2, or any molecule as its bonds are stretched. In such cases, standard approximations for the single-reference approach usually fail, often quite completely. Thus, in practice, the worlds of weak- and strong-correlation have divided.[5]

In previous work,[6] we showed that the partition theory in ref 7 plays a role analogous to that of the Kohn−Sham (KS) formalism in density functional theory (DFT). In Kohn−Sham theory,[2] a reference system is created which is much easier to solve and in which the interactions between electrons have been turned off. In partition theory,[7,8] the reference system has been constructed from isolated effective fragments (e.g., atoms) between which there are no interactions. In both theories, the total electronic density of the system is used as the connection between the reference and reality; it remains unchanged from one to the other and so uniquely defines the reference. Many other analogies are made within the paper. Suffice it to say that, just as KS DFT is particularly well-suited to weakly correlated systems, partition theory is well suited, though not limited to, weakly interacting fragments. We illustrate our method with an analysis of a system of two electrons moving independently in a simple one-dimensional potential. In ref 6, a model calculation was shown in which only integer particle numbers occurred, as determined by symmetry. Just as in pure partition theory, much more is gained in going from that case[9] to the asymmetric case,[10] leading to fractional occupations. Unlike in ref 6, here, we perform a calculation with

* Corresponding author e-mail: pelliott@uci.edu.
† UC Irvine Physics.
‡ Rutgers University and Princeton University.
§ Purdue University.
|| UC Irvine Chemistry.

10.1021/ct9000119 CCC: $40.75
Published on Web 03/26/2009

noninteger occupations, which is the more general case that will be encountered in molecular calculations.

We start with the relevant background information on DFT, including the KS scheme and how partition theory can be used to break a system into fragments. Following this, we review density functional partition theory (DFPT) before generalizing the analysis of ref 6. Next, we perform a DFPT calculation on a one-dimensional model system of a heteronuclear diatomic molecule, leading to fractionally occupied fragments, before we conclude with a discussion of significance.

2. Background

In this section, we review both Kohn−Sham DFT and partition theory, highlighting the analogies between them.

2.1. Kohn−Sham Density Functional Theory. In the KS[2] approach to DFT, one constructs a set of noninteracting equations:

$$\left[-\frac{1}{2}\nabla^2 + v_s(\mathbf{r})\right]\phi_j(\mathbf{r}) = \varepsilon_j\phi_j(\mathbf{r}) \tag{1}$$

where the orbitals $\phi_j(\mathbf{r})$ are defined to reproduce the exact density, $n(\mathbf{r})$, of the interacting system of interest. The KS potential $v_s(\mathbf{r})$ is unique via the Hohenberg−Kohn theorem.[1] The total energy is then rewritten in terms of the reference system:

$$E[n] = T_S[n] + U[n] + E_{XC}[n] + \int d^3r\, n(\mathbf{r})\, v(\mathbf{r}) \tag{2}$$

where T_S is the KS kinetic energy, U the Hartree energy, E_{XC} the unknown XC energy, and $v(\mathbf{r})$ the one-body external potential. The (in principle exact) total energy can be found by solving eq 1 and inserting the resulting density in the expression above, eq 2. The most important result of ground-state DFT is that the KS potential of eq 1 is given by

$$v_s(\mathbf{r}) = v(\mathbf{r}) + v_H(\mathbf{r}) + v_{XC}(\mathbf{r}) \tag{3}$$

where

$$v_H[n](\mathbf{r}) = \frac{\delta U[n]}{\delta n(\mathbf{r})} = \int d^3r' \frac{n(\mathbf{r}')}{|\mathbf{r} - \mathbf{r}'|} \tag{4}$$

is the Hartree potential and

$$v_{XC}[n](\mathbf{r}) = \frac{\delta E_{XC}[n]}{\delta n(\mathbf{r})} \tag{5}$$

is the XC potential. Thus, if one knows E_{XC} as a density functional, a closed set of self-consistent equations results, which can be solved for any system. With good approximations to $E_{XC}[n]$, this scheme has proven useful in many applications.[11]

2.2. Partition Theory. On the other hand, partition theory[7] provides a method for breaking a system into a sum of fragments. Begin from the one-body potential, $v(\mathbf{r})$, which is typically a sum of contributions, most from individual nuclei, for example,

$$v(\mathbf{r}) = -\sum_\beta \frac{Z_\beta}{|\mathbf{r} - \mathbf{R}_\beta|} \tag{6}$$

where Z_β is the atomic charge of a nucleus at point $\mathbf{R}_\beta$. In partition theory, we group these contributions into N_f fragments of our choosing:

$$v(\mathbf{r}) = \sum_{\alpha=1}^{N_f} v_\alpha(\mathbf{r}) \tag{7}$$

and each $v_\alpha(\mathbf{r})$ is the sum over one or more nuclei. The simplest possible choice is to divide the system into two parts ($N_f = 2$), which we call binary fragmentation. These parts would obviously be the two nuclei in a diatomic molecule but could also be the nuclei of a chemical group extracted from a large molecule, or those of a molecule interacting with a surface. One can imagine many cases for which that could prove useful; two examples can be seen in Figure 1. An alternative choice is atomization, in which every term in eq 6 above is separated, and the number of fragments matches the number of nuclei.

Once the fragments have been picked, the partition problem is to find fragment densities $n_\alpha(\mathbf{r})$ such that they add to the total molecular density:

$$\sum_{\alpha=1}^{N_f} n_\alpha(\mathbf{r}) = n(\mathbf{r}) \tag{8}$$

Within partition theory, this is done by minimizing the total energy of the independent fragments, E_f, with the constraint that the sum of the fragment densities must match the molecular density, that is, eq 8. The total energy of the fragments is

$$E_f = \sum_{\alpha=1}^{N_f} \varepsilon_\alpha \tag{9}$$

where ε_α is the energy of each fragment. Since there is no constraint that a fragment's particle number, N_α, be an integer, the Perdew, Parr, Levy, and Balduz (PPLB) formulation[12,13] is used. Thus

$$\varepsilon_\alpha = (1 - \nu_\alpha)E_\alpha[n_{p_\alpha}] + \nu_\alpha E_\alpha[n_{p_\alpha+1}] \tag{10}$$

where $E_\alpha[n]$ is the energy density functional for each fragment α. The fragment particle number is $N_\alpha = p_\alpha + \nu_\alpha$, p_α and $p_\alpha + 1$ are the lower and upper bordering integers of N_α, and $0 \le \nu_\alpha < 1$. The PPLB scheme is simply that of the fragment in contact with an infinite but distant reservoir.

We note the following:

• If all fragments are separated from each other, these fragment densities become exactly those of the isolated fragments, $n_\alpha^{(0)}(\mathbf{r})$.

• One solves the Hamiltonian for each isolated fragment independently of the other fragments. It is the sum of these fragment energies that is minimized.

• It may appear that finding the minimum requires first solving for the molecular density and, so, is even more work than solving the initial problem. But an exactly analogous statement can be made about KS DFT, whose true value is

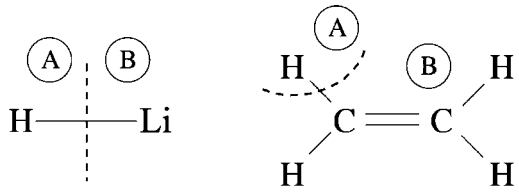

Figure 1. Two examples of binary fragmentation into fragments A and B. The figure on the left shows a lithium hydride molecule at equilibrium bond length, while on the right, an ethene molecule is shown with one substituent cornered off as one of two fragments. Due to the lack of symmetry, in both cases, the fragments will have noninteger occupations at equilibrium bond lengths.

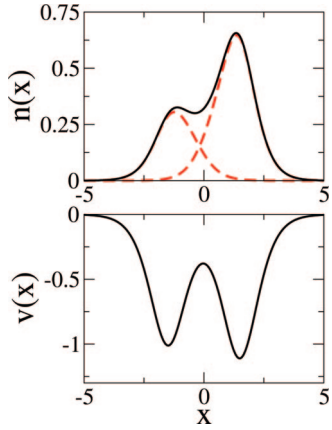

Figure 2. Top panel: The exact density (solid line) for two noninteracting fermions in the potential defined in eq 26 with $R = 3$ and shown below. The two exact partition densities (dashed lines) for this system. Bottom panel: The corresponding molecular potential (solid line) as defined in eq 26.

only apparent when approximations are made. Below, we show the same thing for partition theory.

The process of finding the minimum produces an extremely useful conceptual tool. Minimizing the Lagrangian:

$$\mathscr{G} = E_f - \mu\left(\sum_{\alpha=1}^{N_f} N_\alpha - N\right) + \int d^3r\, v_p(\mathbf{r})\left(\sum_{\alpha=1}^{N_f} n_\alpha(\mathbf{r}) - n(\mathbf{r})\right) \tag{11}$$

where $N_\alpha = \int d^3r\, n_\alpha(\mathbf{r})$, yields the solution to the partition problem.[7] The Lagrange multiplier μ is identified as the chemical potential of the molecule,[8] while the Lagrange multiplier that constrains the sum of the fragment densities to be the molecular density is a potential, dubbed the partition potential, $v_p(\mathbf{r})$. This is a global property of the molecule, uniquely defined once we have chosen a particular fragmentation. It has the interesting aspect that, when added to any fragment potential, the sum is exactly that potential for which the fragment density is a ground-state density. In the upper panel of Figure 2, the exact total density for a model system is shown. It is the solution for two noninteracting fermions in the potential shown in the lower panel of Figure 2 and is discussed in detail later, in the illustration. Solving the partition problem yields the two fragment densities, which are also shown in the upper panel of Figure 2. It can be seen that adding these two fragment densities will give the

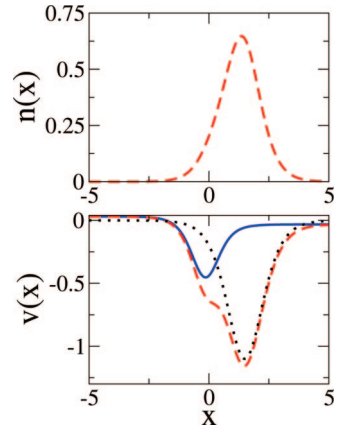

Figure 3. Top panel: The fragment density (dashed line) for the B atom of Figure 1. Bottom panel: The exact partition potential $v_p(x)$ (solid line) for this system, the nuclear potential $v_B(x)$ (dotted line), and the fragment potential $v_B(x) + v_p(x)$ (dashed line). This potential has the fragment density shown in the upper panel as its ground-state density, and the same is true for the A atom.

total density. In the lower panel of Figure 3, we show the exact partition potential for this problem. When added to a fragment potential, it gives an effective potential for each fragment; this is shown as the dashed line in the lower panel of Figure 3. The ground-state density of this effective potential can be seen in the upper panel of Figure 3, it is exactly the same as the fragment density shown in the upper panel of Figure 2.

We emphasize here that, once a choice of fragmentation has been made, the entire procedure is then unambiguously defined and leads to unique densities. The user chooses fragments depending on which aspects they wish to study, usually guided by chemical intuition.

The conceptual structure of partition theory has deep roots, going back to Moffitt's proposed solution of the atoms in molecules (AIM) problem, the ultimate partition into "atoms".[14] Some of the fundamental concepts of partition theory were introduced by Parr et al.[15] in prescient work which reformulated the AIM problem within the framework of DFT. They introduced three central ideas:

1. The electron density of a molecule should be decomposed *exactly* into a sum of contributions from individual atoms.

2. This decomposition should be made unique by minimizing the *promotion energy*, the increase of the sum of the energies (the density functionals) of the individual atoms caused by meeting constraint 1.

3. The electron numbers on the individual atoms need not be integers.

Palke[16] applied these ideas to an analysis of the H_2 molecule. Building upon the Parr et al. work, Guse[17] developed the conceptual structure further, carrying out a Legendre transformation on the sum of the atomic energies before the minimization, thereby introducing a Lagrange parameter without recognizing explicitly that it plays the role of an external potential, which is the same for all of the atoms. Rycklewski and Parr[18] reformulated the theory in terms of wave functions. Ayers and Parr[19] recognized that

the atoms in the molecule were changing in response to an effective external potential in a significant contribution to chemical reactivity theory, but that potential was not identified with Guse's Lagrange multiplier. Perdew et al. (PPLB)[12,13] constructed a rigorous generalization of DFT for noninteger systems, and Parr[20] used its conceptual structure only to give physical meaning to the notion that atoms-in-molecules could have noninteger electron numbers. Thus, several of the essential elements of the conceptual structure of partition theory had been present in the literature for two decades before the current formulation.[7]

3. Density Functional Partition Theory

In this section, we expand upon the methodology developed in ref 6, which allows one to *calculate a molecular density and energy from individual calculations on fragments* via a self-consistent loop. In this sense, it is the analog of the KS method, in which the energy is found from self-consistent calculations on noninteracting electrons. Clearly, such a capability could in general have tremendous significance for many areas of current research, from $O(N)$ scaling to quantum mechanics/molecular mechanics (QM/MM) methods.

To do so, think of the total fragment energy, eq 9, as analogous to the sum of orbital energies in KS theory. Then, define the partition energy as

$$E_p = E - E_f \tag{12}$$

analogous to the Hartree-XC energy in KS theory. If $E_f^0 = \sum_\alpha \varepsilon_\alpha^0$ is the total energy of the isolated fragments, then we can write

$$E_p = E_{dis} + E_{rel} \tag{13}$$

where E_{rel} is the fragment relaxation energy (the promotion energy[15]):

$$E_{rel} = E_f^0 - E_f = \sum_{\alpha=1}^{N_f} \Delta\varepsilon_\alpha = \sum_{\alpha=1}^{N_f} (\varepsilon_\alpha^0 - \varepsilon_\alpha) \tag{14}$$

and $E_{dis} = E - E_f^0$ is the dissociation energy. For any bound molecule, $E_{dis} < 0$. Furthermore, since ε_α^0 is the ground-state energy for the isolated fragment and ε_α is an expectation value of the same Hamiltonian, $\Delta\varepsilon_\alpha \le 0$ always. Thus, $E_p < 0$. Note that these energies are typically much smaller than total electronic energies and vanish as the molecule is stretched.

We can consider the partition energy as a functional, $E_p[\{n_\alpha\}]$, of the fragment densities alone for the given external potential and choice of fragmentation. We now examine the effect of making small variations in one fragment density, $\delta n_\alpha(\mathbf{r})$, to the partition energy. The first term of eq 13 is the ground-state energy of the system relative to that of the isolated parts, so variations in the density are zero because we are at its minimum. For E_{rel}, the second term, only the αth fragment energy changes. Since the fragment density minimizes the αth fragment in the presence of $v_p(\mathbf{r})$, then $v_p(\mathbf{r}) = -\delta\varepsilon_\alpha/\delta n_\alpha(\mathbf{r})$, so that

$$v_p(\mathbf{r}) = \frac{\delta E_p[\{n_\alpha\}]}{\delta n_\alpha(\mathbf{r})} \tag{15}$$

that is, given any expression for $E_p[\{n_\alpha\}]$, we can extract the corresponding partition potential, $v_p(\mathbf{r})$, and then calculate new fragment densities, which are then used to generate a new partition potential, and so on. Thus, approximating $E_p[\{n_\alpha\}]$ produces a closed loop, and a direct scheme for doing a DFPT calculation. The steps of a DFPT calculation are as follows:

(1) Guess the fragment densities $\{n_\alpha\}$. A reasonable first guess would be $\{n_\alpha^0(\mathbf{r})\}$, the densities of the isolated fragments. This naturally leads to integer occupations, usually those of the neutral fragements.

(2) Construct the partition potential, $v_p(\mathbf{r})$, using eq 15.

(3) Solve for each $n_\alpha(\mathbf{r})$ in its respective fragment potential $v_\alpha(\mathbf{r}) + v_p(\mathbf{r})$, retaining the values of the fragment occupations, $\{N_\alpha\}$.

(4) Cycle steps 2 and 3 until self-consistency, and evaluate E_f.

(5) Repeat with small changes of the occupation numbers, and continue to find the lowest value of E_f.

(6) Along with the fragment densities, this yields the total molecular density and the molecular energy (via $E = E_f + E_p$).

This is the method we have used in our illustration, and it is guaranteed to yield the molecular density and energy, once self-consistent potentials can be found at each value of the occupations. In a larger calculation, it would be optimum to take variations in the fragment occupations also and find both occupations and potentials simultaneously self-consistently.

In principle, any electronic-structure method can be used to calculate the fragments. However, in practice, most of such methods will not provide a way to functionally differentiate the corresponding E_p. Even within KS DFT, one does not usually know the noninteracting kinetic energy, T_S, as a functional of the density. Only with an explicit density functional can the corresponding derivative needed for the partition potential be taken.

To derive the expression for $v_p(\mathbf{r})$ in DFPT, we begin with the universal functional, defined via the Levy constrained search:[21,22]

$$F[n] = \min_{\Psi\to n} \langle\Psi|\hat{T} + \hat{V}_{ee}|\Psi\rangle \tag{16}$$

Then, the ground-state energy of any density is given by

$$E[n] = F[n] + \int d^3r\, n(\mathbf{r})\, v(\mathbf{r}) \tag{17}$$

where $v(\mathbf{r})$ is its corresponding one-body potential. Thus,

$$\varepsilon_\alpha = F[n_\alpha] + V_\alpha[n_\alpha] \tag{18}$$

where, for simplicity, we assume N_α is an integer; otherwise, eq 10 must be used. Thus, E_p is

$$E_p[n] = F[n] - \sum_{\alpha=1}^{N_f} F[n_\alpha] + \sum_{\alpha=1}^{N_f}\sum_{\beta\neq\alpha}^{N_f} \int n_\alpha(\mathbf{r})\, v_\beta(\mathbf{r}) \tag{19}$$

Now

$$\frac{\delta F[n]}{\delta n_\alpha(\mathbf{r})} = \frac{\delta F[n]}{\delta n(\mathbf{r})} = \mu - v(\mathbf{r}) \tag{20}$$

and

$$\frac{\delta F[n_\alpha]}{\delta n_\alpha(\mathbf{r})} = \mu - v_\alpha(\mathbf{r}) - v_p(\mathbf{r}) \tag{21}$$

so we can write the partition potential in terms of functional derivatives of the universal functional:

$$v_p(\mathbf{r}) = \frac{\delta F[n]}{\delta n(\mathbf{r})} - \frac{\delta F[n_\alpha]}{\delta n_\alpha(\mathbf{r})} + \sum_{\beta\neq\alpha}^{N_f} v_\beta(\mathbf{r}) \tag{22}$$

This gives an expression for $v_p(\mathbf{r})$ for each of the N_f fragments. From eqs 17 and 2, the universal functional can be decomposed into $F[n] = T_S[n] + U[n] + E_{XC}[n]$, leading to

$$v_p[\{n_\alpha\}](\mathbf{r}) = \frac{\delta T_s[n]}{\delta n(\mathbf{r})} - \frac{\delta T_s[n_\alpha]}{\delta n_\alpha(\mathbf{r})} + v_{XC}[n](\mathbf{r}) - v_{XC}[n_\alpha](\mathbf{r}) + \sum_{\beta\neq\alpha}^{N_f} (v_\beta(\mathbf{r}) + v_H[n_\beta](\mathbf{r})) \tag{23}$$

for any α and using the fact that the Hartree potential is linear in $n(\mathbf{r})$. Explicit density functional expressions are needed for both $T_S[n]$ and $E_{XC}[n]$. However, since the expression only depends on differences between the functional derivatives of these, some of the error due to approximating these may cancel.

We point out that DFPT is close in spirit (not in execution) to previous work by other authors. Cortona's crystal potential (called embedding potential by later workers)[23,24] is analogous to our $v_p(\mathbf{r})$, but the procedure for finding it is distinct from the variational framework of DFT. And, he does not provide an explicit functional for it. Wesolowski and Warshel[25] gave an explicit form to it and applied it to a two-part system instead of a crystal, with solvation effects specifically in mind. Carter and collaborators[26,27] applied these ideas to adsorbates on and defects in metals, giving a functional form for the embedding potential that is formally equal to ours but has quite a different interpretation. We highlight six key features of DFPT: (1) We can break the system up into an arbitrary number of fragments. (2) We do not suppose that the densities of the parts can be varied independently when their densities are constrained to add to the density of the whole. (3) We obtain the partition potential as a Lagrange multiplier, which allows relaxation of the constraint in a variational procedure that lies outside the pre-established domain of DFT. (4) Our partition potential acts on all parts and is the same for all. (5) We achieve electronegativity equalization through the use of PPLB. (6) We do not fix the density of any part of our system. All fragment densities are self-consistent with respect to one another.

4. Illustration

In ref 6, we illustrated DFPT on a model system of a homonuclear diatomic molecule. We found, as expected, that DFPT gave exactly the right energy and density. While this demonstrated the principle of DFPT, a more powerful example of its usefulness and relevance to real systems is a heteronuclear diatomic molecule. Unlike the symmetric case, the covalently bonded fragments will contain fractional numbers of electrons, necessitating the use of the PPLB formalism.[12] In partition theory, the AB heteronuclear system has been studied[10] for insight into molecular dissociation.

For one- or two-electron systems, the kinetic energy density functional is given exactly by the von Weizsäcker functional:

$$T_W[n] = \frac{1}{8}\int d^3r \frac{|\nabla n(\mathbf{r})|^2}{n(\mathbf{r})} \tag{24}$$

and if we study noninteracting fermions, then $E_p[n]$ as a density functional is known exactly. Taking the functional derivative with respect to a fragment density yields the partition potential, which for a binary fragmentation of a system is

$$v_p(\mathbf{r}) = v_B(\mathbf{r}) + \left(\frac{n'^2(\mathbf{r})}{8n^2(\mathbf{r})} - \frac{n''(\mathbf{r})}{4n(\mathbf{r})}\right) - \left(\frac{n'^2_A(\mathbf{r})}{8n^2_A(\mathbf{r})} - \frac{n''_A(\mathbf{r})}{4n_A(\mathbf{r})}\right) \tag{25}$$

and vice-versa for the A fragment. If we work in one dimension, then the fragments can be solved for easily.

For this example, we use a $1/\cosh^2(x)$ potential for each "nucleus", giving the total potential for a diatomic system with separation R as

$$v(x) = v_A(x) + v_B(x) = -\frac{1}{\cosh^2(x + R/2)} - \frac{1.1}{\cosh^2(x - R/2)} \tag{26}$$

Here, the A fragment plays the role of a Lewis base, while B is a Lewis acid. The small difference in nuclear charges is chosen so as to mimic the effect of screening in an interacting system. The total particle number is two, allowing us to use the von Weizsäcker functional even when fractional charges are present.[28]

The minimization of the Lagrangian, eq 11, in the partition problem is over both the density $n_\alpha(x)$ and the occupation N_α. As described above, we find self-consistent solutions for fixed values of N_α. In Figure 4, we plot the molecular energy found after three iteration cycles for five occupation numbers. We can clearly see that there is a minimum at $N_A = 0.655$, and in fact, it is already extremely close to the exact molecular energy. The convergence for the other occupation numbers is very slow, but the minimum at $N_A = 0.655$ remains even after 10 iteration steps. For practical calculation, the occupancy may be set on the fly, but for the purposes of this demonstration, this procedure is sufficient.

To see how the density converges for each iteration, we will use the final occupation $N_A = 0.655$ from now on. In Figure 5, we show the convergence for one of the two fragment densities for this problem, through several self-consistency cycles. The total potential is the same as that shown in the lower panel of Figure 2, while the two fragment

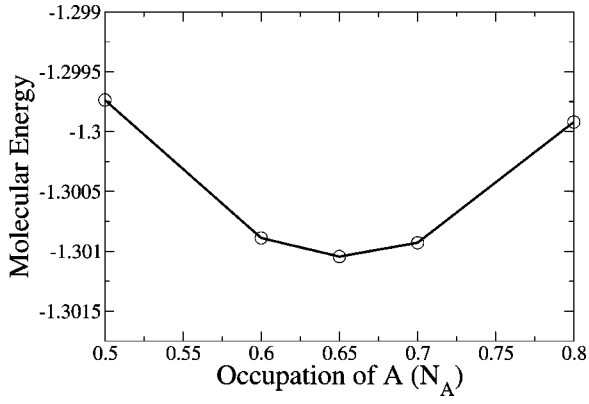

Figure 4. The molecular energy after three iteration cycles as a function of the fractional occupation of the A fragment (N_A) used in each DFPT calculation. The occupation on B is thus $2 - N_A$. The initial fragment densities are the same for each calculation and are simply those of the respective free fragments. The minimum occurs at $N_A = 0.655$, which is then the occupation used in all subsequent calculations.

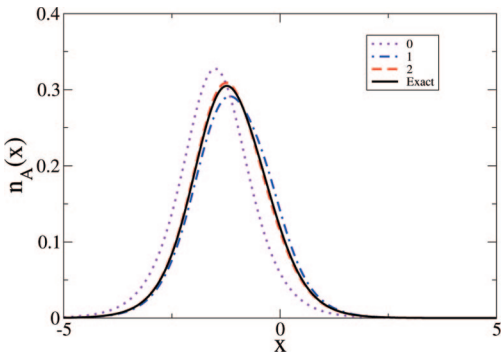

Figure 5. The density for the left (A) fragment as defined by eq 26 with $R = 3$ for the first three self-consistency cycles, labeled 0, 1, and 2, respectively. Also shown is the exact fragment density. Even after just two cycles, the fragment density is almost on top of the exact density, on this scale. For more self-consistency steps, it continues converging toward the exact answer. Calculations were performed using three-site finite difference formulas for derivatives and 2001 grid points with a grid spacing of 0.013 au.

potentials, $v_A(x)$ and $v_B(x)$, are given in eq 26 with $R = 3$. For the initial fragment densities (cycle 0), we use the densities for the two isolated fragments. We then use these to construct a partition potential from eq 25, which is then used to construct effective fragment potentials, $v_\alpha(x) + v_p(x)$. If we then solve for each fragment density in this new potential, we find the cycle 1 density, shown as the dotted−dashed line in Figure 5. It can be seen that the density for this fragment has been shifted toward the other "nucleus", as compared to the isolated case. This is due to the partition potential lowering the fragment potential, v_A, so as to move density into the bonding region, as would be expected.

In Figure 6, the solid line is the total molecular density, found by directly solving for two noninteracting fermions in total potential $v(x)$. It is the same as that shown in Figure 2. In both this case and for the fragments, the density is found by solving the Schrödinger equation numerically on a real-space grid. Derivatives of the density are found using a finite-difference scheme. If we sum the A fragment density shown

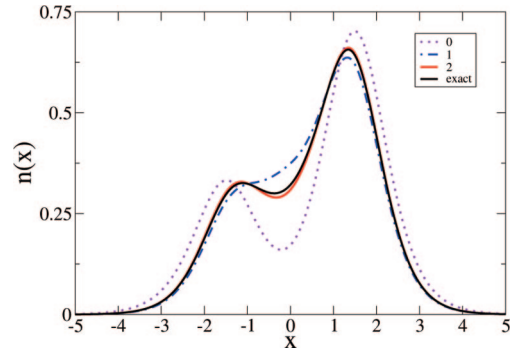

Figure 6. Molecular densities for various cycles 0, 1, and 2 of the self-consistency calculation for this system. Also shown is the exact density for the full system. The density after just two cycles is very close to the exact density, and after three cycles it cannot be distinguished from the exact density on this scale. Convergence continues as more cycles are added, as can seen in Figure 7.

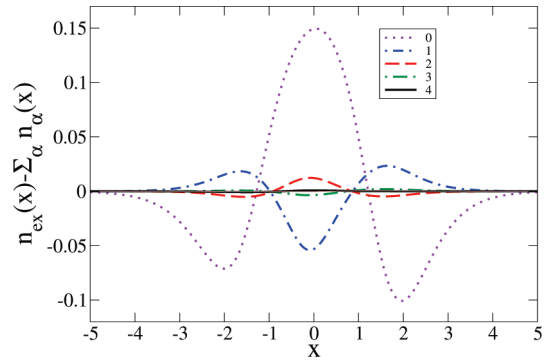

Figure 7. Difference between the exact molecular density, $n_{ex}(x)$, and the sum of the fragment densities for each self-consistency cycle of the DFPT calculation. It is the difference between each of the DFPT densities in Figure 6 and the exact density. After each cycle, this difference decreases, and the convergence to the exact answer is clear.

in Figure 5 with its counterpart on B at each iteration step, we find the corresponding molecular density. These are plotted in Figure 6, and it can be seen that the density at each self-consistency cycle is converging to the exact answer. The convergence toward the exact molecular density can be seen more clearly in Figure 7, where we show the density differences from the overlapped "atomic" densities. We add in the results for more iteration steps, and it is clear that the error decreases with every iteration.

The energy of the molecule may also be calculated using eq 12 for each set of fragment densities. Again, we see the calculation converge to the exact energy of −1.30106. The energy of the initial guess was −1.26067, while after three cycles, it was −1.30104, essentially converged for this level of calculation.

5. Significance

We have demonstrated that, with an explicit expression for the partition energy functional E_p, a self-consistent DFPT calculation can be performed on fragments and that the result converges to the molecular answer. Unlike ref 6, here the fragments have noninteger occupations. The fragments are

solved individually, which, for large interacting systems, would greatly reduce computational cost.

One may wonder, what is the point of our methodology? After all, in order to find the partition potential exactly, we need to know the functional for the entire problem, so we have saved nothing. The point is that one can construct simple approximations to the partition energy as a functional of the fragment densities, which will yield new and different approximations to the many-atom problem. In principle, one can even apply a high-accuracy quantum chemical method to the solution for a fragment and, via an approximate partition functional, embed that solution in the entire molecule (QM/MM). Another useful possibility is to perform, for example, a molecular mechanics simulation and then use overlapped atomic densities in an approximate partition potential to apply to the fragment of interest, where accurate energy differences are needed. Work is ongoing to explore the most useful approximations in different situations.

Acknowledgment. K.B. and P.E. acknowledge support under NSF grant CHE-0809859. This article is dedicated to John Perdew, without whose functionals and exact conditions it would never have been possible.

References

(1) Hohenberg, P.; Kohn, W. *Phys. Rev.* **1964**, *136*, B 864.

(2) Kohn, W.; Sham, L. J. *Phys. Rev.* **1965**, *140*, A 1133.

(3) Hartree, D. R. *Proc. Cambridge Phil. Soc.* **1928**, *24*, 89.

(4) Fock, V. *Z. Phys.* **1930**, *61*, 126.

(5) Fulde, P. *Electron Correlations in Molecules and Solids*; Springer-Verlag: Berlin, 1991; pp 5−454.

(6) Elliott, P.; Burke, K.; Cohen, M. H.; Wasserman, A. Manuscript submitted.

(7) Cohen, M. H.; Wasserman, A. *J. Phys. Chem. A* **2007**, *111*, 2229.

(8) Cohen, M. H.; Wasserman, A. *J. Stat. Phys.* **2006**, *125*, 1125.

(9) Cohen, M. H.; Wasserman, A.; Burke, K. *J. Phys. Chem. A* **2007**, *111*, 12447.

(10) Cohen, M. H.; Wasserman, A.; Car, R.; Burke, K. *J. Phys. Chem. A* **2009**, *113*, 2183.

(11) *A Primer in Density Functional Theory*; Fiolhais, C., Nogueira, F., Marques, M., Eds.; Springer-Verlag: New York, 2003; pp 1−256.

(12) Perdew, J. P.; Parr, R. G.; Levy, M.; Balduz, J. L., Jr. *Phys. Rev. Lett.* **1982**, *49*, 1691.

(13) Perdew, J. P. In *Density Functional Methods in Physics*; Dreizler, R. M., da Providencia, J., Eds.; Plenum: New York, 1985; p 265.

(14) Moffitt, W. *Proc. R. Soc. London, Ser. A* **1951**, *210*, 245.

(15) Parr, R. G.; Donnelly, R. A.; Levy, M.; Palke, W. E. *J. Chem. Phys.* **1978**, *68*, 3801.

(16) Palke, W. E. *J. Chem. Phys.* **1980**, *72*, 2511.

(17) Guse, M. P. *J. Chem. Phys.* **1981**, *75*, 828.

(18) Rychlewski, J.; Parr, R. G. *J. Chem. Phys.* **1986**, *84*, 1696.

(19) Ayers, P. W.; Parr, R. G. *J. Am. Chem. Soc.* **2001**, *123*, 2007.

(20) Parr, R. G. *Int. J. Quantum Chem.* **1984**, *26*, 687.

(21) Levy, M. *Proc. Natl. Acad. Sci. U. S. A.* **1979**, *76*, 6062.

(22) Levy, M. *Phys. Rev. A: At., Mol., Opt. Phys.* **1982**, *26*, 1200.

(23) Cortona, P. *Phys. Rev. B: Condens. Matter Mater. Phys.* **1991**, *44*, 8454.

(24) Cortona, P. *Phys. Rev. B: Condens. Matter Mater. Phys.* **1992**, *46*, 2008.

(25) Wesolowski, T. A.; Warshel, A. *J. Phys. Chem. A* **1993**, *97*, 8050.

(26) Govind, N.; Wang, Y. A.; Carter, E. A. *J. Chem. Phys.* **1999**, *110*, 7677.

(27) Huang, P.; Carter, E. A. *J. Chem. Phys.* **2006**, *125*, 084102.

(28) Sagvolden, E.; Perdew, J. P. *Phys. Rev. A: At., Mol., Opt. Phys.* **2008**, *77*, 012517.

CT9000119

JCTC Journal of Chemical Theory and Computation

DFT Calculations on Charge-Transfer States of a Carotenoid-Porphyrin-C_{60} Molecular Triad

Tunna Baruah[†] and Mark R. Pederson*[,‡]

University of Texas at El Paso, El Paso, Texas 79968,

and Naval Research Laboratory, Washington, D.C. 20375

Received January 13, 2009

Abstract: We present a first-principles study on the ground and excited electronic states of a carotenoid-porphyrin-C_{60} molecular triad. In addition, we illustrate a method for using DFT-based wave functions and densities to simulate complicated charge-transfer dynamics. Since fast and efficient calculations of charge-transfer excitations are required to understand these systems, we introduce a simple DFT-based method for calculating total energy differences between ground and excited states. To justify the procedure, we argue that some charge-transfer excitations are asympototically ground-state properties of the separated systems. Further justification is provided from numerical experiments on separated alkali atoms. The donor-chromophore-acceptor system studied here can absorb and store light energy for several hundreds of nanoseconds. Our density-functional calculations show that the triad can possess a dipole moment of 171 D in a charge-separated state. The charge-transfer energy technique is used to obtain the energies of the excited states. The charge separated excited states with a large dipole moment will create large polarization of the solvent. We use a model to estimate the stabilization of the excited-state energies in the presence of polarization. The calculated excited-state energies are further used to calculate the Einstein's A and B coefficients for this molecular system. We use these transition rates in a kinetic Monte-Carlo simulation to examine the electronic excitations and possible charging of the molecule. Our calculations show that the solvent polarization plays a crucial role in reordering the excited-state energies and thereby in the charge-separation process.

Introduction

Solar energy is an abundant source of alternative energy. Nearly 75% of the solar radiation striking the upper atmosphere reaches the surface of the earth. The natural light harvesting systems such as plants or bacteria have evolved in ways that allow for a relatively efficient mechanism for converting and storing solar energy. This is done through a complex network of donor−acceptor systems which funnel the absorbed energy into a reaction center where the charge separation occurs. To replicate such light-harvesting systems, a plethora of donor−acceptor molecular diads and triads have been synthesized and tested for efficient photovoltaic properties. In this paper, we study from first principles one such molecular donor−acceptor triad system containing a carotenoid, a porphyrin, and a C_{60} molecule.

This carotenoid-porphyrin-C_{60} molecular triad (see Figure 1) was first synthesized by Liddell et al.,[1] and many experimental studies have been reported (see refs 2−4 and references therein). In the experiments a pulse laser at 590 nm was used to excite the porphyrin which then leads to a cascade of transitions between the three components. The charge-separated state was found to have a lifetime of hundreds of nanoseconds. This charge-separated state has a large dipole moment of 153 D.[2] The large dipole moment and long lifetime can be exploited to build a molecular solar-cell.

* Corresponding author e-mail: pederson@dave.nrl.navy.mil.
[†] University of Texas at El Paso.
[‡] Naval Research Laboratory.

10.1021/ct900024f CCC: $40.75
Published on Web 03/19/2009

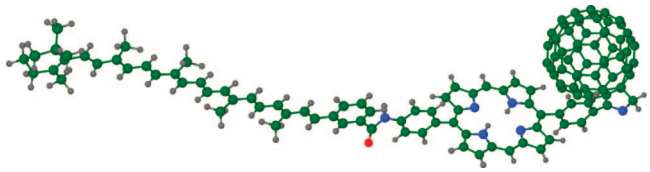

Figure 1. The triad molecule containing a carotenoid-porphyrin-buckyball.

It is known that photoinduced charge transfer (CT) as seen in photosynthesis is a complex nonradiative process where the transfer of energy depends on many different physical characteristics of the system. Developing a first-principles method that is both fast and relatively accurate presents a significant challenge as there are many different effects that must be included. Effects that must be included to get a full quantitative understanding of photoinduced charge transfer include vibrational effects, electronic transitions, energy transport, and polarization effects. In this work we discuss some computatationally efficient density-functional strategies that can be used and refined to allow for some predictive understanding in this area. We combine various methods to obtain a reliable description of the transitions involving absorption of light. Here we present a simple density-functional theory (DFT) based approach for the study of excited charge-separated states, the solvent polarization and stabilization of the charge separated states, and finally any possible radiative transitions. From a combination of density-functional-determined properties a kinetic Monte-Carlo method is used to determine charge-transfer rates. We show that the radiative transitions leading to charge separation are rare events but can be accelerated through a bias caused by an external electric field or due to the presence of counterions. This study is done for radiation density of solar radiation and forms a sequel to our earlier study of the electronic ground-state properties of this molecular triad.[5]

Simple Charge Transfer Systems

One of the goals of this paper is to perform simulations on large molecules for which charge-transfer energies and rates are the relevant figures of merit. It is highly desireable to find fast methods for calculating such excitation energies. Davidson and Nitzsche[6] performed delta-SCF calculations on excited-state within Hartree−Fock early on. They identified at least one case where errors could be made if orthogonality between the ground and excited-state singlets were not maintained. From the standpoint of excited-state calculations within density-functional-based approximations, Perdew and Levy discussed conditions for which extrema of the density-functional energy could be used for excited states in a seminal paper.[7] It is interesting to note that in introducing their ideas they include a quotation from an even earlier piece of literature that is worthwhile reflecting on here: "*One of the most important and controversial questions in density-functional theory concerns the extent to which excited states can be studied by these methods*".[8] While the statement on the controversy is probably as true today as it was in 1984−1985, the need for considering many ways to address this problem is probably more urgent since we are at least a quarter of a century closer to the time when replacements and/or more efficient uses of petroleum resources will be required. The ability to calculate excited states will be key to availing *this generation* of new scientists with tools for computationally improving many technologies that are needed for addressing relatively short-term societal needs. While the scientific debate and iterative improvement of the most ideal way for computing excited states should continue, progress toward deploying a multifaceted array of computational methods for addressing excited states during the next quarter of the century could prove to be truly convenient with respect to more effectively developing technologies that address current issues.

As such we introduce an efficient albeit imperfect means for the calculation of charge-transfer energies in a forthcoming section. The method could be used with almost any type of functional or mean-field quantum-mechanical theory and could be improved upon. For practical reasons it is most attractive to determine the effectiveness of such a method on the standard density-functional methods. In particular we note that we have not relied on either self-interaction corrections[9−11] or exact exchange to stabilize the process. Instead, we include the strong constraint of orthogonalization to the many-electron ground-state reference state. Before discussing this in reference to the light-harvesting triad, we perform some calculations on very simple charge-transfer systems.

Charge Transfer within Ground-State DFT. In this section, we carefully discuss the charge-transfer energy that relates to removal of an electron from one neutral alkali atom and subsequent attachment of this electron to a different albeit identical alkali atom that is at a large distance from the original atom. The purpose of this discussion is to show that this charge-transfer excitation energy depends entirely on ground-state properties of the alkali neutral and charged states. From the arguments presented here we conclude that even within the strictest possible formulation of density-functional theory, the lowest charge-transfer excitation energy in these systems is a ground-state property and is rigorously amenable to calculation within the strictest possible density-functional framework.

We start by considering the case of an isolated alkali atom with either a net positive or net negative charge. These systems are spin unpolarized, and therefore their ground-state energies and densities are rigorously attainable within the original and strictest version of density-functional theory. If we now turn on a static electric or magnetic field, the energy of the charged alkali atom changes due to two effects. To first order, there is direct interaction between the net charge of the alkali atom and the electric field. The system has no net moment so there is not a first-order interaction between a charged alkali and an applied magnetic field. In addition there are small second-order effects related to the field-induced polarization terms. The conclusion of this discussion is that the ground-state energy of a positively (U_I) or negatively (U_A) charged alkali atom is rigorously attainable from density-functional theory. From the definition of ionization energies and electron affinities, the energy of the charged ground states relative to the neutral ground states

Table 1. Calculated Ionization Energies (Ip) and Electron Affinities (A) of Hydrogen-Like Atoms[a]

	affinity		ionization		charge transfer	
atom	DFT	EXP	DFT	EXP	DFT	EXP
H	0.76	0.75	13.6	13.6	12.84	12.85
Li	0.51	0.61	5.59	5.39	5.08	4.78
Na	0.55	0.55	5.36	5.13	4.81	4.58
K	0.51	0.50	4.45	4.34	3.93	3.84
Rb	0.51	0.49	4.22	4.17	3.71	3.62
Cs	0.48	0.47	3.83	3.89	3.35	3.42

[a] Included in the table are results from large-basis sets PBE-GGA calculations and experiment.[18] All energies are in eV.

are given by $U_I = U_o + I$ and $U_A = U_o - A$ with U_o being the energy of the neutral ground state. In many systems (including alkali atoms) I and A are both positive quantities according to the common sign conventions that we also use in this paper.

We now discuss the ground state of the neutral alkali atom. While the practice of using spin-polarized energy functionals is exceedingly well accepted and common in many applications, the original version of density-functional theory was only applicable to nondegenerate ground states. Early arguments to extending density-functional theory to spin-polarized ground states noted that an infinitesimal magnetic field would split the energy of a doublet state yielding a nondegenerate ground state. For the present case of interest (one unpaired electron outside of a closed shell), this simply means that we can in principle calculate the ground-state energy $U_o(B)$ as a function of applied field and extract the ground-state energy at zero field and the spin susceptibility. From this discussion it follows immediately that for two infinitely separated alkali atoms, the charge-transfer energy is a ground-state property given by C = I-A. Further, for two well-separated alkali atoms the charge-transfer energy is given by I-A-1/R with R being the separation between the two atoms. The 1/R stabilization is simply due to the classical coulomb interaction of two charged particles and also immediately falls out by considering the difference of the coulomb energy of two neutral atoms compared to two oppositely charged atoms.

This energy is correct to $O(R^{-4})$ for the case of two alkalis. The lowest correction term arises from the polarization-induced stabilization of each ion that occurs due to the electric field of the other counterion. This energy depends linearly upon the sum of the polarizabilities of the counterions. As in the case of the coulomb interaction, monopole-induced-dipole stabilization as well as other electrostatic interactions between the separated ion are extractable from ground-state density-functional calculations. In Table 1, the charge-transfer energies for pairs of alkali atoms are presented and compared to experiment using the PBE-GGA.[12] As discussed below, the agreement with experiment is good.

Charge-Transfer Energies between Two Well-Separated Alkalis. In Table 1, we present electron affinites calculated within the PBE-GGA for H, Li, Na, K, Rb, and Cs. Very extensive basis sets were used for these calculations. We started with the basis sets developed by Porezag and Pederson[13] for ground-state density-functional calculations. The NRLMOL code was used for the calculations.[14−17] This work optimizes each Gaussian exponent in the problem by variationally minimizing the atomic energy with respect to variation of each nonlinear exponent and the linear expansion coefficients. As discussed in that paper the shortest range Gaussian function must scale as $Z^{10/3}$ to ensure that the energy of the 1s-core electrons are all converged to the same absolute error. Since the anions are expected to be more diffuse than the neutral atoms, we have appended additional long-range single-Gaussian functions to the basis as well and have also used some r^2 gaussians to represent the s-functions. For lithium we have used a total of 11 Gaussian exponents that range between 3200 and 0.005 bohr^{-2}. In addition to 11 s- functions generated from these maximum and minimum values we have also included the r^2 s-type gaussians that fall in the range of 1.28 to 0.02827 bohr^{-2}. For Rb, which has a much larger Z, we have used a total of 23 bare gaussians ranging between 84105050 and 0.005 bohr^{-2}. The basis for the functions contained all 23 of the single Gaussian and also included 17 r^2 functions with decay parameters ranging between 9612 and 0.0211 bohr^{-2}. The p-type orbitals utilized 20 functions ranging between 81517 and 0.005 bohr^{-2}. The 17 d-type functions with the same decay constants as the r^2 s-type functions were used. The calculations in Table 1 are well converged with respect to basis set. Examination of the tables reveals that from calculations on the isolated species, the charge-transfer energies of these systems can be calculated with very high accuracy as compared to experiment.[18]

If one attempts to self-consistently determine the energy of the well separated cation and anion using a standard ground-state density-functional the system quickly finds the real ground state consisting of two neutral atoms. Part of the problem is that the standard DFT iterative method reorders occupation numbers to account for Fermi-level misalignments. This sort of a problem is related but slightly different than the problem that occurs when two well separated systems with different electronegativities are computationally treated as a single system. In such cases, fractional charges are known to occur on the atoms.[19−21]

The misalignment present for the cation−anion pair is in fact physical in this case as it correctly identifies the fact that the electronic configuration of the charge separated state is not the ground state. A computational method that allows for minimization of the functional within the constraint of orthogonality to the ground state does not have this shortcoming. In the forthcoming sections where we wish to apply this procedure to excitations with well-separated but not infinitely separated electron−hole pairs, we introduce a constrained variational method to perform the calculations.

It has long been recognized that the commonly used density-functionals are not self-interaction free.[9−11] As touched upon elsewhere in this paper and a multitude of other papers (see ref 22 and references therein), one of the manifestations of functionals devoid of self-interaction corrections are unbound anions. By unbound, one generally means that the orbital eigenvalue lies above zero. However highly charged anionic systems are experimentally known to exist for long periods of time. At the macroscale, such systems are referred to as capacitors, but nanoscale analogs

such as molecular dianions are known to exist. Compton et al. have provided convincing arguments as to why a dianion can be long-lived even if the dianion is unstable relative to the anion. See refs 23 and 24 and references therein. To the extent that such systems are experimentally known to be unstable the best-possible quantum-mechanical theory, which would be self-interaction free, should provide positive eigenvalues and unbound states. There should be a sensible way of describing such systems within a quantum-mechanical framework. In this regard, the shortcoming of unbound anionic systems within standard DFT functionals is only one example of a larger class of problems, some of which are experimentally observable, that should have a sensible solution. Convergence in such systems, if this word can be used, would most likely be obtained through the use of either implicit or explicit constraints. By implicit constraints we refer to the use of localized basis functions or possibly imposition of a vanishing boundary condition. By explicit constraints we refer to methods that would be similar in scope to those suggested by Watson[25] and Boyer[26] for stabilizing anions and dianions or more recently by Van Voorhis for stabilizing charge-transfer states.[27−29] In each of these cases, a methodology has been developed for including external potentials that force a charge state or charge rearrangement that would be otherwise unstable. The tacit assumption in all of these cases is that the resulting structure is representative of physical systems that could be prepared through the application of external electric fields. Imposition of constraints has proven to be valuable for a variety of practical applications.

A Constrained Excited-State Method

In this section we discuss an attempt for developing a practical means for calculating excited states using the standard approximations to the density-functional theory. Prior to the development of density-functional theory, a transition-state approach due to Slater which used the X_α-method as an approximation to Hartree−Fock was investigated and used with some success for describing localized excitations in atoms and defects. From the standpoint of using density-functional-based approximations, Perdew and Levy discussed conditions for which extrema of the density-functional theory could be used for excited states.[7] Further they review efforts aimed at extending DFT to the lowest-energy state of each symmetry and the efforts due to Theophilou[30] which asserts that the M lowest-energy states are a functional of the average density of these states provided that the M lowest-energy states are constrained to be orthogonal to one another. In regard to such attempts they note that not all excited-state densities are expected to be v-representable.

In the method proposed below, a variational formalism for excited states is developed; however, the variations are performed in a way that do not require v-representable excited-state densities. In developing this method we introduce a constraint of orthogonality between the many-electron Slater determinants that are constructed from the ground- and excited-state of interest. Imposition of such a constraint would appear naturally if one thinks in terms of many-electron wave functions. This constraint leads to a set of single-particle orbitals that do not move in a local Hamiltonian and therefore do not guarantee that the resulting excited-state density is v-representable.

To motivate this method, we assume that a set of orthonormal single-particle orbitals have been determined from a mean-field method such as Hartree−Fock or density-functional theory. Starting with the expression for the total energy and the set of single-particle orbitals that minimize the energy we then wish to build a set of approximate many-electron excited-state Slater determinants that are efficiently optimized from the standpoint of a variational principle. The variational principle that seems most reasonable is to require that the energy of an approximate excited state is minimized relative to all possible variations that maintain orthogonality of the excited state to the ground-state wave function. Once such a set of wave functions are identified, it is possible to imagine using the ground and low-lying excited configurations as a basis for constructing a more exact set of ground- and excited-state orbitals through a configuration-interaction procedure. Further it is assumed that the energies of the resulting set of Slater determinants can be reasonably well approximated from the energy functional that has been used to construct the ground-state energy. In this work, we limit our applications to standard GGA energy functionals. However, the formalism described here can be used within any of the functionals developed by Perdew and collaborators. The computational formalism described here is motivated with the idea that the precise functional that would lead to the best excited states could be developed in concert with the use of this variational procedure. In order to prevent the procedure from leading to a set of orbitals that have collapsed into the ground-state manifold, we introduce the constraint that the many-electron excited-state Slater determinants must be orthogonal to the many-electron ground-state Slater determinant that is composed of the ground-state orbitals. Before continuing we emphasize that if we construct two many-electron Slater determinants (Φ) and (Ψ) from two different sets of orthonormal wave functions ($\phi_1,\phi_2...\phi_N$) and ($\psi_1,\psi_2,...,\psi_N$), the overlap of the two many-electron wave functions ($\Phi|\Psi$) vanishes as long if ($\phi_i|\psi_j$) = 0 for some value of i and all values of j. Alternatively the overlap of the two many-electron wave functions vanishes if ($\psi_i|\phi_j$) = 0 for some value of i and all values of j.

We begin by constructing a single Slater determinant from the single particle self-consistent lowest N Kohn−Sham orbitals ϕ to describe the ground-state wave function as

$$\Psi(\{\vec{R}_n\}) = A(\phi_1\phi_2\cdots\phi_N) \tag{1}$$

where N is the number of particles. Here, "A" represents the antisymmetrizing operator which simply makes an N-electron Slater determinent out of the N single-particle orbitals. The wave functions for single excitations can be constructed from $N - 1$ of the original occupied orbitals ϕ_i (with $i \neq h$) and an unoccupied orbital which we refer to as ϕ_p

$$\Phi = A(\phi_1\phi_2\cdots\phi_{h-1},\phi_p,\phi_{h+1}\cdots\phi_N) \tag{2}$$

where subscripts h and p refer to the hole and particle states. It is important to emphasize the occupied ϕ-orbitals are only

defined up to an arbitrary unitary transformation so the most optimal hole state is only constrained to lie in the space spanned by the occupied Kohn−Sham orbitals. The ground-state density ρ_g is determined by the Kohn−Sham orbitals with occupancy f as $\rho_g = \sum_i^N f_i|\phi_i|^2$. The nonself-consistent density is then given by $\rho_{ex} = \rho_g - \rho_h + \rho_p$ where $\rho_h = |\phi_h|^2$ and $\rho_p = |\phi_p|^2$. The self-consistent ground-state Hamiltonian is

$$H_g = H(\rho_g) \tag{3}$$

Generally, one can approximate the excited-state Hamiltonian in terms of

$$H_{ex} = H(\rho_{ex})$$

However, it is generally not possible to self-consistently determine H_{ex} if one attempts to iterate using standard iterative procedures. Doing so will often lead to the collapse of the second set of orbitals onto the first set. It is clear that such a collapse violates the original orthogonality constraint between the excited-state and ground-state determinants.

To make further progress we first consider a parameter dependent perturbative Hamiltonian of the form

$$\Delta H = \alpha(H_{ex} - H_g) \tag{4}$$

where α is only a tuning parameter. The ϕ_h and ϕ_p are the active orbitals which start out orthogonal to one another and to all the passive ground-state Kohn−Sham orbitals. If we vary the passive excited-state orbitals in the space that is orthogonal to ϕ_h and ϕ_p, we are guaranteed to produce a total energy that is lower than that of the rigid excitation. Further the SD composed of these new passive orbitals and the particle orbital would still be orthogonal to the ground-state SD. To determine the improved excited-state passive orbitals we perturbatively update these orbitals using the following expression

$$\phi_h' = \phi_h + \alpha \sum_{j<N} \frac{\langle \phi_j|\Delta H|\phi_h\rangle|\phi_j\rangle}{\epsilon_j - \epsilon_h} \tag{5}$$

and

$$\phi_k' = \phi_k + \alpha \sum_{j>N} \frac{\langle \phi_j|\Delta H|\phi_k\rangle|\phi_j\rangle}{\epsilon_j - \epsilon_k} k \neq h \tag{6}$$

In the above $h \leq N$ and $k \leq N$. Further, instead of holding the active particle orbital rigid, which would indeed be a somewhat unphysical constraint on the orbitals, it is possible to refine the method further by relaxing the particle orbital in the space of the unoccupied orbitals using exactly the same purturbative approach

$$|\phi_p'\rangle = |\phi_p\rangle + \alpha \sum_{j>N} \frac{\langle \phi_j|H'|\phi_p\rangle}{\epsilon_j - \epsilon_p}|\phi_j\rangle \tag{7}$$

This approach is intuitively more palatable since it is unreasonable to expect the particle orbital to be an eigenfunction of the ground-state Hamiltonian. The resulting set of orbitals depart from orthonormality at second-order. To produce a set of α-dependent orthonormal orbitals we first renormalize the relaxed hole orbital (giving us ϕ_h''). We then Schmidt orthogonalize all passive relaxed orbitals ϕ_k' (k ≠ h) to the relaxed hole−electron ϕ_h''. Finally the passive occupied states and active particle states are orthonormalized using Löwdin's method of symmetric orthonormalization.[31] By following this prescription we are now furnished with a set of α-dependent orthonormal orbitals that can be used to construct an α-dependent Slater determinant that is orthogonal to the ground-state Slater determinant. The excited states can then be expressed as

$$\Phi_{ex} = A(\phi_1''\phi_2''...\phi_{h-1}''\phi_{h+1}''...\phi_N''\phi_p'') \tag{8}$$

The orthogonality between the ground-state Slater determinant and the individual excited-state determinant follows since $\langle \phi_i''|\phi_h''\rangle = 0$ for $i \neq h$. The orthogonality to the ground state is achieved because it is possible to find a unitary transformation (actually there are an infinite number of such unitary transformations) on the original orbital set (ϕ_i) which creates a new set of orthonormal orbitals which span the same space as the Kohn−Sham ground-state orbitals and lead to the same density and energy. These orbitals can be written as $(\psi_1, \psi_2, ..., \psi_{h-1}, \phi_h'', \psi_{h+1}, ..., \psi_N)$ with ϕ_h'' identically equal to the relaxed hole electron.

The density is then calculated from the occupied passive and active orbitals as

$$\rho' = \sum_j |\phi_{j\neq h}''|^2 + |\phi_p''|^2$$

From this density the coulomb energy and exchange correlation energies may be calculated, and the orbitals can also be used to calculate the kinetic energy and the interaction of the density with an external potential. The same procedure is repeated with different values of α. From a set of α and corresponding total energies, the α for lowest energy is determined. The best-excited-state Slater determinant can then be determined by minimizing the energy as a function of α. Once the best α is determined, this provides us with a new way of estimating an excited-state single-electron Hamiltonian H_{ex} which gives a new Δ_H. Given the improved ΔH we can return to eq 4 above and further improve the estimation of the single-particle orbitals. The process can be iterated until self-consistency is established.

In this method the excited-state density is varied by varying the parameter α. In practice, three different α are chosen, and the α_{lowest} is varied using the Newton−Raphson method. The same procedure can again be repeated to refine the α_{lowest} parameter and thereby the energy. This method is inexpensive, since the diagonalization is not required and the α_{lowest} can be extracted relatively inexpensively. The only computationally intensive part is the calculation of coulomb energy for the new density ρ'. However, the procedure needs to be repeated for each set of the particle-hole excited states in question. Also the orthogonality between two excited states is not achieved exactly at present. However, this is a problem that can be solved as well using projection methods and/or

explicit orthonormalization methods similar to the ones discussed above.

Computational Details

The calculations reported here were carried out with the NRLMOL code.[14−17] The calculations were performed at the all-electron level with generalized gradient approximation for exchange-correlation potential. The code uses a large Gaussian basis with polarization functions. The basis set for each atom uses the same set of primitive Gaussians thereby reducing computation. The coefficients of the contracted Gaussians are optimized for each atom.[13] The grid for calculation is variational in that the error in integrals is minimized with respect to the number of points.[15] Moreover, the coulomb potential is calculated analytically. For the triad calculations the electronic structures were calculated using 5 s-type, 4 p-type, and 2 d-type basis functions for carbon, nitrogen, and oxygen atoms. These were contracted from 12 primitive Gaussians for carbon and 13 primitives for oxygen and nitrogen atoms. For hydrogen 4 s-type and 3 p-type functions contracted from a set of 6 primitives were used. The calculations are done at the all-electron level and use generalized gradient approximation for exchange-correlation functionals.[12]

Results and Discussion

We have performed calculations for different systems from small atoms to large molecules. The purpose of this calculation is to examine the cases where the ΔSCF method will be more suitable and where the present method will have an edge. As the simplest case, we have calculated the excitation energies of the first and second row atoms H - Ar. Since our treatment is based on the perturbation method, the small atoms are expected to show the worst agreement with experiment. One way of improving the results for small atoms will be to include higher order terms in the expansion of the wave functions. Another point worth noting in closed shell inert atoms is the necessity for including the long-range Gaussians in the basis. In the inert atoms such as He, the excited electronic state will be spread over a much larger space than the tightly bound ground state which requires long-range Gaussians.

Applications to Atoms and Molecules. The results of our calculations on atoms along with the experimental values are tabulated in Table 2. The experimental values are taken from the NIST Atomic Structure Database. The values show that the perturbative treatment adopted in the present method does not perform very well for closed shell atomic systems. However, such a deficiency is expected due to the relatively large perturbation for the atoms.

We have performed calculations on several small atoms and molecules to gauge the applicability of the method. The HOMO−LUMO excitation energies for the singlet and triplet states are shown in Table 3 and are compared with other available values from the literature.[32−37] All these calculations are spin unrestricted. The basis set effect is large in small molecules also. The basis set used here is large, but improvements can be made. The results are not perfect but show reasonable accuracy. For small atoms and molecules, the relaxations of the passive orbitals due to a charge rearrangement is expected to be larger than relaxations due to less localized excitations in large molecules. In almost all cases, the constrained orthogonality method overestimates experiment. This could indicate that further iterations over the perturbative approach could improve the agreement between theory and experiment. Another point is that these are vertical excitations and therefore exclude the effects due to the rearrangements of ions.

Table 2. Calculated Excited State Energies (eV) For Atoms Using the Constrained Orthogonality Method (COM), ΔSCF, and Experiment[a]

atom	state	COM	ΔSCF	expt
H	2s	11.95	9.90	10.20
H	2p	10.78	9.91	10.20
H	3s	12.44	11.69	12.09
He	1s2s(^{1}S)	22.32	20.32	19.82
He	1s2s(^{3}S)	22.17	19.48	20.62
He	1s2p(^{1}P)	23.80	20.82	20.96
He	1s2p(^{3}P)	23.67	20.38	21.22
Li	$1s^2$2p	1.89	1.89	1.85
Be	$1s^2$2s2p(^{3}P)	3.44	1.63	2.72
Ne	[He]$2s^2$$2p^5$3s(^{1}S)	17.91	16.74	16.62
Na	[Ne]3p	1.91	1.91	2.10
Mg	[Ne]3s3p	3.71	2.73	2.71
Ar	$3s^2$3p5(2P(1/2)4s	11.67	11.64	11.72
Ar	$3s^2$3p5(2P(1/2)4p	12.87	12.59	13.28
Kr	$4s^2$$4p^5$5s	10.23	10.17	9.91

[a] See ref 11.

Table 3. Calculated Excited State Energies (eV) for Small Molecules Using the Constrained Orthogonality Method (COM), ΔSCF, and Experiment[32−36a]

system	state	COM	ΔSCF	expt
N_2	singlet	8.49	8.48	9.31
	triplet	7.50	7.49	8.04
H_2O	singlet	7.50	7.45	7.40
	triplet	7.13	7.07	7.20
CO	singlet	7.20	7.51	8.51
	triplet	5.67	5.91	6.32
CO_2	singlet	9.04	8.70	
	triplet	8.02	8.13	
O_3	singlet	1.94	1.88	1.95
	triplet	1.43	1.36	1.45
LiH	triplet	3.15	3.07	3.25
	singlet	3.85	3.44	3.61
HF	singlet	11.41	11.65	
	triplet	11.38	8.61	
HCN	singlet	8.91	9.11	
	triplet	7.93	6.61	
O_2	singlet	1.65		1.64

[a] The theoretically calculated results are vertical excitations. For LiH, in the experimental column, we have used configuration interaction results of ref 37.

Ground-State Properties of the Triad

We have optimized two different geometries of the triad molecule using density-functional theory at the all-electron generalized gradient level, details of which can be found in ref 5. A linear structure nearly 50 Å long was found to be lower in energy, and therefore all subsequent calculations are done on this structure. The ground state of the molecule has a permanent dipole moment of 9 Debye, and its highest

Table 4. Eigenvalues (eV) and Molecular Parentage of the Ten Highest Occupied and Ten Lowest Unoccupied Orbitals ($-\epsilon_{Fermi} = 4.30$ eV)

hole			particle		
index	$-\epsilon$	parentage	index	$-\epsilon$	parentage
1	5.77	C_{60}	11	4.13	C_{60}
2	5.74	C_{60}	12	4.08	C_{60}
3	5.70	C_{60}	13	3.83	C_{60}
4	5.68	porphyrin	14	3.30	carotene
5	5.60	C_{60}	15	3.13	porphyrin
6	5.56	carotene	16	3.09	porphyrin
7	5.25	porphyrin	17	3.03	C_{60}
8	5.00	porphyrin	18	3.00	C_{60}
9	4.97	carotene	19	2.88	C_{60}
10	4.30	carotene	20	2.71	C_{60}

occupied and lowest unoccupied orbitals (HOMO and LUMO) are found on the carotenoid and the C_{60}, respectively. The gap between these two levels with zero spatial overlap is 0.17 eV from eigenvalue difference. The details of the ground-state electronic structure can be found in ref 5.

Excited States

While the calculation of the ground state is straightforward, obtaining an accurate description of the excited states from DFT especially for the charge-separated particle-hole states is difficult. To understand the transitions between various components we first need to calculate the energies of the relevant excited states. For that purpose, we consider a set of the highest ten occupied orbitals and ten lowest unoccupied orbitals over an energy range of 3 eV. These sets of orbitals in consideration are listed in Table 4.

As listed in the table these orbitals are mostly on one component of the triad. We label the states by HN/PM where H(P) refers to the location of the hole (particle) which can be carotenoid (C), porphyrin, and buckyball (B). N,M refer to the state number given in Table 4. From these two sets of occupied and unoccupied orbitals we have derived a set of 100 singly excited particle-hole states. A number of these excited states have large overlap between the particle and the hole orbitals when both the orbitals are on the same component. We have carried out the method described above to estimate the excited-state energies. This computationally inexpensive approach incorporates the charge polarization effects and the long-range $1/R$ interaction between the particle and hole, referred to as "electron-transfer self-interaction",[38] without requiring the added expense of a complete self-interaction correction[9−11] treatment of the passive orbitals. In the separated fragment limit, the method correctly reproduces the CT excitation ($I - A - 1/R$) which *depends only on ground-state quantities*. For the porphyrin-porphyrin excitations, our corrected excitation energy (2.05 eV) differs only slightly from the eigenvalue difference (1.87 eV) and is in excellent agreement with experiment (1.98)[39] and TDLDA calculations (2.16 eV).[40] However, for the large dipole excitation where TDLDA has been shown to fail,[38] the eigenvalue difference of 0.17 eV dramatically underestimates our corrected excitation energy of 2.46 eV in good agreement with an estimate based on the carotenoid ionization energy, the fullerene affinity, and the fullerene-carotenoid separation ($I - A - 1/R = 2.5$ eV). Our TDDFT calculation on the excitation of the triad also does not yield the charge-transfer energies.[41]

Polarization

The dipole moments of some of the singly excited particle-hole states are quite large (∼171 Debye). The electric field of such large dipoles will in turn induce dipoles on the nearby molecules or on the solvents around them. The electric field due to these induced dipoles in turn stabilizes the dipole state. The solvent polarization is important since the photoinduced charge separation is observed when experiments have been performed on molecules solvated in 2-methyltetrahydrofuran or benzonitrile but not in toluene. Similar dipole-induced polarization will also appear in a molecular crystal as well. We demonstrate below that in the molecular crystal the dipole induced polarization will lower the energies of the excited states, and this stabilization depends on the square of the dipole moments and also on the molecular volume or concentration. This is demonstrated by considering the energy of a classical array of polarizable particles on a lattice. To estimate the orientation and lattice packing of an assembly of the triad, we have optimized the total energy of a dimer assuming a classical van-der-Waals (vdW) pair potential between the atoms on different molecules. The intramolecular bonds are held rigid during this procedure. The triad dimerizes such that the total dipole moment vanishes. Further DFT calculations on the dimer suggest that the repulsive interaction is significantly underestimated by the available vdW parameters, and the dimer cell volume thus derived is likely to be a lower bound. However, the stabilization energy can still be estimated in terms of the dimers at lattice positions. The stabilization energy is $\Delta E_i = E_x^i - E_g$, where E_x^i is the energy of the lattice with the central molecule in the i^{th} excited-state and E_g is the energy of the lattice with the ground-state dimer at each site. The energy of the dipole lattice is calculated variationally using a method developed for determining the dielectric constant of a fullerene crystal from the molecular polarizability and unit cell volumes (see ref 42). This energy is written as

$$E = \frac{1}{2}\sum_{\mu\neq\nu}\left[\frac{\vec{p}_\mu\cdot\vec{p}_\nu}{|r_{\mu\nu}|^3} - \frac{3(\vec{p}_\mu\cdot\vec{r}_{\mu\nu})(\vec{p}_\nu\cdot\vec{r}_{\mu\nu})}{|r_{\mu\nu}|^5}\right] + \sum_{\mu,\nu}\frac{1}{2}\vec{p}_\mu^{\,i}\alpha_{\mu\nu}^{-1}\cdot\vec{p}_\nu^{\,i}\delta_{\mu\nu} \quad (9)$$

In the above equation $\vec{p}_\mu$ and $\vec{p}_\mu^{\,i}$ are the total and induced dipole at lattice position $\vec{r}_\mu$ and $\vec{r}_{\mu\nu} = \vec{r}_\mu - \vec{r}_\nu$. The polarizability tensor α is calculated from self-consistent total energy and dipole moment of the molecule as a function of various applied electric field along the three Cartesian directions.[42−44] The eigenvalues of the polarizability tensor are 878, 220, and 199 Å^3 where the first eigenvector is along the molecular axis. The stabilization energy also depends on the molecular volume and orientation. The stabilization energies of a few excited states with large dipole moments are shown in Figure 2. The stabilization of the large dipole states depend critically on the molecular volume as can be

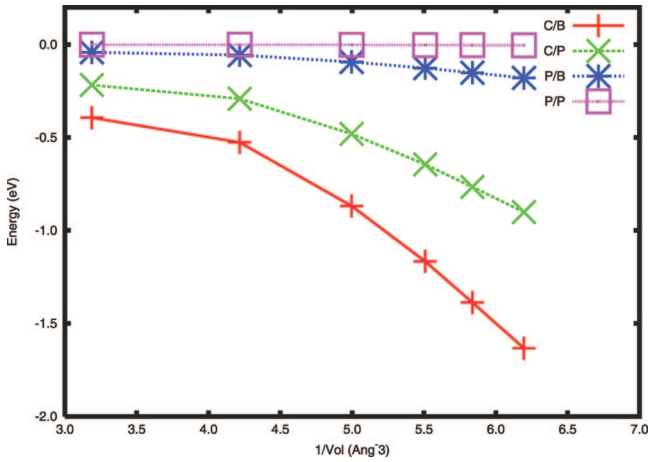

Figure 2. Change in energy levels of four excited states due to polarization effects. The labels C, P, and B refer to carotenoid, porphyrin, and buckyball. A/B refers to hole and particle localizations. The stabilization energy as a function of molecular volume is shown for lattice model.

seen from the figure. We find that it is necessary to increase the vdW dimer volume to avoid polarization induced divergences for the large dipole states (C10/B11−13 in our notation).

The polarization induced divergence is also present in the Clausius-Mossotti expression which relates the dielectric constant to the ratio of the polarizability to unit-cell volume. This divergence is not entirely unphysical as it is to some degree reflecting the fact that a crystal composed of highly polarizable particles will indeed breakdown when either a large enough internal or external electric field is applied. In a real system, this dielectric breakdown could be avoided by moving the charges.

The polarization lowers the energies of the large dipole states significantly bringing the theoretical energy levels closer to the experimental ones. In Figure 2 the stabilization of some of the particle-hole states are plotted as a function of inverse volume. Due to their small dipole moments, the ground and the porphyrin-porphyrin excited-state energies are nearly unaffected by cell volumes. Reduction of the transverse cell dimensions lowers the large-dipole excited states energies steeply leading to polarization induced breakdown. The stabilization energy decreases monotonically with increasing volume.

Dipole Transition Probabilities for KMC

In the experiment the triggering radiation was sent as a pulsed laser at 590 nm which corresponds to the porphyrin absorption frequency.[1] It was observed by Liddel et al. that the final charge separated state was reached following a series of transitions involving the P*-C_{60}^{1}, P*-C_{60}^{-}, and the C+-P-C_{60}− states.

When bathed in a radiation density similar to that of sunlight, a large number of dipole allowed transitions between various electronic states as well as vibronic states can occur. In this paper, we concentrate only on the electronic dipole-allowed transitions and examine whether a sequence of dipole allowed transition can lead to one of the charge-separated states. To find the possible sequence of radiative transitions leading to the charge-separated state, we have calculated Einstein's A and B coefficients. At this stage, the transition probabilities are calculated at temperature $T = 0$ and only to first-order. These probabilities are then used in a kinetic Monte-Carlo simulation to obtain the risetime of the charge-separated states.

The transition probability γ is determined as $\gamma_{ij} = A_{ij}\Theta(\epsilon_i - \epsilon_j) + B_{ij}u(\omega_{ij})$ and $\gamma_{ii} = -\sum_j \gamma_{ij}$. Note that the spectral power distribution contains an Arrhenius-like factor of $e^{-\Delta/kT}$ with Δ being the relevant excitation energy. B_{ij} is obtained from the dipolar transition matrix elements between the particle-hole states constructed from the unperturbed ground-state Kohn−Sham orbitals and $A_{ij} = (2\hbar\omega^3/\pi^2c^3)B_{ij}$.[46] The incident solar radiation with energy density $u(\omega)d\omega$ can be simulated as blackbody radiation at temperature $T = 6000$ K attenuated by a factor (R_s^2/D^2) where R_s and D are the radii of the sun and average earth trajectory. The lifetime of the i^{th} state is $\tau = \gamma_{ii}^{-1}$. At each $\tau/20$, the transition is determined to happen if a random number is less than 1/20. At this point a second random number is used to determine to which state the molecule evolves. This is weighted to ensure correct branching ratios stipulated by $1/\gamma_{ij}$. First, the simulations were carried out for a million steps, and the total time spent in each state is noted. The Einstein A and B coefficients depend on dipole matrix elements between particle and hole states.

In this work we have used the ground-state Kohn−Sham orbitals for estimating the dipole matrix elements. However, a more accurate and more involved approach to calculating these dipole matrix elements would be to calculate the many-electron dipole matrix element between the two Slater determinants. This would account for both direct and indirect relaxation effects. By direct, we refer to the fact that the particle state relaxes slightly due to the change in density. For the dipole matrix elements that connect the HOMO and LUMO porphyrin levels we find that this effect is quite small and that the matrix elements change by less than 1.5%. We also point out that there are other small corrections to this approximation at the many-electron level since the passive orbitals have also been allowed to relax. Inclusion of such effects would certainly be an improvement.

The Monte-Carlo simulations are first carried out for the molecule in gas phase. The large dipole states C10/B11−13 lie above the ground state by 2.46, 2.51, and 2.80 eV. The porphyrin excited state lies about 2 eV above the ground state. The dipole moments of these states are nearly 171 Debye. In the isolated molecule, the incident solar radiation fails to excite the molecule to any of the large dipole states. This situation is similar to when the experiments are done using toluene as solvent. Experimentally, CT is not observed when the triad is solvated in toluene (dipole moment μ = 0.375 D) but is observed in 2-MTHF (μ = 1.47 D) and benzonitrile (μ = 4.18 D).[1] Carbonera et al. have estimated from electrochemical measurements that the energy of the charge separated state in 2-MTHF is 1.24 eV above the ground state.[45] This is clearly an effect of the solvent polarization. The polar solvent encourages CT by lowering the energy of the CT states. If the polarization is ignored,

Table 5. Mean Time and Number of Transitions to Reach the Carotenoid/Buckyball States versus Applied Bias

E_d (a.u.)	time (s)	transitions
0.0000	inf	
−0.0010	5.2	1.3×10^5
−0.0020	0.06	1448.7
−0.0030	5.5×10^{-3}	175.1
−0.0040	4.3×10^{-4}	68.2
−0.0050	7.4×10^{-5}	70.1

then the large dipole states C10/B11−13 lie above the porphyrin excited states. Also the energy ordering of these states does not match that of the experiment without accounting for polarization of the solvents. The molecule spends 99.8% of its time in the ground state. As we have mentioned earlier the energy shift due to polarization depends on the molecular volume. We have estimated the time taken to reach any of the charge-transfer states from carotenoid HOMO to any one of the C_{60} T_{1u} LUMO states taking into account the energy shifts due to polarization. These are the lowest energy states with a hole in the carotenoid and a particle on the buckyball. For these calculations, a molecular volume of $100 \times 35 \times 35$ $\{a.u.\}^3$ was chosen. This volume reduces the energies of the lowest HOMO−LUMO transition to 1.17 eV, close to the experimental values. The Monte-Carlo simulations were allowed to go up to 10 million steps in a given run, and the runs were repeated for 100,000 times to obtain good averages. We find that on average about 62 s are taken to reach the target CT states. This is slower compared to charge transfer in biological systems and not fast enough for a useful solar cell.

Another situation where the energies of the CT states will be lowered is when there are counterions present in the sorrounding. One way of testing this hypothesis is to apply a bias field to lower the energies of the dipole states. Applied negative bias along the direction of the largest dipole moment state will lower the energy of that state. We have carried out this test by applying a uniform field in the range of −0.005 au to +0.005 au along the dipoles of the excited states of interest. The average time taken to reach any of the carotenoid-buckyball CT states is shown in Table 5. The initial state in this calculation was taken as the ground state. The average risetime is calculated from 10^5 such samplings. We note that in the actual sample the field will not be a uniform one. The local electric field in the sample can be caused by a large dipole moment of a neighboring excited molecule (possibly) or due to the presence of counterions and/or polar solvents in the environment (definitely). A similar counterion activated charge transfer is shown to occur in a DNA molecule in ref 47. A field of the order of 0.001 au can be easily created by counterions. To illustrate the possibility of large counterion induced electric fields we have placed a dissociated Na^+-Cl^- pair about 7 Å from C_{60} and the carotenoid center. The leads to an average electric field on the order of 0.0013 au. SCF calculations demonstrate the emergence of a large dipole. This effect is nearly independent of counterion type.

Carbonera et al. have proposed a CT reaction pathway which includes the porphyrin excited-state and also buckyball singlet to triplet excitations leading finally to the $C^{+\cdot}$P-$C_{60}^{-\cdot}$ state.[45] We have ignored the spin polarization and spin−orbit interaction to limit the computational expenses. Our calculations show that in the absence of solvent polarization, the C^+-P-C_{60}^- state lies about 0.3−0.4 eV above the porphyrin excited states. Thus incident radiation is necessary to excite the triad to the large dipole state. The difference in the energies arises because the experiments are carried out on molecules solvated in a polar media. The polarization effects would also occur in a lattice of molecules although it is different from the solvent effect. These polarization effects can change excited-state ordering and will be treated self-consistently in future. In the future, we will also include the nonradiative vibration assisted transitions in our calculations.

In summary, we present and discuss a method to calculate the excited-state energies from density-functional theory and apply it to calculate the energies of the charge-transfer states. We have carried out a DFT-based calculation on the radiative transitions on a large molecular triad. We present a scheme to calculate the charge-transfer energies from DFT which is computationally efficient. The method has been applied it to a large molecular triad. The charge separated states have large dipole moments. We show that medium polarization would lower the energies of the charge-separated states with large dipole moments. We examine the charge-transfer process using a kinetic Monte Carlo approach where we use Einstein's A and B coefficients. We show that the transition to the charge-separated states is catalyzed by several factors such as applied electric field and most notably the presence of counterions in the material. The one-second charging time obtained here suggests an absorption power of ∼30−100 mWatt/m^2 per monolayer of the molecule. In the presence of counterions in the solvent, the transition to a charge separated state can trigger a domino-like effect.

Acknowledgment. The authors acknowledge ONR (Grant No. N000140211046) and the DoD CHSSI Program. T.B. acknowledges a UTEP startup grant, URI, NSF Advance program at UTEP, and NSF Grants No. HRD-0317607 and NIRT-0304122. T.B. gratefully acknowledges the Texas Advanced Computing Center (TACC) at The University of Texas at Austin for providing HPC resources that have contributed to part of the research results reported within this paper. Part of the calculations were performed on Cray XD1 at UTEP. Other parts of the work were performed on the SGI-Altix system at NRL-DC under the auspices of the DoD HPCMP. The authors thank CCS, NRL, especially W. L. Anderson and Dr. Jeanie E. Osburn, for providing computational resources. We thank John Perdew for sharing his wisdom and functionals on many occasions.

References

(1) Liddell, P. A.; Kuciauskas, D.; Sumida, J. P.; Nash, B.; Nguyen, D.; Moore, A. L.; Moore, T. A.; Gust, D. *J. Am. Chem. Soc.* **1997**, *119*, 1400.

(2) Smirnov, S. N.; Liddell, P. A.; Vlassioul, I. V.; Teslja, A.; Kiciauskas, D.; Braun, C. L.; Moore, A. L.; Moore, T. A.; Gust, D. *J. Phys. Chem. A* **2003**, *107*, 7567.

(3) Kuciauskas, D.; Liddell, P. A.; Lin, S.; Stone, S. G.; Moore, A. L.; Moore, T. A.; Gust, D. *J. Phys. Chem. B* **2000**, *104*, 4307.

(4) Andreasson, J.; Kodis, G.; Terazono, Y.; Liddell, P. A.; Bandyopadhyay, S.; Mitchell, R. H.; Moore, T. A.; Moore, A. L.; Gust, D. *J. Am. Chem. Soc.* **2004**, *126*, 15926.

(5) Baruah, T.; Pederson, M. R. *J. Chem. Phys.* **2006**, *125*, 164706.

(6) Davidson, E. R.; Nitzsche, L. E. *J. Am. Chem. Soc.* **1979**, *101*, 6524.

(7) Levy, M.; Perdew, J. P. *Phys. Rev. B* **1985**, *31*, 6264.

(8) Callaway J.; March N. H. *Solid State Physics*; Academic: New York, 1984.

(9) Perdew, J. P.; Zunger, A. *Phys. Rev. B* **1981**, *23*, 5048.

(10) Pederson, M. R.; Heaton, R. A.; Lin, C. C. *J. Chem. Phys.* **1985**, *82*, 2688.

(11) Heaton, R. A.; Pederson, M. R.; Lin, C. C. *J. Chem. Phys.* **1987**, *86*, 258.

(12) Perdew, J. P.; Burke, K.; Ernzerhof, M. *Phys. Rev. Lett.* **1996**, *77*, 3865.

(13) Porezag, D. V.; Pederson, M. R. *Phys. Rev. A* **1999**, *60*, 2840.

(14) Pederson, M. R.; Porezag, D. V.; Kortus, J.; Patton, D. C. *Phys. Status Solidi B* **2000**, *217*, 197.

(15) Pederson, M. R.; Jackson, K. A. *Phys. Rev. B* **1990**, *41*, 7453.

(16) Pederson, M. R.; Jackson, K. A. *Phys. Rev. B* **1991**, *43*, 7312.

(17) Jackson, K. A.; Pederson, M. R. *Phys. Rev. B* **1990**, *42*, 3276.

(18) Andersson, C. K. T.; Sundstrom, J.; Kiyan, I. Y.; Hanstorp, D.; Pegg, D. J. *Phys. Rev. A* **2000**, *62* (111), 022503.

(19) Ruzsinszky, A.; Perdew, J. P.; Csonka, G. I.; et al. *J. Chem. Phys.* **2007**, *126*, 104102.

(20) Ruzsinszky, A.; Perdew, J. P.; Csonka, G. I.; et al. *J. Chem. Phys.* **2006**, *125*, 194112.

(21) Ossowski, M. M.; Boyer, L. L.; Mehl, M. J.; Pederson, M. R. *Phys. Rev. B* **2003**, *68*, 245107.

(22) Tozer, D. J.; De Proft, F. *J. Phys. Chem. A* **2005**, *109*, 8923.

(23) Compton, R. N.; Tuinman, A. A.; Klots, C. E.; Pederson, M. R.; Patton, D. C. *Phys. Rev. Lett.* **1997**, *78*, 4367.

(24) Hettich, R. L.; Compton, R. N.; Ritchie, R. H. *Phys. Rev. Lett.* **1991**, *67*, 1242.

(25) Watson, R. E. *Phys. Rev.* **1958**, *111*, 1108.

(26) Boyer, L. L. *Phys. Rev. Lett.* **1985**, *54*, 1940.

(27) Wu, Q.; Van Voorhis, T. *J. Chem. Phys.* **2006**, *125*, 164105.

(28) Wu, Q.; Van Voorhis, T. *J. Chem. Theory Comput.* **2006**, *2*, 765–774.

(29) Wu, Q.; Cheng, C. L.; Van Voorhis, T. *J. Chem. Phys.* **2007**, *127*, 164119.

(30) Theophilou, A. K. *J. Phys. C* **1979**, *12*, 5419.

(31) Lowdin, P. O. *J. Chem. Phys.* **1950**, *18*, 365.

(32) Marshal, D. Ph.D. Thesis, University of Wisconsin, 2006.

(33) Tilford, S. G.; Simmons, J. D. *J. Phys. Chem. Ref. Data* **1972**, *1*, 147.

(34) Krupenie, P. H. *J. Phys. Chem. Ref. Data* **1972**, *1*, 423.

(35) Lofthus, A.; Krupenie, P. H. *J. Phys. Chem. Ref. Data* **1972**, *6*, 113.

(36) Swanson, N.; Celotta, R. J. *Phys. Rev. Lett.*, **1975**, *35*, 783.

(37) Boutalib, A.; Gadea, F. X. *J. Chem. Phys.* **1992**, *97*, 1144.

(38) Dreuw, A.; Head-Gordon, M. *J. Am. Chem. Soc.* **2004**, *126*, 4007.

(39) Edwards, L.; Dolphin, D. H.; Gouterman, M.; Adler, A. D. *J. Mol. Spectrosc.* **1971**, *38*, 16.

(40) Gisbergen, S. J. A.; Rosa, A.; Ricciardi, G.; Baerends, E. J. *J. Chem. Phys.* **1999**, *111*, 2499.

(41) Spallanzani, N.; Rozzi, C. A.; Varsano, D.; Manghi, F.; Rubio, A.; Baruah, T.; Pederson, M. R. To be published.

(42) Pederson, M. R.; Quong, A. A. *Phys. Rev. B* **1992**, *46*, 13584.

(43) Zope, R. R.; Baruah, T.; Pederson, M. R.; Dunlap, B. *Int. J. Quantum Chem.* **2008**, *108*, 307.

(44) Pederson, M. R.; Baruah, T. *Lect. Ser. Comput. Comput. Chem.* **2005**, *3*, 156.

(45) Carbonera, D.; Valentin, M. D.; Corvaja, C.; Agostini, G.; Giacometti, G.; Liddell, P. A.; Kuciauskas, D.; Moore, A. L.; Moore, T. A.; Gust, D. *J. Am. Chem. Soc.* **1998**, *120*, 4398.

(46) Slater, J. C. *Quantum Theory of Matter*; McGraw Hill Book Company: 1951.

(47) Barnett, R. N.; Cleveland, C. L.; Joy, A.; Landman, U.; Schuster, G. B. *Nature* **2001**, *294*, 567.

CT900024F

JCTC Journal of Chemical Theory and Computation

Adiabatic Connection and the Kohn−Sham Variety of Potential−Functional Theory

E. K. U. Gross* and C. R. Proetto[⊥]

Institut für Teoretische Physik, Freie Universität Berlin, Arnimallee 14, D-14195 Berlin, Germany, and European Theoretical Spectroscopy Facility (ETSF)

Received January 18, 2009

Abstract: In potential−functional theory the total electronic energy is expressed as a functional of the external potential. We discuss how approximations, $T_s^{app}[v]$, of the noninteracting kinetic energy functional can be exploited for interacting systems. Two possibilities are discussed: (a) Via an adiabatic connection formula, $T_s^{app}[v_0]$ can be used directly with the external potential v_0 of the interacting system, and (b) by employing the variational principle of density functional theory, the kinetic energy functional $T_s^{app}[v_s]$ is evaluated at the Kohn−Sham potential v_s, which, in turn, is determined by an iterative procedure. Advantages and disadvantages of the two approaches are discussed.

The Kohn−Sham equations of density functional theory (DFT) are the method of choice to calculate medium to large electronic systems of up to 10000−100000 electrons. The basic strategy of the Kohn−Sham method is to map the interacting electronic system of interest onto a system of noninteracting particles such that the latter has the same ground-state density as the interacting system. Solving the Kohn−Sham single-particle Schrödinger equations rather than the interacting many-body Schrödinger equation makes the problem numerically tractable. However, for larger systems, even the solution of the Kohn−Sham equations becomes too costly. Here, orbital-free DFT,[1] that is, the representation of the total energy as an explicit functional of the density, is the ultimate method. Alternatively, one may express the total energy as a functional of the external potential.[2] This alternative approach, called potential−functional theory (PFT), will be addressed in this communication. The approach has its roots in semiclassical Wigner−Kirkwood-type expansions.[3−5] The design of more refined semiclassical approximations was outlined in the 1960s by Kohn and Sham[6] in one-dimensional systems. Three-dimensional generalizations have also been formulated.[7] On the basis of the work of Kohn and Sham, highly accurate potential functionals in 1D have recently been developed by Elliot et al.[8]

We start from the many-body Hamiltonian

$$\hat{H}[v] = \sum_{i=1}^{N} v(\mathbf{r}_i) + \hat{T} + \hat{W}_{ee} \tag{1}$$

where $\hat{T}$ is the kinetic energy and $\hat{W}_{ee}$ is the Coulomb repulsion of the electrons. Restricting ourselves to potentials $v(\mathbf{r})$ having a nondegenerate ground state, the Schrödinger equation

$$\hat{H}[v]\Psi[v] = E[v]\Psi[v] \tag{2}$$

implies that the ground-state wave function $\Psi[v]$ is uniquely determined by the potential $v(\mathbf{r})$. Consequently, the ground-state density

$$\rho[v](\mathbf{r}) = \int d^3r_2 ... \int d^3r_N \left|\Psi[v](\mathbf{r}, \mathbf{r}_2, ..., \mathbf{r}_N)\right|^2 \tag{3}$$

is a unique functional of the potential, and so is the total energy

$$E[v] = T[v] + W[v] + \int \rho[v](\mathbf{r})\cdot v(\mathbf{r}) d^3r \tag{4}$$

with

$$T[v] = \langle \Psi[v] | \hat{T} | \Psi[v] \rangle \tag{5}$$

* To whom correspondence should be addressed. E-mail: hardy@physik.fu-berlin.de.

⊥ Permanent address: Centro Atómico Bariloche and Instituto Balseiro, 8400, S. C. de Bariloche, Río Negro, Argentina.

10.1021/ct9000334 CCC: $40.75
Published on Web 03/23/2009

$$W[v] = \langle \Psi[v] | \hat{W}_{ee} | \Psi[v] \rangle \quad (6)$$

The basic idea of PFT is to find good approximations for $T[v]$ and $W[v]$ so that the total energy of a given system, characterized by the external potential $v_0(\mathbf{r})$, is obtained directly by plugging $v_0(\mathbf{r})$ in the functional (eq 4).

Most potential functionals known to date have been obtained by semiclassical considerations.[3−6] Highly accurate approximations have recently been constructed[8] for the kinetic energy and the density of noninteracting particles in one spatial dimension (1D). To use these approximations as part of the total energy functional of interacting systems, it appears desirable to have a coupling constant integration formula (or adiabatic connection) in PFT. We will deduce such a formula in the following. Consider the λ-dependent Hamiltonian

$$H_\lambda[v] = \hat{T} + \lambda \hat{W}_{ee} + \sum_{i=1}^{N} v(\mathbf{r}_i) \quad (7)$$

where λ with $0 \leq \lambda \leq 1$ allows us to switch off the electron−electron interaction. The $v(\mathbf{r})$ is an external potential which, in contrast to the adiabatic connection of DFT, is independent of λ. For the time being, we restrict ourselves to systems where for each λ, the ground-state solution $\Psi_\lambda[v]$ of the Schrödinger equation

$$H_\lambda[v]\Psi_\lambda[v] = E_\lambda[v]\Psi_\lambda[v] \quad (8)$$

is nondegenerate. Evidently, the fully interacting ($\lambda = 1$) total energy can then be written as

$$E_{\lambda=1}[v] = E_{\lambda=0}[v] + \int_0^1 \frac{dE_\lambda[v]}{d\lambda} d\lambda \quad (9)$$

Let us first evaluate the total energy functional of noninteracting particles $E_{\lambda=0}[v]$. The (nondegenerate) ground-state wave function of noninteracting particles is the determinant

$$\Psi_s[v](\mathbf{r}_1 ... \mathbf{r}_N) = \frac{1}{\sqrt{N!}} \det\{\varphi_j[v](\mathbf{r}_k)\} \quad (10)$$

with orbitals satisfying the single-particle Schrödinger equation (atomic units are used)

$$\left(-\frac{\nabla^2}{2} + v(\mathbf{r})\right)\varphi_j[v](\mathbf{r}) = \epsilon_j[v]\varphi_j[v](\mathbf{r}) \quad (11)$$

The total energy of the noninteracting system then reads

$$E_{\lambda=0}[v] = T_s[v] + \int \rho_s[v](\mathbf{r}) v(\mathbf{r}) d^3r \quad (12)$$

with

$$T_s[v] = \sum_{j=1}^{N} \int d^3r \varphi_j^*[v](\mathbf{r})\left(-\frac{\nabla^2}{2}\right)\varphi_j[v](\mathbf{r}) \quad (13)$$

$$\rho_s[v](\mathbf{r}) = \sum_{j=1}^{N} |\varphi_j[v](\mathbf{r})|^2 \quad (14)$$

The integrand of the coupling constant integral can be evaluated using the Hellmann−Feynman theorem

$$\frac{dE_\lambda[v]}{d\lambda} = \left\langle \Psi_\lambda[v] \left| \frac{\partial \hat{H}_\lambda[v]}{\partial \lambda} \right| \Psi_\lambda[v] \right\rangle = \langle \Psi_\lambda[v] | \hat{W}_{ee} | \Psi_\lambda[v] \rangle \quad (15)$$

Defining

$$W_\lambda[v] := \langle \Psi_\lambda[v] | \hat{W}_{ee} | \Psi_\lambda[v] \rangle \quad (16)$$

the total energy at full interaction can then be written as

$$E_{\lambda=1}[v] = T_s[v] + \int \rho_s[v](\mathbf{r}) v(\mathbf{r}) d^3r + \int_0^1 W_\lambda[v] d\lambda \quad (17)$$

This is the adiabatic connection formula of PFT. $T_s[v]$ and $\rho_s[v]$ are exactly the functionals for which highly accurate approximations have recently become available.[8] $W_\lambda[v]$, on the one hand, can be approximated using standard many-body perturbation theory, that is, Feynman diagrams with

$$\hat{H}_s[v] = \hat{T} + \sum_{i=1}^{N} v(\mathbf{r}_i) \quad (18)$$

representing the unperturbed Hamiltonian. This leads to approximations of the form

$$W_\lambda[v] = W_\lambda[G_s[v]] \quad (19)$$

where $G_s[v](\mathbf{x},\mathbf{x}')$ is the Green's function associated with the noninteracting Hamiltonian (eq 18). The functional $G_s[v]$, on the other hand, can be approximated very accurately, at least in 1D, using the semiclassical approach described in refs 6 and 8. Hence, the adiabatic connection formula of PFT can readily be used to evaluate the total energy of interacting systems without ever solving any interacting or noninteracting Schrödinger equation. Despite this attractive feature, the approach described so far has some drawbacks:

(i) In practice, evaluation of the functional $W_\lambda[G_s[v]]$ in eq 19 may be rather costly.

(ii) In the context of DFT, the noninteracting kinetic energy functional, $T_s^D[\rho_{int}]$, evaluated at the interacting ground-state density ρ_{int}, represents a major contribution to the total energy. In PFT, an analogous role is played by the functional $T_s[v]$ (cf. eqs 13 and 17). The latter, however, has to be evaluated at the external potential, $v_0(\mathbf{r})$, that is, the bare nuclear Coulomb potential in the case of atoms, molecules, and solids. The density of noninteracting particles moving in the bare nuclear Coulomb potential is much more localized than the interacting density, $\rho_{int}(\mathbf{r})$, and consequently, $T_s[v_0]$ will be much larger than $T_s^D[\rho_{int}]$. It is expected that, in terms of numbers, $T_s^D[\rho_{int}]$ is much closer to the fully interacting kinetic energy, $T^D[\rho_{int}]$, than $T_s[v_0]$ is to $T[v_0]$. The difference, $T[v_0] - T_s[v_0]$, is of course accounted for by the coupling constant integral $\int_0^1 W_\lambda[v]d\lambda$. However, since $T[v_0] - T_s[v_0]$ is expected to be larger than $T^D[\rho_{int}] - T_s^D[\rho_{int}]$, one has to work harder to construct sufficiently accurate approximations for the potential functional $W_\lambda[v]$ than for the corresponding density functional $W_\lambda^D[\rho]$.

(iii) The approach described so far is not variational. In fact, a variational principle has been formulated as well.[2,9] Employing the Rayleigh−Ritz principle, one simply minimizes the total energy functional

$$E_{v_0}[v] = \langle\Psi[v]|\hat{T} + \hat{W}_{ee} + \sum_{i=1}^{N} v_0(\mathbf{r}_i)|\Psi[v]\rangle = T[v] + W[v] + \int \rho[v](\mathbf{r})v_0(\mathbf{r})\mathrm{d}^3r \quad (20)$$

with respect to $v(\mathbf{r})$. Hence, for the exact functional, the following Euler−Lagrange equation is satisfied

$$\left.\frac{\delta E_{v_0}[v]}{\delta v(\mathbf{r})}\right|_{v_0} = 0 \quad (21)$$

In practice, however, this variational principle is not very useful. For an approximate functional, $E^{app}_{v_0}[v]$, the stationary point will generally be achieved at an approximate external potential, $v_0^{app}(\mathbf{r})$, which is the solution of the Euler equation

$$\left.\frac{\delta E^{app}_{v_0}[v]}{\delta v(\mathbf{r})}\right|_{v_0^{app}} = 0 \quad (22)$$

The variationally optimized external potential $v_0^{app}(\mathbf{r})$, however, is not really of interest because, after all, the true external potential, $v_0(\mathbf{r})$, is known. Furthermore, at the true external potential, $E^{app}_{v_0}[v_0]$ will usually not be stationary, which may cause difficulties, for example, in the calculation of vibrational spectra. However, the variational eq 22 may be useful as a quality check for the approximate functional $E^{app}_{v_0}[v]$. One may either compare $v_0(\mathbf{r})$ and $v_0^{app}(\mathbf{r})$ directly, or one may assess the difference $E^{app}_{v_0}[v_0] - E^{app}_{v_0}[v_0^{app}]$.

The three difficulties mentioned above can all be overcome by another flavor of PFT, namely, by representing the total energy as a functional of the Kohn−Sham potential, $v_s(r)$, rather than the external potential. This idea was recently proposed by Yang and co-workers.[2] The crucial point is to exploit the standard variational principle of DFT

$$\left.\frac{\delta E_{v_0}[\rho]}{\delta \rho(r)}\right|_{\rho_0} = 0 \quad (23)$$

where the total energy functional is given by

$$E_{v_0}[\rho] = T_s^D[\rho] + \int \rho(\mathbf{r})v_0(\mathbf{r})\mathrm{d}^3r + E_H[\rho] + E_{xc}[\rho] \quad (24)$$

where $v_0(r)$ is the fixed external potential of the system at hand and $E_H[\rho]$ and $E_{xc}[\rho]$ are the usual Hartree and exchange−correlation energy functionals of DFT. Assuming noninteracting v representability, the ground-state density $\rho(\mathbf{r})$ of an interacting system with external potential $v(\mathbf{r})$ can be represented as the ground-state density of noninteracting particles moving in the Kohn−Sham potential $v_s(\mathbf{r})$. The uniqueness of $v_s(\mathbf{r})$ follows from the Hohenberg−Kohn theorem, while the existence of $v_s(\mathbf{r})$ (i.e., v representability) has been demonstrated[10] in the ensemble sense for systems on an arbitrarily fine but discrete real-space grid. Hence, we can represent the densities $\rho(\mathbf{r})$ as $\rho_s[v_s](\mathbf{r})$ with the functional $\rho_s[v]$ given by eq 14. Consequently, substituting $\rho_s[v_s](\mathbf{r})$ for $\rho(\mathbf{r})$ in eq 24, the variational principle (eq 23) of DFT can be recast in the form

$$\left.\frac{\delta E_{v_0}[v_s]}{\delta v_s(r)}\right|_{v_{s,0}} = 0 \quad (25)$$

with

$$E_{v_0}[v_s] := T_s^D[\rho_s[v_s]] + \int \rho_s[v_s](\mathbf{r})v_0(\mathbf{r})\mathrm{d}^3r + E_H[\rho_s[v_s]] + E_{xc}[\rho_s[v_s]] \quad (26)$$

where $v_{s,0}$ is the Kohn−Sham potential corresponding to the interacting ground-state density $\rho_0(r)$ of the external potential $v_0(\mathbf{r})$

$$v_{s,0}(\mathbf{r}) = v_s[\rho_0](\mathbf{r}) \quad (27)$$

It is easy to see that

$$T_s^D[\rho_s[v_s]] = T_s[v_s] \quad (28)$$

with the potential functional $T_s[v]$ defined in eq 13. Hence, the total energy functional (eq 26) can be written as

$$E_{v_0}[v_s] = T_s[v_s] + \int \rho_s[v_s](\mathbf{r})v_0(\mathbf{r})\mathrm{d}^3r + E_H[\rho_s[v_s]] + E_{xc}[\rho_s[v_s]] \quad (29)$$

As opposed to the external potential functional (eq 17), eq 29 has to be evaluated at the Kohn−Sham potential $v_{s,0}(\mathbf{r})$. The latter is determined from the variational principle (eq 25); using the exact definition (eq 13) of the functional $T_s[v]$, one immediately verifies that

$$\frac{\delta T_s[v_s]}{\delta v_s(\mathbf{r})} = -\int \mathrm{d}^3r' v_s(\mathbf{r}')\frac{\delta \rho_s[v_s](\mathbf{r}')}{\delta v_s(\mathbf{r})} \quad (30)$$

and the variational principle (eq 25) yields the desired potential as

$$v_{s,0}(\mathbf{r}) = v_0(\mathbf{r}) + v_H[\rho_s[v_{s,0}]] + v_{xc}[\rho_s[v_{s,0}]] \quad (31)$$

where, as usual

$$v_H[\rho](\mathbf{r}) := \frac{\delta E_H[\rho]}{\delta \rho(\mathbf{r})} = \int \frac{\rho(\mathbf{r}')}{|\mathbf{r} - \mathbf{r}'|}\mathrm{d}^3r' \quad (32)$$

$$v_{xc}[\rho](\mathbf{r}) := \frac{\delta E_{xc}[\rho]}{\delta \rho(\mathbf{r})} \quad (33)$$

In ref 2, the above variational approach was employed with the exact functional $T_s[v_s]$ to put the optimized effective potential method on a firm variational basis. Here, we exploit the variational approach with approximate functionals $T_s^{app}[v_s]$ and $\rho_s^{app}[v_s]$. We propose to determine the desired potential $v_{s,0}(\mathbf{r})$ by the following iteration

$$\rho^{n+1}(\mathbf{r}) = \rho_s^{app}[v_s^{(n)}](\mathbf{r}) \quad (34)$$

$$v_s^{(n+1)}(\mathbf{r}) = v_0(\mathbf{r}) + v_H[\rho^{n+1}](\mathbf{r}) + v_{xc}[\rho^{n+1}](\mathbf{r}) \quad (35)$$

Clearly, eqs 34 and 35 would represent the usual Kohn−Sham self-consistency loop if the new density ρ^{n+1} had to be evaluated from the exact functional (eq 14), that is, by solving the one-body Schrödinger equation with the potential $v_s^{(n)}(\mathbf{r})$. By using the approximate (but explicit) functional $\rho_s^{app}[v_s^{(n)}]$

in eq 34, the costly step of solving the Schrödinger equation is avoided. The charm of this procedure is that it only relies on the well-established time-proven approximations for the density functional $v_{xc}[\rho]$ and on the noninteracting potential functionals $\rho_s^{app}[v]$ and $T_s^{app}[v]$, both of which are accurately known within the recent semiclassical approximations.[8]

It should be noted that the above derivation of the variational eq 31 relies on the exact noninteracting functionals $T_s[v_s]$ and $\rho_s[v_s]$. For approximate functionals, $T_s^{app}[v_s]$ and $\rho_s^{app}[v_s]$, the Euler eq 25 takes the form

$$\left.\frac{\delta T_s^{app}[v_s]}{\delta v_s(\mathbf{r})}\right|_{v_{s,0}} = -\int d^3r'(v_0(\mathbf{r}') + v_H[\rho_s^{app}[v_{s,0}]](\mathbf{r}') + v_{xc}[\rho_s^{app}[v_{s,0}]](\mathbf{r}'))\left.\frac{\delta\rho_s^{app}[v_s](\mathbf{r}')}{\delta v_s(\mathbf{r})}\right|_{v_s,0} \quad (36)$$

This general variational equation is, of course, much more complicated than eq 31. As a consequence, in each iterative step, the following nonlinear equation

$$\left.\frac{\delta T_s^{app}[v_s]}{\delta v_s(\mathbf{r})}\right|_{v_s^{(n+1)}} = -\int d^3r'(v_0(\mathbf{r}') + v_H[\rho^{(n+1)}](\mathbf{r}') + v_{xc}[\rho^{(n+1)}](\mathbf{r}'))\left.\frac{\delta\rho_s^{app}[v_s](\mathbf{r}')}{\delta v_s(\mathbf{r})}\right|_{v_s^{(n+1)}} \quad (37)$$

has to be solved to obtain the new potential v_s^{n+1}. This raises the question whether, for certain approximations, the variational eq 36 still takes the simple form of eq 31. This is expected, if $T_s^{app}[v_s]$ and $\rho_s^{app}[v_s]$ come from the same semiclassical expansion for the one-body Green's function, $G^{app}[v_s](\mathbf{r})$. In the Appendix, we show explicitly that this is the case for two specific varieties of semiclassical Green's functions.

Employing the iteration (eqs 34 and 35) and plugging the resulting $v_{s,0}(\mathbf{r})$ in the functional of eq 29, the total energy of the interacting system is evaluated without ever solving the interacting or noninteracting Schrödinger equation. This procedure is clearly a very efficient way to exploit PFT for interacting particles. We expect the approach to become the method of choice for very large interacting many-body systems.

Acknowledgment. C.R.P. was supported by the European Community through a Marie Curie IIF (MIF1-CT-2006-040222). We acknowledge support by the Deutsche Forschungsgemeinschaft. It is an exceptional pleasure to contribute, jointly with my colleague César Proetto, to this scientific celebration of John Perdew. Although we live on different continents, John has been one of my closest scientific friends since the early 1980s when we first met at a NATO school in Portugal. All of John's scientific work has been a great source of inspiration. We have enjoyed numerous discussions. My first Ph.D. student, Stefan Kurth, became John's postdoc. For some time, Manfred Lein acted as a "flying dutchman" between our groups, which even triggered John to make a short excursion into TDDFT. This little contribution celebrating your 65th birthday deals with two of your favorite topics, Kohn−Sham theory and the adiabatic connection.

Appendix

Semiclassical Approximations in PFT. An alternative expression for the noninteracting kinetic energy functional as given by eq 13 is the following

$$T_s[v] = \int d^3x t_s[v](\mathbf{x}) \quad (A1)$$

with

$$t_s[v](\mathbf{x}) = \frac{1}{2\pi i}\oint_C d\varepsilon[\varepsilon - v(\mathbf{x})]G_s[v](\mathbf{x},\varepsilon) \quad (A2)$$

The integration in eq A2 is in the complex ε-plane, along any closed contour C which encloses the occupied energy levels.[6] $G_s[v](\mathbf{x},\varepsilon)$ is the diagonal of the noninteracting one-body Green function, which is the solution of

$$\left[-\frac{1}{2}\nabla^2 + v(\mathbf{x}) - \varepsilon\right]G_s(\mathbf{x},\mathbf{x}',\varepsilon) = \delta(\mathbf{x}-\mathbf{x}') \quad (A3)$$

Throughout this appendix, we use the shorthand notation $G_s[v](\mathbf{x},\varepsilon) \equiv G_s[v](\mathbf{x},\mathbf{x},\varepsilon)$. The density can be expressed as a contour integral as well

$$\rho_s[v](\mathbf{x}) = \frac{1}{2\pi i}\oint_C d\varepsilon G_s[v](\mathbf{x},\varepsilon) \quad (A4)$$

Taking the functional derivative of eq A1 with respect to $v(\mathbf{y})$, we obtain the identity

$$\frac{\delta T_s[v]}{\delta v(\mathbf{y})} = -\rho_s[v](\mathbf{y}) + \int d^3x \oint_C \frac{\varepsilon\, d\varepsilon}{2\pi i}\frac{\delta G_s[v](\mathbf{x},\varepsilon)}{\delta v(\mathbf{y})} - \int d^3x v(\mathbf{x})\frac{\delta\rho_s[v](\mathbf{x})}{\delta v(\mathbf{y})} \quad (A5)$$

Equation A5 is valid both for the exact, $G_s[v](\mathbf{x},\varepsilon)$, and for approximate, $G_s^{app}[v](\mathbf{x},\varepsilon)$, Green's functions. In the former case, comparison with the result of eq 30 reveals that for consistency between both expressions, the first and second terms on the right-hand side of eq A5 should cancel each other. In the following, we will show that this cancellation also holds for approximate Green's functions, provided that $G_s^{app}[v](\mathbf{x},\varepsilon)$ satisfies two conditions. The first one

$$G_s^{app}[v](\mathbf{x},\varepsilon) = G_s^{app}[k(v(\mathbf{x}),\varepsilon)] \quad (A6)$$

requires that $G_s^{app}[v](\mathbf{x},\varepsilon)$ depends on v and ε exclusively through its functional dependence on $k(v(\mathbf{x}),\varepsilon) = [2(\varepsilon - v(\mathbf{x}))]^{1/2} \equiv k(\mathbf{x})$. This condition is obviously satisfied for all semiclassical approximations.

The second condition

$$\frac{\delta G_s^{app}[v](\mathbf{x},\varepsilon)}{\delta v(\mathbf{y})} = \frac{\delta G_s^{app}[v](\mathbf{y},\varepsilon)}{\delta v(\mathbf{x})} \quad (A7)$$

requires symmetry under exchange of coordinates. This condition is obviously satisfied for local Thomas−Fermi−von-Weizsäcker-type approximations

$$G_s^{app}[k(\mathbf{x})] = g(k(\mathbf{x}),\nabla k(\mathbf{x}),\nabla^2 k(\mathbf{x}),...) \quad (A8)$$

It is straightforward to verify that the symmetry condition (eq A7) also holds for the exact Green's function. To prove

the cancellation of the first two terms on the right-hand side of eq A5 under these conditions, we first realize that

$$\begin{aligned}\int \mathrm{d}^3x \frac{\delta G_s^{\mathrm{app}}[v](\mathbf{x},\varepsilon)}{\delta v(\mathbf{y})} &= \int \mathrm{d}^3x \frac{\delta G_s^{\mathrm{app}}[v](\mathbf{y},\varepsilon)}{\delta v(\mathbf{x})} \\ &= \int \mathrm{d}^3x \int \mathrm{d}^3z \frac{\delta G_s^{\mathrm{app}}[v](\mathbf{y},\varepsilon)}{\delta k(\mathbf{z})} \frac{\delta k(\mathbf{z})}{\delta v(\mathbf{x})} \\ &= -\int d^3x \int d^3z \frac{\delta G_s^{\mathrm{app}}[v](\mathbf{y},\varepsilon)}{\delta k(\mathbf{z})} \frac{1}{k(\mathbf{z})} \delta(\mathbf{x}-\mathbf{z})\end{aligned} \tag{A9}$$

In the first equality above, we have used the condition in eq A7. In the second equality, eq A6 was used. In the third line, we have used $\delta k(\mathbf{z})/\delta v(\mathbf{x}) = -\delta(\mathbf{x}-\mathbf{z})/k(\mathbf{z})$. Proceeding from eq A9 and noting now that $1/k(\mathbf{z}) = \partial k(\mathbf{z})/\partial\varepsilon$, we obtain

$$\begin{aligned}\int \mathrm{d}^3x \frac{\delta G_s^{\mathrm{app}}[v](\mathbf{x},\varepsilon)}{\delta v(\mathbf{y})} &= -\int \mathrm{d}^3x \int \mathrm{d}^3z \frac{\delta G_s^{\mathrm{app}}[v](\mathbf{y},\varepsilon)}{\delta k(\mathbf{z})} \frac{\partial k(\mathbf{z})}{\partial \varepsilon} \delta(\mathbf{x}-\mathbf{z}) \\ &= -\int \mathrm{d}^3x \frac{\delta G_s^{\mathrm{app}}[v](\mathbf{y},\varepsilon)}{\delta k(\mathbf{x})} \frac{\partial k(\mathbf{x})}{\partial \varepsilon} \\ &= -\frac{\partial G_s^{\mathrm{app}}[v](\mathbf{y},\varepsilon)}{\partial \varepsilon}\end{aligned} \tag{A10}$$

Inserting this into the second term on the right-hand side of eq A5, we obtain

$$\begin{aligned}\oint_C \frac{\varepsilon\,\mathrm{d}\varepsilon}{2\pi\mathrm{i}} \int \mathrm{d}^3x \frac{\delta G_s^{\mathrm{app}}[v](\mathbf{x},\varepsilon)}{\delta v(\mathbf{y})} &= -\oint_C \frac{\varepsilon\,\mathrm{d}\varepsilon}{2\pi\mathrm{i}} \frac{\partial G_s^{\mathrm{app}}[v](\mathbf{y},\varepsilon)}{\partial \varepsilon} \\ &= +\oint_C \frac{\mathrm{d}\varepsilon}{2\pi\mathrm{i}} G_s^{\mathrm{app}}[v](\mathbf{y},\varepsilon) \\ &= \rho_s^{\mathrm{app}}[v](\mathbf{y})\ \text{q.e.d.}\end{aligned} \tag{A11}$$

The second equality above follows from partial integration in the complex plane, with the "boundary" contribution of the contour integral being zero. Through this cancellation, eq A5 reduces to eq 30, with $T_s[v]$ replaced by $T_s^{\mathrm{app}}[v]$ and $\rho_s[v](\mathbf{x})$ by $\rho_s^{\mathrm{app}}[v](\mathbf{x})$. In turn, this implies that the general variational eq 36 reduces to

$$v_{s,0}(\mathbf{x}) = v_0(\mathbf{x}) + v_H[\rho_s^{\mathrm{app}}[v_{s,0}]](\mathbf{x}) + v_{xc}[\rho_s^{\mathrm{app}}[v_{s,0}]](\mathbf{x}) \tag{A12}$$

provided that the approximate functionals $T_s^{\mathrm{app}}[v]$ and $\rho_s^{\mathrm{app}}[v]$ come from approximate Green's functions $G_s^{\mathrm{app}}[v]$ satisfying the conditions in eqs A7 and A8.

As a further example for the validity of the variational result of eq 31 for approximate functionals of $T_s[v]$ and $\rho_s[v]$, we now discuss the recently developed semiclassical approximations of Elliot et al.[8] Adding and subtracting NE_F, eqs A1 and A2 can be written in the more convenient form

$$T_s[v] = \int \mathrm{d}x[E_F - v(x)]\rho_s[v](x) + \int \mathrm{d}x \oint_C d\varepsilon(\varepsilon - E_F)\frac{G_s[v](x,\varepsilon)}{2\pi\mathrm{i}} \tag{A13}$$

where, in order to make contact with the work of Elliot et al., we restrict ourselves to the 1D case. Taking again the functional derivative with respect to $\delta v(y)$, we obtain

$$\frac{\delta T_s[v]}{\delta v(y)} = -\rho_s[v](y) + \int \mathrm{d}x[E_F - v(x)]\frac{\delta \rho_s[v](x)}{\delta v(y)} + \int \mathrm{d}x \oint_C \mathrm{d}\varepsilon \frac{(\varepsilon - E_F)}{2\pi\mathrm{i}} \frac{\delta G_s[v](x,\varepsilon)}{\delta v(y)} \tag{A14}$$

The particular model studied by Elliot et al.[8] consists of a one-dimensional box with potential $v(x)$, $0 \le x \le L$, and $E_F > v(x)$ everywhere. Hard-wall boundary conditions were imposed at $x = 0$ and L. The corresponding $G_s^{\mathrm{semi}}[v](x,\varepsilon)$ is given by

$$G_s^{\mathrm{semi}}[v](x,\varepsilon) = \frac{f(\Theta)}{k(x)} \tag{A15}$$

with $f(\Theta) = \{\cos\Theta(L) - \cos[2\Theta(x) - \Theta(L)]\}/\sin\Theta(L)$, $k(x) = [2(\varepsilon - v(x))]^{1/2}$, and $\Theta(x) = \int_0^x \mathrm{d}x' k(x')$. One easily verifies that $G_s^{\mathrm{semi}}[v](0,\varepsilon) = G_s^{\mathrm{semi}}[v](L,\varepsilon) = 0$. Inserting $G_s^{\mathrm{semi}}[v](x,\varepsilon)$ from eq A15 into the 1D version of eq A4, the semiclassical expression for the density is[8]

$$\rho_s^{\mathrm{semi}}[v](x) = \frac{k_F(x)}{\pi} - \frac{\sin 2\Theta_F(x)}{2T_F k_F(x)\sin\alpha(x)} \tag{A16}$$

where $\alpha(x) = \pi\tau_F(x)/T_F$, $\tau_F(x) = \int_0^x \mathrm{d}x'/k_F(x')$, and $T_F = \tau_F(L)$; also, $k_F(x) = [2(E_F - v(x))]^{1/2}$. The first term on the right-hand side of eq A16 is the 1D analogue of the 3D Thomas−Fermi density; the second term, which is of the same order in $\hbar$ as the first, ensures satisfaction of the hard-wall boundary condition $\rho_s^{\mathrm{semi}}[v](0) = \rho_s^{\mathrm{semi}}[v](L) = 0$. Considering that, from eq A15

$$\frac{\delta G_s^{\mathrm{semi}}[v](x,\varepsilon)}{\delta v(y)} = \delta(x-y)\frac{f(\Theta)}{k^3(x)} + \frac{1}{k(x)}\frac{\delta f(\Theta)}{\delta v(y)} \tag{A17}$$

and inserting the first term on the right-hand side of eq A17 in the last term on the right-hand side of eq A14, we obtain

$$\int \mathrm{d}x\delta(x-y)\oint_C \frac{\mathrm{d}\varepsilon}{2\pi\mathrm{i}}(\varepsilon - E_F)\frac{f(\Theta)}{k^3(x)} = \frac{\rho_s^{\mathrm{semi}}[v](y)}{2} - [E_F - v(y)]\oint_C \frac{\mathrm{d}\varepsilon}{2\pi\mathrm{i}}\frac{f(\Theta)}{k^3(y)} \tag{A18}$$

Following the same steps as those in ref 8, the last contribution in eq A18 is found to be another half of $\rho_s^{\mathrm{semi}}[v](x)$. As the contribution from the second term in the right-hand side of eq A17 to eq A14 can be proved to be null, we obtain again the desired result

$$\frac{\delta T_s^{\mathrm{semi}}[v]}{\delta v(y)} = \int \mathrm{d}x[E_F - v(x)]\frac{\delta \rho_s^{\mathrm{semi}}(x)}{\delta v(y)} \tag{A19}$$

which translates also in this case to a variational equation of the type of eq A12, with the label "app" replaced by "semi".

References

(1) Lignères V. L.; Carter, E. A. *An Introduction to Orbital-Free Density Functional Theory*; Springer: Netherlands, 2005; and references therein.

(2) Yang, W.; Ayers, P. W.; Wu, Q. Potential Functionals: Dual to Density Functionals and Solution to the v-Representability Problem. *Phys. Rev. Lett.* **2004**, *92*, 146404.

(3) Wigner, E. P. On the Quantum Correction for Thermodynamic Equilibrium. *Phys. Rev.* **1932**, *40*, 749.

(4) Kirkwood, J. G. Quantum Statistics of Almost Classical Assemblies. *Phys. Rev.* **1933**, *44*, 31.

(5) Dreizler, R. M.; Gross, E. K. U. *Density Functional Theory*; Springer-Verlag: Berlin, Germany, 1990; pp 75−137.

(6) Kohn, W.; Sham, L. J. Quantum Density Oscillations in an Inhomogeneous Electron Gas. *Phys. Rev.* **1965**, *137*, A1697.

(7) Thorpe, M. A.; Thouless, D. J. Oscillations of the Nuclear Density. *Nucl. Phys. A* **1970**, *A156*, 225.

(8) Elliot, P.; Lee, D.; Cangi, A.; Burke, K. Semiclassicals Origins of Density Functionals. *Phys. Rev. Lett.* **2008**, *100*, 256406.

(9) Schuck, P.; Viñas, X. A Variational Wigner−Kirkwood Theory of Finite Nuclei. *Phys. Lett. B* **1993**, *302*, 1.

(10) Chayes, J. T.; Chayes, L.; Ruskai, M. B. Density Functional Approach to Quantum Lattice Systems. *J. Stat. Phys.* **1985**, *38*, 497.

CT9000334

JCTC Journal of Chemical Theory and Computation

Structure Dependence of Hyperpolarizability in Octopolar Molecules

C. Cardoso,*,† P. E. Abreu,‡ and F. Nogueira†

CFC, Physics Department, Coimbra University, P-3004-516, Coimbra, Portugal, and Chemistry Department, Coimbra University, P-3004-535, Coimbra, Portugal

Received October 31, 2008

Abstract: Recent Hyper Rayleigh Scattering measurements report a significant increase of second-order hyperpolarizability upon introduction of positive charges at the pyridyl end groups in trispyridyl octopolar chromophores. We calculated the geometries, linear response, and first-order hyperpolarizabilities of a series of six trispyridyl molecules both in the neutral and protonated forms. The calculations were performed with *ab initio* and semiempirical methods. The results are in good agreement with the experimental values and a correlation between the first hyperpolarizability and two structural properties, the N−C bond elongation and the C−C bond length alternation, $\langle \Delta r \rangle$ was established. To test these effects we computed the hyperpolarizability for several constrained geometries and confirmed the importance of planarity on the hyperpolarizability values. However the $\langle \Delta r \rangle$ values alone seem to have little influence both on the hyperpolarizability and on the gap values. Replacing the triple C≡C bond by a double C=C bond in the conjugation bridge has no significant effect due to the strong hyperpolarizability dependence on the pyridyl-benzene dihedral angle.

1. Introduction

Photonics is playing an ever-increasing role in today's technology by efficiently replacing electronics in electro-optic devices. In this context, researchers have been focusing on the search for materials with large optical nonlinearities and for their application in the fields of high speed data transmission, processing and storage.[1−6] Organic molecules are promising candidates since their properties can be custom-tailored, and their dielectric constants and refractive indixes are much smaller than those of the most common inorganic molecules. A second-order Non-Linear Optical (NLO) chromophore typically contains a conjugated π-electron system, asymmetrically substituted by electron donor and acceptor groups, through which a charge transfer occurs. In such systems the dominant first hyperpolarizability component is along the direction of charge transfer.

In the early 1990s it was shown that, for a given conjugation bridge, there is an optimal combination of donor and acceptor strengths or ground-state polarization to maximize the dipole moment-first hyperpolarizability product, $\mu\beta$. Beyond a certain point, increased donor−acceptor strength or further ground-state polarization attenuates $\mu\beta$.[7,8] Bond length alternation, i.e., the average difference in length between single and double bonds in the molecule, was also shown to be a relevant parameter in the optimization of the hyperpolarizability of molecules.[9−11] Recently, the possibility of modulating NLO properties at the molecular level using molecules which respond to electrochemical or chemical inputs such as protons or metal cations has been explored.[12−15] In chemosensitive systems of the donor-π-acceptor type, interaction with a cationic species alters the electron density of the terminal sites, resulting in a modulation of the internal charge transfer character of the dye molecule which leads to a change in the optical response.[16−18] There have been several reports of modulation of the two-photon absorption and fluorescence properties of linear chromophores upon cation binding or protonation/deprotonation at the terminal donor substituent.[19−22]

The antiparallel alignment of the dipole moments of one-dimensional chromophores leads the majority of π-conju-

* Corresponding author e-mail: cmcardoso@teor.fis.uc.pt.
† CFC, Physics Department.
‡ Chemistry Department.

10.1021/ct800464t CCC: $40.75
Published on Web 03/02/2009

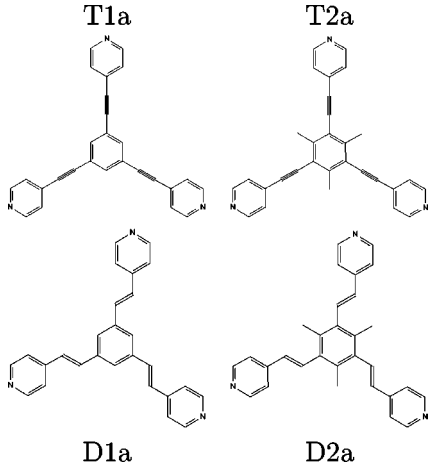

Figure 1. One example of each series: **D1**, **D2**, **T1**, and **T2**. The rest of the series corresponds to different locations of the nitrogen atom in the pyridyl rings, as shown in Figure 2.

gated organic molecules to crystallize in centrosymmetric space groups, having therefore null second-order bulk susceptibility. One of the solutions to achieve dipole minimization without losing the molecular hyperpolarizability is the use of noncentrosymmetric octopolar systems, since their symmetry ensures cancelation of the dipole moment.[1,23−34] Despite the growing impact that octopolar systems are having in the field of nonlinear optics, few studies report on organic NLO octopoles with switchable second-order nonlinearity.[35−38] Theoretical calculations on octopolar tris-acetylene benzenes suggest that the second-order hyperpolarizability β could increase more than 1 order of magnitude upon introduction of positive charges at the pyridyl end groups.[39−42] Asselberghs et al. report a strong increase of the charge transfer character and, consequently, of second-order hyperpolarizability upon introduction of positive charges at the terminal pyridyl groups of octopolar 1,3,5-trisalkynylbenzenes.[37] In a work by Oliva et al. the origin of the first-order NLO response was attributed, for the neutral systems, to octopolar contributions, while the enhanced response after protonation was attributed to the involvement of dipolar excited states yielding dipolar contributions to the NLO outcome.[38]

In the present work we explore the relation between protonation, bond length alternation, and enhanced hyperpolarizability in octopolar chromophores. We performed calculations for several prototypical chromophores of neutral and protonated 1,3,5-trispyridylbenzene in order to determine the parameters that influence its hyperpolarizability. We studied the influence of the conjugation bridge by considering both a C−C≡C−C bridge connecting the pyridyl rings to the central benzene ring (we refer to these systems as the **T** series) and a C−C=C−C bridge (the **D** series, see Figure 1). We also compared the hyperpolarizability values for normal (**T1** and **D1** series) and methylated compounds (**T2** and **D2** series, Figure 1), both in the neutral and the protonated forms. Finally, we assessed the effect of the location of the pyridyl nitrogen (series **T1a**, **T1b**, etc. --- see Figure 2).

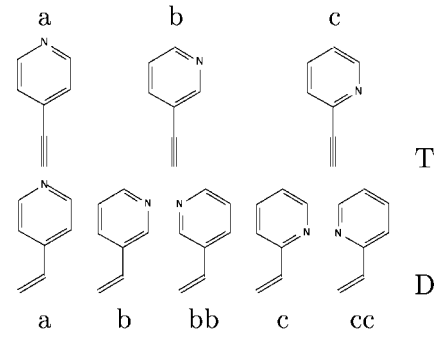

Figure 2. Nitrogen location in the pyridyl rings of the molecules under study.

Table 1. Calculated and Experimental First Hyperpolarizability Component β_{xxx0} for the **T** Series

	B3LYP (au)	PM3 (au)	PM6 (au)	Exp.[37] (au)	CPHF[38] (au)
Neutral					
1a	804	796	753		
1b	229	240	525		
1c	722	938	653	926	417
2a	2446	1722	3262	1389	1346
2b	1763	916	1920		
2c	2860	2002	3537	1041	1198
3+					
1a	6415	6430	7405		
1b	3548	4701	4049		
1c	3438	4561	2350	2199	1844
2a	9815	9848	8837	16895	5248
2b	6231	6146	4070		
2c	5944	3302	2718	4397	3044

2. Computational Methods

We obtained the ground-state geometries, hyperpolarizability, and optical properties of all these molecules within Density Functional Theory (DFT) and Time Dependent Density Functional Theory (TDDFT), using B3LYP for exchange and correlation.[43,44] The molecular geometries were optimized with the GAMESS-US code[45] using a 6−311G+(d,p)[46] basis set of wave functions. The static second-order hyperpolarizabilities were computed using the finite fields method within the same level of theory. The OCTOPUS code[47,48] was used to compute the ground-state Electron Localization Function (ELF)[49] and the optical absorption spectra. The ground-state geometries and hyperpolarizability values were again computed using MOPAC2007,[50] with the PM3[51−54] and PM6[55] Hamiltonians.

3. Results and Discussion

The discussion of our results will be done in four steps: i) comparison of our results for the second-order nonlinear polarizabilities with experimental (Hyper Rayleigh Scattering -- HRS) and other computational results; ii) comparison between the **T** and **D** series; iii) discussion of the computed molecular geometries and ELF, and their relation with the hyperpolarizability values; and iv) report on DFT energy levels and Kohn−Sham orbitals and linear response.

3.1. Nonlinear Optical Properties. In Table 1, we compare the static β_{xxx0} component computed for the **T** series within DFT/B3LYPPM3, and PM6 semiempirical methods

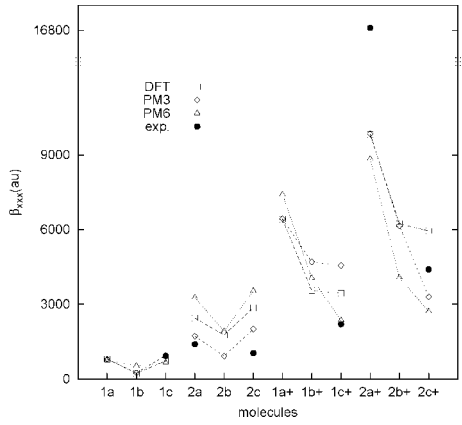

Figure 3. Comparison between calculated and experimental[37] hyperpolarizability component β_{xxx0} for the **T** series.

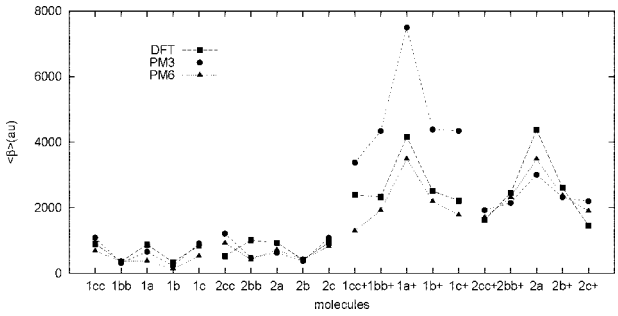

Figure 4. $\langle\beta_{HR}\rangle$ in atomic units, computed within DFT/B3LYP, PM3 and PM6 methods for the **D** series.

to HRS experimental values, obtained within the three level model.[37] In order to make the comparison easier, the same results are plotted in Figure 3.

The present results, obtained both *ab initio* and semiempirically, reproduce very well the trend of the experimental results.[37] The increase of the computed hyperpolarizability with protonation and the larger hyperpolarizability of molecules belonging to the **2** series (compared with series **1**) reflect the stronger donor character of the CH_3 group and are in agreement with experiment. Within each of the neutral series the calculated hyperpolarizability values are very similar, whereas in the case of the protonated series the differences are larger: molecules **a** present hyperpolarizability values significantly larger than molecules **b** and **c**. This is particularly noticeable for the **T2** series computed within the PM3 and PM6 methods. This is again in good agreement with the HRS results. The DFT/B3LYP results are also in good agreement with Coupled Perturbed Hartree−Fock (CPHF) results.[38] The small differences can be attributed to the use of different basis sets and computation methods.

In Figure 6 we show also the intrinsic hyperpolarizability, β_{int}, as defined by Zhou et al.[56] This property gives a scale-independent intrinsic value, useful as a metric that takes into account the molecular size. In the case of the present series, and since the molecules have the same size and number of π electrons, its value depends only on the energy gap. β_{int} follows very closely the variation of the absolute β values. The exceptions are the protonated **T1c** and **T2c** molecules, which show a small increase of β_{int} with respect to **T1b** and **T2b**, contrary to what happens to the absolute β.

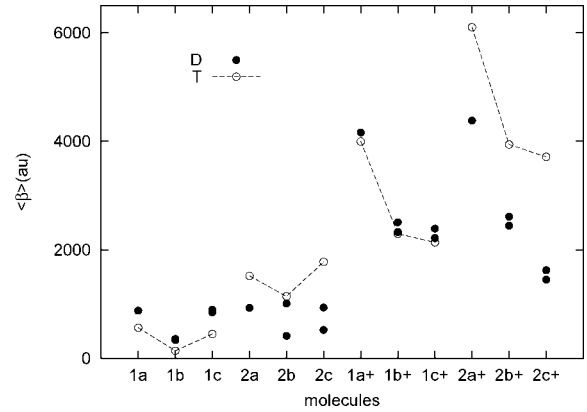

Figure 5. Comparison between the computed DFT/B3LYP $\langle\beta_{HR}\rangle$ values for the **T** and **D** molecules. In the plot, the **1b**, **1c**, **2b**, and **2c** symbols include also, for the **D** series, the values of **1bb**, **1cc**, **2bb**, and **2cc**.

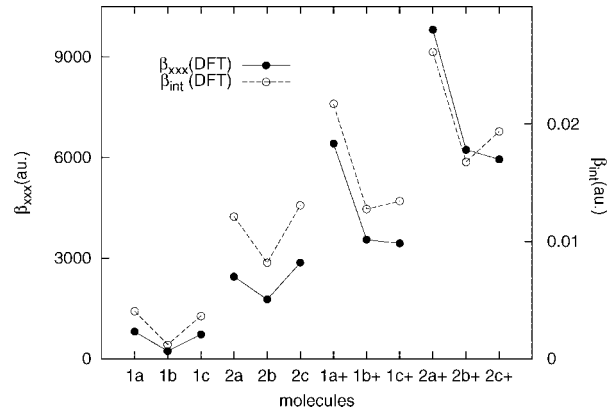

Figure 6. Comparison of the absolute hyperpolarizability values with the intrinsic hyperpolarizability.

Although the calculated values reproduce well the experimental trends, the absolute values show some discrepancies. The molecule with the largest hyperpolarizability presents also the largest deviation from the experimental results. Although DFT methods are expected to overestimate hyperpolarizability, as in fact happens for the other molecules, the measured value for $\mathbf{T2a}^{3+}$ is 1.8 times larger than the computed β_{xxx0}. The experimental value reported for this particular molecule is 16895 ± 578 au. The DFT/B3LYP values do not fall in this range. These differences may have several origins: the basis set, the exchange and correlation functional, and the neglect of solvent effects.

In order to test the basis set used in the *ab initio* calculations we performed also some calculations with the Z3POL basis set,[57,58] a basis set specially tailored for the calculation of electrical properties. The β_{xxx0} obtained with Z3POL for the neutral and protonated **T2a** molecules are 2352 and 9584 au, whereas the 6−311G+(d,p) values are 2446 and 9815 au, respectively. The results are not significantly different, showing that 6−311G+(d,p) is adequate for the task at hand.

Among the DFT exchange and correlation functionals used in the calculation of nonlinear optical properties, the hybrid methods, like the B3LYP used in the present study, represent a significant improvement on the pure DFT methods.[59,60] Sałek et al. reports mean absolute errors of 9% for dynamic

Table 2. $\langle\beta_{HR}\rangle$ in Atomic Units, Computed within DFT/B3LYP, PM3, and PM6 Methods

	D			T		
	B3LYP	PM3	PM6	B3LYP	PM3	PM6
Neutral						
1cc	898	1087	682	-	-	-
1bb	358	318	371	-	-	-
1a	880	660	377	567	662	626
1b	339	223	142	141	168	356
1c	847	918	526	449	622	504
2cc	1011	1210	925	-	-	-
2bb	523	477	421	-	-	-
2a	932	626	715	1521	1178	2150
2b	416	375	425	1142	692	1608
2c	938	1082	822	1780	1370	2252
3+						
1cc	2393	3379	1293	-	-	-
1bb	2330	4345	1925	-	-	-
1a	4162	7499	3495	3998	5392	4750
1b	2510	4391	2197	2299	2902	2556
1c	2217	4345	1785	2139	2820	1692
2cc	1626	1933	1707	-	-	-
2bb	2447	2151	2319	-	-	-
2a	4384	3010	3488	6104	7326	7398
2b	2614	2320	2372	3942	4092	2974
2c	1453	2200	1906	3714	2164	2372

hyperpolarizabilities.[59] However there are some problems for systems with large charge transfer. In cases like para-nitroaniline the hyperpolarizability calculations underestimate the experimental values by 16% at low frequencies and by 30% to more than 40% at higher frequencies.[61] This could also explain why the molecules with larger hyperpolarizability show also larger discrepancies to experimental results.

Solvent measurements indicate a large shift in the hyperpolarizability values for charge transfer molecules[62] in solutions with large dielectric constants. Allin et al. reports ratios as large as 6 between the hyperpolarizabilities calculated in vacuo and in a solvent (the average ratio is 3.7).[63] Although solvent effects should be less important in octopolar than in linear dipolar molecules,[37] the neglect of these effects adds to the previous innacuracies.

All these effects must be taken into account when comparing the calculated values with the experimental ones. Nevertheless, and since the most important trends are well reproduced, the present results allow for a detailed analysis and the drawing of interesting conclusions.

The DFT/B3LYP hyperpolarizability results obtained for the **D** series are summarized in Table 2 and plotted in Figure 4. PM3 and PM6 semiempirical results are, in general, similar and in reasonable agreement with the DFT results. There are, however, some exceptions. The geometries obtained for protonated molecules using the two semiempirical Hamiltonians and DFT/B3LYP show significant differences, and this is reflected in the hyperpolarizability values. DFT geometries and, therefore, hyperpolarizability values, are closer to PM6 values, both predicting off-plane pyridyl rings. The planar geometries obtained within the PM3 Hamiltonian for the **D1** molecules lead to significantly larger hyperpolarizability values. The effect of geometry in hyperpolarizability is discussed in the next sections.

The hyperpolarizability values of the **D** series are of the same order of magnitude and display a similar pattern of

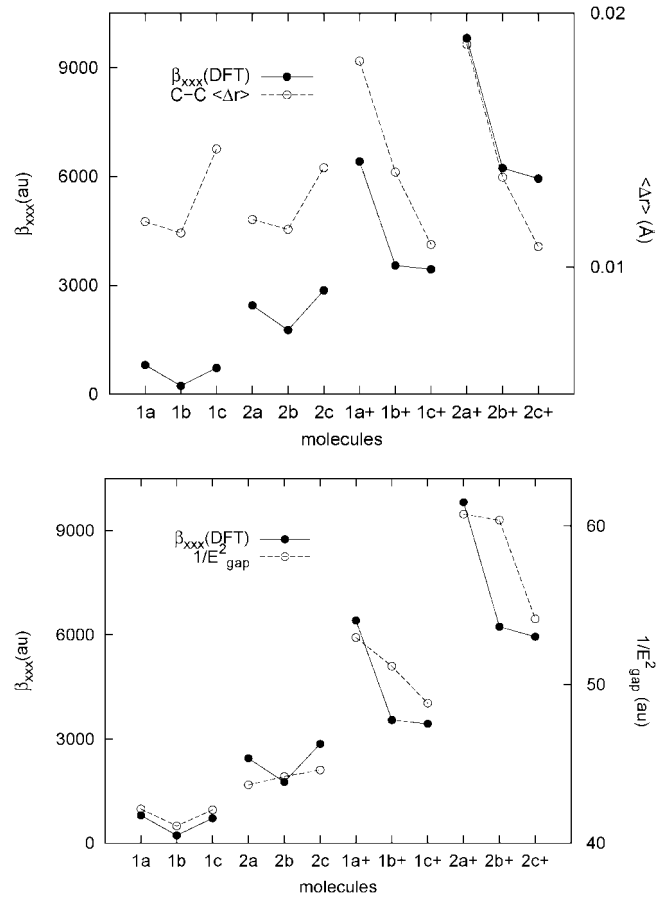

Figure 7. C−C bond length deviation (top) and energy gaps (bottom) calculated within DFT/B3LYP for the **T** series and compared with β_{xxx}.

modulation to those of the **T** molecules (Figure 5). This is in agreement with the results reported Lee et al., in which no significant hyperpolarizability enhancement is seen when the double C−C bond is replaced by a triple bond in a series of compounds.[64] The protonated series presents larger hyperpolarizability than the neutral forms, as in the **T** molecules. However, the increase on hyperpolarizability seen from the **T1** to the **T2** series, due to the presence of electron rich CH_3 groups which increase the donor−acceptor strength, does not happen for the **D** series. **D2** molecules yield hyperpolarizability values similar to the **D1** series and present lower values than its **T2** counterparts. The reason for this is discussed below.

3.2. Energy Gaps. From now on we will focus on the DFT/B3LYP results. Calculations show that, for the **T** series, protonation decreases the HOMO−LUMO energy gap. There is also a decrease on the energy gap from the **T1** to the **T2** series. Figure 7 shows that the hyperpolarizability values follow very closely the trend of the energy gap, as predicted by the three-level model for octopolar molecules.[65] The **D** series presents a more complex scenario. There is still a decrease of the gap from the neutral to the protonated series. However, for the neutral molecules, and contrarily to what happens in the **T** series, the **D2** energy gap is larger than the **D1** gap and so is its hyperpolarizability. For the charged molecules the hyperpolarizability and the energy gap of the **D1** and **D2** are similar but do not present a common trend.

3.3. Molecular Geometries. *3.3.1. T Series.* The molecular DFT/B3LYP geometry optimization, performed within the C_3 point group symmetry for the **T** molecules, results mainly in planar geometries. The only exception is the molecule **T2a** in the neutral form, which has the pyridyl rings tilted by 22°. This deviation does not seem to affect its hyperpolarizability, since, in the neutral series, this is the molecule that has the largest hyperpolarizability and HRS values. Also, the bonds from the central ring to the three pyridyl rings are not exactly linear, with calculations yielding bond angles that can be as large as 8°. There are however other differences in the molecular geometries which seem to be more important from the point of view of nonlinear optics. The most significant differences are a consequence of protonation.

We computed the elongation of the C−N and C−C bonds, $\langle R_{av} - R_{opt}\rangle$, ($R_{opt}(N - C) = 1.334$ Å, $R_{opt}(C - C) = 1.388$ Å),[66] using the DFT/B3LYP optimized geometries. Protonation leads to a significant elongation of the C−N bonds in the pyridyl rings: the average value of this elongation for the neutral molecules is 0.003 Å and increases to 0.020 Å for the protonated molecules. This effect follows the large increase in the hyperpolarizability values.

The mean deviation of the C−C bond lengths from their average value, $\langle \Delta r\rangle_{C-C}$, which was already identified as relevant for dipolar molecules,[9−11] is superimposed with the C−N bond elongation. Figure 7 presents a plot of $\langle \Delta r\rangle_{C-C}$ and $\langle \beta_{HR}\rangle$ values. Since the molecules in each series differ only on the N site in the pyridyl rings, only the C−C bonds in the pyridyl rings and the bonds connecting the pyridyl rings to the conjugation bridge were considered. In fact, the bond length alternation in the central ring is almost negligible, with a maximum of $\langle \Delta r\rangle = 0.004$ Å. Within each series $\langle \Delta r\rangle_{C-C}$ follows very closely the hyperpolarizability values, with maxima for the protonated **1a** and **2a** molecules. It is possible that a larger $\langle \Delta r\rangle_{C-C}$ or C−N elongation would increase further the hyperpolarizability. The ideal value determined by Marder[67] for push−pull polyenes is $0.03 < \langle \Delta r\rangle < 0.05$ Å.

Protonation enhances the bond length alternation for molecules **T1a**, **T1b**, **T2a**, and **T2b** and has the opposite effect on molecules **T1c** and **T2c**. However, the N−C elongation causes the hyperpolarizability of the protonated molecules to be larger even for the latter molecules. This indicates that the two structure related effects that influence the hyperpolarizability values, C−N bond elongation due to protonation and the variation of $\langle \Delta r\rangle_{C-C}$ with the N site, happen mainly within the pyridyl rings.

3.3.2. D Series. In the case of the **D** series, the three methods used to optimize the molecular geometries predict different structures. In particular for the **D1** series, PM3 and PM6 methods predict respectively, on plane and off-plane pyridyl rings, which leads also to different values of hyperpolarizability as will be described below. DFT/B3LYP geometries for the neutral **D1** molecules are close to PM3 results. Although in the protonated case DFT/B3LYP geometries present also off-plane pyridyl rings, the deviations from planarity are smaller than 30°, whereas PM6 geometries show deviations close to 90°. The computed dihedral angles are summarized in Table 3.

Table 3. Pyridyl-Central Benzene Dihedral Angle[a]

	neutral			protonated		
	B3LYP	PM3	PM6	B3LYP	PM3	PM6
1a	−179	180	−12	156	180	86
1b	171	180	82	131	180	83
1bb	170	180	81	133	180	96
1c	179	180	166	138	180	81
1cc	176	180	140	132	180	61
2a	110	96	41	111	−122	72
2b	98	71	115	100	126	102
2bb	92	75	33	90	−120	103
2c	117	125	137	91	−120	59
2cc	115	123	94	93	−77	44

[a] In degrees, computed within DFT/B3LYP, for the **D** series.

We will focus from now on only on the DFT/B3LYP results. The **D1** neutral molecules are mainly planar, with pyridyl ring torsion angles below 3°. Upon protonation, the distortion increases to values around 50°. **D1** is an exception, presenting an almost planar geometry. In the case of the **D2** series, due to steric crowding, the CH_3 group forces the pyridyl rings to be almost perpendicular to the central benzene ring, and protonation does not lead to significant changes on the torsion angles.

As the hyperpolarizability values of the **T** molecules were well correlated with structural parameters, we looked for other structural parameters that could explain the differences between the **T** and **D** series. **T1** and **T2** molecules are mainly planar, whereas **D1** molecules are planar and **D2** molecules have the pyridyl rings tilted with respect to the central benzene ring plane. This means that the stronger CH_3 electron donor character of the **D2** series, which was expected to enhance its hyperpolarizability, is somehow canceled by the rotation of the pyridyl rings due to the same CH_3 groups. The relation between the deviation from planarity and the hyperpolarizability values can be seen in Figure 8. As the dihedral angle deviates from 180°, the computed β values decrease.

We compared again the hyperpolarizability values with the $\langle \Delta r\rangle$ of the pyridyl rings. For the neutral molecules, $\langle \Delta r\rangle$ shows small variations, with values between 0.007 and 0.009 Å. In this case the modulation of hyperpolarizability follows very closely the variations of the dihedral angle. In the charged molecules, $\langle \Delta r\rangle$ ranges from 0.009 to 0.022 Å. The three properties, dihedral angle, $\langle \Delta r\rangle$, and hyperpolarizability follow the same trend, revealing the effect of the two structural parameters in the calculated hyperpolarizability values.

The calculated values suggest that, independently of the bond order present in the conjugation bridge between the donor and acceptor groups, hyperpolarizability is somehow controlled by the planarity of the molecules, the donor and acceptor strengths, and the bond length alternation. All the **T** molecules are planar, and therefore the hyperpolarizability values are determined by the donor and acceptor strengths (series **T1** vs series **T2**) and, within each series, by the C−C bond length alternation. For the **D** series, the dependence on the pyridyl dihedral angle can mask the increase of the donor−acceptor strength.

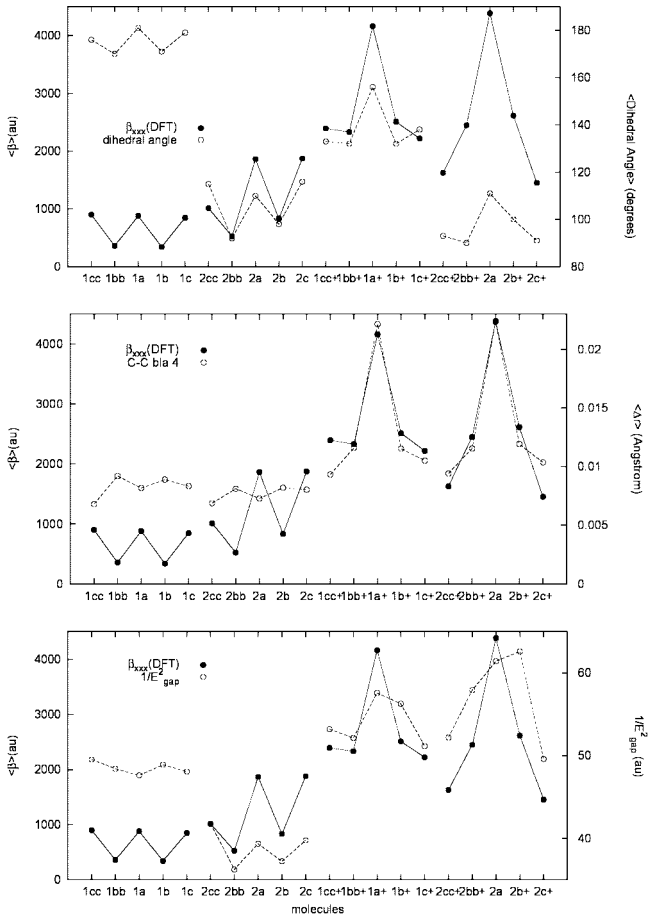

Figure 8. Torsion angles (top), C−C bond length deviation (center), and energy gaps (bottom) calculated within DFT/B3LYP for the **D** series.

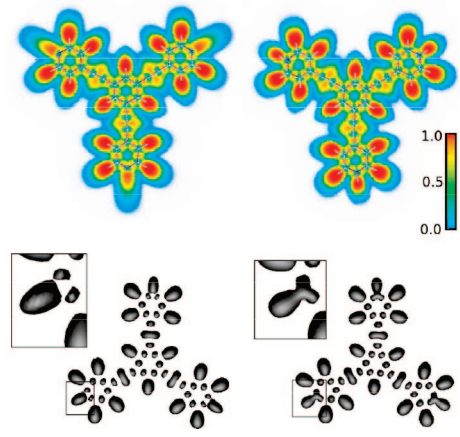

Figure 9. ELF for the z=0 slab (top) and ELF=0.75 isosurface (bottom) for neutral (left) and protonated (right) **T1a** molecule.

3.4. Electron Localization Function. The origin of the N−C bond elongation is clarified by the analysis of the Electron Localization Function (ELF). Figure 9 shows the ELF, calculated for the neutral and protonated **T1a** molecule. In both cases there is a regular alternation between the maxima (bonds) and minima (nuclear sites, except H) of the ELF along the molecular plane. The C≡C triple bond in the conjugation bridge is clearly seen as a characteristic torus around the bond axis. The main difference appears in the pyridyl rings. For the neutral molecule the N lone pair is seen as a diffuse ELF gradient (Figure 9, left), whereas in the protonated molecule ELF presents a higher and more constant value around the H and N nuclei (Figure 9, right). A very similar analysis can be made for all the other **T** series molecules. The same happens for the **D** series. Again, the main difference appears in the pyridyl rings. For the neutral molecules the N lone pair is seen as a diffuse ELF gradient, even more diffuse than in the **T** series, whereas in the protonated molecules ELF presents a higher and more constant value around the H and N nuclei.

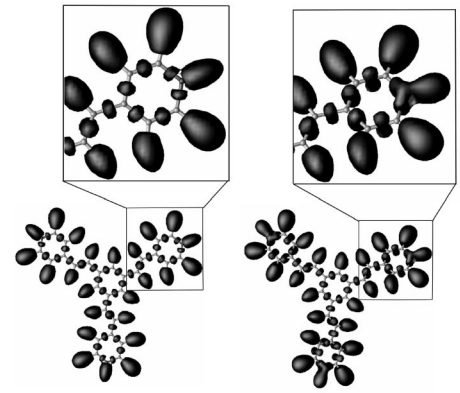

Figure 10. 0.75 ELF isosurface for neutral (left) and protonated (right) **D1a** molecule.

One way of optimizing the first hyperpolarizability, that has already proved to be successful, is the localization of states obtained through a bump on the potential energy.[68] This causes a modulation of conjugation, and the system becomes closer to the three-level model system. A similar effect can be seen in Figures 9 and 10, in which the isosurface ELF=0.75, corresponding to a considerably high electron localization, is plotted. In the neutral molecule, the isosurface corresponding to the N lone pair does not reach the N site (Figures 9 and 10, left). The charged molecule, however, presents an isosurface that encompasses the H and N nuclei (Figures 9 and 10, right). Therefore we can conclude that protonation results in an increase of the electron localization around N, attracting part of the electrons of the N−C bond. As a consequence, the N−C bond order decreases and the bond length increases, leading to a decrease of the conjugation of the pyridyl ring and a modulation of the conjugation of the system.

3.5. Wave Functions. Figure 11 shows the Kohn−Sham HOMO and LUMO orbitals for the neutral and protonated **T1a** molecule, computed with the Octopus code, as an example of the general behavior. The highest occupied energy levels are distributed by a set of two almost degenerate orbitals and another set of three orbitals with slightly lower energies. The neutral molecules show two unoccupied orbitals above HOMO with very similar energies, whereas the protonated molecules LUMO shows a set of three unoccupied orbitals. LUMO orbitals, both in the neutral and charged cases, extend over the whole molecule allowing the charge to travel from the donor to the acceptor fragments, a necessary condition for a large hyperpolarizability. Protonation seems to modify the HOMO orbitals. In the neutral case, three of the five highest occupied orbitals do not extend

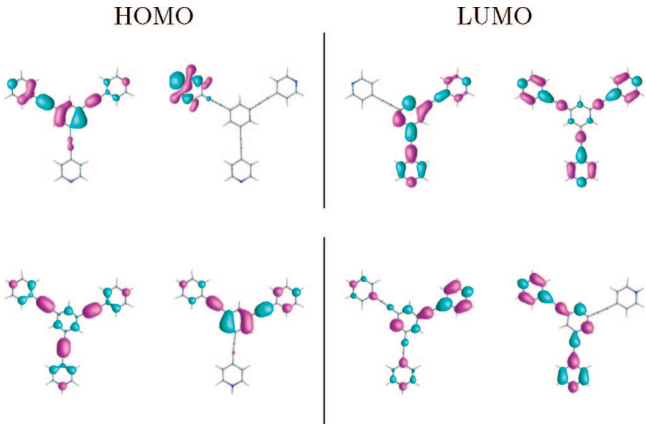

Figure 11. Kohn−Sham orbitals for neutral (top) and protonated (bottom) **1a** molecules. Symmetry related degenerate orbitals are not shown.

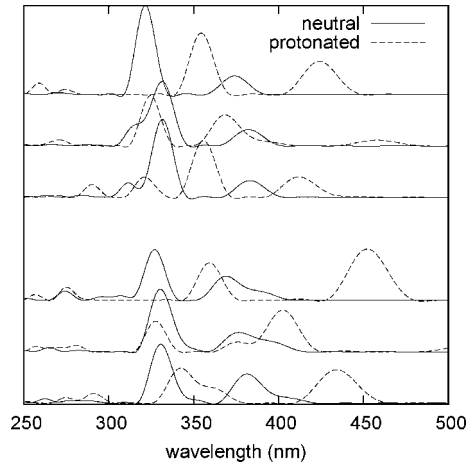

Figure 12. Calculated absorption spectra for, from top to bottom, **T1a**, **T1b**, **T1c**, **T2a**, **T2b**, and **T2c**. The solid (dashed) lines correspond to the neutral (protonated) molecules.

beyond the pyridyl rings, reducing the possibility of charge transfer, whereas in the charged case the wave functions extend over the whole molecule.

3.6. Linear Response. In Figure 12 we present the absorption spectra computed for the **T** molecules, in the neutral and charged forms (as, to our knowledge, no experimental absorption spectra exist for the **D** molecules, we will only discuss our results for the **T** series). The neutral molecules show a first peak (set of peaks in the case of **T1b**) between 300 and 350 nm and a less intense structure between 350 and 400 nm. For molecules **T1a**, **T1c**, **T2a**, and **T2c** protonation causes a shift of the spectrum toward higher wavelengths, consistent with the decrease in E_{gap}. It also leads to an increase of the peak separation and a decrease of the difference in magnitude of the two major absorption peaks. The molecules **T1b** and **T2b** show a slightly different behavior. The shift due to protonation, contrary to the decrease of E_{gap}, is small and toward lower wavelengths, indicating other transitions other than HOMO−LUMO.

For the **T2** series there is a shoulder at the right-hand side of the peak at higher wavelength which can be explained by the energy distribution of the levels just below HOMO. For the charged molecules, there is a shift of the same peak toward higher wavelengths: from **T1a** to **T2a**, the peak at 425 nm is shifted to 450 nm; from **T1b** to **T2b** the peak at 370 goes to 400 nm. These results are in good agreement with the experimental results which report, for the protonated forms of **T1c**, **T2a**, and **T2c**, broader, red-shifted absorption bands with high molar absorptivities, when compared to the neutral forms.[37,38] Our results show, however, peaks slightly shifted toward higher wavelengths than the experimental values, possibly due to solvent effects.

The two main peaks of the absorption spectra of the neutral molecules can be attributed to transitions between the HOMO states and the first and second sets of unoccupied states. The eigenvalue differences between HOMO and LUMO states range from 2.7 to 2.9 eV (459−427 nm) and between HOMO and LUMO+1 states from 3.0 to 3.4 eV (413−365 nm). This explains the splitting between the two main peaks of the absorption spectra, although it does not give their exact location. For the protonated molecules, the two main peaks correspond to transitions from the two sets of highest energy occupied states. The HOMO−LUMO eigenvalue differences range from 2.5 to 2.8 eV (496−443 nm), and the HOMO-1−LUMO gap ranges from 3.1 to 3.3 eV (376−400 nm), in agreement with the red-shifted absorption spectra of the protonated molecules.

4. Interplay between Geometric and Electronic Properties

To date, the vast majority of effective chromophores, concerning the electro-optic activity, are planar conjugated π-electron systems with electron-donor and-acceptor moieties at their ends. As mentioned above, these chromophores exhibit a dominant intramolecular charge-transfer transition from the ground-state to the first excited-state and produce effective polarization along the π-conjugated axis. Recent results[69−72] suggest that molecules with twisted π-electron systems bridging donor (D) and acceptor (A) substituents exhibit large hyperpolarizabilities. The twist-induced reduction in D-π-A conjugation leads to aromatic stabilization and formal charge-separated zwitterionic ground states, relatively low-energy optical excitations, and large dipole moment changes from the ground state to the first excited-state.

In order to study in more detail the interplay between the molecular structures and the electronic properties we computed the **T** series hyperpolarizability for several values of the pyridyl rings torsion angle and of the $\langle \Delta r \rangle$, without a previous geometry relaxation. In Figure 13 we plot β_{xxx} and $1/E_{gap}^2$ for different torsion angles for the neutral and protonated **T1a** molecule. Contrarily to what happens to the chromophores reported by Kang et al.[69] the increase of the torsion angle decreases significantly the hyperpolarizability: β_{xxx} is 4 to 5.5 times larger in the case of the planar geometries than when the pyridyl rings are perpendicular to the central ring. The same happens to $1/E_{gap}^2$. However the values change in a smaller range: for the neutral molecules $1/E_{gap}^2$ is 1.5 times larger for the planar geometry than for the geometry with a 90° torsion angle, whereas for the protonated molecule there is no significant variation.

We also varied the $\langle \Delta r \rangle$ values for the protonated form of **T1a** by changing the length of the C−C bonds in the pyridyl rings. In doing so, $\langle \Delta r \rangle$ ranges from the value of the

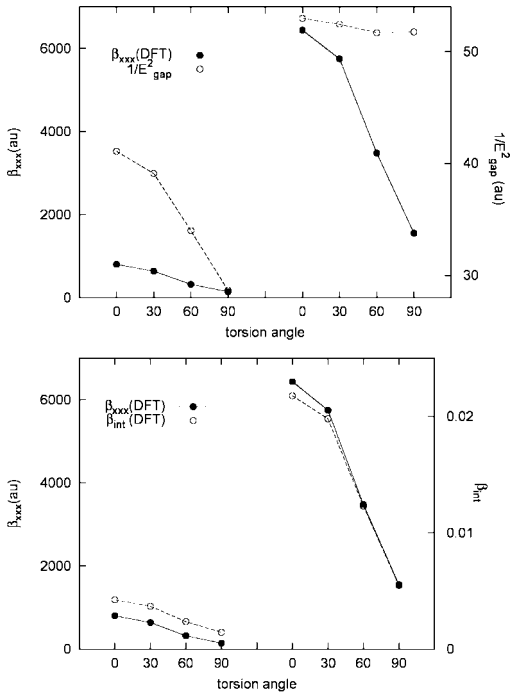

Figure 13. In the upper graph we plot β_{xxx} and $1/E^2_{gap}$ calculated for different torsion angles for the molecule **T1a**, both in the neutral (left) and in the protonated (right) case. In the second graph we plot the absolute and the intrinsic value of the hyperpolarizability. The intrinsic and absolute hyperpolarizability follow the same trend, as expected, since neither the size of the molecule nor the number of π electrons change.

optimized geometry to less than half of that valuer. However, there are no significant changes in the hyperpolarizability values neither in the energy gaps.

5. Conclusions

Ab initio calculations correctly reproduce the large hyperpolarizabilities of the charged octopolar molecules, including the significant increase of first hyperpolarizability upon protonation reported in previous studies. The HOMO−LUMO energy gap decreases upon protonation, its inverse square being related to the β values, in agreement with the three-level model. Linear response TDDFT calculations are also in good agreement with the experimental absorption spectra, reproducing the bathochromic shift of the peaks upon protonation, due to the gap reduction mentioned above. DFT/B3LYP calculations allowed the identification of the levels involved in the transitions.

Ab initio hyperpolarizability values of the protonated octopolar **D** molecules follow closely the values calculated for the corresponding **T** molecules, both in the neutral and protonated cases. The calculated values suggest that, independently of the bond order present in the conjugation bridge between the donor and acceptor groups, hyperpolarizability is mainly controlled by the planarity of the molecules, the donor and acceptor strengths, and the bond length alternation. All the **T** molecules are planar, and therefore the hyperpolarizability values are determined by the donor and acceptor strengths and, to a lesser degree, by the C−C bond length alternation. For the **D** series, the dependence on the pyridyl torsion angle can mask the increase of the donor−acceptor strength.

Changes in the molecules' geometries were also analyzed, and a correlation between the molecular structures and the first hyperpolarizability, β, was suggested. Several parameters affecting β were identified: i) the C−N bond elongation upon protonation, which follows from the localization of the electrons around H and N, as seen in the ELF plots, and accompanies the increase of the β values; ii) the planarity of the molecules; and iii) the C−C bond length alternation, already identified as relevant for dipolar molecules. To test these effects we computed the hyperpolarizability for several constrained geometries, thus confirming the importance of planarity on the hyperpolarizability values.

Acknowledgment. This work was supported by Fundação para a Ciência e a Tecnologia (FCT), within the project POCI/FIS/58309/2004.

References

(1) Zyss, J.; Ledoux, I. *Chem. Rev.* **1994**, *94*, 77.

(2) *Nonlinear Optics of Organic Molecules and Polymers*; Nalwa, H. S., Miyata, S., Eds.; CRC Press: FL, 1997.

(3) Kuzyk, M. G. *SPIE Proc.* **1997**, 3147.

(4) Marder, S. R.; Perry, J. W.; Schaefer, P. W. *Science* **1989**, *245*, 626.

(5) Clays, K.; Wostyn, K.; Olbrechtes, G.; Persoons, A.; Watanabe, A.; Nogi, K.; Duan, X.-M.; Okada, S.; Oikawa, H.; Nakanishi, H.; Brédas, J. L. *J. Opt. Soc. Am. B* **2000**, *17*, 256.

(6) Marder, S. R. *Chem. Commun.* **2006**, 131.

(7) Marder, S. R.; Beratan, D. N.; Cheng, L.-T. *Science* **1991**, *252*, 103.

(8) Marder, S. R.; Gorman, C. B.; Tiemann, B. G.; Cheng, L.-T. *J. Am. Chem. Soc.* **1993**, *115*, 3006.

(9) Gorman, C. B.; Marder, S. R. *Proc. Natl. Acad. Sci. U.S.A.* **1993**, *90*, 11297.

(10) Marder, S. R.; Perry, J. W.; Tiemann, B. G.; Gorman, C. B.; Biddle, S. L.; Gilmour, S.; Bourhill, G. *J. Am. Chem. Soc.* **1993**, *115*, 2524.

(11) Bourhill, G.; Brédas, J.-L.; Cheng, L.-T.; Marder, S. R.; Meyers, F.; Perry, J. W.; Tiemann, B. G. *J. Am. Chem. Soc.* **1994**, *116*, 2619.

(12) Feringa, B. L. *Molecular Switches*; Wiley-VCH: Weinheim, 2001.

(13) Irie, M. *Chem. Rev.* **2000**, *100*, 1683.

(14) Coe, B. J. *Chem.--Eur. J.* **1999**, *5*, 2464.

(15) Asselberghs, I.; Clays, K.; Persoons, A.; Ward, M. D.; McCleverty, J. *J. Mater. Chem.* **2004**, *14*, 2831.

(16) Rurack, K. *Spectrochim. Acta, Part A* **2001**, *57*, 2161.

(17) Meyers, F.; Marder, S. R.; Perry, J. W. Viley-VCH: Weinheim, 1998.

(18) Verbiest, T.; Houbrechts, S.; Kauranen, M.; Clays, C.; Persoons, A. *J. Mater. Chem.* **1997**, *7*, 2175.

(19) Pond, S. J. K.; Tsutsumi, O.; Rumiand, M.; Kwon, O.; Zojerand, E.; Brédas, J. L.; Marder, S. R.; Perry, J. W. *J. Am. Chem. Soc.* **2004**, *126*, 9291.

(20) Kim, H. M.; Jeonga, M.-Y.; Ahn, H. C.; Jeon, S.-J.; Cho, B. R. *J. Org. Chem.* **2004**, *69*, 5749.

(21) Werts, M. H. V.; Gmouh, S.; Mongin, O.; Pons, T.; Blanchard-Desce, M. *J. Am. Chem. Soc.* **2004**, *126*, 16294.

(22) Asselberghs, I.; Zhao, Y.; Clays, K.; Persoons, A.; Comito, A.; Rubin, Y. *Chem. Phys. Lett.* **2002**, *364*, 279.

(23) Zyss, J. *Nonlinear Opt.* **1991**, *1*, 3.

(24) Zyss, J.; Pecaut, J.; Levy, J. P.; Masse, R. *Acta Crystallogr., Sect. B: Struct. Sci.* **1993**, *49*, 334.

(25) Ledoux, I.; Zyss, J.; Siegel, J.; Brienne, J.; Lehn, J. M. *Chem. Phys. Lett.* **1990**, *440*, 172.

(26) Ray, P. C.; Das, P. K. *Chem. Phys. Lett.* **1995**, *244*, 153.

(27) Chao, B. R.; Park, S. B.; Lee, S. J.; Son, K. H.; Lee, S. H.; Kang, T. I.; Cho, M.; Jeon, S.-J. *J. Am. Chem. Soc.* **2001**, *123*, 6421.

(28) Hennrich, G.; Asselberghs, I.; Clays, K.; Persoons, A. *J. Org. Chem.* **2004**, *69*, 5055.

(29) Traber, B.; Wolff, J. J.; Rominger, F.; Oeser, T.; Gleiter, R.; Goebel, M.; Wortmann, R. *Chem.--Eur. J.* **2004**, *10*, 1227.

(30) Stadler, S.; Brauchle, Ch.; Brandl, S.; Gompper, R. *Chem. Mater.* **1996**, *8*, 676.

(31) Luo, Y.; Cesar, A.; Agren, H. *Chem. Phys. Lett.* **1996**, *252*, 389.

(32) Zhu, W.; Wu, G.-S. *J. Phys. Chem. A* **2001**, *105*, 9568.

(33) Dhenaut, C.; Ledoux, I.; Samuel, I. D. W.; Zyss, J.; Bourgault, M.; Bozec, H. L. *Nature* **1995**, *374*, 339.

(34) Viau, L.; Bidault, S.; Maury, O.; Brasselet, S.; Ledoux, I.; Zyss, J.; Ishow, E.; Nakatani, K.; Le Bozec, H. *J. Am. Chem. Soc.* **2004**, *126*, 8386.

(35) Sporer, C.; Marcen, S.; Montant, S.; Létard, J. F.; Freysz, E.; Rovira, C.; Ratera, I.; Ruiz-Molina, D.; Veciana, J. *Polyhedron* **2003**, *22*, 1851.

(36) Cifuentes, M. P.; Humphrey, M. G. *J. Organomet. Chem.* **2004**, *689*, 3968.

(37) Asselberghs, I.; Hennrich, G.; Clays, K. *J. Phys. Chem. A* **2006**, *110*, 6271.

(38) Oliva, M. M.; Casado, J.; Navarrete, J. T. L.; Hennrich, G.; Delgado, M. C. R. *J. Phys. Chem. C* **2007**, *111*, 18778.

(39) Ray, P. C.; Leszczynski, J. *Chem. Phys. Lett.* **2004**, *399*, 162.

(40) Ray, P. C.; Leszczynski, J. *J. Phys. Chem. A* **2005**, *109*, 6689.

(41) Ray, P. C. *Chem. Phys. Lett.* **2004**, *394*, 354.

(42) Ray, P. C. *Chem. Phys. Lett.* **2004**, *395*, 269.

(43) Becke, A. D. *J. Chem. Phys.* **1993**, *98*, 5648.

(44) Stephens, P. J.; Devlin, F. J.; Chablowski, C. F.; Frisch, M. J. *J. Phys. Chem.* **1994**, *98*, 11623.

(45) Schmidt, M. W.; Baldridge, K. K.; Boatz, J. A.; Elbert, S. T.; Gordon, M. S.; Jensen, J. H.; Koseki, S.; Matsunaga, N.; Nguyen, K. A.; Su, S.; Windus, T. L.; Dupuis, M.; Montgomery, J. A., Jr. *J. Comput. Chem.* **1993**, *14*, 1347.

(46) Krishnan, R.; Binkley, J. S.; Seeger, R.; Pople, J. A. *J. Chem. Phys.* **1980**, *72*, 650.

(47) Castro, A.; Appel, H.; Oliveira, M.; Rozzi, C. A.; Andrade, X.; Lorenzen, F.; Marques, M. A. L.; Gross, E. K. U.; Rubio, A. *Phys. Status Solidi B* **2006**, *243*, 2465.

(48) Marques, M. A. L.; Castro, A.; Bertsch, G. F.; Rubio, A. *Comput. Phys. Commun.* **2003**, *151*, 60.

(49) Becke, A. D.; Edgecombe, K. E. *J. Chem. Phys.* **1990**, *92*, 5397.

(50) Stewart, J. J. P. *Stewart Computational Chemistry*; Colorado Springs, CO, U.S.A. http://openmopac.net (accessed Feb 2007).

(51) Stewart, J. J. P. *J. Comput. Chem.* **1989**, *10*, 209.

(52) Stewart, J. J. P. *J. Comput. Chem.* **1989**, *10*, 221.

(53) Stewart, J. J. P. *J. Comput. Chem.* **1991**, *12*, 320.

(54) Stewart, J. J. P. *J. Mol. Model.* **2004**, *10*, 155.

(55) Stewart, J. J. P. *J. Mol. Model.* **2007**, *13*, 1173.

(56) Zhou, J.; Kuzyk, M. G.; Watkins, D. S. *Opt. Lett.* **2006**, *31*, 2891.

(57) Benkova, Z.; Sadlej, A. J.; Oakes, R. E.; Bell, S. E. J. *J. Comput. Chem.* **2005**, *26*, 145.

(58) Benkova, Z.; Sadlej, A. J.; Oakes, R. E.; Bell, S. E. J. *Theor. Chem. Acc.* **2005**, *113*, 238.

(59) Sałek, P.; Helgaker, T.; Vahtras, O.; Grenz, H. A.; Jonsson, D.; Gauss, J. *Mol. Phys.* **2005**, *103*, 439.

(60) Cohen, A. J.; Handy, N. C.; Tozer, D. J. *Chem. Phys. Lett.* **1999**, *303*, 391.

(61) Sałek, P.; Vahtras, O.; Helgaker, T.; Ågren, H. *J. Chem. Phys.* **2002**, *117*, 9630.

(62) Teng, C. C.; Garito, A. F. *Phys. Rev. B* **1983**, *28*, 6766.

(63) Allin, S. B.; Leslie, T. M.; Lumpkin, R. S. *Chem. Mater.* **1996**, *8*, 428.

(64) Lee, S. H.; Park, J. R.; Jeong, M.-Y.; Kim, H. M.; Li, S.; Song, J.; Ham, S.; Jeon, S.-J.; Cho, B. R. *Chem. Phys. Chem* **2006**, *7*, 206.

(65) Joffre, M.; Yaron, D.; Silbey, R. J.; Zyss, J. *J. Chem. Phys.* **1992**, *97*, 5607.

(66) Krygowski, T.; Cyrański, M. *Tetrahedron* **1995**, *52*, 10225.

(67) Marder, S. R.; Gorman, C. B.; Meyers, F.; Perry, J. W.; Bourhill, G.; Brédas, J.-L.; Pierce, B. M. *Science* **1994**, *265*, 632.

(68) Pérez-Moreno, J.; Zhao, Y.; Clays, K.; Kuzyk, M. G. *Opt. Lett.* **2007**, *32*, 59.

(69) Kang, H.; Facchetti, A.; Jiang, H.; Cariati, E.; Righetto, S.; Ugo, R.; Zuccaccia, C.; Macchioni, A.; Stern, C. L.; Liu, Z.; Ho, S.-T.; Brown, E. C.; Ratner, M. A.; Marks, T. J. *J. Am. Chem. Soc.* **2007**, *129* (11), 3267–3286.

(70) Keinan, S.; Zojer, E.; Brédas, J.-L.; Ratner, M. A.; Marks, T. J. *THEOCHEM* **2003**, *633*, 227.

(71) Albert, I. D. L.; Marks, T. J.; Ratner, M. A. *J. Am. Chem. Soc.* **1998**, *120*, 11174.

(72) Albert, I. D. L.; Marks, T. J.; Ratner, M. A. *J. Am. Chem. Soc.* **1997**, *119*, 3155.

CT800464T

JCTC Journal of Chemical Theory and Computation

Excitation Energies in Time-Dependent (Current-) Density-Functional Theory: A Simple Perspective

C. A. Ullrich*

Department of Physics and Astronomy, University of Missouri, Columbia, Missouri 65211

Received November 24, 2008

Abstract: This paper gives a simple and pedagogical explanation, using density matrices of two-level systems, how to calculate excitation energies with time-dependent density-functional theory. The well-known single-pole approximation for excitation energies is derived here in an alternative way and extended to time-dependent current-density-functional theory.

1. Introduction

Time-dependent density-functional theory (TDDFT)[1] is a universal approach to electronic dynamics and excitations. Just like ground-state density-functional theory (DFT), where the rigorous theorems by Hohenberg, Kohn, and Sham[2,3] prove a one-to-one correspondence between ground-state densities and potentials, there is a similar existence theorem for TDDFT, due to Runge and Gross,[4] which establishes the time-dependent density as a fundamental variable.

Many of the concepts that were pioneered by John Perdew for ground-state DFT have now begun to make an important impact also in TDDFT: two prime examples are the self-interaction correction[5] and the discontinuity of the exchange-correlation (XC) potential upon change of particle number.[6] These concepts now find an important place in the discussion of the dynamics of electronic systems.[7−11] Therefore, it seems not inappropriate that the following article, dedicated to honor John Perdew's scientific achievements, addresses a topic in the area of TDDFT.

Many areas in science require an understanding of the electronic excitations of atomic or molecular systems, nanostructures, mesoscopic systems, or bulk materials.[12−15] A wide variety of spectroscopic techniques is being used to characterize the electronic structure and dynamics of these systems by probing their excitation spectra. The performance of any nanoelectronic device, such as a molecular junction, is dominated by its electronic excitation characteristics.[16,17]

The usage of TDDFT as a practical tool to calculate excitation energies started in the mid-90s with the groundbreaking work of Petersilka et al.[18] and Casida.[19] In the Casida-formalism, the excitation energies are obtained from the following eigenvalue problem (in this paper we use Hartree atomic units, $e = m = \hbar = 1$):

$$\begin{pmatrix} \mathbf{A} & \mathbf{K} \\ \mathbf{K}^* & \mathbf{A}^* \end{pmatrix} \begin{pmatrix} \mathbf{X} \\ \mathbf{Y} \end{pmatrix} = \omega \begin{pmatrix} -\mathbf{1} & \mathbf{0} \\ \mathbf{0} & \mathbf{1} \end{pmatrix} \begin{pmatrix} \mathbf{X} \\ \mathbf{Y} \end{pmatrix} \tag{1}$$

Where the matrices $\mathbf{A}$ and $\mathbf{K}$ are defined as follows:

$$A_{ia\sigma,i'a'\sigma'} = \delta_{ii'}\delta_{aa'}\delta_{\sigma\sigma'}(\varepsilon_{a\sigma} - \varepsilon_{i\sigma}) + K_{ia\sigma,i'a'\sigma'} \tag{2}$$

and

$$K_{ia\sigma,i'a'\sigma'} = \int \mathrm{d}^3r \int \mathrm{d}^3r'\, \varphi^*_{i\sigma}(\mathbf{r})\varphi_{a\sigma}(\mathbf{r})\Big[\frac{1}{|\mathbf{r}-\mathbf{r}'|} + f_{\mathrm{xc},\sigma\sigma'}(\mathbf{r},\mathbf{r}',\omega)\Big]\varphi_{i'\sigma'}(\mathbf{r}')\varphi^*_{a'\sigma'}(\mathbf{r}') \tag{3}$$

Here, $\varphi_{i\sigma}$ and $\varepsilon_{i\sigma}$ are the Kohn−Sham orbitals and eigenvalues coming from a self-consistent ground-state DFT calculation; we use the standard convention that i, i',... and a, a',... are indices of occupied and unoccupied orbitals, respectively. The term $f_{\mathrm{xc},\sigma\sigma'}(\mathbf{r}, \mathbf{r}', \omega)$ is the so-called XC kernel,[20] defined as the Fourier transform of

$$f_{\mathrm{xc},\sigma\sigma'}(\mathbf{r},t,\mathbf{r}',t') = \left.\frac{\delta V_{\mathrm{xc},\sigma}(\mathbf{r},t)}{\delta n_{\sigma'}(\mathbf{r}',t')}\right|_{n_\sigma(\mathbf{r},t)=n_{0\sigma}(\mathbf{r})} \tag{4}$$

where $V_{\mathrm{xc},\sigma}(\mathbf{r}, t)$ is the XC potential of TDDFT, and $n_{0\sigma}(\mathbf{r})$ is the ground-state spin density. In general, $f_{\mathrm{xc},\sigma\sigma'}(\mathbf{r}, \mathbf{r}', \omega)$ is a frequency-dependent quantity, but in practice, it is often approximated using frequency-independent expressions. This is known as the adiabatic approximation.

The eigenvalues ω of eq 1 are, in principle, the *exact* excitation energies of the system, provided one starts from an exact Kohn−Sham ground-state calculation and then uses the exact $f_{\mathrm{xc},\sigma\sigma'}$. In practice, of course, static and dynamical

* E-mail: ullrichc@missouri.edu.

10.1021/ct800507m CCC: $40.75
Published on Web 02/02/2009

XC functionals need to be approximated. The formalism of eqs 1−3 can also be recast in the shape of an eigenvalue problem for the squares of the excitation energies:

$$\sum_{a'i'\sigma'} [\delta_{ii'}\delta_{aa'}\delta_{\sigma\sigma'}\omega_{ia\sigma}{}^2 + 2\sqrt{\omega_{ia\sigma}\omega_{i'a'\sigma'}}K_{ia\sigma,i'a'\sigma'}]\xi_{a'i'\sigma'} = \omega^2\xi_{ai\sigma} \tag{5}$$

where $\omega_{ia\sigma} = \varepsilon_{a\sigma} - \varepsilon_{i\sigma}$.

This TDDFT formalism for excitation energies has become very popular for practical applications, due to its unique balance between accuracy and efficiency, allowing the user to study systems that would be impossible to treat with traditional wave function methods, for example in all-electron studies of the photochemistry of large biomolecules.[21,22] The broad spectrum of applications of TDDFT for excited states has been recently reviewed by Elliott et al.[23] From the large body of available literature, the following trends for molecules have emerged. Transition frequencies, calculated with standard gradient-corrected XC functionals, are typically good to within 0.4 eV. Excited-states structural properties such as bond lengths, vibrational frequencies, and dipole moments are essentially as good as those of ground-state calculations (about 1% for bond lengths and about 5% for dipoles and vibrational frequencies). Most importantly for large systems, the computational costs scale as N^3 versus N^5 for wave function methods of comparable accuracy.

While there exist efficient iterative algorithms for solving the full eigenvalue problem (1), it is nevertheless useful to consider approximations, since these can lead to further insight and sometimes even better results. One such method is the Tamm−Dancoff approximation (TDA), which has been known for a long time in nuclear physics.[24] The TDA can be viewed as an approximation to the so-called random-phase approximation (RPA), limited to single particle−hole pairs that are propagating forward in time. In the context and language of quantum chemistry, this approximation is formally identical to the configuration interaction singles (CIS) method. The TDA has been adopted in TDDFT,[25] but with a somewhat different meaning than originally in nuclear physics: one simply neglects the off-diagonal matrices **K** in eq 1 but keeps the matrix **A** as it is; see eq 2. This results in the simpler eigenvalue problem

$$\mathbf{AX} = \omega_{\mathrm{TDA}}\mathbf{X} \tag{6}$$

This TDDFT/TDA approach has some technical advantages over the full TDDFT linear response formalism away from ground-state equilibrium geometry, as shown by Casida et al.[26] The physical meaning of the TDDFT/TDA will become clear when we discuss two-level systems.

In an even more drastic approximation, eq 5 is truncated down to a 1×1 matrix. This yields the so-called small-matrix approximation (SMA),[27] which for spin-saturated systems is given by

$$\omega_{\mathrm{SMA}}{}^2 = \omega_{ia}{}^2 + 4\omega_{ia}K_{ia,ia} \tag{7}$$

This can be further approximated if the correction to the bare Kohn−Sham excitation energy $\omega_{ia\sigma}$ is small, which is known as single-pole approximation (SPA):[18,27]

$$\omega_{\mathrm{SPA}} = \omega_{ia} + 2K_{ia,ia} \tag{8}$$

This approximation can also be viewed as a TDA for a two-level system, as we shall show below.

The original derivation of the SPA[18] proceeded along a different line of thought. The excitation energies of a many-body systems can be represented as the poles of its density−density response function. If the excitation of interest is sufficiently well "isolated" from neighboring excitations, one can focus on a single pole of the response function—hence the name SPA. Carrying out a Laurent expansion in the TDDFT linear response equation then leads to eq 8, where $f_{\mathrm{xc},\sigma\sigma'}(\mathbf{r}, \mathbf{r}', \omega)$ in the matrix element $K_{ia,ia}$ is evaluated at the bare Kohn−Sham excitation energy $\omega_{ia\sigma}$. Evaluating $f_{\mathrm{xc},\sigma\sigma'}$ in eqs 7 and 8 self-consistently at the frequencies ω_{SMA} and ω_{SPA}, respectively, has been termed "dressed" SMA and SPA in the literature.[28] Needless to say, this distinction is irrelevant unless one uses a nonadiabatic approximation for $f_{\mathrm{xc},\sigma\sigma'}$.

It turns out that the SMA and SPA can perform surprisingly well for systems with well-separated excitations, such as simple closed-shell atomic systems[29] or semiconductor nanostructures such as quantum wells.[30,31] We will give a brief example at the end of this paper. From a practical point of view, the SMA and SPA might be seen as merely a curiosity—after all, even large molecular systems can be described with the full Casida TDDFT formalism without resorting to such drastic approximations. Instead, the main importance of the SMA and SPA is as analytical tools that give us insight into how the TDDFT linear response formalism works in combining Kohn−Sham single-particle excitations to form the true excitations.[18,27] Furthermore, they can be extended to treat more complicated processes where excitations involve two close-lying poles[32] or as starting point for the analysis of double or charge-transfer excitations.[28,33]

The main purpose of this paper is to present an alternative, more direct way to derive simplified TDDFT approaches to excitation energies such as SMA and SPA. Instead of starting from Casida's equations or the TDDFT linear response equation and eliminating all excitations except for a single pole, we will simply work with two-level Kohn−Sham systems from the very beginning. This has the advantage that the derivation is very transparent and does not require familiarity with linear response theory; only a basic knowledge of static DFT.

We will show that our two-level system derivation of the SMA and SPA can be extended to systems with phenomenological dissipation in a straightforward manner. Next, we will consider the case of time-dependent current-DFT (TDCDFT), where one deals with XC vector potentials coupling to currents. A generalization of the SMA and SPA for TDCDFT will be derived. To give an example, we will show results for intersubband plasmon excitations in doped quantum wells.

2. Excitation Energies of a Two-Level Kohn−Sham System

2.1. Scalar Potential. Let us consider a two-level system consisting of two orbitals $\varphi_1(\mathbf{r})$ and $\varphi_2(\mathbf{r})$ which are eigenstates of the static Kohn−Sham Hamiltonian

$$H^0 = -\frac{\nabla^2}{2} + V_{\text{ext}}(\mathbf{r}) + \int \mathrm{d}^3r' \frac{n_0(\mathbf{r}')}{|\mathbf{r} - \mathbf{r}'|} + V_{\text{xc}}[n_0](\mathbf{r}) \quad (9)$$

where V_{xc} is the static XC potential, a functional of the ground-state density $n_0(\mathbf{r})$. We assume that initially φ_1 is doubly occupied and φ_2 is empty, and both orbitals are chosen to be real. Now consider a weak perturbation $\lambda H'(\mathbf{r}, t)$ acting on the system. According to time-dependent perturbation theory, the time evolution of the system is given by

$$\varphi(\mathbf{r}, t) = c_1(t)\varphi_1(\mathbf{r}) + \lambda c_2(t)\varphi_2(\mathbf{r}) \quad (10)$$

Let us construct the density matrix of the system as follows:

$$\rho(t) = \begin{pmatrix} \rho_{11} & \lambda\rho_{12} \\ \lambda\rho_{21} & \lambda^2\rho_{22} \end{pmatrix} = \begin{pmatrix} |c_1|^2 & \lambda c_1 c_2^* \\ \lambda c_1^* c_2 & \lambda^2 |c_2|^2 \end{pmatrix} \quad (11)$$

where we explicitly indicate the order of the perturbation through orders of λ. The density matrix obeys the following equation of motion:

$$\dot{\rho} = -i[H, \rho] = -i[H^0 + \lambda H'(t), \rho] \quad (12)$$

Dropping terms of order λ^2, this yields the time evolution of the off-diagonal elements of the density matrix as follows:

$$\dot{\rho}_{12} = -i[(H^0_{11} - H^0_{22})\rho_{12} - H'_{12}\rho_{11}] \quad (13)$$

$$\dot{\rho}_{21} = i[(H^0_{11} - H^0_{22})\rho_{21} - H'_{21}\rho_{11}] \quad (14)$$

where $H^0_{11} = \int \mathrm{d}^3r\ \varphi_1(\mathbf{r})H^0\varphi_1(\mathbf{r})$ and similar for all other matrix elements of H^0 and H'. Since $\rho_{11} = 1 + \mathcal{O}(\lambda^2)$ and defining $H^0_{22} - H^0_{11} = \omega_{21}$ (the bare Kohn−Sham excitation energy), this simplifies to

$$\dot{\rho}_{12} = i[\omega_{21}\rho_{12} + H'_{12}] \quad (15)$$

$$\dot{\rho}_{21} = -i[\omega_{21}\rho_{21} + H'_{21}] \quad (16)$$

Next, we make the ansatz (which will be justified later)

$$\rho_{12}(t) = \tilde{\rho}_{12}(\omega)\mathrm{e}^{-i\omega t} + \tilde{\rho}_{12}(-\omega)\mathrm{e}^{i\omega t} \quad (17)$$

and similar for ρ_{21}, H'_{12}, and H'_{21}. This gives

$$-\omega\tilde{\rho}_{12}(\omega) = [\omega_{21}\tilde{\rho}_{12}(\omega) + \tilde{H}'_{12}(\omega)] \quad (18)$$

$$-\omega\tilde{\rho}_{21}(\omega) = -[\omega_{21}\tilde{\rho}_{21}(\omega) + \tilde{H}'_{21}(\omega)] \quad (19)$$

and an additional two equations for $\tilde{\rho}_{12}(-\omega)$ and $\tilde{\rho}_{21}(-\omega)$ which do not contain any new information. Adding eqs 18 and 19 gives

$$\tilde{\rho}_{12}(\omega) + \tilde{\rho}_{21}(\omega) = -\frac{\tilde{H}'_{12}(\omega)}{\omega_{21} + \omega} - \frac{\tilde{H}'_{21}(\omega)}{\omega_{21} - \omega} \quad (20)$$

Let us now consider the perturbing Hamiltonian:

$$H'(\mathbf{r}, \omega) = \int \mathrm{d}^3r' \left[\frac{1}{|\mathbf{r} - \mathbf{r}'|} + f_{\text{xc}}(\mathbf{r}, \mathbf{r}', \omega)\right]\delta n(\mathbf{r}', \omega) \quad (21)$$

where $\delta n(\mathbf{r}, \omega)$ is the density response. From eqs 10 and 11, we have

$$\delta n(\mathbf{r}, t) = 2|\varphi(\mathbf{r}, t)|^2 = 2\rho_{11}(t)\varphi_1(\mathbf{r})^2 + 2\lambda[\rho_{12}(t) + \rho_{21}(t)]\varphi_1(\mathbf{r})\varphi_2(\mathbf{r}) + 2\lambda^2\rho_{22}(t)\varphi_2(\mathbf{r})^2 \quad (22)$$

where the factor 2 comes from the double occupancy of $\varphi(\mathbf{r}, t)$. Taking the first-order term in λ and Fourier transforming, we get

$$\delta n(\mathbf{r}, \omega) = 2\varphi_1(\mathbf{r})\varphi_2(\mathbf{r})[\tilde{\rho}_{12}(\omega) + \tilde{\rho}_{21}(\omega)] \quad (23)$$

Notice that we do not consider an external perturbation, only the linearized Hartree and XC potentials. We are thus looking for an "eigenmode" of the system in a steady state. This justifies the ansatz (17) made above. We define the double matrix element [cf. eq 3]

$$K_{12,12}(\omega) = \int \mathrm{d}^3r \int \mathrm{d}^3r' \varphi_1(\mathbf{r})\varphi_2(\mathbf{r})\left[\frac{1}{|\mathbf{r} - \mathbf{r}'|} + f_{\text{xc}}(\mathbf{r}, \mathbf{r}', \omega)\right]\varphi_1(\mathbf{r}')\varphi_2(\mathbf{r}') \quad (24)$$

and eq 20 becomes

$$\tilde{\rho}_{12}(\omega) + \tilde{\rho}_{21}(\omega) = -2K_{12,12}(\omega)[\tilde{\rho}_{12}(\omega) + \tilde{\rho}_{21}(\omega)]\left[\frac{1}{\omega_{21} + \omega} + \frac{1}{\omega_{21} - \omega}\right] \quad (25)$$

Canceling $\tilde{\rho}_{12} + \tilde{\rho}_{21}$ on both sides results in

$$1 = -\frac{4\omega_{21}}{{\omega_{21}}^2 - \omega^2}K_{12,12}(\omega) \quad (26)$$

which gives the final result

$$\omega^2 = {\omega_{21}}^2 + 4\omega_{21}K_{12,12}(\omega) \quad (27)$$

This is the same as the "dressed" SMA, eq 7. From the point of view of a two-level system, our derivation shows that the SMA considers the excitation $1 \rightarrow 2$ (absorption) as well as the de-excitation $2 \rightarrow 1$ (stimulated emission). The SPA, eq 8, on the other hand, only includes the excitation $1 \rightarrow 2$ (it is obtained by ignoring the first pole in eq 25). In general, the TDA (6) ignores all de-excitations.

The formalism of this section can easily be extended to the spin-dependent case. Assuming, for simplicity, that the ground-state is spin-unpolarized, we find

$${\omega_\pm}^2 = {\omega_{21}}^2 + 2\omega_{21}[K_{12\sigma,12\sigma}(\omega) \pm K_{12\sigma,12\bar{\sigma}}(\omega)] \quad (28)$$

where the spin-dependent double matrix elements $K_{12\sigma,12\sigma'}(\omega)$ are defined in eq 3.

2.2. Scalar Potential with Phenomenological Dissipation. In many practical situations, it is desirable to introduce dissipation in a simple phenomenological manner.[34,35] Although this sounds easy enough, it is not straightforward

at all for the time-dependent Kohn−Sham equation, but if we work with the Kohn−Sham density matrix, all one needs to do is simply add a relaxation term to the equation of motion. For our two-level system, we have

$$\dot{\rho} = -i[H, \rho] - R \tag{29}$$

where

$$R = \begin{pmatrix} \dfrac{\rho_{11} - \rho_{11}^0}{T_1} & \dfrac{\rho_{12} - \rho_{12}^0}{T_2} \\ \dfrac{\rho_{21} - \rho_{21}^0}{T_2} & \dfrac{\rho_{22} - \rho_{22}^0}{T_1} \end{pmatrix} \tag{30}$$

T_1 and T_2 are phenomenological parameters whose physical meaning is a population relaxation time and a dephasing time. ρ_{jk}^0 are the equilibrium values of the density matrix; in our case, we have $\rho_{11}^0 = 1$ and $\rho_{12}^0 = \rho_{21}^0 = \rho_{22}^0 = 0$. The relaxation term does not introduce any difficulties in the linearization, and eqs 15 and 16 become

$$\dot{\rho}_{12} = i[\Omega_{21}\rho_{12} + H'_{12}] \tag{31}$$

$$\dot{\rho}_{21} = -i[\Omega_{21}^*\rho_{21} + H'_{21}] \tag{32}$$

where $\Omega_{21} = \omega_{21} + i/T_2$. The subsequent derivation then goes through in the same way as in the previous section, and the excitation energies are obtained as

$$\omega = \sqrt{{\omega_{21}}^2 + 4\omega_{21}K_{12,12}(\omega)} - \frac{i}{T_2} \tag{33}$$

The dephasing rate $1/T_2$ thus produces a negative imaginary part of the excitation energy (27), i.e. a finite line width, as expected. In the resulting spectrum, $1/T_2$ is the half-width at half-maximum of the spectral line at the real part of ω. The population relaxation time T_1 does not play any role for excitation energies but becomes important in the nonlinear dynamics of strongly driven systems.[34,35]

2.3. More than Two Levels. Let us briefly sketch how the density matrix formalism works in a subspace with more than two levels. For example, in the case of a spin-unpolarized three-level system, the doubly occupied time-dependent Kohn−Sham orbital is $\varphi(\mathbf{r}, t) = c_1(t)\varphi_1(\mathbf{r}) + \lambda c_2(t)\varphi_2(\mathbf{r}) + \lambda c_3(t)\varphi_3(\mathbf{r})$, which gives the following density matrix

$$\rho(t) = \begin{pmatrix} \rho_{11} & \lambda\rho_{12} & \lambda\rho_{13} \\ \lambda\rho_{21} & \lambda^2\rho_{22} & \lambda^2\rho_{23} \\ \lambda\rho_{31} & \lambda^2\rho_{32} & \lambda^2\rho_{33} \end{pmatrix} = \begin{pmatrix} |c_1|^2 & \lambda c_1 c_2^* & \lambda c_1 c_3^* \\ \lambda c_1^* c_2 & \lambda^2|c_2|^2 & \lambda^2 c_2 c_3^* \\ \lambda c_1^* c_3 & \lambda^2 c_2^* c_3 & \lambda^2|c_3|^2 \end{pmatrix} \tag{34}$$

extending the expressions in eqs 10 and 11. Going through a similar procedure as in section 2.1, considering only the first order in λ, we arrive at

$$\tilde{\rho}_{12} + \tilde{\rho}_{21} = -\frac{4\omega_{21}}{{\omega_{21}}^2 - \omega^2}[(\tilde{\rho}_{12} + \tilde{\rho}_{21})K_{12,12} + (\tilde{\rho}_{13} + \tilde{\rho}_{31})K_{12,13}] \tag{35}$$

$$\tilde{\rho}_{13} + \tilde{\rho}_{31} = -\frac{4\omega_{31}}{{\omega_{31}}^2 - \omega^2}[(\tilde{\rho}_{12} + \tilde{\rho}_{21})K_{13,12} + (\tilde{\rho}_{13} + \tilde{\rho}_{31})K_{13,13}] \tag{36}$$

The off-diagonal matrix elements $K_{12,13}$ and $K_{13,12}$ come in because the first-order density response

$$\delta n(\mathbf{r}, \omega) = 2\varphi_1(\mathbf{r})\varphi_2(\mathbf{r})(\tilde{\rho}_{12} + \tilde{\rho}_{21}) + 2\varphi_1(\mathbf{r})\varphi_3(\mathbf{r})(\tilde{\rho}_{13} + \tilde{\rho}_{31}) \tag{37}$$

which enters in the perturbing Hamiltonian (21) and involves products of the first and second as well as the first and third single-particle orbitals. This shows how the TDDFT linear-response formalism mixes independent single-particle excitations between individual Kohn−Sham levels.

We now define $\xi_{12} = (\tilde{\rho}_{12} + \tilde{\rho}_{21})/(\omega_{21})^{1/2}$ and $\xi_{13} = (\tilde{\rho}_{13} + \tilde{\rho}_{31})/(\omega_{31})^{1/2}$ and end up with

$$({\omega_{21}}^2 + 4\omega_{21}K_{12,12})\xi_{12} + 4\sqrt{\omega_{21}\omega_{31}}K_{12,13}\xi_{13} = \omega^2\xi_{12} \tag{38}$$

$$4\sqrt{\omega_{21}\omega_{31}}K_{13,12}\xi_{12} + ({\omega_{31}}^2 + 4\omega_{31}K_{13,13})\xi_{13} = \omega^2\xi_{13} \tag{39}$$

This is a 2×2 eigenvalue problem which yields two excitation energies, correcting the Kohn−Sham excitation energies ω_{21} and ω_{31}. Equations 38 and 39 can also be directly obtained from the general TDDFT response equation (5) in the case of three spin-unpolarized Kohn−Sham levels. It is thus straightforward to see how Casida's linear response formalism follows from a generalization of our density matrix formalism for $N \to \infty$ spin-dependent levels.

3. Vector Potentials and TDCDFT

Let us now consider the case where the time-dependent Hamiltonian has the following form:

$$H(t) = \frac{1}{2}\left(\frac{\nabla}{i} + \lambda\frac{1}{c}\mathbf{A}(\mathbf{r}, t)\right)^2 + V_{\text{ext}}(\mathbf{r}) + \int \mathrm{d}^3r' \frac{n_0(\mathbf{r}')}{|\mathbf{r} - \mathbf{r}'|} + V_{\text{xc}}[n_0](\mathbf{r}) \tag{40}$$

i.e., the perturbation is given by a vector potential, with the linear term

$$H'(t) = \frac{1}{2ic}(\nabla\cdot\mathbf{A}(t) + \mathbf{A}(t)\cdot\nabla) \tag{41}$$

To obtain the excitation energies in a two-level system, we carry out a similar density-matrix calculation as in the previous section where we considered scalar perturbations. After Fourier transformation, have the following matrix element of the perturbing Hamiltonian:

$$H'_{12}(\omega) = \frac{1}{2ic}\int \mathrm{d}^3r\, \mathbf{A}(\omega)\cdot[\varphi_1(\mathbf{r})\nabla\varphi_2(\mathbf{r}) - \varphi_2(\mathbf{r})\nabla\varphi_1(\mathbf{r})] \tag{42}$$

The general form of the vector potential is $\mathbf{A} = \mathbf{A}_{\text{ext}} + \mathbf{A}_{\text{H}} + \mathbf{A}_{\text{xc}}$, where $\mathbf{A}_{\text{ext}}$ is the external vector potential, e.g., associated with an electromagnetic wave, $\mathbf{A}_{\text{H}}$ is the Hartree vector potential

$$\mathbf{A}_{\mathrm{H}}(\mathbf{r},\omega) = \frac{\nabla}{(i\omega)^2}\int \mathrm{d}^3r' \frac{\nabla'\cdot\delta\mathbf{j}(\mathbf{r}',\omega)}{|\mathbf{r}-\mathbf{r}'|} \quad (43)$$

and the XC vector potential is in general given by

$$\mathbf{A}_{\mathrm{xc}}(\mathbf{r},\omega) = \int \mathrm{d}^3r' \underline{\underline{f_{\mathrm{xc}}}}(\mathbf{r},\mathbf{r}',\omega)\cdot\delta\mathbf{j}(\mathbf{r}',\omega) \quad (44)$$

where $\underline{\underline{f_{\mathrm{xc}}}}$ is the tensorial XC kernel of TDCDFT.

Again, we will assume that the external perturbation $\mathbf{A}_{\mathrm{ext}}$ is absent and that we only consider eigenmodes of the system, driven by the dynamical self-consistent vector potentials $\mathbf{A}_{\mathrm{H}}$ and $\mathbf{A}_{\mathrm{xc}}$. Let us now take the following explicit form for $\mathbf{A}_{\mathrm{xc}}$, proposed by Vignale et al.:[36]

$$\mathbf{A}_{\mathrm{xc},i}(\mathbf{r},\omega) = \frac{c}{i\omega}\nabla\int \mathrm{d}^3r' f_{\mathrm{xc}}^{\mathrm{ALDA}}(\mathbf{r},\mathbf{r}')\delta n(\mathbf{r}',\omega) - \frac{c}{i\omega n_0}\sum_j \nabla_j \sigma_{\mathrm{xc},ij}(\mathbf{r},\omega) \quad (45)$$

where $f_{\mathrm{xc}}^{\mathrm{ALDA}}(\mathbf{r},\mathbf{r}')$ is the XC kernel in adiabatic local-density approximation (ALDA)[1] and the XC viscoelastic stress tensor is defined as a function of the gradients of the velocity field $\mathbf{u}(\mathbf{r},\omega) = \delta\mathbf{j}(\mathbf{r},\omega)/n_0(\mathbf{r})$:

$$\sigma_{\mathrm{xc},ij} = \eta_{\mathrm{xc}}\left(\nabla_j u_i + \nabla_i u_j - \frac{2}{3}\nabla\cdot\mathbf{u}\delta_{ij}\right) + \zeta_{\mathrm{xc}}\nabla\cdot\mathbf{u}\delta_{ij} \quad (46)$$

The quantities η_{xc} and ζ_{xc} are viscosity coefficients of the homogeneous electron gas, defined as[36]

$$\eta_{\mathrm{xc}}(\bar{n},\omega) = -\frac{\bar{n}^2}{i\omega}f_{\mathrm{xc}}^{\mathrm{T}}(\bar{n},\omega) \quad (47)$$

$$\zeta_{\mathrm{xc}}(\bar{n},\omega) = -\frac{\bar{n}^2}{i\omega}\left[f_{\mathrm{xc}}^{\mathrm{L}}(\bar{n},\omega) - \frac{4}{3}f_{\mathrm{xc}}^{\mathrm{T}}(\bar{n},\omega) - \frac{\mathrm{d}^2 e_{\mathrm{xc}}(\bar{n})}{\mathrm{d}\bar{n}^2}\right] \quad (48)$$

where $f_{\mathrm{xc}}^{\mathrm{L}}$ and $f_{\mathrm{xc}}^{\mathrm{T}}$ are the longitudinal and transverse XC kernels and e_{xc} is the XC energy density of a homogeneous electron gas of density $\bar{n}$. In eq 46, η_{xc} and ζ_{xc} are evaluated at the local ground-state density. For our two-level system, the current density can be expressed as

$$\delta\mathbf{j}(\mathbf{r},\omega) = \frac{1}{i}(\tilde{\rho}_{21}(\omega) - \tilde{\rho}_{12}(\omega))(\varphi_1(\mathbf{r})\nabla\varphi_2(\mathbf{r}) - \varphi_2(\mathbf{r})\nabla\varphi_1(\mathbf{r})) \quad (49)$$

where we ignore any diamagnetic contributions to the current since they are of higher order in the perturbation. The derivation of this expression for $\delta\mathbf{j}(\mathbf{r},\omega)$ proceeds along similar lines as the derivation of $\delta n(\mathbf{r},\omega)$, eq 23. The matrix element (42) thus becomes

$$H'_{12} = -\frac{1}{2\omega}\sum_i \int \mathrm{d}^3r\left(\nabla_i \int \mathrm{d}^3r'\left[\frac{1}{\mathbf{r}-\mathbf{r}'} + f_{\mathrm{xc}}^{\mathrm{ALDA}}(\mathbf{r},\mathbf{r}')\right]\delta n(\mathbf{r}',\omega) - \frac{1}{n_0}\sum_j \nabla_j \sigma_{\mathrm{xc},ij}\right)P_i \quad (50)$$

where we defined $P_i(\mathbf{r}) = \varphi_1(\mathbf{r})\nabla_i\varphi_2(\mathbf{r}) - \varphi_2(\mathbf{r})\nabla_i\varphi_1(\mathbf{r})$. After some straightforward manipulation involving partial integration and introducing the abbreviation

$$S_{12,12}(\omega) = \frac{1}{4i\omega}\int \mathrm{d}^3r\left[\frac{\eta_{xc}}{2}\sum_{ij}\left(\nabla_j\frac{P_i}{n_0} + \nabla_i\frac{P_j}{n_0}\right)^2 + \left(\zeta_{xc} - \frac{2}{3}\zeta_{xc}\right)\left(\nabla\cdot\frac{\mathbf{P}}{n_0}\right)^2\right] \quad (51)$$

we obtain

$$\tilde{H}'_{12} = -2\frac{\omega_{21}}{\omega}K_{12,12}(\omega)(\tilde{\rho}_{12} + \tilde{\rho}_{21}) + 2S_{12,12}(\omega)(\tilde{\rho}_{12} - \tilde{\rho}_{21}) \quad (52)$$

Notice that $\tilde{H}'_{12} = -\tilde{H}'_{21}$. From eq 20, we thus get (dropping the subscripts of K and S)

$$\tilde{\rho}_{12} + \tilde{\rho}_{21} = -\frac{-2\frac{\omega_{21}}{\omega}K(\tilde{\rho}_{12} + \tilde{\rho}_{21}) + 2S(\tilde{\rho}_{12} - \tilde{\rho}_{21})}{\omega_{21} + \omega} - \frac{2\frac{\omega_{21}}{\omega}K(\tilde{\rho}_{12} + \tilde{\rho}_{21}) - 2S(\tilde{\rho}_{12} - \tilde{\rho}_{21})}{\omega_{21} - \omega} \quad (53)$$

and similarly

$$\tilde{\rho}_{12} - \tilde{\rho}_{21} = -\frac{-2\frac{\omega_{21}}{\omega}K(\tilde{\rho}_{12} + \tilde{\rho}_{21}) + 2S(\tilde{\rho}_{12} - \tilde{\rho}_{21})}{\omega_{21} + \omega} + \frac{2\frac{\omega_{21}}{\omega}K(\tilde{\rho}_{12} + \tilde{\rho}_{21}) - 2S(\tilde{\rho}_{12} - \tilde{\rho}_{21})}{\omega_{21} - \omega} \quad (54)$$

Using the abbreviation $\beta = 4/({\omega_{21}}^2 - \omega^2)$, we can write this as a system of two coupled equations:

$$(1 + \beta\omega_{21}K)(\tilde{\rho}_{12} + \tilde{\rho}_{21}) - \beta\omega S(\tilde{\rho}_{12} - \tilde{\rho}_{21}) = 0 \quad (55)$$

$$-\frac{{\omega_{21}}^2}{\omega}\beta K(\tilde{\rho}_{12} + \tilde{\rho}_{21}) + (1 + \beta\omega_{21}S)(\tilde{\rho}_{12} - \tilde{\rho}_{21}) = 0 \quad (56)$$

The determinant vanishes if

$$\omega^2 = {\omega_{21}}^2 + 4\omega_{21}(K_{12,12}(\omega) + S_{12,12}(\omega)) \quad (57)$$

which is the desired TDCDFT generalization of the SMA. Again, it is straightforward to repeat the derivation for the spin-dependent case. Assuming, as before, that the ground-state is not spin-polarized, and using the spin-dependent XC vector potential of Qian et al.,[37] we find

$${\omega_\pm}^2 = {\omega_{21}}^2 + 2\omega_{21}[(K_{12\sigma,12\sigma}(\omega) + S_{12\sigma,12\sigma}(\omega)) \pm (K_{12\sigma,12\bar{\sigma}}(\omega) + S_{12\sigma,12\bar{\sigma}}(\omega))] \quad (58)$$

where

$$S_{12\sigma,12\sigma'}(\omega) = \frac{1}{i\omega}\int \mathrm{d}^3r\left[\frac{\eta_{\mathrm{xc},\sigma\sigma'}}{2}\sum_{ij}\left(\nabla_j\frac{P_{i\sigma}}{n_0} + \nabla_i\frac{P_{j\sigma}}{n_0}\right)^2 + \left(\zeta_{\mathrm{xc},\sigma\sigma'} - \frac{2}{3}\eta_{\mathrm{xc},\sigma\sigma'}\right)\left(\nabla\cdot\frac{\mathbf{P}_\sigma}{n_0}\right)^2\right] + \frac{2\delta_{\sigma\sigma'} - 1}{4i\omega}\int \mathrm{d}^3r\, \rho_{\uparrow\downarrow}|\mathbf{P}_\sigma|^2 \quad (59)$$

Table 1. Lowest Intersubband Excitation Energy ω and Linewidth Γ (both in millielectronvolts) of an *n*-Doped 40-nm GaAs/AlGaAs Quantum Well[a]

	KS	ALDA (full)	ALDA (eq 27)	VUC (full)	VUC (eq 57)
ω	7.7445	10.0309	10.0323	10.0950	10.0967
Γ				0.0663	0.0677

[a] VUC stands for the XC vector potential of Vignale et al.[36]

Here, $\rho_{\uparrow\downarrow}(\mathbf{r}, \omega)$ is the so-called spin transresistivity,[38] which is a measure of the spin Coulomb drag effect.[39] It affects only the spin-density excitations.

We point out that eqs 57 and 58 had been derived earlier in an alternative way,[31,40] leading to the same result, except that $S_{12,12}(\omega)$ and $S_{12\sigma,12\sigma'}(\omega)$ are multiplied with $\omega^2/\omega_{21}{}^2$. This difference arises because the alternative derivation starts from an approximation of the Kohn−Sham current−current response function, where the prefactor $\omega^2/\omega_{21}{}^2$ is needed to ensure that the formalism reduces to eq 27 in the appropriate limit. In that sense, the present density-matrix formalism is more consistent: once we have selected a 2-level subspace, no further approximations are involved. Therefore, although the prefactor $\omega^2/\omega_{21}{}^2$ causes only corrections to the excitation energies of order S^2 (which are usually small), eqs 57 and 58 are to be preferred.

In Table 1, we present some results to illustrate the performance of the two-level system approximation. We consider the lowest intersubband transition energy of an *n*-doped 40 nm square GaAs/AlGaAs quantum well with parabolic subbands and an electron concentration of 10^{11} cm^{-1}, using the standard effective-mass approximation.[30]

Table 1 compares the KS transition energy ω_{21} with the ALDA and TDCDFT results. We see that the results using the full TDDFT response equation agree extremely well with the simple SMA approximations, eqs 27 and 57. A more systematic study for closed-shell atoms by Vasiliev et al.[29] came to similar conclusions, although the agreement between SMA and full TDDFT was not as close as for quantum wells. This has to do with the structure and distribution of the quantum well subband levels, which are much better separated than in atoms: the level spacing is $\sim n^2$ for the lowest-lying levels, where n is the subband index, and there is no Rydberg series.

For quantum wells, the finite line width Γ reflects the fact that collective electronic excitations can decay into incoherent single-particle excitations of the electron gas in the (infinite) quantum well plane. Unfortunately, the same physics also leads to a line width for excitations of finite systems such as atoms.[40] To avoid this unphysical effect, approximate XC vector potentials based on the electron gas[36,37] should be applied to extended systems only.[31,41,42]

Acknowledgment. This work was supported by NSF Grant DMR-0553485 and by the Research Corporation.

References

(1) *Time-dependent density functional theory*; Marques, M. A. L., Ullrich, C. A., Nogueira, F., Rubio, A., Burke, K., Gross, E. K. U., Eds.; Springer: Berlin, 2006; Vol. 706.

(2) Hohenberg, P.; Kohn, W. *Phys. Rev.* **1964**, *136*, B864.

(3) Kohn, W.; Sham, L. J. *Phys. Rev.* **1965**, *140*, A1133.

(4) Runge, E.; Gross, E. K. U. *Phys. Rev. Lett.* **1984**, *52*, 997.

(5) Perdew, J. P.; Zunger, A. *Phys. Rev. B* **1981**, *23*, 5048.

(6) Perdew, J. P.; Parr, R. G.; Levy, M.; Balduz, J. L. *Phys. Rev. Lett.* **1982**, *49*, 1691.

(7) Ullrich, C. A.; Reinhard, P.-G.; Suraud, E. *Phys. Rev. A* **2000**, *62*, 053202.

(8) Toher, C.; Filippetti, A.; Sanvito, S.; Burke, K. *Phys. Rev. Lett.* **2005**, *95*, 146402.

(9) Messud, J.; Dinh, P. M.; Reinhard, P.-G.; Suraud, E. *Phys. Rev. Lett.* **2008**, *101*, 096404.

(10) Lein, M.; Kümmel, S. *Phys. Rev. Lett.* **2005**, *94*, 143003.

(11) Mundt, M.; Kümmel, S. *Phys. Rev. Lett.* **2005**, *95*, 203004.

(12) Carter, E. *Science* **2008**, *321*, 800.

(13) Koch, S. W.; Kira, M.; Khitrova, G.; Gibbs, H. M. *Nature Mat.* **2006**, *5*, 523.

(14) Scholes, G. D.; Rumbles, G. *Nature Mat.* **2006**, *5*, 683.

(15) Chelikowsky, J. R.; Kronik, L.; Vasiliev, I. *J. Phys.: Condens. Mat.* **2003**, *15*, R1517.

(16) Nitzan, A.; Ratner, M. A. *Science* **2003**, *300*, 1384.

(17) Koentopp, M.; Chang, C.; Burke, K.; Car, R. *J. Phys.: Condens. Matter* **2008**, *20*, 083203.

(18) Petersilka, M.; Gossmann, U. J.; Gross, E. K. U. *Phys. Rev. Lett.* **1996**, *76*, 1212.

(19) Casida, M. In *Recent Advances in Density Functional Methods*; Chong, D. P., Ed.; World Scientific: Singapore, 1995; Vol. 1, pp 155−192.

(20) Gross, E. K. U.; Kohn, W. *Phys. Rev. Lett.* **1985**, *55*, 2850.

(21) Marques, M. A. L.; Lopez, X.; Varsano, D.; Castro, A.; Rubio, A. *Phys. Rev. Lett.* **2005**, *90*, 258101.

(22) Varsano, D.; Felice, R. D.; Marques, M. A. L.; Rubio, A. *J. Phys. Chem. B* **2006**, *110*, 7129.

(23) Elliott, P.; Burke, K.; Furche, F. In *Recent Advances in Density Functional Methods*; Lipkowitz, K. B., Cundari, T. R., Eds.; Wiley: Hoboken, NJ, 2009; Vol. 26, pp 91−165.

(24) Fetter, A. L.; Walecka, J. D. *Quantum theory of many-particle systems*; Dover: New York, 2003.

(25) Hirata, S.; Head-Gordon, M. *Chem. Phys. Lett.* **1999**, *314*, 291.

(26) Casida, M. E.; Gutierrez, F.; Guan, J.; Cadea, F.-X.; Salahub, D.; Duadey, J.-P. *J. Chem. Phys.* **2000**, *113*, 7062.

(27) Appel, H.; Gross, E. K. U.; Burke, K. *Phys. Rev. Lett.* **2003**, *90*, 043005.

(28) Maitra, N. T.; Zhang, F.; Cave, R. J.; Burke, K. *J. Chem. Phys.* **2004**, *120*, 5932.

(29) Vasiliev, I.; Ogut, S.; Chelikowsky, J. R. *Phys. Rev. Lett.* **1999**, *82*, 1919.

(30) Ullrich, C. A. In *Time-dependent density functional theory*; Marques, M. A. L., Ullrich, C. A., Nogueira, F., Rubio, A., Burke, K., Gross, E. K. U., Eds.; Springer: Berlin, 2006; Vol. 706, pp 271−285.

(31) D'Amico, I.; Ullrich, C. A. *Phys. Rev. B* **2006**, *74*, 121303(R)..

(32) Appel, H.; Gross, E. K. U.; Burke, K. *Int. J. Quantum Chem.* **2006**, *106*, 2840.

(33) Maitra, N. T. *J. Chem. Phys.* **2005**, *122*, 234104.

(34) Załużny, M. *Phys. Rev. B* **1993**, *47*, 3995.

(35) Wijewardane, H. O.; Ullrich, C. A. *Appl. Phys. Lett.* **2004**, *84*, 3984.

(36) Vignale, G.; Ullrich, C. A.; Conti, S. *Phys. Rev. Lett.* **1997**, *97*, 4878.

(37) Qian, Z.; Constantinescu, A.; Vignale, G. *Phys. Rev. Lett.* **2003**, *90*, 066402.

(38) D'Amico, I.; Vignale, G. *Phys. Rev. B* **2000**, *62*, 4853.

(39) Weber, C. P.; Gedik, N.; Moore, J. E.; Orenstein, J.; Stephens, J.; Awschalom, D. D. *Nature (London)* **2005**, *437*, 1330.

(40) Ullrich, C. A.; Burke, K. *J. Chem. Phys.* **2004**, *121*, 28.

(41) van Faassen, M. *Int. J. Mod. Phys. B* **2006**, *20*, 3419.

(42) Nazarov, V. U.; Pitarke, J. M.; Takada, Y.; Vignale, G.; Chang, Y.-C. *Phys. Rev. B* **2007**, *76*, 205103.

CT800507M

JCTC Journal of Chemical Theory and Computation

Optical Absorptions of New Blue-Light Emitting Oligoquinolines Bearing Pyrenyl and Triphenyl Endgroups Investigated with Time-Dependent Density Functional Theory

Jianmin Tao*,† and Sergei Tretiak‡

Theoretical Division and Center for Nonlinear Studies and Center for Integrated Nanotechnology, Los Alamos National Laboratory, Los Alamos, New Maxico 87545

Received December 1, 2008

Abstract: The optical absorption spectra of a family of four n-type conjugated oligomers, oligoquinolines, which can be commercially used to develop high-performance light-emitting diodes for their many desirable properties, have been recently calculated from time-depedent density functional theory (TDDFT) within the adiabatic approximation for the dynamical exchange-correlation potential. In this work, we investigate the optical absorption of two new family members of the blue-light emitting oligoquinolines bearing pyrenyl and triphenyl endgroups in gas phase and chloroform ($CHCl_3$) solution employing the adiabatic TDDFT. The ionization potentials and electron affinities of these two oligoquinoline molecules are also calculated with the ground-state DFT, from which the adiabatic dynamical exchange-correlation potential is constructed. We show that the calculated optical absorptions are in good agreement with experiments. The ionization potentials obtained with the DFT methods agree well with the experimental estimates, while the electron affinities are significantly underestimated in comparison with experiments. A natural transition orbital analysis for selected excited states with the largest oscillator strengths shows that the electronic charge is slightly redistributed in the process of electronic excitations.

I. Introduction

In recent years, n-type (electron transport) organic light-emitting materials have been increasingly gaining popularity in the development of high-performance organic light-emitting diodes (OLEDs)[1,2] because of their ultralow cost, light weight, and flexibility. A common feature of these nanoscale molecules is that they have a backbone chain with overlapping π orbitals. On the one hand, they exhibit the property of a semiconductor because the π orbitals form delocalized valence-band hole and conduction-band electron. On the other hand, these nanoscale conjugated molecules possess several important properties that traditional inorganic semiconductors lack. For example, they are easily deposited on any low-cost substrates[3−7] such as glass, plastic, or metal foils. Therefore, OLED materials are particularly well suited for large-area displays.[4] Fabrication of high-resolution, full-color, and flat-panel displays[3] depends upon many factors. Apart from the optimization of device structure for OLEDs, A crucial step to improve the device performance is to design and synthesize new materials with improved properties[8−13] in charge conductivity, electroluminescence efficiency and power efficiency, thermal stability, operational lifetime, brightness, and color purity.

Jenekhe and collaborators[1] have synthesized a series of four n-type (electron transport) blue-light-emitting oligomers, oligoquinolines. They found that these organic materials can be used to fabricate high-efficiency light-emitting diodes. Recently, we have performed a theoretical investigation[14] of the optical absorption spectra of these molecules and utilized the natural transition orbitals to analyze the delocalization properties of several selected excited states, including the lowest one. The theoretical study has provided a detailed understanding of experimental measurements.

* To whom correspondence should be addressed. E-mail: jtao@lanl.gov.

† Theoretical Division and Center for Nonlinear Studies.

‡ Center for Integrated Nanotechnology.

10.1021/ct800523j CCC: $40.75
Published on Web 03/25/2009

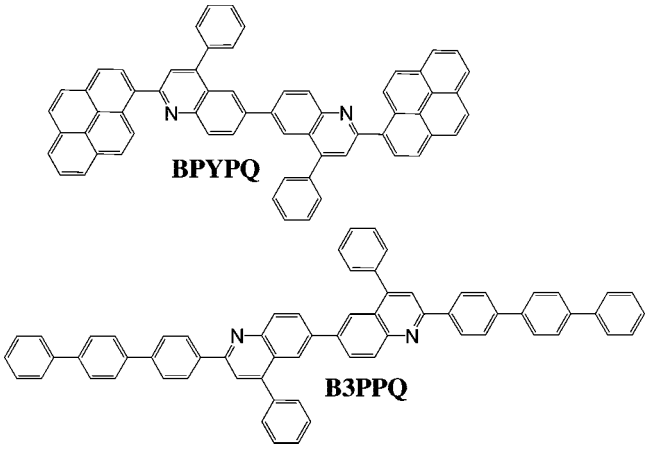

Figure 1. Molecular structures of the computationally studied blue-light-emitting oligoquinolines.

More recently, two new family members of the blue-light emitting oligoquinolines bearing pyrenyl and triphenyl end-groups have been synthesized and their important photochemistry properties such as optical absorption and emission as well as ionization potentials and electron affinities have been experimentally evaluated.[2] It has been found that these new pyrenyl- and triphenyl-bearing oligoquinoline molecules, 6,6′-bis(2-(1-pyrenyl)-4-phenylquinoline) (BPYPQ) and 6,6′-bis(2-(1-triphenyl)-4-phenylquinoline) (B3PPQ), have many desirable properties such as excellent thermal stability, high melt transitions, high quantum yields, and bright blue electroluminescence with high efficiency. They are highly emissive electron transport materials for OLEDs and have been used as emitters in recent fabrication of OLED devices. To get a better understanding of these experiments and to provide a deep physical insight into these phenomena, it is necessary to perform theoretical calculations. The method we choose for the calculation of dynamical properties such as optical absorption is time-dependent density functional theory,[15,16] while the ground-state density functional theory (DFT)[17] is employed to evaluate the equilibrium properties. TDDFT and DFT techniques currently provide optimal combination of accuracy and low computational cost for a broad variety of large molecules.

Kohn−Sham ground-state DFT[18,19] is the most popular method in electronic structure calculations because of its high computational efficiency. In this theory, only the exchange-correlation (XC) energy, which includes all unknown many-body effects, must be approximated as a functional of the electron density. In this paper, we employ several commonly used XC energy functionals to calculate the ionization potentials and the electron affinities of BPYPQ and B3PPQ molecules, whose chemical structures are shown in Figure 1. The density functionals we use here include two pure density functionals [the local spin density approximation (LSDA) and the Tao-Perdew-Staroverov-Scuseria (TPSS)[20] meta-generalized gradient approximation (meta-GGA)] and three hybrid functionals (TPSSh,[21] B3LYP,[22] and PBE0;[23,24] see discussion below). Then we employ the time-dependent DFT linear response theory[25,26] to calculate the optical absorptions of these two new family members of oligoquinolines, BPYPQ and B3PPQ. The dynamical XC potential is constructed, as usual, within the adiabatic approximation.[27] See refs 28−31 for the discussion of the nonadiabatic approximation.

Previous calculations[14,32−42] show that the adiabatic XC potentials constructed from a ladder of widely used density functionals yield excitation energies of molecules in fairly good agreement with experiments. Hybrid functionals such as PBE0 (a hybrid of PBE with 25% exact exchange) and TPSSh (a hybrid of TPSS with 10% exact exchange) yield excitation energies consistently in better agreement[14,42] with experiments than their parental nonhybrid functionals PBE GGA[43] and TPSS meta-GGA. In particular, PBE0, which benefits from the more amount of exact exchange, gives a very good performance in the prediction of low-lying excitations. This excellent improvement probably is a balanced effect between the error concellation between semilocal exchange and semilocal correlation (no exact exchange should be mixed in) and the improvement of the asymptotic behavior of the exchange potential (as much as exact exchange should be mixed in). Recently, Perdew, Staroverov, Tao, and Scuseria[44] have constructed a fourth-rung hyper-GGA, a fully nonlocal functional of the density, which satisfies many additional constraints beyond those[45,46] that the TPSS meta-GGA already satisfies. Specifically, we employ the TDDFT adiabatic PBE0 functional to evaluate the optical absorptions of BPYPQ and B3PPQ. The results obtained with the adiabatic LSDA, TPSS meta-GGA and hybrid TPSSh, and three-parameter hybrid B3LYP (with 1/5 exact exchange), are also presented for comparison. To spell out our results, a natural transition orbital analysis[47] for three selected excited states with the largest oscillator strengths is carried out.

II. Computational Method

All calculations are performed using the GAUSSIAN 03 program.[48] First we optimize the ground-state geometries of BPYPQ and B3PPQ by performing the self-consistent ground-state calculations with respective density functionals. Then we evaluate the vertical excitation energies of these two oligomers based on the optimized ground-state geometries with the respective adiabatic density functionals. Ionization potentials and electron affinities are estimated from the ground-state DFT self-consistent calculations. For consistency, the same basis set 6−31G(d) was used in all calculations. Because the Perdew−Wang parametrization[49] for the LSDA correlation energy is used as the local part in the PBE and TPSS correlation functionals, for consistency, this parametrization was used for all LSDA calculations. The TDDFT calculations of BPYPQ and B3PPQ in chloroform solvent were performed using PCM (polarizable continuum model)[50] method, which was shown[14] to yield almost the same results as CPCM (conductor-like PCM) method[51−53] for the family of oligoquinoline molecules. For systems with high dielectric constant, both methods are equivalent. See refs 54−57 for detailed discussion of PCM method.

III. Results and Discussion

A. Ionization Potentials and Electron Affinities. Ionization potentials are calculated as the difference in total

Table 1. Ionization Potentials (IPs) and Electron Affinities (EAs) (In Units of eV) of BPYPQ and B3PPQ, Evaluated with the Basis Set 6-31G(d) and Geometries Optimized on the Respective Density Functionals

		exptl	LSDA	TPSS	TPSSh	B3LYP	PBE0
BPYPQ	IP	5.86	5.91	5.65	5.82	5.93	6.11
	EA	2.66	2.00	1.75	1.66	1.54	1.59
	η[a]	1.60	1.96	1.95	2.08	2.20	2.26
B3PPQ	IP	5.78	6.01	5.70	5.90	6.03	6.24
	EA	2.58	1.96	1.70	1.59	1.46	1.51
	η[a]	1.60	2.03	2.00	2.16	2.29	2.37

[a] η is the molecular hardness defined by η =(IP − EA)/2.

Table 2. Singlet and Triplet Vertical Excitation Energies (ω_S^g, ω_T^n, n = the nth excited state) in eV, the Transition Oscillator Strength ($f^{abs,n}$), and the Dipole Moment of the Ground State in Debye of BPYPQ Molecule in Gas Phase (μ_g) and Chloroform Solution (μ_{sol}), Calculated Using the Five Adiabatic Density Functionals with the Basis Set 6−31G(d) and the Geometry Optimized on the Respective Density Functionals with the Same Basis (1 eV = 8065.5 cm^{-1} = 0.03675 hartree)[a]

	gas	gas	gas	gas	gas	gas	gas	bgas	sol	sol	sol	sol	sol	sol	sol	sol
	$\omega_S^{abs,1}$	$f^{abs,1}$	$\omega_S^{abs,4}$	$f^{abs,4}$	$\omega_S^{abs,14}$	$f^{abs,14}$	ω_T^{abs}	μ_g	$\omega_S^{abs,1}$	$f^{abs,1}$	$\omega_S^{abs,4}$	$f^{abs,4}$	$\omega_S^{abs,12}$	$f^{abs,12}$	ω_T^{abs}	μ_{sol}
LSDA	2.10	0.558	2.48	0.358	3.06	0.286	1.90	1.031	2.08	0.714	2.47	0.499	3.03	0.384	1.90	1.645
			$\omega_S^{abs,3}$	$f^{abs,3}$	$\omega_S^{abs,12}$	$f^{abs,12}$				$\omega_S^{abs,5}$	$f^{abs,5}$	$\omega_S^{abs,12}$	$f^{abs,12}$			
TPSS	2.21	0.473	2.58	0.392	3.17	0.334	1.85	1.112	2.19	0.610	2.56	0.536	3.15	0.400	1.86	1.761
			$\omega_S^{abs,5}$	$f^{abs,5}$	$\omega_S^{abs,11}$	$f^{abs,11}$				$\omega_S^{abs,5}$	$f^{abs,5}$	$\omega_S^{abs,10}$	$f^{abs,10}$			
TPSSh	2.61	0.852	3.16	0.506	3.48	0.271	1.88	1.138	2.58	1.081	3.14	0.503	3.45	0.314	1.89	1.784
			$\omega_S^{abs,5}$	$f^{abs,5}$	$\omega_S^{abs,9}$	$f^{abs,9}$					$\omega_S^{abs,5}$	$f^{abs,5}$	$\omega_S^{abs,7}$	$f^{abs,7}$		
B3LYP	2.89	1.275	3.44	0.501	3.64	0.092	1.98	1.122	2.85	1.998	3.42	0.513	3.61	0.122	1.98	1.744
			$\omega_S^{abs,5}$	$f^{abs,5}$	$\omega_S^{abs,9}$	$f^{abs,9}$					$\omega_S^{abs,5}$	$f^{abs,5}$	$\omega_S^{abs,14}$	$f^{abs,14}$		
PBE0	3.04	1.516	3.62	0.448	3.79	0.071	1.88	1.190	3.00	1.817	3.60	0.479	4.09	0.096	1.89	1.839
									ω_{1st}^{abs}		ω_{2nd}^{abs}		ω_{3rd}^{abs}			
exptl									3.26		3.60		4.34			

[a] Experimental values measured in chloroform are obtained from ref 2.

Table 3. Singlet and Triplet Vertical Excitation Energies (ω_S^g, ω_T^n, n = the nth excited state) in eV, the Transition Oscillator Strength ($f^{abs,n}$), and the Dipole Moment of the Ground State in Debye of B3PPQ Molecule in Gas Phase (μ_g) and Chloroform Solution (μ_{sol}), Calculated Using the Five Adiabatic Density Functionals with the Basis Set 6−31G(d) and the Geometry Optimized on the Respective Density Functionals with the Same Basis (1 eV = 8065.5 cm^{-1} = 0.03675 hartree)[a]

	gas	gas	gas	gas	gas	gas	gas	gas	sol	sol	sol	sol	sol	sol	sol	sol
	$\omega_S^{abs,1}$	$f^{abs,1}$	$\omega_S^{abs,4}$	$f^{abs,5}$	$\omega_S^{abs,13}$	$f^{abs,13}$	ω_T^{abs}	μ_g	$\omega_S^{abs,1}$	$f^{abs,1}$	$\omega_S^{abs,5}$	$f^{abs,5}$	$\omega_S^{abs,13}$	$f^{abs,13}$	ω_T^{abs}	μ_{sol}
LSDA	2.34	1.235	2.78	0.598	3.27	0.575	2.09	1.137	2.31	1.421	2.75	0.721	3.26	0.593	2.09	1.457
			$\omega_S^{abs,4}$	$f^{abs,4}$	$\omega_S^{abs,13}$	$f^{abs,13}$				$\omega_S^{abs,4}$	$f^{abs,4}$	$\omega_S^{abs,14}$	$f^{abs,14}$			
TPSS	2.49	1.209	2.93	0.425	3.42	0.503	2.079	1.234	2.46	1.378	2.89	0.430	3.42	0.391	2.09	1.602
			$\omega_S^{abs,5}$	$f^{abs,5}$	$\omega_S^{abs,16}$	$f^{abs,16}$				$\omega_S^{abs,10}$	$f^{abs,10}$	$\omega_S^{abs,15}$	$f^{abs,15}$			
TPSSh	2.86	1.779	3.42	0.502	3.95	1.047	2.16	1.267	2.83	1.998	3.74	0.772	3.92	0.856	2.18	1.636
			$\omega_S^{abs,7}$	$f^{abs,7}$	$\omega_S^{abs,12}$	$f^{abs,12}$				$\omega_S^{abs,6}$	$f^{abs,6}$	$\omega_S^{abs,11}$	$f^{abs,11}$			
B3LYP	3.12	2.197	3.86	0.542	4.09	0.923	2.29	1.265	3.08	2.429	3.81	0.498	4.06	0.642	2.30	1.632
			$\omega_S^{abs,6}$	$f^{abs,6}$	$\omega_S^{abs,12}$	$f^{abs,12}$				$\omega_S^{abs,6}$	$f^{abs,6}$	$\omega_S^{abs,12}$	$f^{abs,12}$			
BPE0	3.27	2.373	4.02	0.957	4.30	0.962	2.23	1.306	3.23	2.609	4.02	0.842	4.28	1.099	2.24	1.676
									ω_{1st}^{abs}		ω_{2nd}^{abs}					
exptl									3.32		4.04					

[a] Experimental values measured in chloroform are obtained from ref 2.

energies between the positive ion and the corresponding neutral in their ground states (using the spin-unrestricted DFT formalism) at their geometries optimized with respective density functionals. The results are displayed in Table 1, and the experimental estimates are also listed for comparison. From Table 1, we observe that LSDA, TPSS, and TPSSh give the IPs of BPYPQ and B3PPQ that are closest to the experimental estimates, while B3LYP and PBE0 yield slightly higher values, compared to the experimantal ones.

Electron affinities are calculated as the difference between the total energies of the negative ion and the corresponding neutral in their ground states (using the spin-unrestricted DFT formalism) at their geometries optimized with respective density functionals. The results are summarized in Table 1. We observe from Table 1 that all the density functional values are too low. The nonhybrid functionals (LSDA and TPSS meta-GGA) yield the estimates that are closer to the experimental values than hybrid functionals (TPSSh, B3LYP, and PBE0). As discussed in refs 21 and 58, since negative ions are unstable in the ground-state of semilocal local density functionals that suffer from self-interaction error, the ground-state energies of negative ions are estimated in practice with the artificial stabilization by the use of finite basis sets. That explains the large deviation of the density functional estimates of the electron affinities from the experimental values.

B. Optical Absorption. Tables 2 and 3 show the summary of the calculated properties of BPYPQ and B3PPQ in

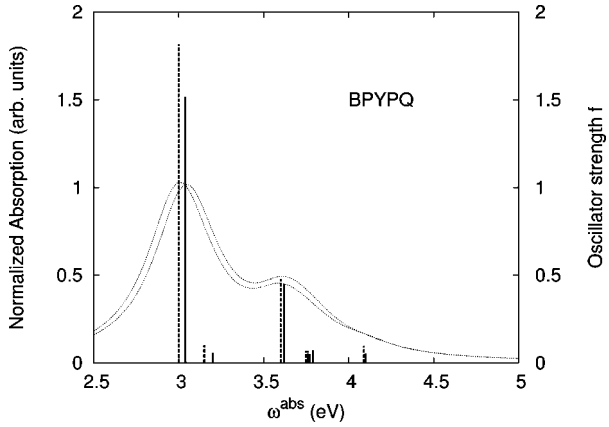

Figure 2. Normalized absorption *I* of eq 1 (in arbitrary units) (right side) and oscillator strength *f* (left side) of BPYPQ. The solid and dashed curves represent the normalized absorption in gas phase and solution, while the solid and dashed "sticks" represent the oscillator strength in gas phase and solution, respectively.

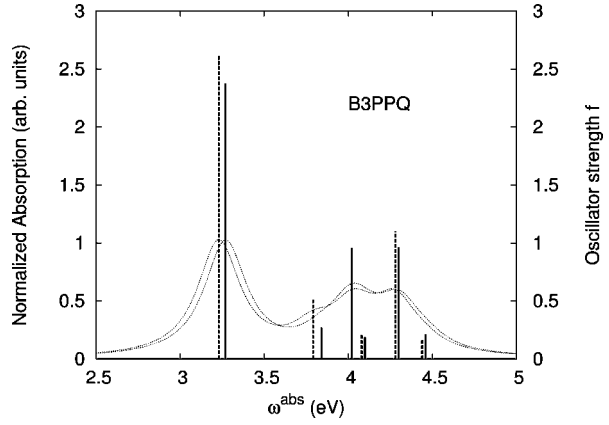

Figure 3. Normalized absorption *I* of eq 1 (in arbitrary units) (right side) and oscillator strength *f* (left side) of B3PPQ. The solid and dashed curves represent the normalized absorption in gas phase and solution, while the solid and dashed "sticks" represent the oscillator strength in gas phase and solution, respectively.

gas phase and in solution, respectively. These calculated properties include the excitation energies of three singlet states with the largest oscillator strengths in the UV−vis region, the corresponding oscillator strengths, and the excitation energy of the first triplet state, in gas phase and solution. The ground-state dipole moments of BPYPQ and B3PPQ in gas phase and solution are also calculated and presented in Tables 2 and 3, respectively. The experimentally observed excitation energies are listed for comparison. Of course, this comparison can be made only approximately because vibrational progression and disorder effects are not included in our calculations. This can make a difference of up to 0.1−0.2 eV.

From Table 2, we observe that the first or lowest-frequency peak of BPYPQ occurs at 3.00 eV (the experimental value is 3.26 eV) with the largest oscillator strength $f = 1.82$ and that a higher-frequency peak occurs at 3.60 eV (the same as the experimental value) with the oscillator strength $f = 0.48$, almost three times smaller than the largest oscillator strength. The third or the highest-frequency absorption peak occurs at about 4.09 eV (4.34 eV for the experimental measurement), with a very small oscillator strength $f = 0.1$. The oscillator strength of the third absorption peak is underestimated significantly with the adiabatic B3LYP and PBE0 functionals. The adiabatic LSDA, TPSS, and TPSSh functionals yield a more realistic oscillator strength, although it is still too small, compared to the experimental observation, where the experimental intensity of the third absorption band is quite noticeable.[2] This discrepancy of theory from experiment for the third peak absorbance may arise from many effects such as temperature, disorder, vibrational progression, etc. These factors have not been taken into consideration in our calculations. We also observe a persistent red shift for the first two peaks from gas phase to solution. This red shift (of about 10 meV) also occurs for the lowest triplet excitation. The dipole moment of BPYPQ is vanishingly small if all the atoms are in a same plane because of its high symmetry. However, this geometry is not the ground-state geometry. In the ground state, there are dihedral angles between two benzene rings connected by a σ-bond. These dihedral angles effectively reduce the symmetry of the molecule, resulting in a large ground-state dipole moment. While the effect of the solvent−solute interaction on the optical absorption is small, it has a significan effect on the ground-state dipole moment and causes the noticeable increase of the oscillator strength in solution, compared to that in gas phase. The absorptions calculated with other adiabatic TDDFT functionals are in fairly good agreement with experiments. The accuracy increases when we go from LSDA, TPSS meta-GGA, TPSSh, and B3LYP to PBE0.

Table 3 shows that in gas phase the first two absorptions of B3PPQ occur at 3.27 and 4.02 eV, respectively, with the oscillator strength of the first peak being about twice that of the second peak. Interestingly, our calculation shows that there should be another absorption peak, which occurs at a higher frequency 4.30 eV. The absorption intensity of the third peak is nearly the same as the second. Since these two peaks are located closely, they may combine to form a broader single peak. Therefore, we may only observe two absorption peaks in total in the experiment. In solution, the three peaks are expected to occur at slightly lower frequency because of the red shift, as shown in Table 3. The solvent−solute effects on the absorption and the ground-state moment are the same as those for BPYPQ.

To simulate the experimentally observed absorptions with our calculated data (see Figures 2 and 3), a simple analytic expression[14] for the normalized absorption intensity or peak magnitude is assumed as

$$I(\omega) = \sum_i f(\omega_i)\delta_m(\omega - \omega_i) \Big/ \sum_i f(\omega_i) \qquad (1)$$

where $\delta_m(x)$ is a δ-like function defined by

$$\delta_m(x) = \frac{m}{\pi}\frac{1}{1 + m^2x^2} \qquad (2)$$

Here m is determined by a fit to experiments; $m = 5.0$ for BPYPQ and 7.0 for B3PPQ. This form has been used[14] to

Table 4. TDDFT Natural Transition Orbital Analysis for the Three Excited States with the Largest Oscillator Strengths in BPYPQ in Gas Phase[a]

Excited state	Electron	Hole
$\|1\rangle$ $\Delta E = 3.04$ eV $f = 1.516$ $W = 92.4\%$	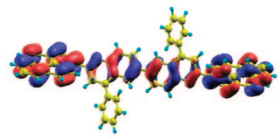	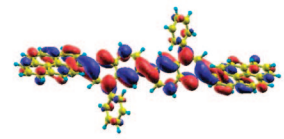
$\|5\rangle$ $\Delta E = 3.62$ eV f = 0.448 $W = 60.4\%$	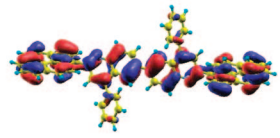	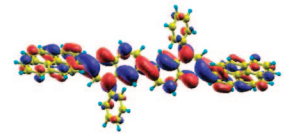
$\|9\rangle$ $\Delta E = 3.79$ eV f = 0.071 $W = 58.1\%$	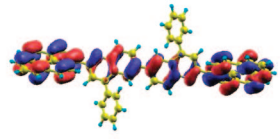	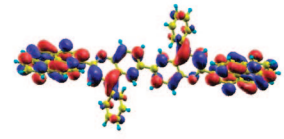

[a] ΔE is the excitation energy, f is the corresponding oscillator strength, and W is the weight of the plotted orbital in the respective transition density matrix.

Table 5. TDDFT Natural Transition Orbital Analysis for the Three Excited States with the Largest Oscillator Strengths in B3PPQ in Gas Phase[a]

Excited state	Electron	Hole
$\|1\rangle$ $\Delta E = 3.27$ eV $f = 2.373$ $W = 94.9\%$	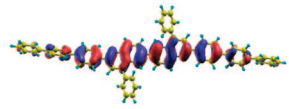	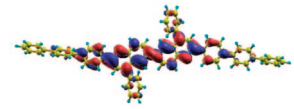
$\|6\rangle$ $\Delta E = 4.02$ eV f = 0.957 $W = 57.6\%$	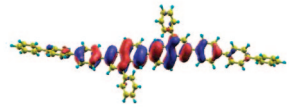	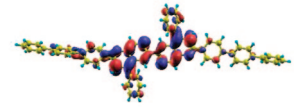
$\|12\rangle$ $\Delta E = 4.30$ eV f = 0.962 $W = 52.6\%$	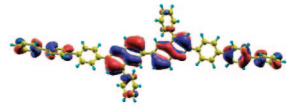	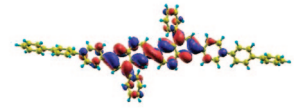

[a] ΔE is the excitation energy, f is the corresponding oscillator strength, and W is the weight of the plotted orbital in the respective transition density matrix.

simulate the optical absorption spectra of other four family members of oligoquinoline molecules. In our simulation, we did not employ the most commonly used Gaussian function. These two functions[59] (eq 1 and Gaussian function) have similar properties and are equivalent in the limit of $m \rightarrow \infty$, but the former gives a better fit to experiments. As displayed in Figure 2, our simulation for the absorption of BPYPQ shows two peaks, whose locations or absorption frequencies are close to the experimentally observed, while the third peak is almost invisible because of a very small absorption intensity. Figure 3 shows a large absorption peak at the lowest frequency and other two smaller peaks at higher frequencies, latter of which may combine to form a broader one.

Finally, we employ the natural transition orbital representation for excited states to analyze the corresponding excited states. The results are plotted and displayed in Tables 4 and 5, respectively. The orbitals we employ here are calculated

with the adiabatic PBE0 functional, which yield the most accurate excitation energies for the entire family of oligoquinoline molecules. It is clear that these low-lying excited states arise from $\pi-\pi^*$ excitations, as illustrated by their transition orbitals shown in Tables 4 and 5. From the weight ($W = 92\%$), we can see that the lowest excited state, $|1\rangle$, can be well represented by a single-pair of transition orbitals (see Table 4). It arises from a delocalized excitation involving the entire conjugated backbone of the BPYPQ oligomer. The side phenyl rings do not participate substantially in this optical excitation. Excited state $|5\rangle$ contributing to the second absorption peak is largely delocalized in the middle section of the molecule, compared to excited state $|1\rangle$, while excited state $|9\rangle$ contributing to the third absorption peak is mainly delocalized in the endgroups of the molecule. We note that excited states $|5\rangle$ and $|9\rangle$ are multiconfigurational, that is, they can be represented only by several pairs of transition orbitals. Here only the dominant ones are shown in Table 4.

The B3PPQ orbitals are slightly less delocalized, compared to those of BPYPQ, while the molecular structure of the former has a longer backbone. This is reflected by the higher excitation energies of B3PPQ. The same trend for the lowest triplet excitation is also observed by comparing Table 2 with Table 3. The oscillator strengths of B3PPQ corresponding to three selected excitations are much larger than those of BPYPQ. From Table 5, we can see that, like BPYPQ, these selected excited states also arise from $\pi-\pi^*$ excitations. The large weight $W = 95\%$ of the lowest excited-state suggests that excited state $|1\rangle$ can essentially be represented by a single-pair of transition orbitals. The side- and end-phenyl rings do not participate in this lowest-frequency optical excitation. Excited state $|6\rangle$ responsible for the second absorption peak is mainly delocalized in the middle section of the molecule, while excited state $|12\rangle$ is partly delocalized in the middle section and partly in the ending sections. Compared to excited states $|1\rangle$ and $|6\rangle$, it is much more delocalized. Table 5 also shows that there are slight charge redistributions during the excitations, with the electronic density flow toward the center of the molecules.

IV. Conclusion

In this paper, we have employed the adiabatic TDDFT approach to study the optical absorption of two new family members of the blue-light emitting oligoquinolines bearing pyrenyl and triphenyl endgroups, BPYPQ and B3PPQ, in gas phase and chloroform ($CHCl_3$) solution. Ionization potentials and electron affinities, which are important in photochemistry, are also calculated using the ground-state DFT. Our calculations of excitation energies are in good agreement with the experimental measurements in chloroform solution, while the absorption intensity or oscillator strength for two higher-frequency absorptions are significantly underestimated for BPYPQ. The ionization potentials agree well with the experimental estimates, while the electron affinities are underestimated.

Our results show that there are two absorption peaks for B3PPQ molecules in gas phase and solution, and the second peak located at a higher frequency may be split into two peaks, as experimentally observed for BPYPQ molecule. The first absorption peak arises from the lowest singlet−singlet transition, whereas the other arises from the multiconfigurational transition. Our simulation of the experimental spectra with the TDDFT data calculated from the adiabatic PBE0 functional shows that there are two main absorption peaks. This prediction agrees with experiments. However, it is questionable whether the third peak can be observed. This discrepancy of the theory from the experimental observation for the third peak intensity may arise from the fact that many effects (temperature, disorder, etc.) that affect the experiment have not been taken into account in our calculations. Our calculations also show that the solvent effects on computed electronic transitions are negligible. To get a detailed understanding of these excitations, an analysis of the natural transition orbitals corresponding to the selected excited states has been made. We find that for both BPYPQ and B3PPQ molecules, the low-lying optically active excited states are $\pi-\pi^*$ excitations with varying degree of spatial delocalization and charge transfer character.

We emphasize here that the order of accuracy of the five adiabatic density functionals in predicting the low-lying excitation energies of molecules, as found in our previous studies,[14,42] that is, LSDA < TPSS < TPSSh < B*3*LYP < PBE0, continue to hold, as shown in Tables 2 and 3.

Acknowledgment. The authors thank Ekaterina Badaeva for technical help and Chao Wu for helpful discussions. This work was supported by the U.S. Department of Energy under the Grant No. LDRD-PRD X9KU at Los Alamos National Laboratory.

References

(1) Tonzola, C. J.; Kulkarni, A. P.; Gifford, A. P.; Kaminsky, W.; Jenekhe, S. A. *Adv. Funct. Mater.* **2007**, *17*, 863.

(2) Hancock, J. M.; Gifford, A. P.; Tonzola, C. J.; Jenekhe, S. A. *J. Phys. Chem. C* **2007**, *111*, 6875.

(3) Forrest, S. R. *Nature* **2004**, *428*, 911.

(4) Kraft, A.; Grimsdale, A. C.; Holmes, A. B. *Angew. Chem., Int. Ed.* **1998**, *37*, 402.

(5) Mitschke, U.; Bauerle, P. J. *J. Mater. Chem.* **2000**, *10*, 1471.

(6) Kim, D. Y.; Cho, H. N.; Kim, C. Y. *Prog. Polym. Sci.* **2000**, *25*, 1089.

(7) Kulkarni, A. P.; Tonzola, C. J.; Babel, A.; Jenekhe, S. A. *Chem. Mater.* **2004**, *16*, 4556.

(8) Heeger, A. J.; Heeger, D. J.; Langan, J.; Yang, Y. *Science* **1995**, *270*, 1642.

(9) Sirringhaus, H.; Kawase, T.; Friend, R. H.; Shimoda, T.; Inbasekaran, M.; Wu, W.; Woo, E. P. *Science* **2000**, *290*, 2123.

(10) Menard, E.; Meitl, M.; Sun, Y.; Park, J.-U.; Shir, D.-L.; Nam, Y.-S.; Jeon, S.; Rogers, J. *Chem. Rev.* **2007**, *107*, 1117.

(11) Granstrom, M.; Petritsch, K.; Arias, A. C.; Lux, A.; Andersson, M. R.; Friend, R. H. *Nature* **1998**, *395*, 257.

(12) Yu, G.; Gao, J.; Hummelen, J. C.; Wudl, F.; Heeger, A. J. *Science* **1995**, *270*, 1789.

(13) Sirringhaus, H.; Brown, P. J.; Friend, R. H.; et al. *Nature* **1999**, *401*, 685.

(14) Tao, J.; Tretiak, S.; Zhu, J.-X. *J. Phys. Chem. B* **2008**, *112*, 13701.

(15) Giuliani, G. F.; Vignale, G. *Quantum Theory of the Electron Liquid*; Cambridge University Press: 2005.

(16) *Time-Dependent Density Functional Theory*; Lecture Notes in Physics Vol. 706; Marques, M. A. L., Ullrich, C. A., Nogueira, F., Rubio, A., Burke, K., Gross, E. K. U., Eds.; Springer: Berlin, 2006.

(17) Perdew, J. P.; Kurth, S. In *A Primer in Density Functional Theory*; Lecture Notes in Physics Vol. 620; Fiolhais, C., Nogueira, F., Marques, M., Eds.; Springer: Berlin, 2003.

(18) Kohn, W.; Sham, L. J. *Phys. Rev.* **1965**, *140*, A1133.

(19) Parr, R. G.; Yang, W.; *Density Functional Theory of Atoms and Molecules*; Oxford University Press: Oxford, U.K., 1989.

(20) Tao, J.; Perdew, J. P.; Staroverov, V. N.; Scuseria, G. E. *Phys. Rev. Lett.* **2003**, *91*, 146401.

(21) Staroverov, V. N.; Scuseria, G. E.; Tao, J.; Perdew, J. P. *J. Chem. Phys.* **2003**, *119*, 12129; **2004**,, *121*, 11507(E).

(22) Stephens, P. J.; Devlin, F. J.; Chabalowski, C. F.; Frisch, M. J. *J. Phys. Chem.* **1994**, *98*, 11623.

(23) Ernzerhof, M.; Scuseria, G. E. *J. Chem. Phys.* **1999**, *110*, 5029.

(24) Adamo, C.; Barone, V. *J. Chem. Phys.* **1999**, *110*, 6158.

(25) Petersilka, M.; Gossmann, U. J.; Gross, E. K. U. *Phys. Rev. Lett.* **1996**, *76*, 1212.

(26) Bauernschmitt, R.; Ahlrichs, R. *Chem. Phys. Lett.* **1996**, *256*, 454.

(27) Zangwill, A.; Soven, P. *Phys. Rev. Lett.* **1980**, *45*, 204; *Phys. Rev. A* **1980**,, *21*, 1561.

(28) Gross, E. K. U.; Kohn, W. *Phys. Rev. Lett.* **1985**, *55*, 2850.

(29) Vignale, G.; Kohn, W. *Phys. Rev. Lett.* **1996**, *77*, 2037.

(30) Tao, J.; Vignale, G. *Phys. Rev. Lett.* **2006**, *97*, 036403.

(31) Tao, J.; Vignale, G.; Tokatly, I. V. *Phys. Rev. B* **2007**, *76*, 195126.

(32) Tozer, D. J.; Handy, N. C. *J. Chem. Phys.* **1998**, *109*, 10180.

(33) Stratmann, R. E.; Scuseria, G. E. *J. Chem. Phys.* **1998**, *109*, 8218.

(34) Adamo, C.; Scuseria, G. E.; Barone, V. *J. Chem. Phys.* **1999**, *111*, 2889.

(35) Schipper, P. R. T.; Gritsenko, O. V.; van Gisbergen, S. J. A.; Baerends, E. J. *J. Chem. Phys.* **2000**, *112*, 1344.

(36) Sala, F. D.; Görling, A. *Int. J. Quantum Chem.* **2003**, *91*, 131.

(37) Jacquemin, D.; Bouhy, M.; Perpete, E. A. *J. Chem. Phys.* **2006**, *124*, 204321.

(38) Tretiak, S. *Nano Lett.* **2007**, *7*, 2201.

(39) Adams, R. D.; Captain, B.; Hall, M. B.; Trufan, E.; Yang, X. Z. *J. Am. Chem. Soc.* **2007**, *129*, 12328.

(40) Sancho-García, J. C. *Chem. Phys. Lett.* **2007**, *439*, 236.

(41) Igumenshchev, K. I.; Tretiak, S.; Chernyak, V. Y. *J. Chem. Phys.* **2007**, *127*, 114902.

(42) Tao, J.; Tretiak, S.; Zhu, J.-X. *J. Chem. Phys.* **2008**, *128*, 084110.

(43) Perdew, J. P.; Burke, K.; Ernzerhof, M. *Phys. Rev. Lett.* **1996**, *77*, 3865.

(44) Perdew, J. P.; Staroverov, V. N.; Tao, J.; Scuseria, G. E. *Phys. Rev. A* **2008**, *78*, 052513.

(45) Staroverov, V. N.; Scuseria, G. E.; Tao, J.; Perdew, J. P. *Phys. Rev. B* **2004**, *69*, 075102.

(46) Perdew, J. P.; Ruzsinszky, A.; Tao, J.; Staroverov, V. N.; Scuseria, G. E.; Csonka, G. I. *J. Chem. Phys.* **2005**, *123*, 062201.

(47) Martin, R. L. *J. Chem. Phys.* **2003**, *118*, 4775.

(48) Frisch, M. J., Trucks, G. W.; Schlegel, H. B.; Scuseria, G. E.; Robb, M. A.; Cheeseman, J. R.; Zakrzewski, V. G.; Montgomery, Jr., J. A.; Stratmann, R. E.; Burant, J. C.; Dapprich, S.; Millam, J. M.; Daniels, A. D.; Kudin, K. N.; Strain, M. C.; Farkas, O.; Tomasi, J.; Barone, V.; Cossi, M.; Cammi, R.; Mennucci, B.; Pomelli, C.; Adamo, C.; Clifford, S.; Ochterski, J.; Petersson, G. A.; Ayala, P. Y.; Cui, Q.; Morokuma, K.; Malick, D. K.; Rabuck, A. D.; Raghavachari, K.; Foresman, J. B.; Cioslowski, J.; Ortiz, J. V.; Stafanov, B. B.; Liu, G.; Liashenko, A.; Piskorz, P.; Komaromi, I.; Gomperts, R.; Martin, R. L.; Fox, D. J.; Keith, T.; Al-Laham, M. A.; Peng, C. Y.; Nanayakkara, A.; Gonzalez, C.; Challacombe, M.; Gill, P. M. W.; Johnson, B.; Chen, W.; Wong, M. W.; Andres, J. L.; Gonzalez, C.; Head-Gordon, M.; Replogle, E. S.; Pople, J. A. *Gaussian 03.*; Gaussian, Inc.: Pittsburgh PA, 2003.

(49) Perdew, J. P.; Wang, Y. *Phys. Rev. B* **1992**, *45*, 13244.

(50) Cancès, E.; Mennucci, B.; Tomasi, J. *J. Chem. Phys.* **1997**, *107*, 3032.

(51) Barone, V.; Cossi, M. *J. Phys. Chem. A* **1998**, *102*, 1995.

(52) Cossi, M. *Chem. Phys. Lett.* **2003**, *384*, 179.

(53) Cossi, M.; Rega, N.; Scalmani, G.; Barone, V. J. *Comp. Chem.* **2003**, *24*, 669.

(54) Cancès, M. T.; Mennucci, B.; Tomasi, J. *J. Chem. Phys.* **1997**, *107*, 3032.

(55) Cossi, M.; Barone, V.; Mennucci, B.; Tomasi, J. *Chem. Phys. Lett.* **1998**, *286*, 253.

(56) Mennucci, B.; Tomasi, J. *J. Chem. Phys.* **1997**, *106*, 5151.

(57) Mennucci, B.; Cancès, E.; Tomasi, J. *J. Phys. Chem. B* **1997**, *101*, 10506.

(58) Rösch, N.; Trickey, S. B. *J. Chem. Phys.* **1997**, *106*, 9840.

(59) Arfken, G. *Mathematical Methods for Physicists*, 3rd ed.; Academic Press: New York, 1985.

CT800523J

JCTC Journal of Chemical Theory and Computation

Förster Energy Transfer and Davydov Splittings in Time-Dependent Density Functional Theory: Lessons from 2-Pyridone Dimer

Espen Sagvolden,*,† Filipp Furche,*,† and Andreas Köhn‡

University of California, Irvine, Department of Chemistry, 1102 Natural Sciences II, Irvine, California 92697-2025, and University of Mainz, Institute of Physical Chemistry, D-55099 Mainz, Germany

Received December 12, 2008

Abstract: The Davydov or exciton splitting of vertical excitation energies is commonly used to estimate the excitation energy transfer rate between chromophores. Here we investigate the S_1-S_2 Davydov splitting in 2-pyridone dimer as a function of the monomer separation, R. We assess the ability of various functionals to reproduce the Davydov splitting at finite R predicted by the approximate coupled cluster singles doubles method CC2. While semilocal functionals fail qualitatively because of spurious charge-transfer intruder states, global hybrids with a large fraction of exact exchange, such as BHandH-LYP, reproduce the CC2 splittings within few wavenumbers. We analyze our results by comparison to lowest-order intermolecular perturbation theory in the spirit of Förster and Dexter. At equilibrium hydrogen bond distance, the Förster–Dexter splittings are too small by up to a factor of 2.

1. Introduction

Excitation energy transfer (EET), the direct migration of energy from a donor to an acceptor chromophore, underlies natural and artificial light harvesting. In photosynthesis[1] and light-driven ion pumps,[2] antenna chromophores transfer solar excitation energy to a reaction center by EET. EET is also essential in excitonic solar cells, allowing the migration of excitons to the interface where charge-separation takes place.[3] Fluorescence resonance energy transfer (FRET) has found widespread use in biology, because the R^{-6} dependence of the EET rate on the chromophore distance R may be used as a spectroscopic ruler.[4]

Quantitative prediction of EET rates from first principles is a challenge for electronic structure methods. According to Förster theory,[5] electronic excitation energy can be transferred from one molecule to a neighboring molecule if their excitation energies are nearly degenerate. It is generally assumed that nuclear relaxation of the donor excited electronic state takes place on a time scale much faster than energy transfer, so the relevant criterion for transfer is nonzero overlap of the donor emission and the acceptor absorption spectra. In his ground-breaking 1948 paper,[5] Förster used intermolecular perturbation theory to derive his well-known result for the EET rate

$$k_{\mathrm{ET}} = K|\langle \Psi^{\mathrm{A}}_{\mathrm{gs}}\Psi^{\mathrm{B}}_{\mathrm{ex}}|\hat{V}|\Psi^{\mathrm{A}}_{\mathrm{ex}}\Psi^{\mathrm{B}}_{\mathrm{gs}}\rangle|^2 = K\left|\int d\mathbf{r}d\mathbf{r}'\frac{\rho^{\mathrm{A}}(\mathbf{r})\rho^{\mathrm{B}}(\mathbf{r}')}{|\mathbf{r}-\mathbf{r}'|}\right|^2 \quad (1)$$

where K accounts for the vibrational density of states and Franck–Condon factors. Here, $\rho^{\mathrm{A}}(\mathbf{r})$ and $\rho^{\mathrm{B}}(\mathbf{r})$ are the transition densities of the unperturbed chromophores. $\hat{V}$ is the sum of electron–electron interactions between electrons on opposite subsystems. $\Psi^{\mathrm{A}}_{\mathrm{gs}}$ and $\Psi^{\mathrm{B}}_{\mathrm{gs}}$ are the unperturbed chromophore ground states, while $\Psi^{\mathrm{B}}_{\mathrm{ex}}$ and $\Psi^{\mathrm{B}}_{\mathrm{ex}}$ are the excited states. The second equality is only correct at long-range, where Dexter exchange effects become negligible. In case of dimers, the splitting of the degenerate vertical monomer excitation energies is called Davydov splitting,[6] $\Delta\Omega$. The Davydov splitting may be related to the energy transfer rate by first-order degenerate perturbation theory

* To whom correspondence should be addressed. E-mail: esagvold@uci.edu (E.S.); filipp.furche@uci.edu (F.F.).

† University of California.

‡ University of Mainz.

10.1021/ct800551g CCC: $40.75
Published on Web 03/20/2009

$$k_{\mathrm{ET}} \approx \frac{K}{4}|\Delta\Omega|^2 \tag{2}$$

We will consider the vertical splitting between the electronic energy eigenvalues of the two supersystem states evaluated at a common nuclear geometry. This splitting is also often called exciton splitting.

According to eq 1, k_{ET} is proportional to the square of the classical Coulomb (or Hartree) interaction of the transition densities $\rho^{\mathrm{A}}(\mathbf{r})$ and $\rho^{\mathrm{B}}(\mathbf{r})$. Since the transition densities integrate to zero, eq 1 is dominated by a transition dipole−transition dipole (hereafter called dipole−dipole) interaction at long-range, if the monomer excitations are dipole-allowed

$$k_{\mathrm{ET}} = K\left|\frac{\mathbf{p}_{\mathrm{A}}\cdot\mathbf{p}_{\mathrm{B}} - 3(\mathbf{n}\cdot\mathbf{p}_{\mathrm{A}})(\mathbf{n}\cdot\mathbf{p}_{\mathrm{B}})}{R^3}\right|^2 + O\left(\frac{1}{R^8}\right) \tag{3}$$

where $\mathbf{R}$ is the vector between the centers of the subsystems, $\mathbf{n} = \mathbf{R}/|\mathbf{R}|$, and $\mathbf{p}_{\mathrm{A/B}}$ are the monomer transition dipole moments. At shorter range, the dipole−dipole description is incorrect, because higher-order multipole moments,[7] overlap effects,[8] polarization effects, and the effects of exchange of one or more electrons among the subsystems[9] no longer vanish. In intramolecular EET it may also be difficult to uniquely define two subsystems with separate electronic eigenstates.

An alternative route to EET rates is to extract the exciton splitting $\Delta\Omega$ from a supermolecular calculation, bypassing the limitations of intermolecular perturbation theory. The resulting exciton splittings are directly comparable to spectroscopic results. A detailed comparison of the two approaches to EET was presented by Tretiak et al.[10,11]

Time-dependent density-functional theory (TDDFT)[12] lends itself easily both to the transition density interaction approach and the Davydov splitting approach. It would be beneficial to be able to use TDDFT for EET in biological systems because of the favorable relationship between accuracy and computational cost offered by modern TDDFT methods.[13]

Förster theory has been extensively studied. Several questions have been addressed in articles by other authors. In addition to works mentioned above, the spatial locality of an excitation[10] and the effect of molecular bridges linking two chromophores,[7,14] and of solvents[8,15] have been studied. The Davydov-splitting approach in TDDFT has been studied by Hsu et al.[8] in a basis consisting of the subsystem excitations. In the present paper, we will evaluate the performance of common density functional methods in computing the Davydov splitting using the 2-pyridone dimer as an example. The 2-pyridone dimer is an experimentally well-characterized[16−19] representative of a large family of hydrogen bound dimers and DNA base pairs. In section 2, we will give a short introduction to linear response theory in TDDFT. In section 4, we present benchmark results for various functionals as we vary the length of the hydrogen bond linking the two 2-pyridone monomers.

2. Introduction to Linear Response Theory in TDDFT

From linear response theory in TDDFT within the adiabatic approximation, the excitation energies, Ω, are given by the solutions of the symplectic eigenvalue problem[20−22]

$$(\Lambda - \Omega\Delta)|X, Y\rangle = 0 \tag{4}$$

The excitation vectors

$$|X, Y\rangle = \begin{pmatrix} X \\ Y \end{pmatrix} \tag{5}$$

represent Kohn-Sham (KS) transition density matrices, where $X \in L_{\mathrm{virt}} \times L_{\mathrm{occ}}$ and $Y \in L_{\mathrm{occ}} \times L_{\mathrm{virt}}$. Here, L_{occ} is the Hilbert space of occupied orbitals and L_{virt} the Hilbert space of unoccupied ground-state KS-orbitals. The superoperators Λ and Δ are given by

$$\Lambda = \begin{pmatrix} A & B \\ B & A \end{pmatrix} \qquad \Delta = \begin{pmatrix} 1 & 0 \\ 0 & -1 \end{pmatrix} \tag{6}$$

where 1 is the identity matrix

$$A_{ia\sigma,jb\sigma'} = (\varepsilon_a - \varepsilon_i)\delta_{ij}\delta_{ab}\delta_{\sigma\sigma'} + (ia\sigma|jb\sigma') + f^{\mathrm{xc}}_{ia\sigma,jb\sigma'} - c_x\delta_{\sigma\sigma'}(ab\sigma|ij\sigma) \tag{7}$$

$$B_{ia\sigma,jb\sigma'} = (ia\sigma|jb\sigma') + f^{\mathrm{xc}}_{ia\sigma,jb\sigma'} - c_x\delta_{\sigma\sigma'}(ja\sigma|ib\sigma) \tag{8}$$

The labels i and j denote occupied and a and b unoccupied orbitals and $(ia\sigma|jb\sigma')$ is a two-electron repulsion integral in Mulliken notation. $f^{\mathrm{xc}}_{ia\sigma jb\sigma'}$ is given by

$$f^{\mathrm{xc}}_{ia\sigma,jb\sigma'} = \int d\mathbf{r}d\mathbf{r}'\phi_i(\mathbf{r})\phi_a(\mathbf{r})f^{\mathrm{xc}}_{\sigma\sigma'}(\mathbf{r},\mathbf{r}')\phi_j(\mathbf{r}')\phi_b(\mathbf{r}') \tag{9}$$

Within the adiabatic approximation, the exchange-correlation (xc) kernel $f^{\mathrm{xc}}_{\sigma\sigma'}$ is the second functional derivative of the semilocal part of the chosen xc-functional

$$f^{\mathrm{xc}}_{\sigma\sigma'}(\mathbf{r},\mathbf{r}') = \frac{\delta^2 E^{\mathrm{xc,sl}}}{\delta\rho_\sigma(\mathbf{r})\delta\rho'_\sigma(\mathbf{r})} \tag{10}$$

c_{x} is the Hartree−Fock exchange mixing coefficient. In TDHF, $c_{\mathrm{x}} = 1$ and in semilocal functionals it is 0. In global hybrids, it takes values between 0 and 1. The TDDFT-based approach to Davydov splittings of Hsu et al.[8] uses Förster's intermolecular interaction theory. Hsu et al.[8] explore the problem in a basis formed by the local monomer excitations using the isolated monomer KS-eigenvalues and orbitals. They derive their estimate of the Davydov splitting by calculating the first-order perturbation of the excitation energy from the interaction between the subsystems. Their basis includes only local excitations in the monomers (as opposed to charge-transfer excitations between monomers), which are the relevant excitations in Förster theory. This provides a theory correct to the level where either the KS-eigenvalues deviate from the monomer values, the dimer orbitals deviate from linear combinations of pairwise degenerate monomer orbitals or the charge-transfer excitations mix with the local excitations.

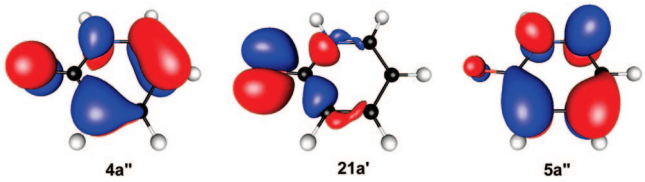

Figure 1. Monomer π (4a''), n (21a'), and π^* (5a'')-orbitals. Molecular orbital (MO) plots were generated using a contour value of 0.05 and PBE/aug-def2-TZVP orbitals.

3. Computational Details

Ground-state structures were optimized using second-order Møller−Plesset theory (MP2) within the resolution-of-the-identity (RI) approximation[23−25] and polarized triple-ζ valence (def2-TZVPP)[26] basis sets. The coordinate file is given as Supporting Information. The structure was confirmed to be a minimum by a force constant calculation[27,28] using PBE0[29] and polarized triple-ζ valence (def2-TZVP)[26] basis sets with additional diffuse augmentation from aug-cc-pVTZ.[30] Starting from this geometry, we increased the distance between the monomers by stretching the hydrogen bonds by increments of 1 au and reoptimized the ground-state geometry in C_{2h} keeping the hydrogen bond length fixed. For this set of geometries, vertical singlet excitation energies were computed using the local density approximation (LDA),[31−33] Perdew−Burke−Ernzerhof generalized gradient approximation (PBE),[34] B3LYP global hybrid,[35−38] PBE0 global hybrid,[29] and BHandH-LYP global hybrid[35−37,39] functionals, as well as configuration interaction with single excitations (CIS), time-dependent Hartree−Fock (TDHF) and the approximate coupled cluster singles doubles method CC2.[59,60] The TDHF and CIS calculations were performed using def2-TZVPP[26] basis sets, with diffuse augmentation from aug-cc-pVTZ,[30] CC2 using an aug-cc-pVQZ basis,[30] and the TD-DFT calculations using def2-TZVP[26] basis sets with diffuse augmentation from aug-cc-pVTZ.[30] All calculations were performed using the TURBOMOLE package[40−48] using an m4 grid for DFT calculations. Interaction matrix elements from monomer transition densities were calculated according to eq 1, including exchange and overlap effects where applicable. These calculations were performed using an implementation described in ref 7.

4. Results

4.1. 2-Pyridone Monomer. We found a monomer ground-state structure with C_s symmetry. We computed the monomer vertical excitation energies, transition densities and transition dipole moments at the RI-MP2 ground-state structure. In all computations, the HOMO is the 4a'' orbital (Figure 1). The 5a'' orbital (Figure 1) is the LUMO in all computations with semilocal and hybrid density functionals. In TDHF (and implicitly CC2 and CIS) the 22a' (an oxygen lone pair) orbital is the LUMO. While all hybrid functionals as well as TDHF, CIS and CC2 yield the first A' excitation as the S_1-state, LDA and PBE incorrectly predict the A'' excitation to be S_1. In Table 1 we display the vertical excitation energy and transition dipole moment of the lowest A' excitation of the monomer.

Table 1. Vertical Excitation Energy, ΔE (in eV), and Transition Dipole Moment, μ (in Debye), in the Length Representation and the Assignment of the Lowest A' and A'' Excitations[a,b]

	$2^1A'$			$1^1A''$		
	ΔE	μ	assignment	ΔE	μ	assignment
LDA	3.99	2.00	$\pi \rightarrow \pi^*$	3.53	0.09	$n \rightarrow \pi^*$
PBE	3.99	2.00	$\pi \rightarrow \pi^*$	3.58	0.09	$n \rightarrow \pi^*$
B3-LYP	4.26	2.33	$\pi \rightarrow \pi^*$	4.44	0.10	$n \rightarrow \pi^*$
PBE0	4.35	2.37	$\pi \rightarrow \pi^*$	4.60	0.11	$n \rightarrow \pi^*$
BHandH-LYP	4.58	2.67	$\pi \rightarrow \pi^*$	5.40	0.36	$\pi \rightarrow C(3s)$
TDHF	4.89	3.00	$\pi \rightarrow \pi^*$	5.73	0.42	$\pi \rightarrow C(3s)$
CIS	5.19	3.39	$\pi \rightarrow \pi^*$	5.74	0.43	$\pi \rightarrow C(3s)$
CC2	4.36	2.50	$\pi \rightarrow \pi^*$	4.54	0.04	$n \rightarrow \pi^*$
CASPT2[a]	4.37	n/a	$\pi \rightarrow \pi^*$	4.99	n/a	$n \rightarrow \pi^*$
MRCI-Q[b]	4.70	n/a	$\pi \rightarrow \pi^*$	n/a	n/a	n/a

[a] Ref 49. [b] Ref 50.

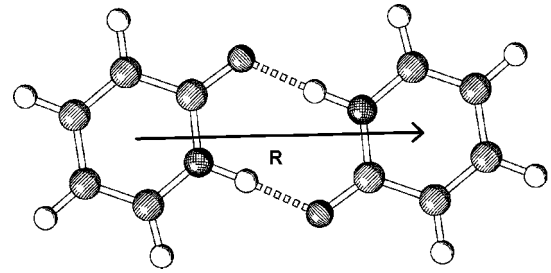

Figure 2. Structure of the 2-pyridone dimer. We will use two length scales in this article. The distance, R, between the centers of the monomers, as defined above, and the elongation of the hydrogen bond relative to its equilibrium value (in integer steps from 0a.u. to 8a.u.). At the equilibrium structure, $R = 11.15$ au.

The $\pi \rightarrow \pi^*$ transition giving rise to the lowest A' excitation is almost a pure 4a''→5a'' transition in TDDFT. In CC2, however, is it dominated by 4a'' → 6a'' and some weight of 4a'' → 7a''. This is in keeping with the MRCI-Q results reported by Barbatti et al.[50] With CIS and TDHF, the 4a'' → 5a'' transition gets approximately the same weight as the 4a'' → 6a'' transition.

The lowest A'' excitation is dominated by the 4a'' → 22a' transition in TDHF and CIS. In CC2, it is dominated by 21a' → 6a'' with some 21a' → 7a'. In all TDDFT computations, the lowest A'' excitation is almost purely 21 → 5a'', except BHandH-LYP, where there is also some degree of 21a' → 6a''.

4.2. 2-Pyridone Dimer Ground-State and Vertical Excitations. The RI-MP2 ground-state structure of the 2-pyridone dimer was found to have C_{2h} symmetry and is displayed in Figure 2. Monomer states of A' symmetry split into dimer eigenstates with A_g and B_u symmetry, while the monomer states of A'' symmetry split into A_u and B_g states. The lowest A_g and B_u excitation energies are given in Table 2. On the basis of the monomer computations, methods predicting the lowest monomer A' transition to be 4a'' → 5a'', should predict that the lowest A_g and B_u transitions are transitions between the occupied states 4a_u and 4b_g and the virtual states 5a_u and 5b_g. This turns out to be the case. Likewise, the CC2 excitation is dominated by transitions from 4a_u and 4b_g into 6a_u and 6b_g.

Table 2. Vertical Excitation Energy, ΔE (in eV), and Transition Dipole Moment, μ (in Debye) of the 2-Pyridone Dimer[a]

	2^1A_g		1^1B_u	
	ΔE	μ	ΔE	μ
LDA	3.348	0.00	3.382	0.65
PBE	3.371	0.00	3.403	0.62
B3-LYP	4.176	0.00	4.333	0.70
PBE0	4.328	0.00	4.511	3.05
BHandH-LYP	4.616	0.00	4.752	3.47
TDHF	4.936	0.00	5.062	3.89
CIS	5.226	0.00	5.375	4.44
CC2	4.290	0.00	4.426	3.23

[a] All excitations have $\pi \rightarrow \pi^*$ character.

Table 3. Davydov Splitting between the Lowest Singlet A_g Excitation and the Lowest Singlet B_u Excitation at Different Values of the Elongation of the Hydrogen Bonds[a]

method	0 au	1 au	2 au	3 au	4 au	5 au	6 au	7 au	8 au
LDA	278	53	10	2	0	0	0	0	0
PBE	259	50	9	2	0	0	0	0	0
B3-LYP	1266	629	423	291	209	159	125	100	82
PBE0	1480	727	428	292	214	164	130	104	85
BHandH-LYP	1101	716	493	356	267	208	165	134	110
TDHF	1019	745	544	408	314	248	200	163	135
CIS	1205	897	662	500	387	306	247	202	167
CC2	1099	682	456	323	239	183	144	115	93

[a] Distances in a.u. relative to the equilibrium bond length. Note that the lowest singlet excited states for LDA and PBE are charge transfer states, not the localized excitations we are studying. All splittings in cm^{-1}.

For symmetry reasons, the A_g excitations are dipole forbidden and the transition dipole moment of the B_u state should be roughly $\sqrt{2}$ times the transition dipole moment of the monomer A' excitation. As can be seen from comparison of Tables 1 and 2, this is true for PBE0, BHandH-LYP, TDHF, CC2, and CIS, but not for B3-LYP, PBE, and LDA. As will be discussed below, this is due to an admixture of charge-transfer excitations into the local excitations in the case of B3-LYP and the incorrect ordering of local and charge transfer excitations with semilocal functionals.

4.3. Dimer Davydov Splittings. We will now investigate how the design of a density functional affects the splitting at ranges where chromophores (in this case the 2-pyridone monomers) are separated by several au. This is an important regime, both to real cases of energy transfer in nature and to the application of energy transfer as a spectroscopic ruler.

The calculated Davydov splittings of the 2^1A_g and 1^1B_u are displayed in Table 3 and Figure 3. An experimental value for the Davydov splitting is reported for the dimer in the gas phase. Müller et al.[19] found a splitting on the order of 40−50 cm^{-1}. This value, however, refers to a vibronically resolved spectrum and cannot easily be related to the splitting of vertical excitation energies, as considered here. Strong relaxation effects seem to play a role and warrant further investigations which are beyond the scope of the present work. As benchmark, we use results from CC2 calculations, which is the most accurate level of theory that is applicable to a system of the present size. CC2 yields accurate excitation energies for systems with single reference ground states. The

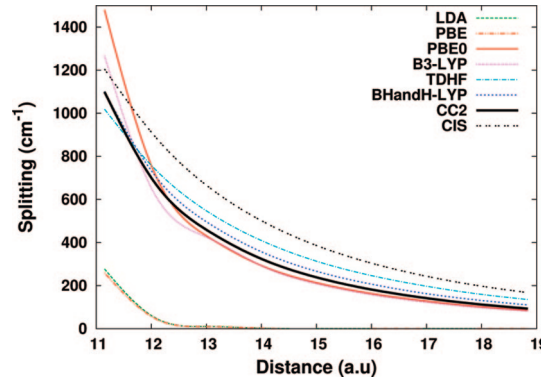

Figure 3. Decay of the Davydov splitting calculated by different methods. Splittings in cm^{-1}. R is the distance between the centers of the two monomers, the equilibrium distance is 11.15 au.

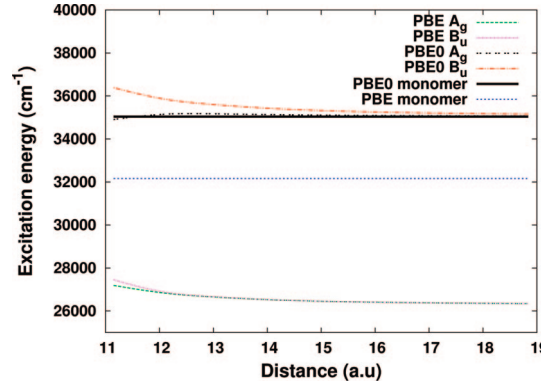

Figure 4. Decay of the first splitting calculated by PBE and PBE0 in cm^{-1}. One sees that while the PBE dimer excitation energies are far away from the PBE monomer first excitation energy, the PBE0 dimer excitation energy tends to its monomer excitation energy as the range increases. This indicates that the lowest PBE0 excitation is local while that of PBE is a charge-transfer excitation. LDA (not displayed) has the same behavior as PBE.

D_1 diagnostic of Janssen and Nielsen[51] is in the range of 0.07−0.08, indicating that CC2 should be reliable here. Furthermore, the T_2 measure for double excitations is in the area of 8−10%. This is also indicative that we should be able to rely on the CC2 calculations.

The global hybrid functional BHandH-LYP($c_x = 0.5$) predicts the Davydov splitting accurately within the entire tested range. TDHF($c_x = 1$) fares well at the equilibrium hydrogen bond length but overestimates the splitting as the hydrogen bonds are stretched. B3-LYP($c_x = 0.20$) and PBE0($c_x = 0.25$) overestimate the splitting at the equilibrium hydrogen bond length but perform better when the hydrogen bond is stretched. One can clearly see the dependence of the splitting on the Hartree−Fock mixing coefficient c_x. As the distance between the monomers increases to 8 au greater than the equilibrium distance, one can observe a clear tendency toward increased splitting with respect to c_x going from B3-LYP to PBE0, BHandH-LYP, and TDHF.

LDA and PBE, however, fail completely to predict the correct splitting. Already at the equilibrium distance the splitting between the lowest A_g and B_u states is significantly

Table 4. Oscillator Strength f (Length Representation) and Excitation Energy ΔE (in eV) for the Two Lowest Pairs of Singlet Excited States Evaluated When the Hydrogen Bond Has Been Stretched by 8 au

	f			ΔE		
excitation	LDA	PBE	PBE0	LDA	PBE	PBE0
2^1A_g	0	0	0	3.24	3.27	4.35
3^1A_g	0	0	0	3.99	3.99	4.75
1^1B_u	5×10^{-8}	7×10^{-8}	0.18	3.24	3.27	4.36
2^1B_u	0.12	0.12	4×10^{-7}	4.00	4.00	4.75

Table 5. Energy of 2^1B_u Minus the Energy of the 3^1A_g in cm^{-1}[a]

method	0 au	1 au	2 au	3 au	4 au	5 au	6 au	7 au	8 au
LDA	260	364	286	208	153	116	90	71	58
PBE	291	368	286	207	153	116	91	72	58
PBE0	−678	−155	−28	−5	−1	0	0	0	0

[a] This is the LDA and PBE predictions for the Davydov splitting between the localized excited states. The PBE0 states shown are charge transfer excitations. The splitting for PBE at 4 au failed to converge.

less than for the other functionals, and from there the splitting rapidly falls off to zero as the hydrogen bond length is stretched.

The reason for this discrepancy is that the first excited-state in the LDA and PBE calculations is not the localized excitation, but rather the corresponding charge-transfer (CT) excitation. It is well-known[52,53] that both Hartree−Fock, semilocal density functionals and their hybrids will estimate the energy of CT excitations to be the Kohn−Sham gap $\varepsilon_{LUMO} - \varepsilon_{HOMO}$ at large R, while the correct excitation energy in the large R limit is the monomer excitation energy. For semilocal functionals, the Kohn−Sham gap is generally lower than the actual charge transfer excitation energy.[54] The PBE HOMO−LUMO gap at 8 au is 3.27 eV and the LDA gap is 3.24 eV, which coincides with the excitation energies of the 2^1A_g and 1^1B_u states given in Table 4. Both for LDA and PBE, the excitation energy of the 3^1A_g state is 3.99 eV and that of the 2^1B_u state is 4.00 eV, close or identical to the monomer excitation energies reported in Table 1. Also, the oscillator strength of a long-range charge-transfer excitation is negligible because of the vanishing overlap between eigenstates centered on opposite systems. We observe that for LDA and PBE, the oscillator strength for the transition to 1^1B_u is close to zero, while that of the transition to 2^1B_u is not. In contrast, for PBE0 the excitation energy of the 2^1A_g and 1^1B_u states equal the vertical excitation energy to the $2^1A'$ state of the monomer and the oscillator strength of the 1^1B_u transition is not small. We conclude that in LDA and PBE, the first pair of excitations are spurious charge transfer excitations, while the local excitations relevant to our investigation is the second pair of excitations. Table 5 displays the splitting of the second pair of excited states, showing the relevant Davydov splitting predicted by LDA and PBE.

However, even in the case of B3-LYP and PBE0, there is significant admixture of the CT excitations into the lowest excitations at short-range. At long-range, the dimer molecular

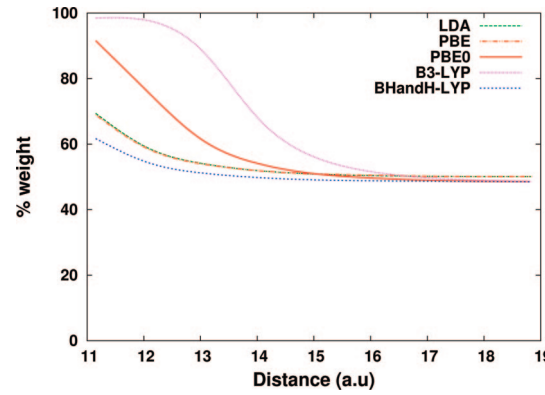

Figure 5. Weight of the dominant configuration in the 2^1A_g excitation as a function of the distance, R, between the centers of the monomers.

orbitals are linear combinations of pairs of degenerate monomer orbitals, and

$$|a''_{A/B}\rangle = \frac{1}{\sqrt{2}}(\langle a_u| \pm \langle b_g|) \tag{11}$$

Here, $|a''_{A/B}\rangle$ denotes a monomer orbital in the a'' irreducible representation (IRREP) of C_s and $|a_u\rangle$ and $|b_g\rangle$ are the corresponding dimer orbitals in the a_u and b_g IRREPs of C_{2h}. If the monomer $S_0 \rightarrow S_1$ excitation is a pure $4a'' \rightarrow 5a''$ transition, the TDDFT excitation vector for the resulting A_g dimer state has the form

$$\begin{aligned} |^1A_g\rangle_{loc} &= \frac{1}{\sqrt{2}}(|4a''_A\rangle\langle 5a''_A| + |4a''_B\rangle\langle 5a''_B|) \\ &= \frac{1}{\sqrt{2}}(|4a_u\rangle\langle 5a_u| + |4b_g\rangle\langle 5b_g|) \end{aligned} \tag{12}$$

for a local excitation and

$$\begin{aligned} |^1A_g\rangle_{CT} &= \frac{1}{\sqrt{2}}(|4a''_A\rangle\langle 5a''_B| + |4a''_B\rangle\langle 5a''_A|) \\ &= \frac{1}{\sqrt{2}}(|4a_u\rangle\langle 5a_u| - |4b_g\rangle\langle 5b_g|) \end{aligned} \tag{13}$$

for a CT excitation. This is similar for the B_u states. Thus, the local and CT excitations are plus and minus linear combinations of *two* dimer configurations with 50% weight each. The deviation of the weight of the dimer configurations from 50% thus implies the admixture of CT character into the local excitation and vice versa.

In Figure 5 and Figure 6 we have plotted the weight of the dominant configuration in the excitations into the 2^1A_g and 1^1B_u states, respectively. The graphs for PBE and LDA stay close to 50% at all ranges. This means that the excitations into their 2^1A_g and 1^1B_u states have pure charge transfer character at all ranges. Likewise, the graphs for BHandH-LYP display the same behavior. However, in this case the excitations into the 2^1A_g and 1^1B_u states have purely local character. The behavior of PBE0 and B3-LYP is different. In the case of the excitation into 2^1A_g, a single configuration has a large weight in PBE0 and yet more so in B3-LYP when the monomers are not too far apart, indicating a large admixture of CT character. As the distance

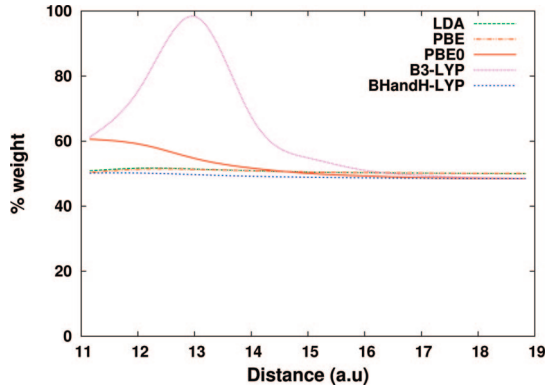

Figure 6. Weight of the dominant configuration in the 1^1B_u excitation as a function of R.

between the monomers increases, they fall off to 50%, meaning that the transition has acquired almost purely local character. For PBE0 the excitation into 1^1B_u appears to be purely local at all ranges based in Figure 6. However, the B3-LYP curve starts at close to 60% at the equilibrium distance, then jumps up to close to 100% when the monomers have been pulled 2a.u. apart and then returns to 50%. This avoided crossing behavior might indicate that the excitation into 1^1B_u at the dimer equilibrium structure is incorrectly predicted to be a charge transfer state by B3-LYP. This is also supported by the low dimer transition dipole moment 1^1B_u reported for B3-LYP in Table 2. As the monomers are pulled apart, it then appears that an even admixture of charge transfer and local excitations arises. At long-range, the local excitation is below the charge transfer excitation. In particular for B3-LYP, the excitations into 2^1A_g and 1^1B_u do not have corresponding weights of local excitations before the hydrogen bond has been stretched approximately 4 au For PBE0, both excitations become purely local at smaller range. The different extent of configuration mixing in PBE0 and B3-LYP rationalizes the bump in the B3-LYP graph in Figure 3 for values of R between 11 au and 13 au.

4.4. Intermolecular Perturbation Theory. Förster's dipole−dipole expression goes as $1/R^6$, with the separation distance R between the chromophores. This is not so at shorter range, however, where higher order transition multipole interactions (which give terms which go as $1/R^8$, $1/R^{10}$, etc.) and Dexter exchange start playing a role. Fückel et al.[7] found for another system that the dipole−dipole approximation was accurate for distances in excess of approximately 50 Å. The Davydov splitting approach also predicts the same $1/R^6$ long-range decay since the splitting goes like $1/R^3$ at long-range. Figure 3 shows the splitting of each method relative to the distance between the centers of the two monomers. Using eq 1, we have calculated the full Coulomb interaction between the monomer transition densities, V_{12}^{AB}, at the equilibrium hydrogen bond length (Table 7) and when it has been stretched 8 au (Table 6). Even when the hydrogen bonds are 8 au longer than their equilibrium length, one observes a significant discrepancy (approximately a factor 2/3) between the splitting calculated from the dipole−dipole interaction and the splitting from the supermolecular calculation. Hence, the dipole−dipole term is insufficient at this range. This is in keeping with the findings of Fückel et al.[7]

Table 6. Splitting, $\Delta\Omega$ (cm^{-1}), at 8 au from our TDDFT Calculations Compared to Twice the Full Transition Density Interaction (V_{12}^{AB}, Calculated Using Eq 1) and Twice the Dipole-Dipole Interaction (Labeled dip-dip)[a]

method	$\Delta\Omega$	$2V_{12}^{AB}$ (Coul+exch)	$2V_{12}^{AB}$ (Coul only)	2 dip-dip	monomer dipole
LDA	58	n/a	n/a	34	0.784
PBE	58	n/a	n/a	35	0.784
B3LYP	82	81	81	51	0.914
PBE0	85	84	84	53	0.931
BHandH-LYP	110	109	109	70	1.049
TDHF	134	135	135	89	1.177

[a] The column labeled (Coul only) contains only the Coulomb interaction between the transition densities. The (Coul+exch) column contains also the exchange part. Also displayed is the size of the monomer transition dipole moment in au.

Table 7. Splitting, $\Delta\Omega$ (cm^{-1}), at 0 au from our TDDFT Calculations Compared to Twice the Full Transition Density Interaction (V_{12}^{AB}, Calculated Using Eq 1) and Twice the Dipole−Dipole Interaction (Labeled dip-dip)[a]

method	$\Delta\Omega$	$2V_{12}^{AB}$ (Coul+exch)	$2V_{12}^{AB}$ (Coul only)	2 dip-dip	monomer dipole
LDA	260	n/a	n/a	169	0.734
PBE	291	n/a	n/a	170	0.733
B3LYP	1266	566	636	252	0.877
PBE0	1480	596	668	264	0.897
BHandH-LYP	1101	769	856	348	1.031
TDHF	1019	909	992	451	1.175

[a] The column labeled (Coul only) contains only the Coulomb interaction between the transition densities. The (Coul+exch) column contains also the exchange part. Also displayed is the size of the monomer transition dipole moment in au.

However, the splitting appears to be very well described by the full Coulomb interaction of monomer transition densities, while Dexter exchange does not appear to play any significant role at this range. Hence, using the interaction of transition densities appears sufficient at this range. This also implies that, at this range, the ability of a functional to correctly predict the Davydov splitting is determined exclusively by its ability to correctly reproduce the monomer transition density.

As we can see from Table 7, however, at equilibrium distance there is a dramatic discrepancy between the splitting as predicted by the transition densities of the monomers and the splitting from the supermolecular calculations. This is a regime where exact exchange in the functional matters, so it is reasonable that including exchange would improve the splittings from the monomer calculations. However, Dexter exchange makes the already-too-small splitting even smaller. It would seem reasonable to assume that since the monomer geometry does not change much as one stretches the hydrogen bond, this is not due to a qualitative change in the ability of functionals to predict the transition densities. Likely, first-order perturbation theory is insufficient at the dimer equlibrium structure. Higher-order effects, such as induction, begin to play a role, as well as nonvanishing overlap of the monomer wave functions. Accounting for all these effects is cumbersome, and convergence of the perturbation series is not guaranteed. The breakdown of intermolecular perturbation theory calls into question the equivalence between the exciton splitting method and För-

ster's transition density interaction at a more fundamental level than the mere insufficiency of the dipole−dipole interaction or the neglect of exchange. Thus, even in the hydrogen-bonded pyridone dimer, the chromophore interaction is too strong for a perturbative treatment in Förster's spirit.

Fink et al.[55] have studied EET between two benzene molecules. They found that TD-DFT with B3-LYP suffered from the same problem of intruder charge-transfer excitation states as we found in our computations only with LDA and PBE. The conclusion of ref 55 was thus that TDDFT was unreliable for EET calculations and that TDHF was the preferable choice. Our present results suggest that this is an overly pessimistic view: Although B3-LYP fails, global hybrid functionals with a larger fraction of exact exchange perform well, while TDHF overestimates the monomer transition dipole moment leading to spuriously large couplings at long-range.

5. Conclusion

We have tested the ability of various modern functionals to correctly predict the Davydov splitting. Semilocal functionals seem unsuitable for routine treatments of the Davydov splitting at realistic chromophore separations because of charge-transfer intruder states, in line with previous observations.[52,55,56] The global hybrid functional BHandH-LYP is in good agreement with splittings calculated with CC2 over the investigated range. We conclude that the method of choice for larger applications is hybrid TDDFT with a large fraction of exact exchange, calibrated by higher level methods such as CC2. Whether range-separated hybrid functionals[57,58] improve on the BHandH-LYP results further remains to be investigated.

There is an observable breakdown of the equivalence between the exciton splitting method and Förster's perturbative approach at equilibrium distance even for the hydrogen-bonded 2-pyridone dimer. We attribute this to the breakdown of first-order degenerate perturbation theory when the coupling becomes too strong. More effort is necessary to develop methods that accurately predict EET rates over the full range of chromophore separations.

Acknowledgment. We would like to dedicate this work to John P. Perdew on the occasion of his 65th birthday. Useful discussions are acknowledged with Dmitrij Rappoport, Ingolf Warnke, Robert Send, and Nathan Crawford. E.S. and F.F. acknowledge funding from the Center for Functional Nanostructures (CFN) of the Deutsche Forschungsgemeinschaft (DFG) within Project C3.9. A.K. acknowledges support from the Deutsche Forschungsgemeinschaft. Part of this research was carried out at the University of Karlsruhe.

Supporting Information Available: RI-MP2/def2-TZVPP ground-state structures of the 2-pyridone monomer and 2-pyridone dimer. This material is available free of charge via the Internet at http://pubs.acs.org.

References

(1) Engel, G. S.; Calhoun, T. R.; Read, E. L.; Ahn, T.-K.; Mancal, T.; Cheng, Y.-C.; Blankenship, R. E.; Fleming, G. R. *Nature* **2007**, *446*, 782.

(2) Balashov, S. P.; Imasheva, E. S.; Boichenko, V. A.; Anton, J.; Wang, J. M.; Lanyi, J. K. *Science* **2005**, *309*, 2061.

(3) Gregg, B. A. *J. Phys. Chem. B* **2003**, *107*, 4688.

(4) Stryer, L.; Haugland, R. P. *Proc. Nat. Acad. Sci.* **1967**, *58*, 719.

(5) Förster, T. *Ann. Phys.* **1948**, *437*, 55.

(6) Kasha, M.; Rawls, H. R.; Bayoumi, M. A. E. *Pure Appl. Chem.* **1965**, *11*, 371.

(7) Fückel, B.; Köhn, A.; Harding, M. E.; Diezemann, G.; Hinze, G.; Basché, T.; Gauss, J. *J. Chem. Phys.* **2008**, *128*, 074505.

(8) Hsu, C.-P.; Fleming, G. R.; Head-Gordon, M.; Head-Gordon, T. *J. Chem. Phys.* **2001**, *114*, 3065.

(9) Dexter, D. L. *J. Chem. Phys.* **1953**, *21*, 836.

(10) Tretiak, S.; Mukamel, S. *Chem. Rev.* **2002**, *102*, 3171.

(11) Tretiak, S.; Middleton, C.; Chernyak, V.; Mukamel, S. *J. Phys. Chem. B* **2000**, *104*, 4519.

(12) *Time-Dependent Density Functional Theory*; Marques, M., Ullrich, C. A., Nogueira, F., Rubio, A., Burke, K., Gross, E. K. U. , Eds.; Spinger: Berlin, 2006; Vol. 23.

(13) Elliot, P.; Furche, F.; Burke, K. Excited states from time-dependent density functional theory. In *Reviews in Computational Chemistry*; Lipkowitz, K. B., Cundari, T. R. , Eds.; 2009; Vol. 26, p 91.

(14) Russo, V.; Curutchet, C.; Mennucci, B. *J. Phys. Chem. B* **2007**, *111*, 853.

(15) Iozzi, M. F.; Mennucci, B.; Tomasi, J. *J. Chem. Phys.* **2004**, *120*, 7029.

(16) Held, A.; Pratt, D. W. *J. Am. Chem. Soc.* **1990**, *112*, 8629.

(17) Matsuda, Y.; Ebata, T.; Mikami, N. *J. Chem. Phys.* **1999**, *110*, 8397.

(18) Müller, A.; Talbot, F.; Leutwyler, S. *J. Chem. Phys.* **2000**, *112*, 3717.

(19) Müller, A.; Talbot, F.; Leutwyler, S. *J. Chem. Phys.* **2002**, *116*, 2836.

(20) Casida, M. E. In *Recent Advances in Density Functional Methods, Part I*; Chong, D. P. , Ed.; World Scientific: Singapore, 1995; Vol. 1, Chapter 5, pp 155−192.

(21) Furche, F. *J. Chem. Phys.* **2001**, *114*, 5982.

(22) Furche, F.; Ahlrichs, R. *J. Chem. Phys.* **2002**, *117*, 7433.

(23) Ahlrichs, R. *Phys. Chem. Chem. Phys.* **2004**, *6*, 5119.

(24) Weigend, F.; Häser, M. *Theor. Chem. Acc.* **1997**, *97*, 331.

(25) Weigend, F.; Häser, M.; Patzelt, H.; Ahlrichs, R. *Chem. Phys. Lett.* **1998**, *294*, 143.

(26) Schäfer, A.; Huber, C.; Ahlrichs, R. *J. Chem. Phys.* **1994**, *100*, 5829.

(27) Deglmann, P.; Furche, F.; Ahlrichs, R. *Chem. Phys. Lett.* **2002**, *362*, 511.

(28) Deglmann, P.; Furche, F. *J. Chem. Phys.* **2002**, *117*, 9535.

(29) Perdew, J. P.; Ernzerhof, M.; Burke, K. *J. Chem. Phys.* **1996**, *105*, 9982.

(30) Kendall, R. A.; Dunning, T. H.; Harrison, R. J. *J. Chem. Phys.* **1992**, *96*, 6796.

(31) Dirac, P. A. M. *Proc. Royal Soc. (London) A* **1929**, *123*, 714.

(32) Slater, J. C. *Phys. Rev.* **1951**, *81*, 385.

(33) Perdew, J. P.; Wang, Y. *Phys. Rev. B* **1992**, *45*, 13244.

(34) Perdew, J. P.; Burke, K.; Ernzerhof, M. *Phys. Rev. Lett.* **1996**, *77*, 3865.

(35) Vosko, S. H.; Wilk, L.; Nusair, M. *Can. J. Phys* **1980**, *58*, 1200.

(36) Becke, A. D. *Phys. Rev. A* **1988**, *38*, 3098.

(37) Lee, C.; Yang, W.; Parr, R. G. *Phys. Rev. B* **1988**, *37*, 785.

(38) Becke, A. D. *J. Chem. Phys.* **1993**, *98*, 5648.

(39) Becke, A. D. *J. Chem. Phys.* **1993**, *98*, 1372.

(40) *TURBOMOLE*, version V5−10; TURBOMOLE GmbH: Karlsruhe, Germany, 2008. www.turbomole.com.

(41) Ahlrichs, R.; Bär, M.; Häser, M.; Horn, H.; Kölmel, C. *Chem. Phys. Lett.* **1989**, *162*, 165.

(42) Hättig, C.; Weigend, F. *J. Chem. Phys.* **2000**, *113*, 5154.

(43) Hättig, C.; Köhn, A. *J. Chem. Phys.* **2002**, *117*, 6939.

(44) Hättig, C. *J. Chem. Phys.* **2003**, *118*, 7751.

(45) Hättig, C.; Hellweg, A.; Köhn, A. *Phys. Chem. Chem. Phys.* **2006**, *8*, 1159.

(46) Köhn, A.; Hättig, C. *J. Chem. Phys.* **2003**, *119*, 5021.

(47) Eichkorn, K.; Weigend, F.; Treutler, O.; Ahlrichs, R. *Theor. Chem. Acc.* **1997**, *97*, 119.

(48) Weigend, F.; Häser, M. *Theor. Chem. Acc.* **1997**, *97*, 331.

(49) Sobolewski, A. L.; Adamowicz, L. *J. Phys. Chem.* **1996**, *100*, 3933.

(50) Barbatti, M.; Aquino, A. J. A.; Lischka, H. *Chem. Phys.* **2008**, *349*, 278.

(51) Janssen, C. L.; Nielsen, I. M. B. *Chem. Phys. Lett.* **1998**, *290*, 423.

(52) Dreuw, A.; Weisman, J. L.; Head-Gordon, M. *J. Chem. Phys.* **2003**, *119*, 2943.

(53) Hieringer, W.; Görling, A. *Chem. Phys. Lett.* **2006**, *419*, 557.

(54) Tozer, D. J. *J. Chem. Phys.* **2003**, *119*, 12697.

(55) Fink, R. F.; Pfister, J.; Zhao, H. M.; Engels, B. *Chem. Phys.* **2008**, *346*, 275.

(56) Dreuw, A.; Fleming, G. R.; Head-Gordon, M. *Phys. Chem. Chem. Phys.* **2003**, *5*, 3247.

(57) Yanai, T.; Tew, D. P.; Handy, N. C. *Chem. Phys. Lett.* **2004**, *393*, 51.

(58) Vydrov, O. A.; Scuseria, G. E. *J. Chem. Phys.* **2006**, *125*, 234109.

(59) Christiansen, O.; Koch, H.; Jörgensen, P. *Chem. Phys. Lett.* **1995**, *243*, 409.

(60) Hättig, C. *J. Chem. Phys.* **2003**, *118*, 7751.

CT800551G

JCTC Journal of Chemical Theory and Computation

Calculation of Quasi-Particle Energies of Aromatic Self-Assembled Monolayers on Au(111)

Yan Li,* Deyu Lu, and Giulia Galli

Chemistry Department, University of California, Davis, California 95616

Received October 31, 2008

Abstract: We present many-body perturbation theory calculations of the electronic properties of phenylene diisocyanide self-assembled monolayers (SAMs) on a gold surface. Using structural models obtained within density functional theory (DFT), we have investigated how the SAM molecular energies are modified by self-energy corrections and how they are affected by the presence of the surface. We have employed a combination of GW (G = Green's function; W = screened Coulomb interaction) calculations of the SAM quasi-particle energies and a semiclassical image potential model to account for surface polarization effects. We find that it is essential to include both quasi-particle corrections and surface screening in order to provide a reasonable estimate of the energy level alignment at a SAM−metal interface. In particular, our results show that within the GW approximation the energy distance between phenylene diisocyanide SAM energy levels and the gold surface Fermi level is much larger than that found within DFT, e.g., more than double in the case of low packing densities of the SAM.

1. Introduction

The study of the self-assembly of molecular monolayers of materials and their applications for electronic and optical devices has been an active field of research for the past 2 decades.[1] In particular, aromatic self-assembled monolayers (SAMs) have been proposed to be promising candidates for electron-transport applications because of the delocalized nature of their π electrons and the relatively small energy gap between the highest occupied molecular orbital (HOMO) and the lowest unoccupied molecular orbital (LUMO), which may give rise to low barriers for electron or hole transport. In order to predict such barriers and thus the performance of SAM−metal devices, it is essential to understand, at the microscopic level, the structural and electronic properties of the molecule−electrode interfaces.

Density functional theory (DFT) has been widely used to study these properties, and usually the structure and energetics of SAM−metal interfaces are reasonably well described, as compared, e.g., to experimental findings. On the other hand, the deficiencies of DFT in describing energy levels in small molecules are well-known: the Kohn−Sham energy eigenvalues are usually not a good representation of molecular orbital energies, and the predicted HOMO−LUMO gap is in most cases underestimated with respect to the experimentally measured difference of electron removal and addition energies. As a consequence, the conductance of electrons or holes estimated using $|E_F - E_{HOMO}|$ or $|E_F - E_{LUMO}|$ is often seriously overestimated (E_F is the Fermi level). Moreover, the electrostatic polarization from the metal substrate, partly missing in conventional DFT calculations, may also significantly affect the values of electron removal and addition energies. For example, it was recently reported that the computed conductance of single-molecule benzenediamine−gold junctions as obtained within DFT is about 7 times larger than that in experiment[2] and the self-energy correction and surface polarization effect were estimated to shift the HOMO level by −3 and +1 eV, respectively.

In order to gain insight into the alignment of SAM−metal energy levels beyond semilocal DFT approximations, we have carried out calculations of SAM quasi-particle energies using many-body perturbation theory within the GW approximation (G = Green's function; W = screened Coulomb interaction). We have also included surface polarization effects by using a semiclassical image potential model, which was proposed and successfully employed in several recent studies of organics−metal interfaces or

* Corresponding author e-mail: ynli@ucdavis.edu.

10.1021/ct800465f CCC: $40.75
Published on Web 01/09/2009

junctions.[2,3] In particular, we have studied SAMs of 1,4-phenylene diisocyanide (PDI) on Au(111), and we have considered different surface coverages. The energetic, electronic, and vibrational properties of PDI SAMs adsorbed on the Au(111) surface have been reported in an earlier work,[4] and here we use the structural model determined in ref 4 to investigate the energy level alignment at the interface.

It has been suggested that aromatic isocyanides may have promising transport properties: the presence of a triple bond in the isocyanide group (−NC) may effectively connect pπ orbitals residing on the aromatic moiety and the dπ orbitals pointing out of the gold surface, thus providing a good network of delocalized electrons and thereby lowering the barrier for charge injection from the metal into the organic semiconductor.[5] However, no consensus has been reached about the performance of such systems from electrical conductivity measurements.[6−11] For example, the study of Chu et al. on the conductance of alkanes and biphenyl- and diphenylacetylene bridges with thiol and isocyanide terminals suggested that the conductivity is enhanced by an order of magnitude when the thiol−gold linkage is replaced with an isocyanide−gold linkage,[11] while the opposite trend was reported by other groups.[10]

Most of the existing theoretical investigations of transport properties of isocyanide molecules have been based on DFT in the local density (LDA) or generalized-gradient-corrected (GGA) approximations and on nonequilibrium Green function calculations.[12,13] One of these studies[12] reported that in a system comprising a single PDI molecule sandwiched between two gold electrodes the gold Fermi level (E_F) is in near-resonance with the delocalized LUMO state of the PDI molecule, leading to a large zero-bias conductance (45.8 μS) that is much higher than that of benzenedithiol (4.8 μS) calculated using the same method.[14] Similarly, a moderate electron barrier $|E_{LUMO} - E_F| \sim 0.7$ eV was obtained within DFT for the low-density PDI SAM adsorbed on the Au(111) surface.[4] These predictions appear to be consistent with the experimental findings of Chu et al.[11] However, as was already mentioned, transport calculations using energy levels obtained using DFT within LDA or GGA usually overestimate conductance values, because they underestimate energy barriers for charge transport.[15,16] Therefore, it is important to explore ways to obtain the relative position of the SAM and metal surface energy levels, beyond local and semilocal DFT approximations.

The rest of the paper is organized as follows: in section 2, we describe the method and geometrical models used in our calculation. In section 3, we present the GW self-energy calculations and compare them to the DFT results. In section 4, we describe the semiclassical model for the polarization effect from the metal substrate. Section 5 concludes the paper.

2. Methods

Because of the complexity and large computational cost of quasi-particle energy calculations of a system comprising a SAM and a metal, we have split our calculation into two parts: the self-energy corrections for a free-standing PDI SAM were first obtained through a GW self-energy calculation, and we assume that this correction term remains the same after the slight structural relaxation of the SAM upon adsorption on the metal surface. Surface polarization effects were then included as an external perturbation to the orbitals of the adsorbed SAM through a semiclassical image potential model.

The free-standing PDI SAMs were arranged in $(\sqrt{3} \times \sqrt{3})$ or (3×3) unit cells, which correspond to high ($\Theta = 1$) and low coverage ($\Theta = {}^1/_3$), respectively. The nearest-neighbor distances, d_{NN}, are 5.10 and 8.83 Å for the two packing densities, assuming a lattice constant of 4.16 Å for the underlying Au(111) surface in the adsorbate system, as determined from DFT calculations for bulk gold.[4] The two-dimensional periodic SAM was then placed in a supercell with a 10 Å vacuum separation between SAMs in neighboring supercells in the self-consistent ground-state calculations. The Brillouin zone was sampled with a $6 \times 6 \times 1$ Monkhorst−Park grid of k points for high coverage and a $3 \times 3 \times 1$ grid for the low-coverage structure. The SAM band structures were generated by non-self-consistent calculations along the edges of the irreducible Brillouin zone.

Both DFT and GW calculations were performed using the ABINIT code.[17,18] Geometries of the free-standing PDI SAMs were first fully relaxed, and their ground-state properties were evaluated by performing plane-wave pseudopotential calculations within DFT, in the Perdew−Burke−Ernzerhof (PBE) GGA.[19] We employed norm-conserving pseudopotentials generated with the PBE exchange and correlation functionals, and details can be found in ref 4. Wave functions were expanded in plane waves with an energy cutoff of 50 Ry. DFT energy eigenvalues and wave functions were then used to construct the inverse dielectric matrix $\varepsilon_{G,G'}^{-1}$ (G and G' indicate the reciprocal lattice vectors) and evaluate the self-energy operator Σ in the GW approximation. The frequency dependence of the dielectric matrix was approximated by the plasmon-pole model (PPM) proposed by Godby and Needs.[20] The self-energy correction for orbital i was then estimated as $\Delta E_i = \langle \Psi_i | \Sigma - V_{xc} | \Psi_i \rangle$, where V_{xc} is the DFT exchange-correlation (xc) potential and $|\Psi_i\rangle$ is the DFT wave function of orbital i. In the high-coverage case ($\Theta = 1$), the matrix elements of the self-energy operator were evaluated with a 25 Ry energy cutoff for the exchange part Σ_x and a 15 Ry energy cutoff for the correlation part Σ_c; a total of 400 conduction bands (~60 eV above E_{HOMO}) were included. In the low-coverage case ($\Theta = {}^1/_3$), a 25 Ry cutoff for Σ_x, a 10 Ry cutoff for Σ_c, and 700 conduction bands (~45 eV above E_{HOMO}) were used. Further increasing the energy cutoffs or the number of conduction bands has little influence on the magnitude of the quasi-particle gap, while both HOMO and LUMO are slightly shifted to lower energies.

For finite (nonperiodic) systems, one needs to eliminate spurious interactions between different supercells, when one evaluates the electron removal and addition energies. In order to do so in our GW calculations, we used the two-dimensional Coulomb cutoff technique proposed in ref 21, For high-density PDI SAMs, the differences between quasi-particle energies computed with or without a Coulomb cutoff are on the order of 0.1−0.2 eV.

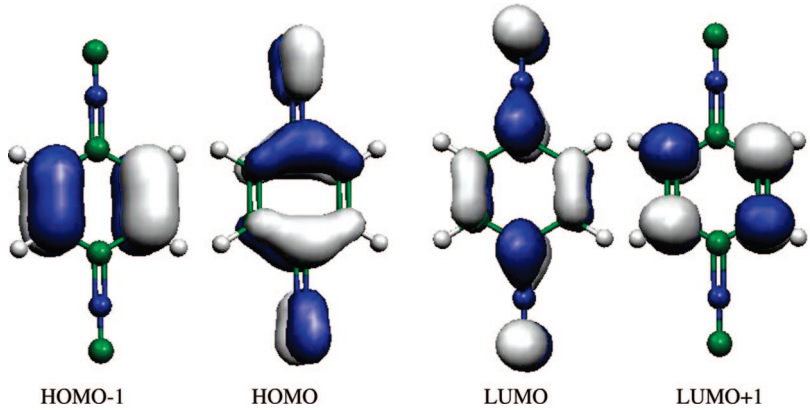

Figure 1. Isosurface plots of HOMO−1, HOMO, LUMO, and LUMO+1 states of the PDI molecule in the gas phase, as obtained within DFT/PBE. The corresponding orbital energies are −7.6, −6.9, −3.1, and −2.5 eV, from left to right.

3. Quasi-Particle Energies of PDI SAMs

The PDI molecule contains an aromatic ring and two isocyanide groups. The molecular orbitals can be separated into two groups: those derived from the benzene molecular orbitals and those mainly localized on the isocyanide groups. The HOMO−1, HOMO, LUMO, and LUMO+1 states of gas-phase PDI and the corresponding DFT orbital energies are shown in Figure 1: these are derived from the doubly degenerate HOMOs and LUMOs of benzene. The degeneracy present in benzene is now lifted in the HOMO and LUMO of the PDI molecule, defined as π_P and π_P^*; the π orbitals on the benzene ring couple to those on the isocyanide groups, and their energy levels are drawn closer, with a gap of 3.8 eV. At the same time, the HOMO−1 and LUMO+1 states remain the same as those in benzene, and they are thus defined as π_B and π_B^*. The energy difference between π_B and π_B^* (∼5.1 eV) is close to the corresponding one of the benzene molecule computed within DFT.[3] The GW quasi-particle gap of gas-phase benzene is estimated to be about 10.5 eV, i.e., ΔE_g ($=E_g^{GW} - E_g^{DFT}$) ∼ 5 eV, and one expects a similar ΔE_g for gas-phase PDI. Indeed, the total energy differences of the neutral molecule and corresponding cation−anion yield $E_{HOMO} = -9.5$ eV and $E_{LUMO} = -0.9$ eV ($E_g = 8.6$ eV). These energy levels were obtained using *Gaussian03*,[22] DFT/PBE with a aug-cc-pvTZ basis set.

When PDI molecules are arranged into a periodic SAM structure, the molecular energy levels broaden and shift with respect to those of the isolated molecule because of intermolecular interactions within the SAM. Figure 2a plots the DFT band structure of the (3 × 3) PDI SAM. The occupied bands are nearly dispersionless and so are the lower unoccupied bands. Other bands higher in energies show moderate dispersion. In contrast, for the ($\sqrt{3} \times \sqrt{3}$) high-density SAM (Figure 2b), the dispersion within the bands becomes more pronounced. In addition, the energy bands are found to shift down by about 1 eV relative to those of the low-density SAM. This is caused by the local charge polarization effect between the aromatic moiety and the two isocyanide groups because of the strong acceptor nature of the latter. At high density, the molecules experience a deeper potential well formed by the two local dipole layers at the SAM edges, and therefore the energy levels shift down with respect to the vacuum level. For the same reason, π_B and π_B^* are located at lower energy in PDI than in benzene, even in the gas phase. An opposite trend is found when the −NC group is replaced by the $-NH_2$ group, which is a strong electron donor.

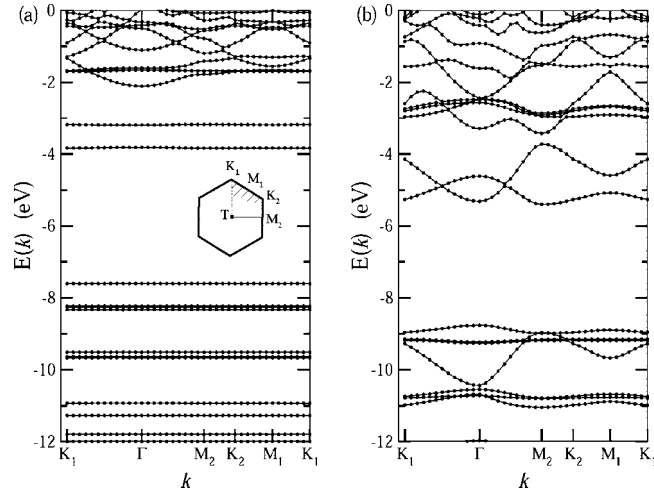

Figure 2. DFT/PBE band structure of PDI SAMs at low and high packing densities (see the text). Inset: irreducible Brillouin zone in the *x*−*y* plane. All energies have been adjusted to the vacuum energy level.

Next, we calculate the GW self-energy corrections to the DFT energy bands. At low coverage, because the bands are mostly dispersionless, the corrections are expected to be similar at different *k* points. Indeed, the GW corrections at, for example, Γ and *K* differ by only a few tens of millielectronvolts. Table 1 shows the DFT Kohn−Sham orbital energies E^{DFT} and GW quasi-particle energies E^{GW} at Γ = (0, 0, 0). The states labeled as $\sigma_\pm$ correspond to σ orbitals localized on the isocyanide groups with even or odd horizontal mirror symmetry, respectively. Although DFT energies of $\sigma_\pm$ states are nearly degenerate with that of the π_B state, self-energy corrections are larger for these localized states and the GW quasi-particle energies turned out to be about 0.6 eV below that of π_B. All energies here have been adjusted relative to the vacuum energy level, which is taken as the plane-averaged Hartree potential (containing both electronic and ionic contributions) in the middle of the vacuum region.

Table 1. DFT/PBE Single-Particle Energies and GW Quasi-Particle Energies (in eV) of Orbitals of the (3 × 3) PDI SAM Structure at the Γ Point[a]

	E^{DFT}	V_{xc}^{DFT}	Σ_x	$\Sigma_c(E^{DFT})$	ΔE	E^{GW}
π_B	−8.34	−13.06	−15.57	0.67	−1.50	−9.84
σ_+	−8.27	−13.58	−18.68	2.21	−2.20	−10.47
σ_-	−8.23	−13.65	−18.71	2.20	−2.19	−10.42
π_P	−7.60	−13.98	−16.00	0.33	−1.40	−9.01
π_P^*	−3.81	−13.09	−8.31	−1.13	3.06	−0.75
π_B^*	−3.19	−12.49	−7.45	−1.48	2.98	−0.21

[a] V_{xc}^{DFT}, Σ_x, and $\Sigma_c(E^{DFT})$ correspond to the expectation values of the DFT xc potential and the exchange and correlation parts (evaluated with DFT energies) of the self-energy operator, respectively. $E^{GW} = E^{DFT} + \Delta E = E^{DFT} + [\Sigma(E^{GW}) - V_{xc}^{DFT}]$, in which $\Sigma(E^{GW})$ is obtained from Σ_x and $\Sigma_c(E^{DFT})$ by linear expansion.

A few observations from Table 1: first, the energy levels of occupied states shift down and those of unoccupied state shift up when GW corrections are added to the DFT eigenvalues. This shift is not symmetric. For example, the energies of the π_P and π_B orbitals are shifted by −1.50 and −1.40 eV, while those of the π_P^* and π_B^* orbitals are shifted by 3.06 and 2.98 eV, respectively. Second, self-energy corrections are strongly dependent on the localization of the single-particle wave functions. For more localized states such as $\sigma_\pm$, the correction is about 0.7 eV larger than that for delocalized π_P and π_B states. Third, the quasi-particle gap is 8.3 eV, much larger than the DFT/PBE, HOMO−LUMO gap, but it is still smaller than the quasi-particle gap of the gas-phase PDI molecule (8.6 eV). The energy distance between π_B and π_B^* also increases from 5.1 to 9.6 eV, and it is close to that of the gas-phase benzene molecule (10.5 eV) estimated within GW.[3] The fact that the energy separations are smaller in the SAM than in the isolated molecule indicates that even at low density there exists a weak screening within the SAM that reduces the separation between HOMO and LUMO, in comparison with the case of an isolated molecule.

Similarly, one expects the GW gap of SAMs to further decrease as the packing density increases. This is indeed the case for the high-density SAM, as shown in Table 2. Self-energy corrections are presented at different k points: Γ, K_1, and M_2. One finds that although the dispersion of the DFT bands can be as large as 1−1.5 eV (see also Figure 2b) the GW corrections (ΔE) for different k points amount to a shift that is almost rigid. The vertical gaps between π_P and π_P^* are 7.9, 7.3, and 7.2 eV at the three k points shown in Table 2, obviously smaller than the corresponding values at low packing density.

Although a direct comparison with the experiment is not available for the energy levels of the PDI molecule and PDI SAM, we can estimate possible inaccuracies of our GW approach by comparing it with the experimental results obtained for the benzene molecule. We carried out quasi-particle calculations for benzene using a face-centered-cubic supercell of lattice constant $a = 18.5$ Å. Electronic wave functions were obtained from DFT/LDA ground-state calculations and expanded in plane waves with an energy cutoff of 50 Ry. GW corrections were evaluated with energy cutoffs of 20 and 10 Ry for the exchange and correlation parts, respectively, and with a total of 1000 conduction bands (∼50 eV above E_{HOMO}). Using the PPM by Godby and Needs, we found quasi-particle energies of the HOMO (−8.35 eV) and LUMO (1.85 eV) levels of benzene in good agreement with those obtained by Niehaus et al., who carried out GW calculations with Gaussian-type orbitals.[23] However, both energies are shifted by about 1 eV compared with values obtained from experiments[24,25] and by doing total energy differences within LDA. There are several factors contributing to this energy shift: (1) As mentioned earlier in section 2, we found that the GW-corrected orbital energies always shift downward when one increases the plane-wave energy cutoff for the self-energy operator or includes more conduction bands for the dielectric matrix calculation. The convergence on the latter was found to be rather slow. The asymptotic limit of the quasi-particle energies was obtained by varying the energy cutoff of the sum over conduction bands measured from the HOMO level (defined as E_c), similar to the procedure of Umari et al.[26] By extrapolating the GW corrections to $E_c \rightarrow \infty$, we found $E_{HOMO}^{\infty} = -8.65$ eV and $E_{LUMO}^{\infty} = 1.46$ eV. (2) Another possible source of error is the use of a PPM instead of explicit energy integration over the frequency dependence of the dielectric function. It has been demonstrated earlier that GW calculations with PPM yield reasonable results for the ionization potential and electron affinity of selected isolated systems.[27] Yet, the influence of PPM on aromatic systems such as PDI SAMs is not clear. Furthermore, we found that that using different PPMs such as those proposed by Godby and Needs[20] and by von der Linden and Horsch,[28] the GW energy corrections can differ by about 0.3−0.4 eV. (3) Additional corrections may be obtained by performing self-consistent GW calculation and/or by going beyond the random-phase approximation for the dielectric matrix. For the sake of completeness, we note that the GW results on the benzene molecule reported by Tiago and Chelikowsky[29] are in good agreement with experiment. Several numerical approximations different from those used here were adopted in ref 29, and the origin of the discrepancy between our and ref 23 results and Tiago and Chelikowsky's results is not fully understood. Overall, it is not unreasonable to expect that the position of the HOMO and LUMO levels of the PDI molecule and of the SAMs computed here may be rigidly shifted upward with respect to experiment by approximately the same amount.

In summary, we found that through application of GW self-energy corrections to the Kohn−Sham energy levels of PDI SAM structures the HOMO−LUMO gap is significantly increased, with the occupied and unoccupied bands shifted in opposite directions. The magnitude of the shift depends on the localization of the orbitals, but it only varies slightly within the same band. At high packing density, screening among neighboring molecules decreases the HOMO−LUMO gap by about 1 eV. Because it was found that low coverage of PDI SAM is energetically more favorable on the Au(111) surface,[4] we will focus on the (3 × 3) structure in the following and apply the GW energy corrections computed above to the adsorbed SAM structure. However, before doing so, we discuss the surface polarization in the next section.

Table 2. DFT/PBE and GW Energies (in eV) of Orbitals of the ($\sqrt{3} \times \sqrt{3}$) PDI SAM Structure at Three Different *k* Points

	$\Gamma = (0, 0, 0)$				$K_1 = (1/3, 1/3, 0)$				$M_2 = (1/2, -1/2, 0)$		
	E^{DFT}	ΔE	E^{GW}		E^{DFT}	ΔE	E^{GW}		E^{DFT}	ΔE	E^{GW}
π_B	−10.44	−1.36	−11.80	π_B	−9.27	−1.12	−10.39	σ_+	−9.19	−2.06	−11.24
σ_+	−9.26	−2.08	−11.34	σ_+	−9.18	−2.06	−11.23	σ_-	−9.16	−2.04	−11.20
σ_-	−9.23	−2.06	−11.29	σ_-	−9.15	−2.04	−11.19	π_P	−8.99	−1.23	−10.21
π_P	−8.76	−1.16	−9.92	π_P	−8.96	−1.22	−10.18	π_B	−8.96	−1.05	−10.01
π_B^*	−5.31	2.17	−3.14	π_P^*	−5.26	2.38	−2.88	π_P^*	−5.39	2.34	−3.06
π_P^*	−4.61	2.60	−2.00	π_B^*	−4.14	2.41	−1.73	π_B^*	−3.72	2.53	−1.19

4. Polarization from the Metal Substrate

It is well-known that in DFT the xc potential within local or semilocal approximations fails to reproduce the asymptotic image potential tail shape of a metal surface.[30,31] Long-range many-body effects, absent in most conventional DFT approximations, are expected to screen the Coulomb potential experienced by an added hole or electron and thus effectively decrease the HOMO−LUMO gap of the isolated SAM. In principle, this effect can be captured by performing GW calculations for the whole SAM-on-metal system (see, e.g., ref 3). Because of the complexity and huge computational cost to carry out such calculations on a large metallic system, here we adopt a semiempirical treatment. To account for this polarization effect from the metal substrate, we add the following correction term to the quasi-particle energy level $E^{GW}(j)$ calculated for a given SAM molecular orbital j:

$$\Delta P^{surface}(j) = \int_{z>z_1} dr\, [V_{im}(r) - V_{xc}^{Au(111)}(r)]\rho_j^{SAM}(r) \quad (1)$$

$$V_{im}(r) = -\frac{e^2}{4|z - z_0|} \quad (2)$$

where $V_{im}(r)$ and $V_{xc}^{Au(111)}(r)$ are the image potential and the DFT xc potential of a clean Au(111) surface, respectively; $\rho_j^{SAM}(r)$ is the electron density of orbital j of the SAM. To evaluate $V_{xc}^{Au(111)}$ and ρ_j^{SAM}, DFT calculations were carried out separately for the two subsystems, adopting the atomic positions determined in the optimized SAM−Au(111) system.[4] z_0 is the image plane position, and z_1 is the where $V_{xc}^{Au(111)}(r)$ starts to deviate from the effective local quasi-particle xc potential, assuming that the latter crosses smoothly from $V_{xc}^{Au(111)}(r)$ to $V_{im}(r)$ at z_1. z_0 and z_1 were therefore determined by computing the intersection of the plane-averaged potentials $V_{xc}^{Au(111)}(z)$ and $V_{im}(z)$, as shown in Figure 3. This approximation is consistent with GW calculations for Al surfaces;[30,31] our fitted mirror-plane position is about 1.0 Å above the first layer of gold atoms, which compares well with the corresponding values adopted for graphite[3] and gold[2] surfaces in similar instances.

We note that in order to treat surface polarization effects as an external perturbation the adsorbate orbitals are required to be well separated from the metal substrate. This is true, for example, in the case of benzene molecules physisorbed on the graphite surface.[3] Although the PDI molecules are chemisorbed on Au(111), with a binding energy of about 0.5 eV,[4] the LUMO-like adsorbate orbitals are found to be only weakly coupled to the metal surface. Indeed, for these states, approximately 90% of the wave function is localized on the SAM itself. Therefore, the use of eq 1 is justified. By

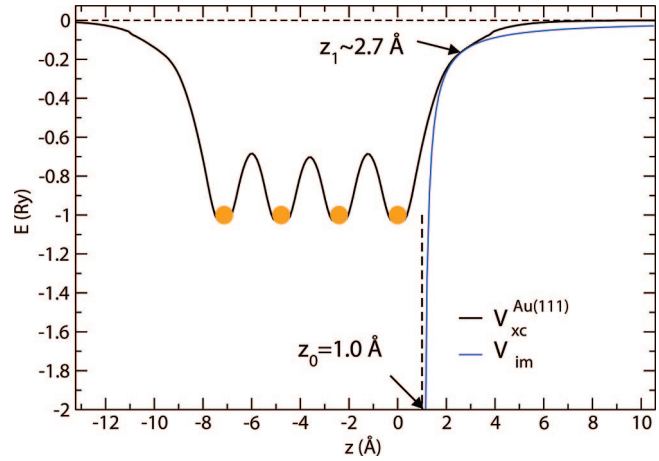

Figure 3. Plane-averaged DFT/PBE xc potential (V_{xc}) calculated from a clean Au(111) slab and a classical image potential $V_{im} = -1/4|z - z_0|$. The origin is set at the first layer of gold atoms, and z_0 and z_1 were fitted by setting the intersection of the two curves at z_1.

application of the correction in eq 1, the energy levels of LUMO-like states are lowered by about 0.5 eV. When this term is combined with the self-energy correction obtained for the isolated SAM, the LUMO level is predicted to shift up by about 1.5−2 eV from the DFT values. This means that the value of the electron barrier is at least more than doubled with respect to those found in DFT. On the other hand, the HOMO-like states are more strongly coupled to the metal substrate than the LUMO-like states, and the perturbation approach used here to evaluate surface polarization effects may no longer be appropriate. However, because the GGA calculation already yielded a rather large lower bound for $E_F - E_H$ (3 eV), these states will not contribute to the low bias conductance.

Although the self-energy correction and surface polarization have opposite effects on the energy levels of the adsorbate orbitals, the balance of these two effects depends on the details of the molecular nature of the adsorbate and the interaction at the molecule−metal interface, which may vary from system to system. However, our results clearly indicate that it is important to go beyond a DFT treatment to obtain a realistic energy alignment at the interface, especially when considering transport properties. For example, functionalized diamondoid molecules adsorbed on the Au(111) surface were found to have a negative electron affinity from electron photoemission experiments,[32] while LDA calculations on similar systems predicted a LUMO level below the vacuum level.[33] A more realistic picture could be obtained when both the self-energy correction and screening

effects were included, in agreement with quantum Monte Carlo results.[34]

5. Conclusion

In summary, we have carried out ab initio calculations of the electronic properties of aromatic isocyanide SAMs adsorbed on the Au(111) surface. By combining many-body perturbation theory under the GW approximation and a classical image potential model, we have investigated energy level alignments at the molecule−metal interface, beyond the DFT/LDA or GGA, commonly used in the literature to study SAMs on gold. In particular, the LUMO-like states of the SAMs were found to shift upward by about 1.5−2 eV from the corresponding DFT energies, when both self-energy corrections and surface polarization effects are taken into account. In the future, additional systematic GW calculations on aromatic molecules, including benzene, are needed to establish the correct position of the LUMO level of PDI and the LUMO-like levels of the SAMs and thus determine quantitatively the upward shift compared to DFT. However, even when using the lower bound of our estimate of the LUMO-like level position ($|E_F - E_{LUMO}| \sim 2$ eV), we find a rather high barrier for electron transport for PDI SAMs. This finding is qualitatively different from that inferred from DFT results, predicting a LUMO level at near-resonance with the metal Fermi level.[12] Experimentally, there exist a wide range of measured conductance for aromatic isocyanide monolayers sandwiched between gold electrodes,[6,7,10,11] with no definitive answer about the position of the molecular HOMO and LUMO levels relative to the metal Fermi level. Our results indicate that PDI SAMs may not be very promising materials for electron transport compared to, e.g., thiolate or other SAMs.

Acknowledgment. This work was funded by NSF Grant DMR-0213618 and by DOE/BES Grant DE-FG02-06ER46262. Some of the calculations were performed at the NERSC and the SDSC facilities.

References

(1) Wang, W.; Lee, T.; Reed, M. A. *Rep. Prog. Phys.* **2005**, *68*, 523–544.

(2) Quek, S.; Venkataraman, L.; Choi, H.; Louie, S.; Hybertsen, M.; Neaton, J. *Nano Lett.* **2007**, *7*, 3477–3482.

(3) Neaton, J. B.; Hybertsen, M. S.; Louie, S. G. *Phys. Rev. Lett.* **2006**, *97*, 216405.

(4) Li, Y.; Lu, D.; Swanson, S.; Scott, J.; Galli, G. *J. Phys. Chem. C* **2008**, *112*, 6413–6421.

(5) Chen, J.; Wang, W.; Klemic, J.; Reed, M. A.; Axelrod, B. W.; Kaschak, D. M.; Rawlett, A. M.; Price, D. W.; Dirk, S. M.; Tour, J. M.; Grubisha, D. S.; Bennett, D. W. *Ann. N.Y. Acad. Sci.* **2002**, *960*, 69–99.

(6) Chen, J.; Calvet, L. C.; Reed, M. A.; Carr, D. W.; Grubisha, D. S.; Bennett, D. W. *Chem. Phys. Lett.* **1999**, *313*, 741–748.

(7) Hong, S.; Reifenberger, R.; Tian, W.; Datta, S.; Henderson, J. I.; Kubiak, C. P. *Superlattices Microstruct.* **2000**, *28*, 289–303.

(8) Dupraz, C. J.-F.; Beierlein, U.; Kotthaus, J. P. *ChemPhysChem* **2003**, *4*, 1247–1252.

(9) Lee, J.; Lientschnig, G.; Wiertz, F.; Struijk, M.; Janssen, R.; Egberink, R.; Reinhoudt, D.; Hadley, P.; Dekker, C. *Nano Lett.* **2003**, *3*, 113–117.

(10) Kim, B.; Beebe, J.; Jun, Y.; Zhu, X.-Y.; Frisbie, C. *J. Am. Chem. Soc.* **2006**, *128*, 4970–4971.

(11) Chu, C.; Ayres, J.; Stefanescu, D.; Walker, B.; Gorman, C.; Parsons, G. *J. Phys. Chem. C* **2007**, *111*, 8080–8085.

(12) Xue, Y.; Ratner, M. A. *Phys. Rev. B* **2004**, *69*, 085403.

(13) Bai, P.; Li, E.; Neerja; Collier, P. *IEEE Trans. Nanotechnol.* **2005**, *4*, 422–429.

(14) Xue, Y.; Ratner, M. A. *Phys. Rev. B* **2003**, *68*, 115406.

(15) Toher, C.; Filippetti, A.; Sanvito, S.; Burke, K. *Phys. Rev. Lett.* **2005**, *95*, 146402.

(16) Toher, C.; Sanvito, S. *Phys. Rev. Lett.* **2007**, *99*, 056801.

(17) ABINIT 5.1.2. The ABINIT code is a common project of the Université Catholique de Louvain, Corning Inc., and other contributors (URL: http://www.abinit.org).

(18) Gonze, X.; et al. *Z. Kristallogr.* **2005**, *220*, 558−562.

(19) Perdew, J. P.; Burke, K.; Ernzerhof, M. *Phys. Rev. Lett.* **1996**, *77*, 3865–3868.

(20) Godby, R. W.; Needs, R. J. *Phys. Rev. Lett.* **1989**, *62*, 1169–1172.

(21) Rozzi, C. A.; Varsano, D.; Marini, A.; Gross, E. K. U.; Rubio, A. *Phys. Rev. B* **2006**, *73*, 205119.

(22) Frisch, M. J. et al. *Gaussian 03*, revision C.02; Gaussian, Inc.: Wallingford, CT, 2004.

(23) Niehaus, T. A.; Rohlfing, M.; Sala, F. D.; Carlo, A. D.; Frauenheim, T. *Phys. Rev. A* **2005**, *71*, 022508.

(24) Herzberg, G. *Molecular Spectra and Molecular Structure: Electronic Spectra and Electronic Structure of Polyatomic Molecules*; Van Nostrand: New York, 1989; Vol. III, p 665.

(25) Burrow, P. D.; Michejda, J. A.; Jordan, K. D. *J. Chem. Phys.* **1987**, *86*, 9–24.

(26) Umari, P.; Stenuit, G.; Baroni, S. cond-mat arXiv:0811.1453, 2008.

(27) Rohlfing, M.; Louie, S. G. *Phys. Rev. B* **2000**, *62*, 4927–4944.

(28) von der Linden, W.; Horsch, P. *Phys. Rev. B* **1988**, *37*, 8351–8362.

(29) Tiago, M. L.; Chelikowsky, J. R. *Phys. Rev. B* **2006**, *73*, 205334.

(30) Eguiluz, A. G.; Hanke, W. *Phys. Rev. B* **1989**, *39*, 10433–10436.

(31) White, I. D.; Godby, R. W.; Rieger, M. M.; Needs, R. J. *Phys. Rev. Lett.* **1998**, *80*, 4265–4268.

(32) Yang, W. L. *Science* **2007**, *316*, 1460–1462.

(33) Wang, Y.; Kioupakis, E.; Lu, X.; Wegner, D.; Yamachika, R.; Dahl, J. E.; Carlson, R. M. K.; Louie, S. G.; Crommie, M. F. *Nat. Mater.* **2008**, *7*, 38–42.

(34) Drummond, N. D.; Williamson, A. J.; Needs, R. J.; Galli, G. *Phys. Rev. Lett.* **2005**, *95*, 096801.

CT800465F

JCTC Journal of Chemical Theory and Computation

AM05 Density Functional Applied to the Water Molecule, Dimer, and Bulk Liquid†

Ann E. Mattsson*,† and Thomas R. Mattsson*,‡

Multiscale Dynamic Materials Modeling, MS 1322, Sandia National Laboratories, Albuquerque, New Mexico 87185-1322, and High Energy Density Physics Theory, MS 1189, Sandia National Laboratories, Albuquerque, New Mexico 87185-1189

Received November 14, 2008

Abstract: We compare results for water obtained with the AM05 exchange-correlation density functional (Armiento, R.; Mattsson, A. E. *Phys. Rev. B* **2005**, *72,* 085108) with those obtained with five other pure functionals: LDA, PBE, PBEsol, RPBE, and BLYP. For liquid water, AM05 yields an O−O pair correlation function that is more structured than the ones of PBE and BLYP, which, in turn, are more structured than the one of RPBE. However, LDA and PBEsol yields more structured water than AM05. We show that AM05 yields a H_2O dimer binding energy of 4.9 kcal/mol. The result is thus within 0.15 kcal/mol of CCSD(T) level theory (5.02 ± 0.05 kcal/mol). We confirm that accuracy in the water dimer binding energy is not a strong indicator for the fidelity of the resulting structure of liquid water.

1. Introduction

Quantitative results for a broad range of systems in combination with a relatively low computational cost has made density functional theory (DFT)[1,2] the foundation of most large-scale quantum mechanical simulations. The limiting factor for the accuracy of the calculations is the approximation for the exchange-correlation (XC) functional. While the local density approximation (LDA) functional, proposed in early DFT works, gives resonably accurate properties for solid-state systems, the application of DFT to systems of interest in chemistry did not emerge until more advanced functionals were constructed, work where John Perdew and co-workers have been instrumental. Today, for single character systems, like bulk solids or strictly molecular systems, the wide use of DFT is a testament to the theory's advantages. The use of XC functionals is, however, largely divided depending on the application. In fact, only a few functionals, among them the Perdew−Burke−Ernzerhof (PBE) functional,[3] are extensively used for both solid and molecular systems. The quest for even more accurate functionals has been most vigorously pursued for chemistry applications, and for high accuracy in molecular systems the use of hybrid functionals is now considered vital. For solids, local and semilocal functionals, such as LDA and different general gradient approximations (GGAs), such as PBE, are mostly employed even though, also here, more accurate functionals have been developed lately.

For some time,[4] it has been evident that one of the largest challenges in the field resides in developing a functional that can bridge the gap between molecular and solid systems. Thus, the performance of several hybrid functionals have recently been investigated for solid-state systems (see for example refs 5 and 6), sometimes with very good results. However, in addition to accuracy, the speed of the calculation has emerged as an additional major consideration: DFT is increasingly being employed for larger systems and for longer molecular dynamics (MD) simulations, both applications requiring as fast functional evaluations as possible. While some hybrids are accurate for solid-state systems, the computational overhead compared to a GGA type functional is prohibiting for these applications. In a recent study,[7] we showed that the Armiento and Mattsson functional of 2005 (AM05),[8] while being of the fast GGA type preferred in large calculations, is as accurate as the best hybrids for solid-state systems.

† This article is part of the Perdew 2009 Special Issue.

* Corresponding author. E-mail: aematts@sandia.gov; trmatts@sandia.gov.

† Multiscale Dynamic Materials Modeling.

‡ High Energy Density Physics Theory.

10.1021/ct8004968 CCC: $40.75
Published on Web 03/03/2009

There is thus ample motivation to investigate the performance of the AM05 functional[8] for molecules and liquids. Our focus here is on the structure of liquid water. We also calculate the structure and binding energy of the water dimer because it explores the hydrogen bonding pertinent to the liquid water structure. The chemical bonding in the water molecule is only explored via the structure; a more extensive study of molecules using AM05 will be published elsewhere.[9]

We, in addition to AM05, for benchmarking purposes include three GGA type functionals commonly used in studies of molecular systems in general and water in particular: BLYP,[10,11] RPBE,[12] and PBE.[3] These functionals are shown to not perform as well as AM05 for solids,[7] but they have reasonable performace for molecular systems and are thus the preferred functionals for applications, such as liquid water, requiring a fast functional.

Although not normally used for water, we also include LDA in the comparisons. First, LDA plays an important role in elucidating the differences between functionals. For example, AM05 is a subsystem functional; it is made to reproduce the exact combined XC energy for two reference systems, the uniform electron gas and the jellium surface. AM05 thus shares one of its reference systems, the uniform electron gas, with LDA. A main conclusion of this work is that AM05 does not share the deficiencies of LDA for molecular systems. Second, LDA performs very well for a number of heavy transition metals; see for example ref 7. When studying the interface between molecules and solids, it is important that the properties of *both* the solid and the molecular components are taken into account accurately. When deciding on which functional to use for heterogeneous systems, it is important to know not only how well a functional performs for one component (LDA describes Pt well) but also how poorly it performs for the other (LDA overbinds molecules significantly).

The recently constructed PBEsol[13] functional yields almost exactly the same lattice constants and bulk moduli as AM05, for important and large classes of solids.[14−16] Results also agree for other properties,[17] but sometimes differences have been shown.[18] Despite mostly giving the same results as AM05, PBEsol is constructed according to very different principles than AM05. In particular, PBEsol is not expected to give good molecular properties.[13] In contrast, nothing in the construction of AM05 would prevent it from performing well also for molecules. It is thus interesting to compare the performance of PBEsol to that of AM05 also for systems of less solid-state character, and we therefore include PBEsol in this comparison.

Another functional that we would have liked to compare results with for the studied systems is the meta-GGA functional of Tao, Perdew, Staroverov, and Scuseria[19] (TPSS). However, TPSS is not available in the code we use and is not readily implemented in it. But others have used TPSS in studies[20,21] comparable to ours. Even though it is not advisable to compare too closely results obtained by very different codes, some information can be extracted by relating results for the common functionals (in this case PBE and BLYP) in two studies to the functional of interest (here TPSS). We are thus able to, to some extent, relate results otained by others with TPSS to those obtained here using AM05.

In this study we focus on pure functionals. However, in the chemistry community there is a considerable interest in hybrid functionals in general and the B3LYP functional in particular. In the same way as we are able to compare TPSS results by others to our results for pure functionals, as described above, we are also able to compare B3LYP results obtained by others for the water dimer. Liquid water radial distrubution functions have been calculated using hybrid functionals (see for example ref 27), but we have not found a B3LYP study that can be compared to ours. We also note that B3LYP performs slightly worse than PBE for solids.[6]

2. Method

First-principles simulations involve a number of approximations, fundamental as well as technical. Because the purpose of functional development is to improve the fundamental accuracy of the theory, it is particularly important to maintain the best possible technical precision in calculations for the purpose of functional development. The accuracy of contemporary exchange-correlation functionals has raised the requirements for overall precision.

2.1. XC Functionals. In the Kohn−Sham DFT computational scheme[2] the ground-state electron energy is obtained via the solution of the Kohn−Sham (KS) equations. Although all many-body effects can *formally* be accounted for within the XC functional, the crucial question is how good the approximation of this quantity is.

As discussed above, PBE[3] gives reasonable accuracy for both molecular and solid-state systems, and it has been tested and used extensively in calculations for large classes of different materials and properties. Even though there are more accurate functionals for specific materials, it appears to be the functional with most broad range performance. In contrast, the BLYP and RPBE functionals show unsatisfactory performance for solid-state systems[7] while they perform well for molecular systems. PBE and BLYP are both used extensively for water,[20,22−30] and RPBE has been suggested to give a water structure in good agreement with experimental results.[23] While the performance of LDA lies between that of the PBE and the BLYP/RPBE functionals for solid-state systems,[7] LDA is well-known to give too structured water. AM05 and PBEsol perform very well for solid-state systems, but they have not previously been tested for water. A brief review of the functionals used in this study was presented in ref 7. Here we only discuss AM05 because it is the main topic of this paper.

Kohn and Mattsson discussed the creation of an XC functional from a surface-oriented model system and its possible combination with another treatment where this model was unsuitable.[31,32] The approach was formalized and generalized in the subsystem functional scheme by Armiento and Mattsson.[33] The fundamental idea is to create several separate subsystem functionals, each accurately describing a specific model system, and then use an interpolation function[34] that based on the nature of the real system in each point determines how much of each subsystem functional

to use in this point. Because LDA is based on the uniform electron gas model system, it is a subsystem functional and can be easily incorporated in the subsystem functional scheme. The ideas of the subsystem functional scheme were made concrete in the AM05 functional.[8] Subsystem functionals based on two model systems are used: the LDA functional based on the uniform electron gas and a surface functional derived from the Airy gas[31] in combination with the jellium surfaces.[35] The interpolation function is based on the magnitude of the dimensionless gradient:[8] If the dimensionless gradient of the real system is large, the system in this point is surface-like, while if it is small, the system is more uniform electron gas like.

The AM05 surface exchange functional is a parametrization of the Airy electron gas data.[31] For correlation, Armiento and Mattsson derived a semicompatible surface correlation from the XC data available for jellium surface models, based on the idea that both the Airy gas and jellium surface models are related to similar surface physics.

Note that AM05 stems from a completely different theoretical framework than functionals originally referred to as GGAs. The subsystem functional scheme is not based on gradient expansions, and thus AM05 is "not a GGA" in the theoretical sense. However, it is of the same form as a GGA and can be easily implemented in a code using the same input quantities as, e.g., PBE does.[16]

The AM05 functional is the first functional constructed according to the subsystem functional scheme. It can be seen as a consistent theoretical improvement over LDA because it reproduces the exact XC energy for *two* types of model systems, the uniform electron gas *and* the jellium surfaces, describing two situations with fundamentally different physics. The subsystem functional scheme offers a promising alternative approach to further improved functionals, by exploiting exact XC model systems and adding them to the ones already reproduced.

Applying AM05 to water in the current work (see Table 2), we see how this formal theoretical improvement over LDA translates into significantly improved numerical results for molecular systems. Because AM05 and traditional GGA functionals are constructed according to such different philosophies, traditional theoretical comparisons are hard to make.[13,14] Performanace assessments of AM05 compared to other GGA functionals have to be based on results from high-precision calculations.

2.2. Numerical Precision. While the XC functional determines the fundamental *accuracy* of the calculation, there is a second source of errors, the numerical *precision* in solving the Kohn−Sham equations. The numerical precision is determined by implementation-related approximations, such as choice of basis sets, pseudopotential quality, approximate matrix diagonalization methods, plane-wave cutoff energies, etc. (see ref 36). In general, the precision can be successively improved by increasing the computational expense (i.e., by converging the calculations).

The concept of precision is particularly important in the area of functional development. When the differences between functionals are small,[37] the precision of the calculations has to be high enough to resolve them.

In this study we use the pseudopotential, plane-wave VASP 5.1 code,[5,38−40] with projected augmented wave (PAW) core potentials,[41,40] ported to the Cray platform.[42] In a recent publication,[28] it was shown that with appropriate settings, VASP yields high precision MD results for water.

The PAW implementation in VASP 5.1 allows use of multiple XC functionals on the same set of core potentials[40] while retaining high precision. The difference in AM05 results using existing LDA or PBE core potentials in VASP 5.1 has been carefully studied[7] and shown to be minimal. In this study we use PBE core potentials for all functionals except LDA, where the LDA core potentials are used instead.

Pseudopotentials should reproduce the results of all-electron calculations. The VASP PAW core potentials have been extensively evaluated (see for example refs 5 and 7) and are of high quality. However, because we want to have good control over numerical errors in this study, we nevertheless consider transferability errors. Transferability can be improved by using a harder core potential, requiring a larger plane wave basis (cutoff). To investigate the effect of potential hardness, we used two types of PAW core potentials, one softer (nominally needing a 400 eV cutoff) and one harder (nominally needing a 700 eV cutoff), for a subset of the functionals tested, in the molecule and dimer calculations. For the more demanding MD calculations, we used the 400 eV potentials. Because the dimer binding energies differ a mere 0.2 kcal/mol between the 400 and 700 potentials, as seen in Table 2, they are unlikely to yield different results for the liquid structure. The water structures resulting from the two different core potentials are indeed very similar, as shown in ref 28.

In order to minimize the possibility that numerical errors obscure the differences between functionals, we use more stringent than normal settings in all our calculations. To minimize interactions with periodic copies, a cubic cell with 12 Å sides is used for the molecule and the dimer calculations. In the self-consistent loop, the convergence criterium is set to at least 1.0×10^{-5} eV. All calculations are gamma point only, and a 500 eV cutoff is used for the 400 eV potentials while the harder 700 eV potential calculations are done with a 1000 eV cutoff.

In order to minimize effects of system size, we study a cell of 64 water molecules. The simulations are performed in the NVT ensemble using a Nose thermostat,[44] deuterium mass, and the velocity verlet algorithm with a 0.5 fs time step. Because the average temperature is fixed, the energy shift due to time integration errors is absorbed in the thermostat degreee of freedom. The energy absorbed by the thermostat is of the order 1K/ps, see ref 28 for a more extensive discussion on basis set convergence, energy drift, and thermalization between hydrogen and oxygen degrees of freedom. The MD simulations are between 15 and 50 ps long, depending on temperature/rate of thermalization for the different functionals. As shown in Figure 4, the different functionals yield highly different structures for liquid water at 300 K. For example, while RPBE-water is liquid with rather rapid thermalization behavior already at 300 K, PBE and AM05-water are glassy with significant structure and long thermalization time. RPBE gives a pair correlation

Table 1. Properties of the Water Molecule, the OH Distance (R_{OH}), and the HOH Angle (∠HOH), As Obtained with Six Functionals: AM05, PBE, LDA, PBEsol, BLYP, and RPBE, Compared to 'Best ab Initio'[49] (CCSD(T)), As Described in Ref 43[a]

	R_{OH} (Å)		∠HOH (deg)	
functional	PAW 400 eV	PAW 700 eV	PAW 400 eV	PAW 700 eV
AM05	0.974	0.971	104.8	104.4
PBE	0.972	0.969	104.5	104.2
LDA	0.974	0.971	105.3	105.0
PBEsol	0.973		104.7	
BLYP	0.973		104.8	
RPBE	0.973		104.2	
best ab initio[49]	0.959		104.2	

[a] For AM05, LDA, and PBE, results using two different sets of PAW core functions (labeled by their nominal energy cutoffs of 400 resp 700 eV, see text) are shown. The differences in results between the two sets is at the level of 0.3%, demonstrating that the softer potentials, employed in the MD simulations, also are of high fidelity.

function similar to ones extracted from experiments.[45−48] However, as will be discussed later, important effects not included in traditional DFT-MD simulations, like ours, call into question the relevance of direct comparisons to experimental findings.

We furthermore investigated the influence of initial state for AM05 and BLYP by annealing from structures equilibrated at higher temperature. The AM05-water was thermalized at 500 K and annealed to 300 K, followed by equilibration at 300 K. No significant difference in final structure was detected between this run and one continued from a PBE simulation. For BLYP, we went even further and investigated three different 400 K geometries followed by anneal to 300 K and 28, 22, and 24 ps simulations at 300 K. All three annealed runs eventually reached a structure similar to that of a BLYP run continued from a PBE final geometry as well as the PBE structure itself. Finally, the PBEsol simulations were continued from the corresponding final AM05 geometry. For all temperatures, the change to PBEsol resulted in a slightly more structured geometry.

3. Results

3.1. Water Monomer and Dimer. The results for molecular properties of water and the water dimer are presented in Table 1 and Table 2.

For the water monomer, the differences in results obtained with different functionals are small. AM05 lies between LDA and PBE, as is mostly the case for geometric properties like lattice constants.[7] The only significant difference is that LDA yields a slightly larger bond angle than the semilocal functionals. Overall, LDA performs as well for the water monomer as any of the semilocal functionals. However, none of the functionals tested here acheive the accuracy of hybrid functionals, that generally display a shorter OH distance, closer to the 'best ab initio' value.

Our results for the water dimer (see Figure 1) binding energies for PBE, BLYP, and LDA agree to within 0.1 kcal/mol to the energies reported by Xu and Goddard.[43] For the water dimer, LDA and PBEsol give a dimer binding energy

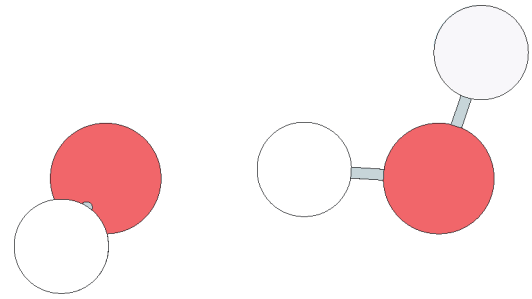

Figure 1. The water dimer. The R_{OO} value in Table 2 is the distance between the two oxygen atoms. ΔR_{OH} is the elongation of the O−H bond of the hydrogen binding hydrogen (the hydrogen atom between the two oxygens) compared to the O−H bond length in the monomer.

that is significantly too large, while BLYP and RPBE give that which is too small. AM05 and PBE both give dimer binding energies close to that of the best ab initio. That AM05 yields results close to those of PBE for this molecular system is interesting. A common view is that a functional constructed to perform well for solids, such as AM05 and PBEsol, would work less well than PBE for molecular systems.[13] The results for the water dimer clearly show that while this might be the case for PBEsol, this reasoning applies less well to functionals such as AM05, constructed according to the subsystem functional approach. It is also interesting to note that while AM05 gives geometrical dimer properties in between LDA and PBE, this is not the case for the binding energy of the dimer, where AM05 binds even less hard than PBE.

Water dimer binding energies and distances between oxygen atoms are calculated with several functionals in ref 21 among them TPSS, BLYP, and PBE. Our results for the binding energies for PBE and BLYP agree well with those results and we can thus conclude that the TPSS binding energy of 4.53 kcal/mol can be directly compared to our results, placing it slightly below the AM05 and PBE results. The agreement between the O−O distances calculated by us and in ref 21 is also good, and we can thus place the TPSS value of approximately 2.900 Å very close to the PBE value. Similar considerations place B3LYP results presented in ref 43 at 4.57 kcal/mol and 2.926 Å.

Figure 2 shows a summary of Table 2 and the TPSS results from ref 21 and the B3LYP results of ref 43, and AM05 and TPSS falls outside of trends drawn from the other pure functionals. For TPSS this is not too surprising because it is a meta-GGA and thus already by construction different from GGAs. That AM05 also falls outside of trends might be more surprising but is probably reflecting its very different theoretical foundation in the subsystem functional scheme. Figure 2 also shows the dramatic improvement AM05 gives compared to LDA for molecular systems, which is encouraging for using the subsystem functionals scheme, that relates LDA and AM05, for developing an even more accurate and generally applicable functional in the future.

3.2. Structure of Water. The importance of water as ubiquitous actor in the chemistry and biology of life can hardly be overestimated. An improved understanding of the interaction between water and ions, proteins, and solid

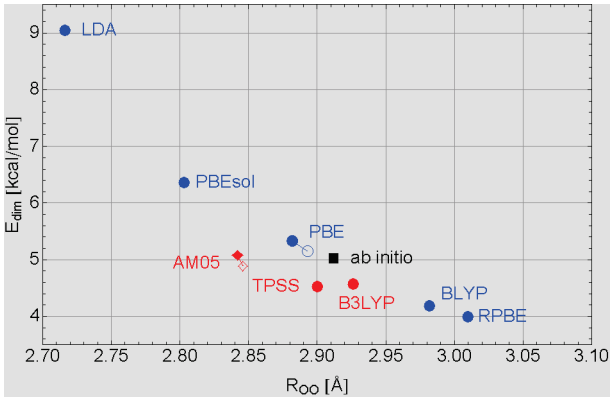

Figure 2. Dimer binding energy versus oxygen−oxygen distance, calculated with eight different functionals and compared to best ab initio (solid symbols). The TPSS results are taken from ref 21 and the B3LYP results from ref 43 For AM05 and PBE the calculations have also been performed with a harder PAW potential; those results are shown with open symbols. The numerical precision is significantly higher than the differences between functionals. Trends obtained by comparing LDA, PBEsol, PBE, BLYP, and RPBE cannot be applied to TPSS and AM05.

Table 2. Properties of the Water Dimer for Six Functionals: AM05, PBE, LDA, PBEsol, BLYP, and RPBE[a]

	E_{dim}, kcal/mol	R_{OO}, Å	ΔR_{OH}, Å
best ab initio[50]	5.02	2.912	0.006
AM05 (400)	5.08	2.842	0.013
AM05 (700)	4.89	2.846	0.013
PBE (400)	5.33	2.882	0.011
PBE (700)	5.15	2.893	0.011
LDA (400)	9.05	2.716	0.019
PBEsol (400)	6.36	2.803	0.015
BLYP (400)	4.19	2.982	0.008
RPBE (400)	3.99	3.010	0.007

[a] The properties are the dimer binding energy (E_{dim}), distance between the oxygen atoms (R_{OO}), and elongation of the hydrogen−oxygen bond compared to the water monomer (ΔR_{OH}), and they are compared to 'best ab initio'[50] (CCSD(T)), according to ref 43.

surfaces is hence highly sought. However, water is not only of importance in biochemistry, nanotechnology, and surface science/catalysis, but the structural and thermophysical properties of water under high energy-density conditions[51−54] largely determine the gravitational properties of water-rich giant planets like Neptune.[55] It is therefore not surprising that the structure of liquid water has been subject to intense theoretical efforts over the past few years.[20,23−30] The amount of recent work also suggests that the definitive consensus regarding first-principles simulation of water has not yet emerged.

For several reasons, liquid water is a particularly difficult system to study computationally. First, the low mass of the hydrogen (deuterium) atoms limits the molecular dynamics time step, making simulations over several tens of picoseconds computationally very demanding. Second, the mass ratio between oxygen and hydrogen atoms and the strong O−H bonds, in comparison to the weak hydrogen bonds, yields normal modes of very different frequencies, in turn, resulting in slow thermalization and sensitivity with respect to thermostats and equilibration times. Third, both hydrogen

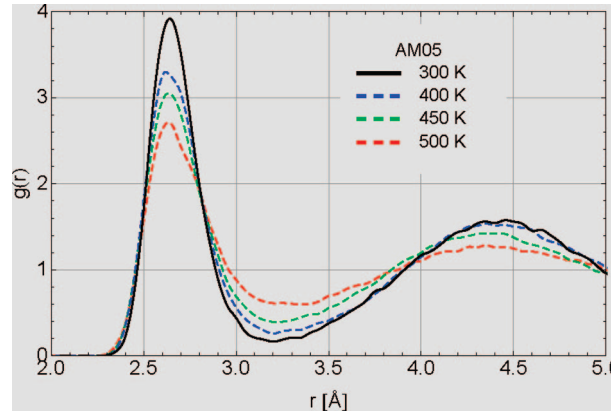

Figure 3. Oxygen−oxygen radial distribution function for AM05 as a function of temperature: 300 K (black), 400 K (blue dashed), 450 K (green dashed), and 500 K (red dashed).

and deuterium atoms are light enough to be influenced by quantum nuclei effects.[24,29] Fourth, long-range van der Waals/dispersion forces can be important in dense systems like liquid water.[30] None of the functionals included in this study is constructed with van der Waals/dispersion properties as a focus.

Taken together, there are thus good reasons to *avoid* liquid water as a system for benchmarking XC functionals. However, given the fundamental importance of liquid water, it is necessary to assess functional performance despite the technical challenges.

Our main result for AM05, the O−O pair correlation function, is presented in Figure 3. Just like PBE and LDA, AM05 yields overstructured liquid water at 300 K. As expected, the structure becomes less ordered with increased temperature. The overstructuring compared to experiment, however, remains also for higher temperatures.

Although the results for AM05 are the main focus of the paper, it is important to directly compare the functional's behavior to that of other functionals. The numerical challenges mentioned above limits the reliability of conclusions based only on comparisons with literature results. One example is the spread in average temperature resulting from NVE simulations; when changes in temperature of a few tens of Kelvin change the liquid structure, it is difficult to compare results with high confidence. In order to make as direct comparisons as possible, we therefore performed extensive additional simulations with other functionals using the same thermostats, timesteps, convergence criteria, etc.

In Figure 4, we compare the O−O pair-correlation function (radial distribution function) at 300 K for six different exchange-correlation functionals: AM05, PBE, LDA, PBEsol, BLYP, and RPBE. The overall relative results for PBE, BLYP, and RPBE are in agreement with most previous simulations, for example those of refs 23, 24, and 20. In ref 20 O−O radial distribution function results are given for, among others, TPSS, BLYP, and PBE. While the differences between radial distribution functions obtained with the different functionals is suppressed by the different temperatures obtained in the NVE runs, it is clear that TPSS gives more structured water than PBE and BLYP. In the comparison in Figure 4, the O−O radial distribution function

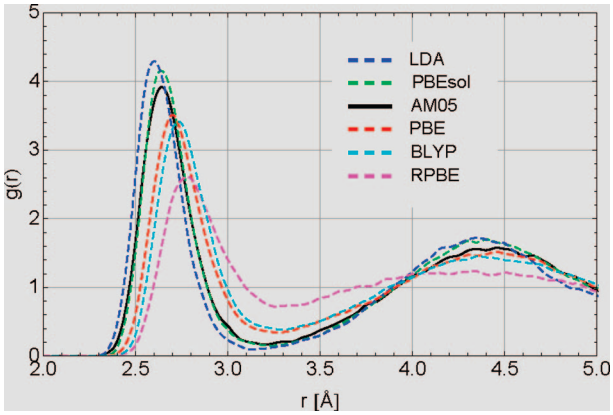

Figure 4. Oxygen−oxygen radial distribution function at 300 K for six functionals, in order of maximum peak height: LDA (blue dashed), PBEsol (green dashed), AM05 (black), PBE (red dashed), BLYP (turqoise dashed), and RPBE (purple dashed). The TPSS radial distribution function from Figure 8 of ref 20 would fall between AM05 and PBE. The structure of DFT water at 300 K thus ranges from very glassy (LDA) to liquid (RPBE) depending on the exchange-correlation functional used.

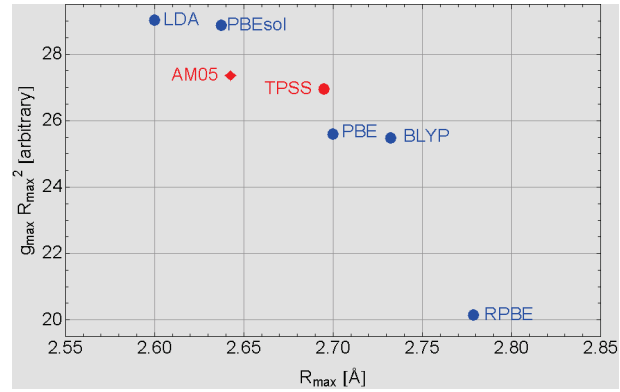

Figure 5. A measure related to the number of atoms in the first hydration shell versus the position of the maximum of the first peak (R_{max}, g_{max} is the maximum peak height). g_{max} and R_{max} for TPSS are estimated by comparing the TPSS, PBE, and BLYP radial distribution function from Figure 8 of ref 20 to the radial distribution functions for PBE and BLYP in Figure 4.

obtained with TPSS would end up between the PBE and the AM05 ones.

From the perspective of applying DFT as a first-principles theory, the results in Figure 4 can readily be interpreted as negative and even discouraging:[56] is there a reason to trust a theory where one can dial the answer for a property like the O−O pair correlation function simply by changing the XC functional? However, from a more fundamental point of view, the results are stimulating: which properties of the different functionals are responsible for their markedly different behavior, and how can one improve upon them?

It is clear from Figure 4 that the maximum peak heights are inversly proportional to the radial positions of the peaks. If the functionals only differed in their preference for a certain nearest neighbor distance, thus this trend being a pure geometrical effect, the number of atoms in the first hydration shell obtained from integrating over the first peak would remain constant. As no significant broadening of the peak would be associated with such a geometrical effect, a good measure would be a constant value of $g_{max}R_{max}^2$. In Figure 5 we show this measure versus the position of the peak. The difference in radial distribution function obtained by LDA and PBEsol, and by PBE and BLYP, lends itself to such an interpretation because no significant broadening of these peaks is seen in Figure 4. If the difference between AM05 and TPSS is also a pure geometrical effect, it is harder to determine because we do not have a direct comparison between these radial distribution functions. However, because TPSS and AM05 also give very similar dimer binding energies (see Figure 2), it is plausible that the difference is indeed purely geomerical. On the other hand, the differences between (LDA, PBEsol), (PBE, BLYP), (AM05, TPSS), and RPBE are *not* purely geometrical, and other effects must also play a role. It is, for example, evident that the RPBE peak has a significant broadening compared to the other functionals. It also appears that the differences in peak heights between TPSS and PBE, and between PBEsol and AM05, are not pure geometrical effects because they have almost the same peak position but not the same peak heights.

We can make a number of observations by comparing the results from properties of dimer binding in Table 2 with that of the structure of liquid water. For water at 300 K, AM05 and PBE yield similarly overstructured, glassy water. Interestingly, the difference in liquid water structure between RPBE and PBE is larger than the difference between AM05 and PBE.

The glassy character of water for both AM05 and PBE is intriguing because AM05 and PBE give similar, correct binding energy for the water dimer (see Table 2). RPBE behaves differently; it significantly underestimates the water dimer binding energy while it was shown by Astaghiri, Pratt, and Kress[23] to give a liquid structure at normal conditions relatively close to that of experiments.[45−48] While we confirm that RPBE yields a significantly less ordered liquid structure than that from BLYP, PBE, and AM05, the disparity in results between dimer binding energy and liquid structure for several functionals suggests that the structure of liquid water is not determined by the fundamental building block: the hydrogen bond between two water molecules.

The importance of quantum effects on liquid water has been a subject of much work in the past using empirical potentials as well as DFT, resulting in a wide range of conclusions. Although a comprehensive review of past work on this topic is significantly beyond the scope of the present work, we would like to mention that very recent large-scale DFT path-integral simulations have concluded that quantum effects reduce the structuring of liquid water[29] compared to BLYP simulations using classical hydrogens, a possibility raised by Schwegler et al.[24] as an explanation for the overstructuring of BLYP and PBE water. It has also been demonstrated that inclusion of van der Waals forces reduces the structuring compared to BLYP without dispersion corrections.[30] With quantum and van der Waals effects independently resulting in qualitative changes in structure, simulations where the hydrogen atoms are treated as classical particles performed with traditional functionals lacking well

defined van der Waals contributions should not yield water structure in agreement with experiments at normal conditions. While quantum nuclear effects seems to only affect the peak height, inclusion of van der Waals contributions also seems to affect the first peak position. Further studies are thus needed in order to determine more accurately which of the pure functionals studied here that yields the best results if quantum nuclear and van der Waals effects are both taken into account self-consistently.

4. Summary and Discussion

Problems involving both molecules and solids remain one of the main challenges for DFT. PBE[3] is one of very few functionals extensively used for both solid and molecular systems, a strong testament to its versatility. The work of John Perdew and co-workers have thus created a framework within which a considerable range of systems can be analyzed with confidence. Directly related to confidence is a question of increasing importance: how to make quantitative estimations of the systematic uncertainties of DFT for a particular problem. This task is in practice often approached by performing calculations with multiple XC functionals. The broad use of PBE makes it an obvious functional to employ for this purpose; the remaining question is which additional functionals to include in a suite of calculations in order to gain the most information of the limitations of DFT.

The subsystem functional AM05 is based on two exact reference systems: the uniform electron gas and the surface jellium. AM05 hence constitutes a systematic improvement upon LDA by adding a description of physics derived from a surface model system to the physics derived from the uniform electron gas model system already well described by LDA. The functional's systematic improvement upon LDA has already been demonstrated for solid-state systems[7] and is established here for hydrogen bonded molecular systems by the results for the water dimer in Figure 2 and the liquid water in Figure 4. This substantial and consistent improvement over LDA supports the subsystem functional approach as a sound theoretical basis for further development. Furthermore, the AM05 functional performs as well as PBE[3] for water dimer binding energy and is slightly more structured than PBE for liquid water.

When combined with AM05's previously demonstrated high accuracy for solids,[7] these results suggest AM05 as a promising candidate to describe the physics and chemistry of solid−molecular interfaces and other mixed systems. As a functional developed on a foundation different from traditionals GGAs, AM05 brings different strenghts and weaknesses and does not follow the same trends as other functionals, as evident from Figure 2, Figure 4, and Figure 5. We suggest AM05 as a valuable additional functional to include in the analysis, in particular when experimental data is either scarce or unavailable, and it is important to estimate the systematic errors in a DFT calculation.

Acknowledgment. We sincerely thank Georg Kresse for the early opportunity to use VASP 5.1 and Joachim Paier for his implementation of BLYP in the code. We are grateful to Paul Kent for sharing code modifications enabling VASP to run massively parallel on the Cray XT4 platform. The simulations were run on the Sandia High Performance Computing (HPC) machines Red Storm and Thunderbird. We acknowledge support from the LDRD office at Sandia. Sandia is a multiprogram laboratory operated by Sandia Corporation, a Lockheed Martin Company, for the United States Department of Energy's National Nuclear Security Administration under contract DE-AC04-94AL85000.

References

(1) Hohenberg, P.; Kohn, W. *Phys. Rev.* **1964**, *136*, B864.

(2) Kohn, W.; Sham, L. J. *Phys. Rev.* **1965**, *140*, A1133.

(3) Perdew, J. P.; Burke, K.; Ernzerhof, M. *Phys. Rev. Lett.* **1996**, *77*, 3865.

(4) Mattsson, A. E. *Science* **2002**, *298*, 759.

(5) Paier, J.; Marsman, M.; Hummer, K.; Kresse, G.; Gerber, I. C.; Ángyán, J. G. *J. Chem. Phys.* **2006**, *124*, 154709. Paier, J.; Marsman, M.; Hummer, K.; Kresse, G.; Gerber, I. C.; Ángyán, J. G. *J. Chem. Phys.* **2006**, *125*, 249901.

(6) Paier, J.; Marsman, M.; Kresse, G. *J. Chem. Phys.* **2007**, *127*, 024103.

(7) Mattsson, A. E.; Armiento, R.; Paier, J.; Kresse, G.; Wills, J. M.; Mattsson, T. R. *J. Chem. Phys.* **2008**, *128*, 084714.

(8) Armiento, R.; Mattsson, A. E. *Phys. Rev. B* **2005**, *72*, 085108.

(9) Muller, R. P.; Mattsson, A. E.; Janssen, C. L. To be published.

(10) Becke, A. D. *Phys. Rev. A* **1988**, *38*, 3098.

(11) Lee, C.; Yang, W.; Parr, R. G. *Phys. Rev. B* **1988**, *37*, 785.

(12) Hammer, B.; Hansen, L. B.; Nørskov, J. K. *Phys. Rev. B* **1999**, *59*, 7413.

(13) Perdew, J. P.; Ruzsinszky, A.; Csonka, G. I.; Vydrov, O. A.; Scuseria, G. E.; Constantin, L. A.; Zhou, X.; Burke, K. *Phys. Rev. Lett.* **2008**, *100*, 136406.

(14) Mattsson, A. E.; Armiento, R.; Mattsson, T. R. *Phys. Rev. Lett.* **2008**, *101*, 239701.

(15) Ropo, M.; Kokko, K.; Vitos, L. *Phys. Rev. B* **2008**, *77*, 195445.

(16) Information about and subroutines for the AM05 functional are available at the AM05 web site: http://dft.sandia.gov/functionals/AM05.html.

(17) Stroppa, A.; Kresse, G. *New J. Phys* **2008**, *10*, 063020.

(18) Feibelman, P. J. *Phys. Chem. Chem. Phys.* **2008**, *10*, 4688.

(19) Tao, J.; Perdew, J. P.; Staroverov, V. N.; Scuseria, G. E. *Phys. Rev. Lett.* **2003**, *91*, 146401.

(20) VandeVondele, J.; Mohamed, F.; Krack, M.; Hutter, J.; Sprik, M.; Parrinello, M. *J. Chem. Phys.* **2005**, *122*, 014515.

(21) Santra, B.; Michaelides, A.; Scheffler, M. *J. Chem. Phys.* **2007**, *127*, 184104.

(22) Feibelman, P. J. *Science* **2002**, *295*, 5552.

(23) Asthagiri, D.; Pratt, L. R.; Kress, J. D. *Phys. Rev. E* **2003**, *68*, 041505.

(24) Schwegler, E.; Grossman, J. C.; Gygi, F.; Galli, G. *J. Chem. Phys.* **2004**, *121*, 5400.

(25) Sit, H.-L.; Marzari, N. *J. Chem. Phys.* **2005**, *122*, 204510.

(26) Lee, H. S.; Tuckerman, M. *J. Chem. Phys.* **2006**, *125*, 154507.

(27) Guidon, M.; Schiffmann, F.; Hutter, J.; VandeVondele, J. *J. Chem. Phys.* **2008**, *128*, 214104.

(28) Rempe, S. L.; Mattsson, T. R.; Leung, K. *Phys. Chem. Chem. Phys.* **2008**, *10*, 4685.

(29) Morrone, J. A.; Car, R. *Phys. Rev. Lett.* **2008**, *101*, 017801.

(30) Lin, I.-C.; Seitsonen, A. P.; Coutinho-Neto, M. D.; Tavernelli, I.; Rothlisberger, U. *J. Phys. Chem. B* **2009**, *113*, 1127.

(31) Kohn, W.; Mattsson, A. E. *Phys. Rev. Lett.* **1998**, *81*, 3487.

(32) Mattsson, A. E.; Kohn, W. *J. Chem. Phys.* **2001**, *115*, 3441.

(33) Armiento, R.; Mattsson, A. E. *Phys. Rev. B* **2002**, *66*, 165117.

(34) Perdew, J. P.; Tao, J.; Armiento, R. *Acta Phys. Chim. Debrecina* **2003**, *36*, 25.

(35) Lang, N. D.; Kohn, W. *Phys. Rev. B* **1970**, *1*, 4555.

(36) Mattsson, A. E.; Schultz, P. A.; Desjarlais, M. P.; Mattsson, T. R.; Leung, K. *Modelling Simul. Mater. Sci. Eng.* **2005**, *13*, R1.

(37) Mattsson, A. E.; Armiento, R.; Schultz, P. A.; Mattsson, T. R. *Phys. Rev. B* **2006**, *73*, 195123.

(38) (a) Kresse, G.; Hafner, J. *Phys. Rev. B* **1993**, *47*, R558. Kresse, G.; Hafner, J. *Phys. Rev. B* **1994**, *49*, 14251. (b) Kresse, G.; Furthmüller, J. *Phys. Rev. B* **1996**, *54*, 11169.

(39) The calculations were made using version 5.1.38 of the VASP code.

(40) Paier, J.; Hirschl, R.; Marsman, M.; Kresse, G. *J. Chem. Phys.* **2005**, *122*, 234102.

(41) (a) Blöchl, P. E. *Phys. Rev. B* **1994**, *50*, 17953. (b) Kresse, G.; Joubert, D. *Phys. Rev. B* **1999**, *59*, 1758.

(42) Kent, P. R. C. *J. Phys.: Conf. Ser.* **2008**, *125*, 012058.

(43) Xu, X.; Goddard, W. A., III. *J. Phys. Chem. A* **2004**, *108*, 2305.

(44) Nose, S. *J. Chem. Phys.* **1984**, *81*, 511.

(45) Soper, A. K. *Chem. Phys.* **2000**, *258*, 121.

(46) Soper, A. K. *J. Phys.: Condens. Matter* **2007**, *19*, 335206.

(47) Hura, G.; Sorenson, J. M.; Glaeser, R. M.; Head-Gordon, T. *J. Chem. Phys.* **2000**, *113*, 9140.

(48) Head-Gordon, T.; Hura, G. *Chem. Rev.* **2002**, *102*, 2651.

(49) Tschumper, G. S.; Leininger, M. L.; Hoffman, H. B. C.; Waleev, E. F.; Schaefer, H. F., III; Quack, M. *J. Chem. Phys.* **2002**, *116*, 690.

(50) Klopper, W.; van Duijneveldt-van de Rijdt, J. G. C. M.; van Duijneveldt, F. B. *Phys. Chem. Chem. Phys.* **2000**, *2*, 2227.

(51) Cavazzoni, C.; Chiarotti, G. L.; Scandolo, S.; Tosatti, E.; Bernasconi, M.; Parrinello, M. *Science* **1999**, *283*, 44.

(52) Schwegler, E.; Galli, G.; Gygi, F.; Hood, R. Q. *Phys. Rev. Lett.* **2001**, *87*, 265501.

(53) Goldman, N.; Fried, L. E.; Feng, I.; Kuo, W.; Mundy, C. J. *Phys. Rev. Lett.* **2005**, *94*, 217801.

(54) Mattsson, T. R.; Desjarlais, M. P. *Phys. Rev. Lett.* **2006**, *97*, 017801.

(55) French, M.; Mattsson, T. R.; Nettelman; N.; Redmer, R. *Phys. Rev. B* **2009**, *79*, 054107.

(56) Bukowski, R.; Szalewicz, K.; Groenenboom, G. C.; van der Avoird, A. *Science* **2007**, *315*, 1249.

CT8004968

JCTC Journal of Chemical Theory and Computation

The Many-Body Exchange-Correlation Hole at Metal Surfaces

Lucian A. Constantin*,† and J. M. Pitarke‡,§

Department of Physics and Quantum Theory Group, Tulane University, New Orleans, Louisiana 70118, CIC nanoGUNE Consolider, Tolosa Hiribidea 76, E-20018 Donostia, San Sebastian, Basque Country, and Materia Kondentsatuaren Fisika Saila (UPV/EHU), DIPC, and Centro Física Materiales (CSIC-UPV/EHU), 644 Posta kutxatila, E-48080 Bilbao, Basque Country

Received December 13, 2008

Abstract: We present a detailed study of the coupling-constant-averaged exchange-correlation hole density at a jellium surface, which we obtain in the random-phase approximation of many-body theory. We report contour plots of the exchange-only and exchange-correlation hole densities, the integration of the exchange-correlation hole density over the surface plane, the on-top correlation hole, and the energy density. We find that the on-top correlation hole is accurately described by local and semilocal density-functional approximations. We also find that for electrons that are localized far outside the surface the main part of the corresponding exchange-correlation hole is localized at the image plane.

I. Introduction

The exchange-correlation (xc) energy of a many-electron system is the only density functional that has to be approximated in the Kohn−Sham (KS) formalism of density functional theory (DFT).[1] It is formally defined by the following equation derived from the Hellmann−Feynman theorem:[2]

$$E_{\rm xc}[n] = \frac{1}{2}\int {\rm d}\mathbf{r}\int {\rm d}\mathbf{r}'\int_0^1 {\rm d}\lambda\,\frac{\rho_2^\lambda(\mathbf{r}',\mathbf{r})}{|\mathbf{r}-\mathbf{r}'|} - U[n] \quad (1)$$

where $n(\mathbf{r})$ is the density of a spin-unpolarized system of N electrons, $U[n] = (1/2)\int {\rm d}\mathbf{r}\, n(\mathbf{r})n(\mathbf{r}')/|\mathbf{r}-\mathbf{r}'|$ is the Hartree energy, and $\rho_2^\lambda(\mathbf{r}',\mathbf{r})$ is the reduced two-particle density matrix

$$\rho_2^\lambda(\mathbf{r}',\mathbf{r}) = N(N-1)\sum_{\sigma,\sigma',\ldots,\sigma_{\rm N}}\int {\rm d}\mathbf{r}_3\ldots{\rm d}\mathbf{r}_{\rm N}\times |\Psi^\lambda(\mathbf{r}'\sigma',\mathbf{r}\sigma,\mathbf{r}_3\sigma_3,\ldots,\mathbf{r}_{\rm N}\sigma_{\rm N})|^2 \quad (2)$$

Here, $\Psi^\lambda(\mathbf{r}_1\sigma_1,\ldots,\mathbf{r}_{\rm N}\sigma_{\rm N})$ is the antisymmetric wave function that yields the density $n(\mathbf{r})$ and minimizes the expectation value of $\hat{T}+\lambda\hat{V}_{\rm ee}$, where $\hat{T}=-\sum_{i=1}^N\nabla_i^2/2$ and $\hat{V}_{\rm ee} = (1/2)\sum_i\cdot\sum_{j\neq i}(1/|\mathbf{r}_i-\mathbf{r}_j|)$ are the kinetic energy and the electron−electron interaction operators. Equation 2 shows that $\rho_2^\lambda(\mathbf{r}',\mathbf{r})\,{\rm d}\mathbf{r}'\,{\rm d}\mathbf{r}$ is the joint probability of finding an electron of arbitrary spin in d$\mathbf{r}'$ at $\mathbf{r}'$ and an electron of arbitrary spin in dr at r, assuming that the Coulombic interaction is $\lambda/|\mathbf{r}-\mathbf{r}'|$. In the case of noninteracting KS electrons (i.e., λ=0), $\rho_2^{\lambda=0}(\mathbf{r}',\mathbf{r})$ is the *exchange-only* reduced two-particle density matrix that is expressible in terms of KS orbitals. (Unless otherwise stated, atomic units are used throughout, that is, $e^2=\hbar=m_{\rm e}=1$.)

Hence, the xc energy can be expressed as the electrostatic interaction between individual electrons and the corresponding (and surrounding) coupling-constant-averaged xc hole density $\bar{n}_{\rm xc}([n];\mathbf{r},\mathbf{r}')$, as follows

$$E_{\rm xc}[n] = \int {\rm d}\mathbf{r}\, e_{\rm xc}(\mathbf{r}) = \frac{1}{2}\int {\rm d}\mathbf{r}\int {\rm d}\mathbf{r}'\,\frac{n(\mathbf{r})\bar{n}_{\rm xc}([n];\mathbf{r},\mathbf{r}')}{|\mathbf{r}-\mathbf{r}'|} \quad (3)$$

where (see eqs 1 and 3):

$$\bar{n}_{\rm xc}([n];\mathbf{r},\mathbf{r}') = \frac{1}{n(\mathbf{r})}\int_0^1 {\rm d}\lambda\,\rho_2^\lambda(\mathbf{r}',\mathbf{r}) - n(\mathbf{r}') \quad (4)$$

and $e_{\rm xc}(\mathbf{r})$ is the xc energy density. The xc hole density $n_{\rm xc}([n];\mathbf{r},\mathbf{r}')$ is the result of three effects: self-interaction

* Corresponding author e-mail: lconstan@tulane.edu.
† Tulane University.
‡ CIC nanoGUNE Consolider.
§ UPV/EHU, DIPC, and CSIC-UPV/EHU.

10.1021/ct800553t CCC: $40.75
Published on Web 03/02/2009

correction to the Hartree approximation, Pauli exclusion principle, and the electron correlation due to Coulombic repulsion between electrons.

The adiabatic-connection fluctuation-dissipation theorem provides an elegant path to the *exact* coupling-constant-averaged xc hole density,[3−6] which can be written as follows[7]

$$\bar{n}_{\rm xc}([n];\mathbf{r},\mathbf{r}') = \frac{1}{n(\mathbf{r})}\Big[-\frac{1}{\pi}\int_0^\infty d\omega \int_0^1 d\lambda\, \chi^\lambda(\mathbf{r},\mathbf{r}';\omega) - n(\mathbf{r})\delta(\mathbf{r}-\mathbf{r}')\Big] \quad (5)$$

where $\chi^\lambda(\mathbf{r},\mathbf{r}';\omega)$ is the density-response function of the interacting system at coupling strength λ and satisfies, in the framework of time-dependent density-functional theory (TDDFT), the following exact Dyson-type equation[8]

$$\chi_\lambda(\mathbf{r},\mathbf{r}';\omega) = \chi_0(\mathbf{r},\mathbf{r}';\omega) + \int d\mathbf{r}_1\, d\mathbf{r}_2\, \chi_0(\mathbf{r},\mathbf{r}_1;\omega) \times \left\{\frac{\lambda}{|\mathbf{r}_1-\mathbf{r}_2|} + f_{{\rm xc},\lambda}[n](\mathbf{r}_1,\mathbf{r}_2;\omega)\right\}\chi_\lambda(\mathbf{r}_2,\mathbf{r}';\omega) \quad (6)$$

Here, $\chi_0(\mathbf{r},\mathbf{r}';\omega)$ is the density-response function of noninteracting KS electrons (which is exactly known in terms of KS orbitals),[9] and $f_{{\rm xc},\lambda}[n](\mathbf{r},\mathbf{r}';\omega)$ is the Fourier transform with respect to time $[f_{{\rm xc},\lambda}[n](\mathbf{r},\mathbf{r}';\omega) = \int_{-\infty}^{\infty} dt\, e^{i\omega t} f_{{\rm xc},\lambda}[n](\mathbf{r},t,\mathbf{r}',0)]$ of the *unknown* λ-dependent xc kernel, formally defined by

$$f_{{\rm xc},\lambda}[n](\mathbf{r},t,\mathbf{r}',t') = \frac{\delta v_{\rm xc}^\lambda[n](\mathbf{r},t)}{\delta n(\mathbf{r}',t')} \quad (7)$$

where $v_{\rm xc}^\lambda[n](\mathbf{r},t)$ is the exact time-dependent xc potential of TDDFT. When $f_{{\rm xc},\lambda}[n](\mathbf{r},\mathbf{r}';\omega)$ is taken to be zero, eq 6 reduces to the random phase approximation (RPA). If the interacting density response function $\chi_\lambda(\mathbf{r},\mathbf{r}';\omega)$ is replaced by the noninteracting KS density-response function $\chi_0(\mathbf{r},\mathbf{r}';\omega)$, then eq 5 yields the *exchange-only* hole density.

The scaling relation of the correlation hole density at coupling constant λ[10,11] leads to the following equation for the coupling-constant-averaged correlation hole density:

$$\bar{n}_{\rm c}([n];\mathbf{r},\mathbf{r}') = \int_0^1 d\lambda \left(\frac{\lambda}{w}\right)^3 n_{\rm c}^{\,w}\left([n_{w/\lambda}],\frac{\lambda}{w}\mathbf{r},\frac{\lambda}{w}\mathbf{r}'\right) \quad (8)$$

where $0 < w \ll 1$ is a fixed constant, and $n_\gamma(\mathbf{r}) = \gamma^3 n(\gamma\mathbf{r})$ is a uniformly scaled density.[12] Equation 8 shows that the whole many-body problem is equivalent to the knowledge of the universal correlation hole density at a small, fixed coupling strength w.

There is a "Jacob's ladder"[13] classification (in RPA and beyond RPA) of nonempirical approximations to the angle-averaged xc hole density

$$\bar{n}_{\rm xc}([n];\mathbf{r},u) = \frac{1}{4\pi}\int d\Omega\, \bar{n}_{\rm xc}([n];\mathbf{r},\mathbf{r}') \quad (9)$$

where $d\Omega$ is the differential solid angle around the direction of $\mathbf{u} = \mathbf{r}' - \mathbf{r}$. The simplest rung of the ladder is the local spin density approximation (LSDA) of the xc hole density $\bar{n}_{\rm xc}(n_\uparrow, n_\downarrow; u)$ that has as ingredients only the spin densities. (For the RPA-based LSDA xc hole and for the LSDA xc hole, see refs 14 and 15 and refs 14, 16, and 17 respectively.) The next rung is the generalized gradient approximation (GGA) xc hole density $\bar{n}_{\rm xc}(n_\uparrow, n_\downarrow, \nabla n_\uparrow, \nabla n_\downarrow, u)$ (see ref 14 for the smoothed GGA exchange hole model, ref 18 for the PBE-GGA[19] correlation hole, and ref 15 for the RPA-based GGA hole model. For a GGA xc hole constructed for solids, see ref 20). The third rung on this ladder is the nonempirical meta-GGA xc hole density[21] $\bar{n}_{\rm xc}(n_\uparrow, n_\downarrow, \nabla n_\uparrow, \nabla n_\downarrow, \tau_\uparrow, \tau_\downarrow, u)$ that depends on spin densities and their gradients, as well as the positive KS kinetic energy densities $\tau_\uparrow$ and $\tau_\downarrow$, and that was constructed to satisfy many exact constraints (for an RPA-based meta-GGA xc hole model, see also ref 21).

Jellium is a simple model of a simple metal, in which the ion cores are replaced by a uniform positive background of density $\bar{n} = 3/4\pi r_s^3 = k_F^3/3\pi^2$ and the valence electrons in the spin-unpolarized bulk neutralize this background. r_s is the bulk density parameter, and k_F is the magnitude of the bulk Fermi wavevector. At a jellium surface, the plane $z = 0$ separates the uniform positive background ($z > 0$) from the vacuum ($z < 0$), and the electrons can leak out into the vacuum. This electron system is translationally invariant in the plane of the surface.

The exchange hole at a jellium surface was studied in ref 22 (using a finite linear-potential model[23]) and in refs 24 and 25 (using the infinite barrier model (IBM)[26]). The behavior of the xc hole at a jellium surface was investigated at the RPA level using IBM orbitals.[27] Hence, existing calculations of the exchange-only and xc hole at a jellium surface invoke either a finite linear-potential model or the IBM for the description of single-particle orbitals. An exception is a self-consistent calculation of the RPA xc hole density reported briefly in refs 28 and 29 in which accurate LSDA single-particle orbitals were employed.

In this article, we present extensive self-consistent calculations of the *exact*-exchange hole and the RPA xc hole at a jellium surface. We report contour plots of the corresponding hole densities, the integration of the xc hole density over the surface plane, and the on-top correlation hole. We find that the on-top RPA correlation hole $\bar{n}_{\rm c}([n\,];{\rm r},{\rm r})$ is accurately described by the on-top RPA-based LSDA hole, in accord with the work of Perdew et al.[5,30,31]

II. Exact-Exchange Hole and the RPA xc Hole at a Jellium Surface

Let us consider a jellium surface with the surface plane at $z = 0$. Using its translational invariance in a plane perpendicular to the z axis, we can write the coupling-constant-averaged xc hole density of eq 5 as follows[29]

$$\bar{n}_{\rm xc}([n];r,z,z') = -\frac{1}{2\pi}\int_0^\infty dq_\parallel\, q_\parallel J_0(q_\parallel r) \times \left[\frac{1}{\pi n(z)}\int_0^1 d\lambda \int_0^\infty d\omega \times \chi^\lambda(q_\parallel,z,z',\omega) - \delta(z-z')\right] \quad (10)$$

where $r = |\mathbf{r}_\parallel - \mathbf{r}_\parallel'|$, and $\mathbf{q}_\parallel$ is a two-dimensional (2D) wavevector. $\chi^\lambda(q_\parallel, z, z', \omega)$ represents the 2D Fourier transform of the interacting density response function of eq 6, which in the RPA is obtained by neglecting the xc kernel $f_{\rm xc}$. The exact-exchange hole density is obtained by simply

replacing in eq 10 $\chi^{\lambda}(q_{\|}, z, z', \omega)$ by the corresponding KS noninteracting density response function $\chi^{0}(q_{\|}, z, z', \omega)$.

For the evaluation of eq 10, we follow the method described in ref 7. We consider a jellium slab, and we assume that the electron density $n(z)$ vanishes at a distance $z_0 = 2\lambda_F$ ($\lambda_F = 2\pi/k_F$ is the bulk Fermi wavelength) from either jellium edge.[32] We expand the single-particle wave functions entering the evaluation of $\chi^{0}(q_{\|}, z, z', \omega)$ in a sine Fourier representation, and the density-response functions $\chi^{0}(q_{\|}, z, z', \omega)$ and $\chi_{\lambda}(z, z'; q_{\|}, \omega)$ in a double-cosine Fourier representation. We also expand the Dirac delta function entering eq 10 in a double-cosine representation (see eq A2 of ref 7). We take all the occupied and unoccupied single-particle orbitals and energies to be the LSDA eigenfunctions and eigenvalues of a KS Hamiltonian, as obtained by using the Perdew−Wang parametrization[33] of the Ceperley−Alder xc energy of the uniform electron gas.[34]

In the calculations presented below, we considered jellium slabs with several bulk parameters r_s and a thickness $a = 2.23\lambda_F$ for the positive background. For $r_s = 2.07$, such a slab corresponds to about four atomic layers of Al(100) and it was used in the wavevector analysis of the RPA[35] and beyond-RPA[20,36] xc surface energy.

In Figures 1 and 2, we show contour plots for the exact-exchange hole density and the self-consistent RPA xc hole density, respectively. In the bulk, both the exchange-only hole and the xc hole are spherical and the xc hole is more localized, as in the case of a uniform electron gas. Near the surface, both the exchange-only hole and the xc hole happen to be distorted, the center of gravity being closer to the surface when correlation is included. For an electron that is localized far outside the surface, the corresponding exchange-only hole and xc hole remain localized near the surface; Figures 1 and 2 show that the introduction of correlation results in a flatter hole, which in the case of an electron that is infinitely far from the surface becomes completely localized at a plane parallel to the surface. This is the image plane. We recall that the RPA xc hole density is exact in the limit of large separations (where $u = |\mathbf{r} - \mathbf{r}'| \rightarrow \infty$) and yields therefore the exact location of the image plane.

The integration of the xc hole density over the whole surface plane,

$$b_{xc}([n], z, z') = \int_0^{\infty} \mathrm{d}r\, \bar{n}_{xc}([n]; r, z, z') \qquad (11)$$

represents a quantity of interest for a variety of theoretical and experimental situations (see, for example, refs 37 and 38). Below we show that $b_{xc}([n]; z, z')$ represents a suitable quantity to describe the behavior of the xc hole corresponding to a given electron located at an arbitrary distance from the surface. In Figure 3, we plot this quantity, versus z', for $r_s = 2.07$ and a given electron located at $z = 0.5\lambda_F$, $z = 0$, $z = -0.5\lambda_F$, and $z = -1.5\lambda_F$. We see from this figure that (i) correlation damps out the oscillations that the exchange hole exhibits in the bulk part of the surface, and (ii) in the case of a given electron located far from the surface into the vacuum the main part of the exchange-only and the xc hole is found to be near the surface (see also Figures 1 and 2), although the exchange-only hole appears to be much more delocalized with a considerable weight within the bulk.

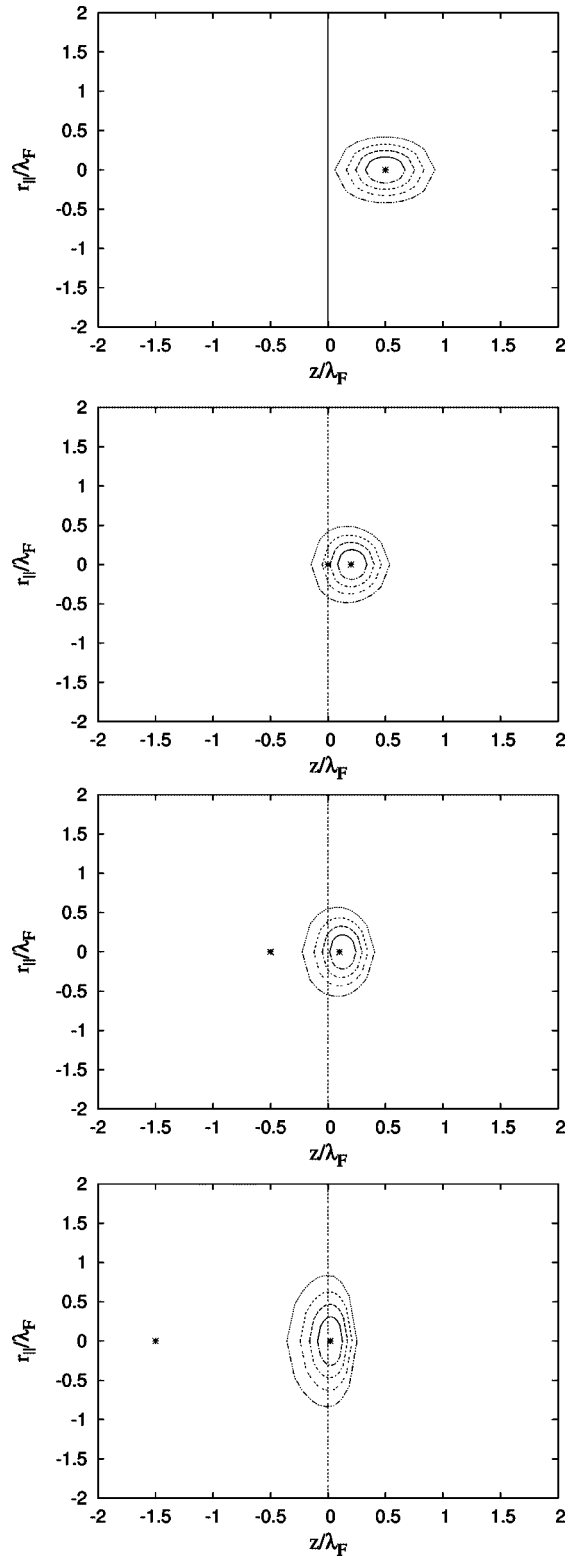

Figure 1. Contour plots of the exchange hole density $\bar{n}_x(r_{\|}, z, z')$ for several fixed values of the electron position: $z = 0.5\lambda_F$ (inside the bulk), $z = 0$ (on the surface), $z = -0.5\lambda_F$ (in the vacuum), and $z = -1.5\lambda_F$ (far outside the surface in the vacuum). The bulk parameter is $r_s = 2.07$, the jellium surface is at $z = 0$, and $r_{\|} = \pm|\mathbf{r}_{\|} - \mathbf{r}_{\|}'|$.

Let us now focus on the on-top xc hole. The LSDA accurately accounts for short wavelength contributions to the xc energy;[30] thus, all the nonempirical approximations of the xc hole have been constructed to recover the LSDA on-

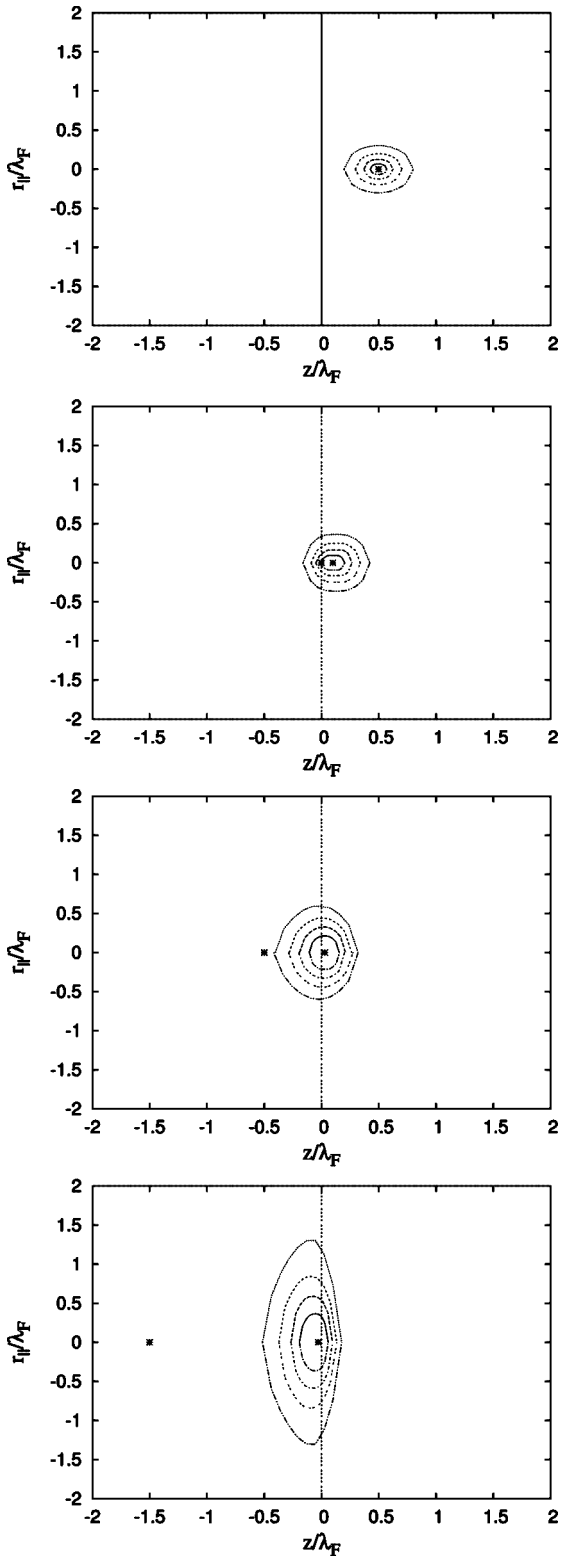

Figure 2. Contour plots of the RPA coupling-constant-averaged xc hole density $\bar{n}_x(r_{||}, z, z')$ for several fixed values of the electron position: $z = 0.5\lambda_F$ (inside the bulk), $z = 0$ (on the surface), $z = -0.5\lambda_F$ (in the vacuum), and $z = -1.5\lambda_F$ (far outside the surface in the vacuum). The bulk parameter is $r_s = 2.07$, the jellium surface is at $z = 0$, and $r_{||} = \pm|\mathbf{r}_{||} - \mathbf{r}_{||}'|$. See also Figure 1 of ref 29.

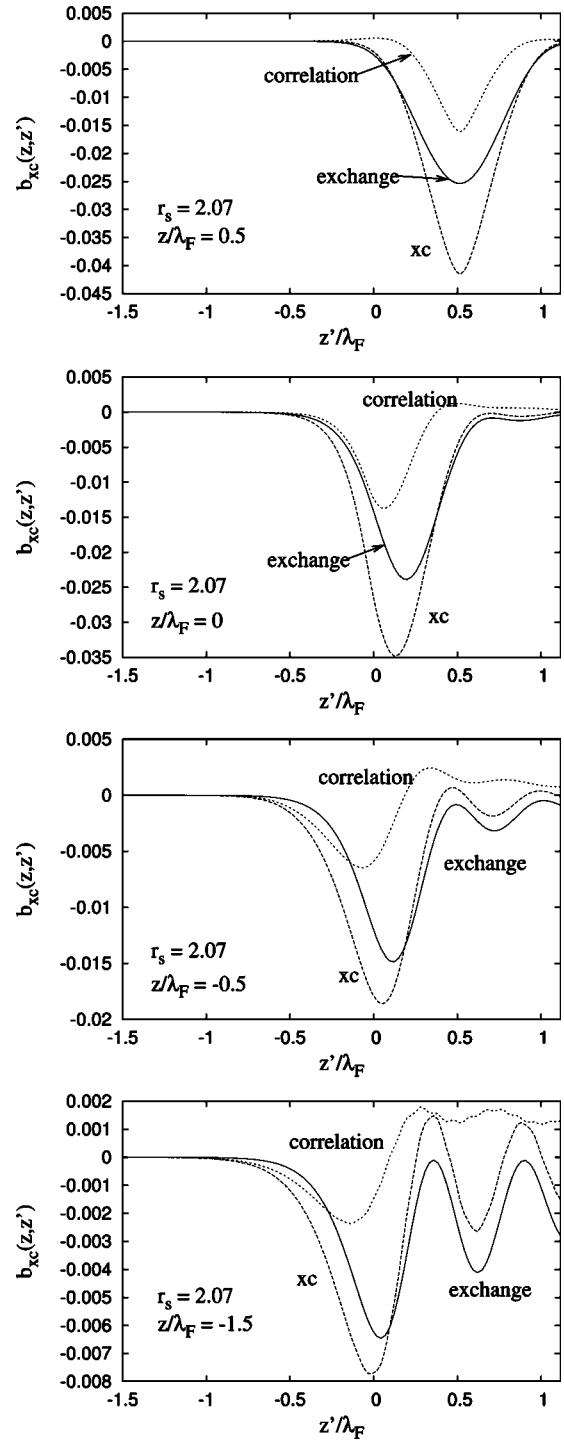

Figure 3. $b_{xc}(z, z')$ of eq 11 versus z'/λ_F for the same positions of the electron as in Figures 1 and 2. The bulk parameter is $r_s = 2.07$, and the jellium surface is at $z = 0$.

top xc hole $\bar{n}_{xc}^{LSDA}(r, r)$. The slowly varying electron gas was treated within RPA by Langreth and Perdew.[5] For a spin-unpolarized system, the gradient correction to the LSDA on-top correlation hole density is[31]

$$\bar{n}_c^{GEA}(\mathbf{r}, \mathbf{r}) = \bar{n}_c^{LSDA}(\mathbf{r}, \mathbf{r}) + \frac{|\nabla n|^2}{72\pi^3 n^2} \qquad (12)$$

In Figure 4, we show the on-top correlation hole for the exact RPA, the RPA-based LSDA (see ref 15) and the RPA-based GEA of eq 12. We see that for a jellium surface the RPA-based LSDA on-top correlation hole nearly coincides with

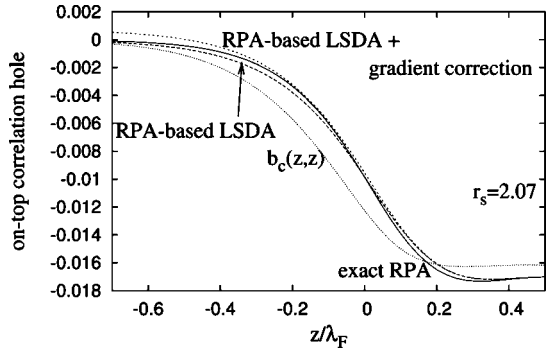

Figure 4. On-top coupling-constant-averaged correlation hole $\bar{n}_c(\mathbf{r}, \mathbf{r})$ at a jellium surface. Also shown is $b_c(z, z)$ of eq 11. The bulk parameter is $r_s = 2.07$, and the jellium surface is at $z = 0$.

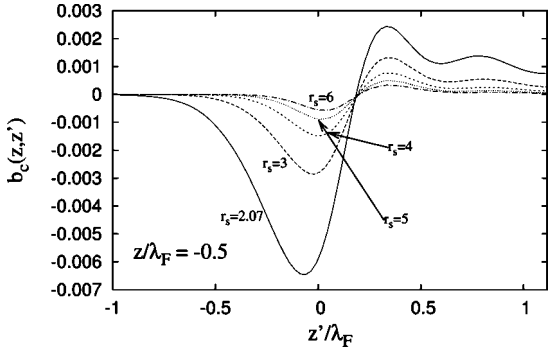

Figure 5. Correlation hole $b_c(z, z')$ of an electron at position $z = -0.5\lambda_F$ for several values of the bulk parameter $r_s = 2.07$, 3, 4, 5, and 6. The jellium surface is at $z = 0$.

the corresponding exact RPA on-top correlation hole; this is in contrast with the case of strong inhomogeneous systems (e.g., Hooke's atom).[30] The gradient correction of eq 12 improves the already accurate RPA-based LSDA on-top correlation hole in the slowly varying density region but is inaccurate in the tail of the density. Figure 4 also shows that the integrated $b_c(z, z)$ of eq 11 is more (less) negative in the vacuum (bulk) than the actual on-top correlation hole.

At this point, we would like to emphasize that, while the RPA on-top correlation hole in the bulk is too negative but finite, the on-top correlation hole diverges in the bulk within a TDDFT scheme that uses a wavevector and frequency-independent xc kernel like in the adiabatic local-density approximation (ALDA)

$$f_{xc,\lambda}^{ALDA}[n](\mathbf{r}, \mathbf{r}', \omega) = \frac{d v_{xc}^{\lambda,unif}[n(\mathbf{r})]}{dn(\mathbf{r})}\delta(\mathbf{r} - \mathbf{r}') \qquad (13)$$

or the energy-optimized local-density approximation of ref 39 (see the discussion after eq 3.9 of ref 39). Here, $v_{xc}^{\lambda,unif}[n(r)]$ is the xc potential of a uniform electron gas of density $n(r)$. An xc kernel borrowed from a uniform gas xc kernel that has the correct large-wavevector behavior (see, for example, the xc kernels of refs 40−42) would yield a finite on-top correlation hole. Figure 5 shows the integrated correlation hole of eq 11 for an electron at the vacuum side of the surface, at the position $z = -0.5\lambda_F$ and for several values of the electron-density parameter $r_s = 1.5$, 2.07, 3, 4, 5, and 6.

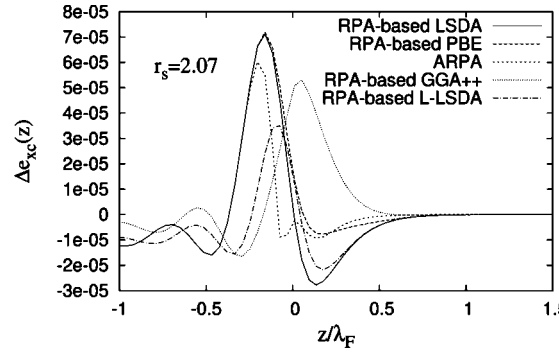

Figure 6. $\Delta e_{xc}(z) = e_{xc}^{RPA}(z) - e_{xc}^{approx}(z)$ versus z/λ_F at a surface of a jellium slab, for several xc approximations: RPA-based LSDA,[15] RPA-based PBE,[15] ARPA-GGA,[47] RPA-based GGA++,[38] and RPA-based L-LSDA (eq 14 with $C = 0.3$). The bulk parameter is $r_s = 2.07$, and the edge of the positive background is at $z = 0$.

In the bulk, the correlation hole exhibits damped oscillations with r_s-dependent amplitude and a period that does not depend on the electron density and is close to the period ($\sim 0.56\lambda_F$) of the corresponding oscillations exhibited by the exchange-only hole.

Finally, we look at the xc energy density e_{xc} defined in eq 3. We note that adding to the actual e_{xc} of eq 3 an arbitrary function of the position r that integrates to zero yields the same total xc energy.[43] The Laplacian of the density $\nabla^2 n$ integrates to zero for finite systems, it plays an important role in the gradient expansion of the kinetic-energy density,[44−46] and it is an important ingredient in the construction of density-functional approximations for the kinetic energy density[44,45] and the xc energy.[45]

We define the simplest possible Laplacian-level RPA-based LSDA (the RPA-based L-LSDA) xc energy density:

$$e_{xc}^{L-LSDA-RPA}(\mathbf{r}) = e_{xc}^{LSDA-RPA}(\mathbf{r}) - C\nabla^2 n(\mathbf{r}) \qquad (14)$$

where C is a constant parameter that we find by minimizing the difference between $e_{xc}^{RPA-L-LSDA}$ and e_{xc}^{RPA}. We find $C = 0.3$ for a jellium slab with $r_s = 2.07$, and its value gets larger as r_s increases.

In Figure 6, we show $\Delta e_{xc}(z) = e_{xc}^{RPA}(z) - e_{xc}^{approx}(z)$ versus z/λ_F for a jellium slab with $r_s = 2.07$ and several RPA-based approximations for $e_{xc}^{approx}(z)$. The RPA-based PBE[15] improves considerably the behavior of the RPA-based LDA. The ARPA-GGA[47] is a GGA functional that fits the RPA xc energy density of the airy gas and is remarkably accurate for jellium surfaces. The RPA-based GGA++ is the RPA version of the GGA++ of ref 38 ($e_{xc}^{RPA-GGA++} = e_{xc}^{RPA-LSDA}F_{xc}(l)$, where $l = r_s^2\nabla^2 n/n$ is a reduced Laplacian and $F_{xc}(l)$ is defined in eq 3 of ref 38). Although the GGA++ functional was constructed for the Si crystal, we observe that the RPA-based GGA++ improves over the RPA-based LSDA in the bulk near the jellium surface, showing that it can be a good approximation for systems with small oscillations. (In the bulk, close to the jellium surface, there are Friedel oscillations as well as quantum oscillations due to the finite thickness of the jellium slab.) We note finally that $e_{xc}^{RPA-L-LSDA}$ significantly reduces the local error of the

RPA-based LSDA near the jellium surface, although by construction $E_{xc}^{RPA-L-LSDA} = E_{xc}^{RPA-LSDA}$.

III. Conclusions

We presented extensive self-consistent calculations of the *exact*-exchange hole and the RPA xc hole at a jellium surface.

We presented a detailed study of the RPA xc hole density at a metal surface. When the electron is in the vacuum, its hole remains localized near the surface (its minimum is on the image plane) and has damped oscillations in the bulk. We find that the on-top correlation hole is accurately described by local and semilocal density-functional approximations, as expected from ref 5. We also find that for an electron that is localized far outside the surface the main part of the corresponding xc hole is completely localized at a plane parallel to the surface, which is the image plane.

Because of an integration by parts that occurs in the underlying gradient expansion, a GGA (or meta-GGA) hole is meaningful only after averaging over the electron density $n(r)$.[18,20] This average smooths the sharp cutoffs used in the construction of the angle-averaged GGA xc hole density. The wavevector analysis of the jelium xc surface energy is an important and hard test for the LSDA, GGA, and meta-GGA angle-averaged xc hole densities, showing not only the accuracy of the xc hole but also the error cancellation between their exchange and correlation contributions. Thus, refs 20, 21, and 35 showed that the TPSS meta-GGA[21] and the PBEsol GGA[20] xc hole densities improve considerably the accuracy of their LSDA and PBE counterparts at jellium surfaces, both within RPA and beyond RPA.[48]

The exchange energy density does not have a gradient expansion,[49] as does the kinetic energy density. However, the existence of gradient expansion of the xc energy density is still an open problem. We use our RPA xc hole density to compare the xc energy densities of several approximations. The most accurate ones are ARPA-GGA of ref 47 and RPA-based L-LSDA of eq 14.

Acknowledgment. We thank J. P. Perdew and J. F. Dobson for many valuable discussions and suggestions. J.M.P. acknowledges partial support by the Spanish MEC (Grant No. FIS2006-01343 and CSD2006-53) and the EC sixth framework Network of Excellence NANOQUANTA. L.A.C. acknowledges NSF support (Grant No. DMR05-01588).

References

(1) Kohn, W.; Sham, L. J. *Phys. Rev.* **1965**, *140*, A1133.

(2) Perdew, J. P.; Kurth, S. In *A Primer in Density Functional Theory*; Fiolhais, C., Nogueira, F., Marques, M., Eds.; Springer: New York, 2003; p 1.

(3) Callem, H. B.; Welton, T. R. *Phys. Rev.* **1951**, *83*, 34.

(4) Harris, J.; Griffin, A. *Phys. Rev. B* **1975**, *11*, 3669.

(5) (a) Langreth, D. C.; Perdew, J. P. *Phys. Rev. B* **1977**, *15*, 2884; (b) **1980**, *21*, 5469; (c) **1982**, *26*, 2810.

(6) Gunnarsson, O.; Lundqvist, B. I. *Phys. Rev. B* **1976**, *13*, 4274.

(7) (a) Pitarke, J. M.; Eguiluz, A. G. *Phys. Rev. B* **1998**, *57*, 6329; (b) **2001**, *63*, 045116.

(8) Gross, E. K. U.; Dobson, J. F.; Petersilka, M. In *Density Functional Theory II*; Nalewajski, R. F., Ed.; Topics in Current Chemistry 181; Springer: Berlin, 1996; p 81.

(9) Gross, E. K. U.; Kohn, W. *Phys. Rev. Lett.* **1985**, *55*, 2850.

(10) Levy, M. *Phys. Rev. A* **1991**, *43*, 4637.

(11) Levy, M. *Bull. Am. Phys. Soc.* **1990**, *35*, 822.

(12) Levy, M.; Perdew, J. P. *Int. J. Quantum Chem.* **1994**, *49*, 539.

(13) Perdew, J. P.; Schmidt, K. In *Density Functional Theory and Its Application to Materials*; Van Doren, V., Van Alsenoy, C., Geerlings, P., Eds.; American Institute of Physics: Melville, NY, 2001.

(14) Ernzerhof, M.; Perdew, J. P. *J. Chem. Phys.* **1998**, *109*, 3313.

(15) Yan, Z.; Perdew, J. P.; Kurth, S. *Phys. Rev. B* **2000**, *61*, 16430.

(16) Perdew, J. P.; Wang, Y. *Phys. Rev. B* **1992**, *46*, 12947.

(17) Gori-Giorgi, P.; Perdew, J. P. *Phys. Rev. B* **2002**, *66*, 165118.

(18) Perdew, J. P.; Burke, K.; Wang, Y. *Phys. Rev. B* **1996**, *54*, 16533.

(19) Perdew, J. P.; Burke, K.; Ernzerhof, M. *Phys. Rev. Lett.* **1996**, *77*, 3865.

(20) Constantin, L. A.; Perdew, J. P.; Pitarke, J. M. Unpublished work.

(21) Constantin, L. A.; Perdew, J. P.; Tao, J. *Phys. Rev. B* **2006**, *73*, 205104.

(22) (a) Sahni, V.; Bohnen, K.-P. *Phys. Rev. B* **1984**, *29*, 1045; (b) **1985**, *31*, 7651.

(23) Sahni, V.; Ma, C. Q.; Flamholz, J. S. *Phys. Rev. B* **1978**, *18*, 3931.

(24) Juretschke, H. J. *Phys. Rev.* **1953**, *92*, 1140.

(25) Moore, I. D.; March, N. H. *Ann. Phys. (N.Y.)* **1976**, *97*, 136.

(26) Newns, D. M. *Phys. Rev. B* **1970**, *1*, 3304.

(27) Inglesfield, J. E.; Moore, I. D. *Solid State Commun.* **1978**, *26*, 867.

(28) (a) Pitarke, J. M.; Eguiluz, A. G. *Bull. Am. Phys. Soc.* **1994**, *39*, 515; (b) **1995**, *40*, 33.

(29) Nekovee, M.; Pitarke, J. M. *Comput. Phys. Commun.* **2001**, *137*, 123.

(30) Burke, K.; Perdew, J. P.; Langreth, D. C. *Phys. Rev. Lett.* **1994**, *73*, 1283.

(31) Burke, K.; Perdew, J. P.; Ernzerhof, M. *J. Chem. Phys.* **1998**, *109*, 3760.

(32) $z_0 = 2\lambda_F$ is sufficiently large for the physical results to be accurate.

(33) Perdew, J. P.; Wang, Y. *Phys. Rev. B* **1992**, *45*, 13244.

(34) Ceperley, D. M.; Alder, B. J. *Phys. Rev. Lett.* **1980**, *45*, 566.

(35) Pitarke, J. M.; Constantin, L. A.; Perdew, J. P. *Phys. Rev. B* **2006**, *74*, 045121.

(36) Constantin, L. A.; Pitarke, J. M.; Dobson, J. F.; Garcia-Lekue, A.; Perdew, J. P. *Phys. Rev. Lett.* **2008**, *100*, 036401.

(37) Nekovee, M.; Foulkes, W. M.; Needs, R. J. *Phys. Rev. B* **2003**, *68*, 235108.

(38) Cancio, A. C.; Chou, M. Y. *Phys. Rev. B* **2006**, *74*, 081202(R).

(39) Dobson, J. F.; Wang, J. *Phys. Rev. B* **2000**, *62*, 10038.

(40) Corradini, M.; Del Sole, R.; Onida, G.; Palummo, M. *Phys. Rev. B* **1998**, *57*, 14569.

(41) Constantin, L. A.; Pitarke, J. M. *Phys. Rev. B* **2007**, *75*, 245127.

(42) Pitarke, J. M.; Perdew, J. P. *Phys. Rev. B* **2003**, *67*, 045101.

(43) Tao, J.; Staroverov, V. N.; Scuseria, G. E.; Perdew, J. P. *Phys. Rev. A* **2008**, *77*, 012509.

(44) Constantin, L. A.; Ruzsinszky, A. *Phys. Rev. B*, submitted for publication.

(45) Perdew, J. P.; Constantin, L. A. *Phys. Rev. B* **2007**, *75*, 155109.

(46) (a) Kirzhnitz, D. A. *Sov. Phys. JETP* **1957**, *5*, 64. (b) Kirzhnitz, D. A. In *Field Theoretical Methods in Many-Body Systems*; Pergamon: Oxford, 1967.

(47) Constantin, L. A.; Ruzsinszky, A.; Perdew, J. P. *Phys. Rev. B*, to be submitted for publication.

(48) In ref 20, the PBEsol wavevector analysis of a jellium surface was compared to an accurate TDDFT calculation that used the xc kernel of ref 42.

(49) Perdew, J. P.; Wang, Y. In *Mathematics Applied to Science*; Goldstein, J. A., Rosencrans, S., Sod G., Eds.; Academic: Boston, 1988.

CT800553T

JCTC Journal of Chemical Theory and Computation

Some Fundamental Issues in Ground-State Density Functional Theory: A Guide for the Perplexed

John P. Perdew,*,† Adrienn Ruzsinszky,† Lucian A. Constantin,† Jianwei Sun,† and Gábor I. Csonka‡

Department of Physics and Quantum Theory Group, Tulane University, New Orleans, Louisiana 70118, and Department of Inorganic and Analytical Chemistry, Budapest University of Technology and Economics, H-1521 Budapest, Hungary

Received December 3, 2008

Abstract: Some fundamental issues in ground-state density functional theory are discussed without equations: (1) The standard Hohenberg−Kohn and Kohn−Sham theorems were proven for a Hamiltonian that is not quite exact for real atoms, molecules, and solids. (2) The density functional for the exchange-correlation energy, which must be approximated, arises from the tendency of electrons to avoid one another as they move through the electron density. (3) In the absence of a magnetic field, either spin densities or total electron density can be used, although the former choice is better for approximations. (4) "Spin contamination" of the determinant of Kohn−Sham orbitals for an open-shell system is not wrong but right. (5) Only to the extent that symmetries of the interacting wave function are reflected in the spin densities should those symmetries be respected by the Kohn−Sham noninteracting or determinantal wave function. Functionals below the highest level of approximations should however sometimes break even those symmetries, for good physical reasons. (6) Simple and commonly used semilocal (lower-level) approximations for the exchange-correlation energy as a functional of the density can be accurate for closed systems near equilibrium and yet fail for open systems of fluctuating electron number. (7) The exact Kohn−Sham noninteracting state need not be a single determinant, but common approximations can fail when it is not. (8) Over an open system of fluctuating electron number, connected to another such system by stretched bonds, semilocal approximations make the exchange-correlation energy and hole-density sum rule too negative. (9) The gap in the exact Kohn−Sham band structure of a crystal underestimates the real fundamental gap but may approximate the first exciton energy in the large-gap limit. (10) Density functional theory is not really a mean-field theory, although it looks like one. The exact functional includes strong correlation, and semilocal approximations often *overestimate* the strength of static correlation through their semilocal exchange contributions. (11) Only under rare conditions can excited states arise directly from a ground-state theory.

I. Introduction

The pleasure of doing density functional theory (DFT) arises from (1) the deep fundamental and intellectual challenge that it presents, (2) the great practical utility and importance of the subject, which is now central to most electronic structure calculations in quantum chemistry and condensed matter physics, and (3) the opportunity to work or communicate with a good company of others who share this interest or passion.

This short article contains no equation, table, or new result. Instead it reviews some fundamental issues in DFT. Nearly all the answers it presents can be found in the literature (and

* Corresponding author e-mail: perdew@tulane.edu.
† Tulane University.
‡ Budapest University of Technology and Economics.

10.1021/ct800531s CCC: $40.75
Published on Web 03/02/2009

even the given references are sketchy and incomplete), yet some of the answers are unknown to or forgotten by the users and even the developers of this theory. These answers, to the extent that they are not quite right or complete, will be corrected, refined, and extended in future work.

II. What Is the Hamiltonian?

The magic of Kohn−Sham density functional theory[1−7] is that it transforms a computationally heavy many-electron problem into a computationally more tractable problem of noninteracting electrons moving in a self-consistent field, in a way that is exact in principle for the ground-state energy and density. This theory tells us much that we wish to know about what atoms, molecules, nanostructures, and solids can exist, with what geometries and other properties, and how much energy is needed to break bonds or remove electrons, etc.

The standard Hohenberg−Kohn (HK)[1] and Kohn−Sham (KS)[2] theorems that undergird DFT were proven for an electronic ground-state of a particular Hamiltonian of an N-electron system: the sum of the nonrelativistic kinetic energy of the electrons, the interaction of the electrons with a static scalar external potential which is a function of electron position (typically but not exclusively arising from Coulomb attraction to the nuclei), and the instantaneous Coulomb repulsion among pairs of electrons. For this Hamiltonian, the HK theorem asserts that the Hamiltonian itself (and in particular its ground-state wave function and energy) is determined in principle by the ground-state electron density; degeneracy is not a problem.[3]

The KS theorem asserts that the ground-state density can be found by solving exact self-consistent one-electron Schrödinger equations for Kohn−Sham orbitals with occupation numbers 1 or 0. The density is found by summing the squares of the occupied orbitals. The total energy is the sum of the kinetic energy of the occupied orbitals, the interaction of the density with the external potential, the Hartree electrostatic energy of the density interacting with itself, and the exchange-correlation energy. The multiplicative effective potential seen by a Kohn−Sham orbital arises from the external potential, the Hartree electrostatic potential due to the density, and a multiplicative position-dependent exchange-correlation potential which is the functional derivative of the exchange-correlation energy. The Kohn−Sham orbitals themselves are manifestly functionals of the density.

In the simplest version of spin-density functional theory,[8] the interacting Hamiltonian also includes the interaction of the electron spins with a position-dependent external magnetic field pointing along a fixed z-axis. Then the exchange-correlation energy becomes a functional of the separate up- and down-spin densities, and the exchange-correlation potentials for the up- and down-spin electrons can differ. Even in the absence of an external magnetic field, this spin-density version is the one that is almost always used in electronic-structure calculations.

The underlying interacting Hamiltonian is realistic but not exact for the real atoms, molecules, nanostructures, and solids that need to be described. First there are relativistic corrections,[5,6,9] which can be treated rigorously in a covariant reformulation of the theory that also takes into account electron currents. When the relativistic effects are not too large, they can also be treated perturbatively for all the electrons or fully for core electrons and perturbatively for the valence electrons. Second, the nuclei are not really sources of a *static* external potential, because they move. The ground-state problem can be reformulated using a multicomponent DFT[4,5,10] employing also the densities of the various kinds of nuclei, or, if the nuclei are sufficiently massive (i.e., classical), then the effect of their motions on the electrons can be accounted for using the standard Born−Oppenheimer adiabatic approximation.[4,5]

III. What Is the Exchange-Correlation Energy?

Thanks to the work of Levy,[3] the exact density functional for the exchange-correlation energy can be defined from a search over many-electron wave functions constrained to yield a given density. Thus many exact conditions (constraints which this functional must satisfy)[7] can be derived, but actually implementing the search (directly or indirectly[11]) would be harder than the already-very-hard traditional N-electron wave function approaches (which are impractical for the large-N case that is often of interest). So, simplifying approximations need to be made.

Fortunately the exchange-correlation energy is a relatively small part of the total energy of a typical system, although it is by far the largest part of "nature's glue" that binds atoms together.[12] It arises because the electrons do not move randomly through the density but avoid one another, an effect that lowers the expectation value of the electron−electron Coulomb interaction (and more so when the electrons are closer together). The exchange-correlation energy consists of three contributions. The first is the potential energy of exchange (the Fock integral of the Kohn−Sham orbitals, including the self-exchange or self-interaction correction). The second is the potential energy of correlation (due to the effect of Coulomb repulsion on the interacting wave function). Both potential energies are negative because the expectation value of the repulsive electron−electron Coulomb interaction is thereby reduced. The third is a smaller positive kinetic energy of correlation (due to the extra swerving motion of the electrons as they avoid one another).

The motion of the electrons through the density (Figure 1) is like the motion of shoppers through a crowded mall.[13] Each shopper is surrounded by his or her "personal space", and each electron is surrounded by its exchange-correlation hole density. Just as a shopper never bumps into himself or herself, an electron never interacts with itself. Thus the exact exchange-correlation energy provides a self-interaction correction to the Hartree electrostatic energy.

IV. Spin Densities or Total Density?

When the external magnetic field tends to zero, the exact spin-density functional theory[8] does not reduce to the exact total-density functional theory,[2] except in spin-unpolarized systems. While both theories should deliver the same ground-

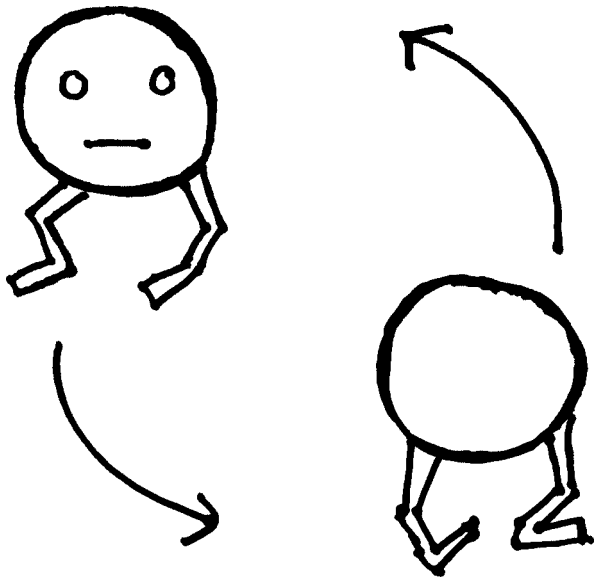

Figure 1. Electrons moving through the density swerve to avoid one another, like shoppers in a mall. The resulting reduction of the potential energy of mutual Coulomb repulsion is the main contribution to the negative exchange-correlation energy. The swerving motion also makes a small positive kinetic energy contribution to the correlation energy.

state energy and total density in this limit, only the former should deliver the separate exact densities of spin-up and spin-down electrons. When the exchange-correlation energy is approximated, even the energy and total density will typically differ (with better results[14] from the spin-density functional calculation, since its inputs are richer and more detailed).

V. Is Spin Contamination Bad for Us?

The underlying interacting Hamiltonian of DFT, in a uniform or zero magnetic field, commutes with the square of the total electron spin and with its z-component. Then the real interacting ground-state wave function can be chosen as an eigenstate of both spin operators.

In open-shell systems, the wave function of the noninteracting Kohn−Sham system (typically and preferably a single Slater determinant of orbitals, as discussed in section VIII) is often *not* an eigenfunction of the square of total spin. This has been called "spin contamination",[15] and "restricted open-shell Kohn-Sham"[16] methods have been developed to avoid it. But it is a contamination only to one who regards the Kohn−Sham wave function as an approximation to the true wave function. The more correct interpretation is that the Kohn−Sham determinant is an auxiliary quantity that generates the true ground-state spin densities. It comes from a spin-dependent Kohn−Sham potential and thus from a noninteracting Hamiltonian which does not commute with the square of the total spin. In some cases, this is the only way to generate the interacting ground-state spin densities in a noninteracting system.[17] Kohn−Sham theory is only designed to yield the ground-state total energy and spin densities and not unrelated observables.

The exact exchange-correlation energy can be written[18,19] as an average over the electron−electron coupling constant that continuously connects the Kohn−Sham noninteracting system to the real interacting one, while holding the spin densities fixed. If the real interacting wave function is not a spin singlet (S=0), then the wave functions in this "adiabatic connection" may not be eigenfunctions of the square of the total spin, except at full or physical coupling strength.

VI. Can Symmetries Break?

As discussed in the preceding section, the Kohn−Sham noninteracting wave function need not display the symmetries of the interacting wave function. But of course it must produce the correct spin densities, which are influenced by symmetry. For example, the exact ground-state of the H_2 molecule is a spin singlet (S=0) at any bond length and thus is spin-unpolarized, with equal up- and down-spin densities. Semilocal approximations typically produce a spin-unpolarized density out to a critical bond length and then break symmetry by gradually localizing an up-spin electron on one nucleus and a down-spin electron on the other.[19] While this leads to an incorrect spin-density, it still leads to the correct dissociation limit for the energy, with an intuitive picture of separate atoms at dissociation. The lower-level functionals can then be regarded[20] as faithful approximations to a theory in which the basic objects are not the up- and down-spin densities but the total density and on-top pair density. Probably functionals on the first four rungs of the ladder of approximations (as defined in section VII) require spin-symmetry breaking, while those on the fifth rung seem more properly to describe static correlation (sections IX and XI) without spin-symmetry breaking.[21]

VII. Are All Approximations Created Equal?

The exchange-correlation energy can be written as the integral over all space of a position-dependent exchange-correlation energy density (which is not unique, although its integral is). The approximation is said to be semilocal if this energy density depends only on the electron density and orbitals in an infinitesimal neighborhood of the given position, and otherwise it is said to be fully nonlocal. On the ladder[22] of density functional approximations (Figure 2), the first rung or local spin-density approximation[2,8] employs only the local spin densities, the second rung or generalized gradient approximation (GGA) [e.g., refs 23 and 24] adds the gradients of the local spin densities, and the third rung or meta-GGA adds the positive orbital kinetic energy density [e.g., refs 25−28] (or, almost equivalently,[29] the Laplacians of the spin densities). Such semilocal functionals often work because of proper accuracy for a slowly varying density or because of error cancelation between exchange and correlation over "normal" regions of space in which such a cancelation is expected.[30] When the semilocal exchange and correlation holes satisfy the same sum rules as the exact holes (section IX), error cancelation can occur because the exact exchange-correlation hole is usually more localized around its electron (and thus more semilocal) than the exact exchange hole. The "abnormal" regions in which no error cancelation is expected include one-electron, nonuniform high-density, and rapidly varying regions (in which exchange

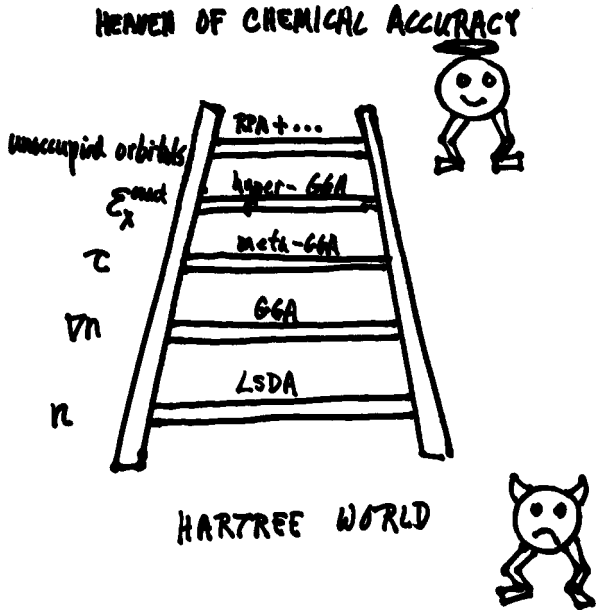

Figure 2. The Jacob's ladder of density functional approximations to the exchange-correlation energy adds local ingredients successively, leading up in five steps from the Hartree world ($E_{xc} = 0$) of weak or no chemical bonding to the heaven of chemical accuracy (with errors in energy differences of order 1 kcal/mol=0.0434 eV).

dominates correlation). A second class of abnormal systems includes the open systems of fluctuating electron number discussed in sections IX and XI (over which the semilocal holes do not satisfy the exact sum rules).

There are also two fully nonlocal rungs: the fourth rung or hyper-GGA [e.g., ref 30], which adds the exact exchange energy density, and the fifth rung or generalized random phase approximation [e.g., ref 31], which adds the unoccupied orbitals. Climbing up the ladder, the approximations become more complicated, more sophisticated, and typically more accurate. Computation times increase modestly from the first to the third rungs and much more steeply after that. The added ingredients on each higher rung of the ladder can be used to satisfy more exact constraints (nonempirical approach[32]), or to better fit data (semiempirical approach), or both. The first three rungs and the fifth require no fitting, but empiricism seems unavoidable[30] on the fourth rung. The ladder classification is not an exclusive one. Although it finally brings in van der Waals interaction on the fifth rung, there are simpler ways to do that, some involving an approximation for the exchange-correlation energy as a double integral of a function of the densities and their gradients at two points in space.[33]

Mel Levy has stressed that, when an investigator reports a "failure of density functional theory", he or she is typically reporting the failure of a given density functional approximation and should say that. Users should also report results on several different rungs, where possible, both as a check on consistency and as guidance for functional developers.

It appears that the densities and energies (if not the Kohn−Sham potentials) of most atoms, and of most molecules and solids close to equilibrium, can be evaluated with increasingly satisfactory accuracy by climbing the first three or semilocal rungs of the ladder.[26−28] But, wherever stretched bonds connect open subsystems of fluctuating electron number,[34−38] full nonlocality may be unavoidably needed, as discussed in sections IX and XI.

Readers who still ask "Which functional should I choose?" could consult ref 39.

VIII. Is One Slater Determinant Enough?

Starting from the Levy constrained search,[3] many different formally exact Kohn−Sham theories can be constructed.[40] In all of them, a search is made over a class of simple objects (of given electron number N) that all yield a given ground-state density (or spin densities), to find the one that minimizes the expectation value of the kinetic energy. The various components of the total energy are then defined for this density, and the total energy is minimized over all N-electron densities. The class might be all single Slater determinants, all fermion wave functions, or most generally all ensembles. The minimizing object then represents the state of the Kohn−Sham noninteracting system of that density; it is either a single determinant, or a linear combination of a few determinants, or an ensemble of such wave functions. The more this class is restricted, the greater the chance that it may be an empty set for the interacting ground-state density of interest. In other words, the desired interacting ground-state density may not be "noninteracting v-representable"[41] over a restricted class, in which case even the "exact" Kohn−Sham theory will fail. Even if a minimizing Slater determinant exists for a given density, it might be an excited state (not a ground state) of the Kohn−Sham noninteracting system.

It seems likely that, for most but perhaps not all real ground-state systems of interest, one can find a Kohn−Sham noninteracting system that is in its ground-state and described by a single Slater determinant. The commonly used density functional approximations are only expected to be reliably accurate when a single Slater determinant can be found. These approximations, whether nonempirical or semiempirical, are all based on general properties of or fits to systems in which the Kohn−Sham wave function is a single Slater determinant (and thus the orbital occupation numbers are integers). In particular, semilocal functionals are accurate in part because they model an on-top hole density that is exact for exchange[42] and often accurate for correlation.[43] If one Slater determinant is not enough, then these approximations cannot be reliably accurate. In other words, if energy-minimized self-consistent calculations with an approximate functional and broken symmetry do not lead to integer occupation numbers for all the orbitals, be careful.

IX. Are Open Systems Different from Closed Ones?

A closed system is one with a fixed number of electrons. It can be composed of several open subsystems among which the electron numbers fluctuate (Figure 3). Since correlation suppresses fluctuation,[44] the fluctuation between subsystems at the noninteracting or Kohn−Sham level is expected to be greater than or equal to that in the real interacting system.

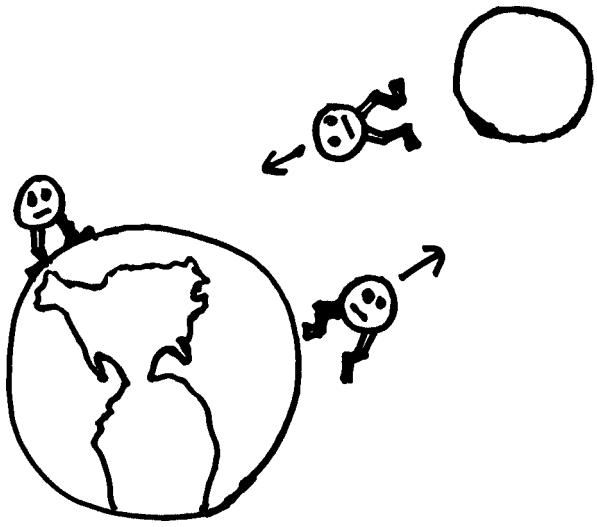

Figure 3. Weakly correlated electrons can fluctuate between the moon (an isolated open system of fluctuating electron number) and the earth (a reservoir). But strongly correlated electrons can localize and thus not fluctuate. The Hartree−Fock approximation neglects correlation, while semilocal approximations often overestimate it.

When fluctuation occurs, some occupied Kohn−Sham orbitals share an electron between the two open subsystems, equivalent to a noninteger occupation number (section VIII) in each. If these open systems are sufficiently separated (connected by *stretched* bonds), then semilocal functionals can make serious errors not only in their separate exchange and correlation energies but also in the sum of the two,[34−38] whose magnitude can be greatly overestimated. These errors can be related directly to the sum rules on the exact exchange[38] and exchange-correlation[35] hole densities around an electron, which integrate to −1 over a closed system but to a value between 0 and −1 over an open system of fluctuating electron number.

It is known[34,35] that the exact energy of an isolated open system varies linearly as a function of its average electron number between adjacent integer numbers. This result follows from both the exact ensemble approach to the open subsystem[34] and the exact wave function approach to the combined closed system.[35] The semilocal functionals make the energy variation concave upward[34,35,38] over this range. (In contrast, the exact-exchange-only or Hartree−Fock approximation makes it concave downward[38] and thus requires a strong negative static correlation correction at noninteger average electron number in order to recover the correct straight-line behavior.)

The resulting "many-electron self-interaction error"[37,45] (or "delocalization error"[46]) of semilocal functionals produces some striking failures thereof: (a) Many asymmetric molecules AB dissociate not to neutral atoms A and B but improperly to fractionally charged fragments $A^{+q}...B^{-q}$.[36−38] (b) Radical symmetric molecules A_2^{+1} at infinite bond length have the correct charge state $A^{+0.5}...A^{+0.5}$ but thereby energies far below the proper energy of $A...A^{+1}$ [e.g., ref 37]. (c) Long-range charge transfers are overestimated.[47] (d) Because the transition states of chemical reactions have long stretched bonds, the energy barriers that control the reaction rates are underestimated or even absent [e.g., ref 30].

The exact energy of an isolated open system has a derivative discontinuity at integer average electron number, where one straight line meets another.[34] As a result, the exact Kohn−Sham potential (and specifically the functional derivative of the exchange-correlation energy) jumps discontinuously by an additive constant at each integer.[34,35,48−50] This is counterintuitive to one who regards the Kohn−Sham potential as a physical object, but not to one who recalls that it is a mathematical object that acts on a nonphysical system of noninteracting electrons.

X. Is the Kohn−Sham Band Gap Wrong?

The jump of the Kohn−Sham potential (discussed in the last paragraph of section IX) also explains[51−54,46] how the fundamental band gap of an insulator (ionization energy minus electron affinity) can be larger than the gap in the exact Kohn−Sham band structure. (Note that accurate fundamental gaps for semiconductors are predicted not by the band structure of the Kohn−Sham potential but by that of a hybrid of the multiplicative Kohn−Sham and nonmultiplicative Hartree−Fock potentials.[55]) Since in an atom the first excitation energy is often approximated by the difference between the lowest unoccupied and highest occupied exact Kohn−Sham orbital energies,[56] it follows that in a large-gap insulator the gap in the exact Kohn−Sham band structure approximates the first exciton energy (the least energy to create an electron−hole pair localized on one atom), which is smaller than the fundamental gap. The fundamental gap (if it is direct or optical one) is however the limit of a Rydberg series of exciton energies.

XI. Can DFT Describe Strong Correlations?

Some practitioners of "strong correlation" define it as "anything not described by DFT" but probably mean by that "some things not described correctly by the common semilocal density functional approximations". "Strong correlation" has two different meanings: (1) It can refer for example to the correlations present in a superconductor or a Luttinger liquid, which may have a small effect on bonding energies but are qualitatively different from the correlations given by low-order perturbation theory or by the random phase approximation. (2) It can refer to static correlations[57] that arise from near- or exact degeneracies at the Kohn−Sham level and are especially important when there are stretched bonds between open systems of fluctuating electron number[34−38] (section IX). (In the limit of infinite stretch, there is degeneracy between the bonding and unoccupied antibonding molecular orbitals that are shared between two open subsystems, each of fluctuating electron number.) These static correlations can be large and important on the scale of bonding energies. Even in equilibrium, they can perhaps arise from subsystems composed of localized d-electrons (as in some transition-metal oxides) or f-electrons (as in some lanthanides and actinides).[38] Static correlation, also known as electron localization or the suppression of electron fluctuation, can occur in both molecules and solids.

It is often said that DFT (at least in semilocal approximations) is a "mean field approximation" (like Hartree−Fock theory) which "does not include strong correlation". Neither of these statements is really correct. DFT solves mean-field-like equations but includes in principle all correlations via the exact exchange-correlation functional. Semilocal approximations account for static correlation not in the correlation term but in the exchange term.[57] In the case of stretched bonds between open systems of fluctuating electron number (section VIII), they typically *overestimate* the magnitude of the sum of exact exchange and exact correlation (including static correlation).[38] This error is often reduced in hybrid functionals that mix a fraction $a \approx 0.25$[58] of exact exchange with a fraction 1-a of semilocal exchange plus full semilocal correlation. But in other cases (e.g., stretched spin-restricted singlet H_2) they somewhat *underestimate* the magnitude of the static correlation, and in these cases the hybrid functionals can be worse than the semilocal ones. Accurate description of these strong correlations seems to require fully nonlocal (fourth- or even fifth-rung) functionals.

Strong correlations of type (2) above are often treated with a "DFT+U" approach, where the positive empirical parameter U can be understood[59,38] as an energy penalty for fractional occupation that corrects the semilocal DFT error described in sections IX and XI.

XII. Do Excited States Arise Directly from a Ground-State Theory?

In principle, the ground-state density in the absence of a magnetic field determines the Hamiltonian and thus all excited states and their energies. But solutions of the exact Kohn−Sham equations do not predict exact excited-state energies and densities, except under special circumstances.[60,61] If the ground-state density functional for the energy has extrema lying above the minimum, those extrema predict the energies and densities of excited states. In particular, self-consistent solutions of the exact Kohn−Sham equations in which all spin−orbitals have occupations 1 below (or at) and 0 above a Fermi level represent either ground or excited states.

In principle and in practice, excited-state energies can be found from time-dependent DFT or from excited-state DFT.[4−6]

Note Added after ASAP Publication. This article was released ASAP on March 2, 2009. On March 3, 2009 additional information was added to ref 24. Additional information was added to ref 63 on March 17, 2009. The correct version was posted on March 18, 2009.

Acknowledgment. J.P.P. thanks Gus Scuseria, Kieron Burke, and Mel Levy for putting together this special issue as well as Tulane University, Ulli Diebold, and Kieron Burke for bringing so many of his friends and colleagues together for the DFT Fest in March 2008 and all of them for participating, with special thanks to those who have contributed articles.[62−89] This work was supported in part by the National Science Foundation (DMR-0501588).

References

(1) Hohenberg, P.; Kohn, W. *Phys. Rev.* **1964**, *136*, B 864.

(2) Kohn, W.; Sham, L. J. *Phys. Rev.* **1965**, *140*, A1133.

(3) Levy, M. *Proc. Natl. Acad. Sci. U.S.A.* **1979**, *76*, 6062.

(4) Parr, R. G.; Yang, W. *Density-Functional Theory of Atoms and Molecules*; Oxford University Press: New York, 1989.

(5) Dreizler, R. M.; Gross, E. K. U. *Density Functional Theory*; Springer-Verlag: Berlin, 1990.

(6) *A Primer in Density Functional Theory*; Fiolhais, C., Nogueira, F., Marques, M., Eds.; Springer-Verlag, Berlin: 2003.

(7) Perdew, J. P.; Kurth, S. in ref 6.

(8) Barth, U.; Hedin, L. *J. Phys. C* **1972**, *5*, 1629.

(9) Dreizler, R. M.; Engel, E. In *Density Functionals: Theory and Applications*; Joubert, D. P., Ed.;Lecture Notes in Physics 500, Springer-Verlag: Berlin, 1998.

(10) Kreibich, T.; van Leeuwen, R; Gross, E. K. U. *Phys. Rev. A* **2008**, *78*, 022501.

(11) Bartlett, R. J.; Lotrich, V. F.; Schweigert, I. V. *J. Chem. Phys.* **2005**, *123*, 062205.

(12) Kurth, S.; Perdew, J. P. *Int. J. Quantum Chem.* **2000**, *77*, 814.

(13) Tran, H. T.; Perdew, J. P. *Am. J. Phys.* **2003**, *71*, 1048.

(14) Gunnarsson, O.; Lundqvist, B. I.; Wilkins, J. W. *Phys. Rev. B* **1974**, *10*, 1310.

(15) Baker, J.; Scheiner, A.; Andselm, A. *Chem. Phys. Lett.* **1993**, *216*, 380.

(16) Filatov, M.; Shaik, S. *Chem. Phys. Lett.* **1998**, *288*, 689.

(17) Pople, J. A.; Gill, P. M. W.; Handy, N. C. *Int. J. Quantum Chem.* **1995**, *56*, 303.

(18) Langreth, D. C.; Perdew, J. P. *Solid State Commun.* **1975**, *17*, 1425.

(19) Gunnarsson, O.; Lundqvist, B. I. *Phys. Rev. B* **1976**, *13*, 4274.

(20) Perdew, J. P.; Savin, A.; Burke, K. *Phys. Rev. A* **1995**, *51*, 4531.

(21) Fuchs, M.; Niquet, Y.-M.; Gonze, X.; Burke, K. *J. Chem. Phys.* **2005**, *122*, 094116.

(22) Perdew, J. P.; Schmidt, K. In *Density Functional Theory and Its Applications to Materials*; Van Doren, V. E., Van Alsenoy, K., Geerlings, P., Eds.; American Institute of Physics: Melville, NY, 2001.

(23) Perdew, J. P.; Burke, K; Ernzerhof, M. *Phys. Rev. Lett.* **1996**, *77*, 3865; **1997**, *78*, 1396 (E).

(24) Perdew, J. P.; Ruzsinszky, A.; Csonka, G. I.; Vydrov, O. A.; Scuseria, G. E.; Constantin, L. A.; Zhou, X.; Burke, K. *Phys. Rev. Lett.* **2008**, *100*, 136406; **2009**, *102*, 033902 (E).

(25) Tao, J.; Perdew, J. P.; Staroverov, V. N.; Scuseria, G. E. *Phys. Rev. Lett.* **2003**, *91*, 146401.

(26) Staroverov, V. N.; Scuseria, G. E.; Tao, J.; Perdew, J. P. *J. Chem. Phys.* **2003**, *119*, 12129.

(27) Staroverov, V. N.; Scuseria, G. E.; Tao, J.; Perdew, J. P. *Phys. Rev. B* **2004**, *69*, 075102.

(28) Furche, F.; Perdew, J. P. *J. Chem. Phys.* **2006**, *124*, 044103.

(29) Perdew, J. P.; Constantin, L. A. *Phys. Rev. B* **2007**, *75*, 155109.

(30) Perdew, J. P.; Staroverov, V. N.; Tao, J.; Scuseria, G. E. *Phys. Rev. A* **2008**, *78*, 052513.

(31) Constantin, L. A.; Pitarke, J. M.; Dobson, J. F.; Garcia-Lekue, A.; Perdew, J. P. *Phys. Rev. Lett.* **2008**, *100*, 036401.

(32) Perdew, J. P.; Ruzsinszky, A.; Tao, J.; Staroverov, V. N.; Csonka, G. I. *J. Chem. Phys.* **2005**, *123*, 062201.

(33) Dion, M.; Rydberg, H.; Schroeder, E.; Langreth, D. C.; Lundqvist, B. I. *Phys. Rev. Lett.* **2004**, *92*, 246401.

(34) Perdew, J. P.; Parr, R. G.; Levy, M.; Balduz, J. L. *Phys. Rev. Lett.* **1982**, *49*, 1691.

(35) Perdew, J. P. In *Density Functional Methods in Physics*; Dreizler, R. M., da Providencia, J. Eds.; Plenum: New York, 1985.

(36) Ruzsinszky, A.; Perdew, J. P.; Csonka, G. I.; Vydrov, O. A.; Scuseria, G. E. *J. Chem. Phys.* **2006**, *125*, 194112.

(37) Ruzsinszky, A.; Perdew, J. P.; Csonka, G. I.; Vydrov, O. A.; Scuseria, G. E. *J. Chem. Phys.* **2007**, *126*, 104102.

(38) Perdew, J. P.; Ruzsinszky, A,; Csonka, G. I.; Vydrov, O. A.; Scuseria, G. E.; Staroverov, V. N.; Tao, J. *Phys. Rev. A* **2007**, *76*, 040501 (R).

(39) Rappoport, D.; Crawford, N. R. M.; Furche, F.; Burke, K. In *Computational Inorganic and Bioinorganic Chemistry*; Solomon, E. I., King, R. B., Scott, R. A., Eds.; Wiley: Chichester, in press.

(40) Levy, M.; Perdew, J. P. In *Density Functional Methods in Physics*; Dreizler, R. M., da Providencia, J., Eds.; Plenum: New York, 1985.

(41) Levy, M. *Phys. Rev. A* **1982**, *26*, 1200.

(42) Ziegler, T.; Rauk, A.; Baerends, E. J. *Theor. Chim. Acta* **1977**, *43*, 261.

(43) Burke, K.; Perdew, J. P.; Ernzerhof, M. *J. Chem. Phys.* **1998**, *109*, 3760.

(44) Ziesche, P.; Tao, J.; Seidl, M.; Perdew, J. P. *Int. J. Quantum Chem.* **2000**, *77*, 819.

(45) Mori-Sanchez, P.; Cohen, A. J.; Yang, W. *J. Chem. Phys.* **2006**, *125*, 201102.

(46) Mori-Sanchez, P.; Cohen, A. J.; Yang, W. *Phys. Rev. Lett.* **2008**, *100*, 146407.

(47) Tozer, D. J. *J. Chem. Phys.* **2003**, *119*, 12697.

(48) Sagvolden, E.; Perdew, J. P. *Phys. Rev. A* **2008**, *77*, 012517.

(49) Sagvolden, E.; Perdew, J. P.; Levy, M. *Phys. Rev. A* **2009**, *79*, 026501.

(50) Gori-Giorgi, P.; Savin, A. *Int. J. Quantum Chem.* **2009**, . in press.

(51) Perdew, J. P.; Levy, M. *Phys. Rev. Lett.* **1983**, *51*, 1884.

(52) Sham, L. J.; Schlueter, M. *Phys. Rev. Lett.* **1983**, *51*, 1888.

(53) Perdew, J. P. *Int. J. Quantum Chem.* **1986**, *30*, 4519.

(54) Gruening, M.; Marini, A.; Rubio, A. *Phys. Rev. B* **2006**, *74*, 161103.

(55) Brothers, E. N.; Izmaylov, A. F.; Normand, J. O.; Barone, V.; Scuseria, G. E. *J. Chem. Phys.* **2008**, *129*, 011102.

(56) Savin, A.; Umrigar, C.; Gonze, X. *Chem. Phys. Lett.* **1998**, *288*, 391.

(57) Handy, N. C.; Cohen, A. J. *Mol. Phys.* **2001**, *99*, 403.

(58) Perdew, J. P.; Ernzerhof, E.; Burke, K. *J. Chem. Phys.* **1996**, *105*, 9982.

(59) Cococcioni, M.; de Gironcoli, S. *Phys. Rev. B* **2006**, *71*, 035105.

(60) Perdew, J. P.; Levy, M. *Phys. Rev. B* **1985**, *31*, 6264.

(61) Freire, H. J. P.; Egues, J. C. *Phys. Rev. Lett.* **2007**, *99*, 026801.

(62) Tempel, D. G.; Martinez, T. J.; Maitra, N. T. *J. Chem. Theory Comput.* this issue.

(63) Gaiduk, A. P.; Chulkov, S.; Staroverov, V. N. *J. Chem. Theory Comput.* this issue.

(64) Gori-Giorgi, P.; Vignale, G.; Seidl, M. *J. Chem. Theory Comput.* this issue.

(65) Savin, A. *J. Chem. Theory Comput.* this issue.

(66) Li, Y.; Lu, D.; Galli, G. *J. Chem. Theory Comput.* this issue.

(67) Kurth, S.; Proetto, C. R.; Capelle, K. *J. Chem. Theory Comput*. this issue.

(68) Odashima, M. M.; Capelle, K.; Trickey, S. B. *J. Chem. Theory Comput.* this issue.

(69) Ruzsinszky, A.; Csonka, G. I.; Scuseria, G. E. *J. Chem. Theory Comput.* this issue.

(70) Csonka, G. I.; French, A. P.; Johnson, G. P.; Stortz, C. A. *J. Chem. Theory Comput.* this issue.

(71) Sun, J. *J. Chem. Theory Comput.* this issue.

(72) Constantin, L. A.; Pitarke, J. M. *J. Chem. Theory Comput.* this issue.

(73) Tao, J.; Tretiak, S *J. Chem. Theory Comput.* this issue.

(74) Mattsson, A. E.; Mattsson, T. R. *J. Chem. Theory Comput.* this issue.

(75) Chen, L. *J. Chem. Theory Comput.* this issue.

(76) Ernzerhof, M. *J. Chem. Theory Comput.* this issue.

(77) Sagvolden, E.; Furche, F.; Koehn, A. *J. Chem. Theory Comput.* this issue.

(78) Elliott, P.; Cohen, M.; Wasserman, A.; Burke, K. *J. Chem. Theory Comput.* this issue.

(79) Cohen, A. J.; Mori-Sanchez, P.; Yang, W. *J. Chem. Theory Comput.* this issue.

(80) Gross, E. K. U.; Proetto, C. *J. Chem. Theory Comput.* this issue.

(81) Cardoso, C.; Abreu, P.; Nogueira, F. *J. Chem. Theory Comput.* this issue.

(82) Kannemann, F.; Becke, A. J. *J. Chem. Theory Comput.* this issue.

(83) Hesselmann, A.; Goerling, A.; Gimon, T.; Ipatov, A. *J. Chem. Theory Comput.* this issue.

(84) Kuemmel, S.; Karlowski; A.; Armiento, R. *J. Chem. Theory Comput.* this issue.

(85) Andrade, X.; Castro, A.; Zueco, D.; Echenique, P.; Alonso, J. L.; Falceto, F.; Rubio, A. *J. Chem. Theory Comput.* this issue.

(86) Henderson, T.; Scuseria, G. E.; Weintraub, E. *J. Chem. Theory Comput.* this issue.

(87) Zheng, J.; Zhao, Y.; Truhlar, D. *J. Chem. Theory Comput.* this issue.

(88) Ullrich, C. *J. Chem. Theory Comput.* this issue.

(89) Pederson, M.; Baruah, T. *J. Chem. Theory Comput.* this issue.

CT800531S

JCTC Journal of Chemical Theory and Computation

Standard Free Energy of Binding from a One-Dimensional Potential of Mean Force

Slimane Doudou, Neil A. Burton, and Richard H. Henchman*

School of Chemistry, The University of Manchester, Oxford Road, Manchester, M13 9PL, United Kingdom, and Manchester Interdisciplinary Biocentre, The University of Manchester, 131 Princess Street, Manchester M1 7DN, United Kingdom

Received June 20, 2008

Abstract: A practical approach that enables one to calculate the standard free energy of binding from a one-dimensional potential of mean force (PMF) is proposed. Umbrella sampling and the weighted histogram analysis method are used to generate a PMF along the reaction coordinate of binding. At each point, a restraint is applied orthogonal to the reaction coordinate to make possible the determination of the volume sampled by the ligand. The free energy of binding from an arbitrary unbound volume to the restrained bound form is calculated from the ratio of the PMF integrated over the bound region to that of the unbound. Adding the free energy changes from the standard-state volume to the unbound volume and from the restrained to the unrestrained bound state gives the standard free energy of binding. Exploration of the best choice of binding paths is also made. This approach is first demonstrated on a model binding system and then tested on the benzamidine−trypsin system for which reasonable agreement with experiment is found. A comparison is made with other methods to obtain the standard free energy of binding from the PMF.

Introduction

The binding free energy is a fundamental property of many molecular systems[1−9] such as those encountered in drug design, catalysis, and self-assembly. Consequently, the development of free energy methods plays a pivotal role in research. Typically, these methods can be used either to calculate the free energy of the bound and unbound states separately, in approaches such as the MM/PBSA[10−12] and LIE[1,13]methods, or to evaluate the free energy difference between bound and unbound states. Free energy difference methods proceed through decoupling the interactions between the ligand and its receptor, giving a nonphysical pathway[8,10,14,15] or by displacing the ligand along a physical pathway of binding.[10,12,16−21]Although the decoupling free energy methods are commonly used to calculate the binding free energy, the pathway methods also provide mechanistic and kinetic information on the real process of binding. The immediate output of a binding-pathway free energy method is not a free energy difference but a potential of mean force (PMF), which is defined as the negative logarithm of the probability of being at a given value of a specified reaction coordinate. Sampling realistic binding pathways is an ongoing challenge, and the path usually has to be selected and biased to achieve converged sampling, an exception to this being transition path sampling.[22]Many different pathway methods have been developed. These include umbrella sampling,[23] adaptive force bias,[24] the Jarzynski method,[25] and metadynamics.[26] While newer methods such as the adaptive force bias method should be more efficient, umbrella sampling has been one of the most widely used methods to study binding in solution.[12,16−20,27−30]

For protein−ligand systems, the relationship between the standard free energy of binding ΔG° and the change in the PMF on binding, hereafter referred to as the PMF depth, ΔW_R, is controversial, and they are often assumed to be equivalent.[31−34] Even in the few studies that examine that relationship, there are differing formulations.[10,12,18,21,30,35−37] In the simple case of spherical symmetry, the association force constant can be calculated by integrating the PMF over the bound region and by accounting for the radial Jacobian

* Corresponding author phone: +44 (0)161 306 5194; fax: +44 (0)161 306 5201; e-mail: henchman@manchester.ac.uk.

10.1021/ct8002354 CCC: $40.75
Published on Web 03/10/2009

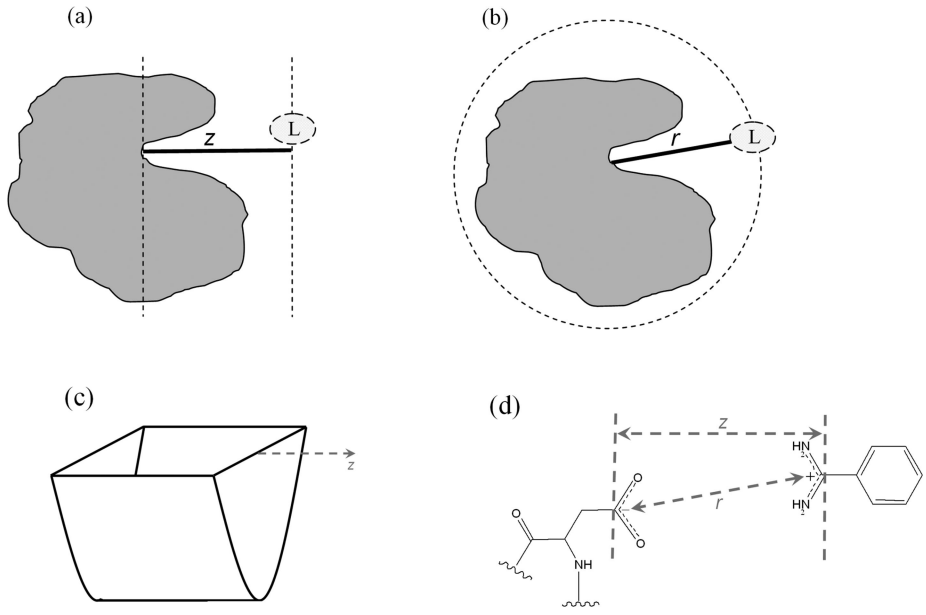

Figure 1. (a) *z*-Component reaction coordinate and (b) the distance *r* reaction coordinate between the protein on the left and the ligand on the right. (c) The three-dimensional PMF of the model binding site. (d) The *z*-component and the distance *r* reaction coordinates between the carboxylate of Asp 189 and the amidine carbon of benzamidine.

and standard-state concentration.[10,30,35−37] In protein−ligand systems, there are two major problems. First, there is no such symmetry due to the complex shapes of the proteins. Second, there are limitations on sampling since the ligand would need to sample all the space around the protein. This makes necessary more general formulations. Gilson and co-workers[10] suggest calculating the standard free energy of binding from the PMF by defining w_b as the average PMF depth in the bound region and adding to it a term that accounts for the change in the ligand's translational and rotational volumes upon binding. Their PMF is a six-dimensional function of the ligand's position and orientation. The problem with using a PMF of such high dimensionality is that the extensive sampling required makes it difficult to calculate. A similar approach was employed by Lee and Olson,[12,18] but they use w_{min}, the minimum of the PMF, instead of w_b and their PMF is a function of a one-dimensional reaction coordinate. Woo and Roux[21] have a different approach in which they apply multiple restraints to the ligand, determine a radial one-dimensional PMF, and then remove the restraints. The standard free energy of binding is then obtained from the equilibrium binding constant using a complex derivation that involves calculating a surface area integral for the ligand at a large distance from the receptor and multiplying this by terms to add and remove the restraints, by the PMF integral over the bound state, and by the standard concentration. Information about the PMF depth is contained implicitly in the PMF integral.

In this work, a strategy is described to obtain the standard free energy of binding from a one-dimensional PMF. Our approach is similar to Woo and Roux's[21] but is constructed in a simpler manner that permits an easier implementation and physical interpretation of the terms involved. The choice of reaction coordinate is important in formulating the method and achieving converged sampling. The PMF is obtained along a one-dimensional *z*-component reaction coordinate between the protein and the ligand while applying restraints orthogonal to this reaction coordinate. The protein is oriented so that the *z*-axis points directly out of the binding site. The orthogonal restraints serve a dual purpose: they make it possible to calculate the area sampled by ligand orthogonal to the reaction coordinate and they limit the sampling required in each window. The use of a *z*-component rather than a radial reaction coordinate *r* is illustrated in Figure 1a and 1b and ensures that the configurational areas at each point along the reaction coordinate are similar in size rather than increasing as $4\pi r^2$. Small, constant areas are easier to sample than areas that increase in size. An extra term accounting for the $4\pi r^2$ increase in area as the ligand unbinds would be required if a flat PMF is desired in the bulk solvent.[36,38,39] Computing the ratio of the integrated PMF over the bound and unbound regions leads to the free energy of binding from a specified unbound volume to a bound restrained state. The orthogonal restraint permits the calculation of the unbound volume. Adding the free energy changes from the standard volume to this unbound volume and from the restrained to the unrestrained bound state determines the standard free energy of binding. The approach is used on a model system to demonstrate its performance. It is then applied to calculate the standard Gibbs free energy of binding of trypsin to benzamidine along a suitably chosen binding path and then compared with experiment.

Methods

Standard Free Energy of Binding from the PMF. The reaction coordinate of the PMF is chosen to be the *z*-component.[40,41] Orthogonal harmonic restraints are applied along the *x* and *y* axes to restrict the ligand to an area that is easily determined and capable of being sampled for the length of the simulations. The free energy change of binding ΔG_{PMF} between the bound and unbound sections of the PMF

is given by

$$\Delta G_{\mathrm{PMF}} = -RT \ln\left(\frac{Q_{\mathrm{b,R}}}{Q_{\mathrm{u,R}}}\right) \quad (1)$$

where $Q_{\mathrm{b,R}}$ and $Q_{\mathrm{u,R}}$ are the partition functions for the bound and unbound regions, respectively, and the subscript R denotes the use of orthogonal restraints. Their ratio is computed by integrating the PMF over the bound and unbound regions using the following equation:

$$\frac{Q_{\mathrm{b,R}}}{Q_{\mathrm{u,R}}} = \frac{\int_{\mathrm{bound}} \exp\left(\frac{-W_{\mathrm{R}}(z)}{RT}\right) \mathrm{d}z}{\int_{\mathrm{unbound}} \exp\left(\frac{-W_{\mathrm{R}}(z)}{RT}\right) \mathrm{d}z} = \frac{l_{\mathrm{b}}}{l_{\mathrm{u}}} \exp\left(\frac{-\Delta W_{\mathrm{R}}}{RT}\right) \quad (2)$$

where $W_{\mathrm{R}}(z)$ is the PMF as a function of z and defined to be zero at its lowest point when the ligand is bound. The cutoff between the bound and unbound regions is chosen to be the value of z where the PMF becomes constant within statistical noise and the ligand is in the bulk. The unbound region is defined up to an arbitrary upper limit that cancels in the full expression for ΔG° given below. The PMF depth ΔW_{R} is defined as the lowest point, zero, minus the exponential average of the PMF over the entire unbound region, giving

$$\Delta W_{\mathrm{R}} = RT \ln\left[\int_{\mathrm{unbound}} \exp\left(\frac{-W_{\mathrm{R}}(z)}{RT}\right) \mathrm{d}z / \int_{\mathrm{unbound}} \mathrm{d}z\right] \quad (3)$$

The bound and unbound lengths, l_{b} and l_{u}, are configurational integrals of the PMF

$$l_{\mathrm{b}} = \int_{\mathrm{bound}} \exp\left(\frac{-W_{\mathrm{R}}(z)}{RT}\right) \mathrm{d}z \quad (4)$$

$$l_{\mathrm{u}} = \int_{\mathrm{unbound}} \exp\left(\frac{-(W_{\mathrm{R}}(z) + \Delta W_{\mathrm{R}})}{RT}\right) \mathrm{d}z = \int_{\mathrm{unbound}} \mathrm{d}z \quad (5)$$

which are both independent of the orthogonal restraints. The definition of ΔW_{R} ensures that l_{u} equals the length of the reaction coordinate in the unbound region. The lowest values for $W(z)$ in the binding site contribute the most to the integrals and make the calculations of the ratio of the partition functions insensitive to the cutoff.[42] To determine the standard free energy of binding ΔG°, the free energy ΔG_{V} for changing from the standard-state volume $V^{\circ} = 1661$ Å^3, which corresponds to a 1 M concentration, to the sampled unbound volume and the free energy ΔG_{R} to remove the orthogonal restraints when the ligand is bound are included to give the expression

$$\Delta G^{\circ} = \Delta G_{\mathrm{PMF}} + \Delta G_{\mathrm{V}} + \Delta G_{\mathrm{R}} \quad (6)$$

These three free energy terms are depicted in Figure 2. The second term of eq 6, ΔG_{V}, is the ratio of the sampled unbound volume $V_{\mathrm{u,R}}$ to the standard-state volume V° and can be written as

$$\Delta G_{\mathrm{V}} = -RT \ln\left(\frac{V_{\mathrm{u,R}}}{V^{\circ}}\right) \quad (7)$$

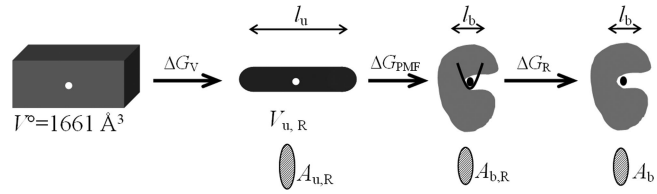

Figure 2. Schematic showing the decomposition of the standard Gibbs free energy of binding ΔG° into the volume reduction term ΔG_{V}, the potential of mean force term ΔG_{PMF}, and the term for the removal of the orthogonal restraints ΔG_{R}.

The unbound volume $V_{\mathrm{u,R}}$ is determined from the distances that the ligand samples along the x, y, and z directions. In the x and y directions, the area $A_{\mathrm{u,R}}$ for the unbound ligand is obtained from the partition function of the orthogonal restraint potential, which is given by

$$A_{\mathrm{u,R}} = \int_{-\infty}^{+\infty} \exp\left(\frac{-k_{xy}x^2}{2RT}\right) \mathrm{d}x \int_{-\infty}^{+\infty} \exp\left(\frac{-k_{xy}y^2}{2RT}\right) \mathrm{d}y = \frac{2\pi RT}{k_{xy}} \quad (8)$$

The reaction coordinate distance spanning the unbound region in the z direction equals l_{u}. $V_{\mathrm{u,R}}$ is simply the distance l_{u} multiplied by the area in the x and y directions

$$V_{\mathrm{u,R}} = l_{\mathrm{u}} \times A_{\mathrm{u,R}} = l_{\mathrm{u}} \frac{2\pi RT}{k_{xy}} \quad (9)$$

ΔG_{R} is calculated using a free energy perturbation approach from the exponential average of turning on the harmonic restraint as follows:

$$\Delta G_{\mathrm{R}} = RT \ln\left\langle \exp\left(\frac{-k_{xy}(\Delta x^2 + \Delta y^2)}{2RT}\right)\right\rangle_{k_{xy}=0} \quad (10)$$

where Δx and Δy are the displacements relative to the restraint minimum for the simulation without orthogonal restraints. The perturbation is carried out using the simulation without restraints as the reference state because the configuration space sampled will include all the important subset of states when the restraint is applied. A perturbation in the reverse direction would not sample all the important states when the restraint is removed. Substituting ΔG_{PMF} and ΔG_{V} from eqs 1, 2, 7, and 9 into eq 6 gives a clear relationship between the standard free energy of binding and the PMF depth as

$$\Delta G^{\circ} = \Delta W_{\mathrm{R}} - RT \ln\left(\frac{l_{\mathrm{b}} A_{\mathrm{u,R}}}{V^{\circ}}\right) + \Delta G_{\mathrm{R}} \quad (11)$$

which is independent of length l_{u}. The equivalent binding equilibrium constant, K_{a}, is

$$K_{\mathrm{a}} = \frac{l_{\mathrm{b}} A_{\mathrm{u,R}}}{V^{\circ}} \exp\left(\frac{\Delta G_{\mathrm{R}} - \Delta W_{\mathrm{R}}}{RT}\right) \quad (12)$$

Equation 12 has the following interpretation: ΔW_{R} does not contain the integration of the PMF over the bound length so this must be included in the form of l_{b}; it does contain

integration over $A_{u,R}$ so this must be removed by multiplication by $A_{u,R}$ (division by $1/A_{u,R}$) since it concerns the unbound state; it does not contain integration over V° when unbound so this must be included by dividing by V°; it contains integration over the orthogonal restraints when bound so this contribution is removed by multiplying by $\exp(\Delta G_R/RT)$. Defining ΔG_R in terms of the ratio of orthogonal areas, we have

$$\Delta G_R = -RT \ln\left(\frac{A_{b,R}}{A_b}\right) \tag{13}$$

where $A_{b,R}$ and A_b are the bound areas available to the ligand with and without the orthogonal restraints, and setting $V_b = l_b A_b$ leads to the insightful relationship

$$\Delta G^\circ = \Delta W_R - RT \ln\left(\frac{V_b}{V^\circ}\frac{A_{u,R}}{A_{b,R}}\right) \tag{14}$$

If the PMF is three-dimensional in x, y, and z, then an analogous expression can be derived for ΔG° as

$$\Delta G^\circ = \Delta W_{3D} - RT \ln\left(\frac{V_b}{V^\circ}\right) \tag{15}$$

where ΔW_{3D} is the minimum in the three-dimensional PMF obtained by integrating over all system coordinates except x, y, and z of the ligand. Equating eqs 14 and 15 yields the relationship

$$\Delta W_{3D} = \Delta W_R - RT \ln\left(\frac{A_{u,R}}{A_{b,R}}\right) \tag{16}$$

Model Binding Site. The approach is first applied to a model binding site. The three-dimensional PMF, as shown in Figure 1c, is harmonic in the x and y directions with a force constant k_b of 20 kcal mol^{-1} Å^{-2} and a step function in z with a length l_b of 0.5 Å. ΔW_{3D} is chosen to be -10 kcal mol^{-1}. Equation 16 is used to calculate the value of ΔW_R. Equation 8 gives the required areas $A_{u,R}$ and $A_{b,R}$ and the force constant when bound equals $k_{xy} + k_b$. Five orthogonal force constants k_{xy} are tested: 0, 1, 5, 10, and 50 kcal mol^{-1} Å^{-2}.

Trypsin−Benzamidine Setup and Molecular Dynamics Protocol. The protein−ligand system examined is the inhibitor benzamidine binding to the enzyme bovine trypsin (PDB code 3PTB) whose function is to degrade dietary proteins. This system has commonly been used as a benchmark for computational methods.[33,43−46] The same five orthogonal force constants k_{xy} are tested: 0, 1, 5, 10, and 50 kcal mol^{-1} Å^{-2}. The protein is modeled with the AMBER 99 force field[47] and solvated with 9284 TIP3P[48] water molecules using the leap module of AMBER 9.[49] Nine Cl^- ions are added to neutralize the system. The ligand, benzamidine, is modeled with the GAFF force field,[50] and its charges are derived using the RESP method.[51] This setup results in a system comprising 31 100 atoms in a box of size $66 \times 62 \times 75$ Å^3.

The energy minimization and molecular dynamics simulations are performed with the Sander module of AMBER 9. Periodic boundary conditions and the particle mesh Ewald method are used with a nonbonded cutoff of 9 Å. The system is first energy-minimized using 1000 steps of each of the steepest descent and conjugate gradient methods. It is then heated at constant volume to 298 K in a 50-ps molecular dynamics simulation with Langevin temperature regulation. Bonds involving hydrogen atoms are constrained using the SHAKE algorithm allowing a 2-fs integration time step. Subsequently, the system is switched to a constant pressure of 1 bar and further equilibrated for 1 ns.

Umbrella Sampling. Umbrella sampling is adopted to determine the PMF from the binding site to solution in water, whereby a harmonic restraint is placed at successive points along the reaction coordinate ξ and probabilities at each point are accumulated. The restraining potential employed has the harmonic form

$$V(\xi) = \frac{1}{2}k(\xi - \xi_0)^2 \tag{17}$$

where ξ_0 is the target distance and k is the force constant. The weighted histogram analysis method[52,53] is used to convert the probabilities into the PMF along the reaction coordinate. The reaction coordinate here is defined as either the z-component of the distance between the C7 atom of benzamidine and the Cγ atom of ASP 189, as shown in Figure 1d, or the radial distance r. The radial distance when the ligand is bound is ~3.8 Å. The path extends linearly out of the binding site and is divided into 28 windows at 1 Å intervals, with each window having the ligand placed at the desired value of the reaction coordinate, starting from 4 to 31 Å, remaining well within the simulation box. The restraint force constant of the umbrella potential is set to 1 kcal mol^{-1} Å^{-2}. Each window is simulated for 1 ns.

Choice of the Binding Path. A suitable linear path, to which this approach is applied, was chosen by performing short umbrella sampling simulations along 17 different linear paths at different orientations from the binding pocket to the bulk as illustrated in Figure 3. One of these trajectories is along the central z-axis, which coincides with the long axis of the ligand when bound. The other trajectories are chosen with combinations of four different polar angles θ (5°, 10°, 15°, and 20°) and four different azimuthal angles φ (0°, 90°, 180°, and 270°). The radial distance reaction coordinate is employed. Each window on every path is simulated for only 50 ps to offset the expense of simulating the larger number of paths. An alternative approach where each window is started from the last configuration of the preceding window to create a nonlinear path was also examined but was found to be dissatisfactory, as reported in the results.

Results

Standard Free Energy of Binding of the Model System. Figure 4 shows the PMFs for the model system with four different orthogonal restraints. The PMF depths ΔW_R are seen to decrease with smaller orthogonal force constant k_{xy} and tend to negative infinity in the limit of $k_{xy} = 0$ when the unbound ligand samples an infinite volume. Using the arbitrary unbound length l_u of 10 Å, Table 1 summarizes l_b,

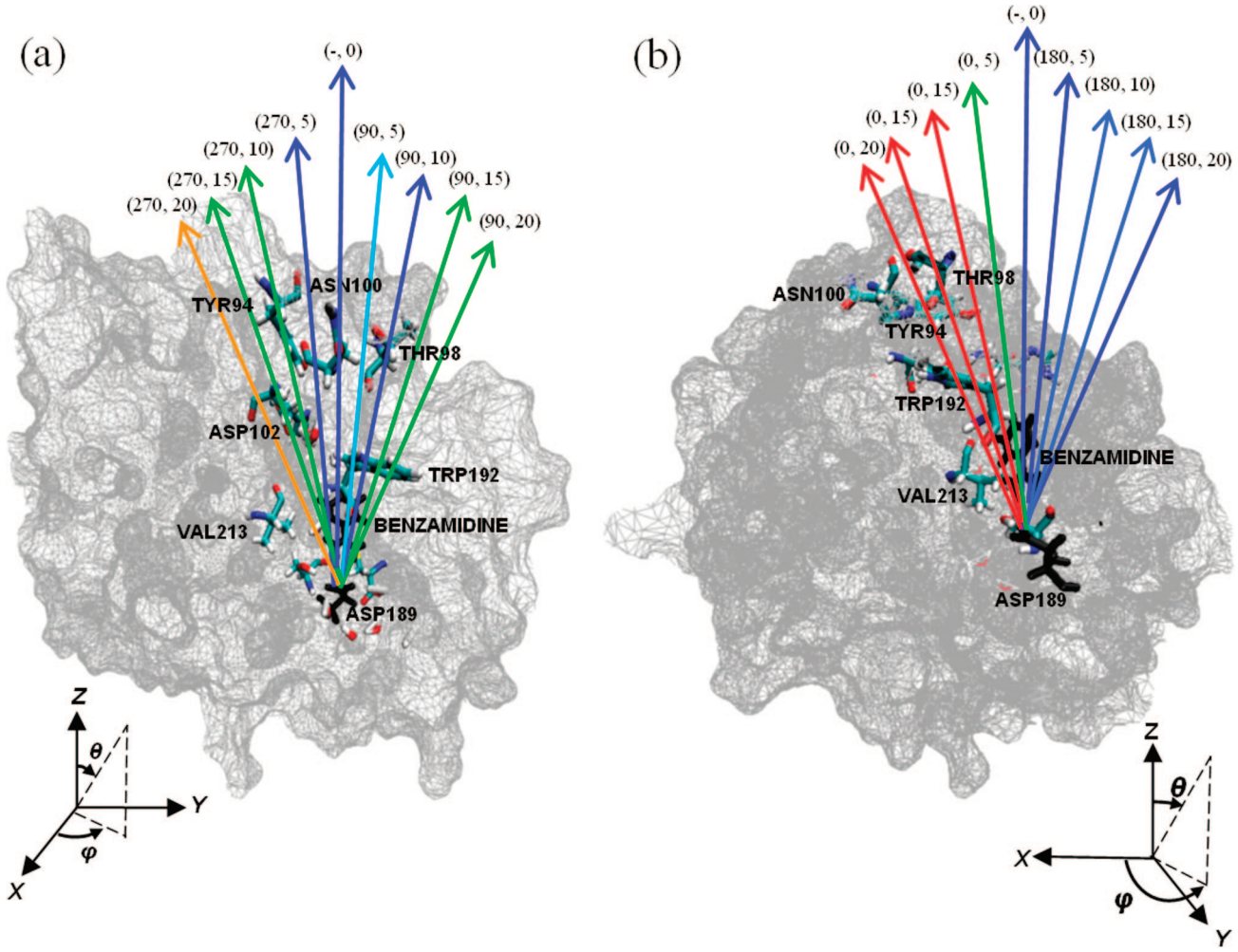

Figure 3. Seventeen paths considered for umbrella sampling that connect the binding site to the bulk in the (a) *yz* plane and (b) *xz* plane. Each path is labeled by its azimuthal and polar angles relative to the central path. Asp 189 and benzamidine are in black. Paths are colored according to their PMF depths, ΔW_R, with blue the deepest and red the shallowest.

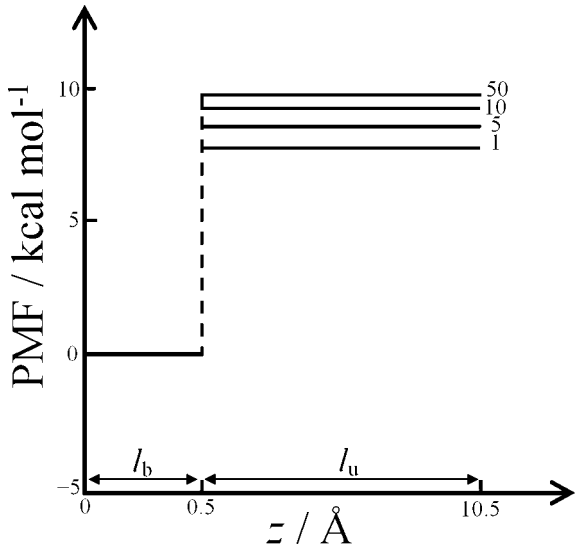

Figure 4. PMFs along the *z*-component reaction coordinate for the model binding system with orthogonal force constants of 1, 5, 10, and 50 kcal mol^{-1} Å^{-2}.

$A_{u,R}$, ΔW_R, ΔG_{PMF}, ΔG_V, ΔG_R, and $\Delta G°$ for different values of k_{xy}. The unbound area $A_{u,R}$ orthogonal to the reaction coordinate decreases with larger k_{xy}, and ΔW_R and ΔG_{PMF} become more favorable as would be expected since the ligand is binding from a smaller unbound volume. The unbound volumes $V_{u,R}$ range from 37 Å^3 for k_{xy} = 1 kcal mol^{-1} Å^{-2} to 0.74 Å^3 for k_{xy} = 50 kcal mol^{-1} Å^{-2}. Consequently, the free energy change ΔG_V for contracting from the standard-state volume to the unbound volume increases from 2.2 to 4.5 kcal mol^{-1}. The free energy change ΔG_R for turning off the restraints in the binding site decreases from 0.0 to −0.7 kcal mol^{-1} with larger k_{xy}. The same value is obtained for the standard free energy of binding $\Delta G° = -4.2$ kcal mol^{-1}, regardless of k_{xy}. This value is consistent with that predicted by eq 15 using $V_b = 0.092$ Å^3 as determined by an analogue of eq 9. It would also be independent of l_u because this cancels between ΔG_{PMF} and ΔG_V.

Standard Free Energy of Binding of Trypsin−Benzamidine. Figure 5a−e shows the PMFs obtained using a *z*-component reaction coordinate with orthogonal restraints of 0, 1, 5, 10, and 50 kcal mol^{-1} Å^{-2}, respectively, for different sampling times for the trypsin−benzamidine system. The central path was used for this run since it is one of the most favorable paths. If the other five most favorable paths are extended to 1-ns sampling per window, similar ΔW_R results are found, confirming the choice of the central path. A more detailed examination of the alternative paths is

Table 1. Standard Free Energy of Binding ΔG° and Its Components for Different Orthogonal Restraints k_{xy} for the Model System

k_{xy}/(kcal mol^{-1} Å^{-2})	l_b/(Å)	$A_{u,R}$/(Å^2)	ΔW_R/(kcal mol^{-1})	ΔG_{PMF}/(kcal mol^{-1})	ΔG_v/(kcal mol^{-1})	ΔG_R/(kcal mol^{-1})	ΔG°/(kcal mol^{-1})
0	0.5	$+\infty$	$+\infty$	$+\infty$	$-\infty$	0.0	
1	0.5	3.7	−8.2	−6.4	2.2	−0.0	−4.2
5	0.5	0.74	−9.0	−7.3	3.2	−0.1	−4.2
10	0.5	0.37	−9.3	−7.6	3.6	−0.2	−4.2
50	0.5	0.074	−9.8	−8.0	4.5	−0.7	−4.2

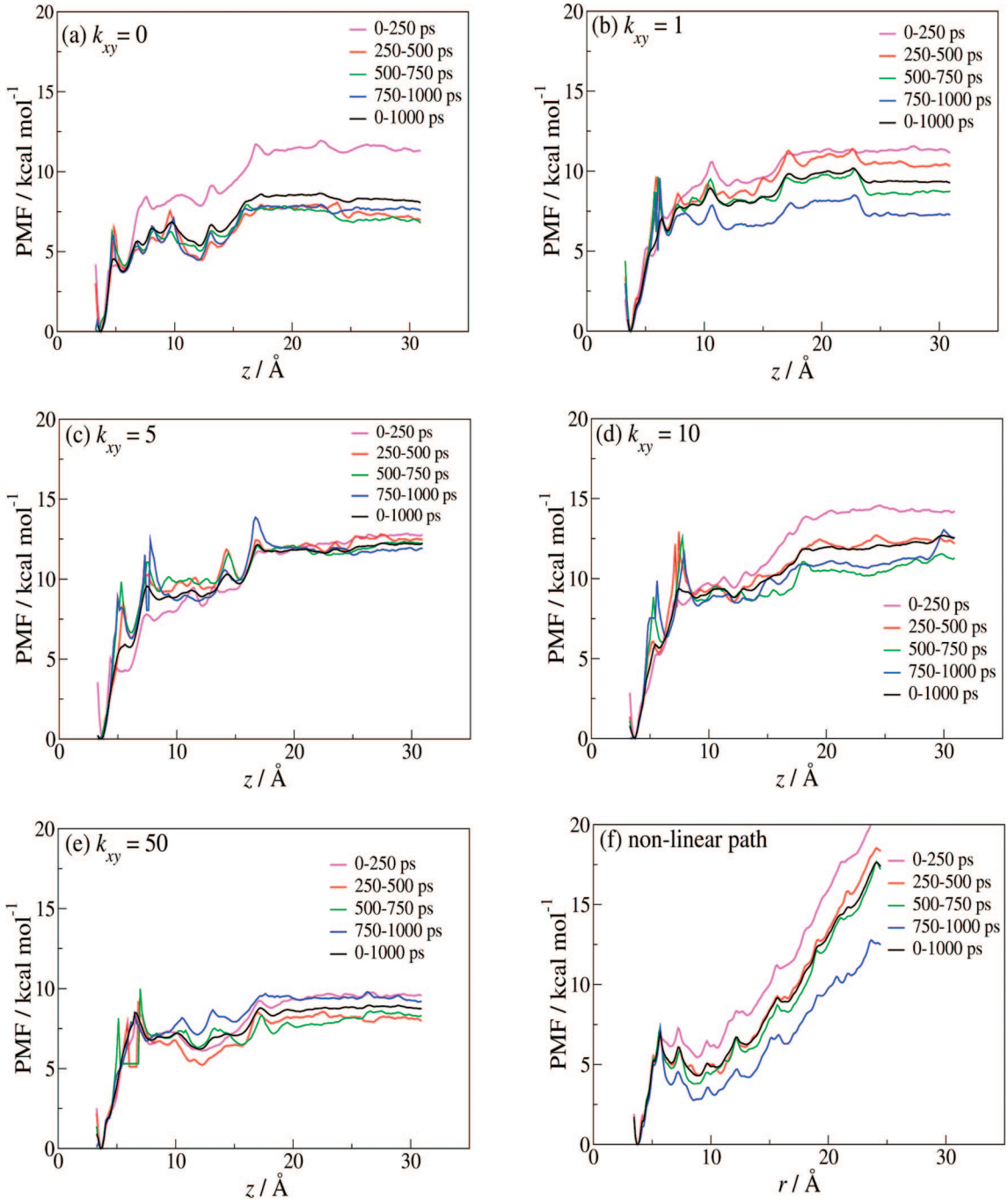

Figure 5. PMFs from umbrella sampling for trypsin−benzamidine using the *z*-component reaction coordinate with an orthogonal force constant k_{xy} (kcal mol^{-1} Å^{-2}) of (a) 0, (b) 1, (c) 5, (d) 10, and (e) 50. (f) PMF using the radial reaction coordinate and the nonlinear path, for which each window starts from the last frame of the preceding one. PMFs are shown averaged over 250-ps intervals (magenta, red, green, blue) and over the full 1 ns (black).

provided below. The PMFs with orthogonal restraints of 5 and 50 kcal mol^{-1} Å^{-2} are seen to converge slightly better than those at 0, 1, and 10 kcal mol^{-1} Å^{-2}. We might expect that the convergence would be worse for weaker restraints since the ligand has to sample a greater volume. In the limit of zero force constant, this volume would be infinite.

Table 2. Standard Free Energy of Binding $\Delta G°$ and Its Components for Different Orthogonal Restraints k_{xy} for the Trypsin−Benzamidine System

k_{xy}/(kcal mol^{-1} Å^{-2})	l_b/(Å)	$A_{u,R}$/(Å^2)	ΔW_R/(kcal mol^{-1})	ΔG_{PMF}/(kcal mol^{-1})	ΔG_V/(kcal mol^{-1})	ΔG_R/(kcal mol^{-1})	$\Delta G°$/(kcal mol^{-1})
0	0.54		−8.3 (1.0)	−6.4			
1	0.41	3.7	−9.6 (0.8)	−7.5	2.0	−1.2 (0.4)	−6.7 (0.9)
5	0.59	0.74	−11.9 (0.1)	−10.0	3.0	−2.0 (0.5)	−9.0 (0.5)
10	0.53	0.37	−11.9 (0.8)	−10.0	3.4	−2.3 (0.6)	−8.9 (1.0)
50	0.49	0.074	−8.7 (0.4)	−6.7	4.4	−3.2 (0.6)	−5.5 (0.7)

However, for the 1-ns trajectories run here, a significant difference is not observed.

Table 2 summarizes l_b, $A_{u,R}$, ΔW_R, ΔG_{PMF}, ΔG_V, ΔG_R, and $\Delta G°$ for different values of k_{xy}. The cutoff between the bound and unbound regions of the PMF is chosen to be 17 Å and the maximum value of the reaction coordinate is chosen to be 31 Å, so the length l_u in the unbound region equals 14 Å. The bound length l_b is similar for different orthogonal restraints. The unbound area $A_{u,R}$ is unchanged from the model system. ΔW_R and ΔG_{PMF} again become more favorable with larger k_{xy}, with the exception of a less favorable value of ΔW_R for $k_{xy} = 50$ kcal mol^{-1} Å^{-2}. ΔG_V increases from 2.0 to 4.4 kcal mol^{-1}, while ΔG_R decreases from −1.2 to −3.2 kcal mol^{-1} for the same range of k_{xy}. These values of ΔG_R are larger than those in the model system, presumably because the minimum of the orthogonal restraint in the trypsin−benzamidine system no longer matches up with the effective minimum of the binding site as it was assumed to do in the model system. The final standard free energies of binding $\Delta G°$ range from −5.5 to −9.0 kcal mol^{-1}, comparing reasonably well with the experimental value[54,55] of −6.3 kcal mol^{-1}. Our estimates of the standard errors of the mean free energy differences ΔW_R are given in parentheses in Table 2 and utilize the four 250-ps time frames (Figure 5) to estimate errors due to inadequate sampling. The errors on l_b are estimated in the same manner and are found to be negligible compared to ΔW_R; standard errors in ΔG_R are also taken over the 250-ps time periods. The final errors on $\Delta G°$ are found to lie between 0.5 and 1.0 kcal mol^{-1}. Other errors arising from the force field accuracy and possible incomplete sampling cannot be reliably estimated.

Other Linear and Nonlinear Paths. The PMF along the nonlinear radial path for trypsin−benzamidine is displayed in Figure 5f, averaged over different time slices of the simulations. There are two clear problems with this PMF: the first is that it is not converged and decreases with time; the second is that the PMF does not become constant at long range as would be expected once the ligand is fully solvated. This is because the ligand never actually leaves the protein surface over the entire 25 Å reaction coordinate. Although such paths are possibly more realistic in describing binding, such an approach was not pursued further due to the excessively long reaction coordinate, poor convergence, and difficulty in defining the unbound volume.

For the linear paths approach, the PMF values of all 17 paths are color-coded and displayed in Figure 6. In principle, all PMFs should produce the same ΔW_R; however, in practice, they do not due to convergence problems arising from the short simulation timescales and steric clashes between the ligand and protein. The PMFs of all paths are plotted in Figure 6 at 1 Å intervals with a common reference point in the bulk solvent. The lowest values of the PMFs are colored blue and the highest are colored red. The plot shows that paths with $\varphi = 180°$ all have favorable PMFs with large binding energies, and Figure 3b indicates that this

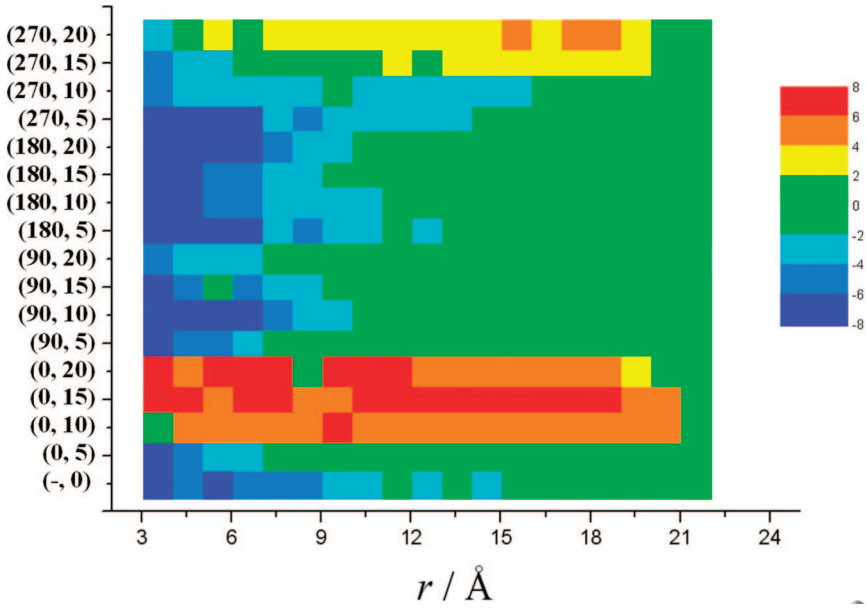

Figure 6. Color-coded PMFs along the distance reaction coordinate for each of the 17 linear paths in the (φ, θ) notation. The points with the blue color have the lowest value of $W(z)$ and those with red the highest.

is the open end of the protein where fewer residues occupy the path of the ligand. Other favorable paths include (−, 0°), (90°, 10°), (180°, 5°), and (270°, 5°). Most paths give conventional binding PMFs in that there is a minimum at the bound state and the PMF curve flattens off in the unbound region. However, for paths having $\varphi = 0°$ and $\theta = 10°$, 15°, or 20°, a tryptophan residue (Trp 192 in Figure 3) blocks the way of the ligand. This forces it away from these paths, resulting in unreasonable PMFs for the short timescale of simulation used.

Discussion

In this work, we show how to obtain the standard free energy of binding $\Delta G°$ from a one-dimensional PMF and apply it to a model binding system and the trypsin−benzamidine system. The PMF along the *z*-component of the reaction coordinate is calculated by applying restraints to the ligand orthogonal to the reaction coordinate. We calculate the ratio of the partition functions of the bound and unbound states from the PMF. The sampled unbound volume is computed from the volume spanned within the orthogonal restraint along the unbound section of the PMF. $\Delta G°$ is obtained from the free energy of contraction from the standard volume to the unbound volume, then to the bound state with restraints, and then to the bound state. Our approach gives reasonable results in comparison with experiment for the trypsin−benzamidine system,[54,55] and the results are reasonably independent of the size of the orthogonal restraint. The main exception appears to be for $k_{xy} = 50$ kcal mol^{-1} Å^{-2} for which a less favorable value of $\Delta G°$ is obtained. This may arise because the larger force constant is constraining the ligand too tightly to a linear path, bringing it too close to the protein, and leading to a nonconverged PMF.

It is clear that $\Delta G°$ is not ΔW_R as is often assumed.[31−34] Nor is it always obtained by augmenting ΔW_R with the change in free energy from the standard volume to the bound volume. Because the one-dimensional PMF includes averaging over the ligand's orthogonal coordinates *x* and *y*, one must know the *xy* area sampled in the unbound region to work out the volume sampled in the unbound region and therefore determine the free energy for scaling to it from the standard volume. Equation 14 for $\Delta G°$ becomes equivalent to that of Lee and Olson[12,18] when $A_{u,R} = A_{b,R}$. This equality will hold in the limit of an infinitely large orthogonal force constant, when confinement by the protein would be negligible, or when sampling is very short. Usually $A_{u,R}$ would exceed $A_{b,R}$ because the binding site also confines the ligand, and so omitting this term would overestimate $\Delta G°$ and make it less favorable. Short sampling may not allow the ligand to adequately explore the larger $A_{u,R}$. It is curious to note that the $\Delta G°$ values obtained do not differ substantially from ΔW_R obtained without an orthogonal restraint or any consideration of the standard-state concentration. This is purely coincidental. If a different standard-state concentration were used, $\Delta G°$ would change but ΔW_R would not. Use of a three-dimensional PMF and eq 15 to get $\Delta G°$ would avoid the need to define an orthogonal restraint. However, this suffers from the disadvantage in the case of umbrella sampling that many more umbrella potentials would be required to span the three-dimensional space. Similar issues apply to the rotational entropy. If an angular restraint were to be applied to sample smaller angular volumes, the free energy change from $8\pi^2$ in solution to the unbound angular volume would be required. The change in rotational entropy here is assumed to be included in ΔW_R.

Comparing the approach of Woo and Roux,[21] their derivation includes the calculation of a surface area integral at the unbound state and a PMF integral over the bound region. They apply translational, rotational, and conformational restraints on the large ligand used in that study. Their partition function ratio is made up of four terms: S^*, a surface area integral over what is effectively a patch of a sphere of arbitrary radius 40 Å, and I^*, the integral of the PMF over the bound region up to this radius, and free energy terms for turning on and off the restraints. S^* corresponds to our $A_{u,R}$ and I^* to our $l_b \exp(-\Delta W_R/RT)$. Our method is a simpler formulation expressed in terms that have a clear physical interpretation. The use of a *z*-component versus a radial reaction coordinate leads to a number of advantages: there is a simple expression for the unbound area $A_{u,R}$ independent of the cutoff; there is no need for a Jacobian, which results in a flat PMF in the unbound region; the area to be sampled is roughly constant at each value of the reaction coordinate; and ΔW_R is exponentially averaged over the entire unbound region, reducing its statistical error. The interdependence of I^* and S^* on the cutoff and the dependence of the PMF on the radial Jacobian make it difficult to consider more than one radial point in the unbound region. Combining these attributes of the method gives a simple relationship between $\Delta G°$ and ΔW_R (eq 11 or 14).

The trypsin−benzamidine system has been previously studied using umbrella sampling and grand canonical simulations by Resat et al.[45] They obtained a rather different PMF with a depth of −25 kcal mol^{-1} and a pronounced barrier of 10 kcal mol^{-1} at a reaction coordinate distance of ∼5 Å. The larger PMF depth could be due to less equilibration and a rigid protein. Gervasio et al.[33] studied the same system with metadynamics using a two-dimensional reaction coordinate made up of a distance and a ligand orientation. They found good agreement with experiment although it should be noted that they do not include the standard-state dependence in their comparison.

We also examined multiple unbinding pathways of benzamidine from trypsin. One protocol that involves no assumption of the unbinding pathway uses a nonlinear radial trajectory, similar to the approach of Hajjar et al.[56] Having a nonlinear umbrella-sampling trajectory would give more realistic information on the binding mechanism; however, this approach has a number of shortcomings: it results in deep, unconverged PMFs and would require a long reaction coordinate to the bulk since the ligand remains bound to the protein surface even at large distances. Serial simulations are also required since each window is started from the preceding one. Despite all the disadvantages of this protocol, it may more accurately represent the binding mechanism whereby the ligand may first bind to the protein somewhere on the surface at a distance from the binding site rather then directly into the binding site from solution. Calculating the

PMF of the ligand along linear pathways avoids the problem in the nonlinear protocol because the ligand reaches the bulk solvent along a much shorter reaction coordinate and each window, being independent of the previous one, can be run in parallel. Multiple trajectories were also used by Karplus and van der Vaart[57] but to obtain a PMF in targeted MD calculations. Hajjar et al.[56] use multiple trajectory umbrella sampling in addition to nonlinear paths. The linear paths method allows us to identify the most favorable binding paths that the ligand can follow. It also generates an approximate free energy landscape of the ligand near the protein's binding site. This landscape tells us the expected result that PMF is governed by sterics so that the lowest and most converged PMFs span regions that are least occupied by the protein. One path is then chosen to estimate the standard free energy of binding using the z-component reaction coordinate and orthogonal restraints as discussed earlier. Although the PMFs may appear barrierless, they represent an average over many configurations and do not necessarily imply that individual binding or unbinding trajectories have no barriers.

Conclusions

We introduce an approach to calculate the standard free energy of binding $\Delta G°$ from a one-dimensional potential of mean force. The PMF is calculated using a z-component reaction coordinate with orthogonal restraints. The ratio of the bound and unbound partition functions is calculated from the PMF, and the standard-state concentration is accounted for by determining the unbound volume sampled by the ligand through application of restraining potentials. The final expression for $\Delta G°$ depends on the bound length along the reaction coordinate, the unbound area orthogonal to the reaction coordinate, the standard volume, the orthogonal restraining potential, and the PMF depth ΔW_R. We demonstrate how to get $\Delta G°$ from the PMF for a model binding system and go on to apply it to the PMF of benzamidine binding to trypsin to predict $\Delta G°$ to range from -5.5 to -9.0 kcal mol^{-1}, in good agreement with experiment at -6.3 kcal mol^{-1}. We emphasize how the formulation is simpler when using a z-component reaction coordinate rather than a radial one and make clear how the formulation depends on the dimensionality of the PMF.

Acknowledgment. S.D. thanks the School of Chemistry at the University of Manchester, the Algerian government for funding, and also Dr. Richard Dimelow for providing the WHAM code to generate the PMFs from the umbrella sampling simulations. R.H.H. is funded by EPSRC Grant EP/E026222/1.

References

(1) Brandsdal, B. O.; Österberg, F.; Almlöf, M.; Feierberg, I.; Luzhkov, V. B.; Åqvist, J. *Adv. Protein Chem.* **2003**, *66*, 123–158.

(2) Chipot, C.; Pohorille, A. *Free Energy Calculations: Theory and Applications in Chemistry and Biology*; Springer: Berlin, 2007.

(3) Gilson, M. K.; Zhou, H.-X. *Annu. Rev. Biophys. Biomol. Struct.* **2007**, *36*, 21–42.

(4) Gohlke, H.; Klebe, G. *Angew. Chem., Int. Ed.* **2002**, *41*, 2644–2676.

(5) Meirovitch, H. *Curr. Opin. Struct. Biol.* **2007**, *17*, 181–186.

(6) Raha, K.; Merz, J. K. M.; David, C. S. *Annual Reports in Computational Chemistry*; Elsevier: Amsterdam, 2005; pp 113−130.

(7) Rodinger, T.; Pomès, R. *Curr. Opin. Struct. Biol.* **2005**, *15*, 164–170.

(8) Shirts, M. R.; Mobley, D. L.; Chodera, J. D. *Annual Reports in Computational Chemistry*; Elsevier: Amsterdam, 2007; pp 41−59.

(9) Wong, C. F.; McCammon, J. A. *Adv. Protein Chem.* **2003**, *66*, 87–121.

(10) Gilson, M. K.; Given, J. A.; Bush, B. L.; McCammon, J. A. *Biophys. J.* **1997**, *72*, 1047–1069.

(11) Swanson, J. M. J.; Henchman, R. H.; McCammon, J. A. *Biophys. J.* **2004**, *86*, 67–74.

(12) Lee, M. S.; Olson, M. A. *Biophys. J.* **2006**, *90*, 864–877.

(13) Åqvist, J.; Medina, C.; Samuelsson, J.-E. *Protein Eng.* **1994**, *7*, 385–391.

(14) Jorgensen, W. L.; Buckner, J. K.; Boudon, S.; Tirado-Rives, J. *J. Chem. Phys.* **1988**, *89*, 3742–3746.

(15) Wang, J.; Deng, Y.; Roux, B. *Biophys. J.* **2006**, *91*, 2798–2814.

(16) Bui, J. M.; Henchman, R. H.; McCammon, J. A. *Biophys. J.* **2003**, *85*, 2267–2272.

(17) Dang, L. X.; Kollman, P. A. *J. Am. Chem. Soc.* **1990**, *112*, 503–507.

(18) Lee, M. S.; Olson, M. A. *J. Phys. Chem. B* **2008**, *112*, 13411–13417.

(19) Palma, R.; Himmel, M. E.; Brady, J. W. *J. Phys. Chem. B* **2000**, *104*, 7228–7234.

(20) Tsunekawa, N.; Miyagawa, H.; Kitamura, K.; Hiwatari, Y. *J. Chem. Phys.* **2002**, *116*, 6725–6730.

(21) Woo, H. J.; Roux, B. *Proc. Natl. Acad. Sci. U.S.A.* **2005**, *102*, 6825–6830.

(22) Bolhuis, P. G.; Dellago, C.; Chandler, D. *Faraday Discuss.* **1998**, *110*, 421–436.

(23) Torrie, G. M.; Valleau, J. P. *Chem. Phys. Lett.* **1974**, *28*, 578–581.

(24) Darve, E.; Pohorille, A. *J. Chem. Phys.* **2001**, *115*, 9169–9183.

(25) Jarzynski, C. *Phys. Rev. Lett.* **1997**, *78*, 2690–2693.

(26) Laio, A.; Parrinello, M. *Proc. Natl. Acad. Sci. U.S.A.* **2002**, *99*, 12562–12566.

(27) Boresch, S.; Tettinger, F.; Leitgeb, M.; Karplus, M. *J. Phys. Chem. B* **2003**, *107*, 9535–9551.

(28) Deng, Y.; Roux, B. *J. Chem. Theory Comput.* **2006**, *2*, 1255–1273.

(29) Hermans, J.; Wang, L. *J. Am. Chem. Soc.* **1997**, *119*, 2707–2714.

(30) Pranata, J.; Jorgensen, W. L. *Tetrahedron* **1991**, *47*, 2491–2501.

(31) Baştuğ, T.; Chen, P.-C.; Patra, S. M.; Kuyucak, S. *J. Chem. Phys.* **2008**, *128*, 155104.

(32) Charlier, L.; Nespoulous, C.; Fiorucci, S.; Antonczak, S.; Golebiowski, J. *Phys. Chem. Chem. Phys.* **2007**, *9*, 5761–5771.

(33) Gervasio, F. L.; Laio, A.; Parrinello, M. *J. Am. Chem. Soc.* **2005**, *127*, 2600–2607.

(34) Ghoufi, A.; Malfreyt, P. *J. Chem. Phys.* **2006**, *125*, 224503.

(35) Justice, M. C.; Justice, J. C. *J. Solution Chem.* **1976**, *5*, 543–561.

(36) Prue, J. E. *J. Chem. Educ.* **1969**, *46*, 12–16.

(37) Shoup, D.; Szabo, A. *Biophys. J.* **1982**, *40*, 33–39.

(38) Khavrutskii, I. V.; Dzubiella, J.; McCammon, J. A. *J. Chem. Phys.* **2008**, *128*, 044106.

(39) Trzesniak, D.; Kunz, A. P. E.; van Gunsteren, W. F. *Chem. Phys. Chem.* **2007**, *8*, 162–169.

(40) Dang, L. X.; Pettitt, B. M. *J. Am. Chem. Soc.* **1987**, *109*, 5531–5532.

(41) Setny, P. *J. Chem. Phys.* **2008**, *128*, 125105.

(42) Mihailescu, M.; Gilson, M. K. *Biophys. J.* **2004**, *87*, 23–36.

(43) Essex, J. W.; Severance, D. L.; TiradoRives, J.; Jorgensen, W. L. *J. Phys. Chem. B* **1997**, *101*, 9663–9669.

(44) Jiao, D.; Golubkov, P. A.; Darden, T. A.; Ren, P. *Proc. Natl. Acad. Sci. U.S.A.* **2008**, *105*, 6290–6295.

(45) Resat, H.; Marrone, T. J.; McCammon, J. A. *Biophys. J.* **1997**, *72*, 522–532.

(46) Schwarzl, S. M.; Tschopp, T. B.; Smith, J. C.; Fischer, S. *J. Comput. Chem.* **2002**, *23*, 1143–1149.

(47) Wang, J.; Cieplak, P.; Kollman, P. A. *J. Comput. Chem.* **2000**, *21*, 1049–1074.

(48) Jorgensen, W. L.; Chandrasekhar, J.; Madura, J. D.; Impey, R. W.; Klein, M. L. *J. Chem. Phys.* **1983**, *79*, 926–935.

(49) Case, D. A.; Darden, T. A.; Cheatham, T. E., III; Simmerling, C. L.; Wang, J.; Duke, R. E.; Luo, R.; Merz, K. M.; Pearlman, D. A.; Crowley, M.; Walker, R. C.; Zhang, W.; Wang, B.; Hayik, S.; Roitberg, A.; Seabra, G.; Wong, K. F.; Paesani, F.; Wu, X.; Brozell, S.; Tsui, V.; Gohlke, H.; Yang, L.; Tan, C.; Mongan, J.; Hornak, V.; Cui, G.; Beroza, P.; Mathews, D. H.; Schafmeister, C.; Ross, W. S.; Kollman, P. A. AMBER9; University of California, San Francisco: San Francisco, CA, 2006.

(50) Wang, J.; Wolf, R. M.; Caldwell, J. W.; Kollman, P. A.; Case, D. A. *J. Comput. Chem.* **2004**, *25*, 1157–1174.

(51) Bayly, C. I.; Cieplak, P.; Cornell, W. D.; Kollman, P. A. *J. Phys. Chem.* **1993**, *97*, 10269–10280.

(52) Dimelow, R. J.; Bryce, R. A.; Masters, A. J.; Hillier, I. H.; Burton, N. A. *J. Chem. Phys.* **2006**, *124*, 114113.

(53) Kumar, S.; Rosenberg, J. M.; Bouzida, D.; Swendsen, R. H.; Kollman, P. A. *J. Comput. Chem.* **1992**, *13*, 1011–1021.

(54) Mares-Guia, M. *Arch. Biochem. Biophys.* **1968**, *127*, 317–322.

(55) Talhout, R.; Engberts, J. B. F. N. *Eur. J. Biochem.* **2001**, *268*, 1554–1560.

(56) Hajjar, E.; Perahia, D.; Debat, H.; Nespoulous, C.; Robert, C. H. *J. Biol. Chem.* **2006**, *281*, 29929–29937.

(57) van der Vaart, A.; Karplus, M. *J. Chem. Phys.* **2007**, *126*, 164106.

CT8002354

JCTC Journal of Chemical Theory and Computation

Computations of Absolute Solvation Free Energies of Small Molecules Using Explicit and Implicit Solvent Model

Devleena Shivakumar,[†,§] Yuqing Deng,[†,‡,||] and Benoît Roux*[,†,‡]

Department of Biochemistry & Molecular Biology, University of Chicago, 929 East 57th Street, Chicago, Illinois 60637, and Biosciences Division, Argonne National Laboratory, 9700 South Cass Avenue, Argonne, Illinois 60439

Received October 20, 2008

Abstract: Accurate determination of absolute solvation free energy plays a critical role in numerous areas of biomolecular modeling and drug discovery. A quantitative representation of ligand and receptor desolvation, in particular, is an essential component of current docking and scoring methods. Furthermore, the partitioning of a drug between aqueous and nonpolar solvents is one of the important factors considered in pharmacokinetics. In this study, the absolute hydration free energy for a set of 239 neutral ligands spanning diverse chemical functional groups commonly found in drugs and drug-like candidates is calculated using the molecular dynamics free energy perturbation method (FEP/MD) with explicit water molecules, and compared to experimental data as well as its counterparts obtained using implicit solvent models. The hydration free energies are calculated from explicit solvent simulations using a staged FEP procedure permitting a separation of the total free energy into polar and nonpolar contributions. The nonpolar component is further decomposed into attractive (dispersive) and repulsive (cavity) components using the Weeks−Chandler−Anderson (WCA) separation scheme. To increase the computational efficiency, all of the FEP/MD simulations are generated using a mixed explicit/implicit solvent scheme with a relatively small number of explicit TIP3P water molecules, in which the influence of the remaining bulk is incorporated via the spherical solvent boundary potential (SSBP). The performances of two fixed-charge force fields designed for small organic molecules, the General Amber force field (GAFF), and the all-atom CHARMm-MSI, are compared. Because of the crucial role of electrostatics in solvation free energy, the results from various commonly used charge generation models based on the semiempirical (AM1-BCC) and QM calculations [charge fitting using ChelpG and RESP] are compared. In addition, the solvation free energies of the test set are also calculated using Poisson−Boltzmann (PB) and Generalized Born model of solvation (GB), which are two widely used continuum electrostatic implicit solvent models. The protocol for running the absolute solvation free energy calculations used throughout is automated as much as possible, with minimum user intervention, so that it can be used in large-scale analysis and force field optimization.

1. Introduction

An accurate determination of solvation free energy of a molecule plays a critical role in numerous areas of biomedical, chemical, and industrial research, and its evaluation is a long-standing and constantly evolving challenge in computational chemistry.[1,2] For example, estimating the desolvation

* Corresponding author phone: (773) 834-3557; fax: (773) 702-0439; e-mail: roux@uchicago.edu.

† University of Chicago.

‡ Argonne National Laboratory.

§ Current address: Schrodinger, Inc., 120 West 45th Street, 29th Floor, New York, NY 10036-4041.

|| Current address: Zymeworks Inc., 540-1385 West Eighth Ave., Vancouver, BC V6H 3V9, Canada.

10.1021/ct800445x CCC: $40.75
Published on Web 03/24/2009

penalty for a ligand and its receptor upon formation of a bound complex is an important component in drug design.[2] Another example is in the area of pharmacokinetics, where partitioning between various solvents (the so-called "log *P*") and acid−base equilibrium is useful in determining absorption properties.[3–5] Solvation free energies are highly sensitive to the details of the molecular mechanical force field parameters used to describe the solvent and the solute molecules, such as atomic partial charges, Lennard-Jones radii, and the well depth. The calculation of the absolute solvation free energy is, thus, a critical test of the accuracy of a force field, and the underlying method to represent the interaction between the solute and the solvent. Because absolute solvation free energies have been experimentally determined for several small molecules, it provides a direct comparison between the experimental and calculated values.

Despite its importance, the calculation of "absolute" solvation free energies presents a challenge to computational chemists. Both the dynamic and the thermodynamic properties of a molecular solute are strongly influenced by the microscopic structure and organization of the solvent molecules in its surrounding. The current methods to treat solvation generally follow one of two approaches. The first one involves the explicit simulation of a large number of solvent molecules with periodic boundary conditions.[6] Alternatively, the effect of solvation can be incorporated implicitly, via continuum approximations.[7] While molecular dynamics free energy perturbation (FEP/MD) with explicit solvent molecules provides the most realistic, and arguably most accurate, treatment of solvation,[8] the approach is often limited in practice by the computational cost.[9] On the other hand, there is a vast range of available implicit solvent methods differing widely in sophistication, computational cost, and accuracy.[7] The family of methods constructed on the basis of continuum electrostatic solvation models are particularly appealing because of their ability to accurately reproduce solvation in polar liquids while remaining computationally inexpensive.[10–13]

Several groups have shown that the Poisson−Boltzmann (PB) models[14,15] are capable of reproducing polar explicit solvent forces between solute and solvent.[16,17] The performance of continuum electrostatic models is highly dependent on the input parameters, such as the effective atomic Born radii.[11,18–21] A good agreement with PB has been observed for the electrostatic or polar component of the solvation energy using an optimized set of radii.[18,21,22] In implicit solvation models based on continuum electrostatics, the free energy to insert the uncharged solute into the solvent, the so-called nonpolar contribution, must be treated separately. Such free energy contribution to solvation has been traditionally approximated from models based on the solvent-accessible surface area (SASA).[22–25] However, more sophisticated statistical mechanical treatments have shown that the cavity creation term is dependent on both the SASA and the solvent-accessible volume term, with a crossover at large solute sizes (>10 Å).[26,27] Furthermore, decomposition of the nonpolar solvation free energy in simulation with explicit water molecules indicates that the effects from the repulsive and the dispersive van der Waals interactions are both considerable and of opposite sign.[28] In fact, not accounting for the attractive van der Waals interactions between solvent and solute atoms in the SASA-based model introduces important inaccuracies,[29–32] and efforts have been made to design reasonably accurate and computationally tractable approximations to the nonpolar free energy contribution. Along those lines, Tan et al. have recently developed an implicit solvent model methodology treating explicitly the nonpolar solvation energy corresponding to the cavity creation and the attractive dispersion.[33] This implicit solvation model was implemented in the Amber simulation program (Amber9 and newer versions).

In the present study, we compute the absolute hydration free energy using FEP/MD with explicit water molecules for a set of 239 small molecules that are representative of the chemical functionalities found in drug design. The set includes saturated hydrocarbons, unsaturated hydrocarbons, strained systems, conjugated and aromatic systems, all major polar functional groups, as well as heterocyclic systems. The FEP/MD simulations with explicit solvent molecules are based on the TIP3P water model.[34] To increase the computational efficiency, the FEP/MD simulations are generated using the Spherical Solvent Boundary Potential (SSBP) approach,[35] which consists of keeping a small number of explicit solvent molecules in the vicinity of the solute, and representing the remaining bulk implicitly via an effective solvent boundary potential. Two widely used fixed charge general force fields are considered to model the small molecules. The first is the generalized Amber force field (GAFF)[36] established recently, and the second is the CHARMm-MSI force field,[37] which was developed almost a decade earlier. Both are biomolecular force fields constructed from simple analytical functions. Because they share a similar functional form, a comparison of the calculated absolute solvation free energy using these two force fields is meaningful and of general interest.

For the same test set of small molecules and force field parameters, we compare the FEP/MD results to the free energies obtained from two commonly used implicit solvent models, PB/SA and GB/SA.[38] For the purpose of this comparison, the total solvation free energy is separated into polar (electrostatics) and nonpolar contributions to provide more insight, following a step-by-step reversible work to materialize the solute in solution.[7,39] The nonpolar component obtained in FEP/MD is further decomposed into purely repulsive and dispersive terms using the separation scheme for the Lennard-Jones 6-12 pair potential introduced in the WCA theory[40] and implemented in an earlier study of side chain analogues.[28] Correspondingly, the nonpolar component obtained with the implicit solvation models is separated into a repulsive and an attractive component using an optimized continuum decomposition.[33] Although such a decomposition scheme of the solvation free energy is path dependent by definition,[41] the analysis based on a specific step-by-step reversible work provides a useful framework for dissecting the free energy because each individual contribution can be associated with a microscopic process with a clear and well-defined physical meaning.[7] Here, the decomposition of the solvation free energy allows a comparison of the various

Table 1. Table Showing the Chemical Functional Group and Number of Small Molecules from Each Class Used in the Present Study

type	number	type	number
alkanes	8	esters	15
alkenes	10	ethers	11
alkynes	5	halogen, bromo	10
alcohols	17	halogen, chloroalkanes	11
aldehydes	6	halogen, chloroalkenes	5
aliphatic amines	16	halogen, chloroarenes	3
amides	5	halogen, flouro	6
arenes	14	halogen, iodo	8
aromatic amines	14	bifunamine	3
ketones	12	multiple halogens	15
bifunctional	5	nitriles	5
branched alkanes	7	cycloalkanes	5
carboxylic	5	sulfides	5
nitro	7		
disulfides	2		
total	239		

contributions terms from explicit as well as implicit solvent methods. Furthermore, decomposition of nonpolar solvation energy into repulsive and attractive contributions is advantageous to better understand the factors governing hydrophobic solvation and protein stability. In particular, it is shown that the nonpolar component of the free energy correlates strongly with log *P* and SASA values. All of the computational methodologies and force field parameters are described in the next section.

2. Method and Force Fields

a. Test Set. The absolute free energy of solvation for 239 neutral molecules (Table 1) was computed using three separate methods: molecular dynamics free energy perturbation (FEP/MD) simulation in explicit TIP3P solvent molecules,[34] finite-difference Poisson−Boltzmann (PB) continuum electrostatic,[10] and Generalized Born plus a surface area term (GB/SA).[11] This set of methods enables us to evaluate the accuracy of the commonly used point-charge models and force fields used in molecular modeling of small molecules. The test set consisting of 239 molecules was curated from earlier work in the literature.[42,43] The initial structures were obtained from the NIST Chemistry WebBook database. The molecules chosen for this comparative study have diverse chemical functional groups commonly encountered in drug design. These include saturated hydrocarbons, unsaturated hydrocarbons, conjugated and aromatic systems, all major polar functional groups, as well as heterocyclic and ionic systems. The diverse chemical functionalities include, alkanes, alkenes, alkynes, branched alkanes, alcohols, aldehydes, ketones, esters, carboxylic acid, cycloalkanes, arenas, aliphatic amines, aromatic amines, amides, bifunctional amines, ammonia, nitriles, nitro, thiols, sulfides, disulphides, ethers, fluoro, chloroalkanes, chloroalkenes, chloroarenes, bromo, iodo, multiple halogens, and bifunctional groups. A table summarizing the list of compounds under each category and their experimental solvation energy is shown in Supporting Information Table T1.

b. The Force Fields. The GAFF (Generalized Amber Force Field)[36] and the CHARMm-MSI force field[37] considered for the current study share a similar functional form:

$$V = \sum_{\text{bonds}} k_b(b - b_0)^2 + \sum_{\text{angles}} k_\theta(\theta - \theta_0)^2 + \sum_{\text{dihedrals}} k_\varphi(1 + \cos(n\varphi - \delta)) + \sum_{\text{nonbonded}} \varepsilon_{ij}\left[\left(\frac{R_{\min,ij}}{r_{ij}}\right)^{12} - \left(\frac{R_{\min,ij}}{r_{ij}}\right)^{6}\right] + \frac{q_i q_j}{\varepsilon r_{ij}} \quad (1)$$

Here, the first term accounts for the bond stretching energy when the atom moved $(b - b_0)$ from equilibrium. The second term in the potential energy function accounts for bond angle bending from equilibrium $(\theta - \theta_0)$. The third term corresponds to the twisting in the dihedral or the torsional angle with multiplicity n, and phase shift δ. The force constants for bond length, bond angle, and torsional angle are k_b, k_θ, and k_ϕ, respectively. The last term represents the standard 12-6 Lennard-Jones potential used to calculate the nonbonded interactions between pairs of atoms (i, j), where ε and $R_{\min}$ represent the well depth and radius parameters of the potential, respectively.

The ligand structures were read into the Antechamber program to generate the individual parameter and topology files based on the general Amber force field (GAFF). In addition, *tleap* program (Amber9 version) was used to generate topology and parameter file in Amber format for the implicit solvent simulations. The CHARMM format of the GAFF parameter file was used to generate the input topology and parameter file for small molecules compatible with the CHARMM program format. These files were used in all of the explicit solvent simulations using the CHARMM program. The GAFF potential function consists of 35 basic and 22 special atom types based on element type, hybridization, aromaticity, and chemical environment. The combination of basic and special atom types covers almost all of the organic chemical space that is made up of C, N, O, S, P, H, F, Cl, Br, and I atoms, making it a complete force field to study pharmaceutical ligand phase space. The van der Waals parameters of GAFF are the same as those used by the traditional Amber force field.[36] Also, GAFF uses a simple additive harmonic energy function consisting of bond, angle, dihedral, and Lennard-Jones 12-6 potential term as the traditional CHARMM and Amber force fields as described above, making it compatible in a broader perspective with these force fields. Both GAFF and CHARMm-MSI are complete force fields in the sense that they aim at covering most small organic molecules. GAFF can be assigned to a wide range of molecules in automatic fashion using the Antechamber package,[44] while the CHARMm-MSI force field can be automatically assigned to small molecules using the InsightII program (Accelrys). This makes both force fields practical to be applied to a large number of ligands in a database screening in docking studies.

The CHARMm-MSI force field parameters were assigned to the 239 small molecules in our test set using the InsightII program by specifying the force field file, CHARMM.cfrc (Insight II Version 2000 − Molecular Modeling System).

Perl scripts were used to automate the input file generation step with the InsightII program.

c. Charge Methods. The charge method plays a crucial role in any molecular mechanics calculations. While the set of atomic partial charges is closely associated with the rest of the force field, combining the nonelectrostatic part of a force field with sets of atomic partial charges derived from a variety of approaches is quite common when considering large databases of ligands. For the sake of clarity, we will be implicitly referring only to the nonelectrostatic part of the GAFF and CHARMm-MSI potential function when invoking those names hereon. Because the charges have a very large impact on the resulting solvation energies,[28,45,46] it is often worthwhile considering different strategies to generate them. In Amber's ff99 and ff94, the charges are derived by using the HF/6-31G* method. The idea behind using this as a preferred method is that it exaggerates the dipole moment of most of the residues by 10−20%, which in turn mimics the polarization in the condensed phase simulations. The CHARMM22 charges were obtained by fitting of solute−water dimer energies from SCF/6-31G*. In the present study, we compare three different charge models: two methods based on fitting partial charges to the electrostatic potential, ChelpG[47] and restrained electrostatic potential fit (RESP),[48] and a third method based on semiempirical AM1-BCC model.[49,50] The AM1-BCC method is a computationally inexpensive method used to generate high-quality atomic charges for condensed phase simulations. The AM1 atomic charges are "population" quantities based on occupation of the molecular orbital and do not reproduce the electrostatic potential (ESP) of a molecule. The simple additive bond charge corrections (BCC) are added to these AM1 atomic charges to generate the AM1-BCC charges, which better reproduce the ESP. The parametrizations of the BCC were carried out by Bayley and co-workers by fitting to the HF/6-31G* ESP of a training set of >2700 molecules.[50] Henceforth, the models considered will be GAFF/AM1-BCC, GAFF/ChelpG, GAFF/RESP, CHARMm-MSI/AM1-BCC, CHARMm-MSI/ChelpG, and CHARMm-MSI/RESP. The performance of three commonly used charge methods was compared in this work. They are ab initio methods such as RESP and ChelpG and a semiempirical method, AM1-BCC. For each molecule, these three methods are used to derive a set of atom-centered point charges.

AM1-BCC charges for our test set containing 239 molecules were obtained using the Antechamber package (ver 2.7). The Antechamber and mopac programs were used to calculate the AM1-Mulliken population charges for each small molecule. The am1bcc program was used to assign atom types and bond types according to AM1-BCC definitions, and then assign the BCC values for the atoms.

ChelpG (charges from electrostatic potentials using a grid) charges were obtained using the Gaussian program.[51] In this method, the atomic charges were fitted to reproduce the molecular electrostatic potential (MEP) at a number of grid points around the molecule. After the MEP was evaluated at all valid grid points, atomic charges were derived that reproduce the MEP in the most optimum way. The only additional constraint in the fitting procedure was that the sum of all atomic charges equals that of the overall charge of the system.

RESP (restrained electrostatic potential fit) charges are based on a restrained least-squares fitting algorithm to best reproduce the quantum mechanical electrostatic potential of a molecule. The potential was evaluated at a large number of points defined by four shells of surfaces at 1.4, 1.6, 1.8, and 2.0 times the VDW radii. These distances have been shown to be appropriate for deriving charges that reproduce typical intermolecular interactions (energies and distances). Also, during the RESP charge fitting, the equivalent atoms were made to bear the same charges because equivalent atoms are indistinguishable during the molecular dynamical simulations. The value of the electrostatic potential at each grid point was calculated from the quantum mechanical wave function using the Gaussian 03 program.[51] The charges derived using this procedure are basis set dependent. The electrostatic potential for the small molecules in our test set was calculated at the HF/6-31G* level of theory. The 3-21G* basis set was used for the iodine atom. The Respgen utility of the Antechamber package was used to generate the input files for two-stage fitting. The partial atomic charges were fitted to the electrostatic potential using the RESP program and Antechamber package.

d. Generating Input Files. Because our ultimate goal is the practical application of these methods for screening databases containing multiple small molecules used in protein−ligand docking studies, emphasis was given to making the input file generation steps automated with the help of programs such as Antechamber and InsightII, and simple perl scripts. To efficiently handle hundreds of small molecules in any molecular mechanics calculations, one needs to automatically assign the parameters and generate the residue topology file rather than hand-editing individual molecule. The stand-alone version of Antechamber program v2.7 serves this purpose by automatically perceiving atom types and assigning bond type and bond order from the three-dimensional geometry of the molecule.[44] However, it should be kept in mind that when using Antechamber, the user has to provide the total charge of the molecule for accurate charge calculation; otherwise the program perceives the default total charge of 0. Because in our case only neutral molecules were used, we used the default total charge. The Antechamber program was used to generate the input topology and parameter files for both the Amber and the CHARMM programs when using GAFF. The InsightII program and perl scripts were used to automate the input file preparatory step when the CHARMm-MSI force field was used. All of the explicit solvent simulations were set up and performed with the CHARMM program in an automated manner using a suite of perl scripts, keeping in mind the broader application of this method in screening large databases of ligands. The only input that was supplied was a coordinate file for the small molecule, for example, mol2 or PDB format.

e. Solvation Free Energy Protocols. The absolute free energy of solvation for the small molecules was calculated using FEP/MD with explicit solvent molecules. The FEP/

MD simulations were carried out using the PERT module of the program CHARMM v31.[52] Three staging or coupling parameters, s, ξ, and λ, were used to separate the absolute solvation free energy in terms of its polar and nonpolar components.[28] The latter was further decomposed into purely repulsive and attractive terms using the WCA scheme. The free energy contribution from the core repulsion was calculated by setting the staging parameter s to 0.0, 0.2, 0.3, 0.4, 0.5, 0.6, 0.7, 0.8, 0.9, and 1.0. For each value of s, two trajectories of 70 ps were run for both the initial and the final states. Only the last 60 ps of each trajectory was used in the free energy calculations. The free energy contributions from electrostatics and from the van der Waals dispersion interactions were both calculated using a standard linear coupling scheme. For the dispersive attraction, the coupling parameter ξ was set to 0.0, 0.1, 0.2, 0.3, 0.4, 0.5, 0.6, 0.7, 0.8, 0.9, and 1.0. For the electrostatic free energy contribution, the coupling parameter λ was set to 0.0, 0.1, 0.2, 0.3, 0.4, 0.5, 0.6, 0.7, 0.8, 0.9, and 1.0. In both cases, interaction energy samples were collected from the last 20 ps of two 30 ps trajectories, and the samples were processed by the weighted histogram analysis method (WHAM).[53] All free energies were calculated with 400 explicit TIP3P water molecules, with the influence of the remaining bulk being incorporated via the SSBP.[35] The system temperature was held fixed at 300 K with Langevin dynamics. A friction constant of 5 ps^{-1} was applied on the oxygen atoms of all of the water molecules. The integration time step of the dynamics was 2 fs. All bonds containing hydrogen atom were fixed with SHAKE constraints. The center of mass of the solute was constrained to the center of the solvent sphere with a harmonic potential with a force constant of 1.0 kcal $Å^{-2}$ mol^{-1}.

The solvation energies for the 239 small molecules were obtained using two implicit solvent methods, the GB/SA model in Nucleic Acid Builder (NAB)[54] and the PB. The NAB molecular modeling package was used to perform the MM-GB/SA calculations with the Amber force field. NAB is a high-level language that can perform the force field calculations, such as molecular dynamics and minimization similar to the Amber program.[54] The NAB and Amber program have the same GB implementation. The ΔG_{polar} was obtained using the GB method as implemented in the NAB program using a dielectric constant of 80 for the water phase. Each atom in a molecule was represented as a sphere of radius R_i with a charge q_i at its center; the interior of the atom was assumed to be filled uniformly with a material of dielectric constant 1. The Born radii were computed according to the method of Onuchic, Bash, and Case or the "OBC" model (implemented as igb = 5 in NAB, version 5).[55] The effective Born radius of an atom reflects the degree of its burial inside the molecule. In the "OBC" model, the effective radii are rescaled using parameters proportional to the degree of the atom's burial.

The $\Delta G_{nonpolar}$ contribution to the total solvation free energy was estimated using a term proportional to the total solvent accessible surface area (SASA) of the molecule, with proportionality constant derived from experimental solvation energies of small nonpolar molecules. A fast LCPO algorithm[56] was used to compute an analytical approximation to the SASA of the molecule.

The PB continuum solvent method with new and improved nonpolar solvation model in Amber9 was used in this study. This implicit solvent model decomposes the total solvation free energy into polar and nonpolar. The polar component of the total solvation free energy was obtained by using a grid-based finite difference solution to the PB equation with zero salt concentration and modified Bondi radii (corresponding to mbondi2 in Amber) for small molecules.[55] A grid spacing of 0.2 was used for generating the grids. The $\Delta G_{nonpolar}$ was obtained as a combination of two terms representing separate cavity or repulsive term and a dispersive or attractive term using an optimized 6-12 decomposition scheme using the methodology implemented as igb = 10 in Amber9.[33]

For the continuum solvent calculations, the starting structures of the small molecules were subjected to 500 steps each of SD and ABNR energy minimizations, followed by 1 ns of MD simulations using GB (igb = 5 in Amber). The PB was performed on the final snapshot of the equilibrated structure. As a comparison, we also calculated the PB electrostatic energy using PBEQ solver[18,21,57] in the CHARMM program using the same set of radii (mbondi2 in Amber) and PB parameters. The effect of conformational fluctuations on the magnitude of the solvation free energy was examined in the case of four small molecules: methyl hexanoate, methyl propyl ether, octanal, and 5-nonanone. Those molecules were chosen because they have the highest number of the rotatable bonds and are among the most flexible in the test set of 239 molecules studied here. The MD simulations for 10 and 20 ns duration for each of the molecule in vacuum were carried out to generate an ensemble of conformations using both the CHARMM and the NAB programs. The solvation free energy for the snapshots was then calculated perturbatively for the implicit solvent methods described above, PB/CHARMM and GBSA/NAB.

3. Results and Discussion

a. Comparison of the Charge Methods. For each set of Lennard-Jones parameters from GAFF and CHARMm-MSI force fields, we calculate the absolute solvation free energies using atomic partial charges obtained from three different methods. The first two methods are based on the electrostatic potential from the quantum mechanics (QM): ChelpG and RESP. The third method, AM1-BCC, is based on a semiempirical AM1 determination of charge followed by bond charge correction (BCC). The correlation plot between the experimental (ΔG_{exp}) and calculated (ΔG_{calc}) absolute solvation free energies is shown in Figure 1. When using GAFF/RESP and GAFF/ChelpG, the correlation coefficient R^2 between the absolute ΔG_{exp} and ΔG_{calc} corresponds to 0.84 and 0.80, respectively. Thus, the two QM methods show good overall performance in terms of reproducing the experimental results, the GAFF/RESP being slightly better than the GAFF/ChelpG. The major outliers using the GAFF/RESP model are (the error in absolute solvation free energy is shown in parentheses) 1,4-dimethylpiperazine (5.1), aze-

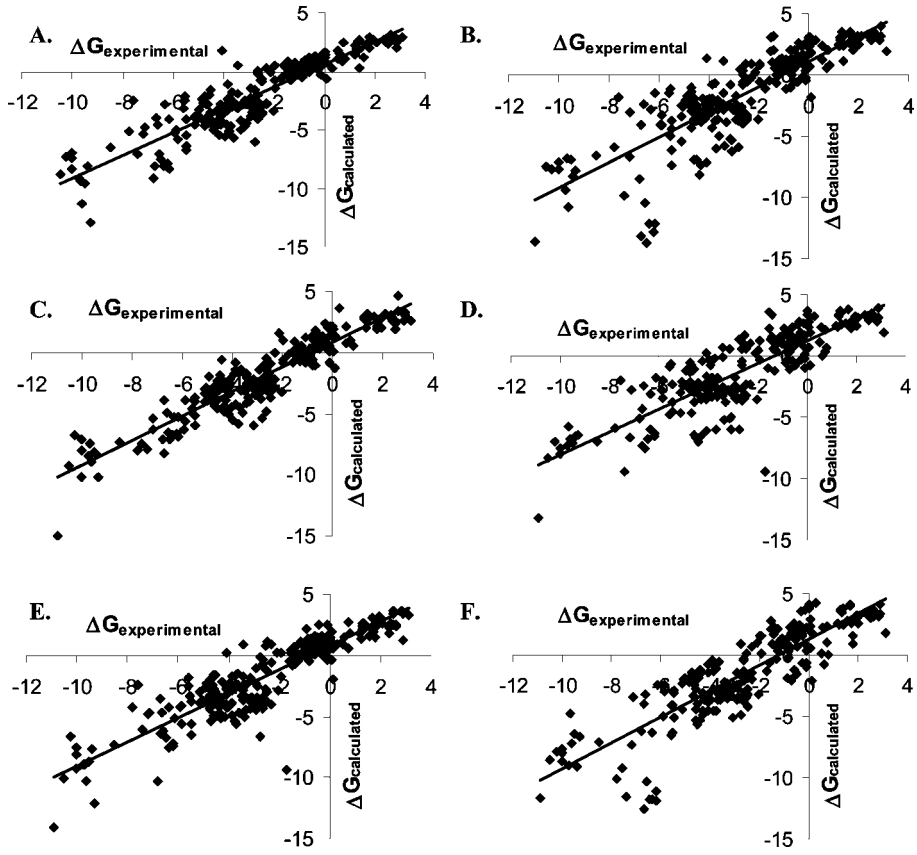

Figure 1. Plot showing correlation between experimental (*x*-axis; $\Delta G_{\text{experimental}}$, kcal/mol) and calculated (*y*-axis; $\Delta G_{\text{calculated}}$, kcal/mol) absolute solvation free energies obtained using explicit solvent simulations on 241 neutral molecules. Absolute solvation free energy calculated using the following models: GAFF/RESP ($R^2 = 0.84$) (A), CHARMm-MSI/RESP ($R^2 = 0.72$) (B), GAFF/ChelpG ($R^2 = 0.80$) (C), CHARMm-MSI/ChelpG ($R^2 = 0.72$) (D), GAFF/AM1-BCC ($R^2 = 0.87$) (E), and CHARMm-MSI/AM1-BCC ($R^2 = 0.76$) (F). The energies are in kcal/mol.

tidine (3.4), 1,2-ethanediol (−3.6), *N*-methylacetamide (3.0), 2-ethylpyrazine (3.1), propylaminoformamidine (−5.2), and methyl formate (−3.3). Upon discarding these top outliers, the R^2 between the absolute solvation free energy (ΔG_{exp} and ΔG_{calc}) improved from 0.82 to 0.88. On the other hand, the semiempirical charge AM1-BCC method is able to reproduce the absolute solvation free energies for our test set with a higher correlation coefficient ($R^2 = 0.87$). The major outlier with the GAFF/AM1-BCC method was 1-heptanol (3.8). When using the CHARMm-MSI Lennard-Jones parameters, we see that the overall correlation between the absolute ΔG_{exp} and ΔG_{calc} is worse for all three charge models, CHARMm-MSI/AM1-BCC, CHARMm-MSI/RESP, and CHARMm-MSI/CHelpG. However, a similar trend was observed between the performances of the three charge models. The R^2 between the absolute ΔG_{exp} and ΔG_{calc} from the CHARMm-MSI/RESP, CHARMm-MSI/ChelpG, and CHARMm-MSI/AM1-BCC corresponds to 0.72, 0.72, and 0.76, respectively (Figure 1B). The results show that for both force fields, the two QM methods, RESP and ChelpG, performed similarly in reproducing the experimental absolute solvation free energies, whereas the semiempirical AM1-BCC performed slightly better than the former two.

In an attempt to compare the performance of different charge models, the compounds were grouped depending on their chemical nature, and the average unsigned error (AUE) in the absolute solvation energy was calculated for each group (Figure 2). We observe that for small molecules containing hydrocarbons, such as linear and branched alkanes, alkenes, alkynes, cycloalkanes, polar groups such as aldehydes, ketones, carboxylic acids, esters, ethers, aliphatic amines, nitro, sulfides, and the majority of the halogenated molecules, the AUE in solvation energy is similar between the two QM charge methods (Figure 2). The major outliers are the small molecules containing hydrophobic ring structure (arenes), and a polar functional group like alcohols, amides, groups containing amines and another chemical group (bifunctional), and compounds with iodine. For the bulky arene hydrocarbons and compounds with an iodo functional group, the calculated solvation free energies with RESP charges yield better agreement with the experimental solvation free energies as compared to the ChelpG charges.

In the calculation of absolute solvation energies, the results obtained from the semiempirical AM1-BCC charges perform as well as those obtained with QM charges. In case of nitrogen-containing polar functional groups, such as amines, amides, nitro, and bifunctional groups with at least one amino function, the AM1-BCC performs better than the ChelpG and RESP, for a given force field. It is somewhat surprising that the AM1-BCC charges outperform the RESP for the above functional groups. This can be attributed to the five BCC parameters that were adjusted in the original AM1-BCC model to improve agreement with experimental data of amines, nitro, and unsaturated aromatic hydrocarbon

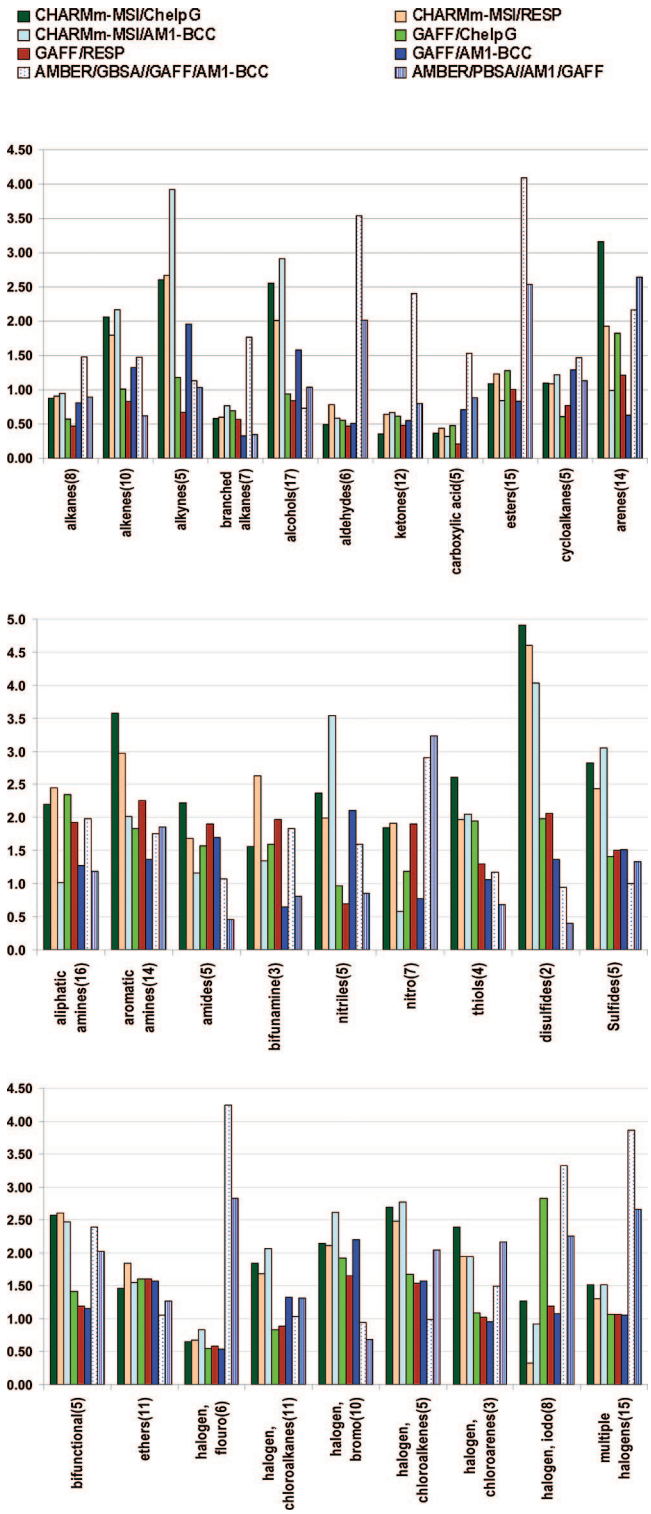

Figure 2. Average unsigned error [AUE] in the absolute solvation free energies. The AUE is shown in the *y*-axis, and the chemical functionalities in the small molecules are plotted in the *x*-axis. The solid bars represent the solvation free energies calculated using explicit solvent/FEP method in CHARMM. The bars with dotted line and stripes represent the solvation free energy calculated using GB and PB model in Amber9.

groups.[50] The AM1-BCC model also outperforms the RESP and ChelpG in case of bulky arene molecules, such as 1,3-dimethyl naphthalene, benzene, biphenyl, etc., for the above-mentioned reason.

For the small molecules containing alkyne and nitrile functional groups, AM1-BCC underperforms as compared to the two QM charge models. A possible explanation can be the AM1 population charges are insufficient to model the electron delocalization in the highly unsaturated compounds. The nitriles were also among the major outliers in a previous study using implicit solvent GB/SA and SGB/NP model[58] and indicate the challenges associated with obtaining accurate charge distributions for nitrogen-containing species. Overall, the AM1-BCC charge model appears to perform well with both the GAFF or CHARMm-MSI force field and the explicit solvent FEP/MD in reproducing the experimental absolute solvation free energies. Considering the fact that the AM1-BCC model was not parametrized to work with the GB/SA (or PB) model, the low AUE in solvation free energies calculated with implicit solvent models is extremely encouraging. Because the AM1-BCC charge generation method is very fast as compared to the RESP and ChelpG methods, the present results suggest that it can be a preferred practical method for screening database containing thousands of diverse small molecules.

b. Comparison of the Lennard-Jones Parameters/Force Fields. We compare the absolute solvation free energies for small molecules using two popular fixed charge force fields that are commonly used as a general force field for small molecules, GAFF and CHARMm-MSI. The former is a general version of the traditional biomolecular Amber force field that was recently developed, and the latter is a part of the CHARMm force field distributed commercially by MSI. Both of them use a similar functional form of the harmonic potential energy function to describe their additive force field equations based on bond, angle, dihedral, and nonbonded Lennard-Jones parameters.

Comparing the overall reproduction of the experimental absolute solvation free energies with any given charge method, we find that GAFF performs better than CHARMm-MSI. For example, using the GAFF/AM1-BCC method ($R^2 = 0.87$), we obtain a better correlation between the experimental and calculated solvation free energy when using the CHARMm-MSI/AM1-BCC ($R^2 = 0.76$, Figure 1). The AUE in absolute solvation free energies obtained from GAFF and CHARMm-MSI for different chemical functions is shown in Figure 2. For a given charge method, GAFF performs better than CHARMm-MSI for several functional groups, such as alkenes, alkynes, arenes, aromatic amines, nitriles, bifunctional groups, and small molecules with chloride functional group. Interestingly, in this study, the disulfides and sulfides are one of the major outliers in the CHARMm-MSI force field, which point in the direction of need for improvement in the sulfur atomic parameters in MSI force field. GAFF performs well even for those small molecules for which CHARMm-MSI has trouble reproducing the absolute solvation free energies. On the other hand, GAFF has high AUE [AUE > 1.5 kcal/mol] in reproducing the absolute solvation free energy for chemical functional groups such as amides, sulfides, ethers, bromo, and chloro-alkenes.

c. Comparison of the Explicit and Implicit Solvent Models. The accuracy of commonly used continuum solvent models, such as PB and GB, depends sensitively upon the

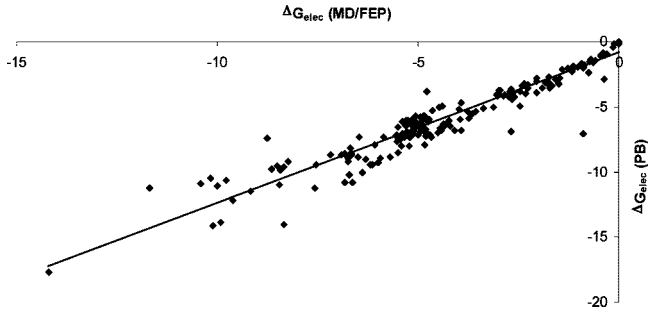

Figure 3. Comparison of the electrostatic component of the absolute solvation free energy between explicit solvent and implicit solvent model. The implicit solvent is modeled using PB in the Amber9 program. The explicit solvent results are from the FEP/MD and CHARMM v31 program. The correlation coefficient is 0.92. The calculations were done with the GAFF/AM1-BCC model. The energies are in kcal/mol.

parameters like atomic charges, the solute and solvent dielectric coefficients, and the atomic Born radii, which are used to define the solute−solvent dielectric boundary. Here, we compare the electrostatic component of the absolute solvation free energies obtained using the GB and PB continuum solvation models and compare it with its counterpart from the explicit solvent simulation, FEP/MD. We find that the electrostatic components obtained by solving the PB equation are in better agreement ($R^2 = 0.91$) with the explicit solvent simulation as compared to the GB model ($R^2 = 0.81$) [Figure 3]. Such a good performance of continuum PB in approximating the electrostatic free energy from FEP/MD has been observed in several previous studies.[18,22,29]

The decomposition scheme implemented in the implicit solvent module (igb = 10) in the Amber9 program was used to separate the nonpolar solvation free energy into repulsive ($\Delta G_{\text{rep-PB}}$) and attractive or dispersive ($\Delta G_{\text{att-PB}}$) components.[33] In this optimized 6-12 decomposition scheme, the SASA has been used to correlate the repulsive (cavity) term only, and a surface-integration approach is used to compute the attractive (dispersion) term. We benchmark the corresponding values for the repulsive and attractive terms with the similar counterparts obtained using WCA decomposition from the explicit solvent simulation using CHARMM ($\Delta G_{\text{rep-explicit}}$ and $\Delta G_{\text{att-explicit}}$). The correlation plot comparing the two components of the nonpolar solvation free energy is shown in Figure 4A and B. The $\Delta G_{\text{att-PB}}$ shows a correlation coefficient of 0.94 with $\Delta G_{\text{att-explicit}}$, whereas the $\Delta G_{\text{rep-PB}}$ has a correlation coefficient of 0.96 with $\Delta G_{\text{rep-explicit}}$.

We observe a very good correlation between the repulsive and attractive component of the nonpolar solvation free energy ($\Delta G_{\text{rep-explicit}}$) calculated using the WCA decomposition via FEP/MD simulation with explicit solvent and the SASA ($R^2 = 0.95$) approximation (Figure 5). However, the total nonpolar contribution obtained from both PB and explicit solvent simulations shows poor correlation with the SASA approximation (Figure 5). This suggests that implicit solvent models that rely exclusively on the SASA approximation to model the total nonpolar contribution might lead to considerable errors and should be used with caution.

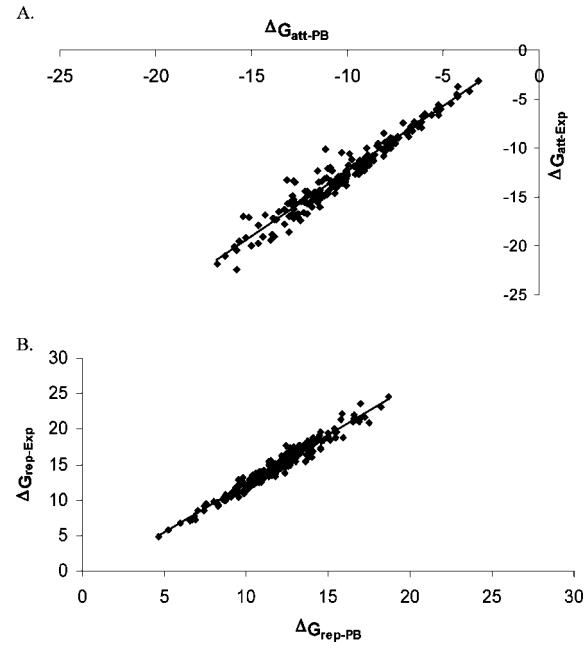

Figure 4. Comparison of the nonpolar components of the absolute solvation free energy between explicit solvent and implicit solvent model. The correlation between the attractive component of the nonpolar solvation energy obtained from FEP/MD with explicit solvent ($\Delta G_{\text{att-exp}}$) and PB implicit continuum solvent ($\Delta G_{\text{att-PB}}$) is 0.95. In the continuum PB model, the nonpolar part of the solvation energy is obtained from the Amber9 program. The FEP/MD results are from the CHARMM v31 program. The calculations were done with the GAFF/AM1-BCC model. The energies are in kcal/mol.

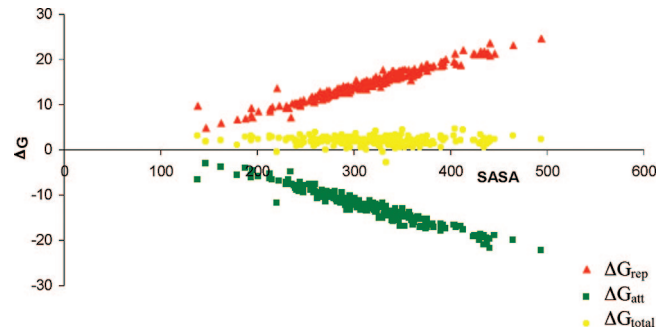

Figure 5. Plot showing correlation between total nonpolar solvation free energy (kcal/mol), and its repulsive and attractive components calculated using explicit solvent FEP/MD with solvent accessible surface area (SASA, Å^2).

In an attempt to better understand the performance of the PB solver implemented in the two popular molecular mechanics program, CHARMM and Amber, we compared the electrostatic solvation free energies between the two. The modified Bondi radii (corresponding to mbondi2 in Amber) were extracted from Amber and read in as a stream file in the PBEQ solver in CHARMM. With a grid spacing of 0.2, reentrant water surface, and probe density of 1.4, we find an excellent correlation between the electrostatic component of the solvation energy using the PB solvers from CHARMM and Amber ($R^2 > 0.99$) (Supporting Information, Figure S1).

In the present study, we used a single energy-minimized conformation to calculate the solvation free energies with the implicit solvation model. This is actually a common

Table 2. Table Showing the Average Solvation Free Energy and Single Snapshot Using Implicit Solvent Models, PB and GB[a]

molecule	$\Delta G_{experiment}$	PB (10 ns)	PB (20 ns)	PB (1 snapshot)	GB (10 ns)	GB (20 ns)	GB (1 snapshot)
methyl hexanoate	−2.49	−4.27	−4.25	−4.59	−6.07	−5.93	−6.07
methyl propyl ether	−1.59	−1.21	−1.22	−0.97	−2.18	−2.12	−2.14
octanal	−2.29	−3.71	−3.77	−4.14	−5.66	−5.58	−5.7
5-nonanone	−2.67	−2.78	−2.77	−2.97	−4.78	−4.68	−4.6

[a] All energies are reported in kcal/mol.

practice in docking and scoring with implicit solvation models. However, the neglect of conformational flexibility can cause some problems, as shown in a previous study.[59] To ascertain the impact of conformational flexibility on the solvation free energy, we compared the solvation free energy obtained using the single solute conformation with that from a proper ensemble average. The solvation free energy was calculated pertubatively from an ensemble of conformations generated by an extensive MD simulation of the molecule in a vacuum using the following expression:

$$e^{-\Delta G/k_B T} = \frac{1}{N}\sum_i e^{-\Delta W(\mathbf{X}_i)/k_B T} \quad (2)$$

where $\Delta W(\mathbf{X}_i)$ is the potential of mean force incorporating the effect of solvent implicitly for the conformation $\mathbf{X}_i$, k_B is the Boltzmann constant, and T is absolute temperature. We obtained the average solvation free energy using both the PB and the GB implicit solvent simulations, for four of the most flexible molecules in our set (number of rotatable bonds larger than 5). These molecules are methyl hexanoate, 5-nonanone, octanal, and methyl propyl ether. The results are shown in Table 2. Comparing the average solvation free energy obtained from the above method with that of the single solute conformation reported in this Article, we find that the solvation free energy estimated from a single energy-minimized snapshot is within 0.5 kcal/mol for all four flexible molecules. These estimates are comparable to the results from a previous study where for the energy-minimized conformation in vacuum (called "BestVac" in Mobley et al.[59]) the rms error was on the order of 0.34 kcal/mol. They showed that an approach based on energy-minimum conformations in vacuum gives the lowest errors.

d. log *P*. The molecular hydrophobicity or log P of a small molecule is an important descriptor to measure differential solubility of a solute in two immiscible solvent media, hydrophobic and hydrophilic solvent.[4] For example, the partition coefficient of a solute between octanol and water is represented by

$$\log P_{oct/wat} = \log([\text{solute}]_{oct}/[\text{solute}]_{wat}) \quad (3)$$

It is commonly used in the QSAR studies and drug design to study the drug absorption, bioavailability, metabolism, and toxicity. However, the force field-based simulations are not commonly used to calculate this quantity as the simulations in octanol solvent pose significant challenges due to complex structure formations, such as micelles.

Here, we compare the correlation between the experimental log $P_{oct/wat}$ with the repulsive component of the nonpolar solvation free energy ($\Delta G_{rep\text{-}explicit}$) obtained using explicit solvent FEP/MD. The experimental data for log $P_{oct/wat}$ have been taken almost entirely from the recommended values in the compilation by Hansch and co-workers.[60] The data cover a range of 7.0 log units from ca. −2 to +5. It shows high correlation with the cavity or repulsive term, $\Delta G_{rep\text{-}explicit}$. Such a high correlation is intriguing. A possible explanation is that log P is a measure of hydrophobicity, and therefore is correlated with $\Delta G_{rep\text{-}explicit}$. Also, the SASA is correlated with the $\Delta G_{rep\text{-}explicit}$ as well as log P with a correlation coefficient of 0.95.

Within a particular chemical series, the log P is linearly correlated with $\Delta G_{rep\text{-}explicit}$ with a high correlation coefficient (Figure 6). For example, for alcohols, such as methanol, ethanol, propanol, butanol, pentanol, hexanol, heptanol, and octanol, the correlation coefficient between log P and $\Delta G_{rep\_Explicit}$ is 0.996. For amines, such as methylamine, ethylamine, 1-propanamine, 1-butylamine, 1-pentanamine, *N*-ethylethamine, *N*,*N*-dimethylamine, *N*,*N*-diethylethanamine, *N*-propylpropan-1-amine, trimethylamine, piperidine, and pyrrolidine, the correlation coefficient is 0.93. For nitro-containing small molecules, such as nitroethane, 1-nitropropane, 2-nitropropane, 1-nitrobutane, nitrobenzene, 3-nitrophenol, and 1-methyl-2-nitro-benzene, the correlation coefficient is 0.99.

The physical significance for such a correlation may be that a larger SASA facilitates solvation in a more hydrophobic solvent, such as octanol. It reflects the importance of van der Waals interaction in the organic solvent, which in turn is related to the cavitation of the solute. The nature of the chemical function governs the slope and the intercept of this log P versus $\Delta G_{rep\text{-}explicit}$ linear curve. We believe that the FEP/MD simulations, similar to the ones used in this study, could provide important information about the molecular descriptor properties such as hydration and log P. Further studies in making a physics-based accurate log P predicting tool are currently underway and will be reported elsewhere.

4. Conclusion

In this study, we computed the absolute solvation free energy for a diverse set of 239 neutral molecules using FEP/MD with explicit solvent and compared the results with experimental data as well as with two widely used implicit solvent models (GB/SA and PB). We evaluated the performance of two popular general force fields, GAFF and CHARMm-MSI, used to model small molecules and ligands in drug design. Also, we examined the sensitivity of the free energy to the atomic partial charges generated via ab initio QM (ChelpG and RESP) and semiempirical (AM1-BCC) methods.

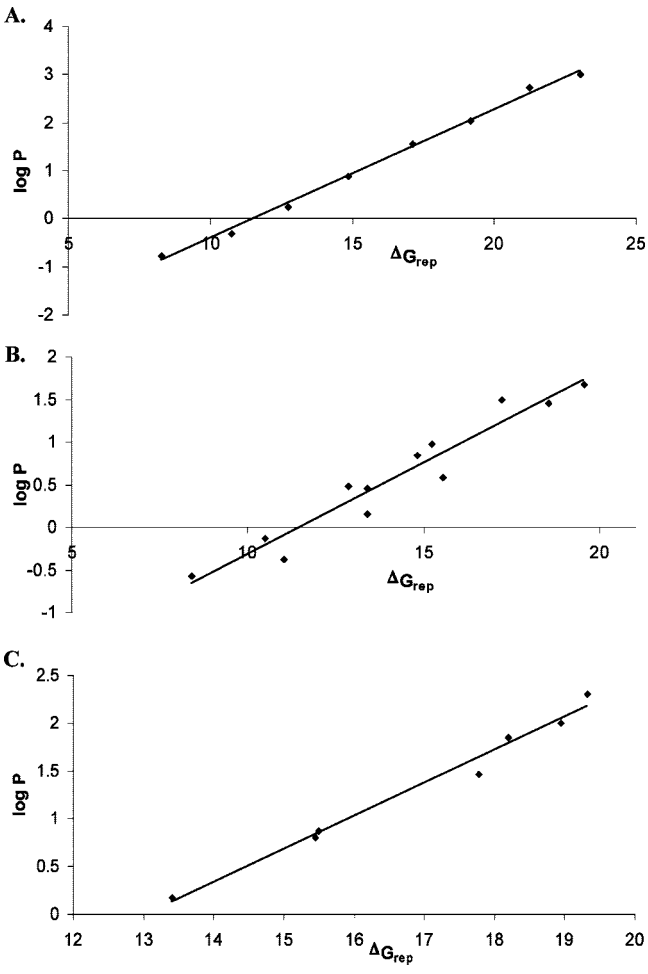

Figure 6. Correlation of log *P* with nonpolar solvation free energy ($\Delta G_{rep\_explicit}$). The correlation coefficient for alcohols, such as methanol, ethanol, propanol, butanol, pentanol, hexanol, heptanol, octanol, is 0.996 (A). For amines, such as methylamine, ethylamine, 1-propanamine, 1-butylamine, 1-pentanamine, *N*-ethylethamine, *N,N*-dimethylamine, *N,N*-diethylethanamine, *N*-propylpropan-1-amine, trimethylamine, piperidine, and pyrrolidine, the correlation coefficient is 0.93 (B). For nitro-containing small molecules, such as nitroethane, 1-nitropropane, 2-nitropropane, 1-nitrobutane, nitrobenzene, 3-nitrophenol, and 1-methyl-2-nitro-benzene, the correlation coefficient is 0.99 (C).

Our analysis indicates that the GAFF force field with the AM1-BCC atomic charges generally outperforms the others for a majority of chemical functionalities. However, the AM1-BCC charges need to be revisited for some unsaturated chemical functional groups, such as nitriles and alkynes, to provide better agreement with experiment. The origin of the problem is clearly the partial charges because those same functional groups show good correlation with experimental values when RESP charges are used. Also, our studies show that the sulfur-containing groups are particularly troublesome in case of the CHARMm-MSI force field.

Concerning the performance of implicit solvent models, it is observed that the electrostatic component obtained by solving the finite-difference PB equation is in better agreement with the explicit solvent simulations as compared to the GB model. The underperformance of GB as compared to PB noted here is somewhat surprising because the accuracy of GB is generally believed to deteriorate for large complex macromolecules, but to be quite adequate in the case of small molecules such as those considered here. On the other hand, the repulsive and the attractive components of the nonpolar solvation free energy show excellent correlation between the implicit and the explicit solvent simulations. The repulsive components of nonpolar solvation free energy obtained using the implicit and explicit solvent models are also highly correlated with the SASA. However, the total nonpolar solvation free energy is poorly correlated with SASA. This suggests that implicit solvent models that use only SASA to approximate the total nonpolar contribution are less accurate and should be used with caution.

Interestingly, log *P* appears to be highly correlated with the cavity or repulsive component of the nonpolar solvation free energy, $\Delta G_{rep\text{-}explicit}$, as well as the SASA. Within particular chemical series, log *P* displays an almost perfect linear correlation with the $\Delta G_{rep\text{-}explicit}$. Although the reasons for such a high correlation are not entirely clear, it is possible that it reflects the importance of van der Waals interaction in the organic solvent such as octanol, which is related to the size of the cavity needed to insert the solute.

Continued efforts are needed to assess the accuracy of atomic partial charges and other aspects of molecular mechanical force fields. Such assessment is critically important for the progress of computational structural biology. The present study shows how force field development and validation could benefit from extensive free energy computations performed on a large-scale basis.

Acknowledgment. This work was supported by the National Science Foundation through Grant MCB-0630140, and by Grant 2006-264-R2 from the Laboratory-Directed Research and Development (LDRD) program at Argonne National Laboratory, and by the U.S. Department of Energy (DOE), Office of Basic Energy Sciences, under Contract no. DE-AC02-06CH11357. D.S. thanks Jeff Klauda for supplying the AMBER99 force field conversion for use in the CHARMM program.

Supporting Information Available: Please contact authors for the decomposition of the nonpolar estimates, molecular structures of the molecules, and assigned atomic partial charges. The absolute solvation free energy for the test set is provided, along with the correlation plot between the electrostatic component of the solvation energy using the PB solvers from CHARMM and Amber. This material is available free of charge via the Internet at http://pubs.acs.org.

References

(1) Karplus, M. Molecular Dynamics Simulations of Biomolecules. *Acc. Chem. Res.* **2002**, *35*, 321–323.

(2) Shoichet, B. K.; Leach, A. R.; Kuntz, I. D. Ligand Solvation in Molecular Docking. *Proteins: Struct., Funct., Genet.* **1999**, *34*, 4–16.

(3) Vedani, A.; Dobler, M.; Lill, M. A. The Challenge of Predicting Drug Toxicity in silico. *Basic Clin. Pharm. Toxicol.* **2006**, *99*, 195–208.

(4) Lipinski, C. A.; Lombardo, F.; Dominy, B. W.; Feeney, P. J. Experimental and Computational Approaches to Estimate Solubility and Permeability in Drug Discovery and Development Settings. *Adv. Drug Delivery Rev.* **2001**, *46*, 3–26.

(5) Jorgensen, W. L. The Many Roles of Computation in Drug Discovery. *Science* **2004**, *303*, 1813–1818.

(6) Brooks, C. L., III; Karplus, M.; Pettitt, B. M. Proteins a Theoretical Perspective of Dynamics, Structure and Thermodynamics. In *Advances in Chemical Physics*; Prigogine, I., Rice, S. A., Eds.; John Wiley and Sons: New York, 1988.

(7) Roux, B.; Simonson, T. Implicit Solvent Models. *Biophys. Chem.* **1999**, *78*, 1–20.

(8) Kollman, P. Free Energy Calculations: Applications to Chemical and Biochemical Phenomena. *Chem. Rev.* **1993**, *93*, 2395–2417.

(9) Shirts, M. R.; Pitera, J. W.; Swope, W. C.; Pande, V. S. Extremely Precise Free Energy Calculations of Amino Acid Side Chain Analogs: Comparison of Common Molecular Mechanics Force Fields for Proteins. *J. Chem. Phys.* **2003**, *119*, 5740–5761.

(10) Warwicker, J.; Watson, H. C. Calculation of the Electric Potential in the Active Site Cleft due to α-helix Dipoles. *J. Mol. Biol.* **1982**, *157*, 671–679.

(11) Still, W. C.; Tempczyk, A.; Hawley, R. C.; Hendrickson, T. Semianalytical Treatment of Solvation for Molecular Mechanics and Dynamics. *J. Am. Chem. Soc.* **1990**, *112*, 6127–6129.

(12) Edinger, S. R.; Cortis, C.; Shenkin, P. S.; Friesner, R. A. Solvation Free Energies of Peptides: Comparison of Approximate Continuum Solvation Models with Accurate Solution of the Poisson-Boltzmann Equation. *J. Phys. Chem. B* **1997**, *101*, 1190–1197.

(13) Schaefer, M.; Karplus, M. A Comprehensive Analytical Treatment of Continuum Electrostatics. *J. Phys. Chem. B* **1996**, *100*, 1578–1599.

(14) Klapper, I.; Hagstrom, R.; Fine, R.; Sharp, K.; Honig, B. Focusing of Electric Fields in the Active site of Cu-Zn Superoxide Dismutase: Effects of Ionic Strength and Amino-acid Modification. *Proteins* **1986**, *1*, 47–59.

(15) Sharp, K. A.; Honig, B. Electrostatic Interactions in Macromolecules: Theory and Applications. *Annu. Rev. Biophys. Biophys. Chem.* **1990**, *19*, 301–332.

(16) Wang, J.; Tan, C.; Tan, Y. H.; Lu, Q.; Luo, R. Poisson-Boltzmann Solvents inMolecular Dynamics Simulations. *Commun. Comput. Phys.* **2008**, *3*, 1010–1031.

(17) Jean-Charles, A.; Nicholls, A.; Sharp, K.; Honig, B.; Tempczyk, A.; Hendrickson, T.; Still, C. Electrostatic Contributions to Solvation Energies: Comparison of Free Energy Perturbation and Continuum Calculations. *J. Am. Chem. Soc.* **1991**, *113*, 1454–1455.

(18) Nina, M.; Beglov, D.; Roux, B. Atomic Radii for Continuum Electrostatics Calculations Based on Molecular Dynamics Free Energy Simulations. *J. Phys. Chem. B* **1997**, *101*, 5239–5248.

(19) Jayaram, B.; Sprous, D.; Beveridge, D. L. Solvation Free Energy of Biomacromolecules: Parameters for a Modified Generalized Born Model Consistent with the AMBER Force Field. *J. Phys. Chem. B* **1998**, *102*, 9571–9576.

(20) Cramer, C. J.; Truhlar, D. G. Implicit Solvation Models: Equilibria, Structure, Spectra, and Dynamics. *Chem. Rev.* **1999**, *99*, 2161–2200.

(21) Banavali, N. K.; Roux, B. Atomic Radii for Continuum Electrostatics Calculations on Nucleic Acids. *J. Phys. Chem. B* **2002**, *106*, 11026–11035.

(22) Swanson, J. M. J.; Henchman, R. H.; McCammon, J. A. Revisiting Free Energy Calculations: A Theoretical Connection to MM/PBSA and Direct Calculation of the Association Free Energy. *Biophys. J.* **2004**, *86*, 67–74.

(23) Eisenberg, D.; McLachlan, A. D. Solvation Energy in Protein Folding and Binding. *Nature* **1986**, *319*, 199–203.

(24) Chothia, C. Hydrophobic Bonding and Accessible Surface Area in Proteins. *Nature* **1974**, *248*, 338–339.

(25) Sharp, K. A.; Nicholls, A.; Fine, R. F.; Honig, B. Reconciling the Magnitude of the Microscopic and Macroscopic Hydrophobic Effects. *Science* **1991**, *252*, 106–109.

(26) Lum, K.; Chandler, D.; Weeks, J. D. Hydrophobicity at Small and Large Length Scales. *J. Phys. Chem. B* **1999**, *103*, 4570–4577.

(27) Rajamani, S.; Truskett, T. M.; Garde, S. Hydrophobic Hydration from Small to Large Lengthscales: Understanding and Manipulating the Crossover. *Proc. Natl. Acad. Sci. U.S.A.* **2005**, *102*, 9475–9480.

(28) Deng, Y.; Roux, B. Hydration of Amino Acid Side Chains: Nonpolar and Electrostatic Contributions Calculated from Staged Molecular Dynamics Free Energy Simulations with Explicit Water Molecules. *J. Phys. Chem. B* **2004**, *108*, 16567–16576.

(29) Wagoner, J. A.; Baker, N. A. Assessing Implicit Models for Nonpolar Mean Solvation Forces: The Importance of Dispersion and Volume Terms. *Proc. Natl. Acad. Sci. U.S.A.* **2006**, *103*, 8331–8336.

(30) Gallicchio, E.; Zhang, L. Y.; Levy, R. M. The SGB/NP Hydration Free Energy Model Based on the Surface Generalized Born Solvent Reaction Field and Novel Nonpolar Hydration Free Energy Estimators. *J. Comput. Chem.* **2002**, *23*, 517–529.

(31) Pitera, J. W.; van Gunsteren, W. F. The Importance of Solute-Solvent van der Waals Interactions with Interior Atoms of Biopolymers. *J. Am. Chem. Soc.* **2001**, *123*, 3163–3164.

(32) Floris, F.; Tomasi, J. Evaluation of the Dispersion Contribution to the Solvation Energy. A Simple Computational Model in the Continuum Approximation. *J. Comput. Chem.* **1989**, *10*, 616–627.

(33) Tan, C.; Tan, Y.-H.; Luo, R. Implicit Nonpolar Solvent Models. *J. Phys. Chem. B* **2007**, *111*, 12263–12274.

(34) Jorgensen, W. L.; Chandrasekhar, J.; Madura, J. D.; Impey, R. W.; Klein, M. L. Comparison of Simple Potential Functions for Simulating Liquid Water. *J. Chem. Phys.* **1983**, *79*, 926–935.

(35) Beglov, D.; Roux, B. Finite Representation of an Infinite Bulk System: Solvent Boundary Potential for Computer Simulations. *J. Chem. Phys.* **1994**, *100*, 9050–9063.

(36) Wang, J.; Wolf, R. M.; Caldwell, J. W.; Kollman, P. A.; Case, D. A. Development and Testing of a General Amber Force Field. *J. Comput. Chem.* **2004**, *25*, 1157–1174.

(37) Momany, F. A.; Rone, R. Validation of the General-Purpose Quanta3. 2/CHARMM force-field. *J. Comput. Chem.* **1992**, *13*, 888.

(38) Case, D. A.; Cheatham, T. E., III; Darden, T.; Gohlke, H.; Luo, R.; Merz, J. K. M.; Onufriev, A.; Simmerling, C.; Wang, B.; Woods, R. The Amber Biomolecular Simulation Programs. *J. Comput. Chem.* **2005**, *26*, 1668–1688.

(39) Levy, R. M.; Zhang, L. Y.; Gallicchio, E.; Felts, A. K. On the Nonpolar Hydration Free Energy of Proteins: Surface Area and Continuum Solvent Models for the Solute-Solvent Interaction Energy. *J. Am. Chem. Soc.* **2003**, *125*, 9523–9530.

(40) Weeks, J. D. C.; Andersen, D.; Hans, C. Role of Repulsive Forces in Determining the Equilibrium Structure of Simple Liquids. *J. Chem. Phys.* **1971**, *54*, 5237–5247.

(41) Boresch, S.; Archontis, G.; Karplus, M. Free Energy Simulations: the Meaning of the Individual Contributions from a Component Analysis. *Proteins* **1994**, *20*, 25–33.

(42) Chambers, C. C.; Hawkins, G. D.; Cramer, C. J.; Truhlar, D. G. Model for Aqueous Solvation Based on Class {IV} Atomic Charges and First Solvation Shell Effects. *J. Phys. Chem.* **1996**, *100*, 16385–16398.

(43) Maple, J. R.; Cao, Y.; Damm, W.; Halgren, T. A.; Kaminski, G. A.; Zhang, L. Y.; Friesner, R. A. A Polarizable Force Field and Continuum Solvation Methodology for Modeling of Protein-Ligand Interactions. *J. Chem. Theory Comput.* **2005**, *1*, 694–715.

(44) Wang, J.; Wang, W.; Kollman, P. A.; Case, D. A. Automatic Atom Type and Bond Type Perception in Molecular Mechanical Calculations. *J. Mol. Graphics Modell.* **2006**, *25*, 247–260.

(45) Mobley, D. L.; Dumont, E.; Chodera, J. D.; Dill, K. A. Comparison of Charge Models for Fixed-Charge Force Fields: Small-Molecule Hydration Free Energies in Explicit Solvent. *J. Phys. Chem. B* **2007**, *111*, 2242–2254.

(46) Nicholls, A.; Mobley, D. L.; Guthrie, J. P.; Chodera, J. D.; Bayly, C. I.; Cooper, M. D.; Pande, V. S. Predicting Small-Molecule Solvation Free Energies: An Informal Blind Test for Computational Chemistry. *J. Med. Chem.* **2008**, *51*, 769–779.

(47) Breneman, C. M.; Wiberg, K. B. Determining Atom-centered Monopoles from Molecular Electrostatic Potentials. The Need for High Sampling Density in Formamide Conformational Analysis. *J. Comput. Chem.* **1990**, *11*, 361–373.

(48) Bayly, C. I.; Cieplak, P.; Cornell, W. D.; Kollman, P. A. A Well Behaved Electrostatic Potential based Method using Charge Restraints for Deriving Atomic Charges−The RESP Model. *J. Phys. Chem.* **1993**, *40*, 10269–10280.

(49) Jakalian, A.; Bush, B. L.; Jack, D. B.; Bayly, C. I. Fast, Efficient Generation of High-Quality Atomic Charges. AM1-BCC Model: I. Method. *J. Comput. Chem.* **2000**, *21*, 132–146.

(50) Jakalian, A.; Jack, D. B.; Bayly, C. I. Fast, Efficient Generation of High-Quality Atomic Charges. AM1-BCC Model: II. Parameterization and Validation. *J. Comput. Chem.* **2002**, *23*, 1623–1641.

(51) Frisch, M. J.; Trucks, G. W.; Schlegel, H. B.; Scuseria, G. E.; Robb, M. A.; Cheeseman, J. R.; Montgomery, J. A., Jr.; Vreven, T.; Kudin, K. N.; Burant, J. C.; Millam, J. M.; Iyengar, S. S.; Tomasi, J.; Barone, V.; Mennucci, B.; Cossi, M.; Scalmani, G.; Rega, N.; Petersson, G. A.; Nakatsuji, H.; Hada, M.; Ehara, M.; Toyota, K.; Fukuda, R.; Hasegawa, J.; Ishida, M.; Nakajima, T.; Honda, Y.; Kitao, O.; Nakai, H.; Klene, M.; Li, X.; Knox, J. E.; Hratchian, H. P.; Cross, J. B.; Bakken, V.; Adamo, C.; Jaramillo, J.; Gomperts, R.; Stratmann, R. E.; Yazyev, O.; Austin, A. J.; Cammi, R.; Pomelli, C.; Ochterski, J. W.; Ayala, P. Y.; Morokuma, K.; Voth, G. A.; Salvador, P.; Dannenberg, J. J.; Zakrzewski, V. G.; Dapprich, S.; Daniels, A. D.; Strain, M. C.; Farkas, O.; Malick, D. K.; Rabuck, A. D.; Raghavachari, K.; Foresman, J. B.; Ortiz, J. V.; Cui, Q.; Baboul, A. G.; Clifford, S.; Cioslowski, J.; Stefanov, B. B.; Liu, G.; Liashenko, A.; Piskorz, P.; Komaromi, I.; Martin, R. L.; Fox, D. J.; Keith, T.; Al-Laham, M. A.; Peng, C. Y.; Nanayakkara, A.; Challacombe, M.; Gill, P. M. W.; Johnson, B.; Chen, W.; Wong, M. W.; Gonzalez, C.; Pople, J. A. *Gaussian 03*, revision C.02; Gaussian, Inc.: Wallingford, CT, 2004.

(52) Brooks, B. R.; Bruccoleri, R. E.; Olafson, B. D.; States, D. J.; Swaminathan, S.; Karplus, M. CHARMM: a Program for Macromolecular Energy, Minimization, and Dynamics Calculations. *J. Comput. Chem.* **1983**, *4*, 187–217.

(53) Souaille, M. a. R. B. Extension to the Weighted Histogram Analysis Method: Combining Umbrella Sampling with Free Energy Calculations. *Comput. Phys. Commun.* **2001**, *135*, 40–57.

(54) Macke, T.; Case, D. A. Modeling unusual nucleic acid structures. In *Molecular Modeling of Nucleic Acids*; Leontes, N. B., SantaLucia, J. J., Eds.; American Chemical Society: Washington, DC, 1998; pp 379−393.

(55) Onufriev, A.; Bashford, D.; Case, D. A. Exporling Protein Native States and Large-scale Conformational Changes with a Modified Generalized Born Model. *Proteins* **2004**, *55*, 383–394.

(56) Weiser, J.; Shenkin, P. S.; Still, W. C. Approximate Atomic Surfaces from Linear Combinations of Pairwise Overlaps (LCPO). *J. Comput. Chem.* **1999**, *20*, 217–230.

(57) Roux, B. Influence of the Membrane Potential on the Free Energy of an Intrinsic Protein. *Biophys. J.* **1997**, *73*, 2980–2989.

(58) Rizzo, R. C.; Aynechi, T.; Case, D. A.; Kuntz, I. D. Estimation of Absolute Free Energies of Hydration Using Continuum Methods: Accuracy of Partial Charge Models and Optimization of Nonpolar Contributions. *J. Chem. Theory Comput.* **2006**, *2*, 128–139.

(59) Mobley, D. L.; Dill, K. A.; Chodera, J. D. Treating Entropy and Conformational Changes in Implicit Solvent Simulations of Small Molecules. *J. Phys. Chem. B* **2008**, *112*, 938–946.

(60) Leo, A.; Hoekman, D. H.; Hansch, C. *Explor. QSAR, Hydrophob., Electron., Steric Const.*; American Chemical Society: Washington, DC, 1995.

CT800445X

JCTC Journal of Chemical Theory and Computation

A Single Reference Perturbation Theory beyond the Møller−Plesset Partition

Feiwu Chen*

Department of Chemistry, University of Science and Technology Beijing, Beijing 100083, People's Republic of China

Received July 21, 2008

Abstract: A new single reference perturbation partition is proposed for restricted open-shell Hartree−Fock (ROHF) and complete active space self-consistent field (CASSCF) orbitals. It is a sum of one-particle operator which is implicitly defined. When the operator acts on a ROHF or CASSCF orbital, the resultant eigenvalue is the orbital's corresponding orbital energy coming from the ROHF or CASSCF calculation. HF, F_2, and N_2 with stretched bonds are used for the size extensivity test. Results indicate that the first three-order energies calculated with the new partition are size extensive. Single reference perturbation calculations for H_2O, NH_3, and CH_4 with CASSCF orbitals have been performed and compared with other methods like MRCI, MRCI+Q, MRPT2, and MRPT3. The single reference nature of the present perturbation theory is also shown with computations of the singlet−triplet separation of the CH_2 and SiH_2 radicals.

1. Introduction

The Rayleigh−Schrödinger perturbation theory with the Møller−Plesset partition (MP)[1] has been widely used in electronic structure calculations because of its inexpensive computational cost and size extensivity. MP partition is defined as a sum of the Fock operator which is only valid for restricted closed-shell problems. For open-shell problems, unrestricted Hartree−Fock (UHF), restricted open-shell Hartree−Fock (ROHF), and complete active space self-consistent field (CASSCF) computations are usually performed instead. Because of spin contamination, the UHF wave function and its corresponding MP perturbation series will not be discussed here further. Because no single particle operator is properly defined for ROHF and CASSCF orbitals, the application of MP perturbation series is largely limited. Although Epstein−Nesbet partition[2] can be used sometimes as an alternative, yet its corresponding perturbation series are not size extensive.[3] It is because the perturbation series are not invariant with respect to the orbital unitary transformation.[4]

Encouraged by the success of the MP partition for restricted closed-shell problems, many perturbation approaches[3,5−19] have been attempted for open-shell problems. The basic strategy is to define an analogous single particle operator such as the Fock operator based on a physical intuition or a mathematical consideration. Among these methods, to list just a few, there are opt1 and opt2,[6] and MROPT,[7] of Davidson's group, and MRMP2[8] of Hirao, CASPT2 and CASPT3 of Roos.[11] The interested reader can find more details from ref 20.

Rintelman et al.[21] investigated extensively the size extensivity problem of MRMP2[8] and CASPT2[11] with a series of basis sets and three challenging molecules, HF, N_2, and F_2, which are stretched away from their equilibrium geometries to have some multireference character. Rolik et al. presented a multireference perturbation theory.[17] Szabados et al. reformulated it later and obtained a size extensive second-order theory.[18] However, higher orders of the series violate the size-extensivity requirement. On the basis of the multireference perturbation theory by Chen et al.,[22] we derived a size extensive second-order multireference perturbation theory through a theoretical analysis on a supermolecule consisting of N noninteracting H_2 molecules.[19]

In this paper, a new single reference perturbation partition is proposed for ROHF and CASSCF orbitals. The size extensivity as well as the accuracy of the first three-order perturbation energies based on this partition will be examined numerically. The single reference nature of the present partition will also be investigated with the CH_2 and SiH_2 radicals.

* Corresponding author. E-mail: chenfeiwu@sas.ustb.edu.cn.

10.1021/ct800546g CCC: $40.75
Published on Web 02/23/2009

2. Theory

ROHF and CASSCF are two common approaches for open-shell problems. CASSCF are also widely used to account for the nondynamic correlation energy in multireference problems. ROHF orbitals and orbital energies are obtained for a given system by minimizing its electronic energy E[37]

$$E = 2\sum_k \langle k|\hat{h}|k\rangle + \sum_{k,l}[2(kl|\hat{g}|kl) - (kl|\hat{g}|lk)] + f(2\sum_m \langle m|\hat{h}|m\rangle + f\sum_{m,n}[2a(mn|\hat{g}|mn) - b(mn|\hat{g}|nm)] + 2\sum_k\sum_m[2(km|\hat{g}|km) - (km|\hat{g}|mk)])$$

where a, b, and f are constants, indices k and l are used for closed-shell orbitals, m and n for open-shell obitals, $\hat{h}$ and $\hat{g}$ are one- and two-particle operators respectively. A CASSCF wave function for a given system has the following form

$$\Psi = \sum_k c_k \Phi_k$$

where Φ_k is a configuration function. These configurations are constructed by a complete distribution of a number of active electrons among a set of active orbitals.[38] The CASSCF wave function can be regarded as a small full configuration interaction function. But it is optimized variationally not only with respect to the expansion coefficients c_k but also with respect to the orbitals within the configuration Φ_k.

In order to apply Rayleigh−Schrödinger perturbation theory to the problems discussed above a zero-th Hamiltonian should be defined at first. Similar to the Fock operator, a single particle operator $\hat{F}$ for a ROHF or CASSCF orbital ϕ_i is defined implicitly below

$$\hat{F}\varphi_i = \varepsilon_i\varphi_i \tag{1}$$

provided that all orbitals are orthonormalized with each other. The eigenvalue ε_i is the orbital energy of the corresponding orbital ϕ_i, which is originally from a ROHF or CASSCF calculation. For a restricted closed-shell problem the operator $\hat{F}$ is reduced to the Fock operator. For other cases, an explicit form of the operator $\hat{F}$ is in general unknown or maybe does not exist in reality. However, the information given in eq 1 is enough to define the zero-th Hamiltonian $\hat{H}_0$ in Rayleigh−Schrödinger perturbation theory. Of course, some kind of generalized Fock operator may be defined explicitly for these cases. However, the reason that we do not follow this approach is that the orbitals optimized with ROHF and CASSCF have been well tested and widely used for years.

Corresponding to the single particle operator $\hat{F}$ in eq 1, the zero-th Hamiltonian $\hat{H}_0$ has the following form

$$\hat{H}_0 = \sum_i \hat{F}(i) \tag{2}$$

The summation in the above equation is carried out over all electrons in a system of interest. It is assumed that the eigenvalues and eigenfunctions of $\hat{H}_0$ are known as

$$\hat{H}_0\Phi_i^{(0)} = E_i^{(0)}\Phi_i^{(0)}, \quad i = 1, 2, 3, ...$$

In the current implementation of this perturbation theory, spin-adapted configuration interaction functions are used as $\Phi_i^{(0)}$. Thus, $E_i^{(0)}$ is just a sum of the orbital energies of those molecular orbitals in the corresponding configuration function $\Phi_i^{(0)}$. The system Hamiltonian operator $\hat{H}$ can then be decomposed into two parts, $\hat{H}_0$ and $\hat{V}$, i.e.

$$\hat{H} = \hat{H}_0 + \lambda\hat{V} \tag{3}$$

where $\hat{V}$ is supposed to be a small perturbation operator to the unperturbed $\hat{H}_0$, λ is a perturbation parameter. With these preparations, application of the Rayleigh−Schrödinger perturbation theory to the atomic and molecular systems is straightforward. The corresponding perturbation formula[4,30] is

$$E_i = E_i^{(0)} + V_{ii}\lambda + \sum_{j\neq i}\frac{V_{ij}V_{ji}}{E_i^{(0)} - E_j^{(0)}}\lambda^2 + \left[\sum_{j,k\neq i}\frac{V_{ij}V_{jk}V_{ki}}{(E_i^{(0)} - E_j^{(0)})(E_i^{(0)} - E_k^{(0)})} - V_{ii}\sum_{j\neq i}\frac{V_{ij}V_{ji}}{(E_i^{(0)} - E_j^{(0)})^2}\right]\lambda^3 + ... \tag{4}$$

where $V_{ij} = \langle\Phi_i^{(0)}|\hat{V}|\Phi_j^{(0)}\rangle$, λ is set equal to unity for the final energy E_i.

For the purpose of comparison, the multireference perturbation series[22] are also included here

$$E_p = \varepsilon_p^{(0)} + \sum_{i,j\leq n}\sum_{a>n}\frac{u_p^{(0)}(i)H_{ia}H_{aj}u_p^{(0)}(j)}{\varepsilon_p^{(0)} - H_{aa}}\lambda^2 + \sum_{i,j\leq n}\sum_{\substack{a,b>n\\ a\neq b}}\frac{u_p^{(0)}(i)H_{ia}H_{ab}H_{bj}u_p^{(0)}(j)}{(\varepsilon_p^{(0)} - H_{aa})(\varepsilon_p^{(0)} - H_{bb})}\lambda^3 + ... \tag{5}$$

where $u_p^{(0)}(i)$ is the i-th component of the p-th eigenvector and $\varepsilon_p^{(0)}$ is the p-th eigenvalue in the reference space. The dimension of the reference space is n. H_{ij} is the Hamiltonian matrix element with respect to the i-th and j-th configuration functions. λ is a perturbation parameter as described in eq 4 and is set equal to unity for the final energy E_p.

3. Results and Discussion

For a supermolecular system composed of m monomers, which are separated by so large a distance that the interaction among them can be negligible, the size extensivity error (SEE) can then be defined as

$$\text{SEE} = E(A_1 + A_2 + ... + A_m) - [E(A_1) + E(A_2) + ... + E(A_m)] \tag{6}$$

If the monomers are the same, the SEE can be computed as follows

$$\text{SEE} = E(m \times A)/m - E(A) \tag{7}$$

Equation 7 is used for all SEE calculations in this study.

All ROHF and CASSCF orbitals and orbital energies in this study were calculated with GAMESS[23] and Gaussian.[36]

Table 1. Size Extensivity Error (hartree) Check for N_2, HF, and F_2 Supermolecules

method	SRPT1	SRPT2	SRPT3
no. of HFs		CASSCF(2,2)	
1	0	0	0
2	0.00000000	−0.00000000	0.00000000
3	0.00000000	−0.00000000	0.00000000
4	0.00000000	−0.00000000	0.00000000
no. of F_2s		CASSCF(2,2)	
1	0	0	0
2	0.00000000	−0.00000008	0.00000005
3	0.00000000	−0.00000008	−
4	0.00000000	−0.00000008	−
		N_2 dimer	
CASSCF(2,2)	0.00000000	0.00000000	−0.00000000
CASSCF(4,4)	0.00000000	0.00000000	0.00000000
CASSCF(6,6)	0.00000000	0.00000000	−0.00000001

MELDF[24] and our group programs were used to calculate matrix elements and perturbation energies.

A. Size Extensivity Test. As discussed in the first part of this paper, Rintelman et al. [21] investigated the size extensivity error with three molecular series, HF, N_2, and F_2, and several different levels of basis sets, Pople's 6−31G(d,p),[25,26] 6−311G(d,p),[27] and Dunning's cc-pVDZ, cc-pVTZ, and cc-pVQZ.[28] It was shown that the SEEs increased as the basis set was enlarged. However, the changes are not so much, and the errors are almost at the same order of magnitude. On the basis of this observation, only 6−31G(d,p) for the above three molecular series is used in this study. The stretched bond lengths of HF, N_2, and F_2 are the same as in ref 21 and are 1.60 Å, 1.50 Å, and 1.50Å, respectively. The distance between monomers of N_2 and F_2 is 200 Å to make sure that interactions between monomers can be neglected. However, the distance between HF monomers is 2000 Å in order to quench the possible dipole−dipole interactions. The CASSCF convergence threshold is 10^{-8} for supermolecular series of HF, F_2, and N_2.

In Table 1, SEEs are calculated with the first-, second-, and third-order perturbation theory in eq 4 (denoted as SRPT1, SRPT2, and SRPT3) with partition eq 2. Results of HF supermolecules are listed in the upper part of the table. The complete active space is CASSCF(2,2). SEE is very small and is less than the CASSCF convergence threshold. As the basis set changes to 6−31G, the unpublished SEEs are still at about the same level. The effects of HF geometries on the SEE have also been investigated though the results have not been presented in the Table 1. The bond length of HF is chosen as 1.4 Å, which is between the equilibrium bond length[30] 0.92 Å and the elongated bond length 1.6 Å studied above. These unpublished SEEs calculated with basis set 6−31G and 6−31G(d,p) are all also less than the CASSCF convergence threshold.

In the middle part of the Table 1 are the results of F_2 supermolecules. They are more challenging examples for the SEE test. The active space is CASSCF(2,2) which is the same as used in the HF case. The core orbital 1*s* of the fluorine atom is frozen in the calculations. The SEEs are all at the order of 10^{-8} hartree. Though they are slightly larger than the results of HF supermolecules, SEEs are still at the same level as the convergence threshold set for CASSCF calculations. Thus, the SEEs are not from the perturbation theory itself but due to the accuracy of CASSCF.

The SEE results of N_2 dimer are listed in the bottom of the Table 1. Three different complete active spaces, CASSCF(2,2), CASSCF(4,4), and CASSCF(6,6) are exploited to investigate the impact of active spaces on SEE. The absolute values of SEEs are below or close to the accuracy threshold 10^{-8} set for CASSCF calculations. These results indicate that SEEs are not dependent on the active space.

The SEEs of the above three molecular series are the smallest numerical data available in the literature so far. They are only dependent on the accuracy of CASSCF calculations. On the basis of this numerical observation, it is concluded that the first three-order perturbation energies with the partition eq 2 are size extensive.

Table 2. Total Energies (hartree) for the Ground State of H_2O Calculated with Different Methods

method	CASSCF(2,2)	CASSCF(4,4)	CASSCF(6,6)
CASSCF	−76.028093	−76.073481	−76.108960
MRCI	−76.214391	−76.227688	−76.229860
MRCI+Q	−76.232834	−76.241006	−76.243466
MRPT2	−76.261841	−76.249367	−76.234849
MRPT3	−76.214391	−76.221040	−76.227849
SRPT1	−76.023135	−76.022580	−76.022519
SRPT2	−76.215623	−76.223225	−76.223123
SRPT3	−76.223403	−76.220441	−76.220101

Table 3. Total Energies (hartree) for the Ground State of NH_3 Calculated with Different Methods

method	CASSCF(2,2)	CASSCF(4,4)	CASSCF(6,6)
CASSCF	−56.206428	−56.236639	−56.266567
MRCI	−56.392364	−56.396398	−56.399209
MRCI+Q	−56.405136	−56.410243	−56.413800
MRPT2	−56.423838	−56.413585	−56.403748
MRPT3	−56.389412	−56.392987	−56.397138
SRPT1	−56.195183	−56.194773	−56.194503
SRPT2	−56.381911	−56.383932	−56.385328
SRPT3	−56.393340	−56.391289	−56.389208

B. Total Energies of H_2O, NH_3, and CH_4. Experimental geometries[30] of H_2O, NH_3, and CH_4 are used. The basis set is the Pople's 6−31G(d, p).[25,26] Total energies of H_2O, NH_3, and CH_4 at the ground states are calculated with the first three-order perturbation theory with partition eq 2 and are compared with other methods: CASSCF, multireference configuration interaction (MRCI), MRCI with Davidson correction[29] (MRCI + Q), and multireference second- and third-order perturbation theory (MRPT2 and MRPT3) in eq 5.

The results are listed in Table 2, Table 3, and Table 4. It can be seen from the tables that total energies are improved substantially with MRCI+Q over the results of MRCI. MRPT2 overestimates the energies especially with a small complete active space like CASSCF(2,2) in comparison with MRCI results. MRPT3 counteracts these discrepancies significantly. As the complete active space increases from CASSCF(2,2) to CASSCF(6,6) the MRPT2 and MRPT3 results converges very closely to MRCI energies. As expected, the CASSCF energies, which is actually the multireference zeroth-order energies, becomes lower as the CASSCF active space enlarged.

Table 4. Total Energies (hartree) for the Ground State of CH_4 Calculated with Different Methods

method	CASSCF(2,2)	CASSCF(4,4)	CASSCF(6,6)
CASSCF	−40.217021	−40.235347	−40.257266
MRCI	−40.385722	−40.383480	−40.385818
MRCI+Q	−40.397641	−40.395588	−40.398550
MRPT2	−40.405016	−40.392464	−40.387637
MRPT3	−40.386805	−40.382938	−40.384963
SRPT1	−40.201530	−40.201327	−40.201130
SRPT2	−40.369367	−40.364530	−40.365727
SRPT3	−40.386128	−40.379376	−40.378295

The single reference calculations are listed at the bottom of the Table 2, 3, and 4. Unlike the CASSCF energies, the ground-state energies of SRPT1 are almost unchanged with respect to the three types of CASSCF wave functions. This is also true for the energies calculated with SRPT2 and SRPT3. The reason for this is that the perturbation series in eq 4 considers only the ground-state configuration and its corresponding excitation configurations such as the single and double excitation configurations. Therefore, the nondynamical correlation from the CASSCF wave functions has not been taken into account. In this sense, it may be said that the present perturbation theory is not sensitive to the CASSCF orbitals. Nevertheless, like the Møller−Plesset second-order perturbation theory, SRPT2 recovers most of the correlation energy. The biggest energy difference between MRCI and SRPT3 is 10^{-2} hartree for NH_3. The energy differences for H_2O and CH_4 are at the order of 10^{-3} hartree. Considering the cheap computational cost of the single reference perturbation theory, the performances of SRPT2 and SRPT3 are satisfactory.

C. The Singlet−Triplet Separation in CH_2 and SiH_2. Computations of the singlet−triplet separation in CH_2 are a challenging problem for any perturbation theory. Detailed discussions on this can be found in ref 20. The purpose here is to investigate whether the present partition can be applied to a multireference problem. As can be seen from the above discussions in part B, the first three-order energies of the present partition are not changed so much though the complete active space is enlarged. Since they are essentially single reference problems in nature, the above three test cases may be not good enough to show the single reference character inherent in the present partition. Because of its well-known multireference character, CH_2 can be regarded as a proper example to fulfill the present purpose.

The calculations are performed with the DZP basis and the theoretically optimized geometry as used by Bauschlicher and Taylor.[31] The 1s orbital of CH_2 is frozen during the calculations. In Table 5 only single reference perturbation calculations are presented. The singlet−triplet separations are listed in the last column. It can be seen from the upper part of the table that the singlet−triplet gaps are still far away from the FCI result if only RHF orbitals for the singlet state and ROHF orbitals for the triplet state are used for the calculations. But the gaps listed in the lower part of the table are still not improved even with CASSCF(2,2) and CASSCF(6,6) orbitals for the singlet state. As pointed out by Bauschlicher and Taylor,[31] there are two important configurations in the singlet state. Thus, the possible reason for the above failure may be due to the fact that the perturbation series with partition eq 2 is a single reference perturbation theory and cannot solve the multireference problem of the singlet state. In order to check this, the multireference second- and third-order calculations, MRPT2 and MRPT3 in eq 4, have been performed for the singlet state with CASSCF(2,2) and CASSCF(6,6) active spaces. The results are presented in Table 6. It can be seen clearly from the table that the singlet−triplet gaps are improved considerably in comparison with the results listed in Table 5 and are close to the FCI result.[31] As the active spaces are increased from CASSCF(2,2) to CASSCF(6,6), the gaps are getting much closer to the FCI result. The best result was obtained with CASSCF(6,6) at the third-order level. The gap is only 0.22 kcal/mol bigger than the FCI result.

Table 5. The Singlet−Triplet Separation in CH_2 Calculated with Single Reference Perturbation Theory

method	$^1A_1$ (hartree)	$3B_1$ (hartree)	Δ (kcal/mol)
FCI[a]	−39.027183	−39.046260	11.97
method	RHF	ROHF	Δ (kcal/mol)
SRPT1	−38.886297	−38.927947	26.14
SRPT2	−38.996127	−39.042348	29.00
SRPT3	−39.016593	−39.043335	16.78
method	CASSCF(2,2)	ROHF	Δ (kcal/mol)
SRPT1	−38.885662	−38.927947	26.53
SRPT2	−38.998686	−39.042348	27.40
SRPT3	−39.017087	−39.043335	16.47
method	CASSCF(6,6)	ROHF	Δ (kcal/mol)
SRPT1	−38.885298	−38.927947	26.76
SRPT2	−39.000520	−39.042348	26.25
SRPT3	−39.015873	−39.043335	17.23

[a] See ref 31.

Table 6. The Singlet−Triplet Separation in CH_2 Calculated with the Single- And Multireference Perturbation Theory

method	$^1A_1$ (hartree)	$3B_1$ (hartree)	Δ (kcal/mol)
FCI[a]	−39.027183	−39.046260	11.97
method	MRPT + CASSCF(2,2)	SRPT + ROHF	Δ (kcal/mol)
2nd order	−39.027875	−39.042348	9.08
3rd order	−39.023129	−39.043335	12.68
method	MRPT + CASSCF(6,6)	SRPT + ROHF	Δ (kcal/mol)
2nd order	−39.025273	−39.042348	10.71
3rd order	−39.023912	−39.043335	12.19

[a] See ref 31.

Another example for this preliminary test is SiH_2. The geometries for the singlet and triplet state are the same as that used by Bauschlicher and Taylor.[32] The basis sets for H is the Dunning's double-ζ basis set[33] with a 2p polarization function ($\alpha = 1.0$) added. The basis set for Si is [5s3p] contractions of the Huzinaga[34] (12s8p) Si basis given by McLean and Chandler[35] with a 3d polarization function ($\alpha = 0.3$) added. The 3s component of the 3d set is deleted. These basis sets for SiH_2 are the same as that in the original work of Bauschlicher and Taylor.[32]

Table 7. The Singlet−Triplet Separation in SiH_2 Calculated with the Single- and Multireference Perturbation Theory

method	$^1A_1$ (hartree)	$3B_1$ (hartree)	Δ (kcal/mol)
FCI[a]	−290.110207	−290.082313	17.5
	MRPT + CASSCF(2,2)	SRPT + ROHF	
2nd order	−290.106628	−290.072361	21.5
3rd order	−290.106525	−290.078602	17.5
	MRPT + CASSCF(6,6)	SRPT + ROHF	
2nd order	−290.104278	−290.072361	20.0
3rd order	−290.106201	−290.078602	17.3

[a] See ref 32.

In all calculations only the outer-shell six electrons of the SiH_2 radical are considered for correlation. Like the CH_2 case, the single reference perturbation theory is also not enough to describe the singlet state. Therefore, multireference perturbation calculations with CASSCF(2,2) and CASSCF(6,6) orbitals have been carried out instead. As for the triplet state, it is found that the energies calculated with ROHF orbitals and single reference perturbation theory, especially the SRPT3, are comparable to the full CI result obtained by Bauschlicher and Taylor.[32] All results are summarized in Table 7. In comparison with the FCI result, the errors of the singlet−triplet gaps calculated with SRPT2 and MRPT2 are 4 and 3.5 kcal/mol for CASSCF(2,2) and CASSCF(6,6), respectively. However, as the perturbation level increases to the third-order, i.e., SRPT3 for the triplet and MRPT3 for the singlet, the errors of the singlet−triplet gaps becomes surprisingly small, i.e., zero for CASSCF(2,2) and 0.2 kcal/mol for CASSCF(6,6).

The above calculations in parts B and C demonstrate that the single reference perturbation theory with the partition eq 2 is valid and effective for single reference problems whenever ROHF and CASSCF orbitals are available. More studies with the present theory for open-shell problems such as the geometry optimization are under investigation.

4. Conclusions

A single reference perturbation theory with a new partition is presented. The perturbation partition has been proposed for ROHF and CASSCF orbitals. Through numerical studies on the size extensivity test with HF, F_2, and N_2 supermolecules, it has been shown that the first three-order perturbation series with the present partition are size extensive. The ground-state energies of H_2O, NH_3, and CH_4 calculated with the present perturbation partition are accurate. The biggest energy difference between MRCI and SRPT3 is 10^{-2} hartree for NH_3. The energy differences for H_2O and CH_4 are at the order of 10^{-3} hartree. The single reference nature of present partition has also been demonstrated with the computations on the singlet−triplet gap of the CH_2 and SiH_2 radicals.

The present perturbation partition can be considered as a natural extension of Møller−Plesset partition beyond Hartree−Fock orbitals and can be used for single reference problems where the perturbation theory with the Møller−Plesset partition is not applicable.

Acknowledgment. The author would like to thank the National Natural Science Foundation of China (grant nos. 20473011 and 20773011) for financial support.

References

(1) Møller, C.; Plesset, M. S. *Phys. Rev.* **1934**, *46*, 618.

(2) (a) Epstein, P. S. *Phys. Rev.* **1926**, *28*, 695. (b) Nesbet, R. K. *Proc. R. Soc. London Ser. A* **1955**, *230*, 312.

(3) Witek, H. A.; Nakano, H.; Hirao, K. *J. Chem. Phys.* **2003**, *118*, 8197.

(4) Chen, F. *Computational methods in quantum chemistry*; Science Press: Beijing, P. R. China, 2008; pp 166−170.

(5) Davidson, E. R.; MacMurchie, L. E.; Day, S. J. *J. Chem. Phys.* **1981**, *74*, 5491.

(6) Murray, C. W.; Davidson, E. R. *Chem. Phys. Lett.* **1991**, *187*, 451.

(7) (a) Kozlowski, P. W.; Davidson, E. R. *J. Chem. Phys.* **1994**, *100*, 3672. (b) Kozlowski, P. W.; Davidson, E. R. *Chem. Phys. Lett.* **1994**, *222*, 615. (c) Kozlowski, P. W.; Davidson, E. R. *Chem. Phys. Lett.* **1994**, *226*, 440. (d) Kozlowski, P. W.; Davidson, E. R. *Int. J. Quantum Chem.* **1995**, *53*, 149.

(8) (a) Hirao, K. *Chem. Phys. Lett.* **1992**, *190*, 374–380. (b) Hirao, K. *Chem. Phys. Lett.* **1992**, *196*, 397–403. (c) Hirao, K. *Chem. Phys. Lett.* **1993**, *201*, 59.

(9) Dyall, K. G. *J. Chem. Phys.* **1995**, *102*, 4909.

(10) Werner, H. J. *Mol. Phys.* **1996**, *89*, 645.

(11) Roos, B. O.; Andersson, K.; Fulscher, M. K.; Malmqvist, P.-A.; Serrano-Andres, L.; Pierloot, K.; Merchan, M. *Adv. Chem. Phys.* **1996**, *93*, 219.

(12) Knowles, P. J.; Andrews, J. S.; Amos, R. D.; Handy, N. C.; Pople, J. A. *Chem. Phys. Lett.* **1991**, *186*, 130.

(13) Lauderdale, W. J.; Stanton, J. F.; Gauss, J.; Watts, J. D.; Barttlett, R. J. *Chem. Phys. Lett.* **1991**, *87*, 21.

(14) (a) Head-Gordon, M.; Oumi, M.; Maurice, D. *Mol. Phys.* **1999**, *96*, 593. (b) Head-Gordon, M.; Maslen, P. E.; White, C. A. *J. Chem. Phys.* **1998**, *108*, 616. (c) Maslen, P. E.; Head-Gordon, M. *Chem. Phys. Lett.* **1998**, *283*, 102.

(15) Angeli, C.; Cimiraglia, R.; Evangelisti, S.; Leininger, T.; Malrieu, J.-P. *J. Chem. Phys.* **2001**, *114*, 10252.

(16) (a) Wolinski, K.; Seller, H. L.; Pulay, P. *Chem. Phys. Lett.* **1987**, *140*, 225–231. (b) Wolinski, K.; Pulay, P. *J. Chem. Phys.* **1989**, *90*, 3647. (c) Van Dam, B. J. J.; Van Lenthe, J. H.; Pulay, P. *Mol. Phys.* **1998**, *93*, 431.

(17) Rolik, Z.; Szabados, Á.; Surján, P. R. *J. Chem. Phys.* **2003**, *119*, 1922.

(18) Szabados, A.; Rolik, Z.; Tóth, G.; Surján, P. R. *J. Chem. Phys.* **2005**, *122*, 114104.

(19) Chen, F. *Sci. China Ser. B* **2007**, *50*, 483.

(20) Davidson, E. R.; Jarzecki, A. A. Multi-reference perturbation theory. In *Recent Advances in Computational Chemistry*; Hirao, K., Ed.; World Scientific Publishing: Singapore, 1999; Vol. 4, pp31−63.

(21) Rintelman, J. M.; Adamovic, I.; Varganov, S.; Gordon, M. S. *J. Chem. Phys.* **2005**, *122*, 044105.

(22) Chen, F.; Davidson, E. R.; Iwata, S. *Int. J. Quantum Chem.* **2002**, *86*, 256.

(23) Gamess Schmidt, M. W.; Baldridge, K. K.; Boatz, J. A.; Elbert, S. T.; Gordon, M. S.; Jensen, J. H.; Koseki, S.; Natsunaga, N.; Nguyen, K. A.; Su, S. J.; Windus, T. L.; Dupuis, M.; Montgomery, J. A. *J. Comput. Chem.* **1993**, *14*, 1347.

(24) MELD is a set of electronic structure programs written by McMurchie L. E., Elbert, S. T.; Langhoff S. R.; Davidson, E. R. with extensive modifications by Feller, D.; Rawlings, D. C. Available from http://php.indiana.edu/∼davidson.

(25) Hehre, W. J.; Ditchfield, R.; Pople, J. A. *J. Chem. Phys.* **1972**, *56*, 2257.

(26) (a) Ditchfield, R.; Hehre, W. J.; Pople, J. A. *J. Chem. Phys.* **1971**, *54*, 724. (b) Hariharan, P. C.; Pople, J. A. *Theor. Chim. Acta* **1973**, *28*, 213.

(27) Krishnan, R.; Binkley, J. S.; Seeger, R.; Pople, J. A. *J. Chem. Phys.* **1980**, *72*, 650.

(28) Dunning, T. H., Jr. *J. Chem. Phys.* **1989**, *90*, 1007.

(29) Langhoff, S. R.; Davidson, E. R. *Int. J. Quantum Chem.* **1974**, *8*, 61.

(30) Szabo, A.; Ostlund, N. S. *Modern Quantum Chemistry: Introduction to Advanced Electronic Structure Theory*; Macmillan: New York, 1982.

(31) Bauschlisher, C. W.; Taylor, R. P. *J. Chem. Phys.* **1986**, *85*, 6510.

(32) Bauschlisher, C. W.; Taylor, R. P. *J. Chem. Phys.* **1987**, *86*, 1420.

(33) Dunning, Jr., T. H. *J. Chem. Phys.* **1970**, *53*, 2823.

(34) Huzinaga, S. Department of Chemistry Report, University of Alberta, Edmonton, Alberta, Canada, 1971.

(35) McLean, A. D.; Chandler, G. S. *J. Chem. Phys.* **1980**, *72*, 5639.

(36) Frisch, M. J.; Trucks, G. W.; Schlegel, H. B.; Scuseria, G. E.; Robb, M. A.; Cheeseman, J. R.; Montgomery, J. A., Jr.; Vreven, T.; Kudin, K. N.; Burant, J. C.; Millam, J. M.; Iyengar, S. S.; Tomasi, J.; Barone, V.; Mennucci, B.; Cossi, M.; Scalmani, G.; Rega, N.; Petersson, G. A.; Nakatsuji, H.; Hada, M.; Ehara, M.; Toyota, K.; Fukuda, R.; Hasegawa, J.; Ishida, M.; Nakajima, T.; Honda, Y.; Kitao, O.; Nakai, H.; Klene, M.; Li, X.; Knox, J. E.; Hratchian, H. P.; Cross, J. B.; Bakken, V.; Adamo, C.; Jaramillo, J.; Gomperts, R.; Stratmann, R. E.; Yazyev, O.; Austin, A. J.; Cammi, R.; Pomelli, C.; Ochterski, J. W.; Ayala, P. Y.; Morokuma, K.; Voth, G. A.; Salvador, P.; Dannenberg, J. J.; Zakrzewski, V. G.; Dapprich, S.; Daniels, A. D.; Strain, M. C.; Farkas, O.; Malick, D. K.; Rabuck, A. D.; Raghavachari, K.; Foresman, J. B.; Ortiz, J. V.; Cui, Q.; Baboul, A. G.; Clifford, S.; Cioslowski, J.; Stefanov, B. B.; Liu, G.; Liashenko, A.; Piskorz, P.; Komaromi, I.; Martin, R. L.; Fox, D. J.; Keith, T.; Al-Laham, M. A.; Peng, C. Y.; Nanayakkara, A.; Challacombe, M.; Gill, P. M. W.; Johnson, B.; Chen, W.; Wong, M. W.; Gonzalez, C.; Pople, J. A. *Gaussian 03W, revision D.01*; Gaussian, Inc.: Wallingford, CT, 2004.

(37) Roothaan, C. C. *Rev. Mod. Phys.* **1960**, *32*, 179.

(38) (a) Roos, B.; Tayor, P.; Siegbahn, P. *Chem. Phys.* **1980**, *48*, 157. (b) Siegbahn, P.; Heiberg, A.; Roos, B.; Levy, B. *Phys. Scr.* **1980**, *21*, 323. (c) Siegbahn, P.; Almlof, J.; Heiberg, A.; Roos, B. *J. Chem. Phys.* **1981**, *74*, 2384.

CT800546G

JCTC Journal of Chemical Theory and Computation

Adaptive Finite Element Method for Solving the Exact Kohn−Sham Equation of Density Functional Theory

Eric J. Bylaska,*,† Michael Holst,*,‡ and John H. Weare*,§

William R. Wiley Environmental Molecular Sciences Laboratory, Pacific Northwest National Laboratory, P.O. Box 999, Richland, Washington 99352, and Department of Mathematics and Department of Chemistry and Biochemistry, University of California, San Diego, La Jolla, California 92093

Received August 26, 2008

Abstract: Results of the application of an adaptive piecewise linear finite element (FE) based solution using the FETK library of M. Holst to a density functional theory (DFT) approximation to the electronic structure of atoms and molecules are reported. The severe problem associated with the rapid variation of the electronic wave functions in the near singular regions of the atomic centers is treated by implementing completely unstructured simplex meshes that resolve these features around atomic nuclei. This concentrates the computational work in the regions in which the shortest length scales are necessary and provides for low resolution in regions for which there is no electron density. The accuracy of the solutions significantly improved when adaptive mesh refinement was applied, and it was found that the essential difficulties of the Kohn−Sham eigenvalues equation were the result of the singular behavior of the atomic potentials. Even though the matrix representations of the discrete Hamiltonian operator in the adaptive finite element basis are always sparse with a linear complexity in the number of discretization points, the overall memory and computational requirements for the solver implemented were found to be quite high. The number of mesh vertices per atom as a function of the atomic number Z and the required accuracy ε (in atomic units) was estimated to be $v(\varepsilon, Z) \approx 122.37(Z^{2.2346}/\varepsilon^{1.1173})$, and the number of floating point operations per minimization step for a system of N_A atoms was found to be $O(N_A{}^3 v(\varepsilon, Z))$ (e.g., with $Z = 26$, $\varepsilon = 0.0015$ au, and $N_A = 100$, the memory requirement and computational cost would be ∼0.2 terabytes and ∼25 petaflops). It was found that the high cost of the method could be reduced somewhat by using a geometric-based refinement strategy to fix the error near the singularities.

1. Introduction

Kohn−Sham density functional theory (DFT)[1,2] which can be used to predict the structures, properties, and reactivities for a wide variety of solid state and molecular systems has become a state of the art tool. In many cases it can achieve chemical accuracy at a smaller cost than traditional quantum chemistry methods. It is now routine at this level of theory to perform simulations containing hundreds of atoms, and on today's parallel supercomputers, simulations containing over a thousand atoms are feasible; making realistic descriptions of material surfaces and defects possible. While current implementations of DFT are very efficient and the results are adequate for many cases,[3,4] the much wider application of these approaches to the even more demanding systems encountered in complex technology problems are limited. The limitations are that they use basis sets[5,6] and/or pseudopotentials[7] that are highly engineered, they scale as $O(N_A{}^3)$

* E-mail: eric.bylaska@pnl.gov (E.J.B.); mholst@ucsd.edu (M.H.); jweare@ucsd.edu (J.H.W.).

† Pacific Nortwest National Laboratory.

‡ Department of Mathematics, University of California, San Diego.

§ Department of Chemistry and Biochemistry, University of California, San Diego.

10.1021/ct800350j CCC: $40.75
Published on Web 03/05/2009

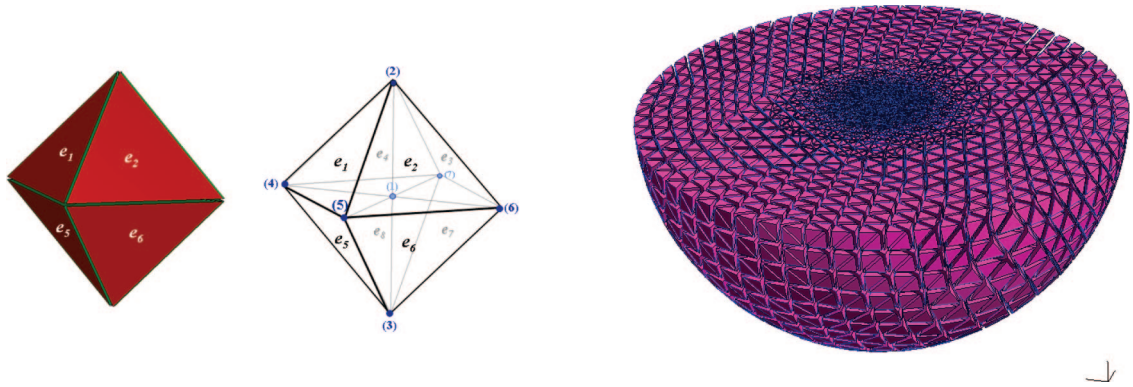

Figure 1. Examples of 3D finite element meshes. (left) Tetrahedral domain containing 8 elements and 7 vertex nodes. The elements are labeled e_l, and the nodes are labeled (m) in this figure. (right) Adaptive hemisphere domain containing 453 608 elements and 81 406 vertex nodes.

or $O(N_A^4)$ in the number of atoms, and the parallel scalings of existing solution methods are not good enough to exploit the performance of the next generation parallel computers. Hence, there is still a need to investigate other computational methods for solving DFT.

There have been a number of efforts to develop fast ab initio solvers based on real space solutions to the DFT equations.[8−27] Uniform finite difference gridding coupled with multilevel solvers has led to significant progress in the calculation of large systems[8−14] with large numbers of processors (~10 000 processors).[10] While these methods are often robust enough for predicting structural properties, they are not very efficient for describing multiple length scales and as a result do not have an accurate description near the atomic centers. In particular, when the interaction between the electron and the nucleus is described by the proper singular potential, $-(Ze/|\vec{r} - \vec{R}_I|)$, the singular behavior at $|\vec{r} - \vec{R}_I|$ can cause trouble with convergence. In fact, this kind of potential cannot be represented by uniform meshes methods. Adaptive finite element methods on the other hand, which can telescope down to the singularity, can in principle describe this kind of potential, and if used with a low order elements (i.e., piecewise finite elements) all the quantum mechanical operators can be represented by $O(N)$ sparse matrices, which can in principle limit the communications per processor to be $O(1)$.

Even though adaptive real space methods for DFT have shown some promise for describing singular electron−ion interactions, these methods have needed to use large number of elements for high Z atoms to describe the singular potential accurately. Earlier work by Bylaska et al.,[18] in which they developed a multilevel eigenvalue solver based on structured adapted mesh refinement and finite difference gridding worked well for simple systems such as H, and H_2^+. However, by $Z = 10$ (i.e., N_e), errors as large as 1 hartree were seen with this approach. These large errors led Kohn et al. to replace the atomic singular potentials with pseudopotentials and replace the finite difference solver with an adaptive finite element solver.[19] This new solver improved the accuracy somewhat, but at the time, it was too computationally intensive to be considered as a practical alternative to standard DFT solvers. Recently, Fattebert et al. have revisited these solvers and have shown them to be competitive with fast Fourier transform (FFT) solvers when very stiff pseudopotentials are used;[20] however, this work still had to rely on using pseudopotentials. Recent work by Batcho using spectral element methods[24] and Harrison et al. using a multiwavelet (high-order) basis,[21−23] has also been shown to be computationally competitive with standard DFT solvers and in some cases surpass them.

In this paper, we present an overview of our implementation of an unstructured adaptive finite element (FE) first principles solver and apply it to DFT equations which contain atomic singular potentials to estimate its overall memory and computational requirements. This solver is based on the FETK finite element framework of Holst.[28] The implementation is unique in that tetrahedral elements are used rather than parallelepipeds, and it also makes use of completely unstructured simplex meshes that have the advantage of being able to resolve the near singular features around atomic nuclei with minimal computational resources. This type solver has several potential advantages. It has compact support, it can be controlled by systematically increasing the number of the basis functions, it produces sparse matrices, it allows for the variable resolution in real space and can exactly represent potentials with "Z/r" singularities, and it does not require the use of a computationally intensive transform.

In section 2, a concise review of the FE method is given, and in section 3, the formulation of FE DFT equations is presented. In section 4, by using test problems which incorporate the critical issues of multiple length scales and the singular behavior of the potential, the overall memory and computational requirements per atom needed by the solver are estimated. The solver is then illustrated for several atoms and molecules including H, He, Li, Ne, H_2^+, and Li_2. Finally conclusions are given in section 5.

2. Background of the Finite Element (FE) Method

In the FE procedure,[29−34] the solution domain Ω (e.g., Figure 1) is divided up into connected polyhedral subregions or elements, $\{e_l\}_{l=1}^{L}$, where L is the number of elements. For each element e_l, a set of T_l nodes is chosen.

$$\{\vec{N}_t^{e_l} = (x_t^{e_l}, y_t^{e_l}, z_t^{e_l})\}_{t=1}^{T_l} \quad (1)$$

From these nodes, a global set of nodes is defined from the union of the element nodes,

$$\{\vec{N}_m\}_{m=1}^{M} = \cup_{l=1}^{L}\{\vec{N}_t^{e_l}\}_{t=1}^{T_l} \tag{2}$$

where M is the number of nodes in the finite element mesh. Nodes may be located at an element vertex, face, edge, or in its interior. A set of T_l basis functions are then defined for each element e_l. The basis functions are defined such that they are nonzero only inside the element, represented as simple low order polynomials, and have a value of 1 at its associated node, i.e.

$$\phi_t^{e_l}(\vec{x}) = \phi_t^{e_l}(x,y,z) = \sum_{n_1}\sum_{n_2}\sum_{n_3} a_{t,n_1,n_2,n_3} x^{n_1} y^{n_2} z^{n_3} \tag{3}$$

Using these basis functions, any piecewise polynomial function may be expanded as follows

$$u(\vec{x}) = \sum_{l=1}^{L}\sum_{t=1}^{T_l} \tilde{c}_{t,l}\phi_t^{e_l}(\vec{x}) \tag{4}$$

where $\tilde{c}_{t,\,l}$ are the expansion coefficients. This expansion is somewhat intricate given that neighboring elements share nodes with one another, which in turn results in certain expansion coefficients being equal to one another. For example, the expansion of a function using the finite element mesh shown in Figure 1 necessitates that the following coefficients be equal

$$\begin{aligned} c_1 = \tilde{c}_{11} = \tilde{c}_{12} = \tilde{c}_{13} = \tilde{c}_{14} = \tilde{c}_{15} = \tilde{c}_{16} = \tilde{c}_{17} = \tilde{c}_{18} \\ c_2 = \tilde{c}_{41} = \tilde{c}_{42} = \tilde{c}_{43} = \tilde{c}_{44} \\ c_3 = \tilde{c}_{45} = \tilde{c}_{46} = \tilde{c}_{47} = \tilde{c}_{48} \\ c_4 = \tilde{c}_{21} = \tilde{c}_{34} = \tilde{c}_{35} = \tilde{c}_{28} \\ c_5 = \tilde{c}_{22} = \tilde{c}_{31} = \tilde{c}_{36} = \tilde{c}_{25} \\ c_6 = \tilde{c}_{23} = \tilde{c}_{32} = \tilde{c}_{37} = \tilde{c}_{26} \\ c_7 = \tilde{c}_{24} = \tilde{c}_{34} = \tilde{c}_{38} = \tilde{c}_{27} \end{aligned} \tag{5}$$

To facilitate this mapping, a local to global index, $\tilde{m}(t, l)$, is defined. By using this index, the finite element expansion can then written as

$$u(\vec{x}) = \sum_{l=1}^{L}\sum_{t=1}^{T_l} c_{\tilde{m}(t,l)}\phi_t^{e_l}(\vec{x}) \tag{6}$$

Compared to eqs 5 and 6, this expansion is fairly uncomplicated. However, it can be simplified even further by introducing the following assembled finite element basis.

$$\eta_m(\vec{x}) = \sum_{l=1}^{L}\sum_{t=1}^{T_l} \phi_t^{e_l}(\vec{x})\delta_{m,\tilde{m}(t,l)} \tag{7}$$

With this assembled basis, the finite element expansion is

$$u(\vec{x}) = \sum_{m=1}^{M} c_m\eta_m(\vec{x}) \tag{8}$$

To facilitate the definition of the finite elements e_l and the corresponding basis functions as shown in eq 3, standard elements $\tilde{e}$ and their corresponding basis functions are introduced. This is done so that the basis functions and integrals for elements of different shapes are calculated readily, through a variable transformation, from the basis functions and integrals for a standard element. In this work, 3D tetrahedral elements with nodes at the vertices are used. The standard 3D tetrahedral element $\tilde{e}$ which covers the domain $[\tilde{x} = 0{:}1, \tilde{y} = 0{:}1 - \tilde{x}, \tilde{z} = 1 - \tilde{x} - \tilde{y}]$, is shown in Figure 2, and its standard local basis functions are

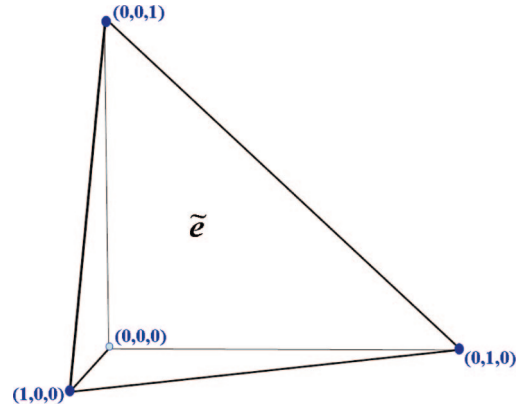

Figure 2. Standard 3D piecewise tetrahedral element.

$$\begin{aligned} \tilde{\phi}_1(\tilde{x},\tilde{y},\tilde{z}) &= 1 - \tilde{x} - \tilde{y} - \tilde{z} \\ \tilde{\phi}_2(\tilde{x},\tilde{y},\tilde{z}) &= \tilde{x} \\ \tilde{\phi}_3(\tilde{x},\tilde{y},\tilde{z}) &= \tilde{y} \\ \tilde{\phi}_4(\tilde{x},\tilde{y},\tilde{z}) &= \tilde{z} \end{aligned} \tag{9}$$

Integrals over the tetrahedral standard element,

$$I^{\tilde{e}}(\tilde{f}) = \int_{\tilde{e}} f(\vec{\tilde{x}})\,\mathrm{d}\vec{\tilde{x}} = \int_0^1 \mathrm{d}\tilde{z}\int_0^{1-\tilde{z}}\mathrm{d}\tilde{y}\int_0^{1-\tilde{z}-\tilde{y}}\mathrm{d}\tilde{x}\,\tilde{f}(\vec{\tilde{x}}) \tag{10}$$

can be computed for polynomial functions

$$\tilde{f}(\vec{\tilde{x}}) = \tilde{f}(\tilde{x},\tilde{y},\tilde{z}) = \tilde{x}^{n_1}\tilde{y}^{n_2}\tilde{z}^{n_3} \tag{11}$$

using the following analytic formula,

$$\begin{aligned} I^{\tilde{e}}(\tilde{x}^{n_1}\tilde{y}^{n_2}\tilde{z}^{n_3}) &= \int_0^1 \mathrm{d}\tilde{z}\int_0^{1-\tilde{z}}\mathrm{d}\tilde{y}\int_0^{1-\tilde{z}-\tilde{y}}\tilde{x}^{n_1}\tilde{y}^{n_2}\tilde{z}^{n_3} \\ &= \tilde{P}(n_1,0)\tilde{P}(n_2,n_1+1)\tilde{P}(n_3,n_1+n_2+2) \end{aligned} \tag{12}$$

where

$$\tilde{P}(a,b) = \sum_{k=0}^{b}\binom{b}{k}\frac{(-1)^k}{(a+k+1)} \tag{13}$$

Equations 12 and 13 are straightforward to compute. However, because the basis functions are only of a certain polynomial order $O(n)$, the integrals of eq 10 only need to be calculated to the same order in the finite element procedure. Therefore, the computation of the integrals of eq 10 can be further simplified by using a numerical method. In this work, the following formula is used

$$I^{\tilde{e}}(\tilde{f}) \approx \sum_{q=1}^{Q} w_q\tilde{f}(\vec{\tilde{x}}_q) \tag{14}$$

Table 1. 5-Point Tetrahedral Integration Points and Weights

formula type	points	weight
5-pt formula	(1/4, 1/4, 1/4)	−2/15
	(1/6, 1/6, 1/6)	3/40
	(1/2, 1/6, 1/6)	3/40
	(1/6, 1/2, 1/6)	3/40
	(1/6, 1/6, 1/2)	3/40

where $\{\vec{\tilde{x}}_q\}_{q=1}^{Q}$ and $\{w_q\}_{q=1}^{Q}$ are the integration point and weights respectively. Many different sets of integration points and weights can be constructed for use in eq 14; however, the computation will be more efficient for small Q. A 5-point formulation that can be used to integrate the standard 3D tetrahedral element to second-order is given in Table 1.

The affinte variable transformation is used to convert the basis function and integrals over an arbitrarily sized tetrahedral element e_l with vertices $\vec{x}_1^{e_l}$, $\vec{x}_2^{e_l}$, $\vec{x}_3^{e_l}$, and $\vec{x}_4^{e_l}$ in terms of a standard element $\tilde{e}$. This variable transformation is linear and invertible. It is defined by

$$\vec{x} = F^{e_l}\vec{\tilde{x}} + \vec{b}^{e_l} \tag{15}$$

or more explicitly by

$$\begin{aligned} x &= x_{e_l}(\tilde{x},\tilde{y},\tilde{z}) = F_{11}^{e_l}\tilde{x} + F_{12}^{e_l}\tilde{y} + F_{13}^{e_l}\tilde{z} + b_1^{e_l} \\ y &= y_{e_l}(\tilde{x},\tilde{y},\tilde{z}) = F_{21}^{e_l}\tilde{x} + F_{22}^{e_l}\tilde{y} + F_{23}^{e_l}\tilde{z} + b_2^{e_l} \\ z &= z_{e_l}(\tilde{x},\tilde{y},\tilde{z}) = F_{31}^{e_l}\tilde{x} + F_{32}^{e_l}\tilde{y} + F_{33}^{e_l}\tilde{z} + b_3^{e_l} \end{aligned} \tag{16}$$

where the matrix F^{e_l} is the Jacobean matrix and b^{e_l} is the location of the origin in the transformation.

$$F^{e_l} = \begin{bmatrix} (x_2^{e_l} - x_1^{e_l}) & (x_3^{e_l} - x_1^{e_l}) & (x_4^{e_l} - x_1^{e_l}) \\ (y_2^{e_l} - y_1^{e_l}) & (y_3^{e_l} - y_1^{e_l}) & (y_4^{e_l} - y_1^{e_l}) \\ (z_2^{e_l} - z_1^{e_l}) & (z_3^{e_l} - z_1^{e_l}) & (z_4^{e_l} - z_1^{e_l}) \end{bmatrix} \tag{17}$$

$$\vec{b}^{e_l} = \begin{bmatrix} x_1^{e_l} \\ y_1^{e_l} \\ z_1^{e_l} \end{bmatrix} \tag{18}$$

The inverse affine transformation is then

$$\vec{\tilde{x}} = (F^{e_l})^{-1}(\vec{x} - \vec{b}^{e_l})\vec{x} \tag{19}$$

or

$$\begin{aligned} \tilde{x} &= \tilde{x}_{e_l}(x,y,z) = (F^{e_l})_{11}{}^{-1}(x - b_1^{e_l}) + \\ &(F^{e_l})_{12}{}^{-1}(y - b_2^{e_l}) + (F^{e_l})_{13}{}^{-1}(z - b_3^{e_l}) \\ \tilde{y} &= \tilde{y}_{e_l}(x,y,z) = (F^{e_l})_{21}{}^{-1}(x - b_1^{e_l}) + \\ &(F^{e_l})_{22}{}^{-1}(y - b_2^{e_l}) + (F^{e_l})_{23}{}^{-1}(z - b_3^{e_l}) \\ \tilde{z} &= \tilde{z}_{e_l}(x,y,z) = (F^{e_l})_{31}{}^{-1}(x - b_1^{e_l}) + \\ &(F^{e_l})_{32}{}^{-1}(y - b_2^{e_l}) + (F^{e_l})_{33}{}^{-1}(z - b_3^{e_l}) \end{aligned} \tag{20}$$

where

$$\begin{aligned} (F^{e_l})_{11}{}^{-1} &= \frac{F_{22}^{e_l}F_{33}^{e_l} - F_{32}^{e_l}F_{23}^{e_l}}{|F^{e_l}|} \\ (F^{e_l})_{21}{}^{-1} &= \frac{F_{31}^{e_l}F_{23}^{e_l} - F_{21}^{e_l}F_{33}^{e_l}}{|F^{e_l}|} \\ (F^{e_l})_{31}{}^{-1} &= \frac{F_{21}^{e_l}F_{32}^{e_l} - F_{31}^{e_l}F_{22}^{e_l}}{|F^{e_l}|} \\ (F^{e_l})_{12}{}^{-1} &= \frac{F_{32}^{e_l}F_{13}^{e_l} - F_{12}^{e_l}F_{33}^{e_l}}{|F^{e_l}|} \\ (F^{e_l})_{22}{}^{-1} &= \frac{F_{11}^{e_l}F_{33}^{e_l} - F_{31}^{e_l}F_{13}^{e_l}}{|F^{e_l}|} \\ (F^{e_l})_{32}{}^{-1} &= \frac{F_{31}^{e_l}F_{12}^{e_l} - F_{11}^{e_l}F_{32}^{e_l}}{|F^{e_l}|} \\ (F^{e_l})_{13}{}^{-1} &= \frac{F_{12}^{e_l}F_{23}^{e_l} - F_{22}^{e_l}F_{13}^{e_l}}{|F^{e_l}|} \\ (F^{e_l})_{23}{}^{-1} &= \frac{F_{21}^{e_l}F_{13}^{e_l} - F_{11}^{e_l}F_{23}^{e_l}}{|F^{e_l}|} \\ (F^{e_l})_{33}{}^{-1} &= \frac{F_{11}^{e_l}F_{22}^{e_l} - F_{21}^{e_l}F_{12}^{e_l}}{|F^{e_l}|} \end{aligned} \tag{21}$$

Using this transformation, the global FE basis functions are written in terms of the standard local basis functions by

$$\phi_t^{e_l}(\vec{x}) = \begin{cases} \tilde{\phi}_t((F^{e_l})^{-1}\vec{x}) & \text{for } \vec{x} \in e_l \\ 0 & \text{otherwise} \end{cases} \tag{22}$$

and the gradients are written as

$$\frac{\mathrm{d}}{\mathrm{d}x^{(i)}}\phi_t^{e_l}(\vec{x}) = \begin{cases} \displaystyle\sum_{j=1}^{3}(F^{e_l})_{ji}{}^{-1}\frac{\mathrm{d}}{\mathrm{d}\tilde{x}^{(j)}}\tilde{\phi}_t((F^{e_l}\vec{x})) & \text{for } \vec{x} \in e_l \\ 0 & \text{otherwise} \end{cases} \tag{23}$$

With this transformation, the integral of a function f over an element is then

$$I^{e_l}(f) = \int_e f(\vec{x})\,\mathrm{d}\vec{x} \approx |F^{e_l}| \sum_{q=1}^{Q} w_q f(F^{e_l}\vec{\tilde{x}}_q) \tag{24}$$

The following element integrals are also needed for our adaptive multilevel finite element (FE) first principles solver.

$$G_r^{e_l}(f) = \int_{e_l}\phi_r^{e_l}(\vec{x})f(\vec{x})\,\mathrm{d}\vec{x} \approx |F^{e_l}| \sum_{q=1}^{Q}\tilde{\phi}_r(\vec{\tilde{x}}_q)f(F^{e_l}\vec{\tilde{x}}_q) \tag{25}$$

$$M_{rs}^{e_l} = \int_{e_l}\phi_r^{e_l}(\vec{x})\phi_s^{e_l}(\vec{x})\,\mathrm{d}\vec{x} \approx |F^{e_l}| \sum_{q=1}^{Q} w_q\tilde{\phi}_r(\vec{\tilde{x}}_q)\tilde{\phi}_s(\vec{\tilde{x}}_q) \tag{26}$$

$$K_{rs}^{e_l}(f) = \int_{e_l} \phi_r^{e_l}(\vec{x}) f(\vec{x}) \phi_s^{e_l}(\vec{x})\, \mathrm{d}\vec{x}$$

$$\approx |F^{e_l}| \sum_{q=1}^{Q} w_q \tilde{\phi}_r(\vec{\tilde{x}}_q) f(F^{e_l}\vec{\tilde{x}}_q) \tilde{\phi}_s(\vec{\tilde{x}}_q) \quad (27)$$

$$K_{rs}^{e_l}(u) = \int_{e_l} \phi_r^{e_l}(\vec{x}) \Big(\sum_{l'=1}^{L} \sum_{t=1}^{T_{l'}} c_{\tilde{m}(t,l')} \phi_t^{e_{l'}}(\vec{x}) \Big) \phi_s^{e_l}(\vec{x})\, \mathrm{d}\vec{x}$$

$$\approx |F^{e_l}| \sum_{q=1}^{Q} w_q \tilde{\phi}_r(\vec{\tilde{x}}_q) \Big(\sum_{t=1}^{T_l} c_{\tilde{m}(t,l)} \tilde{\phi}_t(\vec{\tilde{x}}_q) \Big) \tilde{\phi}_s(\vec{\tilde{x}}_q) \quad (28)$$

$$R_{rs}^{e_l}(f, \rho) = \int_{e_l} \phi_r^{e_l}(\vec{x}) f(\rho(\vec{x})) \phi_s^{e_l}(\vec{x})\, \mathrm{d}\vec{x}$$

$$\approx |F^{e_l}| \sum_{q=1}^{Q} w_q \tilde{\phi}_r(\vec{\tilde{x}}_q) f(\rho(F^{e_l}\vec{\tilde{x}}_q)) \tilde{\phi}_s(\vec{\tilde{x}}_q) \quad (29)$$

$$T_{rs}^{e_l} = \int_{e_l} \nabla \phi_r^{e_l}(\vec{x}) \cdot \nabla \phi_s^{e_l}(\vec{x})\, \mathrm{d}\vec{x}$$

$$\approx |F^{e_l}| \sum_{q=1}^{Q} w_q \Bigg[\sum_{i=1}^{3} \Bigg(\sum_{j=1}^{3} (F^{e_l})_{ji}^{-1} \frac{\mathrm{d}}{\mathrm{d}\tilde{x}^{(j)}} \tilde{\phi}_r(\vec{\tilde{x}}_q) \Bigg) \times \Bigg(\sum_{k=1}^{3} (F^{e_l})_{ki}^{-1} \frac{\mathrm{d}}{\mathrm{d}\tilde{x}^{(k)}} \tilde{\phi}_s(\vec{\tilde{x}}_q) \Bigg) \Bigg] \quad (30)$$

$$D_r^{e_l}(u_D) = -\int_{e_l} \phi_r^{e_l}(\vec{x}) \nabla^2 u_D(\vec{x})\, \mathrm{d}\vec{x}$$

$$= \int_{e_l} \nabla \phi_r^{e_l}(\vec{x}) \cdot \nabla u_D(\vec{x})\, \mathrm{d}\vec{x}$$

$$= \int_{e_l} \nabla \phi_r^{e_l}(\vec{x}) \cdot \nabla \Big(\sum_{l'=1}^{L} \sum_{t=1}^{T_{l'}} c_{\tilde{m}(t,l')} \phi_t^{e_{l'}}(\vec{x}) \Big)\, \mathrm{d}\vec{x}$$

$$= \sum_{t=1}^{T_l} c_{\tilde{m}(t,l)} T_{rt}^{e_l} \quad (31)$$

3. Formulation of FE DFT Equations

The electronic wave functions in density functional theory (DFT) in atomic units are given by the solutions to the following Kohn−Sham eigenvalue problem[1]

$$H\psi_i(\vec{x}) = \Big(-\frac{1}{2}\nabla^2 + V_{\mathrm{ext}} + V_{\mathrm{H}} + V_{\mathrm{xc}} \Big) \psi_i(\vec{x}) = \varepsilon_i \psi_i(\vec{x}) \quad (32)$$

$$\int_{\Omega} \psi_i(\vec{x}) \psi_j(\vec{x})\, \mathrm{d}\vec{x} = \delta_{ij} \quad (33)$$

where ε_i is an eigenvalue, and the wave functions $\{\psi_i\}$ satisfy the orthonormality constraints of a symmetric operator. In general, we require the lowest $N_e/2$ eigenvalues and wave functions for a spin-paired system, where N_e is the number of electrons in the system. The formulation for spin-unrestricted and fractionally occupied systems[2] are not presented here; however, generalizing the following equations to do so is quite straightforward. The external potential represents the external electrostatic field imposed on the system. For molecular systems V_{ext} represents the ion−electron interaction,

$$V_{\mathrm{ext}}(\vec{x}) = \sum_{I=1}^{N_A} \frac{-Z_I}{|\vec{x} - \vec{R}_I|} \quad (34)$$

where N_A is the number atoms, Z_I is the nuclear charge of atom I, and $\vec{R}_I$ is location of atom I. The Hartree potential, V_H, and the exchange-correlation potential, V_{xc}, are the effects of electron−electron interactions. Both of these potentials are functions of the electron density

$$\rho(\vec{x}) = \sum_{i=1}^{N_e/2} |\psi_i(\vec{x})|^2 \quad (35)$$

The exchange and correlation potential, V_{xc}, is a straightforward parametrized function of the electron density, e.g. Dirac exchange formula,[35]

$$V_{\mathrm{xc}}(\vec{x}) = -\Big(\frac{3}{\pi}\rho(\vec{x})\Big)^{1/3} = -\Bigg(\frac{3}{\pi}\sum_{i=1}^{N_e/2} |\psi_i(\vec{x})|^2\Bigg)^{1/3} \quad (36)$$

and the Hartree potential V_H is the solution to the Poisson equation

$$\nabla^2 V_{\mathrm{H}}(\vec{x}) = -4\pi\rho(\vec{x}) = -4\pi \sum_{i=1}^{N_e/2} |\psi_i(\vec{x})|^2 \quad (37)$$

Since both V_{xc} and V_H are functions of ρ, the Kohn−Sham eigenvalue problem must be solved self-consistently by an iterative algorithm. The standard approach for these type of problems is a Gummel-like iteration involving two computationally intensive kernels at each iteration:

(1) Calculation of the Hartree potential through the solution of the Poisson equation.

(2) Calculation of the eigenfunctions of the linearized generalized eigenvalue problem where the updated Hartree and exchange-correlation potentials are taken to be frozen.

The FE Poisson and FE DFT eigenvalue equations are generated by representing the Hartree potential and Kohn−Sham wave functions as a finite element expansion,

$$V_{\mathrm{H}}(\vec{x}) = \sum_{m=1}^{M} v_m \eta_m(\vec{x}) \quad (38)$$

$$\psi_i(\vec{x}) = \sum_{m=1}^{M} c_m^i \eta_m(\vec{x}) \quad (39)$$

and defining the boundary conditions for eqs 32 and 37. More extensive derivations of the weak formulation of the FE DFT and Poisson equations can be found in the work of Pask et al.[14] and Fattebert et al.[20] Free-space boundary conditions and periodic boundary conditions are the most common boundary conditions used for solving the Kohn−Sham eigenvalue equations. In this work, we chose to use free-space boundary conditions, i.e.

$$\begin{aligned} V_{\mathrm{H}}(|\vec{x}| \rightarrow \infty) &= 0 \\ \psi_i(|\vec{x}| \rightarrow \infty) &= 0 \end{aligned} \tag{40}$$

The problem with applying these boundary conditions is that the solution domain Ω does not go out to ∞. For eq 32, this is not a problem since the wave functions for most molecular systems decay exponentially and can readily be set to zero at $\partial\Omega$. However, for eq 37 with free-space boundary conditions, the potential decays $\propto 1/r$; hence, we must first calculate the boundary conditions on $\partial\Omega$. To do this, we use a high-order multipole expansion of the density to define the following far field expansion of the Hartree potential at the boundary,

$$V_{\mathrm{H}}(\vec{x} \in \partial\Omega) = \sum_{l=0}^{L_{\mathrm{MAX}}} \sum_{m=-l}^{l} N_{lm} M_{lm} \frac{T_{lm}(\hat{x})}{|\vec{x}|^{l+1}} \tag{41}$$

$$N_{lm} = \begin{cases} 1 & \text{for } m = 0 \\ 2\dfrac{(l-|m|)!}{(l+|m|)!} & \text{for } |m| > 0 \end{cases} \tag{42}$$

$$M_{lm} = \int_{\Omega} |\vec{x}'|^l \rho(\vec{x}') T_{lm}(\hat{x}')\, \mathrm{d}\vec{x}' \tag{43}$$

$$T_{lm}(\hat{x}) = \begin{cases} P_{l|m|}(\cos\theta) & \text{for } m = 0 \\ P_{l|m|}(\cos\theta)\cos|m|\varphi & \text{for } m > 0 \\ P_{l|m|}(\cos\theta)\sin|m|\varphi & \text{for } m < 0 \end{cases} \tag{44}$$

where $\hat{x} = (\cos\varphi \sin\theta, \sin\varphi \sin\theta, \cos\theta)$ and $P_{lm}(z)$ is an associated Legendre polynomial.[36] To include this boundary condition in the solution to Poisson equation the potential is broken up into two parts $V_{\mathrm{H}}(\vec{x}) = u(\vec{x}) + u_D(\vec{x})$, where the homogeneous part $u(\vec{x})$ is defined to be zero on the boundary, and the boundary part, $u_D(\vec{x})$, is the finite element expansion of eq 41. The solution to the homogeneous expansion coefficients, u_n, for the Hartree potential in eq 38) is then found by solving the following systems of linear equations,

$$A_{mn} u_n = f_n \tag{45}$$

where

$$A_{mn} = \sum_{l=1}^{L} \sum_{r=1}^{T_l} \sum_{s=1}^{T_l} \delta_{m,\tilde{m}(r,l)} \delta_{n,\tilde{m}(s,l)} (-T_{rs}^{e_l}) \tag{46}$$

and

$$f_n = \sum_{l=1}^{L} \sum_{r=1}^{T_l} \delta_{m,\tilde{m}(r,l)} \left(-4\pi G_r^{e_l} \left(\sum_{i=1}^{N_e/2} |\psi_i(\vec{x})|^2 \right) + D_r^{e_l}(u_D(\vec{x})) \right) \tag{47}$$

In this work, a standard preconditioned conjugate gradient solver was used to solve these equations.

Similarly, substituting eq 39 into eqs 32 and 33 produces the following generalized eigenvalue problem

$$H_{mn} c_n^i = \varepsilon_i S_{mn} c_n^i \tag{48}$$

and orthonormality conditions

$$\sum_{m=1}^{M} \sum_{n=1}^{M} c_m^i S_{mn} c_n^j = \delta_{ij} \tag{49}$$

where

$$S_{mn} = \int_{\Omega} \eta_m(\vec{x}) \eta_n(\vec{x})\, \mathrm{d}\vec{x} \tag{50}$$

$$H_{mn} = \int_{\Omega} \eta_m(\vec{x}) H \eta_n(\vec{x})\, \mathrm{d}\vec{x} \tag{51}$$

A formula for the matrix S_{mn} in terms of eq 26 can be readily be obtained by substituting eq 7 into eq 50.

$$S_{mn} = \int_{\Omega} \{ \sum_{l=1}^{L} \sum_{t=1}^{T} \phi_t^{e_l}(\vec{x}) \delta_{m,\tilde{m}(t,l)} \} \{ \sum_{k=1}^{L} \sum_{s=1}^{T} \phi_t^{e_l}(\vec{x}) \delta_{n,\tilde{m}(s,k)} \}\, \mathrm{d}\vec{x} \tag{52}$$

$$\begin{aligned} S_{mn} &= \int_{\Omega} \left\{ \sum_{l=1}^{L} \sum_{r=1}^{T_l} \phi_r^{e_l}(\vec{x}) \delta_{m,\tilde{m}(t,l)} \right\} \left\{ \sum_{k=1}^{L} \sum_{s=1}^{T_k} \phi_s^{e_k}(\vec{x}) \delta_{n,\tilde{m}(s,k)} \right\} \mathrm{d}\vec{x} \\ &= \sum_{l=1}^{L} \sum_{k=1}^{L} \sum_{r=1}^{T_l} \sum_{s=1}^{T} \delta_{m,\tilde{m}(r,l)} \delta_{n,\tilde{m}(s,k)} \int_{\Omega} \phi_r^{e_l}(\vec{x}) \phi_s^{e_k}(\vec{x})\, \mathrm{d}\vec{x} \\ &= \sum_{l=1}^{L} \sum_{k=1}^{L} \sum_{r=1}^{T_l} \sum_{s=1}^{T_k} \delta_{m,\tilde{m}(r,l)} \delta_{n,\tilde{m}(s,k)} \delta_{k,l} \int_{e_l} \phi_r^{e_l}(\vec{x}) \phi_s^{e_l}(\vec{x})\, \mathrm{d}\vec{x} \\ &= \sum_{l=1}^{L} \sum_{r=1}^{T_l} \sum_{s=1}^{T} \delta_{m,\tilde{m}(r,l)} \delta_{n,\tilde{m}(s,l)} \int_{e_l} \phi_r^{e_l}(\vec{x}) \phi_s^{e_l}(\vec{x})\, \mathrm{d}\vec{x} \\ &= \sum_{l=1}^{L} \sum_{r=1}^{T} \sum_{s=1}^{T_l} \delta_{m,\tilde{m}(r,l)} \delta_{n,\tilde{m}(s,l)} M_{rs}^{e_l} \end{aligned} \tag{53}$$

Similarly, a formula for the matrix H_{mn} in terms of eqs 30, 27, and 29 can also be obtained.

$$\begin{aligned} H_{mn} = \sum_{l=1}^{L} \sum_{r=1}^{T_l} \sum_{s=1}^{T_l} \delta_{m,\tilde{m}(r,l)} \delta_{n,\tilde{m}(s,l)} \Bigg(& \frac{1}{2} T_{rs}^{e_l} + K_{rs}^{e_l}(V_{\mathrm{ext}}) + \\ & K_{rs}^{e_l}(V_{\mathrm{H}}) + R_{rs}^{e_l}(V_{\mathrm{xc}}, \sum_{i=1}^{N_e/2} |\psi_i(\vec{x})|^2) \Bigg) \end{aligned} \tag{54}$$

Standard preconditioned eigenvalue solvers used in plane-wave DFT programs were used to solve the generalized eigenvalue equations.[20,37] However, as pointed out by Kohn et al., one potential problem in solving the Kohn−Sham equations with adaptivity is that the condition number of the discrete Kohn−Sham equations is dependent on the number of levels of refinement and that as many as two times the iterations will be needed for each new level of refinement.[19] In this work, we took a very simple approach to this problem. We first solved the equations at a coarse level of refinement and then projected it down for use as input at a finer level of refinement.

4. Adaptive FE DFT Solutions of Atoms and Molecules

The Kohn−Sham DFT equations contain several length scales because of the steepness of the atomic potentials. It is well-known that uniform FE meshes are not very efficient for these types of problems. Ideally, an FE mesh could be

adaptively refined only in the regions near the atom centers. However, in general, generating adaptive meshes of good quality is a difficult problem. Straightforward adaptive refinement procedures usually result in "nonconforming" meshes or meshes with hanging nodes. A globally "conforming" FE mesh is defined as a collection of elements which meet only at vertices and faces. While it is possible to develop a FE method based on nonconforming meshes, in general, FE meshes need to be conforming to ensure continuity of interpolated functions.[30,33] A basic algorithm to refine an existing conforming mesh is as follows. In the first step, the elements that have been selected for refinement are bisected. This step more then likely will produce a nonconforming mesh. The next step in the algorithm is then to mark for refinement the elements which contain hanging nodes. These steps proceed interactively until a conforming mesh is produced.[38,39] Many variants on this basic algorithm are possible. For example, the bisection could be along the longest edge or the newest vertex. In this work we used the conforming adaptive mesh refinement based on longest edge bisection. The exact algorithm used in our calculations is given in Scheme 1.

The adaptive FE solver was tested initially on the hydrogen-like atom. The Hamiltonian for this test problem has a deceptively simple form with only a single potential term.

$$H = -\frac{1}{2}\nabla^2 - \frac{Z}{|\vec{x}|} \tag{55}$$

The solutions to this eigenvalue problem are well-known and analytical solutions are available. However, the singular behavior at the origin can cause significant problems for numerical methods. In the case of the FE solver, a mesh vertex must be at the atom center (origin) in order for the Hamiltonian matrix of the FE solver not to contain a singularity in any of its elements. The lowest energy solution and energy are $\psi(\vec{x}) = (Z^{3/2}/\sqrt{\pi})\exp(-Z|\vec{x}|)$ and $\varepsilon = -Z^2/2$. Note that the severity of the singularity with increasing Z is reflected in the increasing localization of the solution.

Scheme 1: Conforming Adaptive FE Mesh Generation Algorithm.

1. Estimate the error $\gamma(e_l)$ for each element e_l in the FE mesh using the following formula

$$\gamma(e_l) = \left(\frac{1}{2}\{\xi(\vec{x}_2) + \xi(\vec{x}_3) + \xi(\vec{x}_4) - \xi(\vec{x}_1)\} - \xi(\vec{x}_c)\right)\frac{|F^{e_l}|}{6} \tag{56}$$

where $\vec{x}$, $\vec{x}_2$, $\vec{x}_3$, and $\vec{x}_4$ are the four vertices of the tetrahedral element e_l, $\vec{x}_c$ is its geometric center, and $\xi(\vec{x})$ is a user defined weight function having dimensions of density in atomic units.

2. Set refinement queues $Q_1 = Q_2 = \varnothing$.

3. Place elements with large errors ($\gamma(e_l) > \varepsilon$) in the refinement queue Q_1.

4. If $Q_1 = \varnothing$, then go to step 9.

5. If $Q_1 > \varnothing$, then proceed to step 6; otherwise, go to step 1.

6. Bisect the elements in Q_1 (removing from Q_1) using either $q-q$ tetrahedral bisection or $b-b$ bisection using the longest edge as shown in Figure 3 and place the nonconforming elements created in refinement queue Q_2.

7. Set $Q_1 \leftarrow Q_2$.

8. Go to step 5.

9. Done with refinement.

To define the adaptive FE mesh for this problem, local adaptivity was carried out starting from a uniform mesh using the geometric-based refinement strategy given in Scheme 1 with the following weight (atomic density) function

$$\xi(\vec{x}) = \frac{Z^3}{\pi}\exp(-2Z|\vec{x}|) \tag{57}$$

The initial uniform mesh used was generated by uniformly refining a seven element tetrahedral mesh four times using $q-q$ refinement (as shown in Figure 3) with the boundary vertices set to be at a radius of 10 au, resulting in mesh composed of 32 768 finite elements with 6017 vertices. For a given γ, the number of elements generated by refinement procedure was found to be nearly independent of Z. Furthermore, the number of vertices grows very rapidly for small tolerances, since at the lowest tolerance $\gamma = 10^{-4}$ there are approximately 11 000 vertices in the FE mesh, whereas at $\gamma = 10^{-7}$ there are approximately 220 000 vertices in the FE mesh. The number of vertices as a function of γ was found to be approximately,

$$v(\gamma) \approx 200\exp(-\log_{10}(\gamma)) \tag{58}$$

where v is the number of vertices.

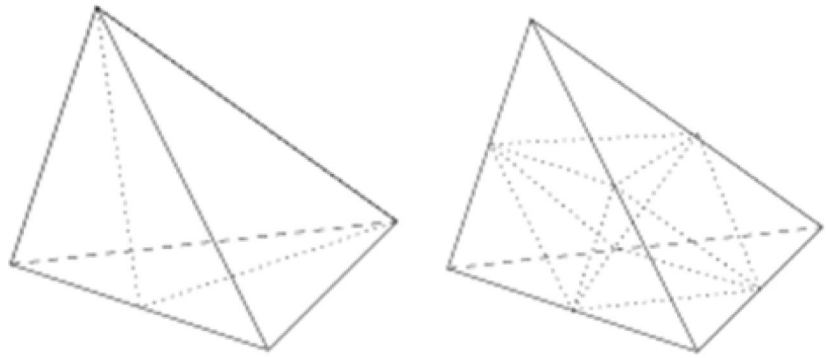

Figure 3. $b-b$ tetrahedral bisection (left) and $q-q$ tetrahedral bisection (right).

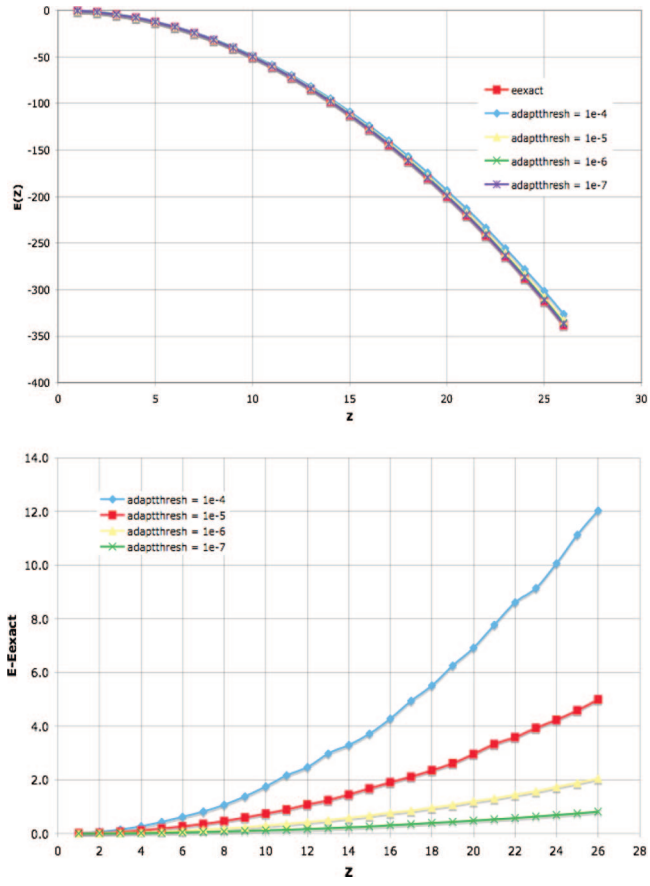

Figure 4. Eigenvalues and errors for the hydrogen-like atom as a function Z.

Not surprisingly, the placement of the elements was found to very dependent on Z. In particular, for higher Z the majority of elements were found to be very close to the atom center, while for lower Z the majority of elements were found to be located away from the atom center. For example, at a $\gamma = 10^{-7}$ refinement, the number of verticies within 1.0 au of the atom center was found to be 32 011 and 214 543 repectively for $Z = 1$ and $Z = 26$, while the number of elements outside this radius was found to be 162 103 and 6212 respectively. Furthermore, it was found that increasing the refinement threshold only increased the number of elements very near the atom centers, while the number of elements away from the atom center remained nearly constant.

In Figure 4, the lowest eigenvalues and errors of the hydrogen-like atoms ($Z = 1...26$) are shown at increasing levels of refinement. Not surprisingly, the accuracy of the solution improved significantly when adaptive refinement was applied. For a given refinement tolerance, the error grew quadratically as a function of Z. For $Z = 1$, the errors were found to be 0.0150 au ($\gamma = 10^{-4}$), 0.0069 au ($\gamma = 10^{-5}$), 0.0029 au ($\gamma = 10^{-6}$), and 0.0012 au ($\gamma = 10^{-7}$). When the singularity was strengthened, the errors were considerably larger. For $Z = 26$, the errors were found to be 12.0348 au ($\gamma = 10^{-4}$), 4.9934 au ($\gamma = 10^{-5}$), 2.0517 au ($\gamma = 10^{-6}$), and 0.08194 au ($\gamma = 10^{-7}$). Even though accurate solutions can be obtained with the current adaptive FE solver based on piecewise linear elements, extremely small adaptive tolerances (large FE meshes) will be required. On the basis of least-squares fitting, the error in terms of γ and Z was found to be approximately given by the following relation in atomic units.

$$\varepsilon(\gamma, Z) \approx 0.64423\exp(0.89503\log_{10}(\gamma))Z^2 \qquad (59)$$

Using eqs 58 and 59, one can estimate the number of vertices needed to obtain accuracies in the millihartree range.

$$v(\varepsilon, Z) \approx 122.37\frac{Z^{2.2346}}{\varepsilon^{1.1173}} \qquad (60)$$

For example, for $Z = 26$ and $\gamma = 10^{-14}$, the error and number of vertices needed are $\varepsilon \approx 0.0015$ au and $v \approx 240, 520, 857$. Hence, in order for the current adaptive FE solver to obtain chemical accuracies for molecules containing atoms with modest Z, the memory requirements are expected to be quite large (>10 Gb/atom). Given that the number of floating point operations per minimization step for a system of N_A atoms will be $O(N_A{}^3 v(\varepsilon, Z))$ the overall memory requirement and computational cost of a simulation can be estimated. For example, to calculate 100 Fe atoms ($Z = 26$) at an accuracy of $\varepsilon = 0.0015$ au will require on the order of 2 terabytes at a cost of 25 petaflops per step.

The next test cases for the adaptive FE solver was the H, He, Li, and Ne atoms at the DFT level using the local density approximation (LDA) exchange-correlation functional.[40] Since the solutions to these equations are spherically symmetric, the accuracy of these FE DFT solutions can be checked by comparing them to solutions of the 1D-radial Kohn−Sham equation.

$$\left(-\frac{1}{2}\frac{d^2}{dr^2} + \frac{l(l+1)}{2r^2} - \frac{Z}{r} + 4\pi\int\frac{\rho(r')}{|r-r'|}r'^2\,dr' + V_{xc}(r)\right)\psi_{il}(r) = \varepsilon_{il}\psi_{il}(r) \qquad (61)$$

Table 2. LDA Energies and Errors in Atomic Units of H, He, Li, and Ne at Increasing Levels of Refinement

refinement	E_{LDA} (H)	error (H)	E_{LDA} (He)	error (He)	E_{LDA} (Li)	error (Li)	E_{LDA} (Ne)	error (Ne)
uniform	−0.438492	4.02E−02	−2.383364	4.51E−01	−5.624508	1.72E+00	−75.145028	5.31E+01
γ = 1e-2	−0.441826	3.68E−02	−2.602388	2.32E−01	−6.674924	6.69E−01	−117.391255	1.08E+01
γ = 1e-3	−0.456391	2.23E−02	−2.731748	1.03E−01	−7.031348	3.13E−01	−123.228792	5.00E+00
γ = 1e-4	−0.468855	9.82E−03	−2.789752	4.51E−02	−7.230246	1.14E−01	−126.047943	2.19E+00
γ = 1e-5	−0.474739	3.93E−03	−2.817929	1.69E−02	−7.294580	4.93E−02	−127.367719	8.66E−01
γ = 1e-6	−0.477234	1.44E−03	−2.830797	4.04E−03	−7.323754	2.01E−02	−127.917138	3.16E−01
γ = 1e-7	−0.477879	7.91E−04	−2.833847	9.89E−04	−7.333440	1.04E−02	*a*	*a*
γ = 1e-8	−0.478194	4.77E−04	*a*	*a*	*a*	*a*	*a*	*a*

[a] Required more than 2 GB of memory.

This 1D-radial equation was solved with a Hermann−Skilman telescoping grid and an Adams fifth-order predictor-correction method.[7] From solving this simplified equation, the exact LDA energies for H, He, Li, and Ne were found to be −0.47867, −2.83484, −7.34386, and −128.2335 au, respectively. For the adaptive FE solutions, the initial uniform FE mesh and the adaptive FE meshes were generated in the same way as the hydrogen-like atoms above, except that the weight functions were taken to be the all electron densities obtained from the solutions to the 1D-radial Kohn−Sham equation.

The LDA energies and errors for H, He, Li, and Ne are reported in Table 2. As expected, the accuracy of the solutions significantly improved when adaptive mesh refinement was applied. Just as for the non-self-consistent hydrogen-like problem, the error grew quadratically as a function of Z for a given refinement tolerance. The errors were also found to be of the same order as with the non-self-consistent hydrogen-like problem, confirming that the essential difficulties of the Kohn−Sham eigenvalues equation are the result of the singular behavior of the atomic potentials.

The next test case for the adaptive FE solver was for the simplest molecule, H_2^+. This problem is very similar to the hydrogen atom in that there is only one electron; however, unlike the hydrogen atom, there are now two centers with singularities located at $\vec{R}_1$ and $\vec{R}_2$. The Hamiltonian for this molecule is,

$$H = -\frac{1}{2}\nabla^2 - \frac{Z_1}{|\vec{x} - \vec{R}_1|} - \frac{Z_2}{|\vec{x} - \vec{R}_2|} \tag{62}$$

where $Z_1 = Z_2 = 1$. Having more than one center complicates the FE mesh generation considerably. To define the adaptive FE mesh for this problem, the geometric-based refinement strategy given in Scheme 1 was used with the following weight function,

$$\xi(\vec{x}) = \frac{Z_1^3}{\pi}\exp(-2Z_1|\vec{x} - \vec{R}_1|) + \frac{Z_2^3}{\pi}\exp(-2Z_2|\vec{x} - \vec{R}_2|) \tag{63}$$

The singularities at the ion centers were accommodated by modifying the initial uniform mesh (6017 vertices, $R = 10a_0$) by moving the vertex nearest to each ion center to lie on top of it. The adaptive solver produced solutions that were similar in accuracy to the hydrogen atom. In Figure 5, the binding energy curve for increasing levels of refinement is shown. The binding energy of H_2^+ at a distance $|\vec{R}_1 - \vec{R}_2|$ is defined as the total energy of molecule at this distance minus the energy of the molecule at infinite separation. Even though large errors are seen with the uniform mesh, the agreement with the analytic result with, even low levels of, adaptive refinement is remarkably good, producing smooth binding energy curves.

As a final test case for the adaptive FE solver, we chose to calculate the binding energy curve for Li_2. This seemingly simple molecule is difficult to calculate. The ground-state solution has three molecular orbitals ($1\sigma_g$, $1\sigma_u$, and $2\sigma_g$) shown in Figure 6. The bottom two molecular orbitals are very localized on the atoms. The top molecular orbital is

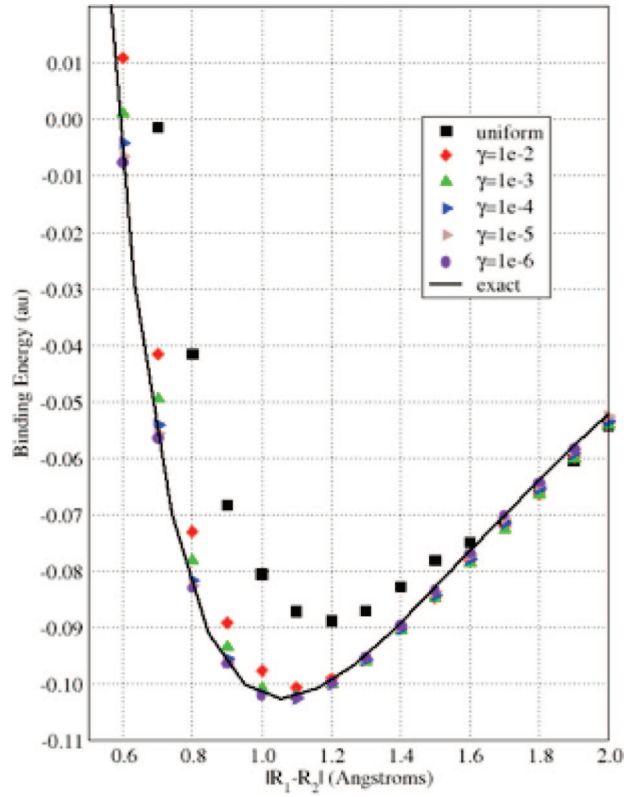

Figure 5. Binding energy curves for H_2^+ obtained with adaptive gridding defined by the geometric-based refinement strategy.

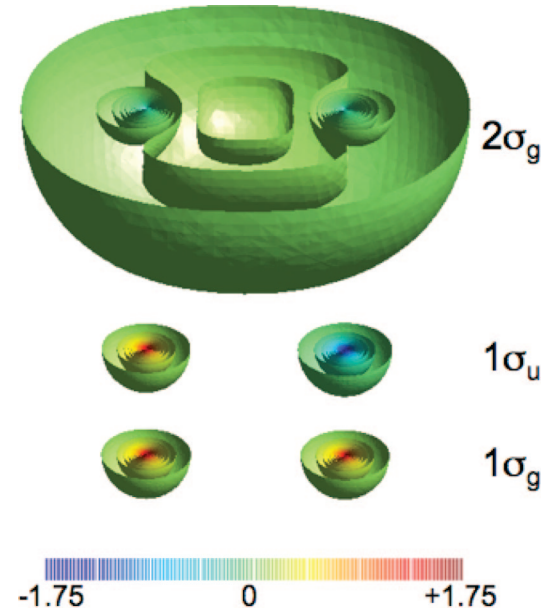

Figure 6. Ground-state molecular orbitals ($1\sigma_g$, $1\sigma_u$, and $2\sigma_g$) of LDA for Li_2 obtained with the FE DFT solver.

considerably more delocalized, but it also contains a localized part. To define the adaptive FE mesh for this problem, the geometric-based refinement strategy given in Scheme 1 was used with the following weight function,

$$\xi(\vec{x}) = \rho^{\mathrm{LDA}}_{\mathrm{Li\ atom}}(|\vec{x} - \vec{R}_1|) + \rho^{\mathrm{LDA}}_{\mathrm{Li\ atom}}(|\vec{x} - \vec{R}_2|)$$

where, $\rho^{\mathrm{LDA}}_{\mathrm{Li\ atom}}(r)$ was obtained by using a spline fit of the solution to eq 61 for the Li atom. The same initial mesh as

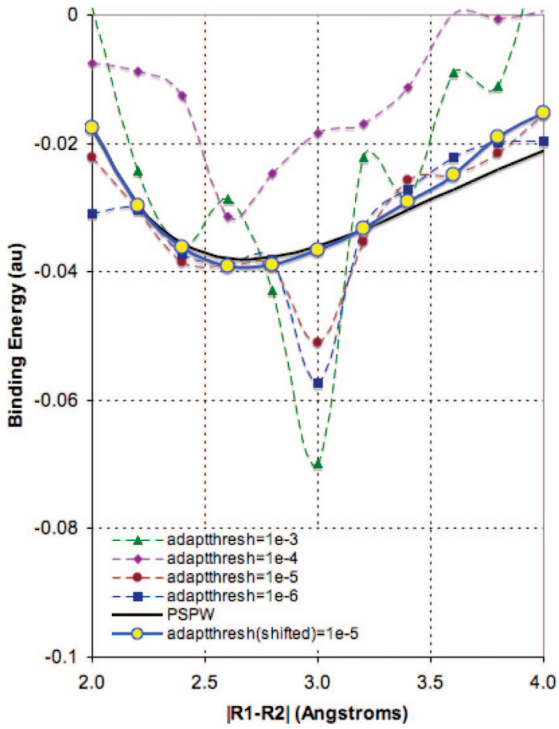

Figure 7. Binding energy curves for Li_2 obtained with adaptive gridding defined by the geometric-based refinement strategy. The "adaptthresh(shifted)=1e-5" curve was obtained with a $\gamma = 1e-5$ adaptive mesh where the initial mesh was modified by shifting procedure of eq 64. The PSPW curve, shown for comparison, was obtained with a NWChem pseudopotential planewave calculation.[4]

for the H_2^+ molecule was used, and vertices nearest to each ion center were moved to lie on top of them.

In Figure 7, the binding energy curve for increasing levels of refinement is shown. Even though a strategy very similar to what was used for the H_2^+ molecule was used, very large errors in the binding energy curves are seen with adaptive refinement at $\gamma = 1e-6$. In analyzing the solution, it was found that the majority of error was from the eigenvalues of the $1\sigma_g$ and $1\sigma_u$ molecular orbitals. Since these orbitals are very localized on the atoms, their eigenvalues are expected to be nearly constant as a function of $|\vec{R}_1 - \vec{R}_2|$. However, it was found that their eigenvalues fluctuated by as much as 0.1 au for the uniform mesh down to 0.01 au for the $\gamma = 1e-6$ mesh. While these errors are slightly smaller than the absolute errors seen for the Li atom in Table 2, they are still too large relative to the LDA binding energy of Li_2, which is roughly 0.04 au.

It was found that the errors in the binding energy for Li_2 could be reduced further by shifting a cloud of vertices near the ion center instead of just a single vertex nearest to each ion center ($\vec{v}_{\text{nearest}}$). To do this, for each ion each of the vertices in the mesh ($\vec{v}_i$) were moved by

$$\vec{v}_i = \vec{v}_i + (\vec{R}_I - \vec{v}_{\text{nearest}}) f(|\vec{v}_i - \vec{v}_{\text{nearest}}|) \qquad (64)$$

where $f(r)$ is the screening function

$$f(r) = 1 - \left[1 - \exp\left(-\left(\frac{r}{R}\right)^N\right)\right]^N \qquad (65)$$

and N and R are adjustable parameters, chosen to be 8 and 1.5 au, respectively, which define the atom center region. When this initial shifting procedure is used, it was found that an accurate binding energy curve was obtained by the $\gamma = 1e-5$ adaptive mesh (adaptthresh(shifted)=1e-5 curve in Figure 7). This result suggests that the placement of the mesh close to the atom centers is the main source of error, and an overlapping grid method can be used to reduce the errors (cancelation of errors) in structure and bond energies of the system. We note that carefully choosing mesh close to atom centers in order to reduce integration errors was also used by Batcho.[24] In this work, the mesh was generated by partitioning the volume around each singularity with a cube that was subdivided into six pyramids.

5. Conclusion

We have implemented an unstructured adaptive FE DFT program. The severe problem associated with the rapid variation of the electronic wave functions in the near singular regions of the atomic centers was treated by using unstructured simplex meshes that resolve these features around atomic nuclei. This approach uses a minimal amount of computational resources by concentrating the computational work in the regions in which the shortest length scales are necessary and provides for low resolution in regions for which there is no electron density. The matrix representations of the discrete Hamiltonian operator in the adaptive finite element basis are always sparse due to the local support nature of finite element basis functions. As a result, application of the Hamiltonian operator is $O(N)$ in the number of discretization points.

The overall memory and computational requirements for the solver implemented were found to be quite high. By using the solution to the hydrogen-like atom, the overall memory and computational requirements per atom needed by the solver were estimated. The number of mesh vertices per atom as a function of the atomic number Z and the required accuracy ε was estimated to be $v(\varepsilon, Z) \approx 122.37(Z^{2.2346}/\varepsilon^{1.1173})$. These meshing requirements were also found to hold for the full DFT solutions. The errors in the LDA energies of H, He, Li, and Ne were found to be of the same order as the hydrogen-like atom, which confirmed that the essential difficulty of solving the Kohn−Sham eigenvalue equation is the result of the singular behavior of the atomic potentials. This estimate can be used determine the overall memory requirement and computational cost of a simulation, since the number of floating point operations per DFT minimization step for a system of N_A atoms will be $O(N_A^3 v(\varepsilon, Z))$ (e.g., $Z = 26$, $\varepsilon = 0.0015$ au, and $N_A = 100$, the memory requirement and computational cost would be ~2 terabytes and ~25 petaflops).

Despite the high cost of the method, it was found that strategies for fixing the error near the atomic potential singularities, such as a geometric-based refinement strategy can be used to reduce the errors in structure and bond energies of the system. In this work, to define the adaptive FE mesh for a problem, local adaptivity was carried out by starting from an uniform mesh and adapting using a conforming adaptation procedure where the error was

determined by using a weight function composed of the sum of the atomic densities for the problem. For the simple H_2^+ molecule this strategy was found to work very well. However, for the Li_2 molecule very large errors in the binding energy curves were seen even when the geometric-based adaptive refinement procedure was used. It was found that the errors in the binding energy for Li_2 could be reduced further by shifting a cloud of vertices near the ion center instead of just a single vertex nearest to each ion center ($\vec{v}_{\text{nearest}}$) in the initial uniform mesh. When this initial shifting procedure was used in combination with the geometric-based adaptation procedure, it was found that an accurate binding energy curve could be obtained. These results showed that the placement of the mesh close to the atom centers is the main source of error in the method, and it suggests that an overlapping grid method could be used to reduce the errors ("cancellation of errors") in structure and bond energies of the molecule.

At present, our adaptive FE DFT solver uses piecewise linear elements which are $O(h^2)$ accurate. It was shown at this low order of accuracy that very large FE meshes will be needed to obtain the millihartree or better accuracy desired for molecules and materials with large Z atoms. Unless very large machines are used, the memory requirements (and computational cost) is unlikely to be competitive with more standard solution methods. Others have shown that memory and computational requirements of FE DFT can be substantially reduced by using higher-order FE elements[19,20] or spectral element methods.[21−24] However, to date these methods have relied on using parallelpiped elements along with a special treatement of the singularity by pseudopotentials[19,20] or with a special integration technique.[22,24] Our current work differs from these prior works in that we use tetrahedral elements rather than parallelpiped elements. This allows for considerably more flexibility in the grid generations as opposed to parallelpiped elements. Future work will focus on higher order FE DFT solvers which make use of tetrahedral elements.

Acknowledgment. This research was supported by the DOE ASCR Multiscale Mathematics program and the DOE BES Geosciences program. The Pacific Northwest National Laboratory (PNNL) is operated by Battelle Memorial Institute. Some of the calculations were performed on the MPP2 computing system at the Molecular Science Computing Facility in the William R. Wiley Environmental Molecular Sciences Laboratory (EMSL) at PNNL. EMSL is a national scientific user facility sponsored by the Department of Energy's Office of Biological and Environmental Research and located at Pacific Northwest National Laboratory. We also wish to thank the Scientific Computing Staff, Office of Energy Research, and the U.S. Department of Energy for a grant of computer time at the National Energy Research Scientific Computing Center (Berkeley, CA).

References

(1) Kohn, W.; Sham, L. J. Self-consistent equations including exchange and correlation effects. *Phys. Rev.* **1965**, *140*, A1133–A1138.

(2) Parr, R. G.; Yang, W. G. *Density-Functional Theory of Atoms and Molecules*; Oxford University Press: New York, 1989.

(3) Apr, A.; Gao, F.; Kristić, P. S.; Wells, J. C.; Windus, T. L. NWChem for Material Science. *Comput. Mater. Sci.* **2003**, *28*, 209–221.

(4) Bylaska, E. J.; de Jong, W. A.; Govind, N.; Kowalski, K.; Straatsma, T. P.; Valiev, M.; Wang, D.; Apra, E.; Windus, T. L.; Hammond, J.; Nichols, P.; Hirata, S.; Hackler, M. T.; Zhao, Y.; Fan, P.-D.; Harrison, R. J.; Dupuis, M.; Smith, D. M. A.; Nieplocha, J.; Tipparaju, V.; Krishnan, M.; Wu, Q.; Van Voorhis, T.; Auer, A. A.; Nooijen, M.; Brown, E.; Cisneros, G.; Fann, G. I.; Fruchtl, H.; Garza, J.; Hirao, K.; Kendall, R.; Nichols, J. A.; Tsemekhman, K.; Wolinski, K.; Anchell, J.; Bernholdt, D.; Borowski, P.; Clark, T.; Clerc, D.; Dachsel, H.; Deegan, M.; Dyall, K.; Elwood, D.; Glendening, E.; Gutowski, M.; Hess, A.; Jaffe, J.; Johnson, B.; Ju, J.; Kobayashi, R.; Kutteh, R.; Lin, Z.; Littlefield, R.; Long, X.; Meng, B.; Nakajima, T.; Niu, S.; Pollack, L.; Rosing, M.; Sandrone, G.; Stave, M.; Taylor, H.; Thomas, G.; van Lenthe, J.; Wong, A.; Zhang, Z. *NWChem, A Computational Chemistry Package for Parallel Computers*;, Version 5.1, Pacific Northwest National Laboratory: Richland, WA, 2007.

(5) Dunning, T. H., Jr.; Peterson, K. A.; Woon, D. E. Gaussian Basis Sets for Use in Correlated Calculations. In *Encyclopedia of Computational Chemistry*; Schleyer, P.v.R., Ed.; John Wiley & Sons Ltd: New York, 1997.

(6) Dunlap, B. I.; Connolly, J. W. D.; Sabin, J. R. On some approximations in applications of X theory. *J. Chem. Phys.* **1979**, *71*, 3396–3402.

(7) Hamann, D. R. Generalized norm-conserving pseudopotentials. *Phys. Rev. B* **1989**, *40*, 2980–2987.

(8) Tsuchida, E.; Tsukada, M. Electronic-structure calculations based on the finite-element method. *Phys. Rev. B* **1995**, *52*, 5573–5578.

(9) Bernholc, J.; Briggs, E. I.; Sullivan, D. J.; Brabec, C. J.; Nardelli, M. B.; Rapcewicz, K.; Roland, C.; Wensell, M. Real-space multigrid methods for large-scale electronic structure problems. *Int. J. Quantum Chem.* **1997**, *65*, 531–543.

(10) Bernholc, J.; Hodak, M.; Lu, W. C. Recent developments and applications of the real-space multigrid method. *J. Phys.: Condensed Matter* **2008**, *20*, 294205.

(11) Chelikowsky, J. R.; Troullier, N.; Saad, Y. Finite-Difference-Pseudopotential Method: Electronic Structure Calculations without a Basis. *Phys. Rev. Lett.* **1994**, *72*, 1240–1243.

(12) Chelikowsky, J. R.; Troullier, N.; Wu, K.; Saad, Y. Higher-order finiet-difference pseudopotential method: An application to diatomic molecules. *Phys. Rev. B* **1994**, *50*, 11355–11364.

(13) Briggs, E. I.; Sullivan, D. J.; Bernholc, J. Large-scale electronic-structure calculations with multigrid acceleration. *Phys. Rev. B* **1995**, *52*, R5471–R5474.

(14) Pask, J. E.; Klein, B. M.; Sterne, P. A.; Fong, C. Y. Finite-element methods in electronic-structure theory. *Comput. Phys. Commun.* **2001**, *135*, 1–34.

(15) Cho, K.; Arias, T. A.; Joannopoulos, J. D.; Lam, P. K. Wavelets in Electronic Structure Calculations. *Phys. Rev. Lett.* **1993**, *71*, 1808–1811.

(16) Lippert, R. A.; Arias, T. A.; Edelman, A. Multiscale Computation with Interpolating Wavelets. *J. Comput. Phys.* **1998**, *140*, 278–310.

(17) Arias, T. A. Multiresolution analysis of electronic structure: semicardinal and wavelet bases. *Rev. Mod. Phys.* **1999**, *71*, 267–311.

(18) Bylaska, E. J.; Kohn, S. R.; Baden, S. B.; Edelman, A.; Kawai, R.; Ong, M. E. G.; Weare, J. H.; Scalable Parallel Numerical Methods and Software Tools for Material Design. In *Proceeding of the Seventh SIAM Conference on Parallel Processing for Scientific Computing*, San Francisco, CA, 1995.

(19) Kohn, S.; Weare, J.; Ong, E.; Baden, S. Parallel Adaptive Mesh Refinement for Electronic Structure Calculations. In *Eigth SIAM Conference on Parallel Processing for Scientific Computing*, Minneapolis, MN, 1997.

(20) Fattebert, J. L.; Hornung, R. D.; Wissink, A. M. Finite element approach for density functional theory. *J. Comput. Phys.* **2007**, *223*, 759–773.

(21) Harrison, R. J.; Fann, G. I.; Yanai, T. G.; Gan, Z.; Beylkin, G. Multiresolution quantum chemistry: Basic theory and initial applications. *J. Chem. Phys.* **2004**, *121*, 11587–11598.

(22) Yanai, T.; Fann, G. I.; Gan, Z. T.; Harrison, R. J.; Beylkin, G. Multiresolution quantum chemistry in multiwavelet bases: Hartree-Fock exchange. *J. Chem. Phys.* **2004**, *121*, 6680–6688.

(23) Yanai, T.; Fann, G. I.; Gan, Z. T.; Harrison, R. J.; Beylkin, G. Multiresolution quantum chemistry in multiwavelet bases: Analytic derivatives for Hartree-Fock and density functional theory. *J. Chem. Phys.* **2004**, *121*, 2866–2876.

(24) Batcho, P. F. Computational method for general multicenter electronic structure calculations. *Phys. Rev. E* **2000**, *61*, 7169–7183.

(25) Modine, N. A.; Zumback, G.; Kaxiras, E. Adaptive-coordinate real-space electronic-structure calculations for atoms, molecules and solids. *Phys. Rev. B* **1997**, *55*, 10289–10301.

(26) Torsti, T.; Lindberg, V.; Makkonen, I.; Ogando, E.; Rasanen, E.; Saarikoski, H.; Puska, M. J.; Nieminen, R. M. Real-space electronic-property calculations for nanoscale structures. In *Handbook of Theoretical and Computational Nanotechnology*; Rieth, M., Schommers, W., Eds.; Forschungszentrum Karlsruhe: Germany, 2006.

(27) Modine, N. A.; Zumbach, G.; Kaxiras, E. Adaptive coordinate real-space electronic structure calculations for atoms, molecules and solids. *Phys. Rev. B* **1997**, *55*, 10289–10301.

(28) Holst, M. Adaptive numerical treatment of elliptic systems on mainfolds. *Adv. Comput. Math.* **2001**, *15*, 139–191.

(29) Axelsson, O.; Barker, V. A. *Finite Element Solution of Boundary Value Problems: Theory and Computation*; SIAM: Philadelphia, 2001.

(30) Braess, D. *Finite Elements: Theory, Fast Solvers and Applications in Solid Mechanics*, 2nd ed.; Cambridge Univeristy Press: Cambridge 2005.

(31) Brenner, S. C.; Scott, L. R., *The Mathematical Theory of Finite Element Methods*, 2nd ed.; Springer-Verlag: New York, 2002.

(32) Strang, G. Piecewise Polynomials and the Finite Element Method. *Bull. Am. Math. Soc.* **1973**, *79*, 1128–1137.

(33) Norrie, D. H.; de Vries, G. *The Finite Element Method*; Academic Press: New York, 1973.

(34) Zienkiewicz, O. C.; Morgan, M. *Finite Elements and Approximation*, Dover Publications: New York, 1983.

(35) Dirac, P. A. M. Note on exchange phenomena in the Thomas atom. *Proc. Cambridge Philos. Soc.* **1930**, *26*, 376–385.

(36) Sansone, G. *Orthogonal Functions*, revised English ed.; Dover Publications: New York, 1991.

(37) Hasnip, P. J.; Pickard, C. J. Electronic energy minimisation with ultrasoft pseudpotentials. *Comput. Phys. Commun.* **2006**, *174*, 24–29.

(38) Bank, R. E.; Holst, M. A New Paradigm for Parallel Adaptive Meshing Algorithms. *Siam J. Sci. Comput.* **2000**, *22*, 1411–1443.

(39) Arnold, D. N.; Mukherjee, A.; Pouly, L. Locally Adapted Tetrahedral Meshes using Bisection. *Siam, J. Sci. Comput.,* **2000**, *22*, 431–448.

(40) Vosko, S. H.; Wilk, L.; Nusair, M. Accurate Spin-Dependent Electron Liquid Correlation Energies for Local Spin-Density Calculations - A Critical Analysis. *Can. J. Phys.* **1980**, *58*, 1200–1211.

CT800350J

JCTC Journal of Chemical Theory and Computation

Distributed Gaussian Valence Bond Surface Derived from Ab Initio Calculations

Jason L. Sonnenberg,[†] Kim F. Wong,[‡] Gregory A. Voth,[‡] and H. Bernhard Schlegel*,[†]

Department of Chemistry, Wayne State University, Detroit, Michigan 48202, and Department of Chemistry, University of Utah, Salt Lake City, Utah 84112

Received November 6, 2008

Ⓦ **This paper contains enhanced objects available on the Internet at http://pubs.acs.org/JCTC.**

Abstract: The experimental and computational results for the tautomerization reaction of 2-pyridone are reviewed. G3, G4, CBS-APNO, and W1 model chemistries are used to generate state-of-the-art reaction energetics for the tautomerization reaction with and without catalytic water molecules in both the gas and aqueous phases. Reactive, electronic potential energy surface surfaces for use in molecular dynamics simulations were generated for these reactions following a recently improved empirical valence bond formulation. The form of molecular mechanics potentials needed for a satisfactory fit is also discussed.

1. Introduction

Over the last century, the keto−enol tautomerism of 2-pyridone (PY) and 2-hydroxypyridine (HY) has been probed by nearly every available experimental[1−13] and theoretical method.[7,10−34] This seemingly innocuous proton-transfer reaction has garnered so much attention because it serves as the archetype model system for hydrogen bonding, proton-transfer tautomerism, and proton-shuttling mechanisms in chemical, biological, and medicinal reactions. Most recently, Hatherley and co-workers used microwave spectroscopy to determine that the gas-phase energy difference between PY and HY is 3.2 ± 0.4 kJ/mol with HY being the more stable species.[8] This value is larger than the ΔG value determined from X-ray photoelectron spectroscopy (PES),[6] but it agrees quite well with Beak's value of 3.3 kJ/mol determined from ultraviolet (UV) spectroscopy.[2] The experimental values are collected in Table 1.

With a gas-phase tautomerization energy smaller than 4.2 kJ/mol (1 kcal/mol, aka chemical accuracy), the PY/HY system has been a formidable challenge for computational chemistry from the beginning. Although semiempirical and molecular mechanics methods provide qualitative agreement with experiment and can describe the PY → HY activation barrier $E^{\ddagger}$ correctly,[15] it was recognized early on that correlation and zero-point vibrational energies are crucial.[16] Following earlier calculations by Schlegel et al. (ref 16), many investigators employed second-order Møller−Plesset perturbation theory (MP2) with a wide variety of basis sets.[10,13,19,21,23,29] While increasing the basis set size beyond triple-ζ (TZ) with the addition of polarization and diffuse functions improved the activation barrier, it unfortunately results in an underestimation of the tautomerization energy because of the well-known correlation energy overestimation by MP2.[35] Predicted tautomerization energies can be brought back into chemical accuracy by utilizing MP4[10] or spin-component-scaled MP2 (SCS-MP2).[36] Density functional theory (DFT) generates reliable molecular structures but the corresponding energetics, with the exception of the BHandHLYP functional,[28,30] are inherently wrong: PY is

Table 1. Experimental Data for the PY → HY Reaction[a]

ΔH	ΔG	T	method	ref
gas phase:				
−3.2 ± 0.4		356	microwave	8
	−3.3	405	UV	2
−2.5 ± 0.4[b]			PES	4
	−2.4 ± 0.21	403	X-ray PES	6
aqueous phase:				
14.2		298	heats of solution	1

[a] Energies and temperatures are in kJ/mol and K, respectively. [b] ΔH was calculated with data ranging from 348 to 728 K using the van't Hoff equation.

* To whom correspondence should be addressed. E-mail: hbs@chem.wayne.edu.

[†] Wayne State University.

[‡] University of Utah.

10.1021/ct800477y CCC: $40.75
Published on Web 03/11/2009

Table 2. Computed Energies (kJ/mol) for the Gas-Phase PY → HY reaction[a]

theory	$\Delta E^{\ddagger}$	$\Delta H^{\ddagger}$	$\Delta G^{\ddagger}$	ΔE	ΔH	ΔG
HF/6-31G(d,p)	207.1[c]			−6.5[h]	−7.3[h]	
HF/6-31++G(d,p)[g]				−5.17	−5.8	
HF/TZV(2df,2dp)[e]				−3.8		
MP2/6-31G(d,p)	147.2[b]	134.0[b]		−9.2[c]		
MP2/6-31+G(d,p)[d]	151.4	138.4	139.4	−8.6	−8.0	
MP2/6-31++G(d,p)[d]	151.3	139.1	144.6	−8.7	−7.1	
MP2/6-311+G(d,p)	149.3	137.3	139.0	−11.6	−10.2	−8.3
MP2/6-311++G(d,p)[d]	149.3			−11.8		
MP2/TZV(2df,2dp)[e]				−11.2		
SCS-MP2/TZV(2df,2dp)//B3LYP/TZV(2df,2dp)[e]				−4.6		
MP4(SDTQ)//MP2/6-311++G(d,p)[f]				−3.62		
CISD/3-21G//HF/3-21G[j]	188.0			12.0		
CISD/DZP1[i]				0.28		
QCISD/TZV(2df,2dp)//B3LYP/TZV(2df,2dp)[e]				−2.9		
QCISD(T)/TZV(2df,2dp)//B3LYP/TZV(2df,2dp)[e]				−4.2		
PBE/TZV(2df,2dp)[e]				6.3		
BP86/TZV(2df,2dp)[e]				5.9		
BLYP/TZV(2df,2dp)[e]				7.9		
B3PW91/6-31++G(d,p)[g]				1.61	1.3	
B3LYP/6-31G(d,p)[b]	148.1	135.0				
B3LYP/6-31+G(d,p)[d]	154.3	140.8	141.3	1.9	1.5	
B3LYP/6-31++G(d,p)[d]	154.2	140.8	141.2	1.8	1.4	
B3LYP/6-311++G(d,p)[d]	158.8	145.1	145.6	3.6	3.3	
B3LYP/6-311++G(2d,2p)[d]	157.6	144.1	144.6	1.5	1.1	1.5
BHandHLYP/6-311++G(2d,2p)[d]	176.6	162.6	163.2	−4.2	−4.6	−4.2
BHandHLYP/TZV(2df,2dp)[e]				−2.9		
G3	159.5	142.3	143.0	−3.8	−4.9	−4.4
G4	156.1	143.1	143.6	−4.2	−4.3	−3.9
CBS-APNO	157.8	144.9	145.1	−4.7	−5.3	−4.9
W1	155.5	142.2	142.7	−3.9	−4.4	−4.1

[a] ΔE is electronic energy and does not include zero-point energy corrections. Enthalpies are at 0 K, while Gibbs free energies are at 298 K. [b] Ref 13. [c] Ref 21. [d] Ref 30. [e] Ref 28. [f] Ref 10. [g] Ref 24. [h] Ref 23. [i] Ref 18. [j] Ref 17.

Table 3. Computed Energies (kJ/mol) for the Gas-Phase $PY(H_2O)_n$ → $HY(H_2O)_n$ Reactions[a]

theory	$\Delta E^{\ddagger}$	$\Delta H^{\ddagger}$	$\Delta G^{\ddagger}$	ΔE	ΔH	ΔG
$PY(H_2O)$ → $HY(H_2O)$:						
HF/6-31G(d,p)[d]	117.2			0.4		
MP2/6-31G(d,p)[b]	57.3			−4.2		
MP2/6-31G(d,p)[d]	55.6			−5.4		
MP2/6-311+G(d,p)	61.3	45.8	51.5	−5.6	−4.4	−3.3
MP2/6-311++G(d,p)[c]				−5.6		
MP4(SDTQ)//MP2/6-311++G(d,p)[c]				1.27		
CISD/3-21G//HF/3-21G[f]	56.0			12.0		
B3LYP/6-31G(d,p)[d]	52.3			3.3		
B3LYP/TZ2P[d]	61.1			5.9		
B3LYP/6-311++G(d,p)[c]				8.65		
B3LYP/6-311++G(2d,2p)[e]	63.1	47.2	52.3	7.1	6.9	7.5
B3LYP/aug-cc-pVTZ//B3LYP/6-311++G(d,p)[c]				7.66		
BHandHLYP/6-311++G(2d,2p)[e]	77.6	60.5	65.9	3.1	2.9	3.5
G3	68.5	51.7	58.0	1.9	0.92	1.4
G4	67.7	52.0	56.1	1.0	0.82	1.2
CBS-APNO	64.0	46.2	52.8	0.98	0.41	0.89
$PY(H_2O)_2$ → $HY(H_2O)_2$:						
MP2/6-31G(d,p)[b]	39.7			−1.3		
MP2/6-311+G(d,p)	69.8	47.2	54.7	1.2	1.9	2.5
CISD/3-21G//HF/3-21G[f]	43.0			19.0		
B3LYP/6-31G(d,p)[d,g]	56.5			13.8		
B3LYP/6-311++G(2d,2p)[e]	67.6	45.4	52.6	12.5	12.1	12.8
BHandHLYP/6-311++G(2d,2p)[e]	85.5	61.4	69.2	9.4	9.0	9.7
G3	75.1	57.3	67.0	4.3	5.7	6.3
G4	77.5	55.0	60.9	7.0	6.2	6.9
$PY(H_2O)_3$ → $HY(H_2O)_3$:						
MP2/6-311+G(d,p)	94.1	67.7	77.3	6.8	6.7	6.5
G3[h]				13.3	12.8	14.7
G4[h]				13.7	14.6	17.5

[a] ΔE is electronic energy and does not include zero-point energy corrections. Enthalpies are at 0 K, while Gibbs free energies are at 298 K. [b] Ref 29. [c] Ref 10. [d] Ref 21. [e] Ref 30. [f] Ref 17. [g] In this calculation, one water is a proton shuttle, and the other is part of the first solvation shell. [h] Transition state calculations were not feasible for this system and level of theory.

predicted to be the most stable tautomer in the gas-phase.[10,13,21,24,28,30,31] Piacenza and Grimme showed convincing evidence that the poor DFT energies arise from the exchange potentials and inclusion of at least 50% Hartree−Fock (HF) exchange "corrects" those exchange potentials as seen in the BHandHLYP results.[28] The necessity of HF exchange in DFT functionals coupled with the MP2 overestimation of the correlation energy suggests that the gas-phase tautomer-

Table 4. Computed Energies (kJ/mol) for the Aqueous Phase $PY(H_2O)_n \rightarrow HY(H_2O)_n$ Reactions[a]

theory	$\Delta E^{\ddagger}$	$\Delta H^{\ddagger}$	$\Delta G^{\ddagger}$	ΔE	ΔH	ΔG
PY → HY:						
MP2/6-311+G(d,p)/IEF-PCM	161.8	148.7	149.6	5.7	5.3	6.0
B3LYP/6-31G(d)/Onsager[c]		158.2[b]	144.8		14.2[b]	13.4
B3LYP/6-311++G(2d,2p)/Onsager[d]			150.1			15.2
B3LYP/6-311++G(2d,2p)/DPCM[d]			176.1			15.4
BHandHLYP/6-311++G(2d,2p)/Onsager[d]			167.7			7.9
BHandHLYP/6-311++G(2d,2p)/DPCM[d]			193.5			10.2
G3/IEF-PCM	168.9	155.0	155.5	14.1	12.4	12.6
G4/IEF-PCM	168.9	155.5	155.9	13.6	12.5	12.7
$PY(H_2O) \rightarrow HY(H_2O)$:						
MP2/6-311+G(d,p)/IEF-PCM	63.9	47.0	53.8	3.1	3.5	4.8
B3LYP/6-31G(d)/Onsager[c]		61.2[b]			11.6[b]	
B3LYP/6-311++G(2d,2p)/Onsager[d]			52.4			13.1
B3LYP6-311++G(2d,2p)/DPCM[d]			70.2			14.6
BHandHLYP/6-311++G(2d,2p)/Onsager[d]			64.7			7.4
BHandHLYP/6-311++G(2d,2p)/DPCM[d]			84.7			13.4
G3/IEF-PCM	73.1	62.2	69.7	12.0	10.8	11.6
G4/IEF-PCM	72.3	55.1	59.6	11.4	10.6	11.0
$PY(H_2O)_2 \rightarrow HY(H_2O)_2$:						
MP2/6-311+G(d,p)/IEF-PCM	71.3	47.7	54.6	4.9	4.9	4.7
B3LYP/6-31G(d)/Onsager[c]		69.5[b]	51.5		17.2[b]	16.4
B3LYP/6-311++G(2d,2p)/Onsager[d]			52.5			15.8
B3LYP/6-311++G(2d,2p)/DPCM[d]			74.6			15.7
BHandHLYP/6-311++G(2d,2p)/Onsager[d]			68.6			12.3
BHandHLYP/6-311++G(2d,2p)/DPCM[d]			94.3			12.9
G3/IEF-PCM	81.7	67.5	77.3	12.2	10.9	11.7
G4/IEF-PCM	80.4	56.1	62.3	11.3	11.2	11.9
$PY(H_2O)_3 \rightarrow HY(H_2O)_3$:						
MP2/6-311+G(d,p)/IEF-PCM	82.4	70.0	78.5	7.6	7.9	8.7
B3LYP/6-31G(d)/Onsager[c]					20.7[b]	19.3
G3/IEF-PCM[e]				13.7	13.2	15.2
G4/IEF-PCM[e]				13.0	11.4	10.9

[a] ΔE is electronic energy and does not include zero-point energy corrections. Enthalpies are at 0 K, while Gibbs free energies are at 298 K unless noted otherwise. [b] Values at 298 K. [c] Ref 31. [d] Ref 30. [e] Transition state calculations were not feasible for this system and level of theory.

ization energetics are dominated by the differences in the exchange energy. Such an illation is supported by HF results that are within chemical accuracy when employing a polarized double-ζ (DZ) or larger basis set.[16,19,21,23,24,28] QCISD, with and without perturbative triples, has predicted tautomerization energies of 4.2 and 2.9 kJ/mol, respectively, indicating that the triples correction is necessary to avoid underestimation of the reaction energy.[28] A representative selection of computational results is presented in Tables 2 and 3.

Because the magnitude of the gas-phase tautomerization barrier prevents rapid proton transfer at room temperature, proton shuttling mechanisms involving explicit water[10,20,21,29−31] and formic acid[13] solvent molecules were investigated. Barone and Adamo were the first to theoretically show that one water molecule reduces the gas-phase tautomerization barrier and switches the lowest energy state from HY to PY.[21] They also demonstrated that addition of a second water molecule to represent bulk solvent actually *increases* the tautomerization barrier because of the hydrogen-bonding interaction with the carbonyl moiety. Maris et al. later confirmed Barone and Adamo's single-molecule proton shuttle findings using MP2, MP4, and DFT methods.[10] One formic acid molecule acting as a proton shuttle was also shown to affect the reaction barrier in the same fashion.[13] In 2005, two groups independently examined the affects of a proton shuttle involving two water molecules and found that both DFT[30] and MP2[29] methods predict a further reduction in the proton-transfer barrier.

Given that inclusion of explicit solvent molecules in addition to those involved in the proton shuttle counterbalances the barrier reduction of the shuttles, a more uniform representation of bulk solvent has been pursued. Wong and co-workers applied the self-consistent reaction field (SCRF) Onsager model to the uncatalyzed 2-pyridone/2-hydroxypyridine tautomerization in cyclohexane and acetonitrile.[19] These results were later confirmed by Wang and Boyd, who also investigated the reaction in chloroform.[22] The same SCRF method was applied to model the tautomerization in water.[21,30,31] For all four solvents, the equilibrium shifts such that the PY species is now favored in solution, which agrees well with experimental results. Barone and Adamo found that inclusion of the bulk solvent via SCRF theory, increased the barrier to proton transfer and stabilized PY for the single water molecule shuttle with and without an explicit solvation shell water.[21] Fu et al. also observed such effects for one and two water proton shuttles.[30] Tsuchida and Yamabe[31] continued the energetic exploration of multiwater proton shuttles in solution and reported that a three-molecule proton shuttle actually *increases* the tautomerization barrier relative to the two-molecule shuttle rather than reducing it. Unfortunately the reported three-molecule proton shuttle transition state (TS) corresponds to a proton transfer between the three

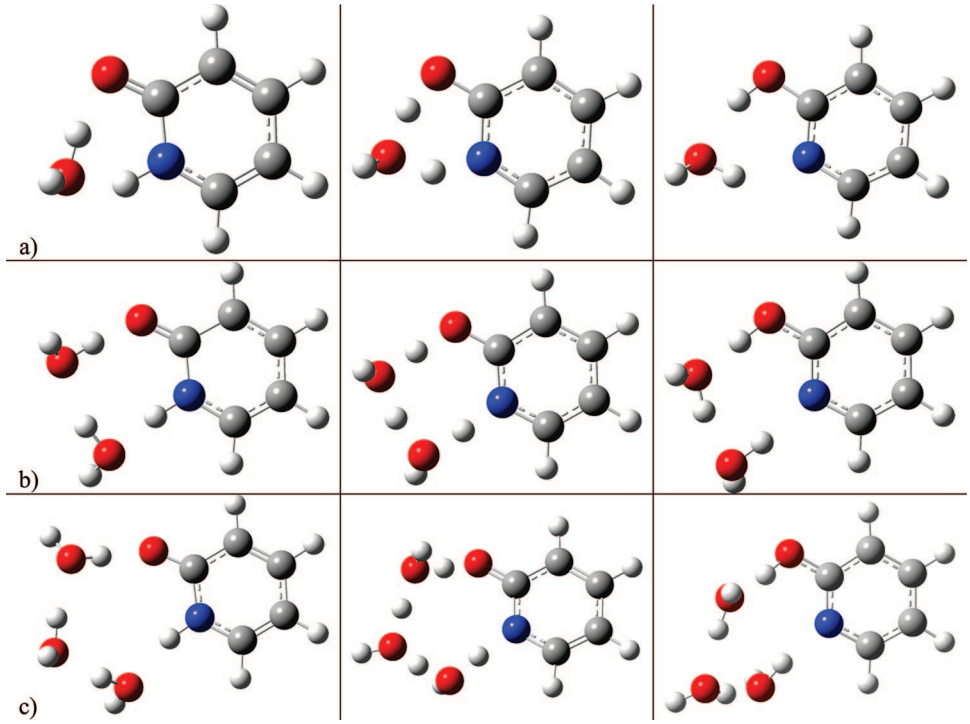

Figure 1. PY$(H_2O)_n$ (reactant), TS$(H_2O)_n$ (transition state), and HY$(H_2O)_n$ (product) geometries for proton-shuttling tautomerization reactions with (a) one, (b) two, and (c) three catalytic water molecules. Carbon, nitrogen, oxygen, and hydrogen are depicted in gray, blue, red, and white, respectively.

Ⓦ Movies of the molecules shown in panels a, b, and c along the reaction paths are available.

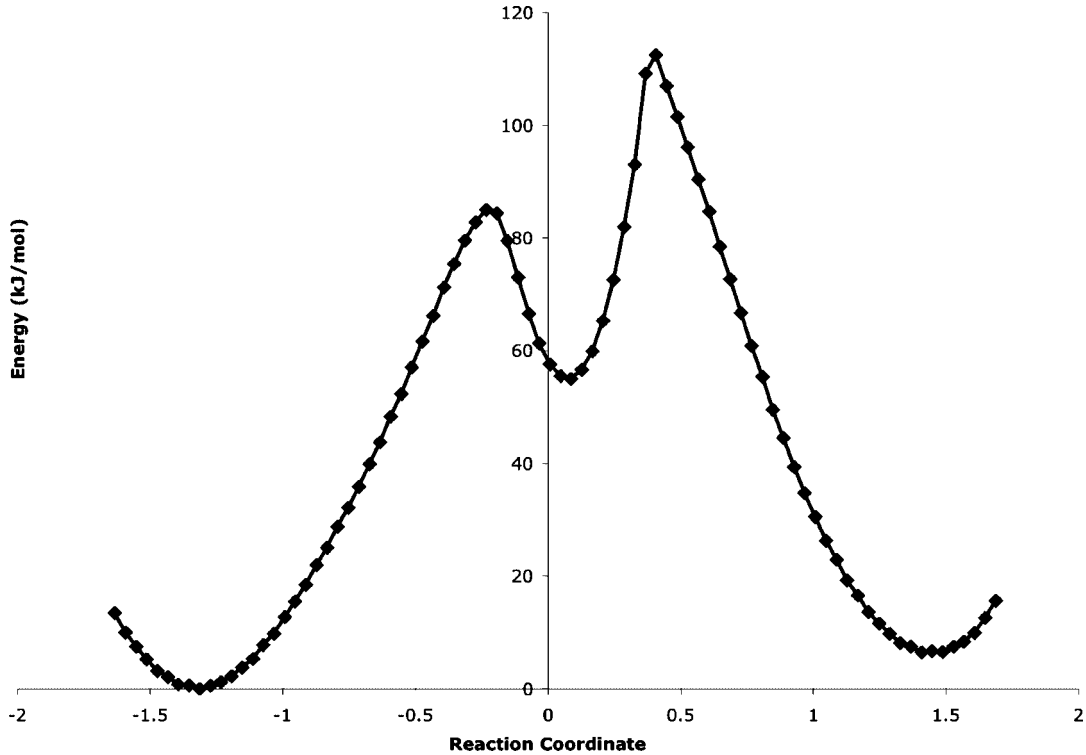

Figure 2. Potential of mean force along the reaction path for the gas-phase, uncatalyzed PY → HY tautomerization employing the $K = 5$ DG-EVB surface. The artificial minimum near the TS results from the quadratic forms of H_{11} and H_{22}.

water molecules rather than true proton shuttling. The correct TS for the three-water proton shuttle for the PY to HY tautomerization is included in Tables 3 and 4 and the structure is available in the Supporting Information for the present paper.

This paper provides benchmark reaction energetics for the PY$(H_2O)_n$ → HY$(H_2O)_n$ ($n = 0-3$) tautomerization reactions in the gas and solution phases. The influence of proton-shuttling water molecules in both phases is also discussed. A reactive electronic potential energy surface for use in

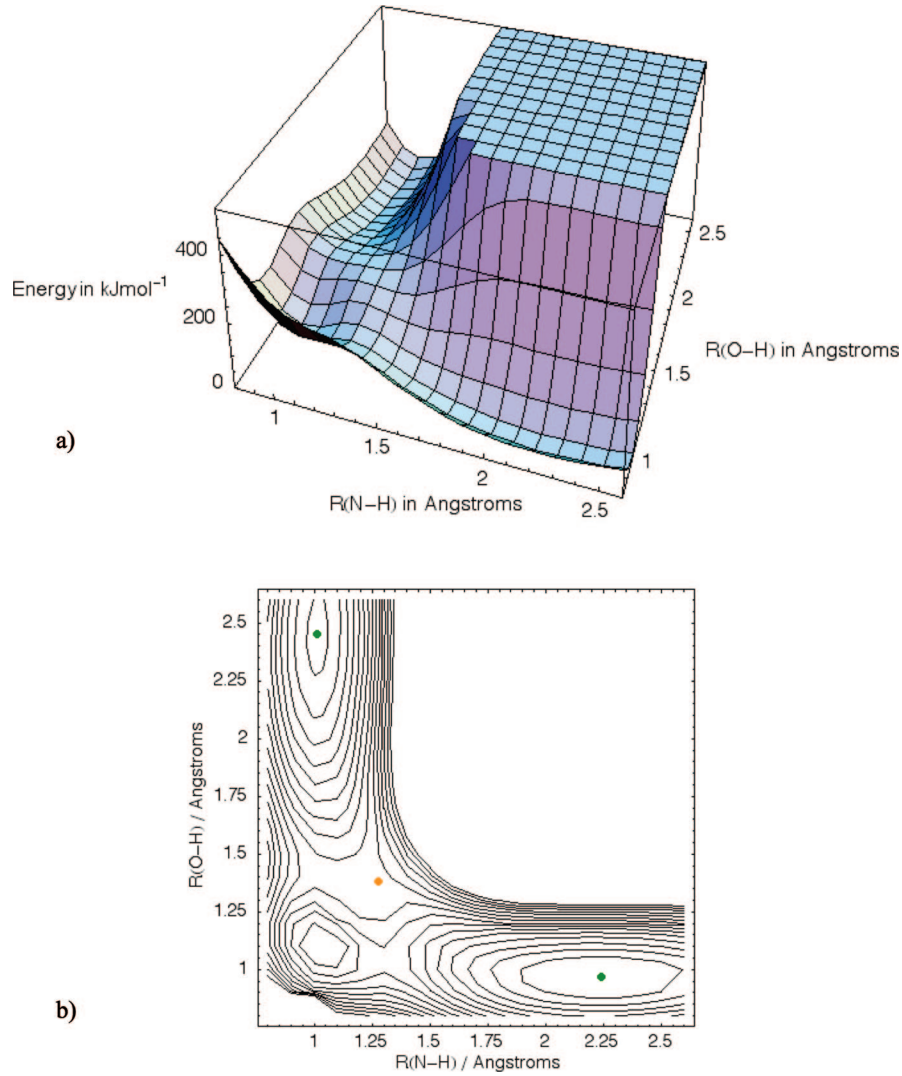

Figure 3. Two-dimensional DG-EVB potential energy surface for the gas-phase, uncatalyzed PY → HY tautomerization, employing the $K = 5$ fit with quadratic H_{nn}. The PY valley is in the back, left-hand corner, while the HY valley is up front in the right-hand corner in both plots. The minima are denoted with a green dot and the TS with an orange dot.

molecular dynamics simulations is then generated from the highly accurate ab initio results following a recently improved EVB formulation using a superposition of states[37,38] and distributed Gaussians.[39,40] The importance of utilizing improved molecular mechanics force fields that go beyond the quadratic approximation utilized in most dynamics calculations is addressed.

2. Computational Methods

The G3,[41] G4,[42] CBS-APNO,[43] and W1[44] model chemistries were employed to determine tautomerization energetics to within ±4.7, ±3.5, ±2.2, and ±1.3 kJ/mol, respectively. Additional data points along the reaction path were generated at the MP2/6-311+G(d,p) level of theory[45−47] using the second-order predictor-corrector reaction path following integrator of Hratchian and Schlegel.[48,49] All stationary points along the reaction path were optimized with the Berny algorithm[50] and confirmed with harmonic vibrational frequency analysis. Bulk solvation effects were accounted for via IEF-PCM in the SCRF framework with a dielectric value of 78.39 and UFF atomic radii.[51−53] All electronic structure calculations were computed using a development version of the Gaussian suite,[54] while the EVB fits and analysis were done in Mathematica version 5.2[55] using the EVB Toolkit for Mathematica[56] developed by the authors. Preliminary MD calculations employed the development version of AMBER 10.[57]

3. Results and Discussion

The discussion begins with calculated results for the pyridone tautomerization reaction, in both the gas and aqueous phases, which has been studied extensively. The effect of proton shuttling waters on reaction energetics and barrier heights is examined for one to three catalytic waters. A new TS structure for the proton-shuttling mechanism involving three catalytic water molecules is given to correct an existing error in the literature. The general form of valence bond potential surfaces for reactions is described, and then some technical aspects of building reliable reactive potential energy surfaces are discussed.

3.1. Reaction Energetics. Our gas- and aqueous-phase results for the pyridone tautomerization are presented in

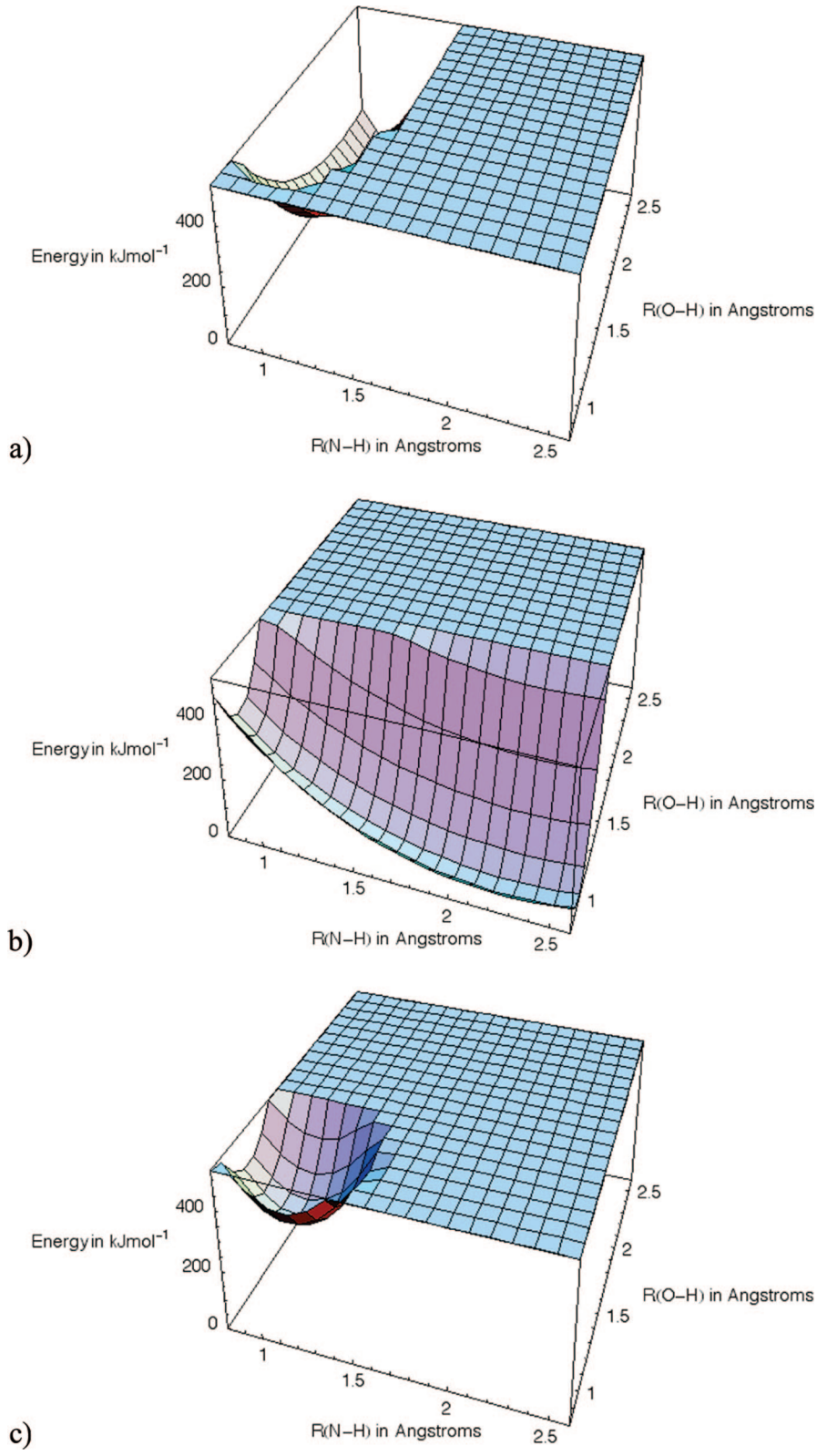

Figure 4. Decomposition of the DG-EVB potential energy surface for the gas-phase, uncatalyzed PY → HY tautomerization employing the $K = 5$ fit with quadratic H_{nn}: (a) H_{11}, (b) H_{22}, and (c) the first term of eq 4, $(H_{11} + H_{22})/2$. The PY valley is in the back, left-hand corner, while the HY valley is up front in the right-hand corner in all plots.

Tables 2−4. For the uncatalyzed tautomerization, the system size is small enough that all four model chemistries, G3, G4, CBS-APNO, and W1 are tractable calculations. Differences of less than 1 kJ/mol between theory and experiment should be considered excellent agreement for systems of this size, thus the gas-phase W1 results can be taken as a "gold standard" for evaluation of other computed results. Of the three remaining model chemistries, the error in barrier heights and reaction energetics increases as G4 < G3 < CBS-APNO when compared to the W1 results. Although CBS-APNO calculations were still feasible for the gas-phase tautomerization reaction catalyzed with one water molecule, only G3

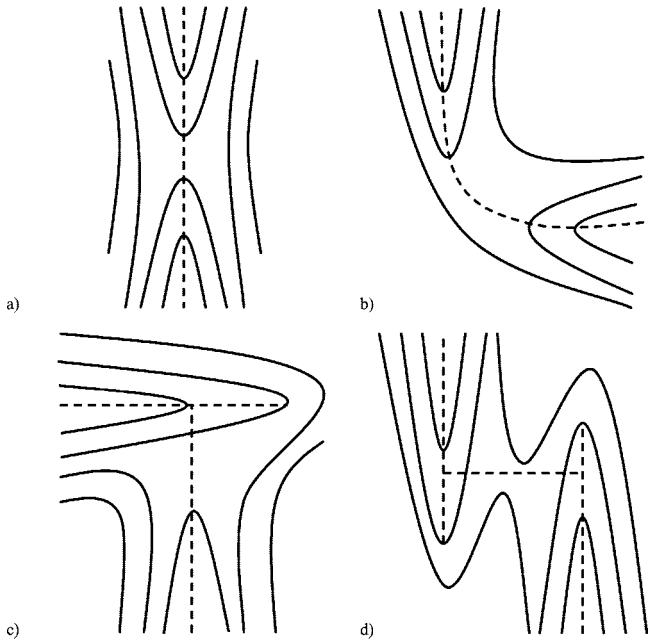

Figure 5. Various classes of reaction channels near the TS on reactive potential energy surfaces: (a) I-shaped valley, (b) L- or V-shaped valley, (c) T-shaped valley, (d) H- or X-shaped valley.

and G4 model chemistry results were computed for gas-phase reactions with more than one water molecule and for all aqueous reactions. For the aqueous results, the agreement between G4 and experiment is very good for the uncatalyzed tautomerization, thus all further discussions of energetics will refer to the G4 results unless noted otherwise.

As seen previously,[10,21] HY is the lower energy gas-phase tautomer only when no proton-shuttling water is present. The addition of one, two, or three water catalysts stabilizes PY by an additional 5.2, 6.0, and 6.7 kJ/mol, respectively. Interestingly, the catalytic waters always form a prereactive complex which minimizes the hydrogen bonding distances prior to transferring the H atom (see Supporting Information). In the aqueous systems, PY is always the lower energy tautomer regardless of the number of catalytic water molecules present. As seen in Table 4, the aqueous reaction energy computed with polarizable continuum models becomes essentially constant once catalytic water molecules are employed as proton shuttles. Therefore the number of catalytic water molecules actually participating in the ground-state tautomerization reaction is determined by the barrier height, *not* the over all reaction energy. Such trends in reaction barriers for additional catalytic waters have been seen previously.[58] In both phases, the reaction barrier decreases by ~90 kJ/mol with the addition of one catalytic water molecule. Additional water molecules actually *increase* the barrier height by ~10 kJ/mol for two water molecules, which agrees with earlier computational studies.[21,30] Since multiple water catalysts increase the reaction barrier height, electronic potential energy surfaces will only be constructed for the two reactions, PY → HY and PY(H_2O) → HY(H_2O).

3.2. Reactive Potential Energy Surfaces. A prerequisite step in molecular dynamic (MD) studies is the construction of a reliable reactive electronic potential energy surface. A reactive potential energy surface $V(\mathbf{q})$, where $\mathbf{q}$ is the vector of molecular coordinates, can be constructed by means of a superposition of reactant and product configuration, ψ_1 and ψ_2, interacting via an empirical Hamiltonian, $\hat{\mathbf{H}}$.[59]

$$\Psi = c_1\psi_1 + c_2\psi_2 \tag{1}$$

$$\hat{\boldsymbol{H}} = \begin{bmatrix} H_{11} & H_{12} \\ H_{21} & H_{22} \end{bmatrix} \tag{2}$$

$$H_{11} = \langle\psi_1|\hat{H}|\psi_1\rangle, H_{12} = H_{21} = \langle\psi_1|\hat{H}|\psi_2\rangle, H_{22} = \langle\psi_2|\hat{H}|\psi_2\rangle \tag{3}$$

$$V(\mathbf{q}) = \tfrac{1}{2}[H_{11}(\mathbf{q}) + H_{22}(\mathbf{q})] - \sqrt{\{\tfrac{1}{2}[H_{11}(\mathbf{q}) - H_{22}(\mathbf{q})]\}^2 + H_{12}^2(\mathbf{q})} \tag{4}$$

H_{11} and H_{22} are the energy surfaces for the reactant and product potentials, respectively, and H_{12} is the resonance integral that must be represented by an approximate functional form. The construction of reactive potential energy surfaces as a superposition of two or more states has a long history as evidenced in the review by Balint-Kurti.[60] In 1929, London showed that a qualitatively correct potential energy surface for the H + H_2 exchange reaction could be generated from two configurations.[61] In a 1938 Faraday discussion on reaction kinetics, Eyring reported the potential energy surface for the same hydrogen exchange reaction calculated from the interaction of five configurations.[62] At the same conference, Evans and Polanyi described a surface for the Cl^- + CH_3Cl S_N2 reaction built from a reactant and a product configuration.[63] The ensuing discussion pointed out that the two approaches are equivalent and identical to the method used in an earlier work on the barriers for ionic reactions.[64] Evans also provided an early application of this approach to the Diels−Alder reaction.[65] Subsequent variations on this method differ primarily in the manner of approximating the H_{11}, H_{22}, and H_{12} matrix elements.

An empirical valence bond (EVB) approach for estimating the matrix elements was employed by Warshel for comparing reactions in solution and enzymes.[66] Pross and Shaik used a qualitative, valence-bond, configuration-mixing approach to investigate organic reactions.[67] More relevant to the present work, Chang and Miller[68,69] constructed accurate potential energy surfaces by fitting a superposition of two EVB configurations to ab initio energies, gradients and Hessians using a generalized Gaussian for H_{12}. Minichino and Voth generalized the Chang-Miller method[68] for N-state systems and provided a scheme to correct gas-phase ab initio data for solutions.[70]

From a pedagogical point of view, EVB surfaces can be classified by the approximation employed in H_{12}. In addition to the simple choice of setting H_{12} equal to a constant (Constant-EVB) that reproduces experimental or high-level ab initio barrier heights, two methods have emerged for constructing accurate reactive EVB surfaces: DWI-EVB and DG-EVB. DWI-EVB represents $H_{12}(\mathbf{q})$ as a distance weighted interpolation (DWI), aka Shepard interpolation, around a set of molecular configurations (called Shepard points) where the energy, gradient, and Hessian are available.[71−74] DG-EVB builds upon the Chang−Miller method[68] and expands

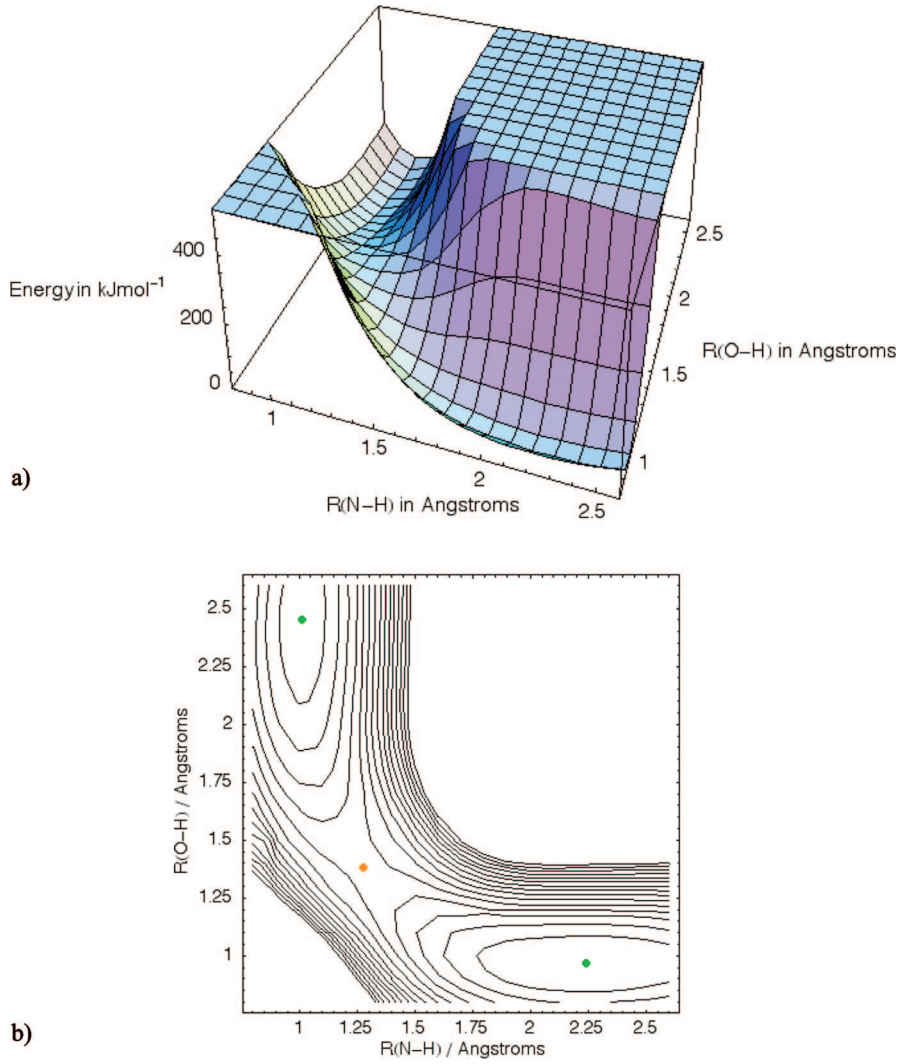

Figure 6. Two-dimensional DG-EVB potential energy surface for the gas-phase, uncatalyzed PY → HY tautomerization employing the $K = 5$ fit with repulsive H_{nn}. The PY valley is in the back, left-hand corner, while the HY valley is up front in the right-hand corner in both plots. The minima are denoted with a green dot and the TS with an orange dot.

$H^2_{12}(\mathbf{q})$ into a set of distributed Gaussians (DG) centered on a set of molecular configurations.[39,40] In our DG-EVB approach, the following form of $H^2_{12}(\mathbf{q})$ is used to reproduce electronic structure data,

$$H^2_{12}(\mathbf{q}) = \sum_{K}^{N_{\mathrm{cfg}}} \sum_{i \geq j \geq 0}^{N_{\mathrm{dim}}} B_{ijK} g(\mathbf{q}, \mathbf{q}_K, i, j, \alpha_K) \tag{5}$$

$$H^2_{12}(\mathbf{q}) = [H_{11}(\mathbf{q}) - V(\mathbf{q})][H_{22}(\mathbf{q}) - V(\mathbf{q})] \tag{6}$$

$$\Delta\mathbf{q}_K = \mathbf{q} - \mathbf{q}_K \tag{7}$$

$$\begin{aligned} g(\mathbf{q}, \mathbf{q}_K, 0, 0, \alpha_K) &= (1 + \tfrac{1}{2}\alpha_K|\Delta\mathbf{q}_K|^2)\exp[-\tfrac{1}{2}\alpha_K|\Delta\mathbf{q}_K|^2] \\ g(\mathbf{q}, \mathbf{q}_K, i, 0, \alpha_K) &= (\Delta\mathbf{q}_K)_i \exp[-\tfrac{1}{2}\alpha_K|\Delta\mathbf{q}_K|^2] \\ g(\mathbf{q}, \mathbf{q}_K, i, j, \alpha_K) &= (1 - \tfrac{1}{2}\delta_{ij})(\Delta\mathbf{q}_K)_i(\Delta\mathbf{q}_K)_j \exp[-\tfrac{1}{2}\alpha_K|\Delta\mathbf{q}_K|^2] \end{aligned} \tag{8}$$

where $g(\mathbf{q}, \mathbf{q}_K, i, j, \alpha_K)$ are s-, p-, and d-type Gaussians centered at a number of molecular configurations, $\mathbf{q}_K$, on the potential energy surface and $\mathbf{B}$ is a vector of coefficients. It is important to note that nonstandard s- and d-type Gaussians are employed to precondition the resulting set of linear equations (see Appendix) that are passed to a GMRES[75] (aka DIIS[76−78]) solver. For a more exhaustive discussion of the DG-EVB method please see ref 39.

Previously the gas-phase, uncatalyzed, 2-pyridone tautomerization reaction was utilized as a test system for the DG-EVB method employing a GMRES solver.[40] In that work, a simple quadratic function was employed for H_{11} and H_{22}

$$H_{nn}(\mathbf{q}) = E_n + \mathbf{g}_n^{\mathrm{T}}\cdot\Delta\mathbf{q} + \tfrac{1}{2}(\Delta\mathbf{q}^{\mathrm{T}}\cdot\tilde{\mathbf{H}}_n\cdot\Delta\mathbf{q}), \quad \Delta\mathbf{q} = \mathbf{q} - \mathbf{q}_n \tag{9}$$

where E_n, $\mathbf{g}_n$, and $\tilde{\mathbf{H}}_n$ are the ab initio energy, gradient, and Hessian, respectively, of the reactant or product. Preliminary MD calculations using the published distributed-Gaussian surfaces discovered a false minimum in the potential of mean force (PMF) plot shown in Figure 2, as a result of an oversimplified form for H_{11} and H_{22}. To investigate the artificial minimum in the PMF plot, a two-dimensional relaxed scan of the 2-pyridone N−H and O−H bond lengths was computed at the HF/6−311+G(d,p) level of theory. The resulting DG-EVB surface for those HF geometries indicated

that a "swimming hole" had formed behind the TS (see Figure 3). The source of the "swimming hole", as shown in Figure 4, was the interaction of H_{11} and H_{22} in the first term of eq 4. Although H_{12} can correct H_{11} and H_{22}, thereby producing an improved V along the reaction path, it cannot completely counterbalance the additive interaction of the quadratic valence bond potentials near the TS. For L- or V-shaped reaction channels, arising from reactions where two coordinates dominate the reaction path, as in the pyridone tautomerization, a simple quadratic potential is too rudimentary and could generate artificial holes in the EVB surface. The T-, H-, or X-shaped reaction channels[80] shown in Figure 5 may also generate artificial minima in the DG-EVB surface when simple quadratic potentials are used as a consequence of geometry, but I-shaped reaction channels should not.

The ground-state potential generated by the interaction of H_{11} and H_{22} via H_{12} is given in eq 4. For this expression to be a good model of the true potential, $V_{\text{true}}(\mathbf{q})$, the first term must always be greater than $V_{\text{true}}(\mathbf{q})$, since the square root in the second term must be positive and real for the ground-state potential.

$$\tfrac{1}{2}(H_{11}(\mathbf{q}) + H_{22}(\mathbf{q})) \geq V_{\text{true}}(\mathbf{q}) \tag{10}$$

In the region around the TS or around any test point, we can approximate $V_{\text{true}}(\mathbf{q})$ by a Taylor series truncated at second order

$$V_{\text{TS}}(\mathbf{q}) \approx V_{\text{TS}}^0 + (\mathbf{V}_{\text{TS}}')^{\text{T}}(\mathbf{q} - \mathbf{q}_{\text{TS}}) + \tfrac{1}{2}(\mathbf{q} - \mathbf{q}_{\text{TS}})^{\text{T}}\tilde{\mathbf{V}}_{\text{TS}}''(\mathbf{q} - \mathbf{q}_{\text{TS}}) \tag{11}$$

with trust radius $\boldsymbol{\tau}_{\text{TS}}$ defining the region where the approximation is valid. The sum of $H_{11}(\mathbf{q})$ and $H_{22}(\mathbf{q})$ can also be approximated by a quadratic function around the TS.

$$V_{\text{sum}}(\mathbf{q}) = \frac{H_{11}(\mathbf{q}) + H_{22}(\mathbf{q})}{2} \approx V_{\text{sum}}^0 + (\mathbf{V}_{\text{sum}}')^{\text{T}}(\mathbf{q} - \mathbf{q}_{\text{TS}}) + \tfrac{1}{2}(\mathbf{q} - \mathbf{q}_{\text{TS}})^{\text{T}}\tilde{\mathbf{V}}_{\text{sum}}''(\mathbf{q} - \mathbf{q}_{\text{TS}}) \tag{12}$$

Note that the minimum for $V_{\text{sum}}(\mathbf{q})$ is between the minima for $H_{11}(\mathbf{q})$ and $H_{22}(\mathbf{q})$, that is, possibly but not necessarily near the transition state. The quadratic expansions for $V_{\text{sum}}(\mathbf{q})$ and $V_{\text{TS}}(\mathbf{q})$ can now be compared to see if eq 4 can produce a suitable surface with the given potentials for $H_{11}(\mathbf{q})$ and $H_{22}(\mathbf{q})$. In particular, we require $V_{\text{sum}}(\mathbf{q}) - V_{\text{TS}}(\mathbf{q}) \geq 0$ to satisfy equation 10.

$$\begin{aligned}
&V_{\text{sum}}(\mathbf{q}) - V_{\text{TS}}(\mathbf{q}) = V_{\text{diff}}(\mathbf{q}) = \\
&V_{\text{diff}}^0 + (\mathbf{V}_{\text{diff}}')^{\text{T}}(\mathbf{q} - \mathbf{q}_{\text{TS}}) + \tfrac{1}{2}(\mathbf{q} - \mathbf{q}_{\text{TS}})^{\text{T}}\tilde{\mathbf{V}}_{\text{diff}}''(\mathbf{q} - \mathbf{q}_{\text{TS}}) \\
&V_{\text{diff}}^0 = (V_{\text{sum}}^0 - V_{\text{TS}}^0), \\
&\mathbf{V}_{\text{diff}}' = (\mathbf{V}_{\text{sum}}' - \mathbf{V}_{\text{TS}}'), \tilde{\mathbf{V}}_{\text{diff}}'' = (\tilde{\mathbf{V}}_{\text{sum}}'' - \tilde{\mathbf{V}}_{\text{TS}}'') \\
&\mathbf{q}_{\text{min}} = -(\tilde{\mathbf{V}}_{\text{diff}}'')^{-1}\mathbf{V}_{\text{diff}}', \\
&V_{\text{diff}}(\mathbf{q}_{\text{min}}) = V_{\text{diff}}^0 - \tfrac{1}{2}\mathbf{V}_{\text{diff}}'(\tilde{\mathbf{V}}_{\text{diff}}'')^{-1}\mathbf{V}_{\text{diff}}'
\end{aligned} \tag{13}$$

where $\mathbf{q}_{\text{min}}$ is the minimum of $V_{\text{diff}}(\mathbf{q})$ (or a higher order stationary point if $\tilde{V}_{\text{diff}}''$ has one or more negative eigenvalues). A number of cases can be considered.

(a) If $V_{\text{diff}}(\mathbf{q}_{\text{min}})$ is positive and all the eigenvalues of $\tilde{\mathbf{V}}_{\text{diff}}''$ are positive, then eq 10 holds for all $\mathbf{q}$ within the trust region of the quadratic expansion and a reliable potential energy surface can be constructed in this region with a suitable choice for $H_{12}^2(\mathbf{q})$ (however, this may require additional molecular configurations).

(b) If $V_{\text{diff}}(\mathbf{q}_{\text{min}})$ is negative or some of the eigenvalues of $\tilde{\mathbf{V}}_{\text{diff}}''$ are negative, then eq 10 is not satisfied in some regions. This can lead to a "swimming hole" similar to the one observed in the simple potential for pyridone. This can be analyzed further by determining where $V_{\text{diff}}(\mathbf{q})$ is negative.

(i) If $V_{\text{diff}}(\mathbf{q}_{\text{min}})$ is negative and $\mathbf{q}_{\text{min}}$ is within the trust radius of the transition state, $|\mathbf{q}_{\text{min}} - \mathbf{q}_{\text{TS}}| < \boldsymbol{\tau}_{\text{TS}}$, then there is clearly a problem.

(ii) For other cases, one needs to find the minimum of $V_{\text{diff}}(\mathbf{q})$ with the constraint $|\mathbf{q}_{\text{min}} - \mathbf{q}_{\text{TS}}| = \boldsymbol{\tau}_{\text{TS}}$. If $V_{\text{diff}}(\mathbf{q}_{\text{min}}) < 0$ for this constrained minimization, then there is a problem. Even if $V_{\text{diff}}(\mathbf{q}_{\text{min}}) > 0$, there may still be problems outside the trust region of the transition state, especially if some of the eigenvalues of $\tilde{\mathbf{V}}_{\text{diff}}''$ are negative. In this case, the location of $\mathbf{q}_{\text{min}}$ may suggest regions for additional molecular configurations to test the surface and to fit $H_{12}^2(\mathbf{q})$.

The analysis described above can be repeated for any additional points used for fitting the surface. It should be emphasized that if eq 10 is not satisfied, the form of $H_{11}(\mathbf{q})$ and $H_{22}(\mathbf{q})$ *must* be modified to avoid spurious deformations of the surface. This is *independent* of the model used for $H_{12}(\mathbf{q})$ and the resulting EVB surface (e.g., DWI-EVB and DG-EVB).

To improve our model valence bond potentials and bring them more in line with modern molecular mechanics potentials, a nonbonding, van der Waals, exponential-6 term from the universal force field (UFF)[80] was added to H_{nn} for coordinates of interest.

$$\begin{aligned}
&H_{nn}(\mathbf{q}) = \\
&C + \mathbf{g}_n^{\text{T}}\cdot\Delta\mathbf{q} + \tfrac{1}{2}(\Delta\mathbf{q}^{\text{T}}\cdot\tilde{\mathbf{H}}_n\cdot\Delta\mathbf{q}) + \sum_i A_{\text{UFF}}^i \exp[-B_{\text{UFF}}^i\Delta\mathbf{q}^i] \\
&\Delta\mathbf{q} = \mathbf{q} - \mathbf{q}_n, C = E_n - \sum_i A_{\text{UFF}}^i \exp[-B_{\text{UFF}}^i\Delta\mathbf{q}^i]
\end{aligned} \tag{14}$$

In eq 14, A_{UFF}^i and B_{UFF}^i are UFF exponential-6 parameters, $\Delta\mathbf{q}^i$ is the repulsive coordinate value (e.g., H—O in PY and N—H in HY) for H_{nn}, and C is a constant ensuring the ab initio energy is recovered at the DG-EVB data points, $\mathbf{q} = \mathbf{q}_n$. Alternatively, the harmonic bond-stretch terms could be replaced by Morse potentials but this requires the determination of Morse parameters for bonds of interest. Both capabilities have been added to the development version of AMBER 10, so that eq 10 can be satisfied. The exponential-6 term has the advantage of less work because all the necessary parameters are already in the literature. In Figure 6, it can been seen that the additional repulsive term does remove the "swimming hole" behind the TS. Since the α values for the $K = 5$ DG-EVB fit are nearly independent of the form of H_{nn}, simple quadratic valence bond potentials may be useful in accelerating the α values optimization process for very large molecular systems, such as enzymes.

The improved form of H_{nn} was utilized to build a DG-EVB surface for the pyridone tautomerization catalyzed by a proton-shuttling water in the gas phase. With $K = 5$, α values of {1.2, 1.3, 1.9, 1.8, 1.8} and four repulsive coordinates, the maximum error along the reaction path is 2.37 kJ/mol. The absence of artificial "swimming holes" in the surface indicates that our improved H_{nn} is acceptable for the current application. It is important to note that one should always test the accuracy both on and off of the reaction path to ensure the quality of the surface.

4. Conclusions

This work reviewed the experimental and computational results for the tautomerization reaction of 2-pyridone. State of the art G3, G4, CBS-APNO, and W1 model chemistries were employed along with the IEF-PCM method to elucidate the gas- and solution-phase tautomerization reaction energetics with and without proton shuttling water molecules. The new data clearly show how the addition of both catalytic water and bulk solvent renders the tautomerization energy in solution nearly constant at 11 kJ/mol in favor of $PY(H_2O)_n$. Since the reaction energy is nearly constant, the reaction barrier correlates with the number of catalytic water molecules employed in the tautomerization. Again it is clear that while reaction channels employing two and three proton-shuttling waters are possible, these channels actually have *higher* barriers than the reaction path utilizing one catalytic water.

Reactive electronic potential energy surfaces suitable for use in molecular dynamics simulations were generated for PY → HY and $PY(H_2O)$ → $HY(H_2O)$ reactions using the DG-EVB formalism. Investigation of our previously published PY → HY surface illuminated a shortcoming in our ground-state molecular mechanics potentials, namely that harmonic force fields do not guarantee an EVB surface free of spurious deformations. This shortcoming can be overcome by including a repulsive term in the force field for at least the bonds that are breaking and forming. This new form of H_{nn} was successfully used to generate new DG-EVB surfaces that possess no artificial minima along or besides the reaction path. Employing a H_{nn} functional form that satisfies eq 10 lays the foundation for applying the DG-EVB methodology to large-scale biological simulations.

Acknowledgment. The Office of Naval Research (N00014-05-1-0457) supported this research. The authors thank Dr. Shinichi Yamabe for providing his three-water proton shuttle TS and are grateful for computer time from the Wayne State University Grid.

Supporting Information Available: The EVB Toolkit for Mathematica is free software available for download along with all DG-EVB surfaces on the "Software" tab at http://chem.wayne.edu/schlegel/. Cartesian coordinates of the stationary points along with animated GIFs of the gas-phase, MP2 IRC geometries for the four, tautomerization reactions. This material is available free of charge via the Internet at http://pubs.acs.org.

Appendix

For a symmetric 2 × 2 EVB Hamiltonian matrix,

$$\hat{\mathbf{H}}_{\mathrm{EVB}} = \begin{bmatrix} H_{11} & H_{12} \\ H_{21} & H_{22} \end{bmatrix} \tag{15}$$

the analytical solution for the coupling term is

$$H_{12}^2(\mathbf{q}) = [H_{11}(\mathbf{q}) - \varepsilon_{\mathrm{EVB}}(\mathbf{q})][H_{22}(\mathbf{q}) - \varepsilon_{\mathrm{EVB}}(\mathbf{q})] \tag{16}$$

where $\varepsilon_{\mathrm{EVB}}$is the lowest eigenvalue of the matrix and $H_{11}(\mathbf{q})$ and $H_{22}(\mathbf{q})$ are the reactant and product valence bond states. $H_{11}(\mathbf{q})$ and $H_{22}(\mathbf{q})$ can be described by a force field potential or as a Taylor series expansion about the minimum from ab initio calculations. With the valence bond states defined, the goal here is to provide a prescription for $H_{12}^2(\mathbf{q})$ such that the resulting EVB surface approximates the ab initio surface, that is, $\varepsilon_{\mathrm{EVB}} = \varepsilon_{\Psi}$. The Chang−Miller approach approximates $H_{12}^2(\mathbf{q})$ as a generalized Gaussian

$$H_{12}^2(\mathbf{q}) = A \exp[\mathbf{B}^{\mathrm{T}}\cdot\Delta\mathbf{q} - \tfrac{1}{2}\Delta\mathbf{q}^{\mathrm{T}}\cdot\tilde{\mathbf{C}}\cdot\Delta\mathbf{q}], \Delta\mathbf{q} = \mathbf{q} - \mathbf{q}_{\mathrm{TS}} \tag{17}$$

where the parameters A (a scalar), $\mathbf{B}$ (a vector), and $\tilde{\mathbf{C}}$ (a matrix) are chosen to reproduce the ab initio energy, gradient, and Hessian at the transition state. In this form, H_{12}^2 diverges for large $\Delta\mathbf{q}$ when $\tilde{\mathbf{C}}$ contains one or more negative eigenvalues. While refinements are available for controlling the asymptotic behavior of the Chang−Miller approach, recasting eq 17 in terms of a quadratic polynomial times a spherical Gaussian

$$H_{12}^2(\mathbf{q}) = A[1 + \mathbf{B}^{\mathrm{T}}\cdot\Delta\mathbf{q} + \tfrac{1}{2}\Delta\mathbf{q}^{\mathrm{T}}\cdot(\tilde{\mathbf{C}} + \alpha\tilde{\mathbf{I}})\cdot\Delta\mathbf{q}]\exp[-\tfrac{1}{2}\alpha|\Delta\mathbf{q}|^2] \tag{18}$$

keeps the coupling element bounded at the asymptotes. The distributed Gaussian (DG) approach generalizes the above polynomial times a Gaussian prescription to utilize ab initio information at other potential energy surface points in addition to the transition state. Here, $H_{12}^2(\mathbf{q})$ is approximated as an expansion about a set of distributed Gaussians centered on a set of molecular configurations $\mathbf{q}_K$

$$H_{12}^2(\mathbf{q}) = \sum_{K}^{N_{\mathrm{cfg}}} \sum_{i\geq j\geq 0}^{N_{\mathrm{dim}}} B_{ijK} g(\mathbf{q}, \mathbf{q}_K, i, j, \alpha_K) \tag{19}$$

$$g(\mathbf{q}, \mathbf{q}_K, 0, 0, \alpha_K) = (1 + \tfrac{1}{2}\alpha_K|\Delta\mathbf{q}_K|^2)\exp[-\tfrac{1}{2}\alpha_K|\Delta\mathbf{q}_K|^2] \tag{20}$$

$$g(\mathbf{q}, \mathbf{q}_K, i, 0, \alpha_K) = (\Delta\mathbf{q}_K)_i \exp[-\tfrac{1}{2}\alpha_K|\Delta\mathbf{q}_K|^2] \tag{21}$$

$$g(\mathbf{q}, \mathbf{q}_K, i, j, \alpha_K) = (1 - \tfrac{1}{2}\delta_{ij})(\Delta\mathbf{q}_K)_i(\Delta\mathbf{q}_K)_j \exp[-\tfrac{1}{2}\alpha_K|\Delta\mathbf{q}_K|^2] \tag{22}$$

$$\Delta\mathbf{q}_K = \mathbf{q} - \mathbf{q}_K \tag{23}$$

where N_{cfg} is the number of ab initio data points used for the fitting, N_{dim} is the number of system coordinates, $g(\mathbf{q},\mathbf{q}_K,i,j,\alpha_K)$ are the s-, p-, and d-type Gaussians and B_{ijK} are the expansion coefficients. The term involving the unit matrix in eq 18 was accumulated into the s-type Gaussian

(eq 20) to precondition the system of linear equations for faster convergence when utilizing iterative solution methods. The non-standard form of the d-type Gaussian is for similar reasons. If the number of Gaussian centers K is equal to the number of data points where H_{12}^2 are evaluated, eq 19 describes a system of linear equations

$$\mathbf{F}^{\mathrm{T}} = \mathbf{B}^{\mathrm{T}}\tilde{\mathbf{D}}^{\mathrm{T}}$$

or

$$\mathbf{F} = \tilde{\mathbf{D}}\mathbf{B} \quad (24)$$

that can be solved using singular value decomposition or by an iterative procedure, such as GMRES. The vector $\mathbf{F}$ stores the coupling terms evaluated at the N_{cfg} ab initio configurations

$$\mathbf{F} = \begin{bmatrix} H_{12}^2(\mathbf{q}_1) \\ H_{12}^2(\mathbf{q}_2) \\ \vdots \\ H_{12}^2(\mathbf{q}_{N_{\mathrm{cfg}}-1}) \\ H_{12}^2(\mathbf{q}_{N_{\mathrm{cfg}}}) \end{bmatrix} \quad (25)$$

where (see eq 16)

$$H_{12}^2(\mathbf{q}_K) = [H_{11}(\mathbf{q}_K) - \varepsilon_\Psi(\mathbf{q}_K)][H_{22}(\mathbf{q}_K) - \varepsilon_\Psi(\mathbf{q}_K)] \quad (26)$$

When first and second derivatives are available for H_{nn} and the ab initio energy, ε_Ψ, the derivative of the coupling terms can also be utilized in the DG fitting procedure. In this case, the $\mathbf{F}$ vector has the following elements

$$\mathbf{F} = \begin{bmatrix} H_{12}^2(\mathbf{q}_1) \\ \vdots \\ H_{12}^2(\mathbf{q}_{N_{\mathrm{cfg}}}) \\ \partial H_{12}^2(\mathbf{q}) \big/ \partial \mathbf{q}|_{\mathbf{q}=\mathbf{q}_1} \\ \vdots \\ \partial H_{12}^2(\mathbf{q}) \big/ \partial \mathbf{q}|_{\mathbf{q}=\mathbf{q}_{N_{\mathrm{cfg}}}} \\ \partial^2 H_{12}^2(\mathbf{q}) \big/ \partial \mathbf{q}^2|_{\mathbf{q}=\mathbf{q}_1} \\ \vdots \\ \partial^2 H_{12}^2(\mathbf{q}) \big/ \partial \mathbf{q}^2|_{\mathbf{q}=\mathbf{q}_{N_{\mathrm{cfg}}}} \end{bmatrix} \quad (27)$$

The corresponding unsymmetric matrix $\tilde{\mathbf{D}}$ contains the values and derivatives of the Gaussian bases

$$\tilde{\mathbf{D}} = \begin{bmatrix} g(\mathbf{q}_1, \mathbf{q}_1, \{i,j\}, \alpha_K) & \cdots & g(\mathbf{q}_1, \mathbf{q}_{N_{\mathrm{cfg}}}, \{i,j\}, \alpha_K) \\ \vdots & \ddots & \vdots \\ g(\mathbf{q}_{N_{\mathrm{cfg}}}, \mathbf{q}_1, \{i,j\}, \alpha_K) & \cdots & g(\mathbf{q}_{N_{\mathrm{cfg}}}, \mathbf{q}_{N_{\mathrm{cfg}}}, \{i,j\}, \alpha_K) \\ \partial g(\mathbf{q}, \mathbf{q}_1, \{i,j\}, \alpha_K) \big/ \partial \mathbf{q}|_{\mathbf{q}=\mathbf{q}_1} & \cdots & \partial g(\mathbf{q}, \mathbf{q}_{N_{\mathrm{cfg}}}, \{i,j\}, \alpha_K) \big/ \partial \mathbf{q}|_{\mathbf{q}=\mathbf{q}_1} \\ \vdots & \ddots & \vdots \\ \partial g(\mathbf{q}, \mathbf{q}_1, \{i,j\}, \alpha_K) \big/ \partial \mathbf{q}|_{\mathbf{q}=\mathbf{q}_{N_{\mathrm{cfg}}}} & \cdots & \partial g(\mathbf{q}, \mathbf{q}_{N_{\mathrm{cfg}}}, \{i,j\}, \alpha_K) \big/ \partial \mathbf{q}|_{\mathbf{q}=\mathbf{q}_{N_{\mathrm{cfg}}}} \\ \partial^2 g(\mathbf{q}, \mathbf{q}_1, \{i,j\}, \alpha_K) \big/ \partial \mathbf{q}^2|_{\mathbf{q}=\mathbf{q}_1} & \cdots & \partial^2 g(\mathbf{q}, \mathbf{q}_{N_{\mathrm{cfg}}}, \{i,j\}, \alpha_K) \big/ \partial \mathbf{q}^2|_{\mathbf{q}=\mathbf{q}_1} \\ \vdots & \ddots & \vdots \\ \partial^2 g(\mathbf{q}, \mathbf{q}_1, \{i,j\}, \alpha_K) \big/ \partial \mathbf{q}^2|_{\mathbf{q}=\mathbf{q}_{N_{\mathrm{cfg}}}} & \cdots & \partial^2 g(\mathbf{q}, \mathbf{q}_{N_{\mathrm{cfg}}}, \{i,j\}, \alpha_K) \big/ \partial \mathbf{q}^2|_{\mathbf{q}=\mathbf{q}_{N_{\mathrm{cfg}}}} \end{bmatrix} \quad (28)$$

where $\{i,j\}$ indicates that the columns of the matrix are elements obtained from cycling through all permutations denoted in the summation over these indices in eq 19. This square matrix has dimensions $DG_{\mathrm{dim}} = N_{\mathrm{cfg}} \times [1 + N_{\mathrm{dim}} + N_{\mathrm{dim}} \times (N_{\mathrm{dim}} + 1)/2]$. If the second derivatives of H_{12}^2 are unavailable, the dimensions of $\tilde{\mathbf{D}}$ are $N_{\mathrm{cfg}} \times (1 + N_{\mathrm{dim}})$. Additionally if the gradients are also unavailable, the matrix will have N_{cfg} rows. Once the solution to the $\mathbf{B}$ vector is known, eq 19 determines H_{12}^2 for all coordinates $\mathbf{q}$. The quality of the resulting PES, nonetheless, depends on the quality of the fit.

References

(1) Cook, M. J.; Katritzky, A. R.; Hepler, L. G.; Matsui, T. *Tetrahedron Lett.* **1976**, *31*, 2685.

(2) Beak, P. *Acc. Chem. Res.* **1977**, *10*, 186.

(3) Bensaude, O.; Dreyfus, M.; Dodin, G.; Dubois, J.-E. *J. Am. Chem. Soc.* **1977**, *99*, 4438.

(4) Guimon, C.; Garrabe, G.; Pfister-Guillouzo, G. *Tetrahedron Lett.* **1979**, *28*, 2585.

(5) Bensaude, O.; Chevrier, M.; Dubois, J.-E. *J. Am. Chem. Soc.* **1979**, *101*, 2423.

(6) Brown, R. S.; Tse, A.; Vederas, J. C. *J. Am. Chem. Soc.* **1980**, *102*, 1174.

(7) Scanlan, M. J.; Hillier, I. H.; MacDowell, A. A. *J. Am. Chem. Soc.* **1983**, *105*, 3568.

(8) Hatherley, L. D.; Brown, R. D.; Godfrey, P. D.; Pierlot, A. P.; Caminati, W.; Damiani, D.; Melandri, S.; Favero, L. B. *J. Phys. Chem.* **1993**, *97*, 46.

(9) Held, A.; Pratt, D. W. *J. Am. Chem. Soc.* **1993**, *115*, 9708.

(10) Maris, A.; Ottaviani, P.; Caminati, W. *Chem. Phys. Lett.* **2002**, *360*, 155.

(11) Frey, J. A.; Leist, R.; Tanner, C.; Frey, H.-M.; Leutwyler, S. *J. Chem. Phys.* **2006**, *125*, 114308.

(12) Hazra, M. K.; Samanta, A. K.; Chakraborty, T. *J. Chem. Phys.* **2006**, *125*, 214302.

(13) Hazra, M. K.; Chakraborty, T. *J. Phys. Chem. A* **2006**, *110*, 9130.

(14) Krebs, C.; Hofmann, H.-J.; Köhler, H.-J.; Weiss, C. *Chem. Phys. Lett.* **1980**, *69*, 537.

(15) Lledós, A.; Bertrán, J. *Tetrahedron Lett.* **1981**, *22*, 775.

(16) Schlegel, H. B.; Gund, P.; Fluder, E. M. *J. Am. Chem. Soc.* **1982**, *104*, 5347.

(17) Field, M. J.; Hillier, I. H. *J. Chem. Soc., Perkin Trans. II* **1987**, 617.

(18) Moreno, M.; Miller, W. H. *Chem. Phys. Lett.* **1990**, *171*, 475.

(19) Wong, M. W.; Wiberg, K. B.; Frisch, M. J. *J. Am. Chem. Soc.* **1992**, *114*, 1645.

(20) Del Bene, J. E. *J. Phys. Chem.* **1994**, *98*, 5902.

(21) Barone, V.; Adamo, C. *J. Phys. Chem.* **1995**, *99*, 15062.

(22) Wang, J.; Boyd, R. J. *J. Phys. Chem.* **1996**, *100*, 16141.

(23) Chou, P.-T.; Wei, C.-Y.; Hung, F.-T. *J. Phys. Chem. B* **1997**, *101*, 9119.

(24) Dkhissi, A.; Houben, L.; Smets, J.; Adamowicz, L.; Maes, G. *J. Mol. Struct.* **1999**, *484*, 215.

(25) Dkhissi, A.; Ramaekers, R.; Houben, L.; Adamowicz, L.; Maes, G. *Chem. Phys. Lett.* **2000**, *331*, 553.

(26) Alkorta, I.; Elguero, J. *J. Org. Chem.* **2002**, *67*, 1515.

(27) Müller, A.; Losada, M.; Leutwyler, S. *J. Phys. Chem. A* **2004**, *108*, 157.

(28) Piacenza, M.; Grimme, S. *J. Comput. Chem.* **2004**, *25*, 83.

(29) Li, Q.-S.; Fang, W.-H.; Yu, J.-G. *J. Phys. Chem. A* **2005**, *109*, 3983.

(30) Fu, A.; Li, H.; Du, D.; Zhou, Z. *J. Phys. Chem. A* **2005**, *109*, 1468.

(31) Tsuchida, N.; Yamabe, S. *J. Phys. Chem. A* **2005**, *109*, 1974.

(32) Esboui, M.; Jainane, N.; Lakhdar, Z. B. *Chem. Phys. Lett.* **2006**, *430*, 195.

(33) Wolfe, S.; Weinberg, N.; Hsieh, Y.-H. *Theor. Chem. Acc.* **2007**, *118*, 265.

(34) Hsieh, Y.-H.; Weinberg, N.; Wolfe, S. *Can. J. Chem.* **2008**, *86*, 81.

(35) Jensen, F. *Introduction to Computational Chemistry*, 2nd ed.; John Wiley & Sons Ltd.: West Sussex, England, 2007; pp 162−169.

(36) Grimme, S. *J. Chem. Phys.* **2003**, *118*, 9095.

(37) Venkatnathan, A.; Voth, G. A. *J. Chem. Theory Comput.* **2005**, *1*, 36.

(38) Ceotto, M.; Ayton, G. S.; Voth, G. A. *J. Chem. Theory Comput.* **2008**, *4*, 560.

(39) Schlegel, H. B.; Sonnenberg, J. L. *J. Chem. Theory Comput.* **2006**, *2*, 905.

(40) Sonnenberg, J. L.; Schlegel, H. B. *Mol. Phys.* **2007**, *105*, 2719.

(41) Curtiss, L. A.; Raghavachari, K.; Redfern, P. C.; Rassolov, V.; Pople, J. A. *J. Chem. Phys.* **1998**, *109*, 7764.

(42) Curtiss, L. A.; Redfern, P. C.; Raghavachari, K. *J. Chem. Phys.* **2007**, *126*, 84108.

(43) Montgomery, J. A.; Ochterski, J. W.; Petersson, G. A. *J. Chem. Phys.* **1994**, *101*, 5900.

(44) Martin, J. M. L.; de Oliveira, G. *J. Chem. Phys.* **1999**, *111*, 1843.

(45) Møller, C.; Plesset, M. S. *Phys. Rev.* **1934**, *46*, 618.

(46) Clark, T.; Chandrasekhar, J.; Spitznagel, G. W.; Schleyer, P. v. R. *J. Comput. Chem.* **1983**, *4*, 294.

(47) Krishnan, R.; Binkley, J. S.; Seeger, R.; Pople, J. A. *J. Chem. Phys.* **1980**, *72*, 650.

(48) Hratchian, H. P.; Schlegel, H. B. *J. Chem. Phys.* **2004**, *120*, 9918.

(49) Hratchian, H. P.; Schlegel, H. B. *J. Chem. Theory Comput.* **2005**, *1*, 61.

(50) Hratchian, H. P.; Schlegel, H. B. Finding minima, transition states, and follow reaction pathways on ab initio potential energy surfaces. In *Theory and Applications of Computational Chemistry: The First Forty Years*; Elsevier: New York, 2005; pp 195.

(51) Cancès, M. T.; Mennucci, B.; Tomasi, J. *J. Chem. Phys.* **1997**, *107*, 3032.

(52) Cossi, M.; Scalmani, G.; Rega, N.; Barone, V. *J. Chem. Phys.* **2002**, *117*, 43.

(53) Mennucci, B.; Cancès, M. T.; Tomasi, J. *J. Phys. Chem. B* **1997**, *101*, 10506.

(54) Frisch, M. J.; Trucks, G. W.; Schlegel, H. B.; Scuseria, G. E.; Robb, M. A.; Cheeseman, J. R.; Montgomery, J. A., Jr.; Vreven, T.; Scalmani, G.; Mennucci, B.; Barone, V.; Petersson, G. A.; Caricato, M.; Nakatsuji, H.; Hada, M.; Ehara, M.; Toyota, K.; Fukuda, R.; Hasegawa, J.; Ishida, M.; Nakajima, T.; Honda, Y.; Kitao, O.; Nakai, H.; Li, X.; Hratchian, H. P.; Peralta, J. E.; Izmaylov, A. F.; Kudin, K. N.; Heyd, J. J.; Brothers, E.; Staroverov, V.; Zheng, G.; Kobayashi, R.; Normand, J.; Sonnenberg, J. L.; Ogliaro, F.; Bearpark, M.; Parandekar, P. V.; Ferguson, G. A.; Mayhall, N. J.; Iyengar, S. S.; Tomasi, J.; Cossi, M.; Rega, N.; Burant, J. C.; Millam, J. M.; Klene, M.; Knox, J. E.; Cross, J. B.; Bakken, V.; Adamo, C.; Jaramillo, J.; Gomperts, R.; Stratmann, R. E.; Yazyev, O.; Austin, A. J.; Cammi, R.; Pomelli, C.; Ochterski, J. W.; Ayala, P. Y.; Morokuma, K.; Voth, G. A.; Salvador, P.; Dannenberg, J. J.; Zakrzewski, V. G.; Dapprich, S.; Daniels, A. D.; Strain, M. C.; Farkas, O.; Malick, D. K.; Rabuck, A. D.; Raghavachari, K.; Foresman, J. B.; Ortiz, J. V.; Cui, Q.; Baboul, A. G.; Clifford, S.; Cioslowski, J.; Stefanov, B. B.; Liu, G.; Liashenko, A.; Piskorz, P.; Komaromi, I.; Martin, R. L.; Fox, D. J.; Keith, T.; Al-Laham, M. A.; Peng, C. Y.; Nanayakkara, A.; Challacombe, M.; Chen, W.; Wong, M. W.; Pople, J. A. *Gaussian DV*; revision G.01; Gaussian, Inc.: Wallingford, CT, 2007.

(55) *Mathematica*; 5.2 ed.; Wolfram Research: Champaign, IL, 2005.

(56) Sonnenberg, J. L.; Schlegel, H. B. The Empirical Valence Bond Toolkit for Mathematica. http://chem.wayne.edu/schlegel/ (accessed November, 2008).

(57) Case, D. A.; Darden, T. A.; Cheatham, T. E., III.; Simmerling, C. L.; Wang, J.; Duke, R. E.; Luo, R.; Crowley, M.; Walker, R. C.; Zhang, W.; Merz, K. M.; Wang, B.; Hayik, S.; Roitberg, A.; Seabra, G.; Kolossvary, I.; Wong, K. F.; Paesani, F.; Vanicek, J.; Wu, X.; Brozell, S. R.; Steinbrecher, T.; Gohlke, H.; Yang, L.; Tan, C.; Mongan, J.; Hornak, V.; Cui, G.; Mathews, D. H.; Seetin, M. G.; Sagui, C.; Babin, V.; Kollman, P. A. *AMBER 10*; University of California: San Francisco, 2008.

(58) Takahashi, K.; Kramer, Z. C.; Vaida, V.; Skodje, R. T. *Phys. Chem. Chem. Phys.* **2007**, *9*, 3864.

(59) Villa, J.; Warshel, A. *J. Phys. Chem. B* **2001**, *105*, 7887.

(60) Balint-Kurti, G. G. *Adv. Chem. Phys.* **1975**, *30*, 137.

(61) London, F. *Z. Elektrochem.* **1929**, *35*, 552.

(62) Eyring, H. *Trans. Farad. Soc.* **1938**, *34*, 3.

(63) Evans, M. G.; Polanyi, M. *Trans. Farad. Soc.* **1938**, *34*, 11.

(64) Ogg, R. A.; Polanyi, M. *Trans. Farad. Soc.* **1934**, *31*, 604.

(65) Evans, M. G.; Warhurst, E. *Trans. Farad. Soc.* **1938**, *34*, 614.

(66) Warshel, A.; Weiss, R. M. *J. Am. Chem. Soc.* **1980**, *102*, 6218.

(67) Pross, A.; Shaik, S. S. *J. Am. Chem. Soc.* **1982**, *104*, 187.

(68) Chang, Y.-T.; Miller, W. H. *J. Phys. Chem.* **1990**, *94*, 5884.

(69) Chang, Y.-T.; Minichino, C.; Miller, W. H. *J. Chem. Phys.* **1992**, *96*, 4341.

(70) Minichino, C.; Voth, G. A. *J. Phys. Chem. B.* **1997**, *101*, 4544.

(71) Higashi, M.; Truhlar, D. G. *J. Chem. Theory Comput.* **2008**, *4*, 790.

(72) Albu, T. V.; Corchado, J. C.; Truhlar, D. G. *J. Phys. Chem. A* **2001**, *105*, 8465.

(73) Kim, Y.; Cochado, J. C.; Villa, J.; Xing, J.; Truhlar, D. G. *J. Chem. Phys.* **2000**, *112*, 2718.

(74) Lin, H.; Pu, J.; Albu, T. V.; Truhlar, D. G. *J. Phys. Chem. A* **2004**, *108*, 4112.

(75) Saad, Y.; Schultz, M. H. *SIAM J. Sci. Stat. Comput* **1986**, *7*, 856.

(76) Pulay, P. *Chem. Phys. Lett.* **1980**, *73*, 393.

(77) Pulay, P. *J. Comput. Chem.* **1982**, *3*, 556.

(78) Pulay, P. Direct inversion in interative subspace (DIIS). In *Molecular Quantum Mechanics: Analytic Gradients and Beyond*; Csaszar, A. G., Fogarasi, G., Schaefer, H. F., III., Szalay, P. G., Eds.; ELTE Institute of Chemistry: Budapest, Hungary, 2007; pp 71.

(79) Shaik, S. S.; Schlegel, H. B.; Wolfe, S. *Theoretical Aspects of Physical Organic Chemistry: The SN2 Mechanism*; John Wiley & Sons, Inc.: New York, 1992.

(80) Rappé, A. K.; Casewit, C. J.; Colwell, K. S.; Goddard, W. A., III.; Skiff, W. M. *J. Am. Chem. Soc.* **1992**, *114*, 10024.

CT800477Y

JCTC Journal of Chemical Theory and Computation

A Combined Charge and Energy Decomposition Scheme for Bond Analysis

Mariusz P. Mitoraj,[†,‡] Artur Michalak,[‡] and Tom Ziegler*[,†]

Department of Chemistry, University of Calgary, 2500 University Drive NW, Calgary, Alberta Canada, and Department of Theoretical Chemistry, Faculty of Chemistry, Jagiellonian University, R. Ingardena 3, 30-060 Cracow, Poland

Received November 19, 2008

Abstract: In the present study we have introduced a new scheme for chemical bond analysis by combining the Extended Transition State (ETS) method [*Theor. Chim. Acta* **1977**, *46*, 1] with the Natural Orbitals for Chemical Valence (NOCV) theory [*J. Phys. Chem. A* **2008**, *112*, 1933; *J. Mol. Model.* **2007**, *13*, 347]. The ETS-NOCV charge and energy decomposition scheme based on the Kohn−Sham approach makes it not only possible to decompose the deformation density, $\Delta\rho$, into the different components (such as σ, π, δ, etc.) of the chemical bond, but it also provides the corresponding energy contributions to the total bond energy. Thus, the ETS-NOCV scheme offers a *compact*, qualitative, and quantitative picture of the chemical bond formation within one common theoretical framework. Although, the ETS-NOCV approach contains a certain arbitrariness in the definition of the molecular subsystems that constitute the whole molecule, it can be widely used for the description of different types of chemical bonds. The applicability of the ETS-NOCV scheme is demonstrated for single (H_3X-XH_3, for X = C, Si, Ge, Sn) and multiple ($H_2X=XH_2$, $H_3CX\equiv XCH_3$, for X = C, Ge) covalent bonds between main group elements, for sextuple and quadruple bonds between metal centers (Cr_2, Mo_2, W_2, $[Cl_4CrCrCl_4]^{4-}$), and for double bonds between a metal and a main group element ($(CO)_5Cr=XH_2$, for X = C, Si, Ge, Sn). We include finally two applications involving hydrogen bonding. The first covers the adenine-thymine base pair and the second the interaction between C−H bonds and the metal center in the alkyl complex.

Introduction

Chemical bonding theory predates quantum mechanics with the work by Lewis from 1916.[1] In the Lewis picture, molecules are formed from atoms (fragments) by the grouping of electrons into lone and bonding pairs. The Lewis picture has since 1916 been consolidated and expanded upon, most often with the help of quantum mechanics. Especially useful in this regard has been the formulation of valence bond[2,3] and molecular orbital[4,5] theory.

The many useful schemes that are available for analyses of the chemical bond emphasizes different aspects of bonding. One group focuses on the charge rearrangement associated with electron pairing, as the molecule is formed from atoms (fragments). Schemes and concepts that belong to this category are Bond Order Orbitals[6,7] and the very similar Natural Bond Orbitals (NBO),[8−12] Atoms in Molecules (AIM),[13] the Electron Localization Function (ELF),[14] the Laplacian of the electron density (∇^2_ρ),[13,15] the deformation density ($\Delta\rho$),[16] population schemes,[17,18] and Charge Decomposition Analysis (CDA).[19−23]

A second group of bonding schemes puts the focus on the decomposition of the bond energy into chemically meaningful contributions. Such decomposition schemes include the Kitaura−Morokuma method,[24] the Extended Transition State (ETS) scheme,[25−27,66−69] the Block Localized Wave Function Energy Decomposition, BLW-ED, presented by Mo,[28] and the kindred Absolutely Localized Molecular Orbitals Energy Decomposition Analysis (ALMO-

* Corresponding author. E-mail: ziegler@ucalgary.ca.
[†] University of Calgary.
[‡] Jagiellonian University.

10.1021/ct800503d CCC: $40.75
Published on Web 03/02/2009

EDA) by Head-Gordon.[29] Further, the Natural Energy Decomposition Analysis (NEDA) theory by Schenter,[30] the Molecular Energy Decomposition for Atoms in Molecule by Francisco,[31] the energy decomposition schemes by Mayer,[32] Korchowiec,[33] Liu,[34] and Bagus,[35] and finally Symmetry Adapted Perturbation Theory (SAPT) scheme.[36,37]

A third useful category provides descriptors of the chemical bond in terms of bond-orders (or bond multiplicity indices). Examples are the work of Pauling,[38] Wiberg,[39] Jug,[40] Mayer,[41] and Ciosłowski,42 as well as Nalewajski, Köster, and Mrozek.[43−49]

One of several useful schemes that link the concepts of bond-order, bond-orbitals, and charge rearrangement with the deformation density is the method based on Natural Orbitals for Chemical Valence (NOCV).[50−54] In this scheme a few eigenfunctions (NOCV) of the deformation density matrix (ΔP) is used to describe bond formation of the molecules from atoms or fragments in a compact form.[50−54,56] The related eigenvalues can in addition be used as valence indices as well as a measure of the change in the density associated with bond formation. However, the NOVC scheme[50−54] does not provide information about the energetics related to the charge rearrangement.

To remedy this, we shall in the present account combine the NOCV scheme with the Extended Transition State (ETS) method.[25−27] We hope in this way to provide a compact analysis of the chemical bond in terms of orbitals (NOCVs) describing the charge rearrangement and the corresponding energy contributions from these orbitals to the chemical bond. Other schemes such as (NBO),[8−12] BLW-ED,[28] and (ALMO-EDA)[29] can be used to combine energy decomposition with charge analysis. Also, our scheme shares with other analysis methods a certain degree of arbitrariness. Thus, the bonding picture that it provides depends on the choice of fragments used to describe the formation of the combined molecule.

Nevertheless we hope in the following to illustrate that the NOCV-ETS method provides a *compact* analysis of chemical bonding. To this end we shall in the following illustrate the use of our scheme in connection with single and multiple bonds between main-group elements, between main-group elements and metals, and between two metals.

Theory

The Extended Transition State Method (ETS). Consider the formation of the molecule AB from the two fragments A^0 and B^0. Let further the heat of formation be given by $\Delta E_{int} = E_{AB} - E_A - E_B$, where E_{AB}, E_A^0, and E_B^0 are the energies of AB, A^0, and B^0, respectively. The ETS scheme[25−27] decomposes ΔE_{int} into a number of chemically meaningful components representing different steps toward the formation of AB from A^0 and B^0 as:

$$E_{AB} - E_A^0 - E_B^0 = \Delta E_{int} = \Delta E_{prep} + \Delta E_{elstat} + \Delta E_{Pauli} + \Delta E_{orb} \quad (1)$$

In the first step we distort the two fragments A^0 and B^0 from their equilibrium geometries to the structures they will have in the combined complex. The corresponding energy required for this distortion is given as ΔE_{prep} in eq 1. This term is often referred to as the distortion or preparation energy. The "distortion" might also involve the promotion of the fragments to another electronic state. We shall refer to the "distorted" fragments as A and B. The corresponding energies are E_A and E_B, respectively. Thus, $\Delta E_{prep} = E_A + E_B - E_A^0 - E_B^0$.

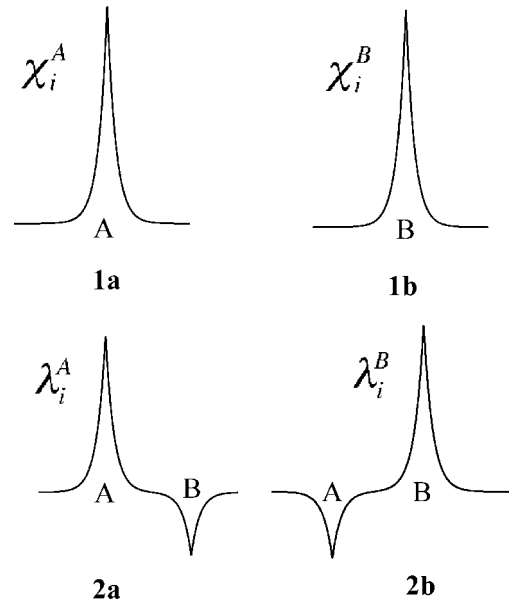

Figure 1. Schematic representation of fragment orbitals on A and B without Löwdin orthogonalization (1a, 1b) and with Löwdin orthogonalization (2a, 2b).

In the Kohn−Sham theory, A and B are represented by the Slater determinants Ψ^A and Ψ^B, respectively. Here Ψ^A is built from the occupied one-electron spin orbitals of fragment A, $\{\chi_j^A, j = 1,n_A\}$, and Ψ^B from the corresponding set on B, $\{\chi_k^B, k = 1,n_B\}$. We illustrate in Figure 1 a fragment orbital χ_j^A as **1a** and a fragment orbital χ_k^B as **1b**. Further, the occupied orbitals making up Ψ^A and Ψ^B form the set $\{\chi_i = 1,n\}$ with $n = n_A + n_B$.

In the second step we bring the distorted fragments from infinite separation to their final positions in the combined compound without changing their densities, ρ_A and ρ_B. The associated energy change $\Delta\tilde{E}^0$ due to this step is given by

$$\Delta\tilde{E}^0 = \Delta E_{elstat} + \Delta E_{XC}^0 \quad (2)$$

Here

$$\Delta E_{elstat} = \sum_{\substack{\nu\in A \\ \mu\in B}} \frac{Z_\nu Z_\mu}{R_{\nu\mu}} + \sum_{\mu\in A}\int \frac{\rho_B(r)Z_\mu}{|R_\mu - r|}dr + \sum_{\nu\in B}\int \frac{\rho_A(r)Z_\mu}{|R_\nu - r|}dr + \int\frac{\rho_A(r_1)\rho_B(r_2)}{r_{12}}dr_1dr_2 \quad (3)$$

represents the change in electrostatic interaction energy when the two distorted fragments are combined in the final molecule while the densities are kept frozen. On the other hand ΔE_{XC}^0 represents the corresponding change in the Kohn−Sham exchange correlation energy[25]

$$\Delta E^0_{XC} = \sum_{\gamma}^{\alpha\beta}\sum_{\tau}^{\alpha\beta}\{E^{\gamma,\tau}_{XC}[(\rho^{\gamma}_A + \rho^{\gamma}_B);(\rho^{\tau}_A + \rho^{\tau}_B)] - E^{\gamma,\tau}_{XC}[\rho^{\gamma}_A;\rho^{\tau}_A] - E^{\gamma,\tau}_{XC}[\rho^{\gamma}_B;\rho^{\tau}_B]\} \quad (4)$$

Here ρ^{τ}_A,ρ^{τ}_B with $\tau = \alpha,\beta$ are the spin densities of A and B, respectively. The electrostatic contribution ΔE_{elstat} enters as the second term in the expression for ΔE_{tot} of eq 1.

It is readily seen that $\tilde{E}^0 = E^0_A + E^0_B + \Delta E_{prep} + \Delta E_{elst} + \Delta E^0_{XC}$ corresponds to the energy of the simple product wave function $\Psi^A\Psi^B$. However, $\Psi^A\Psi^B$ is not antisymmetric with respect to the interchange of all electron indices. As a consequence it does not fully satisfy the Pauli exclusion principle. The product function $\Psi^A\Psi^B$ is further not normalized if the occupied orbitals on the different fragments A and B overlap.

In the third step we construct from $\Psi^A\Psi^B$ the normalized and antisymmetrized wave function

$$\Psi^0 = N\hat{A}\{\Psi^A\Psi^B\} \quad (5)$$

with the corresponding energy E^0.

The wave function Ψ^0 can[24−27] in Kohn−Sham theory be represented by a single Slater determinant as

$$\Psi^0 = |\lambda_1\lambda_2,...\lambda_i\lambda_j,...\lambda_n| \quad (6)$$

where the set $\{\lambda_i;i = 1,n\}$ is obtained from $\{\chi_i;i = 1,n\}$ by a Löwdin orthogonalization[55] and given by

$$\lambda_i = \sum_j S^{-1/2}_{ij}x_j \quad (7)$$

Here, S is the overlap matrix for the set $\{\chi_i = 1,n\}$. We illustrate in Figure 1a fragment orbital λ^A_j as **2a** and a fragment orbital λ^B_k as **2b**. Further, the density corresponding to ψ^0 can be written as:

$$\rho^0 = \sum_i^n \lambda^*_i\lambda_i = \sum_i^n\sum_j^n S_{ij}\chi_i\chi_j = \sum_i^n\sum_j^n \Delta P^{Pauli}_{ij}\chi_i\chi_j + \rho^A + \rho^B \quad (8)$$

Here ΔP^{Pauli} is the (deformation) density matrix in the basis $\{\chi_i = 1,n\}$ representing the Pauli deformation density $\Delta\rho^{Pauli} = \rho^0 - \rho^A - \rho^B$. It follows from eq 8 that $\Delta P^{Pauli}_{ij} = (S_{ij} - \delta_{ij})$.

It is readily shown[25] that the energy difference $\Delta\tilde{E}_{Pauli} = E^0 - \tilde{E}^0$ between ψ^0 and $\psi^A\psi^B$ can be expressed as

$$\Delta\tilde{E}_{Pauli} = E^0[\rho^0] - E^A[\rho^A] - E^B[\rho^B] = \sum_i^{occ}\sum_j^{occ}\Delta P^{Pauli}_{ij}F_{ij}[\rho^{Pauli}_T] \quad (9)$$

where $\rho^{Pauli}_T = 1/2^0_\rho + 1/2\rho_A + 1/2\rho_B$, whereas the Kohn−Sham matrix elements are given as:

$$F_{ij}[\rho] = \int x_i(1)\{-1/2\nabla^2 + V_{Ne}(1) + V_C[\rho]\}x_j(1)d\tau_1 \quad (10)$$

where $\rho = \rho_T$. In eq 10), $V_C[\rho]$ is the Coulomb potential due to ρ and $V_{XC}[\rho]$ is the corresponding exchange correlation potential, whereas $V_{Ne}(1)$ is the nuclear-electron attraction potential due to all the atoms of the combined molecule. We note that eq 10 is derived by expanding $E^0 = E[\rho^0]$ on the one hand and $\tilde{E}^0 = E[\rho^A + \rho^B]$ on the other from the density $\rho^{Pauli}_{TS} = 1/2^0_\rho + 1/2(\rho^A + \rho^B)$ at the midpoint (transition state) between ρ^0 and $\rho^A + \rho^B$.[25] It is customary[24,25] to combine $\Delta\tilde{E}_{Pauli}$ of eq 9 and Δ^0_{XC} of eq 4 into the total Pauli or "exchange repulsion" term[24] ΔE_{Pauli} as

$$\Delta E_{Pauli} = \Delta\tilde{E}_{Pauli} + \Delta E^0_{XC} \quad (11)$$

We note that ΔE_{Pauli} enters as the third contribution to ΔE_{tot} in eq 1. It follows further from the derivation so far that $E^0 - E^0_A - E^0_B = \Delta E_{prep} + \Delta E_{elstat} + \Delta E_{Pauli}$.

The total Pauli repulsion ΔE_{Pauli} of eq 11 is dominated by $\Delta\tilde{E}_{Pauli}$ of eq 9 which is positive and destabilizing. The destabilization comes from the extra nodes added to $\{\lambda_i;i = 1,n\}$, see **2a** and **2b** of Figure 1, compared to $\{\chi_i;i = 1,n\}$, see **1a** and **1b** of Figure 1, in order to make the set $\{\lambda_i;i = 1,n\}$ orthogonal and satisfy the Pauli exclusion principle through Ψ^0. Thus, the added nodes will cause the energy of ψ^0 to be higher than that of $\Psi^A\Psi^B$ due to an increase of the kinetic energy.[24,25] The term ΔE_{Pauli} is in general responsible for an increase in the kinetic energy when chemical bonds are formed.[57]

It is customary[26,27] to combine ΔE_{Pauli} and ΔE_{elstat} under the heading of steric interaction energy as $\Delta E_{steric} = \Delta E_{Pauli} + \Delta E_{elstat}$. Defined in this way, ΔE_{steric} represents the total interaction energy between the two fragments described alone by their occupied orbitals according to Ψ^0 of eq 5 without any involvement of virtuals. This definition is especially meaningful for the interaction between neutral fragments where ΔE_{steric} invariably is positive.[69,72] The definition is consistent with the picture of steric interactions as originating from the penetrations of two electronic charge clouds ρ_A and ρ_B. Such a penetration leads to an increase in kinetic energy due to ΔE_{Pauli}. However, the increase in kinetic energy is to some degree compensated for by ΔE_{elstat}. This interaction, as defined in eq 3, is normally attractive for neutral fragments,[69,72] as the density ρ_A on one fragment only partially can shield the stabilizing (attractive) interaction of the nuclei on the same fragment A with the density ρ_B on the other fragment. In qualitative theories such as the Hückel method, ΔE_{elstat} is considered to be zero and ΔE_{Pauli} represents the steric interaction. However from a quantitative point of view, such an approximation is too severe. The two terms ΔE_{elstat} and ΔE_{Pauli} give rise to two large numbers of opposite sign that increases numerically as the fragments A and B are brought closer together. On the other hand, their sum ΔE_{steric} is numerically much smaller and chemically meaningful.

For the interaction of charged fragments one might modify ΔE_{elstat} as $\Delta E_{elstat} = \Delta\tilde{E}_{elstat} + V_{AB.}$ Here V_{AB} is an effective potential describing the interaction of the net charges on the two fragments. In that case $\Delta\tilde{E}_{steric} = \Delta\tilde{E}_{elstat} + \Delta E_{Pauli}$. Futher, V_{AB} would have to be added as an extra term to the total bonding energy. Such a modification has not been implemented yet. At the moment we can only say that for the interaction of charged fragments, ΔE_{steric} as defined above contains both $\Delta\tilde{E}_{steric}$ and V_{AB}. Of the many examples given

in the following, only the one dealing with $[Cl_4CrCrCl_4]^{4-}$ involves charged fragments. We shall qualify the use of ΔE_{steric} when we discuss $[Cl_4CrCrCl_4]^{4-}$.

The last term of eq 1, ΔE_{orb}, is called the orbital interaction term. It represents the interactions between the occupied molecular orbitals on one fragment with the unoccupied molecular orbitals of the other fragment, as well as the mixing of occupied and virtual orbitals within the same fragment (intrafragment polarization). The orbital interaction term represents the energy change when going from the Ψ^0 state, characterized by the density matrix P^0 to the final wave function, Ψ, characterized by P and the density ρ. A full expression for ΔE_{orb} will be given shortly after a discussion of the deformation density $\Delta\rho = \rho - \rho^0$.

Natural Orbitals for Chemical Valence (NOCV) and the Extended Transition State Method (ETS). In the Natural Orbitals for Chemical Valence (NOCV) approach[50−54] the deformation density

$$\Delta\rho^{orb} = \rho - \rho^{o} = \sum_{\mu}^{N}\sum_{\nu}^{N}\Delta P_{\mu\nu}^{orb}\lambda_\mu\lambda_\nu \qquad (12)$$

is expressed in terms of a set of orthonormal fragment spin−orbitals $\{\lambda_i;i = 1,N\}$ with $N = n + nv$. This set is generated by a separate Löwdin orthogonalization of the n occupied fragment orbitals $\{\chi_i;i = 1,n\}$ and nv virtual fragment orbitals $\{\chi_j;j = n + 1,n + nv\}$, followed by a Schmidt orthogonalization of the virtual set on the occupied set. The set $\{\lambda_i = i = 1,n + nv\}$ includes the occupied and orthonormal fragment orbitals $\{\lambda_i;i = 1,n\}$ introduced previously as well as a an additional set of virtual fragment orbitals $\{\lambda_i;i = 1 + 1,n + nv\}$ that are orthogornal to each other and the occupied set $\{\lambda_i;i = 1,n\}$. The Schmidt (rather than Löwdin) orthogonalization of all virtual orbitals on the occupied ensures that ρ^0 is represented by a diagonal matrix within the set $\{\lambda_i;i = n + 1,n + nv\}$.

The NOCVs are now constructed by a diagonalization of the deformation density matrix $\Delta P_{\mu\nu}^{orb}$ of eq 12 expressed in the set of orthogonalized fragment spin−orbitals. Thus, the NOCVs satisfy the equation:

$$\Delta P^{orb}C_i = v_i C_i \qquad (13)$$

where C_i is a vector containing the coefficients that expands ψ_i in the basis of orthogonalized fragment orbitals λ_j as $\psi_i = \sum_j C_{ij}\lambda_j$.

The deformation density, $(\Delta\rho^{orb})$, can in the NOCV representation be expressed as a sum of pairs of complementary orbitals (ψ_{-k}, ψ_k) corresponding to eigenvalues equal in absolute value but opposite in signs:[50−54]

$$\Delta\rho^{orb}(r) = \sum_{k=1}^{N/2} v_k[-\Psi_{-k}^2(r) + \Psi_k^2(r)] = \sum_{k=1}^{N/2}\Delta\rho_k(r) \qquad (14)$$

The structure of the eigenvalues in complementary pairs is a consequence of the fact that the set λ is orthonormalized and that ΔP is traceless. The complementary pairs of NOCV define the channels for electron charge transfer between the molecular fragments.[50−54] This "pairing" property is also characteristic for Inter-Reactant-Modes (the charge-flow channels describing changes in atomic populations) defined within the Charge Sensitivity Analysis by Nalewajski et al.[96,97]

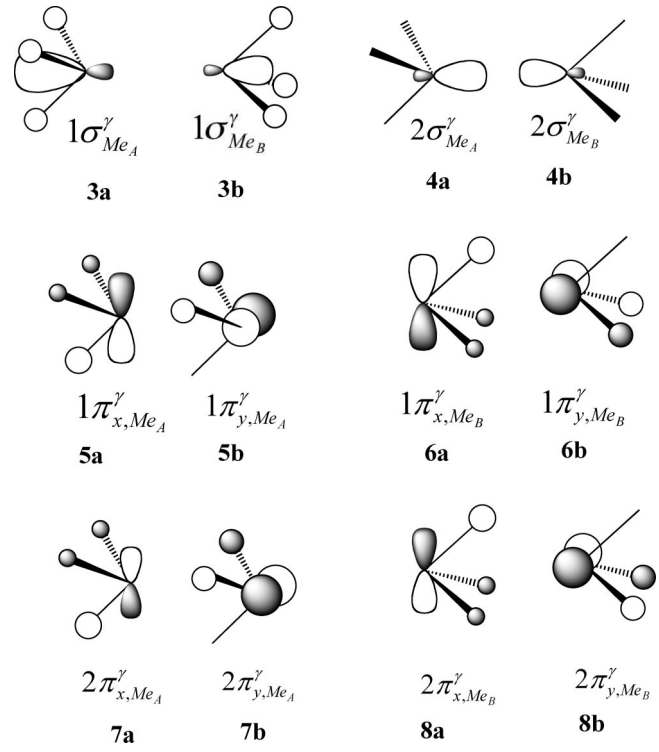

Figure 2. Schematic representation of fragment spin−orbitals in the two methyl radicals Me_A and Me_B.

We can further combine the NOCV and ETS methods in a ETS-NOCV charge and energy decomposition scheme by providing an expression for ΔE_{orb}.

The term ΔE_{orb} is given by:

$$\Delta E_{orb} = E[\rho] - E[\rho^0] \qquad (15)$$

where $E[\rho]$ is the energy of the final molecule and $E[\rho^0]$ is the energy E^0 associated with Ψ^0 of eq 6. An expansion of $E[\rho] = E[\rho^0 + \Delta\rho^{orb}]$ as well as $E[\rho^0]$ from the density $\rho^{TS} = 1/2\rho + 1/2\rho^0$ at the midpoint (transition state) between ρ and ρ^0 allows us to express ΔE_{orb} as:

$$\Delta E_{orb} = \sum_{\nu}^{N}\sum_{\mu}^{N}\Delta P_{\mu\nu}^{orb}F_{\mu\nu}^{TS} = Tr(\Delta P^{orb}F^{TS}) \qquad (16)$$

Here $\Delta P_{\mu\nu}^{orb}$of eq 16 is over orthogonalized Löwdin orbitals $\{\lambda_\mu = 1,N\}$ and $F_{\mu\nu}^{TS}$ is a matrix element similar to that of eq 10 with $\rho = \rho^{TS}$ and χ replaced by λ.

It follows from eq 13 that the NOCVs (ψ_i) are related to the set λ by a unitary transformation C. We can thus write:

$$\Delta E_{orb} = Tr(\Delta P^{orb}F^{TS}) = Tr(C^{+}\Delta P^{orb}CC^{+}F^{TS}C) = \sum_{k=1}^{N/2} v_k[-F_{-k,-k}^{TS} + F_{k,k}^{TS}] = \sum_{k=1}^{N/2}\Delta E_k^{orb} \qquad (17)$$

where C diagonalizes ΔP^{orb}. Further, $F_{-k,-k}^{TS}$ and $F_{k,k}^{TS}$ are diagonal matrix elements of the type defined in eq 10 over ψ_{-k} and ψ_k, respectively, with $\rho = \rho^{TS}$. Also eq 17 makes

Table 1. ETS-NOCV Energy Decomposition of the X−X Bond in H_3X-XH_3[a]

X	ΔE_{Pauli}	ΔE_{elstat}	ΔE_{steric}[b]	$\Delta E_{orb}{}^{\sigma}$[c]	$\Delta E_{orb}^{\pi x}$	$\Delta E_{orb}{}^{\pi y}$	$\Delta E_{orb}{}^{\pi}$[d]	ΔE_{orb}[e]	ΔE_{prep}	ΔE_{int}[f]	d(XX)[g]
C	205.9	−129.3	76.5	−173.3	−7.2	−7.2	−14.4	−187.7	17.8	−93.4	1.53
Si	97.1	−79.3	17.8	−88.3	−2.0	−2.0	−4.0	−92.3	0.6	−73.9	2.35
Ge	107.9	−88.5	19.4	−84.4	−2.0	−2.0	−4.0	−88.4	0.6	−68.4	2.43
Sn	93.7	−84.1	9.6	−66.6	−1.2	−1.2	−2.4	−69.0	0.4	−59.0	2.82

[a] kcal/mol. [b] The total steric repulsion, $\Delta E_{steric} = \Delta E_{Pauli} + \Delta E_{elstat}$. [c] The total stabilization energy from the σ-orbital interactions illustrated in Figure 4 for X = C. [d] The total stabilization energy from the π-orbital interactions illustrated in Figure 5 for X = C, $\Delta E_{orb}^{\pi} = \Delta E_{orb}^{\pi x} + \Delta E_{orb}^{\pi y}$. [e] $\Delta E_{orb} = \Delta E_{orb}^{\sigma} + \Delta E_{orb}^{\pi}$. [f] $\Delta E_{int} = \Delta E_{steric} + \Delta E_{prep} + \Delta E_{orb}$. [g] XX bond lengths in angstroms.

use of the fact that the trace of the product of two matrices is invariant to a unitary transformation of the two matrices.

The advantage of the expression for ΔE_{orb} in terms of NOCVs, eq 17, rather than orthogonalized fragment orbitals, eq 16, is that only a few complementary pairs might contribute significantly to ΔE_{orb} whereas the contributions to ΔE_{orb} in eq 16 might come from several products of orthogonalized Löwdin orbitals. We see further that for each complementary NOCV pair, representing one of the charge delocalization $\Delta\rho_k$, not only can we visualize $\Delta\rho_k$ but also provide the energy contributions ΔE_{orb}^k to the bond energy from $\Delta\rho_k$.

Computational Details

All the DFT calculations presented here were based on the Amsterdam Density Functional (ADF) program.[58−62] The Becke−Perdew exchange-correlation functional[63,64] was applied. A standard double-ζ STO basis with one set of polarization functions was adopted for the elements H, C, N, O, Si, Cl while a standard triple-ζ basis set was employed for the transition metals, Cr, Mo, W, and for the heavier main group elements, Ge, Sn. Auxiliary *s, p, d, f,* and *g* STO functions, centered on all nuclei, were used to fit the electron density and obtain accurate Coulomb potentials in each SCF cycle. Relativistic effects were included using the ZORA approximation.[65−67]

Results and Discussion

Single Bonds between the Main-Group Elements, H_3X-XH_3. Let us first analyze the formation of a single X−X bond in H_3X-XH_3, where X = C, Si, Ge, Sn. We consider X_2H_6 formed from the two radicals $H_3X^{\uparrow}$ and $^{\downarrow}XH_3$ of opposite spin.

Starting with X = C, the first step in the formation of the H_3C-CH_3 single-bond is the distortion of the two methyl radicals from their equilibrium geometry to the structure that they have in the combined molecule. The associated energy is given by ΔE_{prep} of eq 1 and amounts to a destabilization of ΔE_{prep} = 17.8 kcal/mol, Table 1. The distortion is the result of steric interactions between the two methyl fragments in H_3C-CH_3. The distortion energy is seen to be much smaller for the heavier congeners X = Si, Ge, and Sn where the distance between the two H_3X fragments in the combined X_2H_6 compound is much larger, Table 1.

The second step involves bringing the distorted fragments, $H_3C^{\uparrow}$ and $^{\downarrow}CH_3$, from infinity to their final positions in the molecule, without any change in their electronic densities. This step gives rise to the electrostatic interaction ΔE_{elstat} of eq 1. This interaction, as defined in eq 3, is normally attractive for neutral fragments, as the density on one fragment only partially can shield the stabilizing (attractive) interaction of the nuclei on the same fragment with the density on the other fragment. The reduced shielding is due to interpenetration of the two fragment densities. For C_2H_6 the contribution from ΔE_{elstat} amounts to −129.3 kcal/mol, Table 1. For the higher congeners ΔE_{elstat} becomes less stabilizing from Si to Sn as the interpenetration decreases with increasing X−X bond distance, Table 1.

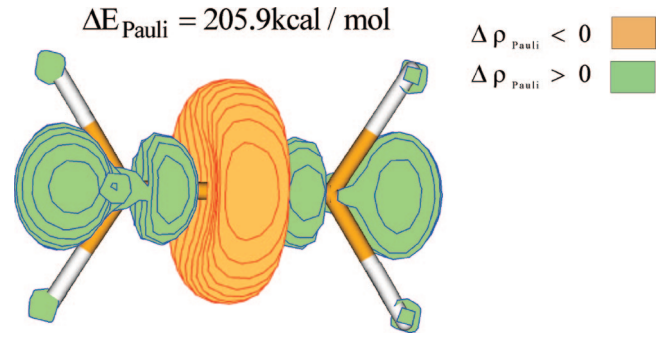

Figure 3. The contour of the Pauli deformation density $\Delta\rho^{Pauli}$ for C_2H_6. The numerically smallest contour values are ±0.01 a.u. The corresponding Pauli repulsion energy is ΔE_{Pauli} = 205.9 kcal/mol.

In the third step we construct the Kohn−Sham Slater determinant Ψ^0 of eq 6 from the orthogonalized set of occupied orbital $\{\lambda_i; i = 1,n\}$. The orbital λ_i consists of χ_i with an out-of-phase contribution from all occupied orbitals of the same spin residing on other fragments, see Figure 1. The out-of-phase contribution will make ΔE_{Pauli} of eq 11 positive. We say that occupied orbitals $\{\chi_i; i = 1,n\}$ of the same spin but on different fragments interact, destabilizing each other. Futher, ΔE_{Pauli} has contributions from both spins so that $\Delta E_{Pauli} = \Delta E_{Pauli}^{\alpha} + \Delta E_{Pauli}^{\beta}$.

In C_2H_6 the leading contribution to ΔE_{Pauli} is from the repulsive interaction between the SOMO $2\sigma_{Me_A}^{\alpha}$ (**4a** for $\gamma = \alpha$) on fragment A with a C−H bonding orbital $1\sigma_{Me_B}^{\alpha}$ (**3b** for $\gamma = \alpha$) on the other fragment as well as the SOMO $2\sigma_{Me_B}^{\beta}$ (**4b** for $\gamma = \beta$) on fragment B interacting repulsively with $1\sigma_{Me_A}^{\beta}$ (**3a** for $\gamma = \beta$) on the other fragment, see Figure 2. Another contribution is from the destabilizing interactions of the two occupied C−H bonding orbitals $1\pi_{x,Me_A}^{\gamma}$; $1\pi_{y,Me_A}^{\gamma}$ (**5a**,**b**) on one fragment with the corresponding occupied $1\pi_{x,Me_B}^{\gamma}$; $1\pi_{y,Me_B}^{\gamma}$orbitals (**6a**,**b**) on the other fragment for $\gamma = \alpha,\beta$; see Figure 2.

The changes in the electron density, $\Delta\rho^{Pauli}$, due to the Pauli interaction are presented in Figure 3. We can clearly see the outflow of the electron density from the bonding region due to the antibonding nature of the set $\{\lambda_i; i = 1,n\}$.

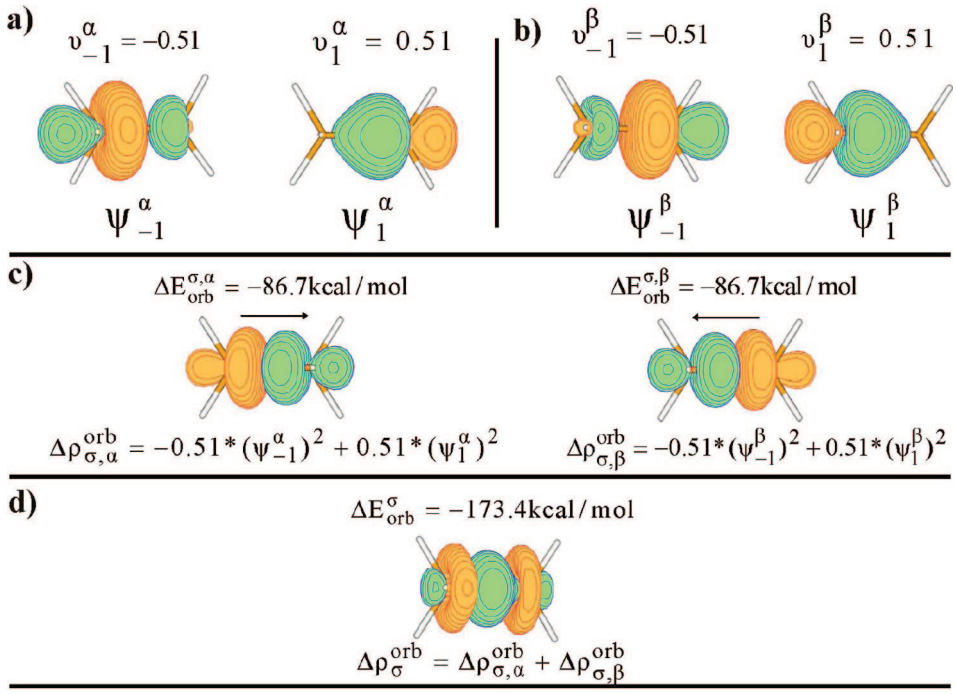

Figure 4. (a) Contours of complementary NOVCs ($\psi^{\alpha}_{-1},\psi^{\alpha}_{+1}$) representing donation from Me_A (left) to Me_B (right) and corresponding eigenvalues ($\upsilon^{\alpha}_{-1},\upsilon^{\alpha}_{+1}$) in C_2H_6. The numerically smallest contour values are ±0.1 a.u. (b) Contours of complementary NOVC's ($\psi^{\beta}_{-1},\psi^{\beta}_{+1}$) representing donation from Me_B (right) to Me_A (left) and corresponding eigenvalues ($\upsilon^{\beta}_{-1},\upsilon^{\beta}_{+1}$) in C_2H_6. The numerically smallest contour values are ±0.1 a.u. (c) Contours of sigma donation ($\Delta\rho^{orb}_{\sigma,\alpha}$) from Me_A to Me_B (left) and sigma donation ($\Delta\rho^{orb}_{\sigma,\beta}$) from Me_B to Me_A (right). The smallest contour values are ±0.0 a.u. The corresponding orbital stabilization energies are $\Delta E^{\sigma,\alpha}_{orb} = \Delta E^{\sigma,\beta}_{orb} = -86.7$ kcal/mol. (d) Total sigma donation $\Delta\rho^{orb}_{\sigma} = \Delta,\rho^{orb}_{\sigma,\alpha} + \Delta\rho^{orb}_{\sigma,\beta}$ and corresponding stabilization energies $\Delta E^{\sigma}_{orb} = \Delta E^{\sigma,\alpha}_{orb} + \Delta E^{\sigma,\beta}_{orb} = -173.4$ kcal/mol. The smallest contour values are ±0.01 a.u.

In other words, the antisymmetrization of the wave function in eq 6 reduces the electron density in the overlap region.[69] It follows from Table 1 and Figure 3 that the corresponding energy change due to the Pauli repulsion is $\Delta E_{Pauli} = 205.9$ kcal/mol. For the higher congeners, ΔE_{Pauli} becomes less repulsive from Si to Sn as the X−X bond distance increases and the overlaps between occupied orbitals on different fragments become smaller, Table 1. It follows from Table 1 that $\Delta E_{steric} = \Delta E_{Pauli} + \Delta E_{elstat}$ is destabilizing due to ΔE_{Pauli}. It is further seen that ΔE_{steric} decreases for X_2H_6 from X = C to X = Sn as the X−X bond length increases.

The final step in the $H_3C{-}CH_3$ bond formation is the inclusion of the virtual fragment orbitals on $H_3C^{\uparrow}$ and $^{\downarrow}CH_3$. The result is the density change $\Delta\rho^{orb}$ defined in eqs 12−14. Associated with $\Delta\rho^{orb}$ is the energy change ΔE_{orb} of eq 1 which is defined in eqs 15−17. The most important contributions to $\Delta\rho^{orb}$ and ΔE_{orb} are due to the in-phase interaction of the virtual orbital $2\sigma^{\beta}_{Me_A}$ (**4a** for $\gamma = \beta$) on A with the destabilized SOMO $2\sigma^{\beta}_{Me_B}$ (**4b** for $\gamma = \beta$) on fragment B, giving rise to a transfer of charge ($\Delta\rho^{orb}_{\sigma,\beta}$) from B to A as well as the interaction of the destabilized SOMO $2\sigma^{\alpha}_{Me_A}$ (**4a** for $\gamma = \alpha$) on A with the virtual orbital $2\sigma^{\alpha}_{Me_B}$ (**4b** for $\gamma = \alpha$) on B resulting in the transfer of charge from A to B ($\Delta\rho^{orb}_{\sigma,\alpha}$). The two interactions are combined responsible for the formation of the σ-bond.

The two complementary Natural Orbitals for Chemical Valence (NOCV) responsible for the σ-transfer of density from A to B are shown as $\psi^{\alpha}_{-1},\psi^{\alpha}_{1}$ in Figure 4a whereas the complementary NOVC's representing the σ-transfer of density from B to A are shown as ($\psi^{\beta}_{-1},\psi^{\beta}_{1}$) in Figure 4b. Figure 4c holds the σ-deformation density for the A-to-B transfer given as $\Delta\rho^{orb}_{\sigma,\alpha} = -0.51(\psi^{\alpha}_{-1})^2 + 0.51(\psi^{\alpha}_{1})^2$ with the corresponding orbital stabilization energy $\Delta E^{\sigma,\alpha}_{orb} = -86.7$ kcal/mol as well as σ-deformation density for the B-to-A transfer given as $\Delta\rho^{orb}_{\sigma,\beta} = -0.51(\psi^{\beta}_{-1})^2 + 0.51(\psi^{\beta}_{1})^2$ with the corresponding orbital stabilization energy $\Delta E^{\sigma,\beta}_{orb} = -86.7$ kcal/mol. We have finally presented in Figure 4d the total σ-orbital deformation density $\Delta\rho^{orb}_{\sigma} = \Delta\rho^{orb}_{\sigma,\alpha} + \Delta\rho^{orb}_{\sigma,\beta}$ along with the total σ-orbital interaction energy $\Delta E^{\sigma}_{orb} = -173.4$ kcal/mol. The term ΔE^{σ}_{orb} clearly represents the σ-orbital interaction energy associated with the formation of the σ-bond. It follows further from Table 1 that ΔE^{σ}_{orb} decreases for X_2H_6 from X = C to X = Sn as the X−X bond length increases.

There is one more stabilizing orbital interaction, ΔE^{σ}_{orb}, that contributes to ΔE_{orb} in eq 1. It involves a transfer (polarization) from the occupied and destabilized C−H bonding orbitals $1\pi^{\gamma}_{x,Me_A}$; $1\pi^{\gamma}_{y,Me_A}$ (**5a**,**b**) and $1\pi^{\gamma}_{x,Me_B}$; $1\pi^{\gamma}_{y,Me_B}$ (**6a**,**b**) to the virtual C−H antibonding orbitals $2\pi^{\gamma}_{x,Me_A}$; $2\pi^{\gamma}_{y,Me_A}$ (**7a**,**b**) and $2\pi^{\gamma}_{x,Me_B}$; $2\pi^{\gamma}_{y,Me_B}$ (**8a**,**b**), where λ can be either α or β, see Figutre 2. Although these fragment orbitals involve C−H σ (**5**,**6**) and C−H σ^* (**7**,**8**) components, they are in accord with common practice given the designation π to emphasize the transformation properties of the contributing p-orbital combinations on the carbons. The term ΔE^{π}_{orb} does not represent the formation of a π-bond but rather a relief of repulsive Pauli interaction between occupied C−H bonding fragment orbitals on opposite fragments by donating

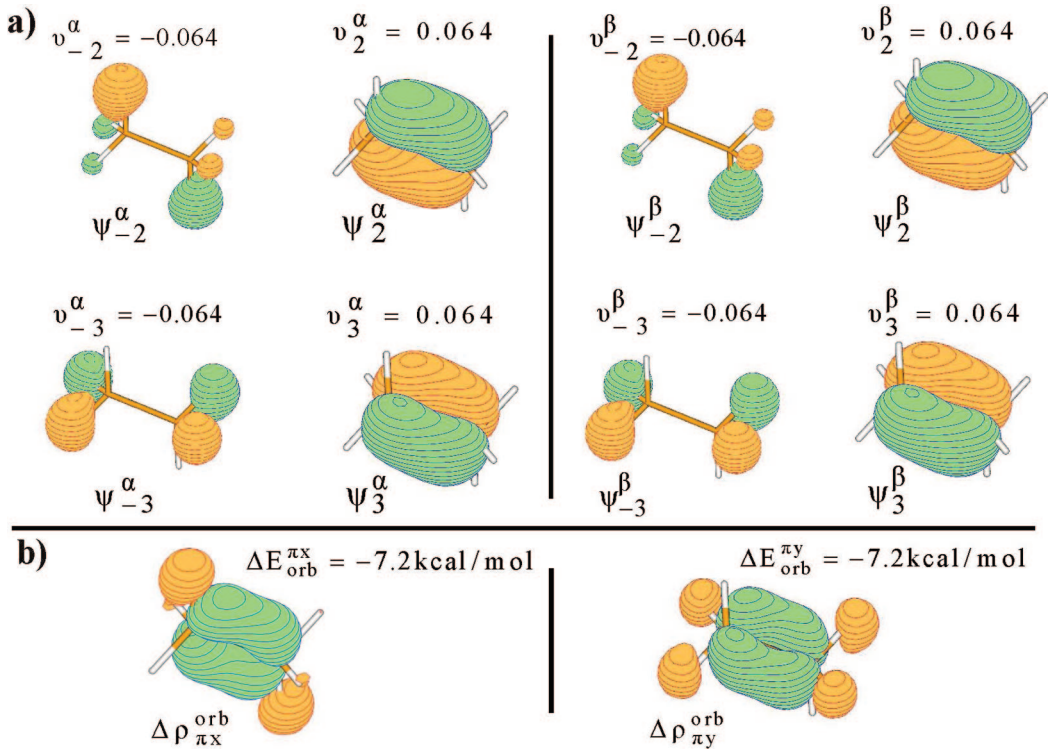

Figure 5. (a) Contours of the π-type NOCVs in C_2H_6. The numerically smallest contour values are ± 0.1 a.u. (b) The π-deformation density contributions, $\Delta\rho^{orb}_{\pi x}$, $\Delta\rho^{orb}_{\pi y}$, and corresponding energies $\Delta E^{\pi x}_{orb}$, $\Delta E^{\pi y}_{orb}$. The numerically smallest contour values are ± 0.005 a.u.

Table 2. ETS-NOCV Energy Decomposition of the Double X=X Bond in the C_2H_4 and Ge_2H_4 Systems[a]

X	ΔE_{steric}[b]	ΔE^{σ}_{orb}	ΔE^{π}_{orb}[a]	ΔE^{π}_{orb}[b]	ΔE_{orb}[c]	ΔE_{prep}[d]	ΔE_{int}[e]	d(XX)[f]
C	107.9	−220.6	−67.8	−5.7	−294.1	6.5	−179.7	1.33
Ge-planar	27.1	−76.3	−22.0	−3.0	−101.3	51.2	−23.0	2.27
Ge-bent	22.0	−75.2	−37.0	−2.6	−114.8	51.9	−40.9	2.37

[a] kcal/mol. [b] The total steric repulsion, $\Delta E_{steric} = \Delta E_{Pauli} + \Delta E_{elstat}$. [c] $\Delta E_{orb} = \Delta E^{\sigma}_{orb} + \Delta E^{\pi 1}_{orb} + \Delta E^{\pi 2}_{orb}$. [d] The distortion (or preparation) term includes the difference in energy between the singlet ground state and the triplet excited state of GeH_2 fragments. [e] $\Delta E_{int} = \Delta E_{steric} + \Delta E_{prep} + \Delta E_{orb}$. [f] XX bond lengths in angstroms.

density from these orbitals (**5**,**6**) to the virtual (**7**,**8**) pair. In this process we are trading C−H bonding and C−C antibonding interactions with C−H antibonding and C−C bonding interactions.

We give in Figure 5a the complementary pairs of NOCVs $(\psi^{\gamma}_{-2},\psi^{\gamma}_{2})$ and $(\psi^{\gamma}_{-3},\psi^{\gamma}_{3})$ describing the change of charge due to the π-orbital interactions. The corresponding deformation densities are given in Figure 5b as $\Delta\rho^{orb}_{\pi x}$ and $\Delta\rho^{orb}_{\pi x}$. The related stabilization energies are $\Delta E^{\pi x}_{orb} = \Delta E^{\pi y}_{orb} = (1)/(2)\Delta E^{\pi}_{orb} = -7.2$ kcal/mol; see Table 1. We note that ΔE^{π}_{orb} decreases in absolute terms for X_2H_6 from X = C to X = Sn as the X−X bond length increases and overlap between orbitals on the two XH_3 fragments diminish.

The results collected in Table 1 are in good qualitative agreement with experiment as well as with other theoretical investigations[98] based on the ETS scheme.

Double Bonds between the Main-Group Elements, $H_2X{=}XH_2$. Turning next to the double bonds between main group elements, we shall consider ethylene and its heavier homologue Ge_2H_4.[68,72−74] Planar ethylene with D_{2h} symmetry can be considered formed from two ground-state triplet carbenes $H_2C{\uparrow\uparrow}$ and $\downarrow\downarrow CH_2$ of opposite spin-polarization. The steric term ΔE_{steric} is somewhat larger for ethylene than for ethane because of the shorter C−C bond length, Table 2.

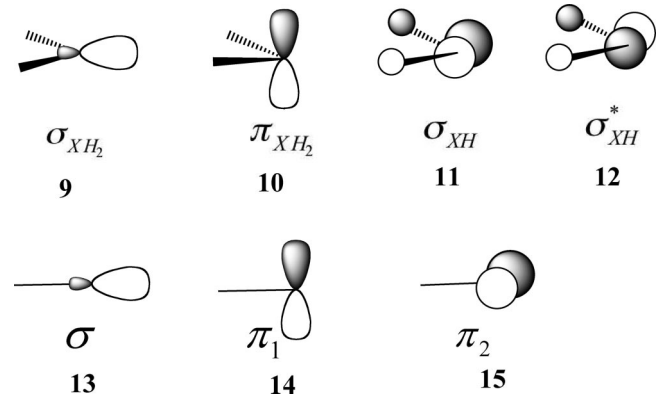

Figure 6. Schematic representation of XH_2 and XCH_3 fragment orbitals.

The carbene units[73−75] each have two singly occupied orbitals σ_{CH_2} (**9**) and π_{CH_2} (**10**); see Figure 6. They give rise to a σ- and a π-bond, respectively. In molecular orbital theory the σ-component is represented by σ_{CC} which is a bonding combination of σ_{CH_2} (**9**) on the two carbenes whereas the π-component is represented by π_{CC} which is the correspond-

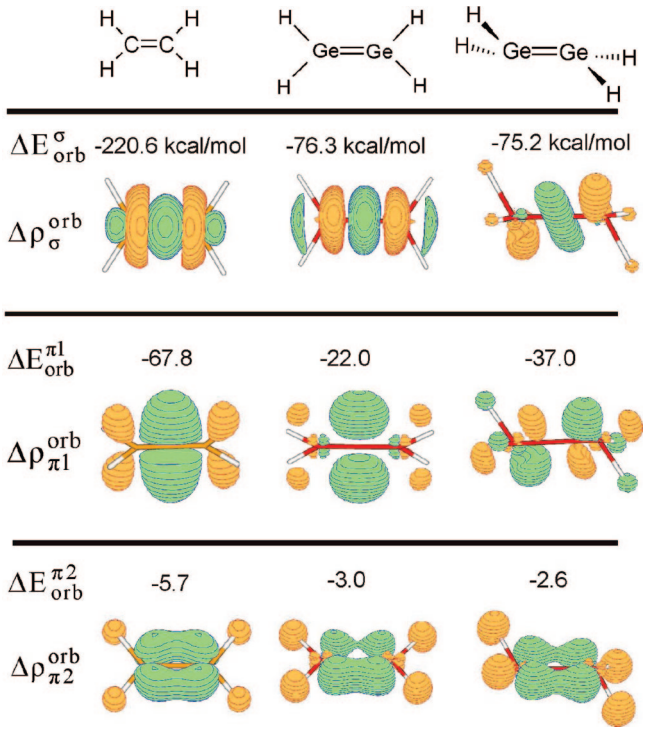

Figure 7. The contours of deformation density contributions $\Delta\rho_{\sigma}^{orb}$, $\Delta\rho_{\pi 1}^{orb}$, $\Delta\rho_{\pi 2}^{orb}$ for ethylene (left), hypothetical planar germanium system (middle), and the real trans-bent germanium homologue (right). The numerically smallest contour values are ±0.01 a.u. The last component, $\Delta\rho_{\pi 2}^{orb}$, was plotted with the contour values ±0.005 a.u. In addition the corresponding energies ΔE_{orb}^{σ}, $\Delta E_{orb}^{\pi 1}$, $\Delta E_{orb}^{\pi 2}$ are shown.

ing bonding combination of π_{CH_2} (**10**) on the two carbenes. The NOCVs for planar ethylene are given as Supporting Information. As for C_2H_6, bonds in C_2H_4 are formed by the shift of density from fragment A to B in one spin component and from B to A in the other component with a net buildup of charge in the bonding region. However, for C_2H_4 both a σ-components (σ_{CH_2}) and a π component (π_{CH_2}) is involved.

We present in the left-hand column of Figure 7 the contributions to the orbital interaction deformation density $\Delta\rho^{orb}$ from the σ- and π-bond as $\Delta\rho_{\sigma}^{orb}$ and $\Delta\rho_{\pi 1}^{orb}$, respectively, where we have summed over spin components. There is a noticeable accumulation of charge in the bonding region for both $\Delta\rho_{\sigma}^{orb}$ and $\Delta\rho_{\pi 1}^{orb}$. The corresponding contributions to ΔE_{orb} are given by $\Delta E_{orb}^{\sigma} = -220.6$ kcal/mol and $\Delta E_{orb}^{\pi 1} = -67.8$ kcal/mol, respectively. Thus our analysis finds in agreement with the common perception that the σ-bond is stronger than the π-bond. There is one more contribution to $\Delta\rho^{orb}$ and ΔE_{orb} given by $\Delta\rho_{\pi 2}^{orb}$ and$\Delta E_{orb}^{\pi 2}$, respectively. It is very similar to ΔE_{orb}^{π} of ethane and it involves the relief of Pauli repulsion by transferring density from the occupied and Pauli destabilized C−H bonding carbene fragment orbitals σ_{XH} (**11**) to the empty C−H antibonding carbene fragment orbitals σ_{XH}^{*} (**12**), see Figure 6. The stabilization amounts to $\Delta E_{orb}^{\pi 2} = -5.7$ kcal/mol.

Also presented in the second column of Figure 7 is planar Ge_2H_4 with triplet GeH_2 as the reference. The corresponding energy decomposition is given in Table 2. We find a reduction in both σ- and π-bond strength with $\Delta E_{orb}^{\sigma} = -76.3$ kcal/mol and $\Delta E_{orb}^{\pi 1} = -22.0$ kcal/mol as one would expect from the increase in the X−X bond distance in going from X = C to X = Ge. In reality Ge_2H_4[68,72] is trans-bent, Figure 7. Such a bending allows occupied Pauli destabilized and occupied spin−orbitals σ_{GeH_2} (**9**) on one fragment to overlap not only with empty σ_{GeH_2} orbitals on the other fragment but also with the corresponding empty π_{GeH_2} orbitals (**10**). As a result, $\Delta\rho_{\sigma}^{orb}$ for trans-bent Ge_2H_4 exhibits transfer of density from σ_{CH_2} to the bonding region; see third column of Figure 7. The bending allows as well occupied and Pauli-destabilized π_{GeH_2} spin−orbitals (**10**) on one fragment to interact not only with empty π_{GeH_2} orbitals on the other fragment but also with the corresponding empty σ_{GeH_2} orbitals (**9**). As a result $\Delta\rho_{\pi 1}^{orb}$ for trans-bent Ge_2H_4 exhibits some transfer of density from π_{GeH_2} to σ_{GeH_2}; see third column of Figure 7. It follows from Table 2 that $\Delta E_{orb}^{\sigma} = -75.2$ kcal/mol and $\Delta E_{orb}^{\pi 1} = -37.0$ kcal/mol, respectively, in the trans-bent conformation. Thus, the deformation from planarity slightly reduces the strength of the σ-bond while considerably strengthening the π-bond. Trans-bending is favorable when the overlap between the two π_{XH_2} orbitals is weak in the planar conformation of X_2H_4, as is increasingly the case through the heavier congeners of ethylene.

Strictly speaking, a σ/π separation is not possible when Ge_2H_4 is trans-bent. However, during the bending process, the ETS-NOCV scheme affords two major contributions to $\Delta\rho^{orb}$ (and ΔE_{orb}). Further, in the planar case these contributions correlate with $\Delta\rho_{\sigma}^{orb}$ and $\Delta\rho_{\pi}^{orb}$, respectively. We have for this reason maintained the same designation for the major components throughout the bending process. For the same reason we refer throughout to the two major contributions to ΔE^{orb} as $\Delta E_{orb}^{\pi 1}$ and $\Delta E_{orb}^{\pi 2}$, respectively. We note that $\Delta E_{orb}^{\pi 2}$, from the plane not influenced by the bending, is virtually unperturbed. We find it a useful characteristics of the ETS-NOCV scheme that the same basic components are maintained when the symmetry of the molecule is reduced.

In the case of GeH_2 the electronic ground-state is a singlet with two electrons in σ_{GeH_2} whereas π_{GeH_2} is empty. It is thus necessary to add a correction of 47.2 kcal /mol to ΔE_{prep} representing the difference in energy between the singlet and triplet states of two GeH_2 units. We might also perform the analysis of the bonding in X_2H_4 with the singlet state of XH_2 as the reference. However, the occupations of the σ_{XH_2} (**9**) and π_{XH_2} (**10**) orbitals in the final X_2H_4 complex is much closer to the triplet state of XH_2 than the singlet. This makes the triplet a natural choice. Nevertheless, it is important to underline that the bonding analysis depends on the reference. On the other hand, the relative energies of bent and planar species are invariant as are the bond energies as long as use is made of XH_2 in its electronic ground state.

Triple Bonds between the Main-Group Elements, RX≡XR. In order to demonstrate the application of the ETS-NOCV scheme to triple bonds between main group elements, we will discuss the X≡X bonding in RX≡XR, with R = CH_3 and X = C, Ge.

Let us start the discussion with the triple C≡C bond in the linear 2-butyne formed from the two units MeC↑↑↑ and ↓↓↓CMe having the opposite spin polarization. These units are each generated by promoting CMe from its doublet ${}^2E_y(\sigma^2\pi_{\lambda}^1;\gamma = 1,2)$ ground-state to its ${}^4A_2(\sigma^1\pi_1^1\pi_2^1)$ quartet

Table 3. ETS-NOCV Energy Decomposition of the Triple X≡X Bond in the RX≡XR Systems, R = CH_3, X = C, Ge[a]

X	ΔE_{steric}[b]	ΔE^{σ}_{orb}	$\Delta E^{\pi 1}_{orb}$	ΔE^{π}_{orb}[b]	ΔE^{π}_{orb}[b]	ΔE_{prep}[d]	ΔE_{int}[e]	d(XX)[f]
C	120.2	−209.7	−88.8	−88.8	−387.3	63.9	−203.18	1.21
Ge-linear	25.5	−102.1	−24.4	−24.1	−150.6	94.9	−30.2	2.20
Ge-bent	23.3	−104.5	−27.3	−34.2	−166.0	96.2	−46.5	2.29

[a] kcal/mol. [b] The total steric repulsion, $\Delta E_{steric} = \Delta E_{Pauli} + \Delta E_{elstat}$. [c] $\Delta E_{orb} = \Delta E^{\sigma}_{orb} + \Delta E^{\pi 1}_{orb} + \Delta E^{\pi 2}_{orb}$. [d] The distortion (or preparation) term includes the difference in energy between the doublet ground state and the excited quartet state of XH_2 fragments. [e] $\Delta E_{int} = \Delta E_{steric} + \Delta E_{prep} + \Delta E_{orb}$. [f] XX bond lengths in angstroms.

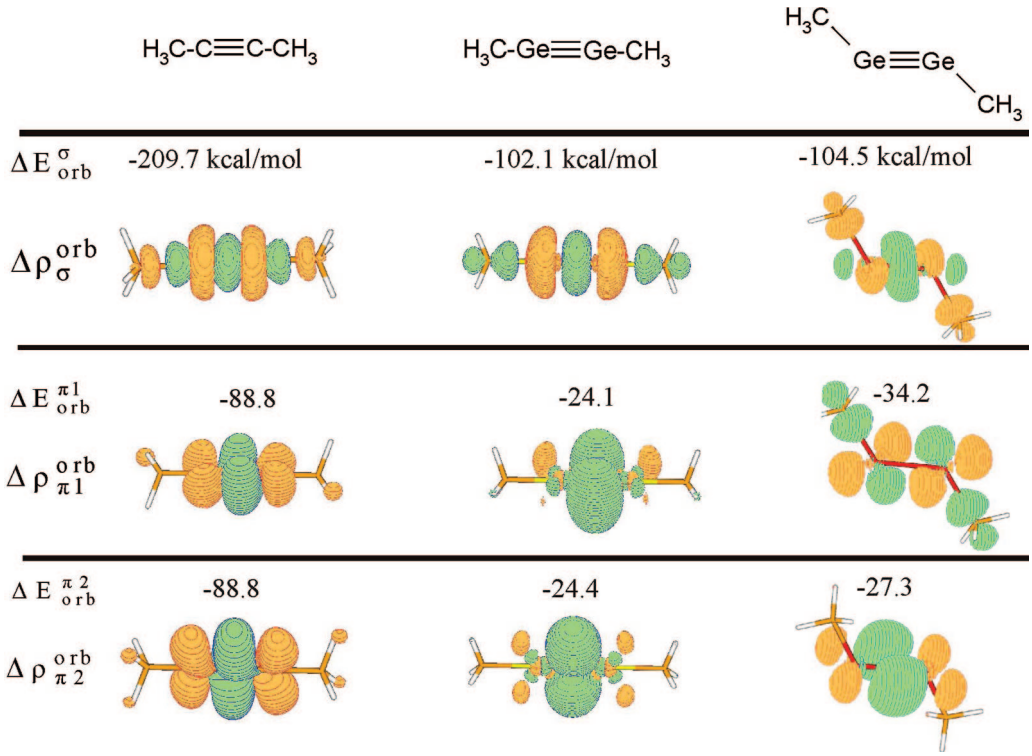

Figure 8. The contours of deformation density contributions $\Delta\rho^{orb}_{\sigma}$, $\Delta\rho^{orb}_{\pi 1}$, $\Delta\rho^{orb}_{\pi 2}$ for the triple bonds in the 2-butyne (left), hypothetical linear germanium system (middle), and the real trans-bent germanium homologue (right). The numerically smallest contour value are ±0.002 a.u. In addition the corresponding energies, ΔE^{σ}_{orb}, $\Delta E^{\pi 1}_{orb}$, $\Delta E^{\pi 2}_{orb}$ have been presented.

excited-state for the price of 63.2 kcal/mol for two CMe units. This energy is part of ΔE_{prep} given in Table 3.

The σ-component of the C≡C bond is made up from σ_A (**13**) and σ_B, on the two different fragments, H_3CC, CCH_3, respectively; see Figure 6. Similarly, the two equivalent π-type contributions to the C≡C bond are built from $\pi_{1,A}$ (**14**), $\pi_{2,A}$ (**15**), on one H_3CC fragment and $\pi_{1,B}$, $\pi_{2,B}$ of the second CCH_3 fragment; see Figure 6. The NOCVs representing the formation of the triple bond in $H_3CC{\equiv}CCH_3$ are given as Supporting Information. The deformation density contributions, $\Delta\rho^{orb}_{\sigma}$, $\Delta\rho^{orb}_{\pi 1}$, $\Delta\rho^{orb}_{\pi 2}$, representing the formation of one σ- and two π-components of the C≡C bond are shown in the left column of Figure 8. Also shown are the corresponding energies, ΔE^{σ}_{orb}, $\Delta E^{\pi 1}_{orb}$, $\Delta E^{\pi 2}_{orb}$. It is clear that the σ-bond contribution of $\Delta E^{\sigma}_{orb} = -209.7$ kcal/mol is stronger than the total π-bonding contribution given by $\Delta E^{\pi 2}_{orb} = -177.5$ kcal/mol.

Turning next to the corresponding $H_3CGe{\equiv}GeCH_3$ system, we promote in a way similar to acetylene the GeMe fragment from its doublet $^2E_{\gamma}$ ($\sigma^2\pi^1_{\chi};\gamma = 1,2$) ground-state to its $^4A_2$ ($\sigma^2\pi^1_{\chi}\pi^1_{\bar{\chi}}$) quartet excited-state for the price of 94.9 kcal/mol for two GeMe units and add this contribution to ΔE_{prep} given in Table 3.

Considering first the $H_3CGe{\equiv}GeCH_3$ system with a linear structure, the σ- and π-contributions to ΔE_{orb} are significantly weaker (−102.1 and −24.4, −24.1, respectively) compared with 2-butyne, as it is shown in the middle column of Figure 8. This is directly related to the increase in the XX distance as we go from X = C to X = Ge; see the last column of Table 3.

Experimentally and theoretically the heavier alkyne homologues, RX≡XR, are known to adopt a trans-bent geometry.[75−84,90−94] The last column of Figure 8 indicates that the σ- and π-components, $\Delta\rho^{orb}_{\sigma}$, $\Delta\rho^{orb}_{\pi 2}$, of the Ge≡Ge bond in the bent-structure are slightly stronger (by 2.4, 2.9 kcal/mol, respectively) compared with the linear analogue. However, the second component of the Ge≡Ge bond, $\Delta E^{\pi 1}_{orb}$, exhibits the most significant increase in the strength, by 10.0 kcal/mol, compared with the linear system. In fact the bending makes it possible for the occupied and Pauli-destabilized π_1 orbital on one GeMe fragment to interact not only with the empty π_1 fragment orbital of the other fragment but also the corresponding empty σ component. The mixing appears as a donation of density from π_1 to σ in $\Delta\rho^{orb}_{\pi 1}$, Figure 8. We note again that we have used a σ/π notation for the contributions to $\Delta\rho^{orb}$ and ΔE_{orb} in trans-bent MeGe≡GeMe.

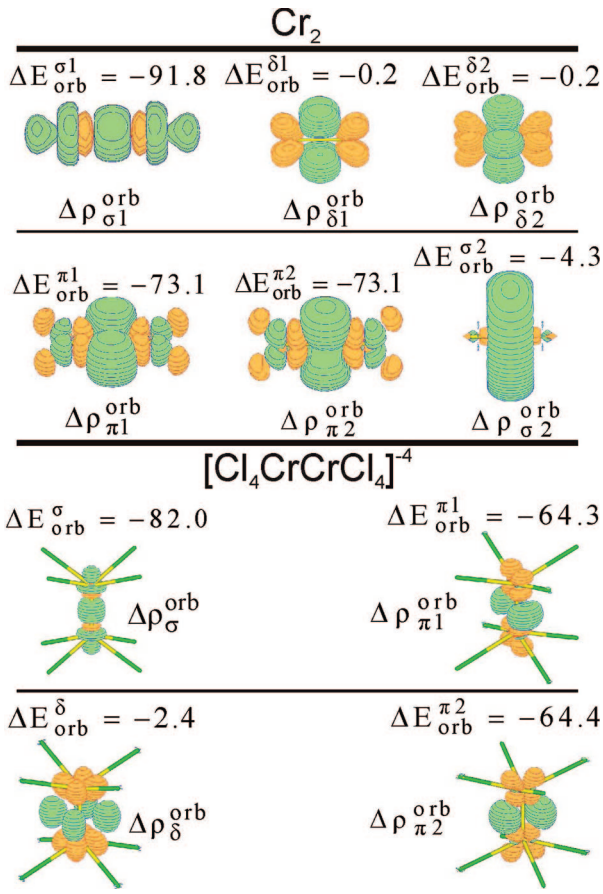

Figure 9. The contours of deformation density contributions describing the two σ-, two π-, and two δ-components of the hextuple bond in the Cr_2 dimer (upper part). The numerically smallest contour values are ±0.003 a.u. The only contour $\Delta\rho_{\sigma 2}^{orb}$ was plotted with the smaller contour values, ±0.001a.u., to improve the quality of visibility. In addition the deformation density components describing the quadruple bond in the $[Cl_4CrCrCl_4]^{4-}$ system have been displayed (lower part). The numerically smallest contour values are ±0.007 a.u. For all of the deformation density contributions, the corresponding energies have been presented.

It is again gratifying to see that the ETS-NOCV scheme affords a simple compact picture of the Ge≡Ge triple bond in terms of three components even when the σ/π separation is broken by distortions such as the trans-bent.

Multiple Bonds between the Metal Centers, Cr_2, Mo_2, W_2, $[Cl_4CrCrCl_4]^{4-}$. Up to now we have applied the ETS-NOCV scheme to a description of bonds between main-group elements. We shall next switch to a discussion of multiple bonds between metal centers. As the first (simple) example we consider the hextuple bonds in the dimers, X_2, with X = Cr, Mo, W. Each of the X_2 molecules was built from two atoms of opposite spin-polarization with the septet valence configuration $(nd_\sigma^1 nd_{\pi 1}^1 nd_{\pi 2}^1 nd_{\delta 1}^1 nd_{\delta 2}^1 (n+1)s^1)$. The septet electronic configuration is the ground-state for chromium and molybdenium atoms whereas the quintet state is characteristic for tungsten.[87,92−94] Therefore we included in the total bonding term the energy describing the promotion from the ground quintet to the excited septet state for tungsten. Additionally, we will also characterize the quadruple Cr−Cr bond in the anion $[Cl_4CrCrCl_4]^{4-}$ with D_{4h} symmetry (eclipsed conformation) made up from the two $CrCl_4^{2-}$ fragments of C_{4v} symmetry each holding four unpaired electrons with the opposite spins and the $nd_\sigma^1 nd_{\pi 1}^1 nd_{\pi 2}^1 nd_\delta^1$ configuration. We found the quintet as a ground state for $CrCl_4^{2-}$ units.

The NOCV deformation density contributions from the components of the sextuple CrCr bond have been displayed in the upper part of Figure 9. Pairing of the five singly occupied *d*-orbitals on each metal center gives rise to one σ-, two π-, and the two δ-components represented by the $\sigma 1$, $\pi 1$, $\pi 2$, $\delta 1$, $\delta 2$ contributions to $\Delta\rho^{orb}$ andΔE_{orb}, Figure 9 and Table 4. We have in addition from $(n+1)s$ the $\sigma 2$ component.

The data presented in Table 4 for Cr_2 lead to the conclusion that the main energy contributions come from the total π-bonding, $\Delta E_{orb}^{\pi 1} + \Delta E_{orb}^{\pi 2} = -146.2$ kcal/mol, as well as $\sigma 1$ with $\Delta E_{orb}^{\sigma 1} = -91.8$ kcal/mol, whereas the δ-components ($\Delta E_{orb}^{\delta 1} + \Delta E_{orb}^{\delta 2} = -0.4$ kcal/mol) and the $\sigma 2$ component ($\Delta E_{orb}^{\sigma 2} = -4.3$ kcal/mol) from the 4*s* orbitals add very little to the bond strength. The same relative strengths of the bond-components can be found for the molybdenum and tungsten dimers. However, the total bond energy, ΔE_{tot}, increases (in absolute term) when going from the chromium (−31.3 kcal/mol) to the tungsten dimer (−88.7 kcal/mol). Similar conclusions were drawn from the experimental and as well as from the other theoretical investigations.[72,87−91] The factor responsible for the trend in ΔE_{int} is the steric repulsion, ΔE_{steric}. This term systematically decreases when chromium atoms are replaced by their group analogues. Further, the decrease in the steric repulsion is directly related to the decrease in the Pauli contribution, ΔE_{Pauli},[72] as the distance XX increase from X = Cr to X = W, the last column of Table 4. More precisely,[72] for chromium where 3*p*, 3*s*, and 3*d* are of the same radial extension, occupied 3*d* orbitals on one center experience Pauli repulsion from occupied 3*p*,3*s* orbitals on the other center. This effect is not present to the same extent for the heavier congeners where *ns*,*np* are much more contracted than *nd*.

Finally, let us briefly describe the character of the CrCr bond in $[Cl_4CrCrCl_4]^{4-}$. It follows from the lower part of Figure 9 that the four deformation density contributions, $\Delta\rho_\sigma^{orb}$, $\Delta\rho_{\pi 1}^{orb}$, $\Delta\rho_{\pi 2}^{orb}$, $\Delta\rho_\delta^{orb}$ with the corresponding energies ΔE_{orb}^{σ},$\Delta E_{orb}^{\pi 1}$, $\Delta E_{orb}^{\pi 2}$, ΔE_{orb}^{δ} accounts for the formation of the Cr−Cr bond in $[Cl_4CrCrCl_4]^{4-}$. Again, the largest contributions to the strength of the quadruple Cr−Cr bond come from the σ- and π-bonding whereas the δ-component is the weakest. We note that the term ΔE_{steric} in $[Cl_4CrCrCl_4]^{4-}$ also contains the coulomb interaction V_{AB} between the two net charges ($q = -2$) on the two $[Cl_4Cr]^{2-}$ fragments as discussed in the theoretical section in connection with the introduction of ΔE_{steric} near eq 10.

Multiple Bonds between Main-Group Elements and Metal Center, $(CO)_5Cr{=}XH_2$. The analysis up to now has been of bonds between either two main-group elements or two metal centers. We shall in this section apply the ETS-NOCV scheme to bonds between transition metals and main-group elements. Consider to this end the carbene-type complex $Cr(CO)_5XH_2$ (with X = C, Si, Ge, Sn). Let the complex further be formed from the square pyramidal metal

Table 4. ETS-NOCV Energy Decomposition of the Hextuple Bond in the X_2 Dimers (X = Cr, Mo, W) and the Quadruple Bond in the $[Cl_4CrCrCl_4]^{4-}$ Molecule[a]

X	ΔE_{orb}^{σ}[a]	ΔE_{orb}^{σ}[b]	ΔE_{orb}^{π}[a]	ΔE_{orb}^{π}[b]	ΔE_{orb}^{δ}[a]	ΔE_{orb}^{δ}[b]	ΔEsteric[b]	ΔE_{int}[c]	d(XX)[d]
Cr_2	−91.8	−4.3	−73.1	−73.1	−0.2	−0.2	211.4	−31.3	1.64
Mo_2	−90.0	−6.7	−74.7	−74.7	−2.5	−2.5	173.2	−77.9	1.98
W_2	−74.2	−13.8	−75.0	−75.0	−5.7	−5.7	150.7	−88.7[e]	2.04
$[Cl_4CrCrCl_4]^{4-}$	−82.0	–	−64.3	−64.4	−2.4	–	189.0	−24.1	1.88

[a] kcal/mol. [b] The total steric repulsion, $\Delta E_{steric} = \Delta E_{Pauli} + \Delta E_{elstat}$. [c] $\Delta E_{int} = \Delta E_{steric} + \Delta E_{prep} + \Delta E_{orb}$, $\Delta E_{orb} = \Delta E_{orb}^{\sigma 1} + \Delta E_{orb}^{\sigma 2} + \Delta E_{orb}^{\delta 1} + \Delta E_{orb}^{\sigma 2} + \Delta E_{orb}^{\pi 1} + \Delta E_{orb}^{\pi 2}$. [d] XX bond lengths in angstroms. [e] For W_2 the term ΔE_{int} includes 10.0 kcal/mol from the promotion of the quintet ground state of the tungsten atoms to their septet excited states.

Table 5. ETS-NOCV Energy Decomposition of the Double Bond in the $(CO)_5Cr{=}XH_2$ complexes[a]

X	ΔE_{steric}[b]	ΔE_{orb}^{σ}	ΔE_{orb}^{π}	ΔE_{orb}	ΔE_{prep}	ΔE_{int}[c]	$\Delta E_{HOMO/LUMO}$[d]
C	20.6	−51.9	−46.3	−98.2	19.0[e]	−58.6	1.42
Si	23.7	−55.9	−19.0	−74.9	3.8	−47.4	1.67
Ge	21.7	−51.8	−15.4	−67.2	4.3	−41.2	2.49
Sn	13.5	−45.6	−9.7	−55.3	4.5	−37.3	2.63

[a] kcal/mol. [b] The total steric repulsion, $\Delta E_{steric} = \Delta E_{Pauli} + \Delta E_{elstat}$. [c] $\Delta E_{int} = \Delta E_{steric} + \Delta E_{prep} + \Delta E_{orb}$, $\Delta E_{orb} = \Delta E_{orb}^{\sigma} + \Delta E_{orb}^{\pi}$. [d] The difference in energies (eV) between occupied d_{π} of $Cr(CO)_5$ and the LUMO π_{XH_2}. [e] Distortion term includes the difference in energy between the triplet ground state and the singlet excited state of CH_2 fragment.

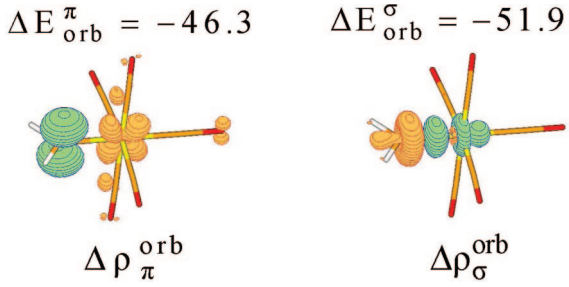

Figure 10. The contours of deformation density contributions $\Delta\rho_{\sigma}^{orb}$, $\Delta\rho_{\pi}^{orb}$ describing the σ- and π-components of the carbene bond in the $(CO)_5Cr{=}CH_2$ complex together with the corresponding energies ΔE_{σ}^{orb}, ΔE_{π}^{orb}. The numerically smallest contour values are ±0.01 a.u.

fragment $Cr(CO)_5$ with a low-spin d^6 ground-state configuration and the XH_2 ligand in its singlet state. For CH_2, the ground state is a triplet and we must add 15.5 kcal/mol to ΔE_{prep}; see Table 5.

Figure 10 exhibits the leading deformation density contributions $\Delta\rho_{\pi}^{orb}$ and $\Delta\rho_{\sigma}^{orb}$ together with the corresponding energies, ΔE_{orb}^{π}, ΔE_{orb}^{σ}. The σ-bond contribution $\Delta\rho_{\sigma}^{orb}$ is due to donation from the occupied σ_{CH_2} orbital into the empty d_{z2} orbital of the metal-based fragment, with d_{z2} pointing toward the carbene. The associated σ-bond formation energy is $\Delta E_{orb}^{\sigma} = -51.9$ kcal/mol. The second component, $\Delta\rho_{\pi}^{orb}$, represents the π-back-donation from an occupied d_{π} orbital of the metal into the empty π_{CH_2} type orbital of CH_2. The corresponding energy is given by $\Delta E_{orb}^{\pi} = -46.3$ kcal/mol.

The σ-bond strength ΔE_{orb}^{σ} is seen to change little along the homologue series X = C, Si, Ge. On the other hand, the π-bond strength ΔE_{orb}^{π} is much larger for X = C than for the other elements, Table 5, as the overlap between d_{π} and π_{XH_2} drops sharply from X = C to X = Si because of the increased Cr−X bond distance. Further, ΔE_{orb}^{π} decreases steadily from X = Si to X = Sn as the energy gap between d_{π} and π_{XH_2} increases, Table 5.

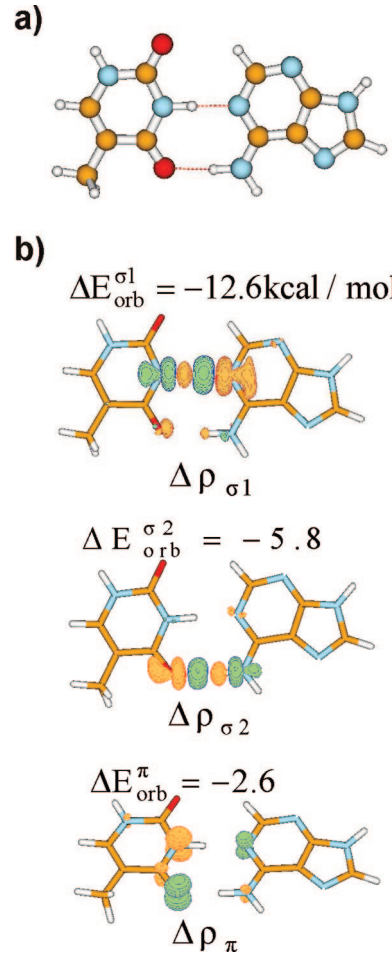

Figure 11. The adenine and thymine fragments in the base pair between the two nucleobases (panel a). The contours of the deformation densities describing the NH−N ($\Delta\rho_{\sigma 1}$) and NH−O ($\Delta\rho_{\sigma 2}$) hydrogen bonds as well as the π-resonance ($\Delta\rho_{\pi}$). Also shown are the corresponding energy contributions, $\Delta E_{orb}^{\sigma 1}$, $\Delta E_{orb}^{\sigma 2}$, ΔE_{orb}^{π} (panel b). The numerically smallest contour values are ±0.01 a.u.

Our bond analysis of $Cr(CO)_5XH_2$ conforms to the known Dewar−Chatt−Duncanson model[85,86] with σ-donation from σ_{XH_2} to d_{z2} and π-back-donation from d_{π} to π_{XH_2}. We find that the charge involved in the σ_{XH_2} to d_{z2} donation is 0.92 (C), 0.83 (Si), 0.81 (Ge), and 0.80 (Sn) whereas the corresponding numbers for the d_{π} to π_{XH_2} π-back-donation are 0.77 (C), 0.65 (Si), 0.53 (Ge), and 0.40 (Sn).

The Hydrogen Bond in Deoxyribonucleic Acid (DNA) between Nucleobases. We shall as another example of a donor−acceptor interaction briefly consider the hydrogen bond in DNA between two nucleobases typified by the

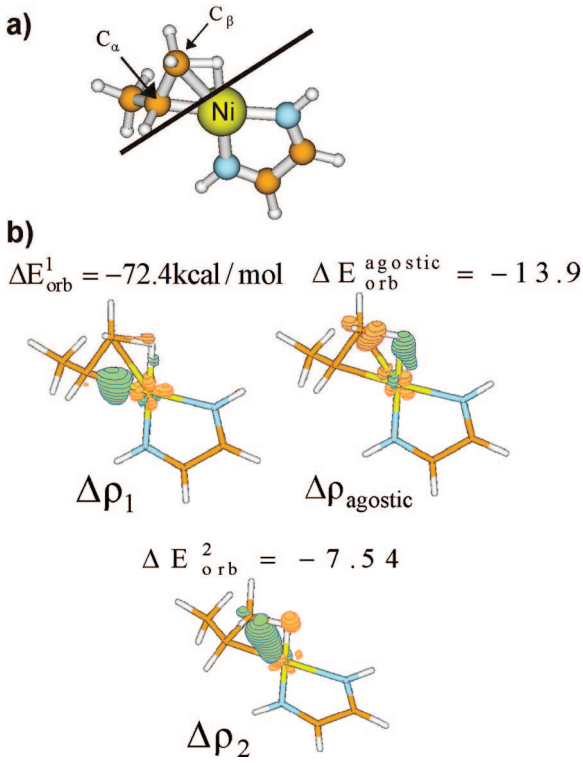

Figure 12. (a) Definition of the fragment separation in the β-agostic propyl-based complex. (b) The contours of the deformation densities describing the two σ bonds (C_α-Ni, $\Delta\rho 1$), ($C\beta$-Ni, $\Delta\rho 2$), and the agostic interaction ($C\beta H\cdots Ni$, $\Delta\rho_{agostic}$). Also shown are the corresponding energy contributions, ΔE^1_{orb}, ΔE^2_{orb}, $\Delta E^{agostic}_{orb}$. The numerically smallest contour values are ± 0.01 a.u. for $\Delta\rho_1$ and $\Delta\rho_{agostic}$. The corresponding values for $\Delta\rho_2$ are ± 0.005 a.u.

Table 6. ETS-NOCV Energy Decomposition Results for the Adenine-Thymine Base Pair (A-T)

BP86/TZ2P	kcal/mol
ΔE_{int}	−13.0
ΔE_{orb}	−22.0
ΔE_{Pauli}	38.7
ΔE_{prep}	2.1
ΔE_{elstat}	−31.9
ΔE_{int} (experiment)[99]	−12.1
ΔE_{int} (other theoretical results)[100]	−13.2

adenine-thymine base pair, Figure 11a. This system has previously been studied both experimentally[99] and theoretically.[100] It follows from Figure 11b that three deformation density components ($\Delta\rho_{\sigma 1}$, $\Delta\rho_{\sigma 2}$, $\Delta\rho_\pi$) contribute to the A-T bonding. The energetically most important contributions ($\Delta E^{\sigma 1}_{orb}$, $\Delta E^{\sigma 2}_{orb}$) come from the donor−acceptor interactions ($\Delta\rho_{\sigma 1}$, $\Delta\rho_{\sigma 2}$) between the occupied lone pairs of oxygen (from thymine) and nitrogen (from adenine) and the two unoccupied σ^* orbitals of the N−H bonds. We note that the hydrogen bond involving the nitrogen lone pair ($\Delta\rho_{\sigma 1}$) has a more stabilizing contribution with $\Delta E^{\sigma 1}_{orb} = -12.6$ kcal/mol compared to $\Delta\rho_{\sigma 2}$ involving the oxygen lone pair for which $\Delta E^{\sigma 2}_{orb} = -5.8$ kcal/mol, Figure 11b and Table 6. This is in line with the fact that nitrogen is the better donor. The deformation density $\Delta\rho_\pi$ illustrates the minor participation of π-type orbitals in the A-T bonding. Thus density depletion in the σ-network gives rise to density buildup in the π-framework and visa versa. This so-called Resonance Assisted Hydrogen Bonding (RAHB)[100] between the adenine and thymine subsystems amounts to $\Delta E^{\pi}_{orb} = -2.6$ kcal/mol. Hydrogen bonding in the A-T pair has already been fully analyzed and understood in a previous ETS study.[100] However, the analysis given here illustrate that the ETS-NOCV scheme is able to capture the essential bonding aspects in a few plots as illustrated in Figure 11b. The theoretical bond energies presented in Table 6 are seen to be in good agreement with experiment.

Agostic Bond Interactions in Transition Metal Alkyl Complexes. We shall as our last example study the agostic bonding interactions in a nickel-based β-agosctic propyl complex[101] formed between a C_β−H bond of the propyl group and a nickel center (Figure 12a). It is clear from Figure 12b that three components ($\Delta\rho_1$, $\Delta\rho_2$, $\Delta\rho_{agostic}$) are present in the bond between the propyl group and the nickel center. The dominant contribution, $\Delta\rho_1$, with $\Delta E^1_{orb} = -72.4$ kcal/mol comes from the σ-bond formed between C_α of the propyl group and the nickel center. The second energetically relevant component, $\Delta\rho_{agostic}$, with $\Delta E^{agostic}_{orb} = -13.9$ kcal/mol describes the β-agostic interaction between the C_β−H bond and nickel. Finally, the last component, $\Delta\rho_2$, exhibits direct formation of a weak C_β−Ni σ-bond, with $\Delta E^2_{orb} = -7.54$ kcal/mol. We should point out that a very useful feature of the ETS-NOCV scheme is that we can separate (and simultaneously quantify) the β-agostic interaction between the C_β−H bond of propyl ($\Delta\rho_{agostic}$) from the two Ni−C sigma bonds ($\Delta\rho_1$, $\Delta\rho_2$).

Concluding Remarks

In the present study we have combined the Extended Transition State (ETS) scheme with the Natural Orbitals for Chemical Valence (NOCV) method. It has been shown that the ETS-NOCV charge and energy decomposition scheme offers a compact picture of chemical bond formation within one common theoretical framework. Thus, it not only makes it possible to obtain a qualitative picture of the different components of the chemical bond (σ, π, δ, etc.) by visualization of the deformation density contributions, $\Delta\rho_k$, but it also provides the corresponding quantitative energies, ΔE^{orb}_k. Although, our description of bonding is based on a subjective division of a molecule into subsystems (fragments) with a particular electronic structure, we have demonstrated the applicability of the ETS-NOCV scheme in a description of various types of chemical bonds. They include single, double, and triple bonds between main group elements, sextuple and quadruple bonds between metal centers, and double bonds between a metal and a main group element.

The ETS scheme has previously been used to extract the various components (σ, π, δ, etc.) of the chemical bond for highly symmetrical molecules where ΔE_{orb} is blocked by symmetry.[20−22,25−27,59−62] However, without high symmetry such a separation into the σ, π, δ components was not possible. The distinctive advantage of the new ETS-NOCV charge and energy decomposition scheme is that we do not need a specific point group symmetry for a given molecule to assess the σ, π, δ contributions to the chemical bond. In

fact they can be easily identified by visualization of the deformation density contributions, $\Delta\rho_k$, and quantified by providing the corresponding energies, ΔE_k^{orb}, (see eq 17), even for molecules with no symmetry. Accordingly ETS and NOCV combined significantly broadens the spectrum of applications for the ETS scheme. We have here illustrated the applicability of the ETS-NOCV scheme with applications ranging from strong single and multiple bonds to weak hydrogen bonding interactions.

Acknowledgment. This work was supported by NSERC as well as a research grant from the Polish Ministry of Science and Higher Education in Poland (N N204 227534). T.Z. thanks the Canadian Government for a Canada Research Chair.

References

(1) Lewis, G. N. *J. Am. Chem. Soc.* **1916**, *38*, 762.

(2) Heitler, W.; London, F. *Z. Phys.* **1927**, *44*, 455.

(3) Shaik, S.; Hilberty, P. C. *Rev. Comput. Chem.* **2004**, *20*, 1.

(4) Mulliken, R. S. *Phys. Rev.* **1932**, *40*, 55.

(5) Hückel, E. *Trans. Faraday Soc.* **1934**, *30*, 59.

(6) Jug, K. *J. Am. Chem. Soc.* **1977**, *99*, 7800.

(7) Jug, K. *J. Am. Chem. Soc.* **1978**, *100*, 6581.

(8) Foster, J. P.; Weinhold, F. *J. Am. Chem. Soc.* **1980**, *102*, 7211.

(9) Reed, A. E.; Weinhold, F. *J. Chem. Phys.* **1985**, *83*, 1736.

(10) Reed, A. E.; Weinhold, F. *J. Chem. Phys.* **1983**, *78*, 4066.

(11) Reed, A. E.; Weinhold, F. *J. Chem. Phys.* **1986**, *84*, 5687.

(12) Reed, A. E.; Curtiss, L. A.; Weinhold, F. *Chem. Rev.* **1998**, *88*, 899.

(13) Bader, R. F. W. *Atoms in Molecules. A Quantum Theory*; University Press: Oxford, 1990.

(14) Becke, A.; Edgecombe, K. E. *J. Chem. Phys.* **1990**, *92*, 5397.

(15) Esterhuysen, C.; Frenking, G. *Theoret. Chem. Acc.* **2004**, *111*, 381.

(16) Coppens, P. *Electron Distribution and the Chemical Bond*; Plenum Press: New-York, 1982.

(17) Löwdin, P. O. *J. Chem. Phys.* **1950**, *18*, 365.

(18) Mulliken, R. S. *J. Chem. Phys.* **1955**, *23*, 1833.

(19) Dapprich, S.; Frenking, G. *J. Phys. Chem.* **1995**, *99*, 9352.

(20) Frenking, G.; Fröhlich, N. *Chem. Rev.* **2000**, *100*, 717.

(21) Frenking, G.; Wichmann, K.; Fröchlich, N.; Grobe, J.; Golla, W.; Le Van, D.; Krebs, B.; Läge, M. *Organometallics* **2002**, *21*, 2921.

(22) Frenking, G. *Science* **2005**, *310*, 796.

(23) Frenking, G.; Loschen, C.; Krapp, A.; Fau, S.; Strauss, S. H. *J. Comput. Chem.* **2006**, *28*, 117.

(24) Kitaura, K.; Morokuma, K. *Int. J. Quantum Chem.* **1976**, *10*, 325.

(25) Ziegler, T.; Rauk, A. *Theor. Chim. Acta* **1977**, *46*, 1.

(26) Ziegler, T.; Rauk, A. *Inorg. Chem.* **1979**, *18*, 1755.

(27) Ziegler, T.; Rauk, A. *Inorg. Chem.* **1979**, *18*, 1558.

(28) Mo, Y.; Gao, J.; Peyerimhoff, S. D. *J. Chem. Phys.* **2000**, *112*, 5530.

(29) Khaliullin, R. Z.; Cobar, E. A.; Lochan, R. C.; Bell, A. T.; Head-Gordon, M. *J. Phys. Chem. A* **2007**, *111*, 8753.

(30) Schenter, G. K.; Glendening, E. D. *J. Phys. Chem.* **1996**, *100*, 17152.

(31) Fransisco, E.; Pendás, M.; Blanco, M. A. *J. Chem. Theory Comput.* **2006**, *2*, 90.

(32) Mayer, I.; Hamza, A. *Int. J. Quantum Chem.* **2005**, *103*, 798.

(33) Korchowiec, J.; Uchimaru, T. *J. Chem. Phys.* **2000**, *112*, 1623.

(34) Liu, S., Govind, N. *J. Phys. Chem. A* 2008.

(35) Bagus, P. S.; Hermann, K.; Bauschlicher, C. W. *J. Chem. Phys.* **1984**, *80*, 4378.

(36) Jeziorski, B.; Moszynski, R.; Szalewicz, K. *Chem. Rev* **1994**, *94*, 1887.

(37) SAPT96 is an ab initio program for many-body symmetry adapted perturbation theory calculations of intermolecular interaction written by Bukowski, R.; Jankowski, P.; Jeziorski, B; Jeziorski, M.; Kucharski, S. A.; Moszynski, R.; Rybak, S; Szalewicz, K.; Williams, H. L.; Wormer, P. E. S. University of Delaware and University of Warsaw, 1996.

(38) Pauling, L. *The nature of the chemical bond*; Cornell Univ. Press: Ithaca, 1941.

(39) Wiberg, K. *Tetrahedron* **1968**, *24*, 1093.

(40) Gopinathan, M. S.; Jug, K. *Theoret. Chim. Acta* **1983**, *63*, 497.

(41) Mayer, I. *Chem. Phys. Lett.* **1984**, *97*, 270.

(42) Ciosłowski, J.; Mixon, S. T. *J. Am. Chem. Soc.* **1991**, *113*, 4142.

(43) Nalewajski, R. F.; Köster, A. M.; Jug, K. *Theor. Chim. Acta* **1993**, *85*, 463.

(44) Nalewajski, R. F.; Mrozek, J. *Int. J. Quantum Chem.* **1994**, *51*, 187.

(45) Nalewajski, R. F.; Mrozek, J.; Formosinho, S. J.; Varandas, A. J. C. *Int. J. Quantum Chem.* **1994**, *52*, 1153.

(46) Nalewajski, R. F.; Mrozek, J.; Mazur, G. *Can. J. Chem.* **1996**, *74*, 1121.

(47) Nalewajski, R. F.; Mrozek, J.; Michalak, A. *Int. J. Quantum Chem.* **1997**, *61*, 589.

(48) Nalewajski, R. F.; Mrozek, J.; Michalak, A. *Pol. J. Chem.* **1998**, *72*, 1779.

(49) Michalak, A.; De Kock, R.; Ziegler, T. *J. Phys. Chem. A,* **2008**, *112*, 7256.

(50) Michalak, A.; Mitoraj, M.; Ziegler, T. *J. Phys. Chem. A.* **2008**, *112* (9), 1933.

(51) Mitoraj, M.; Michalak, A. *Organometallics* **2007**, *26* (26), 6576.

(52) Mitoraj, M.; Michalak, A. *J. Mol. Model.* **2007**, *13*, 347.

(53) Mitoraj, M.; Michalak, A. *J. Mol. Model.* **2008**, *14*, 681.

(54) Mitoraj, M.; Zhu, H.; Michalak, A.; Ziegler, T. *Int. J. Quantum Chem.* 2008, DOI:, 10.1002/qua.21910.

(55) Löwdin, P. O. *J. Chem. Phys.* **1950**, *18*, 364.

(56) Pakiari, A. H.; Fakhraee, S.; Azami, S. M. *Int. J. Quantum Chem.* **2008**, *108*, 415.

(57) Hurley, A. C. *J. Chem. Phys.* **1962**, *37*, 449.

(58) TeVelde, G.; Bickelhaupt, F. M.; Baerends, E. J.; Fonseca Guerra, C.; Van Gisbergen, S. J. A.; Snijders, J. G.; Ziegler, T. *J. Comput. Chem.* **2001**, *22*, 931, and refs therein.

(59) Baerends, E. J.; Ellis, D. E.; Ros, P. *Chem. Phys.* **1973**, *2*, 41.

(60) Baerends, E. J.; Ros, P. *Chem. Phys.* **1973**, *2*, 52.

(61) te Velde, G.; Baerends, E. J. *J. Comput. Phys.* **1992**, *99*, 84.

(62) Fonseca, C. G.; Visser, O.; Snijders, J. G.; te Velde, G.; Baerends, E. J. In *Methods and Techniques in Computational Chemistry*; METECC-95; Clementi, E., Corongiu, G., Eds.; STEF: Cagliari, Italy, 1995; p 305.

(63) Becke, A. *Phys. Rev. A* **1988**, *38*, 3098.

(64) Perdew, J. P. *Phys. Rev. B* **1986**, *34*, 7406.

(65) van Lenthe, E.; Baerends, E. J.; Snijders, J. G. *J. Chem. Phys.* **1993**, *99*, 4597.

(66) van Lenthe, E.; Baerends, E. J.; Snijders, J. G. *J. Chem. Phys.* **1993**, *101*, 9783.

(67) van Lenthe, E.; van Leeuwen, R.; Baerends, E. J.; Snijders, J. G. *Int. J. Quantum Chem.* **1996**, *57*, 281.

(68) Jacobsen, H.; Ziegler, T. *J. Am. Chem. Soc.* **1994**, *116*, 3667.

(69) Bickelhaupt, F. M.; Baerends, E. J. Kohn-Sham Density Functional Theory: Predicting and Understanding Chemistry. *Reviews in Computational Chemistry*; Lipkowitz, K. B., Boyd, D. B., Eds.; Wiley-VCH: New York, 2000; Vol. 15, pp 1−86.

(70) Mitoraj, M.; Zhu, H.; Michalak, A.; Ziegler, T. *J. Org. Chem.* **2006**, *71*, 9208.

(71) Mitoraj, M.; Zhu, H.; Michalak, A.; Ziegler, T. *Organometallics* **2007**, *26*, 1627.

(72) Ziegler, T. Periodic Trends in Bond Energies: A Density Functional Study In *Computational Thermochemistry ACS Symposium Series 677*; Irikura, K. K., Frurip, D. J., Eds.; American Chemical SocietyWshington, DC, 1998; pp 369−383.

(73) Wagman, D. D.; Evans, W. H.; Parker, V. B.; Schumm, R. H.; Halow, I.; Bailey, S. M.; Churney, K. L.; Nuttall, R. L. *J. Phys. Chem. Ref. Data* **1982**, *11* (suppl. 2), xxx–xxx.

(74) Langhoff, S. A.; Bauschlicher, C. W., Jr.; Taylor, P. W. *Chem. Phys. Lett.* **1991**, *180*, 88.

(75) Pu, L.; Twamley, B.; Power, P. P. *J. Am. Chem. Soc.* **2000**, *122*, 3524.

(76) Phillips, A. D.; Wright, R. J.; Olmstead, M. M.; Power, P. P. *J. Am. Chem. Soc.* **2002**, *124*, 5930.

(77) Stender, M.; Phillips, A. D.; Wright, R. J.; Power, P. P. *Angew. Chem., Int. Ed.* **2002**, *41*, 1785.

(78) Wiberg, N.; Niedermayer, W.; Fischer, G.; Noth, H.; Suter, M. *Eur. J. Inorg. Chem.* **2002**, 1066.

(79) Sekiguchi, A.; Kinjo, R.; Ichinohe, M. *Science (Washington, DC)* **2004**, *305*, 1755.

(80) Pignedoli, C. A.; Curioni, A.; Andreoni, W. *ChemPhysChem* **2005**, *6*, 1795.

(81) Malcolm, N. O. J.; Gillespie, R. J.; Popelier, P. L. A. *J. Chem. Soc., Dalton Trans.* **2002**, 3333.

(82) Allen, T. L.; Fink, W. H.; Power, P. P. *J. Chem. Soc., Dalton Trans.* **2000**, 407.

(83) Bridgeman, A. J.; Ireland, L. R. *Polyhedron* **2001**, *20*, 2841.

(84) Jung, Y.; Brynda, M.; Power, P.; Head-Gordon, M. *J. Am. Chem. Soc.* **2006**, *128*, 7185.

(85) Dewar, M. J. S. *Bull. Soc. Chim.* **1951**, *18*, C71.

(86) Chatt, J.; Duncanson, J. A. *J. Chem. Soc.* **1953**, *3*, 2939.

(87) Thomas, E. J.; Murray, J. S.; O'Connor, C. J.; Politzer, P. *J. Mol. Struct.* **1999**, *487*, 177.

(88) Roos, B. O. *Collect. Czech. Chem. Commun.* **2003**, *68*, 265.

(89) Roos, B. O.; Borin Antonio, C.; Gagliardi, L. *Angew. Chem., Int. Ed.* **2007**, *46*, 1469.

(90) Bondybey, V. E.; English, J. H. *Chem. Phys. Lett.* **1983**, *94*, 443. Takagi, N.; Nagase, S. *Organometallics* **2007**, *26*, 469.

(91) Simard, B.; Lebeault-Dorget, M.-A.; Marijnissen, A.; Meulen, J. J. *J. Chem. Phys.* **1998**, *108*, 9668. Takagi, N.; Nagase, S. *Organometallics* **2007**, *26*, 3627.

(92) Sugiyama, Y.; Sasamori, T.; Hosoi, Y.; Furukawa, Y.; Takagi, N.; Nagase, S.; Tokitoh, N. *J. Am. Chem. Soc.* **2006**, *128*, 1023. Pis Diez, R. *Int. J. Quantum Chem.* **2000**, *76*, 105.

(93) Balasubramanian, K.; Dingguo, D. *Chem. Phys. Lett.* **1997**, *265*, 538.

(94) Radius, U.; Breher, F. *Angew. Chem., Int. Ed.* **2006**, *45*, 3006.

(95) Lai, C.-H.; Su, M.-d. *J. Comput. Chem.* **2008**, *29*, 2487.

(96) Nalewajski, R. F.; Korchowiec, J.; Michalak, A. In *Reactivity Criteria in Charge Sensitivity Analysis*; Nalewajski, R. F., Ed.;Topics in Current Chemistry, Vol. *183*: Density Functional Theory - Theory of Chemical Reactivity; Springer-Verlag: Heidelberg, 1996; pp 25−141.

(97) Nalewajski, R. F. *J. Math. Chem.* **2008**, *44*, 802.

(98) Kovàcs, A.; Esterhuysen, C.; Frenking, G. *Chem. Eur. J.* **2005**, *11*, 1813.

(99) Yanson, K.; Teplitsky, A. B.; Sukhodub, L. F. *Biopolymers* **1979**, *18*, 1149.

(100) Guerra, C. F.; Bickelhaupt, F. M.; Snijders, J. G.; Baerends, E. J. *Chem. Eur. J.* **1999**, *5*, 3581.

(101) Johnson, L. K.; Mecking, S.; Brookhart, M. *J. Am Chem Soc.* **1996**, *118*, 267.

CT800503D

JCTC Journal of Chemical Theory and Computation

Water Dimer Cation: Density Functional Theory vs Ab Initio Theory

Han Myoung Lee* and Kwang S. Kim*

Center for Superfunctional Materials and Center for Basic Sciences, Department of Chemistry, Pohang University of Science and Technology, Pohang 790-784, Korea

Received November 24, 2008

Abstract: By using density functional theory (DFT) and high-level ab initio theory, the structure, interaction energy, electronic property, and IR spectra of the water dimer cation [$(H_2O)_2^+$] are investigated. Two previously reported structures of the water dimer cation [disproportionated ionic (Ion) structure and hydrazine-like (OO) structure] are compared. For the complete basis set (CBS) limit of coupled cluster theory with single, double, and perturbative triple excitations [CCSD(T)], the Ion structure is much more stable (by 11.7 kcal/mol). This indicates that the ionization of water clusters produce the hydronium cation moiety (H_3O^+) and the hydroxy radical. The transition barrier for the interconversion from the Ion/OO structure is ∼15/∼9 kcal/mol. It is interesting to note that the calculation results of the water dimer cation vary seriously depending on calculation methods. Möller−Pleset second-order perturbation (MP2) theory gives reasonable relative energies in favor of the Ion structure but reports unreasonable frequencies for the OO structure. On the other hand, most DFT calculations with various functionals overstabilize the OO structure. However, the DFT results with MPW1K and BH&HLYP functionals are very close to the CCSD(T)/CBS results. Thus, as for the validity test of the DFT functionals for ionized molecular systems, the energy comparison of two water dimer cation structures would be a very important criterion.

I. Introduction

Numerous experimental and theoretical studies have been carried out on aqua clusters (neutral water clusters,[1] anion-water clusters,[2] and cation-water clusters[3]). The investigation of neutral water clusters has provided the information on neutral H-bonds. The studies of electron−water clusters have provided the information on the electron affinity (EA) of neutral water and the hydration of an electron.[4] Through the study of the hydronium-water clusters,[5] the hydration and coordination chemistry of hydronium cation or proton are understood. There have also been a number of studies on the hydration and dissociation phenomena of acids, bases, and salts,[6] which are important in understanding the nature of water as a solvent. In addition, the studies of the ionization and the ionized state of the water molecule are very useful for understanding the water cluster cations.[7,8]

The ionization of water clusters is widely seen in neutron irradiation of the cooling water in a nuclear atomic plant, in the photoreaction of water, and in aqueous environments.[9] The ionization energy of the water molecule is 12.61 eV.[8] Water cluster cations [$(H_2O)_n^+$] were experimentally produced under special conditions in the gas phase.[10] A few theoretical investigations for water cluster cations were performed.[11−13] For the water dimer cation, the hydrazine-like (OO) structures and disproportionated ionic (Ion) structure were suggested.[11,12] Therefore, we investigate the structures, energetics, spectra, and dynamics of the water dimer cations [$(H_2O)_2^+$] using high level ab initio calculations. Here, we note serious failures of most DFT calculations except for a few functionals. Thus, the comparison of the DFT and CCSD(T) results for the water dimer cation is also addressed.

* Corresponding authors phone: 82-54-279-2110; fax: 82-54-279-8137; e-mail: abcd0lhm@postech.ac.kr (H.M.L.) and kim@postech.ac.kr (K.S.K.).

10.1021/ct800506q CCC: $40.75
Published on Web 03/02/2009

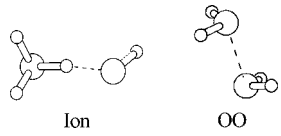

Figure 1. Disproportionated ionic (Ion) structure and hydrazine-like (OO) structure of the water dimer cation $(H_2O)_2^+$.

II. Calculation Methods

The OO structure and the Ion structure of the water dimer cation are shown in Figure 1. We optimized the two structures and calculated their frequencies using various DFT methods of Becke's exchange and Lee−Yang−Parr correlation functionals (BLYP),[14] Becke's exchange and Perdew−Wang correlation functionals (BPW91),[15] Handy's family functional including gradient-corrected correlation (HCTH-407),[16] Becke's three-parameters for exchange and Lee−Yang−Parr correlation functionals (B3LYP),[17] Perdew−Burke−Ernzerhof hybrid functional (PBE1PBE),[18] modified Perdew−Wang one-parameter model for kinetics (MPW-1K),[19] Becke's half HF-LSDA (Hartree−Fock Local Spin Density Approximation) exchange and Lee−Yang−Parr correlation functionals (BH&H),[20] and Becke's half HF-LSDA−Becke exchange and Lee−Yang−Parr correlation functionals (BH&HLYP)[21] with the 6-311++G** basis set.[22] The MP2 optimizations and frequency calculations were also carried out using the aug-cc-pVDZ (abbreviated as aVDZ) and the aug-cc-pVTZ (aVTZ) basis sets.[23] The MP2 single-point calculations with the aug-cc-pVQZ (aVQZ) basis set were also done on the MP2/aVTZ geometries (MP2/aVQZ//MP2/aVTZ). To obtain more accurate results, the CCSD(T) optimizations and frequency calculations were performed using the aVDZ and aVTZ basis sets. The CCSD(T) single-point calculations using the aVQZ basis set were also done on the CCSD(T)/aVTZ geometries (CCSD(T)/aVQZ//CCSD(T)/aVTZ). The 1s orbitals of oxygen atoms were frozen in the correlation calculations. All the "d" and "f" orbitals used here are the spherical harmonic basis functions (5d and 7f).

For the Ion structure, which has the charged H-bonding between one hydronium cation and one neutral hydroxyl radical, the basis set superposition energy (BSSE) correction can be made. However, in the OO structure the positive charge is almost equally distributed in two water molecules, so the BSSE correction cannot be made properly. In order to compare the two structures at equal conditions, it is better not to make the BSSE corrections. Thus, the BSSE corrections are not considered in this system.

All the optimizations were done with the minimization of total energy without any symmetry constraints. We calculated the zero-point-energy (ZPE) uncorrected total energy (ΔE_e) at the equilibrium states of the Born−Oppenheimer potential surfaces and the ZPE-corrected total energy (ΔE_0). The enthalpy/free energy changes ($\Delta H_r/\Delta G_r$) at room temperature and 1 atm were obtained using the frequency calculations. The CBS limit interaction energies were obtained with the extrapolation scheme utilizing that the electron correlation error is proportional to N^{-3} for the aug-cc-pV*N*Z basis set [$\Delta E_{CBS} = (\Delta E_N N^{-3} \Delta E_{N-1}(N-1)^3)/(N^3 - (N-1)^3)$].[24] The DFT and MP2 calculations were carried out by using the Gaussian 03 suite of programs,[25] and the CCSD(T) calculations were performed by using the Molpro2002.6 package.[26] The approximate resolution of the identity MP2 (RI-MP2) calculations[27] was also carried out by using the Turbomole5.6 package.[28] However, these results are essentially the same, with the MP2 values within 0.1 kcal/mol, so these results are not reported here.

Table 1. Various DFT/6-311++** Interaction Energies (kcal/mol) of the Ion and OO Structures of the Water Dimer Cation, $(H_2O)_2^+$ [a]

	$-\Delta E_e$ ($-\Delta E_0$)	
method	Ion structure	OO structure
BLYP	49.3 (46.5)	58.4 (54.0)
BPW91	49.1 (46.4)	57.2 (52.8)
HCTH407	48.0 (45.2)	56.6 (52.1)
B3LYP	49.8 (46.8)	51.5 (46.7)
PBE1PBE	50.3 (47.4)	49.8 (45.0)
MPW1K	49.9 (46.9)	42.9 (37.9)
BH&H	55.5 (52.6)	48.9 (43.8)
BH&HLYP	49.9 (46.7)	41.4 (36.1)

[a] Interaction energy between the neutral water monomer and the water monomer cation. ΔE_e is the ZPE-uncorrected energy at the equilibrium point of the Born−Oppenheimer potential surfaces, and ΔE_0 is the ZPE-corrected energy.

III. Results and Discussion

For the water monomer, the vertical/adiabatic IP (IP_v/IP_a) calculated on the basis of the unrestricted open-shell approach is 12.70/12.61 eV at the MP2/aVDZ level of theory, 12.86/12.77 eV at the MP2/aVTZ level, 12.51/12.42 eV at the CCSD(T)/aVDZ level, 12.68/12.57 eV at the CCSD(T)/aVTZ level, and 12.74/12.64 eV at the CCSD(T)/aVQZ//CCSD(T)/aVTZ level. These values are close to the experimental IP (12.61 eV).[8] The O−H distance and H−O−H bond angle of the water monomer cation are 1.002 Å and 109.1° at the CCSD(T)/aVTZ level, which shows 0.04 Å longer O−H distances and 4.9° wider bond angle than those of the neutral water monomer (0.962 Å and 104.2° at the CCSD(T)/aVTZ level). The O−H bond strength becomes weaker and the H−H repulsion is greater due to the ionization.

We calculated the interaction energy between the neutral water monomer and the water monomer cation [ΔE(dimer cation) = E(dimer cation) − E(water monomer) − E(water monomer cation)], where the geometries for water monomers are relaxed in the dimer. From the optimization of water dimer cation, the OO structure of the "anti" form has one imaginary frequency, while the asymmetric OO structure of the "gauche" form has all real frequencies. Thus, the asymmetric OO structure is shown in Figure 1. As in Table 1, the OO structure is much more stable than the Ion structure at the BLYP, BPW91, and HCTH407 levels of theory. The B3LYP and PBE1PBE calculations predict that both structures are compatible. On the other hand, MPW1K, BH&H, and BH&HLYP calculations predict that the Ion structure is much more stable than the OO structure. Table 2 lists the interaction energies of the two structures of the water dimer cation at the MPW1K, BH&HLYP, MP2/aVDZ,

Table 2. DFT, MP2, and CCSD(T) Interaction Energies (kcal/mol) of the Two Structures of the Water Dimer Cation, $(H_2O)_2^+$ [a]

	Ion structure				OO structure			
method	$-\Delta E_e$	$-\Delta E_0$	$-\Delta H_r$	$-\Delta G_r$	$-\Delta E_e$	$-\Delta E_0$	$-\Delta H_r$	$-\Delta G_r$
MPW1K/6-311++G**	49.87	46.88	48.17	40.06	42.90	37.87	39.29	30.69
MPW1K/aVDZ	48.86	45.99	47.26	39.25	42.49	37.33	38.74	30.12
MPW1K/aVTZ	48.93	45.94	47.24	39.19	41.48	36.51	37.92	29.33
BH&HLYP/6-311++G**	49.88	46.74	47.99	39.94	41.12	36.08	37.50	29.30
BH&HLYP/aVDZ	48.83	45.82	47.07	39.09	40.45	35.46	36.88	28.64
BH&HLYP/aVTZ	48.84	45.73	46.99	38.97	39.73	34.75	36.18	27.90
MP2/aVDZ	45.92	42.91	44.15	36.25	40.68	30.17	31.71	23.23
MP2/aVTZ	46.48	43.47	44.73	36.80	40.40	30.69	32.18	24.00
MP2/aVQZ//[b]	46.47	43.45	44.72	36.78	40.48	30.77	32.26	24.08
CCSD(T)/aVDZ	45.96	46.11	47.81	38.07	39.49	34.75	36.66	26.46
CCSD(T)/aVTZ	46.68	46.48	47.81	38.79	39.51	34.76	36.67	26.49
CCSD(T)/aVQZ//[c]	46.69	46.49	47.82	38.81	39.52	34.77	36.68	26.50
CCSD(T)/CBS	46.70	46.50	47.83	38.82	39.53	34.78	36.69	26.51

[a] The ZPE and thermal energy corrections at the MP2/aVQZ//MP2/aVTZ and CCSD(T)/aVQZ//CCSD(T)/aVTZ levels were made using the MP2/aVTZ and CCSD(T)/aVTZ values, respectively. [b] MP2/aVQZ//MP2/aVTZ. [c] CCSD(T)/aVQZ//CCSD(T)/aVTZ.

Table 3. Conformational Characteristics and Geometrical Parameters [Distances (r/Å) and Rotational Constants (A in GHz)] of the Two Structures of the Water Dimer Cation, $(H_2O)_2^+$ [a]

	Ion structure			OO structure			
method	r_{O-H}	r_{O-O}	A	r_{O-H}	r_{O-O}	A	H_2O: r_{O-H}
B3LYP/6-311++G**	0.998	2.501	244.4	0.979	2.128	140.5	0.962
MPW1K/6-311++G**	0.986	2.470	252.1	0.968	2.052	143.9	0.951
MPW1K/aVDZ	0.989	2.481	242.3	0.970	2.046	142.4	0.954
MPW1K/aVTZ	0.987	2.476	243.4	0.968	2.040	143.4	0.951
BH&HLYP/6−311++G**	0.983	2.497	257.9	0.967	2.053	144.6	0.951
BH&HLYP/aVDZ	0.986	2.503	247.6	0.970	2.049	143.1	0.953
BH&HLYP/aVTZ	0.984	2.500	246.7	0.967	2.047	143.8	0.950
MP2/aVDZ	0.998	2.520	232.5	0.984	2.039	138.3	0.966
MP2/aVTZ	0.996	2.496	234.9	0.980	2.023	139.1	0.961
CCSD(T)/aVDZ	0.998	2.534	228.6	0.984	2.047	138.3	0.967
CCSD(T)/aVTZ	0.995	2.507	233.3	0.980	2.033	139.6	0.962

[a] r_{O-H} is the average values for the O−H distances. The r_{O-H} of the water monomer is also listed for comparison.

MP2/aVTZ, MP2/aVQZ//MP2/aVTZ, CCSD(T)/aVDZ, CCSD(T)/aVTZ, CCSD(T)/aVQZ//CCSD(T)/aVTZ, and CCSD(T)/CBS levels of theory. Except for the MP2/aVQZ//MP2/aVTZ and CCSD(T)/aVQZ//CCSD(T)/aVTZ calculations, the two structures (OO and Ion) were fully optimized and their frequencies were calculated at each calculation level in Table 2. Although most DFT functionals predict that the OO structure is more stable than or at least comparable to the Ion structure, the most reliable CCSD(T)/CBS results show that the Ion structure is much more stable by 11.72 kcal/mol than the OO structure. Thus, only the MPW1K and BH&HLYP results among many DFT calculations are listed in Table 2 for comparison. The MPW1K and BH&HLYP results for the larger basis sets are closer to the CCSD(T)/CBS results. BH&H/6-311++G** predicts almost reasonable relative energy difference, but the interaction energy is overestimated. It is clear that most other functionals completely fail to predict the right energetics of the water dimer cation. We also note that the higher stability of the Ion structure over the OO structure retains even if the temperature rises to room temperature (298 K). Thus, the water dimer cation has the form of a hydronium cation and a hydroxyl radical. The experimental IP_v and IP_a of the water dimer are known to be 12.1 and 11.2 eV.[29,30] On the unrestricted open-shell approach, the calculated IP_v of the water dimer is 11.9 eV at the CCSD(T)/aVQZ// CCSD(T)/aVTZ level. Using the Ion structure, the calculated IP_a of the water dimer is 10.8 eV at the CCSD(T)/aVQZ//CCSD(T)/aVTZ level. These calculated IPs are in good agreement with the experimental data.

Table 3 lists the optimized geometrical parameters of Ion and OO structures at the B3LYP, MPW1K, BH&HLYP, MP2, and CCSD(T) levels. The Ion structure shows longer O−H distance and shorter O−O distance than the OO structure. The Ion structure has a larger rotational constant A than the OO structure. The optimized Cartesian coordinates of water dimer cations (OO and Ion structures) at the CCSD(T)/aVTZ level are listed in the Supporting Information.

The barrier height for the interconversion between the OO and Ion structures of the water dimer cation was calculated at the MPW1K/6-311++G** and MP2/aVDZ levels of theory. The transition state in the interconversion is higher in energy by 8.15 and 9.78 kcal/mol (15.11 and 15.02 kcal/mol) than the OO structure (Ion structure) at the MPW1K/6-311++G** and MP2/aVDZ levels. At the CCSD(T) single-point calculations, the transition state is higher in energy by 8.14 kcal/mol (14.59 kcal/mol) than the OO (Ion) structure with the MPW1K/6-311++G** geometries and is higher in energy by 9.69 kcal/mol (16.12 kcal/mol) than the OO (Ion) structure on the MP2/aVDZ geometries. These transition energy barriers are somewhat high.

Table 4. Scaled Frequencies [ν(cm^{-1})] and the IR Intensities (as subscripts) (10 km/mol) of O−H Stretching Modes for H_2O, H_2O^+, and $(H_2O)_2^+$ (Ion and OO structures) at the DFT, MP2, and CCSD(T) Levels of Theory[a]

method	scale[b]	H_2O	H_2O^+	Ion structure	OO structure
B3LYP/6-311++G**	0.956	3750, 3650	3246, 3196	3595_{45}, 3523_{14}, 3465_{16}, 2157_{45}	3550_{47}, 3549_{0}, 3482_{0}, 3434_{70}
MPW1K/6-311++G**	0.916	3750, 3650	3259, 3210	3585_{41}, 3510_{17}, 3474_{18}, 2170_{282}	3546_{51}, 3544_{3}, 3478_{0}, 3420_{104}
MPW1K/aVDZ	0.920	3752, 3648	3252, 3194	3582_{37}, 3502_{15}, 3468_{17}, 2143_{268}	3546_{49}, 3543_{3}, 3472_{0}, 3415_{93}
MPW1K/aVTZ	0.921	3749, 3651	3248, 3205	3583_{38}, 3512_{15}, 3476_{16}, 2122_{273}	3545_{50}, 3543_{3}, 3479_{0}, 3419_{97}
BH&HLYP[c]	0.917	3748, 3652	3252, 3207	3577_{43}, 3506_{15}, 3484_{21}, 2346_{262}	3549_{52}, 3547_{5}, 3483_{0}, 3419_{124}
BH&HLYP/aVDZ	0.920	3750, 3650	3243, 3188	3577_{40}, 3500_{15}, 3476_{19}, 2297_{254}	3552_{50}, 3549_{5}, 3478_{0}, 3415_{112}
BH&HLYP/aVTZ	0.922	3747, 3653	3241, 3200	3573_{40}, 3506_{14}, 3484_{19}, 2282_{257}	3545_{51}, 3543_{4}, 3481_{0}, 3414_{117}
MP2/aVDZ	0.957	3764, 3636	3308, 3232	3596_{35}, 3519_{7}, 3502_{24}, 2221_{261}	6092_{9999}, 3537_{37}, 3532_{10}, 3442_{0}
MP2/aVTZ	0.952	3760, 3640	3304, 3245	3592_{37}, 3520_{6}, 3508_{25}, 2157_{272}	5663_{9999}, 3528_{47}, 3526_{2}, 3447_{0}
CCSD(T)/aVDZ	0.962	3757, 3643	3277, 3207	3604_{33}, 3522_{15}, 3486_{13}, 2288_{247}	3542_{40}, 3540_{4}, 3460_{0}, 3419_{11}
CCSD(T)/aVTZ	0.958	3752, 3648	3279, 3225	3602_{43}, 3528_{19}, 3476_{16}, 2248_{315}	3537_{50}, 3536_{5}, 3467_{0}, 3424_{14}

[a] The frequencies of H_2O and H_2O^+ are also reported for comparison. [b] Scale factors (see the text). [c] BH&HLYP/6-311++G**.

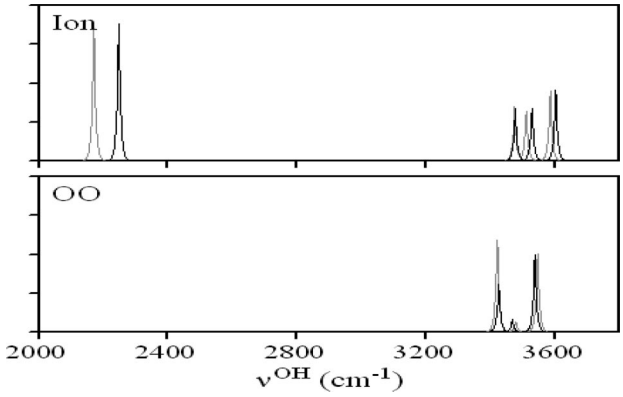

Figure 2. MPW1K/6-311++G** (gray) and CCSD(T)/aVTZ (black) predicted IR spectra for the O−H stretching frequencies of the water dimer cation.

The experimental ν_3, ν_1, and ν_2 frequencies of the water monomer cation are known to be 3259, 3213, and 1408 cm^{-1}.[7] We employed the scale factors (0.956 at the B3LYP/6−311++G** level, 0.916 at the MPW1K/6-311++G** level, 0.952 at the MP2/aVTZ level, 0.962 at the CCSD(T)/aVDZ level, and 0.958 at the CCSD(T)/aVTZ level) to match the average value of calculated symmetric and asymmetric stretch frequencies (ν_1 and ν_3) of the neutral H_2O with the corresponding experimental value (3700 cm^{-1}).[31] The calculated frequencies of the water monomer cation are 3246, 3196, and 1354 cm^{-1} at the B3LYP/6-311++G** level; 3259, 3210, and 1332 cm^{-1} at the MPW1K/6-311++G** level; 3304, 3245, and 1400 cm^{-1} at the MP2/aVTZ level; 3277, 3207, and 1413 cm^{-1} at the CCSD(T)/aVDZ level; and 3279, 3225, and 1413 cm^{-1} at the CCSD(T)/aVTZ level. In the water monomer cation, the strength of O−H bonds is weakened due to the ionization as compared with the neutral water monomer. The asymmetric and symmetric O−H stretching frequencies and bending frequency are red-shifted by 473, 422, and 163 cm^{-1} at the CCSD(T)/aVTZ level in comparison with those of pure neutral water monomer, respectively.

We have calculated the frequencies of the Ion and OO structures of the water dimer cation at the DFT, MP2, and CCSD(T) levels (Figure 2 and Table 4). For the OO structure, the MP2 calculations with aVDZ and aVTZ basis sets fail to produce reasonable frequencies, while DFT and CCSD(T) calculations give reasonable frequencies as shown in Table 4. At the CCSD(T)/aVTZ level, the OO structure shows four weakly red-shifted O−H stretching frequencies of 3424, 3467, 3536, and 3537 cm^{-1}, while the Ion structure shows one strongly red-shifted peak and three weakly red-shifted peaks at 2248, 3476, 3528, and 3602 cm^{-1}. One strongly red-shifted frequency (2248 cm^{-1} at the CCSD(T)/aVTZ level) of the Ion structure is of the hydronium moiety (H_3O^+) interacting with the hydroxyl radical (OH).

IV. Concluding Remarks

At the CCSD(T)/CBS level of theory, the Ion structure is much more stable than the OO structure. The Ion structure is composed of a hydronium cation and a hydroxyl radical. On the other hand, most DFT calculations with various functionals favor the OO structure. Nevertheless, the DFT results with MPW1K and BH&HLYP functionals are very close to the CCSD(T)/CBS results. Thus, the energy comparison of the two structures of the water dimer cation would be an interesting example for the validity test of the DFT functionals. The MP2 calculations give reasonable relative energies but unreasonable frequencies for the OO structure. Therefore, in order to obtain reliable stabilities and frequencies of water dimer cation, the CCSD(T) calculations are required. However, the DFT(MPW1K) is an alternative to obtain reliable results for this system with much less computing time. The calculated spectra are provided to facilitate future experiments.

Acknowledgment. This work was supported by KOSEF (EPB Center: R11-2008-052-01000), BK21, Global Research Laboratory Project (KICOS), and a Korea Research Foundation Grant (KRF-2006-353-C00022) funded by Korea Government (MOEHRD). We would like to acknowledge the support from KISTI Supercomputing Center (KSC-2007-S00-3005 and KSC-2008-K08-0002).

Supporting Information Available: Optimized structures of water dimer cations (OO and Ion structures) at the CCSD(T)/aVTZ level. This material is available free of charge via the Internet at http://pubs.acs.org.

References

(1) (a) Pribble, R. N.; Zwier, T. S. *Science* **1994**, *265*, 75. (b) Liu, K.; Brown, M. G.; Carter, C.; Saykally, R. J.; Gregory, J. K.; Clary, D. C. *Nature* **1996**, *381*, 501. (c) Nauta, K.; Miller, R. E. *Science* **2000**, *287*, 293. (d) Kim, K. S.; Dupuis,

M.; Lie, G. C.; Clementi, E. *Chem. Phys. Lett.* **1986**, *131*, 451. (e) Franken, K. A.; Jalaie, M.; Dykstra, C. E. *Chem. Phys. Lett.* **1992**, *198*, 59. (f) Kim, J.; Kim, K. S. *J. Chem. Phys.* **1998**, *109*, 5886. (g) Xantheas, S. S.; Dunning, T. H. *J. Phys. Chem.* **1992**, *96*, 7505. (h) Lee, H. M.; Suh, S. B.; Lee, J. Y.; Tarakeshwar, P.; Kim, K. S. *J. Chem. Phys.* **2000**, *112*, 9759. (i) Buck, U.; Huisken, F. *Chem. Rev.* **2000**, *100*, 3863.

(2) (a) Combariza, J. E.; Kestner, N. R. *J. Phys. Chem.* **1994**, *98*, 3513. (b) Combariza, J. E.; Kestner, N. R.; Jortner, J. *J. Chem. Phys.* **1994**, *100*, 2851. (c) Baik, J.; Kim, J.; Majumdar, D.; Kim, K. S. *J. Chem. Phys.* **1999**, *110*, 9116. (d) Kim, J.; Lee, H. M.; Suh, S. B.; Majumdar, D.; Kim, K. S. *J. Chem. Phys.* **2000**, *113*, 5259. (e) Xantheas, S. S.; Dunning, T. H. *J. Phys. Chem.* **1994**, *98*, 13489. (f) Lee, H. M.; Kim, D.; Kim, K. S. *J. Chem. Phys.* **2002**, *116*, 5509.

(3) (a) Cunningham, A. J.; Payzant, J. D.; Kebarle, P. *J. Am. Chem. Soc.* **1972**, *94*, 7627. (b) Lau, Y. K.; Ikuta, S.; Kebarle, P. *J. Am. Chem. Soc.* **1982**, *104*, 1462. (c) Feller, D.; Glendening, E. D.; Kendall, R. A.; Peterson, K. A. *J. Chem. Phys.* **1994**, *100*, 4981. (d) Kim, J.; Lee, S.; Cho, S. J.; Mhin, B. J.; Kim, K. S. *J. Chem. Phys.* **1995**, *102*, 839. (e) Glendening, E. D.; Feller, D. *J. Phys. Chem.* **1995**, *99*, 3060. (f) Lee, H. M.; Kim, J.; Lee, S.; Mhin, B. J.; Kim, K. S. *J. Chem. Phys.* **1999**, *111*, 3995. (g) Park, J.; Kolaski, M.; Lee, H. M.; Kim, K. S. *J. Chem. Phys.* **2004**, *121*, 3108. (j) Miller, D. J.; Lisy, J. M. *J. Am. Chem. Soc.* **2008**, *130*, 15393.

(4) (a) Coe, J. V.; Lee, G. H.; Eaton, J. G.; Arnold, S. T.; Sarkas, H. W.; Bowen, K. H. *J. Chem. Phys.* **1990**, *92*, 3980. (b) Ayotte, P.; Johnson, M. A. *J. Chem. Phys.* **1997**, *106*, 811. (c) Jordan, K. D.; Wang, F. *Annu. Rev. Phys. Chem.* **2003**, *54*, 367. (d) Lee, H. M.; Suh, S. B.; Tarakeshwar, P.; Kim, K. S. *J. Chem. Phys.* **2005**, *122*, 044309. (e) Lee, H. M.; Lee, S.; Kim, K. S. *J. Chem. Phys.* **2003**, *119*, 187. (f) Desfrancois, C.; Khelifa, N.; Lisfi, A.; Schermann, J. P.; Eaton, J. G.; Bowen, K. H. *J. Chem. Phys.* **1991**, *95*, 7760.

(5) (a) Lee, H. M.; Tarakeshwar, P.; Park, J.; Kolaski, M. R.; Yoon, Y. J.; Yi, H.-B.; Kim, W. Y.; Kim, K. S. *J. Phys. Chem. A* **2004**, *108*, 2949. (b) Jiang, J.-C.; Wang, Y.-S.; Chang, H.-C.; Lin, S. H.; Lee, Y. T.; Niedner-Schatteburg, G.; Chang, H.-C. *J. Am. Chem. Soc.* **2000**, *122*, 1398. (c) Park, M.; Shin, I.; Singh, N. J.; Kim, K. S. *J. Phys. Chem. A* **2007**, *111*, 10692.

(6) Singh, N. J.; Olleta, A. C.; Kumar, A.; Park, M.; Yi, H.-B.; Bandyopadhyay, I.; Lee, H. M.; Tarakeshwar, P.; Kim, K. S. *Theor. Chem. Acc.* **2006**, *115*, 127.

(7) (a) Brown, P. R.; Davies, P. B.; Stickland, R. J. *J. Chem. Phys.* **1989**, *91*, 3384. (b) Huet, T. R.; Pursell, C. J.; Ho, W. C.; Dinelli, B. M.; Oka, T. *J. Chem. Phys.* **1992**, *97*, 5977. (c) Dopfer, O. *J. Phys. Chem. A* **2000**, *104*, 11693. (d) Dopfer, O.; Roth, D.; Maier, J. P. *J. Phys. Chem. A* **2000**, *104*, 11702. (e) Dopfer, O.; Roth, D.; Maier, J. P. *J. Chem. Phys.* **2001**, *114*, 7081.

(8) (a) Lias, S. G.; Barmess, J. E.; Liebman, J. F.; Holmes, J. L.; Levin, R. D.; Mallard, W. G. *J. Phys. Chem. Ref. Data Suppl.* **1988**, *17*, 1. (b) Hunter, E. P. L.; Lias, S. G. *J. Phys. Chem. Ref. Data* **1998**, *27*, 413.

(9) (a) Shafer, N.; Bersohn, R. *J. Chem. Phys.* **1991**, *94*, 4817. (b) Liu, K.; Cruzan, J. D.; Saykally, R. J. *Science* **1996**, *271*, 929. (c) Bednarek, J.; Plonka, A.; Hallbrucker, A.; Mayer, E. *Radiat. Phys. Chem.* **1998**, *53*, 635. (d) Garrett, B. C.; Dixon, D. A.; Camaioni, D. M.; et al. *Chem. Rev.* **2005**, *105*, 355.

(10) (a) Shinohara, H.; Nishi, N.; Washida, N. *J. Chem. Phys.* **1986**, *84*, 5561. (b) de Visser, S. P.; de Koning, L. J.; Nibbering, N. M. M. *J. Phys. Chem.* **1995**, *99*, 15444. (c) Jongma, R. T.; Huang, Y.; Shi, S.; Wodtke, A. M. *J. Phys. Chem. A* **1998**, *102*, 8847. (d) Angel, L.; Stace, A. J. *Chem. Phys. Lett.* **2001**, *345*, 277.

(11) (a) Barnett, R. N.; Landman, U. *J. Phys. Chem.* **1995**, *99*, 17305. (b) Barnett, R. N.; Landman, U. *J. Phys. Chem. A* **1997**, *101*, 164.

(12) (a) Novakovskaya, Y. V.; Stepanov, N. F. *J. Phys. Chem. A* **1999**, *103*, 3285. (b) Gill, P. M. W.; Radom, L. *J. Am. Chem. Soc.* **1988**, *110*, 4931.

(13) (a) Muller, I. B.; Cederbaum, L. S. *J. Chem. Phys.* **2006**, *125*, 204305. (b) Tachikawa, H. *J. Phys. Chem. A* **2004**, *108*, 7853.

(14) (a) Becke, A. D. *Phys. Rev A* **1988**, *38*, 3098. (b) Lee, C.; Yang, W.; Parr, R. G. *Phys. Rev. B* **1988**, *37*, 785.

(15) Perdew, J. P.; Burke, K.; Wang, Y. *Phys. Rev. B* **1996**, *54*, 16533.

(16) Boese, A. D.; Handy, N. C. *J. Chem. Phys.* **2001**, *114*, 5497.

(17) Becke, A. D. *J. Chem. Phys.* **1993**, *98*, 5648.

(18) Perdew, J. P.; Burke, K.; Ernzerhof, M. *Phys. Rev. Lett.* **1997**, *78*, 1396.

(19) Lynch, B. J.; Fast, P. L.; Harris, M.; Truhlar, D. G. *J. Phys. Chem. A* **2000**, *104*, 4811.

(20) Note that BH&H means $0.5E_X^{HF} + 0.5E_X^{LSDA} + E_C^{LYP}$ functional.

(21) Note that BH&HLYP means $0.5E_X^{HF} + 0.5E_X^{LSDA} + 0.5\Delta E_{X\text{-}Becke88} + E_C^{LYP}$ functional.

(22) Krishnan, R.; Binkley, J. S.; Seeger, R.; Pople, J. A. *J. Chem. Phys.* **1980**, *72*, 650.

(23) Dunning, T. H., Jr. *J. Chem. Phys.* **1989**, *90*, 1007.

(24) (a) Helgaker, T.; Ruden, T. A.; Jorgensen, P.; Olsen, J.; Klopper, W. *J. Phys. Org. Chem.* **2004**, *17*, 913. (b) Min, S. K.; Lee, E. C.; Lee, H. M.; Kim, D. Y.; Kim, D.; Kim, K. S. *J. Comput. Chem.* **2008**, *29*, 1208. (c) Lee, E. C.; Kim, D.; Jurecka, P.; Tarakeshwar, P.; Hobza, P.; Kim, K. S. *J. Phys. Chem. A* **2007**, *111*, 3446.

(25) Frisch, M. J.; Trucks, G. W.; Schlegel, H. B.; Scuseria, G. E.; Robb, M. A.; Cheeseman, J. R.; Zakrzewski, V. G.; Montgomery, J. A., Jr.; Stratmann, R. E.; Burant, J. C.; Dapprich, S.; Millam, J. M.; Daniels, A. D.; Kudin, K. N.; Strain, M. C.; Farkas, O.; Tomasi, J.; Barone, V.; Cossi, M.; Cammi, R.; Mennucci, B.; Pomelli, C.; Adamo, C.; Clifford, S.; Ochterski, J.; Petersson, G. A.; Ayala, P. Y.; Cui, Q.; Morokuma, K.; Salvador, P.; Dannenberg, J. J.; Malick, D. K.; Rabuck, A. D.; Raghavachari, K.; Foresman, J. B.; Cioslowski, J.; Ortiz, J. V.; Baboul, A. G.; Stefanov, B. B.; Liu, G.; Liashenko, A.; Piskorz, P.; Komaromi, I.; Gomperts, R.; Martin, R. L.; Fox, D. J.; Keith, T.; Al-Laham, M. A.; Peng, C. Y.; Nanayakkara, A.; Challacombe, M.; Gill, P. M. W.; Johnson, B.; Chen, W.; Wong, M. W.; Andres, J. L.; Gonzalez, C.; Head-Gordon, M.; Replogle, E. S.; Pople, J. A. *Gaussian 03, Revision A.1*; Gaussian, Inc.: Pittsburgh, PA, 2003.

(26) Amos, R. D.; Bernhardsson, A.; Berning, A.; Celani, P.; Cooper, D. L.; Deegan, M. J. O.; Dobbyn, A. J.; Eckert, F.; Hampel, C.; Hetzer, G.; Knowles, P. J.; Korona, T.; Lindh, R.; Lloyd, A. W.; McNicholas, S. J.; Manby, F. R.; Meyer, W.; Mura, M. E.; Nicklass, A.; Palmieri, P.; Pitzer, R.; Rauhut, G.; Schutz, M.; Schumann, U.; Stoll, H.; Stone, A. J.; Tarroni, R.; Thorsteinsson, T.; Werner, H.-J. *MOLPRO, version 2002.6*.

(27) (a) Feyereisen, M.; Fitzgerald, G.; Komornicki, A. *Chem. Phys. Lett.* **1993**, *208*, 359. (b) Weigend, F.; Häser, M. *Theor. Chem. Acc.* **1997**, *97*, 331.

(28) Ahlrichs, R.; Bär, M.; Häser, M.; Horn, H.; Kölmel, C. *Chem. Phys. Lett.* **1989**, *162*, 165.

(29) Tomoda, S.; Achiba, Y.; Kimura, K. *Chem. Phys. Lett.* **1982**, *87*, 197.

(30) Ng, C. Y.; Trevor, D. J.; Tiedemann, P. W.; Ceyer, S. T.; Kronebusch, P. L.; Mahan, B. H.; Lee, Y. T. *J. Chem. Phys.* **1977**, *67*, 4235.

(31) Fraley, P. E.; Rao, K. N. *J. Mol. Spectrosc.* **1969**, *29*, 348.

CT800506Q

JCTC Journal of Chemical Theory and Computation

Representative Amino Acid Side Chain Interactions in Proteins. A Comparison of Highly Accurate Correlated *ab Initio* Quantum Chemical and Empirical Potential Procedures

Karel Berka,[†,‡] Roman Laskowski,[§] Kevin E. Riley,[||] Pavel Hobza,[†] and Jiří Vondrášek*[,†]

Institute of Organic Chemistry and Biochemistry, Academy of Sciences of the Czech Republic and Center for Complex Molecular Systems and Biomolecules, Flemingovo náměstí 2, Prague 6, 166 10 Czech Republic, Department of Physical and Macromolecular Chemistry, Faculty of Natural Sciences, Charles University in Prague, Hlavova 8, Prague 2, 128 43 Czech Republic, EMBL Outstation - Hinxton, European Bioinformatics Institute, Wellcome Trust Genome Campus, Hinxton, Cambridge CB10 1SD, U.K., and Department of Chemistry, P.O. Box 23346, University of Puerto Rico, Rio Piedras, Puerto Rico 00931

Received November 25, 2008

Abstract: Interactions between amino acid side chains play a crucial role both within a folded protein and between the interacting protein molecules. Here we have selected a representative set of 24 of the 400 (20 × 20) possible interacting side chain pairs based on data from Atlas of Protein Side-Chain Interactions. For each pair, we obtained its most favorable interaction geometry from the structural data and computed the interaction energy in the gas phase using several different, commonly used, *ab initio* and force field methods, namely Møller−Plesset perturbation theory (MP2), density functional theory combined with symmetry-adapted perturbation theory (DFT-SAPT), density functional theory empirically augmented with an empirical dispersion term (DFT-D), and empirical potentials using the OPLS-AA/L and Amber03 force fields. All the methods were compared against a reference method taken to be the CCSD(T) level of theory extrapolated to the complete basis set limit. We found a high degree of agreement between the different methods, even though the range of binding energies obtained was extremely large. The most computationally intensive methods yielded the best results. Among the less computationally time-consuming methods, the DFT-D method as well as parm03 force field provided consistently good results when compared to the reference values. We also tested how representative the chosen geometries of the side chains were and investigated the effect on the binding energies of the dielectric constant of the surrounding medium.

Introduction

The building blocks of proteins are the twenty naturally occurring L-amino acids, which are distinguished by their different side chain structures and chemical compositions. The sequence of amino acids defining a given protein determines both its overall 3D structure and, at the local level, the interactions it makes with other molecules when carrying out its biological function. A change to a single amino acid (e.g., due to a point mutation) can either have relatively little effect[1,2] or seriously harm the organism.[3]

The packing of a protein 3D structure into its final, fully folded form is governed by the noncovalent interactions of its side chains. The hydrophobic interactions in the protein's

* Corresponding author phone: (+420) 220-410-324; fax: (+420) 220-410-320; e-mail: jiri.vondrasek@uochb.cas.cz.

[†] Academy of Sciences of the Czech Republic and Center for Complex Molecular Systems and Biomolecules.

[‡] Charles University in Prague.

[§] European Bioinformatics Institute.

[||] University of Puerto Rico.

10.1021/ct800508v CCC: $40.75
Published on Web 02/25/2009

core[4,5] are of particular importance, as they, along with hydrogen bonds,[6] salt bridges, and disulfide bonds, determine the overall stability and architecture of the protein.

The packing of side chains in a protein is known to be very tight,[7] and two opposing models have been proposed to describe it.[8] The first, the "nuts and bolts in a jar" model, suggests that the main driving force of protein folding is the hydrophobic effect of the surrounding water molecules; consequently, the side chains are crammed together as the protein folds, and their packing is essentially random and the result of entropic factors. In the second, the "jigsaw puzzle" model, energetic (enthalpic) contributions play a more significant role in determining how the side chains come together; consequently, the packing is nonrandom. A large number of studies have analyzed the available 3D structural data in the Protein Data Bank (PDB) and have shown that side chains do indeed have preferred interaction geometries; their packing is not entirely random.[9−12]

Thus, for an accurate energetic picture of protein structure, it is necessary to describe the interactions between amino acid side chains properly. The potential energy landscapes of proteins are most often approximated as a sum of electrostatic charge−charge and Lennard-Jones contributions including exchange-repulsion and dispersion terms. Other energy contributions, such as charge transfer, do not appear to be significant in this schema. There is a reasonable degree of correlation between the molecular mechanics energy landscapes on the one hand and the distributions of amino acid pairs and their geometries observed in protein structures on the other, which suggests that the intrinsic pairwise interaction energies do contribute to packing of side chains in proteins rather than being overwhelmed by the numerous interactions with other atoms within the protein and with the solvent.[13]

The interaction energy functions can generally be divided into two types: an atomic level energy function, whose form is based unambiguously on physical principles, and an energy function based on statistics at the amino acid level, such as the Miyazawa-Jernigan potential.[14,15] The most ideal way to treat these systems is to apply high-level correlated *ab initio* quantum mechanical methods to compute the noncovalent interactions within a protein, incorporating all possible energy contributions. However, these methods are currently limited to small- or medium-sized molecular models. Significant progress has recently been made in overcoming the well-known deficiency of the density functional theory (DFT) approaches in describing dispersion interactions.[16,17] Nevertheless, it is still not possible to make calculations on entire proteins at this level in a reasonable amount of time and at a high (or even medium) level of accuracy. Therefore, a promising approach is to develop improved potential functions for modeling macromolecular interactions involves combining protein structural analysis and quantum mechanical calculations on small molecule models of amino acids.

We have previously obtained a reasonable level of accuracy for determining the interaction energies between amino acid side chains using high-level *ab initio* methods.[18,19] Such characteristics are of utmost importance for the analysis and design of protein structures and can shed light on the enthalpic background of protein stabilization and, to some extent, on the folding process. It must be mentioned here that lower-level theoretical calculations, such as the DFT methods, can incorrectly predict the energetics (and geometries) of these structures. Another fundamental question currently driving research in protein packing is how a single amino acid change in a protein sequence affects the 3D structure.[20] Determining a practical correlation between the two would help move the field of structure prediction and design forward.

Table 1. Computational Methods Used

method	description
CCSD(T)|CBS	reference method—CCSD(T) level of theory, extrapolated to the complete basis set limit (CBS)[27]
RI-MP2|aDZ	MP2 with the aug-cc-pVDZ basis set and resolution of identity approximation
RI-MP2|aTZ	MP2 with the aug-cc-pVTZ basis set and resolution of identity approximation
SCSMI-MP2|TZ	spin-component scaling MP2 perturbation theory, parametrized for molecular interactions (MI) with the cc-pVTZ basis set[32]
DFT-SAPT|aDZ	DFT-symmetry-adapted intermolecular perturbation theory with density fitting with the aug-cc-pVDZ basis set
DFT|TZVP	DFT with the TPSS functional and TZVP basis
DFT-D|TZVP	DFT with the TPSS functional and the TZVP basis set augmented with an empirical dispersion[34]
RI-DFT-D|TZVP	DFT with the TPSS functional and the TZVP basis set augmented with an empirical dispersion and resolution of identity approximation[36]
OPLS	OPLS-AA/L force field[38]
parm03	Duan et al. Amber parm03 force field[39]

Here we explore the intramolecular interaction energies for selected pairs of amino acid side chains. For each pair, we use an empirically determined representative geometry and compare the energies computed using several different *ab initio* and force field methods with the reference method. The interaction geometries are obtained from the Web version of the Atlas of Protein Side-Chain Interactions.[21] The energy calculations are performed using ten different approaches, summarized in Table 1. The estimated CCSD(T)/CBS method is taken as the reference method, whose energies are assumed to be the closest to the "true" energy values and against which all the other methods are compared.

Materials and Methods

1. Representative Set of Amino Acid Side Chain Pairs. To obtain a representative set of amino acid side chain pairs, we extracted data from a specially updated version of the Atlas of Protein Side-Chain Interactions[21] The Web atlas is based on a printed atlas published in 1992 by Singh and Thornton[22] and analyzes the interaction geometries of all 20 × 20 amino acid side chain pairs as found in experimentally determined 3D structural models of proteins. For each side chain pair, the atlas shows how one side chain is distributed with respect to the other in 3D. The preferred interaction geometries are revealed by clusters in the distributions. The atlas lists the clusters by size and selects a representative side chain pairing for each one.

Table 2. Statistical Data for Selected Pairs Taken from the Updated Version of the Side Chain Atlas[a]

A1	A2	code	$N_{clustered\ contact}$ of $N_{detected\ contacts}$	$p_{A1}p_{A2}$	p_{AA}	$p_{AA}/(p_{A1}p_{A2})$
Leu	Leu	LL	143 of 47638	0.850	3.032	3.57
Val	Leu	VL	107 of 27218	0.660	1.733	2.62
Ile	Leu	IL	82 of 26652	0.518	1.697	3.28
Val	Val	VV	192 of 19723	0.513	1.255	2.45
Ile	Ile	II	112 of 18624	0.315	1.186	3.76
Ala	Leu	AL	159 of 15282	0.771	0.973	1.26
Leu	Tyr	LY	74 of 12030	0.326	0.766	2.35
Phe	Phe	FF	42 of 11127	0.165	0.708	4.30
Leu	Thr	LT	172 of 8233	0.510	0.524	1.03
Lys[b]	Glu[b]	KE	187 of 7755	0.389	0.494	1.27
Arg[b]	Asp[b]	RD	493 of 7391	0.295	0.470	1.60
Leu	Trp	LW	45 of 6487	0.136	0.413	3.04
Leu	Gly	LG	165 of 6368	0.685	0.405	0.59
Tyr	Tyr	YY	51 of 5179	0.125	0.330	2.64
Thr	Thr	TT	238 of 4262	0.307	0.271	0.89
Tyr	Pro	YP	61 of 4149	0.165	0.264	1.60
Thr	Ser	TS	149 of 3132	0.328	0.199	0.61
Asp[b]	His	DH	75 of 2383	0.134	0.152	1.13
Gln	Asn	QN	106 of 2217	0.165	0.141	0.86
Met	Met	MM	19 of 1973	0.034	0.126	3.73
Met	Cys	MC	9 of 641	0.025	0.041	1.65

[a] The part of the total number of detected contacts between selected residue pairs which constitutes the most populated clustered motif, whose representative was used for further energetic analysis. The values of $p_{A1}p_{A2}$ are probabilities in percents that these two residues would be in protein sequences based on the detected numbers of residues within the side chain atlas data set. The value of p_{AA} is the frequency in percents of the observed contact between side chains. Their proportion is thus a measure of preferences between side chains. [b] Charged residues were treated also as neutral.

The atlas is derived using a set of nonhomologous protein chains selected from the structures in the Protein Data Bank (PDB). No two chains have a mutual sequence identity greater than 20%, and the chains are only taken from structures solved by X-ray crystallography to a resolution of 2.0 Å or better. The data in the printed version of the atlas were derived from 62 protein structures, whereas the Web version uses 533. For the current study, we have used the atlas as updated in October 2006, applying 2548 structures.[21]

Interacting side chains are considered to be those having a center-to-center distance between their closest two atoms (excluding backbone atoms) of less than the sum of their van der Waals radii, plus 1 Å to allow for coordinate error. The two amino acids must be at least 4 residues apart in the protein's sequence.

The cluster representatives for a given distribution are determined by considering each side chain in turn. The root-mean-square distance (rmsd) to all other side chains in the distribution is computed using the three atoms that define the side chain's frame of reference. Any side chain with an rmsd of less than 1.5 Å from the selected side chain is considered a "neighbor". The side chain with the largest number of neighbors is taken to be the cluster representative of the largest cluster. This side chain and all its neighbors are then removed from the distribution, and the calculation is repeated to obtain the cluster representative of the second largest cluster, etc.

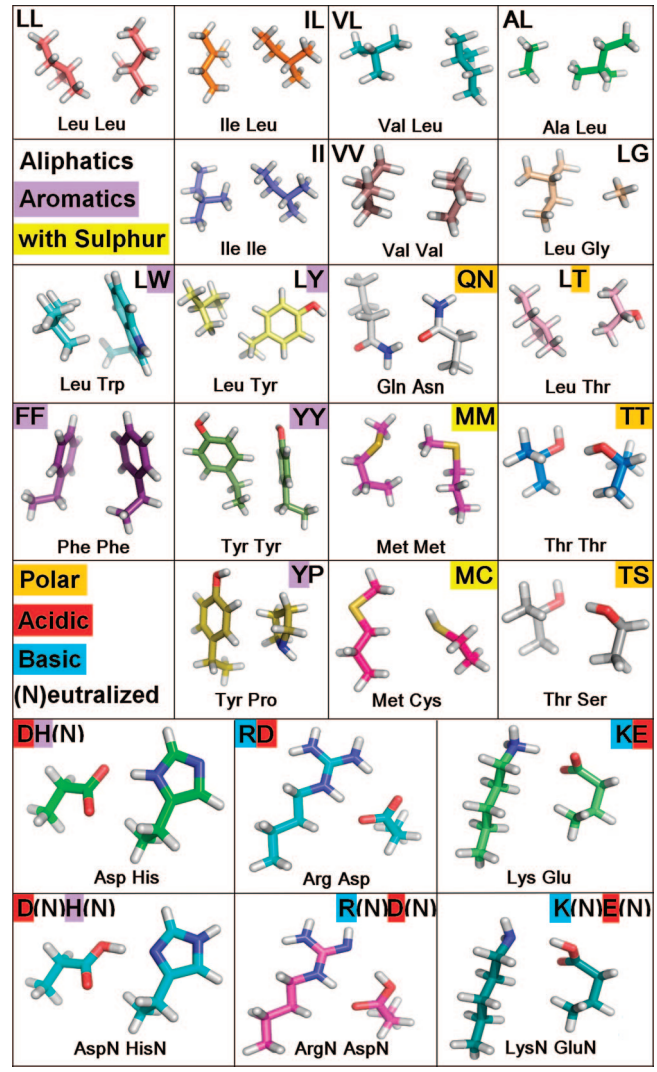

Figure 1. Set geometries of the amino acid residues truncated at the Cα atom and optimized with DFT|TPSS|TZVP, from which the geometries with Cβ fragmentation were derived by the deletion of the Cα methyl group and the insertion of a hydrogen atom in the former methyl direction.

For this study, 24 of the 400 side chain pairs were chosen to be representative of different types of side chain interactions: hydrophobic−hydrophobic, polar−polar, charged−charged, and intermingled interactions (see Table 2 and Figure 1). The side chain pair corresponding to the top cluster representative in each of these 24 distributions was understood to represent that distribution and its geometry used for the various energy calculations described below.

2. System Preparation. As the side chain atlas contains only the heavy atom positions for each cluster representative, the missing hydrogens were added using the Pymol 0.99rc6 package.[23] Two types of model subsystem were defined based on the hydrogenated amino acids: the first contained only the amino acid side chain starting from the C_β atom (C_β model), while the second consisted of the amino acid side chain plus the backbone C_α atom (C_α model). Hydrogen atoms were added at the point of cutting (i.e., either the C_α or C_β atom) in order to complete the valence shell. Proline was modeled as propane or tetrahydropyrrole in the C_β and C_α models, respectively. The positions of hydrogens were

then optimized for each pair at the DFT|TZVP[24] level using the relax procedure in the Turbomole package.[25] The coordinates of the heavy atoms were kept fixed during the entire computational procedure without initial optimization.

3. Reference Interaction Energy in Vacuo. The reference pair stabilization energies were determined in vacuo at the estimated CCSD(T) level of theory and extrapolated to the complete basis set limit (CBS). The CCSD(T)|CBS interaction energy was approximated as[26,27]

$$\Delta E_{CCSD(T)|CBS} = \Delta E_{MP2|CBS} + (\Delta E_{CCSD(T)} - \Delta E_{MP2})_{|small\ basis\ set} \quad (1)$$

The former term, $\Delta E_{MP2|CBS}$, was determined using the Helgaker[28] extrapolation scheme.

The Hartree−Fock and second-order Møller−Plesset (MP2) correlation energies necessary for the extrapolation to the complete basis set limit were determined using systematically improved basis sets; here we have used the aug-cc-pVXZ (X=D, T) basis sets in Turbomole (abbreviated as aXZ). The CCSD(T) term was calculated with a smaller basis set, 6−31G*(0.25, 0.15), in the Molpro 2006 package.[29] The use of this smaller basis set is justified because the accuracy of the quantity (called the CCSD(T) correction term) defined as the difference between the MP2 and CCSD(T) interaction energies (unlike MP2 and CCSD(T) interaction energies themselves) is much less dependent on the size of the basis set and the 6−31G*(0.25, 0.15) basis set has been shown to yield satisfactory values of this difference.[26] The CCSD(T) correction term evaluated for the uracil dimer with this basis set agreed very well[30] with values calculated with the aug-cc-pVDZ and aug-cc-pVTZ basis sets. All the interaction energies were corrected for the basis set superposition error using the counterpoise scheme of Boys and Bernardi.[31] MP2 electronic energies were computed with the resolution of the identity approach (RI-MP2), which has been shown to introduce negligible errors. The frozen core approximation was used systematically throughout the story.

4. Spin-Component Scaling Perturbation Theory SCSMI-MP2. In an attempt to compensate for the overestimation of dispersion contributions generally seen with the MP2 method, the spin-component-scaled MP2 method as parametrized for molecular interactions (SCSMI-MP2) was used.[32] In this method, the parallel and antiparallel spin-contributions of the MP2 correlation energy are empirically scaled with two scaling factors, $c_{PS} = 1.75$ and $c_{AS} = 0.17$. These parameters differ from those of the original SCS-MP2 method described by Grimme:[33]

$$E_{SCSMI\text{-}MP2} = c_{PS}E_{PS} + c_{AS}E_{AS} \quad (2)$$

The parameters were fitted against molecular interaction energies computed at the CCSD(T)|CBS level for the S22 set.[27] The SCSMI-MP2 energies were calculated using the Molpro 2006 package[29] along with the cc-pVTZ basis set (abbreviated as TZ). We prefer to use the SCSMI-MP2 over the original Grimme SCS-MP2 procedure since the former procedure describes not only the stacked interactions but also H-bonding accurately. The original SCS-MP2 procedure works well for stacking interactions, but H-bonded stabilization energies are underestimated.

5. DFT-Based Interaction Energy Augmented with an Empirical Dispersion Term. The energies were also computed using the DFT-D|TZVP method,[34] in which the DFT energies calculated with a TPSS functional in a TZVP basis set are augmented by an empirical dispersion term parametrized against the CCSD(T)|CBS energies in the S22 set.[27] The DFT energies were calculated with the Gaussian03 package.[35]

A faster DFT algorithm using the resolution of the identity approximation and empirically augmented dispersion was also utilized (RI-DFT-D).[36] The RI-DFT-D energies were calculated employing the Turbomole package.[25] This technique provides excellent interaction energies not only for the H-bonded, dispersion-bound and mixed complexes included in the S22 set[34] but also for these noncovalent complexes in general. A strong point of the method is its relatively low computational cost, making it an ideal candidate for calculations on large complexes with hundreds of atoms or even for on-the-fly molecular dynamics simulations.

6. Empirical Force-Field Interaction Energy. All the molecular mechanical force-field calculations were performed using the Gromacs 3.3 package[37] with the built-in OPLS-AA/L (OPLS)[38] and ported parm03[39] force fields. The porting of parm03 was performed according to the method of Sorin and Pande.[40] The amino acid topology and partial charges were changed as follows:

OPLS - The terminal Cα or Cβ methyl group was assigned the same atomic types and partial charges as the other methyl groups.

parm03 - All the original atoms have their original partial charges and the newly added hydrogens on C_α or C_β were assigned to provide the integral charge on the entire residue.

7. SAPT Decomposition of the Interaction Energy in Vacuo. In the DFT-SAPT method,[41] the interaction energy is given as the sum of first- and second-order energies ($E^{(1)}$, $E^{(2)}$) as well as of the δ(HF) term. The first-order energy term contains the electrostatic ($E^{(1)}_{el}$) and exchange-repulsion ($E^{(1)}_{ex}$) contributions, the second-order term includes the induction, exchange-induction, dispersion, and exchange-dispersion contributions. The charge-transfer energy is considered to be part of the induction energy. The δ(HF) energy estimates the contributions from the higher-order energy terms using the Hartree−Fock approximation. In this study, we used the PBE0AC exchange-correlation potential[42] along with the aug-cc-pVDZ basis set (and its corresponding density-fitting basis sets). The PBE0AC functional has been shown to yield accurate first-order as well as induction and dispersion values. The aug-cc-pVDZ set is large enough to provide a reliable estimate of the electrostatic, induction, and exchange components. The dispersion component is underestimated by about 10−20% in this basis set (see ref 41) but should serve well enough for the purpose of comparison. Here we have implemented a gradient-controlled shift procedure required for the asymptotic correction of the exchange-correlation potential, which needs a computed difference (shift) between the vertical ionization potential

and HOMO energy calculated using the same DFT method as used for the DFT-SAPT computation.[42] The DFT-SAPT interaction energy calculated with the aug-cc-pVDZ basis set provides highly accurate interaction energies for DNA base pairs, and if the dispersion energy is augmented by 10−15%, the resulting interaction energies agree fairly well with the CCSD(T)|CBS values.[43] The DFT-SAPT thus provides reasonably accurate stabilization energies as well as their components for various types of noncovalent complexes.

The DFT-SAPT calculation for each pair of selected residues was performed with the density fitting using the Molpro 2006 package.[29] In order to express the obtained DFT-SAPT results in terms of commonly understood physical quantities, the exchange-induction and exchange-dispersion terms were added to the induction and dispersion terms, respectively. The ionization potentials were calculated at the PBE0|TZVP level, while the HOMO values were taken from the aug-cc-pVDZ calculation with the Gaussian03 package.[35]

Results and Discussion

1. Representative Side Chain Pairs. While the most populated types of contacts between the amino acids are mainly those containing leucine, we selected a set of 24 amino acid pairs to best represent the full spectrum of interaction types that occur within proteins, making sure that our set included at least one of each of the 20 natural amino acids (see Figure 1 and Table 2). The most common types of interaction are generally those involving aliphatic-aliphatic contacts, reflecting their tendency to be localized in a protein's hydrophobic core. Thus the largest group within our set comprised aliphatic-aliphatic side chain interactions: LL, IL, VL, AL, II, VV, and LG. The next largest groups consisted of aliphatic-aromatic interactions - LW, LY, and YP - and nonpolar−polar interactions - LT, MC, and MM. An interesting set of contacts are those between aromatic side chains: YY and FF. Polar−polar contacts are represented by the interactions between threonine and serine: TS and TT. A very special type of interaction is that between aromatic and charged residues, DH(N), where the histidine is taken to be neutral, or D(N)H(N), where both residues are taken to be neutral. A typical salt-bridge conformation between charged residues is represented by RD and KE. The final group contains unphysical salt-bridge interactions, where both charged residues are neutralized: R(N)D(N) and K(N)E(N). This situation never happens in solution; however, these complexes would be stable in the gas phase and provide a test case for neutralized charged residues found in force fields.

It is interesting to note how the numbers of expected and observed contacts differ (see Table 2). The expected contact value, $p_{A1}p_{A2}$, is defined as the product of the observed frequencies of all the amino acid side chains detected in the atlas data set. The observed contact value, p_{AA}, is defined as the frequency of the given contact pair divided by the total number of all observed contacts. The observed values differ slightly from the expected values. The ratio between the observed and expected contacts varies between 4.30 for Phe-Phe to 0.59 for Leu-Gly.

2. Comparison of Binding Energies. To assess the performance of the various energy calculation methods used in this study properly for a range of binding energies spanning 2 orders of magnitude - from the most stable pair, RD, to the least stable, LG - we employed two types of statistics: relative and absolute deviation (see the legend of Table 3). The calculated CCSD(T)|CBS binding energies (see Methods) are taken to be the "true" binding energies of these side chain-side chain interactions as they are, to our knowledge, the most accurate binding energies that can be systematically obtained for all of the complexes described in this work. We should add here that the CCSD(T)/CBS method is the only *ab initio* method that provides accurate interaction energies for different types of noncovalent complexes (keeping in mind that MP2 tends to greatly overbind dispersion bound structures). All the other wave function theory (WFT) as well as DFT procedures which are used in the realm of noncovalent complexes are parametrized, i.e. contain one or more parameters, making it possible to fit the obtained values on the benchmark data. Consequently, using these methods we cannot be certain whether the interaction energies for different types of noncovalent complexes are all reliable.

The CCSD(T)|CBS interaction energies vary over a wide range of values (see column 2 of Table 3). The most stable pairs in the gas phase are the salt bridges between the charged residues RD and KE, having interaction energies of the order of 100 kcal/mol. The second most stable are the DH(N) interactions representing a charged residue interacting with an uncharged residue. Neutralizing the charged residues dramatically lowers the interaction energy, as exemplified by the next group of interactions - D(N)H(N), R(N)D(N) and K(N)E(N) - which have energies between 10 and 18 kcal/mol. Interestingly, neutralization affects charged systems differently: salt bridges R(N)D(N) and K(N)E(N) have only 12% of their former interaction energy, whereas the Asp-His pair's interaction energy decreases to only 58%. The next most stable interaction groups consist of polar contacts, QN, TT, and TS, whose interaction energies are around 5 kcal/mol, and aromatic systems, YY, LW, YP, FF, and LY, whose interaction energies cluster around 4 kcal/mol. The energies of nonpolar pairs containing methionine - MM and MC - are approximately 1.5 kcal/mol, while the final group contains the aliphatic nonpolar pairs (LL, VV, IL, II, LT, VL, VL, AL, and LG), whose binding energies seem to depend mainly on the contact surface between them, favoring more lengthy and more "treelike" structures such as those of leucine or valine.

3. Comparison of Computational Methods. Columns 3−11 of Table 3 show the interaction energies obtained from the nine other computational methods tested here. As can be seen, the methods tend to yield similar absolute values and exhibit a high degree of correlation from the highest to the lowest energy values. This correlation can be more clearly seen in Chart 1. However, there are interesting discrepancies between the methods, which will be discussed next.

For H-bonded complexes, the use of a larger basis set with the RI-MP2 method yields higher-quality stabilization energies while overestimating stabilization results for stacking

Chart 1. Correlations between the Computational Methods[a]

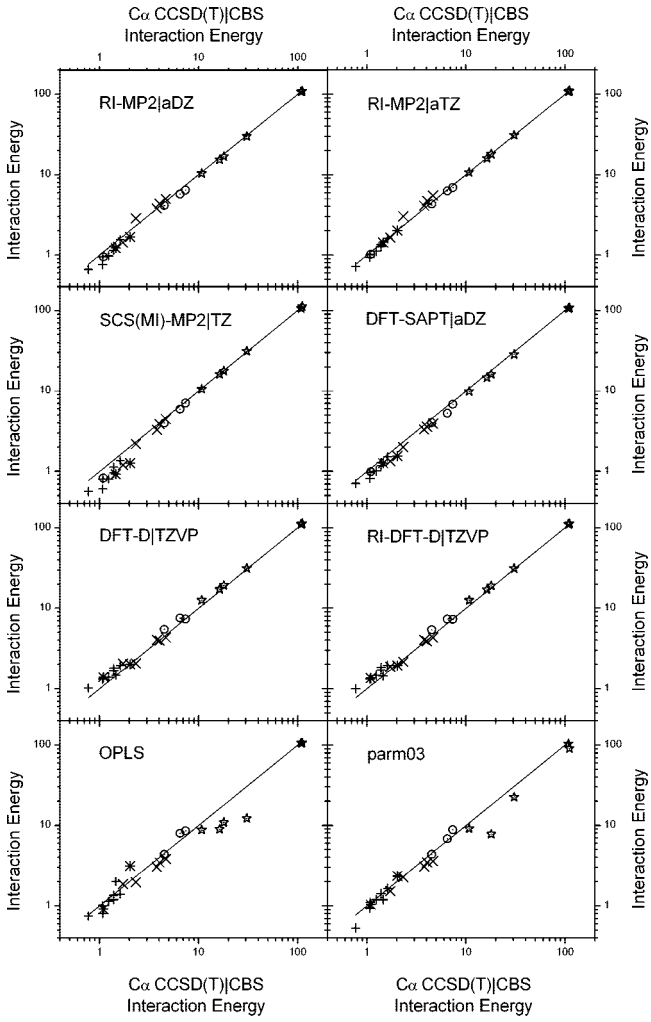

[a] The energies were divided into 5 groups: + - aliphatic-residue-only systems; × - systems with at least one aromatic residue; ✳ - systems containing sulfur; ⊙ - systems with at least one polar residue; and * - systems with at least one charged residue. The systems falling into several groups were arbitrarily added to the more polar group according to the participating amino acids.

complexes. This overestimation is more pronounced when aromatic systems participate in an interaction. Investigating different AA pairs containing at least one aromatic residue (YY, LW, YP, and FF), we found that they exhibit this systematic overbinding and have larger maximal relative errors when larger basis sets are employed. Such behavior when the MP2 method is employed is well-known, with various examples being possible to find in the S22 data set.[19]

The spin component scaled perturbation theory, SCSMI-MP2, performs well on aromatic pair systems but significantly underestimates stabilization energies for loosely bound pairs (interactions whose binding energies are below a threshold of approximately 2 kcal/mol, which is especially true for AL, MC, and MM pairs). This is probably a result of the fitting procedure for this method[32] being carried out in order to obtain minimal errors in the absolute values, and not in terms of relative numbers (i.e., percentagewise), which led to a situation in which contributions from the systems with small binding energies would be underrepresented. Thus the error of the method is relatively modest (0.60 kcal/mol), but larger relative errors occur when stabilization energies are around 1 kcal/mol.

The DFT-SAPT interaction energies are slightly lower than the MP2 ones. Evidently, the DFT-SAPT method does not suffer from an overestimation of the stabilization energies for pairs containing aromatic systems.

The DFT-D method generally overestimates the stabilization energies of these complexes. For polar or charged contacts, the binding energies can be overestimated by up to 2 kcal/mol (approximately 2% of the total interaction energy). At the other extreme, the overestimation of the interaction strength for loosely bound pairs, such as Leu-Gly, is typically around 0.3 kcal/mol.

The errors seen for results obtained using the SCSMI-MP2 are similar in magnitude but opposite in sign to those produced using the DFT-D method. It can also be said that, in terms of absolute energies, the SCSMI-MP2 produces more accurate results, while the DFT-D method yields better results when errors are measured on a relative (i.e., in terms of percentage) scale. It should also be noted here that, as is well-known, the traditional DFT method fails to describe dispersion interactions correctly. Recently introduced modern density functionals, like e.g. the Zhao and Truhlar's MO6 suite of density functionals, do cover the dispersion energy and provide a very good estimate of stabilization energies and geometries for a large spectrum of noncovalent complexes.[44]

The OPLS-AA/L force field yields results that are slightly unbalanced; several residues are not parametrized for the computation of interaction energies with accuracies similar to those of previous methods. In particular, histidine and methionine exhibit relative errors that are higher than those seen for any other method (DH, DH(N), MM, and MC).

The parm03 force field generally behaves better than the OPLS-AA/L force field. When omitting neutralized charged residues (because of parametrization), the parm03 force field has relative errors comparable to those of the MP2|aDZ method. As the largest errors can be found for the most strongly bound complexes (from RD to QN), the absolute errors of parm03 are significantly higher than those observed for any of the *ab initio* quantum mechanics methods discussed previously.

Surprisingly, both force-field methods were found to perform generally well. Their major weakness concerns the parametrization for the neutralized charged residues (D(N)H(N), R(N)D(N), and K(N)E(N)). It should be noted that the parm03 force field does not even contain a neutralized arginine residue.

To summarize the results, the most accurate method (other than the benchmark CCSD(T)/CBS method) for calculations of interaction energies between amino acid residues in proteins is MP2|aug-cc-pVTZ, which is also the most computationally intensive technique considered here. The less demanding SCSMI-MP2 and DFT-D methods yield similar accuracy with comparable computational expense. The fastest *ab initio* method is RI-DFT-D, which tends to overestimate

Chart 2. Correlation between the Different Fragmentations[a]

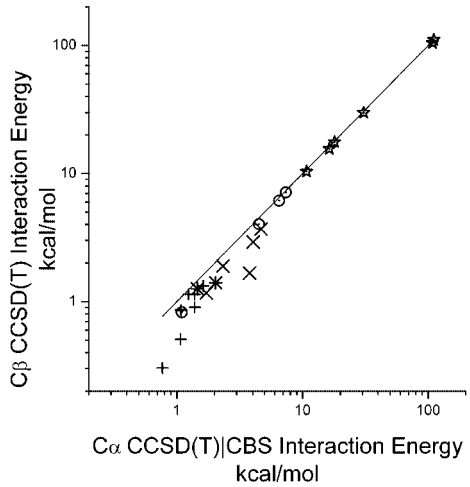

[a] The energies were divided into 5 groups: + - aliphatic-residue-only systems; × - systems with at least one aromatic residue; ✷ - systems containing sulfur; ⊙ - systems with at least one polar residue; and * - systems with at least one charged residue. The systems falling into several groups were arbitrarily added only to the more polar group.

interaction energies slightly. The best force-field method is parm03 force field, especially when strongly bound pairs are omitted.

4. Effects of Different Fragmentation (C_α vs C_β Models). The analysis of interaction energies above was based on our C_α model, i.e. where the amino acid side chains were methylated at the C_α position. Are the results markedly different if one uses the C_β model, i.e. residues starting at the C_β atom, instead?

The last column in Table 3 shows the energies obtained from the CCSD(T)|CBS calculations for the C_β model. The average difference between the interaction energies from the two models is approximately 0.3 kcal/mol. Interestingly, this energy loss caused by removing the C_α methyl group is comparable to the interaction energy for the methane dimer, which is around 0.33−0.46 kcal/mol for two methane molecules in close contact.[45] The simple explanation of this fact is that the smaller system - stabilized mainly by dispersion, the smaller interaction energy is. One additional feature of the different fragmentation has to be also taken into account (see Chart 2). In many cases the position of Ca methyl groups improves contact between interacting residues which results in higher stabilization energy than expected based on C_β geometry.

The interaction energy loss varies according to the nature of the interaction. The differences tend to be small for interactions involving charged residues. In the case of RD, for instance, the difference is 0.06 kcal/mol, which is negligible. On the other hand, when at least one aromatic residue, e.g. LW and YY, participates in the interaction the interaction energy, loss due to the demethylation is quite significant. This may be attributable to a difference in the interaction of the system, with the electronic density of the π-system caused by the fragmentation.

Last but not least, an interesting interaction is that between tyrosine and proline (YP). The interaction energy loss here is strongly affected by the opening of the proline ring due to the loss of the main-chain C_α atom. This effect has recently been reported by Biedermannova et al.[46] in interactions between aromatic side chains and proline.

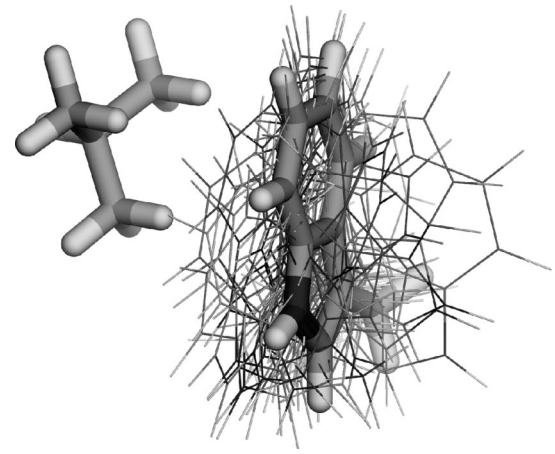

Figure 2. The cluster of LW with a cluster representative.

5. Cluster Representatives. In all the calculations above, the geometry used for each side chain pair is that of the representative of the pair's largest cluster in the Side Chain Atlas. It is natural to ask how valid and meaningful this choice of geometry is. To address this issue we used both the DFT-D and RI-DFT-D methods to compute the interaction energies for all the members of a single cluster and compared these against the energy of that cluster representative. We selected the leucine-tryptophan pair, LW, as it has an intermediate total number of observed contacts (6487) and thus should be more typical than such extreme cases as LL and MC, with 47,638 and 641 contacts, respectively. Moreover, considering that the number of geometries in the cluster is 45 (Figure 2), the number of interaction energies to be computed is sufficiently small for them to be completed in a reasonable time. Finally, to decrease the total calculation time even further, only the C_β fragments were used.

The DFT-D method gave an interaction energy of −2.76 ± 0.550 kcal/mol when averaged over all the Leu-Trp cluster members, which is identical to the energy obtained from the cluster representative using both the DFT-D and RI-DFT-D methods (see Supporting Information Table S1). The RI-DFT-D method yielded a slightly different average cluster value of −2.63 kcal/mol. In this method, however, the median value of the individual energies in the cluster was much closer to the representative's energy than the median value given by DFT-D: −2.75 vs −2.80 kcal/mol, respectively. One can therefore conclude that the geometry of the cluster representative really does approximate to some average energy conformation for the two interacting side chains.

6. Full Optimization of Geometries. To test the relevance of the cluster representative further, we performed a full optimization of their geometry using the C_β model and RI-DFT-D *in vacuo*. In most cases, the geometry changed only negligibly (see Supporting Information Table S2). The differences come mostly for the interactions involving proline, glycine, charged, and polar residues. The largest changes were observed for charged and polar residues,

Table 3. Interaction Energies for Amino Acid Pairs Calculated Using Several Approaches in the Gas Phase[a]

code	CCSD(T) CBS	RI-MP2 aDZ	RI-MP2 aTZ	SCSMI-MP2 TZ	DFT-SAPT aDZ	DFT TZVP	DFT-D TZVP	RI-DFT-D TZVP	OPLS	parm03[b]	CCSD(T) CBS Cβ
RD	−110.80	−109.37	−110.21	−111.71	−107.52	−110.60	−112.93	−112.73	−105.71	−90.37	−110.74
KE	−108.40	−107.36	−107.75	−105.64	−105.78	−108.27	−110.90	−110.86	−106.02	−103.57	−104.67
DH(N)	−30.64	−29.88	−30.91	−31.06	−28.35	−28.83	−31.47	−31.30	−12.20	−22.36	−29.82
D(N)H(N)	−17.97	−16.81	−17.94	−17.68	−16.05	−16.26	−19.29	−19.03	−10.90	−7.80	−17.61
R(N)D(N)	−16.32	−15.29	−15.92	−16.18	−14.68	−14.71	−17.17	−17.01	−8.94		−15.57
K(N)E(N)	−10.76	−10.36	−10.65	−10.50	−9.87	−9.81	−12.60	−12.51	−8.80	−9.11	−10.38
QN	−7.37	−6.41	−6.92	−7.06	−6.83	−5.66	−7.35	−7.31	−8.61	−8.84	−7.14
TT	−6.50	−5.74	−6.28	−5.93	−5.27	−4.81	−7.53	−7.32	−7.96	−6.83	−6.15
YY	−4.66	−4.99	−5.51	−4.49	−3.94	1.35	−4.35	−4.31	−3.84	−3.62	−3.70
TS	−4.50	−4.12	−4.30	−3.99	−4.05	−3.36	−5.47	−5.41	−4.38	−4.40	−4.03
LW	−4.04	−4.38	−4.74	−3.88	−3.58	1.00	−3.97	−3.91	−3.46	−3.46	−2.93
YP	−3.79	−3.78	−4.11	−3.32	−3.34	0.44	−4.06	−4.09	−3.05	−3.09	−1.67
FF	−2.33	−2.85	−3.04	−2.19	−2.01	1.11	−2.07	−2.15	−1.97	−2.26	−1.89
MM	−2.03	−1.67	−2.01	−1.27	−1.56	1.22	−2.01	−1.94	−3.14	−2.35	−1.40
LY	−1.72	−1.43	−1.66	−1.21	−1.34	0.96	−2.07	−1.88	−1.86	−1.52	−1.17
LL	−1.62	−1.54	−1.60	−1.36	−1.52	0.00	−1.93	−1.96	−1.40	−1.66	−1.33
MC	−1.46	−1.22	−1.43	−0.93	−1.27	0.25	−1.48	−1.44	−2.01	−1.20	−1.26
VV	−1.39	−1.14	−1.28	−0.96	−1.18	0.44	−1.79	−1.83	−1.36	−1.43	−0.90
IL	−1.39	−1.28	−1.35	−1.12	−1.29	0.06	−1.68	−1.70	−1.19	−1.41	−1.14
II	−1.24	−0.98	−1.11	−0.80	−1.01	0.62	−1.39	−1.47	−1.13	−1.20	−1.14
LT	−1.09	−0.95	−1.02	−0.83	−0.99	0.02	−1.40	−1.36	−0.91	−1.05	−0.83
VL	−1.08	−0.94	−1.01	−0.81	−0.97	0.11	−1.34	−1.33	−0.81	−1.11	−0.86
AL	−1.07	−0.76	−0.93	−0.60	−0.82	0.71	−1.31	−1.32	−1.00	−0.94	−0.51
LG	−0.77	−0.66	−0.71	−0.56	−0.71	−0.09	−1.02	−1.00	−0.75	−0.53	−0.30
	MRE [%]	*10.96*	*6.52*	*16.05*	*12.01*	*83.61*	*13.04*	*12.64*	*19.54*	*13.55*	*19.68*
	MRX [%]	*28.82*	*−30.62*	*43.57*	*23.69*	*166.28*	*−32.92*	*−31.88*	*60.19*	*56.58*	*60.52*
	MAE	*0.47*	*0.26*	*0.48*	*0.79*	*2.03*	*0.63*	*0.58*	*2.11*	*2.22*	*0.66*
	MAX	*1.43*	*−0.85*	*2.76*	*3.28*	*6.01*	*−2.50*	*−2.45*	*18.44*	*20.43*	*3.73*
	RMS	0.48	0.36	0.60	0.88	1.40	0.73	0.68	4.16	4.78	0.77

[a] All the energies are in kcal/mol. Descriptive statistics: MRE is the unsigned mean relative error, MRX is the signed maximal relative error, MAE is the unsigned mean absolute error, MAX is the signed maximal absolute error, and RMS is the signed root mean square error. [b] Neutral arginine is not defined in the Amber03 force field.

suggesting that the contacts between these residues are shielded by the environment around the charged/polar pair. In the case of Gly and Pro, the interactions tend to involve their main-chain rather than side-chain atoms. The geometries of the nonpolar residue pairs were essentially unchanged upon the optimization, indicating that the stabilization of these pairs is mostly of enthalpic origin.

7. SAPT Decomposition of the Interaction Energies. From the SAPT results shown in Table 4, one can immediately draw a conclusion as to the dominant sources of pair stabilization. From the data, two different groups of side chain interactions may be distinguished: (1) polar and charged residues, which are stabilized mostly by the electrostatic term, and (2) nonpolar residues, which are mostly stabilized by the dispersion term.

However, several specific examples are worth noting: (1) the charged and polar residues in contact are mostly stabilized by the electrostatic term; (2) on the other hand, polar residues in contact with nonpolar residues (LT, MC) are stabilized mostly by the dispersion term. The ratio between the dispersion and electrostatic contributions ranges from 0.05 for charged salt bridges to 9.43 in the case of the Leu-Leu pair. This ratio corresponds to the nonpolarity of the interaction. As expected, the lowest value comes from the salt bridges, while polar contacts have a ratio close to unity and contacts between aromatic residues are lower than those for purely nonpolar aliphatic to aliphatic contacts.

8. Effect of the Solvent. There are many methods for treating amino acid pair interactions within a protein's interior. The most common technique of mimicking the hydrophobic environment in the protein's core is to use implicit solvation models: generalized Born models (GB),[47,48] nonlinear or linear Poisson−Boltzmann models (PB),[49] or a polarizable continuum model (PCM).[50] The most important parameter is usually the dielectric constant of a particular solvent (generally water), which represents the influence of the environment. To model the influence of a protein interior properly is a more complicated task. Several models have been proposed - low dielectric constant ($\varepsilon \sim 2-4$)[51] and high dielectric constant ($\varepsilon \sim 20-40$)[52] as well as more complex models with variable dielectric constants in the interior and at the outer regions of a protein.[53−55]

In this study, we modeled the influence of the protein core environment as solvation by diethyl ether ($\varepsilon = 4.34$), whereas the influence of water was modeled by a dielectric constant $\varepsilon = 80.0$.

We calculated the interaction energies for these two values of dielectric constant using the PCM method (see Table 5 for the results). It appears that the largest influence of the environment is to cause a steep drop of the binding energy for interactions involving charged residues and all the interactions in which the electrostatic contribution is the major term of the interaction. The values obtained for protein environment computations decrease to almost 30% of the gas-phase interaction energy values, whereas, within the water environment, the binding energies are diminished to 2−5% of their gas-phase values. The charged residues are only rarely buried in a protein interior and almost exclusively

Table 4. SAPT Decomposition for Cα in Comparison with the CCSD(T)|CBS Interaction Energies[a]

AA-AA	CCSD(T)	DFT-SAPT	E^1_{pol}	E^1_{exch}	E^2_{ind}	E^2_{disp}	δHF	E^2_{disp}/E^1_{pol}
RD	−110.80	−107.52	**−101.94**	22.28	−14.39	−7.21	−6.25	0.07
KE	−108.40	−105.78	**−96.03**	7.93	−9.99	−4.52	−3.16	0.05
DH(N)	−30.64	−28.35	**−35.96**	35.80	−12.10	−9.24	−6.85	0.26
D(N)H(N)	−17.97	−16.05	**−26.38**	33.71	−8.09	−8.89	−6.40	0.34
R(N)D(N)	−16.32	−14.68	**−19.51**	17.83	−4.04	−6.39	−2.57	0.33
K(N)E(N)	−10.76	−9.87	**−9.52**	6.79	−1.84	−4.20	−1.09	0.44
QN	−7.37	−6.83	**−10.02**	11.23	−2.21	−4.17	−1.66	0.42
TT	−6.50	−5.27	**−9.85**	12.67	−1.76	−4.96	−1.37	0.50
YY	−4.66	−3.94	−3.86	8.93	−0.34	**−7.88**	−0.79	2.04
TS	−4.50	−4.05	**−3.52**	2.92	−0.50	−2.71	−0.25	0.77
LW	−4.04	−3.58	−2.42	6.20	−0.25	**−6.56**	−0.55	2.71
YP	−3.79	−3.34	−2.25	5.24	−0.28	**−5.61**	−0.44	2.49
FF	−2.33	−2.01	−0.65	3.12	−0.13	**−4.08**	−0.26	6.28
MM	−2.03	−1.56	−1.96	5.28	−0.11	**−4.38**	−0.38	2.23
LY	−1.72	−1.34	−1.12	3.80	−0.09	**−3.70**	−0.22	3.30
LL	−1.62	−1.52	−0.21	0.71	−0.01	**−1.98**	−0.03	9.43
MC	−1.46	−1.27	−0.98	2.65	−0.12	**−2.62**	−0.19	2.67
VV	−1.39	−1.18	−0.47	2.01	−0.05	**−2.53**	−0.12	5.38
IL	−1.39	−1.29	−0.25	0.85	−0.01	**−1.83**	−0.04	7.32
II	−1.24	−1.01	−0.56	1.89	−0.02	**−2.23**	−0.09	3.98
LT	−1.09	−0.99	−0.29	0.88	−0.02	**−1.52**	−0.04	5.24
VL	−1.08	−0.97	−0.26	0.89	−0.01	**−1.55**	−0.04	5.96
AL	−1.07	−0.82	−0.66	2.18	−0.02	**−2.21**	−0.10	3.35
LG	−0.77	−0.71	−0.12	0.44	−0.01	**−0.99**	−0.02	8.25

[a] E^1_{pol} is the first-order electrostatics, $E^1_{exch}$is the first-order repulsion, E^2_{ind} is the second-order induction, E^2_{disp} is the second-order dispersion, δ_{HF} is the estimate of higher-order terms and E^2_{disp}/E^1_{pol} is the ratio between the dispersion and electrostatic terms. The most stabilizing terms are boldface.

Table 5. Solvent Effects on the Interaction Energies Calculated by the DFT-D/TPSS|TZVP with PCM in kcal/mol[a]

AA-AA	vacuum	ether		water	
RD	−112.93	−30.70	(27.2%)	−3.23	(2.9%)
KE	−110.90	−33.24	(30.0%)	−7.91	(7.1%)
DH(N)	−31.47	−10.88	(34.6%)	−2.31	(7.3%)
D(N)H(N)	−19.29	−13.86	(71.9%)	−10.45	(54.2%)
R(N)D(N)	−17.17	−7.36	(42.9%)	−2.34	(13.6%)
K(N)E(N)	−12.60	−8.38	(66.5%)	−5.89	(46.7%)
QN	−7.35	−4.45	(60.5%)	−2.55	(34.7%)
TT	−7.53	−5.56	(73.8%)	−4.10	(54.4%)
YY	−4.35	−3.77	(86.7%)	−3.28	(75.4%)
TS	−5.47	−3.18	(58.1%)	−1.59	(29.1%)
LW	−3.97	−3.46	(87.2%)	−3.02	(76.1%)
YP	−4.06	−2.84	(70.0%)	−2.27	(55.9%)
FF	−2.07	−1.55	(74.9%)	−1.26	(60.9%)
MM	−2.01	−1.73	(86.1%)	−1.55	(77.1%)
LY	−2.07	−1.84	(88.9%)	−1.72	(83.1%)
LL	−1.93	−1.87	(96.9%)	−1.85	(95.9%)
MC	−1.48	−1.04	(70.3%)	−0.83	(56.1%)
VV	−1.79	−1.73	(96.6%)	−1.70	(95.0%)
IL	−1.68	−1.64	(97.6%)	−1.62	(96.4%)
II	−1.39	−1.34	(96.4%)	−1.32	(95.0%)
LT	−1.40	−1.32	(94.3%)	−1.28	(91.4%)
VL	−1.34	−1.30	(97.0%)	−1.28	(95.5%)
AL	−1.31	−1.28	(97.7%)	−1.27	(96.9%)
LG	−1.02	−0.98	(96.1%)	−0.96	(94.1%)

[a] The percents in parentheses are relative to the vacuum value.

play a role there as a part of an active site. Their role as a stabilization element in a protein interior is highly improbable.

In terms of the modulation of binding energy strengths with the introduction of solvents, the nonpolar (aliphatic and aromatic) residues behave quite differently than the polar ones. The introduction of neither water nor ether (i.e., protein environment) strongly affects the binding energies for complexes containing these types of amino acid side chains (which is especially true for aliphatic-aliphatic interactions). Generally, solvent effects lower the binding energy of a complex containing nonpolar residues by at most ∼25%. This finding has critical implications in terms of the role of nonpolar interactions in stabilizing a protein.

Conclusion

Here we have calculated the reference binding energies for 24 different pairs of amino acid side chain interactions at the benchmark level of theory (CCSD(T)|CBS). The geometries of the studied structures were derived from X-ray crystal structure data to a resolution of 2.0 Å or better. We expect the resulting interaction energies to be very close to the (still unknown) true interaction energies and to be equally reliable for different types of side chain interactions. One key point concerning the data obtained for these complexes is that each of the interactions was evaluated as attractive. This would not be the case for pairs of similarly charged side chains, and there are no such examples in our set. However, the fact that all the interactions studied here are attractive supports the idea that enthalpic stabilization plays a key role in protein stabilization and that the interactions are nonrandomly distributed within the protein structure. This finding is supported by the geometry optimization of the most populated pairwise interactions, which does not result in any significant changes to the conformations of the interacting side chains taken from the atlas. Allow us to emphasize again that such an essential statement can be made only when using the highly accurate CCSD(T)/CBS procedure. We are certainly aware that all these conclusions concern the stabilization energy and for comparison with experiment it is inevitable to pass to stabilization enthalpy; i.e. to include the zero point vibration energy (ZPVE) term. We determined this term for the weakest pair: the leucine-glycine. Adding the ZPVE (MP2/TZVP] to ΔE we obtained ΔH=−0.3 kcal/

mol. Evidently, the above-mentioned fact that all interaction pairs are attractive remains unchanged even when the ZPVE is taken into account.

In terms of gas-phase binding energies, the strongest interactions were found to be those between two oppositely charged side chains. In general, the strength of a gas-phase interaction is positively correlated with the polarity of the side chains involved in the interaction. Interactions between aromatic side chains are generally stronger than those between aliphatic ones, which has been observed in many previous studies and is chiefly attributable to π-π and CH-π interactions. Amazingly, the range of binding energies observed in this study is extremely large, spanning from -0.77 kcal/mol (LG) to -110.80 kcal/mol (RD). Although polar interactions tend to be the strongest in the gas phase, it is important to keep in mind that these are the types of interactions that are most strongly affected by the introduction of a solvents such as water and ether (which mimics the environment within a protein interior). The introduction of solvent thus dramatically reduces the overall range of binding energies, with interaction energies ranging from -0.83 kcal/mol (MC) to -10.45 kcal/mol (D(N)N(N)) in aqueous solution (as computed using DFT-D).

There are many computational methods that can be used to study protein structure; in this work, we have assessed the performance of several commonly used *ab initio* and force-field techniques in terms of their abilities to produce the accurate binding energies for side chain-side chain complexes (using the estimated CCSD(T)|CBS results as a reference). Not surprisingly, it was found that the computationally intensive MP2|aTZ method yields the most accurate binding energies. The less computationally demanding SCSMI-MP2|TZ and DFT-D|TZVP methods were shown to prove reasonably accurate binding energy results for these complexes, with both techniques yielding better values for strongly bound complexes than for weakly bound ones. The fastest electronic structure method with reasonable accuracy was RI-DFT-D|TZVP. In terms of the force-field methods, the widely used parm03 force field was found to yield the best-balanced interaction energy results.

Acknowledgment. This work was supported by Grant Nos. 203/05/0009, 203/06/1727, and 203/05/H001 from the Czech Science Foundation, Grant No. A400550510 from the Grant Agency of the Academy of Sciences of the Czech Republic, and Grant No. LC512 from the Ministry of Education, Youth and Sports (MSMT) of the Czech Republic. It was also a part of the research projects nos. Z40550506 and MSM6198959216. The authors acknowledge the support from the Praemium Academiae award of the Academy of Sciences of the Czech Republic, awarded to P.H. in 2007. K.R. gratefully acknowledges the support of the NSF EPSCOR program (EPS-0701525).

Supporting Information Available: Interaction energy for the whole cluster of the Leu-Trp pair calculated for Cβ fragmentation (Table S1) and rmsd between the structures before and after full geometry optimization of the pairs (Table S2). This material is available free of charge via the Internet at http://pubs.acs.org.

References

(1) Taverna, D. M.; Goldstein, R. A. *J. Mol. Biol.* **2002**, *315* (3), 479.

(2) Taverna, D. M.; Goldstein, R. A. *Proteins: Struct., Funct., Genet.* **2002**, *46* (1), 105.

(3) McKusick, V. A. *Mendelian Inheritance in Man; A Catalog of Human Genes and Genetic Disorders*; The Johns Hopkins University Press: Baltimore, MD, U.S.A., 1998.

(4) Dill, K. A. *Biochemistry* **1990**, *29* (31), 7133.

(5) Richards, F. M.; Lim, W. A. *Q. Rev. Biophys.* **1993**, *26* (4), 423.

(6) Mcdonald, I. K.; Thornton, J. M. *J. Mol. Biol.* **1994**, *238* (5), 777.

(7) Richards, F. M. *J. Mol. Biol.* **1974**, (82), 1.

(8) Bromberg, S.; Dill, K. A. *Protein Sci.* **1994**, *3* (7), 997.

(9) Banerjee, R.; Sen, M.; Bhattacharya, D.; Saha, P. *J. Mol. Biol.* **2003**, *333* (1), 211.

(10) Chakrabarti, P.; Bhattacharyya, R. *Prog. Biophys. Mol. Biol.* **2007**, *95* (1−3), 83.

(11) Misura, K. M. S.; Morozov, A. V.; Baker, D. *J. Mol. Biol.* **2004**, *342* (2), 651.

(12) Mitchell, J. B. O.; Laskowski, R. A.; Thornton, J. M. *Proteins: Struct., Funct., Bioinf.* **1998**, *29* (3), 370.

(13) Morozov, A. V.; Misura, K. M. S.; Tsemekhman, K.; Baker, D. *J. Phys. Chem. B* **2004**, *108* (24), 8489.

(14) Jernigan, R. L.; Bahar, I. *Curr. Opin. Struct. Biol.* **1996**, *6* (2), 195.

(15) Miyazawa, S.; Jernigan, R. L. *J. Mol. Biol.* **1996**, *256* (3), 623.

(16) Andersson, Y.; Hult, E.; Apell, P.; Langreth, D. C.; Lundqvist, B. I. *Solid State Commun.* **1998**, *106* (5), 235.

(17) Rapcewicz, K.; Ashcroft, N. W. *Phys. Rev. B* **1991**, *44* (8), 4032.

(18) Vondrasek, J.; Bendova, L.; Klusak, V.; Hobza, P. *J. Am. Chem. Soc.* **2005**, *127* (8), 2615.

(19) Jurecka, P.; Sponer, J.; Cerny, J.; Hobza, P. *Phys. Chem. Chem. Phys.* **2006**, *8* (17), 1985.

(20) Holmes, J. B.; Tsai, J. *J. Mol. Biol.* **2005**, *354* (3), 706.

(21) Laskowski, R. A. M. S.; Thornton, J. M. Atlas of Side-chain Interactions. http://www.ebi.ac.uk/thornton-srv/databases/sidechains. (accessed Oct 31, 2008).

(22) Singh, J.; Thornton, J. M. *Atlas of Protein Side-Chain Interactions*; 1992.

(23) DeLano, W. L. *The PyMOL Molecular Graphics System, 0.99rc6*; DeLano Scientific: Palo Alto, CA, U.S.A., 2002.

(24) Riley, K. E.; Op't Holt, B. T.; Merz, K. M., Jr. *J. Chem. Theory Comput.* **2007**, *3* (2), 407.

(25) Ahlrichs, R.; Bar, M.; Haser, M.; Horn, H.; Kolmel, C. *Chem. Phys. Lett.* **1989**, *162* (3), 165.

(26) Jurecka, P.; Hobza, P. *Chem. Phys. Lett.* **2002**, *365* (1−2), 89.

(27) Jurecka, P.; Sponer, J.; Cerny, J.; Hobza, P. *Phys. Chem. Chem. Phys.* **2006**, *8* (17), 1985.

(28) Halkier, A.; Helgaker, T.; Jorgensen, P.; Klopper, W.; Koch, H.; Olsen, J.; Wilson, A. K. *Chem. Phys. Lett.* **1998**, *286* (3−4), 243.

(29) Werner, H.-J.; Knowles, P. J.; Lindh, R.; Manby, F. R.; Schütz, M.; Celani, P.; Korona, T.; Rauhut, G.; Amos, R. D.; Bernhardsson, A.; Berning, A.; Cooper, D. L.; Deegan, M. J. O.; Dobbyn, A. J.; Eckert, F.; Hampel, C.; Hetzer, G.; Lloyd, A. W.; McNicholas, S. J.; Meyer, W.; Mura, M. E.; Nicklass, A.; Palmieri, P.; Pitzer, R.; Schumann, U.; Stoll, H.; Stone, A. J.; Tarroni, R.; Thorsteinsson, T. *MOLPRO, version 2006.1, a package of ab initio programs*; 2007. See http://www.molpro.net.

(30) Valdes, H.; Klusak, V.; Pitonak, M.; Exner, O.; Stary, I.; Hobza, P.; Rulisek, L. *J. Comput. Chem.* **2007**, 861.

(31) Boys, S. F.; Bernardi, F. *Mol. Phys.* **1970**, *19* (4), 553.

(32) Distasio, R. A.; Head-Gordon, M. *Mol. Phys.* **2007**, *105* (8), 1073.

(33) Grimme, S. *J. Chem. Phys.* **2003**, *118* (20), 9095.

(34) Jurecka, P.; Cerny, J.; Hobza, P.; Salahub, D. R. *J. Comput. Chem.* **2007**, *28* (2), 555.

(35) Frisch, M. J. T. G. W.; Schlegel, H. B.; Scuseria, G. E.; Robb, M. A.; Cheeseman, J. R.; Montgomery, J. A., Jr.; Vreven, T.; Kudin, K. N.; Burant, J. C.; Millam, J. M.; Iyengar, S. S.; Tomasi, J.; Barone, V.; Mennucci, B.; Cossi, M.; Scalmani, G.; Rega, N.; Petersson, G. A.; Nakatsuji, H.; Hada, M.; Ehara, M.; Toyota, K.; Fukuda, R.; Hasegawa, J.; Ishida, M.; Nakajima, T.; Honda, Y.; Kitao, O.; Nakai, H.; Klene, M.; Li, X.; Knox, J. E.; Hratchian, H. P.; Cross, J. B.; Bakken, V.; Adamo, C.; Jaramillo, J.; Gomperts, R.; Stratmann, R. E.; Yazyev, O.; Austin, A. J.; Cammi, R.; Pomelli, C.; Ochterski, J. W.; Ayala, P. Y.; Morokuma, K.; Voth, G. A.; Salvador, P.; Dannenberg, J. J.; Zakrzewski, V. G.; Dapprich, S.; Daniels, A. D.; Strain, M. C.; Farkas, O.; Malick, D. K.; Rabuck, A. D.; Raghavachari, K.; Foresman, J. B.; Ortiz, J. V.; Cui, Q.; Baboul, A. G.; Clifford, S.; Cioslowski, J.; Stefanov, B. B.; Liu, G.; Liashenko, A.; Piskorz, P.; Komaromi, I.; Martin, R. L.; Fox, D. J.; Keith, T.; Al-Laham, M. A.; Peng, C. Y.; Nanayakkara, A.; Challacombe, M.; Gill, P. M. W.; Johnson, B.; Chen; W.; Wong, M. W.; Gonzalez, C.; Pople, J. A. *Gaussian 03, Revision C.02*; Gaussian, Inc.: Wallingford, CT, 2004.

(36) Cerny, J.; Jurecka, P.; Hobza, P.; Valdes, H. *J. Phys. Chem. A* **2007**, *111* (6), 1146.

(37) Van Der Spoel, D.; Lindahl, E.; Hess, B.; Groenhof, G.; Mark, A. E.; Berendsen, H. J. *J. Comput. Chem.* **2005**, *26* (16), 1701.

(38) Kaminski, G. A.; Friesner, R. A.; Tirado-Rives, J.; Jorgensen, W. L. *J. Phys. Chem. B* **2001**, *105* (28), 6474–6487.

(39) Duan, Y.; Wu, C.; Chowdhury, S.; Lee, M. C.; Xiong, G. M.; Zhang, W.; Yang, R.; Cieplak, P.; Luo, R.; Lee, T.; Caldwell, J.; Wang, J. M.; Kollman, P. *J. Comput. Chem.* **2003**, *24* (16), 1999.

(40) Sorin, E. J.; Pande, V. S. *Biophys. J.* **2005**, *88* (4), 2472.

(41) Hesselmann, A.; Jansen, G.; Schutz, M. *J. Chem. Phys.* **2005**, *122* (1), 14103.

(42) Hesselmann, A.; Jansen, G. *Chem. Phys. Lett.* **2002**, *362* (3−4), 319.

(43) Hesselmann, A.; Jansen, G.; Schutz, M. *J. Am. Chem. Soc.* **2006**, *128* (36), 11730.

(44) Zhao, Y.; Truhlar, D. G. *Theor. Chem. Acc.* **2008**, *120* (1−3), 215.

(45) Tsuzuki, S.; Uchimaru, T.; Tanabe, K. *Chem. Phys. Lett.* **1998**, *287* (1−2), 202.

(46) Bendova-Biedermannova, L.; Hobza, P.; Vondrasek, J. *Proteins: Struct., Funct., Bioinf.* **2008**, *72* (1), 402.

(47) Onufriev, A.; Bashford, D.; Case, D. A. *J. Phys. Chem. B* **2000**, *104* (15), 3712.

(48) Tsui, V.; Case, D. A. *Biopolymers (Nucleic Acid Sci.)* **2001**, *56*, 257.

(49) Wagoner, J.; Baker, N. A. *J. Comput. Chem.* **2004**, *25* (13), 1623.

(50) Riley, K. E.; Vondrašek, J.; Hobza, P. *Phys. Chem. Chem. Phys.* **2007**, *9* (41), 5555.

(51) Gilson, M. K.; Honig, B. H. *Biopolymers* **1911**, *1986*, 2097.

(52) Antosiewicz, J.; McCammon, J. A.; Gilson, M. K. *J. Mol. Biol.* **1994**, *238* (3), 415.

(53) Archontis, G.; Simonson, T. *J. Phys. Chem. B* **2005**, *109* (47), 22667.

(54) Schutz, C. N.; Warshel, A. *Proteins: Struct., Funct., Genet.* **2001**, *44* (4), 400.

(55) Fitch, C. A.; Karp, D. A.; Lee, K. K.; Stites, W. E.; Lattman, E. E.; Garcia-Moreno, E. B. *Biophys. J.* **2002**, *82* (6), 3289.

CT800508V

JCTC Journal of Chemical Theory and Computation

"Mindless" DFT Benchmarking

Martin Korth and Stefan Grimme*

Organisch-Chemisches Institut, Universität Münster, Corrensstrasse 40, D-48149 Münster, Germany

Received November 26, 2008

Abstract: A diversity-oriented approach for the generation of thermochemical benchmark sets is presented. Test sets consisting of randomly generated "artificial molecules" (AMs) are proposed that rely on systematic constraints rather than uncontrolled chemical biases. In this way, the narrow structural space of chemical intuition is opened up and electronically difficult cases can be produced in an unforeseeable manner. For the calculation of chemically meaningful relative energies, AMs are systematically decomposed into small molecules (hydrides and diatomics). Two different example test sets containing eight-atom, single-reference, main group AMs with chemically very diverse and unusual structures are generated. Highly accurate all-electron, estimated CCSD(T)/complete basis set reference energies are also provided. They are used to benchmark the density functionals S-VWN, BP86, B-LYP, B97-D, PBE, TPSS, PBEh, BH-LYP, B3-PW91, B3-LYP, B2-PLYP, B2GP-PLYP, BMK, MPW1B95, M05, M05-2X, PW6B95, M06, M06-L, and M06-2X. In selected cases, an empirical dispersion correction (DFT-D) has been applied. Due to the composition of the sets, it is expected that a good performance indicates "robustness" in many different chemical applications. The results of a statistical analysis of the errors for the entire set with 165 entries (average reaction energy of 117 kcal/mol, dubbed as the MB08-165 set) perfectly fit to the "Jacob's ladder" metaphor for the ordering of density functionals according to their theoretical complexity. The mean absolute deviation (MAD) decreases very strongly from LDA (20 kcal/mol) to GGAs (MAD of about 10 kcal/mol) but then was less pronounced to hybrid-GGAs (MAD of about 6−8 kcal/mol). The best performance (MAD of 4.1−4.2 kcal/mol) is found for the (fifth-rung) double-hybrid functionals B2-PLYP-D and B2GP-PLYP-D, followed by the M06-2X meta-hybrid (MAD of 4.8 kcal/mol). The significance of the proposed approach for thermodynamic benchmarking is discussed and related to the observed performance ranking also regarding wave function based methods.

1. Introduction

Especially with the rise of the density functional theory (DFT) based zoo of electronic structure methods in the past decade, benchmarking has become an intrinsically important task in quantum chemistry.[1−7] With state-of-the-art functionals that approach the accuracy of high-level wave function theory techniques at least for a variety of "standard" applications,[8,9] it is now becoming more and more obvious that the evaluation of new or improved methods via benchmarking suffers from two major problems. First, high-quality experimental reference data are not always at hand, and it is often impossible to produce the corresponding theoretical data as an alternative in reasonable time spans. The second—but sometimes overlooked—problem is the composition of the test sets that is often strongly biased by factors like availability, chemical intuition, and the professional interest in "good" results, all leading to a pronounced narrowness of the chemical space under consideration.

An example of the influence of such a bias is the bad performance of the PBE[10] density functional for common benchmark sets, which stands in opposition to its good

* Corresponding author phone: +49-251-83-33241; fax: +49-251-83-36515; e-mail: grimmes@uni-muenster.de.

10.1021/ct800511q CCC: $40.75
Published on Web 03/04/2009

performance for a variety of real-life problems[5] and to its popularity in solid-state physics. The reason for the discrepancy in this case is also due to the fact that the common tests rely heavily on atomization energies. This produces a strong bias toward an accurate description of the free atoms relative to molecules,[11,12] which is not representative for many chemical applications.

A closer examination of the composition of existing benchmark sets reveals another problem. For example in the so-called Gn thermochemistry sets,[2] the individual compounds are explicitly selected according to the high accuracy of the experimental reference data. This leads to an accumulation of very stable, easily accessible compounds and thus to a lot of entries without much diverse information regarding their electronic structure (e.g., a large number of alkane derivatives with very similar electronic properties). In recent years, the composition of these sets was questioned and new benchmarks with model systems and theoretical reference values came up.[3,5,9] Because their composition is also guided by chemical intuition, these sets are nevertheless limited to the known chemical space, which has been proven to be very narrow in comparison with the chemical universe of possible compounds.[13]

An obvious way to open up the chemical space of test sets is to make use of random procedures in their generation. On the other hand, a completely randomized ansatz is not only impractical but also counterproductive: many biases correspond to some partial knowledge about the system of interest and the neglect of this knowledge results in a greatly diminished efficiency for the construction of test sets. Therefore, the only possible way of dealing with biases in benchmarking is the preferably complete transformation of *unperceived biases into known constraints*. In this spirit, one can make use of random elements constrained by systematic and controllable specifications to avoid unsystematic and uncontrolled criteria for the construction of benchmark sets.

On the basis of this insight, we here make a first suggestion of how to address the "selection" problem in practice and propose a diversity-oriented benchmarking procedure that is inspired by the "mindless chemistry" approach of Bera et al. for the problem of isomer-minima search.[14] Our ansatz is to randomly generate molecular systems for the calculation of relative energies, which are then used for thermochemical benchmarking purposes. Our goal is to produce theoretically demanding test cases in an unforeseeable manner through an opening of the chemical space beyond chemical intuition. This work is also rooted in the strong belief that only robust electronic structure methods will be useful in practice. The term "robust" here means that reliable results are provided even in electronically complicated situations ("extrapolative power"). It can be expected that only robust quantum chemical methods will provide good results also in an opened chemical space. The interest in molecular systems and relative energies reflects the "chemical" orientation of our approach, but algorithms for different properties and systems can surely be set up analogously.

2. Theory of Diversity Oriented Benchmarking

The basic idea of our approach is the generation of what we will call an "artificial molecule" (AM). An AM is not a molecule in the classical sense but a randomly generated minimum on an energetic hypersurface for a random conglomerate of a (predefined) set of atoms. To make sure that the generated systems are of use for quantum chemical research, we developed the following procedure for the generation of AMs. In the first step, the benchmark specification parameters are chosen to determine the general conditions (i.e., the constraints to randomness) of the test set:

1 How many systems are generated?
2 How many atoms does one AM contain?
3 How are the atoms chosen from the periodic system of elements?
4 How are the atoms arranged in space?
5 What is the desired complexity of electronic structure (e.g., total charge, number of open shells, or multireference character)?
6 What reaction scheme is applied?

The second step is the generation of structures, in accordance with the answers to the first four questions. In the third step, one has to ensure that the intended number of molecules has the specified electronic structure according to the fifth question. The fourth step is the generation of reference data. This way, a vast amount of completely different benchmark sets can be systematically generated, characteristically depending on the countless possible answers to the above named questions. It has to be kept in mind that while the basic principle of our approach is completely general and unbiased, any generated benchmark set itself is necessarily constrained. We would like to emphasize that the restrictions we have applied for the generation of the example benchmark sets that we present in the following paragraphs (e.g., single reference cases and CCSD(T) reference values) are limitations of the generated test sets but not of the mindless benchmarking approach itself. While it would surely be a tedious task (that we found unreasonable to undertake for the benchmarking of current DFT methods), the use of multireference methods is in no way incompatible with our benchmarking approach. Along these lines, we have also excluded complicated spin states to keep the example benchmark set generation simple, not because our approach is generally limited in this direction (comparison of different density functionals also becomes problematic because they may yield different spin states as the lowest state). When speaking of the generation of electronically demanding test cases, it has to be kept in mind that alongside multireference character other reasons for electronic complexity (e.g., unusual bonding, small gaps, spin contamination) exist. In general, one cannot say that all multireference cases are necessarily electronically difficult (the multiplet of an atom being an example) and vice versa for single-reference molecules. The advantage of "mindless" benchmarking is the transparency of the process, which turns unperceived biases into known constraints, i.e. that it forces the originator of a benchmark set to explicitly determine the

Table 1. Initial and Final Element Distributions (in percent) for the MB08-931 and MB08-ORG Benchmark Sets

	MB08-931			MB08-ORG		
element	initial	final	ratio[a]	initial	final	ratio[a]
H	69.2	64.8	0.94	61.8	58.2	0.94
Li	3.3	3.5	1.061	1.9	1.0	0.53
Be	3.3	3.6	1.091	0.5	0.0	0.00
B	3.3	4.7	1.42	1.0	1.8	1.80
C	3.3	3.9	1.18	15.5	17.6	1.14
N	3.3	3.8	1.15	3.9	4.3	1.10
O	3.3	2.9	0.88	3.9	4.5	1.15
F	3.3	3.2	0.97	1.0	1.3	1.30
Na	1.1	1.1	1.00	1.0	0.3	0.30
Mg	1.1	1.2	1.09	1.0	1.2	1.20
Al	1.1	2.0	1.82	1.0	1.5	1.50
Si	1.1	1.4	1.27	1.9	2.4	1.26
P	1.1	1.2	1.09	1.9	2.7	1.42
S	1.1	1.7	1.55	1.9	1.9	1.00
Cl	1.1	1.4	1.27	1.9	1.3	0.68

[a] Ratio of final to initial distribution.

boundary conditions to all dimensions of complexity found in the test set.

We have generated two different test sets for the illustration of our approach. For both sets we initially generated 300 random AMs. All systems contain exactly eight atoms, and only main group elements up to chlorine, excluding the noble gases helium and neon, are considered. The two test sets differ in their elemental composition; i.e., the atoms were chosen randomly with different probabilities for the different elements. For the first set, termed "MB08-931", the elemental probabilities were chosen so that the occurrence of the atoms Na to Cl is one-third of the occurrence of the atoms Li to F, which in turn is one-third of the occurrence of hydrogen (see Table 1). For the second set, termed "MB08-ORG", the element probabilities were chosen to roughly reproduce the element distribution found in organic compounds (see Table 1).[15]

The atoms were always placed randomly on the corners of a cube with an initial edge length of 2 b and then freely optimized on the PBE/TZVP[10,16] level. All systems were chosen to be uncharged, and open-shell calculations were restricted to (low-spin) doublet states.

Only systems that converged within a limit of 100 SCF and 100 geometry optimization steps and had a HOMO/LUMO gap of more than 0.5 eV (PBE/TZVP) were considered further. The number of open-shell AMs were chosen to be about 25% of all systems. To screen out multireference cases, an RCCSD(T)/cc-pVDZ[17] calculation was performed and systems with a T1-diagnostic larger than 0.02 or a D1-diagnostic larger than 0.10 were dropped (with both diagnostics rounded to two digits after the decimal point). Note that, when done automatically, checks for double entries and correct spin states have to be included in the benchmark set generation algorithm.

For both sets, a systematic decomposition into hydrides (for the group 1−4 elements) and homonuclear diatomic molecules (for the group 5−7 elements) was chosen as the reaction scheme. The only allowed reactant beside these products and the reactant AM is molecular hydrogen. The stoichiometry is restricted to integer numbers. The first three reactions from the MB08-931 set are given as an example:

$$2\mathrm{AM}_{(\mathrm{HHHCOHHH})} + 0\mathrm{H}_2 \rightarrow 2\mathrm{CH}_4 + 1\mathrm{O}_2 + 2\mathrm{H}_2$$

$$2\mathrm{AM}_{(\mathrm{HHOHPHNH})} + 0\mathrm{H}_2 \rightarrow 1\mathrm{N}_2 + 1\mathrm{O}_2 + 1\mathrm{P}_2 + 5\mathrm{H}_2$$

$$2\mathrm{AM}_{(\mathrm{NLiBHCHHB})} + 8\mathrm{H}_2 \rightarrow 4\mathrm{BH}_3 + 2\mathrm{CH}_4 + 2\mathrm{LiH} + 1\mathrm{N}_2$$

The above-described settings were chosen to restrict the test sets to small single-reference main group molecules, as these routinely applicable (black-box type) reference methods like CCSD(T) are known to yield results of high accuracy. A large number of initial structures was generated because we expected a lot of optimizations not to converge and aimed at a set size of about 100 entries. Of course, if the size of the test set is of importance, one can alter the scheme to generate random systems as long as enough systems have passed the following tests. Systems with a fixed number of eight atoms were chosen because a variable number of atoms seemed to be an unnecessary complication in this first study. Furthermore, eight-atom systems are just routinely manageable with high-level methods. Main group elements outweighing chlorine were also regarded as an unnecessary complication and the noble gases on the other side were viewed as too uninteresting for our purpose. Transition metals were excluded because even high-level coupled-cluster methods are known to have problems with the complex electronic situations in transition metal compounds, so the generation of a high-quality reference itself would be too demanding. The use of a cube for the initial starting geometries was believed as simple and sufficient after a few initial tests. An interesting alternative would be a "kick" procedure comparable to the one of Saunders,[18] which was also used by Bera et al.[14] for their isomer-minima search. The choice of the GGA for the optimization and initial screening is further to our disposal and might introduce a subtle bias toward single-reference cases. The SCF and structure optimization iteration limits were chosen to be quite high to avoid the introduction of additional biases through these limits. The goal of the applied threshold (gaps, diagnostics) was to completely screen out cases with very complex electronic structures, where CCSD(T) cannot be assumed to yield accurate reference values.

The basis set converged T1-diagnostic is known to be a reliable indicator for the inherent importance of nondynamical electron correlation, and it is furthermore known that multireference effects are negligible for T1-diagnostic values of less than 0.02.[19] The convergence of the T1-diagnostic with respect to the basis set improvement is a measure for the coupling between the one- and *N*-electron basis sets, which is likely to be small for the single-reference molecules we aim at. In any case, as the T1-diagnostic decreases with larger one-particle basis sets (because more orbital relaxation is necessary for the more incomplete smaller basis sets), we can assume the T1-diagnostic already at the RCCSD/cc-pVDZ level to be a good threshold for the rejection of multireference cases. While the T1-diagnostic can be seen as an average measure over the whole molecule (for which contributions from a small problem area can be swamped

by that of the well described rest of the molecule), the D1-diagnostic is designed to yield a large value for systems with only a small problematic area[20] and is used as a complement for the T1-diagnostic here. We found that a cutoff of 0.10 for the D1-diagnostic leads to results that are consistent with the 0.02 value for the T1-diagnostic. We would like to mention that the T1- and D1-diagnostics are not foolproof and that it could be a possible refinement for our screening approach to use the percentage of atomization energy accounted for by the (T) component as a predictor for higher-order correlation effects, as suggested by Karton et al. (which nevertheless seems to lead to quantitatively comparable results in almost all cases).[21]

As a general reaction scheme, the decomposition of the AMs to small (mainly closed-shell) molecules was chosen. As already mentioned, we think that this is closer to everyday chemistry than the commonly employed atomizations which furthermore introduce a bias for the correct description of the molecule compared to the (mostly) open-shell atoms. However, we have included reference values for the atomization of the AMs in the Supporting Information. While in the present form our approach cannot deal with barrier heights, future benchmarks will include charged compounds with an odd number of electrons to allow investigations of, for example, self-interaction errors in DFT.

To summarize, both sets consist of reactions with small single-reference main group molecules, roughly three-quarters of them being closed-shell cases. The first set was generated with a general chemistry motivated "931" element distribution. The second one resembles element distribution in organic molecules more closely. Despite being single-reference main group molecules, the generated AMs show a large structural diversity with interesting bonding features, and many of them are chemically very unusual (see Figures 1 and 2; example AMs are discussed in section 4.1).

3. Computational Details

After the initial DFT geometry optimizations at the PBE/TZVP level[10,16] and RCCSD/cc-pVDZ[17] single point calculations for the T1- and D1-diagnostics, the reference reaction energy values were produced for the remaining systems as follows.

The RCCSD(T) complete basis set (CBS) limit correlation energy was extrapolated according to the method of Halkier et al.[22] using cc-pVTZ and cc-pVQZ[17] data points and added to the extrapolated SCF energy.[23] Core correlation/polarization effects were estimated by using the relative energy differences of valence RCCSD(T)/cc-pVTZ and all-electron RCCSD(T)/cc-pCVTZ[17] calculations as a correction to the valence RCCSD(T)/CBS results. Our final reaction energies thus correspond to all-electron CCSD(T)/CBS estimates.

These values serve as reference data for DFT single-point calculations with the S-VWN,[24,25] B97-D,[26] B-P86,[27] B-LYP,[28,29] PBE,[10] TPSS,[30] PBEh[31] (also known as PBE0 or PBE1PBE), BH-LYP,[32] B3-PW91,[33] B3-LYP,[33,34] B2-PLYP,[35] B2GP-PLYP-D,[36] BMK,[37] MPW1B95,[38] PW6B95,[39] M05,[9,40] M05-2X,[9,41] M06,[9,42] M06-L,[9,43] and M06-2X[9,42] density functionals using TZVPP[16] and QZVP[44] Gaussian AO basis sets. In standard notation these are written as (5s2p1d)/[3s2p1d] and (7s3p2d1f)/[4s3p2d1f] for hydrogen, (11s3p)/[5s3p] and (15s6p2d1f)/[6s4p2d1f] for lithium, (11s4p)/[5s3p] and (15s7p2d1f)/[7s4p2d1f] for beryllium,

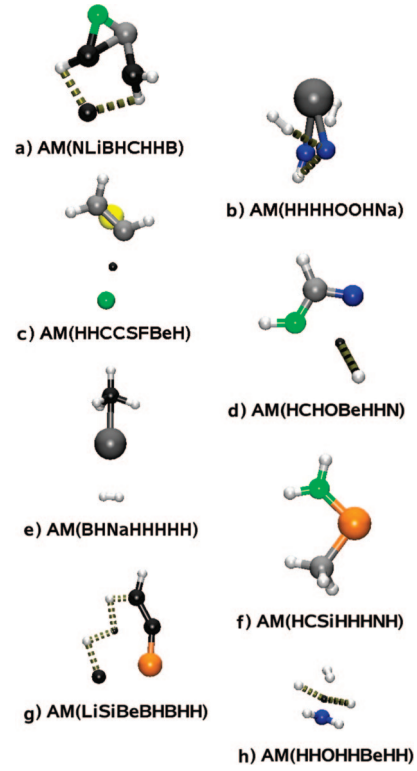

Figure 1. Examples for artificial molecules (AMs) from the MB08-931 benchmark set.

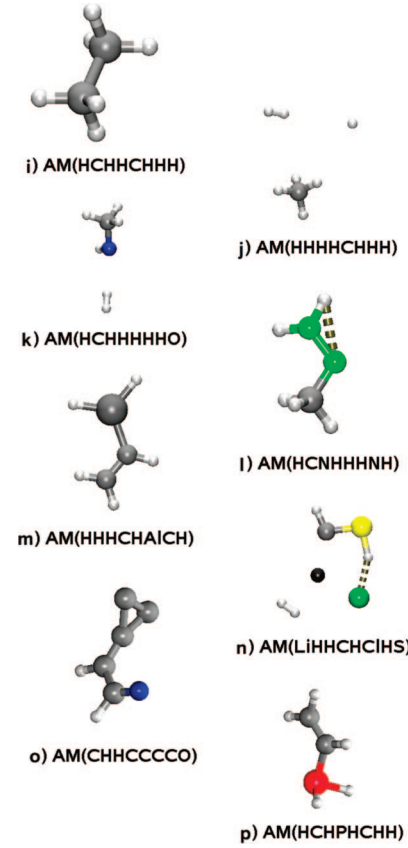

Figure 2. Examples for artificial molecules (AMs) from the MB08-ORG benchmark set.

(11s6p2d1f)/[5s3p2d1f] and (15s8p3d2f1g)/[7s4p3d2f1g] for boron to fluorine, (14s8p1d)/[5s4p1d] and (20s12p4d2f)/[9s5p4d2f] for sodium, (14s8p1d)/[5s4p1d] and (20s12p5d2f)/[9s5p5d2f] for magnesium, and (14s9p2d1f)/[5s5p2d1f] and (20s14p4d2f1g)/[9s6p4d2f1g] for aluminum to chlorine.

All DFT treatments of open-shell species were performed unrestricted. For the local and semilocal functionals and for the second-order perturbation correction of the double-hybrids, the RI approximation for two-electron integrals[45,46] has been used. For all functionals except S-VWN, PBEh, TPSSh, BH-LYP, B3-PW91, BMK, MPW1B95, M05, M05-2X, PW6B95, M06, M06-L, and M06-2X, the DFT-D[26] correction for London dispersion energy was applied (added suffix "-D"). Its impact is small to moderate for the tested functionals (for a more detailed discussion, see below) mainly because relatively small eight-atom systems have been considered. All coupled-cluster calculations were done using Molpro 2006.1,[47] for the MPW1B95 and B3-PW91 calculations, we employed Gaussian 03,[48] and the PW6B95, M05, M05-02X, M06, M06-L, and M06-2X calculations were carried out with NWChem 5.1.[49] For all other calculations we used Turbomole 5.10.[50,51]

4. Results and Discussion

4.1. Benchmark Set Generation. For the MB08-931 example set, 162 (out of 300) geometry optimizations converged, but four of them had a HOMO/LUMO gap smaller than 0.5 eV. From the remaining 75 closed-shell and 83 open-shell systems, all closed-shell and the first 25 randomly generated open-shell systems were chosen. Twelve of these systems were identical to others, four had substantial multireference character, and for one system the RCCSD(T)/cc-pVQZ calculation did not converge. As a result, the first set contains 83 entries, with 21 (25%) open-shell cases, ranging in size from 11 to 44 electrons.

For the MB08-ORG example set, 176 (out of 300) geometry optimizations converged, but for three of them the RCCSD(T)/cc-pVDZ calculations did not converge, and three of them had a HOMO/LUMO gap smaller than 0.5 eV. From the remaining 82 closed-shell and 88 open-shell systems, all closed-shell and the first 27 randomly generated open-shell systems were chosen. Eleven of these systems were identical to others, six had substantial multireference character, and for eight systems the all-electron RCCSD(T)/cc-pCVTZ calculation did not converge. As a result, the second set contains 84 entries, with 19 (23%) open-shell cases, ranging in size from 12 to 50 electrons.

Two AMs of the organic set were also generated within the MB08-931 set (MB08-931 entries 12 and 49), so that the merging of MB08-931 and MB08-ORG leads to a benchmark set with 165 entries that is dubbed in the following (and for future reference) MB08-165. This set contains 39 open-shell systems of which nine have a significant amount of spin contamination (>0.03 deviation from the expected $\langle \hat{S}^2 \rangle$ value of 0.75 at the HF-level).

Not surprisingly, after the generation and selection process, the final element distributions turned out to be different from the one used as guideline. The initial and resulting distributions are both given in Table 1. For the MB08-931 set no element is clearly underrepresented (less than 75% of the guideline distribution), while only aluminum and sulfur are clearly overrepresented (more than 150% of the guideline distribution). For the organic set, Li, Na, and Cl atoms are underrepresented and beryllium was completely screened out, while only boron is clearly overrepresented. The resulting distributions thus reflect the finite size of the sets, but another factor that also seems to be of influence is the element-specific different complexity of possible interactions. For instance, beryllium is found in seven out of the 300 initially generated "organic" structures, whereof three could not be optimized and the other four are skipped as open-shell systems, so that none is found between the finally selected ones. It is important to notice that the resulting distributions nevertheless nicely follow our initial intentions for the composition of the two example benchmarks as "931" and "ORG" sets.

Figures 1 and 2 show eight systems as examples from each test set. Both sets contain a number of chemically reasonable systems like e, f, and l, but while the organic set includes some "conventional molecules" like i (ethane) and k (methanol/H_2), nearly 30% of the 931 set are made up by fragmented systems like h and j. A handful of systems in both sets are quite complex like d and o, and a good part of both sets consists of chemically very unusual systems, like a, g, and n. The coordinates of all systems can be found in the Supporting Information.

4.2. Benchmark Calculations. *Overview and Discussion of the Reference Values.* For the given single-reference main group systems, already our valence CCSD(T)/CBS reference data can be assumed to be of high accuracy. In addition, because DFT functionals include core-correlation, we added an estimate for these effects to our reference data. It is based on the relative energy difference between valence RCCSD(T)/cc-pVTZ and all-electron RCCSD(T)/cc-pCVTZ calculations. As expected, this difference is small (about 1 kcal/mol on average with a maximum of 5 kcal/mol, compared to mean absolute reaction energies of 117 kcal/mol). For a typical density functional, it has little impact on the MAD if valence or all-electron data are taken as reference (e.g., a difference of less than 0.5 kcal/mol for PBE-D/QZVP).

The reference reaction energies should be briefly discussed first. The 931 set contains reaction energies between −199 and 434 kcal/mol and the organic set contains reaction energies between −571 and 302 kcal/mol. Opposed to the commonly employed atomization benchmarks that exclusively consider endothermic reactions, our data contain almost evenly around zero distributed reaction energies (see Figure 3). This means that without any applied bias in this direction our algorithm has generated simultaneously very stable and very unstable AMs. This is a greatly appreciated feature for a general thermodynamic benchmark set for chemistry where endothermic as well as exothermic reactions are of interest.

Overview of the DFT Data. This paragraph gives a short overview of the tables and figures with DFT data that are discussed in detail in the next paragraph.

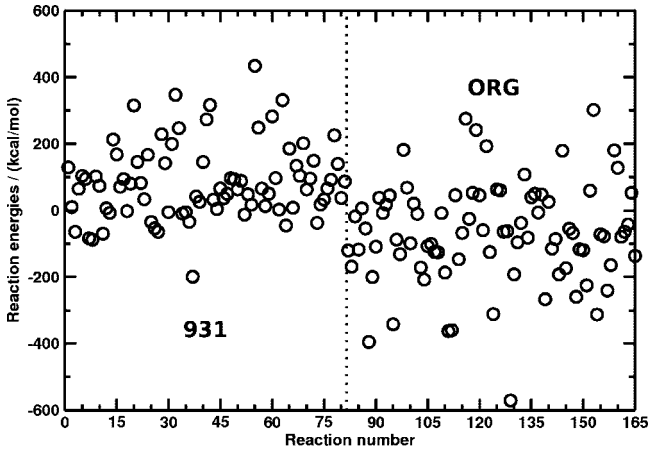

Figure 3. Distribution of reaction energies of both benchmark sets.

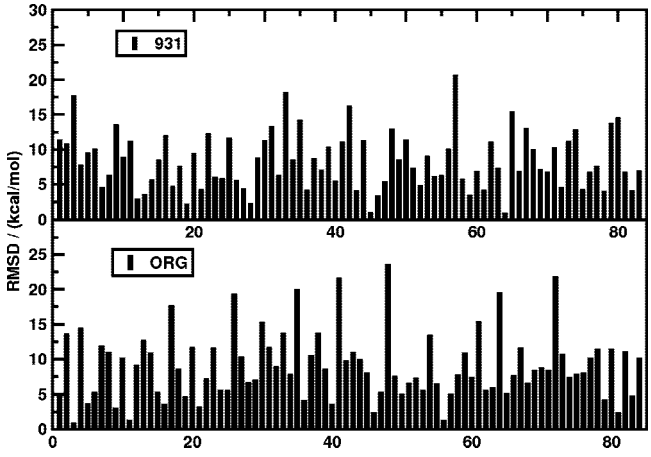

Figure 4. Rmsd averaged over 11 density functionals with the QZVP basis (see the text) for all reactions of both benchmark sets.

Figure 4 shows the root-mean-square deviation (rmsd) over 11 density functionals (S-VWN, PBE-D, B97-D, TPSS-D, PBEh, B3-LYP-D, M05, M05-2X, BMK, MPW1B95, and B2PLYP-D with the QZVP basis set) for the different entries of the two benchmark sets. This analysis is used to spot and check exceptionally problematic cases in the test sets, but it can clearly be seen that both sets are free from sizable outliers.

The mean absolute deviation (MAD), mean deviation (MD), rmsd, and the error spread (Δ, difference of maximum and minimum deviations) for representative density functionals (and for comparison also for HF and some coupled-cluster approximations) for both sets and the combined set are presented in Table 2. Low-order perturbation theory (i.e., MP2) has also been considered, but as expected, this and related methods suffer from spin-contamination in some of the open-shell systems. This makes a comparison with the DFT methods difficult, and therefore, we omit these methods in the present work. The MADs for DFT are also shown graphically in Figure 5. These statistical data are used for the evaluation of the different functionals and to find indicators for the example benchmark set quality. Additional information can be extracted from the histograms in Figure 7, where the error distribution for the functionals with the lowest overall MAD (M06, MPW1B95, BMK, M06-2X, PW6B95, and B2-PLYP-D) is shown. To summarize the results, Table 3 shows DFT and WFT methods in order of their accuracy for the combined MB08-165 set. A complete listing of all results can be found in the Supporting Information.

Discussion of the DFT Data. Turning to Table 2, we first note the very similar performance of all tested density functionals for the two different test sets. It can therefore be concluded that a specific element distribution does not have a substantial impact on the difficulty of the AMs. This clearly supports previous experience that the main distinction for modern electronic structure methods is between main group chemistry and transition metal compounds. Methods that perform well for organic chemistry are usually also applicable to general main-group systems.

In Figure 6 we plotted the relative MAD per element in order to investigate possible element-specific characteristics of the observed errors. These values were obtained by dividing the absolute reaction energy errors between the atoms of the AM according to their number, taking the average over all reactions and 11 functionals, weighting this value with the element occurrence in the set, and dividing it by the corresponding value for hydrogen (which is set to unity in this way). Values larger (smaller) than unity thus indicate higher (smaller) "difficulty" for the corresponding element. While not much can be concluded for the MB08-931 set, it looks as if oxygen is rather problematic (presumably because of the open-shell reaction product O_2) in the MB08-ORG set. A trend can be observed for the second-row where the errors increase with atomic number. A possible reason why sodium is a particularly easy case in both sets could be that it only occurs in simple ionic structures. We expect that a similar error analysis would be extremely helpful for semiempirical approaches where often atom-specific parameters are used. The finding that DFT does not produce very pronounced elemental error distributions is in agreement with its fundamental "ab initio"-like character.

The second conclusion that can be drawn from Table 2 is that albeit basis set incompleteness effects are less severe for DFT than for WFT methods, a thorough analysis should be made at the QZVP one-electron basis set level. Note that the CCSD(T)/cc-pVDZ level of theory (which is quite often used in the literature) performs a lot worse than any tested DFT approach (except LDA)! On the other hand, the extrapolated CCSD(T)/cc-pV(DT)Z data are comparable even to CCSD(T)/cc-pVQZ, which seems to be an important result for future generation of similar reference data for larger systems.

In some cases the now well-established DFT-D method[26] to account for nonlocal London dispersion effects has been applied, which is indicated by the suffix "-D" after the functional name. The MAD values with and without the dispersion correction for selected functionals are given in Tables 2 and 3 for comparison. Because of the relatively small size of the systems studied, dispersion effects are moderate. Except for PBE, application of this correction always leads to a lowering of the MAD ranging from 0.7 kcal/mol (TPSS) over 1.7 kcal/mol (B2-PLYP) to 2.2 kcal/

Table 2. Statistical Performance Indicators (in kcal/mol) for the MB08-931, MB08-ORG, and Both (MB08-165) Benchmark Sets

						MB08-165							
		MB08-931 QZVP		MB08-ORG QZVP		TZVPP				QZVP			
entry	method	MAD	rmsd	MAD	rmsd	MAD	MD	rmsd	$\Delta_{Min-Max}$	MAD	MD	rmsd	$\Delta_{Min-Max}$
						DFT							
1	S-VWN	22.4	28.7	17.9	24.4	19.4	14.1	25.5	134.9	20.3	16.2	26.8	138.5
2	Slater−Dirac	16.2	20.9	14.2	18.6	14.9	7.6	19.4	112.5	15.1	9.9	19.8	95.9
3	PBE-D	10.0	12.4	9.6	12.0	9.6(9.2) [a]	2.8	12.4	86.0	9.8	4.9	12.2	69.6
4	B97-D	9.7	12.3	10.9	14.6	11.5	−5.7	15.2	92.3	10.3	−3.5	13.5	87.1
5	TPSS-D	9.2	11.8	10.7	13.7	10.4(11.1) [a]	−2.7	14.1	79.5	10.0	−0.7	12.8	66.3
6	PBEh	8.0	10.0	9.1	12.0	9.3	−2.9	12.7	86.9	8.6	−0.5	11.1	69.6
7	B3-LYP-D	6.2	8.0	7.0	9.4	7.8(10.0) [a]	−4.8	10.5	55.4	6.6	−2.7	8.8	49.1
8	M05	6.4	8.0	7.5	9.6	8.0	−3.7	10.1	58.7	7.0	−1.3	8.9	57.6
9	M05-2X	7.8	11.3	5.7	8.2	6.3	1.2	8.9	70.0	6.8	3.5	9.9	72.2
10	BMK	5.1	6.3	5.9	8.0	6.5	−2.8	8.8	54.4	5.5	−1.1	7.3	50.9
11	MPW1B95	5.6	6.9	5.6	7.3	6.1	−1.9	8.2	54.7	5.6	0.1	7.1	40.8
12	M06	6.3	8.1	5.6	7.0	7.2	−4.3	9.6	48.5	6.0	−2.2	7.6	40.4
13	M06-2X	5.0	7.1	4.6	6.0	4.6	2.1	6.2	44.6	4.8	3.9	6.6	33.1
14	PW6B95	4.5	5.8	5.1	6.5	5.5	−2.8	7.7	48.6	4.8	−0.7	6.1	33.9
15	B2-PLYP-D	3.7	4.8	4.5	6.1	6.2(7.9) [a]	−5.6	8.4	38.7	4.1	−2.6	5.5	29.7
						WFT							
16	HF	24.0	29.6	28.0	37.0	26.6	−23.0	33.6	133.2	26.1	−22.4	33.7	158.7

		MAD	MD	rmsd	$\Delta_{Min-Max}$
17	CCSD/cc-pVQZ	5.6	−5.2	7.7	34.3
18	CCSD(T)/cc-pVDZ	14.2	−13.9	18.2	78.3
19	CCSD(T)/cc-pVTZ	5.5	−5.3	7.0	24.6
20	CCSD(T)/cc-pVQZ	2.6	−2.5	3.4	11.8
21	CCSD(T)/cc-pV(DT)Z	2.8	−2.4	3.8	17.8

[a] Values without DFT-D[26] dispersion correction in parentheses.

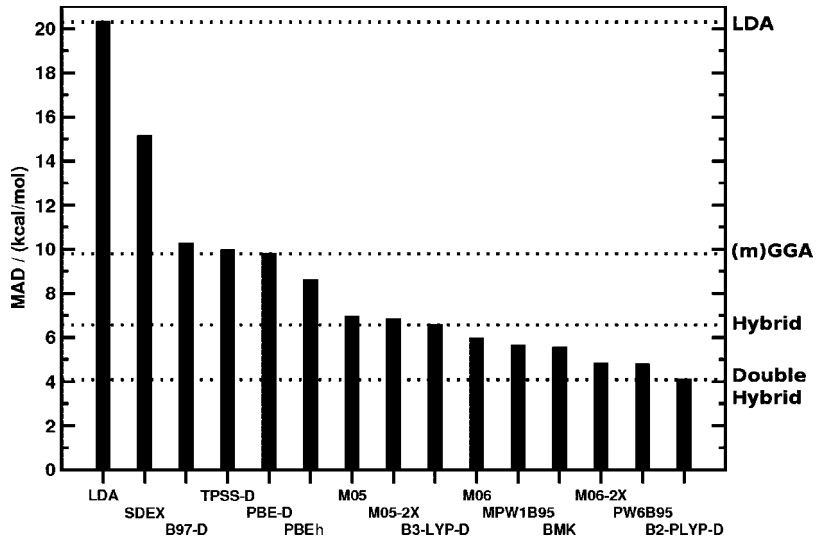

Figure 5. MAD of different density functionals for the MB08-165 set.

mol (B3-LYP). This is consistent with previous experience about the implicit account of dispersion effects by the electronic part of the functionals.[52]

Comparing the performance of the different functionals (Table 2 and Figure 5), one finds that the observed accuracy fits nicely to the "Jacob's ladder" metaphor of Perdew et al.[53] for the ordering of density functionals based upon the information of electron density they use. Suited on the first rung (local density approximation, LDA), the S-VWN functional yields quite bad results, with MADs of 22.4 (MB08-931 set), 17.9 (MB08-ORG set), and 20.3 kcal/mol (MB08-165 set), respectively. Note that exchange-only LDA (Slater−Dirac exchange) produces significantly better results than S-VWN.

The biggest improvement is found when climbing up to the second rung (generalized gradient approximation, GGA). Our examples PBE-D (MADs of 10.0, 9.6 and 9.8 kcal/mol) and B97-D (9.7, 10.9 and 10.3 kcal/mol) yield similar results, although we note a slightly better performance of the nonempirical (PBE) compared to the empirically parametrized functional. The next step up the ladder to the third rung (meta-GGA) with TPSS-D (9.2,

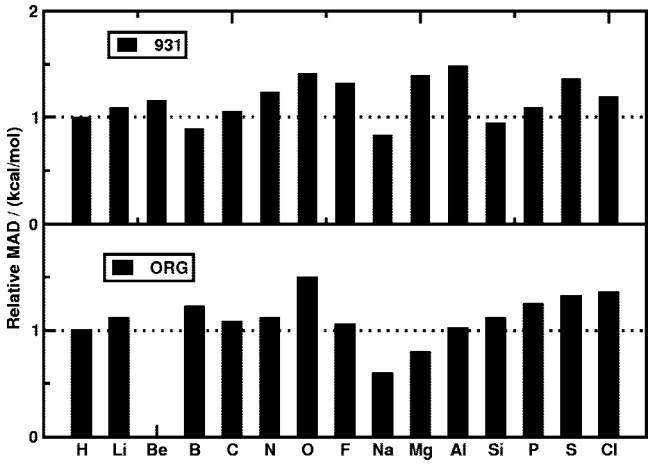

Figure 6. Relative MAD as distributed over the elements (for details, see the text) for the MB08-931 and the MB08-ORG set.

Table 3. Performance (statistical descriptors in kcal/mol) of DFT and WFT[a] Methods for the Combined MB08-165 Benchmark Set

method	rmsd	MAD
CCSD(T)/cc-pVQZ	3.38	2.61
CCSD(T)/cc-pV(DT)Z	3.80	2.82
B2-PLYP-D/QZVP	5.49	4.09
PW6B95/QZVP	6.14	4.78
M06-2X/QZVP[a]	6.59	4.82
B2-PLYP/QZVP	6.63	5.12
CCSD(T)/cc-pVTZ	7.01	5.45
MPW1B95/QZVP	7.13	5.64
BMK/QZVP	7.26	5.53
M06/QZVP[a]	7.60	5.96
CCSD/cc-pVQZ	7.69	5.64
B3-LYP-D/QZVP	8.75	6.58
M05/QZVP	8.88	6.95
B3-PW91/QZVP	9.31	7.04
M05-2X/QZVP	9.89	6.83
B3-LYP/QZVP	10.61	8.19
TPSSh/QZVP	10.98	8.38
PBEh/QZVP	11.09	8.62
B-P86-D/QZVP	11.50	9.27
B-LYP-D/QZVP	12.14	9.23
PBE-D/QZVP	12.24	9.81
TPSS-D/QZVP	12.85	9.97
B97-D/QZVP	13.54	10.27
BH-LYP/QZVP	16.66	12.03
M06-L/QZVP[a]	17.17	11.13
CCSD(T)/cc-pVDZ	18.24	14.25
S-VWN/QZVP	26.78	20.31
HF/QZVP	33.68	26.07

[a] Only valence electrons have been correlated. [b] Two (four for M06-L) entries have been omitted because SCF convergence is lacking.

10.7, and 10.0 kcal/mol) shows no advancement at all, which is in agreement with the results of two recent studies[5,12] on "real" molecules.

The inclusion of nonlocal information from occupied orbitals by adding Fock-exchange on the fourth rung (hyper-

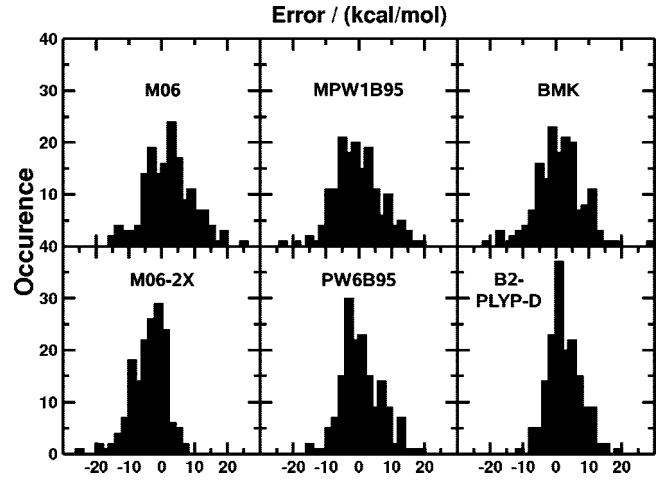

Figure 7. Error distribution for the density functionals with the lowest MADs. The binning interval is 2 kcal/mol.

GGA or hybrids) with PBEh (8.0, 9.1 and 8.6 kcal/mol) and B3-LYP-D (6.2, 7.0, and 6.6 kcal/mol) represents again a big step toward higher accuracy. However, less is gained from the GGA level to hybrids than from LDA to GGAs, i.e., it becomes more and more difficult to climb up the ladder.

Turning to the performance of the hybrid-meta-GGAs (which are mostly represented by highly parametrized forms), one finds a mixed picture. For the M05 and M06 family of functionals, it was possible to incorporate dispersion effects through flexibility and parametrization, and therefore no dispersion correction was applied for these functionals. Compared to conventional hybrids like B3-LYP-D, the MAD increases even slightly for M05 and M05-2X. BMK and MPW1B95 perform a bit better and the best results in this class are found for the PW6B95 (4.5, 5.1, and 4.8 kcal/mol) and M06-2X (5.0, 4.6, and 4.8 kcal/mol) functionals. However, in the SCF calculations with the M06 functionals, we noted in several cases convergence problems, and a few AMs therefore had to be omitted. This behavior is known in the literature.[54] Note also how well MAD, rmsd, and maximum errors provide the same picture about performance, which is a clear indication for the statistical quality of the sets.

The B2-PLYP-D and B2GP-PLYP-D double-hybrid functionals include nonlocal information about correlation, which is absent in any of its competitors, via the second-order perturbation correction. They can therefore be classified as true (but empirical) fifth-rung density functionals. This view is indeed supported by the very good performance of B2-PLYP-D for all benchmark sets with MADs of 3.7, 4.5, and 4.1 kcal/mol, which is again an appreciable step into the right direction. B2GP-PLYP-D that contains more nonlocal information compared to B2-PLYP-D (65 vs 53% Fock-exchange and 36 vs 27% MP2-type correlation) shows indistinguishably good performance. Note that also the maximum errors for the double-hybrids are lower than for any other tested functional (28−30 vs 33.1 kcal/mol for the best other, which is M06-2X).

While the conventional DFT approaches are shown to have reached the basis set limit already at the TZVPP level, the

double-hybrids substantially benefit from a further basis set enlargement because of the included perturbation correction.

Additional information about the performance of the functionals with the lowest MADs (M06, MPW1B95, BMK, M06-2X, PW6B95, and B2-PLYP-D) can be taken from Figure 7, which displays error distributions in a 5 kcal/mol interval. The hybrid-GGAs M06, MPW1B95, and BMK show a behavior very similar to each other, while the M06-2X and the PW6B95 functionals seem to be slightly superior. Nevertheless, they cannot reach the accuracy of B2-PLYP-D, which shows the sharpest and most well-behaved Gaussian-shape error distribution.

This view is further supported by Table 3, where DFT and WFT methods are shown in order of their accuracy for the combined MB08-165 set. As additional functionals, BH-LYP, B3-PW91, and M06-L are included here for comparison. On the basis of the MAD, we tried to identify groups of methods with similar performance. Perusing Table 3, one finds that B2-PLYP-D outperforms the highly parametrized meta-hybrid GGAs, which in turn are even better than CCSD(T) with a sizable AO basis. In the next group, we find three other meta-hybrids that are better than B3-LYP, even when it is corrected for missing dispersion effects. Two almost nonempirical hybrids (TPSSh and PBEh) and uncorrected B3-LYP follow, which are only slightly better than typical GGAs. Here, the old B-P86 seems to be most robust, although we note only a small (probably statistically insignificant) difference between the best and worst (B-P86 and B97-D) GGAs. This seems to be important in many solid-state or surface-science applications, where semilocal functionals are dominant.

5. Concluding Remarks

We present a diversity-oriented approach for the preferably unbiased generation of thermochemical benchmark data. We have addressed the "selection" problem through the random generation of "artificial molecules" (AMs) in accordance with systematic and controllable generation specifications. The most appealing feature of our approach in comparison to existing test sets is the opening of chemical space, which produces electronically demanding cases in an unforeseeable manner. It is hoped that these sets can provide a clear, unbiased, statistically significant, and comprehensive picture about the performance of electronic structure methods at a minimum of computational effort.

For the generation of two example sets, we have chosen several strict constraints (that could have been released or further "randomized") to keep the examples simple and to ensure a high accuracy of the reference data. We ended up with two test sets with chemically very diverse and unusual structures, despite the single-reference main group nature of all generated AMs. For the evaluation of the benchmark sets, we performed DFT calculations, applying several different density functionals, and compared them to highly accurate CCSD(T)/CBS(all electron) estimates. We have found a systematic improvement along "Jacob's ladder" for most of the tested functionals, which is a promising first result for our "mindless" approach and supports the significance of Perdew's metaphor.

Concerning individual density functionals and wave function based methods, the following main conclusions can be drawn:

1. Even for these relatively small systems, B3-LYP is not better than other simple hybrids. Only when the relatively large effect of the dispersion correction (about 2 kcal/mol lowering of the MAD) is included does it outperform the modern and highly parametrized M05 meta-hybrid GGAs that seem to represent relatively inaccurate points in the M0X-parameter space (this also holds for M05-L). However, the performance of B3-LYP for larger molecules is known to deteriorate substantially, and since more accurate and robust alternatives are available, we cannot recommend its application in general.

2. Although no atomizations have been considered, the PBE family of functionals (including TPSS and hybrid versions) performs slightly worse than B3-LYP. This is contrast to some recent applications in, for example, organic chemistry where they outperform B3-LYP and is likely a result of the relatively small size of the systems. As known from previous work on van der Waals complexes, the PBE(h) functionals simulate to some extent medium-range correlation effects related to short-range dispersion[55] that seem to be of some importance even in eight-atom systems.

3. Concerning the meta-hybrid GGAs, the M06 parametrization seems to be a clear step forward, although we also note the good performance of the less parametrized PW6B95 functional. However, meta-GGAs or meta-hybrid-GGAs do not in general represent improvements compared to their GGA counterparts, as seen for the PBE(h)/TPSS(h) pairs.

4. The best functionals contain a relatively large fraction of nonlocal Fock-exchange (about 40−60%) and adding more seems to improve the results (the only exception to this rule is BH-LYP). This is consistent with our choice that only main-group systems have been considered. By construction the sets do not contain cases with strong correlation effects (for which semilocal functionals should work better) but seem to be dominated by self-interaction error including cases (which are better described with "high-X" functionals). This bias is not rooted in the basic ansatz of "mindless" benchmarking but a result of the choice of the necessary (single) reference CCSD(T) method as a basis for evaluation.

5. The dispersion-corrected double-hybrid functionals, despite having only three (two "electronic") adjustable parameters (not counting the global, "black-box"-type dispersion correction), outperform all other tested DFT approaches by a significant margin and yield results in between CCSD(T)/cc-pVTZ and CCSD(T)/cc-pVQZ quality. The fact that two different parametrizations (B2-PLYP and B2GP-PLYP) provide similar rmsd values indicates the robustness of the general idea. This could not be expected, because standard MP2 often breaks down in electronically complicated situations. This supports the previous claim that the Kohn−Sham orbitals greatly improve the behavior of the perturbation treatment used in the double-hybrids.

6. The more approximate coupled-cluster treatments provide results for the MB08-165 set, in full agreement with common knowledge about their behavior: the (T)-correction is of utmost importance (e.g., CCSD/cc-pVQZ is not better

than the best meta-hybrids), single DZ (or even TZ) AO basis set computations are a waste of computer time, and two-point extrapolations provide results that improve like one step in cardinal number (i.e., DT-extrapolation yields results comparable to a single QZ calculation). This further supports the significance of the proposed test set.

All in all, it is hoped that this work will help to pave the way for improved electronic structure methods in chemistry. Future work in this promising direction will explore in particular larger AMs than the eight-atom systems considered herein.

Acknowledgment. This work was supported by the Deutsche Forschungsgemeinschaft in the framework of the SFB 424.

Supporting Information Available: Cartesian coordinates of all AMs and relative energies at various CCSD(T) levels and for all described density functionals. This material is available free of charge via the Internet at http://pubs.acs.org

References

(1) Cioslowski, J., Ed. *Quantum Mechanical Prediction of Thermochemical Data*; Kluwer: Dordrecht, 2001; 1 ff.

(2) Curtiss, L. A.; Raghavachari, K.; Redfern, P. C.; Rassolov, V.; Pople, J. A. *J. Chem. Phys.* **1998**, *109*, 7764–7776.

(3) Lynch, B. J.; Truhlar, D. G. *J. Phys. Chem. A* **2003**, *107*, 8996–8999.

(4) Zhao, Y.; Gonzalez-Garcia, N.; Truhlar, D. G. *J. Phys. Chem. A* **2005**, *109*, 2012–2018.

(5) Grimme, S.; Steinmetz, M.; Korth, M. *J. Org. Chem.* **2007**, *72*, 2118–2126.

(6) Jurecka, P.; Sponer, J.; Hobza, P. *Phys. Chem. Chem. Phys.* **2006**, *8*, 1985–1993.

(7) Johnson, E. R.; Mori-Sanchez, P.; Cohen, A. J.; Yang, W. *J. Chem. Phys.* **2008**, *129*, 204112.

(8) Schwabe, T.; Grimme, S. *Acc. Chem. Res.* **2008**, *41*, 569–579.

(9) Zhao, Y.; Truhlar, D. G. *Acc. Chem. Res.* **2008**, *41*, 157–167.

(10) Perdew, J. P.; Burke, K.; Enzerhof, M. *Phys. Rev. Lett.* **1996**, *77*, 3865–3868.

(11) Csonka, G. I.; Ruzsinszky, A.; Tao, J.; Perdew, J. P. *Int. J. Quantum Chem.* **2005**, *101*, 506–511.

(12) Grimme, S. *J. Phys. Chem. A* **2005**, *109*, 3067–3077.

(13) Fink, T.; Reymond, J.-L. *J. Chem. Inf. Model.* **2007**, *47*, 342–352.

(14) Bera, P. B.; Sattelmeyer, K. W.; Saunders, M.; Schaefer, H. F., III; Schleyer, P. v. R. *J. Phys. Chem. A* **2006**, *110*, 4287–4290.

(15) Clayden, J.; Greeves, N.; Warren, S.; Wothers, P. *Organic Chemistry*; Oxford University Press: Oxford, 2001; p 12.

(16) Schäfer, A.; Huber, C.; Ahlrichs, R. *J. Chem. Phys.* **1994**, *100*, 5829–5835.

(17) Dunning, T. H. *J. Chem. Phys.* **1989**, *90*, 1007–1023.

(18) Saunders, M. *J. Comput. Chem.* **2004**, *25*, 621–626.

(19) Lee, T. J.; Taylor, P. R. *Int. J. Quantum Chem.* **1989**, *S23*, 199–207.

(20) Lee, T. J. *Chem. Phys. Lett.* **2003**, *372*, 362–367.

(21) Karton, A.; Rabinovich, E.; Martin, J. M. L.; Ruscic, B. *J. Chem. Phys.* **2006**, *125*, 144108.

(22) Halkier, A.; Helgaker, T.; Jorgensen, P.; Klopper, W.; Koch, H.; Olsen, J.; Wilson, A. K. *Chem. Phys. Lett.* **1998**, *286*, 243–252.

(23) Halkier, A.; Helgaker, T.; Jorgensen, P.; Klopper, W.; Olsen, J. *Chem. Phys. Lett.* **1999**, *302*, 437–446.

(24) Slater, J. C. *Phys. Rev.* **1951**, *81*, 385–390.

(25) Vosko, S. H.; Wilk, L.; Nusair, M. *Can. J. Phys.* **1980**, *58*, 1200–1211.

(26) Grimme, S. *J. Comput. Chem.* **2006**, *27*, 1787–1799.

(27) Perdew, J. P. *Phys. Rev. B* **2000**, *33*, 8822–8824.

(28) Becke, A. D. *Phys. Rev. A* **1988**, *38*, 3098–3100.

(29) Lee, C.; Yang, W.; Parr, R. G. *Phys. Rev. B* **1988**, *37*, 785–789.

(30) Tao, J.; Perdew, J. P.; Staroverov, V. N.; Scuseria, G. E. *Phys. Rev. Lett.* **2003**, *91*, 146401.

(31) Adamo, C.; Barone, V. J. *J. Chem. Phys.* **1999**, *110*, 6158–6170.

(32) Becke, A. D. *J. Chem. Phys.* **1993**, *98*, 1372–1377.

(33) Becke, A. D. *J. Chem. Phys.* **1993**, *98*, 5648–5652.

(34) Stephens, P. J.; Devlin, F. J.; Chabalowski, C. F.; Frisch, M. J. *J. Phys. Chem.* **1994**, *98*, 11623–11627.

(35) Grimme, S. *J. Chem. Phys.* **2006**, *124*, 034108.

(36) Karton, A.; Tarnopolsky, A.; Lamere, J.-F.; Schatz, G. C.; Martin, J. M. L. *J. Phys. Chem. A* **2008**, *112*, 12868.

(37) Boese, A. D.; Martin, J. M. L. *J. Chem. Phys.* **2004**, *121*, 3405–3416.

(38) Zhao, Y.; Truhlar, D. G. *J. Phys. Chem. A* **2004**, *108*, 6908–6918.

(39) Zhao, Y.; Truhlar, D. G. *J. Phys. Chem. A* **2005**, *109*, 5656–5667.

(40) Zhao, Y.; Schultz, N. E.; Truhlar, D. G. *J. Chem. Phys.* **2005**, *123*, 161103.

(41) Zhao, Y.; Schultz, N. E.; Truhlar, D. G. *J. Chem. Theory Comput.* **2006**, *2*, 364–382.

(42) Zhao, Y.; Schultz, N. E.; Truhlar, D. G. *Theor. Chem. Acc.* **2008**, *120*, 215–241.

(43) Zhao, Y.; Truhlar, D. G. *J. Chem. Phys.* **2006**, *125*, 194101.

(44) Weigend, F.; Furche, F.; Ahlrichs, R. *J. Chem. Phys.* **2003**, *119*, 12753–12762.

(45) Eichkorn, K.; Treutler, O.; Öhm, H.; Häser, M.; Ahlrichs, R. *Chem. Phys. Lett.* **1995**, *242*, 652.

(46) Eichkorn, K.; Weigend, F.; Treutler, O.; Ahlrichs, R. *Theor. Chem. Acc.* **1997**, *97*, 119–124.

(47) Werner, H. J.; et al. MOLPRO version 2006.1, a package of ab initio programs; University College Cardiff Consultants, Ltd.: Cardiff, 2006. See also http://www.molpro.net (accessed Feb 3, 2009).

(48) Frisch, M. J.; Trucks, G. W.; Schlegel, H. B.; Scuseria, G. E.; Robb, M. A.; Cheeseman, J. R.; Montgomery, J. A., Jr.; Vreven, T.; Kudin, K. N.; Burant, J. C.; Millam, J. M.; Iyengar, S. S.; Tomasi, J.; Barone,

V.; Mennucci, B.; Cossi, M.; Scalmani, G.; Rega, N.; Petersson, G. A.; Nakatsuji, H.; Hada, M.; Ehara, M.; Toyota, K.; Fukuda, R.; Hasegawa, J.; Ishida, M; Nakajima, T.; Honda, Y.; Kitao, O.; Nakai, H.; Klene, M.; Li, X.; Knox, J. E.; Hratchian, H. P.; Cross, J. B.; Bakken, V.; Adamo, C.; Jaramillo, J.; Gomperts, R.; Stratmann, R. E.; Yazyev, O.; Austin, A. J.; Cammi, R. Pomelli, C.; Ochterski, J. W.; Ayala, P. Y.; Morokuma, K.; Voth, G. A.; Salvador, P.; Dannenberg, J. J. Zakrzewski, V. G.; Dapprich, S.; Daniels, A. D.; Strain, M. C.; Farkas, O.; Malick, D. K.; Rabuck, A. D.; Raghavachari, K.; Foresman, J. B.; Ortiz, J. V.; Cui, Q.; Baboul, A. G.; Clifford, S.; Cioslowski, J.; Stefanov, B. B.; Liu, G.; Liashenko, A.; Piskorz, P.; Komaromi, I.; Martin, R. L.; Fox, D. J.; Keith, T.; Al-Laham, M. A.; Peng, C. Y.; Nanayakkara, A.; Challacombe, M.; Gill, P. M. W.; Johnson, B.; Chen W.; Wong, M. W.; Gonzalez, C.; Pople, J. A. *Gaussian 03, Revision E.01*; Gaussian, Inc.: Wallingford CT, 2004.

(49) Bylaska, E. J.; et al. *NWChem, A Computational Chemistry Package for Parallel Computers, Version 5.1*; Pacific Northwest National Laboratory: Richland, 2007.

(50) Ahlrichs, R.; et al. *TURBOMOLE V5.10*; University of Karlsruhe: Karlsruhe, 2008. See also: http://www.turbomole.com (accessed Feb 3, 2009).

(51) Ahlrichs, R.; Bär, M.; Häser, M.; Horn, H.; Kömel, C. *Chem. Phys. Lett.* **1989**, *162*, 165–169.

(52) Schwabe, T.; Grimme, S. *Phys. Chem. Chem. Phys.* **2007**, *9*, 3397–3406.

(53) Perdew, J. P.; Ruzsinszky, A.; Tao, J.; Staroverov, V. N.; Scuseria, G. E.; Csonka, G. *J. Chem. Phys.* **2005**, *123*, 062201.

(54) Zhao, Y.; Truhlar, D. G. *J. Chem. Theory Comput.* **2008**, *4*, 1849–1868.

(55) Grimme, S. *Angew. Chem., Int. Ed.* **2006**, *45*, 4460−4464.

CT800511Q

JCTC Journal of Chemical Theory and Computation

Quantum Chemistry on Graphical Processing Units. 2. Direct Self-Consistent-Field Implementation

Ivan S. Ufimtsev[†] and Todd J. Martinez*[,†]

Department of Chemistry and The Beckman Institute, University of Illinois, Urbana, Illinois 61801

Received December 2, 2008

Abstract: We demonstrate the use of graphical processing units (GPUs) to carry out complete self-consistent-field calculations for molecules with as many as 453 atoms (2131 basis functions). Speedups ranging from 28× to 650× are achieved as compared to a mature third-party quantum chemistry program (GAMESS) running on a traditional CPU. The computational organization used to construct the Coulomb and exchange operators is discussed. We also present results using three GPUs in parallel, combining coarse and fine-grained parallelism.

Introduction

Graphical processing units (GPUs) and related massively parallel processors are rapidly emerging as a promising architecture for many methods in computational chemistry, including molecular dynamics[1,2] and quantum chemistry.[3−9] Previously, we demonstrated[5,6] that gains in efficiency of up to 130× over conventional CPUs could be achieved for two-electron Coulomb repulsion integral (ERI) evaluation using NVIDIA graphics cards with algorithms well-tuned to the stream processing[10] architecture underlying modern GPUs. Here, we extend our initial implementation to complete formation of the Fock matrix, which forms the dominant computational step in both Hartree−Fock and density functional self-consistent-field calculations. Our implementation as described here is limited to s- and p-type atom-centered Gaussian basis functions, although extension to higher angular momenta is underway. We assess the efficiency of the resulting code by comparison to GAMESS,[11] a mature third-party quantum chemistry package. Because of the observed 2 order-of-magnitude increase in efficiency, we are able to carry out "on-the-fly" ab initio Monte Carlo simulations of water clusters, and the resulting equilibrium structures are in good agreement with previous studies using local optimization. We also carry out direct SCF calculations on a variety of molecules containing up to 453 atoms (2131 basis functions). These calculations show that the GPU can be as much as 650× faster than conventional CPUs, and calculations on molecules with hundreds of atoms can be completed in minutes. Precision remains a critical issue that limits the size of molecules that can be treated accurately. The newest generation of NVIDIA cards includes double-precision (DP) support, and we comment on this briefly.

We begin with a brief overview of the GPU architecture, focusing on the issues that are most relevant to the current work. More detailed descriptions can be found elsewhere.[12] We then describe the *J*- and *K*-matrix formation algorithms, followed by results and discussion. All numerical results were first obtained on a single GeForce 8800GTX card. However, as we were preparing the manuscript, NVIDIA released a new generation of GPUs (G200) that supports DP floating point operations in hardware. Thus, we also present results obtained on one GeForce 280GTX card as well as on a multi-GPU system containing three such cards running in parallel. The hardware overview and performance sections refer to the G80 GPU hardware. Some parts of our code invoke DP calculations on the GPU, and we comment on this briefly. Everywhere in this Article we use NVIDIA's CUDA[12] (Compute Unified Device Architecture) programming interface that allows control of the GPU via an extension of the standard C language.

Overview of Graphics Hardware

GPUs are an example of a stream processing architecture,[10] emphasizing fine-grained parallelism and efficient utilization

[†] Present address: Department of Chemistry, Stanford University, Stanford, CA 94305.

* Corresponding author phone: (650) 736-8860; e-mail: Todd.Martinez@stanford.edu.

10.1021/ct800526s CCC: $40.75
Published on Web 03/06/2009

of the memory hierarchy. Typical GPUs contain many arithmetic units, which are arranged in groups that share fast access memory and an instruction unit. For example, the GeForce 8800GTX graphics card, which was released in late 2006, has 128 arithmetic units (also referred to as streaming processors, or SPs) organized into 16 streaming multiprocessors (SMs). Each SM (consisting of 8 SPs in the 8800GTX) has its own instruction unit and thus operates independently of the other SMs. The SPs comprising an SM operate together in single instruction multiple data (SIMD) fashion. In other words, at any moment, all 8 SPs on an SM are executing exactly the same instruction on different data streams.

Because the computational units of the GPU operate in parallel, problems should be split into a set of smaller tasks (threads) that are distributed among the different processors. In NVIDIA's CUDA paradigm, all threads are organized into a 1D- or 2D-grid of 1-, 2-, or 3D blocks with up to 512 threads in each block. The choice of grid topology is dictated by the particular problem under consideration; in our case, we use a 2D grid of 2D blocks. Threads in the same block are always executed on the same multiprocessor, providing them access to the SM's shared memory for fast data exchange. In contrast, distinct blocks are not guaranteed to be executed on the same SM. This means that distinct blocks must communicate through the main GPU memory, which is much slower (by 2 orders of magnitude) than the shared memory. In addition, block execution cannot be efficiently synchronized. Therefore, any efficient GPU algorithm should avoid expensive interblock data transfer, having all interthread communication, if any, occur within blocks. The hardware splits the thread blocks into warps with 32 threads in a warp, which are processed by SMs in SIMD fashion with all 32 threads executed by 8 streaming processors in 4 clock cycles. This SIMD execution model requires additional effort when developing GPU-based algorithms, because all threads in the same warp must execute exactly the same set of instructions. A typical case demonstrating violation of this requirement and subsequent deleterious consequences is a simple loop where the number of iterations is determined at runtime. If there are threads in a warp that complete their loop as the others continue iterating, the idle threads will still execute the unnecessary loop instructions until the last thread in the warp is done. Such idle threads, thereby, occupy the hardware resources, which otherwise would be used for useful work, and degrade the algorithm performance.

Several basic strategies for efficient execution on the GPU architecture can be delineated.

(1) The first is data localization. Contiguous threads should access contiguous DRAM addresses to coalesce multithread memory instructions into one memory load/store operation. Otherwise, the overall memory bandwidth can drop by a factor of 10 or even more, completely obviating the computational advantage of the GPU.

(2) The second is little interthread communication. Most streaming-type architectures (including NVIDIAs) do not provide efficient tools for fast interthread data exchange, except when threads belong to the same block. All communication must be restricted to threads within the same block, and ideally there is no communication between threads.

(3) The third is elimination of memory access collisions. Neither CUDA nor the NVIDIA hardware support floating-point atomic memory operations. In other words, if two or more threads write to the same memory address at the same instant of time, the result is unpredictable. It is therefore critical to ensure that potential memory access collisions are avoided, which requires careful attention to the relationship between a thread and the memory it will write to.

(4) The fourth is dense computing. Because thread warps are processed in SIMD fashion, it is imperative to keep the whole warp busy. If some threads in a warp are not carrying out useful work, performance degradation will occur. Because of the efficient warp scheduler, there is little penalty if all threads in a warp are idle; in this case, the entire warp will be removed from execution scheduling.

Self-Consistent-Field Calculations

The evaluation of a large number of two-electron repulsion integrals (ERIs) over N atom-centered basis functions is one of the most computationally intensive tasks in any ab initio Molecular Orbital (MO) or Density Functional Theory (DFT) approach. These integrals are given by:

$$(\phi_\mu\phi_\nu|\phi_\lambda\phi_\sigma) = \int\int \phi_\mu(\vec{r}_1)\phi_\nu(\vec{r}_1)\frac{1}{|\vec{r}_1 - \vec{r}_2|}\phi_\lambda(\vec{r}_2)\phi_\sigma(\vec{r}_2)\,\mathrm{d}\vec{r}_1\,\mathrm{d}\vec{r}_2 \quad (1)$$

where the ϕ are linear combinations (contractions) of atom-centered Gaussian basis function primitives. In our previous work,[6] we explored three different algorithms for ERI evaluation on GPU. The algorithms possess different granularity of the problem decomposition and cover a wide range of possible thread-integral mapping strategies. It was found that the so-called "1 Thread − 1 Contracted Integral" (1T1CI) algorithm was the most efficient at generating the set of all contracted integrals. Another approach, "1 Thread − 1 Primitive Integral" (1T1PI), was the fastest in primitive integral evaluation. However, the subsequent integral transformation step, leading to the final set of contracted integrals, was not very efficient and sometimes required so much labor as to mitigate the advantage of the 1T1PI mapping strategy. We also observed that the time required to transfer calculated ERIs from GPU to CPU memory can be comparable to the ERI calculation time due to limited CPU−GPU bus bandwidth.[6]

This removes the need for the problematic primitive→contracted integral transformation and limits the GPU−CPU communication to matrices of size $O(N^2)$, where N is the number of primitive basis functions. In this case, GPU−CPU communication requires a negligible amount of the total time. We also use an incremental Fock matrix formation procedure ("Fock matrix updating"),[13] where the GPU computes only the difference between Fock operators in successive iterations. This has the usual advantage of minimizing the number of Fock matrix elements that need to be computed, especially as convergence is reached in later iterations. However, an

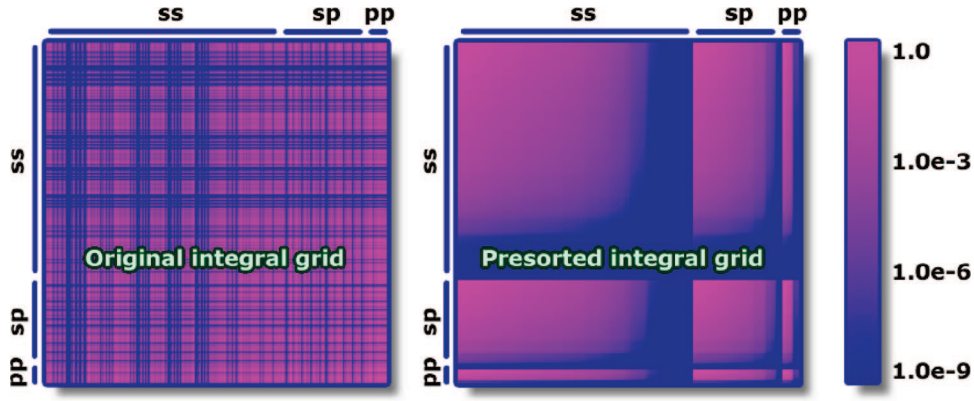

Figure 1. Illustration of ERI organization for *J*- and *K*-matrix construction, using data obtained from a representative calculation on ethane. The row and column indices correspond to *bra* and *ket* pairs of a given primitive integral, and the coloration indicates the magnitude of the Schwartz upper bound for a given integral. After the *ket* and *bra* pairs are ordered by angular momentum, the grid on the left is obtained. The sparse structure of the resulting grid hampers effective parallelization because of load imbalance. Further sorting of the *ket* and *bra* pairs within each angular momentum class according to the magnitude of each pair's contribution to the Schwartz upper bound leads to the grid on the right, which is well-suited for computations on the GPU.

additional advantage in the present context is that the incremental Fock matrix procedure is numerically more accurate when integrals are generated with limited, that is, 32-bit, precision.

In Hartree−Fock (HF) calculations for molecules with up to a few thousand basis functions, most of the computational time is spent on formation of the Fock matrix, comprised of one-electron, Coulomb, and exchange contributions:

$$\mathbf{F(C)} = \mathbf{H}_{\mathbf{core}} + \mathbf{J(C)} - \frac{1}{2}\mathbf{K(C)} \qquad (2)$$

where **C** is the matrix of the molecular orbital (MO) coefficients in the atomic orbital (AO) basis, and $\mathbf{H}_{\mathbf{core}}$ includes all one-electron terms. We construct the *J*- and *K*-matrices entirely on the GPU and transfer the resulting matrices to the CPU, where they are augmented with the one-electron term to yield the final Fock matrix. Subsequent SCF operations, such as the transformation of **F** to an orthogonal basis set and its subsequent diagonalization, are performed either on the GPU (dgemm calls to the NVIDIA CUBLAS library) or on the CPU (dsyevd calls to the Intel MKL 10.0.3.020 library). All operations performed on the CPU are carried out in full 64-bit arithmetic, while the operations on the GPU may be carried out in 32-bit, 64-bit, or hybrid of 32-bit and 64-bit arithmetic as discussed below.

Organization and Prescreening of Integrals

Efficient algorithms on the GPU require careful attention to the relationship between data storage and computation. We view the fundamental data structure in the direct SCF problem as an $N^2 \times N^2$ matrix of integrals, where the row and column indices correspond to $[\mu\nu|$ (*bra*) and $|\lambda\sigma]$ (*ket*) pairs; two such pairs, when combined together, index a primitive $[\mu\nu|\lambda\sigma]$ integral. For each *bra* and *ket* pair, one can define a Schwartz upper bound[14] such that the product of the bounds for *bra* and *ket* provides an upper bound to the corresponding [*bra*|*ket*] integral. The left panel of Figure 1 depicts this structure graphically for the specific case of the ethane molecule, using blue−pink coloration to denote the magnitude of the corresponding bound. The *bra* and *ket* pairs are sorted according to $\mu\nu$ and $\lambda\sigma$ basis function types (our code currently supports s- and p-type basis functions, although implementation of higher orbital momentum functions is underway; and there are three possible combinations if s- and p-functions are involved, *ss*, *sp*, and *pp*), resulting in an ERI grid that is well ordered with respect to $[\mu\nu|\lambda\sigma]$ integral types. As we have discussed previously,[6] this grouping makes it possible to efficiently calculate the different angular momentum classes of integrals. However, incorporating prescreening into the algorithm (ignoring integrals that are known by the Schwartz bound to be below a given numerical threshold) leads to load balancing problems because the integrals that still need to be computed are scattered in irregular fashion throughout the integral matrix. Thus, we further presort the *bra* and *ket* pairs (within each angular momentum class) according to the pair's contribution to the Schwartz bound. This leads to a well-ordered integral grid as shown in the right panel of Figure 1. This arrangement of the integral matrix leads to efficient algorithms on the GPU, as discussed below.

J-Matrix Algorithm

The *J*-matrix is formed directly from primitive ERIs using the 1T1PI algorithm, in which each GPU thread evaluates one primitive ERI (or, as we have discussed previously,[6] a batch of ERIs when higher than *s* angular momentum basis functions are involved). The elements of the *J*-matrix are given as:

$$J_{(\mu\nu)} = \sum_{(\lambda\sigma)} P_{(\lambda\sigma)}(\mu\nu|\lambda\sigma) \qquad (3)$$

Following conventional usage,[15−17] we use parentheses or brackets throughout to indicate that the Greek indices refer to contracted or primitive basis functions, respectively. We build the *J*-matrix directly from primitive integrals as:

$$J_{[\mu\nu]} = \sum_{[\lambda\sigma]} P_{[\lambda\sigma]}[\mu\nu|\lambda\sigma] \tag{4}$$

which is then contracted into the final J-matrix:

$$J_{(\mu\nu)} = \sum_{i,j} J_{[\mu_i\nu_j]} \tag{5}$$

where μ_i denotes the ith primitive function contributing to the μth contracted function. Following Ahmadi and Almlof,[18] we first expand the Cartesian Gaussian primitive pair products in terms of a Hermite Gaussian basis set and preprocess the corresponding density matrix elements $P_{[\lambda\sigma]}$ accordingly. For example, each *ss* pair can be expressed with a single (Λ_0) Hermite basis function, while the three products in an *sp* pair (sp_x, sp_y, and sp_z) are expanded over four Hermite basis functions (Λ_0, Λ_x, Λ_y, and Λ_z). Denoting *bra* and *ket* primitive Hermite products as $[p|$ and $|q]$, eq 4 can be written as:

$$\begin{aligned} J_{[\mu\nu]} &= \sum_{[pq\lambda\sigma]} E_{[p]}^{[\mu\nu]} E_{[q]}^{[\lambda\sigma]} P_{[\lambda\sigma]}[p|q] \\ &= \sum_{[pq]} E_{[p]}^{[\mu\nu]} P_{[q]}[p|q] \\ &= \sum_{[p]} E_{[p]}^{[\mu\nu]} J_{[p]}^{\text{Hermite}} \end{aligned} \tag{6}$$

where $E_{[p]}^{[\mu\nu]}$ are the expansion coefficients of the Hermite pair primitive functions in terms of the primitive Cartesian Gaussian basis functions, and the second line defines the preprocessed density matrix in terms of Hermite primitive pair products, $P_{[q]}$. Generation of all required information about the Hermite primitive pair products and preprocessing of the density matrix is carried out on the CPU. The $[p|q]$ integrals are calculated using the McMurchie−Davidson algorithm[19] on the GPU and contracted with the preprocessed density matrix elements to generate $J_{[p]}^{\text{Hermite}}$. Although the integrals are calculated with 32-bit arithmetic, their accumulation is done with double precision accuracy to minimize numerical error accumulation during the summation.[20] The $J_{[p]}^{\text{Hermite}} \rightarrow J_{[\mu\nu]}$ postprocessing (transformation from Hermite to Cartesian) and subsequent $J_{[\mu\nu]} \rightarrow J_{(\mu\nu)}$ contraction are done on the CPU, leading to the final J-matrix.

It is well-known that efficient evaluation of two-electron integrals requires different subroutines for differing angular momentum classes, for example, (*ss*|*ss*) or (*ss*|*sp*). Because efficient execution on the GPU requires maximizing the amount of work for a given kernel (which can loosely be regarded as a subroutine), we have previously described[6] a supergrid representation of the two-electron integrals that allows one to easily treat integrals of the same type together (see Figure 1). For purposes of computational organization, we imagine the primitive integrals $[p|q]$ arranged in a square grid, shown in Figure 2. The $\mu\nu \leftrightarrow \nu\mu$ and $\lambda\sigma \leftrightarrow \sigma\lambda$ index permutation symmetries for the $[\mu\nu|\lambda\sigma]$ integrals are easily incorporated by pruning the list of $[p|$ and $|q]$ pair products, which comprise the rows and columns and the usual postprocessing (e.g., doubling off-diagonal contributions). Thus, the final two-dimensional grid of primitive integrals is of dimension $N(N+1)/2 \times N(N+1)/2$. The index-symmetry pruned list of $[p|$ and $|q]$ pair products are sorted according to their Schwartz upper bounds:

$$[p|_{\text{Schwartz}} = \sqrt{[p|p]} \tag{7a}$$

$$|q]_{\text{Schwartz}} = |P_{\lambda\sigma}|^{\max}\sqrt{[q|q]} \tag{7b}$$

where we note that the order of the *bra* and *ket* arrays may be different because we include the density matrix element contribution in the *ket* bound. When the angular momentum of one or both of the basis functions involved in a pair product is greater than *s*, we follow the usual practice of using a single $[p|p]$ in eq 7 corresponding to the pair product with $l = 0$. We also use the maximum of the density matrix elements over all angular momentum components (in the Cartesian representation) in the second line of eq 7. If one considers a basis set containing at most $l = 1$ angular momentum basis functions, the procedure thus boils down to first grouping the $[p|$ and $|q]$ lists by the angular momentum of the Cartesian Gaussians ($\mu\nu$ and $\lambda\sigma$) leading to *ss*, *sp*, and *pp* groups for each of $[p|$ and $|q]$. Each of the resulting six lists is then sorted according to the Schwartz bounds given in eq 7. Nine GPU kernels are then called, one for [*ss*|*ss*], [*ss*|*sp*], [*ss*|*pp*], [*sp*|*ss*], and so on. All of the GPU kernels were hand-coded; however, an automatic GPU code generation tool for basis sets with higher angular momentum is currently under development in our group.

At this point, we simplify the description of our implementation by considering only one of the integral classes, for example, [*ss*|*ss*]. All other integral classes are treated similarly. Figure 2 depicts the primitive integral grid for a representative integral class, with the pink/blue color scheme denoting the magnitude of the primitive integral Schwartz upper bounds as in Figure 1. The triangles above and to the left of the grid represent the Schwartz bounds for *ket* and *bra*, respectively. Each small cyan-bordered square in Figure 2 represents a single $[p|q]$ primitive integral. It is easily seen that each row of this integral matrix contributes to a single matrix element of J^{Hermite}. As mentioned above, each primitive integral will be computed by a single GPU thread; that is, each small square will translate to a GPU thread. The organization into thread blocks is indicated by the orange squares; that is, each orange square translates to a thread block. We show a 2×2 arrangement of threads into thread blocks for illustration in Figure 2, but the actual implementation uses an 8×8 arrangement, which we found to be optimal. To utilize memory effectively, the integral matrix is processed by columns, assigning thread blocks to each column. Each thread in each thread block calculates the appropriate primitive integral multiplied by the appropriate preprocessed density matrix element. When all threads in these thread blocks are complete, the next group of columns in the integral matrix is processed. The same thread blocks will treat the integrals in a given row, which ensures that they already have the partially formed matrix elements of J^{Hermite} in shared memory. Once all columns have been processed, reduction along the threads in each row of the

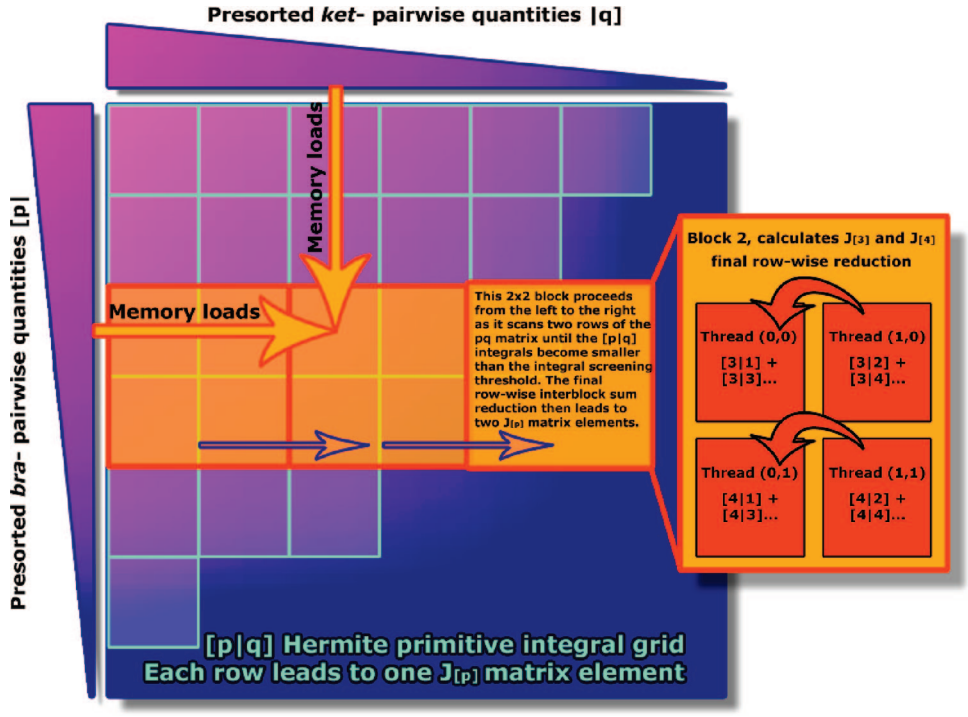

Figure 2. $J_{[p]}$-Matrix formation algorithm for a given angular momentum block, e.g., [*ss*|*ss*]. Cyan-bordered squares depict primitive integrals that need to be evaluated and further contracted into the matrix elements. The *bra*- and *ket*-pair quantities (left and upper triangles) are presorted and lead to a well-organized grid of integrals, whose upper bound is represented by the blue−pink (with pink being largest) color scheme. The orange-bordered squares show those integrals that are evaluated by one block as it scans the integral grid from the left to the right and accumulates the results. Those integrals with Schwartz bound lying below the prescreening threshold (lower-right part of the grid) are ignored. Yellow arrows illustrate the GPU memory load operations.

thread block leads to the final matrix element of J^{Hermite}. These elements are sent to the CPU for postprocessing.

This approach evaluates approximately twice as many integrals as minimally required, because the same integrals are present in distinct rows due to the $[p|q]\leftrightarrow[q|p]$ index permutation symmetry that we do not account for. Our choice was dictated by the interblock communication and memory access collision requirements discussed above, and our implementation completely satisfies both of these requirements. Additionally, this row-wise model is perfectly suitable for multi-GPU parallelization because distinct rows can be sent to different GPUs. Expensive internode communication is avoided because each GPU has all of the data needed to complete its share of the work (these data consist of the pair quantities corresponding to the $[p|$ and $|q]$ lists discussed above).

K-Matrix Algorithm

The computation of the *K*-matrix has very different memory access requirements as compared to the *J*-matrix. Additionally, it is not possible to easily split the work using the pair product representation as outlined for the *J*-matrix above. Therefore, we make no attempt to use the integrals calculated during *J*-matrix construction in the computation of the *K*-matrix. Instead, the *K*-matrix calculation is completely independent of the *J*-matrix calculation. As will be seen below, the data organization is also completely different, and therefore the pair quantities are generated and sorted completely separately. The basic organizational strategy that we use eliminates both interblock communication and memory access collisions by having just one block of GPU threads calculate one $K_{\mu\nu}$ matrix element.

Unlike the *J*-matrix algorithm, the $\mu\lambda\leftrightarrow\lambda\mu$ and $\nu\sigma\leftrightarrow\sigma\nu$ symmetries cannot be exploited because, for example, [*bra*|$\nu\sigma$] and [*bra*|$\sigma\nu$] integrals contribute to distinct *K*-matrix elements and thus reside in different GPU blocks. Exploiting this symmetry would necessitate expensive interblock communication. All [*bra*| and |*ket*] pair-quantities are thus grouped into four rather than three segments (assuming that only s- and p-type basis functions are employed), *ss*, *sp*, *ps*, and *pp*, producing 16 distinct ERI subgrids instead of the nine distinct subgrids depicted in Figure 1. Exploiting the [*bra*|*ket*]↔[*ket*|*bra*] symmetry reduces this to 10 subgrids, because only the upper triangle needs to be considered.

Figure 3 provides more details on the *K*-matrix algorithm using one of the 10 angular momentum subgrids as an example. For each of the angular momentum ERI subgrids, we further group the basis function pairs by the first primitive index. The pair quantities are then sorted by the Schwartz upper bound within each of these classes (angular momentum class and first primitive index), where we do not include the density matrix estimation in the bound computed for either [*bra*| or |*ket*]. Thus, we have a series of [μ...|ν...] blocks (with size $N \times N$) of the integral matrix, each of which contributes to one $K_{\mu\nu}$ matrix element. One GPU thread block is tasked with the evaluation of each $K_{\mu\nu}$ matrix element and winds

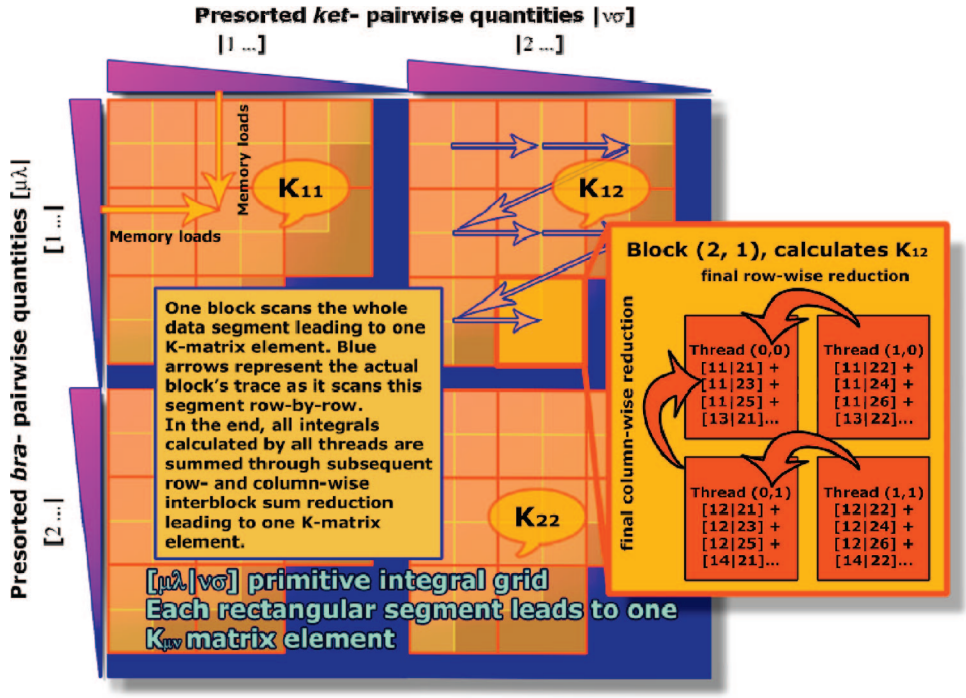

Figure 3. *K*-Matrix formation algorithm. Similar to the *J*-matrix algorithm, but in this case, each GPU thread block scans its own square segment of the integral grid rather than several rows of the whole grid. Each square segment ([1...|1...], [1...|2...], or [2...|2...]) leads to one *K*-matrix element.

its way through the corresponding [μ...|ν...] block as shown for K_{12} in Figure 3. As for the *J*-matrix above, we depict a 2×2 configuration of threads in each thread block, but we use an 8×8 configuration in the code. Even though the Schwartz bounds for neither [*bra*| nor |*ket*] are weighted with the density matrix elements $P_{\lambda\sigma}$, we do utilize the *P*-matrix sparsity. As a thread block scans its way through the [μ...|ν...] block, we monitor the product of the Schwartz upper bound and the density matrix element $P_{\lambda\sigma}$. Once this product falls below the standard ERI threshold (10^{-11} au) multiplied by a "guard" parameter (chosen to be 10^{-5}) for all threads in a warp, we abort the scan of the row and the warp proceeds to the next one. We verified that this procedure does not affect the final SCF energies, while it leads to considerable computational savings. In addition, the integrals are accumulated with double precision accuracy, as described above for Coulomb matrix formation. The McMurchie−Davidson algorithm was used to calculate the ERIs with pre- and postprocessing steps performed inside the GPU kernel. In our *K*-matrix implementation, $O(N^4/2)$ integrals are evaluated. Together with $O(N^4/4)$ ERIs calculated to form the *J*-matrix, the number of integrals calculated at each Fock matrix formation step is $O(3N^4/4)$, that is, 6 times more than the number of unique ERIs. Despite this apparent computational inefficiency, the GPU is still able to achieve significant performance gains as compared to traditional CPU implementations. In addition, the *K*-matrix algorithm possesses the same level of parallelism as does the *J*-matrix algorithm, making the whole Fock matrix formation step suitable for implementation on multi-GPU platforms.

Multi-GPU Parallelization

We have also investigated the possibility of using multiple GPUs in parallel. Our parallel *J*-matrix algorithm maps different rows of the [*p*|*q*] Hermite integral matrix to different GPUs cyclically. Each GPU thus computes its own subset of the $J^{\text{Hermite}}_{[p]}$ matrix that is then copied to the host. In the parallel *K*-matrix algorithm, different GPUs calculate different rows of the *K*-matrix, which are also mapped to the devices cyclically. Tests performed on a 3-GPU (GTX280) system, vide infra, show reasonable speedups of 2.0−2.8× over a single GPU board for both *J*- and *K*-matrix algorithms. We have not made any attempt at dynamic load balancing in our current implementation, and this is expected to improve the scalability even more, bringing it closer to the ideal 3× speedup.

Table 1. Specifications of Several GPU Kernels Invoked during *J*-Matrix Formation on GeForce 8800GTX[a]

kernel	FLOPs	MOPs	registers per thread	active threads per SM	performance (GFLOPS)	bandwidth (Gbytes/s)
ssss	30	12	20	384	88 (175)	131
sssp	55	15	24	320	70 (174)	71
sspp	84	21	24	320	69 (227)	64
pppp	387	21	56	128	97 (198)	20

[a] Four out of nine kernels are presented. The performance values in parentheses correspond to the test code where some memory load operations were removed as described in the text.

Results and Discussion

A detailed analysis of the performance obtained during *J*-matrix formation for a representative test case is presented in Table 1. Statistics are shown for four of the two-electron integral kernels, which are grouped by the angular momentum of the basis functions involved. The number of floating-point and memory operations (FLOPs and MOPs, respectively) for each kernel were determined by hand-counting

instructions in the intermediate assembly level code generated by the compiler. All floating-point instructions (including division and exponentials) were counted as a single FLOP with the exception of fused multiply add (MAD), which was counted as two FLOPs. For memory operations, we have counted 32-, 64-, and 128-bit memory loads/stores as 1, 2, and 4 MOPs, respectively. Because there is limited local memory (registers) on each SM, the amount of local memory required by each thread executing a kernel impacts the number of threads that can execute simultaneously on a single SM. Thus, we show the number of registers required for each thread by the different kernels in Table 1. As this number increases, the number of threads that can be active on a single SM decreases. This is generally expected to reduce the ability to hide memory access latency effectively.

The GPU hides on-board memory access latency (typically constituting hundreds of clock cycles) by time-sliced execution of a large number of parallel threads (up to 768 parallel threads can run on each SM, and one GeForce 8800GTX card has 16 SMs). Once a thread issues a memory access instruction, the warp scheduler switches to other warps, thus keeping the whole device busy. If the number of active warps is not large enough, the computation can stall because all active warps will eventually be waiting for data to return from memory accesses. In fact, the number of active warps is solely determined by the amount of resources (registers, shared memory, etc.) the GPU kernels consume, and it is highly desirable to develop "light" kernels to ensure that many GPU threads can execute in parallel. We present both the number of registers allocated per thread and the consequent number of active threads running on one SM in Table 1. Obviously, the more registers a kernel consumes the less threads are active (i.e., run in parallel), and memory latency hiding becomes less efficient. This adversely affects the sustained bandwidth[21] (last column in Table 1).

A single GeForce 8800GTX card can provide up to 350 GFLOP/s (GFLOPS) computational performance. How much of this power can be harnessed in quantum chemistry calculations? The results from our current implementation are shown in the "performance" column in Table 1. The kernels sustain close to 30% of the theoretical peak performance. Although we consider this level of performance to be quite reasonable for a complex task like Fock matrix formation, one might wonder how to further improve. To determine the extent to which memory bandwidth is controlling the observed performance, we removed the fundamental integral interpolation table and density matrix element loads, replacing the corresponding variables by arbitrary constants. The resulting performance is represented in parentheses in the "performance" column of Table 1. Even though this code transformation does not change the number of FLOPs executed by each kernel, the sustained performance increases by a factor of 2 or even more. This demonstrates that our current implementation is limited by memory bandwidth. Presumably, some part of the memory latency effect is generated by the fundamental integral interpolation table lookup routines that access the device memory in random fashion, making it difficult for the hardware to coalesce such random loads into one memory operation. We are currently developing a scheme that better meets the GPU memory access requirements.

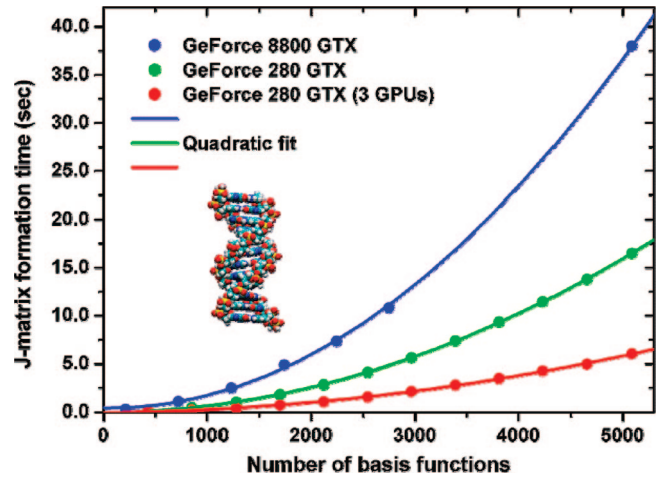

Figure 4. Timings for *J*-matrix construction on a GPU for a series of DNA duplexes using the 3-21G basis set. The solid line is a quadratic fit, showing that our GPU algorithm exhibits ideal quadratic scaling with as few as 500 basis functions. The performance of the algorithm on a multi-GPU system is also shown, indicating its efficient parallel performance.

A series of *J*-matrix formation benchmarks has been performed on duplex-strands of DNA, containing an increasing number of base pairs using the 3-21G basis set. The *J*-matrix formation timings are presented in Figure 4 as a function of the total number of basis functions. Significant acceleration is achieved, allowing the calculation of electronic structure for molecules with up to a thousand basis functions in a matter of seconds. Moreover, the timings are accurately fitted by a quadratic polynomial showing that our algorithm exhibits perfect quadratic scaling already for a few hundred basis functions. This is because of the efficient treatment of prescreening arising from the sorting of the [*bra*| and |*ket*] lists described above. The timings reported in Figure 4 include CPU-side work, for example, sorting and calculation of pair quantities, as well as GPU−CPU data exchange. One can see from Figure 4 that the latest GeForce 280GTX card is significantly faster than the GeForce 8800GTX and furthermore that our parallel implementation achieves a 2.8× speedup using three 280GTX cards.

As pointed out earlier, the GPU architecture is very different from that of CPU, and one might therefore expect that programs optimized for CPU architectures will not fully benefit from the computational power provided by modern streaming processors. Recently, Yasuda[7] reported GPU acceleration of *J*-matrix formation in a development version of the Gaussian electronic structure code. Comparison with the present results allows one to get a sense of the performance gains that can be achieved by careful choice of "stream-friendly" algorithms, as opposed to retrofitting existing CPU algorithms. Thus, we obtained timings on the same GPU hardware used by Yasuda (8800GTX) for *J*-matrix formation for taxol and valinomycin using the 3-21G and 6-31G basis sets. The comparison with timings from our code (including pre- and postprocessing steps performed on the CPU and CPU−GPU data transport overhead) is shown in Table 2. Yasuda's implementation uses

Table 2. *J*-Matrix Formation Time (in seconds) for Taxol and Valinomycin Molecules Using 3-21G and 6-31G Basis Sets[a]

	J-matrix formation time (s)			
	Gaussian on GPU[7]		present work	
molecule	3-21G	6-31G	3-21G	6-31G
taxol	16.8	31.9	0.60	1.65
valinomycin	23.8	57.4	1.05	3.05

[a] Previously reported GPU-accelerated timings based on modifying an existing code (Gaussian) are compared to timings from our code, which has been completely redesigned for stream processors. This comparison emphasizes the gains that can be achieved by redesigning an entire SCF code for stream processing, as opposed to porting an existing CPU algorithm. All timings were obtained on one GeForce 8800GTX card.

multipole methods on the CPU for all far-field contributions (not included in the timings in Table 2), while we evaluate all two-electron integrals explicitly. Thus, this comparison is strongly tilted in favor of Yasuda's implementation. Nevertheless, we find that our code is between 20 and 30 times more efficient than the previous implementation. Of course, neither of these implementations is fully optimized, but the results suggest that there is compelling reason to rethink electronic structure algorithms in the context of streaming processor architectures.

To further demonstrate the effectiveness of quantum chemistry on the GPU, we performed ab initio Monte Carlo (AIMC) simulation of two molecular systems on one GeForce 8800GTX card using the 3-21G basis set: (1) a cluster of 10 rigid water molecules, and (2) the neutral photoactive yellow protein (PYP) chromophore[22] solvated by 45 rigid water molecules. In both cases, the temperature was set at 300 K. Two AIMC runs were performed for the water cluster, and one AIMC run for the solvated PYP chromophore with fixed geometry. Following Wales and Hodges,[23] all MC iterations were grouped into two sets: displacements and rotations, each containing 30 successive MC steps. In the former set, all water molecules were randomly displaced along the three axes, while in the latter set, each water molecule was randomly rotated about the oxygen atom. The displacement and rotation parameters were independently adjusted during the simulations to provide an acceptance ratio of 30−40% in both sets. All water molecules were displaced or rotated in each MC iteration. The initial positions of the water molecules in all three runs were generated randomly; that is, we did not use any pre-equilibration techniques like simulated annealing. The left panel in Figure 5 shows two of the $(H_2O)_{10}$ configurations found after the MC procedure. When further optimized to the nearest energy local minimum, both of these form well-known structures that have been previously characterized.[24] The right panel of Figure 5 shows a snapshot from the solvated PYP chromophore simulation. On average, one MC step required 0.5 and 14 s for the water cluster and solvated chromophore simulations, respectively. Out of these 14 s for the solvated chromophore, a noticeable part of the time was spent on the one-electron integral evaluation (3.4 s) and Fock matrix diagonalization (2.4 s) steps that are currently performed on the host CPU. For bigger systems, the impact of linear algebra (matrix multiplication and diagonalization) will grow in significance because of its cubic scaling as compared to the quadratic scaling of Fock matrix formation. A similar problem emerged as linear scaling electronic structure methods[25] were developed, and we are currently investigating the use of alternatives to diagonalization such as pseudodiagonalization and density matrix purification.[26]

Furthermore, we performed a series of restricted Hartree−Fock direct-SCF benchmarks on caffeine ($C_8N_4H_{10}O_2$), cholesterol ($C_{27}H_{46}O$), buckyball (C_{60}), taxol ($C_{45}NH_{49}O_{15}$), valinomycin ($C_{54}N_6H_{90}O_{18}$), CLN025 (a recently reported[27] "artificial protein," $C_{62}N_{11}H_{97}O_{32}$), and olestra ($C_{156}H_{278}O_{19}$) test molecules, depicted in Figure 6, using the 3-21G and 6-31G basis sets and incremental Fock matrix formation procedure.[13] These tests are run on three different GPU systems: one GeForce 8800GTX, one GeForce 280GTX, and three GeForce 280GTX cards that operate in parallel. Because the GeForce 280GTX supports 64-bit DP floating point operations in hardware, we modified the original *J*-matrix code to perform DP accumulation of the J_p^{Hermite} and $K_{\mu\nu}$ matrix elements to avoid additional error introduced by summation of two-electron integrals of widely varying magnitudes. In this case, the ERIs themselves are still evaluated in 32-bit arithmetic on the GPU. All GPU calculations on the 8800GTX card were performed with 32-bit single precision (SP) accuracy. In all of the benchmarks, an integral screening threshold of 10^{-11} au was used.

Tables 3 and 4 summarize the performance results. The "speedup" column represents the speedups achieved in the first (and generally most time-consuming) direct SCF iteration, as compared to GAMESS ver. 11 Apr 2008 (R1) linked to Intel MKL ver. 10.0.3.020 running on a single Intel Pentium D 3 GHz core. Even though our algorithm calculates a significant number of redundant two-electron integrals (6 times more than the number of unique ERIs), the resulting performance is remarkable. In many cases, the GPU code using a single GTX280 card is more than 100× faster than the CPU. Numbers in parentheses in the "GPU" column of Table 3 represent the fraction of one SCF iteration time required to construct the Fock matrix. For small- and medium-sized molecules, most of the SCF time is devoted to Fock matrix formation. However, for large molecules, the linear algebra calls (we use standard dgemm and dsyevd routines from the NVIDIA CUBLAS and Intel MKL library, correspondingly) become a bottleneck. The olestra molecule is a typical example that experiences such performance degradation (Table 5); the linear algebra functions (on the GPU and CPU) take as much as 50% of the Fock matrix computation time (on the GPU). Because general matrix multiplication and diagonalization algorithms scale cubically with the number of contracted basis functions, this impact will be even larger for larger molecules.

In Table 5, we provide detailed timing information for different parts of the SCF procedure. For small and medium molecules, most of the SCF iteration time is spent on the Fock matrix construction that is done on the GPU. However, for the larger molecules, we find that the linear algebra (performed on the GPU and CPU) begins to constitute a major part of the SCF iteration time. We also

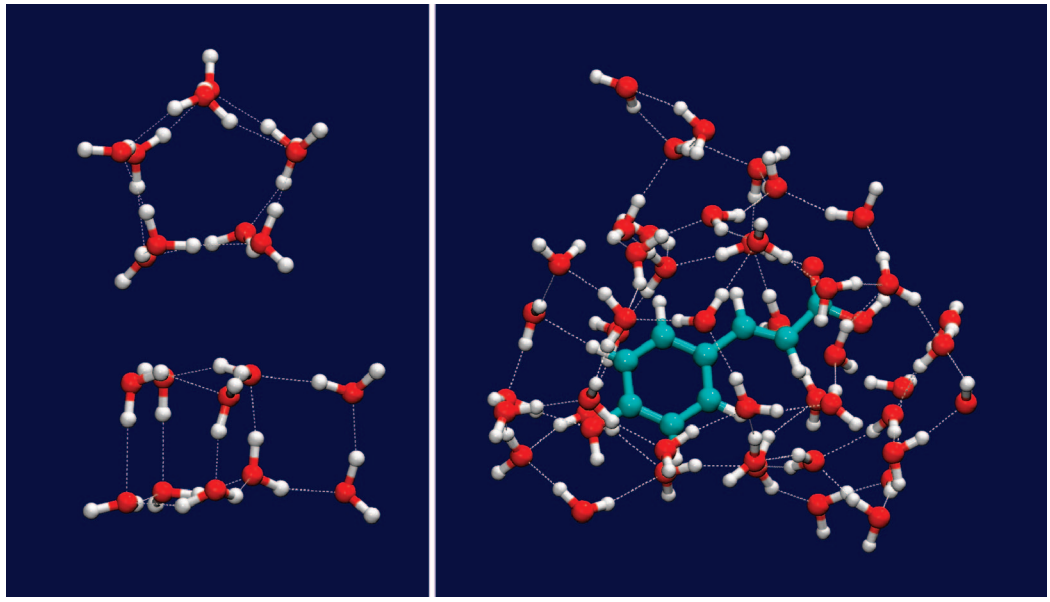

Figure 5. Equilibrated structures from ab initio Monte Carlo simulations at 300 K on the GPU. (Left) Two (upper and lower) representative structures of a cluster with 10 water molecules. (Right) Representative equilibrium structure of the neutral form of the photoactive yellow protein (PYP) chromophore microsolvated with 45 water molecules.

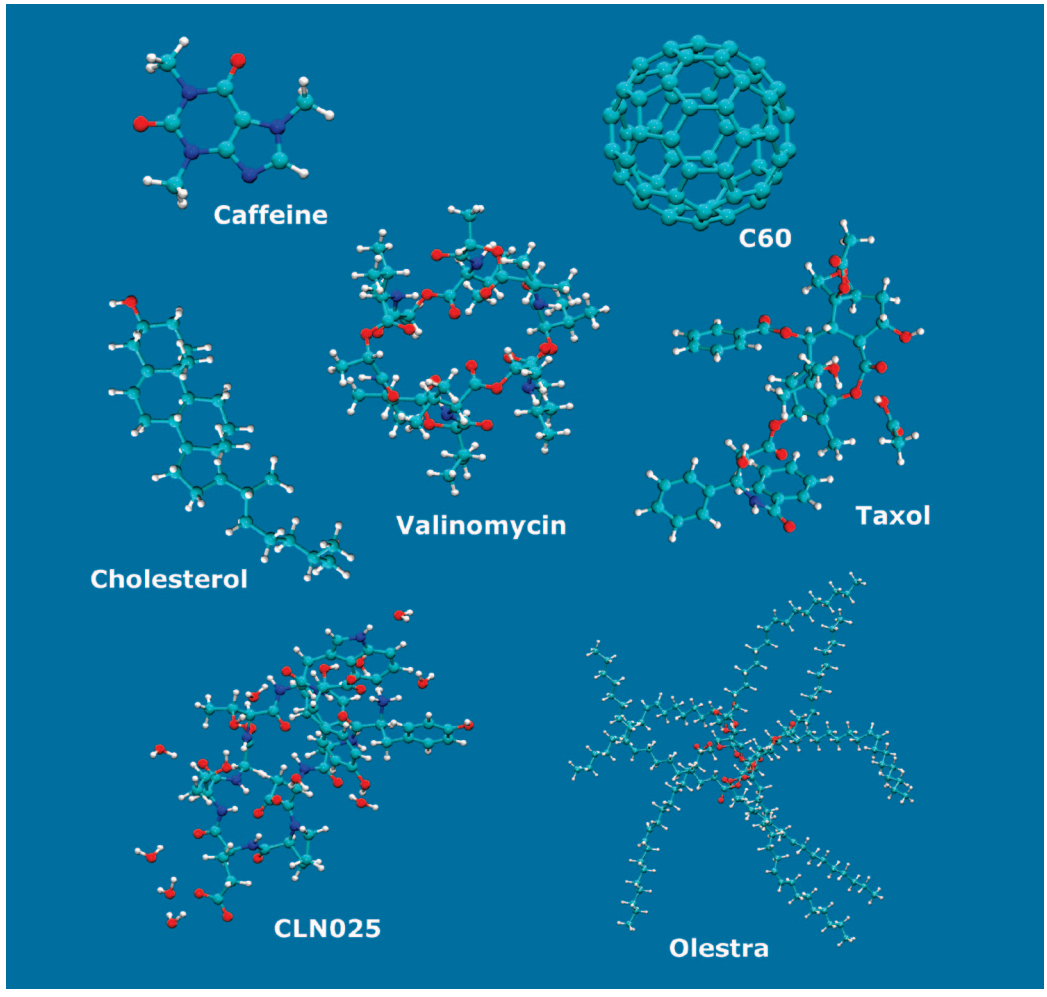

Figure 6. Structures of seven molecules used in the direct-SCF benchmark.

demonstrate that the amount of time required for the presorting of pair quantities is a completely negligible portion of the SCF iteration time. We have pointed out that the dense integral grid resulting from this presorting is critical for efficient GPU computation. However, this step may also be beneficial for traditional CPU imple-

Table 3. Accuracy and Performance of the Direct-SCF Algorithm on One GeForce 280GTX GPU with DP Accumulation of 32-bit Integrals Using the 3-21G Basis Set[a]

	time for the first direct-SCF iteration (s)		electronic energy (au)		
molecule (atoms; basis functions)	GPU	GAMESS	GPU (32 + 64 bit)	GAMESS	speedup
caffeine (24; 146)	0.10 (98%)	4.4	−1605.91830	−1605.91825	44
cholesterol (74; 344)	0.78 (94%)	66.8	−3898.82172	−3898.82189	86
buckyball (60; 540)	3.87 (96%)	353.9	−10 709.08339	−10 709.08392	91
taxol (110; 647)	2.99 (92%)	282.0	−12 560.68286	−12 560.68278	94
valinomycin (168; 882)	5.45 (91%)	729.9	−20 351.98981	−20 351.99038	134
CLN025 (202; 1139)	10.20 (90%)	1405.2	−30 763.37801	−30 763.37882	138
olestra (453; 2131)	19.09 (67%)	12408.1	−49 058.97636	−49 058.97814	650

[a] Reference calculations are performed on a single core of Intel Pentium D 3 GHz processor with full 64-bit DP accuracy. Numbers in parentheses represent the fraction of SCF computation time devoted to Fock matrix formation.

Table 4. Similar to Table *3*, but for 6-31G Basis Set[a]

					GPU speedup		
molecule	electronic energy GPU_{32+64}	ΔE_{32} (mH)	ΔE_{32+64} (mH)	GAMESS CPU time (s)	G80	280GTX	3 × 280GTX
caffeine	−1609.37202	0.06	0.10	7.6	19	28	42
cholesterol	−3904.55935	0.35	0.04	113.9	40	56	120
buckyball	−10 721.02377	−2.84	0.80	589.9	37	57	155
taxol	−12 575.56452	0.07	0.29	476.8	46	64	145
valinomycin	−20 371.17351	3.32	0.61	1226.3	67	90	222
CLN025	−30 791.12220	5.94	1.11	2274.7		92	225
olestra	−49 097.16184	36.55	0.44	14 079.2	199	352	696

[a] Errors in the electronic energy (in millihartree) are shown for both 32-bit (ΔE_{32}, G80) and mixed 32 + 64-bit (ΔE_{32+64}, 280GTX) accumulation of the Fock matrix. In all cases, the two-electron integrals are generated on the GPU using 32-bit arithmetic. Speedups (wall clock time, referencing the first SCF iteration) are quoted for the older 8800GTX card, the newer 280GTX card, and a parallelized implementation using three 280GTX cards (3 × 280GTX). All timings refer to the first SCF iteration.

Table 5. Timing Data (in seconds) for Different Steps of the SCF Procedure (the First Iteration, 3-21G Basis Set)[a]

				Fock matrix (first iteration)			
molecule	density	1e Ints	initial guess	pair sort	*J*	*K*	linear algebra
caffeine	0.00	0.01	0.96	0.00	0.02	0.06	0.02
cholesterol	0.00	0.09	0.99	0.04	0.14	0.55	0.05
buckyball	0.01	0.21	1.05	0.09	0.58	3.04	0.15
taxol	0.02	0.30	1.10	0.11	0.43	2.21	0.22
valinomycin	0.03	0.71	1.25	0.19	0.78	3.97	0.48
CLN025	0.06	1.13	1.48	0.29	1.26	7.66	0.93
olestra	0.28	2.88	3.20	0.67	2.54	9.65	5.95

[a] The Fock matrix formation consists of three steps: presorting of the pair-quantities (done on the host CPU), and the *J*- and *K*-matrix formation steps (done on the GPU) as described in the text. These timing data were obtained using a 2.66 GHz Intel Core2 Quad CPU and a GeForce 280GTX GPU.

mentations, because it will improve cache utilization and the efficiency of integral prescreening.

Another important question under consideration is the accuracy one can attain on the GPU. The 8800GTX hardware used in our first calculations natively supports only 32-bit arithmetic operations; thus only 6−7 significant figures of accuracy should be expected in the final result. This may not be enough for large molecules where the absolute total energy exceeds 10^4 hartree, because one wants energy differences to be accurate at the millihartree level or better. The absolute energy error generated by 32-bit GPU arithmetic (and 32-bit accumulation of the Fock matrix elements) as compared to 64-bit calculations on the CPU (GAMESS) using 6-31G basis sets is shown in the column labeled ΔE_{32} of Table 4. The GPU provides submillihartree accuracy for the taxol molecule, but the absolute errors exceed the millihartree level for larger molecules.

The major contribution to the resulting energy error is made by two-electron integrals with relatively large magnitudes, because the mantissa of a 32-bit number is not capable of holding enough significant figures to provide the required accuracy (typically, 10^{-11} hartree). Yasuda has suggested the computation of the largest ERIs on the CPU with DP accuracy to avoid this problem. Both our *J*- and *K*-matrix algorithms already use presorted integral grids, and splitting the grids into DP and SP subgrids, according to the ERI Schwartz upper bound, is straightforward and will not cause any additional computational overhead. This will be investigated in future work. A second contribution to the precision error lies in the summations that lead to the final *J*- and *K*-matrices. Using the DP capability of the 280GTX, we have implemented these summations in DP, while the integrals themselves are still calculated in 32-bit precision. This leads to the errors listed in the column of Table 4 labeled ΔE_{32+64}. The use of DP accumulation improves the accuracy sometimes by better than an order of magnitude (at negligible computational cost), and calculations on molecules as large as olestra are within "chemical accuracy", typically defined as 1 kcal/mol.

Additionally, because many of the large two-electron integrals are produced by core orbitals that are chemically inert, their corresponding contributions may be expected to cancel (at least partially) when energy differences are computed, as previously shown by Kermes et al. in calculations of the correlation energy.[4] Direct tests performed on a GeForce 8800GTX card (32-bit integrals and 32-bit accumulation) on a cholesterol molecule confirm this. We

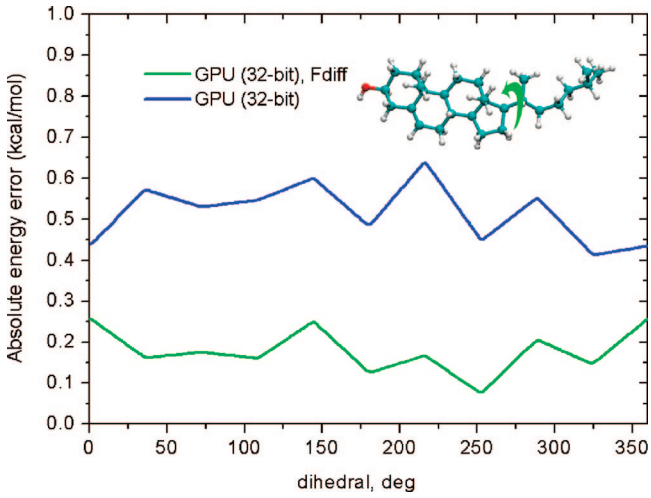

Figure 7. The absolute energy error produced by 32-bit calculations of the cholesterol (3-21G basis set) molecule on the 8800GTX GPU, as the molecule is twisted around one of its bonds. Conventional (blue) and incremental (green) Fock matrix formation approaches are presented. The reference 64-bit data were generated by GAMESS.

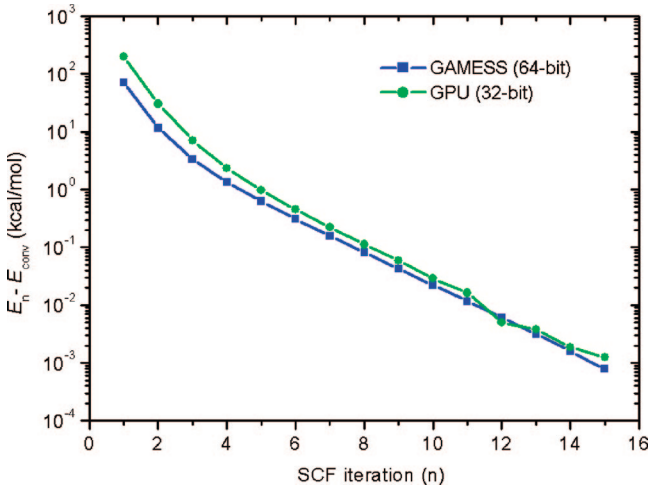

Figure 8. Convergence of the SCF energy for the cholesterol molecule (3-21G basis set) using the 8800GTX GPU and CPU. The convergence behavior is nearly identical, showing that the single precision evaluation of the integrals has no adverse effect on SCF convergence.

twisted the molecule around one of the bonds (see inset in Figure 7) and optimized the molecular geometry with DP accuracy, keeping the corresponding dihedral fixed. The corresponding error generated by 32-bit arithmetic for conventional (blue) and incremental (green) Fock matrix formation techniques is displayed in Figure 7. Two characteristic features can be seen in this figure: (1) the incremental approach much better represents 64-bit results, and (2) in both curves, the deviation from the mean is smaller than the absolute values of the errors (presumably due to cancelation of large integrals).

Finally, we investigated the impact of SP accuracy on the SCF convergence behavior using the cholesterol molecule as an example and GeForce 8800GTX GPU, comparing to the 64-bit GAMESS calculation results. Figure 8 presents the SCF energy error, $E_n - E_{conv}$, as it gradually declines at each subsequent SCF iteration, where E_{conv} is the converged energy, which is different for GPU and CPU. The slight initial offset is due to the less accurate initial guess algorithm used in our program. We disabled SCF acceleration both in our code and in GAMESS. The curves in Figure 8 track each other nearly perfectly, meaning there is no convergence instability introduced by 32-bit GPU arithmetic, up to $\Delta E \approx 0.1$ kcal/mol. Of course, eventually unavoidable precision noise will produce less regular behavior if one attempts to converge the energy beyond the 7−8 significant figures that can be obtained with SP arithmetic.

Conclusions

We have demonstrated that it is possible to achieve two order-of-magnitude increases in efficiency for an entire quantum chemistry calculation using GPUs. The speedups we report here (up to 650×) are for the entire direct SCF iteration, and thus representative of the speedup that can be expected for the full SCF calculation. Because of the exceptional performance, we were able to carry out ab initio Monte Carlo simulations for molecular systems with over a hundred atoms. We obtained this level of performance by developing the algorithms from the ground up for use on stream processing architectures. For example, our algorithm calculates many redundant ERIs in recognition of the fact that it can be more efficient to do redundant computation than random memory accesses and/or interthread communication on GPUs. We have further demonstrated the possibility of parallelization over multiple GPUs, which leads to even more significant performance gains.

We showed that the accuracy achieved for energy differences can be significantly higher than that expected from the absolute energies because of systematic cancelation of precision errors largely due to integrals involving the chemically inert core electrons. We demonstrated that using double precision only to preserve accuracy during summation of the density-ERI products provides "chemical accuracy" in all of the absolute energies reported here (as compared to full double precision calculations on the CPU) at negligible computational cost.

The advances reported here will make large-scale quantum chemistry calculations routine and will be especially useful in increasing the utility of ab initio molecular dynamics (AIMD) simulations. We are currently working on an implementation of analytic gradients that is a prerequisite for efficient use in the AIMD context.

Acknowledgment. This work was supported by the National Science Foundation (CHE-06-26354 and DMR-03025939).

References

(1) Anderson, J. A.; Lorenz, C. D.; Travesset, A. *J. Comput. Phys.* **2008**, *227*, 5342.

(2) Stone, J. E.; Phillips, J. C.; Freddolino, P. L.; Hardy, D. J.; Trabuco, L. G.; Schulten, K. *J. Comput. Chem.* **2007**, *28*, 2618.

(3) Anderson, A. G.; Goddard, W. A., III.; Schroder, P. *Comput. Phys. Commun.* **2007**, *177*, 265.

(4) Kermes, S.; Olivares-Amaya, R.; Vogt, L.; Shao, Y.; Amador-Bedolia, C.; Aspuru-Guzik, A. *J. Phys. Chem.* **2007**, *112A*, 2049.

(5) Ufimtsev, I. S.; Martinez, T. J. *Comput. Sci. Eng.* **2008**, *10*, 26.

(6) Ufimtsev, I. S.; Martinez, T. J. *J. Chem. Theory Comput.* **2008**, *4*, 222.

(7) Yasuda, K. *J. Comput. Chem.* **2008**, *29*, 334.

(8) Yasuda, K. *J. Chem. Theory Comput.* **2008**, *4*, 1230.

(9) Brown, P.; Woods, C.; McIntosh-Smith, S.; Manby, F. R. *J. Chem. Theory Comput.* **2008**, *4*, 1620.

(10) Kapasi, U. J.; Rixner, S.; Dally, W. J.; Khailany, B.; Ahn, J. H.; Mattson, P.; Owens, J. D. *Computer* **2003**, *36*, 54.

(11) Schmidt, M. W.; Baldridge, K. K.; Boatz, J. A.; Elbert, S. T.; Gordon, M. S.; Jensen, J. H.; Koseki, S.; Matsunaga, N.; Nguyen, K. A.; Su, S.; Windus, T. L.; Dupuis, M.; Montgomery, J. A. *J. Comput. Chem.* **1993**, *14*, 1347.

(12) NVIDIA CUDA. Compute Unified Device Architecture Programming Guide Version 2.0; NVIDIA Developer Web Site; http://developer.download.nvidia.com/compute/cuda/2_0/docs/NVIDIA_CUDA_Programming_Guide_2.0.pdf (acccessed September 15, 2008).

(13) Almlof, J.; Faegri, K.; Korsell, K. *J. Comput. Chem.* **1982**, *3*, 385.

(14) Whitten, J. L. *J. Chem. Phys.* **1973**, *58*, 4496.

(15) White, C. A.; Head-Gordon, M. *J. Chem. Phys.* **1996**, *104*, 2620.

(16) Gill, P. M. W. *Adv. Quantum Chem.* **1994**, *25*, 141.

(17) Shao, Y.; Head-Gordon, M. *Chem. Phys. Lett.* **2000**, *323*, 425.

(18) Ahmadi, G. R.; Almlof, J. *Chem. Phys. Lett.* **1995**, *246*, 364.

(19) McMurchie, L. E.; Davidson, E. R. *J. Comput. Phys.* **1978**, *26*, 218.

(20) This double precision accumulation is only implemented on the 280GTX card. Results reported using the 8800GTX carry out the accumulation in single precision arithmetic.

(21) The bandwidth reported in Table 1 is an effective bandwidth that may be higher than the actual bandwidth because of caching (of texture memory).

(22) Ko, C.; Levine, B.; Toniolo, A.; Manohar, L.; Olsen, S.; Werner, H.-J.; Martinez, T. J. *J. Am. Chem. Soc.* **2003**, *125*, 12710.

(23) Wales, D. J.; Hodges, M. P. *Chem. Phys. Lett.* **1998**, *286*, 65.

(24) Day, P. N.; Pachter, R.; Gordon, M. S.; Merrill, G. N. *J. Chem. Phys.* **2000**, *112*, 2063.

(25) Scuseria, G. E. *J. Phys. Chem.* **1999**, *103A*, 4782.

(26) Daniels, A. D.; Scuseria, G. E. *J. Chem. Phys.* **1999**, *110*, 1321.

(27) Honda, S.; Akiba, T.; Kato, Y. S.; Sawada, Y.; Sekijima, M.; Ishimura, M.; Ooishi, A.; Watanabe, H.; Odahara, T.; Harata, K. *J. Am. Chem. Soc.* **2008**, *130*, 15327.

CT800526S

JCTC Journal of Chemical Theory and Computation

Evaluation of B3LYP, X3LYP, and M06-Class Density Functionals for Predicting the Binding Energies of Neutral, Protonated, and Deprotonated Water Clusters

Vyacheslav S. Bryantsev,*,† Mamadou S. Diallo,† Adri C. T. van Duin,‡ and William A. Goddard III*,†

Materials and Process Simulation Center, Beckman Institute, MC 139-74, California Institute of Technology, Pasadena, California 91125, and Department of Mechanical and Nuclear Engineering, The Pennsylvania State University, University Park, Pennsylvania 16801

Received December 10, 2008

Abstract: In this paper we assess the accuracy of the B3LYP, X3LYP, and newly developed M06-L, M06-2X, and M06 functionals to predict the binding energies of neutral and charged water clusters including $(H_2O)_n$, $n = 2-8$, 20), $H_3O^+(H_2O)_n$, $n = 1-6$, and $OH^-(H_2O)_n$, $n = 1-6$. We also compare the predicted energies of two ion hydration and neutralization reactions on the basis of the calculated binding energies. In all cases, we use as benchmarks calculated binding energies of water clusters extrapolated to the complete basis set limit of the second-order Møller−Plesset perturbation theory with the effects of higher order correlation estimated at the coupled-cluster theory with single, double, and perturbative triple excitations in the aug-cc-pVDZ basis set. We rank the accuracy of the functionals on the basis of the mean unsigned error (MUE) between calculated benchmark and density functional theory energies. The corresponding MUE (kcal/mol) for each functional is listed in parentheses. We find that M06-L (0.73) and M06 (0.84) give the most accurate binding energies using very extended basis sets such as aug-cc-pV5Z. For more affordable basis sets, the best methods for predicting the binding energies of water clusters are M06-L/aug-cc-pVTZ (1.24), B3LYP/6-311++G(2d,2p) (1.29), and M06/aug-cc-PVTZ (1.33). M06-L/aug-cc-pVTZ also gives more accurate energies for the neutralization reactions (1.38), whereas B3LYP/6-311++G(2d,2p) gives more accurate energies for the ion hydration reactions (1.69).

1. Introduction

There is growing interest and need for describing various phenomena in inhomogeneous aqueous environments, for example, in the context of solvation of neutral and ionic solutes, ion complexation, solute transport, and partitioning at an organic liquid−water interface. Although the importance of polarization and charge transfer in inhomogeneous aqueous environments has been recognized,[1] it has been difficult to explicitly include them in a broadly applicable classical force field. Moreover, only a few empirical potential functions allow autoionization and charge migration.[2] The majority of theoretical studies of aqueous reactions reported thus far are based on the use of wave function methods and density functional theory (DFT).

The selection of the exchange-correlation functional in DFT is critical for correctly predicting the properties of aqueous systems.[3−5] Todorova et al.[3a] reported that hybrid functionals (B3LYP, X3LYP, PBE0) [modified with short-range Hartree−Fock exchange within a plane wave framework] give better results than generalized gradient approximation (GGA) functionals (BLYP, XLYP, and PBE) in

* Corresponding author phone: (626) 395-2730; fax: (626) 585-0918; e-mail: slava@wag.caltech.edu (V.S.B.), wag@wag.caltech.edu (W.A.G.).

† California Institute of Technology.

‡ The Pennsylvania State University.

10.1021/ct800549f CCC: $40.75
Published on Web 03/12/2009

reproducing the experimental structural (radial distribution function) and dynamical (self-diffusion constant) properties of liquid water. Tuckerman et al.[4] employed ab initio molecular dynamics simulations to probe the structure and transport mechanism of OH^-(aq) in water. They compared the performance of three DFT functionals: BLYP, PW91, and HCTC. They found that the BLYP functional reproduced the experimental findings that the diffusion of OH^-(aq) is slower than that of H^+(aq) and much faster than that of pure water. In contrast, the PW91 (HCTC) functional yields a OH^-(aq) diffusion that is too fast (slow) in comparison to a H^+(aq) diffusion.

McGrath et al.[5] showed that the computed thermodynamic properties of water (e.g., vapor−liquid coexistence curves) are sensitive not only to the density functional used, but also to the size of the basis set employed. PBE predicted a higher critical temperature and boiling point than experiment, while BLYP provided a better performance with small basis sets (double- and triple-ζ basis sets). These results were consistent with the ability of PBE and BLYP to describe the energetics of small water clusters. We have recently developed a computational methodology that gives accurate hydration free energies for ionic solutes.[6] This methodology, which couples DFT with mixed cluster/continuum models, is predicated upon the accurate calculations of the difference in total binding energies between relatively large ion−water clusters ($X^{m\pm}(H_2O)_n$) and pure water clusters ($(H_2O)_n$).[6] Thus, the correct description of water and solute−water clusters is critical for the accurate prediction of the thermodynamic properties of pure water and aqueous solutions.

Several reports devoted to the ability of DFT methods to describe hydrogen bonds in water clusters have appeared in the literature.[7−19] However, these previous studies have focused primarily on small neutral water clusters rarely containing more than six water molecules.[10,15,17] Only a few studies have tested the accuracy of DFT methods to predict the binding energies of $H_3O^+(H_2O)_n$ and $OH^-(H_2O)_n$ clusters.[19] Dahlke and Truhlar showed[13] that most of the hybrid functionals (which include Hartree−Fock exchange) gave more accurate binding energies and many-body components of the full interaction energy than the general-purpose GGA functionals. They also pointed out that these results are highly basis set dependent and that the choice of the appropriate basis set for each DFT method is very important for obtaining accurate results.[12,13] Santra et al.[16] examined the performance of density functionals in the limit of a complete basis set and found that the hybrid functionals (X3LYP and PBE0) gave binding energies for water clusters that were in closer agreement with benchmark binding energies calculated at the second-order Møller−Plesset (MP2)/complete basis set (CBS) level of theory. Similarly, Svozil et al.[15] reported improved results with the hybrid functionals (B3LYP and PBE0) for the description of the autoionization of a water octamer.

Zhao and Truhlar have recently developed the M06 family of local (M06-L) and hybrid (M06, M06-2X) meta-GGA functionals that show promising performance for noncovalent interactions.[20] This includes the binding energies in the two HB6/04 and JHB7 hydrogen-bonded databases. M06-L has been shown to provide accurate reaction energies for neutralization reactions involving small hydronium and hydroxide clusters.[19] In addition, M06-L and M06-2X have been tested to reproduce the relative energies of low-lying isomers of water hexamers.[18]

In this paper, we report a comparative study of the accuracy of the B3LYP[21] and X3LYP[22] functionals and the newly developed M06-L, M06-2X, and M06 functionals[20] to predict the binding energies of neutral ($(H_2O)_n$, $n = 2-8$, 20), protonated ($H_3O^+(H_2O)_n$, $n = 1-6$), and deprotonated ($OH^-(H_2O)_n$, $n = 1-6$) water clusters. B3LYP was selected given its widespread use, and X3LYP was included because of its excellent performance on small water clusters.[10,16] The accuracy of each method was evaluated using several basis sets. We also assessed the effect of basis set superposition error (BSSE) correction as calculated for the smallest basis set. As a benchmark for determining the accuracy of DFT functionals, we employed binding energies calculated at the complete basis set limit of the MP2 theory[23] with coupled-cluster theory with single, double, and perturbative triple excitations [CCSD(T)]/aug-cc-pVDZ corrections that were either compiled from the literature or calculated in this work.

2. Computational Methods

We used the second-order Möller−Plesset perturbation theory (MP2)[23] in the complete basis set (CBS) limit and coupled-cluster theory with singles, doubles, and perturbative triples excitations (CCSD(T))[24] in the aug-cc-pVDZ basis set[25] to determine the benchmark binding energies of hydrogen-bonded complexes against which the density functionals are evaluated. The effect of the basis set size (e.g., larger than aug-cc-pVDZ) on CCSD(T) corrections for water[26] and ion−water[27,28] clusters was shown to be relatively small (<0.2 kcal/mol). Thus, the combination of MP2/CBS with CCSD(T)/aug-cc-pVDZ corrections provides an excellent compromise between accuracy and computational cost and thus has been applied to water clusters as large as octamers.

For the basis set expansion in our MP2 calculations, we used a family of augmented correlation-consistent basis sets[25] (aug-cc-pVnZ, n = D, T, Q, 5). Only the valence electrons were correlated in the MP2 calculations. The largest basis set for geometry optimization was aug-cc-pVTZ. A test calculation for $OH^-(H_2O)$ reveals that the O−O distances differ by only 0.002 Å and the binding energies differ by <0.01 kcal/mol when compared to results obtained after full optimization at the MP2/aug-cc-pVQZ level. A BSSE-corrected intermolecular interaction energy (ΔE^b_e) was calculated with each basis set via the function counterpoise method[29] by taking into account the fragment relaxation energy terms resulting from the geometry change of the isolated fragments during the cluster formation:[30a]

$$\Delta E^b_e = E^{full}(\text{full}) - \sum_{\text{fragm}} E^{full}(\text{fragm}) + \sum_{\text{fragm}} \Delta E^{fragm}_{relax}(\text{fragm}) \quad (1)$$

where E^{full} and E^{fragm} are, respectively, the energies calculated with the full and fragment-only basis sets. Compared to the

method of Valiron and Mayer,[30b] which explicitly considers the hierarchy of *N*-body interactions for calculating the BSSE-corrected interaction energy, eq 1 does not include the three-body and higher many-body corrections. To estimate the MP2/CBS limit of the interaction energy, we utilized both the uncorrected and BSSE-corrected energies in an extrapolation scheme based on a polynomial function of inverse powers of 4 and 5:[31−33]

$$\Delta E(n) = \Delta E_{CBS} + B/(l_{max} + 1)^4 + C/(l_{max} + 1)^5 \quad (2)$$

where $n = 2$, 3, 4, and 5 for $n =$ D, T, Q, and 5 in aug-cc-pV*n*Z, respectively, and ΔE_{CBS}, B, and C are the fitting parameters.

We examined the ability of five density functionals [including two hybrid GGAs (B3LYP and X3LYP), one local meta-GGA (M06-L), and two hybrid meta-GGAs (M06-2X and M06)] to reproduce benchmark binding energies (MP2/CBS + ΔCCSD(T)) for a database of 27 pure, hydroxide, and hydronium water clusters. For each of these functionals, three different basis sets were considered: 6-311++G**, aug-cc-pVTZ, and aug-cc-pV5Z. For B3LYP, we also tested an empirically optimized 6-311++G(2d,2p) basis set. The small 6-311++G** basis set was selected as it provides reasonable dissociation energies for covalent bonds[34] and is computationally affordable for relatively large molecular systems. The geometries of all but $(H_2O)_{20}$ clusters were also optimized with the aug-cc-pVTZ basis set. $(H_2O)_{20}$ clusters were optimized using the aug-cc-pVDZ basis set followed by single-point energy calculations with the aug-cc-pVTZ basis set. Finally, single-point energy calculations for complexes containing up to five water molecules were performed using a very large aug-cc-pV5Z basis set. This basis set is sufficient to give converged DFT interaction energies for water clusters[12,16] and is expected to reflect a true performance of the tested functionals at the basis set limit. The BSSE correction in DFT methods is usually much smaller than in the explicitly correlated methods as MP2 and was investigated only for the smallest 6-311++G** basis set.[10,35] All MP2, CCSD(T), and DFT calculations were carried out using the NWChem 5.1 program package.[36] For the numerical integration grid in the DFT methods, the NWChem default grid was used for $(H_2O)_{20}$ in the aug-cc-pVTZ basis set and the ultrafine grid for the rest of the calculations. This corresponds to a target accuracy of 10^{-6} and 10^{-8} hartree, respectively.

3. Database of Accurate Water Cluster Binding Energies

The compiled database consists of 27 cluster binding energies extrapolated to the CBS limit of the MP2 and CCSD(T) theory. This includes a set of 14 neutral water clusters ($(H_2O)_n$, $n = 2-6,8,20$), 5 hydronium ion clusters ($H_3O^+(H_2O)_n$, $n = 1-3,6$), 7 hydroxide ion clusters ($OH^-(H_2O)_n$, $n = 1-6$), and 1 autoionized water cluster ($H_3O^+(H_2O)_4OH^-$). The structures of these clusters are shown in Figure 1, and the Cartesian coordinates (obtained after geometry optimization at the B3LYP/6-311++G(2d,2p) level of theory) are given in the Supporting Information.

Table 1. Total Water Binding Energies for $OH^-(H_2O)_n$ Clusters (kcal/mol)[a]

method	$OH^-(H_2O)$		$OH^-(H_2O)_2$		$OH^-(H_2O)_3$		$OH^-(H_2O)_4$ (C_s)		$OH^-(H_2O)_4$ (C_4)		$OH^-(H_2O)_5$		$OH^-(H_2O)_6$	
	$-\Delta E_e$	$-\Delta E^b_e$	$-\Delta E_e$	$-\Delta E^b_e$	$-\Delta E_e$	$-\Delta E^b_e$	$-\Delta E_e$	$-\Delta E^b_e$	$-\Delta E_e$	$-\Delta E^b_e$	$-\Delta E_e$	$-\Delta E^b_e$	$-\Delta E_e$	$-\Delta E^b_e$
MP2/aug-cc-pVDZ	26.73	24.68	48.65	45.13	68.07	62.82	85.86	78.40	85.86	78.63	101.95	92.65	117.96	106.26
MP2/aug-cc-pVTZ	27.17	25.85	49.12	47.04	68.22	65.30	86.04	81.85	85.61	81.67	101.87	96.69	117.52	111.12
MP2/aug-cc-pVQZ[b]	26.95	26.12	48.80	47.56	67.76	66.15	85.30	83.03	84.86	82.78	100.86	98.15	116.15	112.86
MP2/aug-cc-pV5Z[b]	26.71	26.27	48.49	47.81	67.36	66.50	84.72	83.51	84.32	83.22	100.16		115.33	
MP2/aug-cc-pV6Z[b]	26.62	26.36												
MP2/CBS (eq 2)	26.40	26.48	47.97	48.10	66.71	66.86	83.84	84.00	83.51	83.66	99.12	99.39	114.19	114.33
MP2/CBS best estimate[c]	26.44 ± 0.04		48.04 ± 0.06		66.79 ± 0.07		83.92 ± 0.08		83.58 ± 0.07		99.26 ± 0.13		114.26 ± 0.07	
MP2/CBS (ref 28)	26.4−26.5		47.8−48.2											
MP2/CBS + ΔCCSD(T)[d]	26.59		48.39		67.58		84.84		84.79		100.66		115.69	

[a] ΔE_e and ΔE^b_e are uncorrected and BSSE-corrected energies, respectively. [b] Single-point energies on MP2/aug-cc-pVTZ-optimized geometries. [c] Obtained as an average of the extrapolated CBS values of ΔE_e and ΔE^b_e. [d] CCSD(T) corrections are calculated using the aug-cc-pVDZ basis set.

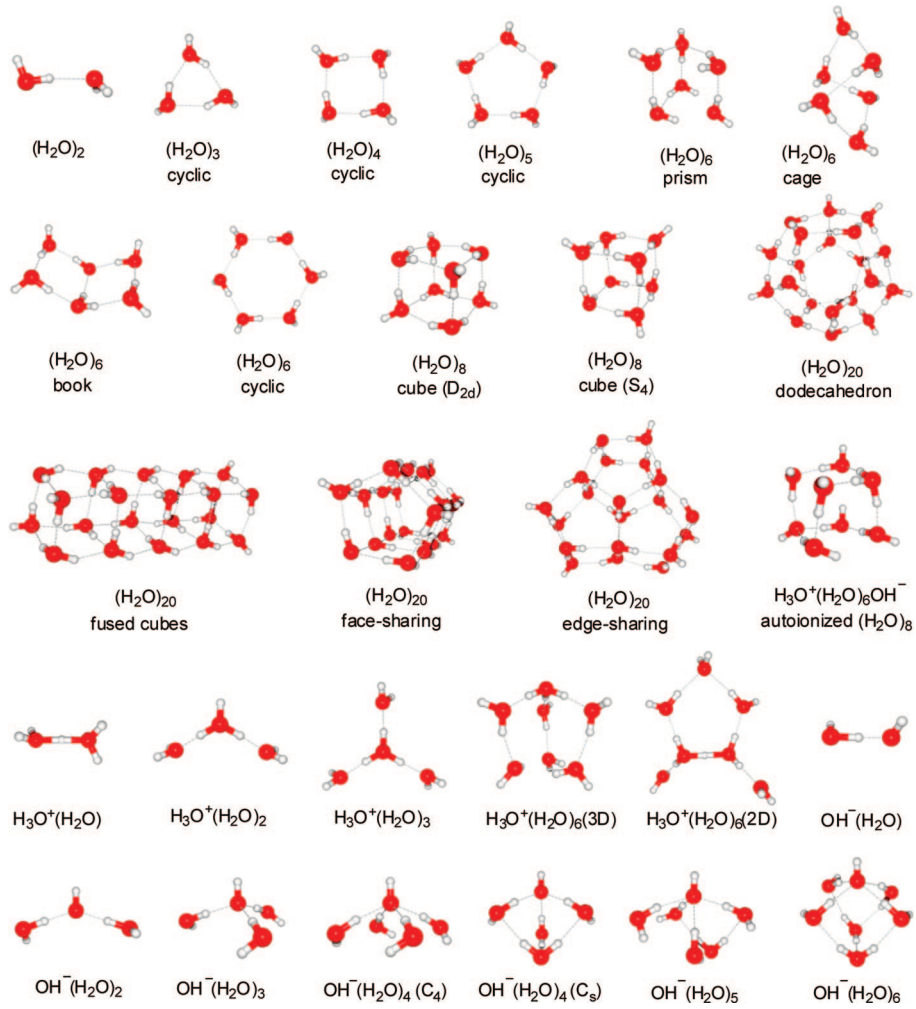

Figure 1. Structures of the studied pure, protonated, and deprotonated water complexes.

The structures and MP2/CBS binding energies of the neutral water clusters were taken from Xantheas and co-workers.[26,31−33] The reference binding energies of the lowest energy protonated water clusters $H_3O^+(H_2O)_{1-3}$ were computed in this study (see section 4.1). The estimated CCSD(T)/CBS interaction energies and the starting geometries of the two $H_3O^+(H_2O)_6$ isomers were taken from Shin et al.[37] (denoted as $2D_a$ and $3D_1$ in Figure 2 of ref 37). For the $OH^-(H_2O)_{1-6}$ clusters, the starting structures were based on the lowest energy conformers reported by Lee et al.[38] The results of high-level ab initio calculations for these systems are presented in section 4.1. The structure and relative energy of the autoionized water octamer [with respect to the S_4 cubic structure] at the MP2/CBS + ΔCCSD(T) level were taken from Svozil et al.[15] We expect the database of binding energies presented in this paper to have an accuracy of 0.5 kcal/mol or better and thus serve as a reliable benchmark for evaluating other methods.

4. Results and Discussion

4.1. Benchmark Binding Energies: MP2 and CCSD(T). The benchmark MP2 binding energies of the $OH^-(H_2O)_{1-6}$ and $H_3O^+(H_2O)_{1-3}$ clusters calculated with a series of correlation-consistent basis sets (aug-cc-pV*n*Z, n = D, T, Q, and 5) are shown in Tables 1 and 2, respectively. Figure 2 illustrates the effects of basis set size on the uncorrected and BSSE-corrected binding energies (ΔE_e and ΔE^b_e) for $OH^-(H_2O)$ and $H_3O^+(H_2O)$ complexes, respectively. A decrease of ΔE_e in going from the aug-cc-pVDZ to the aug-cc-pVTZ basis set is a typical feature of ion−water clusters,[30a] different from that for neutral water clusters.[31−33] However, such a minimum in ΔE_e for the aug-cc-pVTZ basis set becomes less pronounced with increasing size of a cluster and vanishes for $OH^-(H_2O)_{5-6}$.

The results in Tables 1 and 2 suggest that the magnitude of the BSSE correction decreases by 35−50% for each succeeding aug-cc-pV*n*Z set: For $OH^-(H_2O)$, for example, the BSSE correction is 2.05 (aug-cc-pVDZ), 1.33 (aug-cc-pVTZ), 0.83 (aug-cc-pVQZ), 0.44 (aug-cc-pV5Z), and 0.26 (aug-cc-pV6Z) kcal/mol. This trend points to a meaningful extrapolation toward a CBS limit, provided that sufficiently large basis sets are employed. We subsequently tested several extrapolation schemes based on exponential,[39] mixed exponential/Gaussian,[40] and inverse polynomial[31−33,41] functions. We found that a polynomial dependence of inverse powers of 4 and 5 (eq 2) gives the smallest difference of the extrapolated CBS values for the uncorrected and BSSE-corrected binding energies. This is the same CBS extrapolation scheme used by Xantheas and co-workers in their study of neutral water clusters.[31−33] The energies calculated with

Table 2. Total Water Binding Energies for $H_3O^+(H_2O)_n$ Clusters (kcal/mol)[a]

	$H_3O^+(H_2O)$		$H_3O^+(H_2O)_2$		$H_3O^+(H_2O)_3$	
method	$-\Delta E_e$	$-\Delta E^b_e$	$-\Delta E_e$	$-\Delta E^b_e$	$-\Delta E_e$	$-\Delta E^b_e$
MP2/aug-cc-pVDZ	34.05	31.77	57.81	54.35	77.82	73.13
MP2/aug-cc-pVTZ	34.55	33.29	58.13	56.43	77.97	75.68
MP2/aug-cc-pVQZ[b]	34.42	33.70	57.98	57.02	77.70	76.45
MP2/aug-cc-pV5Z[b]	34.27	33.91	57.75	57.28	77.40	76.77
MP2/CBS (eq 2)	34.00	34.18	57.33	57.58	76.89	77.13
MP2/CBS best estimate[c]	34.09 ± 0.09		57.46 ± 0.12		77.01 ± 0.12	
MP2/CBS (ref 27)	34.1−34.2		57.6−57.7			
MP2/CBS + ΔCCSD(T)[d]	33.53		56.85		76.46	

[a] ΔE_e and ΔE^b_e are uncorrected and BSSE-corrected energies, respectively. [b] Single-point energies at the MP2/aug-cc-pVTZ-optimized geometries. [c] Obtained as an average of the extrapolated CBS values of ΔE_e and ΔE^b_e. [d] CCSD(T) corrections are calculated using the aug-cc-pVDZ basis set.

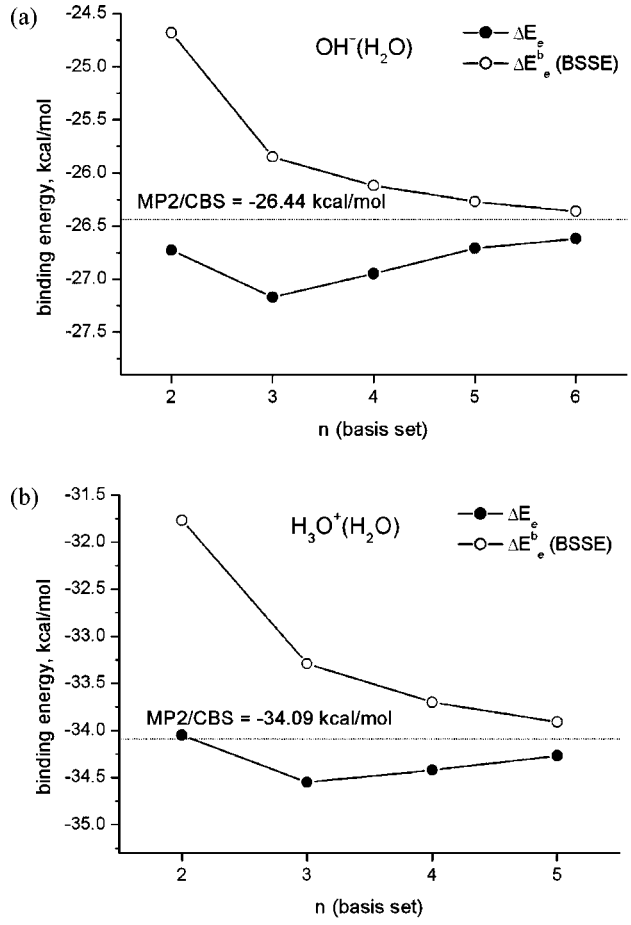

Figure 2. Variation in the MP2 binding energy for (a) $OH^-(H_2O)$ and (b) $H_3O^+(H_2O)$ with basis set size (aug-cc-pV*n*Z, $n = 2-6$), excluding (filled circles) and including (open circles) a BSSE correction. An extrapolated CBS limit is indicated as a horizontal line.

the aug-cc-pVDZ basis set were not included in the extrapolation, except for $OH^-(H_2O)_5$ and $OH^-(H_2O)_6$. The use of three consecutive BSSE-corrected energies for $OH^-(H_2O)_3$ and $OH^-(H_2O)_4$ clusters, with $n = 2-4$ and $n = 3-5$, yields CBS limit energies that are within 0.1 kcal/mol of each other. This gives us confidence that the extrapolation of results for $OH^-(H_2O)_5$ and $OH^-(H_2O)_6$ with only $n = 2-4$ energies available (aug-cc-pV*n*Z, $n =$ D, T, and Q) is reasonably accurate (within ~0.1 kcal/mol).

Our best estimates of the MP2/CBS values are obtained as an average of the extrapolated CBS values of ΔE_e and ΔE^b_e. The difference between these values is quite small and ranges from 0.08 kca/mol for $OH^-(H_2O)_5$ to 0.27 kcal/mol for $OH^-(H_2O)_5$. The results are given in Tables 1 and 2, together with previously reported MP2/CBS binding energies for $OH^-(H_2O)_{1-2}$ and $H_3O^+(H_2O)$.[27,28] Note that, in these previous studies,[27,28] geometry optimization was performed using a smaller aug-cc-pVDZ basis set and a different extrapolation scheme to reach the CBS limit was used. However, both computational protocols yielded very similar CBS values.

The effects of a higher order of electron correlation were examined using single-point CCSD(T)/aug-cc-pVDZ energy calculations at the MP2/aug-cc-pVDZ-optimized geometries. The results are listed in Tables 1−3. The inclusion of higher correlation at the CCSD(T) level decreases the binding energy of $H_3O^+(H_2O)_n$ by ~0.6 kcal/mol. The opposite effect is observed for $OH^-(H_2O)_n$. When the correlation effects are included at the CCSD(T) level, the binding energy progressively increases from ~0.2 kcal/mol for $OH^-(H_2O)$ to ~1.4 kcal/mol for $OH^-(H_2O)_6$. The magnitude of the average CCSD(T) correction for neutral water clusters is small (~0.18 kcal/mol). Overall, the results are variable, ranging from an increase of binding energy by ~0.1 kcal/mol for the $(H_2O)_6$ prism to a decrease in binding energy by ~0.5 kcal/mol for the $(H_2O)_6$ cyclic isomer. These results are consistent with a recent study of $(H_2O)_6$ isomers at the MP2 and CCSD(T) levels using the aug-cc-pVTZ basis set on oxygen and the cc-pVTZ basis set on hydrogen.[18]

4.2. A Comparative Study of the DFT Methods. The benchmark binding energies collected in the previous sections enable us to evaluate the performance of the DFT methods in reproducing the binding energies of neutral, protonated, and deprotonated water clusters. The discussion is organized as follows: We first consider the overall performance of 21 theoretical models resulting from a combination of 5 density functionals, several basis sets, and a set of BSSE-corrected results for our smallest basis set. Then we discuss the ability of DFT methods to accurately predict the relative stability of low-lying structural isomers and describe the binding energies of a series of large water clusters ($(H_2O)_{20}$ isomers). Finally, the density functionals are tested for their ability to reproduce the reaction energies of two ion hydration and neutralization reactions.

4.2.1. Overall Performance of the DFT Methods for an Accurate Database of MP2/CBS + ΔCCSD(T) Binding

Table 3. Comparison of the Benchmark Water Binding Energies (MP2/CBS + ΔCCSD(T)) to Those Obtained with Various DFT Methods (kcal/mol)[a]

	OBS[b]	aug-cc-pVTZ					aug-cc-pV5Z[c]					CBS	
complex	B3LYP	B3LYP	X3LYP	M06-L	M06-2X	M06	B3LYP	X3LYP	M06-L	M06-2X	M06	MP2	CCSD(T)
$(H_2O)_2$	4.97	4.57	4.95	4.74	5.17	4.79	4.55	4.93	4.70	5.09	4.73	4.98[e]	5.01
$(H_2O)_3$ cyclic	15.33	14.35	15.45	15.90	17.03	16.09	14.27	15.35	15.64	16.82	15.78	15.8[e]	15.8
$(H_2O)_4$ cyclic	27.42	26.05	27.76	27.22	28.76	27.33	25.84	27.52	26.69	28.43	26.82	27.6[e]	27.4
$(H_2O)_5$ cyclic	36.13	34.55	36.76	35.08	37.32	35.04	34.24	36.42	34.49	36.91	34.54	36.3[e]	35.9
$(H_2O)_6$ prism	44.03	41.14	44.33	47.31	50.04	47.82						45.9[e]	46.0
$(H_2O)_6$ cage	44.08	41.50	44.60	46.85	49.43	47.20						45.8[e]	45.8
$(H_2O)_6$ book	44.84	42.58	45.49	44.94	47.62	45.09						45.6[e]	45.3
$(H_2O)_6$ cyclic	44.63	42.81	45.51	43.08	46.11	43.36						44.8[e]	44.3
$(H_2O_8$ cube (D_{2d})	70.37	66.28	71.00	73.63	77.34	74.54						72.7[f]	72.6[h]
$(H_2O)_8$ cube (S_4)	70.34	66.24	70.96	73.62	77.34	74.52						72.7[f]	
$(H_2O)_{20}$ dodecahedron[d]	195.12	185.45	198.14	192.76	200.63	187.60						200.1[g]	
$(H_2O)_{20}$ fused cubes[d]	195.67	184.10	198.02	211.80	221.16	212.56						212.6[g]	
$(H_2O)_{20}$ face-sharing[d]	197.19	185.75	199.59	207.72	220.80	210.95						215.0[g]	
$(H_2O)_{20}$ edge-sharing[d]	199.97	188.85	202.56	206.03	223.71	209.16						217.9[g]	
$H_3O^+(H_2O)$	35.29	35.18	35.67	34.33	36.14	34.69	35.05	35.54	34.43	35.97	34.92	34.1	33.5
$H_3O^+(H_2O)_2$	58.64	58.37	59.35	57.14	59.92	57.05	58.18	59.16	57.10	59.61	57.15	57.5	56.9
$H_3O^+(H_2O)_3$	77.97	77.31	78.76	76.27	79.18	76.37	77.10	78.55	76.13	78.82	76.43	77.0	76.5
$H_3O^+(H_2O)_6$ (3*D*)	117.57	114.92	118.58	117.47	121.38	116.10						118.3[i]	117.8[i]
$H_3O^+(H_2O)_6$ (2*D*)	115.83	113.94	117.00	113.81	118.41	114.06						115.7[i]	114.9[i]
$OH^-(H_2O)$	29.01	27.43	27.97	27.29	30.11	27.55	26.92	27.45	26.07	29.39	26.93	26.4	26.6
$OH^-(H_2O)_2$	51.11	48.88	49.90	49.34	52.58	48.81	48.26	49.27	47.85	51.80	48.24	48.0	48.4
$OH^-(H_2O)_3$	69.89	66.88	68.37	70.22	73.29	69.82	66.20	67.67	68.50	72.53	69.07	66.8	67.6
$OH^-(H_2O)_4$ (C_4)	84.63	80.69	82.95	87.63	91.12	87.37	79.99	82.23	85.84	90.35	86.43	83.6	84.8
$OH^-(H_2O)_4$ (C_s)	85.45	81.33	83.83	87.74	91.84	87.25	80.60	83.07	85.73	90.87	86.23	83.9	84.8
$OH^-(H_2O)_5$	99.58	94.61	97.84	104.22	108.23	103.87	93.81	97.00	102.12	107.29	102.59	99.3	100.7
$OH^-(H_2O)_6$	114.32	108.57	112.55	119.19	123.78	119.01						114.3	115.7
$(H_2O)_8$ cube (S_4)−$H_3O^+(H_2O)_6OH^-$	24.42	22.94	23.26	29.64	23.45	30.91						25.3[j]	28.5[j]
MAE MP2, neutral	4.83	9.54	3.95	**2.57**	3.19	2.59							
MAE CCSD(T), neutral	0.83	2.70	0.82	**0.72**	2.30	0.87	1.29	**0.28**	0.64	0.79	0.56		
MAE CCSD(T), protonated	1.23	1.57	1.96	**0.54**	3.10	0.80	1.16	2.13	**0.49**	2.52	0.57		
MAE CCSD(T), deprotonated	**1.52**	3.26	1.79	2.44	6.06	2.16	2.96	1.64	**0.90**	4.90	1.15		
MAE CCSD(T), total	1.29	2.75	1.59	**1.24**	3.80	1.33	2.03	1.33	**0.73**	3.08	0.84		

[a] The lowest mean absolute error (MAE) for the two groups of basis sets is in bold. [b] Using the optimal 6-311++G(2d,2p) basis set (OBS) for B3LYP. [c] aug-cc-pV5Z single-point energies on aug-cc-pVTZ-optimized geometries. [d] aug-cc-pVTZ single-point energies on aug-cc-pVDZ-optimized geometries for the DFT methods. [e] Reference 31. [f] Reference 32. [g] Reference 33. [h] Reference 26. [i] Reference 37. [j] Reference 15.

Energies. Table 3 lists calculated binding energies of water clusters using the five DFT functionals with the 6-311++G(2d,2p) and aug-cc-pV*n*Z basis sets (n = T, 5). The DFT binding energies are compared with the benchmark estimates at the MP2/CBS and CCSD(T)/CBS levels. The MP2/CBS energies are given because they are considered to be reasonably accurate for neutral water clusters[31−33] and can also serve as a benchmark when CCSD(T) calculations are not feasible. DFT binding energies (both uncorrected and BSSE-corrected) calculated with the 6-311++G** basis set are included as Supporting Information (Table 1S). The accuracy of each method (density functional/basis set) is characterized by the mean unsigned error (MUE), averaged over the subset of neutral, protonated, and deprotonated clusters as well as the total data set. Note that the MUE for the largest aug-cc-pV5Z set may be biased since calculations with this basis set did not include clusters containing more than five water molecules.

The M06-L/aug-cc-pV5Z functional with an MUE of 0.73 kcal/mol shows the best overall performance. It gives the most accurate binding energies for $H_3O^+(H_2O)_n$ and $OH^-(H_2O)_n$ clusters. The M06/aug-cc-pV5Z functional with an MUE of 0.84 kcal/mol is the second best. X3LYP, B3LYP, and M06-2X [with the aug-cc-pV5Z basis set] are less accurate than M06-L by a factor of 1.8, 2.8, and 4.3, respectively. The overall accuracy of the M06-L and M06 potentials at the near CBS limit is impressive. However, from the practical point of view, the aug-cc-pV5Z basis set (287 basis functions per H_2O) is expensive even for medium-sized clusters.

If the largest aug-cc-pV5Z basis set is excluded, the best methods ranked by their mean unsigned error (kcal/mol, in parentheses) are M06-L/aug-cc-pVTZ (1.24), B3LYP/6-311++G(2d,2p) (1.29), and M06/aug-cc-pVTZ (1.33). The largest errors of M06-L/aug-cc-pVTZ and M06/aug-cc-pvTZ are due to the overbinding of $OH^-(H_2O)_n$ clusters (on average, by 2.2−2.4 kcal/mol). Interestingly, the DFT binding energy of $OH^-(H_2O)_n$ converges much more slowly with respect to basis set size than that of $(H_2O)_n$ and $H_3O^+(H_2O)_n$. For example, as one goes from the aug-cc-pVTZ to the aug-cc-pV5Z basis set, the M06-L binding energy decreases by 0.3, 0.1, and 1.7 kcal/mol for $(H_2O)_3$, $H_3O^+(H_2O)_3$, and $OH^-(H_2O)_3$, respectively. Thus, very large basis sets are needed for M06-L and M06 to accurately describe the energetics of different types of complexes.

As M06-L and M06 methods show the overall best performance at the basis set limit, this is not the case with the B3LYP functional. B3LYP/6-311++G** systematically overbinds, while B3LYP/aug-cc-pVTZ systematically underbinds, except for small ion−water clusters. On the basis of the performance for small water clusters, the 6-31+G(d,2p) basis set was recommended as an optimal basis set for B3LYP.[13] After testing several basis sets, we found that 6-311++G(2d,2p) provides a better and nearly optimal performance for the data set of binding energies employed in this study. B3LYP/6-311++G(2d,2p) has a mean unsigned error only 0.05 kcal/mol higher than that of M06-L/aug-cc-pVTZ and 0.04 kcal/mol lower than that of M06/aug-cc-pVTZ. However, the B3LYP/6-311++G(2d,2p) method is much more affordable than the M06 and M06-L methods since the 6-311++G(2d,2p) basis set employs approximately half Gaussian basis functions as the aug-cc-pVTZ basis set.

The X3LYP functional with the aug-cc-pV5Z basis set has the lowest MUE for the pure water clusters (0.28 kcal/mol). However, due to sizable errors for $H_3O^+(H_2O)_n$ and $OH^-(H_2O)_n$ clusters, X3LYP ranks fourth for overall performance (an MUE of 1.33 and 1.59 kcal/mol with the aug-cc-pV5Z and aug-cc-pVTZ basis sets, respectively). M06-2X does very poorly in almost each category, significantly overbinding even in the CBS limit, and particularly for $OH^-(H_2O)_n$ clusters. Its mean unsigned error is 3−4 times larger than the error obtained with the best DFT methods utilizing the same basis set (either aug-cc-pVTZ or aug-cc-pV5Z).

The utilization of a relatively small 6-311++G** basis set leads to significant overbinding for all the tested functionals (Table 1S of the Supporting Information). In this case, the mean unsigned errors sorted in increasing order are 4.2 (B3LYP), 5.9 (M06-L), 6.3 (X3LYP), 7.5 (M06), and 9.6 (M06-2X) kcal/mol. The inclusion of the BSSE correction (eq 1) partially compensates an overbinding effect associated with the 6-311++G** basis set, reducing the MUE by a factor of 1.8−3.3: 1.7 (B3LYP), 1.9 (X3LYP), 2.1 (M06-L), 3.1 (M06), and 5.1 (M06-2X) kcal/mol. B3LYP has the lowest error for both the uncorrected and BSSE-corrected binding energies calculated with this basis set.

4.2.2. Relative Stability of Conformational Isomers. The ability of DFT to describe the relative energies of the low-energy isomers is critical for the successful description of water in inhomogeneous environments at extreme conditions and under nanoscale confinement. Below, we compare the performance of B3LYP and M06-L as a test case to illustrate the distinctly different behavior between two classes of functionals. The first group consists of B3LYP and X3LYP functionals, whereas the second group consists of M06-L and M06 functionals. Note that the density functionals within each group behave very similarly.

We first consider the water hexamer isomers. Besides a cyclic structure, which is the most stable for clusters with three to five water molecules, $(H_2O)_6$ can adopt a variety of three-dimensional forms. CCSD(T) calculations yield the following energy ordering of the four hexamer structures: prism < book < cage < cyclic.[18,42] M06-L correctly predicts the energetic ordering of these isomers, but overestimates the energy spacing between them. For example, the energy difference between the cyclic and prism hexamers is 4.2 kcal/mol at the M06-L/aug-cc-pVTZ level, which is 2.5 kcal/mol larger than the benchmark value. In contrast, B3LYP predicts almost the reverse order of the relative stability of the four isomers, although with a much smaller range of energies (0.81 kcal/mol at the B3LYP/6-311++G(2d,2p) level). For a more thorough discussion, the reader is referred to a recent study focused exclusively on the performance of several DFT methods for a set of water hexamers.[18]

For protonated water clusters $H_3O^+(H_2O)_n$, the lowest energy conformers for n = 3−5 have noncyclic two-dimensional structures,[43] but the global minimum for n = 6 is a three-dimensional structure (without zero-point energy

Table 4. Ion Hydration (1−8) and Neutralization (9−32) Reactions Considered in This Study

1	$H_3O^+ + (H_2O)_2 = H_3O^+(H_2O)_2$	17	$H_3O^+(H_2O) + OH^-(H_2O)_4 = 7H_2O$
2	$H_3O^+ + (H_2O)_3 = H_3O^+(H_2O)_3$	18	$H_3O^+(H_2O)_3 + OH^-(H_2O)_3 = 8H_2O$
3	$H_3O^+ + (H_2O)_6 = H_3O^+(H_2O)_6$	19	$H_3O^+(H_2O)_2 + OH^-(H_2O)_4 = 8H_2O$
4	$OH^- + (H_2O)_2 = OH^-(H_2O)_2$	20	$H_3O^+(H_2O) + OH^-(H_2O)_5 = 8H_2O$
5	$OH^- + (H_2O)_3 = OH^-(H_2O)_3$	21	$H_3O^+(H_2O)_6 + OH^-(H_2O) = 9H_2O$
6	$OH^- + (H_2O)_4 = OH^-(H_2O)_4$	22	$H_3O^+(H_2O)_3 + OH^-(H_2O)_4 = 9H_2O$
7	$OH^- + (H_2O)_5 = OH^-(H_2O)_5$	23	$H_3O^+(H_2O)_2 + OH^-(H_2O)_5 = 9H_2O$
8	$OH^- + (H_2O)_6 = OH^-(H_2O)_6$	24	$H_3O^+(H_2O) + OH^-(H_2O)_6 = 9H_2O$
9	$H_3O^+(H_2O) + OH^-(H_2O) = 4H_2O$	25	$H_3O^+(H_2O)_6 + OH^-(H_2O)_2 = 10H_2O$
10	$H_3O^+(H_2O)_2 + OH^-(H_2O) = 5H_2O$	26	$H_3O^+(H_2O)_3 + OH^-(H_2O)_5 = 10H_2O$
11	$H_3O^+(H_2O) + OH^-(H_2O)_2 = 5H_2O$	27	$H_3O^+(H_2O)_2 + OH^-(H_2O)_6 = 10H_2O$
12	$H_3O^+(H_2O)_2 + OH^-(H_2O)_2 = 6H_2O$	28	$H_3O^+(H_2O)_6 + OH^-(H_2O)_3 = 11H_2O$
13	$H_3O^+(H_2O)_3 + OH^-(H_2O) = 6H_2O$	29	$H_3O^+(H_2O)_3 + OH^-(H_2O)_6 = 11H_2O$
14	$H_3O^+(H_2O) + OH^-(H_2O)_3 = 6H_2O$	30	$H_3O^+(H_2O)_6 + OH^-(H_2O)_4 = 12H_2O$
15	$H_3O^+(H_2O)_3 + OH^-(H_2O)_2 = 7H_2O$	31	$H_3O^+(H_2O)_6 + OH^-(H_2O)_5 = 13H_2O$
16	$H_3O^+(H_2O)_2 + OH^-(H_2O)_3 = 7H_2O$	32	$H_3O^+(H_2O)_6 + OH^-(H_2O)_6 = 14H_2O$

correction).[37] Although all DFT methods correctly predict a lower electronic energy for the 3*D* conformer of $H_3O^+(H_2O)_6$, the M06-class functionals provide a slightly more accurate prediction of the relative energy of the 2*D* conformer.

For deprotonated water clusters $OH^-(H_2O)_n$, the hypercoordinated structures with four oxygen neighbors are the most stable species for $n > 4$.[38,44] For $OH^-(H_2O)_4$, however, three-coordinate (C_s) and four-coordinate (C_4) structures are essentially isoenergetic at the MP2/CBS + ΔCCSD(T) level (the C_s isomer is more stable by only 0.05 kcal/mol). The M06-L method with either aug-cc-pVTZ or aug-cc-pV5Z basis set accurately reproduces the small difference in binding energies between these two conformations (within 0.1 kcal/mol). In contrast, B3LYP/6-311++G(2d,2p) overestimates the stability of the three-coordinate cluster by 0.8 kcal/mol. The overall results of our calculations suggest that the M06-L and M06 functionals do a better job than the B3LYP and X3LYP functionals in reproducing relative energetics of isomeric structures of small water clusters.

4.2.3. $(H_2O)_{20}$ Water Clusters. Accurate binding energies for the lowest lying isomers of the four families of stable $(H_2O)_{20}$ clusters were calculated by Fanourgakis et al.[33] at the MP2/CBS level of theory. These benchmark data are used to evaluate the performance of DFT methods for water clusters this large. The results summarized in Table 3 suggest that all DFT methods with optimal basis sets for small water clusters [(6-311++G(2d,2p) for B3LYP and aug-cc-pVTZ for X3LYP, M06-L, and M06] significantly underestimate the binding energies of the $(H_2O)_{20}$ clusters. The average error over the four isomers compared to the MP2/CBS binding energies is 6.3 (M06), 6.8 (M06-L), 11.8 (X3LYP), and 14.4 (B3LYP) kcal/mol. Note that M06-2X/aug-cc-pVTZ yields larger binding energies for $(H_2O)_{20}$ compared to the MP2/CBS values (the average error is 5.2 kcal/mol) due to significant overbinding for smaller water clusters (e.g., by 4.7 kcal/mol for $(H_2O)_8$).

B3LYP and X3LYP correctly predict the edge-sharing prism to be the lowest energy isomer and the face-sharing pentagonal prism to be the second lowest lying isomer. These functionals, however, do not reproduce a much lower stability of the dodecahedron arrangement with respect to the other three families. For example, the dodecahedron is 12.5 kcal/mol less stable than the fused cubes at the MP2/CBS level, whereas there is a very small energy separation between these isomers (<1.0 kcal/mol) at the B3LYP and X3LYP levels. The M06-L and M06 methods predict a high relative energy for the dodecahedral structure, but give the reverse order of stability for the three lowest energy families of minima compared to the MP2/CBS results. Thus, none of the studied DFT methods provide a completely satisfactory description of absolute and relative binding energies of $(H_2O)_{20}$.

4.2.4. Reaction Energies for Ion Hydration and Neutralization Reactions. We examined two types of reactions: ion hydration and neutralization reactions. In the first reaction, an ionic solute is hydrated by a cluster of *n* water molecules to form an ion−water cluster:

$$X^{\pm} + (H_2O)_n = X^{\pm}(H_2O)_n \qquad (3)$$

where $X^{\pm}$ is either H_3O^+ or OH^-. An improved methodology for the calculation of the solvation free energies of charge solutes based on reaction 3 has been recently described in ref 6. Due to the need to locate the low-energy isomers of relatively large solute−water clusters, this approach would benefit from the use of computationally efficient density functional theory. It is thus of interest to examine the accuracy of DFT methods for predicting the energy difference between ion−water clusters and the corresponding neutral water clusters.

Using the most stable isomers, as determined at the MP2/CBS + ΔCCSD(T) level, six reaction energies were calculated with the aug-cc-pV5Z basis set and eight reaction energies were calculated with the other basis sets (Table 4). The mean unsigned error of the reaction energies for all 21 DFT methods is given in Table 5. As expected from the best performance for clusterization energies, M06-L/aug-cc-pV5Z and M06/aug-cc-pV5Z are also the best two methods for reaction energetics (an MUE of 1.09 and 1.25 kcal/mol, respectively). However, these methods are very expensive and not applicable for clusters with more than 5−6 water molecules. The B3LYP/6-311++G(2d,2p) method is of the most practical interest, because it has the next lowest error for the ion hydration reactions (1.69 kcal/mol) and is computationally affordable for relatively large systems. Considerably more expensive M06/aug-cc-pVTZ and M06-L/aug-cc-pVTZ methods have an MUE that is 0.2−0.3 kcal/mol higher than that of B3LYP/6-311++G(2d,2p). Finally, we note that, due to a partial cancellation of systematic errors

Table 5. Mean Unsigned Error (kcal/mol) in Energies of Ion Hydration and Neutralization Reactions Calculated with Various DFT Methods[a]

method	ion hydration[b]	neutralization[c]
MP2/CBS	**0.90**	2.28
B3LYP/6-311++G**	2.53	9.30
B3LYP/6-311++G**(BSSE)	2.29	2.71
B3LYP/6-311++G(2d,2p)	**1.69**	**1.93**
B3LYP/aug-cc-pVTZ	2.12	3.25
B3LYP/aug-cc-pV5Z	2.04	2.49
X3LYP/6-311++G**	2.91	13.22
X3LYP/6-311++G**(BSSE)	2.25	4.54
X3LYP/aug-cc-pVTZ	2.10	2.76
X3LYP/aug-cc-pV5Z	2.07	2.84
M06-L/6-311++G**	3.21	8.82
M06-L/6-311++G**(BSSE)	2.16	2.11
M06-L/aug-cc-pVTZ	1.98	**1.38**
M06-L/aug-cc-pV5Z	**1.09**	**0.95**
M06-2X/6-311++G**	2.69	17.26
M06-2X/6-311++G**(BSSE)	3.44	8.89
M06-2X/aug-cc-pVTZ	3.64	7.33
M06-2X/aug-cc-pV5Z	3.64	5.55
M06/6-311++G**	6.07	13.51
M06/6-311++G**(BSSE)	2.21	5.44
M06/aug-cc-pVTZ	1.87	2.15
M06/aug-cc-pV5Z	**1.25**	**1.02**

[a] Using the most stable isomers at the MP2/CBS + ΔCCSD(T) level, namely, the 3*D* isomer for $H_3O^+(H_2O)_6$, the C_s isomer for $OH^-(H_2O)_4$, and the prism isomer for $(H_2O)_6$. The four lowest errors of each reaction are in bold. [b] Ion hydration reactions: $X^\pm(H_2O)_n = X^\pm + (H_2O)_n$, where $X^\pm = H_3O^+$ and OH^-. Six reaction energies calculated with the aug-cc-pV5Z basis set and eight reaction energies calculated with the other basis sets (Table 4). [c] Neutralization reactions: $H_3O^+(H_2O)_n + OH^-(H_2O)_m = (m + n + 2)H_2O$. Fifteen reaction energies calculated with the aug-cc-pV5Z basis set and 24 reaction energies calculated with the other basis sets (Table 4). The reference reaction energy (MP2/CBS + ΔCCSD(T)) for $H_3O^+ + OH^- = 2H_2O$ is 255.6 ± 0.2 kcal/mol.

in the binding energies of pure water and ion−water clusters,[6] some of the methods that perform poorly for predicting clusterization energies do better for predicting ion hydration energies.

A second reaction of interest is the neutralization of a hydronium ion cluster by a hydroxide ion cluster:

$$H_3O^+(H_2O)_n + OH^-(H_2O)_m = (m + n + 2)H_2O \quad (4)$$

We considered all possible neutralization reactions for the most stable isomers at the CCSD(T)/CBS level (Table 4). They include 15 reactions with the aug-cc-pV5Z basis set and 24 reactions with the smaller basis sets. Table 5 lists the mean unsigned errors of the reaction energies for all 21 methods. Since there is no cancellation of systematic errors in neutralization reactions, the MUE in the reaction energies of this type of reaction is higher than that of ion hydration reactions in most cases. The only methods showing improved performance are M06 and M06-L with the largest aug-cc-pV5Z basis set (an MUE of 0.95−1.02 kcal/mol) and M06-L/aug-cc-pVTZ (an MUE of 1.38 kcal/mol). These are also the best two methods for describing neutralization reactions. In addition, Table 3 shows that M06-L/aug-cc-pvTZ is more accurate than other methods in predicting the energetics of the autoionization of a water octamer cluster ($H_3O^+(H_2O)_6OH^-$).[15] The overall results of our calculations support a conclusion recently drawn from a subset of smaller ion−water clusters[19] that M06-L/aug-cc-pVTZ gives accurate energies for neutralization reactions. B3LYP/6-311++G(2d,2p) has the fourth lowest MUE (1.93 kcal/mol), which is 0.22 kcal/mol lower than that of M06/aug-cc-pVTZ. Finally, we note that although MP2/CBS yields the smallest average error for ion hydration reactions (0.90 kcal/mol), this method is outperformed by the M06-L, B3LYP, and M06 functionals for neutralization reactions (2.28 kcal/mol).

5. Conclusions

We evaluated the ability of five density functionals [including two hybrid GGAs (B3LYP, X3LYP), one local meta-GGA (M06-L), and two hybrid meta-GGAs (M06-2X, M06) with several basis sets] to reproduce accurate binding energies of 27 neutral ($(H_2O)_n$, $n = 2-8$, 20), protonated ($H_3O^+(H_2O)_n$, $n = 1-6$), and deprotonated ($OH^-(H_2O)_n$, $n = 1-6$) water clusters. As a benchmark for determining the accuracy of the DFT method, we used binding energies extrapolated to the complete basis set limit of the MP2 theory with the effects of higher order correlation estimated at the CCSD(T)/aug-cc-pVDZ level. We established the CBS limit of the MP2 and CCSD(T) theory for a series of $OH^-(H_2O)_n$ ($n = 1-6$) and $H_3O^+(H_2O)_n$ ($n = 1-3$) clusters. We subsequently combined our estimates with CBS limit estimates taken from the literature to generate a database of highly accurate binding energies of water clusters that were used as benchmarks to compare the accuracy of the DFT functionals.

The M06-L and M06 functionals coupled with a very large aug-cc-pV5Z basis set show the best overall performance (a mean unsigned error of 0.73−0.84 kcal/mol). However, these methods are very expensive and therefore cannot be routinely used even for medium-sized clusters. If the aug-cc-pV5Z basis set is excluded, the best methods ranked by their mean unsigned error (kcal/mol, in parentheses) are M06-L/aug-cc-pVTZ (1.24), B3LYP/6-311++G(2d,2p) (1.29), M06/aug-cc-PVTZ (1.33), and X3LYP/aug-cc-pVTZ (1.59). The performance of M06-2X is relatively poor. M06-2X/aug-cc-pVTZ has an average error that is 3 times as large as those of the best methods.

The utilization of a relatively small 6-311++G** basis set leads to significant overbinding for all the tested functionals. This effect can be partially compensated by including the BSSE correction. B3LYP has the lowest average error for both the uncorrected and BSSE-corrected binding energies calculated with this basis set.

M06-L and M06 do a good job in reproducing the relative energetics of small clusters. However, none of the functionals gave adequate binding energies for the $(H_2O)_{20}$ clusters. The M06-L, M06, B3LYP, and X3LP methods with their optimal basis sets for small clusters underestimate binding energies for the four lowest lying isomers of stable $(H_2O)_{20}$ clusters.

M06-L and M06 functionals in the CBS limit are the most accurate methods for predicting reaction energetics. M06-L/aug-cc-pVTZ and B3LYP/6-311++G(2d,2p) are the best among the more cost-effective methods. M06-L/aug-cc-

pVTZ shows exceptional performance for neutralization reactions, whereas B3LYP/6-311++G(2d,2p) is more accurate for ion hydration reactions.

Acknowledgment. We are grateful to Dr. George S. Fanourgakis, Dr. Daniel Svozil, and Dr. P. Tarakeshwar for providing us with the Cartesian coordinates of $(H_2O)_{20}$, $H_3O^+(H_2O)_6OH^-$, and $OH^-(H_2O)_{5-6}$ clusters, respectively. This work was performed in part using the Molecular Science Computing Facility (MSCF) in the William R. Wiley Environmental Sciences Laboratory, a national scientific user facility sponsored by the U.S. Department of Energy's Office of Biological and Environmental Research located at the Pacific Northwest National Laboratory, which is operated for the Department of Energy by Battelle.

Supporting Information Available: Cartesian coordinates and energies for optimized clusters at the B3LYP/6-311++G(2d,2p) level of theory and Table 1S comparing the performance of the various DFT methods employing the 6-311++G** basis set. This material is available free of charge via the Internet at http://pubs.acs.org.

References

(1) (a) Mucha, M.; Frigato, T.; Levering, L. M.; Allen, H. C.; Tobias, D. J.; Dang, L. X.; Jungwirth, P. *J. Phys. Chem. B* **2005**, *109*, 7617–7623. (b) Vacha, R.; Buch, V.; Milet, A.; Devlin, J. P.; Jungwirth, P. *Phys. Chem. Chem. Phys.* **2005**, *7* (9), 4736–4747. (c) Wick, C. D.; Kuo, I.-F. W.; Mundy, C. J.; Dang, L. X. *J. Chem. Theory Comput.* **2007**, *3*, 2002–2010. (d) Jorgensen, W. L. *J. Chem. Theory Comput.* **2007**, *3*, 1877–1877. (e) Xie, W.; Gao, J. *J. Chem. Theory Comput.* **2007**, *3*, 1890–1900.

(2) (a) Stillinger, F. H.; David, C. W. *J. Chem. Phys.* **1978**, *69*, 1473–1484. (b) David, C. W. *J. Chem. Phys.* **1996**, *104*, 7255–7260. (c) Halley, J. W.; Rustad, J. R.; Rahman, A. *J. Chem. Phys.* **1993**, *98*, 4110–4119. (d) Corrales, L. R. *J. Chem. Phys.* **1999**, *110*, 9071–9080. (e) Lussetti, E.; Pastore, G.; Smatgiassi, E. *Chem. Phys. Lett.* **2003**, *381*, 287–291. (f) Garofalini, S. H.; Mahadevan, T. S. *J. Phys. Chem. B* **2007**, *111*, 8919–8927. (g) Goddard, W. A., III; Merinov, B.; van Duin, A. C. T.; Jacob, T.; Blanco, M.; Molinero, V.; Jang, S. S. *Mol. Simul.* **2006**, *32*, 251–268.

(3) (a) Todorova, T.; Seitsonen, A. P.; Hutter, J.; Kuo, I.-F. W.; Mundy, C. J. *J. Phys. Chem. B* **2006**, *110*, 3685–3691. (b) VandeVondele, J.; Mohamed, F.; Krack, M.; Hutter, J.; Sprik, M.; Parrinello, M. *J. Chem. Phys.* **2005**, *122*, 014515−1-6.

(4) (a) Tuckerman, M. E.; Marx, D.; Parrinello, M. *Nature* **2002**, *417*, 925–929. (b) Tuckerman, M. E.; Chandra, A.; Marx, D. *Acc. Chem. Res.* **2006**, *39*, 151–158.

(5) McGrath, M. J.; Siepmann, J. I.; Kuo, I.-F. W.; Mundy, C. *J. Mol. Phys.* **2006**, *104*, 3619–3626.

(6) Bryantsev, V. S.; Diallo, M. S.; Goddard, W. A., III. *J. Phys. Chem. B* **2008**, *112*, 9709–9719.

(7) Xantheas, S. S. *J. Chem. Phys.* **1994**, *102*, 4505–4517.

(8) Hall, R. J.; Hillier, I. H.; Vincent, M. A. *Chem. Phys. Lett.* **2000**, *320*, 139–143.

(9) Xu, X.; Goddard, W. A., III. *J. Phys. Chem. A* **2004**, *108*, 2305–2313.

(10) Su, J. T.; Xu, X.; Goddard, W. A., III. *J. Phys. Chem. A* **2004**, *108*, 10518–10526.

(11) Dahlke, E. E.; Truhlar, D. G. *J. Phys. Chem. B* **2005**, *109*, 15677–15683.

(12) Csonka, G. I.; Ruzsinszky, A.; Perdew, J. P. *J. Phys. Chem. B* **2005**, *109*, 21471–21475.

(13) Dahlke, E. E.; Truhlar, D. G. *J. Phys. Chem. B* **2006**, *110*, 10595–10601.

(14) Anderson, J. A.; Tschumper, G. S. *J. Phys. Chem. A* **2006**, *110*, 7268–7271.

(15) Svozil, D.; Jungwirth, P. *J. Phys. Chem. A* **2006**, *110*, 9194–9199.

(16) Santra, B.; Michaelides, A.; Scheffler, M. *J. Chem. Phys.* **2007**, *127*, 1–9.

(17) Shields, G. C.; Kirschner, K. N. *Synth. React. Inorg., Met.-Org., Nano-Met. Chem.* **2008**, *38*, 32–39.

(18) Dahlke, E. E.; Olson, R. M.; Leverentz, H. R.; Truhlar, D. G. *J. Phys. Chem. A* **2008**, *112*, 3976–3984.

(19) Dahlke, E. E.; Orthmeyer, M. A.; Truhlar, D. G. *J. Phys. Chem. B* **2008**, *112*, 2372–2381.

(20) (a) Zhao, Y.; Truhlar, D. G. *J. Chem. Phys.* **2006**, *125*, 1–17, 194101. (b) Zhao, Y.; Truhlar, D. G. *Theor. Chem. Acc.* **2008**, *120*, 215–241.

(21) (a) Becke, A. D. *Phys. Rev. A* **1988**, *38*, 3098–3100. (b) Lee, C. T.; Yang, W. T.; Parr, R. G. *Phys. Rev. B* **1988**, *37*, 785–789.

(22) Xu, X.; Goddard, W. A., III. *Proc. Natl. Acad. Sci. U.S.A.* **2004**, *101*, 2673–2677.

(23) Möller, C.; Plesset, M. S. *Phys. Rev.* **1934**, *46*, 618–622.

(24) (a) Purvis, G. D., III; Bartlett, R. J. *J. Chem. Phys.* **1982**, *76*, 1910–1918. (b) Raghavachari, K.; Trucks, G. W.; Pople, J. A.; Head-Gordon, M. *Chem. Phys. Lett.* **1989**, *157*, 479–483. (c) Watts, J. D.; Gauss, J.; Bartlett, R. J. *J. Chem. Phys.* **1993**, *98*, 8718–8733.

(25) (a) Dunning, T. H., Jr. *J. Chem. Phys.* **1989**, *90*, 1007–1023. (b) Kendall, R. A.; Dunning, T. H., Jr.; Harrison, R. J. *J. Chem. Phys.* **1992**, *96*, 6796–6806.

(26) Xantheas, S. S. *Struct. Bonding (Berlin)* **2005**, *116*, 119–148.

(27) Masamura, M. *Theor. Chem. Acc.* **2001**, *106*, 301–313.

(28) Masamura, M. *Int. J. Quantum Chem.* **2004**, *100*, 28–40.

(29) Boys, S. F.; Bernardi, F. *Mol. Phys.* **1970**, *19*, 553–566.

(30) (a) Xantheas, S. S. *J. Chem. Phys.* **1996**, *104*, 8821–8824. (b) Valiron, P.; Mayer, I. *Chem. Phys. Lett.* **1997**, *275*, 46–55.

(31) Xantheas, S. S.; Burnham, C. J.; Harrison, R. I. *J. Chem. Phys.* **2002**, *116*, 1493–1499.

(32) Xantheas, S. S.; Aprà, E. *J. Chem. Phys.* **2004**, *120*, 823–828.

(33) Fanourgakis, G. S.; Aprà, E.; Xantheas, S. S. *J. Chem. Phys.* **2004**, *121*, 2655–2663.

(34) Bryantsev, V. S.; Diallo, M. S.; Goddard, W. A., III. *J. Phys. Chem. A* **2007**, *111*, 4422–4430.

(35) Zhao, Y.; Truhlar, D. G. *J. Chem. Theory Comput.* **2005**, *1*, 415–432.

(36) Bylaska, E. J.; de Jong, W. A.; Govind, N.; Kowalski, K.; Straatsma, T. P.; Valiev, M.; Wang, D.; Apra, E.; Windus, T. L.; Hammond, J.; Nichols, P.; Hirata, S.; Hackler, M. T.; Zhao, Y.; Fan, P.-D.; Harrison, R. J.; Dupuis, M.; Smith,

D. M. A.; Nieplocha, J.; Tipparaju, V.; Krishnan, M.; Wu, Q.; Van Voorhis, T.; Auer, A. A.; Nooijen, M.; Brown, E.; Cisneros, G.; Fann, G. I.; Fruchtl, H.; Garza, J.; Hirao, K.; Kendall, R.; Nichols, J. A.; Tsemekhman, K.; Wolinski, K.; Anchell, J.; Bernholdt, D.; Borowski, P.; Clark, T.; Clerc, D.; Dachsel, H.; Deegan, M.; Dyall, K.; Elwood, D.; Glendening, E.; Gutowski, M.; Hess, A.; Jaffe, J.; Johnson, B.; Ju, J.; Kobayashi, R.; Kutteh, R.; Lin, Z.; Littlefield, R.; Long, X.; Meng, B.; Nakajima, T.; Niu, S.; Pollack, L.; Rosing, M.; Sandrone, G.; Stave, M.; Taylor, H.; Thomas, G.; van Lenthe, J.; Wong A.; Zhang, Z. *NWChem, A Computational Chemistry Package for Parallel Computers*, version 5.1; Pacific Northwest National Laboratory: Richland, WA, 2007.

(37) Shin, I.; Park, M.; Min, S. K.; Lee, E. C.; Suh, S. B.; Kim, K. S. *J. Chem. Phys.* **2006**, *125*, 1–7, 234305].

(38) Lee, H. M.; Tarkeshwar, P.; Kim, K. S. *J. Chem. Phys.* **2004**, *121*, 4657–4664.

(39) Feller, D. J. *J. Chem. Phys.* **1992**, *96*, 6104–6114.

(40) Peterson, K. A.; Wood, D. E.; Dunning, T. H., Jr. *J. Chem. Phys.* **1994**, *100*, 7410–7415.

(41) (a) Helgaker, T.; Klopper, W.; Koch, H.; Noga, J. *J. Chem. Phys.* **1997**, *106*, 9639–9646. (b) Halkier, A.; Helgaker, T.; Jorgensen, P.; Klopper, W.; Koch, H.; Olson, J.; Wilson, A. K. *Chem. Phys. Lett.* **1998**, *286*, 243–252.

(42) Dahlke, E. E.; Leverentz, H. R.; Truhlar, D. G. *J. Chem. Theory Comput.* **2008**, *4*, 33–41.

(43) (a) Jiang, J. C.; Wang, Y. S.; Chang, H. C.; Lin, S. H.; Lee, Y. T.; Niedner-Schatteburgm, G.; Chang, H. C. *J. Am. Chem. Soc.* **2000**, *122*, 1398–1410. (b) Lee, H. M.; Tarakeshwar, P.; Park, J. W.; Kolaski, M. R.; Yoon, Y. J.; Yi, H.-B.; Kim, W. Y.; Kim, K. S. *J. Phys. Chem. A* **2004**, *108*, 2949–2958. (c) Park, M.; Shin, I.; Singh, N. J.; Kim, K. S. *J. Phys. Chem. A* **2007**, *111*, 10692–10702.

(44) Masamura, M. *J. Comput. Chem.* **2001**, *22*, 31–37.

(45) (a) Li, X.; Teige, V. E.; Iyengar, S. S. *J. Phys. Chem. A* **2007**, *111*, 4815–4820. (b) Śmiechowski, M.; Stangret, J. *J. Phys. Chem. A* **2007**, *111*, 2889–2897. (c) Cappa, C. D.; Smith, J. D.; Messer, B. M.; Cohen, R. C.; Saykally, *J. Phys. Chem. A* **2007**, *111*, 4776–4785.

CT800549F

JCTC Journal of Chemical Theory and Computation

Robust and Reliable Multilevel Minimization of the Kohn−Sham Energy

Branislav Jansík,* Stinne Høst, Mikael P. Johansson, Jeppe Olsen, and Poul Jørgensen

Lundbeck Foundation Center for Theoretical Chemistry, Department of Chemistry, University of Aarhus, DK-8000 Århus C, Denmark

Trygve Helgaker

Centre for Theoretical and Computational Chemistry, Department of Chemistry, University of Oslo, P.O. Box 1033 Blindern, N-0315 Oslo, Norway

Received December 18, 2008

Abstract: Kohn−Sham density-functional calculations are used in many branches of science to obtain information about the electronic structure of molecular systems and materials. Conventional algorithms for minimization of the Kohn−Sham energy have certain deficiencies, however, that may cause divergence or, worse, convergence to unphysical saddle points. We here present a three-level hierarchical minimization strategy which is both more efficient and robust than the conventional algorithms and which does not suffer from the flaws of these algorithms. Using the three-level minimization strategy, the molecular density is built up in a hierarchical fashion in accordance with chemical insight: First, the molecular density is composed by a superposition of atomic densities; next, bonds are formed by performing a simple valence-shell optimization; finally, the molecular description is refined by an optimization in the full molecular basis. Importantly, the density matrix generated at each of the two lower levels in this hierarchy is transferred to the next without loss of information. Examples demonstrate the efficacy and robustness of the proposed scheme.

1. Introduction

A common trend in many fields of science is the increased use of atomistic models for predictions and rationalizations. In particular, theoretical and experimental studies of molecular properties and interactions rigorously based on the laws of quantum mechanics are making important contributions to advances in many branches of science. Kohn−Sham (KS) density-functional theory[1,2] currently represents the best compromise between cost and accuracy in describing the electronic structure of molecules and materials. Indeed, thousands of KS calculations are carried out every day, not only in the fields of chemistry and physics but also in related fields such as molecular biology and medicine, to obtain information of the electronic structure of molecules and materials. As ever more complex calculations are being attempted, it becomes paramount to use algorithms that locate the KS energy minimum reliably and efficiently.[3]

In KS theory, the electronic energy is minimized with respect to variations in the one-electron density matrix. The efficiency and reliability of this minimization depends not only on the optimization algorithm itself but also on the quality of the starting density matrix. Usually, this matrix is obtained by diagonalizing the one-electron Hamiltonian (HCORE) or the Hückel Hamiltonian. Starting density matrices have also been obtained by carrying out an initial molecular calculation in a minimal basis, followed by projection of the obtained density matrix onto the full basis. Recently, van Lenthe et al. demonstrated that a starting density matrix constructed as a superposition of atomic density matrices constitutes the best available approach to date.[4]

Here, we propose a new strategy for the optimization of the KS energy, where the minimization is carried at three

* Corresponding author e-mail: jansik@chem.au.dk.

10.1021/ct800562h CCC: $40.75
Published on Web 03/04/2009

levels of description, of increasing cost and complexity. First, the molecule is formed from separate atoms, by a simple superposition of atomic densities. Next, chemical bonds are formed in a valence-shell description, using a small subset of the full molecular basis. This second level constitutes the crux of our proposed scheme—it allows all the essential elements of molecular bonding to be approximated accurately, at a cost much smaller than that of a full-basis optimization. Finally, and importantly, the information obtained about the system at this second level is transferred—without loss of information—to the third level, where the description is refined in the full molecular basis. Notably, this full-basis optimization begins either inside or close to the local region—the difficult global optimization is essentially completed at the first and second levels, providing a high-quality starting guess for the expensive final refinement.

The proposed three-level method can in principle be combined with any existing method for the minimization of the KS energy from a given starting guess. We here use the augmented Roothaan−Hall (ARH) method,[5] which was recently shown to possess several advantages over the traditional minimization schemes.

In the traditional KS optimization scheme, each iteration consists of two steps: first, a Roothaan−Hall (RH) step, where the KS matrix (the energy gradient) is constructed from the current approximate density matrix and then diagonalized to yield a new density matrix; second, an averaging step, where the density matrix for the next RH iteration is determined as a combination of the new and old density matrices using Pulay's method of direct inversion in the iterative subspace (DIIS).[6] Although successful, this traditional two-step RH/DIIS scheme occasionally fails—in particular, for the larger and more complicated electronic systems often studied by KS theory nowadays. Since only gradient information is used in the RH/DIIS scheme, the optimization may sometimes diverge or converge to a saddle point rather than the ground-state minimum. Whereas divergence is an obvious failure, saddle-point convergence is more pernicious in that it typically leaves the user unaware that the provided solution does not properly represent the electronic ground state.

In the ARH algorithm, the two separate RH and DIIS steps are merged into a single, concerted minimization step that fully exploits the second-derivative (Hessian) information available from the current and previous iterations. At each ARH iteration, a local quadratic model of the KS energy is constructed that is exact (within the quasi-Newton approximation) in the directions of the old density matrices and approximate (but accurate) in the remaining directions. The new density matrix is then obtained by applying the trust-region minimization method to this quadratic model, thereby ensuring that the energy is lowered at each iteration and that a minimum is obtained.[7] Therefore, the ARH method does not suffer from the deficiencies of the RH/DIIS method.[5]

Combining the ARH method with the three-level (3L) method introduced in this paper, we arrive at a highly efficient and robust strategy for KS energy optimizations. Following the introduction of the 3L scheme in Section 2, we demonstrate the efficacy and robustness of the combined ARH-3L method in Section 3, where comparisons are also made with traditional methods. Section 4 contains some final remarks.

2. The Three-Level Optimization of the KS Energy

The optimization of the KS energy presented here is carried out at three consecutive levels, where the density matrix obtained at one level is used as starting guess at the next level. The three optimization levels are as follows: separate atomic optimizations, a valence-basis molecular optimization, and a full-basis molecular optimization. The cost of the optimization is dominated by the full-basis optimization, which is typically an order of magnitude higher than that of the valence-basis optimization, while the cost of the atomic optimizations is negligible. In the following sections, we describe each optimization level in greater detail.

2.1. Atom-in-a-Molecule Density Matrix. To generate an atom-in-a-molecule density matrix, we first carry out a separate canonical ensemble KS optimization for each atom P in the molecule, in an atomic-orbital (AO) basis $|\chi^P\rangle$ consisting of local atom-centered functions. In a canonical ensemble KS calculation, fractional occupation numbers are assigned to the highest occupied AOs if they are not fully occupied to ensure that a spherical symmetric atomic density matrix is obtained.

The eigenvectors of the atomic KS eigenvalue problem are next partitioned as $\mathbf{C}^P = (\mathbf{C}_o^P, \mathbf{C}_u^P)$, where $\mathbf{C}_o^P$ contains the (possibly fractionally) occupied AOs and $\mathbf{C}_u^P$ the unoccupied ones. (In our notation, subscripts 'o' and 'u' denote 'occupied', and 'unoccupied', respectively.) In the $|\chi^P\rangle$ basis, the atom-optimized AOs are then given by

$$|\zeta_o^P, \zeta_u^P\rangle = |\chi^P\rangle(\mathbf{C}_o^P, \mathbf{C}_u^P) \tag{1}$$

and the corresponding spherically symmetric atomic density matrix basis becomes

$$\mathbf{D}^P = \begin{pmatrix} \mathbf{D}_o^P & \mathbf{0} \\ \mathbf{0} & \mathbf{0} \end{pmatrix} \tag{2}$$

where the diagonal matrix $\mathbf{D}_o^P$ contains the (fractional) occupation numbers of the occupied atomic orbitals $\mathbf{C}_o^P$. For an oxygen atom with electronic structure $(1s^2 2s^2 2p^4)$ the occupied atom-optimized AOs are $(\zeta_{1s}\zeta_{2s}\zeta_{2px}\zeta_{2py}\zeta_{2pz})$ with occupation numbers (2,2,4/3,4/3,4/3).

To prepare for the subsequent molecular calculation, we now set up a full atomic (denoted by subscript 'A') basis consisting of the atom-optimized AOs

$$|\zeta_A\rangle = |\zeta_{Ao}, \zeta_{Au}\rangle \tag{3}$$

where the sets of occupied and unoccupied atomic orbitals are given by

$$|\zeta_{Ao}\rangle = |\zeta_o^P, \zeta_o^Q, ...\rangle \tag{4}$$

$$|\zeta_{Au}\rangle = |\zeta_u^P, \zeta_u^Q, ...\rangle \tag{5}$$

Likewise, we generate a molecular density matrix as the superposition of atomic density matrices

$$\mathbf{D}_{\mathrm{A}} = \begin{pmatrix} \mathbf{D}_{\mathrm{Ao}} & \mathbf{0} \\ \mathbf{0} & \mathbf{0} \end{pmatrix} \tag{6}$$

whose occupied part is the superposition (direct sum) of the occupied atomic density matrices

$$\mathbf{D}_{\mathrm{Ao}} = \mathbf{D}_{\mathrm{o}}^{\mathrm{P}} \oplus \mathbf{D}_{\mathrm{o}}^{\mathrm{Q}} \oplus \ldots \tag{7}$$

The resulting atom-in-a-molecule density matrix $\mathbf{D}_{\mathrm{A}}$ satisfies the symmetry and trace conditions of a valid KS density matrix but not the idempotency condition. However, this lack of idempotency does not matter as the density matrix will only be used to construct a KS matrix, from which an idempotent density matrix is obtained from the KS eigenvectors in agreement with the Aufbau principle.

2.2. Valence-Basis Molecular Optimization. In the ATOMS scheme advocated by van Lenthe et al.,[4] a full-basis molecular calculation is now carried out in the full atomic orbital basis $|\chi\rangle = |\chi^{\mathrm{P}},\chi^{\mathrm{Q}},\cdots\rangle$, using the full-basis atom-in-a-molecule density matrix $\mathbf{D}_{\mathrm{A}}$, eq (6), transformed from the $|\zeta_{\mathrm{A}}\rangle$ basis to the $|\chi\rangle$ as a starting guess. We instead first perform a molecular calculation in the smaller atom-optimized AO occupied basis $|\zeta_{\mathrm{Ao}}\rangle \subset |\zeta_{\mathrm{A}}\rangle$, using $\mathbf{D}_{\mathrm{Ao}}$ of eq (7) as a starting guess. The purpose of this valence-basis calculation is to incorporate the essential features of bonding into the density matrix at low cost, before the expensive final refinement of the molecular density matrix in the full atomic orbital basis.

The valence-basis optimization is carried out in the usual manner, by treating the occupied atomic basis functions $|\zeta_{\mathrm{Ao}}\rangle$ as a generally contracted basis with contraction coefficients obtained by multiplying $\mathbf{C}_{\mathrm{Ao}}^{\mathrm{P}}$ on the $|\chi^{\mathrm{P}}\rangle$ atomic contraction coefficients. The occupied atom-optimized AO basis $|\zeta_{\mathrm{Ao}}\rangle$ contains core as well as valence atomic orbitals—for a first-row atom, for example, it contains the atomic orbitals $(\zeta_{1s}\zeta_{2s}\zeta_{2px}\zeta_{2py}\zeta_{2pz})$. Since the 1s core orbitals are reasonably well described by the ζ_{1s} atomic orbitals and change little upon bond formation, they may be omitted from the valence-basis optimization, but this has not been done in the calculations reported here.

The valence-basis calculation may be carried out using any standard KS optimization scheme. We use the ARH algorithm with $\mathbf{D}_{\mathrm{Ao}}$ as the starting density matrix. At convergence, the optimization returns a density matrix $\mathbf{D}_{\mathrm{V}}^{\mathrm{Ao}}$ in the $|\zeta_{\mathrm{Ao}}\rangle$ basis that satisfies the Fock/KS eigenvalue equation

$$\mathbf{F}^{\mathrm{Ao}}(\mathbf{D}_{\mathrm{V}}^{\mathrm{Ao}})\mathbf{C}_{V} = \mathbf{S}^{\mathrm{Ao}}\mathbf{C}_{V}\boldsymbol{\varepsilon}_{\mathrm{V}} \tag{8}$$

providing us with a valence optimized molecular basis as a linear combination of the occupied atom-optimized AOs

$$|\zeta_{\mathrm{V}}\rangle = |\zeta_{\mathrm{Vo}},\zeta_{\mathrm{Vu}}\rangle = |\zeta_{\mathrm{Ao}}\rangle(\mathbf{C}_{\mathrm{Vo}},\mathbf{C}_{\mathrm{Vu}}) \tag{9}$$

where the $\mathbf{S}^{\mathrm{Ao}}$ and $\mathbf{F}^{\mathrm{Ao}}$ are the overlap and Kohn−Sham matrices in the occupied atom-optimized AO basis. We have here partitioned the orbitals as $\mathbf{C}_{\mathrm{V}} = (\mathbf{C}_{\mathrm{Vo}},\mathbf{C}_{\mathrm{Vu}})$, where $\mathbf{C}_{\mathrm{Vo}}$ and $\mathbf{C}_{\mathrm{Vu}}$ contain the occupied and virtual orbitals, respectively. (We use 'V' to denote 'valence', in contrast to 'A' for 'atomic'.) In this valence basis $|\zeta_{\mathrm{V}}\rangle$, the molecular density matrix becomes

$$\mathbf{D}_{\mathrm{V}} = \begin{pmatrix} \mathbf{I} & \mathbf{0} \\ \mathbf{0} & \mathbf{0} \end{pmatrix} \tag{10}$$

where $\mathbf{I}$ is a unit matrix of the dimension of $|\zeta_{\mathrm{Vo}}\rangle$.

In the course of the valence-basis optimization, chemical bonds are formed between neighboring atoms, providing us with a set of local occupied and virtual orbitals with contributions only from neighboring atoms involved in the bond formation. For high locality, diffuse basis functions may be omitted from the optimization of the atomic orbitals.

Returning to the full atom-optimized AO basis eq (3), we see that our atomic and valence-basis KS optimizations have provided us with the following partitioning of the basis

$$|\zeta_{\mathrm{F}}\rangle = |\zeta_{\mathrm{V}},\zeta_{\mathrm{Au}}\rangle = |\zeta_{\mathrm{Vo}},\zeta_{\mathrm{Vu}},\zeta_{\mathrm{Au}}\rangle \tag{11}$$

which, apart from being local, has a definite orbital occupancy associated with each orbital. It may therefore be useful to express the results of a full-basis KS optimization (discussed below) in the $|\zeta_{\mathrm{F}}\rangle$ basis (or in its orthogonalized counterpart), rather than in the atomic-orbital basis, as is usually done. Likewise, it may be useful to express KS response-function calculations and correlated calculations in this basis, as discussed in a forthcoming paper.

2.3. Full-Basis Molecular Optimization. At the beginning of the full-basis optimization, we have a density matrix $\mathbf{D}_{\mathrm{V}}$ [eq (10)] that represents the KS energy minimum in the molecular valence basis $|\zeta_{\mathrm{V}}\rangle$ but not yet in the full basis $|\zeta_{\mathrm{F}}\rangle \supset |\zeta_{\mathrm{V}}\rangle$. In the full basis, the corresponding density matrix is given by

$$\mathbf{D}_{\mathrm{V}}^{\mathrm{F}} = \begin{pmatrix} \mathbf{D}_{\mathrm{V}} & \mathbf{0} \\ \mathbf{0} & \mathbf{0} \end{pmatrix} \tag{12}$$

which (like $\mathbf{D}_{\mathrm{V}}$ in the valence basis) satisfies the symmetry, trace, and idempotency conditions. The molecular valence basis optimized density matrix $\mathbf{D}_{\mathrm{V}}$ is thus transferred to the full basis $|\zeta_{\mathrm{F}}\rangle$ without loss of information. Our final calculation is carried out in the $|\zeta_{\mathrm{F}}\rangle$ basis using $\mathbf{D}_{\mathrm{V}}^{\mathrm{F}}$ as the starting guess for an ARH optimization in this basis.

3. Illustrative Results

To illustrate the performance of the ARH-3L method, we present in Section 3.1 calculations on a Rh complex [(4-dimethylaminopyridine-*N*)dicarbonylchlororhodium [Rh(C_7N_2-H_{10})$(CO)_2$Cl]] at the B3LYP(VWN3)/3−21G level of theory[8−10] and on a model of vitamin B12, at the BP86/AhlrichsVDZ[11,12] level. The valence- and full-basis optimizations are carried out using the ARH method. In Section 3.2, ARH-3L optimizations are compared with optimizations using the RH/DIIS algorithm without RH level shifting. Most electronic-structure programs use a RH/DIIS algorithm with some level shifting in the initial RH iterations and possibly with other modifications so as to accelerate convergence.

In ref 4, van Lenthe et al. demonstrated the usefulness of their ATOMS approach by carrying out B3LYP calculations on 23 transition-metal complexes—in Section 3.3, we compare their results with those of the ARH-3L method.

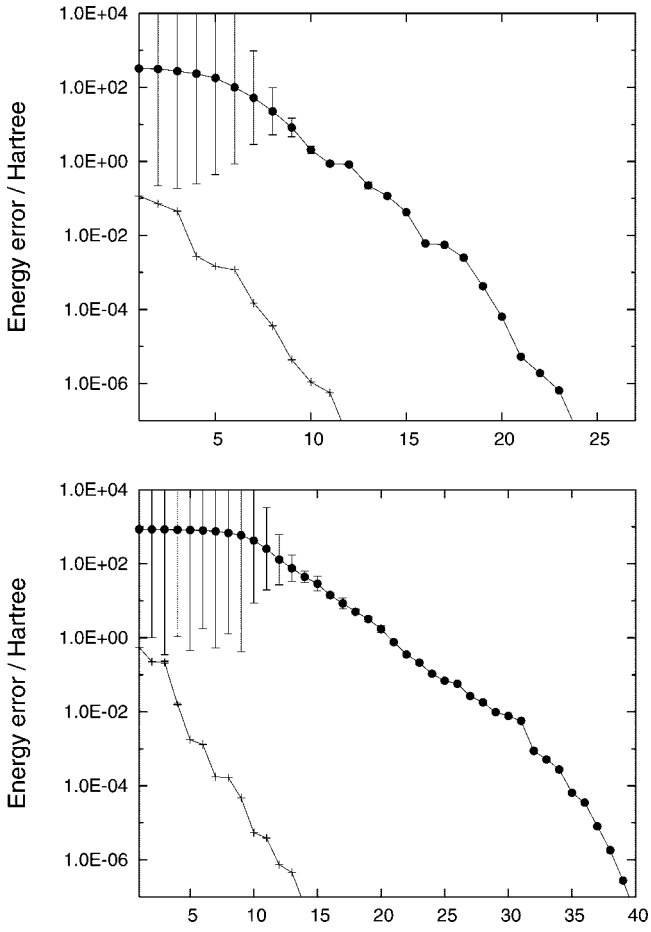

Figure 1. The convergence of calculations on the Rh complex (upper panel) and B12 (lower panel) using the ARH-3L method (plus signs) and ARH with a HCORE initial guess of the density matrix (full circles). The level shifts at each iteration are displayed as error bars.

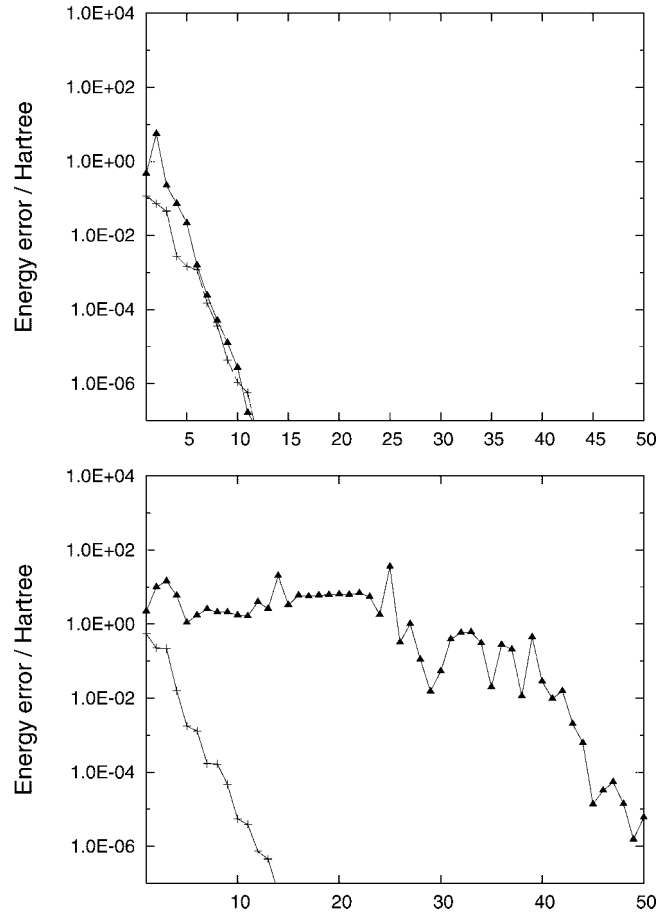

Figure 2. The convergence of calculations on the Rh complex (upper panel) and B12 (lower panel) using the ARH-3L method (plus signs) and RH/DIIS (full triangles) with ATOMS starting density matrix.

All calculations have been carried out with a development version of the Dalton program package.[13] For molecular geometries, see the Supporting Information.

3.1. Convergence of ARH-3L Calculations. In Figures 1 and 2, the convergence of the ARH-3L calculations on the Rh complex (upper panel) and B12 (lower panel) is compared to the convergence obtained using other optimization strategies, by plotting the energy at each full-basis iteration relative to the converged full-basis energy. In Figure 1, the convergence of ARH-3L calculations is compared with that of ARH calculations with a one-electron Hamiltonian (HCORE) starting guess. The error bars represent the magnitudes of the level shifts, plotted on a relative scale. Because of the poor HCORE starting guess, large shifts (up to 3.2 for the Rh complex and 42.4 for B12) are imposed in the global region (first 5−15 iterations) of the ARH optimization. These shifts decrease as the optimizations approach the local region, where no shifts are needed. By contrast, hardly any level shifts are needed in the ARH-3L optimizations, indicating that these optimizations begin close to the local region, bypassing the difficult global and semiglobal regions.

Although ARH calculations with HCORE starting guesses provide useful insight into the performance of the ARH-3L method, better guesses are usually used in electronic-structure programs. In Figure 2, we compare ARH-3L optimizations of the Rh complex (upper panel) and of B12 (lower panel) with optimizations using the plain RH/DIIS algorithm with an ATOMS starting density matrix and without level shifting in the initial iterations.

For the Rh complex, our plain RH/DIIS implementation converges in about the same number of iterations, as does the ARH-3L method. In the more difficult B12 case, the superiority of the ARH-3L method becomes more pronounced; the RH/DIIS method requires significantly more iterations than the ARH-3L method to reach convergence.

3.2. Robustness and Reliability of the ARH Algorithm. To demonstrate the robustness of the ARH algorithm, we here compare the convergence of the full-basis ARH method with that observed with the RH/DIIS implementation for the two test molecules, using the HCORE starting guess—see Figure 3. For both molecules, the ARH convergence is smooth and fast, while the convergence using RH/DIIS is more erratic. For the Rh complex, the optimizations require about the same number of iterations. For B12, on the other hand, the RH/DIIS method fails, whereas the ARH method shows its typical robust global convergence.

Because of the good starting density matrices in the ARH-3L method, it might be thought that the choice of optimization algorithm matters little. This is not the case, as demonstrated by calculations on an imidazolecadmium(2+)

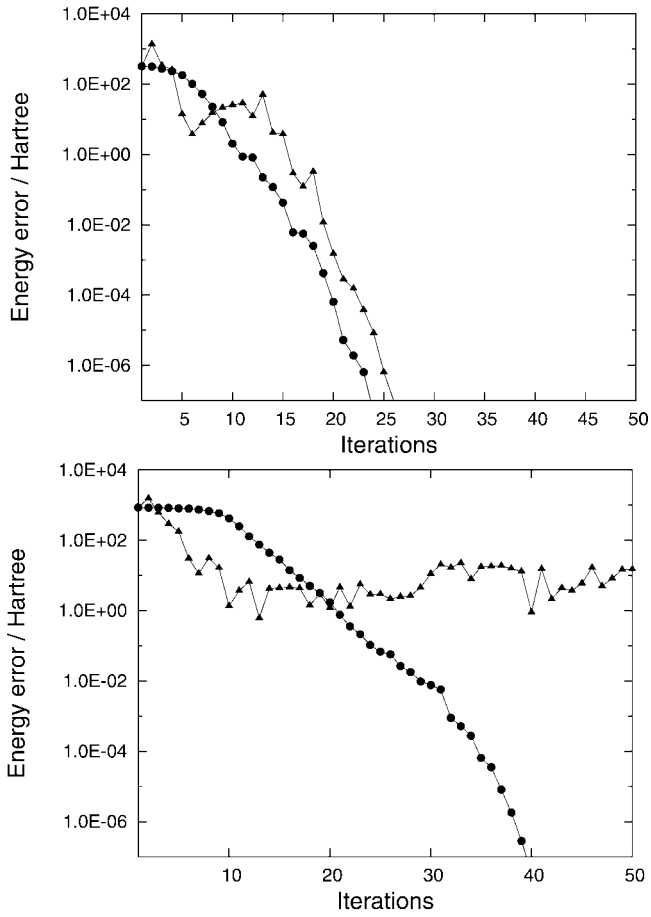

Figure 3. The convergence of calculations on the Rh complex (upper panel) and B12 (lower panel) with the HCORE starting density matrix using the ARH method (full circles) and the RH/DIIS method (full triangles).

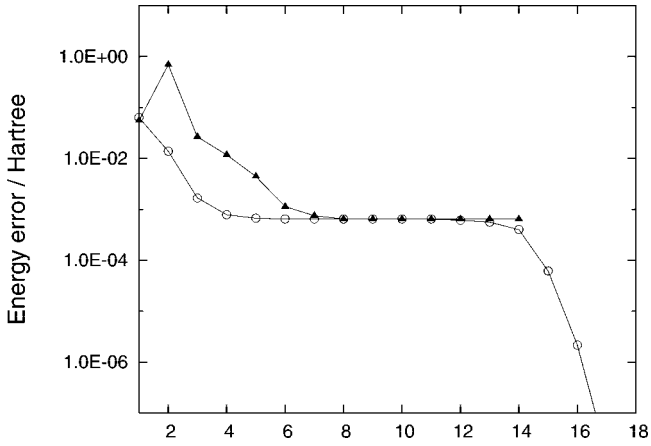

Figure 4. Convergence of full-basis B3LYP(VWN3)/3−21G calculations of imidazolecadmium(2+) using the ARH-3L (open circles) and RH/DIIS (full triangles) methods. Both calculations start from a valence-basis optimized density matrix.

complex, whose full-basis ARH-3L convergence is displayed in Figure 4. The horizontal plateau in Figure 4 arises as the optimization converges toward a saddle point. Close to the saddle point, the ARH algorithm detects a negative Hessian eigenvalue, upon which the optimization turns toward the minimum and converges quickly. From the same starting guess, the RH/DIIS calculation converges (very tightly, with a gradient norm less than 10^{-6}) to the same saddle point in few iterations, without recognizing that a saddle point instead of a minimum has been reached. Moreover, several standard programs also converge to this saddle point.[5] To avoid saddle-point convergence, it is therefore important to use the ARH algorithm, even with very good starting density matrices.

Table 1. Statistics for Calculations on a Test Set of 23 Transition-Metal Complexes[4a]

	ΔE (Hartrees)		num. of iter. (%)			
	max.	mean	best	mean	worst	fail
HCORE	159.63	159.63	291	291	291	22
MINGUESS	2.03	1.57	88	117	175	1
ATOMS	1.93	0.46	100	100	100	0
ARH-3L	0.20	0.06	42	78	94	0

[a] The HCORE, MINGUESS, and ATOMS results are taken from ref 4. In addition, results are given for the ARH-3L algorithm. ΔE is the energy difference between the initial and final iterations. The number of iterations is given in percent relative to the ATOMS calculation. The final column contains the number of optimizations that did not converge.

3.3. Comparison of ARH-3L and ATOMS Starting Density Matrices. We now consider the 23 transition-metal complexes studied by van Lenthe et al., using the RH/DIIS algorithm with the ATOMS starting guess and a predefined level shift in the first iterations.[4] For comparison, van Lenthe et al. reported MINGUESS calculations, where the starting guess was obtained in a preliminary STO-3G calculation and then projected onto the full TZVP basis[14] as well as calculations with the HCORE starting guess. The results of van Lenthe et al. are summarized in Table 1, which contains information on ΔE (the energy in the first iteration relative to the converged energy) and the number of iterations in the optimizations (in percent relative to the ATOMS calculations in the same table). We have augmented the table by including results obtained with the ARH-3L method.

The results in Table 1 demonstrate the superiority of the ARH-3L valence-basis starting guess, whose energy on average is only 0.06 hartree above the converged result, compared with 1.93 hartree for the ATOMS starting guess.

The MINGUESS calculations are not an improvement on the ATOMS calculations because of the errors introduced in the projection onto the TZVP basis. The loss of information that arises when the molecular STO-3G density matrix is projected onto the full basis is thus very significant. In the ARH-3L method, the molecular valence-basis density matrix is transferred to the full basis without loss of information.

On average, the ARH-3L calculations use 22% fewer iterations than do the ATOMS calculations—in the best case, 58% fewer iterations are needed. The ARH-3L method thus converges significantly faster than previous methods, already for these small systems.

4. The Three-Level Approach Summarized

We have presented a novel ARH-3L optimization scheme for the KS energy, consisting of three levels:

1) Atomic canonical-ensemble optimizations in the $|\chi^{P}\rangle$ atomic basis, giving a spherically symmetric atomic density matrix. Superposition of atomic density matrices is used as the starting guess in the valence-basis molecular optimization.

2) A valence-basis molecular ARH optimization in the $|\zeta_{Ao}\rangle$ basis, giving a valence-basis starting guess for the full-basis molecular optimization

3) A full-basis molecular ARH optimization of the KS energy

In the three-level ARH-3L method, information about the molecular system is built up gradually, exploiting chemical insight. Because of the high quality of the valence- and full-basis starting guesses, these minimizations begin close to the local region, bypassing almost entirely the difficult global region. The cost of the first two ARH-3L levels, where the global optimization is carried out, is insignificant compared with that of the third level.

The ARH-3L algorithm is highly cost-effective, requiring significantly fewer iterations than other algorithms, even for the small systems considered here. Bearing in mind that a large proportion of the CPU time allocated to quantum-chemical simulations is actually spent optimizing KS energies, this translates into considerable savings of computational resources. Furthermore, the ARH-3L method exhibits reliable convergence, also when standard methods fail. Last but not least, whereas the traditional methods may converge to saddle points, the ARH-3L method is designed to avoid such points. For both efficiency and reliability, we recommend its use in molecular KS calculations.

Acknowledgment. This work has been supported by the Lundbeck Foundation, the Danish Center for Scientific Computing (DCSC), and the Norwegian Science Research Council through the CeO Centre for Theoretical and Computational Chemistry (Grant no. 179658/V30).

Supporting Information Available: Atomic coordinates. This material is available free of charge via the Internet at http://pubs.acs.org.

References

(1) Hohenberg, P.; Kohn, W. Inhomogeneous Electron Gas. *Phys. Rev.* **1964**, *136*, B864−B871.

(2) Kohn, W.; Sham, L. J. Self-Consistent Equations Including Exchange and Correlation Effects. *Phys. Rev.* **1965**, *140*, B1133−B1138.

(3) Koch, W.; Holthausen, M. C. *A Chemist's Guide to Density Functional Theory*; Wiley-VCH: Weinheim, 2000; p 15.

(4) van Lenthe, J. H.; Zwaans, R.; van Dam, H. J. J.; Guest, M. F. Starting SCF Calculations by Superposition of Atomic Densities. *J. Comput. Chem.* **2006**, *27*, 926–932.

(5) Høst, S.; Jansík, B.; Olsen, J.; Jørgensen, P.; Reine, S.; Helgaker, T. A ground-state-directed optimization scheme for the Kohn−Sham energy. *Phys. Chem. Chem. Phys.* **2008**, *10*, 5344–5348.

(6) Pulay, P. Convergence acceleration of iterative sequences. The case of SCF iteration. *Chem. Phys. Lett.* **1980**, *73*, 393–398.

(7) Fletcher, R. *Practical Methods of Optimization*, 2nd ed.; Wiley: Chichester, 1987; pp 207−211.

(8) Becke, A. D. Density-functional thermochemistry. III. The role of exact exchange. *J. Chem. Phys.* **1993**, *98*, 5648–5652.

(9) Lee, C.; Yang, W.; Parr, R. G. Development of the Colle−Salvetti correlation-energy formula into a functional of the electron density. *Phys. Rev. B* **1988**, *37*, 785–789.

(10) Vosko, S. H.; Wilk, L.; Nusair, M. Accurate spin-dependent electron liquid correlation energies for local spin density calculations: a critical analysis. *Can. J. Phys.* **1980**, *58*, 1200–1211.

(11) Becke, A. D. Density-functional exchange-energy approximation with correct asymptotic behavior. *Phys. Rev. A* **1988**, *38*, 3098–3100.

(12) Perdew, J. P. Density-functional approximation for the correlation energy of the inhomogeneous electron gas. *Phys. Rev. B* **1986**, *33*, 8822–8824.

(13) *Dalton, an ab initio electronic structure program, Release 2.0*; 2005. See http://www.kjemi.uio.no/software/dalton/dalton.html (accessed February 5, 2009).

(14) Schäfer, A.; Huber, C.; Ahlrichs, R. Fully optimized contracted Gaussian basis sets of triple zeta valence quality for atoms Li to Kr. *J. Chem. Phys.* **1994**, *100*, 5829–5835.

CT800562H

JCTC Journal of Chemical Theory and Computation

Intramolecular Nonbonded Attractive Interactions: 1-Substituted Propenes

Kenneth B. Wiberg,*,† Yi-gui Wang,† George A. Petersson,*,‡ and William F. Bailey§

Department of Chemistry, Yale University, New Haven, Connecticut 06520-8107, Department of Chemistry, Wesleyan University, Middletown, Connecticut 06459-0180, and Department of Chemistry, University of Connecticut, Storrs, Connecticut 06269-3060

Received February 2, 2009

Abstract: Whereas *cis*-substituted alkenes are normally significantly less stable than the *trans*-isomers, there is a group of 1-substituted propenes (X = F, OMe, Cl, Br, SMe) where the *cis*-isomers are the more stable. The calculated structures show that there is steric repulsion with the *cis*-isomers. However, this is overcome by attractive Coulombic interactions when X = F or OMe and by attractive dispersive interactions when X = Cl or Br. It was possible to calculate the magnitude of the latter term via the summation of the appropriate MP2 pair energies. The calculated and observed energy differences could be reproduced by a summation of steric, electrostatic, and dispersive interactions.

The *cis*-isomers of disubstituted ethenes are normally less stable than the corresponding *trans*-isomers as a result of a steric interaction between the substituents. As an example, *cis*-2-butene has a higher energy (1.1 kcal/mol) than *trans*-2-butene.[1] Nonbonded intramolecular interactions that stabilize molecules have been of considerable interest. Some 1-substituted propenes are examples of compounds that apparently exhibit attractive intramolecular interactions as evidenced by the fact that the *cis*-isomers are more stable than the *trans*-isomers. These compounds have received considerable study, both experimental[2,3] and computational.[4,5] The experimental observations are recorded in Table 1 along with the derived $\Delta G°$ values and their estimated uncertainties.

The *cis*-isomers of these 1-substituted propenes must be stabilized enough to overcome the normal steric interactions that beset such molecules. These stabilizing interactions may include (1) attractive Coulombic interactions between the substituents, which could result from interaction of bond dipoles that are oriented appropriately;[3b] (2) delocalization of valence electrons associated with one group into a vacant orbital on the other group;[5] and/or (3) stabilizing van der Waals interactions between the groups.

Table 1. Observed Equilibrium Compositions and Free Energy Differences of 1-Substituted Propenes at 30−40° C

compound	% cis	$\Delta G°$ (kcal/mol)	ref
$CH_3CH{=}CHOMe$	71	0.53 ± 0.06	3a
$CH_3CH{=}CHOEt$	81	0.86 ± 0.08	3a
$CH_3CH{=}CHCl$	76	0.68 ± 0.06	3b
$CH_3CH{=}CHBr$	68	0.45 ± 0.06	3c
$CH_3CH{=}CHCN$	61	0.26 ± 0.04	3b

In order to gain further information about the intramolecular interactions within these molecules, we have carried out geometry optimizations at the HF, DFT, and MP2 levels using the aug-cc-pVTZ basis set. CCSD(T)/aug-cc-pVTZ calculations were carried out using the MP2 geometries. The HF calculations do not include electron correlation, so the effect of nonbonded van der Walls attractive terms will not be seen. The use of the density functionals will allow some correction for electron correlation but may not correctly reproduce van der Waals (dispersive) interactions,[6] MP2 provides modest correction for electron correlation, and CCSD(T) gives superior correction for this effect. The latter methods would be expected to reproduce the van der Waals terms.[7] Thus, it was anticipated that a comparison of the relative energies at these different levels would give information on the nature of the intramolecular interactions present in 1-substituted propenes.

* Corresponding author e-mail: kenneth.wiberg@yale.edu.
† Yale University.
‡ Wesleyan University.
§ University of Connecticut.

10.1021/ct900059e CCC: $40.75
Published on Web 03/04/2009

Table 2. Relative Energies (Trans ⇌ Cis) of 1-Substituted Propenes[a]

X	HF	B3LYP	MP2	CCSD[b]	CCSD(T)[b]
F	−0.53	−0.56	−0.70	−0.63	−0.65
OMe	−0.56	−0.63	−0.95	−0.76	−0.80
CN	0.09	−0.11	−0.72	−0.37	−0.50
CH_3	1.56	1.25	1.04	1.13	1.06
Cl	0.01	−0.33	−0.77	−0.49	−0.60
Br	0.18	−0.27	−0.99	−0.63	−0.79
SMe	0.65	−0.26	−0.57	−0.14	−0.35

[a] No zero-point or thermal corrections, in kcal/mol, using aug-cc-pVTZ. [b] aug-cc-pVTZ using MP2/aug-cc-pVTZ geometries.

The substituents F, Cl, Br, CN, and CH_3 lead to conformers that have C_s symmetry with a methyl hydrogen eclipsing the C−C double bond.[8] With X = OMe or SMe, the substituent rotates so that a lone pair may interact with the carbon−carbon double bond. The situation with respect to the enamine, X = NMe_2, was somewhat more complex. The *trans*-isomer of the enamine with C_s symmetry was a stationary point on the potential energy surface with no imaginary frequencies. However, the *cis*-isomer was a transition state, and rotation of the substituent to allow the lone pair to interact with C=C led to a lower energy structure. An MP2 optimization of the *trans*-structure with reduced symmetry also led to a lower energy structure. The rotated structures were minima at B3LYP and CCSD as well as MP2. However, whereas the *trans*-isomer of the enamine presented no steric problems, a methyl of the NMe_2 group in the *cis*-isomer interfered with the terminal methyl at C(2). As a result, the relative energies of the enamine (X = NMe_2) are not comparable to those of the other 1-substituted propenes and will not be further considered.

Since we are primarily interested in the purely electronic interactions that lead to the energy differences, Table 2 gives the results of the calculations, without correction for zero-point energies or the change in energy with temperature. It was not practical for us to carry out geometry optimizations at the CCSD/aug-cc-pVTZ level, and therefore these energies were calculated using the MP2/aug-cc-pVTZ optimized geometries.

Inspection of the results summarized in Table 2 reveals that for the first-row substituents, X = F or OMe, the calculated relative energies are essentially independent of the method used. However, with X = Cl, the HF relative energy is essentially zero, and it became positive, favoring the *trans*-isomer, with X = Br or SMe. In contrast to the HF results, the *cis*-preference is maintained when X = Cl, Br, or SMe using all of the methods that include electron correlation. Taking the CCSD(T) relative energies as the more reliable, MP2 overcorrects somewhat, as is often observed.[9] The negative triple excitations, $e(T)_{ijk}$, partly cancel the positive semijoint third-order pair coupling terms, $e^{(3)}_{ij,jk}$, so the CCSD(T) relative energies are about halfway between the MP2 and the CCSD results. The DFT models also reproduce the *cis* preference and therefore *appear* to include short-range dispersion effects even though they have no terms that include true R^{-6} dispersive effects.[10]

The change in relative energies at the HF level is probably largely the result of steric interactions, as is suggested by the data presented in Tables 3 and 4. The results summarized in Table 3 indicate that the C=C-Me bond angle is larger with the *cis*-isomers than with *trans*-isomers, and this difference increases on going from X = F to Cl and Br. The effect may also be seen in comparing *cis*- and *trans*-2-butene where the *trans*-form is favored.

Table 3. Calculated C=C-Me Angles for 1-Substituted Propenes, MP2/aug-cc-pVTZ

X	cis	trans
F	125.24	122.38
Cl	126.78	122.64
Br	127.00	122.63
CN	125.21	123.78
CH_3	127.22	124.59
OMe	124.54	122.70
SMe	125.14	123.66

Table 4. Calculated CH_3 Rotational Barriers and CH_3 Torsion Frequencies (in cm^{-1}), B3LYP/aug-cc-pVTZ

X	cis	ν	trans	ν
F	1.07 (1.06)[a]	151*i*	2.14 (2.20)[a]	223*i*
OMe	0.71	108*i*	2.12	219*i*
CN	1.44 (1.39)[a]	168*i*	1.91	212*i*
Me	0.98	128*i*	1.96	207*i*
Cl	0.75 (0.62)[a]	109*i*	2.02 (2.17)[a]	215*i*
Br	0.73	116*i*	2.00	214*i*
SMe	0.56	92*i*	1.91	203*i*

[a] Observed values (ref 11).

The data summarized in Table 4 show that the *cis*-isomers have a smaller methyl rotational barrier than *trans*-isomers as observed experimentally[11] and that the methyl torsion frequency is smaller for *cis*-isomers than *trans*-isomers. Both of these observations are consistent with a repulsive interaction between the methyl group and the *cis*-substituent.

The observation that the experimentally observed preference for the *cis*-isomer of 1-fluoropropene is reproduced at all theoretical levels, whereas this is not true for the other halogens, implies that the origin of the *cis*-preference in 1-fluoropropene is different than that responsible for the *cis*-preference of the other 1-halopropenes. In view of the large electronegativity of fluorine in comparison with the other halides, a reasonable hypothesis is there is a significant attractive Columbic interaction between the negatively charged fluorine at C(1) in the *cis*-isomer and the presumably positively charged methyl (a result of being attached to a double bond as well as the inductive effect of the 1-fluoro substituent) as suggested some time ago by Crump.[3b] The effect would be larger for the *cis*-isomer than for the *trans*-isomer because the former has the shorter nonbonded F···Me distance.

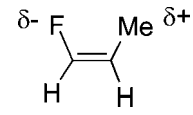

One might examine the validity of this hypothesis by evaluating the magnitude of the electrostatic interaction. This requires some method of obtaining the relevant atomic charges. This has been a continuing problem since atomic

Table 5. Calculated Dipole Moments of Haloethenes (CH_2=CHX) Using aug-cc-pVTZ

compound	calculation	μ_x	μ_y	μ_{total}
CH_2=CHF	CCSD	1.267	0.748	1.471
	Hirshfeld atomic	0.944	0.526	1.081
	Hirshfeld dipole	0.319	0.219	0.387
	Hirshfeld total	1.263	0.745	1.467
CH_2=CHCl	CCSD	1.197	0.907	1.501
	Hirshfeld atomic	0.963	0.712	1.198
	Hirshfeld dipole	0.261	0.173	0.280
	Hirshfeld total	1.185	0.884	1.478
CH_2=CHBr	CCSD	1.156	0.924	1.480
	Hirshfeld atomic	0.953	0.740	1.206
	Hirshfeld dipole	0.201	0.161	0.258
	Hirshfeld total	1.154	0.901	1.464

Table 6. Effective Atomic Charges Based on the Hirshfeld Charges and the Dipole Moments[a]

compound	X	C_1H	C_2H	CH_3	μ(D)
cis-CH_3CH=CHF	−0.218	0.190	−0.010	0.038	1.464 (1.555)
trans-CH_3CH=CHF	−0.226	0.189	−0.009	0.039	1.873 (1.889)
cis-CH_3CH=CHCl	−0.156	0.101	0.023	0.035	1.533 (1.553)
trans-CH_3CH=CHCl	−0.172	0.102	0.027	0.044	2.032 (1.837)
cis-CH_3CH=CHBr	−0.031	0.126	0.075	0.029	1.613 (1.608)
trans-CH_3CH=CHBr	−0.071	0.145	0.076	0.031	1.865 (1.891)

[a] Values in parentheses are the ab initio MP2/aug-cc-pVTZ calculated values.

charges in molecules are not well defined, and different methods for calculating them give different results.[12]

In order to try to obtain some additional information, we have studied the haloethenes (CH_2=CHX). The structures of the haloethenes were calculated at the CCSD/aug-cc-pVTZ level of theory, and the dipole moment components were reoriented to place the C=C bond along the x axis. The calculated dipole moments are given in Table 5.

There is remarkably little difference in the dipole moments of the haloethenes and their components (z is out-of-plane so μ_z is zero), despite the large difference in electronegativity among the halogens. This is the result of a compensating increase in C-X bond length as the smaller electronegativity decreases the halogen charge. One of the more successful definitions of atomic charges is that of Hirshfeld[13] that also gives the atomic dipoles, originating from nonspherical charge distribution about the atoms. The results of these calculations are included in Table 5. It can be seen that the Hirshfeld charges reproduce the ab initio calculated dipole moments quite well when the atomic dipoles are included.

The MP2/aug-cc-pVTZ calculated dipole moments of the 1-halopropenes are summarized in Table 6. Again, there is little change in going from one halogen to another. In this case, we examined several models for calculating atomic charges. One computational method, ChelpG,[14] uses a least-squares fit to the electrostatic potential, with the dipole moments used as a constraint. However, an examination of the halopropenes found large differences in these charges on going from *cis*- to *trans*-isomers (Supporting Information), whereas all other methods for obtaining charges find little difference in charge between *cis*- and *trans*-forms. Therefore, they are clearly not satisfactory for the present purpose.

The atomic charges for the 1-halopropenes were obtained using the NPA,[15] AIM,[16] and Hirshfeld[13] definitions. The CH bond dipoles calculated using NPA are known to be exaggerated,[17] and so the hydrogen charges were combined with the carbon charges. The dipole moments calculated using the NPA and AIM charges[18] varied considerably and did not agree with those from the ab initio calculations. However, the moments calculated using the Hirshfeld charges did not vary much on going from 1-fluoropropene to 1-chloropropene, although they were somewhat too small if the atomic dipoles are not included. Therefore, we further examined the Hirshfeld charges. In order to simplify the calculations, the atomic dipoles were neglected, and the atomic charges were scaled to account for this neglect.

With X = F and Cl, the average ratio of the ab initio dipole moments to those obtained using the Hirshfeld charges was 1.51 ± 0.06. The charges were scaled by this ratio giving the charges summarized in Table 6. The last column in Table 6 has the dipole moments calculated from these charges, and they can be seen to compare favorably with the ab inito values given in parentheses. As expected, the charge on X decreases on going from F to Cl and Br.

Clearly, these effective charges are just approximations, but they do fit the ab initio calculated dipole moments fairly well, and the halogen charges change in the expected fashion. They are, in any event, the best we have been able to obtain.

The differences in the intramolecular electrostatic interactions present in the *cis*- and *trans*-isomers were calculated using these charges, and the results are presented in Table 7. As noted some time ago by Westheimer and Kirkwood,[19] one must account for the fact that the polarizable C=C group lies between the substituents in the *trans*-isomer, and a hydrocarbon dielectric constant of 2 was used for this purpose.

Table 7 also includes *cis*- and *trans*-2-butene in order to have a case where the normal trans preference is found. In order to compare the results with the HF energy differences, it is necessary to include the steric repulsions between the methyl hydrogens and the substituents. They were estimated by calculation of the Pauli repulsion for H···X in the $^3\Sigma$ state and scaling the result by 0.4 in order to reproduce the rotational barrier in ethane (see the Supporting Information). The sum of the Coulombic and steric term fairly well reproduce the HF energy differences, although the steric term for X = F appears to be a little too large as compared to that for X = Cl.

Now, it remains to explain the difference between the HF and MP2 relative energies for the isomers. The MP2 correlation energy is a sum of *pair energies*, one for each pair of occupied SCF orbitals:

$$E^{(2)} = \sum_{i<j}^{occ} e_{ij}^{(2)} = \sum_{i<j}^{occ} \left\{ \sum_{a<b}^{virt} \frac{|\langle ij||ab\rangle|^2}{\varepsilon_i + \varepsilon_j - \varepsilon_a - \varepsilon_b} \right\}$$

The sum of these pair energies is invariant to unitary transformations among the occupied orbitals.[20] We are therefore free to localize the occupied orbitals.[21] The resulting second-order pair correlation energies between halogen lone pair electrons and methyl C−H bond electrons (Figure 1) can be interpreted as *intra*molecular dispersion energies. The details are included as Supporting Information. The method we use is essentially the same as the method employed by Grimme, Műck-Lichtenfeld,

Table 7. Interpretation of the HF Results for 1-Halopropene Isomers

X	qX	qMe	r(X···Me)	qq/r[a]	Δqq/r	Pauli H···X	scaled	total	ΔE_{HF}[b]
cis-F	−0.218	0.038	2.908	−0.946	−0.553	0.775	0.310	−0.243	−0.521
trans-F	−0.226	0.039	3.725	−0.393					
cis-Cl	−0.156	0.035	3.199	−0.567	−0.261	0.997	0.391	0.130	0.101
trans-Cl	−0.172	0.044	4.103	−0.306					
cis-Br	−0.031	0.039	3.299	−0.122	−0.036	1.282	0.513	0.477	0.373
trans-Br	0.071	0.031	4.246	−0.086					
cis-Me	0.007	0.007	3.151	0.005	0.003	3.752	1.501	1.504	1.640
trans-Me	0.006	0.006	3.909	0.005					

[a] The Coulombic effect for the trans isomers were reduced by a factor of 2 (see text). [b] $E_{cis} - E_{trans}$.

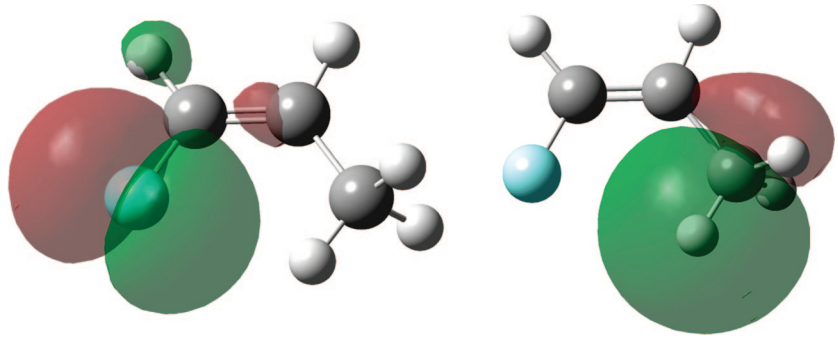

Figure 1. Examples of MP2 localized orbitals for 1-fluoropropene. The full set may be found in the Supporting Information.

Table 8. Interpretation of the HF-MP2 Relative Energy Differences[a]

X	E_{HF}	E_{MP2}	ΔE_{HF}	ΔE_{MP2}	$\Delta E_{MP2} - \Delta E_{HF}$	ΔE_{Disp}	Disp[b]
cis-F	−216.00815	−216.77183	−0.521	−0.707	−0.186	−0.221	−10.634
trans-F	−216.00732	−216.77071					−10.413
cis-Cl	−576.05438	−576.75803	0.101	−0.763	−0.864	−0.926	−12.559
trans-Cl	−576.05454	−576.75681					−11.673
cis-Br	−2688.99619	−2698.74332	0.373	−0.989	−1.362	−1.208	−12.909
trans-Br	−2688.99676	−2698.74174					−11.701
cis-Me	−156.16616	−156.86107	1.640	1.039	−0.601	−0.792	−11.612
trans-Me	−156.16877	−156.86273					−10.820

[a] The total energies are given in atomic units (H), and the energy differences are given in kcal/mol. [b] Total interatomic pair energies not including geminal interactions.

Table 9. Components Contributing to the Relative Energies of the *cis*- and *trans*-Isomers of 1-Substitued Propenes[a]

X	qq/r	steric	Disp	total	MP2	CCSD[b]	CCSD(T)
F	−0.553	0.320	−0.221	−0.464	−0.70	−0.63	−0.65
Cl	−0.261	0.391	−0.926	−0.796	−0.77	−0.49	−0.60
Br	−0.036	0.513	−1.028	−0.731	−0.99	−0.63	−0.79
CH_3	0.003	1.501	−0.792	0.712	1.04	1.13	1.06

[a] No zero-point or thermal corrections, in kcal/mol, using aug-cc-pVTZ. [b] At MP2/aug-cc-pVTZ geometries.

and Antony.[22] These intramolecular dispersion energies are compared with the total MP2 energy differences in Table 8. Given that we are looking at small differences between large numbers, the agreement is rather good. The contribution of the correlation energy to the *cis*−*trans* energy differences is in all cases almost entirely due to intramolecular dispersion.

Combining the results from Tables 7 and 8, we obtain a detailed explanation for the calculated *cis*−*trans* energy differences in Table 2. The summary in Table 9 demonstrates that electrostatic, steric, and dispersion interactions all play significant roles in determining the relative stability of the *cis*- and *trans*-isomers of 1-substituted propenes. In short, the relatively constant energetic preference found favoring the *cis*-isomers of 1-halopropenes masks the varying roles of electrostatic and dispersion interactions within these molecules.

Summary

Although the *cis*-1-substituted propene with X = F, OMe, CN, Cl, Br, and SMe are more stable than their *trans*-isomers, the structural parameters indicate that they are subject to steric repulsion as is found with most compounds of this type. The observed *cis*-preference is due to a combination of Coulombic attraction between X and the terminal methyl (particularly important with X = F or OMe) and a dispersion interaction between X and the terminal methyl group (particularly important with X = Cl, Br, or SMe). The contribution of each of these terms to the relative energies has been estimated making use of model steric calculations,

Hirshfeld atomic charges, and MP2 pair energies. The results are in satisfactory agreement with the differences in calculated total energies.

Calculations

All of the ab initio calculations were carried out using a development version of Gaussian.[23] The Hirshfeld charges were obtained using a local program.[24] The MO plots were made using Gaussview.

Acknowledgment. Research at Yale was supported by the National Science Foundation (Grant CHE-0445847). The work at Wesleyan was supported by Gaussian, Inc.

Supporting Information Available: Calculated energies and structures, comparison of calculated atomic charges, detailed information concerning the MP2 pair energies and the complete ref 23. This material is available free of charge via the Internet at http://pubs.acs.org.

References

(1) Pedley, J. R. *Thermochemical Data and Structures of Organic Compounds*; Thermodynamics Research Center: College Station, TX, 1994.

(2) For a review, see: Lowe, J. P. *Prog. Phys. Org. Chem.* **1968**, *6*, 1.

(3) (a) Salomma, P.; Nissi, P. *Acta Chem. Scand.* **1967**, *21*, 1386. (b) Crump, J. W. *J. Org. Chem.* **1963**, *28*, 953. (c) Harwell, K. E.; Hatch, L. F. *J. Am. Chem. Soc.* **1955**, *77*, 1682.

(4) Hagen, K.; Stolevik, R. *J. Mol. Struct.* **1996**, *376*, 83.

(5) (a) Epiotis, N. D.; Bjorkquist, D.; Bjorkquist, L.; Sarkanen, S. *J. Am. Chem. Soc.* **1973**, *95*, 7558. (b) Epiotis, N. D. *J. Am. Chem. Soc.* **1973**, *95*, 3087. (c) Allen, L. C.; Scartzafava, E. *J. Am. Chem. Soc.* **1971**, *93*, 311. (d) Hu, Z.-Q.; Zhu, X.-D. *Youji Huaxue* **2002**, *22*, 200. (e) Rois, B.; Taddei, F. *THEOCHEM* **1998**, *430*, 113.

(6) Tsuzuki, S.; Uchimara, T.; Tanabe, K. *Chem. Phys. Lett.* **1998**, *287*, 202.

(7) Jeziorski, B.; Szalewicz, K. In *Encyclopedia of Computational Chemistry*; Schleyer, P. v. R., Ed.; Wiley: Chichester, U.K., 1998; pp 1379−1388.

(8) This is the usual observation for alkenes: Wlodarczak, G.; Demaison, J.; Heineking, N.; Csaszar, A. G. *J. Mol. Spectrosc.* **1994**, *167*, 239.

(9) Cremer, D. In *Encyclopedia of Computational Chemistry*; Schleyer, P. v. R., Ed.; Wiley: Chichester, U.K., 1998; pp 1706ff.

(10) Hu, C.-H.; Chong, D. P. In *Encyclopedia of Computational Chemistry*; Schleyer, P. v. R., Ed.; Wiley: Chichester, U.K., 1998; p 675.

(11) (a) Siegel, S. *J. Chem. Phys.* **1957**, *27*, 989. (b) Beaudet, R. A.; Wilson, E. B., Jr. *J. Chem. Phys.* **1962**, *37*, 1133. (c) Beaudet, R. A. *J. Chem. Phys.* **1962**, *37*, 2398. (d) Beaudet, R. A. *J. Chem. Phys.* **1964**, *40*, 2705. (e) Lesarri, A. G.; Cosleoo, J.; Li, X.; Wlodarczak, G.; Demaison, J. *J. Mol. Spectrosc.* **1995**, *172*, 520. (f) Durig, J. R.; Guirgis, G. A. *J. Raman Spectrosc.* **1982**, *13*, 160.

(12) Wiberg, K. B.; Rablen, P. *J. Comput. Chem.* **1993**, *14*, 1504.

(13) Hirshfeld, F. L. *Theor. Chim. Acta* **1977**, *44*, 129. Nalewajski, R. F.; Parr, R. G. *Proc. Natl. Acad. Sci.* **2000**, *97*, 8879. Parr, R. G.; Ayers, P. N.; Nalewajski, R. F. *J. Phys. Chem. A* **2005**, *109*, 3957.

(14) Breneman, C. M.; Wiberg, K. B. *J. Comput. Chem.* **1990**, *11*, 361.

(15) (a) Reed, A. E.; Weinstock, R. B.; Weinhold, F. A. *J. Chem. Phys.* **1985**, *83*, 735. (b) Reed, A. E.; Weinhold, F. A.; Curtiss, L. A. *Chem. Rev.* **1988**, *88*, 899.

(16) Bader, R. F. W. *Atoms in Molecules. A Quantum. Theory*; Clarendon Press: Oxford, U.K., 1990..

(17) Reed, A. E.; Weinhold, F. *J. Chem. Phys.* **1986**, *84*, 2428.

(18) When the atomic dipoles are included, the AIM charges do reproduce the calculated dipole moments. Although these charges are well defined and useful, they are not as convenient as the Hirshfeld charges in comparing charges between related molecules because of the sensitivity of the atomic volumes to changes in electronegativity.

(19) Westheimer, F. H.; Kirkwood, J. G. *J. Chem. Phys.* **1938**, *6*, 513. (a) Kirkwood, J. G.; Westheimer, F. H. *J. Chem. Phys.* **1938**, *4*, 506. (b) Cf. Eucken, A. *Angew. Chem.* **1932**, *45*, 203.

(20) Ochterski, J. W.; Petersson, G. A.; Montgomery, J. A., Jr. *J. Chem. Phys.* **1996**, *104*, 2598.

(21) Montgomery, J. A., Jr.; Frisch, M. J.; Ochterski, J. W.; Petersson, G. A. *J. Chem. Phys.* **2000**, *112*, 6532.

(22) Grimme, S.; Műck-Lichtenfeld, C.; Antony, J. *Phys. Chem. Chem. Phys.* **2008**, *10*, 3327.

(23) Frisch, M. J. et. al. Gaussian development version, 2006. The full reference is given in the Supporting Information.

(24) Rablen, P. R. Ph.D. thesis, Yale, 1994.

CT900059E

JCTC Journal of Chemical Theory and Computation

Development of OPLS-AA Force Field Parameters for 68 Unique Ionic Liquids

Somisetti V. Sambasivarao and Orlando Acevedo*

Department of Chemistry and Biochemistry, Auburn University, Auburn, Alabama 36849

Received January 6, 2009

Abstract: OPLS-AA force field parameters have been developed and validated for use in the simulation of 68 unique combinations of room temperature ionic liquids featuring 1-alkyl-3-methylimidazolium [RMIM] (R = Me, Et, Bu, Hex, Oct), *N*-alkylpyridinium [RPyr], and choline cations, along with Cl^-, PF_6^-, BF_4^-, NO_3^-, $AlCl_4^-$, $Al_2Cl_7^-$, TfO^-, saccharinate, and acesulfamate anions. The new parameters were fit to conformational profiles from gas-phase ab initio calculations at the LMP2/cc-pVTZ(-f)//HF/6−31G(d) theory level and compared to experimental condensed-phase structural and thermodynamic data. Monte Carlo simulations of the ionic liquids gave relative deviations from experimental densities of ca. 1−3% at 25 °C for most combinations and also yielded close agreement over a temperature range of 5 to 90 °C. Predicted heats of vaporization compared well with available experimental data and estimates. Transferability of the new parameters to multiple alkyl side-chain lengths for [RMIM] and [RPyr] was determined to give excellent agreement with charges and torsion potentials developed specific to desired alkyl lengths in 35 separate ionic liquid simulations. As further validation of the newly developed parameters, the Kemp elimination reaction of benzisoxazole via piperidine was computed in 1-butyl-3-methylimidazolium hexafluorophosphate [BMIM][PF_6] using mixed quantum and molecular mechanics (QM/MM) simulations and was found to give close agreement with the experimental free energy of activation.

Introduction

Ionic liquids are a unique class of solvent, generally defined as a material containing only ionic species with a melting point below 100 °C.[1,2] These "designer" solvents are typically composed of a low symmetry organic cation, such as the well-recognized 1-alkyl-3-methylimidazolium [RMIM] and *N*-alkylpyridinium [RPyr] cation classes, and a weakly coordinating inorganic or organic anion with a diffuse negative charge like hexafluorophosphate [PF_6] or tetrafluoroborate [BF_4].[3] Ion components can be fine-tuned through different functional groups to enhance the degree of localized structuring in the liquid phase, which distinguishes ionic liquids from molecular solvents and solutions containing dissociated ions.[4] This distinctive structural behavior[5] in conjunction with their attractive properties, e.g., low viscosities, negligible vapor pressure, and excellent thermal and chemical stabilities, has led to numerous advances in electrochemistry,[6] separation science,[7] catalysis,[8−10] organic synthesis,[11] materials,[12] and applications with lanthanides and actinides.[13]

Ionic liquids are often touted as green alternatives to volatile organic solvents. However, their potential impact on the environment is strongly dictated by ionic liquid selection.[9,14,15] For example, toxicity testing of 1-butyl-3-methylimidazolium [BMIM] and *N*-1-butylpyridinium [BPyr] on *Daphnia magna*, a common fresh water crustacean and aquatic food-chain base, found the cations to be half as toxic as toluene (EC_{50} of ca. 20 mg/L) and increasing the alkyl chain length to dodecyl increased the ecotoxicity by a factor of 2500 (EC_{50} of 4 μg/L).[15] In addition, combinations of [BMIM] with [BF_4] or [PF_6] anions have been determined to possess a negligible biodegradability,[16] allowing for their persistence in the environment for a considerable length of time. More environmentally friendly ionic liquids have

* E-mail: orlando.acevedo@auburn.edu.

10.1021/ct900009a CCC: $40.75
Published on Web 03/12/2009

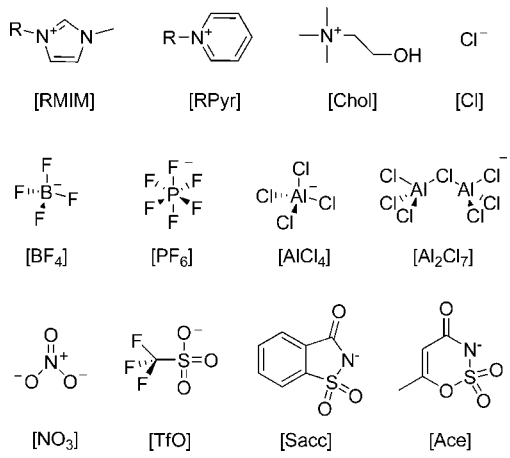

Figure 1. Ionic liquid-forming ions. R = M (methyl), E (ethyl), B (butyl), H (hexyl), and O (octyl).

recently been explored based on the choline cation [Chol],[17] a food-grade additive, and imidazolium derivatives designed for biodegradability[18] in combination with anions based on amino acids,[19] saccharinate [Sacc],[17] and acesulfamate [Ace][17,20] ([Sacc] and [Ace] are used as artificial sweeteners).

This study seeks to develop force field potentials for the atomistic simulation of both widely used ionic liquid combinations and next-generation alternatives with smaller environmental impact. In this respect, OPLS-AA parameters have been created and validated for use in the simulation of 68 unique combinations of room temperature ionic liquids featuring [RMIM] (R = Me, Et, Bu, Hex, Oct), [RPyr], and [Chol] cations, along with [PF_6], [BF_4], [Sacc], [Ace], nitrate [NO_3], chloride [Cl], tetrachloroaluminate [$AlCl_4$], heptachlorodialuminate [Al_2Cl_7], and triflate [TfO] anions (Figure 1). Many of the ions presented in this work have already been featured in other molecular dynamics[21−24] and Monte Carlo[25] studies for a variety of force fields, e.g., CHARMM,[26] AMBER,[27] and OPLS-AA.[28] Therefore it is important to stress that in addition to the parametrization of previously unpublished ionic liquids, e.g., [Chol], [Sacc], and [Ace], this study explored an unprecedented number of cation/anion combinations with two completely different charge and torsion sets for a detailed comparison of parameter transferability. The first charge/torsion set is potentially transferable to any alkyl side-chain length on the [RMIM] and [RPyr] cations (tested up to R = octyl) and the second set is specific to the ionic liquid cations: [EMIM], [BMIM], [MPyr], [EPyr], and [BPyr]. In addition, the current work validated the parameters for temperatures ranging from 5 to 90 °C against experimental densities for 11 unique ionic liquid combinations; most previous work focused on room temperature.

Monte Carlo (MC) simulations of the ionic liquid parameters gave predicted densities and heats of vaporization, ΔH_{vap}, in close agreement with experimentally observed values. The driving force behind the newly developed parameter set is to produce a computationally accurate representation of the reaction medium for use in mixed quantum and molecular mechanics (QM/MM) calculations. The objective is to understand the microscopic details on how ionic liquids influence chemical reactions accelerated and controlled by different cation and anion combinations.[8,9] Our recent work on Diels−Alder reactions in the chloroaluminate ionic liquids [EMIM][$AlCl_4$] and [EMIM][Al_2Cl_7] emphasized the importance of intermolecular interactions on the rate of reaction.[25] In this study, the Kemp elimination ring-opening of benzisoxazole in [BMIM][PF_6] using piperidine as the base has been carried out using QM/MM calculations and was found to give good agreement with the experimental free energy of activation.

Computational Methods

OPLS-AA Force Field. The OPLS-AA force field[28] formalism was chosen to represent the ionic liquids. As a brief overview, the total energy of the ionic systems are evaluated as a sum of individual energies for the harmonic bond stretching and angle bending terms, a Fourier series for torsional energetics, and Coulomb and 12−6 Lennard−Jones terms for the nonbonded interactions, see eqs 1−4. The parameters are the force constants k, the r_o and θ_o reference values, the Fourier coefficients V, the partial atomic charges, q, and the Lennard−Jones radii and well depths, σ and ε.

$$E_{\text{bonds}} = \sum_i k_{b,i}(r_i - r_{o,i})^2 \quad (1)$$

$$E_{\text{angles}} = \sum_i k_{b,i}(\theta_i - \theta_{o,i})^2 \quad (2)$$

$$E_{\text{torsion}} = \sum_i \left[\frac{1}{2}V_{1,i}(1 + \cos\varphi_i) + \frac{1}{2}V_{2,i}(1 + \cos 2\varphi_i) + \frac{1}{2}V_{3,i}(1 + \cos 3\varphi_i) + \frac{1}{2}V_{4,i}(1 + \cos 4\varphi_i)\right] \quad (3)$$

$$E_{\text{nonbond}} = \sum_i \sum_{j>i} \left\{\frac{q_i q_j e^2}{r_{ij}} + 4\varepsilon_{ij}\left[\left(\frac{\sigma_{ij}}{r_{ij}}\right)^{12} - \left(\frac{\sigma_{ij}}{r_{ij}}\right)^{6}\right]\right\} \quad (4)$$

The geometric combining rules regularly used for the Lennard−Jones coefficients are employed: $\sigma_{ij} = (\sigma_{ii}\sigma_{jj})^{1/2}$ and $\varepsilon_{ij} = (\varepsilon_{ii}\varepsilon_{jj})^{1/2}$.[28] Nonbonded interactions are evaluated intermolecularly and for intramolecular atom pairs separated by three or more bonds. In order to use identical parameters for both intra- and intermolecular interactions the 1,4-intramolecular interactions are reduced by a factor of 2.[28] To retain compatibility with OPLS-AA, all present parameters were developed in a similar fashion to recent parametrization efforts by Jorgensen and co-workers.[29−31] Whenever appropriate, published potentials were retained without change. This includes assigning all standard bond stretching and angle bending force constants from OPLS-AA, which may also include some entries from the AMBER-AA force field.[27] All Lennard−Jones parameters also came from the OPLS-AA parameter set except when explicitly stated. The present work then focused on the development of Fourier coefficients, partial charges, and equilibrium geometries, and the validation of multiple ionic liquid combinations.

Ab Initio Calculations. All individual ions, i.e., [RMIM] (R = Me, Et, Bu), [RPyr] (R = Me, Et, Bu), and [Chol] cations with [Cl], [PF_6], [BF_4], [NO_3], [$AlCl_4$], [Al_2Cl_7],

[TfO], [Sacc], and [Ace] anions, were optimized using the Jaguar program[32] at the Hartree−Fock (HF) theory level using the 6−31G(d) basis set with subsequent single-point energy calculations using the local MØller−Plesset second-order perturbation (LMP2)[33] method and the correlation-consistent polarized valence cc-pVTZ(-f) basis set.[34] This LMP2/cc-pVTZ(-f)//HF/6−31G(d) method is the current practice for OPLS-AA parametrization.[31] Vibrational analytical frequency calculations at the HF/6−31G(d) were carried out to confirm all minima as stationary points. The ab initio derived ion geometries were used for the equilibrium bond and angle, r_o and θ_o, reference values in the force field and given in the Supporting Information. Partial charges were computed by fitting the molecular electrostatic potential (ESP) at the atomic centers. For a better description of the charge density, LMP2 dipole moments were also computed along with a coupled perturbed Hartree−Fock (CPHF) term. Charges were symmetrized for similar atoms and used for the Coulombic nonbonded force field partial charges. Torsional energies were fit to reproduce computed LMP2/cc-pVTZ(-f)//HF/6−31G(d) energy scans. Calculations at this level have been reported to yield highly accurate conformational energies with average errors of ca. 0.25 kcal/mol for reported test sets and 0.6 kcal/mol for perfluorolalkanes.[31] Greater detail on the torsional scans and assignment of partial charges are given in Results and Discussion.

Ionic Liquid Simulations. The Metropolis Monte Carlo (MC) simulations were performed with the BOSS 4.6 program.[35] All cations were fully flexible, i.e., all bond stretching, angle bending, and torsional motions were sampled. Anions were simulated as rigid molecules, and as a result no additional intramolecular anion parametrization was necessary. The use of rigid anions in OPLS-AA has been shown to provide an accurate representation of ionic liquid physical properties,[23] including use as a reaction medium for a computed QM/MM Diels−Alder reaction study.[25] Periodic boundary conditions have been applied to boxes containing 190 ion pairs with long-range interactions handled with Ewald summations. In short, Ewald summations calculate the exact electrostatic energy of an infinite lattice of identical copies of the simulation cell. This suppresses artifacts resulting from the simple cutoff of the long-range electrostatic interactions prevalent in the ionic liquid. The liquid-phase simulations were carried out by placing the 380 ions at random positions in the simulation box (see Figure 2), and a temperature value of 1000 °C was initially applied for 10 million configurations in the NVT ensemble to encourage a thorough mixing. The simulations were then equilibrated at 25 °C for 100−200 million MC steps in the NPT ensemble. The heating/NVT and equilibration/NPT simulations on each ionic liquid system were repeated sequentially an average of 4−6 times until the energy and volume of the system no longer decreased. A pressure of 1 atm was used in all cases. The computed densities, heats of vaporization, energy distributions, and conformational properties were very well converged with MC simulations of this length.

In order to compute the heats of vaporization, ΔH_{vap}, MC simulations needed to be performed on the gas-phase ion pair of the corresponding ionic liquid because of the flexibility of the cations. Experimental evidence suggests that ionic liquids go into the vapor phase in ion pairs.[36] Gas-phase simulations consisted of 1 million configurations of equilibration, followed by 2 million configurations of averaging. For the liquids, the systems were periodic and tetragonal with $c/a = 1.5$; as an example, a is ca. 34.3 and 35.5 Å for [BMIM][BF_4] and [BMIM][PF_6] (box sizes for all ionic liquids are given in the Supporting Information).

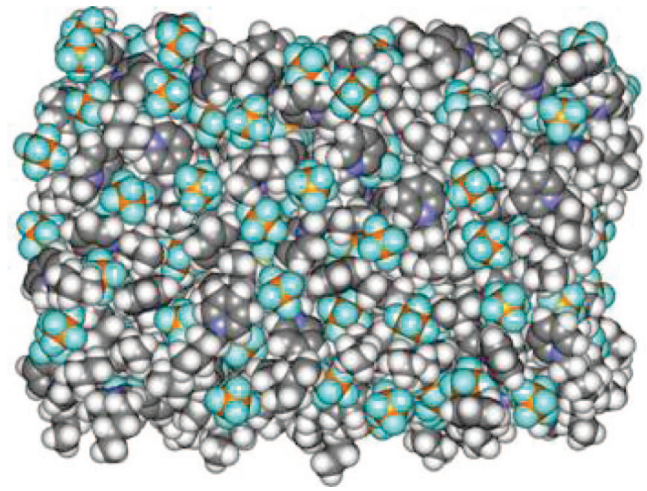

Figure 2. Illustration of an equilibrated [BPyr][PF_6] ionic liquid simulation box.

Solvent−solvent intermolecular cutoff distances of 12 Å were employed for the tail carbon atom of each side chain (methyl and alkyl), a midpoint carbon on the alkyl chain, and the ring carbon between both nitrogens for imidazolium. Cutoff atoms were also based on alkyl side-chain length for *N*-pyridinium using the carbon at the end of the alkyl chain, a midpoint carbon on the side chain, the nitrogen atom, and the carbon ring atom para to the nitrogen. For choline, atoms O and N, along with two Cs bonded to N (methyl and on the chain) were used for cutoffs. Center atoms, e.g., B in BF_4^- and P in PF_6^-, were used for the anions. If any distance is within the cutoff, the entire solvent−solvent interaction was included. Adjustments to the allowed ranges for rotations, translations, and dihedral angle movements led to overall acceptance rates of about 40−50% for new configurations. The ranges for bond stretching and angle bending were set automatically by the BOSS program on the basis of force constants and temperature. All MC calculations were run on a Linux cluster at Auburn University, and all ab initio calculations were performed on computers located at the Alabama Supercomputer Center.

Results and Discussion

Partial Charges. Ab initio calculations at the LMP2/cc-pVTZ(-f)//HF/6−31G(d) theory level were carried out on the isolated gas-phase ions in order to facilitate the transferability of the charge model to multiple ionic liquid combinations. All anions were geometry optimized, and Coulombic charges were assigned from the ESP fits (Table 1). For the cations, multiple low-energy geometry configurations exist stemming primarily from torsion rotations, i.e., the alkyl side

Table 1. Nonbonded Parameters for [Cl], [PF_6], [BF_4], [NO_3], [$AlCl_4$], [Al_2Cl_7], [TfO], Saccharinate [Sac], and Acesulfamate [Ace] Anions[a]

anion	atom type	q (e)	σ (Å)	ε (kcal mol^{-1})
[Cl][b]	Cl	−1.00	3.770	0.148
[BF_4][c]	B	0.8276	3.5814	0.095
	F	−0.4569	3.1181	0.060
[PF_6]	P	1.3400	3.740	0.200
	F	−0.3900	3.1181	0.061
[NO_3]	N	0.794	3.150	0.170
	O	−0.598	2.860	0.210
[$AlCl_4$][d]	Al	0.6452	4.050	0.100
	Cl	−0.4113	3.770	0.148
[Al_2Cl_7][d]	Al	0.5455	4.050	0.100
	ClM[e]	−0.1404	3.770	0.148
	Cl	−0.3251	3.770	0.148
[TfO]	S	1.1887	3.550	0.250
	O	−0.6556	2.960	0.210
	C	0.2692	3.500	0.066
	F	−0.1637	2.950	0.053
[Sac]	C1	−0.0519	3.550	0.070
	C2	−0.1882	3.550	0.070
	C3	−0.0235	3.550	0.070
	C4	−0.2759	3.550	0.070
	C5	0.1293	3.550	0.070
	C6	−0.1968	3.550	0.070
	C9	0.5502	3.750	0.105
	S7	1.2149	3.550	0.250
	N8	−0.6889	3.250	0.170
	OC	−0.5950	2.960	0.210
	OS	−0.6285	2.960	0.210
	HA	0.1132	2.420	0.030
	HB	0.0782	2.420	0.030
[Ace]	C1	−0.8536	3.550	0.070
	C2	0.6670	3.550	0.070
	C6	0.9507	3.750	0.105
	C7	−0.3083	3.500	0.066
	O3	−0.5087	2.900	0.140
	OB	−0.6573	2.960	0.210
	OS	−0.6158	2.960	0.170
	S4	1.3355	3.550	0.250
	N5	−0.8224	3.250	0.170
	HA	0.0666	2.500	0.030
	HB	0.2289	2.420	0.030

[a] All Lennard−Jones (LJ) nonbonded parameters are from the OPLS-AA force field unless otherwise stated. Atom types for [Sacc] and [Ace] are shown in Figure 4. [b] LJ parameter for Cl taken from ref 23. [c] LJ parameter for B taken from ref 24. [d] LJ parameters taken from refs 24 and 25. [e] Corresponds to Cl atom bridging the Al atoms.

chains in the [RMIM] and [RPyr] ions and choline's internal N−C−C−O dihedral. This presented the challenge of developing a single set of charges per cation family that could accurately represent different alkyl lengths and orientations. ESP charges were initially computed for all available [RMIM] and [RPyr] energy-minimized stationary points, where R = Me, Et, and Bu. An average partial charge value for each atom in [RMIM] and [RPyr] was developed by appropriately weighting the contribution of each ground-state structure to the overall conformational population. For example, the partial charges specific to [BMIM] (see values in Figure 3) were computed from a two-state model and the Boltzmann distribution based on gauche and trans side-chain optimized energies for the cation. Charges specific to [EMIM], [MPyr], and [EPyr] are given in the Supporting Information. To assign a final charge set to [RMIM], all charges for [MMIM], [EMIM], and [BMIM] were appropriately weighted and averaged (see Table 2 and Figure 3). For the ring atoms, e.g., NA, CW, HW in [RMIM], departures in charge from symmetry were small in the R = Me, Et, and Bu ions; hence, the atoms were given symmetrical values to facilitate transferability. Charges for the carbon and hydrogen atoms, CS and HS, present in the middle of the alkyl side chains (-CH_2-) were taken directly from OPLS-AA alkane values[28] to allow the simulation of any [RMIM] desired chain length (tested up to octyl in the present work). In the simulations of [MMIM], the CM and HM atom types are used in both methyl groups attached to the 1 and 3 nitrogen positions of the imidazolium. A set of transferable charges for [RPyr] and a specific set for choline were computed in an identical fashion (Table 2).

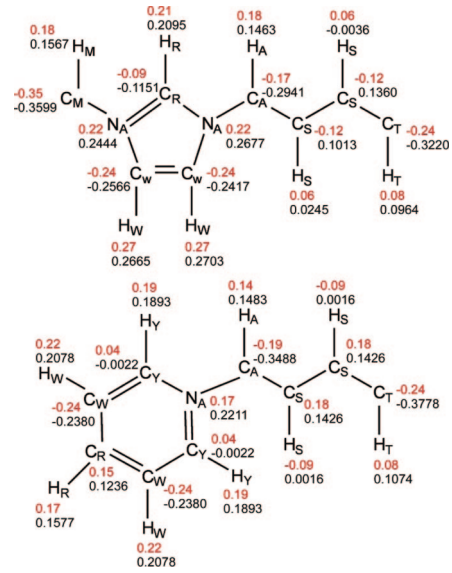

Figure 3. Partial charges assigned for atom types in [RMIM] and [RPyr] in red, and charges exclusively for use in [BMIM] and [BPyr] in black.

The use of averaged point charges was necessary for a fully transferable force field; however, a direct comparison of the accuracy between these [RMIM] and [RPyr] charges versus point charges specific to [EMIM], [BMIM], [MPyr], [EPyr], and [BPyr] was evaluated in this study. Thirty-five ionic liquid combinations were computed using both charge sets, along with the appropriate torsion terms, to compare differences in predicted densities and heats of vaporization for a quantitative evaluation of the final charges presented in Table 2. Most Lennard−Jones (LJ) parameters were taken directly from the OPLS-AA force field; for example, parameters for [RMIM] and [RPyr] were based on imidazole[37] and pyridine,[38] respectively. However, any LJ parameters not assigned from OPLS-AA are specified in Table 1.

Intramolecular Potentials. The resultant geometries from the ab initio calculations were used to obtain the equilibrium bond and angle reference values, r_o and θ_o, for the simulations; the final values are given in the Supporting Information. To allow full flexibility for the cations, appropriate bond and angle force constants, and Fourier coefficients for ring atoms on [RMIM] and [RPyr] were taken directly from published OPLS-AA parameters.[22,37,38] In this work, new

Table 2. Nonbonded Parameters for 1-Alkyl-3-methylimidazolium [RMIM], *N*-Alkylpyridinium [RPyr], and Choline [Chol] Cations[a]

cation	atom type	q (e)	σ (Å)	ε (kcal mol^{-1})
[RMIM]	CR	−0.09	3.55	0.070
	NA	0.22	3.25	0.170
	CW	−0.24	3.55	0.070
	CM	−0.35	3.50	0.066
	CA	−0.17	3.50	0.066
	CS	−0.12	3.50	0.066
	CT	−0.24	3.50	0.066
	HR	0.21	2.42	0.030
	HW	0.27	2.42	0.030
	HM	0.18	2.50	0.030
	HA	0.18	2.50	0.030
	HS	0.06	2.50	0.030
	HT	0.08	2.50	0.030
[RPyr]	CR	0.15	3.55	0.070
	CW	−0.24	3.55	0.070
	CY	0.04	3.55	0.070
	NA	0.17	3.25	0.170
	CM	−0.39	3.50	0.066
	CA	−0.19	3.50	0.066
	CS	0.18	3.50	0.066
	CT	−0.24	3.50	0.066
	HR	0.17	2.42	0.030
	HW	0.22	2.42	0.030
	HY	0.19	2.42	0.030
	HM	0.16	2.50	0.030
	HA	0.14	2.50	0.030
	HS	−0.09	2.50	0.030
	HT	0.08	2.50	0.030
[Chol]	NA	0.1640	3.250	0.170
	CA	−0.3847	3.500	0.066
	CS	−0.1111	3.500	0.066
	CW	0.2318	3.500	0.066
	OY	−0.6547	3.070	0.170
	HA	0.1934	2.500	0.030
	HS	0.1251	2.500	0.030
	HW	0.0398	2.500	0.030
	HY	0.4537	0.000	0.000

[a] Atom types for [RMIM], [RPyr], and [Chol] are given in Figures 3 and 4.

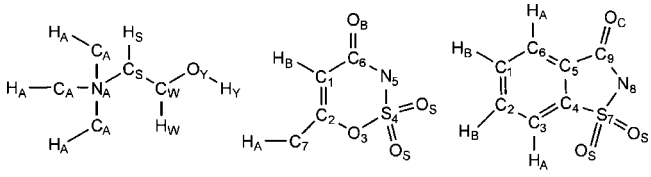

Figure 4. Atom types for choline [Chol], acesulfamate [Ace], and saccharinate [Sacc].

Fourier coefficients for the alkyl side chains of [RMIM] and [RPyr] and an entire new set for the choline cation were developed to reproduce all possible rotations. Vibrational frequencies as is typical of the OPLS force field were not parametrized and will require further refinement of the force constants if greater accuracy is desired. The focus of the ionic liquid OPLS-AA parameter set is to accurately reproduce intermolecular interactions such as density and thermodynamic quantities such as the heats of vaporization.

Torsions. The procedure for establishing the missing Fourier coefficients involved direct adjustment of the OPLS-AA torsional parameters to reproduce the energy differences between conformational energy minima from ab initio calculations. For each dihedral angle, energy profiles were

Table 3. Torsional Fourier Coefficients (kcal/mol) for 1-Alkyl-3-methylimidazolium [RMIM] and Specific to [EMIM] and [BMIM] Charge Sets

torsion	V_1	V_2	V_3	cation
NA-CA-CT-HT	0.000	0.000	0.000	[RMIM]
	0.000	0.000	0.350	[EMIM]
CW-NA-CA-CT	−4.355	−4.575	−1.375	[RMIM]
	−0.599	−1.750	0.290	[EMIM]
CR-NA-CA-CT	−2.000	−0.275	−1.650	[RMIM]
	−0.555	0.479	0.200	[EMIM]
CW-NA-CA-HA	−2.700	−5.650	0.355	[RMIM]
	−0.755	−2.125	0.400	[EMIM]
	−1.400	−2.650	0.175	[BMIM]
CW-NA-CA-CS	−2.110	−5.000	0.345	[RMIM]
	−1.910	−1.500	0.290	[BMIM]
CR-NA-CA-CS	−0.159	0.095	−0.010	[RMIM]
	−1.659	−0.555	−0.375	[BMIM]
NA-CA-CS-CS	−0.788	0.800	0.400	[RMIM]
	−1.788	0.756	−0.288	[BMIM]
HA-CA-CS-HS	0.000	−0.150	0.518	[RMIM]
	0.000	0.000	0.318	[BMIM]

Table 4. Torsional Fourier Coefficients (kcal/mol) for *N*-Alkylpyridinium [RPyr] and Specific to [EPyr] and [BPyr] Charge Sets

torsion	V_1	V_2	V_3	cation
CY-NA-CA-CT	0.000	0.010	0.000	[RPyr]
	0.000	0.150	0.000	[EPyr]
NA-CA-CT-HT	0.000	0.000	0.020	[RPyr]
	0.000	0.000	0.400	[EPyr]
HA-CA-CT-HT	0.000	0.000	0.518	[RPyr]
	0.000	0.000	0.332	[EPyr]
NA-CA-CS-HS	0.000	0.000	0.200	[RPyr]
	−0.700	−0.500	0.000	[BPyr]
HA-CA-CS-HS	0.000	0.000	0.418	[RPyr]
	−1.700	−1.710	0.655	[BPyr]
CY-NA-CA-CS	0.000	−0.050	−0.200	[RPyr]
	0.000	0.180	0.000	[BPyr]
NA-CA-CS-CS	−0.788	0.400	−0.288	[RPyr]
	−0.233	1.400	−0.290	[BPyr]

obtained by rotating the [RMIM] and [RPyr] alkyl side chains and all available [Chol] dihedrals in increments of 15° for each ion with a constrained minimization carried out using the LMP2/cc-pVTZ(-f)//HF/6−31G(d) theory level. Only the dihedrals involved in the torsional potential energy surface were restrained; the remainder of the ion was fully flexible. Each [MMIM], [EMIM], [BMIM], [MPyr], [EPyr], [BPyr], and [Chol] cation was individually parametrized using their specific charge set with coefficients, V_1 to V_3, that gave the best overall fit for all rotatable bonds (Tables 3−5). The resultant Fourier coefficients were then refitted to give the best overall values for the general [RMIM] and [RPyr] cation families, taking into account the general atomic charge sets.

As an example, the energy profiles for the CT-CA-NA-CW/Y and HT-CT-CA-NA rotations in [EMIM] and [EPyr] using the fully transferable parameters (in blue) and the parameters specific to the individual cations (in green) are given in Figure 5; LMP2/cc-pVTZ(-f)//HF/6−31G(d) energy values are presented in black along with the original OPLS-AA parameters in red. Positions of all the minima and maxima were shifted to achieve the lowest possible rms energy error with respect to the quantum mechanical results. The specific charge/torsion parameter sets for the individual

Table 5. Torsional Fourier Coefficients (kcal/mol) for Choline [Chol]

torsion	V_1	V_2	V_3
CW-CS-NA-CA	0.100	0.550	0.650
CA-NA-CA-HA	0.000	0.000	0.825
CS-NA-CA-HA	0.000	0.000	0.940
HS-CS-NA-CA	0.000	1.000	0.700
OY-CW-CS-NA	−6.000	−5.000	3.200
OY-CW-CS-HS	−0.500	−2.500	0.250
HW-CW-CS-NA	−6.000	−7.000	0.750
HW-CW-CS-HS	6.000	−3.000	2.000
HY-OY-CW-CS	−0.356	−0.174	0.350
HY-OY-CW-HW	−3.000	1.000	−2.000
X-NA-X-X[a]	0.000	2.000	0.000

[a] Improper torsion.

cations typically performed better than the generalized parameter set, e.g., the HT-CT-CA-NA rotation in [EMIM] (Figure 5). However, energy profiles for the dihedral rotations were considerably improved using both parameter sets when compared to the unaltered OPLS-AA potentials. The highly transferable [RMIM] and [RPyr] general parameter set enabled most dihedral rotations to be appropriately modeled with good accuracy (multiple energy profiles for [RMIM] and [RPyr] given in the Supporting Information (Figures S3−S10). For example, the energy barriers for dihedral rotations in the 1-propyl-3-methylimidazolium [PMIM] and *N*-1-propylpyridinium [PPyr] cations were well reproduced when using the general [RMIM] and [RPyr] parameter sets despite not being specifically taken into consideration during the parametrization process (Figures S4 and S7). In addition, the simulation of longer alkyl side chains, such as hexyl and octyl, using the [RMIM] and [RPyr] general parameters also gave good agreement with experimental densities and heats of vaporization data, as discussed below.

Density. With satisfactory agreement achieved between the newly developed OPLS-AA parameters and the ab initio calculations for the ionic structures, subsequent MC simulations for 68 unique ionic liquid combinations were carried out. The systems were composed of 190 ion pairs at 25 °C and 1 atm. Each simulation required over 500 million MC configurations to properly equilibrate the periodic boxes using Ewald summations. The computed densities for the solvents are given in Tables 6−8. The imidazolium-based ionic liquids provided the largest amount of experimental data to validate the newly developed force field (Figures 6 and 7). However, in many cases, different experimental measurements varied by as much as 5% per solvent (Table 6). Relative deviations from experimental density values were ca. 1−3% for most [RMIM] ionic liquid combinations using both the fully transferable OPLS-AA force field and the parameters developed specifically for [EMIM] and [BMIM]. The limited amount of reported densities for the [RPyr][BF_4] ionic liquids also compared well with the simulations (Table 7).

Chloroaluminate-based ionic liquids gave slightly larger deviations at ca. 4−5%. Exact agreement could not be expected because the ionic composition of the experimental and modeled systems is not identical. For example, Raman,[39] ^{27}Al NMR,[40] and mass spectra[41] all indicate that when $AlCl_3$ comprises <50% mol of the [EMIM][Cl] ionic liquid melt, [$AlCl_4$] is the only chloroaluminate species present along with chloride ions that are not bound to aluminum. A ratio greater than 1:1 $AlCl_3$-to-[EMIM][Cl] gives [$AlCl_4$] and [Al_2Cl_7] as the principal anionic constituents of the melt from ^{27}Al NMR[42] and negative-ion FAB mass spectra.[43] Despite underestimation of the densities, the simulations for [RMIM][$AlCl_4$] and [RMIM][Al_2Cl_7] reproduced the relative trend of decreasing density with increasing alkyl chain length. In addition, the computed heats of vaporization are strikingly similar to the experimental values for [BMIM][$AlCl_4$] and [HMIM][$AlCl_4$] (Table 6). The OPLS-AA chloroaluminate solvents have previously provided an appropriate reaction medium environment for the Diels−Alder reaction using QM/MM methodology.[25]

The errors in the densities computed for choline-based ionic liquids were significantly larger (see Table 8) despite using the same parametrization procedure as the [RMIM]- and [RPyr]-based ionic liquids. For example, simulation of [Chol][Sacc] gave a predicted density of 1.200 g/cm^3 compared to 1.383 g/cm^3 experimentally and [Chol][Ace] gave a calculated value of 1.206 g/cm^3 (experimental 1.284 g/cm^3).[17] Improvements to the [Chol]-based ionic liquid parameters are difficult, owing to the lack of experimental data available for refinement.

Densities were also computed for 11 ionic liquid combinations over temperatures ranging from 5 to 90 °C and compared with experimentally observed values (Table 9). Various chain lengths were tested for [RMIM] from R = Et to Oct with multiple anions, [BF_4], [PF_6], [$AlCl_4$], and [TfO]. The relative deviations from experiment were ca. 1−3% with the exception of [EMIM][$AlCl_4$], which gave deviations of ca. 4−5%, similar to the simulations at 25 °C. The general trend of a decreasing density as temperature increases was reproduced for all ionic liquids tested (Figure 7). Good agreement was also found between the fully transferable parameters and the charge/torsion set specific to [EMIM] and [BMIM] (Table 9).

Heats of Vaporization. Ionic liquids are generally characterized by vaporization enthalpies that are almost 1 order of magnitude higher than for molecular liquids because of strong electrostatic interactions between the ions.[1] The importance of properly reproducing the heats of vaporization, ΔH_{vap}, in addition to densities for ionic liquids cannot be minimized, as they both serve as key properties representative of molecular size and the average intermolecular interactions.[30] Heats of vaporization are readily computed from the simulation results using equation 5.

$$\Delta H_{vap} = \Delta H_{gas} - \Delta H_{liquid} = E_{total}(gas) - E_{total}(liquid) + RT \quad (5)$$

Experimental evidence suggests that ionic liquids go into the vapor phase in ion pairs.[36] Hence, the E_{total}(gas) term was computed from the average intra- and intermolecular energy for the ion pair in the gas phase from each ionic liquid combination. E_{total}(liquid) is the total potential energy of the liquid consisting of both the average intramolecular energy, E_{intra}(liquid), and the average intermolecular energy, E_{inter}(liquid), from the ionic liquid. The *RT* term is used in place of a *PV*-work term in the enthalpy. The heats of vaporization

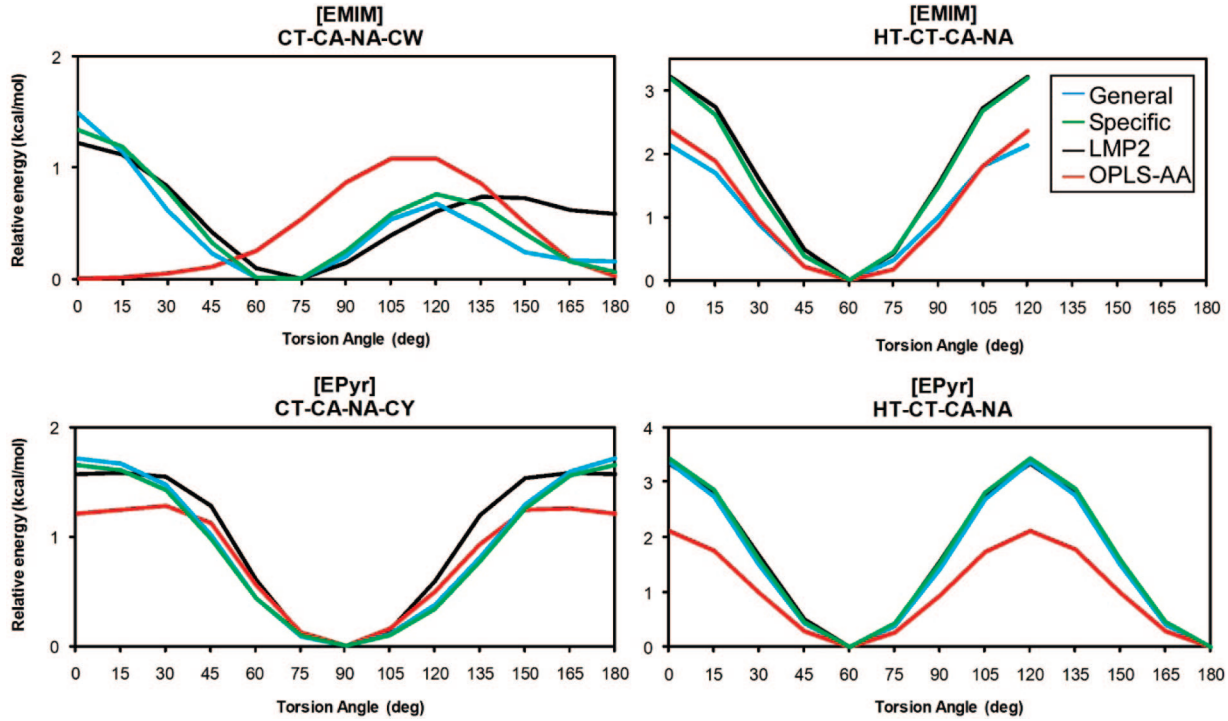

Figure 5. Torsion energy profiles for the rotation around dihedral angles for [EMIM] and [EPyr] cations. The transferable [RMIM] and [RPyr] parameters given in blue, parameters specific to [EMIM] and [EPyr] in green, LMP2/cc-pVTZ(-f)/HF/6−31G(d) in black, and the unaltered OPLS-AA force field in red.

obtained from the MC simulations for the ionic liquids are presented in Tables 6−8, and for [RMIM] in Figure 8.

Comparison between the computed and experimental heats of vaporization, ΔH_{vap}, values is particularly difficult, owing to the large reported deviations between different experimental-based techniques. For example, earlier ΔH_{vap} estimates derived from correlations of Hildebrand's solubility parameter, δ, to solvent-controlled chemical reactions[50] and viscosity data[73] have been found to significantly overestimate experimentally measured ΔH_{vap} values.[1] Accordingly, the new ionic liquid parameters were not adjusted to improve agreement with reported experimental data. Instead, the parameters were fit to reproduce ab initio calculations and directly compared to available experimental values. The MC simulations gave favorable correlations with direct measurements of the ionic liquids using a temperature programmed desorption technique[36] and with more accurate ΔH_{vap} estimates derived from density and surface tensions measurements coupled to Zaitsau et. al's empirical equation.[60] For example, ΔH_{vap} values of 41.9 and 38.3 kcal/mol were computed for the chloroaluminate ionic liquids [BMIM]-[$AlCl_4$] and [HMIM][$AlCl_4$], respectively, using the general [RMIM] parameter set which were found to be in close agreement with the experimentally estimated values of 41.1 and 39.5 kcal/mol.[60] Calculations of [OMIM]-based ionic liquids with [BF_4] and [PF_6] counteranions gave ΔH_{vap} values of 41.9 and 47.3 kcal/mol, respectively, in reasonable agreement with experimentally measured values of 38.7 ± 0.7 and 40.4 ± 1.0 kcal/mol.[36] The computed ΔH_{vap} values of 27.8 and 31.9 kcal/mol for [BMIM][BF_4] and [BMIM][PF_6], respectively, are in good agreement with recent experimental estimates of 30.6 and 37.0 kcal/mol;[49] the simulations confirm earlier estimates of 48.6 and 45.8 kcal/mol[50] from correlations of Hildebrand's solubility parameter to be overestimated.[1] Further comparisons of calculated versus experimental ΔH_{vap} values for [RMIM]-based ionic liquids are given in Table 6.

A general trend found in the calculation of the ΔH_{vap} was a smaller predicted value in the [EMIM] cation-based ionic liquids relative to other [RMIM] values. For example, [RMIM][NO_3] ΔH_{vap} values of 31.8, 18.1, and 28.0 kcal/mol were computed using the general OPLS-AA parameter set for [MMIM], [EMIM], and [BMIM], respectively. Experimental combustion calorimetry in conjunction with ab initio calculations (G3MP2) estimate ΔH_{vap} as 39.1 ± 1.3 and 38.8 ± 1.4 kcal/mol for [EMIM] and [BMIM] in the [NO_3]-based ionic liquids.[62] The computed heats of vaporization are particularly sensitive to the charge sets used, as the specific OPLS-AA charge set reduced the deviation between the ionic liquids and brought the results closer to the estimates with computed values of 25.8 and 31.9 kcal/mol for [EMIM][NO_3] and [BMIM][NO_3]. The general parameters maybe more susceptible to deviations for [EMIM] because of the use of the same atom types CT and HT to model the end carbon and hydrogens as the longer alkyl side chains, such as butyl and hexyl. Earlier parametrization efforts used an atom type specific to [EMIM] to cap the alkyl chain.[23] The use of a polarizable force field may also improve agreement.[74] However, the large differences in the computed ΔH_{vap} values when using the transferable and cation specific OPLS-AA parameters were not seen for the predicted densities (Figure 6) which were generally insensitive to the charge/torsion set used.

Table 6. Calculated and Experimental Liquid Densities (g/cm^3) and Heats of Vaporization (kcal/mol) at 25 °C for 1-Alkyl-3-methylimidazolium [RMIM]-Based Ionic Liquids[a]

ionic liquid	density (calcd)	density (exptl)	refs	ΔH_{vap} (calcd)	ΔH_{vap} (exptl)	refs
[MMIM][BF_4]	1.299	1.373	44	30.1		
[EMIM][BF_4]	1.254 (1.253)	1.279, 1.28	45, 46	18.0 (24.0)		
[BMIM][BF_4]	1.171 (1.178)	1.19, 1.21, 1.26	45, 47, 48	27.8 (30.0)	*30.6*,[e] *48.6*[f]	49, 50
[HMIM][BF_4]	1.105	1.1481, 1.1484, 1.177	44, 51	35.8		
[OMIM][BF_4]	1.044	1.08, 1.0912, 1.105, 1.133	44, 48, 52, 53	41.9	38.7 ± 0.7,[g] *29.2*[e]	36, 49
[MMIM][PF_6]	1.512			33.1		
[EMIM][PF_6]	1.455 (1.455)	1.558[b]	54	21.4 (27.6)		
[BMIM][PF_6]	1.339 (1.342)	1.31, 1.36, 1.368, 1.37	44, 48, 55, 56	31.9 (31.9)	*37.0*,[e] *45.8*[f]	49, 50
[HMIM][PF_6]	1.257	1.24, 1.278, 1.29, 1.292, 1.2935	47, 51, 55, 56	40.1	*33.4*[e]	49
[OMIM][PF_6]	1.181	1.19, 1.22, 1.237	48, 55, 56	47.3	40.4 ± 1.0,[g] *34.5*[e]	36, 49
[MMIM][Cl]	1.175	1.155	57	32.3		
[EMIM][Cl]	1.121 (1.130)	1.110	57	19.3 (25.5)		
[BMIM][Cl]	1.041 (1.060)	1.075, 1.08	55, 57	29.1 (32.0)		
[HMIM][Cl]	1.007	1.03, 1.0338	55, 58	37.5		
[OMIM][Cl]	0.959	1.00, 1.0104, 1.0124	55, 58, 59	44.6	*29.3*[e]	49
[MMIM][$AlCl_4$]	1.260	1.3289	60	31.1	*45.3*[e]	60
[EMIM][$AlCl_4$]	1.226 (1.229)	1.2947, 1.302	24, 60	19.8 (26.3)	*43.6*[e]	60
[BMIM][$AlCl_4$]	1.175 (1.176)	1.238, 1.2381	24, 60	41.9 (32.1)	*41.1*[e]	60
[HMIM][$AlCl_4$]	1.120	1.1952	60	38.3	*39.5*[e]	60
[MMIM][Al_2Cl_7]	1.282	1.341[c]	57, 61	34.0		
[EMIM][Al_2Cl_7]	1.260 (1.249)	1.325[c]	57, 61	22.3 (28.2)		
[BMIM][Al_2Cl_7]	1.206 (1.203)	1.272[c]	57, 61	32.4 (33.6)		
[HMIM][Al_2Cl_7]	1.119			39.2		
[MMIM][NO_3]	1.305			31.8		
[EMIM][NO_3]	1.253 (1.258)			18.1 (25.8)	*39.1 ± 1.3*[h]	62
[BMIM][NO_3]	1.163 (1.175)	1.15343	58	28.0 (31.9)	*38.8 ± 1.4*[h]	62
[HMIM][NO_3]	1.080	1.11658	58	34.9		
[MMIM][TfO]	1.489			32.5		
[EMIM][TfO]	1.420 (1.412)	1.37522, 1.38, 1.390	47, 63 64	21.3 (26.7)		
[BMIM][TfO]	1.297 (1.310)	1.30, 1.30148, 1.3013[d]	64, 65	31.1 (32.7)	*33.8*[f]	50
[HMIM][TfO]	1.241	1.24	64	40.6		
[OMIM][TfO]	1.125	1.12	64, 66	46.5	36.1 ± 0.7[g]	36

[a] Calculated density and ΔH_{vap} values given in parentheses were computed using OPLS-AA charge/torsion parameters specific to [EMIM] and [BMIM]. ΔH_{vap} estimations from experimental data given in italics. R = M (methyl), E (ethyl), B (butyl), H (hexyl), and O (octyl). [b] 23 °C; density computed from crystal structure cell parameters. [c] [RMIM][Cl]−$AlCl_3$ 0.66 melt,[57] which should correspond to exclusively [RMIM][Al_2Cl_7].[61] [d] 22.6 °C. [e] Experimental density and surface tension measurements in conjunction with Kabo's equation[49] was used to estimate ΔH_{vap}. [f] ΔH_{vap} estimated from Hildebrand's solubility parameter, δ, to solvent-controlled Diels−Alder reaction. [g] Temperature-programmed desorption. [h] Experimental combustion calorimetry in conjunction with ab initio calculations (G3MP2) were used to estimate ΔH_{vap}.

Table 7. Calculated Liquid Densities (g/cm^3) and Heats of Vaporization (kcal/mol) at 25 °C for *N*-Alkylpyridinium [RPyr] (R = Me, Et, Bu, Hex, Oct)-Based Ionic Liquids[a]

ionic liquid	density	ΔH_{vap}	ionic liquid	density	ΔH_{vap}
[MPyr][BF_4]	1.300 (1.302)	41.5 (41.0)	[MPyr][PF_6]	1.514 (1.520)	44.9 (44.3)
[EPyr][BF_4][b]	1.250 (1.256)	37.3 (29.8)	[EPyr][PF_6]	1.462 (1.459)	40.3 (33.5)
[BPyr][BF_4][c]	1.169 (1.176)	28.7 (41.1)	[BPyr][PF_6]	1.345 (1.347)	29.8 (39.0)
[HPyr][BF_4][d]	1.091	43.8	[HPyr][PF_6]	1.247	46.2
[OPyr][BF_4]	1.043	52.2	[OPyr][PF_6]	1.170	53.8
[MPyr][$AlCl_4$]	1.246 (1.253)	41.5 (41.3)	[MPyr][Al_2Cl_7]	1.271 (1.267)	44.1 (40.7)
[EPyr][$AlCl_4$]	1.221 (1.217)	37.8 (30.6)	[EPyr][Al_2Cl_7]	1.261 (1.241)	40.8 (28.9)
[BPyr][$AlCl_4$]	1.163 (1.161)	28.1 (36.3)	[BPyr][Al_2Cl_7]	1.181 (1.194)	29.7 (38.9)
[MPyr][NO_3]	1.312 (1.315)	41.6 (41.5)	[MPyr][TfO]	1.506 (1.504)	43.7 (42.5)
[EPyr][NO_3]	1.253 (1.263)	36.4 (29.5)	[EPyr][TfO]	1.421 (1.431)	38.4 (31.6)
[BPyr][NO_3]	1.161 (1.167)	25.2 (35.3)	[BPyr][TfO]	1.306 (1.318)	27.1 (37.3)
[MPyr][Cl]	1.181 (1.184)	44.9 (43.8)	[HPyr][Cl]	1.006	46.5
[EPyr][Cl]	1.122 (1.130)	39.3 (31.9)	[OPyr][Cl]	0.943	52.8
[BPyr][Cl]	1.041 (1.050)	28.3 (38.8)			

[a] Calculated density and ΔH_{vap} values given in parentheses were computed using OPLS-AA charge/torsion parameters specific to [MPyr], [EPyr], and [BPyr]. [b] Experimental density of 1.3020 g/cm^3.[67] [c] Experimental density of 1.2144 and 1.22 g/cm^3.[46,53] [d] Experimental density of 1.16 g/cm^3 at 20 °C.[68]

Kemp Elimination. As an initial test of the newly developed ionic liquid parameters, mixed quantum and molecular mechanical (QM/MM) calculations were carried out on the Kemp elimination of benzisoxazole with piperidine in [BMIM][PF_6] (Scheme 1). The solutes were treated with the PDDG/PM3 semiempirical QM method.[75] PDDG/PM3 has given excellent results in our recent QM/MM studies of the Kemp elimination of 5-nitro-benzisoxazole via catalytic antibody 4B2[76] and the condensed-phase Kemp decarboxylation of benzisoxazole-3-carboxylic acid.[77] Potentials of

Table 8. Calculated Liquid Densities (g/cm^3) and Heats of Vaporization (kcal/mol) at 25 °C for Choline [Chol]-Based Ionic Liquids

ionic liquid	density	ΔH_{vap}	ionic liquid	density	ΔH_{vap}
[Chol][Cl][a]	1.040	78.9	[Chol][$AlCl_4$]	1.192	75.3
[Chol][Ace][b]	1.206	70.9	[Chol][Al_2Cl_7]	1.195	77.5
[Chol][Sacc][c]	1.200	79.2	[Chol][NO_3]	1.159	76.9
[Chol][BF_4]	1.165	75.7	[Chol][TfO]	1.326	76.0
[Chol][PF_6]	1.375	77.8			

[a] Experimental density from crystal structure at 85 °C is 1.12 g/cm^3.[69] [b] Experimental density is 1.284 g/cm^3.[17] [c] Experimental density is 1.383 g/cm^3.[17]

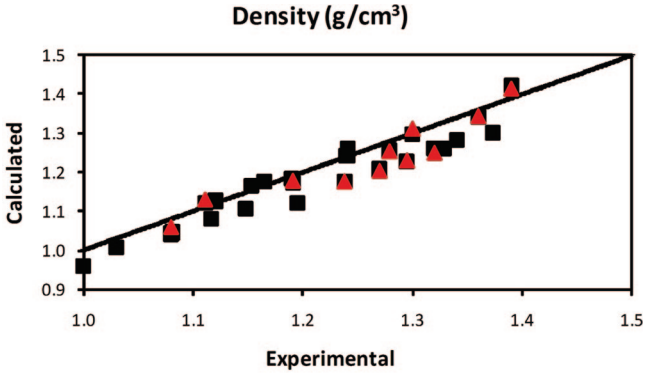

Figure 6. Computed OPLS-AA and experimental results for liquid densities for 1-alkyl-3-methylimidazolium [RMIM]-based ionic liquids (black squares) at 25 °C and 1 atm. Computed values with OPLS-AA parameters specific to [EMIM] and [BMIM] given as red triangles.

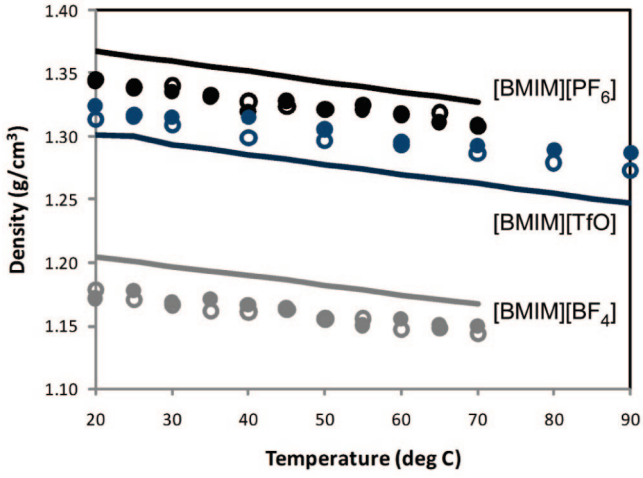

Figure 7. Calculated and experimental liquid densities versus temperature for 1-butyl-3-methylimidazolium [BMIM]-based ionic liquids with [BF_4] in black, [TfO] in blue, and [PF_6] in gray. (○ = general OPLS-AA [RMIM] parameter set, ● = specific OPLS-AA [BMIM] parameter set, and solid lines = experimental values).

mean force (PMF) calculations coupled to Metropolis Monte Carlo (MC) statistical mechanics were used to build a free-energy profile for the ring opening at 25 °C and 1 atm.

A reacting distance, $R_{NH} - R_{CH}$, was used for the proton transfer between the nitrogen on piperidine and the hydrogen on the isoxazole ring (Figure 9); $R_{NH} + R_{CH}$ was kept constant at 2.85 Å. The fixed distance of 2.85 Å was determined to be appropriate from our recent study of the reaction.[76] A second perturbation was necessary, R_{NO}, which entailed the opening of the isoxazole ring via an increasing N−O distance. Combining the $R_{NH} - R_{CH}$ PMF which runs along one reaction coordinate with the R_{NO} PMF in a second direction produced a two-dimensional (2D) PMF. The result is a free-energy map that can be used to identify minima and the transition state present in the reaction. The breaking of the N−O bond was split into ca. 24 windows with an increment of 0.04 Å. Each PMF calculation required 5 million configurations of equilibration followed by 10 million configurations of averaging.

For the hydrogen transfer, a novel method was developed in our recent study of the ring-opening of 5-nitrobenzisoxazole, where it was found that free-energy changes for individual windows can be fit almost perfectly by a fifth order polynomial.[76] Using only 7 windows out of the usual 50 and analytically integrating the values yielded a sextic polynomial for the overall proton-transfer PMF that is essentially identical to running the full simulation. The new methodology provided a 7-fold improvement in speed over traditional PMF methods for the enzymatic calculations, and the largest deviation found between the approximate and the detailed calculation was 1 kcal/mol. The fifth order polynomial quadrature method was used to compute the free energy of activation for the Kemp elimination in a periodic box of 378 [BMIM][PF_6] ionic liquid ions in the NPT ensemble. Ewald sums were used to handle the long-range electrostatics, and electrostatic contributions to the solute−solvent energy were calculated using CM3 charges,[78] with a scale factor of 1.14.

The free-energy surface for the Kemp elimination of benzisoxazole via piperidine is shown in Figure 10. The reaction follows a concerted mechanism where the R_{NO} distance of the isoxazole ring in the transition structure is 2.06 Å while the R_{NH} and R_{CH} distances are 1.10 and 1.75 Å, respectively. Computed changes in free energy yielded a $\Delta G^{\ddagger}$ value of 25.2 kcal/mol after a cratic entropy correction of 1.89 kcal/mol.[79] The level of uncertainty is less than ±1 kcal/mol based on fluctuations in the averages for the individual free-energy perturbation (FEP) windows. The experimental $\Delta G^{\ddagger}$ for the reaction under the same conditions is 22.6 ± 0.5 kcal/mol.[80] The calculations reproduce the activation values well, particularly when considering the computed and experimental uncertainties and the additional overestimation of ca. 1 kcal/mol for the Kemp elimination from the fifth order polynomial methodology.[76] The good agreement suggests that the ionic liquid microenvironment is being appropriately modeled by the new parameters. Further calculations and a detailed analysis of the Kemp elimination in additional ionic liquids and conventional solvents with different bases are currently underway and will be the focus of a future publication.

Conclusions

The development and testing of the OPLS-AA force field for use in the simulation of 68 unique ionic liquids has been described. Charges, equilibrium geometries, and torsional Fourier coefficients were derived to reproduce gas-phase structures and conformational energetics from LMP2/cc-

Table 9. Calculated and Experimental Liquid Densities (g/cm^3) versus Temperature for 1-Alkyl-3-methylimidazolium [RMIM] and *N*-Alkylpyridinium [RPyr] (R = Me, Et, Bu, Hex, Oct)-Based Ionic Liquids[a]

ionic liquid	temp (°C)	density (calcd)	density (exptl)	refs	ionic liquid	temp (°C)	density (calcd)	density (exptl)	refs
[EMIM][BF_4]	20	1.255 (1.260)	1.283	46	[BMIM][TfO]	20	1.314 (1.324)	1.3013	70
	25	1.253 (1.254)	1.279	46		25	1.317 (1.315)	1.30, 1.30148	64, 65
	30	1.255 (1.251)	1.275	46		30	1.309 (1.315)	1.2934	70
	35	1.246 (1.251)	1.271	46		40	1.299 (1.315)	1.2856	70
	40	1.247 (1.246)	1.266	46		50	1.296 (1.305)	1.277	70
[EMIM][TfO]	5	1.431 (1.428)	1.40052	63		60	1.293 (1.296)	1.2699	70
	15	1.431 (1.420)	1.39204	63		70	1.286 (1.293)	1.2623	70
	25	1.425 (1.422)	1.38360	63		80	1.279 (1.289)	1.2545	70
	35	1.414 (1.411)	1.37522	63		90	1.273 (1.288)	1.2469	70
	45	1.412 (1.414)	1.36690	63	[HMIM][BF_4]	25	1.102	1.14532	71
	55	1.401 (1.404)	1.35863	63		35	1.094	1.13851	71
	65	1.397 (1.391)	1.35043	63		45	1.097	1.13167	71
	75	1.393 (1.385)	1.34230	63		55	1.088	1.12489	71
[EMIM][$AlCl_4$]	10	1.240 (1.244)	1.3060	60		65	1.080	1.11816	71
	15	1.238 (1.239)	1.3020	60		75	1.077	1.11147	71
	20	1.234 (1.228)	1.2979	60		85	1.070	1.10484	71
	25	1.229 (1.229)	1.2947	60	[HMIM][PF_6]	5	1.267	1.3101	72
	30	1.222 (1.224)	1.2908	60		10	1.265	1.3060	72
	35	1.221 (1.216)	1.2870	60		15	1.266	1.3019	72
	40	1.217 (1.216)	1.2833	60		20	1.262	1.2979	72
	45	1.214 (1.214)	1.2798	60		25	1.255	1.2937, 1.29341	71, 72
	50	1.209 (1.206)	1.2759	60		30	1.253	1.2896	72
	55	1.207 (1.200)	1.2725	60		35	1.256	1.2854, 1.28578	71, 72
	60	1.203 (1.201)	1.2689	60		40	1.249	1.2813	72
	65	1.200 (1.195)	1.2651	60		45	1.250	1.2772, 1.27792	71, 72
[BMIM][BF_4]	20	1.179 (1.172)	1.2049, 1.2038	70		55	1.244	1.26988	71
	25	1.171 (1.178)	1.2011, 1.2000	70		65	1.237	1.26213	71
	30	1.167 (1.169)	1.1974, 1.1962	70		75	1.232	1.25436	71
	35	1.161 (1.171)	1.1938, 1.1924	70		85	1.229	1.24681	71
	40	1.161 (1.167)	1.1901, 1.1889	70	[OMIM][BF_4]	25	1.034	1.0912	53
	45	1.168 (1.165)	1.1865, 1.1854	70		30	1.037	1.0887	53
	50	1.155 (1.155)	1.1827, 1.1813	70		40	1.039	1.0823	53
	55	1.167 (1.174)	1.1790, 1.1779	70		50	1.028	1.0747	53
	60	1.147 (1.155)	1.1753, 1.1741	70		60	1.027	1.0685	53
	65	1.162 (1.151)	1.1717, 1.1705	70		70	1.025	1.0618	53
	70	1.143 (1.150)	1.1680, 1.1669	70	[OMIM][PF_6]	25	1.178	1.2245	53
[BMIM][PF_6]	20	1.345 (1.343)	1.3698, 1.3681	70		30	1.163	1.2207	53
	25	1.339 (1.338)	1.3657, 1.3641	70		40	1.161	1.2141	53
	30	1.340 (1.335)	1.3616, 1.3600	70		50	1.159	1.2069	53
	35	1.333 (1.331)	1.3574, 1.3557	70		60	1.156	1.1999	53
	40	1.328 (1.319)	1.3533, 1.3518	70		70	1.149	1.1922	53
	45	1.324 (1.328)	1.3492, 1.3475	70	[BPyr][BF_4]	25	1.175 (1.177)	1.2144	53
	50	1.322 (1.321)	1.3451, 1.3435	70		30	1.175 (1.177)	1.2118	53
	55	1.325 (1.321)	1.3410, 1.3394	70		40	1.165 (1.172)	1.2053	53
	60	1.318 (1.318)	1.3369, 1.3352	70		50	1.162 (1.164)	1.1988	53
	65	1.319 (1.311)	1.3327, 1.3311	70		60	1.155 (1.163)	1.1922	53
	70	1.308 (1.309)	1.3286, 1.3270	70		70	1.148 (1.156)	1.1856	53

[a] Calculated density values given in parentheses were computed using OPLS-AA charge/torsion parameters specific to [EMIM], [BMIM], [HMIM], [OMIM], and [BPyr], respectively.

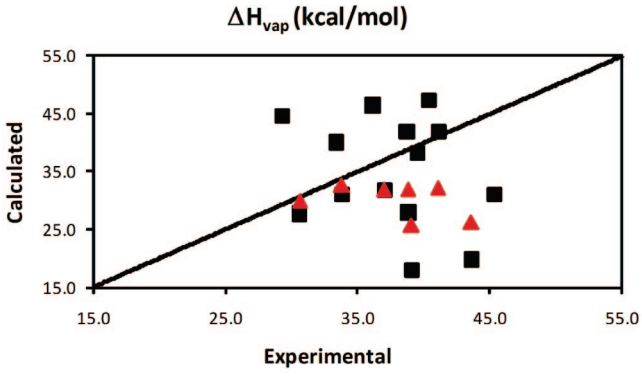

Figure 8. Computed OPLS-AA and experimental results for heats of vaporization for 1-alkyl-3-methylimidazolium [RMIM]-based ionic liquids (black squares) at 25 °C and 1 atm. Computed values with OPLS-AA parameters specific to [EMIM] and [BMIM] given as red triangles.

pVDZ(-f)//HF/6−31G(d) quantum mechanical calculations. Multiple alkyl chain lengths were considered in the fitting process, and the quality of the fits for the transferable force field yielded energy profiles for bond rotations comparable to that of ab initio calculations. In addition, the highly transferable parameters for [RMIM] and [RPyr] were compared to potentials developed specifically for individual ionic liquid cations and good agreement in liquid densities values was found between both sets. Relative deviations from experimental density values were ca. 1−3%; however, chloroaluminate-based ionic liquids had slightly larger deviations at ca. 4−5%. The errors in the densities computed for choline-based ionic liquids were significantly larger but are difficult to improve, owing to the lack of available experimental data for refinement. Agreement between the computed

Scheme 1. Kemp Elimination Reaction of Benzisoxazole with Piperidine

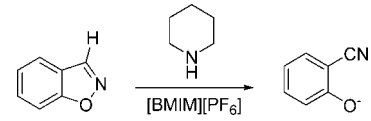

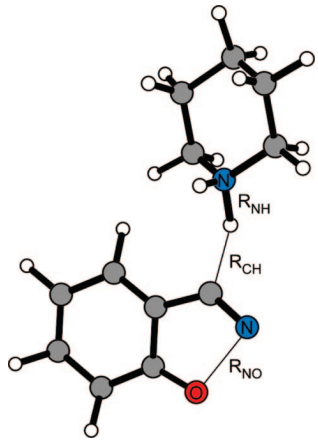

Figure 9. Reaction coordinates, $R_{NH} - R_{CH}$ and R_{NO}, used to locate stationary points from free-energy maps obtained via PMF simulations for the Kemp elimination of benzisoxazole using piperidine. Illustrated structure corresponds to the transition state computed from QM/MM calculations.

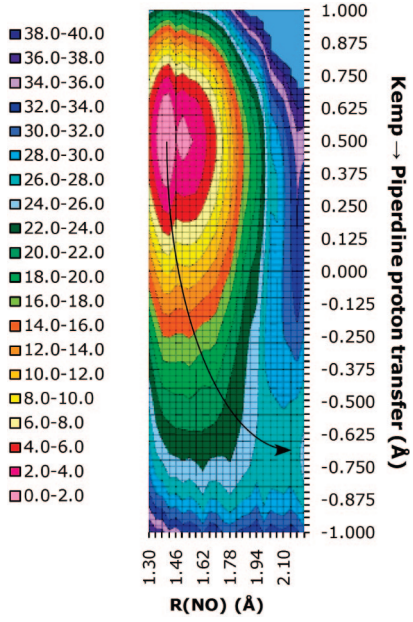

Figure 10. Two-dimensional potentials of mean force (free energy map, kcal/mol) for the Kemp elimination reaction of benzisoxazole via piperidine in [BMIM][PF_6]. Free energy values truncated to 40 kcal/mol for clarity. The arrow follows the reaction path toward product.

ΔH_{vap} and experimental estimates are generally good; however, absolute errors in the vaporization enthalpies are more difficult to assess because of inconsistencies between reported experimental values. In addition, the computed heats of vaporization were found to be more sensitive to the charge set used. The importance of testing the cation and anion parameters in a large number of ionic liquid combinations is highlighted in this work by the liquid simulation of an unprecedented number of ionic liquids, with 35 of the 68 solvents recomputed using specific cation parameters for a detailed comparison of the new parameters set's transferability between different alkyl chain lengths and anion combinations. QM/MM simulations for the Kemp elimination of benzisoxazole using piperidine as the base in [BMIM][PF_6] yielded good agreement with the experimental free energy of activation, i.e., $\Delta G^{\ddagger}$(calcd) = 25.2 ± 1 kcal/mol compared to $\Delta G^{\ddagger}$(exptl) = 22.6 ± 0.5 kcal/mol.[80]

Acknowledgment. Gratitude is expressed to the Alabama Supercomputer Center and Auburn University for support of this research and to Dr. Kasper P. Jensen for helpful discussions.

Supporting Information Available: ESP charges specific to [EMIM], [MPyr], and [EPyr]. Equilibrium bond and angle reference values, r_o and θ_o, and force constants, k, for the simulations. Additional torsion Fourier coefficients for the cations. Additional torsion energy profiles for the cations. Box sizes for all ionic liquids simulated. This material is available free of charge via the Internet at http://pubs.acs.org.

References

(1) Weingaertner, H. *Angew. Chem., Int. Ed.* **2008**, *47*, 654–670.

(2) (a) Forsyth, S. A.; Pringle, J. M.; MacFarlane, D. R. *Aust. J. Chem.* **2004**, *57*, 113–119. (b) Welton, T. *Chem. Rev.* **1999**, *99*, 2071–2083. (c) Seddon, K. R. *J. Chem. Tech. Biotechnol.* **1997**, *68*, 351–356.

(3) Bonhote, P.; Dias, A.-P.; Papageorgiou, N.; Kalyanasundaram, K.; Gratzel, M. *Inorg. Chem.* **1996**, *35*, 1168–1178.

(4) (a) Iwata, K.; Okajima, H.; Saha, S.; Hamaguchi, H. *Acc. Chem. Res.* **2007**, *40*, 1174–1181. (b) Castner, E. W.; Wishart, J. F.; Shirota, H. *Acc. Chem. Res.* **2007**, *40*, 1217–1227.

(5) (a) Hardacre, C.; Holbrey, J. D.; Nieuwenhuyzen, M.; Youngs, T. G. A. *Acc. Chem. Res.* **2007**, *40*, 1146–1155. (b) Hardacre, C.; Holbrey, J. D.; McMath, S. E. J. *J. Chem. Phys.* **2003**, *118*, 273–278.

(6) (a) MacFarlane, D. R.; Forsyth, M.; Howlett, P. C.; Pringle, J. M.; Sun, J.; Annat, G.; Neil, W.; Izgorodina, E. I. *Acc. Chem. Res.* **2007**, *40*, 1165–1173. (b) Tsuda, T.; Hussey, C. L. *Electrochem. Soc. Interface* **2007**, *16*, 42–49. (c) Silvester, D. S.; Compton, R. G. *Z. Phys. Chem.* **2006**, *220*, 1247–1274.

(7) (a) Han, X.; Armstrong, D. W. *Acc. Chem. Res.* **2007**, *40*, 1079–1086. (b) Visser, A. E.; Swatloski, R. P.; Reichert, W. M.; Davis, J. H., Jr.; Rogers, R. D.; Mayton, R.; Sheff, S.; Wierzbicki, A. *Chem. Commun.* **2001**, 135–136. (c) Huddleston, J. G.; Rogers, R. D. *Chem. Commun.* **1998**, 1765–1766.

(8) Pârvulescu, V. I.; Hardacre, C. *Chem. Rev.* **2007**, *107*, 2615–2665.

(9) van Rantwijk, F.; Sheldon, R. A. *Chem. Rev.* **2007**, *107*, 2757–2785.

(10) (a) Welton, T. *Coord. Chem. Rev.* **2004**, *248*, 2459–2477. (b) Wasserscheid, P.; Keim, W. *Angew. Chem., Int. Ed.* **2000**, *39*, 3772–3789.

(11) (a) Sheldon, R. *Chem. Commun.* **2001**, 2399–2407. (b) Haumann, M.; Riisager, A. *Chem. Rev.* **2008**, *108*, 1474–1497. (c) Zhang, Z. C. *Adv. Catal.* **2006**, *49*, 153–237.

(12) (a) Smiglak, M.; Metlen, A.; Rogers, R. D. *Acc. Chem. Res.* **2007**, *40*, 1182–1192. (b) Lodge, T. P. *Science* **2008**, *321*, 50–51.

(13) Binnemans, K. *Chem. Rev.* **2007**, *107*, 2592–2614.

(14) (a) Ranke, J.; Stolte, S.; Störmann, R.; Arning, J.; Jastorff, B. *Chem. Rev.* **2007**, *107*, 2183–2206. (b) Docherty, K. M.; Kulpa, C. F., Jr. *Green Chem.* **2005**, *7*, 185–189. (c) Stolte, S.; Arning, J.; Bottin-Weber, U.; Matzke, M.; Stock, F.; Thiele, K.; Uerdingen, M.; Welz-Biermann, U.; Jastorff, B.; Ranke, J. *Green Chem.* **2006**, *8*, 621–629.

(15) Wells, A. S.; Coombe, V. T. *Org. Process Res. Dev.* **2006**, *10*, 794–798.

(16) Gathergood, N.; Garcia, M. T.; Scammels, P. J. *Green Chem.* **2004**, *6*, 166–175.

(17) Nockemann, P.; Thijs, B.; Driesen, K.; Janssen, C. R.; Van Hecke, K.; Van Meervelt, L.; Kossmann, S.; Kirchner, B.; Binnemans, K. *J. Phys. Chem. B* **2007**, *111*, 5254–5263.

(18) Gathergood, N.; Scammels, P. J.; Garcia, M. T. *Green Chem.* **2006**, *8*, 156–160.

(19) Fukumotu, K.; Yoshizawa, M.; Ohno, H. *J. Am. Chem. Soc.* **2005**, *127*, 2398–2399.

(20) Pernak, J.; Stefaniak, F.; Wglewski, J. *Eur. J. Org. Chem.* **2005**, 650–652.

(21) (a) Lynden-Bell, R. M.; Del Pópolo, M. G.; Youngs, T. G. A.; Kohanoff, J.; Hanke, C. G.; Harper, J. B.; Pinilla, C. C. *Acc. Chem. Res.* **2007**, *2007*, 1138–1145. (b) Pádua, A. A. H.; Costa Gomes, M. F.; Canongia Lopes, J. N. A. *Acc. Chem. Res.* **2007**, *40*, 1087–1096. (c) Wang, Y.; Jiang, W.; Yan, T.; Voth, G. A. *Acc. Chem. Res.* **2007**, *40*, 1193–1199. (d) Cadena, C.; Zhao, Q.; Snurr, R. Q.; Maginn, E. J. *J. Phys. Chem. B* **2006**, *110*, 2821–2832. (e) Hunt, P. A. *Mol. Simul.* **2006**, *31*, 1–10. (f) Canongia Lopes, J. N.; Padua, A. H. *J. Phys. Chem. B* **2004**, *108*, 16893–16898. (g) Liu, Z.; Huang, S.; Wang, W. *J. Phys. Chem. B* **2004**, *108*, 12978–12989. (h) Morrow, T. I.; Maginn, E. J. *Fluid Phase Equilib.* **2004**, *217*, 97–104. (i) de Andrade, J.; Böes, E. S.; Stassen, H. *J. Phys. Chem. B* **2002**, *106*, 3546–3548.

(22) Canongia Lopes, J. N.; Padua, A. A. H. *J. Phys. Chem. B* **2006**, *110*, 19586–19592.

(23) Canongia Lopes, J. N.; Deschamps, J.; Padua, A. H. *J. Phys. Chem. B* **2004**, *108*, 2038–2047.

(24) de Andrade, J.; Böes, E. S.; Stassen, H. *J. Phys. Chem. B* **2002**, *106*, 13344–13351.

(25) Acevedo, O.; Jorgensen, W. L.; Evanseck, J. D. *J. Chem. Theory Comput.* **2007**, *3*, 132–138.

(26) MacKerell, A. D., Jr.; Bashford, D.; Bellott, M.; Dunbrack, R. L.; Evanseck, J. D.; Field, M. J.; Fisher, S.; Gao, J.; Guo, H.; Ha, S.; Joseph-McCarthy, S.; Kuchnir, L.; Kuczera, K.; Lau, F. T. K.; Mattos, C.; Michnick, S.; Ngo, T.; Nguyen, D. T.; Prodhom, B.; Reiher, W. E., III; Roux, B.; Schlenkrich, M.; Smith, J. C.; Stote, R.; Straub, J.; Watanabe, M.; Wiorkiewicz-Kuczera, J.; Yin, D.; Karplus, M. *J. Phys. Chem. B* **1998**, *102*, 3586.

(27) Cornell, W. D.; Cieplak, P.; Bayly, C. I.; Gould, I. R.; Merz, K. M.; Ferguson, D. M.; Spellmeyer, D. C.; Fox, T.; Caldwell, J. W.; Kollman, P. A. *J. Am. Chem. Soc.* **1995**, *117*, 5179–5197.

(28) Jorgensen, W. L.; Maxwell, D. S.; Tirado-Rives, J. *J. Am. Chem. Soc.* **1996**, *118*, 11225–11236.

(29) (a) Jensen, K. P.; Jorgensen, W. L. *J. Chem. Theory Comput.* **2006**, *2*, 1499–1509. (b) Price, M. L. P.; Ostrovsky, D.; Jorgensen, W. L. *J. Comput. Chem.* **2001**, *22*, 1340–1352. (c) Rizzo, R. C.; Jorgensen, W. L. *J. Am. Chem. Soc.* **1999**, *121*, 4827–4836. (d) Jorgensen, W. L.; McDonald, N. A. *J. Phys. Chem. B* **1998**, *102*, 8049–8059.

(30) Jorgensen, W. L.; Tirado-Rives, J. *Proc. Nat. Acad. Sci. U.S.A.* **2005**, *102*, 6665–6670.

(31) (a) Kaminski, G. A.; Friesner, R. A.; Tirado-Rives, J.; Jorgensen, W. L. *J. Phys. Chem. B* **2001**, *105*, 6474–6487. (b) Watkins, E. K.; Jorgensen, W. L. *J. Phys. Chem. A* **2001**, *105*, 4118–4125.

(32) Jaguar, version 6.0, Schrödinger, LLC, New York, NY, 2005.

(33) (a) Saebø, S.; Pulay, P. *Annu. Rev. Phys. Chem.* **1993**, *44*, 213–236. (b) Saebø, S.; Tong, W.; Pulay, P. *J. Chem. Phys.* **1993**, *98*, 2170–2175.

(34) Dunning, T. H., Jr. *J. Chem. Phys.* **1989**, *90*, 1007–1023.

(35) Jorgensen, W. L.; Tirado-Rives, J. *J. Comput. Chem.* **2005**, *26*, 1689–1700.

(36) Armstrong, J. P.; Hurst, C.; Jones, R. G.; Licence, P.; Lovelock, K. R. J.; Satterley, C. J.; Villar-Garcia, I. J. *Phys. Chem. Chem. Phys.* **2007**, *9*, 982–990.

(37) McDonald, N. A.; Jorgensen, W. L. *J. Phys. Chem. B* **1998**, *102*, 8049–8059.

(38) Jorgensen, W. L.; McDonald, N. A. *J. Mol. Struct. (THEOCHEM)* **1998**, *424*, 145–155.

(39) Gale, R. J.; Gilbert, B. P.; Osteryoung, R. A. *Inorg. Chem.* **1978**, *17*, 2728–2729.

(40) Wilkes, J. S.; Frye, J. S.; Reynolds, G. F. *Inorg. Chem.* **1983**, *22*, 3870–3872.

(41) (a) Ackermann, B. L.; Tsarbopoulos, A.; Allison, J. *Anal. Chem.* **1985**, *57*, 1766–1768. (b) Wicelinski, S. P.; Gale, R. J.; Pamidimukkala, K. M.; Laine, R. A. *Anal. Chem.* **1988**, *60*, 2228–2232.

(42) Gray, J. L.; Maciel, G. E. *J. Am. Chem. Soc.* **1981**, *103*, 7147–7151.

(43) Franzen, G.; Gilbert, B. P.; Pelzer, G.; Depauw, E. *Org. Mass Spectrom.* **1986**, *21*, 443–444.

(44) Ohlin, C. A.; Dyson, P. J.; Laurenczy, G. *Chem. Commun.* **2004**, 1070–1071.

(45) Nishida, T.; Tashiro, Y.; Yamamoto, M. *J. Fluorine Chem.* **2003**, *120*, 135–141.

(46) Noda, A.; Hayamizu, K.; Watanabe, M. *J. Phys. Chem. B* **2001**, *105*, 4603–4610.

(47) Zhang, S.; Sun, N.; He, X.; Lu, X.; Zhang, X. *J. Phys. Chem. Ref. Data* **2006**, *35*, 1475–1517.

(48) Branco, L. C.; Rosa, J. N.; Ramos, J. J. M.; Afonso, C. A. M. *Chem. Eur. J.* **2002**, *8*, 3671–3677.

(49) Zaitsau, D. H.; Kabo, G. J.; Strechan, A. A.; Paulechka, Y. U.; Tschersich, A.; Verevkin, S. P.; Heintz, A. *J. Phys. Chem. A* **2006**, *110*, 7303–7306.

(50) Swiderski, K.; McLean, A.; Gordon, C. M.; Vaughan, D. H. *Chem. Commun.* **2004**, 2178–2179.

(51) (a) Letcher, T. M.; Reddy, P. *J. Chem. Thermodyn.* **2005**, *37*, 415–421. (b) Letcher, T. M.; Reddy, P. *Fluid Phase Equilib.* **2004**, *219*, 107–112.

(52) Arce, A.; Rodil, E.; Soto, A. *J. Solution Chem.* **2006**, *35*, 63–78.

(53) Gu, Z.; Brennecke, J. F. *J. Chem. Eng. Data* **2002**, *47*, 339–345.

(54) Matsumotoa, K.; Hagiwara, R. *J. Fluorine Chem.* **2007**, *128*, 317–331.

(55) Huddleston, J. G.; Visser, A. E.; Reichert, W. M.; Willauer,

H. D.; Broker, G. A.; Rogers, R. D. *Green Chem.* **2001**, *3*, 156–164.

(56) Dzyuba, S. V.; Bartsch, R. A. *ChemPhysChem* **2002**, *3*, 161–166.

(57) Fannin, A. A., Jr.; Floreani, D. A.; King, L. A.; Landers, J. S.; Piersma, B. J.; Stech, D. J.; Vaughn, R. L.; Wilkes, J. S.; Williams, J. L. *J. Phys. Chem.* **1984**, *88*, 2614–2621.

(58) Seddon, K. R.; Stark, A. S.; Torres, M.-J., In *Clean Solvents: Alternative Media for Chemical Reactions and Processing*; Abraham, M.; Moens, L., Eds.; ACS Symposium Series 819; American Chemical Society: Washington, DC, 2002; Vol. 3, pp 4−49.

(59) Letcher, T. M.; Deenadayalu, N. *J. Chem. Thermodyn.* **2003**, *35*, 67–76.

(60) Tong, J.; Liu, Q.-S.; Xu, W.-G.; Fang, D.-W.; Yang, J.-Z. *J. Phys. Chem. B* **2008**, *112*, 4381–4386.

(61) Fannin, A. A., Jr.; King, L. A.; Leveisky, J. A.; Wilkes, J. S. *J. Phys. Chem.* **1984**, *88*, 2609–2614.

(62) Emel'yanenko, V. N.; Verevkin, S. P.; Heintz, A.; Schick, C. *J. Phys. Chem. B* **2008**, *112*, 8095–8098.

(63) Rodriguez, H.; Brennecke, J. F. *J. Chem. Eng. Data* **2006**, *51*, 2145–2155.

(64) Ye, C.; Shreeve, J. n. M. *J. Phys. Chem. A* **2007**, *111*, 1456–1461.

(65) (a) Olivier-Bourbigou, H.; Magna, L. *J. Mol. Catal. A: Chem.* **2002**, 182. (b) Fredlake, C. P.; Crosthwaite, J. M.; Hert, D. G.; Aki, S. N. V. K.; Brennecke, J. F. *J. Chem. Eng. Data* **2004**, *49*, 954–964. (c) Tokuda, H.; Hayamizu, K.; Ishii, K.; Susan, M. A. B. H.; Watanabe, M. *J. Phys. Chem. B* **2004**, *108*, 16593–16600.

(66) Papaiconomou, N.; Yakelis, N.; Salminen, J.; Bergman, R.; Prausnitz, J. M. *J. Chem. Eng. Data* **2006**, *51*, 1389–1393.

(67) Valderrama, J. O.; Sanga, W. W.; Lazzus, J. A. *Ind. Eng. Chem. Res.* **2008**, *47*, 1318–1330.

(68) Merck ionic liquid database, http://ildb.merck.de/ionicliquids/en/startpage.html.

(69) Shanley, P.; Collin, R. L. *Acta Crystallogr.* **1961**, *14*, 79–80.

(70) Jacquemin, J.; Ge, R.; Nancarrow, P.; Rooney, D. W.; Costa Gomes, M. F.; Pádua, A. A. H.; Hardacre, C. *J. Chem. Eng. Data* **2008**, *53*, 716–726.

(71) Muhammad, A.; Mutalib, M. I. A.; Wilfred, C. D.; Murugesan, T.; Shafeeq, A. *J. Chem. Thermodyn.* **2008**, *40*, 1433–1438.

(72) Pereiro, A. B.; Tojo, E.; Rodríguez, A.; Canosa, J.; Tojo, J. *J. Chem. Thermodyn.* **2006**, *38*, 651–661.

(73) Lee, S. H.; Lee, S. B. *Chem. Commun.* **2005**, 3469–3471.

(74) Yan, T.; Burnham, C. J.; Del Pópolo, M. G.; Voth, G. A. *J. Phys. Chem. B* **2004**, *108*, 11877–11881.

(75) Repasky, M. P.; Chandrasekhar, J.; Jorgensen, W. L. *J. Comput. Chem.* **2002**, *23*, 1601–1622.

(76) Acevedo, O. *J. Phys. Chem. B*, submitted.

(77) Acevedo, O.; Jorgensen, W. L. *J. Am. Chem. Soc.* **2005**, *127*, 8829–8834.

(78) Thompson, J. D.; Cramer, C. J.; Truhlar, D. G. *J. Comput. Chem.* **2003**, *24*, 1291–1304.

(79) Hermans, J.; Wang, L. *J. Am. Chem. Soc.* **1997**, *119*, 2707–2714.

(80) D'Anna, F.; La Marca, S.; Noto, R. *J. Org. Chem.* **2008**, *73*, 3397–3403.

CT900009A

JCTC Journal of Chemical Theory and Computation

Modeling of the Chiroptical Response of Chiral Amino Acids in Solution Using Explicit Solvation and Molecular Dynamics

Matthew D. Kundrat and Jochen Autschbach*

Department of Chemistry, 312 Natural Sciences Complex, The State University of New York at Buffalo, Buffalo, New York 14260-3000

Received December 1, 2008

Abstract: Molecular dynamics (MD) simulations and TDDFT linear response computations were employed to model the molar rotations of the zwitterionic forms of glycine, alanine, proline, and phenylalanine in aqueous solution. The MD simulations inherently take into account averaging the chiroptical response of different amino acid conformers and also allow the effects from vibrational distortions and explicit solvent perturbations on the optical rotation to be modeled. The results show that the chiroptical response correlates strongly to the conformations of these molecules relative to their carboxylate functional groups. Additionally, the molar rotation of phenylalanine shows a correspondence to the molecule's internal rotation about its phenyl group. These findings may be rationalized with established and revised "sector rules" for optical activity.

Introduction

Molar rotation is among the quintessential properties of chiral molecules. A solution of one enantiomer of a chiral compound will rotate the polarization plane of polarized light either to the left or the right, depending on the absolute configuration of the molecule. Matching the computed molar rotation of such a chiral molecule with experiment to assign its absolute configuration has drawn significant interest, due in part to the advances in time dependent density functional theory (TDDFT), which allows for efficient routine calculations of optical rotations from first principles.[1−10]

Most of the ab initio wave function based and density functional theory modeling of chirality done to date has been with static models of structurally rigid molecules. However, most chiral molecules found in nature can adopt multiple conformations, and are not frozen but are actively vibrating as they are measured at room temperature. Modeling the chiroptical response of flexible molecules by time dependent density functional theory computations on static conformers and averaging their responses based upon respective Boltzmann factors has met with some success.[2,11−19] However, in addition to approximations intrinsic to TDDFT the overall accuracy of such modeling is limited by the accuracy of the Boltzmann factors, which can be difficult to gauge.

Our most recent work in this area involved calculations on the small amino acids, glycine and alanine.[20] The publication served as a validation of the method of using force-field based (classical) molecular dynamics (MD) and an explicit point charge solvent model along with TDDFT to model the chiroptical response properties of these molecules. This MD-based modeling method has several purposes: First the molecular dynamics simulation serves as an engine to generate configurations of the molecules of interest in differing conformations, conformational sampling being essential to the modeling of chiroptical properties of flexible molecules. The second advantage of employing molecular dynamics is that it allows us, through capturing many geometries from the simulation, to model some of the thermal effects on chirality, for instance from vibrations; these effects have drawn much attention from our research group and others.[8,21−30] Third, the molecular dynamics simulation contains explicit water molecules, which through the simple point charge model can serve as an effective means of modeling solvation effects, whose import impact on optical rotation has drawn significant interest as well.[10,11,25,28,30−40]

In keeping with prior publications on the chiroptical response of amino acids,[20,41] this work begins with calcula-

* Corresponding author phone: (716) 645-6800 x2086; fax: (716) 645-6963; e-mail: jochena@buffalo.edu.

10.1021/ct8005216 CCC: $40.75
Published on Web 03/24/2009

tions on glycine, the smallest amino acid. In a recent work, glycine was used to benchmark a method of explicit solvation using point charge water molecules and molecular dynamics to model chiroptical response. Here the method is used to explore the variations in this response with respect to changes in the geometry of the glycine molecule. While not intrinsically chiral, glycine can through the course of molecular dynamics adopt chiral configurations which give rise to nonzero molar rotations. In fact, those molar rotations can be very large. The first section investigates the regular variations of this chiral response as a function of glycine's N−C−C−O dihedral angle over the course of a molecular dynamics simulation and how differing solvation models affect this molar rotation. Comparable trends in the chiroptical response of the smallest chiral amino acid, alanine, are also discussed. The regular variations of molar rotation are correlated with sector rules for amino acid chiroptical activity.

The focus of the paper then shifts to proline, a chiral amino acid known to adopt two different conformations at room temperature, differing in the direction of puckering for its five membered ring. The relative populations of these two conformers obtained by classical molecular dynamics are found to be remarkably similar to that obtained by DFT and those derived from experiment. The dependency of molar rotation upon this configuration is found to be similar to that seen for fixed configurations optimized with DFT. The variation of molar rotation with the N−C−C−O dihedral angle is similar to that of glycine, but with the variations expected from the fact that proline is intrinsically chiral and glycine is not.

The next section deals with phenylalanine, a more conformationaly flexible chiral amino acid which can be found in rotamers whose molar rotation depends on not one but two chromophores. As such, the effects of the rotamer identity, as well as dihedral angles, with respect to the carboxylate and phenyl chromophores, are examined. As with proline and glycine, the variation of the dihedral angle with respect to the COO^- group (the N−C−C−O angle) causes variations in the molar rotation consistent with the sector rule for the carboxylate chromophore. The variation of the $C_\alpha-C_\beta-C_\gamma-C_\delta$ dihedral angle, which relates directly to the geometry about the phenyl chromophore, yields results consistent with recent incarnations of the sector rule for the phenyl chromophore, which are the opposite of what the older sector rule for this group predicted.

Finally, the average molar rotations resulting from thousands of TDDFT calculations of proline and phenylalanine are compared with experiment. The populations of the three different phenylalanine conformers obtained from classical molecular dynamics are more evenly distributed than those obtained from the Boltzmann weighting of DFT optimized structures. The populations of the proline molecule computed by molecular dynamics and those obtained from Boltzmann weighted DFT optimizations both agree very well with experimentally derived values in the literature. This allows us to isolate the effects that the intrinsic dynamics of the solute and dynamic solvation have on the molar rotation for this molecule in solution and to evaluate how well these factors are modeled by the current computational methods.

Computational Methods

Many of the computational methods used in this work are detailed in previous publications[20,41−43] where TDDFT based computations of optical rotations of amino acids were exhaustively benchmarked. All quantum mechanical (QM) data were computed with the Turbomole[44] quantum chemical software, version 5.7.1. Dunning's aug-cc-pVDZ basis set[45] was used for all calculations except those involving the aromatic sector rule, which will be discussed later in this work. The PBE0 functional was employed, since for small amino acids in solution it yields low lying electronic excitations that are reasonably close to those obtained at the CC2 level of theory. For some calculations the conductor-like screening model (COSMO)[46] of solvation was applied to the ground state. Molar rotations were calculated at the wavelength of the sodium D line (589.3 nm) and reported in units of deg·cm^2/(dmol). The center of the mass of the amino acid molecule has been used for the coordinate origin for all response calculations. While the molar rotations computed herein are attributed to the length representation of the electric dipole operator and are formally origin dependent, this dependence is minimized in TDDFT when large basis sets such as aug-cc-pVDZ are used; see our earlier work and the references cited therin.[41]

Geometries used in the quantum mechanical calculations were generated with the GROMACS[47] molecular dynamics program, version 3.3.3, in a fashion similar to that of Mukhopadhyay et al.[33] Molecular dynamics of solvated amino acid molecules were run in a cubic periodic solvent box measuring $25 \times 25 \times 25$ nm^3 with average density of 1.0 g/cc using TIP3P water molecules. Note that the phrases, "TIP3P solvation" and "COSMO solvation" will be used later in this article referring to subsequent DFT calculations which treat the solvent molecules as simple point charges taken from the TIP3P model and those which discard all the explicit water molecules from the molecular dynamics simulation and treat the solvent as a continuum. 256 water molecules from each MD configuration were used in any subsequent DFT calculations; as such, no water molecules greater than 12.5 nm from the center of the solute were included, yielding solvation spheres for QM calculations that were nearly spherical, not cubic. The all-atom OPLS-AA molecular mechanics (MM)[48] force field was used for the simulations, which were carried out at 300K with a time step of 1 fs. Snapshots of the simulations, akin to frames of a motion picture, were taken every 10 ps for glycine and 100 ps for the larger molecules, which was a sufficient duration for energetic and chiroptical response calculations of adjacent MD configurations to be uncorrelated. These geometric configurations were used for subsequent computations of molar rotation. The classical mechanics MD used here captures some of the dynamical effects on the optical rotation. Ideally, of course, the nuclear motion should be treated quantum mechanically. Zero-point and temperature-dependent vibrational and internal rotation corrections on optical rotation using approximate nuclear wave functions suitable for local minima have been considered by

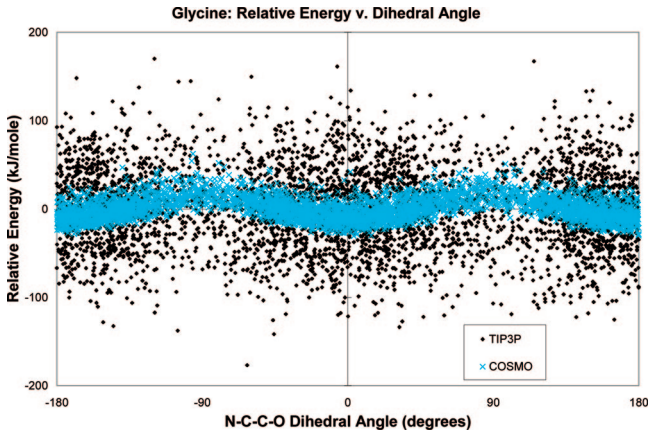

Figure 1. Variation of the energy of a glycine system as a function of the N−C−C−O dihedral angle. The energies reported include either 256 point charge based water molecules or the COSMO solvation model. All energies are reported relative to the average energy for the model. The geometries were generated by molecular dynamics with the GROMACS program, and snapshots were recorded at 10 ps intervals.

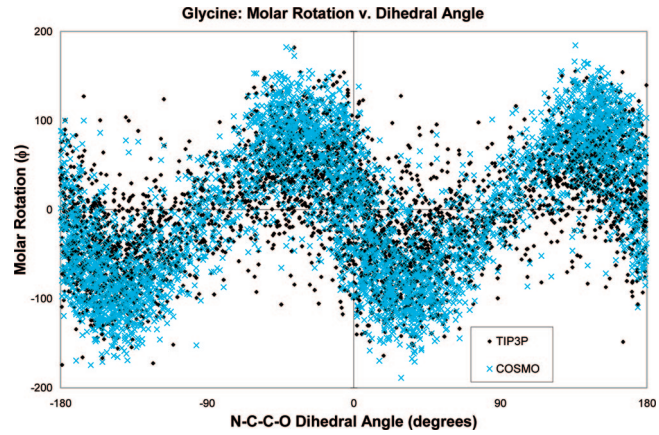

Figure 2. Molar rotation (ϕ) of glycine as a function of the N−C−C−O dihedral angle. The geometries used are from the same dynamics run used for Figures 1 and 5, and include either 256 point charge based water molecules or the COSMO solvation model.

our group previously, [21−24] but this approach has not been adapted for use with solvation models needed for this work. In many aspects the approximations used here and in those previous works are complementary and capture different aspects of the dynamical behavior of the system.

Results and Discussion

Effects of the Dihedral Angles on Energy and Molar Rotation for Glycine and Alanine. All the chiral amino acids studied here can be regarded as derivatives of glycine, the smallest amino acid. The functional groups in glycine and the structural variations thereof are present in the other amino acids as well, and so it is logical to investigate this prototypical molecule first. Among all the structural variables in glycine, one stands out as having the greatest impact on optical activity. It is the O−C−C−N dihedral angle, a structural portion which is present in all amino acids. As this angle varies during the course of a molecular dynamics simulation, the energy of the system and its chiroptical response vary as well. This section shows how the energy and molar rotation of glycine correlate strongly with this dihedral angle.

The relative energy of a solvated glycine molecule as a function of this angle is plotted in Figure 1. The reference point for this relative energy is the average energy at the PBE0/aug-cc-pVDZ level of theory using either explicit TIP3P waters or the COSMO solvent continuum; a comparison of the raw energies of the two different methods would not yield relevant results. The first detail of note from this graph is that the energy of the system varies much more when explicit point charge water molecules are used for solvation than when the COSMO continuum is used. This is to be expected since the large variations in the geometries formed by the explicit waters can lead to greater changes, both positive and negative, of the glycine−water system. For each DFT calculation with COSMO, the continuum is built around the glycine molecule, however distorted its geometry may be. For the calculations using explicit TIP3P waters, the positions and geometries of the solvent molecules can differ vastly between different snapshots of the MD, and how optimally a particular solvent sphere geometry may stabilize the solute varies considerably.

The second point we want to draw attention to in Figure 1 is the correlation between energy and clustering of structures. The energy of the system is calculated at the PBE0/aug-cc-pVDZ level of theory. The geometries with their particular dihedral angles are determined by the all-atoms force field in GROMACS. Depending on the details of the force field and solvent−solute interactions, the geometries of glycine that constitute local minima could potentially differ between the QM and MM methods, but they do not. The trend of the QM energies indicates that the molecule has a local minimum structure with its dihedral angle at 0° (or 180°, due to the degeneracy in the C_{2v} symmetrical carboxylate group). This is in agreement with the QM optimization calculations on glycine in our previous work.[41] In that work we found the glycine structure with the ±90° dihedral to be a saddle point, which is consistent with the data in Figure 1. These data also indicate that the energetics of the MM simulation agree with the QM results.

While the energy of a solvated glycine molecule is an *even* function of its N−C−C−O dihedral angle, the molar rotation, depicted in Figure 2, is an *odd* function. The energy of the glycine molecule increases as the dihedral angle deviates from its ideal at 0°, regardless of the direction of the perturbation. The molar rotation, however, deviates in equal and opposite directions depending on which way the molecule twists. This is in keeping with the sector rule for optical rotation of amino acids.[43] As the N−C−C−O dihedral changes, the functional groups that perturb the symmetry of the otherwise C_{2v} symmetrical carboxylate group move either above or below the horizontal symmetry plane of that group. As the sign of the optical activity "sectors" are opposites on opposite sides of this plane, the molar rotation changes in opposing ways depending on which side of the plane those perturbing groups deviate from.

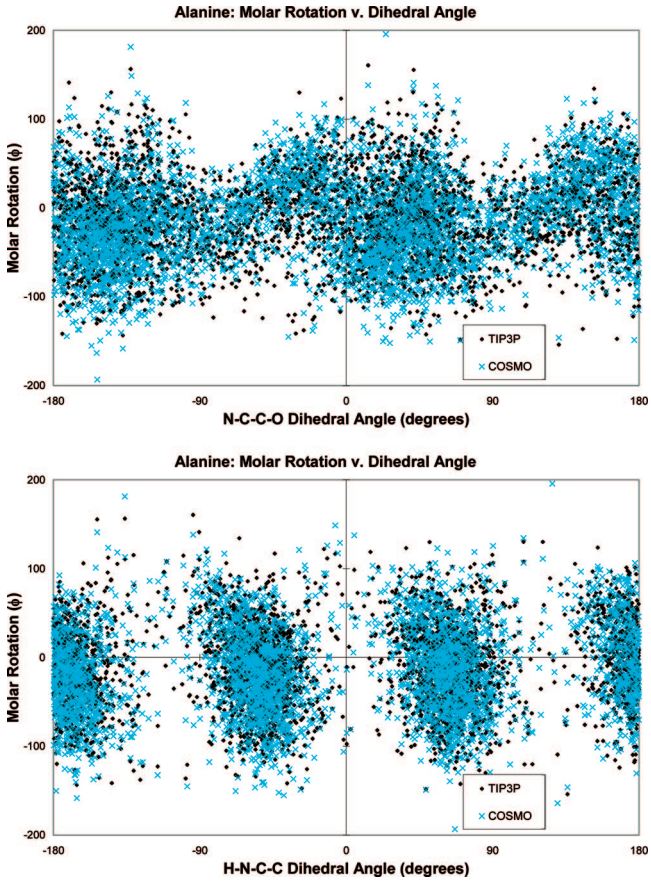

Figure 3. Molar rotation of a solvated alanine zwitterion as a function of the N−C−C−O (top) and H−N−C−C (bottom) dihedral angles.

Also note that every time that the N−C−C−O dihedral angle is an integer multiple of 90°, the molecule assumes approximate C_{2v} symmetry, but the optical rotation may be nonzero because of distortions elsewhere in the molecule as well as movement in the explicit solvation shell where one is present. It is useful here to draw attention to the works of Wiberg et al.,[49] in which the effects of torsional angles on optical activity were also demonstrated, and that of Pecul et al.,[50] where among other things the optical rotation of alanine was modeled. For a comparison with the latter we have performed MD simulations for the alanine zwitterion; the results of which are shown in Figure 3. The plots both show periodic variations of optical rotation as a function of the N−C−C−O dihedral angle. A notable difference is that our plot for the zwitterionic glycine, as well as our results from calculations with the zwitterionic form of alanine depicted in Figure 3, with its C_{2v} symmetrical chromophore, shows symmetrical results when the chromophore is rotated 180°, while the plot for the neutral alanine,[50] with its COOH chromophore whose C_{2v} symmetry is significantly perturbed by its hydrogen atom, shows results that are not quite symmetrical about a 180° rotation.

Since, unlike glycine, alanine is a chiral molecule, the molar rotation need not average to zero when the N−C−C−O dihedral angle approaches a multiple of 90°, though since the molar rotation of alanine is known from experiment to be small (about 2 deg·cm^2/(dmol)) this deviation should not be too great. The variation of the molar rotation of alanine

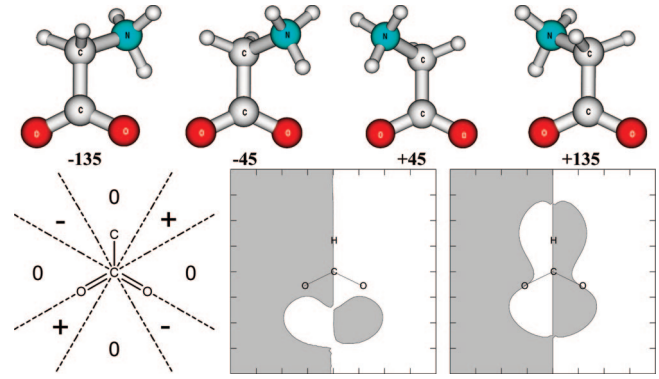

Figure 4. Glycine molecule with differing O−C−C−N dihedrals, Jorgensen's sectors for amino acids (depicted as a set of overlapping carbonyl chromophores, *not* a pentavalent carbon), and sectors computed from TDDFT for the CD of the first excitation (center) and molar rotation (right) of the formate anion (areas of positive rotation are light, negative areas are dark). Jorgensen's sectors shown are above the plane of the page, those below the plane are of the opposite sign. Note that the configurations of glycine with dihedral angles of +45° and −135°, as well as those of −45° and +135°, are equivalant due to the symmetry of the carboxylate group.

with respect to the H−N−C−C dihedral angle, which describes the rotation of the NH_3^+ group, is shown on the bottom of Figure 3. The C_{3v} symmetry of this functional group is readily apparent from the periodicity of the graph, as is the fact that during the molecular dynamics simulation the NH_3^+ group shows a strong tendency to be found near its rotational minima at intervals 120° apart. The periodic variation of molar rotation for the NH_3^+ group is not as obvious, as it is dwarfed by the variation in molar rotation caused by the rotation of the COO^- group which is occurring simultaneously in the molecular dynamics simulation. This is consistent with the fact that for a zwitterionic alanine molecule the COO^- group is the primary chromophore effecting molar rotation at 589.3 nm, and the NH_3^+ group is secondary, just as it has been computed that for a neutral alanine in the gas phase the COOH group is the primary chromophore and the NH_2 group has secondary effects.[50]

Returning to the less complex glycine molecule, the dihedral angles in Figure 2 that are multiples of 90° represent "nodes" in oscillating molar rotation pattern. These are the geometries in which the glycine molecule is most symmetrical, and as such its molar rotations are the smallest in magnitude. Conversely, when the N−C−C−O dihedral angle deviates most from multiples of 90°, the molar rotations tend to be the greatest. Some configurations of glycine where this configuration is far from symmetrical are depicted in Figure 4.

According to a sector rule model for amino acid optical activity derived from CD sector rules by Jorgensen,[51] the glycine configurations with the NH_3^+ group in a positive sector should have positive molar rotation, and those with the NH_3^+ group in a negative sector should have a negative molar rotation. Our computations of a formate anion (to model the carboxylate chromophore), perturbed with a negative point charge, form sectors which are consistent with

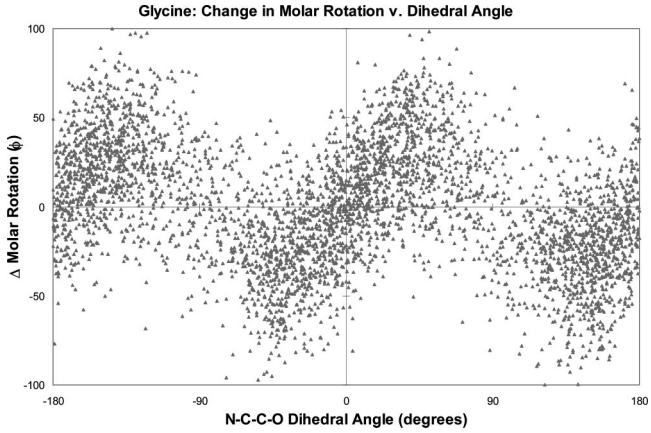

Figure 5. Difference between the molar rotation computed using point charge water molecules and that computed using the COSMO solvent model. $\Delta\phi = \phi_{TIP3P} - \phi_{COSMO}$.

this as well. However, we point out that the sector modeling of glycine by formate is a rather crude model; see our previous publication for details[43] and note the differing signs of the computed CD and optical rotation sectors close to around the C−H bond. The data in Figure 2 confirm that the sector assignment yields the expected sign of the optical rotation. For the conformers where the dihedral angle is near +45° (or −135°, due to the degeneracy caused by the symmetrical COO^- group), the molar rotation is negative. For those molecules with O−C−C−N dihedrals nearing −45° (or +135°), the molar rotation is positive.

One interesting factor that deserves attention is the effect of explicit solvation as a function of dihedral angle on molar rotation. This effect is implied in Figure 2, which shows the molar rotation of glycine solvated by explicit point charge water molecules and that solvated by a continuum. However, the differences are not obvious in Figure 2; therefore, the difference of these two molar rotations has been computed explicitly, and the results are shown in Figure 5.

The periodic "wave" pattern formed by the data in Figure 5 appears to be a somewhat weakened mirror image of the data in Figure 2, as the maxima in Figure 2 coincide with the minima in Figure 5 and vice versa. The rationale for this pattern correlates with the sector rule, and the fact that the location of a perturbing group relative to the carboxylate chromophore affects the optical rotation of the glycine molecule. Here the perturbing entities causing the change in the chiroptical response are not the glycine's NH_3^+ group but the water molecules surrounding it. Due to the nature of the molecular dynamics simulation of a liquid system where the molecules are in close contact, the water molecules occupy the space not taken by the glycine solute. So if the NH_3^+ group happens to occupy a *negative* sector, then the ensemble of water molecules surrounding it will preferentially occupy the *positive* sectors. As such, the use of explicit point charge waters to solvate glycine as opposed to a continuum model has a damping effect on the resulting optical activity.

Proline. The chiral amino acid proline shares the same carboxylate chromophore as its achiral counterpart, glycine. Therefore, one would expect the N−C−C−O dihedral angle

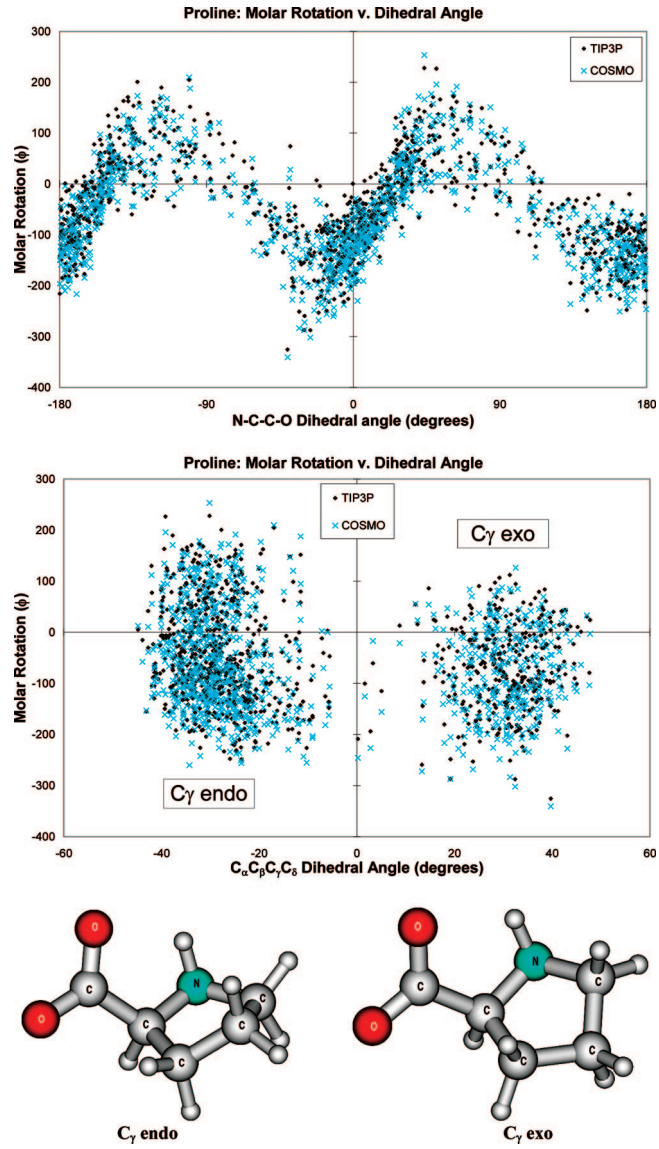

Figure 6. Molar rotation of proline as a function of its N−C−C−O (upper plot) and $C_\alpha-C_\beta-C_\gamma-C_\delta$ (lower plot) dihedral angles, along with illustrations of the proline molecule in its C_γ endo (left structure) and C_γ exo (right structure) conformations. The $C_\alpha-C_\beta-C_\gamma-C_\delta$ dihedral angle is indicative of the envelope conformation of the five-membered ring. If this angle is negative, the molecule is in the C_γ endo conformation; if it is positive, it is C_γ exo.

for this molecule to have a profound effect on its molar rotation as well. As can be seen in Figure 6, this is indeed the case.

The upper plot of Figure 6 has some similarities to the corresponding graph for the glycine molecule. (Note that only 1024 configurations were sampled here compared to 4096 for glycine, since the relative size of the proline molecule required more TDDFT computing time per configuration.) As with glycine, the optimal dihedral angle is close to 0°, which again is in agreement with the geometries optimized by first principles methods. The data also repeat after a period of 180°, owing to the C_{2v} symmetry the carboxylate group possesses in both molecules. Differences can be seen where this periodic wave intercepts zero. In glycine, the molar rotation approaches zero when this dihedral angle approaches

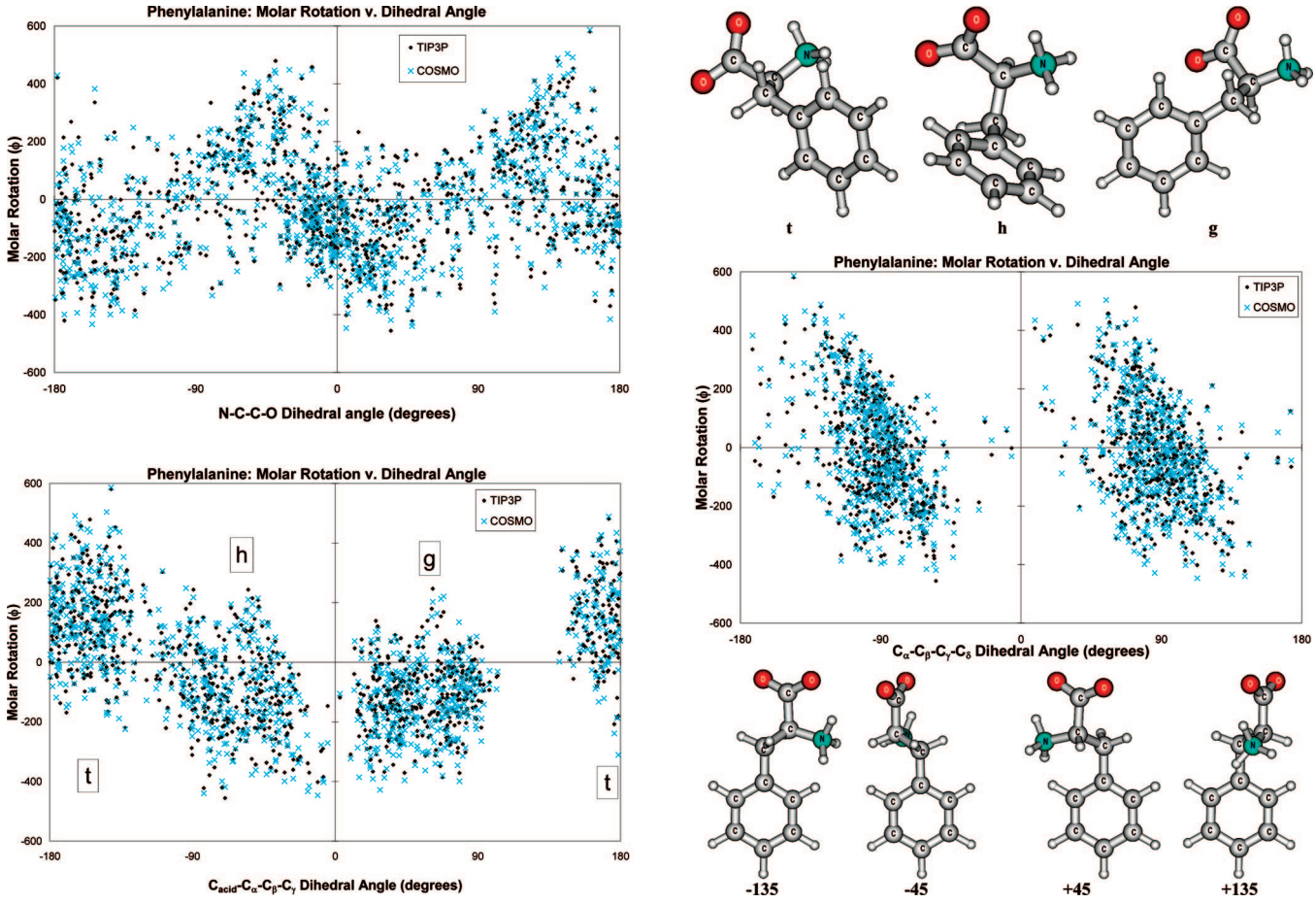

Figure 7. Molar rotation of phenylalanine as a function of its N−C−C−O (top left plot), $C_{acid}-C_\alpha-C_\beta-C_\gamma$ (bottom left plot), and $C_\alpha-C_\beta-C_\gamma-C_\delta$ (right plot) dihedral angles, along with illustrations of phenylalanine in relevant conformations. The $C_{acid}-C_\alpha-C_\beta-C_\gamma$ dihedral defines the molecule as being in a trans (t), gauche (g), or hindered (h) conformation. The $C_\alpha-C_\beta-C_\gamma-C_\delta$ dihedral angle is indicative of how the aromatic ring is twisted with respect to the rest of the molecule.

zero. In proline, this is not the case. Proline, unlike glycine, is inherently chiral in its various conformers. From static DFT calculations[41] and from experimental data, we expect this rotation to be negative. Indeed, the MD average yields about −100 deg·cm^2/(dmol).

It is known both from experiment and prior calculations that the proline molecule tends to form two optimal structures, both significantly populated at room temperature and differing only by the puckering of the ring; see our earlier work and the references cited therein.[41] Prior DFT calculations and some experiments concur that the conformation with the γ carbon in the endo configuration is slightly favored. This more populous conformation has been previously shown to have a molar rotation that is somewhat less negative than its less populous C_γ exo counterpart. The bottom portion of Figure 6 confirms that both the energetic and molar rotation trends seen with frozen isolated proline configurations are reproduced by the molecular dynamics based calculations in this work. In this instance, the C_γ endo conformations, those having a negative $C_\alpha-C_\beta-C_\gamma-C_\delta$ dihedral angle, have a relative "population" of 66% and an average molar rotation of −41.0 with TIP3P waters and −53.9 with COSMO, while the C_γ exo conformers form the balance of the population and have and average molar rotation of −68.1 deg·cm^2/(dmol) with TIP3P waters and −81.6 deg·cm^2/(dmol) with COSMO.

Phenylalanine. The amino acids investigated thus far show a periodic variation of molar rotation as a function of the molecule's N−C−C−O dihedral angle. Phenylalanine, an aromatic amino acid, is no exception in this regard, as can be seen in the top of Figure 7. As phenylalanine has an average molar rotation that is closer to zero than does proline, the "phase" of the wave in its molar rotation plot is more similar to glycine. However, there is significantly more scatter in the molar rotations for phenylalanine than for glycine, or proline for that matter. This is due to a few factors. First, as result of its size and flexibility, phenylalanine has a larger conformational space than glycine or proline. It can be found in three rotamers, differentiated by their $C_{acid}-C_\alpha-C_\beta-C_\gamma$ dihedral angles, which have been shown to differ significantly in their individual specific rotations.[42] Its phenyl functional group is free to flex and bend, moving into different sectors about the carboxylate chromophore even as the N−C−C−O dihedral remains the same, thus causing more variation in molar rotation for a given N−C−C−O dihedral value.

Another factor that may contribute to the scatter seen in the top of Figure 7 is that the phenyl functional group is itself a chromophore that can contribute to the calculated molar rotation. In a prior molecular modeling work[42] this chromophore did not show a significant impact on molar

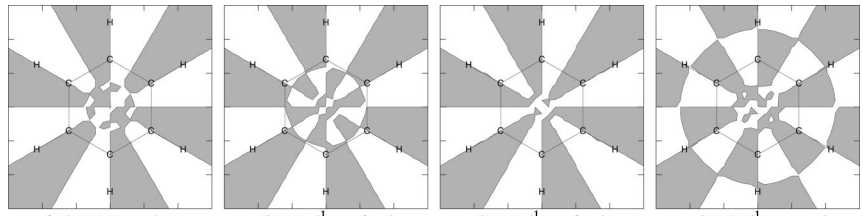

Figure 8. Sign of the molar rotation and CD of the first 3 electronic transitions of benzene as a function of the position of a perturbing group. Positive rotations are indicated by the light areas, while negative rotations are depicted by the dark areas. A point charge of −0.1 was used as a perturber, and the sectors drawn are 1.3 Å above the plane of the ring. A grid size of 0.1 Å was used, and the distortions along the edges of the contour lines (particularly evident in the center of the ring) are caused by the coarseness of the grid. The molar rotation calculations were performed at the PBE0/SVP level of theory, and the CD calculations with CC2/SVP.

rotation, since when held rigid the external perturbations did not perturb the chromophore enough to cause a significant contribution from the electronically forbidden π to π^* transition. But in this study which uses molecular dynamics to generate the geometries, the phenyl ring is free to vibrate, and such distortions (along with asymmetric solvent−solute interactions when explicit waters are used) can promote this otherwise forbidden transition.

The bottom of Figure 7 is an attempt to isolate the effect that the geometry about the phenyl chromophore has on the molar rotation of phenylalanine. As with the carboxylate chromophore, the phenyl group has a local 2-fold axis of symmetry, which is why the left side of the bottom chart is identical to the right side, just as is the case in the top half of the figure. Also, when the $C_\alpha-C_\beta-C_\gamma-C_\delta$ dihedral angle passes through ±90°, when the rest of the phenylalanine molecule is aligned perpendicular to the phenyl ring (in one of its mirror planes), then the molar rotation of the molecule is at a minimum. When this angle deviates from 90°, the molar rotation of the molecule deviates in a positive direction if the change in the dihedral is positive and in a negative direction if the dihedral change is negative. Logically, the opposite effect should be seen as the $C_\alpha-C_\beta-C_\gamma-C_\delta$ dihedral angle passes through 0° or 180°; however, these are energetically disfavored angles, and the molecule is not found in configurations close to this angle often enough to make a determination on the chirality in the vicinity of these energetic maxima.

We expected this variation of optical rotation with the dihedral angle about the phenyl group to be consistent with the historical rationale for chiroptical response caused by the phenyl chromophore: as with the carboxylate chromophore, the space about the phenyl group can be divided into sectors, and the location of the atoms perturbing that space is connected with the sign of the response.[52−54] However the "sectors" that our calculations allude to are of the opposite sign of those illustrated in Smith and co-worker's illustrations of the sector rules in the works cited above. In 2002, with the aid of ab initio methods that the originators of these sector rules did not have the benefit of, Butz and co-workers obtained results similar to ours.[55] This led Butz et al. to set forth a revised sector rule for the benzene chromophore, which is quite similar to the historical model, except with the signs reversed.[56,57] Our results here are consistent with this revised sector rule.

We have earlier demonstrated that an illustration of a sector rule for chiroptical response can be generated by a series of first-principles calculations on the chromophore of interest perturbed by a point charge in varying positions.[43] Here, we illustrate the molar rotation caused by a phenyl chromophore, approximated as a benzene molecule, as it is perturbed by a point charge of −0.1, which has been shown to reasonably approximate the perturbing effects of the remainder of a zwitterionic amino acid molecule. The results are illustrated in Figure 8.

The sectors computed in Figure 8 all exhibit the D_{6h} symmetry of the benzene ring as they must, and as such give us sectors similar to those predicted by Schellman over four decades earlier.[58] One fact is consistent throughout the first three CD transitions shown, corresponding to the ^1L_b, ^1L_a, and half of the ^1B_b excitations:[59] all have the same sign in the region outside of the hydrogen atoms on the benzene ring. As such, in this outer region, where the rest of a phenylalanine molecule is attached, the CD excitations reinforce to give the molar rotation shown on the left of Figure 8. Note these sectors fit with the revised sector rule of Butz et al.,[55] and are precisely the opposite of the historical sector rule cited by Pescitelli et al.[60]

One aspect where our results are similar to those of Pescitelli and co-workers is in the basis set effects on the CD of aromatic compounds. We have found that the addition of diffuse functions to benzene and phenylalanine promotes excitations to diffuse electronic states, some of which occur at lower energies than the first three valence excitations expected from a simple LCAO model. This model has become the de facto standard model for benzene excitations used in textbooks. It has been used by Platt to assign the electronic spectrum of aromatic compounds and is the basis for the benzene sector rule.[59] To create the sector maps of Figure 8 we have used the SVP basis set which yields a collection of electronic excitations and energetic ordering consistent with the LCAO model. Similar results are obtained with the cc-pVDZ basis. Using a diffuse basis (aug-cc-pVDZ, d-aug-cc-pVDZ, etc., or a large set of diffuse s-, p-, d-functions added at the benzene ring center) yielded among the classic b1u, b2u, and e1u transitions several other electronic transitions of differing symmetries. The additional states were obtained both with TDDFT and with an approximate coupled cluster method (CC2). Since the energetic ordering depended on where the perturbing charge was

Table 1. Room Temperature Populations of the Conformers of Proline and Alanine in Solution[a]

proline	C_γ endo	C_γ exo	
molecular dynamics	66.0	34.0	
Boltzmann, DFT optimized	65.5	34.5	
experimentally derived	63	37	
phenylalanine	h	g	t
molecular dynamics	29.4	34.3	36.3
Boltzmann, DFT optimized	21.5	3.1	75.5
experimentally derived	27	24	50

[a] Experimental data are derived from nuclear magnetic resonance measurements and are from the works of Jankowski et al.[61] and Fujiwara et al.[62] for proline and phenylalanine, respectively. The DFT derived Boltzmann populations are from our previous work.[43]

located this situation made it impossible to plot the CD sector maps for the b1u, b2u, and e1u transitions in an automated fashion using a diffuse basis. Fortunately, the sectors for molar rotation, which are affected to varying extents by all CD transitions, remain the same between different basis sets in the "substitution region" outside the carbon ring. While the basis set effects on the ordering of electronic excitations may warrant further investigation, they do not appear to affect conclusions regarding molar rotation aimed at in this work.

Comparison with Experiment

We shall finish this study with a discussion of how the modeling method being presented compares with those previously published, and with experimental data. Glycine is achiral, and its molar rotation should converge to zero over the course of the MD, as has been shown in our preliminary work. Proline and phenylalanine are both chiral molecules that adopt multiple conformations, all of which contribute to the average molar rotation that is observed experimentally. The modeling of the conformational distributions and the ultimate average molar rotations that result are discussed in turn.

The chiroptical properties measured in the laboratory are the result of the interaction of polarized light with molecules in varying conformations. Proline is known to be found in and around two local energetic minima, while phenylalanine has three local minima, illustrated earlier in Figures 6 and 7, respectively. In our earlier works the molecules were optimized to their respective structures, and the populations of the conformers determined by employing their computed relative energies using Boltzmann factors at room temperature. In this work, the "populations" were determined by a molecular dynamics simulation, and are classified on the basis of their dihedral angles. Proline molecules with a negative $C_\alpha-C_\beta-C_\gamma-C_\delta$ dihedral angle were deemed to be of the C_γ endo conformation, and those with a positive angle were C_γ exo. For the phenylalanine molecule, the $C_{acid}-C_\alpha-C_\beta-C_\gamma$ dihedral is the determining factor, with h being $-60°$ (± 60), g being $+60°$ (± 60), and t being 180° (again ± 60). These computed populations, along with experimentally derived data, are summarized in Table 1.

The agreement between dynamically computed populations, statically computed populations, and experimentally derived populations for the proline conformers is excellent. As molar rotation depends in part upon these populations, it is apparent that the conformer distribution should not be a significant source of error for this molecule. In our previous work using static geometries, we found very good agreement between the modeled and measured chiroptical properties of proline.[41] Because the populations of the conformers found by the dynamics simulations in this current work are the same, we thus expect any deviations in the fit of this dynamic model to be caused either by the geometric distortions (vibrations) of the molecular dynamics used to generate the structure, and by the use of a point charge solvation method instead of a continuum.

Table 2. Average Molar Rotation of Proline and Phenylalanine[a]

proline	C_γ endo	C_γ exo		average
molecular dynamics with TIP3P	−41.0	−68.1		−50.1
molecular dynamics with COSMO	−53.9	−81.6		−63.3
DFT optimized static with COSMO	−68.5	−125.5		−101.5
experiment				−99.2
phenylalanine	h	g	t	average
molecular dynamics with TIP3P	−96.2	−109.2	148.2	−11.9
molecular dynamics with COSMO	−93.1	−125.5	149.4	−16.1
DFT optimized static with COSMO	−128.1	124.7	−1.9	−36.8
experiment				−57.0

[a] DFT optimized static data are from our previous work.[43] Experimental data are from Greenstein and Winitz.[63]

The agreement in conformer populations for phenylalanine is not as perfect as it is for proline. One aspect on which dynamic calculations, static calculations, and experimental derivations agree is that the phenylalanine rotamer in which the phenyl ring and carboxylate group are *trans* to each other is the most highly populated. What they do not agree upon is the extent of the dominance of this conformation: our previous work[42] indicated that $^3/_4$ of the molecules should be of this conformation, Fujiwara's experimental data said this population should be closer to $^1/_2$, and the current molecular dynamics puts it at just over $^1/_3$ of the population. The dynamics data indicate a much more even distribution among the conformers than the earlier static computations, which is in somewhat better agreement with experiment. Therefore, we would expect a somewhat better agreement with experiment for the molar rotations modeled in this current work than in previous works. This comparison between the molar rotation from theory and experiment is shown in Table 2.

The molar rotation of proline computed with two optimized geometries and weighted by their Boltzmann factors is in excellent agreement with experiment, differing by only about 2 deg·cm^2/(dmol). When thermal effects are added, by using structures taken from snapshots of the molecular dynamics simulation, this deviation increases to about 36 deg·cm^2/(dmol). When TIP3P waters are substituted for the COMSO continuum, this deviation increases by another 13

deg•cm^2/(dmol). While it is tempting to conclude that the agreement between theory and experiment is clearly worse with the dynamics model and explicit solvation, this is not so clearly the case because of other approximations, most notably those inherent in TDDFT. That is, the supposedly improved solvation treatment may well expose systematic errors in the TDDFT optical rotation computations. The results for phenylalanine are similar. Given the confidence level of time dependent density functional theory, the good agreement between theory and experiment using the static model might be fortuitous, and the data using the dynamics model may be equally as useful. As the field of first principles modeling of optical activity continues to develop, more advanced (and more costly) linear response electronic structure methods such as coupled cluster analyses may become more widely available in computing codes, and more powerful computers should make them practical, but for now TDDFT remains the state of the art method for modeling the optical activity of molecules of this size (and using as many MD configurations as done here).

Conclusions

Molecular dynamics and explicit solvation may be used to generate geometric data suitable for the modeling of molar rotation of conformationally flexible molecules by time dependent density functional theory. The molar rotations of the various conformers of the amino acids studied can be rationalized in terms of the sector rules for the carboxylate and phenyl chromophores. The inclusion of vibrational effects and explicit solvent effects via molecular dynamics both dampened the magnitude of the average molar rotations computed for the molecules studies. The damping effect can also be traced back to the sector rules, this time via a lack of presence of a perturbing group in a given sector. The results highlight the difficulties of obtaining reliable optical rotations for conformationally flexible molecules.

References

(1) Crawford, T. D.; Stephens, P. J. *J. Phys. Chem. A* **2008**, *112*, 1339.

(2) Grimme, S.; Muck-Lichtenfeld, C. *Chirality* **2008**, *20*, 1009.

(3) Pecul, M.; Ruud, K. The ab initio calculation of optical rotation and electronic circular dichroism. In *Advances In Quantum Chemistry*; Elsevier Academic Press Inc: San Diego, 2005; Vol. *50*, p 185.

(4) Stephens, P. J.; McCann, D. M.; Cheeseman, J. R.; Frisch, M. J. *Chirality* **2005**, *17*, S52.

(5) Giorgio, E.; Tanaka, K.; Verotta, L.; Nakanishi, K.; Berova, N.; Rosini, C. *Chirality* **2007**, *19*, 434.

(6) Jansik, B.; Rizzo, A.; Agren, H. *J. Phys. Chem. B* **2007**, *111*, 446.

(7) Tanaka, T.; Kodama, T. S.; Morita, H. E.; Ohno, T. *Chirality* **2006**, *18*, 652.

(8) Kongsted, J.; Pedersen, T. B.; Jensen, L.; Hansen, A. E.; Mikkelsen, K. V. *J. Am. Chem. Soc.* **2006**, *128*, 976.

(9) Autschbach, J. *Comput. Lett.* **2007**, *3*, 131.

(10) Crawford, T. D.; Tam, M. C.; Abrams, M. L. *J. Phys. Chem. A* **2007**, *111*, 12057.

(11) Wiberg, K. B.; Wang, Y. G.; Wilson, S. M.; Vaccaro, P. H.; Jorgensen, W. L.; Crawford, T. D.; Abrams, M. L.; Cheeseman, J. R.; Luderer, M. *J. Phys. Chem. A* **2008**, *112*, 2415.

(12) Kapitan, J.; Baumruk, V.; Kopecky, V.; Bour, P. *J. Phys. Chem. A* **2006**, *110*, 4689.

(13) Tam, M. C.; Crawford, T. D. *J. Phys. Chem. A* **2006**, *110*, 2290.

(14) Carlson, K. L.; Lowe, S. L.; Hoffmann, M. R.; Thomasson, K. A. *J. Phys. Chem. A* **2006**, *110*, 1925.

(15) Mori, T.; Inoue, Y.; Grimme, S. *J. Org. Chem.* **2006**, *71*, 9797.

(16) Marchesan, D.; Coriani, S.; Forzato, C.; Nitti, P.; Pitacco, G.; Ruud, K. *J. Phys. Chem. A* **2005**, *109*, 1449.

(17) da Silva, C. O.; Mennucci, B.; Vreven, T. *J. Org. Chem.* **2004**, *69*, 8161.

(18) Voloshina, E.; Raabe, G.; Estermeier, M.; Steffan, B.; Fleischhauer, J. *Int. J. Quantum Chem.* **2004**, *100*, 1104.

(19) Kondru, R. K.; Wipf, P.; Beratan, D. N. *J. Phys. Chem. A* **1999**, *103*, 6603.

(20) Kundrat, M. D.; Autschbach, J. *J. Chem. Theory Comput.* **2008**, *4*, 1902.

(21) Mort, B. C.; Autschbach, J. *J. Phys. Chem. A* **2005**, *109*, 8617.

(22) Mort, B. C.; Autschbach, J. *J. Phys. Chem. A* **2006**, *110*, 11381.

(23) Mort, B. C.; Autschbach, J. *ChemPhysChem* **2007**, *8*, 605.

(24) Mort, B. C.; Autschbach, J. *ChemPhysChem* **2008**, *9*, 159.

(25) Wilson, S. M.; Wiberg, K. B.; Murphy, M. J.; Vaccaro, P. H. *Chirality* **2008**, *20*, 357.

(26) Crawford, T. D.; Tam, M. C.; Abrams, M. L. *Mol. Phys.* **2007**, *105*, 2607.

(27) Kongsted, J.; Pedersen, T. B.; Strange, M.; Osted, A.; Hansen, A. E.; Mikkelsen, K. V.; Pawlowski, F.; Jorgensen, P.; Hattig, C. *Chem. Phys. Lett.* **2005**, *401*, 385.

(28) Pecul, M.; Marchesan, D.; Ruud, K.; Coriani, S. *J. Chem. Phys.* **2005**, 122.

(29) Kongsted, J.; Pedersen, T. B.; Osted, A.; Hansen, A. E.; Mikkelsen, K. V.; Christiansen, O. *J. Phys. Chem. A* **2004**, *108*, 3632.

(30) Kongsted, J.; Ruud, K. *Chem. Phys. Lett.* **2008**, *451*, 226.

(31) Neugebauer, J. *Angew. Chem., Int. Ed.* **2007**, *46*, 7738.

(32) Mukhopadhyay, P.; Zuber, G.; Wipf, P.; Beratan, D. N. *Angew. Chem., Int. Ed.* **2007**, *46*, 6450.

(33) Mukhopadhyay, P.; Zuber, G.; Goldsmith, M. R.; Wipf, P.; Beratan, D. N. *ChemPhysChem* **2006**, *7*, 2483.

(34) Jensen, L.; Swart, M.; Van Duijnen, P. T.; Autschbach, J. *Int. J. Quantum Chem.* **2006**, *106*, 2479.

(35) Wilson, S. M.; Wiberg, K. B.; Cheeseman, J. R.; Frisch, M. J.; Vaccaro, P. H. *J. Phys. Chem. A* **2005**, *109*, 11752.

(36) Mennucci, B.; Tomasi, J.; Cammi, R.; Cheeseman, J. R.; Frisch, M. J.; Devlin, F. J.; Gabriel, S.; Stephens, P. J. *J. Phys. Chem. A* **2002**, *106*, 6102.

(37) Coriani, S.; Baranowska, A.; Ferrighi, L.; Forzato, C.; Marchesan, D.; Nitti, P.; Pitacco, G.; Rizzo, A.; Ruud, K. *Chirality* **2006**, *18*, 357.

(38) Pecul, M.; Larnparska, E.; Cappelli, C.; Frediani, L.; Ruud, K. *J. Phys. Chem. A* **2006**, *110*, 2807.

(39) Rossi, S.; Lo Nostro, P.; Lagi, M.; Ninham, B. W.; Baglioni, P. *J. Phys. Chem. B* **2007**, *111*, 10510.

(40) Lo Nostro, P.; Ninham, B. W.; Milani, S.; Fratoni, L.; Baglioni, P. *Biopolymers* **2006**, *81*, 136.

(41) Kundrat, M. D.; Autschbach, J. *J. Phys. Chem. A* **2006**, *110*, 4115.

(42) Kundrat, M. D.; Autschbach, J. *J. Phys. Chem. A* **2006**, *110*, 12908.

(43) Kundrat, M. D.; Autschbach, J. *J. Am. Chem. Soc.* **2008**, *130*, 4404.

(44) Ahlrichs, R.; Bar, M.; Haser, M.; Horn, H.; Kolmel, C. *Chem. Phys. Lett.* **1989**, *162*, 165.

(45) Woon, D. E.; Dunning, T. H. *J. Chem. Phys.* **1994**, *100*, 2975.

(46) Schafer, A.; Klamt, A.; Sattel, D.; Lohrenz, J. C. W.; Eckert, F. *Phys. Chem. Chem. Phys.* **2000**, *2*, 2187.

(47) Lindahl, E.; Hess, B.; van der Spoel, D. *J. Mol. Model.* **2001**, *7*, 306.

(48) Jorgensen, W. L.; Maxwell, D. S.; TiradoRives, J. *J. Am. Chem. Soc.* **1996**, *118*, 11225.

(49) Wiberg, K. B.; Wang, Y. G.; Vaccaro, P. H.; Cheeseman, J. R.; Luderer, M. R. *J. Phys. Chem. A* **2005**, *109*, 3405.

(50) Pecul, M.; Ruud, K.; Rizzo, A.; Helgaker, T. *J. Phys. Chem. A* **2004**, *108*, 4269.

(51) Jorgensen, E. C. *Tetrahedron Lett.* **1971**, *13*, 863.

(52) Smith, H. E.; Fontana, L. P. *J. Org. Chem.* **1991**, *56*, 432.

(53) Smith, H. E.; Neergaard, J. R. *J. Am. Chem. Soc.* **1997**, *119*, 116.

(54) Smith, H. E. *Chem. Rev.* **1998**, *98*, 1709.

(55) Butz, P.; Tranter, G. E.; Simons, J. P. *PhysChemComm* **2002**, 91.

(56) Macleod, N. A.; Butz, P.; Simons, J. P.; Grant, G. H.; Baker, C. M.; Tranter, G. E. *Isr. J. Chem* **2004**, *44*, 27.

(57) Macleod, N. A.; Butz, P.; Simons, J. P.; Grant, G. H.; Baker, C. M.; Tranter, G. E. *Phys. Chem. Chem. Phys.* **2005**, *7*, 1432.

(58) Schellman, J. A. *J. Chem. Phys.* **1966**, *44*, 55.

(59) Platt, J. R. *J. Chem. Phys.* **1949**, *17*, 484.

(60) Pescitelli, G.; Di Bari, L.; Caporusso, A. M.; Salvadori, P. *Chirality* **2008**, *20*, 393.

(61) Jankowski, K.; Soler, F.; Ellenberger, M. *J. Mol. Struct.* **1978**, *48*, 63.

(62) Fujiwara, S.; Ishizuka, H.; Fudano, S. *Chem. Lett.* **1974**, *11*, 1281.

(63) Greenstein, J. P.; Winitz, M. *Chemistry of the Amino Acids*; John Wiley & Sons: New York, 1961.

CT8005216

JCTC Journal of Chemical Theory and Computation

Investigation of the Ligand-Field States of the Hexaammine Cobalt(III) Ion with Quantum Chemical Methods

François P. Rotzinger*

Institut des Sciences et Ingénierie Chimiques (ISIC), Ecole Polytechnique Fédérale de Lausanne (EPFL), Station 6, CH-1015 Lausanne, Switzerland

Received January 27, 2009

Abstract: The ligand-field (LF) transition energies of the $Co(NH_3)_6^{3+}$ ion have been computed with multiconfiguration quasidegenerate second-order perturbation theory (MCQDPT2). The water solvent was treated with the polarizable continuum model (PCM), and the environment in crystals was modeled by the $Co(NH_3)_6 \cdot Cl_4^-$ complex. The Co−N bond lengths, calculated for the hydrated cation and the $Co(NH_3)_6 \cdot Cl_4^-$ model compound, agree with those in the crystal structures. The vertical transition energies agree with experiment, whereby those based on $Co(NH_3)_6 \cdot Cl_4^-$ are more accurate than those for the hydrated ion. The 0−0 transitions were based on the OPBE geometries of ground and excited $^1T_{1g}$, $^3T_{1g}$, $^5T_{2g}$ states of the hydrated ion. The $^3T_{1g}$ state is the lowest excited state; the $^5T_{2g}$ state lies higher by >0.6 eV.

Introduction

For the understanding of the photochemical reactivity of hexaammine cobalt(III) complexes, it is desirable to know which excited state is lowest, the $^3T_{1g}$ or the $^5T_{2g}$ ligand-field (LF) state. Their geometries and, therefore, also their reactivities differ. In a low-temperature (8 K) electron spectroscopic study of the hexaammine cobalt(III) ion, the 0−0 transition energies to the lowest singlet ($^1T_{1g}$) and triplet ($^3T_{1g}$) LF states were determined.[1] The spectroscopically unmeasurable quintet state ($^5T_{2g}$) was proposed to lie below or at the same energy as the $^3T_{1g}$ state.[1] Later, in a theoretical treatment of the electron self-exchange reaction of the $Co(NH_3)_6^{2+/3+}$ couple, the energy of the relaxed $^5T_{2g}$ state was found to be higher than those of the $^1T_{1g}$ and $^3T_{1g}$ states according to ZINDO calculations.[2] On the basis of the excited state dynamics of three cobalt(III) complexes with chelating ligands, the $^5T_{2g}$ state was suggested to be the lowest LF state.[3]

Experimental LF transition energies of $Co(NH_3)_6^{3+}$ were measured in aqueous solution[4] and in the solid state,[1] in which the cation is surrounded by water or anions. In this study, the vertical and the 0−0 LF transition energies were investigated with quantum chemical methods by taking into account environmental effects.

* To whom correspondence should be addressed. E-mail: francois.rotzinger@epfl.ch.

Computational Details

The calculations were performed using the GAMESS[5,6] programs. For cobalt, the relativistic effective core potential (ECP) basis set of Stevens et al. (SBKJ)[7] was used. For chlorine, the ECP basis set of Stevens et al.[8] supplemented with a polarization function ($\alpha_d = 0.65$[9]) was taken. For N and H, the 6-31G(d) basis set[10,11] was used ($\alpha_d = 1.00$[9]). Some calculations were performed with tripleζ + polarization basis sets, 6-311G(d) for N and H,[12] and the outermost s and p functions of the SBKJ basis set were uncontracted (SBKJu). Figures 1 and 2 were generated with MacMolPlt.[13]

Hydration was treated using the polarizable continuum model (PCM).[14,15] The cavity was constructed based on the van der Waals radii of the atoms, whereby for cobalt, a value of 2.20 Å was taken. Because of the high charge of $Co(NH_3)_6^{3+}$, a finer tesselation than the default had to be used (NTSALL = 960, the default is 60; in PCM, each atom is represented by a sphere, which is approximated by NTSALL triangles). The DFT calculations were performed with a grid finer (NTHE = 24 and NPHI = 48) than the default (NTHE = 12 and NPHI = 24). The active space for the multiconfiguration quasidegenerate second-order pertur-

10.1021/ct900048r CCC: $40.75
Published on Web 03/26/2009

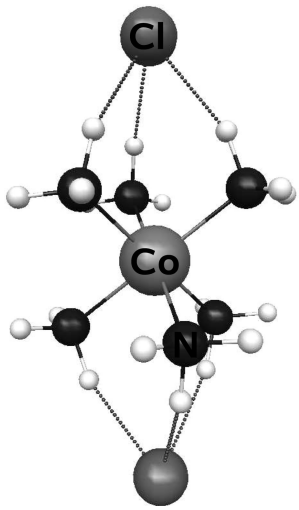

Figure 1. Perspective view of the $Co(NH_3)_6 \cdot Cl_2^+$ ion (MP2 geometry).

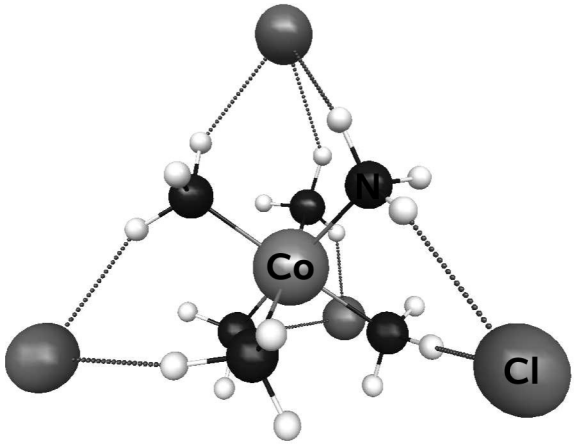

Figure 2. Perspective view of the $Co(NH_3)_6 \cdot Cl_4^-$ ion (OPBE geometry).

bation (MCQDPT2)[16,17] computations was determined via configuration interaction (CI) singles-doubles calculations.[18] A 10 electrons in 10 orbitals (10/10) active space was used for most MCQDPT2 calculations, whereby for each degenerate state, a state-averaged complete active space self-consistent field (CAS-SCF) calculation was performed. Since the symmetries of $Co(NH_3)_6^{3+}$, $Co(NH_3)_6 \cdot Cl_2^+$, and $Co(NH_3)_6 \cdot Cl_4^-$ are lower than O_h, the triply degenerate states split into an A and an E state. The CAS-SCF and the MCQDPT2 calculations were performed by averaging over the A and E states corresponding to the T state of interest. Hydration at the MCQDPT2 level was computed as described elsewhere.[19] Unless noted otherwise, only the 1s MOs of N were treated as frozen cores. Spin−orbit coupling was computed on the basis of the corresponding CAS-SCF wave function via spin−orbit CI with the full Breit−Pauli Hamiltonian including a partial two electron operator.[20−22] Interactions of each state with the others exhibiting the same symmetry and spin or a spin differing by ±1 were taken into account.

The geometry optimizations of the excited states $^1T_{1g}$, $^3T_{2g}$, and $^5T_{2g}$ with PCM hydration were performed at the spin unrestricted level (without spin projection). To achieve SCF convergence, orbital interchanges were restricted (restrct =.t. option in $scf), and level shifting or damping of the Fock matrix was applied (shift =.t. or damp =.t. option). The atomic coordinates of the $^1A_{1g}$, $^1T_{1g}$, $^3T_{2g}$, and $^5T_{2g}$ states of $Co(NH_3)_6^{3+}$ are given in Tables S1−S4 (Supporting Information), and those of $Co(NH_3)_6 \cdot Cl_4^-$ in its ground state are reported in Table S5 (Supporting Information).

Table 1. Co−N Bond Lengths from X-ray Crystal Structures

compound	*d*(Co−N), Å	reference
$[Co(NH_3)_6]_2[Ni(CN)_4]_3 \cdot 2H_2O$	1.964	23
$[Co(NH_3)_6][Co(CN)_6]$	1.97	24
$[Co(NH_3)_6]I_3$	1.96 ± 0.02	25
$[Co(NH_3)_6][ZnCl_4]Cl$	1.967	26
$[Co(NH_3)_6][FeCl_6]$	1.965	27
$[Co(NH_3)_6][SbCl_6]$	1.983	28
$[Co(NH_3)_6][Sb_2F_9]$	1.990 ± 0.005	29
$[Co(NH_3)_6][BrO_3]_3 \cdot {}^1/_2H_2O$	1.959	30
$[Co(NH_3)_6]Cl_2[BF_4]$	1.955	31
$[Co(NH_3)_6]Cl[SiF_6] \cdot 2H_2O$	1.965 ± 0.002	32

Results

Ground State Geometry of $Co(NH_3)_6^{3+}$. The Co−N bond lengths in the crystal structures, reported in Table 1, lie in the range of 1.96 −1.97 Å. The diversity of the anions in the crystals gives rise to different hydrogen bonds with the ammonia ligands. This is the reason why the Co−N bond lengths of the various compounds vary somewhat. Through these H bonds charge is donated to the cation. This strengthens the Co−N bonds compared with the free $Co(NH_3)_6^{3+}$ ion (in the gas phase). The quantum chemically determined Co−N bond lengths in free $Co(NH_3)_6^{3+}$, exhibiting D_3 symmetry, are summarized in Table 2. The Co−N bond lengths vary slightly upon improvement of the basis set from doubleζ + polarization to tripleζ + polarization. The Hartree−Fock (HF) method, neglecting electron correlation, produces too long Co−N bonds whereas MP2, neglecting static electron correlation, yields too short Co−N bonds. With CAS-SCF, neglecting dynamic electron correlation, too long Co−N bonds are obtained. The most accurate Co−N bonds are computed with MCQDPT2(10/10) which takes into account static and dynamic electron correlation. In the MCQDPT2(4/4) calculation with a smaller active space, a part of the static correlation is neglected, which leads to too short Co−N bonds as with MP2. The widely applied BLYP[33−35] and B3LYP[36−38] functionals gave rise to too long Co−N bonds. The PBE[39,40] and PBE0[41] functionals are superior. The OPBE[39,40,42] and OLYP[42] functionals exhibit the OPTX[42] exchange, which is superior to other exchange functionals.[43] OLYP yielded too long Co−N bonds. The best geometries with respect to MCQDPT2(10/10) were obtained with PBE0 and OPBE. For the $Co(NH_3)_6^{3+}$ complexes, these two functionals were assumed to provide the most accurate geometries.

The LF spectrum of the free $Co(NH_3)_6^{3+}$ ion (in the gas phase) is unknown. For comparison with the vis spectra in the solid state,[1] the environment of the cation was modeled by adding two or four chloride ions in the second coordination sphere. $Co(NH_3)_6 \cdot Cl_2^+$ (Table 2ii) exhibits

Table 2. Bond Lengths in $Co(NH_3)_6^{3+}$, $Co(NH_3)_6 \cdot Cl_2^{+}$, and $Co(NH_3)_6 \cdot Cl_4^{-}$ Computed with Various Methods and Basis Sets

method	basis set	d(Co−N), Å	d(N−H), Å
	(i) $Co(NH_3)_6^{3+}$, D_3 Symmetry		
HF	SBKJ/6-31G(d)	2.045	1.010
HF	SBKJ/6-311G(d)	2.042	1.006−1.007
HF	SBKJu/6-311G(d)	2.041	1.006−1.007
MP2[a]	SBKJ/6-31G(d)	1.986	1.025
MP2[b]	SBKJ/6-31G(d)	1.974	1.025−1.026
MP2[a]	SBKJ/6-311G(d)	1.981	1.021
MP2[b]	SBKJ/6-311G(d)	1.966	1.021
CAS-SCF(10/10)	SBKJ/6-31G(d)	2.034	1.009
CAS-SCF(10/7)	SBKJ/6-31G(d)	2.052	1.009−1.010
CAS-SCF(4/4)	SBKJ/6-31G(d)	2.047	1.009
MRMP2(10/10)[b]	SBKJ/6-31G(d)	2.014	1.027
MRMP2(4/4)[b]	SBKJ/6-31G(d)	1.997	1.025−1.026
BLYP	SBKJ/6-31G(d)	2.060	1.034−1.035
B3LYP	SBKJ/6-31G(d)	2.033	1.026
PBE	SBKJ/6-31G(d)	2.028	1.034
PBE0	SBKJ/6-31G(d)	2.006	1.024
OPBE	SBKJ/6-31G(d)	2.021	1.026
OLYP	SBKJ/6-31G(d)	2.052	1.027−1.028
	(ii) $Co(NH_3)_6 \cdot Cl_2^{+}$, D_{3d} Symmetry		
HF	SBKJ/6-31G(d)	2.018	1.005−1.025
MP2[a]	SBKJ/6-31G(d)	1.957	1.020−1.048
BLYP	SBKJ/6-31G(d)	2.027	1.029−1.068
B3LYP	SBKJ/6-31G(d)	2.003	1.021−1.056
PBE0	SBKJ/6-31G(d)	1.974	1.019−1.056
OPBE	SBKJ/6-31G(d)	1.980	1.021−1.065
	(iii) $Co(NH_3)_6 \cdot Cl_4^{-}$, C_3 Symmetry		
HF	SBKJ/6-31G(d)	2.007,[c] 2.002[c]	1.003−1.015
MP2[a]	SBKJ/6-31G(d)	1.947,[c] 1.938[c]	1.018−1.034
MP2[b]	SBKJ/6-31G(d)	1.936,[c] 1.927[c]	1.018−1.034
CAS-SCF(10/10)	SBKJ/6-31G(d)	1.996,[c] 1.989[c]	1.003−1.014
BLYP	SBKJ/6-31G(d)	2.011,[c] 2.003[c]	1.028−1.048
B3LYP	SBKJ/6-31G(d)	1.991,[c] 1.983[c]	1.019−1.036
PBE	SBKJ/6-31G(d)	1.982,[c] 1.975[c]	1.027−1.048
PBE0	SBKJ/6-31G(d)	1.965,[c] 1.958[c]	1.018−1.040
OPBE	SBKJ/6-31G(d)	1.969,[c] 1.962[c]	1.020−1.049
	(iv) $Co(NH_3)_6^{3+}$ in Aqueous Solution[d]		
HF	SBKJ/6-31G(d)	1.998	1.005
PBE	SBKJ/6-31G(d)	1.976	1.029
PBE0	SBKJ/6-31G(d)	1.960	1.019−1.020
OPBE	SBKJ/6-31G(d)	1.967	1.021−1.022
OLYP	SBKJ/6-31G(d)	1.992	1.022−1.023

[a] The 1s levels of N and the 3s/p levels of Co were treated as frozen cores. [b] The 1s levels of N were treated as frozen cores. [c] 3 symmetry equivalent bonds. [d] Hydration modeled using the polarizable continuum model (PCM).

D_{3d} symmetry and is strongly anisotropic (Figure 1). The two added anions give rise to a reduction of the Co−N bonds by 0.03−0.04 Å. The most accurate Co−N bonds (PBE0 and OPBE data) are still too long by ∼0.02 Å compared with the crystal structure data. In the $Co(NH_3)_6 \cdot Cl_4^{-}$ model compound with C_3 symmetry (Table 2iii), the chloride ions form approximately a tetrahedron surrounding the $Co(NH_3)_6^{3+}$ pseudo-octahedron (Figure 2). This model complex is less anisotropic than $Co(NH_3)_6 \cdot Cl_2^{+}$. In $Co(NH_3)_6 \cdot Cl_4^{-}$, the Co−N bond lengths computed with PBE0 and OPBE agree with those of the crystal structures, and therefore this model complex can be considered as acceptable for crystals containing the $Co(NH_3)_6^{3+}$ ion.

In aqueous solution, modeled by the polarizable continuum model (PCM), the Co−N bonds (PBE0 and OPBE data) are as in the $Co(NH_3)_6 \cdot Cl_4^{-}$ model compound (Table 2iv). At least as the geometries are concerned, the water solvent exerts a similar effect on the $Co(NH_3)_6^{3+}$ ion as the lattice anions in the crystals.

Vertical Transitions. The vertical transition energies were computed based on various ground state geometries to probe their sensitivity to the Co−N bond lengths and the environment of the cation (Table 3). At the HF geometry of the free ion, yielding by ∼0.08 Å too long Co−N bonds, the LF transition energies are too low because of the too small crystal-field splitting parameter (Δ). For Co−N bonds fixed at the experimental value, the first singlet−singlet and singlet−triplet transitions, $^1T_{1g} \leftarrow {}^1A_{1g}$ and $^3T_{1g} \leftarrow {}^1A_{1g}$, agree with experiment,[1] but the second transitions, $^1T_{2g} \leftarrow {}^1A_{1g}$ and $^3T_{2g} \leftarrow {}^1A_{1g}$, are underestimated by ∼0.2 eV, and the singlet-quintet $^5T_{2g} \leftarrow {}^1A_{1g}$ transition energy is too low by ∼0.3 eV. Hydration, modeled with PCM, causes a small reduction (∼0.02 eV) of the transition energies. The augmentation of the basis set (from doubleζ + polarization to tripleζ + polarization) yields somewhat lower transition energies. The data based on the MP2 geometry is slightly worse because of the longer Co−N bonds (compared with experiment).

The transition energies based on the HF geometry of $Co(NH_3)_6 \cdot Cl_2^{+}$ are also too low (Table 3iii). The agreement with experiment is better for the more accurate MP2 geometry. For the best geometry (OPBE) based on the best model ($Co(NH_3)_6 \cdot Cl_4^{-}$), the $^1T_{2g} \leftarrow {}^1A_{1g}$, $^3T_{1g} \leftarrow {}^1A_{1g}$, and $^3T_{2g} \leftarrow {}^1A_{1g}$ transition energies agree with experiment, but the $^1T_{1g} \leftarrow {}^1A_{1g}$ energy is overestimated by 0.26 eV (Table 3iv).

The transition energies reported in Table 3 correspond to averages of A and E states because the symmetries of $Co(NH_3)_6^{3+}$, $Co(NH_3)_6 \cdot Cl_2^{+}$, and $Co(NH_3)_6 \cdot Cl_4^{-}$ are lower than O_h (Table 4). A reduction of the symmetry from O_h to D_3 (or D_{3h}) causes a splitting of the T_{1g} and T_{2g} states into $A_2 + E$ (or $A_{2g} + E_g$) and $A_1 + E$ (or $A_{1g} + E_g$) states, respectively. In C_3 symmetry both terms, T_{1g} and T_{2g}, split into A + E. In the $Co(NH_3)_6^{3+}$ ion, the $A_{1/2}$−E splittings are small (0.01 eV), unlike in $Co(NH_3)_6 \cdot Cl_2^{+}$, where the two anions are located in axial positions (Figure 1). This anisotropy causes the larger $A_{1/2}$−E splittings. In contrast to $Co(NH_3)_6^{3+}$, where the $A_{1/2}$ states exhibit slightly lower energies than their corresponding E states, the $A_{1/2}$ energies are higher for $Co(NH_3)_6 \cdot Cl_2^{+}$. Because of the large $A_{1g}-E_g$ splitting of the $^5T_{2g}$ state, $Co(NH_3)_6 \cdot Cl_2^{+}$ is a poor model which is not considered further. The splittings of the singlet and triplet states in $Co(NH_3)_6 \cdot Cl_4^{-}$ are comparable to those of $Co(NH_3)_6 \cdot Cl_2^{+}$, but for $^5T_{2g}$, the A−E splitting is small.

In Table 5 are summarized the vertical transition energies of $Co(NH_3)_6^{3+}$ in the idealized O_h symmetry as well as in the effective D_3 symmetry (Computational Details). Spitting due to spin−orbit (SO) coupling, treated in the D_3* double group, is small (Table 5). The corresponding data for $Co(NH_3)_6 \cdot Cl_4^{-}$ is given in Table 6; the splittings due to spin−orbit coupling are as for $Co(NH_3)_6^{3+}$ but, as already mentioned, the transition energies are higher and more accurate (Table 3). On the basis of the $Co(NH_3)_6^{3+}$ and $Co(NH_3)_6 \cdot Cl_4^{-}$ models, the $^5T_{2g}$ energy is higher than those of the triplet states and lower than those of the singlets.

Table 3. Vertical Ligand-Field Transition Energies[a] of $Co(NH_3)_6^{3+}$

geometry	basis set	$^1T_{1g} \leftarrow {}^1A_{1g}$	$^1T_{2g} \leftarrow {}^1A_{1g}$	$^3T_{1g} \leftarrow {}^1A_{1g}$	$^3T_{2g} \leftarrow {}^1A_{1g}$	$^5T_{2g} \leftarrow {}^1A_{1g}$
		(i) Experimental Data[b]				
		2.60	3.66	1.61	2.14[c]	
		(ii) $Co(NH_3)_6^{3+}$, D_3 Symmetry				
HF	SBKJ/6-31G(d)	2.21	2.96	0.85	1.36	1.21
HF[d]	SBKJ/6-31G(d)	2.66, 2.63[e]	3.48, 3.45[e]	1.36, 1.34[e]	1.93, 1.90[e]	2.14, 2.12[e]
HF[d]	SBKJ/6-311G(d)	2.64	3.45	1.35	1.90	2.10
HF[d]	SBKJu/6-311G(d)	2.59	3.37	1.31	1.86	2.09
MP2[f]	SBKJ/6-31G(d)	2.51	3.31	1.21	1.75	1.86
MP2[f]	SBKJ/6-311G(d)	2.53	3.32	1.22	1.76	1.88
		(iii) $Co(NH_3)_6 \cdot Cl_2^+$, D_{3d} Symmetry				
HF	SBKJ/6-31G(d)	2.46	3.19	1.13	1.62	1.68
MP2[f]	SBKJ/6-31G(d)	2.80	3.58	1.51	2.04	2.32
		(iv) $Co(NH_3)_6 \cdot Cl_4^-$, C_3 Symmetry				
OPBE	SBKJ/6-31G(d)	2.86	3.60	1.57	2.07	2.46

[a] Units: eV. [b] Reference 4. [c] Calculated[44] according to Tanabe and Sugano.[45] [d] d(Co−N) fixed at 1.96 Å. [e] With PCM hydration. [f] The 1s levels of N and the 3s/p levels of Co were treated as frozen cores.

Table 4. A_1-E and A_2-E or $A-E$ Splittings[a] of the T_{2g} and T_{1g} States

geometry	basis set	$^1T_{1g}$	$^1T_{2g}$	$^3T_{1g}$	$^3T_{2g}$	$^5T_{2g}$
		(i) $Co(NH_3)_6^{3+}$, D_3 Symmetry				
HF	SBKJ/6-31G(d)	4.18	8.95	1.88	6.39	3.11
HF[b]	SBKJ/6-31G(d)	4.33, 4.54[c]	11.3, 11.3[c]	2.50, 2.58[c]	8.08, 8.18[c]	4.63, 5.39[c]
HF[b]	SBKJ/6-311G(d)	4.49	10.2	2.34	8.00	5.82
HF[b]	SBKJu/6-311G(d)	4.49	9.25	2.78	8.14	5.82
MP2[d]	SBKJ/6-31G(d)	4.14	8.41	3.10	6.69	6.01
MP2[d]	SBKJ/6-311G(d)	4.41	8.76	3.21	7.07	6.34
		(ii) $Co(NH_3)_6 \cdot Cl_2^+$, D_{3d} Symmetry				
HF	SBKJ/6-31G(d)	36.2	36.5	29.5	41.1	92.1
MP2[d]	SBKJ/6-31G(d)	55.3	44.5	42.7	50.9	270
		(iii) $Co(NH_3)_6 \cdot Cl_4^-$, C_3 Symmetry				
OPBE	SBKJ/6-31G(d)	14.7	55.7	46.3	38.4	4.7

[a] Units: meV. [b] (Co−N) fixed at 1.96 Å. [c] With PCM hydration. [d] The 1s levels of N and the 3s/p levels of Co were treated as frozen cores.

TDDFT based on the BLYP and B3LYP functionals overestimates the (vertical) LF transitions energies (Table S6).

0−0 Transitions. Their computation requires optimized excited state geometries. Because of the Jahn−Teller theorem, the degeneracy is removed and hence these geometries were computed with the OPBE functional and PCM hydration (OPBE-PCM), since this method reproduced the Co−N bond lengths of the $Co(NH_3)_6^{3+}$ ion in the crystal structures (Tables 1 and 2iv). All of these PCM computations had to be performed in C_1 symmetry. Attempts to optimize the geometries of the excited states of the $Co(NH_3)_6 \cdot Cl_4^-$ model compound were unsuccessful. The computed Co−N bond lengths of the ground state and the excited $^1T_{1g}$, $^3T_{1g}$, and $^5T_{2g}$ states are reported in Table 7. In the $^1T_{1g}$ and $^3T_{1g}$ states, the spatial MO occupations are virtually equal, and this is the reason why their geometries differ only marginally. In agreement with Wilson and Solomon's study,[1] these two states exhibit a compressed octahedral structure with a computed shortening of the axial bonds of 0.010 and 0.014 Å for the $^3T_{1g}$ and $^1T_{1g}$ states, respectively, and an elongation of the equatorial bonds of ∼0.15 Å. This data agrees well with the spectroscopically determined[1] values of ∼0.02 (compression) and ∼0.12 Å (elongation). The geometry of the $^5T_{2g}$ state is almost octahedral. In this state, the Co−N bond lengths are elongated by ∼0.17 Å with respect to those

Table 5. Computed Vertical Ligand-Field Transition Energies[a] of $Co(NH_3)_6^{3+}$ Including Spin-Orbit Coupling

O_h	D_3	D_3^*
0.0000 ($^1A_{1g}$)	0.0000 ($^1A_1$)	0.0000 (A_1)
1.36 ($^3T_{1g}$)	1.3608 (^3E)	1.4118 (A_1)
	1.3583 ($^3A_2$)	1.3819 (A_2)
		1.3797 (E)
		1.3402 (E)
		1.3388 (E)
		1.3387 (A_1)
1.93 ($^3T_{2g}$)	1.9327 (^3E)	1.9880 (A_2)
	1.9246 ($^3A_1$)	1.9783 (A_1)
		1.9755 (E)
		1.9531 (E)
		1.9497 (E)
		1.9480 (A_2)
2.14 ($^5T_{2g}$)	2.1415 (^5E)	2.2009 (A_1)
	2.1369 ($^5A_1$)	2.1961 (A_2)
		2.1942 (E)
		2.1897 (A_1)
		2.1895 (E)
		2.1269 (E)
		2.1231 (A_2)
		2.1220 (E)
		2.0934 (E)
		2.0933 (A_1)
2.66 ($^1T_{1g}$)	2.6614 (^1E)	2.6756 (E)
	2.6571 ($^1A_2$)	2.6728 (A_2)
3.48 ($^1T_{2g}$)	3.4838 (^1E)	3.4948 (E)
	3.4725 ($^1A_1$)	3.4830 (A_1)

[a] Units: eV; HF/SBKJ/6-31G(d) geometry with C−N bond lengths of 1.96 Å.

Table 6. Computed Vertical Ligand-Field Transition Energies[a] of $Co(NH_3)_6 \cdot Cl_4^-$ Including Spin-Orbit Coupling

O_h	C_3	C_3*
0.00 ($^1A_{1g}$)	0.0000 (^1A)	0.0000 (A)
1.57 ($^3T_{1g}$)	1.5869 (^3E)	1.6004 (A)
	1.5406 (^3A)	1.5736 (A)
		1.5665 (E)
		1.5292 (E)
		1.5252 (E)
		1.5246 (A)
2.07 ($^3T_{2g}$)	2.0795 (^3E)	2.1267 (A)
	2.0411 (^3A)	2.1194 (E)
		2.0988 (E)
		2.0983 (A)
		2.0008 (E)
		1.9955 (A)
2.46 ($^5T_{2g}$)	2.4643 (^5E)	2.5207 (A)
	2.4596 (^5A)	2.5166 (A)
		2.5141 (E)
		2.5101 (A)
		2.5098 (E)
		2.4466 (E)
		2.4423 (E)
		2.4402 (A)
		2.4142 (A)
		2.4134 (E)
2.86 ($^1T_{1g}$)	2.8669 (^1E)	2.8762 (E)
	2.8522 (^1A)	2.8678 (A)
3.60 ($^1T_{2g}$)	3.6193 (^1E)	3.6381 (E)
	3.5637 (^1A)	3.5740 (A_1)

[a] Units: eV.

Table 7. Co−N Bond Lengths in the $^1A_{1g}$, $^1T_{1g}$, $^3T_{1g}$, and $^5T_{2g}$ States of $Co(NH_3)_6^{3+}$

state	d(Co−N), Å	remarks
$^1A_{1g}$	1.967[a]	D_3 symmetry, (pseudo)octahedron
$^1T_{1g}$	1.953, 1.953, 2.098, 2.098, 2.123, 2.128	compressed (pseudo)octahedron
$^3T_{1g}$	1.957, 1.957, 2.099, 2.100, 2.124, 2.129	compressed (pseudo)octahedron
$^5T_{2g}$	2.129, 2.130, 2.138, 2.138, 2.139, 2.139	∼ regular (pseudo)octahedron

[a] Six symmetry-equivalent Co−N bonds.

Table 8. 0−0 Transition Energies (ΔE)

		ΔE_{calc}, eV		
state	ΔE_{exp},[a] eV	MCQDPT2[b]	OPBE	E_{SO}, cm^{-1}
$^1A_{1g}$				−76.9
$^1T_{1g}$	2.36	2.36 (2.62)	1.70	−10.0
$^3T_{1g}$	1.37	0.95 (1.33)	1.20	−78.6
$^5T_{2g}$		1.60 (2.12)	1.82	−51.7

[a] Reference 1. [b] In parentheses: vertical transitions.

in the $^1A_{1g}$ ground state. A smaller elongation of ∼0.12 Å was estimated by Wilson and Solomon.[1]

The 0−0 transition energies (Table 8) were computed with multiconfiguration quasidegenerate second-order perturbation (MCQDPT2)[16,17] theory and density functional theory using the OPBE functional. These calculations were based on the above-described OPBE-PCM geometries (Table 7). PCM hydration was included to model the effect of the environment of $Co(NH_3)_6^{3+}$. Contributions from spin−orbit coupling (E_{SO}) were taken into account, but they are small (Table 8). E_{SO} was obtained via spin−orbit CI (Computational Details), which was based on the CAS-SCF wave function of the corresponding state including the interactions with other states of appropriate symmetry and spin (Computational Details). Zero point energy corrections were not included because they would be questionable: as mentioned above, it was not possible to optimize the geometries of the excited states of the $Co(NH_3)_6 \cdot Cl_4^-$ model compound. Hence, hydrogen bonding of ammonia with lattice anions could not be treated (see above). The neglect of these H-bonds gives rise to low-frequency rotational modes of the ammonia ligands. In the presence of anions and, therefore, H-bonds, these modes would have much higher frequencies. The MCQDPT2 energy of the $^1T_{1g}$ state agrees with experiment, but that of the $^3T_{1g}$ state is too low by 0.32 eV. Interestingly, the OPBE $^3T_{1g}$ energy is underestimated by only 0.17 eV, but that of $^1T_{1g}$ is inaccurate and too low by 0.66 eV. For the experimentally unknown $^5T_{2g}$ state, the MCQDPT2 and OPBE energies differ by 0.22 eV. On the basis of the more reliable MCQDPT2 energies, the $^5T_{2g}$ state lies above the $^3T_{1g}$ state by 0.65 eV and below the $^1T_{1g}$ state. According to the OPBE energies, which are less reliable, the $^5T_{2g}$ state lies also above the $^3T_{1g}$ state by 0.62 eV, but the $^1T_{1g}$ energy (which deviates strongly from the experimental value) is lower than that of the $^5T_{2g}$ state. The lowest (relaxed) excited state of $Co(NH_3)_6^{3+}$ is the triplet $^3T_{1g}$ state and not the quintet $^5T_{2g}$ state. The vertical transition energies, calculated without chloride ions in the second coordination sphere, were too low by ∼0.2−0.3 eV (Table 3). Possibly, the 0−0 transition energies (Table 8) are also too low by this error.

Table 9. Experimental and Computed Symmetric Stretching Frequencies of $Co(NH_3)_6^{3+}$[a]

	a_{1g}		e_g	
state	exptl[b]	calcd	exptl[b]	calcd
$^1A_{1g}$	490	458, 460[c]	440	425,[d] 426[c]
$^1T_{1g}$	480	454	429	371, 184
$^3T_{1g}$	483	447	434	373, 151
$^5T_{2g}$	∼435[e]	382	-	304[d]

[a] OPBE-PCM geometries, unless noted otherwise. Units: cm^{-1}. [b] Reference 1. [c] $Co(NH_3)_6 \cdot Cl_4^-$ model compound. [d] Average of the two e_g components. [e] Estimated.

Vibrational Frequencies. For the $^1A_{1g}$ ground state, the vibrational frequencies were computed based on the $Co(NH_3)_6^{3+}$ OPBE-PCM and the $Co(NH_3)_6 \cdot Cl_4^-$ OPBE (gas phase) geometries. The computed frequencies are insensitive to the model (Table 9) and lower than the experimental values. The frequencies of the excited $^1T_{1g}$ and $^3T_{1g}$ states are also underestimated, whereby the error of the e_g component is sizable, possibly because the distortion of the PCM geometries is larger than those of $Co(NH_3)_6^{3+}$ in the solid, where the motion of the nearest neighbors is restricted. Assuming an average error of −31 cm^{-1} for the a_{1g} component, the best estimate of the a_{1g} mode for the $^5T_{2g}$ state would be ∼413 cm^{-1}, being somewhat lower than the value estimated from experiment. This difference might again be due to the full relaxation of the PCM geometry.

Discussion

Quantum Chemical Investigations of the Related Low-Spin $Co(CN)_6^{3-}$ and $Co(OH_2)_6^{3+}$Complexes. The vertical LF transitions of the low-spin $Co(CN)_6^{3-}$ ion have been computed[46] at the experimental geometry using DFT-

Table 10. Vertical Ligand Field Transition Energies of $Co(OH_2)_6^{3+}$

electronic state	$Co(OH_2)_6^{3+}$			$Co(OH_2)_6 \cdot (OH_2)_{12}^{3+}$	
	LFDFT[a]	SORCI[a]	TDDFT[a]	LFDFT[a]	exp.[b]
$^1A_{1g}$	0	0	0	0	0
$^1T_{1g}$	15370	15670	16528	15669	16500
$^1T_{2g}$	24537	23600	22017	24726	24700
$^3T_{1g}$	9212	5257	9156	10271	8000
$^3T_{2g}$	13782	10779	9380	14798	12500
$^5T_{2g}$	9660			12649	

[a] From ref 46. [b] From ref 44.

based LF theory (LFDFT)[47] and the spectroscopically oriented configuration interaction method (SORCI).[48] The agreement with experiment is better for the SORCI technique. For the $Co(OH_2)_6^{3+}$ ion (Table 10), the transition energies, computed at the experimental Co−N bond lengths, were taken from Table 19-7 of ref 46 in which the experimental data has been replaced by those of Johnson and Sharpe,[44] who measured transition energies to the singlet and the triplet states. All of the applied methods agree with experiment, whereby it should be noted that SORCI underestimates the $^3T_{1g}$ energy by further 0.1 eV than MCQDPT2 for $Co(NH_3)_6^{3+}$ (Table 3). For $Co(CN)_6^{3-}$ and $Co(OH_2)_6^{3+}$, energies computed with CAS-SCF-based second-order perturbation theory is not available. Environmental effects were not modeled; they were assumed to cancel largely.

The above-mentioned LFDFT and SORCI vertical transition energies agree with experiment because (i) these calculations were performed at the experimental cobalt(III)−ligand bond lengths, and (ii) because systematic errors due to the neglect of environmental effects cancel largely. It should be noted that LF theory is based on the Racah parameters Δ, B, and C, whose expressions are derived from Coulomb and exchange integrals, whereby electron correlation energy is accounted for in an effective, nonspecific way. Since Δ, B, and C are obtained via a fit to experimental data, the errors arising from the approximate treatment of electron correlation cancel partially. The computation of 0−0 transitions is more demanding, since accurate geometries of ground and excited states are required. Because of the differences in metal−ligand bond lengths of ground and excited states, the Coulomb and exchange integrals vary. The parameters Δ, B, and C are not constant for 0−0 transitions, and the error arising from the neglect of electron correlation is different than for vertical transitions. Therefore, 0−0 transitions predicted by LF theory cannot be expected to be accurate, and energies of the relaxed $^5T_{2g}$ states of $Co(OH_2)_6^{3+}$ and $Co(NH_3)_6^{3+}$, estimated on the basis of LF theory, are likely to be affected by those systematic errors.

Geometry of the $Co(NH_3)_6^{3+}$ Ion. The Co−N bond lengths computed with MP2 for the free $Co(NH_3)_6^{3+}$ ion are close to those in the crystal structures (Tables 1 and 2i). However, the MP2 geometry is not correct, since static electron correlation is neglected, and since the gas phase geometry is expected to differ form those in the crystal. In aqueous solution and in crystals, the Co−N bonds are shorter than in the free ion because charge transfer from solvent molecules or anions to the cation strengthens the Co−N bonds. The electronic transition energies in $Ru(NH_3)_6^{2+}$ and $Ru(NH_3)_5(pyr)^{2+}$ (pyr: pyridine) were shown to depend strongly on the solvent-to-solute charge transfer.[49] According to QM/MM computations[49] on these Ru^{II} and Ru^{III} complexes, roughly one electron is transferred from the water solvent to the $Ru(NH_3)_6^{2+/3+}$ and $Ru(NH_3)_5(pyr)^{2+/3+}$ ions. The neglect of this solvent-to-solute charge transfer effect in quantum chemical computations on di- and trivalent cations is responsible for the systematically too long metal−ligand bond lengths. It is interesting to note that PCM, which takes into account electrostatic solute−solvent interactions (the hydrogen bonds are mainly electrostatic) provides Co−N bond lengths being close to those in the crystal structures.

Transition Energies. Experimentally, the $^5T_{2g}$ energy has not been measurable so far. According to ZINDO calculations of Larsson, Ståhl, and Zerner,[2] the vertical $^5T_{2g}$ energy is higher than that of the $^3T_{1g}$, $^3T_{2g}$, and $^1T_{1g}$ states, and lower than that of the $^1T_{2g}$ state. The present calculations suggest that the $^5T_{2g}$ energy is higher than those of the two triplets, and lower than those of the two singlets. The comparison with experimentally available transition energies shows that the computational error is $\leq$0.3 eV (Table 3iv). Because of this error, the present computations do not allow the assessment of the $^5T_{2g}-{}^1T_{1g}$ ordering. However, there is little doubt that the (vertical) $^5T_{2g}$ energy is higher than those of the $^3T_{1g}$ and $^3T_{2g}$ states.

The 0−0 transition energies, computed on the basis of the ZINDO method,[2] increase in the order $^3T_{1g} < {}^1T_{1g} \approx {}^5T_{2g}$. According to the spectroscopic study,[1] the energy ordering is $^5T_{2g} \leq {}^3T_{1g} < {}^1T_{1g}$, and the present computations suggest the ordering $^3T_{1g} < {}^5T_{2g} < {}^1T_{1g}$. The computed $^1T_{1g}$ energy agrees with experiment, but the $^3T_{1g}$ energy is too low by 0.42 eV (Table 8). Because of the magnitude of the $^5T_{2g}-{}^3T_{1g}$ energy difference (Table 8) the statement that the $^5T_{2g}$ energy is higher than the $^3T_{1g}$ energy can be made with confidence. Because of the sizable error in the $^3T_{1g}$ energy, however, the question, whether the $^5T_{2g}$ state lies below the $^1T_{1g}$ state or whether their energies are comparable, remains open. It should be remembered that it was not possible to optimize the geometries of the $^1T_{1g}$, $^3T_{1g}$, and $^5T_{2g}$ states for the $Co(NH_3)_6 \cdot Cl_4^-$ model. Hence, the 0−0 transition energies based on the best model are not available. The environment of the $Co(NH_3)_6^{3+}$ ion had to be represented with PCM water. It should be noted that the geometries of the excited states, computed at the OPBE-PCM level, are fully relaxed. It is an open question, whether in the crystal the excited states can relax completely, since the motion of the lattice anions is restricted. These constraints would also affect the relaxation of the Co−N bonds. The longer Co−N bonds and the lower vibrational frequencies for the computed excited states compared with Wilson et al.'s experimental data in the solid state might also be due to a possible incomplete relaxation in the crystal (whereby inaccuracies in the computations contribute as well). In contrast to $Co(NH_3)_6^{3+}$, for $Co(OH_2)_6^{3+}$, exhibiting a weaker crystal field, the $^5T_{2g}$ state is the lowest excited 0−0 state.[50]

Acknowledgment. I am grateful to Dr. M. W. Schmidt for a nonpublic version of GAMESS.

Supporting Information Available: Tables S1−S4 listing the atomic coordinates of hydrated $Co(NH_3)_6^{3+}$ in its $^1A_{1g}$, $^1T_{1g}$, $^3T_{1g}$, and $^5T_{2g}$ states, Table S5 listing the atomic coordinates of $Co(NH_3)_6 \cdot Cl_4^-$ in the ground state, and Table S6 summarizing the vertical LF transition energies obtained with TDDFT (BLYP and B3LYP). This material is available free of charge via the Internet at http://pubs.acs.org.

References

(1) Wilson, R. B.; Solomon, E. I. *J. Am. Chem. Soc.* **1980**, *102*, 4085.

(2) Larsson, S.; Ståhl, K.; Zerner, M. C. *Inorg. Chem.* **1986**, *25*, 3033.

(3) McCusker, J. K.; Walda, K. N.; Magde, D.; Hendrickson, D. N. *Inorg. Chem.* **1993**, *32*, 394.

(4) Konya, K.; Nishikawa, H.; Shibata, M. *Inorg. Chem.* **1968**, *7*, 1165.

(5) Schmidt, M. W.; Baldridge, K. K.; Boatz, J. A.; Elbert, S. T.; Gordon, M. S.; Jensen, J. H.; Koseki, S.; Matsunaga, N.; Nguyen, K. A.; Su, S. J.; Windus, T. L.; Dupuis, M.; Montgomery, J. A. *J. Comput. Chem.* **1993**, *14*, 1347.

(6) Gordon, M. S.; Schmidt, M. W., In *Theory and Applications of Computational Chemistry, the first forty years*; Dykstra, C. E.; Frenking, G.; Kim, K. S.; Scuseria, G. E. Eds.; Elsevier: Amsterdam, 2005, pp 1167−1189.

(7) Stevens, W. J.; Krauss, M.; Basch, H.; Jasien, P. G. *Can. J. Chem.* **1992**, *70*, 612.

(8) Stevens, W. J.; Basch, H.; Krauss, M. *J. Chem. Phys.* **1984**, *81*, 6026.

(9) Schäfer, A.; Horn, H.; Ahlrichs, R. *J. Chem. Phys.* **1992**, *97*, 2571.

(10) Hehre, W. J.; Ditchfield, R.; Pople, J. A. *J. Chem. Phys.* **1972**, *56*, 2257.

(11) Ditchfield, R.; Hehre, W. J.; Pople, J. A. *J. Chem. Phys.* **1971**, *54*, 724.

(12) Krishnan, R.; Binkley, J. S.; Seeger, R.; Pople, J. A. *J. Chem. Phys.* **1980**, *72*, 99.

(13) Bode, B. M.; Gordon, M. S. *J. Mol. Graphics Modell.* **1998**, *16*, 133.

(14) Tomasi, J. *Theor. Chem. Acc.* **2004**, *112*, 184.

(15) Tomasi, J.; Mennucci, B.; Cammi, R. *Chem. Rev.* **2005**, *105*, 2999.

(16) Nakano, H. *J. Chem. Phys.* **1993**, *99*, 7983.

(17) Nakano, H. *Chem. Phys. Lett.* **1993**, *207*, 372.

(18) Rotzinger, F. P. *J. Phys. Chem. B* **2005**, *109*, 1510.

(19) Rotzinger, F. P. *J. Phys. Chem. A* **1999**, *103*, 9345.

(20) Furlani, T. R.; King, H. F. *J. Chem. Phys.* **1985**, *82*, 5577.

(21) King, H. F.; Furlani, T. R. *J. Comput. Chem.* **1988**, *9*, 771.

(22) Fedorov, D. G.; Gordon, M. S. *J. Chem. Phys.* **2000**, *112*, 5611.

(23) Seitz, K.; Peschel, S.; Babel, D. *Z. Anorg. Allg. Chem.* **2001**, *627*, 929.

(24) Iwata, M.; Saito, Y. *Acta Crystallogr. B* **1973**, *29*, 822.

(25) Barnet, M. T.; Craven, B. M.; Freeman, H. C. *J. Chem. Soc., Chem. Commun.* **1966**, 307.

(26) Meek, D. W.; Ibers, J. A. *Inorg. Chem.* **1970**, *9*, 465.

(27) Beattie, J. K.; Moore, C. J. *Inorg. Chem.* **1982**, *21*, 1292.

(28) Schroeder, D. R.; Jacobson, R. A. *Inorg. Chem.* **1973**, *12*, 210.

(29) Schroeder, D. R.; Jacobson, R. A. *Inorg. Chem.* **1973**, *12*, 515.

(30) Sharma, R. P.; Bala, R.; Sharma, R.; Perez, J.; Miguel, D. *J. Mol. Struct.* **2006**, *788*, 49.

(31) Sharma, R. P.; Bala, R.; Sharma, R.; Venugopalan, P.; Salas, J. M.; Quiros, M. *J. Fluorine Chem.* **2005**, *126*, 1543.

(32) Sharma, R. P.; Bala, R.; Sharma, R.; Rychlewska, U.; Warzajtis, B. *J. Fluorine Chem* **2005**, *126*, 967.

(33) Becke, A. D. *Phys. Rev. A* **1988**, *38*, 3098.

(34) Lee, C.; Yang, W.; Parr, R. G. *Phys. Rev. B* **1988**, *3*, 7–785.

(35) Miehlich, B.; Savin, A.; Stoll, H.; Preuss, H. *Chem. Phys. Lett.* **1989**, *157*, 200.

(36) Becke, A. D. *J. Chem. Phys.* **1993**, *9*, 8–5648.

(37) Stephens, P. J.; Devlin, F. J.; Chablowski, C. F.; Frisch, M. J. *J. Phys. Chem.* **1994**, *98*, 11623.

(38) Hertwig, R. H.; Koch, W. *Chem. Phys. Lett.* **1997**, *268*, 345.

(39) Perdew, J. P.; Burke, K.; Ernzerhof, M. *Phys. Rev. Lett.* **1996**, *77*, 3865.

(40) Perdew, J. P.; Burke, K.; Ernzerhof, M. *Phys. Rev. Lett.* **1997**, *78*, 1396.

(41) Adamo, C.; Barone, V. *J. Chem. Phys.* **1999**, *110*, 6158.

(42) Handy, N. C.; Cohen, A. J. *Mol. Phys.* **2001**, *99*, 403.

(43) Conradie, J.; Ghosh, A. *J. Phys. Chem. B* **2007**, *111*, 12621.

(44) Johnson, D. A.; Sharpe, A. G. *J. Chem. Soc. A* **1966**, 798.

(45) Tanabe, Y.; Sugano, S. *J. Phys. Soc. Jpn.* **1954**, *9*, 753.

(46) Atanasov, M.; Comba, P.; Daul, C. A.; Neese, F. In *Models, Mysteries and Magic of Molecules*; Boeyens, J. C. A.; Ogilvie, J. F., Eds.; Springer: Dordrecht, 2008; pp 411−445.

(47) Atanasov, M.; Daul, C. A.; Rauzy, C. *Struct. Bonding (Berlin)* **2004**, *106*, 97.

(48) Neese, F. *J. Chem. Phys.* **2003**, *119*, 9428.

(49) Pearl, G. M.; Zerner, M. *J. Am. Chem. Soc.* **1999**, *121*, 399.

(50) Johnson, D. A.; Nelson, P. G. *Inorg. Chem.* **1999**, *38*, 4949.

CT900048R

JCTC Journal of Chemical Theory and Computation

Vibrational Spectra of Small Protonated Peptides from Finite Temperature MD Simulations and IRMPD Spectroscopy

A. Cimas,[†] T. D. Vaden,*[,‡] T. S. J. A. de Boer,[‡] L. C. Snoek,[‡] and M.-P. Gaigeot*[,†]

LAMBE UMR8587 Laboratoire Analyse et Modélisation pour la Biologie et l'Environnement, Université d'Evry val d'Essonne, Blvd F. Mitterrand, Bât. Maupertuis, 91025 Evry, France, and Physical and Theoretical Chemistry Laboratory, Chemistry Department, University of Oxford, South Parks Road, Oxford OX1 3QZ, United Kingdom

Received February 1, 2009

Abstract: Finite temperature Born−Oppenheimer DFT-based molecular dynamics simulations are presented for the vibrational spectroscopy of the prototype gas-phase Ala_2H^+ and Ala_3H^+ protonated peptides. The dynamics and the vibrational signatures are used to interpret IR-MPD spectra recorded in the NH/OH stretch region. Molecular dynamics simulations are one way to go beyond the harmonic approximations commonly applied for the calculations of infrared spectra, naturally including all anharmonicities, i.e. mode couplings, vibrational and dipole anharmonicities. The dynamics of the peptides allows understanding of the evolution of the shape and width of the N−H bands when increasing the size of the peptide, as demonstrated here with the two small prototypes Ala_2H^+ and Ala_3H^+. Hence, the conformational dynamics of Ala_2^+ at room temperature participates to the broadening of the IR active bands. The complex N−H broadband of Ala_3H^+ is shown to result from the dynamics of the N−H groups in the different peptide families, with a special role from breaking/reforming of hydrogen bonds involving the N−H groups. Taking this dynamics into account is thus mandatory for the understanding of this band in the 300−400 K experimental spectrum.

Introduction

Characterizing the folding behavior of peptide chains is of fundamental importance for a better understanding of proteins. The conformational structures and dynamics of simple model oligopeptides have been studied in solution by NMR and 2-D IR spectroscopy,[1−3] but the role of the aqueous environment on peptide behavior is an open question. The intrinsic peptide structures and dynamics may be explored in the gas phase, where the solution environment is removed and the folding behavior is determined exclusively from the noncovalent interactions associated with the peptide backbones and/or side chains. This has catalyzed many structural investigations of cold, gas-phase peptides, revealing gas-phase formation of traditional secondary-structure motifs like helices, β-sheets, and β- and γ-turns.[4−9]

For a complete picture of folding behavior in gas-phase oligopeptides it is necessary to include the effects of temperature. At physiological temperatures, entropic differences between conformations can alter the free energy surfaces, and as a result multiple conformational families may be populated and barriers to conformational isomerization may be surmounted. While frozen peptides at 0 K exhibit only one or a few distinct structures, at 298 K peptides are better described in terms of average conformation(s), with a (relatively) rigid backbone and moderate or large-amplitude side-chain motions.[10] The motivation to understand these issues is reflected in the work of Polfer et al.[11] and Gregoire et al.,[12] in which protonated peptide ions are characterized at ∼300 K using Infrared Multiple Photodissociation (IR-

* Corresponding author e-mail: timothy.vaden@chem.ox.ac.uk (T.D.V.), mgaigeot@univ-evry.fr (M.-P.G.).

[†] Université d'Evry val d'Essonne.

[‡] University of Oxford.

10.1021/ct900057s CCC: $40.75
Published on Web 03/20/2009

MPD) spectroscopy with a Free Electron Laser (FEL). Vaden et al. have recently investigated protonated polyalanine peptides, Ala_nH^+, under elevated internal energy conditions by generating the ions via UV photochemical protonation.[13] The 'temperature' of the ions produced in these experiments is roughly estimated about 350 K, so that the peptides structural and dynamical properties extracted from these experiments are relevant for understanding the room temperature physiological medium. When turning to theoretical calculations in order to interpret the IR-MPD recorded features, one should be aware that the local dynamics of the peptides (e.g., hydrogen bonds dynamics, methyl groups rotation, local distortions of the peptide chain) and the conformational isomerization/interconversion dynamics of the peptides as well as anharmonic vibrational effects (i.e., mode couplings, vibrational and dipole anharmonicities) may be pivotal issues for the comprehension of the finite temperature experimental vibrational features. See our recent papers[12,14,15] on these issues.

The dynamics of the molecules (local or more global isomerization/interconversion) and their direct consequences on measured properties such as vibrational spectra can only be accounted for through molecular dynamics (MD) simulations.[16,17] The calculation of infrared spectra through MD relies on dipole time correlation functions recorded along a trajectory.[18] This is well established in the context of classical MD[19−24] but is much more recent in the ab initio MD community. Pioneering studies were done by Parrinello et al. on liquid water,[25−27] and within the past few years, we have shown that ab initio molecular dynamics represents the best method for the calculation of IR spectra of DNA and peptide building blocks in the gas phase or immersed in liquid water[12,14,15,28−30] at room temperature. We have in particular shown that ab initio MD simulations are the proper tool to calculate IR absorption spectra of gas-phase molecules that can exist in multiple isomeric conformations at finite temperature.[14]

Another advantage of MD simulations for the calculation of IR spectra is that vibrational anharmonicities are directly taken into account in the final spectrum. The two successive harmonic approximations usually adopted for the determination of IR spectra from static ab initio calculations, i.e. a harmonic approximation of the potential energy surface at the optimized geometries and a mechanical harmonic approximation for the transition dipole moments, are omitted in MD, because they are not needed. Hence, the finite temperature dynamics take place on all accessible parts of the potential energy surface, be they harmonic or anharmonic. As the calculation of IR spectra with MD is related only to the time-dependent dipole moment, it does not require any harmonic expansion of the transition dipole moments. Therefore, if the dipole moments and their fluctuations are accurately calculated along the trajectory, the resulting IR spectrum should be reliable too, as demonstrated in our previous works.[12,14,28−30] Furthermore, the temperature and the conformational dynamics of the peptide will contribute to vibrational band broadening.

In this article, we apply DFT-based Born−Oppenheimer dynamics at ∼300−400 K on the prototype gas-phase alanine protonated di- and tri-peptides in order to calculate their infrared spectral signatures. Our goal is to interpret the vibrational features at the microscopic level, with a special emphasis on the evolution of the active bands with the peptide size increase. The dynamics and the vibrational signatures are then used to interpret IR-MPD spectra recorded in the NH/OH stretch region. We have chosen these two well-studied small protonated polyalanines (see for instance refs 13 and 31) in order to demonstrate that the peptides dynamical features have to be taken into account to obtain a precise understanding of the relation between experimental features and the underlying molecular structural and dynamical properties, including anharmonicities. Previous investigations reported in the literature on these systems[13,31,32] have combined IR-MPD spectra in the NH/OH or mid-IR amide domains and scaled harmonic DFT frequencies computed for frozen conformations of the peptides, thereby neglecting vibrational anharmonic contributions and local/nonlocal conformational dynamics at the finite temperature of the experiments. The present investigation goes beyond these approximations. Note that these issues have already been addressed on Ala_2H^+ with DFT-based Car−Parrinello modeling in the mid-IR region.[12,14]

IR-MPD Setup

The experimental method and experimental results are unchanged from our previous Ala_nH^+ investigation.[13] The following brief description is given for a better assessment of the interplay between the experiments and the theoretical investigations. Ala_2H^+ and Ala_3H^+ ions were generated by a photochemical protonation scheme (1)−(4), described in detail elsewhere,[33−35] in which intermolecular proton transfer follows resonance-enhanced 2-photon ionization (R2PI) of a phenol-peptide (PhOH..Ala_n, $n = 2,3$) complex.

$$PhOH + Ala_n \rightarrow [PhOH..Ala_n] \quad (1)$$

$$[PhOH..Ala_n] + 2h\nu \rightarrow [PhOH^+..Ala_n]^{\bullet} \quad (2)$$

$$[PhOH^+..Ala_n]^{\bullet} \rightarrow PhO^{\bullet}..Ala_nH^+ \quad (3)$$

$$PhO^{\bullet}..Ala_nH^+ \rightarrow PhO^{\bullet} + Ala_nH^+ \quad (4)$$

Cold $PhOH..Ala_n$ complexes were generated, step (1), by seeding gas-phase Ala_n peptides (using laser desorption by a Continuum Minilite Nd:YAG laser) into a pulsed supersonic expansion of phenol in argon carrier gas. The complexes passed through a skimmer into the extraction region of a linear time-of-flight (TOF) mass spectrometer (R. M. Jordan), where they were ionized, step (2), at ∼278 nm via R2PI using the frequency-doubled output of a Lamda-Physik FL2002 dye laser. Rapid, exothermic proton transfer within the ionized complexes, $[PhOH^+..Ala_n]^{\bullet}$, step (3), followed by endothermic loss of the phenoxy radical $PhO^{\bullet}$, step (4), generated the free protonated peptide ions, Ala_nH^+. Ala_2 samples were obtained from Aldrich, while Ala_3 samples were obtained from Bachem (Germany).

The internal energy content of the protonated cations depends on the excess energy after two-photon ionization

(~60 kJ.mol^{-1}), the ΔH of the proton transfer reaction (3) (~100 kJ.mol^{-1}), and the binding energy of the $PhO^{\bullet}..Ala_nH^+$ complex (estimated to be ~75 kJ.mol^{-1}).[33] As discussed previously, the 'temperatures' of the $Ala_{2,3}H^+$ ions, which depend on the peptide size through the vibrational heat capacities, are not well-characterized but could be anywhere from 250 K to more than 400 K.[13] Previous analyses have assumed temperatures of 350 K as a rough guide, but in the current work we consider several different temperatures, enabling a better characterization of the internal energy content.

The $Ala_{2,3}H^+$ ions were probed with IR-MPD spectroscopy using the idler output (~10−20 mJ/pulse, tunable from 2000−4000 cm^{-1}, with a bandwidth of ~2 cm^{-1}) of a LaserVision KTP/KTA OPO/OPA laser system, tightly focused to a beam diameter ~800 μm, which intersected the ions 400 ns after the UV pulse, in a spatially distinct region downstream from the ionizing UV laser beam. IR-MPD spectra were recorded by monitoring the depletion of the (parent) protonated peptide ion (using active baseline correction[13]) as a function of the IR frequency, since the TOF mass spectra were too congested to unambiguously identify the fragment ions.

DFT-Based Molecular Dynamics

We perform Born−Oppenheimer molecular dynamics simulations (BOMD) with the CP2K package,[36,37] where nuclei are treated classically and electrons quantum mechanically within the DFT (Density Functional Theory) formalism. These simulations solve Newton's equations of motion of the nuclei at finite temperature, while the electronic wave function is obtained at each nucleus conformation by solving the time-independent Schrödinger equation. Forces that act on the nuclei are derived from the Kohn−Sham energy. Details on the molecular dynamics setup are presented in the Supporting Information. Briefly, we use the Becke, Lee, Yang, and Parr (BLYP) gradient-corrected functional[38,39] and Goedecker-Teter-Hutter (GTH) pseudopotentials.[40−42] A double-ζ (DZVP) Gaussian basis set (from the CP2K library) and a 320 Ryd Plane-wave density cutoff have been applied. With this basis set the four structures of Ala_2H^+ from ref 32 have been reoptimized and are found in the same energy order and with similar energy gaps as in refs 14 and 32 i.e. transA1 (least energy), transO1 (+1.32 kcal/mol), transA2 (+1.72 kcal/mol), and cisA3 (+2.57 kcal/mol), with the Zero Point Energy (ZPE) included. Note that the use of a bigger plane-wave basis set in ref 14 led to the energy inversion of conformers transO1 and transA2. The Ala_3H^+ two main conformers identified as A_31 and A_33 in ref 13 with an energy gap of 4.88 kcal/mol from DFT/B3LYP/6−31+G(d,p) optimizations is found at 3.83 kcal/mol with the present BLYP/DZVP optimization, including the ZPE. The BLYP/DZVP present method thus gives similar minima and energy gaps on the potential energy surfaces of Ala_2H^+ and Ala_3H^+ protonated peptides as with e.g. B3LYP and more extended basis sets. In any case, the use of diffuse functions is less critical in charged species.

The dynamics are performed in the microcanonical NVE ensemble (after an equilibration period, see details in the Supporting Information) with a time-step of 0.5 fs. With BOMD, discrepancies between calculation and experiment are expected to be due to the choice of the DFT functional (BLYP throughout this paper), as DFT-based dynamics are only as good as the functional itself allows.

Calculation of the IR absorption coefficient $\alpha(\omega)$ by means of MD makes use of the relation derived from Linear Response Theory involving the Fourier Transform of the dipole time correlation function,[18] as described in our previous works[12,14,28−30]

$$\alpha(\omega) = \frac{2\pi\beta\omega^2}{3n(\omega)cV} \times \int_{-\infty}^{\infty} dt \ \langle \mathbf{M}(t)\cdot\mathbf{M}(0)\rangle \exp(i\omega t) \quad (5)$$

where $\beta = 1/kT$, $n(\omega)$ is the refractive index, c is the speed of light in vacuum, and V is the volume. $\mathbf{M}$ is the total dipole moment of the system, which is the sum of the ionic and electronic contribution.[26] Interpretation of the infrared-active bands into individual atomic displacements is done with the vibrational density of states (VDOS) formalism. This is obtained by Fourier transformation of the atomic velocity autocorrelation functions and is decomposed into individual atomic contributions or into groups of atoms.[30] Note that we do not apply any scaling factor to the vibrational band positions extracted from our calculations.

Setup of the Dynamics

We performed three separate dynamics of the protonated Ala_2H^+ dipeptide and eight dynamics of the protonated Ala_3H^+ tripeptide. The trajectories of Ala_2H^+ span a total 30 ps dynamics, where the average temperature is 290 ± 37 K. The initial configurations (positions and velocities of the atoms) of the dynamics have been taken from the end of the dynamics reported in our previous work.[14] The trajectories of Ala_3H^+ also span a total ~30 ps dynamics with temperatures ranging between 387 ± 38 K and 530 ± 50 K, on average; choice of the temperatures will be explained below. The molecular dynamics simulations of the protonated tripeptide follow our general two-steps setup, i.e. an equilibration phase of 1−3 ps with a control of temperature through velocity rescaling, followed by data collection over trajectories in the microcanonical ensemble (no rescaling of velocities), each one for 3.2−3.7 ps.

We have considered three families of the Ala_3H^+ tripeptide in our ab initio dynamics simulations, as illustrated in Figure 1. The dynamics were initiated from optimized structures found in our previous work[13] (labeled A_31, A_33, and A_35). A_31 and A_33 are the two structures found lower in energy[13,31] in previous works, with their relative energy that depends on the ab initio level of theory (DFT and MP2) and basis set used in the optimization procedures. The family hereafter denoted 'NH_2' corresponds to a tripeptide in which the proton is located on the N-terminal carbonyl group and is initiated from the A_31 optimized conformation of our previous work.[13] The supplementary proton of the family hereafter denoted 'elongated NH_3^+' (or simply 'NH_3^+') is located on the N-terminal NH_3^+ and displays an extended peptide chain, and the dynamics of this family are initiated from the A_35 optimized conformation. This structure lies higher in energy

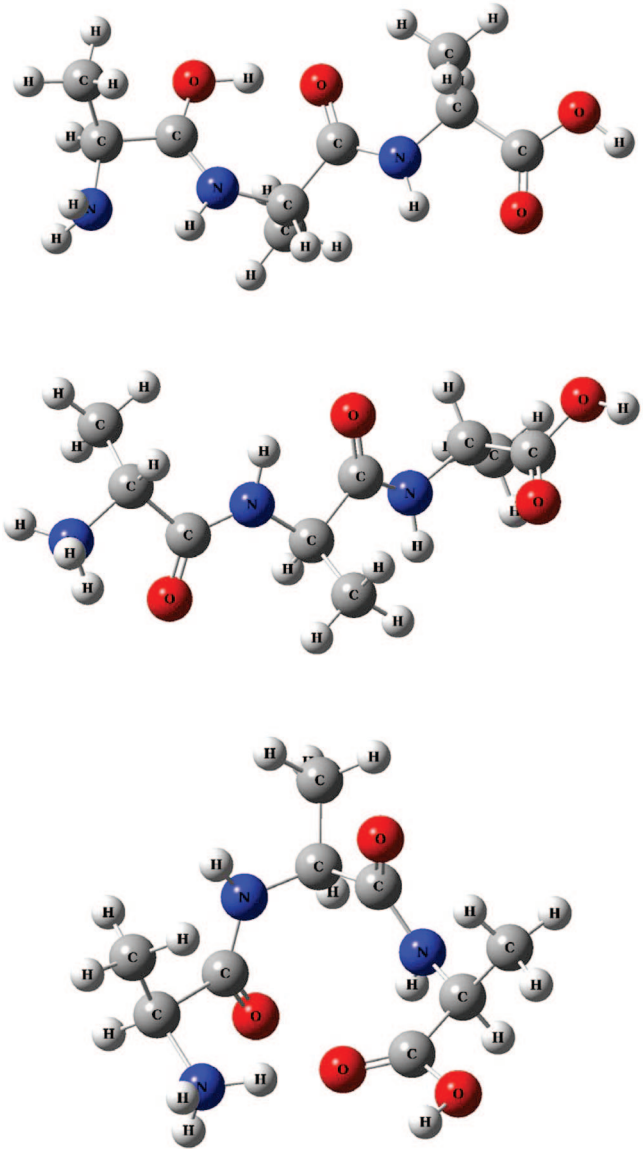

Figure 1. Schematic representation of the main structures of Ala_3H^+ which have been used as initial structures in the DFT-based Born−Oppenheimer dynamics. From top to bottom: NH_2 family, elongated NH_3^+ family, and folded NH_3^+ family. Carbon atoms are represented in dark gray, nitrogen atoms in dark blue, oxygen atoms in red, and hydrogen atoms in light gray.

than the A_31 and A_33 ones[13,31] and was therefore discarded in the previous analysis of the IR-MPD spectra. We have nonetheless investigated this type of conformer in the present work, considering that it could be populated as a result of the method of production of the ions in the present experiment where a photochemical scheme is employed. The other reason is that this conformation is very similar to the one of the Ala_2H^+ that was observed in our previous MD work.[14] The third family investigated is denoted 'folded NH_3^+' (or simply 'folded') and corresponds to a folded chain through a $NH_3^+\cdots O{=}C$ H-bond and is initiated from the A_33 optimized conformation of our previous work.[13]

Two dynamics of the NH_2 family have been performed at 380 ± 36 K and two other dynamics at 460 ± 40 K and 530 ± 50 K, respectively. Two dynamics of the NH_3^+ family have been performed at 380 ± 37 K and a supplementary dynamics at 450 ± 45 K. The trajectory of the folded family has been performed at 400 ± 40 K. The dynamics performed at higher temperatures were begun from the end of lower temperature dynamics, heated up and equilibrated for 2−3 ps, and then evolved in the microcanonical ensemble. As already emphasized, the exact value of the temperature in the related IR-MPD experiments is not well-characterized but roughly estimated about 350 K, thus the average 380−400 K achieved in the dynamics performed on Ala_3H^+. The highest temperatures chosen here are aimed at investigating the temperature effect on the final vibrational features. The final spectra of Ala_2H^+ and of Ala_3H^+ presented here have been averaged over all performed trajectories.

One has to be cautious when trying to compare the calculated IR absorption intensities (calculated within the static or the dynamics formalisms) to those obtained in IR-MPD experiments. Equation 5 is strictly valid for one-photon linear IR absorption spectroscopy. IR-MPD on the other hand is a multiphotonic process leading to the fragmentation of the molecule. The recorded signal is the fragmentation yield with respect to each excitation IR wavelength. It is thus an indirect measurement of IR absorption, in contrast to the usual linear IR spectroscopy. Calculations and experiments are therefore not directly comparable where band intensities are concerned, thereby displaying expected discrepancies. The direct simulation of IR-MPD spectra, with a clear theoretical expression of the signal in terms of dynamical quantities, remains an unsolved problem. Comparisons of experimental and calculated IR intensities will therefore be cautiously discussed in the following analyses.

Structural Analyses along the Trajectories

Ala_2H^+. The dynamics of the protonated Ala_2H^+ dipeptide using DFT-based Car−Parrinello molecular dynamics simulations have already been presented and discussed in our previous work,[14] though in another context. The same dynamical results are obtained here, despite the changes in the dynamical approach (Born−Oppenheimer versus Car−Parrinello) and the basis set representation between the two works. Briefly, the protonated dipeptide undergoes continuous conformational dynamics at room temperature between transA1 and transA2 conformers (see ref 14 for more details about the nomenclature adopted for the isomers). This conformational dynamics corresponds to the $N-C-C_\alpha-O$ torsional rotation of the C-terminal COOH of the peptide, without energy barrier.[14] We also observe proton transfers between the NH_3^+ N-terminal and the neighboring carbonyl on the chain, giving rise to transient periods of time during which the transO1 conformer (NH_2/COH) is populated.[14] Overall, conformations where the N-terminal of the peptide is protonated (NH_3^+) are predominantly populated, with a strong hydrogen bond that is formed between NH_3^+ and the neighboring carbonyl group. Moreover, there is enough energy for the NH_3^+ group to rotate and exchange the hydrogen atom that can be hydrogen bonded to the neighboring carbonyl.

We find that, depending on the orientation of the C-terminal COOH during the dynamics, the amide N−H group

can be located in the vicinity of the carbonyl group of COOH with an average N−H···O═C distance of ∼2.1 Å or away from it with distances of the order of ∼3.2−3.5 Å. The short ∼2.1 Å distances cannot be classified as proper hydrogen bonds, since the corresponding average N−H···O angles of ∼110° are too far from the ideal linearity. Considering the geometrical hindrances of the peptide chain, improper hydrogen bonds between neighboring groups on the chain are expected to occur. We observe that the C-terminal O−H group is never involved in any hydrogen bond and thus remains free over the dynamics. Finally, there is not enough energy in the system to overcome the energy barrier of the trans/cis orientation of the peptide bond.

Ala_3H^+. The two dynamics of the NH_2 family performed at 380 K give rise to the exploration of helical α_L conformations of Ala_3H^+, where Φ (Φ = C1−N−C_α−C2 where C1 is the N-terminal carbonyl atom and C2 is the C-terminal carbonyl atom) and Ψ (Ψ = N1−C_α−C2−N2 where N1 is the N-terminal amide nitrogen atom and N2 is the C-terminal amide nitrogen atom) angles are in the [0/100°] and [100/180°] domains, while the dynamics performed at higher temperatures explore either exclusively helical α_R conformations with Φ and Ψ angles, respectively, in the [0/−100°] and [−100/−180°] domains for the 460 K dynamics or a mixture of α_L and α_R conformations for the higher 530 K temperature dynamics. There is therefore a transition between α_L and α_R conformations of the protonated tripeptide that becomes permitted with the increase of the temperature for the NH_2 family (at least within the time-lengths of the simulations performed here). All dynamics on the NH_3^+ family explore the [90−180°] domain of Φ and both [150−180°] and [−150/−180°] domains of Ψ, which also grossly correspond to helical α_L and α_R conformations of the tripeptide. The domains explored by the folded peptide correspond to [−100/−50°] and [60/130°], respectively, for Φ and Ψ, which is the domain of the polyproline PII structure. As already observed for the Ala_2H^+ dipeptide, the C-terminal COOH of the elongated Ala_3H^+ tripeptide undergoes a rotational motion without energy barrier.

Overall, we do not observe spontaneous conformational interconversion/isomerization of Ala_3H^+ during the dynamics close to room temperature. This becomes permitted around 500 K.

The dynamics of the NH_2 family display an equal population of conformations where there is an attraction between NH_2 and the neighboring backbone amide N−H, which gives rise to an average H_2N···H−N distance of ∼2.1 Å, and population of conformations where there is no attraction between NH_2 and the neighboring amide N−H, as revealed by H_2N···H−N distances above 2.5 Å. The short average H_2N···H−N distance of ∼2.1 Å is associated with an average value of the N−H···N angle of ∼110−120°, which does not characterize N−H···N as a proper H-bond. The attraction between the two groups is nonetheless sufficient to induce an increase of the amide N−H bond length to ∼1.05 Å (∼0.02 Å longer than the average C-terminal N−H amide). The H_2N···H−N can be viewed as an energetically weak H-bond. Therefore, the dynamics of the NH_2 family of the tripeptide display an equal

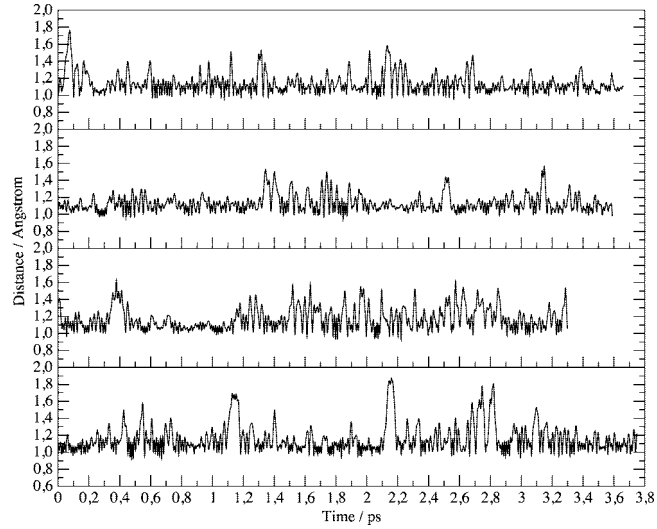

Figure 2. Time evolution of the distance C1−O1−H···O2═C2 for the four dynamics of the NH_2 family of Ala_3H^+ performed in this work, where C1 is the N-terminal carbonyl and C2 is the C-terminal carbonyl. The distance is reported with O1 as the reference.

population of conformations where a weak H_2N···H−N H-bond is formed and where this weak H-bond is broken. Breaking and reforming of this H-bond is observed along all the dynamics performed here.

We have illustrated in Figure 2 the evolution with time of the C−O−H···O═C distance in the NH_2 tripeptide family. Though the supplementary proton of the protonated peptide can be seen hopping between both oxygen sites, it is mainly shared between the two carbonyl groups of the tripeptide with an average H···O distance of ∼1.10−1.13 Å. We can distinguish periods of times during which the supplementary proton is located on the N-terminal C═O (O−H ∼1.0 Å) and other periods of times during which it is located on the C-terminal C═O (which appear as transient and short time spans), but the average localization of the proton is mainly seen in between the two carbonyl groups.

Interestingly, the dynamics of the protonated tripeptide in which the proton is located on the N-terminal NH_3^+ at the beginning of the simulation give rise to the exploration of proton transfer events between the NH_3^+ extremity and the neighboring carbonyl group, as illustrated in Figure 3 where we have reported the evolution with time of the distance NH_3^+···O═C along the three dynamics performed in this work. The supplementary proton either remains at the NH_3^+ terminal giving rise to a strong hydrogen bond between NH_3^+ and the neighboring carbonyl group, with an average NH_3^+···O═C distance of 1.6−1.7 Å, or jumps to the neighboring carbonyl group thus forming an N-terminal amine NH_2 and a protonated C−O−H. The C−O−H remains H-bonded to the amine, with an average C−O−H···N−H distance of 1.6−1.7 Å and an average angle of 130−140°. Note that as observed for Ala_2H^+, there is also enough energy for the NH_3^+ extremity of Ala_3H^+ to rotate and exchange the hydrogen atom that can be hydrogen bonded to the neighboring carbonyl, as can be seen from Figure 3 (bottom). The proton transfer thus proceeds without any energy barrier at the temperature of the simulations performed in the present

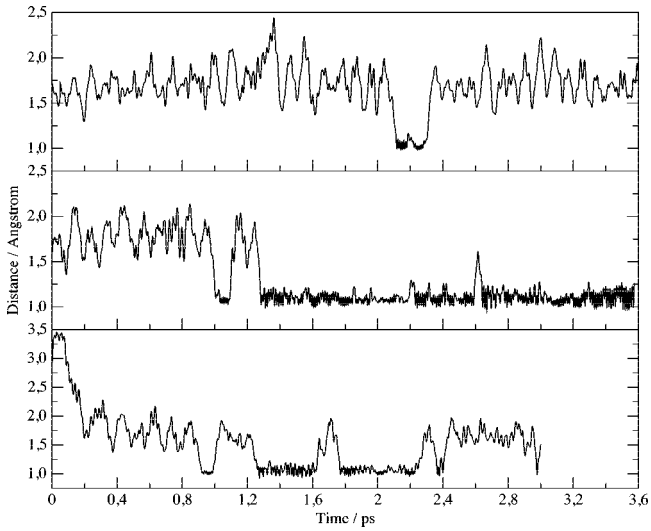

Figure 3. Time evolution of the distance (N-)$H^+\cdots$O1=C1 for the three dynamics of the NH_3^+ family of Ala_3H^+ performed in this work. N−H^+ is one group of the N-terminal NH_3^+.

work. Overall, the configurations protonated at the N-terminus are observed predominantly, but longer statistics would be needed in order to give a more definite statement. The C-terminal N−H and C=O groups form a weak distorted H-bond, with an average distance of 1.9−2.0 Å and an average N−H···O=C angle of 120−130°.

In the case of the folded NH_3^+ family, the dynamics at 400 K shows that there is a rotational motion of the NH_3^+ N-terminal which induces alternate periods of times during which a $NH_3^+\cdots$O=C H-bond between both N- and C-terminal extremities of the folded peptide can be observed and periods of times during which this H-bond is broken. As a consequence, the dynamics explore, on average, an equal percentage of conformations displaying a $NH_3^+\cdots$O=C H-bond between both N-terminal and C-terminal extremities of the folded peptide and of conformations in which this H-bond is lost. We note that the H-bonds are formed for ∼100 fs before breaking again. The $NH_3^+\cdots$O=C H-bond is therefore not energetically strong. As a consequence of the rotation of the NH_3^+, there is formation and breaking of a hydrogen bond between NH_3^+ and the neighboring C=O carbonyl located at the N-terminal of the chain. These two H-bonds can be viewed, on average, to replace each other, while the NH_3^+ rotates. The N-terminal C=O does not form a H-bond with the C-terminal amide N−H, as they are on average apart from each other by ∼2.8 Å. Variations are observed for the dihedral angles around the central N−C_α and C_α−C bonds (variations by ∼60°), which indicate that the skeleton of the folded Ala_3H^+ presumably tries (unsuccessfully) to slightly unfold.

Methyl groups rotate freely along all the dynamics performed, with the amplitude of the $(H_3)C-C_\alpha-C-N$ dihedral angles varying by up to ∼80°. All the peptide groups remain in their trans orientation along all the simulations. The trans/cis peptide bond isomerization barrier is generally estimated as a few tens of kcal.mol $^{-1}$,[32,43,44] and it is too high to be observed spontaneously at the temperatures of the dynamics of the present work.

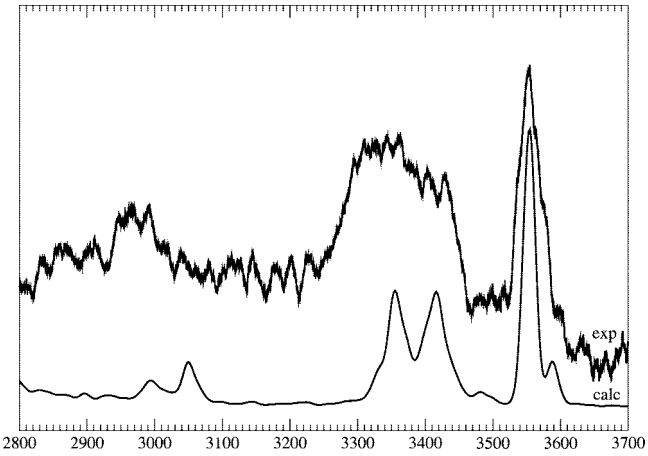

Figure 4. Comparison of the experimental infrared spectrum of Ala_2H^+ (top, from ref 13) and the calculated spectra from DFT-based Born−Oppenheimer dynamics at room temperature (bottom).

Infrared Spectroscopy

Infrared Spectroscopy of Ala_2H^+. The infrared spectrum of the gas phase Ala_2H^+ calculated from our trajectories, superimposed with the experiment, is presented in Figure 4. The theoretical spectrum has been averaged over the three trajectories performed in this work, corresponding to a total of 30 ps dynamics.

It must be emphasized that each of the three dynamics gives different individual active IR features of the protonated dipeptide, depending on the underlying dynamical behavior of the molecule, e.g., depending on the relative population of transA1 or transA2 conformations explored along the trajectories, or the appearance of transO1 conformations along the trajectories. Temperature and conformational dynamics naturally give rise to the breadth of the vibrational bands, without applying any empirical model. Note that the intensities of the calculated bands have been normalized with respect to the experimental 3560 cm^{-1} band. We can see that our calculation then reproduces the intensities of the two other bands very well, even though the linear IR theoretical signal and the IR-MPD experimental signal are not fully comparable, see the Introduction. Our calculations do not make any assumptions about harmonic modes or harmonic dipoles: all anharmonicities are naturally taken into account in the theoretical spectrum. Furthermore, no frequency scaling factors nor translations have been applied to the calculated spectrum. The remaining band shifts with respect to experiment are therefore the result of a combination of the ab initio method (DFT) and the basis set (DZVP) used.

The band located at 3560 cm^{-1} corresponds to the O−H stretch of the C-terminal COOH group of the dipeptide. The calculation matches the experimental band in terms of position and band shape. The shoulder located at ∼3590 cm^{-1} nicely reflects the feature present in the experimental spectrum.

The broadband located between 3300 and 3500 cm^{-1} (including the small feature at ∼3490 cm^{-1}) can be assigned

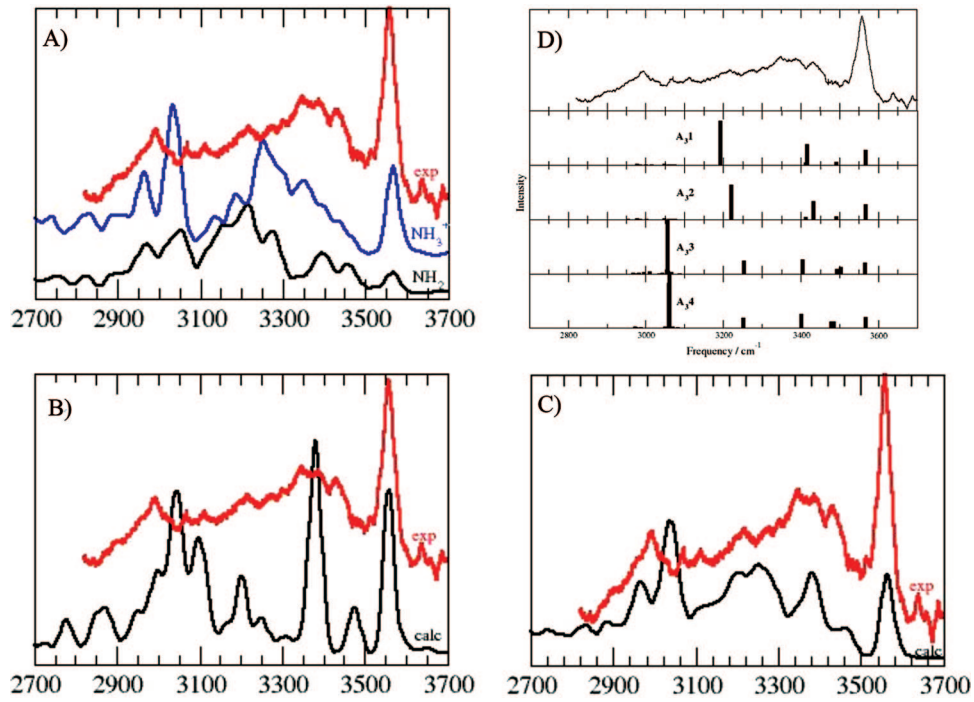

Figure 5. (A-C) Infrared spectra of Ala_3H^+ calculated from DFT-based Born−Oppenheimer dynamics. The spectra are plotted in relation to the conformational families of the tripeptide explored during the trajectories (see text for explanations). The spectra presented for each family have been averaged over the performed dynamics. A: NH_2 (black line) and NH_3^+ (blue line) families; B: folded family (black line); C: the final infrared spectrum of Ala_3H^+ (black line) averaged over all the trajectories performed in this work. Experiment (in red in all graphs) is from ref 13. D: Scaled harmonic frequencies obtained for the four optimized geometries of Ala_3H^+ as obtained in ref 13.

to the N−H stretches from the amide N−H group and from the free N−H groups of the NH_3^+ N-terminal. The symmetric and antisymmetric stretches of the free N−H of the NH_3^+ can be seen at 3415 and 3370 cm^{-1}, respectively, under the broad experimental band. The backbone amide N−H stretch also appears on the higher frequency part of the band, around 3415 cm^{-1}. Although the calculated band nicely reflects the two parts which can be observed in the experimental band, it is nonetheless not broad enough in comparison to the experiment. The breadth of the IR bands in molecular dynamics results from the temperature, conformational dynamics of the molecule, and anharmonicities. The difference observed here may be the signature that the temperature of the simulations is not high enough and that the experiments are indeed performed at a higher temperature. Interestingly, the IR signature of NH_3^+ that is hydrogen bonded to the neighboring C═O carbonyl throughout the simulations is spread over the broad 2500−2850 cm^{-1} region of the spectrum (not shown), thus strongly shifted down from the symmetric and antisymmetric modes of NH_3^+. Strong anharmonicity of the N−H···O═C hydrogen bond is responsible for the *displacement* of this band, whereas anharmonicity and the dynamics of the hydrogen bond at finite temperature are responsible for its *width*. Indeed, the N−H^+···O═C H-bond distance fluctuates by 0.3−0.4 Å around its mean value, and there is enough energy for the NH_3^+ group to rotate and exchange the hydrogen atom which can be hydrogen bonded to the neighboring carbonyl. These complex H-bond dynamics therefore lead to vibrational signatures which are spread over a large frequency domain. Note that our previous harmonic calculations[34] on Ala_2H^+ neglected this point. This is where finite-temperature molecular dynamics simulations are very useful for the calculation of vibrational spectra, as they are not restricted to the harmonic approximations of the modes.

The third double band of the IR spectrum in the investigated 2800−4000 cm^{-1} region is related to combined C_α−H and C−H stretch modes of the methyl groups of the peptide. These bands are shifted to higher frequency relative to the experiment by ∼40 cm^{-1}, and the band spacing between the two bands (∼50 cm^{-1}) is slightly bigger than the experimental one (∼30 cm^{-1}). It is nonetheless remarkable that our calculation predicts an intensity of the band so close to the experiment. Again, the harmonic calculation[34] does not give such intensity to this mode.

Infrared Spectroscopy of Ala_3H^+. Spectra of the protonated alanine tripeptide obtained from the ab initio trajectories are presented in Figure 5. The spectra are plotted in relation with the conformational families of the tripeptide explored during the trajectories: (*i*) the NH_2 family where the supplementary proton is located on the N-terminal carbonyl group, the N-terminal NH_2 displaying an equal population of conformations of weak H_2N···H−N hydrogen bonds and without any such hydrogen bonds, (*ii*) the NH_3^+ family where the supplementary proton is predominantly located on the N-terminal NH_3^+ but can transfer to the neighboring carbonyl during the dynamics, and (*iii*) the folded family where the peptide chain is folded through a weak NH_3^+···O═C H-bond, which has been shown to break/reform during the dynamics. The spectra presented for each family have been averaged over the corresponding dynamics

(apart from family (*iii*) where only one trajectory has been performed). See Figure 5-A and -B for the results presented individually for each family. The final spectrum of Ala_3H^+, presented in Figure 5-C, has been averaged over all the trajectories performed for this molecule. Considering the production method of the ions in the associated experiments, which certainly does not follow a thermalized Boltzmann distribution, such an average in the calculation appears reasonable. In the following, we will mainly concentrate our discussion on the band-positions and the band-shapes of the theoretical spectra in comparison to the experimental spectrum, as again intensities of the calculated spectra and the experimental IR-MPD signals are not strictly identical.

As has already been emphasized for the protonated dipeptide, each dynamics within a conformational family gives different individual active IR features, depending on the underlying dynamical behavior of the molecule at the temperature of the simulations (room temperature and above). At finite temperature, the statistical average of the spectra is meaningful and can thus be compared to the spectrum recorded in the experiment. Temperature and the conformational dynamics of the peptide will induce the broadening of the vibrational bands. Vibrational anharmonicities explored at this temperature, i.e. anharmonicity from the potential energy surface and from the molecular dipole, will induce band shifts and also participate in the broadening of the bands.

The experimental spectrum[13] is reported in all figures. All the spectra display the same vibrational patterns that will be discussed below, whatever the tripeptide family they are related to. The position, intensity, and shape of the individual bands will slightly change depending on the trajectory and the Ala_3H^+ family that is concerned, but the assignments of the bands are maintained. In the following, we discuss the bands of the average spectrum (Figure 5-C) and extract the vibrational assignments from the individual trajectories.

The band located at 3560 cm^{-1} corresponds to the O−H stretch of the C-terminus. As expected from the similar dynamical behavior of the COOH of the protonated dipeptide and tripeptide, this band is located in an identical position for the two peptides. Moreover, the slight asymmetry of this band is correctly reproduced by the calculations.

Based on the band assignments, the 3100−3500 cm^{-1} region can be separated into two parts. The 3300−3500 cm^{-1} frequency region is assigned to the stretches of the N−H groups of the tripeptide not involved in hydrogen bonds along the dynamics, i.e. the symmetric and antisymmetric stretch of the N-terminal amine NH_2, the stretches of the free N−H of the protonated N-terminal NH_3^+, and the stretches of the C-terminal amide N−H. The 3100−3300 cm^{-1} frequency domain is entirely related to the stretching bands of the N-terminal amide N−H group. As previously described, this amide group can be weakly hydrogen bonded to the amine N-terminal in the NH_2 tripeptide family (through a distorted H-bond) and also weakly hydrogen bonded to the C-terminal carbonyl of the peptide in the NH_3^+ family (again distorted H-bond because of steric hindrances). These H-bonds are therefore strong enough to induce the shift toward lower energy of the N-terminal N−H stretch in comparison to the positions of the free N−H groups. Note that the weak attraction of the N-terminal N−H with the carbonyl COOH extremity (over parts of the dynamics) is not strong enough to induce such a shift.

The 3300−3500 cm^{-1} part of the spectrum calculated for the NH_3^+ family is shapeless in comparison to the spectrum of the NH_2 family (Figure 5-A). In this later case, two nonoverlapping active bands can indeed be observed. As a consequence, the 3300−3500 cm^{-1} region of the experimental spectrum is better explained by the spectrum of the NH_2 family of the Ala_3H^+ peptide than by the spectrum of the NH_3^+ family. In contrast, the N-terminal N−H 3100−3300 cm^{-1} frequency domain is better explained by the superposition of spectra coming from the two families. This region is indeed composed of four main peaks that are organized within the same overall patterns in both NH_2 and NH_3^+ families of Ala_3H^+ (with the two higher frequency bands displaying higher intensities than the two lower frequency bands) but with significant band shifts. Hence, the bands of the NH_2 family are down shifted from the bands of the NH_3^+ family, by ∼80−100 cm^{-1} for the two higher frequency bands and by ∼30−40 cm^{-1} for the two lower frequency bands. As a consequence of these band shifts, the superposition of these bands in the final spectrum of Ala_3H^+ presented in Figure 5-C gives rise to a broadband where numerous subpeaks can be seen, nicely in agreement with the experimental vibrational patterns in the 3100−3300 cm^{-1} frequency region.

Though the band positions and band shapes of the spectrum of the folded Ala_3H^+ in the 3100−3500 cm^{-1} domain are different from the two unfolded families (note that there is only one dynamics acquired for the folded tripeptide versus three or four dynamics for each unfolded NH_2/NH_3^+ family, which could participate to these differences), their assignments follow the same lines as for the other two families, i.e. free N−H signatures at higher frequencies and H-bonded N−H signatures at lower frequencies. Note that all skeleton amide N−H stretches participate to the 3480 cm^{-1} band in the spectrum, while the free N−H of NH_3^+ give rise to the 3380 cm^{-1} band (Figure 5-B). The four peaks observed in the 3300−3100 cm^{-1} domain are related to the N−H group of NH_3^+ that was identified as forming a hydrogen bond with the neighboring N-terminal C═O group during the dynamics. This is different from the unfolded families and could be the reason for the different band shapes and intensities of the four bands in comparison to the four bands calculated for the unfolded families.

The final calculated spectrum presented in Figure 5-C, as the addition of the spectra of all families, i.e. unfolded/folded and NH_2/NH_3^+ N-terminus, therefore gives rise to several separate vibrational patterns of the N−H stretching motions, i.e. distinguishable subpeaks, which are in good agreement with the experiment. The overall shape is well reproduced by our calculations. The complex vibrational patterns of this large band are therefore a result of the local dynamics of the N−H groups in the different Ala_3H^+ families, in particular the dynamics of the H-bonded N−H which are different within the tripeptide families.

The 2800−3100 cm^{-1} domain is assigned to the C−H stretches arising from the methyls and the C_α−H groups of the tripeptide. Both CH_3 and C_α−H groups systematically participate in the two bands. All spectra calculated for all Ala_3H^+ families display two main intense bands located between 2900 and 3100 cm^{-1}, followed by a low intensity tail at lower frequency. Our final calculated spectrum therefore displays these properties in the 2800−3100 cm^{-1} domain, while a more featureless band can be observed in the experiment in the same region. There are nonetheless subpeaks that can be distinguished in the experiment which may be related to the separate peaks we obtain in our calculation. Note that these bands are shifted to higher frequency by ∼40 cm^{-1} with respect to the experiment.

As already observed for the Ala_2H^+ dipeptide, the vibrational signatures of NH_3^+ that are hydrogen bonded to the neighboring carbonyl in the NH_3^+ tripeptide family are strongly shifted to lower frequency compared to the other N−H stretches and appear over the extended 2000−2800 cm^{-1} domain. This breadth is entirely due to the vibrational anharmonicities and dynamics of the $N-H^+\cdots O{=}C$ H-bond at the finite temperature of the NH_3^+ family dynamics. Remarkably, the stretching of the protonated C−O−H in the NH_2 family is superimposed on the N−H^+ stretches of the NH_3^+ tripeptide family. It is therefore unfortunately not possible to distinguish both families using the stretching patterns of the H-bonded N−H^+ or C−O−H groups of the peptide, and it is also not possible to give a definite answer as to the location of the supplementary proton along the tripeptide chain. The strong frequency shifts result from the strong anharmonicities of these H-bonds.

The final spectrum of Ala_3H^+ calculated from the dynamics and presented in Figure 5-C agrees well with the experimental spectrum (regardless of band intensities that are indeed expected to give discrepancies). The 3560 cm^{-1} O−H stretch band of the C-terminal COOH of the Ala_3H^+ peptide is perfectly located at the experimental band position with a similar, slightly asymmetrical band-shape. The 3100−3500 cm^{-1} domain of the N−H stretching motions is overall well reproduced in our calculations, although displaying certain discrepancies with the experiment. The extent of the N−H stretch domain calculated here is identical to the experiment. The calculated 3300−3500 cm^{-1} higher frequency part is composed of a shoulder located at 3475 cm^{-1} which is located very close to the 3485 cm^{-1} shoulder in the experiment and a broadband located at 3390 cm^{-1} with a shoulder of low intensity at 3345 cm^{-1}. These two last bands correspond to the 3390 cm^{-1} and 3350 cm^{-1} bands in the experiment, though the 3350 cm^{-1} band is definitely more intense (but again, the calculated and experimental signals are not identical for intensities). Note that the appearance of the 3350 cm^{-1} shoulder in the final spectrum is entirely due to the active mode in the spectrum of the NH_3^+ family. The intense experimental 3435 cm^{-1} band unfortunately does not have a comparable intensity in our calculation. Instead, we have a shoulder located between 3430−3470 cm^{-1} in the final calculated spectrum: the low intensity of this band in our calculation arises from the average of the IR spectra of the NH_2 and NH_3^+ families, where this region has a featureless shape and intensity for the NH_3^+ family, ultimately leading here to the decrease of the intensities of the bands arising from the NH_2 family. The 3100−3300 cm^{-1} lower frequency part of the N−H stretch region displays the same broadband as in the experiment with the appearance of the characteristic subpeaks observed in the experiment. The four main subpeaks that can be distinguished in the experiment (∼3270, 3220, 3120, and 3075 cm^{-1}) can also be found in our calculation (∼3260, 3210, 3145, and 3115 cm^{-1}). Two of the frequencies are therefore only downshifted by 10 cm^{-1} from their experimental counterparts, while the two lower frequencies are shifted to higher frequency by 25−40 cm^{-1}. The double bands and low intensity tail calculated for the C−H stretches in the 2900−3100 cm^{-1} domain are shifted by +40 cm^{-1} from the experiment and are more structured than the experimental bands.

In Figure 5-D, we have reported the scaled harmonic spectra obtained from our previous investigation[13] for the four optimized geometries of lowest energy of Ala_3H^+. As can be immediately observed, the N−H broadband of the experimental spectrum is systematically associated with only two main intense harmonic bands, grossly separated by 200 cm^{-1} and 150 cm^{-1}, respectively, for the NH_2 and NH_3^+ families; hints of a third band located close to the ∼3490 cm^{-1} experimental band can also be seen, with a very low intensity. With these harmonic normal modes, the highest frequencies are related to free N−H groups of the optimized geometries and the lowest frequencies to the hydrogen-bonded backbone N−H. Though these interpretations roughly agree with what has been obtained in the present work from molecular dynamics simulations, one should admit that the IR spectrum extracted here from MD does offer vibrational details in the 3100−3500 cm^{-1} N−H domain that are completely missed by the harmonic calculations, even when adding the four harmonic spectra of Figure 5-D. Last but not least, C−H harmonic modes predicted around 3000 cm^{-1} have no intensity, while the anharmonic spectrum extracted from MD correctly predicts the intensity in this region.

The interpretation given here from MD simulations that the broad and complex N−H vibrational band comes from the intrinsic local dynamics of the N−H groups in the different conformers/isomers of Ala_3H^+, and in particular the breaking/forming of N−H hydrogen bonds, can only be achieved when performing molecular dynamics simulations. Scaled harmonic spectra will never be able to give a definite conclusive interpretation. Moreover, C−H band intensities do not show up correctly with harmonic spectra, while they are correctly obtained through anharmonic molecular dynamics.

Conclusions

We have chosen the two prototype small protonated polyalanines Ala_2H^+ and Ala_3H^+ in order to demonstrate that the peptides dynamical features should be taken into account to obtain a precise understanding of the relation between IR-MPD experimental features obtained at finite temperature and the underlying molecular structural and dynamical properties, including vibrational anharmonicities. We found that the spectra of Ala_2H^+ and Ala_3H^+ calculated from the

DFT-based Born−Oppenheimer dynamics performed in this work are in very good agreement with the experiments (Figures 4 and 5). We recall that no scaling factors nor translations have been applied to the calculated spectra. Once more, we recall that calculated and recorded IR-MPD intensities are not strictly comparable. Our calculations give an interpretation of the recorded vibrational patterns in terms of the dynamics of the gas-phase peptides at finite temperature.

In the case of Ala_2H^+, the conformational dynamics between two conformers of the peptide that mainly differ by a rotation of the COOH C-terminus is responsible for the broad bands in the NH/OH vibrational region. Though α_L/α_R conformational dynamics has been observed for the Ala_3H^+ peptide (when increasing the temperature of the dynamics), it does not have any influence in the N−H/O−H vibrational region. Instead, the local dynamics of the N-terminal backbone amide N−H group does give rise to the complex 3100−3500 cm^{-1} broad IR band, involving forming and breaking of hydrogen bonds at finite temperature. This cannot be grasped by static harmonic calculations as demonstrated by the comparison between harmonic static vibrational spectra and anharmonic dynamical spectra. This adds up to our previous works[12,14,15] where similar conclusions have already been reached. Though the static harmonic spectra may be useful in grossly establishing the "general" conformational features of the Ala_3H^+ protonated peptide from the N−H/O−H vibrational region, it fails in giving a convincing understanding of the complex N−H vibrational band in relation to the peptide conformation. Such understanding is only achieved when the dynamics of the peptide is taken into account. There are still some discrepancies though between the final spectrum extracted from the dynamics and the IR-MPD experimental signal, but we feel that the present work demonstrates once more the real need for the use of molecular dynamics simulations in order to interpret vibrational spectroscopy experiments performed at finite temperature.

We have shown that the calculated O−H stretch band of the C-terminal extremety of the Ala_2H^+ and Ala_3H^+ alanine peptide perfectly matches the experiments. This band is commonly located in both peptides as a result of the free O−H group dynamics in both molecules (not H-bonded). The calculated N−H band of Ala_2H^+ lacks part of the broadness of the experimental band (approximately half the width of the experiment), while the one of Ala_3H^+ reflects the more complex experimental features. The experimental N−H band encompasses the 3300−3500 cm^{-1} domain for Ala_2H^+ and extends to the 3100−3500 cm^{-1} domain for Ala_3H^+. As demonstrated with our dynamics, the 3300−3500 cm^{-1} frequency domain contains the stretching motions of free N−H groups within the di- and tripeptide and displays the same general shape for both peptides, i.e. showing two main subpeaks. In going from Ala_2H^+ to Ala_3H^+, the dynamics of the slightly hydrogen bonded N-terminal amide N−H group gives rise to the 3300−3500 cm^{-1} band. As we have shown, the subpeaks which make up this 200 cm^{-1} large band originate from weak interactions between the N-terminal and the neighboring amide N−H group and reflect the diversity of the local dynamics of the N−H H-bonding patterns within the different families of the tripeptide. This gives rise to different band positions of this amide N−H stretch, thus forming the numerous subpeaks that can be observed in both the experiment and the calculation. We have thus shown that the dynamics of the H-bonded N-terminal amide N−H give rise to the numerous subpeaks arising in the lower frequency part. This is in contrast with the results of Rizzo et al.[9] on longer peptide chains obtained at very low temperature (∼10−20 K), where the individual signatures of each N−H group along the chain can be distinguished among the vibrational signatures.

Band shapes are very well reproduced by our calculations. The slight asymmetry of the O−H band of Ala_3H^+ is obtained as well as the shoulder at high frequency of Ala_2H^+. More remarkably, the band shape of the N−H vibrations is very well generated by our calculations (though not broad enough for Ala_2H^+) and has no equivalence from the harmonic calculations (see for instance refs 13 and 34 and Figure 5-D in the present work). This is due to the natural broadening arising from the finite temperature of the calculations, the conformational dynamics of the molecules in the simulations, and all anharmonicities which are naturally taken into account in the present calculations. Unfortunately, the 3000 cm^{-1} C−H stretch band obtained from the calculations is composed of two separate bands (Ala_2H^+ and Ala_3H^+), while a more compact and shapeless band is observed in the experiments. The position of this band is also systematically shifted by ∼+40 cm^{-1} in our calculations. Interestingly, the anharmonic dynamics performed here give rise to an infrared active C−H band, while harmonic calculations predict no intensity.[13,34]

The final spectrum of Ala_3H^+ has been calculated as the sum of the individual spectra (each one averaged over a few dynamics) from three different peptide families. This summation is essential for the understanding of the broad and complex N−H band. If the 3300−3500 cm^{-1} region of this band may be more easily understood solely from the dynamics of the NH_2 family, this does not hold true for the 3100−3300 cm^{-1} region. There, the combination of signatures arising from the NH_2 and NH_3^+ families (including the folded one) is pivotal to get the long and more shapeless tail composed of subpeaks.

The present DFT-based BO molecular dynamics demonstrate once more the importance of taking into account *in a direct way* the finite temperature dynamics of flexible gas-phase peptides, in order to calculate and interpret gas-phase infrared spectra that are recorded at temperatures of 300−400 K. In the present investigation of Ala_2H^+ and Ala_3H^+, the dynamics are pivotal in relation to the N−H stretching motions. Taking into account the dynamics of the peptides directly allows understanding of the evolution of the shape and width of the N−H bands when increasing the size of the peptide. Our experiments[13] show that the N−H stretch domain continues to evolve with the increase of the peptide chain length, indicating, in view of the present calculations, that there is a change in the dynamics of the N−H amide groups for the longer chains, which is essential to understand in order to get a precise and definite picture of the

conformational dynamics of the gas-phase peptide. This is where our combined experiments and calculations are heading.

Acknowledgment. A.C. and M.-P.G. thank IDRIS (Orsay, France) for generous access to their computational facilities. M.-P.G. acknowledges support from Genopole-France through the program 'ATIGE' Action Thématique Incitative de Génopole. A.C. and M.-P.G. acknowledge the help of the group of J. Hutter for their help with the CP2K code. We are grateful to the Royal Society for a USA/Canada Research Fellowship (T.D.V.) and a University Research Fellowship (L.C.S.), to The Leverhulme Trust (T.B., L.C.S., Grant F/08788G), and to Linacre College (T.D.V.) and Corpus Christi College, Oxford (T.B., L.C.S.) for support.

Supporting Information Available: Details on the DFT-based molecular dynamics simulations performed in this work. This material is available free of charge via the Internet at http://pubs.acs.org.

References

(1) Graf, J.; Nguyen, P. H.; Stock, G.; Schwalbe, H. *J. Am. Chem. Soc.* **2007**, *129*, 1179.

(2) Hamm, P.; Helbing, J.; Bredenbeck, J. *Annu. Rev. Phys. Chem.* **2008**, *59*, 291.

(3) Woutersen, S.; Hamm, P. *J. Phys. Chem. B* **2000**, *104*, 11316.

(4) Abo-Riziq, A.; Crews, B. O.; Callahan, M. P.; Grace, L.; de Vries, M. S. *Angew. Chem., Int. Ed.* **2006**, *45*, 5166.

(5) Brenner, V.; Piuzzi, F.; Dimicoli, I.; Tardivel, B.; Mons, M. *J. Phys. Chem. A* **2007**, *111*, 7347.

(6) Chin, W.; Piuzzi, F.; Dimicoli, I.; Mons, M. *Phys. Chem. Chem. Phys.* **2006**, *8*, 1033.

(7) Chin, W.; Dognon, F. P. J. P.; Dimicoli, I.; Tardivel, B.; Mons, M. *J. Am. Chem. Soc.* **2005**, *127*, 11900.

(8) de Vries, M. S.; Hobza, P. *Annu. Rev. Phys. Chem.* **2007**, *58*, 585.

(9) Stearns, J. A.; Boyarkin, O. V.; Rizzo, T. R. *J. Am. Chem. Soc.* **2007**, *129*, 13820.

(10) Chellgren, B. W.; Creamer, T. P. *Proteins* **2006**, *62*, 411.

(11) Polfer, N. C.; Oomens, J.; Suhai, S.; Paizs, B. *J. Am. Chem. Soc.* **2007**, *129*, 5887.

(12) Grégoire, G.; Gaigeot, M.; Marinica, D.; Lemaire, J.; Schermann, J.; Desfrançois, C. *Phys. Chem. Chem. Phys.* **2007**, *9*, 3082.

(13) Vaden, T. D.; de Boer, T. S. J. A.; Simons, J. P.; Snoek, L. C.; Suhai, S.; Paizs, B. *J. Phys. Chem. A.* **2008**, *112*, 4608.

(14) Marinica, C.; Grégoire, G.; Desfrançois, C.; Schermann, J.; Borgis, D.; Gaigeot, M.-P. *J. Phys. Chem. A* **2006**, *110*, 8802.

(15) Gaigeot, M.-P. *J. Phys. Chem. A* **2008**, *112*, 13507.

(16) Allen, M.; Tildesley, D. *Computer simulation of liquids*; Oxford Science Publications: 1997.

(17) Frenkel, D.; Smit, B. *Understanding molecular simulations*, 2nd edition; Academic Press: 2002.

(18) McQuarrie, D. *Statistical Mechanics*; Harper-Collins Publishers: New York, 1976.

(19) Vuilleumier, R.; Borgis, D. *J. Chem. Phys.* **1999**, *111*, 4251.

(20) Tassaing, T.; Danten, Y.; Besnard, M.; Zoidis, E.; Yarwood, J.; Guissani, Y.; Guillot, B. *Mol. Phys.* **1995**, *84*, 769.

(21) Guillot, B. *J. Chem. Phys.* **1991**, *95*, 1543.

(22) Glover, W.; Madden, P. *J. Chem. Phys.* **2004**, *121*, 7293.

(23) Pavlatou, E.; Madden, P.; Wilson, M. *J. Chem. Phys.* **1997**, *107*, 10446.

(24) Madden, P.; Impey, R. *Chem. Phys. Lett.* **1986**, *123*, 502.

(25) Silvestrelli, P.; Parrinello, M. *J. Chem. Phys.* **1999**, *111*, 3572.

(26) Silvestrelli, P.; Bernasconi, M.; Parrinello, M. *Chem. Phys. Lett.* **1997**, *277*, 478.

(27) Bernasconi, M.; Silvestrelli, P.; Parrinello, M. *Phys. Rev. Lett.* **1998**, *81*, 1235.

(28) Gaigeot, M.-P.; Sprik, M. *J. Phys. Chem. B* **2003**, *107*, 10344.

(29) Gaigeot, M.-P.; Vuilleumier, R.; Sprik, M.; Borgis, D. *J. Chem. Theory Comput.* **2005**, *1*, 772.

(30) Gaigeot, M.; Martinez, M.; Vuilleumier, R. *Mol. Phys.* **2007**, *105*, 2857.

(31) Wu, R.; McMahon, T. B. *J. Am. Chem. Soc.* **2007**, *129*, 11312.

(32) Lucas, B.; Gregoire, G.; Lemaire, J.; Maitre, P.; Ortega, J.; Rupenyan, A.; Reimann, B.; Schermann, J.; Desfrancois, C. *Phys. Chem. Chem. Phys.* **2004**, *6*, 2659.

(33) MacLeod, N. A.; Simons, J. P. *Mol. Phys.* **2007**, *105*, 689.

(34) Vaden, T. D.; de Boer, T. S. J. A.; MacLeod, N. A.; Marzluff, E. M.; Simons, J. P.; Snoek, L. C. *Phys. Chem. Chem. Phys.* **2007**, *9*, 2549.

(35) Vaden, T. D.; de Boer, T. S. J. A.; Simons, J. P.; Snoek, L. C. *Phys. Chem. Chem. Phys.* **2008**, *10*, 1443.

(36) VandeVondele, J.; Krack, M.; Mohamed, F.; Parrinello, M.; Chassaing, T.; Hutter, J. *Comput. Phys. Commun.* **2005**, *167*, 103.

(37) *The CP2K developers group*. http://cp2k.berlios.de/.

(38) Becke, A. *Phys. Rev. A* **1988**, *38*, 3098.

(39) Lee, C.; Yang, W.; Parr, R. *Phys. Rev. B* **1988**, *37*, 785.

(40) Krack, M. *Theor. Chem. Acc.* **2005**, *114*, 145.

(41) Goedecker, S.; Teter, M.; Hutter, J. *Phys. Rev. B* **1996**, *54*, 1703.

(42) Hartwigsen, C.; Goedecker, S.; Hutter, J. *Phys. Rev. B* **1998**, *58*, 3641.

(43) Fischer, G. *Chem. Soc. Rev.* **2000**, *29*, 119.

(44) Mantz, Y.; Gerard, H.; Iftimie, R.; Martyna, G. *J. Am. Chem. Soc.* **2004**, *126*, 4080.

CT900057S

JCTC Journal of Chemical Theory and Computation

Exact Analytic Result of Contact Value for the Density in a Modified Poisson−Boltzmann Theory of an Electrical Double Layer

Ping Lou[†,*,‡] and Jin Yong Lee[*,‡]

Department of Chemistry, Sungkyunkwan University, Suwon 440-746, Korea, and Department of Physics, Anhui University, Hefei 230039, Anhui, P. R. China

Received September 8, 2008

Abstract: For a simple modified Poisson−Boltzmann (SMPB) theory, taking into account the *finite ionic size*, we have derived the exact analytic expression for the contact values of the difference profile of the counterion and co-ion, as well as of the sum (density) and product profiles, near a charged planar electrode that is immersed in a binary symmetric electrolyte. In the *zero ionic size* or *dilute* limit, these contact values reduce to the contact values of the Poisson−Boltzmann (PB) theory. The analytic results of the SMPB theory, for the difference, sum, and product profiles were compared with the results of the Monte-Carlo (MC) simulations [Bhuiyan, L. B.; Outhwaite, C. W.; Henderson, D. *J. Electroanal. Chem.* **2007**, *607*, 54; Bhuiyan, L. B.; Henderson, D. *J. Chem. Phys.* **2008**, *128*, 117101], as well as of the PB theory. In general, the analytic expression of the SMPB theory gives better agreement with the MC data than the PB theory does. For the difference profile, as the electrode charge increases, the result of the PB theory departs from the MC data, but the SMPB theory still reproduces the MC data quite well, which indicates the importance of including steric effects in modeling diffuse layer properties. As for the product profile, (i) it drops to *zero* as the electrode charge approaches *infinity*; (ii) the speed of the drop increases with the *ionic size*, and these behaviors are in contrast with the predictions of the PB theory, where the product is identically 1.

Introduction

Exact relations are always interesting per se from a theoretical perspective. Besides, they aid theoretical development by serving as checks and can be useful tools in assessing different theories. In the theory of an electrical double layer, such relations are the so-called *contact theorems*.[1−4] For example, for a binary symmetric electrolyte with ion diameter a, assuming that the planar electrode has a negative charge, the contact values of the density,[1,2] charge,[3−5] and product[3,4] profiles are given by[1,3,4,6]

$$g_{\mathrm{sum}}(a/2) = \alpha + \frac{b^2}{2} \tag{1}$$

$$g_{\mathrm{diff}}(a/2) = \mathscr{J} + \frac{b^2}{2} \tag{2}$$

and

$$g_-(a/2)g_+(a/2) = \alpha^2 - \mathscr{J}^2 + b^2(\alpha - \mathscr{J}) \tag{3}$$

respectively, where $g_{\mathrm{sum}}(x) = 1/2[g_+(x) + g_-(x)]$ and $g_{\mathrm{diff}}(x) = 1/2[g_+(x) - g_-(x)]$, with the subscripts sum and diff denoting sum and difference. $g_-(x)$ and $g_+(x)$ are the singlet distribution functions for the co-ions (ions with same sign as the surface charge of the electrode) and the counterions (ions with opposite sign to the surface charge of the electrode), respectively. $\mathscr{J} = -\beta z e \int_{a/2}^{\infty} \mathrm{d}x\, [\partial\psi(x)/\partial x] g_-(x)$, where $\psi(x)$ is the electrostatic potential. $b = 2\pi\beta\sigma^2/c_b\varepsilon$ is

* Corresponding author e-mail: loup@ahu.edu.cn (P.L.); jinylee@skku.edu (J.Y.L.).

† Sungkyunkwan University.

‡ Anhui University.

10.1021/ct800375t CCC: $40.75
Published on Web 03/11/2009

the dimensionless electrode charge density, whose dimensioned value is σ.[7] $\alpha = \beta P/2c_b$ and is the osmotic coefficient of the bulk electrolyte, and P the bulk electrolyte pressure. $\beta = 1/k_BT$ (k_B is the Boltzmann constant and T the absolute temperature). e, z, c_b, and ε are the elementary charge, the absolute value of the valence of an ion, the bulk concentration of the ions, and the dielectric constant, respectively. It should be mentioned that the contact value of eq 1 is also valid for an asymmetric electrolyte, which was first derived by Henderson et al.[1]

Recently Bhuiyan et al. examined the contact values of the profiles of the double layer formed by the electrolyte species in a binary symmetric restricted primitive model (RPM) electrolyte next to a planar electrode by means of the Monte Carlo (MC) simulation. They focused on the product profile, instead of the density profile or the charge profile. Because, at large electrode charge, the contact values of these profiles are dominated by the large quadratic term in the electrode charge, it is difficult to extract detailed information from the simulations. Note that in the Poisson−Boltzmann (PB) theory, the counterion and co-ion profiles are exponentials of $\exp[\pm ze\psi(x)/k_BT]$,[8] so its product is identically 1.[7] However, they found that the MC simulation value is not 1 nor even a constant as the electrode charge is varied. The product profile of PB prediction does not agree qualitatively with the simulation result.[7] This is a direct test of the basis of the PB theory.

On the other hand, the finite ionic size may play an important role in a concentrated solution. Since Bikerman[9] first showed that the deviation of the distribution function from Boltzmann's function takes into account the proper volume of the ions, there followed a lot of works.[9−23] For a very comprehensive review of previous works, excellent recent papers[21,22] should be referred to. The simple modified Poisson−Boltzmann (SMPB) model of Kornyshev[23] and Kilicet al.[21,22] for steric effects in electrolytes has been reinvented many times by Borukhov et al.,[15,16] Iglic,[14] and Eigen and Wicke,[12] and also by Dutta.[10] Thus, the following question arises: Can the SMPB theory reproduce Bhuiyan, Outhwaite, and Henderson's MC data?[7] This will give a direct test of the basis of the SMPB theory.

Model and Theory

On the basis of mean-field theory together with the lattice-gas approximation in statistical mechanics,[15,16] the phenomenological free energy of a general electrolyte system can be written as[15,16,24]

$$\Omega = \frac{\varepsilon}{8\pi}\int d^3\mathbf{r}\,(\nabla\psi(\mathbf{r}))^2 - \int d^3\mathbf{r}\sum_i^m \mu_i c_i(\mathbf{r}) + \frac{k_BT}{a^3}\int d^3\mathbf{r}\left[\left(1 - \sum_i^m c_i(\mathbf{r})a^3\right)\times \ln\left(1 - \sum_i^m c_i(\mathbf{r})a^3\right) + \sum_i^m c_i(\mathbf{r})a^3 \ln\left(c_i(\mathbf{r})a^3\right)\right] + \int d^3\mathbf{r}\,\lambda(\mathbf{r}) + \frac{4\pi}{\varepsilon}\sum_i^m e z_i c_i(\mathbf{r}) \quad (4)$$

where $c_i(\mathbf{r})$, μ_i, and z_i are the local concentration, the chemical potential, and the valence of the ionic species i (i = 1,..., m), respectively. a is the effective size of the ions and solvent molecules. The term $(k_BT)/a^3\int d^3\mathbf{r}\,(1 - \sum_i^b c_i(\mathbf{r})a^3)\ln(1 - \sum_i^m c_i(\mathbf{r})a^3)$ is the entropy of the solvent molecules that is responsible for the steric corrections to the PB equation.[15,16]

The last two terms in eq 4, containing the Lagrange multiplier $\lambda(\mathbf{r})$, allow us to regard the local concentration, $c_i(\mathbf{r})$, and the electrostatic potential, $\psi(\mathbf{r})$, as independent fields. Following the method in ref 24 we can obtain

$$\nabla^2\psi(\mathbf{r}) = -\frac{4\pi e}{\varepsilon}\sum_i^m z_i c_i(\mathbf{r}) \quad (5)$$

with

$$c_i(\mathbf{r}) = \frac{c_{ib}\exp(-\beta e z_i\psi(\mathbf{r}))}{1 - \sum_i^m c_{ib}a^3 + \sum_i^m c_{ib}a^3\exp(-\beta e z_i\psi(\mathbf{r}))} \quad (6)$$

where i = 1,..., m and c_{ib} is the bulk concentration of the ionic species i. Equations 5 and 6 are the SMPB equations. Notice that in the *zero size* ($a \to 0$) or *dilute* limit ($c_{ib} \to 0$), eqs 5 and 6 are reduced to the PB equation.[8] It should be pointed out that just like the PB equation, eqs 5 and 6 can be applied to any geometry and boundary conditions.

Here, for comparison with the results of the MC simulations of Bhuiyan et al.,[7] we also consider a binary symmetric electrolyte and assume, without loss of generality, that the planar electrode has a negative charge. Thus, we have m = 2, $z_1 = z$, $z_2 = -z$, $c_{1b} = c_{2b} = c_b$, and eqs 5 and 6 are reduced to

$$\frac{d^2\psi(x)}{dx^2} = \frac{8z\pi e c_b}{\varepsilon}\frac{\sinh(ze\beta\psi(x))}{1 + 2\rho^*\sinh^2\left(\frac{ze\beta\psi(x)}{2}\right)} \quad (7)$$

where $\rho^* = 2c_ba^3$ is the reduced density, and x is the perpendicular distance of the ion from the electrode surface. The singlet distribution functions for the counterions and the co-ions, which are calculated by $g_+(x) = c_1(x)/c_b$ and $g_-(x) = c_2(x)/c_b$, are given by

$$g_+(x) = \frac{\exp(ze\beta\psi(x))}{1 + 2\rho^*\sinh^2\left(\frac{ze\beta\psi(x)}{2}\right)} \quad (8)$$

and

$$g_-(x) = \frac{\exp(-ze\beta\psi(x))}{1 + 2\rho^*\sinh^2\left(\frac{ze\beta\psi(x)}{2}\right)} \quad (9)$$

respectively.

Then, the difference profile $\{^1/_2[g_+(x) - g_-(x)]\}$ is given by

$$g_{diff}(x) = \frac{\sinh(ze\beta\psi(x))}{1 + 2\rho^*\sinh^2\left(\frac{ze\beta\psi(x)}{2}\right)} \quad (10)$$

The sum profile $\{^1/_2[g_+(x) + g_-(x)]\}$ is given by

$$g_{\mathrm{sum}}(x) = \frac{\cosh(ze\beta\psi(x))}{1 + 2\rho^* \sinh^2\left(\frac{ze\beta\psi(x)}{2}\right)} \tag{11}$$

It should be pointed out that the sign of the charge of the electrode is immaterial to the definition of $g_{\mathrm{diff}}(x)$. However, for the sake of definiteness, we have assumed that the electrode has a negative charge and $g_{\mathrm{diff}}(x)$ is either positive or mostly positive (with a positive area). Thus, the individual ion profiles are the sum (for the counterions) and difference (for the co-ions) of $g_{\mathrm{sum}}(x)$ and $g_{\mathrm{diff}}(x)$, i.e., $g_+(x) = g_{\mathrm{sum}}(x) + g_{\mathrm{diff}}(x)$ and $g_-(x) = g_{\mathrm{sum}}(x) - g_{\mathrm{diff}}(x)$.

The product profile is given by

$$g_-(x)g_+(x) = \frac{1}{\left[1 + 2\rho^* \sinh^2\left(\frac{ze\beta\psi(x)}{2}\right)\right]^2} \tag{12}$$

Following the trick in refs 21−23, i.e., integrating eq 7 using the boundary conditions $\psi(x)|_{x=a/2} = \psi_{\mathrm{D}}$, $\psi(x)|_{x\to\infty} = 0$, and $d\psi(x)/dx|_{x\to\infty} = 0$, we can get

$$\sigma = -\sqrt{\frac{c_{\mathrm{b}}\varepsilon}{\pi\beta\rho^*}}\sqrt{\ln\left[1 + 2\rho^* \sinh^2\left(\frac{ze\beta\psi_{\mathrm{D}}}{2}\right)\right]} \tag{13}$$

where $\sigma = -\varepsilon/4\pi\ d\psi(x)/dx|_{x=a/2}$ is the electrode charge density. Then, by combining eqs 10, 11, 12, and 13, it is easy to find that the full analytic expressions for $g_{\mathrm{diff}}(x)$, $g_{\mathrm{sum}}(x)$, and $g_+(x)g_-(x)$ at contact, $x = a/2$, are

$$g_{\mathrm{diff}}(a/2) = \frac{1}{\rho^*}\sqrt{\left[1 - \exp\left(-\frac{b^2}{2}\rho^*\right)\right]} \times \sqrt{\left[1 + (2\rho^* - 1)\exp\left(-\frac{b^2}{2}\rho^*\right)\right]} \tag{14}$$

$$g_{\mathrm{sum}}(a/2) = \frac{1}{\rho^*}\left[1 + (\rho^* - 1)\exp\left(-\frac{b^2}{2}\rho^*\right)\right] \tag{15}$$

and

$$g_-(a/2)g_+(a/2) = e\exp(-b^2\rho^*) \tag{16}$$

Equations 14, 15, and 16 are the *main results* of this paper.

It should be pointed out that there are two different limit orders for eqs 14, 15, and 16 in a mathematical aspect. One is that if $\rho^* \to 0$ then $b \to \infty$. The other is that if $b \to \infty$, then $\rho^* \to 0$. However, only $\rho^* \to 0$ and then $b \to \infty$ are physically sound. This is because ρ^* is an internal parameter of the system, while b is an external parameter. As $\rho^* \to 0$, eqs 14, 15, and 16 are reduced to the following equations:

$$\lim_{\rho^*\to 0} g_{\mathrm{diff}}(a/2) = b\sqrt{1 + \frac{b^2}{4}} \tag{17}$$

$$\lim_{\rho^*\to 0} g_{\mathrm{sum}}(a/2) = 1 + \frac{b^2}{2} \tag{18}$$

and

$$\lim_{\rho^*\to 0} g_-(a/2)g_+(a/2) = 1 \tag{19}$$

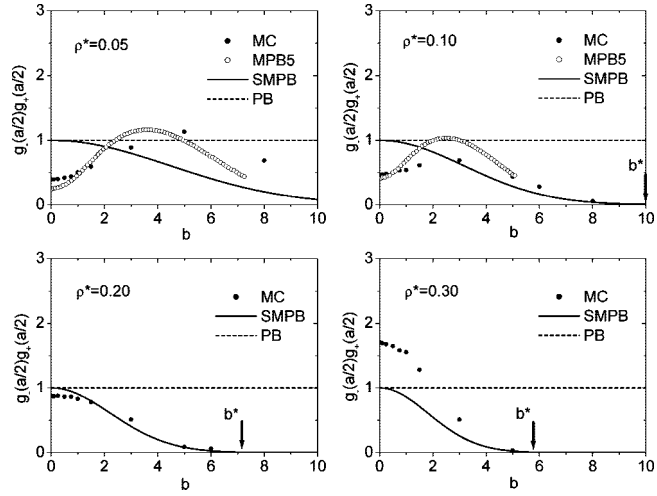

Figure 1. The contact value of the product profile $g_-(a/2)g_+(a/2)$as a function of b at indicated values of the reduced density ρ^*. The filled symbol represents the MC data,[7] the open circle symbol represents the numerical results of MPB5,[7] the solid line is an analytic expression of the SMPB theory (eq 16), and the dashed line is an analytic expression of the PB theory (eq 19). The arrow indicates the value of the parameter b^*, after which the excluded volume effects dominate.

These are the full expressions of the PB theory for $g_{\mathrm{diff}}(x)$, $g_{\mathrm{sum}}(x)$, and $g_-(x)g_+(x)$ at contact.[3]

Results and Discussion

In recent MC simulations, Bhuiyan et al.[7] simulated $g_i(x)$ using the reduced temperature $T^* = \varepsilon a k_{\mathrm{B}}T/(ze)^2 = 0.15$. The simulations were performed in a canonical ensemble using the standard Metropolis algorithm. The techniques that they adopted were similar to those used in the simulations by Boda et al.[25] and Lamperski and Bhuiyan.[26] They employed the Torrie−Valleau[27] parallel charged sheets procedure to account for the long-range Coulomb interactions. In practice, the bulk electrolyte concentration is not known a prior. They overcome it by slight adjustments to the length (perpendicular to the wall) of the central MC box.[28] The number of particles simulated depended essentially on the bulk concentration and varied from about 140 (which corresponds to $\rho^* = 0.02$) to about 800 (which corresponds to $\rho^* = 0.3$). The results of the MC simulations of Bhuiyan et al.[7] are shown in Figure 1 for $g_-(a/2)g_+(a/2)$ by the filled symbol. They found that[7]

$$\lim_{b\to+\infty} g_-(a/2)g_+(a/2) \to 0 \tag{20}$$

and they pointed out that $g_-(a/2)g_+(a/2)$ can exhibit a nontrivial behavior.

The analytical results of the SMPB theory, as well as of the PB theory, for $g_-(a/2)g_+(a/2)$ vs b at different reduced densities, which are given by eqs 16 and 19, are compared with the corresponding MC data[7] in Figure 1. It is clearly seen that $g_-(a/2)g_+(a/2)$ drops to *zero* as $b \to +\infty$, while it is unity from the PB theory (eq 19). Moreover, as ρ^* increases, the speed that $g_-(a/2)g_+(a/2)$ drops to zero increases, which reveals that $g_-(a/2)g_+(a/2) \to 0$ originates from the steric effect. However, it fails to reproduce the MC data[7] at small b. It is worth addressing that, in the previous study,[7] the

numerical results calculated by a plethora of modified Poisson−Boltzmann equations perturbing PB theory (which is called MPB5 and in which the excluded volume term has been evaluated via an inhomogeneous Ornstein−Zernike equation)[28,29] have been used for comparison with the MC data.[7] Due to the limitations of the numerical technique that was used, except for very small b, no convergent solutions of the MPB5 equation could be obtained for $\rho^* = 0.2$ and 0.3;[7] i.e., there are no numerical results of MPB5 for $\rho^* = 0.2$ and 0.3. The numerical results of MPB5 for $\rho^* = 0.05$ and 0.1, which were obtained by Bhuiyan et al,[7] are shown in Figure 1. It can be seen that at small b, the numerical results of the MPB5 are in better agreement with the MC results than the analytical expression of the SMPB theory. This is because the MPB5 includes the fluctuation effects, while the SMPB theory is mean field like. The reason that the analytic expression of the SMPB theory fails to reproduce the MC data[7] at small b can be traced to the neglect of fluctuation effects, which implies that there are remarkable ionic correlations in that regions; i.e., the correlated fluctuations of ion distributions cannot be omitted.[7]

On the other hand, at large b, due to the scarcity of the numerical results of MPB5, it is impossible here to compare the analytic expression of the SMPB theory with the numerical results of MPB5, which is an interesting topic that is worth investigating further. It is noted that we define the parameter b^*, after which the excluded volume effects dominate, such that for $\rho^* = 0.1$ the parameter $b^* = 10$ (shown in Figure 1b by the arrow); from eq 16, we find that b^* satisfies the equation $b^* = (10.0/\rho^*)^{1/2}$. Then, we deduce that $b^* = 14.14$ for $\rho^* = 0.05$, $b^* = 7.07$ for $\rho^* = 0.2$, and $b^* = 5.77$ for $\rho^* = 0.3$ (shown in Figure 1c,d by the arrow, respectively, while for $\rho^* = 0.05$, $b^* = 14.14$ is beyond the range of b shown in Figure 1a), which are in quite good agreement with the MC results.

It is worth pointing out that for a system with $T^* = 0.15$, the Coulombic interaction is strong and correlation and fluctuation effects would be important, which are shown by the behavior of the system at small b. On the other hand, when b is large, a mean field approach can capture the behavior of the system. Note that b is the dimensionless electrode charge density. Larger b means larger external electric field. Thus, we can get the following information: (1) as b increases, the Coulombic interaction, correlation, and fluctuation effects will be restrained by the larger external electric field; (2) the product vanishes at high charge density because of the density saturation of the ionic layer rather than the correlation and fluctuation effects. Therefore, we can conclude that the behavior of $g_-(a/2)g_+(a/2)$ may be controlled mainly by two factors. One is the ionic correlation effect, which controls the behavior of $g_-(a/2)g_+(a/2)$ at small b. The other is the steric effect that is captured by the analytic expression of the SMPB theory, which leads to $g_-(a/2)g_+(a/2) \to 0$ as $b \to +\infty$.

More recently, Bhuiyan and Henderson[30] examined $g_{diff}(a/2)$ by using the extensive simulation results of Bhuiyan et al.[7] The data of Bhuiyan and Henderson[30] and the corresponding analytical results given by eqs 14 (the SMPB theory) and 17 (the PB theory) are shown in Figure 2. It is clearly seen

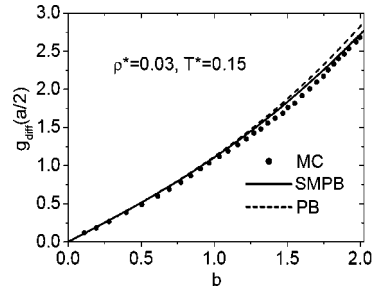

Figure 2. The contact value of the difference profile $g_{diff}(a/2)$ as a function of b at reduced density $\rho^* = 0.03$ and reduced temperature $T^* = 0.15$. The filled symbol represents the MC data,[30] the solid line is an analytic expression of the SMPB theory (eq 14), and the dashed line is an analytic expression of the PB theory (eq 17).

that, at small b, both analytic expressions of eqs 14 and 17 reproduce the data of Bhuiyan and Henderson[30] remarkably well. However, as b increases, the result of the PB theory departs from the data, but the analytical expression of the SMPB theory still reproduces the data quite well, which shows again the importance of including steric effects in modeling diffuse layer properties.

Conclusions

In conclusion, we have obtained the exact analytic expressions for the contact values in the SMPB theory. In particular, we have shown that the exact analytic expression allows us to account for the following behaviors of the contact product that are displayed by the MC simulation:[7] (i) $g_-(a/2)g_+(a/2)$ tends to zero as $b \to +\infty$; (ii) the speed that $g_-(a/2)g_+(a/2)$ drops to zero increases with increasing ρ^*. In addition, for $g_{diff}(a/2)$, the analytical expression of the SMPB theory also reproduces the data of Bhuiyan and Henderson[30] quite well. In contrast, the popular PB theory does not reproduce a vanishing contact value of the product profile at large b. Moreover, only at low ρ^* and small b region does the PB theory reproduce the data of Bhuiyan and Henderson[30] for $g_{diff}(a/2)$. As b increases, the result of the PB theory departs from the MC data. The present study demonstrates that the SMPB theory can give a quick, qualitative insight into the effects of a finite ion size and is worth investigating further.

Acknowledgment. This work was supported by the Korea Science and Engineering Foundation (KOSEF) Grant funded by the Korean Government (MEST) (R11-2007-012-03002-0) (2009).

Appendix

Derivation of Eqs 14, 15, and 16 Using the boundary conditions $\psi(x)|_{x=a/2} = \psi(a/2)$, $\psi(x)|_{x\to\infty} = 0$, and $d\psi(x)/dx|_{x\to\infty} = 0$, at contact, $x = a/2$, we can get the difference, sum, and product profiles as

$$g_{diff}(a/2) = \frac{\sinh(ze\beta\psi(a/2))}{1 + 2\rho^* \sinh^2\left(\frac{ze\beta\psi(a/2)}{2}\right)} \qquad \text{(A1)}$$

$$g_{\mathrm{sum}}(a/2) = \frac{\cosh(ze\beta\psi(a/2))}{1 + 2\rho^* \sinh^2\left(\frac{ze\beta\psi(a/2)}{2}\right)} \quad \text{(A2)}$$

and

$$g_-(a/2)g_+(a/2) = \frac{1}{\left[1 + 2\rho^* \sinh^2\left(\frac{ze\beta\psi(a/2)}{2}\right)\right]^2} \quad \text{(A3)}$$

On the other hand, for the electrode charge density ($\sigma = -\varepsilon/4\pi\ \mathrm{d}\psi(x)/\mathrm{d}x|_{x=a/2}$)

$$\sigma = -\sqrt{\frac{c_b\varepsilon}{\pi\beta\rho^*}}\sqrt{\ln\left[1 + 2\rho^* \sinh^2\left(\frac{ze\beta\psi(a/2)}{2}\right)\right]} \quad \text{(A4)}$$

Equation A4 can be rewritten as

$$\frac{b^2}{2}\rho^* = \ln\left[1 + 2\rho^* \sinh^2\left(\frac{ze\beta\psi(a/2)}{2}\right)\right] \quad \text{(A5)}$$

then

$$1 + 2\rho^* \sinh^2\left(\frac{ze\beta\psi(a/2)}{2}\right) = \exp\left(\frac{b^2}{2}\rho^*\right) \quad \text{(A6)}$$

and

$$\sinh^2\left(\frac{ze\beta\psi(a/2)}{2}\right) = \frac{1}{2\rho^*}\left[\exp\left(\frac{b^2}{2}\rho^*\right) - 1\right] \quad \text{(A7)}$$

where $b = 2\pi\beta\sigma^2/c_b\varepsilon$.

Using the following formulas

$$\sinh(A) = 2\sinh\left(\frac{A}{2}\right)\sqrt{1 + \sinh^2\left(\frac{A}{2}\right)}$$

$$\cosh(A) = 1 + 2\sinh^2\left(\frac{A}{2}\right)$$

and eq A7, we can get

$$\sinh(ze\beta\psi(a/2)) = \frac{\exp\left(\frac{b^2}{2}\rho^*\right)}{\rho^*}\sqrt{\left[1 - \exp\left(-\frac{b^2}{2}\rho^*\right)\right]} \times \sqrt{\left[1 + (2\rho^* - 1)\exp\left(-\frac{b^2}{2}\rho^*\right)\right]} \quad \text{(A8)}$$

and

$$\cosh(ze\beta\psi(a/2)) = \frac{\exp\left(\frac{b^2}{2}\rho^*\right)}{\rho^*}\left[1 + (\rho^* - 1)\exp\left(-\frac{b^2}{2}\rho^*\right)\right] \quad \text{(A9)}$$

Substituting eqs A6, A8, and A9 into eqs A1, A2, and A3, we have

$$g_{\mathrm{diff}}(a/2) = \frac{1}{\rho^*}\sqrt{\left[1 - \exp\left(-\frac{b^2}{2}\rho^*\right)\right]} \times \sqrt{\left[1 + (2\rho^* - 1)\exp\left(-\frac{b^2}{2}\rho^*\right)\right]} \quad \text{(A10)}$$

$$g_{\mathrm{sum}}(a/2) = \frac{1}{\rho^*}\left[1 + (\rho^* - 1)\exp\left(-\frac{b^2}{2}\rho^*\right)\right] \quad \text{(A11)}$$

and

$$g_-(a/2)g_+(a/2) = \exp(-b^2\rho^*) \quad \text{(A12)}$$

References

(1) Henderson, D.; Blum, L.; Lebowitz, J. *J. Electroanal. Chem.* **1979**, *102*, 315.

(2) Carnie, S. L.; Chan, D. C. *J. Chem. Phys.* **1981**, *74*, 1293.

(3) Holovko, M.; Badiali, J. P.; di Caprio, D. *J. Chem. Phys.* **2005**, *123*, 234705.

(4) Holovko, M.; Badiali, J. P.; di Caprio, D. *J. Chem. Phys.* **2007**, *127*, 014106.

(5) Henderson, D.; Bhuiyan, L. B. *Mol. Simul.* **2007**, *33*, 953.

(6) Holovko, M.; Badiali, J. P.; di Caprio, D. *J. Chem. Phys.* **2008**, *128*, 117102.

(7) Bhuiyan, L. B.; Outhwaite, C. W.; Henderson, D. *J. Electroanal. Chem.* **2007**, *607*, 54.

(8) Hunter, R. J. *Foundations of Colloid Science*, 2nd ed.; Oxford University Press: New York, 2001.

(9) Bikerman, J. J. *Philos. Mag.* **1942**, *33*, 384.

(10) Dutta, M.; Bagchi, S. N. *Indian J. Phys.* **1950**, *24*, 61.

(11) Freise, V. *Z. Elektrochem.* **1952**, *56*, 822.

(12) Wicke, E.; Eigen, M. *Z. Elektrochem.* **1952**, *56*, 551.

(13) Levine, S.; Bell, G. M. *J. Phys. Chem.* **1960**, *64*, 1188.

(14) Iglič, A.; Kralj-Iglič, V. *Electrotecnical. Rev. (Slovenia)* **1994**, *61*, 127.

(15) Borukhov, I.; Andelman, D.; Orland, H. *Phys. Rev. Lett.* **1997**, *79*, 435.

(16) Borukhov, I.; Andelman, D.; Orland, H. *Electrochim. Acta* **2000**, *46*, 221.

(17) Manciu, M.; Ruckenstein, E. *Langmuir.* **2002**, *18*, 5178.

(18) Barbero, G.; Evangelista, L. R.; Olivero, D. *J. Appl. Phys.* **2000**, *87*, 2646.

(19) Lue, L. *Langmuir* **1999**, *15*, 3726.

(20) Outhwaite, C. W.; Lamperski, S. *Condens. Matter Phys.* **2001**, *4*, 739.

(21) Kilic, M. S.; Bazant, M. Z.; Ajdari, A. *Phys. Rev. E.* **2007**, *75*, 021502.

(22) Kilic, M. S.; Bazant, M. Z.; Ajdari, A. *Phys. Rev. E.* **2007**, *75*, 021503.

(23) Kornyshev, A. A. *J. Phys. Chem. B.* **2007**, *111*, 5545.

(24) Burak, Y.; Andelman, D. *J. Chem. Phys.* **2001**, *114*, 3271.

(25) Boda, D.; Henderson, D.; Chan, K.-Y. *J. Chem. Phys.* **1999**, *110*, 5346.

(26) Lamperski, S.; Bhuiyan, L. B. *J. Electroanal. Chem.* **2003**, *540*, 79.

(27) Torrie, G. M.; Valleau, J. P. *J. Chem. Phys.* **1980**, *73*, 5807.

(28) Outhwaite, C. W.; Bhuiyan, L. B. *J. Chem. Soc., Faraday Trans.* **1982**, *2*, 775.

(29) Lamperski, S.; Outhwaite, C. W. *Langmuir* **2002**, *18*, 3423.

(30) Bhuiyan, L. B.; Henderson, D. *J. Chem. Phys.* **2008**, *128*, 117101.

CT800375T

JCTC Journal of Chemical Theory and Computation

Computational DFT Study of Ruthenium Tetracarbonyl Polymer

Mika Niskanen, Pipsa Hirva,* and Matti Haukka

Department of Chemistry, University of Joensuu, P.O. Box 111, FI-80101 Joensuu, Finland

Received September 29, 2008

Abstract: Ruthenium tetracarbonyl polymer, $[Ru(CO)_4]_n$, a chainlike compound formed by metal−metal interactions, was studied computationally. We first performed tests with selected pure and hybrid GGA density functionals and ab initio methods at HF and MP2 levels of theory to find the most suitable method. Calculated geometries and molecular orbitals were compared to see effectiveness and possible differences of the methods. Hybrid functionals, especially PBE1PBE and MPW1K, were found to produce accurate geometrical parameters compared to the experimental structure, with reasonable computational cost. Bonding in $[Ru(CO)_4]_n$ chains was studied by calculation of Mayer bond order and theoretical structure factors followed by multipole refinement to get bond critical points according to the quantum theory of atoms in molecules. Ruthenium−ruthenium bonding comparable to that in a $Ru_3(CO)_{12}$ cluster was found with both methods.

1. Introduction

Chainlike compounds having a transition-metal backbone have been intensively studied in recent years. Interest toward these compounds comes from the various properties these one-dimensional chains exhibit: luminescence,[1] solvatochromy[2] and vapochromy,[3] antitumor activity in "platinum blue"-type compounds,[4,5] and catalytic properties in ruthenium chains containing carbonyl ligands.[6,7] Certain transition-metal chain compounds are also semiconductors with use in electronic devices.[8]

Depending on their structure, chain compounds with metal backbone can be divided into different categories. Square planar metal complexes can form stacks where metal atoms line up. This is the case with, for example, Magnus' green salt,[9,10] its derivatives,[11] and many tetracyanoplatinates.[12] One-dimensional coordination polymers do not have real metal backbone. Instead, they have an alternating chain of metal atoms and linking ligands.[13] In supported chains, including EMACs, metal atom chains are surrounded and held together by bridging ligands.[14] Unsupported chains have metal backbone formed by direct metal−metal interactions without aid from the ligands.[15]

The $[Ru(CO)_4]_n$ polymer is an unsupported chain. It was synthesized for the first time by photolysis from concentrated Ru_3CO_{12} solution in tetrahydrofuran using CO atmosphere in the mid 1980s,[16] and the structure was solved in the beginning of the 1990s.[17] Many of the known chainlike transition-metal structures are mixed valence chains or have charges. $[Ru(CO)_4]_n$, however, is neutral, and all ruthenium atoms have the same valence, making the chain rare and interesting.

Most of the previous studies on the unsupported transition-metal chains focus on experimental work. These studies include synthesis,[18] X-ray studies,[15] electrocatalytic properties,[7,19,20] and spectroelectrochemical studies[21] on similar unsupported ruthenium- and osmium-based chains. Computational work includes a study of ruthenium and osmium chain growth from mononuclear $[M(CO)_4Cl_2]$ units and trinuclear $[M_3(CO)_{12}]$ clusters (M = Ru, Os).[22]

The aim of our study was to examine the $[Ru(CO)_4]_n$ polymer and its properties by means of computational chemistry. We tested the efficiency of various modeling methods suitable for modeling unsupported metal chain structures. We selected nine popular density functionals and also traditional wave functional methods on modeling single chains of $[Ru(CO)_4]_n$ polymer. Additionally, we studied bonding by calculating Mayer bond orders and by multipole

* Corresponding author e-mail: pipsa.hirva@joensuu.fi.

10.1021/ct800407h CCC: $40.75
Published on Web 03/02/2009

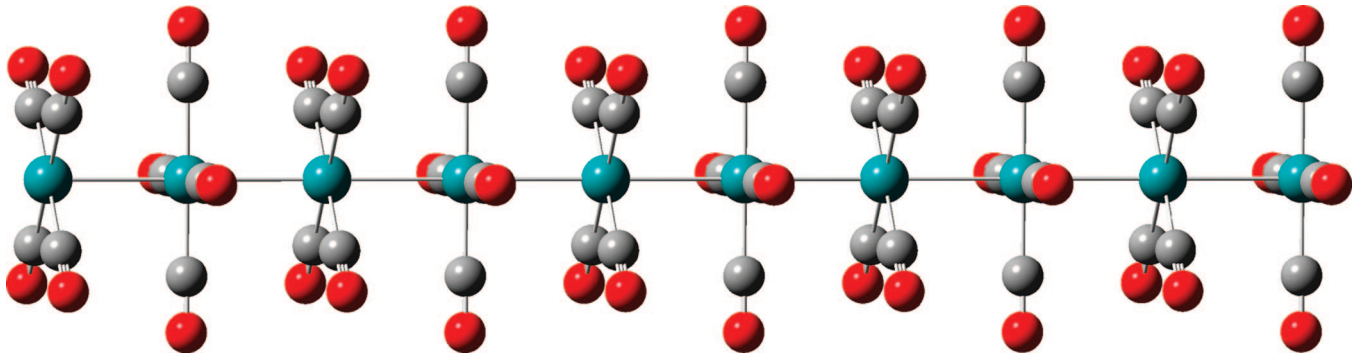

Figure 1. Ten-units-long single chain of $[Ru(CO)_4]_n$. Ru−Ru bond length is 2.86 Å, and C−Ru−Ru−C dihedral angle is 45°.

refinement from calculated theoretical structure factors to locate bond critical points according to the quantum theory of atoms in molecules.[23]

2. Computational Methods

Single chain calculations were carried out with the Gaussian03 program package.[24] Initial geometry tests were made with selected pure GGA density functionals (HCTH,[25] PBEPBE,[26] and VSXC[27]) and hybrid GGA density functionals (B1B95,[28] B3LYP,[29−31] B3PW91,[29,32] B97-2,[33] MPW1K,[34,35] and PBE1PBE[26]). For further studies, we used B1B95, B3PW91, and PBE1PBE (also known as PBE0) functionals. Ab initio calculations with HF and MP2 levels of theory were also performed for comparison. Two different basis sets were tested for ruthenium atom: Huzinaga's all-electron basis set[36] with an additional p-polarization function (433321/4331/421) and Los Alamos National Laboratory 2-double-ζ (LanL2DZ).[37] The latter is a small core ECP basis set, with 16 valence electrons for ruthenium atom, and incorporates mass−velocity and Darwin relativistic effects into the potentials. The basis set used for nonmetal atoms was the standard all-electron basis set 6-31G(d), but effects of increasing it to 6-311+G(d) were also tested. Symmetry was utilized in all models to speed up calculations. Frequency calculations with no scaling were performed to ensure all optimized molecular structures were minima.

For 3D periodic calculations, we used the CRYSTAL program package.[38] Calculations were performed with the PBE1PBE hybrid functional. Basis sets for C[39] and O[40] were selected from the CRYSTAL basis set library. For ruthenium, we used an all-electron basis set developed for the free atom case[41] and modified it for solid-state calculations by removing the most diffuse functions. The final basis set had a contraction of 976311/76311/631.

3. Results and Discussion

3.1. Molecular Models. Models of $[Ru(CO)_4]_n$ chains were based on crystallography information.[17] Our initial testing models were single chain models; interactions between $[Ru(CO)_4]_n$ chains are weak so neighboring chains from crystal structure were excluded for simplicity (Figure 1).

In powder X-ray study, $[Ru(CO)_4]_n$ polymer had been estimated to be roughly an average of 90 monomers long.[17] We built multiple short models $[Ru(CO)_4]_n$ (n = 2, 3, 4, 6, 8, 10) and tested hydrogen, chloride, water, and carbonyl ligands for terminating ends of the models. We also tested a model without a terminating group. Terminating the chain with carbonyl distorted the geometry at the ends of the chain. Water as terminating group constrained symmetry, which was not to our best interest. Effects of the other tested terminating groups on Ru−Ru distance in the middle of the chain can be seen in Figure 2. In longer chains, the effect of terminating group diminished. Ru−Ru distance approached approximate value of 2.88 Å which is in good agreement with the X-ray measured value of 2.86 Å in the crystal. We decided to use nonterminated $[Ru(CO)_4]_n$ chain models for our studies. This way, models were simpler and stabilization energies could be compared reliably.

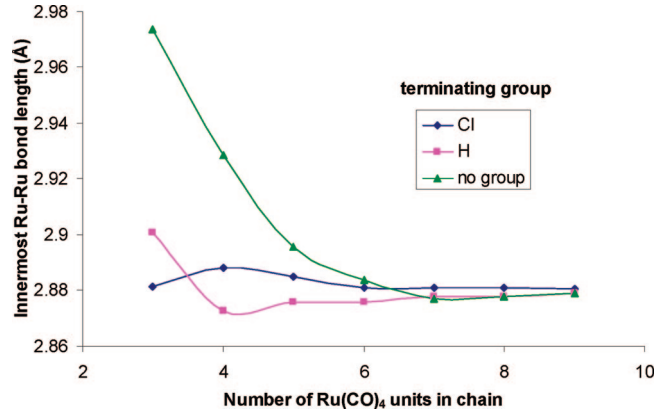

Figure 2. Effect of chain length and terminating group on the innermost Ru−Ru bond length (B3PW91, Huzinaga's AE basis set for ruthenium).

3.2. Tests for Functionals. Functionals were first tested by partial optimization of chains with selected Ru−Ru distances. We made the tests with small models, $[Ru(CO)_4]_n$ (n = 2, 3, 4), where Ru−Ru distances were fixed between values of 2.70 and 3.40 Å with 0.02 or 0.04 Å increments. Selected results for relative energies as a function of Ru−Ru distance can be seen in Figure 3. With VSXC functional, energy rose only slightly when the Ru−Ru bond was lengthened, indicating that the energy minimum could not be found easily. HCTH did better, but energy still increased more slowly than with PBEPBE or its hybrid counterpart PBE1PBE. All the hybrid functionals gave a curve similar to that of PBE1PBE. Moreover, hybrid functionals converged easily, whereas some extra work was needed with pure

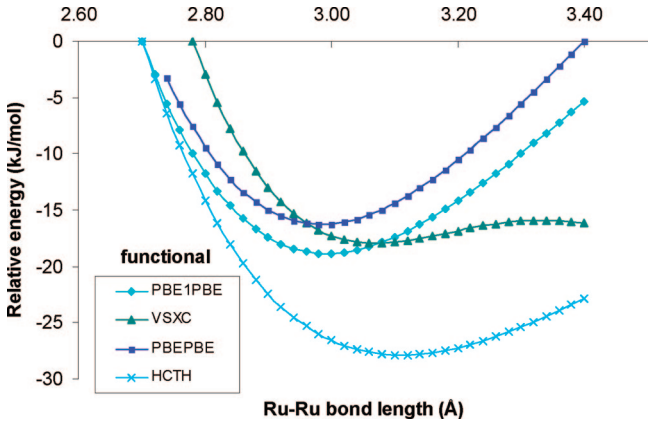

Figure 3. Relative $[Ru(CO)_4]_2$ energies as a function of Ru−Ru bond length. (Huzinaga's AE basis set.) The highest calculated energy with each functional has been set to 0 kJ/mol.

functionals in $n = 3$ and 4 models to reach geometry convergence.

It is not a real surprise that HCTH and VSXC work poorly as it has been noted before that most pure functionals do not work well on transition-metal carbonyl complexes.[42] Therefore, pure functionals were excluded from further studies.

For further testing, we performed full geometry optimizations to longer $[Ru(CO)_4]_n$ ($n = 6, 8, 10$) models using only the tested hybrid functionals and wave functional methods. Innermost Ru−Ru bond lengths for the calculated structures are presented in Table 1.

Many of the hybrid functionals gave results very close to experimental values, namely B3PW91, MPW1K, and PBE1PBE when Huzinaga's AE basis set was used and B1B95, MPW1K, and PBE1PBE when LanL2DZ basis set was used. Changing the metal basis set from Huzinaga's AE to LanL2DZ gave a (systematic) increase of 2−4 pm to Ru−Ru bond lengths with the density functionals. The difference most probably results from the relativistic effects, which the Huzinaga's AE basis set does not account for. However, in our previous tests for different carbonyl complexes of group 8 transition metals (including trinuclear cluster complexes $M_3(CO)_{12}$, M = Fe, Ru, Os), we showed that the relativistic effects are rather small for the 4d elements, both in geometry and in decarbonylation energies.[42] The very stable Huzinaga's basis set was found especially suitable for studying ruthenium carbonyl complexes.

The Hartree−Fock method also reproduced the overall geometry of chains well, but the bond distances were quite far from the experimental values and values of DFT methods. Results obtained by the MP2 method were in good agreement with DFT methods and experimental values for innermost Ru−Ru and Ru−C lengths, but neighboring $Ru(CO)_4$ units are no longer strictly square planar. Furthermore, the computation requirements were considerably higher with the MP2 method, taking roughly 450 times longer than DFT calculations and effectively prohibiting the calculation of longer chains than $[Ru(CO)_4]_8$.

Effects of improving the nonmetal atom basis set to 6-311+G(d) were also tested. Geometries were slightly affected; Ru−Ru bonds were 1 to 2 pm longer and C−O bonds were about 1 pm shorter. However, these changes occurred with all the functionals and did not change their relative results.

$[Ru(CO)_4]_n$ chains with 6−10 units had similar geometry in the central parts of the chain as the real polymers of about 90 units. To see the effect of extending the size of the model, we calculated a one-dimensional periodic single chain describing an infinite polymer, $[Ru(CO)_4]_\infty$.

Obtained bond lengths are shown in Table 2. Optimizations of infinite chains with Huzinaga's AE basis set reproduced the results of longest finite chains with differences less than 1 pm. Again, the most accurate geometry was obtained with the PBE1PBE and MPW1K functionals.

Stabilization energies were calculated with chosen functionals. The energies were calculated using equation $E_{stab} = (E_n/n) - E_1$, where E_n/n is the energy of an n-units-long chain divided by the number of units and E_1 is the energy of a single $Ru(CO)_4$ unit. Results are shown in Figure 4.

The chosen functionals gave similar results with a difference around 15 kJ/mol between PBE1PBE and B3PW91. The energy difference between chains of 9 and 10 units was only 3−4 kJ/mol, and thus the energies were slowly approaching their limiting values.

Ruthenium complexes, which follow the 18-electron rule, usually exhibit a singlet ground state. However, in the case of unsaturated systems, optimizing the spin state can lead to different electronic states, which are close in energy.[43] In our molecular models, the effect can be expected to be the largest at the end groups of the chains, since both of the $Ru(CO)_4$ units are 17-electron systems. The triplet spin state was calculated for the nonterminated models with the PBE1PBE/Huzinaga method, which was found to produce reliable results for the singlet state. In the monomer and dimer, the singlet state was found energetically favored. However, as the chain increased, the energy of the triplet decreased, as can be seen in the stabilization energies in Figure 4. On the other hand, since the central $Ru(CO)_4$ units are saturated, the effect of the end groups converged with increasing the size of the chain. Additionally, the effect of optimizing the spin state was found to have a negligible effect on the optimized geometry parameters of the longer chains ($\Delta d = 0.0005$ Å for the central Ru−Ru bond in $[Ru(CO)_4]_8$).

3.3. Properties of $[Ru(CO)_4]_n$. Selected molecular orbitals of $[Ru(CO)_4]_6$ and $[Ru(CO)_4]_8$ models were calculated and examined with B1B95, B3PW91, and PBE1PBE functionals. The orbitals between HOMO−9 and LUMO+9 and their relative energy levels were almost identical regardless of the functional or metal basis set used. In general, the orbitals were highly delocalized along the chain. As an example, we have drawn selected molecular orbitals delocalized over metal chain (Figure 5a,b) and along the entire molecule (Figure 5c,d). In Figure 5a,b, we can see Ru−Ru bonding and antibonding interactions. We further examined the nature of the M−M bonding with NBO analysis, which revealed that the Ru−Ru bonds consisted mainly of d−d interactions with 25−30% of s and 70−75% of d_{z^2} character.

Table 1. Optimized Structure of $[Ru(CO)_4]_8$ Calculated with Various DFT Methods, HF, and MP2 Method[a]

bond	B1B95	B3LYP	B3PW91	B97-2	MPW1K	PBE1PBE	HF	MP2	exptl[17]
				Huzinaga AE					
Ru−Ru	2.825	2.919	2.878	2.896	2.837	2.849	2.959	2.858	2.860
	−1.2%	2.1%	0.63%	1.3%	−0.80%	−0.38%	3.5%	−0.07%	
Ru−C	1.954	1.970	1.955	1.955	1.951	1.951	2.029	1.935	1.951
	0.15%	0.97%	0.21%	0.21%	0.0%	0.0%	4.0%	−0.82%	
C−O	1.144	1.149	1.148	1.147	1.136	1.146	1.118	1.168	1.133
	0.97%	1.4%	1.3%	1.2%	0.27%	1.1%	−1.3%	3.1%	
				LanL2DZ					
Ru−Ru	2.849	2.954	2.908	2.924	2.859	2.874	2.971	2.843	2.860
	−0.38%	3.3%	1.7%	2.2%	0.035%	0.49%	3.9%	−0.59%	
Ru−C	1.952	1.966	1.951	1.952	1.947	1.947	2.019	1.922	1.951
	0.051%	0.77%	0.0%	0.051%	−0.205%	−0.205%	3.5%	−1.5%	
C−O	1.145	1.150	1.149	1.148	1.136	1.147	1.119	1.169	1.133
	1.1%	1.5%	1.4%	1.3%	0.24%	1.2%	−1.2%	3.2%	

[a] Bond lengths are in angstroms. Percent values are deviations from the experimental value.

Table 2. Optimized Structure of $[Ru(CO)_4]_\infty$ Calculated with HF and Selected DFT Methods[a]

bond	B1B95	B3LYP	B3PW91	B97-2	MPW1K	PBE1PBE	HF	exptl[17]
				Huzinaga AE				
Ru−Ru	2.826	2.923	2.880	2.896	2.838	2.851	2.962	2.860
	−1.2%	0.97%	1.3%	1.3%	−0.77%	−0.31%	3.6%	
Ru−C	1.954	1.970	1.955	1.955	1.951	1.951	2.028	1.951
	0.5%	0.97%	0.21%	0.21%	0.0%	0.0%	3.9%	
C−O	1.144	1.149	1.148	1.147	1.136	1.146	1.118	1.133
	0.97%	1.4%	1.3%	1.2%	0.26%	1.1%	−1.3%	

[a] Bond lengths are in angstroms. Percent values are deviations from the experimental value.

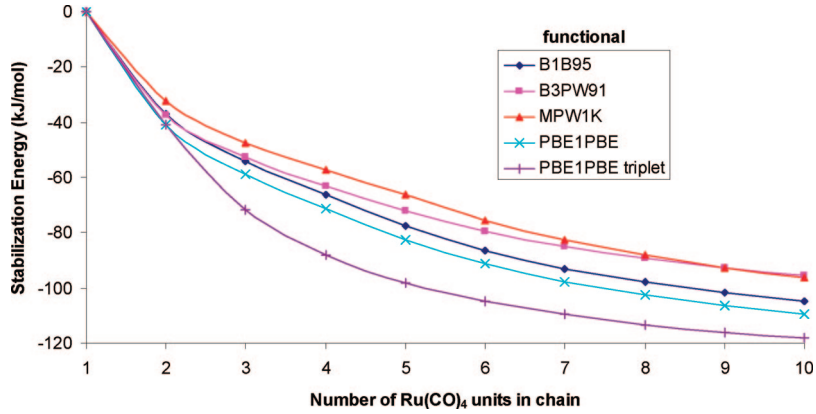

Figure 4. Stabilization energies with chosen functionals.

According to a previous study of compounds with staggered and eclipsed carbonyl groups,[45] staggered conformation maximizes the 1,3 M···C interactions and strengthens M−M bonding. This was also discussed in a powder X-ray study.[17] In our study, it is possible to see bonding 1,3 M···C and 1,4 C···C interactions in calculated molecular orbitals, as shown in Figure 5c,d. These interactions can be observed with only low cutoff values, however, which suggests that their effect on bonding between adjacent $Ru(CO)_4$ units will be minor even if bonding interactions exist.

We wanted to study closer the nature of bonding and interactions in $[Ru(CO)_4]_n$ chains. For this, we calculated Mayer bond orders[46] in the $[Ru(CO)_4]_8$ chain using QMForge.[47] Mayer bond orders in the $Ru_3(CO)_{12}$ cluster were calculated for comparison. Selected results are shown in Table 3.

According to Mayer bond orders, direct Ru−Ru bonding in chains is stronger than that in the $Ru_3(CO)_{12}$ cluster despite similar bond lengths. However, there are six weak 1,3 Ru···C interactions with MBO of 0.11 in a cluster that may strengthen overall bonding by forming weak bridges. Mayer bond orders obtained for 1,3 Ru···C interactions in the $[Ru(CO)_4]_8$ chain were negligible. Even though there are eight of these kinds of interactions between each $Ru(CO)_4$ unit, their contribution to bonding seems to be small or nonexistent, according to our study.

It should be noted that the $Ru_3(CO)_{12}$ cluster was calculated in gas phase and CO groups were in staggered conformation. In an X-ray study[48] the axial CO groups were found to be in eclipsed conformation, favoring 1,4 C···C interactions. However, the eclipsed conformation in the cluster is due to packing effects in solid state, and information on the Mayer bond orders in the single molecule in staggered conformation can be used for comparison with the polymeric chain.

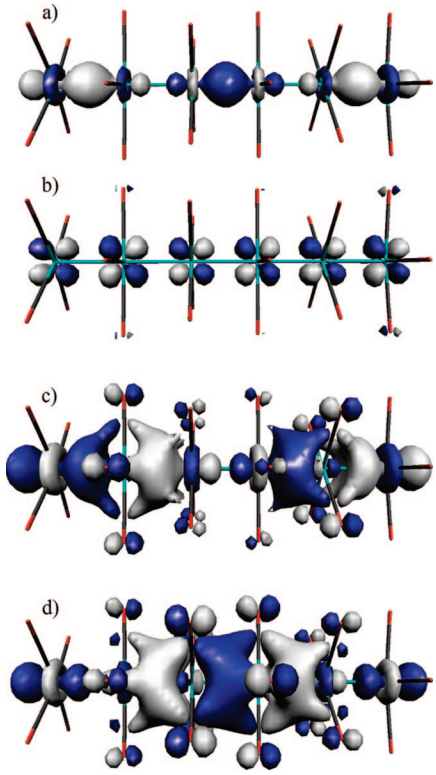

Figure 5. Selected molecular orbitals for $[Ru(CO)_4]_6$. (a) H-7, (b) H-4, (c) H-2, and (d) H-1. A cutoff value of 0.04 was used in (a) and (b), and a cutoff value of 0.02 was used in (c) and (d). Visualization was done with MOLEKEL 4.3.[44]

Table 3. Selected Mayer Bond Orders

atom pair	MBO in $[Ru(CO)_4]_8$	MBO in $Ru_3(CO)_{12}$
Ru−Ru	0.70	0.62
Ru−C	0.88	0.87;[a] 0.94[b]
C−O	2.1	2.1;[a] 2.2[b]
1,3 Ru···C	0.03	0.11;[c] 0.01−0.02
1,4 C···C	0.01	0.02

[a] Axial carbons. [b] Equatorial carbons. [c] 1,3 Ru···C interactions to two axial carbons, bonded on different ruthenium atoms.

3.4. Properties of $[Ru(CO)_4]_n$ Based on 3D Periodic Model. Our second periodic model was a real three-dimensional crystal structure where the neighboring chains were included. Parameters for unit cell and atomic positions were taken from powder X-ray data[17] and optimized using the PBE1PBE functional and CRYSTAL program package.[38] A one-dimensional chain was calculated for comparison. $[Ru(CO)_4]_n$ crystal packing and unit cell borders are shown in Figure 6, and selected structural parameters are shown in Table 4. The optimized unit cell was slightly smaller than the experimental value. However, the overall structure was very well reproduced. 1D and 3D models gave similar Ru−Ru lengths and C−Ru−Ru−C dihedral angles, indicating that the interchain interactions have only a small effect on the geometry of the chains.

Finally, we used CRYSTAL to calculate theoretical structure factors for our optimized 3D periodic crystal structure of $[Ru(CO)_4]_n$ and made multipole refinement with XD2006[49] for the obtained data. Bond critical points, shown

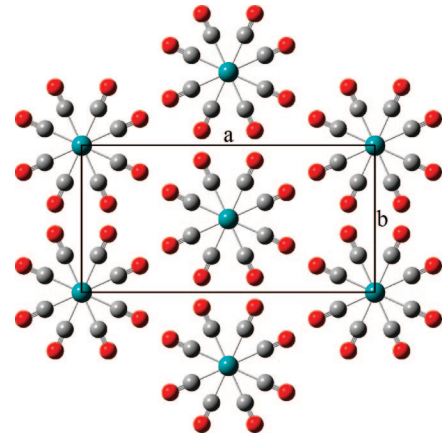

Figure 6. $[Ru(CO)_4]_n$ unit cell and crystal packing.

Table 4. $[Ru(CO)_4]_n$ Structural Parameters

parameter	optimized 1D	optimized 3D	powder X-ray[17]
a		13.94 Å	14.15 Å
b		6.85 Å	7.06 Å
c	5.62 Å	5.64 Å	5.72 Å
Ru−Ru	2.81 Å	2.82 Å	2.860 Å
Ru−C	1.94 Å	1.94 Å	1.951 Å
C−O	1.15 Å	1.15 Å	1.133 Å
C−Ru−Ru−C	44.7°	39.8°	41.0°

in Table 5, were calculated using Bader's quantum theory of atoms in molecules[23] approach, which provides information about atoms and bonding through charge density analysis. This kind of indirect route to topological analysis has been suggested to reduce differences between theory and experiment.[50] Obtained charge density, $\rho(\mathbf{r})$, its Laplacian, $\nabla^2\rho(\mathbf{r})$, kinetic energy density, $G(\mathbf{r})$, potential energy density, $V(\mathbf{r})$, and total energy density, $H(\mathbf{r})$, were compared to values in the experimental charge density study of the $Ru_3(CO)_{12}$ cluster.[48]

The interactions between atoms can be classified on the basis of the sign of the $\nabla^2\rho(\mathbf{r})$ at bond critical point. Negative value means charge is locally concentrated and electrons are shared by both nuclei, which is typical, for example, for covalent interactions (shared shell interactions). Positive value suggests charge is locally depleted and electrons are concentrated in each atom, which is typical, for example, for ionic bonds (closed shell interactions). Further information about the bond can be obtained from energy density values $G(\mathbf{r})$, $V(\mathbf{r})$, and $H(\mathbf{r})$ at bond critical point. These can be calculated from ρ_{BCP} and $\nabla^2\rho_{BCP}$.[51,52] Espinosa et al.[53] further classified interatomic interactions to three categories using the energy density values: pure closed shell interactions ($\nabla^2\rho_{BCP} > 0$, $H_{BCP} > 0$), transit closed shell interactions ($\nabla^2\rho_{BCP} > 0$, $H_{BCP} < 0$), and pure shared shell interactions ($\nabla^2\rho_{BCP} < 0$, $H_{BCP} < 0$). Metal−metal bonds fall in the transit closed shell category, as a typical M−M bond has a low ρ_{BCP}, low and positive $\nabla^2\rho_{BCP}$, and H_{BCP} negative and close to zero.[54]

The values of ρ_{BCP} and $\nabla^2\rho_{BCP}$ in Ru−Ru, Ru−C, and C−O bonds in the $[Ru(CO)_4]_n$ polymer were very similar to corresponding values in the $Ru_3(CO)_{12}$ cluster. The Ru−Ru bonds in $[Ru(CO)_4]_n$ have the typical ρ_{BCP}, $\nabla^2\rho_{BCP}$, and H_{BCP}

Table 5. Selected Parameters in Bond Critical Points[a]

bond critical point	R (Å)	R_{BCP} (Å)	ρ_{BCP} (e Å^{-3})	$\nabla^2\rho_{BCP}$ (e Å^{-5})	G_{BCP} (hartree Å^{-3})	V_{BCP} (hartree Å^{-3})	H_{BCP} (hartree Å^{-3})
				$[Ru(CO)_4]_n$, Optimized			
Ru−Ru	2.819	1.409	0.217	2.33	0.17	−0.18	−0.01
Ru−C	1.938	1.041	0.903	11.2	1.2	−1.6	−0.4
C−O	1.150	0.418	3.440	−39.0	4.5	−11.7	−7.2
1,4 C···C	not found						
1,3 Ru···C	not found						
				$Ru_3(CO)_{12}$, Experimental[48]			
Ru−Ru	2.852	1.425	0.215	2.21	0.17	−0.18	−0.01
Ru−C_{ax}	1.943	1.073	0.903	11.4	1.2	−1.6	−0.4
Ru−C_{ekv}	1.924	1.065	0.985	11.3	1.3	−1.8	−0.5
C−O	1.140	0.442	3.8	−45	5	−14	−9
1,4 C···C	2.815	1.439	0.12	0.99	0.07	−0.07	0.00
1,3 Ru···C	not found						

[a] All shown values are averages. R = distance between atoms, R_{BCP} = distance between first mentioned atom and bond critical point.

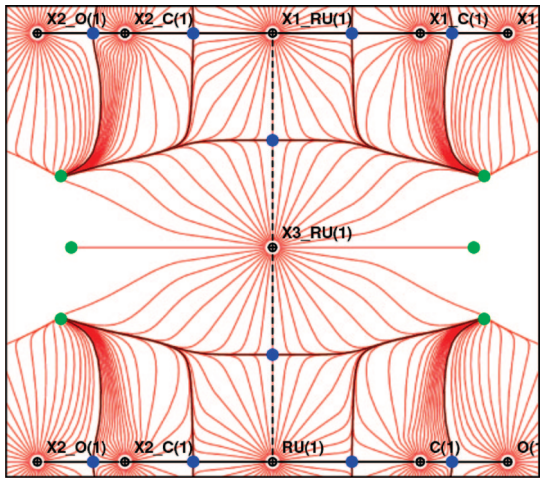

Figure 7. Trajectories with bond critical points (blue) and ring critical points (green) for optimized $[Ru(CO)_4]_n$ 3D model.

values for the M−M bond and belong to the transit closed shell category. Plotted trajectories can be seen in Figure 7. We could not find evidence of 1,3 M···C bonding in the polymer. The possible 1,3 M···C interactions are likely to be too weak to have bond critical points and thus do not play a role in bonding along the Ru chain.

4. Conclusions

Various DFT functionals as well as ab initio methods were tested for modeling ruthenium tetracarbonyl polymer, $[Ru(CO)_4]_n$. Hybrid functionals seem to work well for modeling $[Ru(CO)_4]_n$ in either single chains or crystal state. Functionals PBE1PBE and MPW1K gave especially accurate results. We expect these functionals to perform well with other similar Ru-based linear metal chains such as $[Ru(bpy)(CO)_2]_n$. It is also noteworthy that the model does not need to be longer than six units to obtain geometry and results similar to longer chains.

Mayer bond orders were calculated and a bond critical point search was performed to study bonding in $[Ru(CO)_4]_n$. From the results, we deduced direct Ru−Ru bonding in $[Ru(CO)_4]_n$ to be similar and about the same strength as that in the $Ru_3(CO)_{12}$ cluster. However, overall bonding is stronger in the cluster because of additional interactions from carbonyls. The bonding studies also give a point of comparison for the future when similar chains will be computed. The computational approach and theoretical structure factors may also serve as an aid in the interpretation of experimental data, when satisfactory data is difficult or impossible to get.

Acknowledgment. We thank Matti Tuikka for his comments and advice on charge density studies. The Academy of Finland is gratefully acknowledged for financial support.

References

(1) Stender, M.; White-Morris, R. L.; Olmstead, M. M.; Balch, A. *Inorg. Chem.* **2003**, *42*, 4504.

(2) Yam, V. W.-W.; Wong, K. M.-C.; Zhu, N. *J. Am. Chem. Soc.* **2002**, *124*, 6506.

(3) Buss, C. E.; Mann, K. R. *J. Am. Chem. Soc.* **2002**, *124*, 1031.

(4) Tejel, C.; Cirano, M. A.; Oro, L. A. *Chem.−Eur. J.* **1999**, *5*, 1131.

(5) Davidson, J. P.; Faber, P. J.; Fischer, R. G., Jr.; Mansy, S.; Peresie, H. J.; Rosenberg, B.; Van Camp, L. *Cancer Chemother. Rep., Part 1* **1975**, *59*, 287.

(6) Luukkanen, S.; Homanen, P.; Haukka, M.; Pakkanen, T. A.; Deronzier, A.; Chardon-Noblat, S.; Zsoldos, D.; Ziessel, R. *Appl. Catal., A* **1994**, *185*, 157.

(7) Collomb-Dunand-Sauthier, M.-N.; Deronzier, A.; Ziessel, R. *Inorg. Chem.* **1994**, *33*, 2961.

(8) Caseri, W. R.; Chanzy, H. D.; Feldman, K.; Fontana, M.; Smith, P.; Tervoort, T. A.; Goossens, J. G. P.; Meijer, E. W.; Schenning, A. P. H. J.; Dolbnya, I. P.; Debije, M. G.; de Haas, M. P.; Warman, J. M.; van de Craats, A. M.; Friend, R. H.; Sirringhaus, H.; Stutzmann, N. *Adv. Mater.* **2003**, *15*, 125.

(9) Atoji, M.; Richardson, J. W.; Rundle, R. E. *J. Am. Chem. Soc.* **1957**, *79*, 3017.

(10) Kim, E.-G.; Schmidt, K.; Caseri, W. R.; Kreouzis, T.; Stingelin-Stutzmann, N.; Brédas, J. L. *Adv. Mater.* **2006**, *18*, 2039.

(11) Caseri, W. *Platinum Met. Rev.* **2004**, *48*, 91.

(12) Loosli, A.; Wermuth, M.; Güdel, H.-U.; Capelli, S.; Hauser, J.; Bürgi, H.-B. *Inorg. Chem.* **2000**, *39*, 2289.

(13) Benmansour, S.; Setifi, F.; Gómez-García, C. J.; Triki, S.; Coronado, E. *Inorg. Chim. Acta* **2008**, *361*, 3856.

(14) Berry, J. F.; Cotton, F. A.; Fewox, C. S.; Lu, T.; Murillo, C. A.; Wang, X. *Dalton Trans.* **2004**, *15*, 2297.

(15) Masciocchi, N.; Sironi, A.; Chardon-Noblat, S.; Deronzier, A. *Organometallics* **2002**, *21*, 4009.

(16) Hastings, W. R.; Baird, M. C. *Inorg. Chem.* **1986**, *25*, 2913.

(17) Masciocchi, N.; Moret, M.; Cairati, P.; Ragaini, F.; Sironi, A. *J. Chem. Soc., Dalton Trans.* **1993**, *3*, 471.

(18) Jiang, F.; Yap, G. P. A.; Pomeroy, R. K. *Organometallics* **2002**, *21*, 773.

(19) Chardon-Noblat, S.; Collomb-Dunand-Sauthier, M.-N.; Deronzier, A.; Ziessel, R.; Zsoldos, D. *Inorg. Chem.* **1994**, *33*, 4410.

(20) Chardon-Noblat, S.; Deronzier, A.; Hartl, F.; Slageren, J.; Mahabiersing, T. *Eur. J. Inorg. Chem.* **2001**, *3*, 613.

(21) Hartl, F.; Mahabiersing, T.; Chardon-Noblat, S.; Da Costa, P.; Deronzier, A. *Inorg. Chem.* **2004**, *43*, 7250.

(22) Hirva, P.; Haukka, M.; Jakonen, M.; Pakkanen, T. A. *Inorg. Chim. Acta* **2006**, *359*, 853.

(23) Bader, R. F. W. In *Atoms in Molecules: A Quantum Theory*; Clarendon Press: Oxford, 1990.

(24) Frisch, M. J.; Trucks, G. W.; Schlegel, H. B.; Scuseria, G. E.; Robb, M. A.; Cheeseman, J. R.; Montgomery, J. A., Jr.; Vreven, T.; Kudin, K. N.; Burant, J. C.; Millam, J. M.; Iyengar, S. S.; Tomasi, J.; Barone, V.; Mennucci, B.; Cossi, M.; Scalmani, G.; Rega, N.; Petersson, G. A.; Nakatsuji, H.; Hada, M.; Ehara, M.; Toyota, K.; Fukuda, R.; Hasegawa, J.; Ishida, M.; Nakajima, T.; Honda, Y.; Kitao, O.; Nakai, H.; Klene, M.; Li, X.; Knox, J. E.; Hratchian, H. P.; Cross, J. B.; Bakken, V.; Adamo, C.; Jaramillo, J.; Gomperts, R.; Stratmann, R. E.; Yazyev, O.; Austin, A. J.; Cammi, R.; Pomelli, C.; Ochterski, J. W.; Ayala, P. Y.; Morokuma, K.; Voth, G. A.; Salvador, P.; Dannenberg, J. J.; Zakrzewski, V. G.; Dapprich, S.; Daniels, A. D.; Strain, M. C.; Farkas, O.; Malick, D. K.; Rabuck, A. D.; Raghavachari, K.; Foresman, J. B.; Ortiz, J. V.; Cui, Q.; Baboul, A. G.; Clifford, S.; Cioslowski, J.; Stefanov, B. B.; Liu, G.; Liashenko, A.; Piskorz, P.; Komaromi, I.; Martin, R. L.; Fox, D. J.; Keith, T.; Al-Laham, M. A.; Peng, C. Y.; Nanayakkara, A.; Challacombe, M.; Gill, P. M. W.; Johnson, B.; Chen, W.; Wong, M. W.; Gonzalez, C.; Pople, J. A. Gaussian 03, revision C.02; Gaussian, Inc.: Wallingford, CT, 2004.

(25) Hamprecht, F. A.; Cohen, A. J.; Tozer, D. J.; Handy, N. C. *J. Chem. Phys.* **1998**, *109*, 6264.

(26) Perdew, J. P.; Burke, K.; Ernzerhof, M. *Phys. Rev. Lett.* **1996**, *77*, 3865.

(27) Van Voorhis, T.; Scuseria, G. E. *J. Chem. Phys.* **1998**, *109*, 400.

(28) Becke, A. D. *J. Chem. Phys.* **1996**, *104*, 1040.

(29) Becke, A. D. *J. Chem. Phys.* **1993**, *98*, 5648.

(30) Lee, C.; Yang, W.; Parr, R. G. *Phys. Rev. B* **1988**, *37*, 785.

(31) Stephens, P. J.; Devlin, F. J.; Chabalowski, C. F.; Frisch, M. J. *J. Phys. Chem.* **1994**, *98*, 11623.

(32) Perdew, J. P. In *Electronic Structure of Solids '91*; Ziesche, P., Eschig, H., Eds.; Akademie Verlag: Berlin, 1991; p 11.

(33) Wilson, P. J.; Bradley, T. J.; Tozer, D. J. *J. Chem. Phys.* **2001**, *115*, 9233.

(34) Becke, A. D. *J. Chem. Phys.* **1997**, *107*, 8554.

(35) Adamo, C.; Barone, V. *J. Chem. Phys.* **1998**, *108*, 664.

(36) *Gaussian Basis Sets for Molecular Calculations*; Huzinaga, S., Ed.; Physical Sciences Data 16; Elsevier: Amsterdam, 1984; p 255.

(37) Hay, P. J.; Wadt, W. R. *J. Chem. Phys.* **1985**, *82*, 299.

(38) Dovesi, R.; Saunders, V. R.; Roetti, C.; Orlando, R.; Zicovich-Wilson, C. M.; Pascale, F.; Civalleri, B.; Doll, K.; Harrison, N. M.; Bush, I. J.; Arco, P. D.; Llunell, M. *CRYSTAL06 User's Manual*; University of Torino: Torino, Italy, 2006.

(39) Catti, M.; Pavese, A.; Dovesi, R.; Saunders, V. C. *Phys. Rev. B* **1993**, *47*, 9189.

(40) Gatti, C.; Saunders, V. R.; Roetti, C. *J. Chem. Phys.* **1994**, *101*, 10686.

(41) Towler, M. D. University of Cambridge, Private communication, 2008.

(42) Hirva, P.; Haukka, M.; Jakonen, M.; Moreno, M. A. *J. Mol. Model.* **2008**, *14*, 171.

(43) Carreon-Macedo, J.-L.; Harvey, J. N. *J. Am. Chem. Soc.* **2004**, *126*, 5789.

(44) Flükiger, P.; Lüthi, H. P.; Portmann, S.; Weber, J. *MOLEKEL 4.3*; Swiss National Supercomputing Centre CSCS: Manno, Switzerland, 2000.

(45) Bau, R.; Kirtley, S. W.; Sorrell, T. N.; Winarko, S. *J. Am. Chem. Soc.* **1973**, *96*, 988.

(46) Bridgeman, A. J.; Cavigliasso, G.; Ireland, L. R.; Rothery, J. *J. Chem. Soc., Dalton Trans.* **2001**, *14*, 2095.

(47) Tenderholt, A. L. QMForge, version 2.1; Stanford University: Stanford, CA, 2007. http://qmforge.sourceforge.net.

(48) Gervasio, G.; Bianchi, R.; Marabello, D. *Chem. Phys. Lett.* **2005**, *407*, 18.

(49) Volkov, A.; Macchi, P.; Farrugia, L. J.; Gatti, C.; Mallinson, P.; Richter, T.; Koritsanszky, T. XD2006, a computer program package for multipole refinement, topological analysis of charge densities and evaluation of intermolecular energies from experimental and theoretical structure factors; SUNY at Buffalo: Buffalo, NY, 2006.

(50) Volkov, A.; Abramov, Y.; Coppens, P.; Gatti, C. *Acta Crystallogr., Sect. A* **2000**, *56*, 332.

(51) Abramov, Yu. *Acta Crystallogr., Sect. A* **1997**, *53*, 264.

(52) Espinosa, E.; Molins, E.; Lecomte, C. *Chem. Phys. Lett.* **1998**, *285*, 170.

(53) Espinosa, E.; Alkorta, I.; Elguero, J.; Molins, E. *J. Chem. Phys.* **2002**, *117*, 5529.

(54) Gervasio, G.; Bianchi, R.; Marabello, D. *Chem. Phys. Lett.* **2004**, *387*, 481.

CT800407H

JCTC Journal of Chemical Theory and Computation

Transferable Coarse-Grained Models for Ionic Liquids

Yanting Wang,† Shulu Feng, and Gregory A. Voth*

Center for Biophysical Modeling and Simulation, and Department of Chemistry, University of Utah, 315 South 1400 East Room 2020, Salt Lake City, Utah 84112-0850

Received December 10, 2008

Abstract: The effective force coarse-graining (EF-CG) method was applied to the imidazolium-based nitrate ionic liquids with various alkyl side-chain lengths. The nonbonded EF-CG forces for the ionic liquid with a short side chain were extended to generate the nonbonded forces for the ionic liquids with longer side chains. The EF-CG force fields for the ionic liquids exhibit very good transferability between different systems at various temperatures and are suitable for investigating the mesoscopic structural properties of this class of ionic liquids. The good additivity and ease of manipulation of the EF-CG force fields can allow for an inverse design methodology of ionic liquids at the coarse-grained level. With the EF-CG force field, the molecular dynamics (MD) simulation at a very large scale has been performed to check the significance of finite size effects on the structural properties. From these MD simulation results, it can be concluded that the finite size effect on the phenomenon of ionic liquid spatial heterogeneity (Wang, Y.; Voth, G. A. *J. Am. Chem. Soc.* **2005**, *127*, 12192) is small and that this phenomenon is indeed a nanostructural behavior which leads to the experimentally observed mesoscopic heterogeneous structure of ionic liquids.

1. Introduction

Ionic liquids, also known as room-temperature molten salts, consist of bulky organic cations and/or anions. Because their melting temperatures are around room temperature, they may be used as liquids in industrial applications. In recent years, researchers have extended the possible applications of ionic liquids from solvents[1,2] to other materials, such as lubricants,[3,4] embalming fluids,[5] fuel cells,[6] biocatalysis,[7] and energetic materials.[8] These possible applications are bolstered by the fact that there are many ionic liquid candidates to be chosen from to meet different specific application requirements. Given a target application with a set of specific requirements, it would be valuable to select the best ionic liquid candidates using a computational design approach rather than experimentally testing every possible species one by one. Since ionic liquids can usually be considered as being constructed from smaller components, which can be enumerated, the systematic design of ionic liquids at a coarse-grained level, where each component is treated as one or several coarse-grained (CG) sites, is one possible route to their computational design.

The multiscale coarse-graining (MS-CG) approach[9] calculates the effective nonbonded CG forces between CG sites by a variational fitting to the total forces sampled from atomistic MD simulations. This approach has been successfully applied to ionic liquids,[10] as well as some biomolecular[9,11] and other liquid[12] systems. The MS-CG force fields accurately capture the atomistic local structures at the CG level. However, for the same underlying atomistic system, different MS-CG models must in principle be constructed for different temperatures. In addition, the effective forces cannot easily be transferred to other systems, which may be essential for the systematic computational design of ionic liquids at the CG level.

As an alternative to the general MS-CG approach, the effective force coarse-graining (EF-CG) method[13] was designed to focus more on the transferability and additivity of the resulting CG force field by sacrificing some degree of structural accuracy. With the EF-CG approach, the effective forces between CG sites can be explicitly separated as different contributions from the collective electrostatic and

* Author to whom correspondence should be addressed. Phone: (801)581-7272. Fax: (801)581-4353. Email: voth@chem.utah.edu.

† Current address: Idaho National Laboratory, P.O. Box 1625, Idaho Falls, ID 83415-2208.

10.1021/ct800548t CCC: $40.75
Published on Web 03/02/2009

van der Waals (VDW) interactions, respectively, and are generally more transferable between different temperatures and environments (e.g., surface and bulk). The EF-CG method works especially well for molecules which can be divided into CG sites with good symmetry. This condition is satisfied to some reasonable extent for many ionic liquids. In this study, the EF-CG approach is applied to the imidazolium-based nitrate ionic liquids with various alkyl side-chain lengths. It is shown that a set of effective forces constructed for a short-chain system can be extended to generate the effective force fields suitable for CG molecular dynamics (MD) simulations of the related ionic liquid systems with longer alkyl side chains.

An important structural feature of ionic liquids with an alkyl side chain is the spatial heterogeneity formed by the cationic alkyl tail aggregation.[14] It was revealed by both the all-atom[15,16] and CG[14,17] MD simulations that, in a pure ionic liquid system, the nonpolar cationic tail groups tend to aggregate to form isolated tail domains, while the charged head groups and anions retain their local structures unchanged with various lengths of the side chains. The tail domains were also found to pass through a melting-like transition with increasing temperature.[17] These phenomena were explained by the competition between the collective electrostatic and VDW interactions. In this paper, it will be shown that, despite the approximations made when constructing the EF-CG force fields, the spatial heterogeneity phenomenon is still captured at the CG level with satisfactory accuracy. Additionally, a CG MD simulation with the EF-CG model at a very large spatial scale is reported to connect the tail aggregation mechanism to experimentally observed liquid-crystal-like ionic liquid structures.[18−21]

2. Methods

In this section, the EF-CG methodology and an order parameter quantifying the spatial heterogeneity are briefly reviewed. The construction and manipulation of the EF-CG force fields and the MD simulations at both the atomistic and CG levels are described in detail.

2.1. Effective Force Coarse-Graining Methodology. The EF-CG methodology[13] aims to construct CG models with an enhanced degree of transferability. In order to accomplish this goal, the effective CG force fields should depend on thermodynamic and environmental conditions as little as possible. As a consequence, compared to the general MS-CG approach,[22] the EF-CG methodology usually leads to CG models that have less accuracy in terms of their average local structures.

Before constructing the EF-CG force fields, an all-atom MD simulation at equilibrium must be performed. A coarse-graining strategy is then defined to group atoms together to form one or several CG sites for each molecule. With the atomic positions sampled during the all-atom MD simulation, the bonded coordinate Boltzmann distributions can be determined and fitted iteratively to obtain the bonded CG force fields,[10] while the atomistic nonbonded forces between different atoms $\{\mathbf{f}_{ij}\}$ are also explicitly calculated. For a certain pair of CG sites I and J, all of the atomistic forces between these two sites are summed up and projected on the direction of the unit vector $\hat{\mathbf{R}}_{IJ}$ connecting the center-of-masses of the two CG sites

$$F_{IJ}(R_{IJ}) = \sum_i \sum_j \mathbf{f}_{ij} \cdot \hat{\mathbf{R}}_{IJ} \tag{1}$$

where F_{IJ} is the effective force between CG sites I and J. The magnitude of this projected force F_{IJ} as a function of R is averaged over all pairs with the same type in all sampled MD configurations to obtain the final effective nonbonded EF-CG force between CG sites $\tilde{F}_{IJ}(R)$. Consequently, $\tilde{F}_{IJ}(R)$ is actually an ensemble-averaged effective force over the relative orientation Ω_{IJ} between CG sites I and J, with the probability distribution $P(\Omega_{IJ})$ sampled during the all-atom MD simulation:

$$\tilde{F}_{IJ}(R) = \int \mathrm{d}\Omega \, \tilde{F}_{IJ}(R, \Omega) \tag{2}$$

Different types of atomistic forces, typically electrostatic and VDW interactions, can be calculated separately. The final effective CG forces are simply the sum of all different types of CG forces present in the system.

The effective electrostatic interactions are generally long-range, while the tabulated effective CG forces are usually required by MD simulation software to be short-ranged. It has been found that,[13] for most systems, beyond a certain cutoff around 1 nm, the long-range interactions can be approximated by the electrostatic interactions of the net point charges on the CG sites, so that only the remaining effective short-range forces need be tabulated.

2.2. Heterogeneity Order Parameter. The degree of the spatial heterogeneity of the cationic tail groups in ionic liquids can be gauged by the height of the first peak of the tail−tail radial distribution function (RDF). However, it is more convenient if the spatial heterogeneity can be quantified by a single numerical value. In order to do this, a Gaussian-like *heterogeneity order parameter* (HOP)[17] is defined for each site as

$$\hat{h}_i = \sum_j \exp(-r_{ij}^2/2\sigma^2) \tag{3}$$

where r_{ij} is the modulation of the vector $\boldsymbol{r}_i - \boldsymbol{r}_j$ corrected with the periodic boundary conditions, $\sigma = L/N^{1/3}$ with L the side length of the cubic simulation box and N the total number of the CG sites.

For one configuration, the HOP is computed by averaging over all N_s sites of interest (usually sites of the same type), such that

$$\hat{h} = \frac{1}{N_s} \sum_{i=1}^{N_s} \hat{h}_i \tag{4}$$

The HOP is defined so that it is topologically invariant with the absolute size of the simulation box. For a given topology, the HOP value exhibits finite size effect when very limited number of sites are present, but it approaches a constant value with increasing number of sites. The HOP values $\hat{h}_0$ for the ideally homogeneous systems with $N = n^3$, $n = 1, 2, 3,...$, in a cubic box were computed and listed

Table 1. Heterogeneity Order Parameter $\hat{h}_0$ (Equation *4*) for Uniformly Distributed Systems with Different Number of Sites N_s

N_s	$\hat{h}_0$
1	1.0000
8	4.1464
27	10.8388
64	12.9513
125	15.3220
216	15.5285
343	15.7368
512	15.7431
729	15.7495
1000	15.7495
1728 and larger	15.7496

in Table 1. It can be seen that the HOP approaches a constant value of 15.7496 when $N \geq 729$.

In order to allow the HOP to have a value around zero when the sites distribute almost uniformly, a *reduced* HOP for each configuration is defined as

$$h = \hat{h} - \hat{h}_0 \tag{5}$$

The reduced HOP h allows one to see more clearly how far the structure deviates from the ideal uniform structure.

2.3. Molecular Dynamics Simulations. Without further theoretical development, the EF-CG method cannot decompose explicit many-body interactions into effective pairwise forces. In the case of ionic liquids, the current EF-CG approach is therefore not applicable to the electronically polarizable models, which are known to generate more accurate simulation results for some physical properties of certain species of ionic liquids.[23] Therefore, the atomistic nonpolarizable model was used to perform the all-atom MD simulations for the $EMIM^+/NO_3^-$ system and to generate atomistic MD trajectories for the EF-CG approach. Except the electronic polarization parameters, the force field for the nonpolarizable model is the same as the polarizable model reported in refs 15 and 23.

The DL_POLY simulation package[24] was used to perform both the all-atom and CG MD simulations. After equilibration, the $EMIM^+/NO_3^-$ system with 512 ion pairs first was simulated in a constant *NPT* all-atom MD simulation at $P = 1$ atm and $T = 400$ K for 1 ns, with a time step of 1 fs. The average side length of the cubic simulation box was determined from this *NPT* run to be $L = 50.03 \pm 0.08$ Å. A 1 ns constant *NVT* all-atom MD simulation with the side length of the simulation box fixed to be the above value L was then carried out. One configuration was recorded for every 1 ps (1000 MD steps), so totally 1000 configurations were saved. The EF-CG method was then applied to these configurations to obtain the EF-CG force field for $EMIM^+/NO_3^-$, which was then extended without recalculation to generate the EF-CG force fields for the ionic liquid systems with longer alkyl side chains, as described in the next subsection.

With the various EF-CG force fields, the CG MD simulations were performed for ionic liquids with 512 ion pairs and varying different side-chain lengths at $T = 400$ K. After appropriate equilibration runs, the CG systems were first simulated for 4 ns in a constant *NPT* MD ensemble, and then a 4 ns constant *NVT* MD simulation was performed to collect data. Note that CG simulation time corresponds to much longer atomistic simulation time, because dynamics of the CG systems are generally faster than those of the corresponding atomistic systems. Because the CG sites have heavier masses, the time step for the CG MD runs was set to the larger value of 4 fs. Totally 1000 configurations were sampled for each constant *NVT* CG MD run, with one configuration saved for every 1000 MD steps. The cutoffs for the effective VDW interactions and the real space part of the effective electrostatic interactions were both set to be 14 Å. In the *NVT* runs, the side length of the cubic simulation box was the average values obtained from the preceding *NPT* runs.

2.4. Transferable Coarse-Grained Model of Ionic Liquids. For imidazolium-based ionic liquid cations with an alkyl side chain, most of the positive charges are distributed close to the cationic ring. The net partial charges on the carbon groups, which are five sites or farther from the cationic ring, are so small that they can be effectively considered to be zero. Also, only imidazolium-based ionic liquids with a nitrate anion are studied in this paper. For convenience, the ionic liquid systems are denoted as C_n, where n is the number of carbon groups on the alkyl side chain. For example, $EMIM^+/NO_3^-$ is denoted as C_2, and $HMIM^+/NO_3^-$ is denoted as C_6. Because the structural properties of ionic liquid systems with an even number of carbon groups follow different rules than those for the ILs with odd numbers,[20] in the paper, only those with even numbers are investigated.

The atomistic partial charges and polarizable force fields for C_2 to C_{12} have been reported in ref 15. The CG strategy follows the previous one;[10] the entire nitrate anion is coarse-grained as a single CG site D, the imidazole ring as CG site A, the single methyl group as CG site B, the terminal methyl group on the side chain as CG site E, and the ethyl group adjacent to site E as CG site C, and the other four ethyl groups are denoted as CG sites M1, M2, M3, and M4, ordered from the cationic ring to the terminal of the side chain.

For the ionic liquid systems with different side-chain lengths, the atomistic net partial charges on each CG group are slightly different. To unify the CG models, the atomistic net partial charges were averaged and adjusted so that they have the same values for systems with a side-chain length equal to or larger than C_6. The net partial charges for C_2 were unchanged. The CG scheme for C_2 is shown in Figure 1, and the CG structures for C_2 to C_{12} systems are shown in Figure 2. The partial charges for the CG groups are also given in Figure 2. Since the partial charges for the CG model of C_4 cannot be unified, it is not directly related to the main focus of this study. Therefore, the study of the CG model for the C_4 system is not included in this paper.

The EF-CG approach was applied to C_2 with the effective VDW and electrostatic forces between CG sites computed separately. These force calculations have been reported in ref 13. The tails of the effective VDW forces approach 0 smoothly, and the middle to long-range parts of the effective

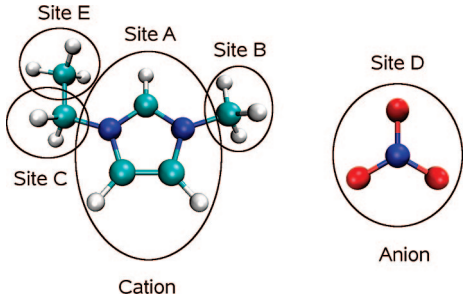

Figure 1. Coarse-graining scheme of $EMIM^+/NO_3^-$ (C_2) ionic liquid.

electrostatic forces are almost equal to the point charge forces, indicating that the EF-CG forces very weakly depend on the environment and thermal conditions. However, because of the multipole interactions, the short-range parts of the effective electrostatic forces are generally quite different from the point charge forces.

For atomic groups with the same atomic structure in different ionic liquid systems or in different positions in the same molecule, such as the CH_2 groups on the alkyl side chain, they should have very similar interactions at the CG level. If the difference caused by the orientation distributions, as shown in eq 2, is negligible, the effective VDW forces between these groups should be the same, and the long-range electrostatic forces should be proportional to their net partial charges. This has been verified by comparing the effective forces obtained for C_2 and C_6 systems (data not shown). Therefore, the effective forces for C_2 can be used as a set of general force fields to construct the CG force fields for imidazolium-based nitrate ionic liquids with arbitrarily long side chains.

The EF-CG force field for C_2 was first extended to construct the effective forces for C_6. The unified CG model for C_6 is shown in Figure 2. The effective VDW forces were copied from the C_2 system to the C_6 system for the CG groups with the same atomic structure, and CG sites M1, M2, M3, and M4 are the same as CG site C. For example, the effective VDW force between sites M1 and E in the C_6 system is the same as that between sites C and E in the C_2 system. The effective electrostatic forces were rescaled by the net partial charges on the CG sites. For example, the effective electrostatic force between CG sites M3 and A in the C_6 system is equal to that between CG sites C and A in the C_2 system multiplied by 0.1235. The total effective forces used to perform the CG MD simulations are the sum of the corresponding effective VDW forces and the modified effective electrostatic forces. For systems with longer side chains (C_8, C_{10}, and C_{12}), more CG sites C with zero partial charges were inserted between CG site C and E in the C_6 system, as shown in Figure 2. Since the effective electrostatic forces for CG sites C and E are all zero, their effective VDW forces are their total effective forces.

3. Results

The EF-CG force fields for ionic liquids with different side-chain lengths extended from C_2 were then used to perform CG MD simulations at $T = 400$ K. The absolute accuracy of these extended force fields was verified by comparing the CG MD simulation results for C_8 with those for the MD simulations with the atomistic polarizable model, which is known to be closer to the experimental results.[23] Besides the difference between the nonpolarizable and polarizable force fields, the modified partial charges for the unified CG

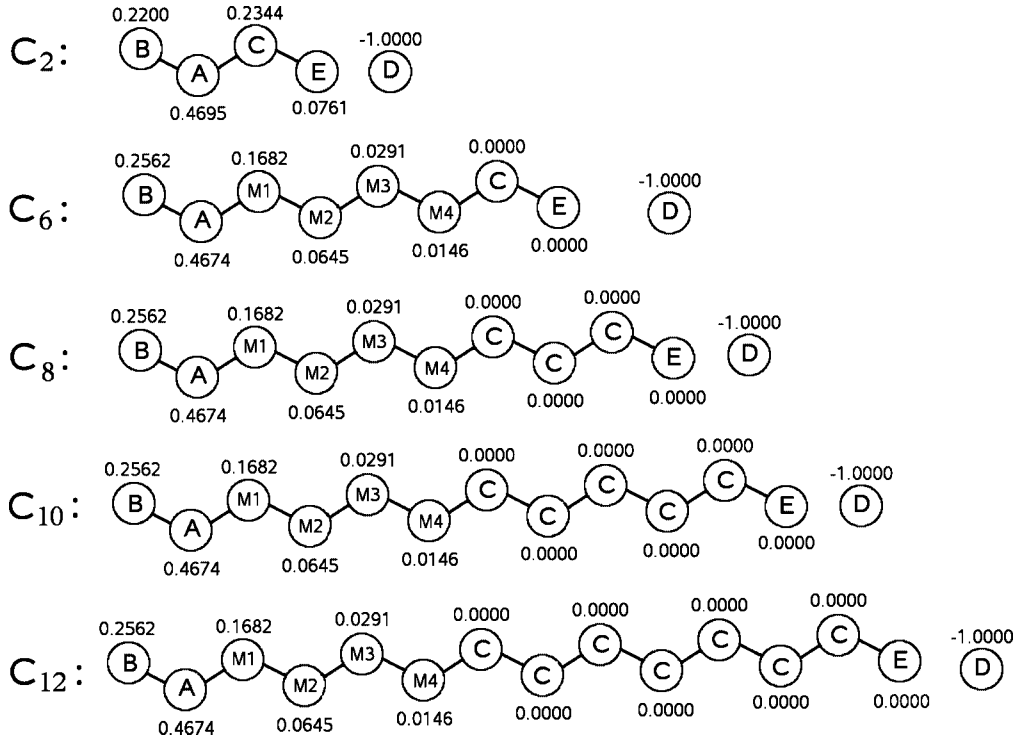

Figure 2. Coarse-grained molecular structures of the imidazolium-based nitrate ionic liquids with various side-chain lengths. The numbers shown on the coarse-grained sites are their effective partial charges.

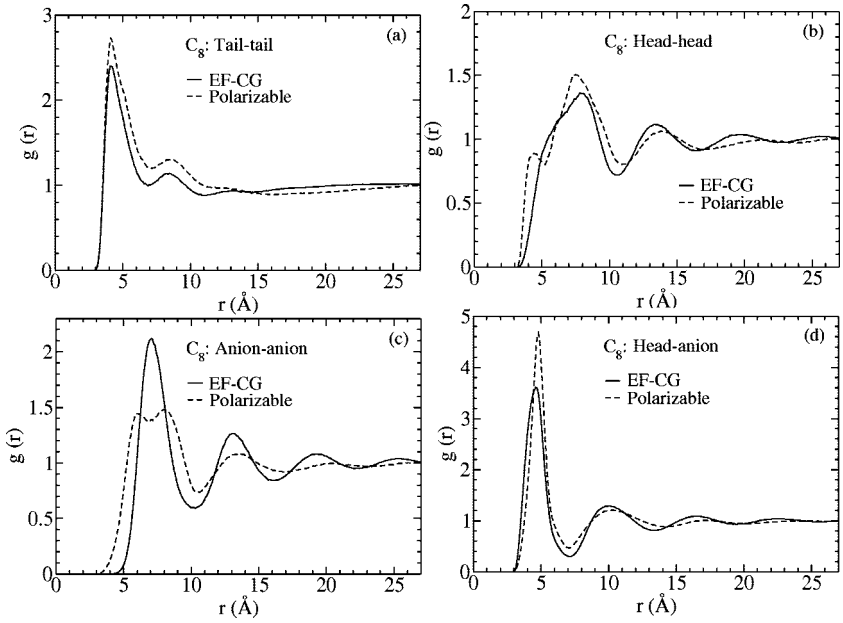

Figure 3. Comparison of radial distribution functions for the C_8 system with the atomistic polarizable model (dashed lines) and the EF-CG model (solid lines): (a) tail−tail (CG sites E−E); (b) head−head (CG sites A−A); (c) anion−anion (CG sites D−D); (d) head−anion (CG sites A−D). See Figure 2 for CG site definitions.

model and the slight difference in the orientation distributions also lead to errors for the CG MD simulations. Nevertheless, the results with the EF-CG model are still close enough to those with the all-atom polarizable model for the purpose of studying the general trends of the global behavior of ionic liquids.

All of the all-atom and CG MD simulations were equilibrated by annealing from $T = 1000$ K down to $T = 400$ K with a temperature interval of 100 K. At each temperature, a 10^6-step constant *NVT* simulation was performed. The systems were then equilibrated at 400 K for a longer time. The systems were verified to be equilibrated at $T = 400$ K by observing that the ionic diffusion constants were nearly unchanged.

3.1. Validity of the Extended Coarse-Grained Force Fields. The results for the CG MD simulations of C_8 are compared with those for the all-atom MD simulations with the atomistic polarizable model previously reported in ref 15. The radial distribution functions (RDFs) between cationic head (CG site A), tail (CG site E), and anions (CG site D) are shown in Figure 3. It can be seen that, although there are some differences in these plots (primarily in the anion−anion structure), the RDFs for the CG MD simulations follow reasonably well those for the simulations with the atomistic polarizable model.

3.2. Thermodynamic and Structural Properties with the Coarse-Grained Models. With the atomistic polarizable model, it has been shown[15] that the density of ionic liquids decreases with increasing side-chain length, which agrees with the experimental results.[25−27] The densities of the ionic liquids with different side-chain lengths simulated by the EF-CG force fields at $T = 400$ K are shown in Figure 4, compared with those obtained with the atomistic polarizable model. For the C_2 system, the atomistic polarizable model gives a significantly higher density, because the electronic polarization effect leads the ions to a closer packed structure.[23] With increasing side-chain length, so that more nonpolar tail groups exist in the system, the polarization effect becomes more localized. Therefore, the density difference is much smaller for the ionic liquids with longer side chains. Despite the numerical differences, the CG model is able to reproduce the trend of decreasing density with increasing alkyl side-chain length.

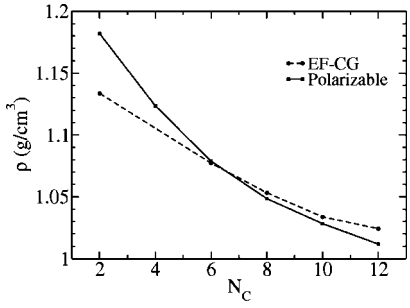

Figure 4. Average densities of the imidazolium-based nitrate ionic liquids with various side-chain lengths from both the atomistic polarizble models (solid line) and the EF-CG models (dashed line).

The reduced HOPs obtained from the CG simulations are shown in Figure 5. With increasing side-chain length, the reduced HOPs for the cationic tail and head groups and for the anions all increase. The tail groups have larger HOPs than the head groups and anions, and the difference increases for the systems with longer side chains. This indicates that the tail groups aggregate more than the head groups and anions, and the tail aggregation is more pronounced for longer side-chain systems. This is consistent with the tail aggregation phenomenon revealed with both the MS-CG[14,17] and atomistic polarizable[15] models.

The RDFs between head groups, tail groups, and anions for different systems from the CG simulations are shown in Figure 6. The peak positions and the plot shapes are relatively

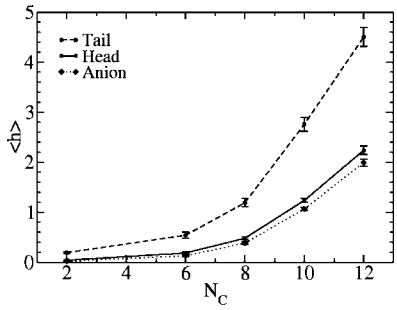

Figure 5. Reduced average heterogeneity order parameter (HOP) values ⟨*h*⟩ of the tail (CG site E), head (CG site A), and anion (CG site D) groups for the imidazolium-based nitrate ionic liquids with various side-chain lengths. See Figure 2 for CG site definitions.

unchanged, indicating that the local structures of these groups are retained for different systems. Because of the stronger tail aggregation of the tail groups, the first peak of the tail−tail RDFs increases with various side-chain lengths. The peaks of the RDFs between head groups and anions also increase with side-chain length, because systems become more heterogeneous with longer chains due to the tail aggregation phenomenon. This is also consistent with the all-atom simulation results with the polarizable model.[15]

From the above results, it can be concluded that, despite the differences in structural and thermodynamic properties, the transferable EF-CG ionic liquid model reproduces the spatial heterogeneity of ionic liquids studied to a satisfactory degree.

3.3. Mesoscopic Ionic Liquid Structure. Before the present work, the largest size MD simulation performed for studying the spatial heterogeneity of ionic liquids contained 512 ion pairs, with a cubic simulation box size of only several nanometers along its edges. As the simulations with a smaller system containing 64 ion pairs show quite different results from the 512 ion-pair system,[15] a question is raised: is the system with 512 ion pairs large enough so that the observed microscopic spatial heterogeneity phenomenon due to tail aggregation is the real nanostructural behavior, or is the finite size simulation structure observed frustrated relative to the real structure having a larger characteristic length scale? The EF-CG model was therefore used to simulate a much larger system to study the change in structural properties. If the observed structure is a frustrated one, the larger system should show a significant structural change compared to the system with 512 ion pairs.

Table 2. Reduced Heterogeneity Order Parameters (Equations *4* and *5*) Measured for C_{12} Systems Containing 512 and 4096 Ion Pairs, Respectively

	512 ion pairs	4096 ion pairs
tail groups	4.50 ± 0.19	4.19 ± 0.11
head groups	2.24 ± 0.08	2.10 ± 0.05
anions	2.00 ± 0.07	1.87 ± 0.05

The EF-CG C_{12} system with 512 ion pairs was thereby duplicated in three dimensions to have a system with 4096 ion pairs. The corresponding all-atom ionic liquid system has a total of 217 088 atoms. After going through the same annealing steps as described above, a 1 ns constant *NPT* run yielded an average side length of the cubic simulation box of 127.8 Å, which is almost exactly twice of the box size of 63.8 Å for the C_{12} system with 512 ion pairs. Therefore, the CG MD simulations with the two sizes yield the same density. A subsequent 1 ns constant *NVT* run was carried out, with 1000 configurations evenly sampled. The time step of these runs was 4 fs.

The HOPs of the 512 and 4096 systems with the EF-CG force fields are compared in Table 2. Although the numbers are not the same, the ones for the system with 4096 ion pairs are only a little smaller than those for the system with 512

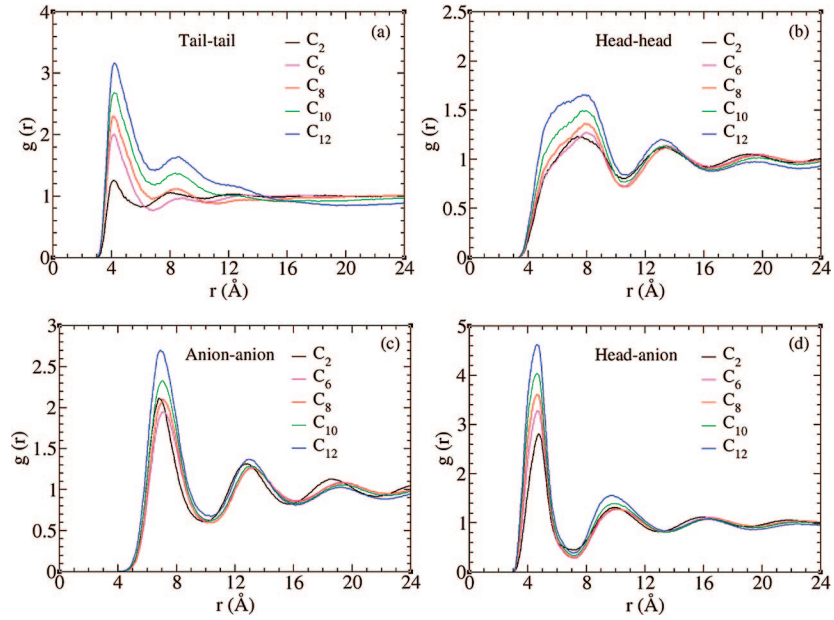

Figure 6. Radial distribution functions of (a) tail−tail (CG sites E−E), (b) head−head (CG sites A−A), (c) anion−anion (CG site D−D), and (d) head−anion (CG sites A−D) by the EF-CG models for imidazolium-based nitrate ionic liquids with various side-chain lengths. See Figure 2 for CG site definitions.

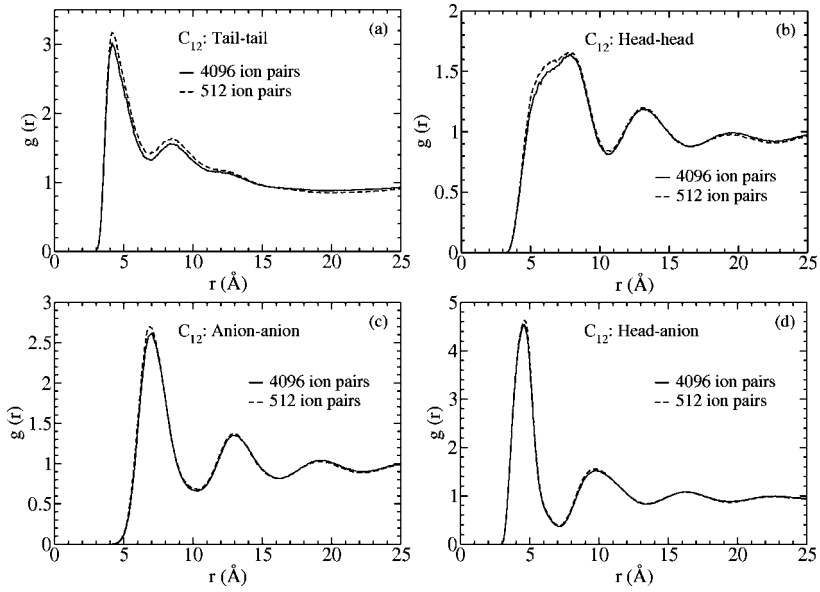

Figure 7. Radial distribution functions of (a) tail−tail (CG sites E−E), (b) head−head (CG sites A−A), (c) anion−anion (CG site D−D), and (d) head−anion (CG sites A−D) for C_{12} with 512 (dashed lines) and 4096 (solid lines) ion pairs by the EF-CG models. See Figure 2 for CG site definitions.

ion pairs. The RDFs of the two systems are compared in Figure 7. The only noticeable difference is that the peaks for the system with 4096 ion pairs are somewhat lower. From these results, it can be concluded that the C_{12} system with 512 ion pairs only has a slightly stronger tail aggregation than the one with 4096 ion pairs, and its finite size effect is not significant for the spatial heterogeneity phenomenon. It can be further anticipated that the observed structure will not change with increasing simulation size beyond 4096 ion pairs. Since the ionic liquid systems with longer side chains have a more significant finite size effect, the size of 512 ion pairs should also be large enough for the other systems investigated (C_2−C_{10}).

4. Conclusions

By sacrificing some degree of accuracy in local liquid structure, the EF-CG method has been successfully applied here to imidazolium-based ionic liquids with varying alkyl side-chain lengths. In addition to the transferability in temperature shown in ref 13, the EF-CG method is also shown here to have good transferability and additivity between systems with various side-chain lengths. Therefore, a small set of effective CG force fields is adequate to represent a series of ionic liquids having different side-chain lengths. This will be of particular importance for building a library of ionic liquid interactions and for the systematic computational design of ionic liquids at the CG level.

For organic systems with large molecules, such as ionic liquids, the finite size effect can generally be significant due to the bulkiness of the underlying molecules. Testing the finite size effect of such systems at the CG level is convenient and efficient. The present EF-CG model for ionic liquids has, for example, been used to verify that the spatial heterogeneity in ionic liquids due to tail aggregation is truly a nanoscale phenomenon.[14−17] Although the finite size effect is still noticeable, the ionic liquid systems with 512 ion pairs were shown to be large enough for the qualitative study of such spatial heterogeneity in ionic liquids with alkyl side chains of C_{12} and shorter in length.

Although the current study has applied the EF-CG method to only the imidazolium-based/nitrate ionic liquids to build a set of transferable CG force fields, the method can be applied to other kinds of ionic liquids, as well as other organic molecular systems. Its extendibility, transferability, and additivity will prove to be important for the systematic computational design of these systems at a coarse-grained level.

Acknowledgment. This research was supported by the Air Force Office of Scientific Research (FA9550-07-1-0251). Allocations of computer time from the Texas Advanced Computing Center (TACC) at The University of Texas at Austin and the National Science Foundation through TeraGrid resources provided by Pittsburgh Supercomputing Center are gratefully acknowledged.

References

(1) Rogers, R. D.; Seddon, K. R. *Science* **2003**, *302*, 792.

(2) Welton, T. *Chem. Rev.* **1999**, *99*, 2071.

(3) Liu, W.; Ye, C.; Gong, Q.; Wang, H.; Wang, P. *Tribol. Lett.* **2002**, *13*, 81.

(4) Mu, Z.; Liu, W.; Zhang, S.; Zhou, F. *Chem. Lett.* **2004**, *33*, 524.

(5) Majewski, P.; Pernak, A.; Grzymislawski, M.; Iwanik, K.; Pernak, J. *Acta Histochem.* **2003**, *105*, 135.

(6) de Souza, R. F.; Padilha, J. C.; Gonçalves, R. S.; Dupont, J. *Electrochem. Commun.* **2003**, *5*, 728.

(7) Sheldon, R. A.; Lau, R. M.; Sorgedrager, M. J.; van Rantwijk, F.; Seddon, K. R. *Green Chem.* **2002**, *4*, 147.

(8) Singh, R. P.; Verma, R. D.; Meshri, D. T.; Shreeve, J. M. *Angew. Chem., Int. Ed. Engl.* **2006**, *45*, 3584.

(9) Izvekov, S.; Voth, G. A. *J. Phys. Chem. B* **2005**, *109*, 2469.

(10) Wang, Y.; Izvekov, S.; Yan, T.; Voth, G. A. *J. Phys. Chem. B* **2006**, *110*, 3564.

(11) Izvekov, S.; Voth, G. A. *J. Chem. Theory Comput.* **2006**, *2*, 637.

(12) Izvekov, S.; Voth, G. A. *J. Chem. Phys.* **2005**, *123*, 134105.

(13) Wang, Y.; Noid, W. G.; Liu, P.; Voth, G. A. *Phys. Chem. Chem. Phys.*, in press. DOI: 10.1039/b819182d.

(14) Wang, Y.; Voth, G. A. *J. Am. Chem. Soc.* **2005**, *127*, 12192.

(15) Wang, Y.; Jiang, W.; Voth, G. A. Spatial Heterogeneity in Ionic Liquids. In *Ionic Liquids IV: Not Just Solvents Anymore*; Brennecke, J. F., Rogers, R. D., Seddon, K. R., Eds.; Ameircan Chemical Society: Washington, DC, 2007; pp 272.

(16) Lopes, J. N. A. C.; Pádua, A. A. H. *J. Phys. Chem. B* **2006**, *110*, 3330.

(17) Wang, Y.; Voth, G. A. *J. Phys. Chem. B* **2006**, *110*, 18601.

(18) Lee, C. K.; Huang, H. W.; Lin, I. J. B. *Chem. Commun.* **2000**, 1911.

(19) Lee, K. M.; Lee, C. K.; Lin, I. J. B. *Chem. Commun.* **1997**, 899.

(20) Holbrey, J. D.; Seddon, K. R. *J. Chem. Soc., Dalton Trans.* **1999**, 2133.

(21) Gordon, C. M.; Holbrey, J. D.; Kennedy, A. R.; Seddon, K. R. *J. Mater. Chem.* **1998**, *8*, 2627.

(22) Izvekov, S.; Parrinello, M.; Burnham, C. J.; Voth, G. A. *J. Chem. Phys.* **2004**, *120*, 10896.

(23) Yan, T.; Burnham, C. J.; Del Pópolo, M. G.; Voth, G. A. *J. Phys. Chem. B* **2004**, *108*, 11877.

(24) Forester, T. R.; Smith, W. *DL_POLY User Manual*; CCLRC, Daresbury Laboratory: Daresbury, Warrington, U.K., 1995.

(25) Huddleston, J. G.; Visser, A. E.; Reichert, W. M.; Willauer, H. D.; Broker, G. A.; Rogers, R. D. *Green Chem.* **2001**, *3*, 156.

(26) Seddon, K. R.; Stark, A.; Torres, M.-J. Alternative Media for Chemical Reactions and Processing. In *Clean Solvents*; Abraham, M., Moens, L., Eds.; ACS Symposium Series 819; American Chemical Society: Washington, DC, 2002.

(27) Tokuda, H.; Hayamizu, K.; Ishii, K.; Bin Hasan Susan, M. A.; Watanabe, M. *J. Phys. Chem. B* **2005**, *109*, 6103.

CT800548T

JCTC Journal of Chemical Theory and Computation

Conformational Motions of HIV-1 Protease Identified Using Reversible Digitally Filtered Molecular Dynamics

Adrian P. Wiley,† Sarah L. Williams,† and Jonathan W. Essex*

School of Chemistry, University of Southampton, Highfield, Southampton, SO17 1BJ, U.K.

Received May 7, 2008

Abstract: HIV-1 protease performs a vital step in the propagation of the HIV virus and is therefore an important drug target in the treatment of AIDS. It consists of a homodimer, with access to the active site limited by two protein flaps. NMR studies have identified two time scales of motions that occur in these flaps, and it is thought that the slower of these is responsible for a conformational change that makes the protein ligand-accessible. This motion occurs on a time scale outside that achievable using traditional molecular dynamics simulations. Reversible Digitally Filtered Molecular Dynamics (RDFMD) is a method that amplifies low frequency motions associated with conformational change and has recently been applied to, among others, *E. coli* dihydrofolate reductase, inducing a conformational change between known crystal structures. In this paper, the conformational motions of HIV-1 protease produced during MD and RDFMD simulations are presented, including movement between the known semiopen and closed conformations, and the opening and closing of the protein flaps.

1. Introduction

Human immunodeficiency virus-1 protease (HIV-1 PR) performs a vital step in the life cycle of HIV and is therefore an important drug target for the treatment of acquired immunodeficiency syndrome (AIDS).[1] The enzyme is responsible for the cleavage of the viral polyproteins to yield their functional constituent proteins, a crucial process for the correct assembly and maturation of the HIV virions.

HIV-1 PR is a homodimeric enzyme of 198 residues, containing two mobile flaps that cover the active site. For convenience, the residues of the two monomers are numbered 1 to 99, and 101 to 199. The HIV-1 PR active site consists of catalytically important, spatially neighboring aspartic acid residues, 25 and 125, at the base of a hydrophobic cleft. Each flap contains two β-sheets (residues 43 to 49 and 52 to 66) connected by a flexible Gly-Gly-Ile-Gly-Gly sequence (residues 48 to 52). Access to the active site requires substantial conformational change in the flap residues, and the nature of this motion has been the topic of much research.

In this paper, an investigation into the flap motions of HIV-1 PR is presented, including molecular dynamics trajectories obtained at a range of temperatures, and reversible digitally filtered molecular dynamics (RDFMD) simulations performed using a variety of protocols. Conformational motions are discussed according to relevant experimental data, and the accessibility of the active site is reported following different opening events.

1.1. Experimental Studies of HIV-1 PR. The HIV-1 PR system has been extensively studied by experimental methods. Abundant structural data of the apoenzyme and the complex formed with a number of substrate analogues and inhibitors is available from the protein data bank (pdb)[2] and HIV structural reference database (HIVSDB).[3,4] A review of the X-ray data was performed using 73 differing structures,[5] locating rigid regions of the protein (such as the residues that surround the active site) and more flexible areas (such as the "flap elbows" around residue 40).

The flap region is seen to exhibit a semiopen conformation in the majority of experimentally determined structures of the free protein, with one structure showing the flaps in an open arrangement allowing access to the active site, obtained with the use of mutations. The flaps have been shown to be in a more ordered, closed conformation in the presence of a ligand. The semiopen (pdb structure 1HHP[6]), open (pdb structure 1TW7[7]) and closed (pdb structure 1G6L[8] observed

* Corresponding author e-mail: J.W.Essex@soton.ac.uk.
† These authors contributed equally to this work.

10.1021/ct800152d CCC: $40.75
Published on Web 03/12/2009

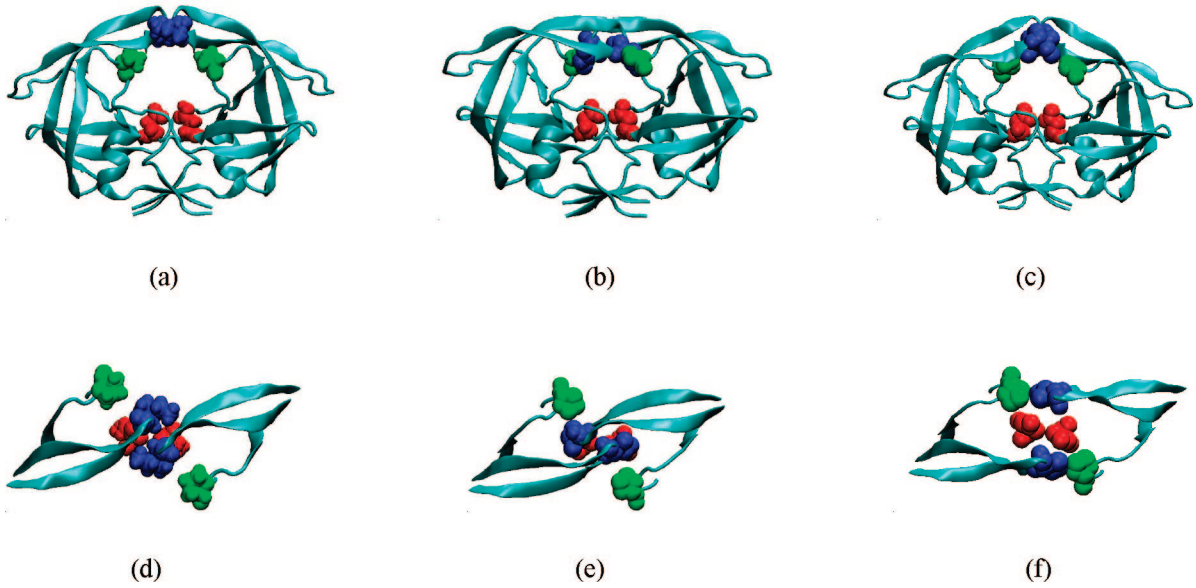

Figure 1. Cartoon representation of HIV-1 PR of semiopen (pdb 1HHP) (a and d), closed (pdb 1G6L) (b and e), open (pdb 1TW7) (c and f)) conformations. For the top view (d, e, and f), only flap and P1 loop residues are shown for clarity (residues 44 to 59, 76 to 83, 144 to 159, and 176 to 183). The van der Waals radii of particularly significant residues are displayed; the active site, residues 25 and 125, are shown in red, the flap tips, residues 50 and 150, are shown in blue, and residues 81 and 181 of the P1 loop are shown in green.

in a tethered dimer) conformations are shown in Figure 1. There is a significant change in the packing of the flap tips, which reach past each other in the closed form but cross in front of the other in the semiopen state. Also shown in Figure 1 are residues 81 and 181 which belong to the hydrophobic P1 loops (residues 79 to 81 and 179 to 181[9]) and are known to be important in flap motions.

In the inhibitor-bound state, all of the available X-ray structures show the flaps to persist in the closed conformation, with one exception, where the structure possesses a metal carborane inhibitor bound to part of the flaps, causing them to be held in an open-type conformation (pdb structure 1ZTZ[10]).

Of particular interest to this study are two NMR studies which shall be referred to in later sections of this paper. In 1999, a model of the flap mobility of HIV-1 PR was proposed by Ishima et al.[11] This was based on a detailed NMR investigation of a mutant that exhibits the same catalytic activity as the wild type protein but is stable in the concentrations required for NMR. The free enzyme was proposed to exist mainly in a semiopen state in solution, and two flap motions were detected. One occurs on a time scale well within 10 ns and involves the flap tip residues, 48 to 52. The other is a larger movement involving more of the flap residues and exists on a time scale of approximately 100 μs. The less ordered protein flaps are proposed to be in an open conformation that allows access to the active site. It was also suggested that an approaching substrate could facilitate the opening of the flaps via interaction with phenylalanine 53.

An extension of the study by Ishima et al., that includes the effects of a bound substrate, was published in 2003.[12] It was proposed that the association rate of substrates was not controlled by diffusion, but by a rare event, such as a flap opening motion. It is noted that the motions previously observed in the free protein are of limited amplitude in the substrate complex.

1.2. Theoretical Studies of Flap Mobility in HIV-1 PR. A number of computational studies of the apoenzyme have sampled a variety of flap conformations, the most successful being those which employed approaches which enhance conformational sampling.

Of studies which used conventional MD and explicit solvent, only one reports significant motion of the flaps. Scott et al. report a large opening event within 3 ns which persists until the end of the 10 ns simulation.[9] In this conformation, the flaps are lying in an asymmetric arrangement with isoleucine 50 interacting with the P1 loop, residues 79 to 81, and with isoleucine 47 and 54. This motion is stabilized by the clustering of hydrophobic sidechains, including those of valine 32, proline 79, and proline 81. Within this hydrophobic cluster is a hydroxyl group of threonine 80, proposed to keep the flap regions mobile by destabilizing the open conformation. The motion is not sampled in the presence of an inhibitor. Scott et al. claim that the simulation results are in agreement with the presence of a motion occurring in a time scale less than 10 ns, reported in the NMR study by Ishima et al. However, the motion described by Ishima et al. should be reversibly sampled well within 10 ns and should include only residues 49 to 52. It seems more likely that a motion more similar to the slower event described by Ishima et al. has been sampled in this study. This motion exists on the 100 μs time scale, in which the protein moves to a less ordered, more open state which is considered to be ligand-accessible. It is possible that Scott et al. have simulated this rare event, but the lack of a reverse path, which has not been previously reported, limits the conclusions that can be taken from this study. Other possible causes for sampling the opening motion have been suggested to be the use of the GROMOS forcefield[13] or issues with

inadequate solvation of the protein cavity.[14] A longer 22 ns MD simulation using explicit solvent, carried out by Perryman et al., does not observe this large conformational change in the WT apoenzyme and only sees one flap of a more flexible mutant move from the intial closed conformation to one similar to the semiopen state.[13]

Several simulations have been carried out using techniques which enhance sampling and these observe an increased range of conformations compared with conventional MD alone. Zhu et al. apply a constraint on the interflap distance in order to sample open conformations of the flaps.[15] The free energy profile calculated for the apoenzyme shows an initial barrier to opening, and after an opening of approximately 3 Å between the α-carbon residues, the profile is flat, suggesting a significant flexibility of the open conformation.

The transition between the closed and semiopen states in the apoenzyme was modeled using a single reaction path method by Rick et al. in 1998.[16] Although neither state allows access to the active site, the transition between semiopen and closed conformations is enzymatically important, possibly describing a closing motion over bound substrates. A loss of β-sheet structure was noted during the simulations, and significant flexibility was reported in the flap tips. Results suggest that the semiopen state exists at a higher potential energy but is stabilized by entropy.

Hornak et al.,[17] Tozzini et al.,[18] Tóth and Borics,[19] and Hamelberg and McCammon[20] all observed flap opening from semiopen/closed starting structures in their simulations. In the Hornak publication,[17] unrestrained molecular dynamics performed on the apo protein using a continuum Generalized-Born solvation model showed multiple conversions between the closed and semiopen forms, along with several reversible large-scale flap opening events. It was noticeable that the most significant opening events were not associated with flap tip curling, as has been postulated elsewhere.[9] In the publication of Hamelberg and McCammon,[20] the accelerated molecular dynamics approach[21] was used to overcome the time scale limitations, and a closed−semiopen−open conformational transition was observed with the use of explicit solvent. In addition, frequent cis−trans isomerization events of the Gly-Gly ω dihedral angles in the flap tips were observed, suggesting that the flexibility if the Gly-rich flap tips contributes to the opening motion. This conclusion is supported by experimental mutagenesis data, which shows that the Gly residues are nearly intolerant of any substitution. A study by Tóth and Borics[19] used Langevin dynamics, a continuum solvent model, and only considered torsion angles, keeping bond angles and distances rigid. Starting from the semiopen conformation, they sampled the open conformation of the flaps in addition to a range of conformations including curling of the flap tips. In addition, Tozzini et al.[18] also observed flap opening among other conformations starting from a coarse-grained model of the semiopen structure. The simulations revealed four types of flap conformation, closed, open, wide-open, and semiopen. They also show that in the open form, the flap-tips have van der Waals contact with the laterally located residue 80 (residue of P1 loop) of the opposite monomer. This observation agrees with the same observation seen in a crystallographic study of the more open HIV-1 PR structure (pdb code 1TW7).[7]

1.3. Protonation State of the Aspartic Acid Dyad. A range of theoretical and experimental studies have been performed to determine the protonation state of the active site of HIV-1 protease, in which the aspartic acids 25 and 125 are in close proximity. At pH 7, both acids would normally be modeled in the deprotonated state,[22] although their close proximity complicates this issue.

A number of experimental studies show that the protonation state of the catalytic dyad is monoprotonated at the active pH range of 5−6, where the stability and activity of this protease is at a maximum.[23,24] At neutral pH, the dyad would lose its proton and become more unstable.[25] In contrast, there is an NMR study by Smith et al. which concludes that the dianionic form exists in solution.[26]

Theoretical studies also report contrasting protonation states for the aspartic acids. Wang et al.[22] suggest a dianionic state as this form gives inter-residue aspartate distances to be closest to the crystal structure. However, the MD simulations in implicit solvent are only 120 ps and showed little deviation from starting structures for any protonation state. The simulations of Scott et al. have been confirmed as using a dianionic dyad in the active site (personal communications), and the reported six counterions used by Perryman et al. also suggests an unprotonated active site.

In support of the monoprotonated form of the active site aspartates are the MD and ab initio studies of Piana et al.[27,28] In the free enzyme, the dyad was considered to be almost ionic, with the aspartic acid residues sharing one proton. It is suggested that the ionic state of the proton may account for the interpretation of the NMR data by Smith et al.[26] Also, at each step of the proposed catalytic cycle, the aspartic acid dyad exists either in the monoprotonated form, or in a transition state, sharing protons with the substrate or with water molecules.

An MD study of the stability of the monoprotonated and deprotonated forms of the aspartic dyad under physiological conditions[29] concluded similar dynamics for both systems, independent of the protonation state of the dyad. A sodium ion was shown to closely bind to the catalytic dyad in the deprotonated state, which blocks the effects of the repulsion. In the absence of this ion, the dimer became unstable, leading to a fully open structure and perhaps explaining the result of Scott et al.

There is therefore no clear choice of protonation state of the aspartic acid in the apoenzyme, and so, in this study, both the monoprotonated and deprotonated states have been investigated.

1.4. Summary. The HIV-1 PR apoenzyme is believed to exist in a semiopen structure in solution and is known to undergo two conformational motions: a limited motion on a time scale well within 10 ns that involves a few residues on the flap tips, and an opening event on a 100 μs time scale (Ishima et al.[11]). Scott et al.[9] report an opening event during 10 ns of simulation which increases the accessibility of the active site although the motion is not reversibly sampled. Perryman et al.[13] report 22 ns of simulation which did not sample the large opening event seen by Scott et al. but

presented results in agreement with the rapid flap curling motion reported by Ishima et al. Hornak et al.[17] and Hamelberg and McCammon[20] have both observed flap opening, the former using unrestrained molecular dynamics in a continuum solvent, and the latter using an enhanced sampling method and accelerated molecular dynamics.

In light of these results, we have applied our own enhanced sampling approach, Reversible Digitally Filtered Molecular Dynamics (RDFMD), to the simulation of flap motion in HIV-1 PR. This approach is computationally efficient and offers the advantage of being useable with explicit solvent models. In addition, these RDFMD simulations are supplemented by a range of normal and high temperature MD simulations, for the monoprotonated and dianionic aspartic acid dyad.

2. Computational Methodology

2.1. Reversible Digitally Filtered Molecular Dynamics. RDFMD is a method of amplifying motions of a specific frequency during a simulation. It has been used to promote conformational motions in the pentapeptide YPGDV,[30] the Syrian hamster prion protein[31] and *E. coli* dihydrofolate reductase.[32] There are a number of interdependent parameters that are associated with the method and a protocol optimized to maximize induced motion in dihedral angles will be applied here.[32,33] This parameter set was previously shown to be suitable for application to flexible regions of protein systems.[32]

RDFMD is performed by the combination of filter sequences separated by periods of traditional molecular dynamics. During the filter sequences, a short simulation is performed in the NVE ensemble with the internal velocities, $v_{\mathrm{int},i}$, saved at each step, i, to create a velocity buffer. A digital filter is a set of coefficients designed to create a certain frequency response. A suitable digital filter is applied to the velocity buffer by multiplying the coefficients of the filter, c_i, by the Cartesian components of the internal velocities, $v_{\mathrm{int},i}$, and summing across the velocity buffer (of length $2m + 1$ steps), as shown in eq 1. Depending on the digital filter applied, the set of velocities produced, v_{filt}, will have certain frequencies of motion amplified or suppressed. The filtered velocities are then multiplied by an amplification factor, A, which determines the level of amplification performed by each filter application and are summed with the original velocities from the center of the velocity buffer, v_0. This creates a new set of velocities, v', as shown in eq 2.

$$v_{\mathrm{filt}} = \sum_{i=-m}^{m} c_i v_{\mathrm{int},i} \tag{1}$$

$$v' = v_0 + A v_{\mathrm{filt}} \tag{2}$$

Simulation can be continued using the coordinate set corresponding to the center of the velocity buffer, with the new velocity set, v'. Another velocity buffer can be filled, to which the digital filter can again be applied, thus progressively amplifying motions of a specific frequency. It is desirable to control the number of steps between filters, d, and if this is to be less than half the buffer length (i.e., if $d < m$), the simulation after the first filter must be run both forward and backward in time, as illustrated in Figure 2. If the time between filter applications is too long, the effects of each filter dissipate before the next is applied, but if too short, the filter sequences are computationally expensive and the system has no time to respond to the amplification of velocities.[32]

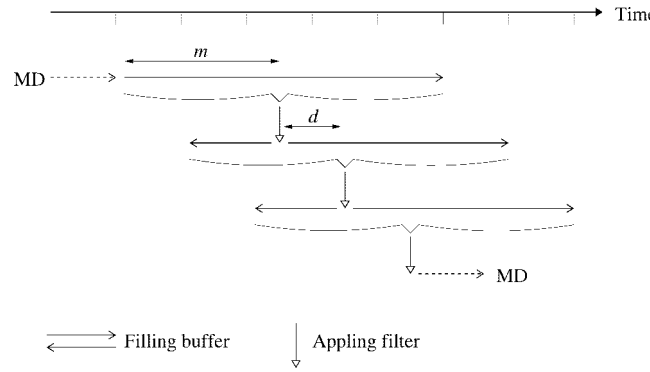

Figure 2. RDFMD sequence showing the delay parameter, d, and the filter length, $2m + 1$.

The repeated application of filters is performed until the internal energies of the targeted residues breach a specified internal temperature cap. This parameter will be discussed in a later section. Once this cap is reached, the filter sequence is ended, and molecular dynamics is performed for a period of time before another set of filters are applied. During this period the effects of the filters are allowed to dissipate, and the simulation temperature quickly returns to that set by a thermostat.

A suitable set of parameters for use with flexible regions of a protein has been optimized on a pentapeptide system[32] and shall be applied here. This includes the use of a digital filter designed to amplify frequencies between $0-100\ \mathrm{cm}^{-1}$ (for which 201 coefficients has been found to be sufficient), an amplification factor of 2, and a delay between filters of either 50 or 100 steps (any value in this region is suggested to be suitable). Filter sequences are separated by 4 ps of molecular dynamics simulation in either the NVT or NPT ensembles. This is sufficient time for the system temperature to return to the desired 300 K, and during this time conformers are sampled for analysis.

Full details of RDFMD, digital filter design, and the methods of optimizing RDFMD parameters can be obtained from previous publications.[30−32]

2.2. Computational Details. The 1HHP pdb structure[6] of the apo enzyme in a semiopen conformation was used as a starting point for both the monoprotonated and unprotonated active site systems. This structure consists of a single monomer, and a transformation of (x, y, z) to $(y, x, -z)$ is used to generate the symmetrical dimer. The crystal structure was checked, and polar hydrogen atoms were placed, using WHAT IF.[34] All other hydrogen atoms were placed and the structures solvated within the XLEAP utility of the AMBER package.[35] In the monoprotonated form of the enzyme, the proton was placed on the OD2 oxygen of aspartate 125, which lies close to the catalytic aspartate of the second monomer. Solvent was added to give a minimum distance of 12 Å from the protein surface to the cell boundary. The

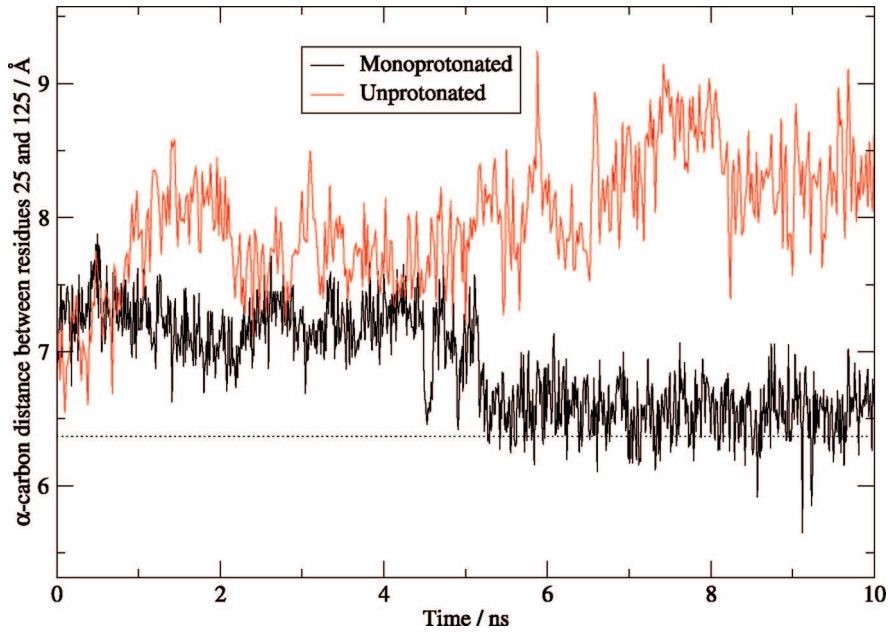

Figure 3. Inter-residue distance between catalytic aspartic acids 25 and 125. Results from 10 ns of MD simulation using the unprotonated and monoprotonated conformations are shown. The dotted line indicates the inter-residue distance in the 1HHP crystal structure.

overall charge was neutralized by the addition of chloride ions within XLEAP. The CHARMM27 force field[36] has been used with TIPS3P[37] explicit solvent.

All simulations presented here have been performed using the NAMD package[38] (NAMD was developed by the Theoretical Biophysics Group in the Beckman Institute at Urbana−Champaign) with cuboid periodic boundary conditions, a particle mesh Ewald treatment of electrostatics (with an interpolation order of 6), a 2 fs time step, and a switching function applied to Lennard−Jones interactions between 9 Å, and the 10.5 Å cutoff. All bonds containing hydrogen atoms have been constrained to equilibrium lengths using SHAKE with a tolerance of 10^{-8} Å. Simulations performed in the NVT ensemble use a Langevin thermostat, with an associated damping parameter. Simulations in the NPT ensemble also use a Nosé−Hoover Langevin barostat (with piston period and decay parameters).

During system setup a total of 96 000 steps of minimization were performed using the conjugate gradient line-search algorithm.[38] The system was then heated in the NVT ensemble for 40 ps at temperatures from 50 to 300 K, at 50 K intervals. A 10 ps^{-1} thermostat damping parameter was used to control the system temperature. An NPT simulation was then used to equilibrate the system pressure to a target of 1 atm; 100 ps of molecular dynamics was performed using a decay parameter of 100 fs and a piston period of 200 fs. A further 200 ps was then performed using a decay parameter of 300 fs and a piston period of 500 fs. The equilibrated system contained 9370 water molecules and 7 chloride ions and had cell dimensions of 61.08, 60.98, and 82.37 Å.

Molecular dynamics simulations are performed in the NVT ensemble using a 5 ps^{-1} thermostat damping parameter. The RDFMD simulations use either the NVT or NPT ensembles between filter sequences (which are performed under NVE conditions), using a 5 ps^{-1} thermostat damping parameter, a barostat decay parameter of 300 fs and a piston period of 500 fs as applicable.

3. Results

It is likely that the protonation state of the catalytic dyad is important for determining the forces in the cavity of the protein, and these may influence the conformational motions of the protein flaps. Initial simulations have therefore been performed with the monoprotonated and unprotonated dyad states and the distance between the α-carbons of the aspartic acid residues are shown in Figure 3. The distance observed in the crystal structure of 1HHP is shown with a dotted line.

The monoprotonated dyad sees two distinct states. The first has an α-carbon separation between residues 25 and 125 of over 7 Å, and the second has a distance less than 7 Å. Visualization of the simulation trajectories (not presented here) indicates that this change, which occurs rapidly at 5 ns, involves the removal of a water molecule from between the aspartic acid sidechains. This water molecule entered the region during the equilibration stage. This is not unexpected, as a water molecule is involved in the reaction catalyzed by HIV-1 PR. The second state has a similar inter-residue distance to that seen in the crystal structure.

The unprotonated dyad begins with an aspartic acid separation similar to that seen in the crystal structure, but this distance quickly increases due to the insertion of several water molecules between the aspartic acid side chains. Similar insertions of water molecules have been previously observed during MD simulations.[29] The resulting structure indicates a distance approximately 2 Å larger than that seen in the crystal structure.

It would therefore appear that the dimer interface is more stable when using a monoprotonated dyad, and subsequent simulation results presented here are all performed on the monoprotonated dyad system.

3.1. Molecular Dynamics. It is difficult to describe the flap motions of HIV-1 PR in graphical form, and analysis is shown by characteristic interaction distances and by snapshots of the protein displayed in a manner consistent to Figure 1. Trajectories of simulations presented in this study may be available by request from the corresponding author. Three conformations are identified during MD simulations, which can be defined by the location of the flap tip isoleucine residues 50 and 150, with respect to important hydrophobic side chains. How open the structure is can be described using the distance between the two flap tips, and the distances between the flap tips and the catalytic residues.

The starting semiopen structure, 1HHP, requires the side chain of the isoleucine flap tips to be closely associated with the side chain of the phenylalanine residue on the opposite flap (for example, an interaction between residues 50 and 153). The closed conformation, seen in crystal structures with inhibitors or substrate analogues, is characterized by the two flaps reaching 'past' each other, interacting with the P1 loop (residues 79 to 81) of the opposite monomer. This can be most clearly seen when looking at the distance between the side chains of the isoleucine flap tips and a proline residue in the P1 loop (residue 81 or 181). The semiopen and closed conformers can be identified using rmsd against the 1HHP and 1G6L pdb structures presented in Figure 1. Superposition is performed over residues 1 to 45, 55 to 99, 101 to 145, and 155 to 199 (those residues deemed not to be part of protein flaps) and the rmsd of the remaining flap residues (46 to 54 and 146 to 154) measured. A third conformation, with the flap tips curled back toward the P1 loop of the same monomer is also frequently observed, and can be defined by the close interaction between the isoleucine 50 to proline 81 (or residue 150 to 181) side-chain distance.

No significant opening events are sampled by the flaps during the 10 ns MD simulation. The first flap (assigned the lower residue numbers) fluctuates between the semiopen and curled conformations (demonstrated by the close distances between residues Ile50 and Phe153 (semiopen) and Ile50 and Pro81 (curled); see Supporting Information) and the distance between the flap tips and the catalytic residues is maintained at approximately 15 Å, indicating the stability of the cavity structure.

The second flap also begins in a state similar to the semiopen form; however, after 0.7 ns, a clearly defined closed conformation is obtained. The rmsd against the semiopen structure increases, and the rmsd against the known closed structure falls from 6 to 3 Å. This change is accompanied the movement of flap tip residue 150 into close proximity with proline 81. After 1.7 ns, the second flap returns to a semiopen conformation. After this point, the flap interchanges between the semiopen and curled forms, in a similar manner to that seen in the first flap.

Conformations adopted by the HIV-1 PR flaps during this simulation are representative of those referred to as semiopen, curled, and closed. Figure 4 shows examples of each of these states. For clarity, only the flap and P1 loop regions of the protein as shown in the top views in Figure 1 are displayed. The nature and timescales of the motions observed suggest that it is the interconversion between these conformers that account for the fast motions (<10 ns) observed by Ishima et al. There is no evidence of flap-opening or of increased accessibility to the active site. It is also worth noting that although the closed conformation is sampled, this only occurs in one flap rather than in both as seen in X-ray structures with bound inhibitors.

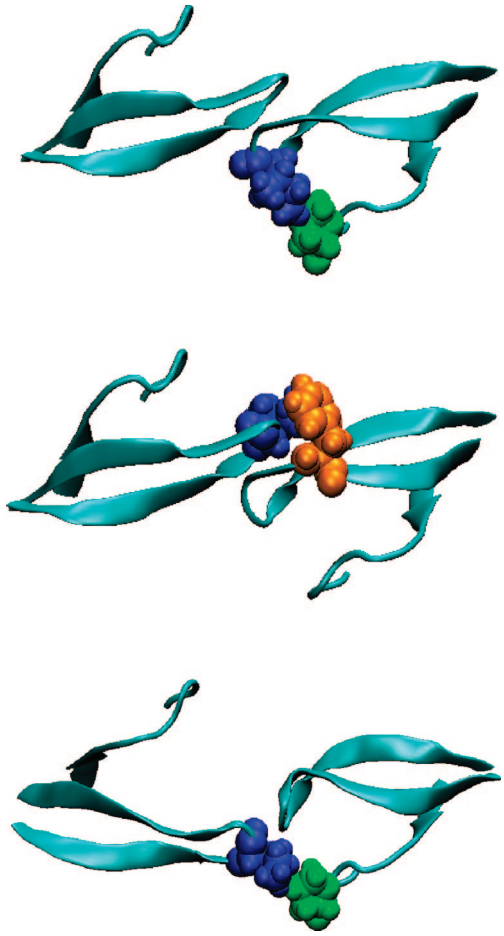

Figure 4. Top: Right-hand flap exhibits curled conformation with close contact between residues 150 (blue) and 181 (green). Middle: Left-hand flap in the semiopen conformation as seen by the close contact between residues 50 (blue) and 153 (orange). Bottom: Left-hand flap in closed conformation, with close contacts between residues 50 (blue) and 181 (green). Conformers obtained after 10 ns (top and middle) or 1.3 ns (bottom) of monoprotonated dyad MD simulation at 300 K. Residues 44 to 59 and 76 to 83 of each flap are shown, as presented in Figure 1.

3.2. Raised Temperature Molecular Dynamics. To assess the flexibility of protein residues, and to determine the stability of the HIV-1 protease system, a range of 10 ns simulations were performed at 50 K intervals from 350 to 500 K. Simulations began from the same starting point as the 300 K simulation, and the temperature was adjusted using the Langevin thermostat. The results are briefly discussed here using the locations of the flap tip residues isoleucine 50 and 150 to describe the conformers observed.

The flap conformations sampled in the 350 K MD simulations are similar to those of the 300 K MD simulation. As in the 300 K simulation, the closed conformation is only attained in one flap, indicating that although mobile between the semiopen, closed and curled conformers, the change to

a stable state with both closed flaps may be outside the 10 ns time scale. It is worth noting the consistency with the results of Perryman et al., performed on a mutant similar to the wild-type protein used here, which sampled transitions from the closed to semiopen form in only one flap within a 22 ns simulation.

The 400 K simulation samples conformations to those at 300 and 350 K. However, the simulation at 450 K observes a significant flap opening event where the second flap moves away from the active site, and another, smaller flap opening event through the curling back of the flap tips (see Supporting Information). This opening could be similar to that reported by Scott et al., although Scott et al. sampled an immediate opening.

At 500 K, the two flaps both drop toward the active site near the start of the simulation, completely excluding water from the protein cavity. There is no experimental data to suggest the existence of this conformation, although a similar event was sampled during a simulation performed by David et al.[39] with an implicit solvent distance-dependent dielectric model. It is possible that the accessibility of this conformation may be associated with a change in the solvation properties of the water model with temperature, but it is more likely to indicate a deficit of the simulation procedures and model for this system using a rapid jump to such a high temperature.

3.3. RDFMD. RDFMD has the ability to selectively enhance motions in certain regions of the protein, without increasing the energy in all degrees of freedom. This is ideal for the HIV-1 PR system, which has been shown to be highly flexible and unstable at elevated temperatures. The flap tip residues are known to be mobile and have been shown to adopt distinct conformers. Indeed, in the recent work of Hamelberg and McCammon,[20] the flexibility of the Gly-rich flap tips has been shown explicitly to contribute to the opening and motions of the flaps. RDFMD is therefore applied to the flap tip residues 49 to 51 and 149 to 151 using the previously described protocol. One hundred filter sequences are performed in an RDFMD simulation, with each sequence being separated by 4 ps of NPT or NVT MD simulation which is pieced into a trajectory for analysis. The protocol used is designed to increase dihedral angle motion in targeted regions as previously described. An important limitation of the RDFMD method when applied to increase dihedral motions is that the frequencies of these motions are similar to those in the ω peptide dihedral. However, by limiting the energy put into the system, ω angle isomerization can be excluded because of the higher energy barriers of isomerization of this dihedral, compared with those of ψ and ϕ. Within each filter sequence, amplification of low frequency motions is therefore repeated only until the targeted residues reach a desired temperature cap. No simulations presented here include isomerization of peptide bonds.

Twelve RDFMD simulations have been performed, visiting each permutation of protocol found by varying either NVT or NPT MD between filter sequences, a temperature cap of 900, 1100, or 1300 K, and 50 or 100 steps between filter applications. A range of protocols are used so to investigate the response of the system to different parameter choices, and to test the reproducibility of results when using this nonequilibrium method. Two of the simulations with a 1300 K temperature cap saw isomerization of the peptide bonds and have therefore been discarded. A total of ten RDFMD trajectories are therefore considered here.

Similar motions to those observed during molecular dynamics simulations are seen using RDFMD, with transitions occurring at an increased rate between closed, curled and semiopen states. However, the RDFMD results discussed here can be grouped into three categories, each sampling a significant motion to a greater extent than seen (if seen at all) during the MD simulations: reversible flap opening, transitions between the semiopen and closed conformations, and flap separation via curled conformations. For each category, the clearest simulation results obtained are presented, along with an indication of how often this type of motion is observed. Simulations that are not presented contain lesser movements or do not sample transitions as completely. Where flap opening motions are noted, the shortest distance between all atoms of residues 45 to 55 and those of 145 to 155 is reported (giving the separation of the flaps looking at the flap tips and four residues either side). This is intended to indicate the extent of accessibility to the active site. Simulation snapshots are considered a clear way of describing conformers sampled and are included as a replacement to full graphical analysis, which is included only where of particular interest.

When considering the motions induced by RDFMD it is important to note that only three residues at the tip of each flap are targeted by the applied protocol.

3.3.1. Reversible Flap Opening. Reversible flap opening is observed in two of the ten 400 ps RDFMD simulations. The simulation presenting the largest opening event used a filter delay of 100 steps, a temperature cap of 1100 K, and NPT MD simulation. Prior to the opening event, both flaps undergo dynamics similar to those reported for MD, with the first flap remaining in the semiopen conformation and the second flap converting between curled and semiopen conformations (indicated by proximity of the isoleucine 150 side chain with the side chains of phenylalanine 53 and proline 181, see Supporting Information).

At 280 and 305 ps, significantly open conformations which are believed to be similar to those reported by Scott et al.[9] are sampled. The flap separation reaches a maximum of 10.1 Å at 305 ps, indicating an opening motion of more than 6.5 Å (see Supporting Information). Snapshots illustrating the significant simulation conformations are shown in Figure 5. As Figure 5a and 5b show, in the most open conformation, flap 2 adopts a curled conformation and the first flap slowly increases its distance from the active site with no interaction with the P1 loop, previously seen to stabilize the curled state. After 320 ps, the opening is reversed, indicated by the decrease in the distance between the nearest flap residues and the flaps return to a conformation where the active site is inaccessible with the flaps approaching a closed conformation at the end of the simulation (Figure 5c and 5d).

This simulation appears to sample more completely the motion reported by Scott et al., with both an opening motion away from the active site, and a closing that Scott et al. did not observe. The secondary structure observed during this

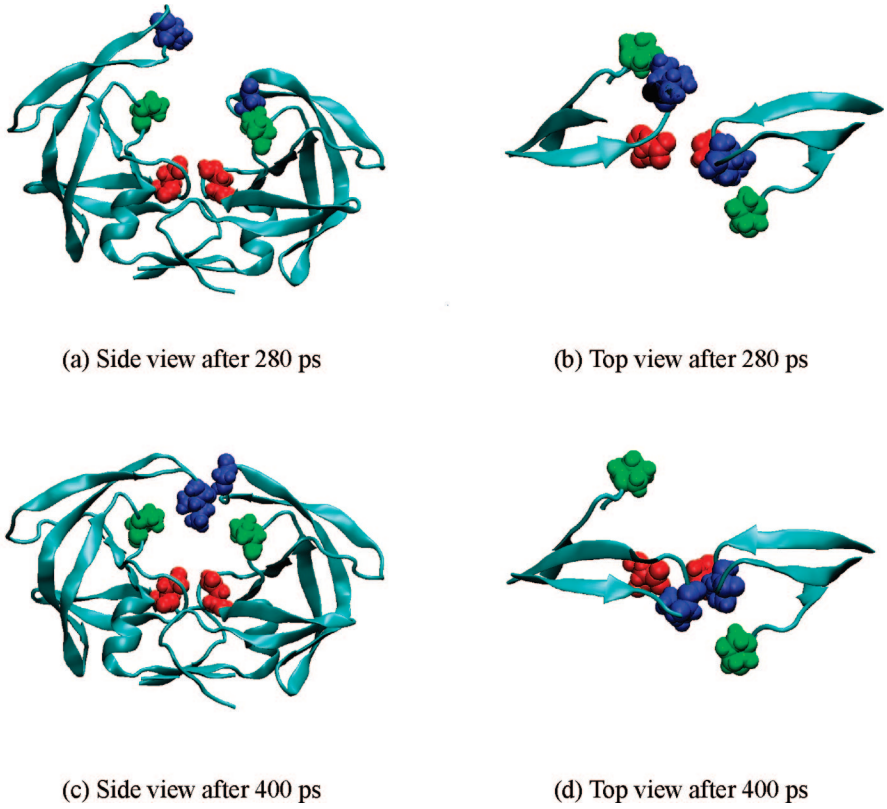

Figure 5. Snapshots of RDFMD simulation using a filter delay of 100 steps, an internal temperature cap of 1100 K and NPT simulation between filter sequences. Presentation is as described in Figure 1.

RDFMD simulation shows no significant differences to that obtained from the 10 ns MD trajectory (analysis not shown), with limited variation in the β-sheet content of the flaps. This is the case for all RDFMD simulations performed in this study.

A complete opening and corresponding closure was also obtained by the RDFMD simulation with a filter delay of 100 steps, a temperature cap of 900 K, and NVT MD simulation between filter sequences. An opening of 8.3 Å is observed in a similar fashion with one flap lifting from the protein cavity, and the other flap adopting a curled conformation. Analysis shows similar results for this lesser opening event (not presented). The opening motion of one flap has therefore been observed in two out of the ten RDFMD simulations performed.

3.3.2. Transitions between the Semiopen and Closed Conformations. One of the ten RDFMD simulations sampled a closed conformation from the initial semiopen starting structure, a conformational change not sampled during the MD simulations where, similar to several of the RDFMD simulations, only one flap moves toward a closed state. In Figure 6, six snapshots from this trajectory are presented. The conformation sampled by the RDFMD simulation where both flaps are in the closed state is similar to the closed 1G6L X-ray structure obtained from a tethered apo dimer and is commonly seen in the presence of an inhibitor. In this conformation, the flap tips swap sides (as shown in Figure 1d and 1e). This conformational change starts after 50 ps during the RDFMD simulation and does not require any significant separation in the flaps (see Supporting Information).

We consider the pathway between the semiopen and closed conformers to be similar to that seen in a reaction path study, published in 1998, by Rick et al.[40] There is little movement in the flap residues that are involved in the β-sheet structure of the protein flaps, and the flap tips (residues 48 to 52 and 148 to 152) do not cross above or below each other but pass directly in front. This is facilitated in the work of Rick et al. by the tips bending toward the direction they are to move in. However, in this simulation, the bend is toward the P1 loop in the opposite direction. The movement therefore is initially similar to the flap curling motion. Once the flaps have crossed, the flap tips straighten to give the closed conformation as seen in Figure 6 at 82 ps. Interestingly, as noted by Rick et al., it is the flap tip residues that are primarily involved in this motion, and these are assigned by Ishima et al. to the faster motion observed in a time scale of less than 10 ns by NMR. However, the single occurrence of this event in this study suggests that the transition of both flaps between semiopen and closed conformations does not occur on this time scale, and it is the semiopen to curled motion that is observed by Ishima et al.

Also noted in this simulation is the occurrence of a brief opening event just before 100 ps, during which a maximum flap separation of 6.5 Å is observed at 127 ps. Figure 6 shows snapshots of the simulation trajectory, in which, at 127 ps, a conformation is seen with strong interactions between the flap tips and the P1 loop of the opposite protein monomers but with no contact between the two flap tips, as in pdb structure 1TW7. From this state the second flap undergoes an opening motion, reaching a maximum flap separation of 9.8 Å and making no contact with the opposite P1 loop. This

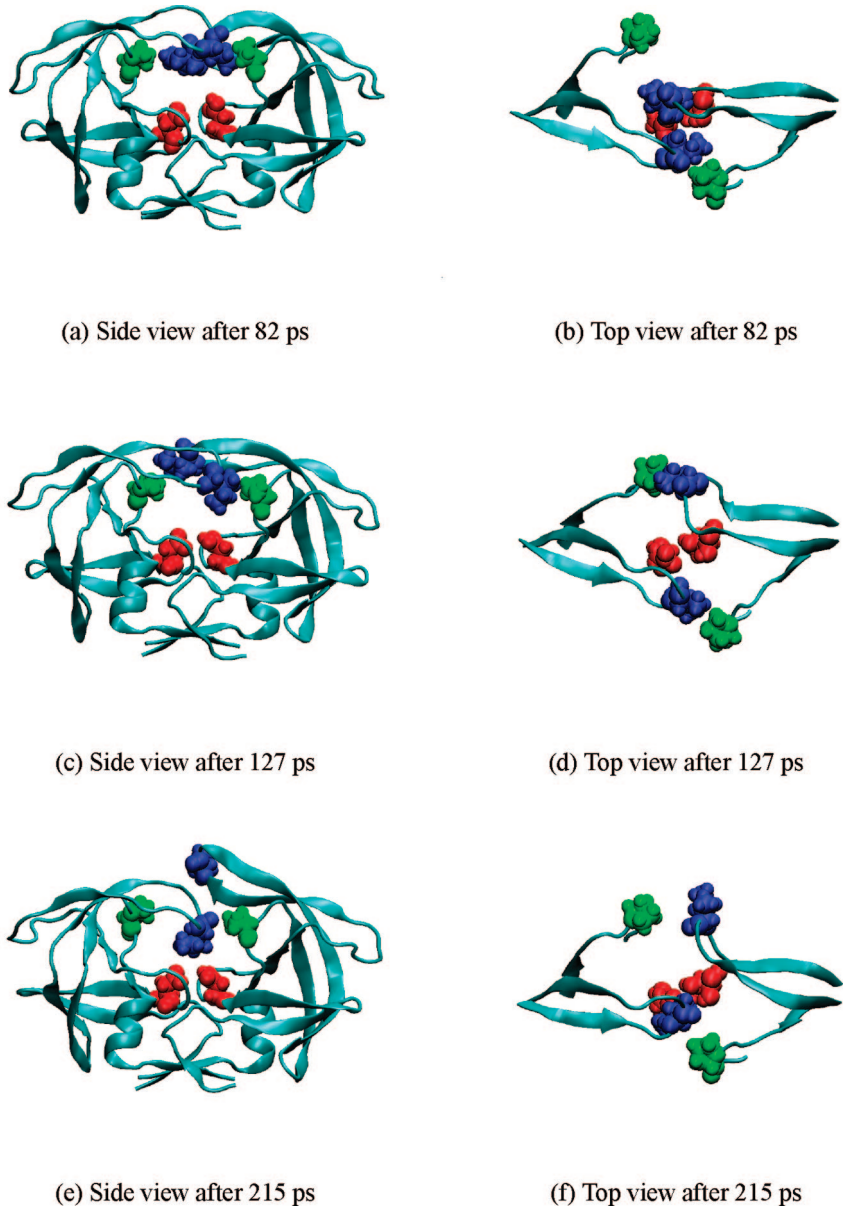

Figure 6. Conformers observed during the 400 ps RDFMD simulation of HIV-1 PR using a filter delay of 100 steps, an internal temperature cap of 1300 K, and NPT simulation between filter sequences. Presentation is as described in Figure 1.

is most clearly seen in Figure 6 at 215 ps. Following this opening motion, the flaps temporarily close back to the closed conformation, with both flaps in contact. The flaps do separate again to a lesser extent, with contact between the flap tips and the P1 loop of the opposite monomers maintained.

This RDFMD simulation has therefore shown a transition between the semiopen and closed conformations in both flaps that was not sampled in the 300 K or raised temperature MD simulations. This motion was observed in only one of the ten RDFMD simulations and could be an important step of the protein's catalytic cycle. It was noted that no flap separation was required to move between states. Also suggested is that flap opening from the closed conformation is possible, perhaps making use of an intermediate state with no contact between the flap tips. Such a state is observed in the open conformation pdb structure 1TW7.

3.3.3. Flap Separation via Curled Conformations. A separation of flaps achieved by both flaps adopting tightly curled conformations was seen in several RDFMD simulations. The simulation with a filter delay of 50 steps, a temperature cap of 900 K, and NPT between simulations showed the largest separation which reached a maximum of 8.4 Å by 400 ps. Of greater interest, despite the smaller opening of 6.7 Å, is the RDFMD simulation with a filter delay of 100 steps, temperature cap of 1100 K, and NVT between simulations, which sampled the opening in a reversible manner (see Supporting Information). Three other RDFMD simulations also sample flap separation via both flaps adopting curled conformations, and with five out of the ten simulations observing this event, it is the most frequently seen of the large motions presented here using RDFMD. It was also noted to a lesser extent very briefly during the 400 K MD simulation, where flap contact was broken for approximately 15 ps.

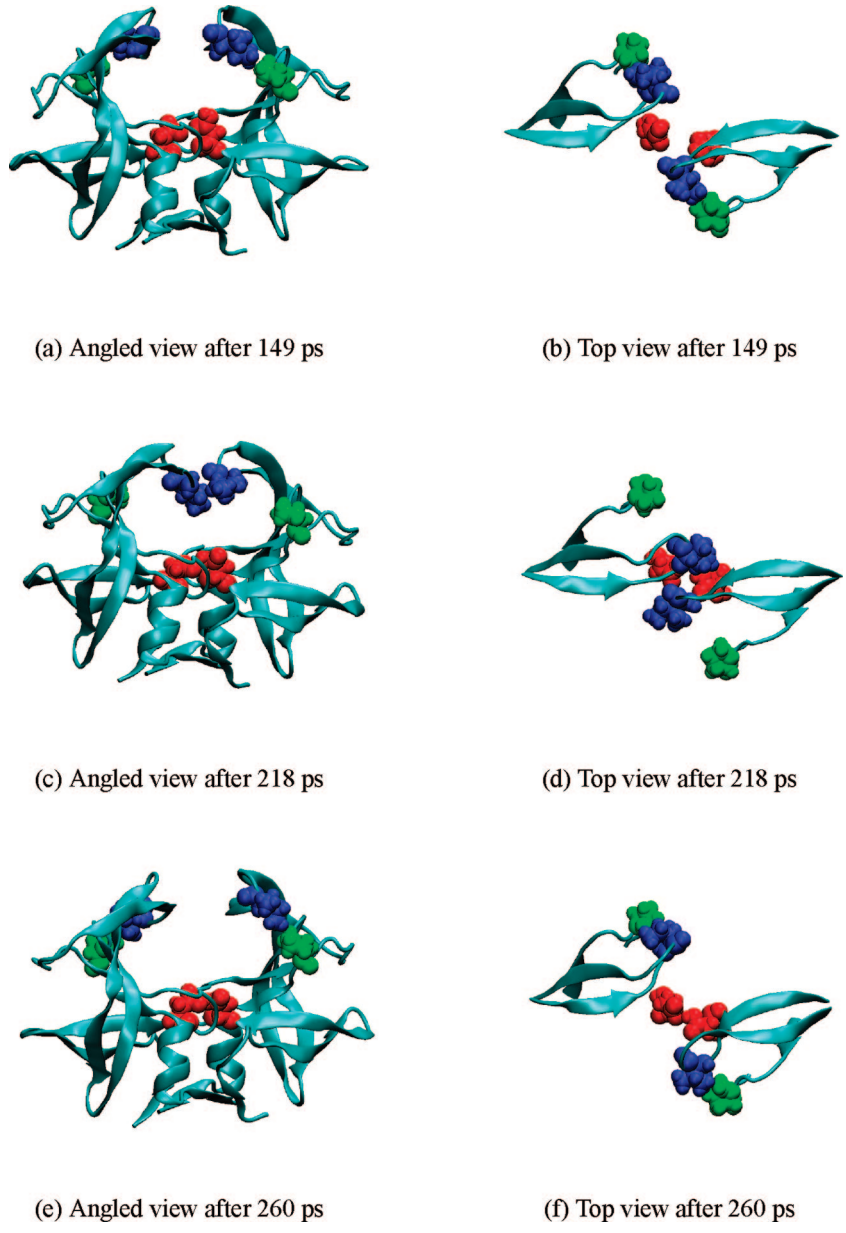

Figure 7. Conformers observed during the 400 ps RDFMD simulation of HIV-1 PR using a filter delay of 100 steps, an internal temperature cap of 1100 K and NVT simulation between filter sequences. Presentation is as described in Figure 1, with an angled view replacing the side view.

Initially, in the simulation with a filter delay of 100 steps, temperature cap of 1100 K, and NVT between simulations, the first flap is seen in a semiopen state and the second flap is curled. After 120 ps, the first flap swaps to the curled conformation. With both flaps curled, the flaps are separated (see Supporting Information). A channel is then revealed with a clear path to the active site for which no movement of the flaps away from the protein cavity and active site is required (as seen in RDFMD simulations already presented here). The flap curling is also an extension of the motion seen frequently within the 10 ns MD simulation and appears to be inherent to the HIV PR protein.

After 212 ps, the extent of the flap curling is decreased, and the contact between the flaps is regained. However, shortly afterward at 250 ps, the second flap moves again into a tightly curled conformation, and another separation of the protein flaps is seen. At 268 ps the second flap returns to the semiopen state and the flaps again close, maintaining contact until the end of the simulation. Snapshots from the simulation showing the reversible nature of the curled opening motion are shown in Figure 7. The side view shown for other simulations is replaced by a view taken from an angle to the protein, revealing the channel that opens above the active site.

4. Discussion

Analysis of the molecular dynamics simulations indicates a stable dimer interface and cavity region using the monoprotonated dyad. A conformational change to and from the closed state in one flap occurs, and the semiopen and curled conformers interconvert at a time scale well within that of the simulation. These two motions are likely to correspond to the fast event described in the NMR study by Ishima et

al. The flaps do not separate in either simulation as seen by Scott et al. although we believe our results to be consistent with those of Perryman et al., who also sampled a closed protein cavity and curling of the flap tips at room temperature.

The opening event described by Ishima et al. as occurring on a 100 μs time scale has not been sampled in the molecular dynamics simulations, and investigation was therefore continued at elevated temperatures. At 350 and 400 K, the protein flaps interconvert between clearly defined semiopen, closed, and curled conformations. Only a brief separation of flap tips is observed at 400 K, and the 350 and 400 K simulations otherwise yield results considered to be similar to those at 300 K. At 450 K, an opening event was sampled in which one flap moves away from the active site. The requirement of such high temperatures to break the otherwise stable contact of the flap tips adds strength to the conclusion that flap opening is outside the time scale of the faster motion observed by Ishima et al. At 500 K, both flaps moved into the protein cavity, adopting a collapsed conformation that indicates an instability of the protein or a breakdown of the simulation model at such a high temperature.

RDFMD simulations show three types of large scale conformational change: the transition of both flaps between the known semiopen and closed conformations, and the increased accessibility of the active site via both reversible flap opening and by flap curling. The flap opening is similar to that reported by Scott et al. although the corresponding closure is also sampled here in two of the ten RDFMD simulations.

The opening via both flaps adopting curled conformations is seen in five of the ten RDFMD simulations presented in this study, of which four sampled the corresponding closure. It is possible that this motion involves overcoming a comparatively smaller energy barrier than an opening by a flap moving away from the cavity. However, since the opening is an extension of a curling motion seen frequently in the MD simulations, it is also possible that the RDFMD method, which amplifies only motions that exist in a simulation buffer, is more likely to sample the double curling event.

It is important to note that RDFMD is seen in this study to induce large motions in the protein by targeting very few residues. This suggests that RDFMD is not necessarily driving the motion, but is assisting the protein in overcoming the initial barriers to flap tip separation. This is consistent with the observation of Hamelberg and McCammon[20] that flexibility of the flap tips contributes to their opening, although it should be noted that the simulations reported here explicitly exclude cis−trans isomerization of ω dihedral angles. The corresponding RDFMD-induced openings and conformational changes involve more residues than those targeted. It is also an important result that the reverse of opening motions are sampled within periods in which filter amplifications are applied. This confirms that RDFMD is not simply disrupting the structure as frequency independent heating may be expected to do, but is successfully assisting in conformational motions inherent to the system. The repeated sampling of the opening events induced by RDFMD, and the similarity of the closed conformer obtained to a known X-ray structure, also adds confidence in RDFMD as a conformational sampling tool.

5. Conclusions

In this manuscript, the application of an enhanced sampling technique, Reversible Digitally Filtered Molecular Dynamics, to the motion of the flaps in HIV-1 PR has been described. A range of motions are sampled in the simulations including the reversible opening of one of the flaps in a fashion similar to that reported by others, transitions between the known semiopen and closed conformations, and finally the reversible opening of the flaps by a mechanism in which both flaps curl back toward the P1 loop of their own monomer. It is important to note that all these motions are seen to be reversible, lending confidence to the results. Furthermore, all these transitions are brought about by amplifying the low frequency vibrational motions in the flap tips.

It must of course be noted that although RDFMD is efficient and capable of being used in explicit solvent, it is a nonequilibrium simulation method. For this reason, a number of RDFMD trajectories have been produced for analysis, and consistency in the conformational transitions observed has been sought. That reversible transitions from the initial semiopen to the known closed structure are observed supports the assertion that RDMFD is successfully assisting in sampling conformational motions inherent to the system. The preponderance of RDFMD trajectories following the double-curling opening mechanism may therefore reflect the presence of this type of motion in normal molecular dynamics.

Acknowledgment. This work has been funded by EPSRC. We acknowledge the contributions of S. Phillips, M. Swain, C. Edge, and R. Gledhill in the development of the RDFMD method. We thank the authors of the NAMD package for the provision of the program and for its continuous improvement. We also thank the EPSRC for the provision of computer resources (grant no. GR/R06137/01). Software to perform RDFMD is available from the authors on request.

Supporting Information Available: Analysis of MD and RDFMD simulations using characteristic interaction distances. This material is available free of charge via the Internet at http://pubs.acs.org.

References

(1) Oroszlan, S.; Luftig, R. B. *Curr. Top. Microbiol. Immunol.* **1990**, *157*, 153–185.

(2) Berman, H. M.; Westbrook, J.; Feng, Z.; Gilliland, G.; Bhat, T. N.; Weissig, H.; Shindyalov, I. N.; Bourne, P. E. *Nucleic Acids Res.* **2000**, *28*, 235–242.

(3) Prasanna, M. D.; Vondrasek, J.; Wlodawer, A.; Bhat, T. N. *Proteins* **2005**, *60*, 1–4.

(4) Prasanna, M. D.; Vondrasek, J.; Wlodawer, A.; Rodriguez, H.; Bhat, T. N. *Proteins* **2006**, *63*, 907–917.

(5) Zoete, V.; Michielin, O.; Karplus, M. *J. Mol. Biol.* **2002**, *315*, 21–52.

(6) Spinelli, S.; Liu, Q. Z.; Alzari, P. M.; Hirel, P. H.; Poljak, R. J. *Biochimie* **1991**, *73*, 1391–1396.

(7) Martin, P.; Vickrey, J. F.; Proteasa, G.; Jimenez, Y. L.; Wawrzak, Z.; Winters, M. A.; Merigan, T. C.; Kovari, L. C. *Structure* **2005**, *13*, 1887–1895.

(8) Pillai, B.; Kannan, K. K.; Hosur, M. V. *Proteins: Struct. Funct. Genet.* **2001**, *43*, 57–64.

(9) Scott, W. R. P.; Schiffer, C. A. *Structure* **2000**, *8*, 1259–1265.

(10) Cigler, P.; Koziesk, M.; Rezacova, P.; Brynda, J.; Otwinowski, Z.; Pokorna, J.; Plesek, J.; Gruner, B.; Doleckova-Maresova, L.; Masa, M.; Sedlacek, J.; Bodem, J.; Kraeusslich, H. G.; Kral, V.; Konvalinka, J. *Proc. Natl. Acad. Sci. U.S.A* **2005**, *102*, 15394–15399.

(11) Ishima, R.; Freedberg, D. I.; Wang, Y. X.; Louis, J. M.; Torchia, D. A. *Structure* **1999**, *7*, 1047–1055.

(12) Katoh, E.; Louis, J. M.; Yamazaki, T.; Gronenborn, A. M.; Torchia, D. A.; Ishima, R. *Protein Sci.* **2003**, *12*, 1376–1385.

(13) Perryman, A. L.; Lin, J. H.; McCammon, J. A. *Protein Sci.* **2004**, *13*, 1108–1123.

(14) Meagher, K. L.; Carlson, H. A. *Proteins* **2005**, *58*, 119–125.

(15) Zhu, Z. W.; Schuster, D. I.; Tuckerman, M. E. *Biochemistry* **2003**, *42*, 1326–1333.

(16) Rick, S. W.; Erickson, J. W.; Burt, S. K. *Proteins* **1998**, *32*, 7–16.

(17) Hornak, V.; Okur, A.; Rizzo, R. C.; Simmerling, C. *Proc. Natl. Acad. Sci. U.S.A.* **2006**, *103*, 915–920.

(18) Tozzini, V.; Trylska, J.; Chang, C. E.; McCammon, J. A. *J. Struct. Biol.* **2007**, *157*, 606–615.

(19) Toth, G.; Borics, A. *J. Mol. Graph. Model.* **2006**, *24*, 465–474.

(20) Hamelberg, D.; McCammon, J. A. *J. Am. Chem. Soc.* **2005**, *127*, 13778–13779.

(21) Hamelberg, D.; Mongan, J.; McCammon, J. A. *J. Chem. Phys.* **2004**, *120*, 11919–11929.

(22) Wang, W.; Kollman, P. A. *J. Mol. Biol.* **2000**, *303*, 567–582.

(23) Hyland, L. J.; Tomaszek, T. A. J.; Meek, T. D. *Biochemistry* **1991**, *30*, 8454–8463.

(24) Ido, E.; Han, H.; Kezdy, F. J.; Tang, J. *J. Biol. Chem.* **1991**, *266*, 24359−24366.

(25) Cheng, Y. E.; Yin, F. H.; Foundling, S.; Blomstrom, D.; Kettner, C. A. *Proc. Natl. Acad. Sci. U.S.A.* **1990**, *87*, 9660–9664.

(26) Smith, R.; Brereton, I. M.; Chai, R. Y.; Kent, S. B. H. *Nat. Struct. Biol.* **1996**, *3*, 946–950.

(27) Piana, S.; Carloni, P. *Proteins* **2000**, *39*, 26–36.

(28) Piana, S.; Carloni, P.; Parrinello, M. *J. Mol. Biol.* **2002**, *319*, 567–583.

(29) Kovalskyy, D.; Dubyna, V.; Mark, A. E.; Kornelyuk, A. *Proteins* **2005**, *58*, 450–458.

(30) Phillips, S. C.; Swain, M. T.; Wiley, A. P.; Essex, J. W.; Edge, C. M. *J. Phys. Chem. B* **2003**, *107*, 2098–2110.

(31) Phillips, S. C.; Essex, J. W.; Edge, C. M. *J. Chem. Phys.* **2000**, *112*, 2586–2597.

(32) Wiley, A. P.; Swain, M. T.; Phillips, S. C.; Edge, C. M.; Essex, J. W. *J. Chem. Theory Comput.* **2005**, *1*, 24–35.

(33) Wiley, A. P.; Gledhill, R. J.; Phillips, S. C.; Swain, M. T.; Edge, C. M.; Essex, J. W. In *The Hilbert-Huang Transform in Engineering: The analysis of molecular dynamics simulations by the Hilbert-Huang transform*; Huang, N., Attoh-Okine, N. O., Eds.; CRC Press: Boca Raton, FL, 2005; pp 246−263.

(34) Vriend, G. *J. Mol. Graph.* **1990**, *8*, 52–56.

(35) Pearlman, D. A.; Case, D. A.; Caldwell, J. W.; Ross, W. S.; Cheatham, T. E.; Debolt, S.; Ferguson, D.; Seibel, G.; Kollman, P. *Comput. Phys. Commun.* **1995**, *91*, 1–41.

(36) Mackerell, A. D.; Bashford, D.; Bellott, M.; Dunbrack, R. L.; Evanseck, J. D.; Field, M. J.; Fischer, S.; Gao, J.; Guo, H.; Ha, S.; Joseph-Mccarthy, D.; Kuchnir, L.; Kuczera, K.; Lau, F. T. K.; Mattos, C.; Michnick, S.; Ngo, T.; Nguyen, D. T.; Prodhom, B.; Reiher, W. E.; Roux, B.; Schlenkrich, M.; Smith, J. C.; Stote, R.; Straub, J.; Watanabe, M.; Wiorkiewicz-Kuczera, J.; Yin, D.; Karplus, M. *J. Phys. Chem. B* **1998**, *102*, 3586–3616.

(37) Jorgensen, W. L.; Chandrasekhar, J.; Madura, J. D.; Impey, R. W.; Klein, M. L. *J. Chem. Phys.* **1983**, *79*, 926–935.

(38) Kale, L.; Skeel, R.; Bhandarkar, M.; Brunner, R.; Gursoy, A.; Krawetz, N.; Phillips, J.; Shinozaki, A.; Varadarajan, K.; Schulten, K. *J. Comput. Phys.* **1999**, *151*, 283–312.

(39) David, L.; Luo, R.; Gilson, M. K. *J. Comput. Chem.* **2000**, *21*, 295–309.

(40) Rick, S. W.; Erickson, J. W.; Burt, S. K. *Proteins* **1998**, *32*, 7–16.

CT800152D

JCTC Journal of Chemical Theory and Computation

Independent-Trajectories Thermodynamic-Integration Free-Energy Changes for Biomolecular Systems: Determinants of H5N1 Avian Influenza Virus Neuraminidase Inhibition by Peramivir

Morgan Lawrenz,[†,‡] Riccardo Baron,*[,†,‡] and J. Andrew McCammon[†,‡,§,||]

Department of Chemistry & Biochemistry, Center for Theoretical Biological Physics, Department of Pharmacology, and Howard Hughes Medical Institute, University of California San Diego, La Jolla, California 92093-0365

Received December 17, 2008

Abstract: Free-energy changes are essential physicochemical quantities for understanding most biochemical processes. Yet, the application of accurate thermodynamic-integration (TI) computation to biological and macromolecular systems is limited by finite-sampling artifacts. In this paper, we employ independent-trajectories thermodynamic-integration (IT-TI) computation to estimate improved free-energy changes and their uncertainties for (bio)molecular systems. IT-TI aids sampling statistics of the thermodynamic macrostates for flexible associating partners by ensemble averaging of multiple, independent simulation trajectories. We study peramivir (PVR) inhibition of the H5N1 avian influenza virus neuraminidase flexible receptor (N1). Binding site loops 150 and 119 are highly mobile, as revealed by N1-PVR 20-ns molecular dynamics. Due to such heterogeneous sampling, standard TI binding free-energy estimates span a rather large free-energy range, from a 19% underestimation to a 29% overestimation of the experimental reference value (-62.2 ± 1.8 kJ mol^{-1}). Remarkably, our IT-TI binding free-energy estimate (-61.1 ± 5.4 kJ mol^{-1}) agrees with a 2% relative difference. In addition, IT-TI runs provide a statistics-based free-energy uncertainty for the process of interest. Using ~800 ns of overall sampling, we investigate N1-PVR binding determinants by IT-TI alchemical modifications of PVR moieties. These results emphasize the dominant electrostatic contribution, particularly through the N1 E277−PVR guanidinium interaction. Future drug development may be also guided by properly tuning ligand flexibility and hydrophobicity. IT-TI will allow estimation of relative free energies for systems of increasing size, with improved reliability by employing large-scale distributed computing.

Introduction

The free-energy change upon binding is the fundamental thermodynamic quantity to evaluate inhibitor affinity for a target protein. Reliable free-energy changes can be estimated by computer simulations via thermodynamic-integration (TI) methods.[1−5] In practice, such calculations are highly accurate for small compounds within the force field and model resolution employed.[6,7] In principle, TI approaches should also provide accurate binding free energies for large biological systems.[8,9] However, TI approaches require a sufficient sampling of the phase-space regions where the Hamiltonians corresponding to two states of the system differ significantly.[1,10,11] Therefore, the practical use of TI-based approaches in the context of macromolecular processes is still rather limited.

* Corresponding author phone: +1-858-534-2913; e-mail: rbaron@mccammon.ucsd.edu.

[†] Department of Chemistry & Biochemistry.

[‡] Center for Theoretical Biological Physics.

[§] Department of Pharmacology.

[||] Howard Hughes Medical Institute.

10.1021/ct800559d CCC: $40.75
Published on Web 03/25/2009

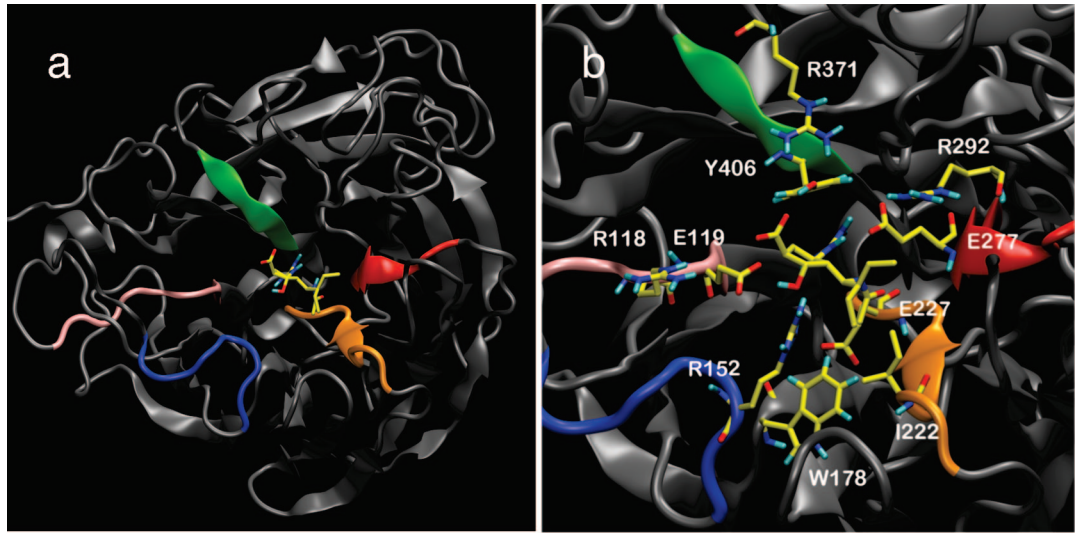

Figure 1. The avian influenza virus N1 neuraminidase protein receptor and its PVR binding site. (a) N1-PVR model structure and scaffold structures containing important PVR-binding residues (green, β-sheet 406; red, β-turn 277; orange, β-turn 222; pink, loop 119; blue, loop 150). (b) Close up of the N1-PVR binding site with key residues highlighted.

Finite sampling problems for a given equilibrium thermodynamic state can be alleviated by multiple independent simulations.[12−14] This enhances phase-space sampling and allows distribution of the computation into a number of independent runs, which is particularly appealing in consideration of the rapid and steady increase of computational power in the form of multiple CPU clusters vs single CPU supercomputers (e.g., http://www.sdsc.edu; http://www.nccs.gov; http://www.bsc.es).

Here, we present the independent-trajectories thermodynamic-integration (IT-TI) approach to calculate free-energy changes for (bio)molecular systems. IT-TI employs multiple, independent TI calculations to calculate a free-energy change of interest, while incorporating both soft-core potentials[15,16] and ligand translational restraints[17,18] to effectively improve the extent of phase-space accessed. Our results show that IT-TI allows significantly increased accuracy compared with standard TI. Using IT-TI in the context of protein−ligand binding and macromolecular association seems particularly motivated for highly flexible binding partners. This is the case for the H5N1 avian influenza neuraminidase receptor studied in this work (Figures 1 and 2).

The avian influenza virus type A, particularly its H5N1 form, is becoming a worldwide pandemic threat due to its high virulence and lethality in birds, rapidly expanding host reservoir, and exceptionally elevated mutation rate (http://www.who.int/csr/disease/avian_influenza). Extraordinary research efforts are devoted to understanding the molecular basis of inhibitor susceptibility to avian influenza viral enzyme neuraminidase (NA) mutations, particularly for the lethal and drug-resistant group 1 NA enzymes that include H5N1.[19−21] The inhibitor peramivir (PVR, also known as BCX-1812 or RWJ-270201; developed by BioCryst Pharmaceuticals, Birmingham, AL; see Scheme 1) is demonstrated to be active in vitro and in vivo against both group 1 and 2 viral NA.[22,23] Therefore, PVR constitutes a promising candidate for further drug-design research.[24]

In this paper, we explore the changes of conformational dynamics and hydration of PVR upon binding to avian influenza virus H5N1 NA (Figure 1). We perform IT-TI calculations that yield an accurate estimate for the N1-PVR free energy of binding, within ~1 kJ mol^{-1} of experiment. Then, we investigate N1-PVR binding determinants and quantify their thermodynamic role in the binding process through IT-TI alchemical modifications of selected PVR moieties. This work represents a first step in the computer-based development of a putative novel class of N1 inhibitors from accurate free-energy calculations. We anticipate that IT-TI will allow, in general, the estimation of relative free energies for systems of increasing size, with improved reliability, by employing large-scale distributed computing.[25]

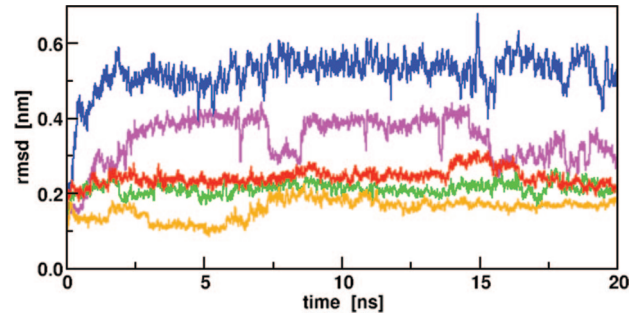

Figure 2. Time series of the C$^{\alpha}$ atom-positional root-mean-square deviation (rmsd) of each N1-PVR binding site loop or secondary structure element from the X-ray structure. Color code as in Figure 1. Running averages over 20-ps windows are used for graphical purposes.

Materials and Methods

Molecular Models. The initial coordinates for the N1 neuraminidase monomer bound to the PVR inhibitor (N1-PVR) were taken from the X-ray crystal structure[26] of N1 bound to oseltamivir (PDB ID: 2HU4; chain A), because no N1-PVR structure has been deposited to date. Atom positional coordinates for PVR were taken from the corresponding N8-PVR structure[26] (PDB ID: 2HTU; chain A) and superimposed onto 2HU4 using the protein backbone C$^{\alpha}$

Scheme 1. Summary of the Modification Perturbations (COO^-, NR_3^+, $TAIL_1$, and $TAIL_1$) for PVR Molecule[a]

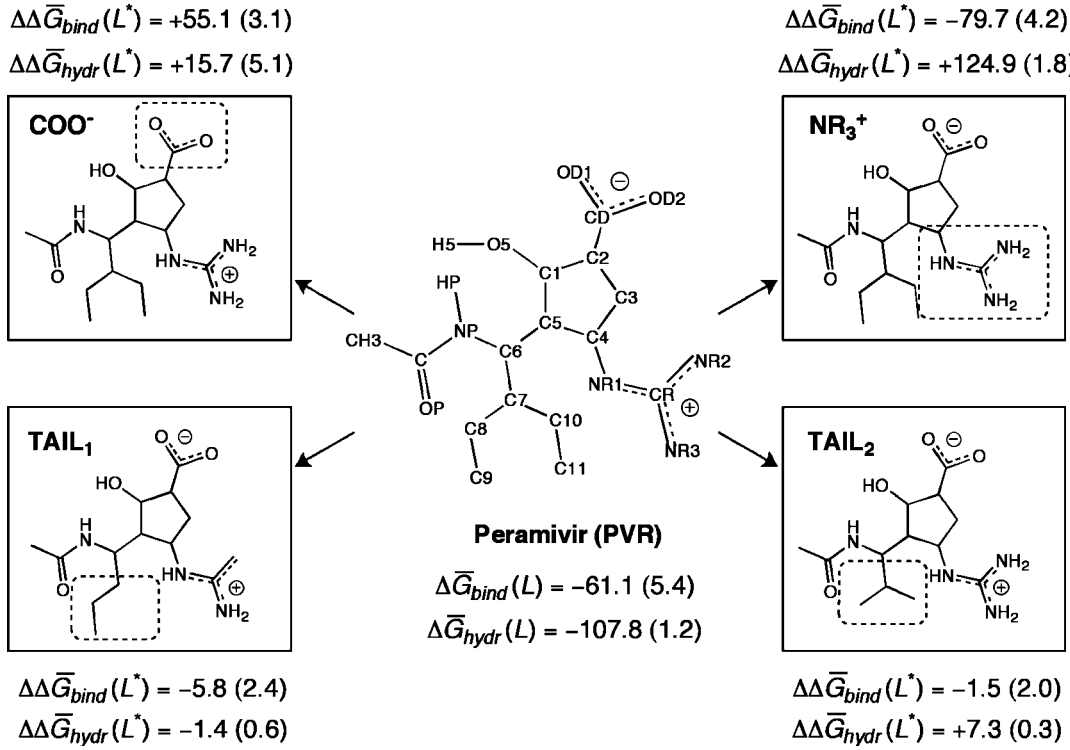

[a] The IT-TI free-energy changes due to PVR hydration $\Delta\bar{G}_{hydr}(L)$ and N1-PVR binding $\Delta\bar{G}_{bind}(L)$ are shown as well as PVR alchemical modification $\Delta\Delta\bar{G}_{hydr}(L^*)$ and $\Delta\Delta\bar{G}_{bind}(L^*)$. All values are given in kJ mol^{-1} with corresponding $\sigma_{\Delta\bar{G}}$ uncertainties between parentheses.

Table 1. System Setup for MD Simulations of PVR Bound to the N1 Active Site (N1-PVR), Free in Water (wt-PVR), and in Vacuum (vc-PVR)

	N1-PVR	wt-PVR	vc-PVR
T [K]	300	300	300
no. Na^+ ions	3	0	0
total system charge [e]	0	0	0
no. solute atoms	3863	30	30
no. water molecules	17046	1748	0
no. atoms in system	55004	5274	30

atoms; this results in superimposition of the oseltamivir and PVR ring atoms. The N1-PVR complex was solvated in (pre-equilibrated) cubic boxes large enough (~8.3 nm^3) to avoid any interactions between mirror images under rectangular periodic boundary conditions. Three randomly chosen water molecules (minimum ion−ion distances of 1.0 nm) were replaced with Na^+ ions to neutralize the system. Initial configurations for the water (wt-PVR) and vacuum (vc-PVR) reference states were defined using the same PVR coordinates. For a summary of N1-PVR, wt-PVR, and vc-PVR simulated systems, see Table 1.

Molecular Dynamics Simulations. All simulations were performed using the GROMOS05 software for biomolecular simulation[27] and the GROMOS force field[28] (45A3 parameter set[7]). Amino acid charges were defined to reproduce an apparent pH 7. GROMOS PVR force-field parameters were derived from existing building blocks[28−30] (Supporting Information, Table S1). The GROMOS compatible SPC water model[31] and previously reported SPC-water compatible parameters for ions[32] were employed. For ligand simulations in vacuo (vc-PVR) the corresponding 45B3 parameter set was employed.

For N1-PVR, a first steepest-descent energy minimization (EM) was performed to relax solvent and ions, while protein atom positions were restrained by using a harmonic potential (force constant $k = 2.5 \times 10^3$ kJ mol^{-1} nm^{-2}). A second EM run without restraints eliminated any residual strain. All EM runs were extended until the energy change per step became <0.5 kJ mol^{-1}. The system was then brought to the reference temperature ($T = 300$ K) in six consecutive MD periods of 25 ps (50 K increments). During the heating of N1-PVR, protein atom positions were restrained with a harmonic potential, using a k from 10^4 to 0 (decreased in steps of 2.5×10^3 kJ mol^{-1} nm^{-2}). In addition, four independent MD runs were initialized by reassigning random velocities from Maxwell−Boltzmann distributions at 5 K. All five independent trajectories were extended (at least 2 ns) to reach equilibration of the separate system Hamiltonian components. Independent trajectories for the wt-PVR and vc-PVR systems were similarly prepared. One MD run for each system was extended for 20 ns and used for conformational analysis (see below).

Newton's equations of motion were integrated using the leapfrog algorithm[33] with a 2-fs time step. The SHAKE algorithm[34] was applied to constrain all bond lengths (relative geometric tolerance of 10^{-4}). All simulations were carried out in the N,p,T ensemble (reference pressure 1 atm) by separately coupling the temperature of solute and solvent degrees of freedom to a 300 K heat bath[35] (relaxation time 0.1 ps) and by coupling the pressure (estimated based on an atomic virial) to

Scheme 2. Thermodynamic Cycles: Annihilation Perturbation[a] and Modification Perturbation[b]

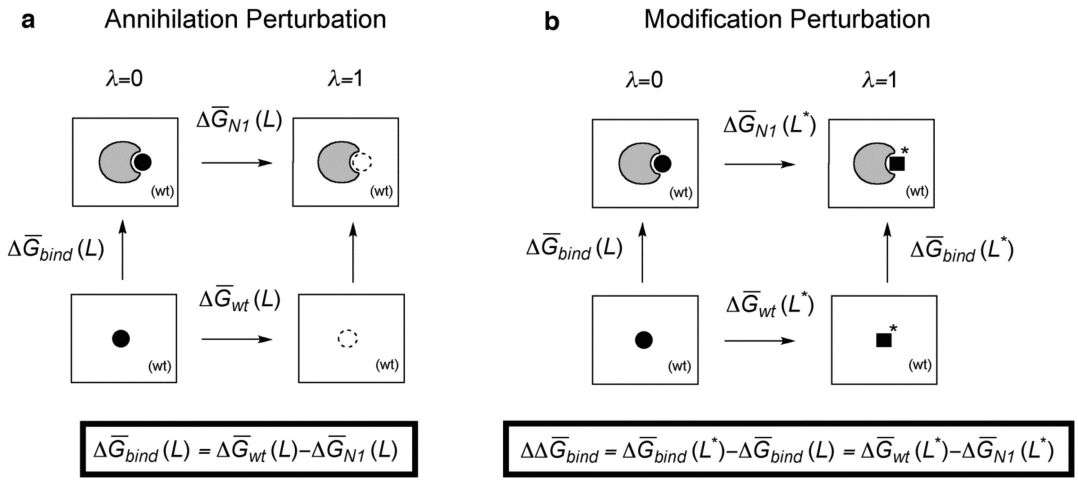

[a] The binding free energy $\Delta\bar{G}_{bind}(L)$ for ligand L can be estimated by an annihilation perturbation ($\lambda = 0 \rightarrow \lambda = 1$) of the nonbonded ligand interactions in the protein and water-solvated thermodynamic states. [b] The impact on the binding free energy, $\Delta\Delta\bar{G}_{bind}(L^*)$, for a ligand modification L* can be estimated by corresponding perturbations ($L \rightarrow L^*$) in both thermodynamic states. An additional cycle was employed to estimate hydration free energies $\Delta G_{hydr}(L)$.

a pressure bath[35] via isotropic coordinate scaling [relaxation time 0.5 ps; isothermal compressibility 4.574×10^{-4} (kJ mol^{-1} nm^{-3})$^{-1}$]. Nonbonded interactions in the range 0.0−0.8 nm were recalculated every time step and in the range 0.8−1.4 nm every five time steps and truncated at 1.4 nm. A reaction-field correction was applied to account for the neglected interactions beyond 1.4 nm,[36] using a relative dielectric permittivity of 61 for the SPC water model.[37] A fast grid-based pairlist-construction algorithm[38] was employed (cell-mask edge of 0.4 nm; atomic-level cutoff) as implemented in the GROMOS05 MD++ module.[27]

Conformational Analysis. Trajectory snapshots were extracted every 2 ps from the 20-ns simulations. Structural fitting was performed by (i) superimposing solute centers of mass (to remove overall translation) and (ii) performing an atom-positional least-squares fitting procedure[39] (to remove overall rotation) using N1 C^{α} atoms or all PVR atoms. Transient N1-PVR interactions identified as important binding motifs were monitored using the GROMOS++ analysis software.[27] Hydrogen bonds were defined to have a maximum hydrogen-acceptor distance of 0.3 nm and a minimum donor-hydrogen-acceptor angle of 125°. An extended hydrogen bond criterion was used (0.35 nm; 120°) to capture additional relevant interactions. Salt bridges and hydrophobic contacts were considered formed for atom pair distances <0.45 nm. Secondary structure elements were defined by the following N1 residue sequences: loop 119, V116−P120; loop 150, T148−S153; loop 277, I222−E227; β-turn 277, H274−C278; β-turn 292, V290−N294; loop 347, G345−K350; loop 371, S368−G373; β-sheet 406, S404−G408; loop 430, R430−W438.

Independent-Trajectories Thermodynamic-Integration Method. The free-energy change between two states A and B can be estimated by thermodynamic integration (TI) as[40]

$$\Delta G_{A\rightarrow B} = \int_{\lambda_A}^{\lambda_B} d\lambda \left\langle \frac{\partial H(\lambda)}{\partial \lambda} \right\rangle_{\lambda} \qquad (1)$$

where $H(\lambda)$ denotes the system Hamiltonian from a single trajectory as a function of the coupling parameter λ and $\langle ... \rangle$ denotes ensemble averaging at a given λ value.

In IT-TI, $H_i(\lambda)$ is the system Hamiltonian for the ith independent trajectory, and the mean free-energy change $\Delta\bar{G}_{A\rightarrow B}$ reads

$$\Delta\bar{G}_{A\rightarrow B} = \int_{\lambda_A}^{\lambda_B} d\lambda \frac{\sum_{i=1}^{N} \left\langle \frac{\partial H_i(\lambda)}{\partial \lambda} \right\rangle_{\lambda}}{N} \qquad (2)$$

where the integration runs over N independent trajectories.

In principle, under the assumptions of (i) infinitely long trajectories and (ii) a fully accessible system phase space, eq 1 will provide an estimate of the free-energy change between two states A and B which is identical to that provided by eq 2. This follows in the limits of validity of the *ergodic hypothesis*. In practice, however, due to the fact that (i) only finite simulation times can be achieved and (ii) the phase space of a solvated macromolecule is far from being fully accessible (i.e., its corresponding free-energy landscape is a very rough and frustrated surface at standard/physiological conditions), eqs 1 and 2 provide significantly different free energy estimates (see Results and Discussion). IT-TI overcomes this practical limitation by enhancing phase-space sampling of the thermodynamic systems of interest, therefore adding to the reliability and predictive power of free-energy calculations.

Two types of thermodynamic perturbations A→B were performed in this study, alternatively employing eq 1 or 2: (i) from ligand L full potential ($\lambda = 0$) to zero nonbonding interactions ($\lambda = 1$); (ii) from the L full potential ($\lambda = 0$) to that of a chemically modified ligand L* ($\lambda = 1$); see Scheme 2. In both cases, soft-core interaction potentials[16] were used for L atoms involved in the perturbation ($s_{LJ} = 0.5$ and $s_C = 0.5$)[27,28] to avoid singularities and to enhance phase-space sampling. Equations 1 and 2 were integrated numerically using the trapezoidal rule.

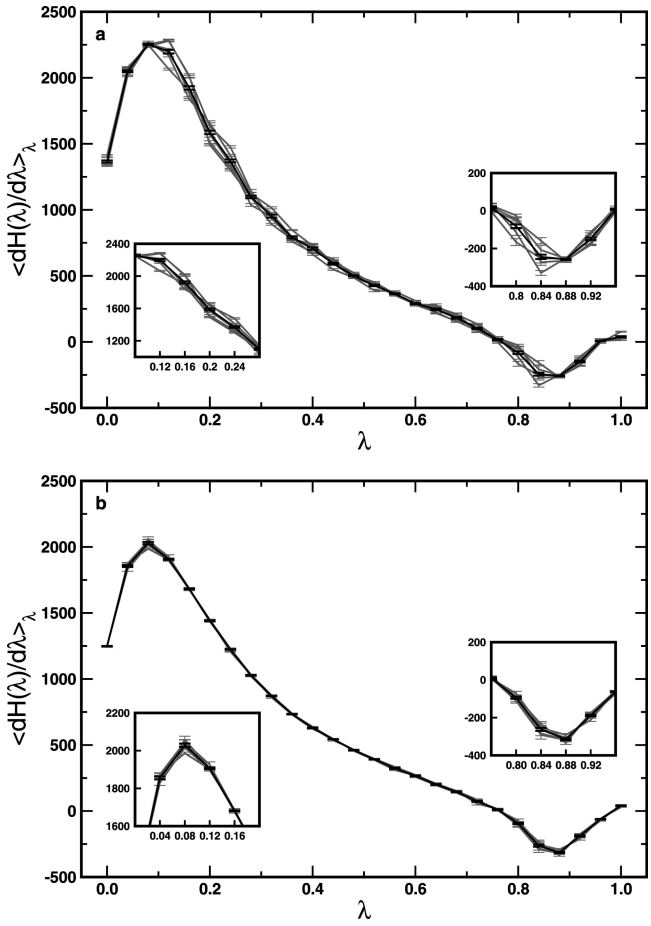

Figure 3. $\langle \partial H(\lambda)/\partial\lambda \rangle_\lambda$ values and corresponding uncertainties $\sigma_{sim}(t)$ vs λ. (a) Annihilation of PVR in N1 binding site ($\Delta\bar{G}_{N1}(L)$; Scheme 2a). (b) Annihilation of PVR in water ($\Delta\bar{G}_{wt}(L)$; Scheme 2a). Black lines: average values over all N individual trajectories. Gray lines: individual trajectory TI curves. Inset panels highlight λ regions where IT-TI averages outperform standard individual TI calculations.

Statistical Analysis of Uncertainties. Two alternative statistical procedures were employed to evaluate the uncertainty σ for $\Delta G_{A\to B}$ or $\Delta\bar{G}_{A\to B}$ free-energy estimates.

First, a simulation standard error $\sigma_{sim}(t)$ of the time-varying Hamiltonian derivative at a given λ can be calculated as

$$\sigma_{sim}(t) = \sqrt{\frac{1}{T-1}\sum_{t=1}^{T}\left[\left(\frac{\partial H_t(\lambda)}{\partial\lambda}\right)_\lambda - \left\langle\frac{\partial H_T(\lambda)}{\partial\lambda}\right\rangle_\lambda\right]^2}/\sqrt{T} \tag{3}$$

with T being the total number of block averages[41] throughout the single ith trajectory or all N concatenated independent trajectories. $(\partial H_t(\lambda)/\partial\lambda)_\lambda$ denotes the Hamiltonian derivative, block-averaged at time t, and $\langle\partial H_T(\lambda)/\partial\lambda\rangle_\lambda$ is the ensemble average over the entire simulation time at a given λ. As an example, $\sigma_{sim}(t)$ uncertainties are reported as error bars for $\langle\partial H_T(\lambda)/\partial\lambda\rangle_\lambda$ vs λ in Figure 3 (solid black curve). Then, a corresponding free-energy uncertainty can be obtained as

$$\sigma_{\Delta G_i} = \left(\int_{\lambda_A}^{\lambda_B} {\sigma_{sim}}^2(t)\,d\lambda\right)^{1/2} \tag{4}$$

This follows from the standard assumption that $(\partial H_t(\lambda)/\partial\lambda)_\lambda$ values are statistically uncorrelated along the time over different values of the coupling parameter λ. However, the $\sigma_{\Delta G_i}$ uncertainty includes the physically based fluctuations of $(\partial H_t(\lambda)/\partial\lambda)_\lambda$, though corresponding noise is typically reduced by block-averaging.[41] Therefore, despite its wide use in the literature, $\sigma_{\Delta G_i}$ is a questionable measure of uncertainty for a free-energy change of interest. For example, considering that overlap of phase space at neighboring λ values is a requirement for smooth $\langle\partial H_T(\lambda)/\partial\lambda\rangle_\lambda$ vs λ curves (Figure 3), one could claim that $(\partial H_t(\lambda)/\partial\lambda)_\lambda$ time series are statistically correlated. Nonetheless, the abovementioned uncertainty defined in eq 4 is representing the lowest possible uncertainty for a free-energy-change estimate from standard TI. Thus, it seems the fairest choice for this study comparing TI vs IT-TI results.

Second, for IT-TI, a statistics-based uncertainty $\sigma_{\Delta\bar{G}}$ on a given free-energy change $\Delta\bar{G}_{A\to B}$ from eq 2 can be calculated as the standard deviation from the mean (standard error) of the N ΔG_i results

$$\sigma_{\Delta\bar{G}} = \frac{\sigma_{\Delta G}}{\sqrt{N}} \tag{5}$$

where $\sigma_{\Delta G}$ is the standard deviation of the free-energy change over the N IT-TI trajectories employed. Importantly, $\sigma_{\Delta\bar{G}}$ has a clear statistical validity,[42] because of its explicit dependence on the repeated independent estimates.

Similarly, for a general overall free-energy change $\Delta\bar{G}_{A\to B}$, calculated as the difference between two free-energy changes $\Delta\bar{G}_B$ and $\Delta\bar{G}_A$, a corresponding uncertainty can be obtained by propagating the respective uncertainties as[42]

$$\sigma_{\Delta\bar{G}_{A\to B}} = \sqrt{(\sigma_{\Delta\bar{G}_A})^2 + (\sigma_{\Delta\bar{G}_B})^2} \tag{6}$$

Then, the relative uncertainty for a given free-energy change A → B reads

$$\sigma_{\Delta\bar{G}_{A\to B}}(\%) = \frac{\sigma_{\Delta\bar{G}_{A\to B}}}{\Delta\bar{G}_{A\to B}} \times 100 \tag{7}$$

In this study, IT-TI runs were extended to obtain sufficiently smooth curves of $\langle\partial H_i(\lambda)/\partial\lambda\rangle_\lambda$ vs λ (Figure 3). IT-TI trajectories were independently equilibrated (0.5 ns) for each of the 26 λ points (from five initial equilibrated $\lambda = 0$ configurations), followed by independent sampling periods (0.5 ns) used for free-energy estimation. Increased sampling (up to 2.5 ns) times were required in the ranges $0.12 \le \lambda \le 0.24$ and $0.76 \le \lambda \le 0.92$. A summary of these calculations is given in Supporting Information, Table S2. All annihilation and modification perturbations fulfilled the criterion $\sigma_{\Delta\bar{G}}(\%) < 6\%$. Only N1−TAIL$_1$ and N1−TAIL$_2$ modification perturbations had larger $\sigma_{\Delta\bar{G}}(\%)$ values (up to 52%) due to the corresponding small $\Delta\bar{G}_{A\to B}$ values (Supporting Information, Table S3).

Separation of Thermodynamic States. For $\Delta\bar{G}_{N1}(L)$ (Scheme 2a), the potential $U(r_L) = {}^{-1}/_2 k (r_L - r_0)^2$ was applied to harmonically restrain ligand translation and ensure its sampling of a finite phase-space volume V_I. An optimal k value of 246.5 kJ mol^{-1} nm^{-2} was estimated from the ensemble-averaged L root-mean-

square deviation (rmsd) by applying the equipartition theorem as[18]

$$\langle \mathrm{rmsd}^2 \rangle = \langle (r_L - r_0)^2 \rangle = \int (r_L - r_0)^2 P(r_L)\, dr_L = \frac{3RT}{k} \quad (8)$$

where r_L is the position of L during 20-ns of unrestrained simulation at $\lambda = 0$, r_0 is the initial position of L in the pre-equilibrated starting configuration, $P(r_L)$ is the 3-D positional probability distribution of L, R is the molar gas constant, and $T = 300$ K. In this study, r_L and r_0 are the instantaneous and initial positions of the PVR C4 ring carbon.

The phase-space volume V_I can be defined as[18]

$$V_I = \int_V \exp[-\beta U(r_L)]\, dr \quad (9)$$

$$V_I = \int_V \exp\left[\frac{1}{2RT} k(r_L - r_0)^2\right] dr = \left(\frac{2\pi RT}{k}\right)^{3/2} \quad (10)$$

where $\beta = 1/RT$. Thus, the correction[17] to the restraining potential bias for $\Delta\bar{G}_{N1}(L)$ in Scheme 2 reads

$$\Delta\bar{G}_{N1}(L) = \int_{\lambda=0}^{\lambda=1} d\lambda \frac{\sum_{i=1}^{N} \left\langle \frac{\partial H_i(\lambda)}{\partial \lambda} \right\rangle_\lambda}{N} + RT \ln(CV_I) \quad (11)$$

Results and Discussion

Conformational Analysis of the N1-PVR Binding Site. Figure 1 shows the six-bladed β-propeller structure of N1 neuraminidase bound to PVR and important active site residues, monitored throughout 20 ns of N1-PVR MD simulation. To investigate N1-PVR receptor flexibility and conformational changes, the C^α atom-positional rmsd from the X-ray crystal structure was monitored for the secondary structure elements forming the N1-PVR binding site (Figure 2). Loop 150 deviates the most (up to ~0.7 nm) to sample stable open-loop configurations (~0.5 units) throughout the MD simulation (Figures 1 and 2, blue). This observation is similar to that recently reported for both apo and oseltamivir-bound N1 neuraminidase (up to ~0.6 nm).[43] Additionally, we find that loop 119 demonstrates significant flexibility and samples conformations with rmsd of ~0.4 and ~0.3 nm in the N1-PVR complex (Figures 1 and 2, pink). The dynamics of loops 150 and 119 in water indicate a significant relaxation from the crystal-packed conformation captured in X-ray experiments. The β-sheet 406 and β-turns 277 and 222 show comparatively lower rmsd deviations (0.1−0.3 nm) and smaller fluctuations on the 20-ns time scale.

Table 2 summarizes the N1-PVR intermolecular hydrogen bonding. Scheme 1 defines PVR atom nomenclature. A dominant multicenter hydrogen bond between N1 E277 and the PVR guanidinium group is stable for the entire simulation time, with PVR NR3 and NR1 atoms alternating as hydrogen donors to E277 carboxyl oxygen atoms OE1 and OE2 (50−69% occurrences). E277 also transiently interacts with the PVR methyl acetamide polar hydrogen (HP; 57%). Yet another hydrogen bond (54%) is observed between the PVR carboxyl oxygen (OD1) and the N1 Y406 hydroxyl (O−H).

Table 2. N1-PVR Intermolecular Hydrogen Bonds from 20 ns of Molecular Dynamics Simulation[a]

donor	acceptor	occurrence (%)
PVR (NR3−HR3)	E277 (OE1)	69
PVR (NR3−HR3)	E277 (OE2)	69
PVR (NR1−HR1)	E277 (OE1)	50
PVR (NR1HR1)	E277 (OE2)	57
PVR (NP−HP)	E277 (OE2)	57
Y406 (O−H)	PVR (OD1)	54
R152 (NH2−H22)[b]	PVR (O5)	44

[a] PVR atom nomenclature as in Scheme 1. OE refers to glutamate carboxyl, O−H to tyrosine hydroxyl, and NH2−H22 to arginine guanidinium. All N1-PVR intermolecular hydrogen bonds occurring >5% are shown. [b] Using extended hydrogen-bonding criterion. See also Materials and Methods.

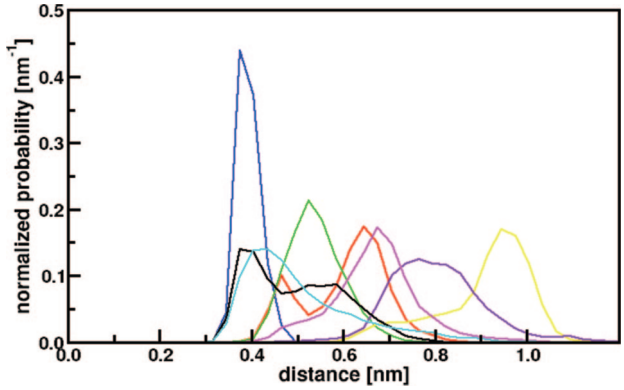

Figure 4. Conformational sampling of PVR moieties in the N1 neuraminidase binding site from 20-ns N1-PVR molecular dynamics simulation. Distance pairs are labeled according to the atoms monitored: PVR CR to N1 E277 (blue), E119 (green), and E227 (red) carboxyl group carbon; PVR CD to N1 R118 (pink), R292 (yellow), and R371 (violet); PVR C11 to N1 I222 side chain carbon (black) and W178 aromatic ring carbon (cyan). See Scheme 1 for PVR atom nomenclature.

Interestingly, the Y406 residue is homologous to other key catalytic tyrosine residues found in the avian influenza virus family of glycosidases (Carbohydrate Active Enzymes database; http://www.cazy.org/). Thus, targeting Y406 could be important for drug design, as suggested by a computational solvent mapping analysis.[44] An extended hydrogen bond between N1 R152 on loop 150 and PVR (O−H group) occurs for 44% of the simulation time (Table 2 and Figure 1) and contributes to the stability of open loop 150 ensemble of configurations.

Figure 4 describes the conformational sampling of PVR in the N1 binding site. N1 protein atoms that maintain strong interactions with either (i) charged ligand moieties (salt bridges) or (ii) hydrophobic groups (hydrophobic packing) display distance probability distributions with one sharp, high-intensity peak. Those residues experiencing varied interactions have broader distributions and/or multiple peaks. Throughout the 20-ns simulation, the PVR guanidinium group (CR atom, Scheme 1) maintains a well-defined salt-bridging interaction with the N1 E277 carboxyl group (0.38 nm average distance). The broad distribution for the PVR CR−N1 E119 distance (0.52 nm) and the doubly peaked distribution for the PVR CR−N1 E227 distance (0.47 and 0.65 nm for first and second peak) correspond to transient

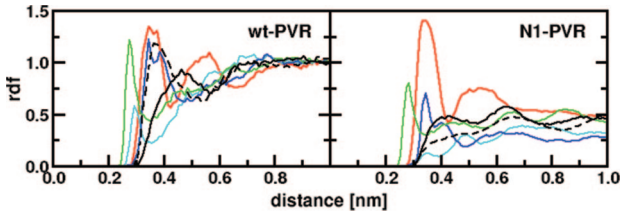

Figure 5. Ensemble-averaged solvation of PVR moieties when free in solution (left panel) or bound to the N1 protein binding site (right panel). Radial distribution functions of the water oxygen atoms from 20-ns molecular dynamics simulations are shown centered on PVR atoms CR (blue), C10 (black solid), C11 (black dashed), CD (red), O5 (green), and NP (cyan). See Scheme 1 for PVR atom nomenclature.

salt bridges formed by these N1 glutamate residues to the PVR guanidinium group.

Stable long-range interactions between PVR and the arginine triad of R118, R371, and R292 residues (Figure 1) are observed along our 20-ns N1-PVR simulation, with distribution peaks at 0.68, 0.8, and 0.96 nm, respectively (Figure 4). This triad of positively charged residues also contributes to binding via the conserved ligand carboxyl group in both the natural ligand, sialic acid, and other synthetic neuraminidases inhibitors (e.g., DANA, oseltamivir, and zanamivir).[26,45] Our results support the fundamental role of R118 and R371 in N1-PVR binding. The distal position of R292 indicates less reliance of PVR on this residue and could account for the retained PVR affinity for the N2 resistance mutation R292K.[23,46]

The PVR aliphatic tail (Scheme 1) has been designed[45] to fill a small hydrophobic subpocket, comprised of W178 and I222 residues, which is conserved among both group 1 and 2 NA (Figure 1). Our MD simulation confirms that PVR tail atoms interact with the branched I222 side chain (C11 peak at 0.40 nm average distance; Figure 4). The same PVR tail atoms are also stably close to the W178 aromatic carbons (C11 peak at 0.42 nm; Figure 4). These results highlight the occurrence of important hydrophobic-packing interactions in the N1 subpocket.

We note that the majority of the conserved residues described above have been suggested to also participate in key interactions between sialic acid and inhibitors DANA, zanamivir, and oseltamivir, as well as PVR, in both group 1 and 2 NA receptors.[26,44−48]

Changes of PVR Hydration upon N1 Binding. PVR hydration and its changes upon N1 binding were also analyzed. Figure 5 shows the radial distribution functions (rdf) for water oxygen atoms from wt-PVR and N1-PVR simulations. The PVR guanidinium group (CR atom; Scheme 1) undergoes ∼0.5 units decrease in its first peak intensity upon N1-PVR binding. We can explain this desolvation effect by considering the tight interaction of this bulky, positively charged PVR group with the negatively charged N1 E277 carboxyl (Figure 4 and Table 2). Desolvation upon N1 binding is also observed for the PVR aliphatic tail by the intensity decrease of its first solvation shell peaks (C10 and C11 atoms, ∼0.5−0.9 units; Figure 5). This is consistent with the formation of more favorable interactions between PVR and N1 residues I222 and W178.

A different hydration behavior can be noticed for the PVR carboxyl group (CD atom), with a similar strong intensity for its first peak at ∼0.35 nm in both wt-PVR and N1-PVR simulations. Its second peak intensity diminishes only marginally upon N1-PVR binding (∼0.3 units). Thus, the PVR carboxyl group is still solvated in the N1 binding site by dynamic water molecules on an ensemble averaged basis. The presence of water molecules in the N1-PVR binding site and the lack of persistent ligand−solvent hydrogen bonds confirm this point. A PVR carboxyl group−N1 Y406 hydroxyl hydrogen bond is transiently formed (54% occurrence; Table 2), allowing this PVR moiety to still repeatedly interact in the N1-PVR binding site with water molecules. Water exchange in charged protein cavities[49] and water-mediated interactions in flexible carbohydrate−protein binding[50] have been previously reported.

The PVR hydroxyl group displays a first peak with reduced intensity when N1-bound (O5 atom, ∼0.5 units; Figure 5). This moiety forms a competing hydrogen bond to N1 R152 (44%; Table 2), yet water molecules are maintained in the first solvation shell upon binding. The PVR acetamide group (NP atom) has limited solvent accessibility due to the adjacent hydrophobic tail. Its solvation is further decreased (∼0.5 units) in the bound state upon formation of a hydrogen bond to N1 E277 (57% occurrence; Table 2).

Overall, the interactions of the PVR guanidinium group with N1 E277, E227, and E119; the PVR carboxyl group with catalytic N1 Y406; and the PVR aliphatic tail with N1 W178 and I222 in the hydrophobic subpocket appear most relevant to drive N1-PVR binding based on conformational and hydration analyses.

IT-TI Free-Energy Change upon N1-PVR Binding. The free-energy change upon N1-PVR binding was estimated using the IT-TI method and compared with standard TI values from single trajectories, as well as with experiment.

Examples of $\langle \partial H_i(\lambda)/\partial\lambda \rangle_\lambda$ vs λ curves are shown for standard TI and the improved IT-TI calculations of the N1 protein and water reference states (Figure 3). The IT-TI curves are smoother than those obtained from individual standard TI runs, because of increased sampling and improved overall statistics obtained through $N = 5$ independent ensembles. Their integration (eq 2) provides $\Delta\bar{G}_{wt}(L)$ and $\Delta\bar{G}_{N1}(L)$ values to estimate $\Delta\bar{G}_{bind}$ (Supporting Information, Table S3). This is summarized in the thermodynamic cycle of Scheme 2a.

Table 3 reports the IT-TI results and their comparison with the available experimental data. Our IT-TI $\Delta\bar{G}_{bind}$ estimate (-61.1 ± 5.4 kJ mol^{-1}) matches the $\Delta\bar{G}^{exp}_{bind}$ value derived from multiple IC_{50} measurements[21,51,52] (-62.2 ± 1.8 kJ mol^{-1}; see Supporting Information, Table S4). A free-energy difference of 1.1 kJ mol^{-1} (i.e., 2% relative difference) has no statistical significance within the above uncertainties. Remarkably, such an IT-TI prediction of the experimental value relies on individual $\Delta\bar{G}_{bind}(N)$ estimates that span a rather large free-energy range (see Table 3). In fact, these standard TI estimates are at variance with the independent calculation performed, ranging from a substantial underestimation ($i = 4$; 19% relative difference) to a substantial overestimation ($i = 5$; 29% relative difference) of the $\Delta\bar{G}^{exp}_{bind}$

Table 3. Free-Energy Change upon N1-PVR Binding[a]

free energy (kJ mol^{-1})			
		uncertainties	
change		$\sigma_{\Delta\bar{G}}$[d]	$\sigma_{\Delta\bar{G}}$(%)[e]
$\Delta\bar{G}_{bind}^{exp}$[b]	−62.2	1.8	3
$\Delta\bar{G}_{bind}$[c]	−61.1	5.4	9
	$\Delta G_{bind}(N)$[f]	$\sigma_{\Delta G_i}$[g]	$\sigma_{\Delta G_i}$(%)
$i = 1$	−63.7	11.0	17
$i = 2$	−55.3	9.0	16
$i = 3$	−55.8	10.1	18
$i = 4$	−80.6	9.9	12
$i = 5$	−50.1	9.7	19

[a] The average $\Delta\bar{G}_{bind}^{exp}$ value from repeated experiments can be compared with the IT-TI $\Delta\bar{G}_{bind}$ estimate. Corresponding $\Delta G_{bind}(N)$ values from individual standard TI trajectories are also reported. [b] Derived using data in refs 21, 51, and 52 (see Supporting Information, Table S4). [c] Equation 2. [d] Equation 5, with propagated uncertainties as in eq 6. [e] Equation 7. [f] Equation 1, $N = 5$. [g] Equation 4.

value. Only one of the individual standard TI results is in good agreement with the $\Delta\bar{G}_{bind}^{exp}$ value (−63.7 ± 11.0 kJ mol^{-1}, $i = 1$; 2% relative difference). The remaining four TI estimates have relative differences >9%. A significantly different N1-PVR binding free-energy estimate of −1180.9 ± 31.8 kJ mol^{-1} has been reported based on MM-PBSA calculations.[48]

The IT-TI free-energy estimate also has a lower $\sigma_{\Delta\bar{G}}$(%) relative uncertainty compared to the $\sigma_{\Delta G_i}$(%) from standard TI, i.e. 9% of the calculated free-energy difference (Table 3). $\sigma_{\Delta G_i}$(%) values associated with independent $\Delta G_{bind}(N)$ estimates are larger, ranging between 12% ($i = 4$) and 19% ($i = 5$). We stress that the uncertainties $\sigma_{\Delta G_i}$ typically evaluated for single standard TI trajectories are not statistical indicators of the ΔG_{bind} accuracy (see Materials and Methods, eq 4). Instead, repeated IT-TI runs allow calculation of the more representative free-energy uncertainty $\sigma_{\Delta\bar{G}}$ (see Materials and Methods, eq. 5). In addition, for this study, the latter is directly comparable to the standard error of $\Delta\bar{G}_{bind}^{exp}$ determined from N experimental values (Supporting Information, Table S4).

Overall, our results underscore the improved predictive power of IT-TI vs standard TI, due to the increased statistical reliability. The large deviations observed among standard TI estimates can be explained, in part, by the flexibility of the N1 binding site. Loops 119 and 150 demonstrate heterogeneous conformational sampling among different λ regions; their rmsd from the initial equilibrated structure reach values up to 0.4 and 0.7 nm, respectively (data not shown). This is consistent with both the dynamic loop behavior from the longer 20-ns MD simulation (Figure 2) and with the large $\sigma_{\Delta G_i}$ values for standard TI estimates (Table 3). We conclude that the IT-TI method significantly aids sampling of thermodynamic macrostates for flexible receptors by ensemble averaging of independent trajectories.

IT-TI Free-Energy Changes for PVR Alchemical Modifications. N1-PVR binding determinants were also investigated using IT-TI free-energy changes upon computer alchemical modifications and their underlying thermodynamic cycle (Scheme 2b). Scheme 1 summarizes the corresponding $\Delta\Delta\bar{G}_{bind}$ values together with the PVR free energy of binding $\Delta\bar{G}_{bind}$. A positive or negative value of $\Delta\Delta\bar{G}_{bind}$ indicates thermodynamically unfavorable or favorable alchemical modifications of the ligand L.

Neutralizing COO^- and NR_3^+ charges has large but opposite effects on ligand binding ($\Delta\Delta\bar{G}_{bind}$ of +55.1 ± 3.1 and −79.7 ± 4.2 kJ mol^{-1}, respectively). The $TAIL_1$ and $TAIL_2$ modifications both have small, favorable impacts on ligand binding ($\Delta\Delta\bar{G}_{bind}$ of −5.8 ± 2.4 and −1.5 ± 2.0 kJ mol^{-1}, respectively). To understand these results, one must look at the effects on receptor−ligand interactions and ligand hydration free-energy changes ($\Delta\Delta\bar{G}_{hydr}$) upon alchemical perturbation. In other words, a given $\Delta\Delta\bar{G}_{bind}$ change can arise from different compensating effects. For example, a positive $\Delta\Delta\bar{G}_{bind}$ value may be driven by (i) unfavorable (enthalpic or entropic) N1−ligand interactions, (ii) a more favorable $\Delta\Delta\bar{G}_{hydr}$, or (iii) a thermodynamically unfavorable combination of the previous effects. Similarly, a negative $\Delta\Delta\bar{G}_{bind}$ value may be driven by (i) favorable (enthalpic or entropic) N1−ligand interactions, (ii) a more unfavorable $\Delta\Delta\bar{G}_{hydr}$, or (iii) a thermodynamically favorable combination of the previous effects. In this section, we address the impact of different IT-TI modification perturbations on N1−ligand binding; in the next section, we consider the ligand hydration free energy. Both are needed to fully describe a given $\Delta\Delta\bar{G}_{bind}$ binding free-energy change.

Throughout the $\lambda = 0 \rightarrow \lambda = 1$ N1−COO^- modification perturbation, R292 and R371 residues move on average apart from the ligand scaffold. The closest arginine, R118, reduces its average distance to the ligand CD atom (Supporting Information, Figure S1a). The important ligand carboxyl−Y406 interaction (Table 2) is partially disrupted, while guanidinium interactions with E119, E227, and E277 are maintained.

During the $\lambda = 0 \rightarrow \lambda = 1$ N1−NR_3^+ modification, N1 R371 samples a more stable conformation close to the ligand CD atom, as revealed by a sharper distance distribution peak (cf. $\lambda = 0$ vs $\lambda = 1$; Supporting Information, Figure S1b). The aforementioned ligand carboxyl−Y406 interaction is destabilized. Moreover, the ligand guanidinium loses its favorable electrostatic interaction with N1 E277, which shifts away from the perturbed moiety. However, the ligand acetamide group is pushed closer to residue R156, which forms a hydrogen bond with atom OP (data not shown). This residue is not observed to closely interact with the unperturbed PVR molecule.

Following the $\lambda = 0 \rightarrow \lambda = 1$ $TAIL_1$ perturbation, I222 and W178 distance distributions for the modified PVR aliphatic tail (C8 and C9 atoms) transition to sharper and fewer peaks (cf. $\lambda = 0$ vs $\lambda = 1$; Supporting Information, Figure S1c,d). On the other hand, the $\lambda = 0 \rightarrow \lambda = 1$ $TAIL_2$ perturbation has a limited effect, as the distributions of tail atoms C8 and C10 with I222 and W178 residues remain predominantly broad (0.4−0.9 nm; Supporting Information, Figure S1e,f).

Role of Ligand Hydration in N1 Binding Thermodynamics. Scheme 1 summarizes the hydration free energy for PVR, $\Delta\bar{G}_{hydr}$, and the changes of this quantity for its

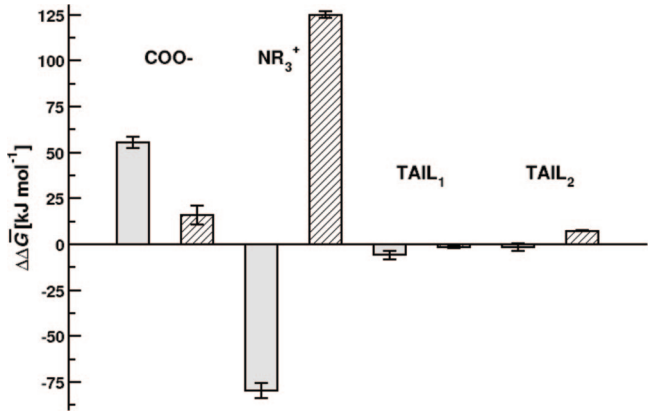

Figure 6. Binding free energies ($\Delta\Delta\bar{G}_{bind}$, gray solid bars) and corresponding hydration free energies ($\Delta\Delta\bar{G}_{hydr}$, diagonal lined bars) for all modification perturbations in this study. Vertical bars display the corresponding uncertainties $\sigma_{\Delta\bar{G}}$. Corresponding free-energy values and uncertainties can be found in Scheme 1 and in Supporting Information, Table S3.

alchemical modifications, $\Delta\Delta\bar{G}_{hydr}$. The corresponding binding free-energy, $\Delta\bar{G}_{bind}$, and changes of this quantity, $\Delta\Delta\bar{G}_{bind}$, are also reported. Figure 6 illustrates the relative components involved for PVR alchemical modifications.

We estimate an IT-TI $\Delta\bar{G}_{hydr}$ value of -107.8 ± 1.2 kJ mol^{-1} for the PVR molecule. No experimental data is available to date for a direct comparison of this result. We note that this value is in qualitative agreement with hydration free energies of a large variety of compounds used to calibrate the force field used in this study.[6,7,30] The value of -820.5 ± 40.2 kJ mol^{-1} reported based on MM-PBSA calculations significantly overestimates the favorable thermodynamic effect of PVR hydration.[48]

The COO^- perturbation gives a positive $\Delta\Delta\bar{G}_{hydr}$ value of 15.7 ± 5.1 kJ mol^{-1}. The PVR carboxyl group gives distinct primary and secondary rdf peaks in water. When deleting its charge, water structure is reduced ($\lambda = 0$ vs $\lambda = 1$; wt-COO^-; Supporting Information, Figure S2). Ligand hydration around this moiety is maintained in the N1 binding site, yet its first solvation shell is displaced (cf. $\lambda = 0$ vs $\lambda = 1$; N1-COO^-; Supporting Information, Figure S2). A sufficiently unfavorable ligand hydration free energy in the unbound state would drive hydrophobic binding. However, this effect is not large enough to compensate for the loss of favorable N1−ligand interactions (see the previous section). The COO^- charge perturbation has the largest unfavorable impact in the N1-bound state, leading to a $\Delta\Delta\bar{G}_{bind}$ value of 55.1 ± 3.1 kJ mol^{-1}.

A different thermodynamic compensation occurs between the bound and unbound states for the NR_3^+ charge perturbation, with a large unfavorable $\Delta\Delta\bar{G}_{hydr}$ value of $+124.9 \pm 1.8$ kJ mol^{-1}. The single solvation peak of the PVR guanidinium group in water shifts to larger distances (cf. $\lambda = 0$ vs $\lambda = 1$; wt-NR_3^+; Supporting Information, Figure S2) due to hydrophobic desolvation of this bulky charge group. The limited hydration of the charged PVR guanidinium in the N1 active site is almost unaffected by the perturbation (cf. $\lambda = 0$ vs $\lambda = 1$; N1-NR_3^+; Supporting Information, Figure S2). The NR_3^+ charge perturbation has the largest unfavorable impact on the unbound state, overcompensating for the loss of N1−ligand favorable interactions (see previous section). This leads to a net $\Delta\Delta\bar{G}_{bind}$ change of -79.7 ± 4.2 kJ mol^{-1}, significantly more favorable than the PVR $\Delta\bar{G}_{bind}$ value. The experimentally observed, improved binding of inhibitors to N2 neuraminidase by hydrophobic substitution at the PVR guanidinium position supports these results.[53]

In water, $TAIL_1$ and $TAIL_2$ modifications increase the solvation around the unperturbed atoms (cf. $\lambda = 0$ vs $\lambda = 1$; Supporting Information, Figure S2) and correlate to the $\Delta\Delta\bar{G}_{hydr}$ values of -1.4 ± 0.6 and 7.3 ± 0.3 kJ mol^{-1}, respectively. In the N1 binding site, a distinct decrease (~0.5 units) for $TAIL_1$ solvation (C9 atom; Supporting Information, Figure S2) agrees with the rearrangement of N1 hydrophobic residues I222 and W178 (see above). The opposite signs of $\Delta\Delta\bar{G}_{hydr}$ offset the changes observed in the protein as well as entropic changes to the aliphatic tail, resulting in similar $\Delta\Delta\bar{G}_{bind}$ values of -5.8 ± 2.4 and -1.5 ± 2.0 kJ mol^{-1} for $TAIL_1$ and $TAIL_2$ alchemical modifications (Figure 6).

Overall, these results emphasize the dominant electrostatic contribution to the free energy of N1 binding for PVR and its alchemically modified variants and suggest that future drug development may also be guided by conveniently tuning ligand flexibility and hydrophobicity.

Conclusion

The independent-trajectories thermodynamic-integration (IT-TI) approach was presented. It allows for estimation of improved free-energy changes for biomolecular systems based on multiple independent simulations. Our results underscore the improved predictive power of IT-TI vs standard TI, due to the increased statistical reliability. Standard TI estimates from individual trajectories span a rather large free-energy estimate range, from a 19% underestimation to a 29% overestimation of the experimental reference value (-62.2 ± 1.8 kJ mol^{-1}). Remarkably, our IT-TI binding free-energy estimate (-61.1 ± 5.4 kJ mol^{-1}) is in excellent agreement, i.e. 2% relative difference. A general formulation is proposed to evaluate corresponding IT-TI free-energy uncertainties that rely on a statistical treatment of error analysis. Overall, IT-TI seems particularly promising in the case of highly flexible protein receptors, ligands, and macromolecular binding partners in general.

Using 20-ns molecular dynamics simulation of the N1-PVR complex, we find a number of key binding interactions. The interactions of the PVR guanidinium group with N1 E277, E227, and E119; the PVR carboxyl group with catalytic N1 Y406; and the PVR aliphatic tail with N1 W178 and I222 in the hydrophobic subpocket appear most relevant to drive N1-PVR binding, based on conformational and hydration analyses. This dynamic, atomistic description was correlated with key thermodynamic contributions to binding.

Furthermore, IT-TI was applied to explore the binding determinants of avian influenza N1 neuraminidase inhibition using alchemical modification of the PVR molecule. Charge annihilation of its carboxyl and guanidinium groups has the largest unfavorable impact in the N1-bound and unbound states, respectively. These results emphasize

the dominant electrostatic contribution to N1-PVR binding free energy. Alchemical modifications of the PVR aliphatic tail suggest that future drug development may also be guided by conveniently tuning ligand flexibility and hydrophobicity.

Finally, this study allows us more general conclusions on free-energy calculations in the context of protein−ligand binding. The key to designing improved inhibitors for a given target relies on an accurate thermodynamic description of both ligand-bound and ligand-unbound receptor and ligand states. Consequently, we suggest that the most reliable and predictive free-energy calculations will likely rely on the use of explicit solvent simulations and MD force fields based also on a direct and general parametrization of solvation thermodynamics. We anticipate the application of the IT-TI approach to develop improved and potent drugs to inhibit flexible macromolecular receptors.

Acknowledgment. The authors thank the members of the McCammon group for useful discussions. This work was supported, in part, by the National Science Foundation grant PHY-0822283, Center for Theoretical Biological Physics, for the computing resources. Additional support has been provided by NSF, NIH, HHMI, and NBCR.

Supporting Information Available: GROMOS force-field parameters for the PVR molecule, Table S1; summary of IT-TI calculations, Table S2; summary of the IT-TI free energies calculated, Table S3; experimental observables used to estimate N1-PVR binding free energy, Table S4; PVR distance distributions during modification perturbations, Figure S1; PVR hydration analysis during modification perturbations, Figure S2. This material is available free of charge via the Internet at http://pubs.acs.org

References

(1) van Gunsteren, W. F.; Beutler, T. C.; Fraternali, F.; King, P. M.; Mark, A. E.; Smith, P. E. *Computation of Free Energy in Practice: Choice of Approximations and Accuracy Limiting Factors*; ESCOM Science Publishers: Leiden, 1993; Vol. 2.

(2) Jorgensen, W. L. *Science* **2004**, *303*, 1813–1818.

(3) McCammon, J. A. *Curr. Opin. Struct. Biol.* **1998**, *8*, 245–249.

(4) Gilson, M. K.; Zhou, H. X. *Annu. Rev. Biophys. Biomol. Struct.* **2007**, *36*, 21–42.

(5) Beveridge, D. L.; DiCapua, F. M. *Annu. Rev. Biophys. Biophys. Chem.* **1989**, *18*, 431–492.

(6) Baron, R.; Trzesniak, D.; de Vries, A. H.; Elsener, A.; Marrink, S. J.; van Gunsteren, W. F. *ChemPhysChem* **2007**, *8*, 452–461.

(7) Schuler, L. D.; Daura, X.; van Gunsteren, W. F. *J. Comput. Chem.* **2001**, *22*, 1205–1218.

(8) Lybrand, T. P.; McCammon, J. A.; Wipff, G. *Proc. Natl. Acad. Sci. U.S.A.* **1986**, *83*, 833–835.

(9) Hünenberger, P. H.; Helms, V.; Narayana, N.; Taylor, S. S.; McCammon, J. A. *Biochemistry* **1999**, *38*, 2358–2366.

(10) Reinhardt, W. P.; Miller, M. A.; Amon, L. M. *Acc. Chem. Res.* **2001**, *34*, 607–614.

(11) Chipot, C.; Pohorille, A. *Free Energy Calculations*; Springer: New York, 2007; Vol. 86.

(12) Zagrovic, B.; van Gunsteren, W. F. *J. Chem. Theory Comput.* **2007**, *3*, 301–311.

(13) Adcock, S. A.; McCammon, J. A. *Chem. Rev.* **2006**, *106*, 1589–1615.

(14) Fujitani, H.; Tanida, Y.; Ito, M.; Jayachandran, G.; Snow, C. D.; Shirts, M. R.; Sorin, E. J.; Pande, V. S. *J. Chem. Phys.* **2005**, *123*, 084108.

(15) Zacharias, M.; Straatsma, T. P.; McCammon, J. A. *J. Chem. Phys.* **1994**, *100*, 9025–9031.

(16) Beutler, T. C.; Mark, A. E.; van Schaik, R. C.; Gerber, P. R.; van Gunsteren, W. F. *Chem. Phys. Lett.* **1994**, *222*, 529–539.

(17) Gilson, M. K.; Given, J. A.; Bush, B. L.; McCammon, J. A. *Biophys. J.* **1997**, *72*, 1047–1069.

(18) Hamelberg, D.; McCammon, J. A. *J. Am. Chem. Soc.* **2004**, *126*, 7683–7689.

(19) Skeik, N.; Jabr, F. I. *Int. J. Infect. Dis.* **2007**, *12*, 233–238.

(20) Le, Q. M.; Kiso, M.; Someya, K.; Sakai, Y. T.; Nguyen, T. H.; Nguyen, K. H.; Pham, N. D.; Ngyen, H. H.; Yamada, S.; Muramoto, Y.; Horimoto, T.; Takada, A.; Goto, H.; Suzuki, T.; Suzuki, Y.; Kawaoka, Y. *Nature* **2005**, *437*, 1108.

(21) Hurt, A. C.; Selleck, P.; Komadina, N.; Shaw, R.; Brown, L.; Barr, I. G. *Antiviral Res.* **2007**, *73*, 228–31.

(22) Chand, P.; Bantia, S.; Kotian, P. L.; El-Kattan, Y.; Lin, T. H.; Babu, Y. S. *Bioorg. Med. Chem.* **2005**, *13*, 4071–4077.

(23) Gubareva, L. V.; Webster, R. G.; Hayden, F. G. *Antimicrob. Agents Chemother.* **2001**, *45*, 3403–3408.

(24) De Clercq, E. *Expert Opin. Emerg. Drugs* **2008**, *13*, 393–416.

(25) Shirts, M.; Pande, V. S. *Science* **2000**, *290*, 1903–1904.

(26) Russell, R. J.; Haire, L. F.; Stevens, D. J.; Collins, P. J.; Lin, Y. P.; Blackburn, G. M.; Hay, A. J.; Gamblin, S. J.; Skehel, J. J. *Nature* **2006**, *443*, 45–49.

(27) Christen, M.; Hünenberger, P. H.; Bakowies, D.; Baron, R.; Burgi, R.; Geerke, D. P.; Heinz, T. N.; Kastenholz, M. A.; Krautler, V.; Oostenbrink, C.; Peter, C.; Trzesniak, D.; van Gunsteren, W. F. *J. Comput. Chem.* **2005**, *26*, 1719–1751.

(28) van Gunsteren, W. F.; Billeter, S. R.; Eising, A. A.; Hünenberger, P. H.; Kruger, P.; Mark, A. E.; Scott, W. R. P.; Tironi, I. G. *Biomolecular Simulation: The GROMOS96 Manual and User Guide*; vdf Hochschulverlag AG an der ETH Zürich and BIOMOS b.v. Groningen: Zürich, Groningen, 1996.

(29) Baron, R.; Bakowies, D.; van Gunsteren, W. F. *J. Pept. Sci.* **2005**, *11*, 74–84.

(30) Lins, R. D.; Hünenberger, P. H. *J. Comput. Chem.* **2005**, *26*, 1400–1412.

(31) Berendsen, H. J. C. *Interaction Models for Water in Relation to Protein Hydration*; Pullman, B. E., Ed.; Reidel: Dordrecht, 1981.

(32) Åqvist, J. *J. Phys. Chem.* **1990**, *94*, 8021–8024.

(33) Hockney, R. W. *Methods Comput. Phys.* **1970**, *9*, 136–211.

(34) Ryckaert, J. P.; Ciccotti, G.; Berendsen, H. J. C. *J. Comput. Phys.* **1977**, *23*, 327–341.

(35) Berendsen, H. J. C.; Postma, J. P. M.; van Gunsteren, W. F.; di Nola, A.; Haak, J. R. *J. Chem. Phys.* **1984**, *81*, 3684–3690.

(36) Tironi, I. G.; Sperb, R.; Smith, P. E.; van Gunsteren, W. F. *J. Chem. Phys.* **1995**, *102*, 5451–5459.

(37) Heinz, T. N.; van Gunsteren, W. F.; Hünenberger, P. H. *J. Chem. Phys.* **2001**, *115*, 1125–1136.

(38) Heinz, T. N.; Hünenberger, P. H. *J. Comput. Chem.* **2004**, *25*, 1474–1486.

(39) McLachlan, A. D. *J. Mol. Biol.* **1979**, *128*, 49–79.

(40) Kirkwood, J. G. *J. Chem. Phys.* **1935**, *3*, 300–313.

(41) Allen, M. P.; Tildesley, D. J. *Computer Simulations of Liquids*; Oxford University Press: New York, 1989.

(42) Taylor, J. R. *An Introduction to Error Analysis. The Study of Uncertainties in Physical Measurements,* 2nd ed.; University Science Books: Sausalito, CA, 1997.

(43) Amaro, R. E.; Minh, D. D.; Cheng, L. S.; Lindstrom, W. M., Jr.; Olson, A. J.; Lin, J. H.; Li, W. W.; McCammon, J. A. *J. Am. Chem. Soc.* **2007**, *129*, 7764–7765.

(44) Landon, M. R.; Amaro, R. E.; Baron, R.; Ngan, C. H.; Ozonoff, D.; McCammon, J. A.; Vajda, S. *Chem. Biol. Drug Des.* **2008**, *71*, 106–116.

(45) Babu, Y. S.; Chand, P.; Bantia, S.; Kotian, P.; Dehghani, A.; El-Kattan, Y.; Lin, T. H.; Hutchison, T. L.; Elliott, A. J.; Parker, C. D.; Ananth, S. L.; Horn, L. L.; Laver, G. W.; Montgomery, J. A. *J. Med. Chem.* **2000**, *43*, 3482–3486.

(46) Chachra, R.; Rizzo, R. C. *J. Chem. Theory Comput.* **2008**, *4*, 1526–1540.

(47) Yen, H. L.; Hoffmann, E.; Taylor, G.; Scholtissek, C.; Monto, A. S.; Webster, R. G.; Govorkova, E. A. *J. Virol.* **2006**, *80*, 8787–8795.

(48) Malaisree, M.; Rungrotmongkol, T.; Decha, P.; Intharathep, P.; Aruksakunwong, O.; Hannongbua, S. *Proteins* **2008**, *71*, 1908–1918.

(49) Baron, R.; McCammon, J. A. *Biochemistry* **2007**, *46*, 10629–10642.

(50) Clarke, C.; Woods, R. J.; Gluska, J.; Cooper, A.; Nutley, M. A.; Boons, G. J. *J. Am. Chem. Soc.* **2001**, *123*, 12238–12247.

(51) Cheng, Y.; Prusoff, W. H. *Biochem. Pharmacol.* **1973**, *22*, 3099–3108.

(52) Collins, P. J.; Haire, L. F.; Lin, Y. P.; Liu, J.; Russell, R. J.; Walker, P. A.; Skehel, J. J.; Martin, S. R.; Hay, A. J.; Gamblin, S. J. *Nature* **2008**, *453*, 1258–1261.

(53) Maring, C. J.; Stoll, V. S.; Zhao, C.; Sun, M.; Krueger, A. C.; Stewart, K. D.; Madigan, D. L.; Kati, W. M.; Xu, Y.; Carrick, R. J.; Montgomery, D. A.; Kempf-Grote, A.; Marsh, K. C.; Molla, A.; Steffy, K. R.; Sham, H. L.; Laver, W. G.; Gu, Y. G.; Kempf, D. J.; Kohlbrenner, W. E. *J. Med. Chem.* **2005**, *48*, 3980–3990.

CT800559D

JCTC Journal of Chemical Theory and Computation

Using Molecular Strain and Aromaticity To Create Ultraweak C−H Bonds and Stabilized Carbon-Centered Radicals

Hooman Shadnia* and James S. Wright

Department of Chemistry, Carleton University, Ottawa K1S 5B6, Canada

Received July 30, 2008

Abstract: An approach based on relief of molecular strain in the parent hydrocarbon, extended conjugation in the radical, and the driving force toward aromaticity is used to design molecules with ultraweak C−H bonds. The molecular strain is generated by two fused rings containing (5,5)-, (5,6)-, or (6,6)-membered ring structures. Homodesmotic reactions are used to calculate the molecular strain enthalpy (MSE) of the parent hydrocarbons and the corresponding radicals, and to analyze how it changes through these reactions. B3LYP calculations are used to obtain the bond dissociation enthalpies (BDEs) for breaking one or more C−H bonds as well as the C−O bond formed after oxygen addition to the radical. Loss of a second H-atom can lead to very low R−H BDE values, especially when the ultimate product is aromatic. Molecular structures based on these ideas may be of interest as novel antioxidants based on carbon-centered radicals.

Introduction

Several research groups have recently analyzed the formation of carbon-centered radicals from their parent hydrocarbons R−H and have shown how such hydrocarbons can be used to design novel antioxidants.[1−4] They identified several factors that led to increased stability, including (i) benzylic resonance stabilization, (ii) unpaired spin delocalization onto oxygen or other (unreactive) heteroatom, (iii) stereoelectronic effects, (iv) electron-withdrawing effects, and (v) steric effects. These effects are primarily focused on stabilization of the carbon-centered radical, with resulting weakening of the C−H bond. We have studied the relative contributions of these and other categories in previous work by the present authors,[5] for a large number of examples. Using the same methodology, in this Article, we calculate gas-phase R−H and R−OO$^\bullet$ bond dissociation enthalpies (BDEs) for a new series of molecules. We analyze the origin of the bond weakening effect and take advantage of a rather neglected structural feature, that is, molecular strain in the parent molecule and the oxygen adduct. We then use this theme, as well as the driving force toward aromatization, to explore a series of hydrocarbons containing fused rings. Some of these proposed compounds have low first and very low second C−H BDEs, forming stable products.

* Corresponding author e-mail: hooman@shadnia.com.

The term "molecular strain" is frequently used in discussing geometries and reactions of small molecules such as cyclopropane and cyclobutane, where the hybrid orbitals do not point along the carbon−carbon bonds, or in structures where the C−H bond orbitals are forced to be eclipsed. A few studies have focused on estimating its origin and magnitude. In early work, Wiberg[6] discussed the origins of strain and provided a quantitative analysis of each source. Other relevant approaches can be found in works of Nicolaides et al.,[7] Bond,[8] and Rogers et al.,[9] who have compared different theoretical methods for calculation of heats of formation and hydrogenation of olefins. Peck et al.[10] have performed similar studies on benzenoid aromatics. In general, most of these methods derive strain energies by comparison between calculated heats of formation of the strained molecules versus the nonstrained congeners.

To provide a basis for comparison, we briefly summarize the magnitude of the effects of different categories of functional groups from previous work by Wright and Shadnia.[5] We found that hyperconjugation effects, for example, as in $(CH_3)_3C-H$, lower the R−H BDE by up to 11 kcal/mol relative to the methyl radical, but have only a minor effect on the R−OO$^\bullet$ BDE. Electron-withdrawing groups, particularly nitro and cyano, decrease the R−H BDE by up to 10 kcal/mol and the R−OO$^\bullet$ BDE by up to 15 kcal/

10.1021/ct900049j CCC: $40.75
Published on Web 03/02/2009

mol. Lone pair donors can also lower the R−H BDE by up to 13 kcal/mol, the strongest effect being seen for the amino group. Conjugative delocalization effects are more powerful and can lower the R−H BDE by up to a full 36 kcal/mol, and also decrease the R−OO• BDE by a maximum of 25 kcal/mol, for example, for trivinylmethane. Benzylic resonance stabilization also is very effective and can decrease the R−H BDE by up to 26 kcal/mol and the R−OO• BDE by up to 23 kcal/mol, as in triphenylmethane. Finally, captodative effects, which were not treated by Scaiano et al.,[1] show some of the largest bond-weakening effects, up to a maximum of 35 and 28 kcal/mol for R−H and R−OO•, respectively. Note that it was not always possible to separate these effects from one another and that molecules containing multiple functional groups do not necessarily act additively. However, this brief summary provides a reference standard against which any novel bond-weakening effects can be compared.

Method of Calculation

A density functional approach using the B3LYP functional with small (6-31G(d)) and large (6-311+G(2d,2p)) basis sets, termed the Medium-Level Model 3 (MLM3) method, was defined previously.[5,11] Briefly, geometries and frequencies are obtained using B3LYP/Small, with a correction factor of 0.98 for frequencies. Single-point energies at the computed minimum are obtained using B3LYP/Large for closed shells, or the restricted open-shell specification ROB3LYP/Large for open-shell radicals. A correction factor of +2.0 kcal/mol is added to the (absolute) enthalpy of doublet radicals, whereas no correction factor is used for triplet states (e.g., the oxygen molecule) or the hydrogen atom. This method gave gas-phase R−H and R−OO• BDEs to within 2 kcal/mol where experimental data were available for comparison. This is sufficiently accurate to make discussion of BDEs and radical stability meaningful.

Most structural features including conjugation and electronic effects are well treated using B3LYP.[5,12] For highly strained hydrocarbons, however, the method has been demonstrated to underestimate the magnitude of molecular strain energies. For example, Walker et al.[13] used homodesmotic reactions (HDRs) and several theoretical techniques to calculate molecular strain energies for a variety of highly strained hydrocarbons. Actual measurements are usually in terms of enthalpies, so we can define the molecular strain enthalpy (MSE) for cyclopropane as the enthalpy change for the reaction cyclopropane + $3CH_3CH_3 \rightarrow 3CH_3CH_2CH_3$ where the HDR matches hybridization types (all sp^3) and C−H substitution patterns (e.g., $3CH_2$ groups for reactants and products, $6CH_3$ groups each). The same approach can be used to define the HDR for a radical; for example, for the cyclopropyl radical the appropriate HDR would be cyclopropyl• + $3CH_3CH_3 \rightarrow CH_3CH^{\bullet}CH_3 + 2CH_3CH_2CH_3$.

In the next section, we investigate the discrepancy between the molecular strain enthalpy (MSE) as calculated by Walker et al.[13] using the more accurate G1 method with that obtained using B3LYP (their calculations and ours). For this discussion, we use their set of highly strained hydrocarbons. It will be shown that the MSE values obtained with B3LYP can be adjusted, so that use of B3LYP methodology becomes as accurate as G1, no matter how highly strained the system.

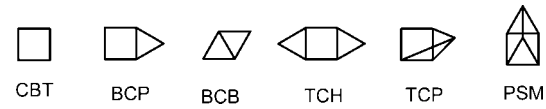

Figure 1. A subset of structures used from the data set of Walker et al.

Table 1. Calculation of Molecular Strain Enthalpy, Defined as the Enthalpy Change, $\Delta H^{\circ}_{298}(g)$, for Homodesmotic Reactions Involving Structures Shown in the First Column (See Figure *1*)[a]

	MSE (Walker et al.[13])		MSE (this work)
structure	G1	B3LYP[b]	B3LYP[c]
CBT	26.0	22.7	23.9
BCP	55.4	46.1	48.4
BCB	66.8	55.7	58.7
TCH	81.5	66.8	70.5
TCP	106.2	90.2	94.2
PSM	143.4	121.7	126.9

[a] All units are in kcal/mol. [b] Small basis = 6-311G(d,p); large basis = 6-311+G(3df,2p); unrestricted open-shell method. [c] Small basis = 6-31G(d); large basis = 6-311+G(2d,2p); restricted open-shell method.

Results and Discussion

A. Correction of B3LYP Values for Strained Systems. A subset of the structures used by Walker et al. is shown in Figure 1. The subset was chosen so as to span the range of values of MSEs in approximately equal increments. These highly strained hydrocarbons show a combination of ring strain and steric strain, the latter caused by eclipsing of C−H bond orbitals. Table 1 shows the molecular strain enthalpy (MSE) obtained for the homodesmotic reaction for each structure, using G1 and B3LYP calculations of Walker, along with our own B3LYP calculation done with the MLM3 method.

As shown in Table 1, MSEs for these compounds (using G1 values) range from the moderately strained cyclobutane (26 kcal/mol) to the very highly strained prismane (143 kcal/mol); this should be sufficient to show any defects in the B3LYP methodology. Comparing B3LYP implementations, our own B3LYP protocol is closer to G1 and is therefore preferable, although both are significantly underestimating the MSE for the more highly strained systems.

Figure 2 shows a plot of our B3LYP values of the MSE versus the G1 values of Walker. There is a near-perfect linear fit with $R^2 = 0.9995$ for the equation:

$$\mathrm{MSE(B3LYP)} = -0.0288 + 0.8821\mathrm{MSE(G1)} \quad (1)$$

Inverting this equation gives

$$\mathrm{MSE(G1)} = +0.0326 + 1.1338\mathrm{MSE(B3LYP)} \quad (2)$$

Thus, the B3LYP method does indeed underestimate the MSE, by about 12%. However, this can be corrected for. Using the above equation, a corrected value for MSE(B3LYP) is equivalent to setting it equal to MSE(G1), which is determined from eq 2. Denoting the corrected value

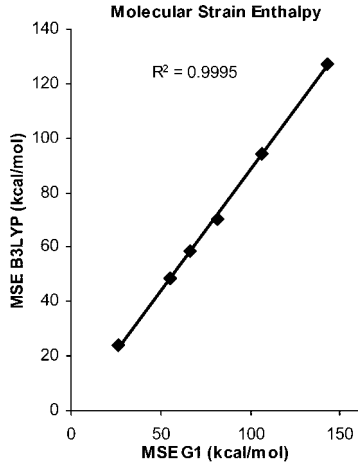

Figure 2. Molecular strain enthalpy (MSE) for B3LYP (our calculation) versus G1 (from Walker et al.).

Table 2. Comparison of the R−H BDE Values Calculated Using B3LYP (Our Work) versus G1 (Walker et al.)[a]

	G1	B3LYP			
structure	BDE	BDE	MSE (parent)	MSE (radical)	BDE*
CBT	100.5	98.5	23.9	25.6	98.8
BCP	100.1	99.0	48.4	50.5	99.3
BCB	101.1	100.4	58.7	62.3	100.9
TCP	103.6	102.9	94.2	100.2	103.6
TCP	113.4	112.6	94.2	112.1	114.9
PSM	107.9	106.9	126.9	139.1	108.5

[a] For the structure codes, see Figure 1. BDE* is the corrected B3LYP value for BDE. All values are in kcal/mol.

asMSE(B3LYP*), the correction factor is Δ = MSE(B3LYP*) − MSE(B3LYP). Because Δ is positive, adding Δ to the absolute enthalpy of the strained system effectively corrects for the B3LYP underestimate.

We have repeated this correlation for radicals using HDRs and obtained the same correlation parameters as those given above (data not shown). Thus, to obtain a BDE, for example, for R−H → R• + H•, the MSE is calculated for parent and radical independently. Absolute enthalpy values $H°_{298}$ are corrected for each, and the (gas-phase) BDE is the enthalpy change for the dissociation reaction.

It is also important to mention that because the magnitudes of MSE for the parent molecule and its radical are often very similar, the B3LYP error on absolute enthalpies of these species is canceled out in calculation of BDE values. Thus, as shown in Table 2 for the structures of Figure 1, even though these structures contain significant amounts of strain (MSE = 25−145 kcal/mol), the difference in MSE of parent and radical is much smaller (2−20 kcal/mol). This leads to the corrected BDE values (BDE*), which differ by no more than 2.6 kcal/mol from the uncorrected BDE values.

B. BDE Values for Fused Ring Systems. Figure 3 shows the ring structures of interest in this Article. Many of these structures have two exchangeable hydrogen atoms. Because they can form intermediate radicals, oxygen adducts, and second dissociation products, a reaction scheme showing the various possibilities is given in Figure 4.

Structures **A1** and **A2**, also shown in Figure 5a, are two forms of pentadiene, that is, the conjugated 1,3-pentadiene

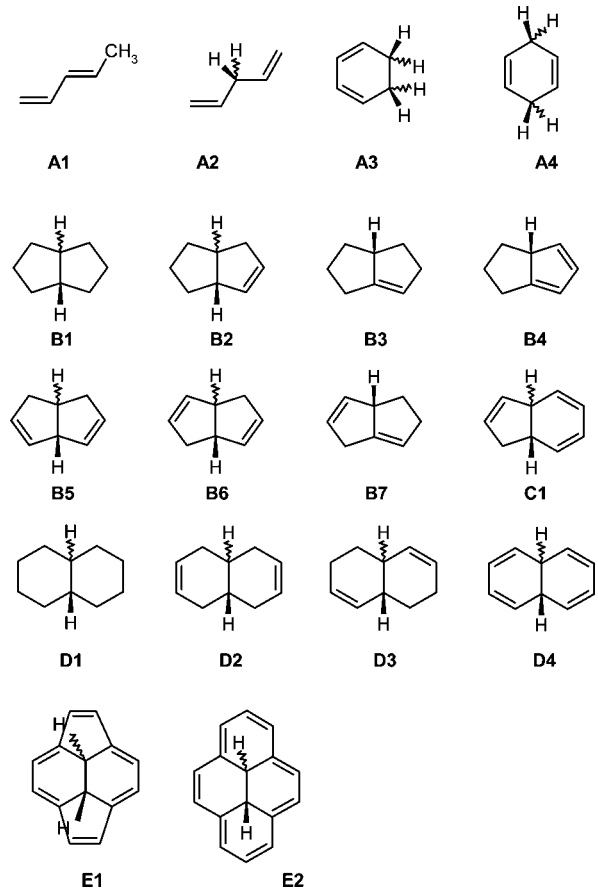

Figure 3. Molecular structures.

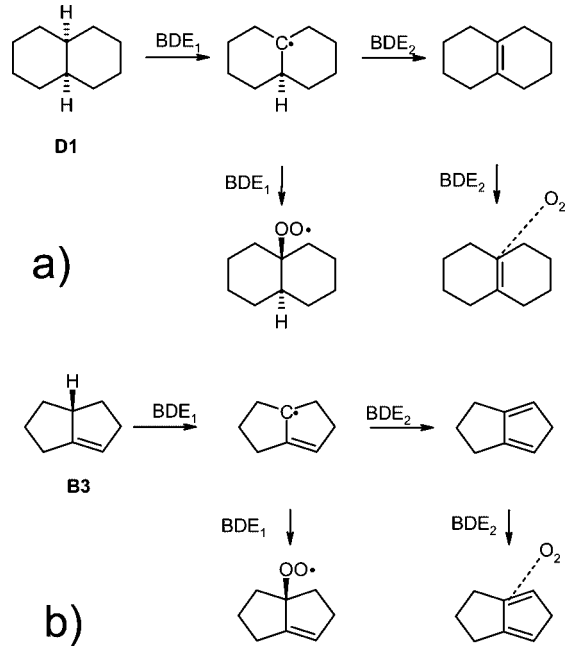

Figure 4. Reactivity scheme. (a) *trans*-**D1** (two exchangeable hydrogen atoms at ring junction), (b) **B3** (second exchangeable H-atom from ring).

and the "skipped diene" 1,4-pentadiene. **A3** and **A4** are the equivalent cyclic structures 1,3-cyclohexadiene and 1,4-cyclohexadiene, respectively. **B1**−**B7** are formed from the fusion of two cyclopentane rings, denoted (5,5), and contain variable amounts of unsaturation. Structures **B1**, **B2**, **B5**, and

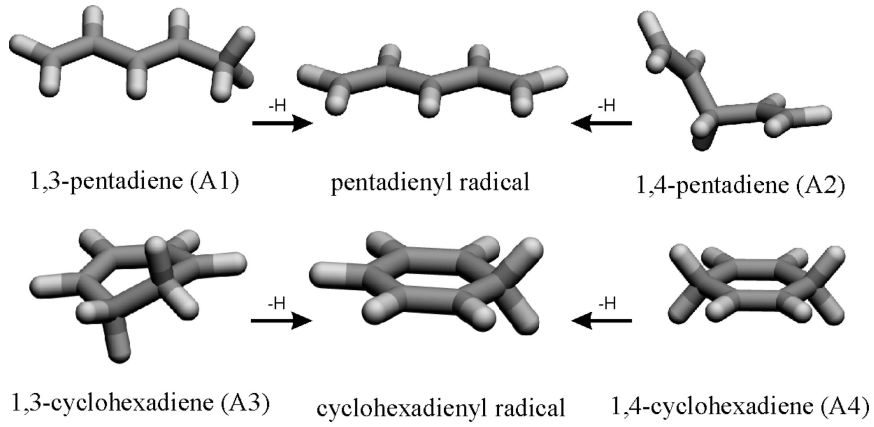

Figure 5. (a) Structures of the pentadienes and their radical; and (b) structures of cyclohexadienes and their radical.

B6 can have *cis*- or *trans*-dihydrogen stereochemistry at the central bond. **C1** is the (5,6) ring combination, whereas **D1**−**D4** are the (6,6) combinations. Finally, **E1** and **E2** are two additional multiring structures.

The MLM3 method was used to calculate gas-phase BDEs for loss of the first H-atom from R−H, denoted R−H BDE_1, and for loss of oxygen after addition to the corresponding radical R•, denoted R−OO• BDE_1. For most of the compounds discussed in this Article, there is an additional weak C−H bond present in the initial carbon radical. Loss of the second H-atom from R• is denoted R−H BDE_2. Similarly, loss of oxygen after addition to the product of this step is denoted R−OO• BDE_2.

The products of the second hydrogen abstraction are closed-shell molecules. In one-half of the cases, addition of oxygen to such molecules results in high-energy molecules, which are nevertheless trapped in a potential minimum. High energies of such adducts are reflected in positive enthalpy changes for the addition reaction, and correspondingly negative BDE values. These high-energy complexes are nevertheless bound by long C−O bonds but must overcome an energy barrier to separate. In other cases, mostly for structures that are less crowded around the radical center, energy minimization gradually increases the C−O bond distance beyond the limits for a covalent bond and results in structures in which oxygen lies in a shallow van der Waals minimum relative to the parent compound. This weak van der Waals interaction results in small positive BDE values in the range of 1−4 kcal/mol. Such cases are identified with an asterisk in Table 3. For all compounds, the four calculated BDE values are given in Table 3.

Corrected values of the R−H BDEs were obtained by applying the correction factor Δ to the parent compound, and a second value of Δ for the radical. The appropriate homodesmotic reactions are given in the Supporting Information. Both corrected (BDE*) and uncorrected R−H BDEs are given in Table 3. No correction factors were determined for oxygen addition reactions. The table also contains a column labeled strain release enthalpy (SRE). This is the difference in (corrected) molecular strain enthalpy between the radical R• and its parent hydrocarbon R−H. The sign follows the convention for enthalpy change, so when the SRE is negative the parent is more strained than the radical.

Table 3. BDE Values of Compounds in Figure 3[a]

	R−H						R−OO•	
structure	BDE_1	SRE	BDE_1*	BDE_2	SRE	BDE_2*	BDE_1	BDE_2
A1	82.7						11.9	
A2	74.1						6.5	
A3	75.2			23.4			8.7	2.4*
A4	75.4			23.4			8.7	2.4*
cis-**B1**	94.9	−0.3	94.8	36.2	−5.3	35.4	32.8	−23.4
trans-**B1**	85.0	−9.1	83.6	39.0	−2.9	38.6	30.9	−19.3
cis-**B2**	87.2	9.4	88.5	44.4	2.9	44.8	24.0	−15.7
trans-**B2**	74.8	−12.4	73.0	44.4	2.9	44.8	−10.4	−15.7
B3	81.9	−2.0	81.6	46.8	32.0	51.4	18.6	−15.8
B4	77.2	2.6	76.9	52.1			6.2	2.5*
cis-**B5**	81.0	3.9	81.5	50.2	8.5	51.4	16.5	−10.9
trans-**B5**	63.4	−11.5	61.7	50.2	8.5	51.4	−15.6	−10.9
cis-**B6**	90.2	12.8	92.0	40.1	27.9	44.1	5.8	−19.4
trans-**B6**	65.9	**−29.9**	61.6	45.9	38.2	51.5	−0.1	−19.4
B7	73.5	−4.3	72.8	51.3	−0.8	51.2	9.5	−12.9
cis-**C1**	69.1	3.8	69.7	26.5			1.1	2.4*
trans-**C1**	61.8	−2.6	61.5	23.0			−5.7	3.2*
cis-**D1**	95.4	1.6	95.6	32.7	8.9	34.0	32.3	−28.7
trans-**D1**	96.0	2.2	96.3	35.6	11.4	37.3	8.1	−28.7
cis-**D2**	87.0	−6.4	86.1	31.5	0.6	31.6	−23.9	3.4*
trans-**D2**	95.3	0.9	95.2	31.5	0.6	31.6	−23.9	3.4*
cis-**D3**	81.2	−1.7	81.7	44.6			16.7	−16.2
trans-**D3**	80.1	−2.7	79.7	44.4			15.6	−15.3
cis-**D4**	60.2	−6.3	59.3	6.8			−4.7	2.6*
trans-**D4**	60.5	−6.0	59.7	6.8			−4.6	2.6*
cis-**E1**	79.1			9.0			6.2	2.5*
trans-**E1**	57.7			25.5			−9.3	1.9*
cis-**E2**	56.0			10.3			−13.2	3.8*
trans-**E2**	46.9			10.3			−13.2	3.8*

[a] All values in kcal/mol. SRE is the corrected strain release enthalpy, and BDE_1* and BDE_2* are the corrected values of BDE_1 and BDE_2.

We found the data in Table 3 for structures **A1**−**A4** to give a surprising result, and further analysis led to development of the main theme of this Article. Thus, the conjugated pentadiene **A1** and the skipped diene **A2** give rise to the same pentadienyl radical; see Figure 5a. Because of 4-center conjugation, the parent hydrocarbon **A1** is more stable than **A2**, which has two isolated double bonds, so **A1** should have the larger R−H BDE_1. As expected, the BDE_1 values of 82.7 and 74.1 kcal/mol for **A1** and **A2**, respectively, reflect this difference in stability of the parent molecule. Note that **A2** is very nonplanar, due to the sp^3 hybridization at the central carbon, thus minimizing any interaction of the isolated π-systems via hyperconjugation through the center methylene group. For the analogous cyclic compounds, both 1,3-cyclohexadiene (**A3**) and 1,4-cyclohexadiene (**A4**) give rise

to the same cyclohexadienyl radical (Figure 5b) and would be expected to follow the above trend in R−H BDE_1. However, their BDEs are essentially identical at 75.3 ± 0.1 kcal/mol.

Why is the cyclic system so different from the straight chains? The carbon skeleton of the cyclohexadienyl radical is planar, as is the 1,4-cyclohexadiene **A4** (Figure 5b). However, the carbon skeleton of 1,3-cyclohexadiene, **A3**, is twisted out of plane by 8°. The adjacent methylene groups show a dihedral angle H−C−C−H of 27° instead of the optimal 60° (in cyclohexane). The resulting steric strain caused by adjacent bond pair repulsions destabilizes **A3**, causing an out-of-plane twist for the conjugated group, partially neutralizing its 4-center conjugation, and giving (coincidentally) the same absolute enthalpy for both **A3** and **A4**.

Loss of a second H-atom from the cyclohexadienyl radical formed in **A3** and **A4** converts the molecule into the closed-shell aromatic benzene ring, so there should be a strong driving force, as reflected in a low value for R−H BDE_2. This is certainly the case, with the remarkably low value of 23.4 kcal/mol for both **A3** and **A4** (the intermediate carbon radical has the same structure for each). The R−H BDE_2 for both **A3** and **A4** is so low that they should transfer the H-atom to any available radical whose BDE for forming the parent molecule is greater than 23.4 kcal/mol, that is, to almost anything. Thus, at the same time the target radical is deactivated by H-atom transfer, the cyclohexadienyl radical will be converted into the highly stable closed-shell molecule benzene.

Next, consider the tendency of molecular oxygen to add to the carbon radical R$^\bullet$ to form R−OO$^\bullet$. For comparison, methane has an R−H BDE of 106.1 and an R−OO$^\bullet$ BDE of 32.0 kcal/mol.[5] To prevent oxygen addition, we need to weaken the R−OO$^\bullet$ bond as much as possible. We showed previously[5] that there is a good correlation between the R−H and R−OO$^\bullet$ BDEs, given by R−OO$^\bullet$ BDE = −67.2 + 0.95 R−H BDE, with correlation coefficient $R^2 = 0.925$. Therefore, in general, molecules with weaker R−H bonds lead to radicals that form weaker R−OO$^\bullet$ bonds, that is, are more resistant to oxygen addition. Structures **A1**−**A4** show this characteristic weakening of the R−OO$^\bullet$ bond as the R−H bond gets weaker. When the second H-atom is lost from **A3** or **A4**, and benzene is formed, molecular oxygen does not form a covalent bond to benzene but forms a weakly bound van der Waals complex. Table 3 shows that the binding energy is only 2.4 kcal/mol, consistent with a van der Waals complex.

Compounds **B1**−**B7** introduce molecular strain into parent R−H and oxygen adduct. Figure 6 shows the parent compound bicyclopentane, **B1**, in both its trans and cis isomers. Clearly, the trans-parent compound is more strained, because its BDE_1 is ca. 11.2 kcal/mol smaller than that for the cis-compound (83.6 vs 94.8 kcal/mol, respectively). Note that where cis and trans isomers are possible, as in **B1**, the R−H BDE_2 can be different, in this case 35.4 versus 38.6 kcal/mol for cis and trans, respectively. The structures of the cis- and trans-radicals are different, and because our optimization procedure begins with the parent compounds,

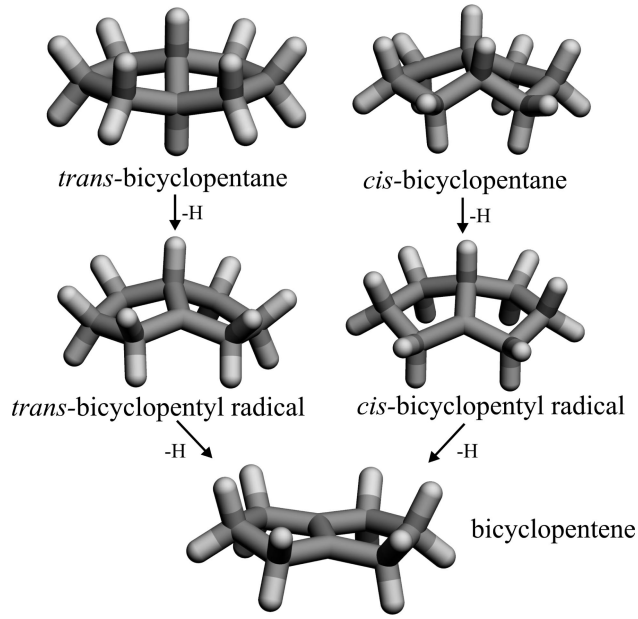

Figure 6. Optimized geometries of bicyclopentanes (*cis*-**B1** and *trans*-**B1**), their radicals, and the ultimate product, bicyclopentene.

different local minima result, which we believe cannot be easily interconverted.

Compounds **B2**−**B7** continue this theme, introducing additional stabilization to the radical by allowing for allylic (**B2**, **B3**, **B6**) or pentadienylic (**B4**, **B5**, **B7**) conjugation. For the allylic case, this causes R−H BDE_1 to drop by 6−10 kcal/mol (compare **B2** vs **B1**) with an equivalent drop in R−OO$^\bullet$ BDE_1. The pentadienylic case is even more dramatic, where for example in *trans*-**B5** the R−H BDE_1 has dropped to a very low 61.7 kcal/mol.

Using only one double bond in *cis*-**B2** and *trans*-**B2** affects the first hydrogen abstraction and reduces R−H BDE_1 to fall within a favorable range (73.0 kcal/mol for *trans*-**B2**) for an antioxidant.[14] Also, the R−OO$^\bullet$ BDE_1 in these compounds has decreased substantially in comparison with **B1**. The *trans*-**B2** compound has negative values for dissociation of oxygen in the first or second step and is therefore resistant to oxygen addition. By moving the position of the double bond, the parent molecule in **B3** is more planar than *trans*-**B2** so the strain release enthalpy for this compound (SRE = −2.0 kcal/mol) falls between those of the *cis*- and *trans*-**B2**. Clearly, the BDE_1 values follow the trend (88.5 > 81.6 > 73.0).

Placing two double bonds on the same ring in **B4** reduces the R−H BDE_1 even further because the radical is stabilized by pentadienylic conjugation. At the same time, because the planar side of the structure (the cyclopentadiene ring) does not interfere with the nonplanar side (cyclopentane), the molecular strain in this structure is diminished, as confirmed by SRE = 2.6 kcal/mol.

Placing both double bonds on different rings in **B5** gives the skipped diene conjugation similar to **A2**. The difference from the strain-free **A2** is that the two isomers of **B5** release different amounts of strain through the hydrogen abstraction reaction (SRE = 3.9 and −11.5 kcal for the *cis*- and *trans*-**B5**, respectively), predictably changing the BDE_1 values from

75.2 kcal/mol for **A2** to 75.2 + (3.9) = 79.1 (ca. 81.5 kcal/mol) for the cis and 75.2 + (−11.5) = 63.6 (ca. 61.7 kcal/mol) for the trans isomer.

When placing two double bonds adjacent to either active hydrogen in *cis*-**B6** and *trans*-**B6**, the conjugative stabilization effect is divided among both first and second hydrogen abstractions. At the same time, in the trans isomer the two cyclopentene rings are highly twisted due to the opposite location of the double bonds, because the structure tends to become planar on the sp^2 centers and nonplanar on the sp^3 centers. Thus, the *trans*-**B6** compound shows the highest amount of strain release enthalpy (SRE = −29.9 kcal/mol), leading to a low BDE_1 of 61.6 kcal/mol. Overall, *trans*-**B6** shows low R−H BDE values and negative BDEs for both oxygen adducts, which makes it another potentially interesting antioxidant. The compound **B7** uses the same skipped diene system as **B5**, with the difference that the double bonds in **B7** give both rings a quasi-planar conformation, which have very little strain, resulting in a small amount of strain release (SRE = −4.3 kcal/mol).

Overall, the calculated SRE values reveal that the trans conformations of (5,5)-membered ring structures in general show considerable strain release (SRE = −9 to −29 kcal/mol), which causes the lowering of R−H BDE_1 values, while the cis conformations show only slight to moderate strain release (SRE = −0.3 to +12.8 kcal/mol) for the first hydrogen abstraction. The variations of the SRE and BDE values reveal that while it is relatively easy to induce molecular strain into a structure, it is difficult to cause it to be released in a hydrogen abstraction reaction. The results also reveal that the position of double bonds and ring fusions needs to be designed properly to give maximum molecular strain for the parents while giving increased conjugation and lower molecular strain for the radical.

Fusing a 5- and 6-membered ring, as in **C1**, allows an additional factor, aromaticity, to stabilize the final product. Now the indene ring can form, containing one benzene unit, so that both R−H BDE_1 and R−H BDE_2 are very low for **C1**, in both cis and trans configurations (69.7, 26.5 vs 61.5, 23.0 kcal/mol, respectively). From the SRE values (3.8, −2.6 kcal/mol for the cis and the trans isomers, respectively), it is clear that these structures undergo only slight changes in molecular strain through the hydrogen abstraction reaction.

This trend can be continued with fusion of two 6-membered rings, as in **D1**−**D4**. The two isomers of **D1** are almost strain-free (SRE = 1.6, 2.2 kcal/mol for cis and trans, respectively) for the abstraction of the first hydrogen. **D2** is similar to **D1** because the double bonds are not conjugated with the central bond. The double bonds in *cis*-**D2** cause a small amount of molecular strain that is released by hydrogen abstraction (SRE = −6.4 kcal/mol), lowering its R−H BDE_1 to 86.1 kcal/mol. **D4** is particularly interesting because in both cis and trans configurations BDE_1 is very low (ca. 59 kcal/mol), and BDE_2 is only 6.8 kcal/mol; that is, after the first dissociation the second H-atom is almost unbound. The SRE values (−6.3, −6.0 kcal/mol for *cis*-**D4** and *trans*-**B4**, respectively) reveal that there is no significant amount of strain release for the abstraction of first hydrogen. Thus, the major driving force is the extended conjugation. For the second step, the driving force is aromatization, forming the product naphthalene.

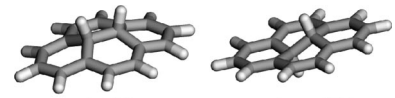

Figure 7. Compounds *cis*-**E2** and *trans*-**E2**.

In general, SRE values reveal that the (5,6)- or (6,6)-membered ring systems are not as useful as the (5,5)-membered ring for taking advantage of molecular strain in lowering R−H BDE values. They can, however, take advantage of conjugation and aromaticity to yield very low R−H BDE values.

An extreme form of this approach to weakening the C−H bond would be *trans*-**E1**, a (6,6,5,5) fragment of a buckyball, where its R−H BDE_1 has dropped to ca. 58 kcal/mol. One could imagine a buckyball that has been modified to include a local single bond, as in **E1**. In that case, the weakening of the C−H bond should be even more extreme.

As a final example consider **E2**, with its (6,6,6,6) structure. As in **D4** and **E1**, the periphery of the parent molecule is fully conjugated, but the molecule is not aromatic (Figure 7). Now the R−H BDE_1 has dropped to 46.9 kcal/mol for the trans isomer, the lowest value in Table 3.

We conclude this discussion with some observations on trends in Table 3. Similar to the comparison made in Table 2, comparison of the values for BDE_1 and the corrected values BDE_1* shows very little difference between the two. Approximately one-half of the entries release strain, whereas the other half increase it; the magnitude of the correction never exceeds ca. 4 kcal/mol and is usually less than 2 kcal/mol. This means that uncorrected values of B3LYP energetics could have been used for these calculations with relatively little error. In general, this also applies to BDE_2 values, although there is one case where the deviation is as large as 6 kcal/mol. The significant amounts of strain introduced into the parent molecule in the trans geometry mean that these structures are "strain traps", which is the cause of their low BDE values.

Relevance to Experimental Work

Ferjančić et al.[15] studied free radical additions to strained cycloalkenes and concluded that the strain relief in the intermediate radical accelerates the addition reaction. The reactions we studied in this work do not involve high energy transition states as those of the Ferjančić study, but they do involve strain relief (in hydrogen abstraction reactions) or gain (in oxygen addition reactions). Thus, it is possible that the strain affects the kinetics of these reactions favorably. This is particularly interesting, because antioxidants that generate carbon radicals are known to have slower reaction rates than those that generate oxygen-centered radicals.

Regarding more highly conjugated compounds, Small et al.[16] have studied the ultraweak σ-bond formed in dimerization of phenalenyl radical and estimated the BDE of this C−C bond to be about 16 kcal/mol. Our calculations show that similar to radicals formed by **E1** and **E2**, the weak C−H bond in phenalenyl radical is the result of increased conjuga-

tion and relief of strain for radical formation. While the phenalenyl radical tends to self-associate and form a dimer, it has been shown[17] that by using appropriately bulky functional groups, a persistent radical can be isolated and even crystallized. A similar steric approach can be used to inhibit the possible dimerization reactions of our about-to-be formed aromatic compounds such as **E1** and **E2**. This approach has been exploited to generate a continuous source of radicals for use as chain-breaking antioxidants.[18]

Verevkin et al.[19] found the compound *cis*-**D4** to be the "thermodynamic sink" (the most stable) of all interconversions of $(CH)_{10}$ compounds. Because they only confined their search to experimentally discovered compounds, the trans compound was not considered. According to our calculation, the trans conformer is 0.3 kcal/mol more stable.

Antioxidant Design

Antioxidants that form carbon-centered radicals by abstraction from a C−H bond are limited in usefulness because they react more slowly than antioxidants based on abstraction from an O−H bond.[20] However, as the R−H BDE drops drastically, these kinetic differences should be reduced. There is an interesting point of comparison with phenolic antioxidants. Phenols are often metabolized biologically to catechols and hydroquinones. These are good H-atom donors and oxidize first to the semiquinone and ultimately to the quinone. Reducing agents such as ascorbate or glutathione are often required to send the reactive semiquinones back to parent catechols (or hydroquinones), or else the very electrophilic quinones can act as tumor initiators by alkylating DNA.[21] When reducing agents are present, the catechol (or phenol) acts as a catalytic antioxidant because the parent compound is regenerated from the reducing power in the cell. However, when oxidation (often autoxidation) exceeds reduction of the oxy-radical, the cell enters into a state of oxidative stress, usually with negative consequences for the organism.

Now consider antioxidants based on carbon-centered radicals as described in Table 3. The first BDE is low, so reaction with a target radical such as peroxyl should be relatively fast. The second BDE is very low, so the reaction will quickly go to completion, forming the relatively stable olefin product. Because olefins are much less electrophilic than quinones, they should pose much less of a tendency to cause oxidative stress. Once formed, the olefin is unlikely to be reduced. Such an antioxidant is then acting in a stoichiometric rather than in a catalytic mode. This will require restoring the supply of starting material. However, due to the presence of two exchangeable H-atoms, the parent compound is acting as a bivalent donor antioxidant. This is an improvement over a monovalent antioxidant. One could continue this theme by designing structures that are polyvalent donors with multiple weak C−H bonds.

Conclusions

Molecular strain and conjugation effects can be effectively used to design structures that produce carbon-centered radicals. Classical substituent effects that stabilize the radical center can be used in combination with molecular strain to design molecules with ultraweak C−H bonds. One possible strategy is to design structural motifs suitable for the quasi-planar orientation of bonds on the radical center, so that the tetrahedral orientation of bonds in the parent and oxygen adduct will be strained. Some simple examples of compounds following this theme were demonstrated, including (5,5)-, (5,6)-, (6,6)-membered fused rings.

Homodesmotic reactions were used to derive correction factors for the absolute enthalpy of both parent and radical. The corrected enthalpies were used to obtain the corrected values of the BDE and the strain release enthalpy (SRE). We demonstrated that this parameter (MSE) can be used to correct for the B3LYP error in highly strained molecules and to obtain BDE values that correspond closely to higher level calculations. The magnitude of this correction however was usually small. The SRE value reveals how much the molecular strain that is engineered in the parent molecules is released through a hydrogen abstraction reaction. The SRE values reveal that the trans isomers of (5,5)-membered systems are ideal "strain traps", which can lower the R−H BDE_1 values by up to 30 kcal/mol.

The fused-ring compounds can undergo subsequent hydrogen loss and show low first and especially low second R−H BDEs. At this stage, these compounds end up as stable closed-shell products, effectively terminating the propagation of oxidative chain reactions. While for classical carbon-centered radicals the reaction rates of C−H bond dissociation are slower than ideal for antioxidant activity, it is likely that the very weak C−H bonds of the parent molecules in our suggested compounds will increase these reaction rates considerably. This leads naturally to the idea of a stoichiometric, bivalent donor antioxidant generating nontoxic products.

Acknowledgment. We thank NSERC for financial support. Computing resources were provided by the HPCVL.

Supporting Information Available: Homodesmotic reactions used to calculate MSE values. This material is available free of charge via the Internet at http://pubs.acs.org.

References

(1) Maillard, B.; Ingold, K. U.; Scaiano, J. C. *J. Am. Chem. Soc.* **1985**, *105*, 5095–5099.

(2) Burton, G. W.; Doba, T.; Gabe, E. J.; Hughes, L.; Lee, F. L.; Prasad, L.; Ingold, K. U. *J. Am. Chem. Soc.* **1985**, *107*, 7053–7065.

(3) Burton, G.; Ingold, K. U. *Acc. Chem. Res.* **1986**, *19*, 194–201.

(4) Shi, H.; Noguchi, N.; Niki, E. *Free Radical Biol. Med.* **1999**, *27*, 334–346.

(5) Wright, J. S.; Shadnia, H. *J. Comput. Chem.*, DOI 10.1002/jcc.21124.

(6) Wiberg, K. B. *Angew. Chem., Int. Ed. Engl.* **1986**, *25*, 312–322.

(7) Nicolaides, A.; Radom, L. *Mol. Phys.* **1996**, *88*, 759–765.

(8) Bond, D. *J. Org. Chem.* **2007**, *72*, 5555–5566.

(9) Rogers, D. W.; McLafferty, F. J. *J. Phys. Chem. A* **2000**, *104*, 9356–9361.

(10) Peck, R.; Schulman, J. M.; Disch, R. L. *J. Phys. Chem.* **1990**, *94*, 6637–6641.

(11) Wright, J. S.; Rowley, C. R.; Chepelev, L. L. *Mol. Phys.* **2005**, *103*, 815–824.

(12) Kollias, A. C.; Domin, D.; Hill, G.; Frenklach, M.; Golden, D. M.; Lester, W. A. *Int. J. Chem. Kinet.* **2005**, *37*, 583–592.

(13) Walker, J. E.; Adamson, P. A.; Davis, S. R. *J. Mol. Struct. (THEOCHEM)* **1999**, *487*, 145–150.

(14) Wright, J. S.; Johnson, E. R.; DiLabio, G. A. *J. Am. Chem. Soc.* **2001**, *123*, 1173–1183.

(15) Ferjančić, Z.; Ćeković, Ź.; Sačić, R. N. *Tetrahedron Lett.* **2000**, *41*, 2979–2982.

(16) Small, D.; Rosokha, S. V.; Kochi, J. K.; Head-Gordon, M. *J. Phys. Chem. A* **2005**, *109*, 11261–11267.

(17) Bowry, V. S.; Stocker, R. *J. Am. Chem. Soc.* **1993**, *115*, 6029–6044.

(18) Frenett, M.; MacLean, P. D.; Barclay, L. R. C.; Scaiano, J. C. *J. Am. Chem. Soc.* **2006**, *128*, 16432–16433.

(19) Verevkin, S. P.; Kümmerlin, M.; Hickl, E.; Beckhaus, H. D.; Rüchardt, C.; Kozhushkov, S. I.; Haag, R.; Boese, R.; Benet-Bucholz, J.; Nordhoff, K.; Meijere, A. *Eur. J. Org. Chem.* **2002**, *14*, 2280–2287.

(20) Zavitsas, A. A.; Chatgilialoglu, C. *J. Am. Chem. Soc.* **1995**, *117*, 10645–54.

(21) Halliwell, B.; Gutteridge, J. M. C. *Free Radicals in Biology and Medicine*; Oxford University Press: Oxford, 1999.

CT900049J

JCTC Journal of Chemical Theory and Computation

Density Functional Theory Calculation of Bonding and Charge Parameters for Molecular Dynamics Studies on [FeFe] Hydrogenases

Christopher H. Chang* and Kwiseon Kim

National Renewable Energy Laboratory, 1617 Cole Boulevard, Golden, Colorado 80401

Received August 18, 2008

Abstract: We have developed and tested molecular mechanics parameters for [FeS] clusters found in known [FeFe] hydrogenases. Bond stretching, angle bending, dihedral and improper torsion parameters for models of the oxidized and reduced catalytic H-cluster, $[4Fe4S]^{+,2+}Cys_4$, $[4Fe4S]^{+,2+}Cys_3His$, and $[2Fe2S]^{+,2+}Cys_4$, were calculated solely from Kohn−Sham density functional theory and Natural Population Analysis. Circumsphere analysis of the cubane clusters in the energy-minimized structure of the full *Clostridium pasteurianum* hydrogenase I showed the resulting metallocluster structures to be similar to known cubane structures. All clusters were additionally stable in molecular dynamics simulations over the course of 1.0 ns in the fully oxidized and fully reduced enzyme models. Normal modes calculated by quasiharmonic analysis from the dynamics data show unexpected couplings among internal coordinate motions, which may reflect the effects of the protein structure on metallocluster dynamics.

Introduction

The biological mechanisms for production of hydrogen gas are a current topic of great interest.[1,2] In particular, [FeFe] hydrogenases are understood to catalyze H_2 production more effectively than the reverse uptake reaction.[3] As naturally occurring enzymes, they must catalyze reduction of protons at $\sim 10^{-7}$ M concentration, ambient or slightly elevated temperatures, and modest reduction potentials. Furthermore, the delivery of electrons from biological electron donors such as ferredoxin and protons from the cellular milieu must be coordinated. These properties make the [FeFe] hydrogenases attractive models for the development of engineered enzymatic catalysts, protein maquettes,[4] or chemical catalysts.

The most complex [FeFe] hydrogenase so far structurally characterized, hydrogenase 1 from *Clostridium pasteurianum*, contains not only the [2Fe]-[4Fe4S] H-cluster but also two auxiliary cubane-type [4Fe4S] clusters with tetracysteinate ligation, a single [4Fe4S] center with unique Cys_3His ligation, and a $[2Fe2S]Cys_4$ cluster. Given that *C. pasteurianum* is a strict anaerobe, it is reasonable to expect these clusters to function either as redox cofactors shuttling between their most reduced and next-most reduced states or as structural centers in one of those two states. Barring the example of the nitrogenase Fe protein which can achieve a remarkable $[4Fe4S]^0$ state, in biological systems this implies cluster valence states of $[2Fe]_H^{I,II;I,I}$, $[4Fe4S]^{2+,+}$, and $[2Fe2S]^{2+,+}$, where Roman numerals refer to the formal valence of individual iron ions, and Arabic numerals to the overall valence of the inorganic cluster core.

In principle, the now widespread availability of user-friendly molecular dynamics and quantum chemistry packages together with communal supercomputing resources brings to bear unprecedented power to simulate and understand the catalytic dynamics of [FeFe] hydrogenases. However, the lack of a complete, consistent set of mechanical parameters derived under a single set of assumptions for the electron transfer and catalytic centers hampers more widespread study of these systems. [2Fe2S] and [4Fe4S] cluster parameters derived from crystallographic study are available (HIC-UP) but with arbitrary force constants. To our knowledge, a systematic effort to derive quantitative bond, angle, and dihedral parameters for the hydrogenase [2Fe], $[4Fe4S]Cys_4$, $[4Fe4S]Cys_3His$, and $[2Fe2S]Cys_4$ centers has not been reported. Here, we use *ab initio* quantum chemistry to generate the force parameters for the metalloclusters. Technical complexities such as the formally multireference

* Corresponding author e-mail: christopher_chang@nrel.gov.

10.1021/ct800342w CCC: $40.75
Published on Web 03/19/2009

character of antiferromagnetically coupled metalloclusters and the challenge of defining dihedral angles in cage structures make this process somewhat tedious. However, the *ab initio* calculation of force parameters for these systems has several attractions. Although the ring or cage structures of [2Fe2S] and [4Fe4S] centers make dihedral definition complicated, their lack of rotational freedom means no rotational isomers need consideration, and thus the behavior of dihedral potential functions away from their cluster-associated values may be reasonably neglected. Furthermore, few ad hoc decisions need to be made regarding particular data to fit. Finally, results may be systematically improved through the use of higher levels of theory, more complete basis sets, and fewer assumptions as needed.

In this spirit, we here report a first-generation set of molecular mechanical parameters and topology files for these centers in their expected functional valence states. Results of these parameters for energy minimization, molecular dynamics, and vibrational analysis are compared to quantum mechanical calculations as well as experimentally measured frequencies for the diatomic ligands on the H-cluster [2Fe] core.

Methods

Structural Models. Models for the catalytic center comprised the basic structure of the $[2Fe]_H$ H-cluster core found in [FeFe] hydrogenase, with the sole cysteinate ligand replaced with methylthiol. The use of a proton to approximate $[4Fe4S]_H$ on this core is precedented.[5−7] The oxidized form of formal iron valence Fe^IFe^{II} was modeled with an open ligation site on the distal Fe motivated by the unusually long Fe_{distal}-X bond observed in the original crystallographic structure of the Clostridial enzyme[8] and the apparent lack of a corresponding ligand in the *Desulfovibrio desulfuricans* [FeFe] hydrogenase structure.[9] The reduced form was modeled with proton ligation to the distal Fe^I. Although this model is of questionable relevance to reaction mechanisms involving solely bridging hydride species,[7,10] it is consistent with other mechanisms that have been proposed,[5] particularly in the presence of a DTMA bridging dithiolate.[11,12] Methylthiolate replaced cysteinate for all [2Fe2S] and [4Fe4S] clusters. For the special [4Fe4S]HisCys$_3$ model, histidine was ligated via N^ε, as modeled in the crystallographic structure for CpI (PDB code 1FEH).

Quantum Chemistry. Geometry optimization and frequency calculations employed the Gaussian 2003 package, rev. C.2, and a BLYP/6−31+G* model chemistry. Coulomb fitting was employed to accelerate the SCF process. Higher symmetries possible for the [2Fe2S]Cys$_4$ and [4Fe4S]Cys$_4$ clusters were not enforced, i.e., all calculations were performed within C_1 symmetry. Geometries were optimized to default criteria (maximum and rms forces of 0.45 and 0.30 mHa/Bohr, displacements of 1.8 and 1.2 mBohr), and the rms change in the density matrix was set to 10^{-8} ("SCF=Tight") with the default pruned (75,302) integration grid. In certain cases, SCF nonconvergence observed for the iron−sulfur clusters was circumvented by constructing initial guesses from localized Natural Bond Orbitals[13] generated from loosely converged Kohn−Sham wave functions. In these cases, broken-spin-symmetry electronic configurations were input, with majority α- and β-spin ions distributed arbitrarily within the model cluster. Frequencies were calculated from analytical second derivatives. Output of the Hessian in internal coordinates was achieved using the Gaussian route flag IOp(7/32) and keyword option Freq=InternalModes. Hessian diagonal elements were scaled by $(0.9945)^2$, based on empirical frequency scaling studies.[14] The Urey−Bradley terms included as part of the CHARMM force field were not calculated, which may simply be thought of as neglecting anharmonicity in the angle bending coordinates. To convert force constants from atomic units (Hartree/Bohr^2 or Hartree/radian^2) to those used in the program package CHARMM (kcal/(mol·Å^2) and kcal/(mol·rad^2)), force constants were further scaled by 2242.3 (bonds) and 627.49 (bends and torsions).

Definition of Dihedral Angles. Where possible, the force constants calculated with density functional theory are used in harmonic potential functions, which differs from the common parametrization as a trigonometric function. This was the case for angles that could be defined with a single minimum-energy value, which in turn depends on both the dynamic rigidity in three-dimensional space as well as the chosen definition of atom types. Thus, although the cage structures of [FeS] clusters imply limited rotational flexibility, to make our force field as simple as possible we have chosen to limit cluster atom types to one per element, per [FeS] cluster type. In doing so, for the auxiliary electron transfer clusters (i.e., not the $[2Fe]_H$ component of the H-cluster), optimum dihedral angles typically clustered as one or more $\pm\theta$ pairs; unfortunately, such a pattern is difficult to encode exactly with either a single harmonic or trigonometric function. Nevertheless, for these cases with multiple minima arising from degeneracy in our atom type definitions, we have chosen simplicity over precision by choosing the lowest multiplicity of a cosine function that places minima near all optimum θ values. A particularly pernicious example is the FEIR-SIR-FEIR-SIR dihedral associated with the iron and sulfide core of the reduced [4Fe4S]HisCys$_3$ cluster, with a multiplicity of 40 and phase angle of 180° to encompass true minima at approximately ±9° and ±91°. The CHARMM potential function $V_{dihedral}=A[1+\cos(n\theta+\varphi)]$, with multiplicity n and phase angle φ produces the requisite minima at 9 and 90 degrees, at the cost of introducing numerous spurious minima. However, the relatively rigid cage topology of this cluster type arising from effective dihedral constraints by bond and angle forces prevents sampling of these spurious dihedral minima, as illustrated in Figure 2. We have made a further approximation in taking the harmonic force constants from our *ab initio* calculations directly as cosine amplitudes. Again, however, the lack of physical transitions among the function's minima and the effective constraints from the stiffer bond and angle force constants makes the fine detail of the high-energy values mostly irrelevant.

Approximations for Fe−C−O/N Bending Parameters. The linear angles found in the Fe−C−(O/N) and *trans* S−Fe−C angles created two particular difficulties in parameter derivation. First, care was required to exclude any

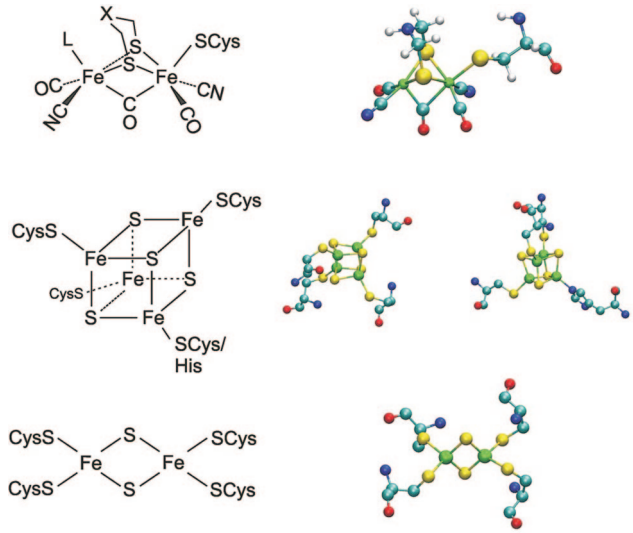

Figure 1. Schematic and CPK representations of [FeFe] hydrogenase electron transfer and catalytic centers considered.

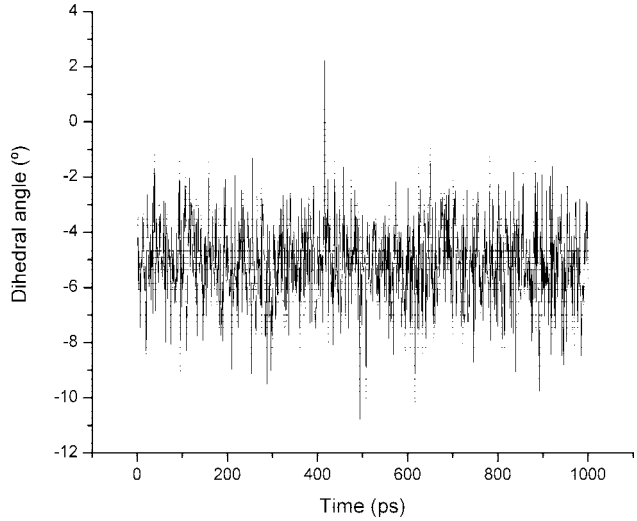

Figure 2. Dynamic stability of the Fe1−S1−Fe2−S2 dihedral angle from $[4Fe4S]^{+}HisCys_3$ over 1 ns simulation time of the *Cp*I hydrogenase.

dihedral angle definitions involving three such atoms; the effects of the singularity produced by a linearity in an A−B−C−D system manifested as sudden atomic accelerations and immediate cessation of dynamics simulations. This observation is the primary driver behind our decision to abandon automatic generation of internal coordinates and the explicit definition of bonding topologies we have used. Second, linear bending coordinates are described along deformations in two orthogonal directions; however, the natural mechanism in classical biomolecular force fields is an improper torsion. The two linear bending force constants calculated quantum mechanically were used as constants to describe one improper torsion and one angle bend. By way of example, the FEL1-CLC-CLO1-OL4 (Fe_{prox}-C_{br}-CO_{prox}-O_{CO}) improper torsion force constant was assigned the DFT-calculated force constant for the linear FEL1-CLO1-OL4 bend within the FEL1/CLO1/CLC plane, and the FEL1-CLO1-OL4 bending constant was assigned the average of the above linear bend constant and that for the FEL1-CLO1-OL4 bend perpendicular to the FEL1/CLO1/OL4 plane as a compromise to describe all possible FEL1-CLO1-OL4 bending motions relative to the FEL1/CLO1/OL4 plane.

van der Waals radii were primarily taken from standard CHARMM atom types, including "S" (sulfide and DTMA thiolate), "CT2" (DTMA methylene C), heme OM (carbonyl O), heme CM (carbonyl C), HA (DTMA methylene H) and HC (HCR hydride), wildcard N (cyanide N, DTMA nitrogen), and heme Fe.[15] We note that the Fe van der Waals interactions are neglected in CHARMM27 with an ε value of 0.0 in the standard Lennard-Jones 6−12 potential form.

Test Simulations. Energy minimization, molecular dynamics, and analysis calculations of the protein system with the exception of frequency estimations were carried out using the NAMD[16] and VMD[17] program packages. Metallocluster normal modes and frequencies were calculated from the trajectory data using the CHARMM program package, version 34.[18] After projecting out translational and rotational motions of the clusters, modes and frequencies were obtained by quasiharmonic analysis.[19] To estimate localized "C−O" and "C−N" stretching frequencies for the H-cluster diatomic ligands, the normal modes were projected onto the appropriate localized mode and vibrational frequency of the localized mode calculated from the weighted rms over the set of normal-mode frequencies[20]

$$\begin{aligned} \Lambda &= \hat{L}^{\dagger}\hat{H}_{\text{int}}\hat{L} \\ \vec{m}'\cdot\Lambda\cdot\vec{m} &= (\vec{m}'\cdot\hat{L}^{\dagger})\hat{H}_{\text{int}}(\hat{L}\cdot\vec{m}) \\ \lambda_m &= \sum_i \lambda_i m_i^2 \lambda = 4\pi^2\nu^2 \\ \nu_m &= \sqrt{\sum_i \nu_i^2 m_i^2} = \sqrt{\sum_i \nu_i^2 w_i} \end{aligned} \tag{1}$$

where L is the matrix of eigenvectors (i.e., normal modes) of the Hessian in internal coordinates H_{int}, $L^{\dagger}$ is its adjoint, Λ is the diagonal matrix of eigenvalues λ_i, $\vec{m}$ is the localized mode vector of interest, ν_i is the frequency of the i^{th} normal mode, ν_m is the frequency of the localized mode of interest, and $w_i = \vec{m}_i' \cdot \vec{m}_i$ is the weight of the i^{th} normal mode in the localized mode.

Simulation parameters other than the force constant and atomic charges considered here were as previously described.[21] Circumsphere plots of iron and sulfide angular coordinates were made with the Python plotting module Plothon version 0.1.2 (now SVGFig[22]). Ellipsoid plots were constructed by determining the appropriate rotations to achieve the desired perspective and then applying these to a reference dynamics frame prior to calculation of anisotropic temperature factors using an in-house VMD script implementing the appropriate calculations.[23] PDB files including the calculated ANISOU records were constructed and used as input to the Raster3D package.[24]

Results and Discussion

Atom Type Definitions. We have limited our efforts to the two most relevant valence states of each metallocluster considered here, given the requirements for reduction of

Table 1. Residue Names, Atom Type Labels, and Atom Names for Metalloclusters Considered

structure	residue	atom types	atom names
[2Fe2S]Cys_4	F2(O/R)	FEK(O/R), SK(O/R)	FE1, FE2, S1, S2
[4Fe4S]Cys_4	F4(O/R)	FEJ(O/R), SJ(O/R)	FE1...FE4, S1...S4
[4Fe4S]Cys_3His	FH(O/R)	FEI(O/R), SI(O/R)	FE1...FE4, S1...S4
$[2Fe]_H$	HC(O/R)	FE(M/L)1, FE(M/L)2, S(M/L)1, S(M/L)2, N(M/L)M, O(M/L)4, N(M/L)5, O(M/L)6, C(M/L)O1, C(M/L)N1, C(M/L)O2, C(M/L)N2, C(M/L)C, HC(M/L)1, HC(M/L)2, CC(M/L)1	FE1, FE2, S1, S2, N1, (O3 or O7),(N4 or N6), O5, C3, C4, C7, C6,C5, (HB1 or HB4), (HB2 or HB3), (CB1 or CB3)

protons to H_2 and typical redox potentials in anaerobic bacterial cytoplasm. For the H-cluster [2Fe] core, we have likewise considered two forms; however, given the greater bonding flexibility as compared to [FeS] cluster cofactors, we were forced to make several choices regarding the nature of the open coordination site found on Fe_{distal}. First, although the nature of the (μ_2,μ_2)-bridging dithiolate ligand has been variously proposed as 1,3-propanedithiolate,[9] di(thiomethyl)-amine,[11,25] or di(thiomethyl)ether,[26] we have chosen di(thiomethyl)amine (DTMA) due to its attraction as a proton transfer intermediary and the presence of Cys299 within hydrogen bonding distance of the central atom of this bridging ligand. This choice in turn favors a proton transfer mechanism involving a terminal binding mode to Fe_{distal}, at least in the initial stages of proton reduction at $[2Fe]_H$. Thus, for the "active oxidized" Fe^IFe^{II} form (as compared to the "inactive oxidized" diferrous form found in certain as-isolated enzymes, e.g., *Desulfovibrio vulgaris*[27,28]), the distal coordination site was left open based on the unusually long Fe−O bond found in the crystallographic structure and on the need for an open site to permit terminal hydride binding. The fully reduced $[2Fe]_H$ unit was modeled as a terminally protonated Fe^IFe^I species.

Our atom type nomenclature in this report is summarized in Table 1. There are three noncatalytic electron carrier cluster types, each with two potential redox states. The oxidized or reduced state is signaled through a terminal "O" or "R", respectively, on the atom type name for Fe and inorganic sulfide atoms. The nature of the cluster is identified through an index character immediately following the element name, with (I, J, K) = ([4Fe4S]Cys_3His, [4Fe4S]Cys_4, [2Fe2S]Cys_4). The bonding changes between oxidized and reduced forms of $[2Fe]_H$ were associated with different nomenclature. Atoms of the oxidized cluster are denoted with "M" following the elemental character, with the exceptions of "HCM1", "HCM2", and "CCM1" denoting DTMA methylene hydrogen atoms pointing toward $Fe_{proximal}$, DTMA methylene hydrogen atoms pointing toward Fe_{distal}, and DTMA methylene carbons, respectively. Terminal carbonyl oxygen atoms are denoted by an index number of "4", the bridging carbonyl oxygen atom by "6", and the terminal cyano nitrogen atoms by "5": thus, "OM6" is the oxygen atom of the bridging CO group. Diatomic ligand carbon atoms bound to $Fe_{proximal}$ have a numeric index of "1"; those bound to Fe_{distal} an index of "2", leading to "CMN2" corresponding to the terminal cyano carbon bound to Fe_{distal}, for example. Nomenclature for reduced $[2Fe]_H$ is identical save for the replacement of "M" with "L" and the terminally bound proton denoted by atom type "HH". The atom naming and typing system is illustrated in Figure 3 for the reduced $[2Fe]_H$ center.

Force constant values and NPA charges are given in their entirety in the Supporting Information. We have generated CHARMM-style topology files with explicit definitions of bond, angle, dihedral angle, and improper torsion angle definitions, allowing the general user to avoid certain problems associated with linear angles found in the $[2Fe]_H$ center and to map cleanly to the available force parameters. In addition, explicit internal coordinate definitions corresponding to the density functional theory-optimized struc-

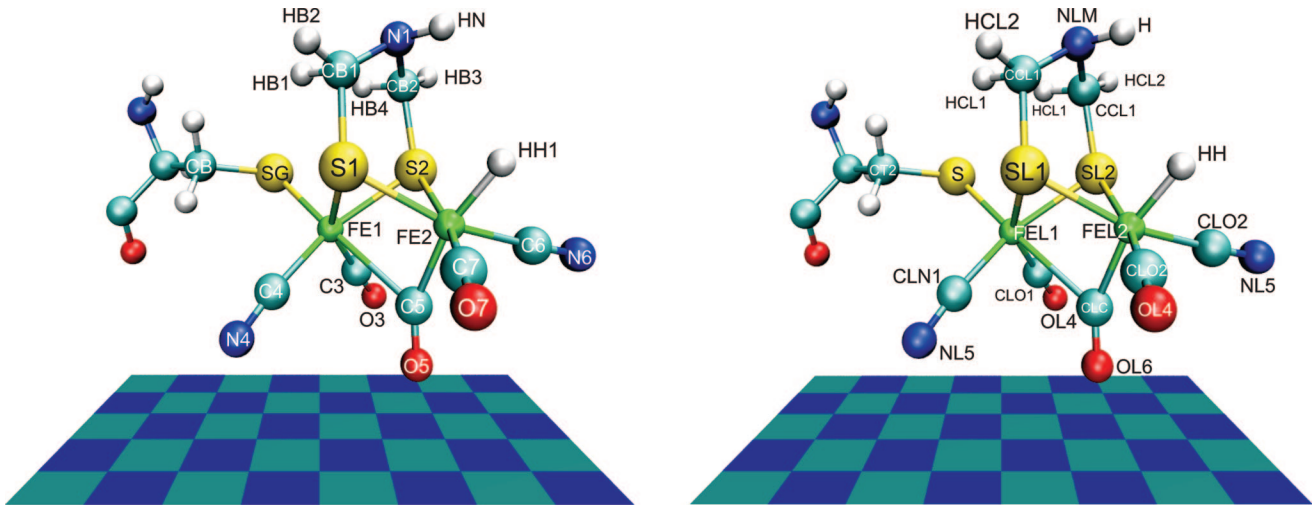

Figure 3. Atom names (left) and types (right) associated with the force field calculated for the reduced $[2Fe]_H$ core of [FeFe] hydrogenases. Oxidized types may be trivially derived from the reduced types by replacing "L" with "M" and neglecting bound hydride "HH".

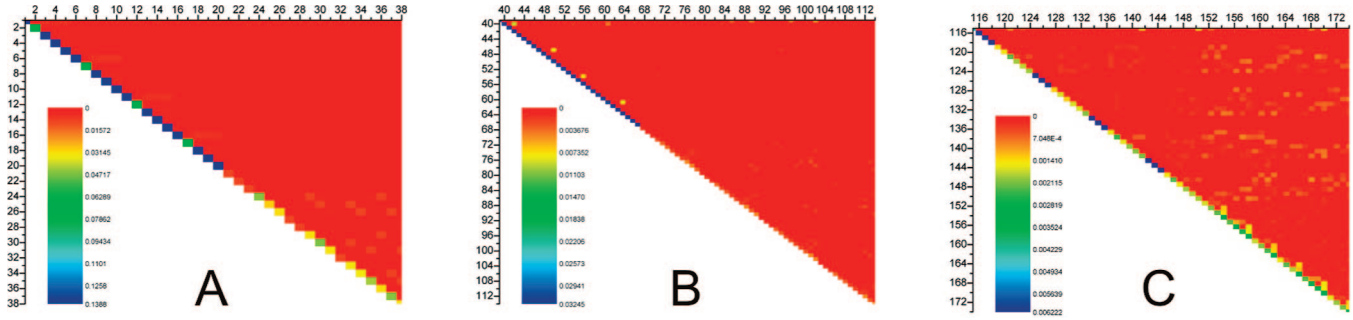

Figure 4. Color maps of Hessian sections calculated for the oxidized [4Fe4S] cluster model. The maximum of the dynamic range is set to the average of the diagonal values for (A) bonds, (B) angles, and (C) dihedrals. Only coordinate couplings within each type of coordinate are shown. Axes are labeled by the internal coordinate indices.

tures for $[2Fe]_H$ are included for automatic regeneration of the complete cluster structure from partial experimental structures, with direct user intervention limited to minor text editing of the Protein Data Bank file. Beyond general build practices for proteins, user responsibility is limited to ensuring proper atom naming in the input PDB file consistent with that in Figure 3 and our convention of naming the Fe atom bound to histidine in $[4Fe4S]Cys_3His$ as FE1.

Quantum Chemistry. Geometry optimizations and charge calculations were straightforward. The three terminal hydrogen charges of methylthiolate were adapted to the two methylene hydrogen atoms of cysteine simply by redistributing the sum of the former three atoms over two, thereby preserving overall the integer charge of the system. Calculation of force constants as diagonal Hessian elements often required repeated calculations with manually specified internal coordinates, as program-generated redundant internal coordinates did not always include those desirable for a molecular mechanics force field. However, after initial storage of force constants in the checkpoint file, such repetitions were very brief, requiring only conversion of Cartesian force constants to internal coordinates and output of the Hessian including the manually specified internal coordinates.

As expected, the orthogonality of coordinates decreases as one moves from two-body bonds, through three-body angles, to four-body dihedral and improper torsions. This is illustrated in Figure 4, where a color map of the upper triangular Hessian for the oxidized $[4Fe4S]^{2+}$ cluster is plotted. The dynamic range maximum was set to the average diagonal value of the bonds (4A), angles (4B), or dihedral angles (4C) to allow visual evaluation of the relative diagonal dominance for each class of parameter. The diagonal dominance is clear in all three cases, with some coordinate coupling becoming apparent for the weakest force constants (dihedrals and impropers). It should be noted that the ring- and cage-type structures of the clusters considered constrain the space of achievable geometries. Thus, errors arising from neglected coupling among weak four-body force constants should be "drowned out" in simulation practice by the much stronger bonding interactions. Nevertheless, for the sake of completeness and to include as much physics as possible in this first-generation force field, we have included these four-body parameters.

Due to the requirement for a complete [2Fe]-[4Fe4S]-(methylthiolate)$_4$ second derivatives calculation to derive the angular parameters governing the linkage between $[2Fe]_H$ and $[4Fe4S]_H$, we have chosen to neglect the four-body terms between these entities and to approximate the Fe−S(Cys)−Fe bending force constant with an arbitrary 500 kcal/(mol·rad^2) value, with the optimum angle left as that observed in the crystallographic structure for *Clostridium pasteurianum* hydrogenase I. The treatment of the [6Fe4S] H-cluster as structurally separable $[2Fe]_H$ and $[4Fe4S]_H$ clusters for the purposes of molecular mechanical/dynamical calculations raises the question of their actual physical autonomy. Recent computational and spectroscopic data have revealed a degree of electronic coupling[29,30] as expected for such a coordinate-covalently linked metallocluster, and careful examination of ^{57}Fe hyperfine couplings in the H_{ox} state confirmed exchange coupling between $[2Fe]_H$ and $[4Fe4S]_H$ in this redox state.[31] The observed exchange coupling (spin polarization) in one-electron theory is distinct from electron "delocalization" between the clusters in the sense of extended molecular orbitals, which was proposed based on examination of the calculated difference electron density between isolated and structurally connected clusters, canonical (i.e., those diagonalizing the approximate one-electron Hamiltonian) frontier orbital shape, and nonadditivity of open-shell iron character in the sulfur K-edge X-ray absorption bands.[30] However, direct physical interpretation of one-electron molecular orbitals, particularly those derived from Kohn−Sham theory,[32] can be physically ambiguous, especially among near-degenerate orbitals that may be mixed without dramatically changing the wave function. Self-interaction error has been raised as a particular source of excessive delocalization in canonical Kohn−Sham orbitals of odd-electron systems.[33,34] Spectral analysis of $[2Fe]_H$, [4Fe4S], and $[6Fe4S]_H$ model complexes shows that the assigned sulfide-to-high-spin-Fe transition intensity in a combined [6Fe4S] model arises from contributions of [4Fe4S] peak intensity, $[2Fe]_H$ low-spin-Fe(I)-to-thiolate tail intensity, and cooperative effects potentially including delocalization;[30] however, it is not clear whether the electronic changes expected from exchange coupling alone could account for the observed nonadditivity, or whether electron delocalization is necessary. The pattern and contour values of difference density suggested that the bulk of electronic reorganization between the isolated and combined cluster models occurred among orbitals on indi-

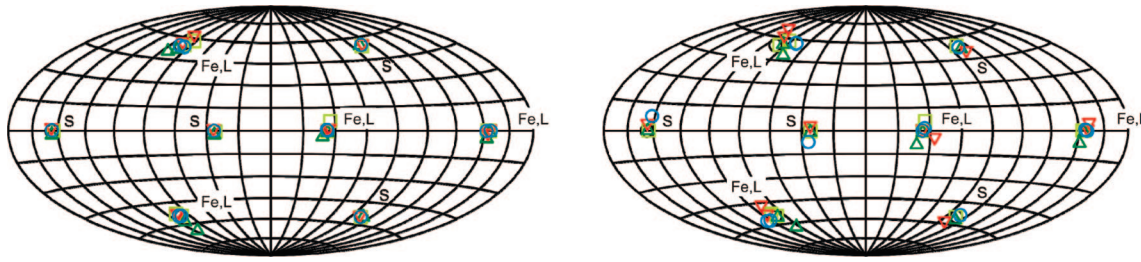

Figure 5. Circumsphere plots of oxidized (left) and reduced (right) CpI [FeFe] hydrogenase [4Fe4S] cluster coordinates, together with maximally symmetric coordinates. Black circle, perfect symmetry; chartreuse square, $[4Fe4S]_{581}$; green triangle, $[4Fe4S]_{582}$; red inverted triangle, $[4Fe4S]_{583}$; blue circle, $Cys_3His[4Fe4S]_{584}$. Cluster numbering is as in PDB entry 1FEH.

Table 2. Experimental and Geometry-Optimized Circumsphere Radii for CpI [4Fe4S] Clusters

	Fe			sulfide			protein ligands		
	Exp	$Comp_{ox}$	$Comp_{red}$	Exp	$Comp_{ox}$	$Comp_{red}$	Exp	$Comp_{ox}$	$Comp_{red}$
HYDA[a]	1.663	1.488	1.590	2.244	2.232	2.468	3.949	3.812	4.118
HYDB	1.689	1.488	1.602	2.245	2.226	2.453	3.974	3.807	4.133
HYDC	1.688	1.484	1.612	2.242	2.222	2.446	3.965	3.804	4.153
HYDD	1.675	1.400	1.753	2.232	2.266	2.324	3.880	3.571	4.087

[a] [4Fe4S] hydrogenase residues are here indexed alphabetically, with increasing lexical value reflecting increasing distance from the catalytic $[2Fe]_H$ H-cluster in the *C. pasteurianum* enzyme structure.

vidual ions, rather than between clusters, a result which could arise from atomic orbital near-degeneracy combined with numerical factors in the SCF procedure as well as small perturbations of the cluster electronic structures induced by exchange coupling. The inclusion of the cubane in a $[2Fe]_H$ computational geometry optimization resulted in a weakening of the Fe_{prox}-Cys bond and a shift of the bridging carbonyl group toward the proximal Fe[29] relative to the protonated cysteine thiol $[2Fe]_H$ models commonly used, which might be explained by differential charge polarization within the $[2Fe]_H$ cluster induced by a proton versus an exchange-coupled [4Fe4S] center. Overall, the existing evidence suggests that direct electron delocalization between clusters is a small effect and that the dominant direct effect of [4Fe4S] linkage is a modest perturbation of the charge distribution on the [2Fe] center as compared with a cysteine thiol model. The observation of discrete $[2Fe]^{I,II}$-$[4Fe4S]^{+}$ ("H_{trans}") and $[2Fe]^{I,I}$-$[4Fe4S]^{2+}$ ("H_{ox}") valence states during activation in the enzyme from *Desulfovibrio desulfuricans*[35] further suggests that the two subclusters retain some electronic autonomy in the enzyme's more oxidized states. Lack of an observable reduced $[4Fe4S]^{+}$ moiety during catalytic turnover may arise from rapid and directional electron transfer from $[4Fe4S]_H$ to $[2Fe]_H$, as opposed to inextricable electronic structure in a nondegenerate ground electronic state. Given the evidence, we assert that for the purposes of deriving molecular mechanical parameters, isolated cluster calculations are suitable as an initial approximation. Nevertheless, the effect of electronic coupling between these subclusters on structure and properties will be an area for future refinement and study of the force field.

Test Simulations—Optimized Geometries. The geometry of the *Clostridium pasteurianum* hydrogenase I was optimized in fully oxidized and fully reduced states with the parameters reported. In order to evaluate the modeled energy-minimized geometries, we compare the angular positions of the iron, sulfide, and bonded ligand atoms to an ideal cluster geometry using the circumsphere methodology of Fee and co-workers.[36] Figure 5 shows overlays of atomic positions associated with all [4Fe4S] clusters in the geometry-optimized CpI hydrogenase in its fully oxidized and reduced states, with an idealized cluster comprising three Platonic tetrahedra circumscribed about a common origin. Comparison to this Platonic ideal and to the clusters examined in ref 28 shows excellent angular overlap, confirming that the derived [4Fe4S] parameters preserve the expected angular distribution of Fe and S ions, while still allowing adjustment to the protein environment.

Average calculated Fe-sulfide and Fe-protein ligand bond lengths were 2.23 ± 0.012 and 2.29 ± 0.086 and 2.43 ± 0.032 and 2.50 ± 0.11 for the minimum-energy oxidized and reduced models, respectively, averaged over the [4Fe4S] clusters in CpI [FeFe] hydrogenase. As compared with experimental values of 2.31 ± 0.029 for Fe-sulfide and 2.27 ± 0.066 for Fe-protein ligand bonds in this protein, the bond lengths in the energy-minimized oxidized CpI hydrogenase model offer satisfactory agreement with experimentally measured values. Circumsphere radii for the Fe, sulfide, and protein ligand atoms are shown in Table 2 for the [4Fe4S] clusters found in CpI hydrogenase. Most notably, the Fe circumsphere radii in the oxidized state are contracted by ~0.2 Å relative to the experimental structure, and the protein ligand circumsphere by 0.14−0.31 Å. The oxidized sulfide circumsphere matches the experimental structure quite closely, with a small relative ~0.02 Å contraction. Save for the [4Fe4S]Cys_3His cluster (HYDD), *in silico* reduction leads to minimum-energy clusters with a slightly (~0.1 Å) contracted Fe sphere and expanded sulfide (0.2 Å) and ligand (0.3 Å) spheres. The Fe circumsphere of the His-ligated cluster actually expands upon reduction; the sulfide and protein ligand circumspheres also expand but less so than the all-cysteinate-ligated iron−sulfur clusters. Expansion upon reduction has been noticed previously[37] and is evident in our gas-phase energy-optimized structures (Supporting

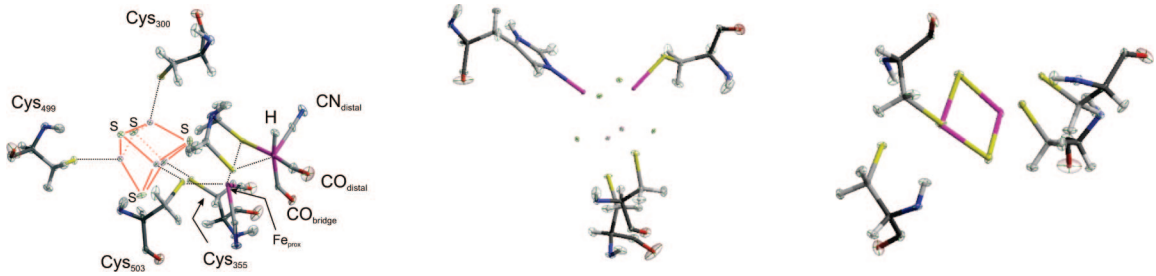

Figure 6. ORTEP-style 50% ellipsoid plots generated from a 1.0 ns molecular dynamics simulation on the CpI hydrogenase model with all clusters reduced. Left, [2Fe]-[4Fe4S]$_H$ with cysteinate ligands; middle, the [4Fe4S]Cys$_3$His auxiliary electron transfer cluster; right, the [2Fe2S]Cys$_4$ auxiliary cluster. Selected group labels and bonds have been drawn into the H-cluster diagram where appropriate to assist in orienting the eye.

Information), consistent with a net Fe−Fe antibonding contribution for the "active" electron, i.e., the electron that enters the oxidized or leaves the reduced cluster form. The substantial compression of the Fe circumspheres in the oxidized models relative to both the gas-phase density functional calculations from which the force constants were derived as well as the experimental protein structure points to a significant role of the protein structure, potential limitations to the classical harmonic potential approximation as applied to redox-active metalloclusters, and possibly subtle effects not yet captured in the current force field. The differences in circumsphere distances involved are satisfyingly small, however, considering the underlying comparison being made between the experimental or gas-phase density functional models on the one hand and the classical mechanical bonding model with protein present on the other.

In order to evaluate the performance of the derived parameters in a broader context, we calculated the geometric properties of [4Fe4S] clusters contained in the PDB database. All structures containing the residue name "SF4" were filtered to eliminate structures containing (1) clusters with multidentate or missing external ligands, (2) clusters with questionable structures, (3) clusters with dual refined positions, (4) clusters falling on a crystallographic symmetry element, such that not all atomic coordinates are explicitly defined, and (5) clusters with bond lengths to external ligands longer than 2.7 Å. The resulting 235 crystallographic protein structures contained 635 [4Fe4S] clusters. We expect these structures to be representative of the oxidized member of the relevant redox couple, due to oxidation during crystallization and limited photoreduction during crystallographic data collection, although this latter assumption is uncertain[38] and depends on specific data acquisition conditions. Average bond lengths, distances between circumcenters, and circumcenter radii were calculated, and the angular circumcenter coordinates were plotted as histograms, as shown in the Supporting Information (Table S2 and Figures S1 and S2). Average circumcenter radii were very close to the experimental [FeFe] hydrogenase values shown in Table 2 as well as to the sulfide and ligand circumsphere radii calculated for the oxidized hydrogenase model. The circumsphere radius calculated for the oxidized hydrogenase [4Fe4S] clusters is ~0.2 Å less than either the DFT-optimized value or the mean experimentally observed value. Angular coordinates of the crystallographic cluster structures cluster around very similar circumsphere theta and phi values to the minimum-energy hydrogenase [4Fe4S] cluster structures shown in Figure 5.

Test Simulations—Dynamics Stability. Figure 6 shows 50% thermal ellipsoid representations for the fully oxidized and reduced models of CpI hydrogenase over 1 ns of molecular dynamics simulation. The Fe and S atoms exhibit narrower distributions than the lighter atoms, as expected. More motion is evident among the second-row atoms of the [2Fe]$_H$ cluster, comparable in magnitude to C/N/O motion in the cysteinate ligands. rms deviations of atomic positions in the protein only, metalloclusters only, and protein + metalloclusters over 1000 frames (1 ns simulation time) were 0.825 ± 0.007 Å, 0.482 ± 0.007 Å, and 0.824 ± 0.007 Å for the oxidized enzyme and 0.835 ± 0.008 Å, 0.363 ± 0.004 Å, and 0.833 ± 0.008 Å for the reduced enzyme, respectively. The reported parameters thus yield dynamically stable structures over at least 1.0 ns of simulated time, with comparable but more restricted motion than the bulk polypeptide.

Test Simulations—Frequencies. By virtue of possessing triply bonded cyanide and carbonyl ligands bound to the H-cluster, [FeFe] hydrogenases show distinctive infrared spectroscopic absorptions well separated from the spectroscopic region associated with amino acid vibrations. Fourier transform infrared spectra of the [FeFe] hydrogenase in its active oxidized state from *Desulfovibrio vulgaris* showed bands in its air-exposed form at 1848, 1983, 2008, 2087, and 2106 cm^{-1}, assigned to CO$_{bridge}$, 2 × CO$_{terminal}$, and 2 × CN$_{terminal}$, in order of increasing energy.[39] Bands seen for the *D. desulfuricans* enzyme at 1802, 1940, 1965, 2079, and 2093 cm^{-1} were assigned to C-X stretches in the ligands C5O5, C7O7, C3O3, C6N6, and C4N4, using our atom naming convention (see Figure 3).[40] Chen, et al. found a similar vibrational manifold for the active oxidized *Clostridium pasteurianum* [FeFe] hydrogenase, with analogous frequencies at 1802, 1948, 1971, 2072, and 2086 cm^{-1}.[41] Notably, the frequencies shift dramatically depending on the redox state of the enzyme and the presence of exogenous CO.[39]

To test the parameter performance in the context of full protein dynamics, we calculated by quasiharmonic analysis the normal modes and frequencies associated with the hydrogenase metalloclusters from the molecular dynamics trajectories. Although the analysis was done only on the metalloclusters and immediately bonded ligand atoms, the

Table 3. Summary of Vibrational Analysis for Isolated Quantum Mechanical H-Cluster Model and Whole-Protein Classical Mechanical Metalloclusters[a]

oxidized				reduced			
QH frequency	quasiharmonic description	QM frequency	QM stretch[b]	QH frequency	quasiharmonic description	QM frequency	QM stretch[b]
2271	CO_{prox} + CN_{prox} (AS) + CO_{br}(S)	2088	0.9940CN_{prox}	2522	CN_{term}	2111	0.9935CN_{term}
2232	CO_{term} + CN_{term}(AS) + CO_{br}(AS)	2076	0.9870CN_{term}	2463	CO_{br} + Fe−H (S)	2088	0.9990CN_{prox}
2136	CO_{prox} + CN_{prox}(S) + CO_{br}(AS) + CO_{term}(AS)	1944	0.0659CO_{prox}, 0.0520CO_{br}, 0.8742CO_{term}	2412	CO_{br} + Fe−H (AS)	1965	0.0386CO_{prox}, 0.1938CO_{br}, 0.7559CO_{term}
1973	CN_{prox}-CO_{br}(S)-CO_{term}(S)	1911	0.8825CO_{prox}, 0.0176CO_{br}, 0.0910CO_{term}	2351	CO_{br} + Fe−H (AS)	1927	0.1870CO_{prox}, 0.2763CO_{br}, 0.1389CO_{term}
1726	CN_{term} stretch and bend	1825	0.0383CO_{prox}, 0.9265CO_{br}, 0.0321CO_{term}	2115	CO_{term}	1904	0.3954CO_{prox}, 0.1744CO_{br}, 0.0040CO_{term}
				2074	CO_{prox}		
				2054	CO_{prox} + CN_{prox} (AS)		
				1956	CN_{prox}		

[a] Frequencies are given in cm^{-1}. Two or more terms imply coupled vibration, specified relative to the first listed local stretch as symmetric (S) or antisymmetric (AS). Vibrations are stretches unless otherwise noted. [b] Coefficients for QM stretches are summed squares of Cartesian eigenvector components of C and O/N atoms involved in the mode. If the mode vector is comprised only of diatomic ligand atom motions, these will sum to 1.0000; deviation from 1.0000 reflects motion distributed among other atoms in the H-cluster model.

dynamics trajectory was extracted from that of the entire enzyme. Hence, the nature of the vibrational modes will not necessarily match the quantum mechanical modes of the isolated cluster, to the extent that polypeptide motions couple with the H-cluster or otherwise lead to mixing of localized C-X stretches in the normal modes. Table 3 summarizes results from both density functional theory calculations on the isolated cluster model and those from quasiharmonic analysis of the dynamics trajectories. Frequencies from the quantum mechanical calculations on the isolated H-cluster show isolated C−N stretches but mixing among the possible C−O stretches with more mixing evident in the reduced H-cluster model. None of the classical modes shows predominantly C-X stretching motions alone—DTMA bridge motions in both H-cluster redox forms and Fe-hydride stretches in the reduced system coupled noticeably with the localized C-X stretches. In addition, C-X stretches coupled among themselves (see the Supporting Information for animations of vibrational modes). The observed mixing in the classical dynamics may reflect the effects of the protein environment on the metallocluster vibrations, particularly electrostatic interactions (e.g., CN_{prox} H-bonding to the Ser232 backbone amide N−H and the CN_{term} Lys358 charge-dipole interaction). The quasiharmonic modes containing significant C-X stretching show frequency ranges for the oxidized and reduced models that bracket the DFT-calculated values for the isolated cluster. Quantitative agreement is not expected at this stage of parameter development, and careful refinement of nonbonded parameters, an account of the protein environment's effect on hydrogen bonding and electronic anisotropy of the cluster[42] via more expensive QM/MM calculations, and possibly a more explicit treatment of static and dynamic electron correlation should be necessary to achieve such agreement. Nevertheless, the data presented support the utility of the calculated parameters for molecular dynamics simulations of known [FeFe] hydrogenase enzymes and related proteins with similar metallocluster species.

Conclusions

We have presented a set of molecular mechanical parameters relevant to $[2Fe2S]^{2+,+}$, $[4Fe4S]^{2+,+}Cys_4$, $[4Fe4S]^{2+,+}Cys_3His$, and $[2Fe]_H^{II,I;I,I}$ metalloclusters found in known [FeFe] hydrogenase enzymes. Modeled minimum-energy hydrogenase structures are consistent with those found experimentally, and the cluster dynamics are stable, while still permitting as much flexibility as is allowed by the quantum mechanical force constants. Calculated vibrational frequencies associated with the catalytic $[2Fe]_H$ CO and CN ligands agree semiquantitatively with those measured experimentally and calculated with density functional theory. It is our hope that the consistent derivation procedure for all four cluster types in both oxidized and reduced states will permit both high-quality simulations of hydrogenase molecular dynamics, particularly of the protein environment immediately around the clusters, as well as allow systematic improvement of these parameters by the modeling community should shortcomings be found. It is expected that the pragmatic interest in alternative fuels combined with fundamental scientific questions of electron transfer and proton dynamics and reduction in hydrogenases will benefit from the availability of these parameters.

Acknowledgment. The work is supported by U.S. Department of Energy under Contract No. DE-AC36-99GO10337. Calculations were done on the "Lester" cluster at the National Renewable Energy Laboratory and the "Jacquard" cluster at the National Energy Research Supercomputing Center, which is supported by the Office of Science of the U.S. Department of Energy under Contract No. DE-AC02-05CH11231.

Supporting Information Available: CHARMM-format topology files for cluster reconstruction and system

setup, CHARMM-format parameter files for simulations, an example of a VMD/PSFGen build script, a table of circumsphere radii for DFT-optimized model clusters, summary data for PDB [4Fe4S] cluster survey, and trajectory (32-bit binary DCD) and structure (text PSF) files for visualizing H-cluster diatomic vibrational modes. This material is available free of charge via the Internet at http://pubs.acs.org.

References

(1) Melis, A.; Seibert, M.; Ghirardi, M. L. Hydrogen Fuel Production by Transgenic Microalgae. In *Transgenic Microalgae as Green Cell Factories*; Leon, R., Gavan, A., Fernandez, E., Eds.; Landes Bioscience: 2007.

(2) Vignais, P. M.; Billoud, B. *Chem. Rev.* **2007**, *107*, 4206–4272.

(3) van Haaster, D. J.; Hagedoorn, P.-L.; Jongejan, J. A.; Hagen, W. R. *Biochem. Soc. Trans.* **2005**, *33*, 12–14.

(4) Jones, A. K.; Lichtenstein, B. R.; Dutta, A.; Gordon, G.; Dutton, P. L. *J. Am. Chem. Soc.* **2007**, *129*, 14844–14845.

(5) Cao, Z.; Hall, M. B. *J. Am. Chem. Soc.* **2001**, *123*, 3734–3742.

(6) Liu, Z.-P.; Hu, P. *J. Am. Chem. Soc.* **2002**, *124*, 5175–5182.

(7) Zhou, T.; Mo, Y.; Liu, A.; Zhou, Z.; Tsai, K. R. *Inorg. Chem.* **2004**, *43*, 923–930.

(8) Peters, J. W.; Lanzilotta, W. N.; Lemon, B. J.; Seefeldt, L. C. *Science* **1998**, *282*, 1853–1858.

(9) Nicolet, Y.; Piras, C.; Legrand, P.; Hatchikian, C. E.; Fontecilla-Camps, J. C. *Structure* **1999**, *7*, 13–23.

(10) Zhou, T.; Mo, Y.; Zhou, Z.; Tsai, K. *Inorg. Chem.* **2005**, *44*, 4941–4946.

(11) Fan, H.-J.; Hall, M. B. *J. Am. Chem. Soc.* **2001**, *123*, 3828–3829.

(12) Greco, C.; Bruschi, M.; De Gioia, L.; Ryde, U. *Inorg. Chem.* **2007**, *46*, 5911–5921.

(13) Weinhold, F. Natural Bond Orbital Methods. In *Encyclopedia of Computational Chemistry*; Schleyer, P. v. R., Allinger, N. L., Clark, T., Gasteiger, J., Kollman, P. A., Schaefer, H. F. I., Schreiner, P. R., Eds.; Wiley Interscience: New York, 1998; Vol. 3, pp 1792−1813.

(14) Scott, A. P.; Radom, L. *J. Phys. Chem.* **1996**, *100*, 16502–16513.

(15) MacKerell, A. D., Jr.; Bashford, D.; Bellott, M.; Dunbrack, R. L., Jr.; Evanseck, J. D.; Field, M. J.; Fischer, S.; Gao, J.; Guo, H.; Ha, S.; Joseph-McCarthy, D.; Kuchnir, L.; Kuczera, K.; Lau, F. T. K.; Mattos, C.; Michnick, S.; Ngo, T.; Nguyen, D. T.; Prodhom, B.; Reiher, W. E., III; Roux, B.; Schlenkrich, M.; Smith, J. C.; Stote, R.; Straub, J.; Watanabe, M.; Wiórkiewicz-Kuczera, J.; Yin, D.; Karplus, M. *J. Phys. Chem. B* **1998**, *102*, 3586–3616.

(16) Phillips, J. C.; Braun, R.; Wang, W.; Gumbart, J.; Tajkhorshid, E.; Villa, E.; Chipot, C.; Skeel, R. D.; Kalé, L.; Schulten, K. *J. Comput. Chem.* **2005**, *26*, 1781–1802.

(17) Humphrey, W.; Dalke, A.; Schulten, K. *J. Mol. Graph.* **1996**, *14*, 33–38.

(18) Brooks, B. R.; Bruccoleri, R. E.; Olafson, B. D.; States, D. J.; Swaminathan, S.; Karplus, M. *J. Comput. Chem.* **1983**, *4*, 187–217.

(19) Karplus, M.; Kushick, J. N. *Macromolecules* **1981**, *14*, 325–332.

(20) Wilson, E. B.; Decius, J. C.; Cross, P. C. *Molecular Vibrations: The Theory of Infrared and Raman Vibrational Spectra*; Dover Publications: New York, 1980.

(21) Chang, C. H.; King, P. W.; Ghirardi, M. L.; Kim, K. *Biophys. J.* **2007**, *93*, 3034–3045.

(22) Pivarski, J. *SVGFig, 1.1.6*; Google Code: 2009. http://code.google.com/p/svgfig/ (accessed March 2009).

(23) Burden, C. J.; Oakley, A. J. *Phys. Biol.* **2007**, *4*, 79–90.

(24) Merritt, E. A.; Bacon, D. J. *Methods Enzymol.* **1997**, *277*, 505–524.

(25) Nicolet, Y.; de Lacey, A. L.; Vernède, X.; Fernandez, V. M.; Hatchikian, E. C.; Fontecilla-Camps, J. C. *J. Am. Chem. Soc.* **2001**, *123*, 1596–1601.

(26) Pandey, A. S.; Harris, T. V.; Giles, L. J.; Peters, J. W.; Szilagyi, R. K. *J. Am. Chem. Soc.* **2008**, *130*, 4533–4540.

(27) Patil, D. S.; Moura, J. J. G.; He, S. H.; Teixeira, M.; Prickril, B. C.; DerVartanian, D. V.; Peck, H. D., Jr.; LeGall, J.; Huynh, B. H. *J. Biol. Chem.* **1988**, *263*, 18732–18738.

(28) Pierik, A. J.; Hagen, W. R.; Redeker, J. S.; Wolbert, R. B. G.; Boersma, M.; Verhagen, M. F. J. M.; Grande, H. J.; Veeger, C.; Mutsaers, P. H. A.; Sands, R. H.; Dunham, W. R. *Eur. J. Biochem.* **1992**, *209*, 63–72.

(29) Fiedler, A. T.; Brunold, T. C. *Inorg. Chem.* **2005**, *44*, 9322–9334.

(30) Schwab, D. E.; Tard, C.; Brecht, E.; Peters, J. W.; Pickett, C. J.; Szilagyi, R. K. *Chem. Commun.* **2006**, 3696–3698.

(31) Silakov, A.; Reijerse, E. J.; Albracht, S. P. J.; Hatchikian, E. C.; Lubitz, W. *J. Am. Chem. Soc.* **2007**, *129*, 11447–11458.

(32) Stowasser, R.; Hoffmann, R. *J. Am. Chem. Soc.* **1999**, *121*, 3414–3420.

(33) Mantz, Y. A.; Gervasio, F. L.; Laino, T.; Parrinello, M. *J. Phys. Chem. A* **2007**, *111*, 105–112.

(34) Kuleff, A. I.; Dreuw, A. *J. Chem. Phys.* **2009**, *130*, 034102.

(35) Roseboom, W.; De Lacey, A. L.; Fernandez, V. M.; Hatchikian, E. C.; Albracht, S. P. J. *J. Biol. Inorg. Chem.* **2005**, *11*, 102–118.

(36) Fee, J. A.; Castagnetto, J. M.; Case, D. A.; Noodleman, L.; Stout, C. D.; Torres, R. A. *J. Biol. Inorg. Chem.* **2003**, *8*, 519–526.

(37) Torres, R. A.; Lovell, T.; Noodleman, L.; Case, D. A. *J. Am. Chem. Soc.* **2003**, *125*, 1923–1936.

(38) Carugo, O.; Carugo, K. D. *Trends Biochem. Sci.* **2005**, *30*, 213–219.

(39) Pierik, A. J.; Hulstein, M.; Hagen, W. R.; Albracht, S. P. *Eur. J. Biochem.* **1998**, *258*, 572–578.

(40) De Lacey, A. L.; Stadler, C.; Cavazza, C.; Hatchikian, E. C.; Fernandez, V. M. *J. Am. Chem. Soc.* **2000**, *122*, 11232–11233.

(41) Chen, Z.; Lemon, B. J.; Huang, S.; Swartz, D. J.; Peters, J. W.; Bagley, K. A. *Biochemistry* **2002**, *41*, 2036–2043.

(42) Dey, A.; Roche, C. L.; Walters, M. A.; Hodgson, K. O.; Hedman, B.; Solomon, E. I. *Inorg. Chem.* **2005**, *44*, 8349–8354.

CT800342W

JCTC Journal of Chemical Theory and Computation

Conformational Transition Map of an RNA GCAA Tetraloop Explored by Replica-Exchange Molecular Dynamics Simulation

Yufen Zhang,[†,‡] Xian Zhao,*[,‡] and Yuguang Mu*[,†]

School of Biological Sciences, Nanyang Technological University, Singapore 637551, and State Key Laboratory of Crystal Materials, Shandong University, Jinan 250100, P.R. China

Received October 9, 2008

Abstract: A 120 ns replica-exchange molecular dynamics simulation in explicit solvent is performed to probe the conformational transitions in 5′-GGGCGCAAGCCU-3′ RNA GCAA tetraloop. The ample structural transition information of the loop is detected on the basis of extensive clustering analysis. The resultant loop structural transition map nicely agrees with the recent ultrafast fluorescence measurement, which confirms the dynamical properties of this tetraloop. Moreover, a new transition pattern that was not disclosed previously is predicted. Meanwhile, the folding free energy landscapes were characterized: the global folding dynamics is coupled mainly with the stem rather than the loop part.

Introduction

Hairpins are elementary structural units responsible for RNA folding.[1,2] Hairpin loop contains a base-paired stem structure and a loop sequence with unpaired nucleotides. Its most obvious property is to function as a "bender" to reverse the direction of backbone. Due to steric hindrance, there exists a minimum of three nucleotides to make a loop structure. However, loops with four nucleotides, known as tetraloops, are found to be much populated.[1,3] Among the four-base tetraloop motif, the family of GNRA (where N is any nucleotide and R is a purine) tetraloops is well structured with unusual stability.[4−6]

The most powerful tools to explore the structure features of RNA tetraloops are crystallography and nuclear magnetic resonance measurements.[5,7] These structural biology tools usually provide a well-defined structure or a structural ensemble with limited fluctuations. With the newly developed techniques, the dynamical features of RNA molecules are attracting attention.[8−10] For example, ^{13}C NMR relaxation measurements discovered substantial dynamic fluctuations in the loop regions of several tetraloops.[11−13] Dynamical properties or structural heterogeneity of the RNA loop can also be resolved by fluorescence spectroscopy.[14,15] For instance, a GAAA tetraloop that was substituted with 2-aminopurine residues and followed by fluorescence-detected temperature-jump relaxation analysis demonstrated the existence of more than a single conformation state with different base stacking patterns in the loop.[14] By incorporating both 2-aminopurine and 7-deazaguanine residues into similar GNRA tetraloops, another group studied the heterogeneity of loop conformation by femtosecond time-resolved fluorescence.[16] What they found not only confirmed the previous observation,[14] but with more position-specific fluorescence decay data, a more detailed dynamic multiconformation model for the tetraloop was proposed.

Molecular dynamics simulations are another powerful tool to explore the conformational dynamics of RNA tetraloops;[17−27] for example, the influence of base substitutions on the stability of GCAA tetraloop has been studied by the free energy perturbation method.[28,29] Most of the theoretical studies were targeted at the folding/unfolding dynamics of short RNA loops. The common features resolved by the modeling studies affirmed the hierarchical properties of folding free energy landscapes and general heterogeneity of loop conformation. However, detailed analysis of the conformational dynamics near the native-structure local mini-

* Corresponding author e-mail: YGMu@ntu.edu.sg (Y.M.) or zhaoxian@icm.sdu.edu.cn (X.Z.).

[†] Nanyang Technological University.

[‡] Shandong University.

10.1021/ct8004276 CCC: $40.75
Published on Web 03/26/2009

mum and direct comparison with available fluorescence experimental data are scarce.

In this paper, the structural transition mechanism of RNA tetraloop near the native-structure minimum at atomic detail was interrogated by a replica exchange molecular dynamics (REMD) simulation in explicit solvent for a GCAA RNA tetraloop. In order to directly compare with experimental data, the alternative stacking patterns of loop residues were monitored. The REMD simulation can overcome the sampling limitations of standard MD methods.[30−32] During REMD simulation, several replicas of a system are simulated at different temperatures in parallel, allowing for exchanges between neighboring replicas at frequent intervals.[30−33] So the REMD simulation can significantly enhance the conformational sampling. This technique has been successfully used for simulations of hairpin loop structure.[22,25,26] The key component in replica exchange simulations is the exchange of configurations between different replicas/temperatures by rescaling the velocities.[34] Such an algorithm helps to overcome large energy barriers and allows large conformational space to be sampled. Meanwhile, it maintains the continuous transformation of structures.[30,35] Together with extensive clustering analysis, the ample structural transition information of the tetraloop was detected. The resultant structural evolution map was able to directly compare with available experimental data, which confirms the predictive power of the current theoretical model.

Methods

The GROMACS program suite[36] and the full atomic Amber parm98 force field[37] were used. With Amber parm98 force field, the dynamics of a UUUU tetraloop RNA was studied by one of us[19] and a good agreement between MD result and NMR relaxation measurement was obtained. To test the reliability of parm98 further, a new Amber force field, parmbsc0,[38] was also employed to perform a constant temperature simulation. All bonds involving hydrogen atoms were constrained in length according to LINCS protocol.[39] This allowed the use of an integration step of 0.002 ps in simulations. Nonbonded pair lists were updated every 5 integration steps.[40] The RNA and the water were separately coupled to an external heat bath with a relaxation time of 0.1 ps. Replica exchange was attempted every 1000 integration steps (2 ps). The trajectories were output every 1 ps. Electrostatic interactions were treated with particle mesh Ewald method with a cutoff of 9 Å, and a cutoff of 14 Å was used in the calculation of van der Waals interactions.

We studied the GCAA tetraloop structure with the sequence of 12-mer single-strand RNA: 5′-GGGCGCAAGCCU-3′. A related NMR hairpin structure (model 1 of PDB accession code 1ZIH)[4] was used as initial structure in this REMD simulation. REMD simulation was carried out with an explicit TIP3P water model,[41] under periodic boundary conditions. The structure was solvated in a cubic box of 42 Å containing 2285 water molecules, 11 Na^+ ions to neutralize the system, and 7255 atoms in total. The REMD simulation was conducted under constant volume with 48 replicas. An exponentially increasing temperature series along the replicas from 300 to 575.5 K was used, which gives approximately uniform acceptance ratios for exchanges between neighboring replicas.[30−32] Exchange probabilities between neighboring replicas were observed of ∼25%. The REMD simulation was continued for 120 ns for each replica. In total, an accumulated simulation time of 5.76 μs was obtained.

The trajectories output from REMD simulation are usually sorted according to temperature. They are discontinuous regarding the structural transformation due to the repeated replica exchange events. These trajectories form canonical ensembles under different temperatures so they are named as ensemble trajectories. According to the exchange information, ensemble trajectories can be resorted in such a way that each trajectory contains continuous structure transitions of the simulated system beginning from each replica. Such trajectories are known as replica trajectories. Evidently, in a replica trajectory, due to the rescaling of velocities during the exchange process, the temperature has no defined meaning.

Root-mean-square deviation of the whole hairpin with respect to the NMR structure[4] (wRMSDnmr) was calculated based on all atoms. Cluster analysis was performed for the corresponding ensembles using the algorithm proposed by Daura et al.[42] The conformations were clustered by their structural similarity, measured by the pairwise rmsd. The related rmsd cutoff was chosen as 2.0 Å. Curves method[43] was used to find the sugar pucker pattern for different conformations in the GCAA tetraloop.

To further study the structural heterogeneity of RNA in direct comparison with NMR measurement, distances of interresidue hydrogen atoms that were employed as nuclear Overhauser effect (NOE) constraints in the work of Jucker et al.[4] were calculated. Forty-seven interresidue distances were selected, of which 22 are within the stem residues and 25 are within the loop and between stem and loop residues. The complete atom pairs and distances are listed in the Supporting Information. For each snapshot, the fraction of NOE distances satisfaction, Q, was calculated:

$$Q_i = N_s/N_{tot}$$

where N_s is the number of interhydrogen distances whose average values are satisfied by the NOE constraints and N_{tot} is the number of total NOE distances. Q_{stem} and Q_{loop} were calculated separately for stem and loop residues. The average interhydrogen distance is calculated by

$$r_{ij}^{avg} = \left(\frac{1}{K}\sum_{k=1} r_{ij}^{-6}\right)^{-1/6}$$

where r_{ij} is the distance and K is the number of snapshots used in the calculation.

Free energy (G, in units of kilojoules per mole) was evaluated by the following equation:

$$G = -k_B T \ln (N_i/N_{ref})$$

where k_B is the Boltzmann constant, T is temperature, N_i refers to the number of members in state i, and N_{ref} refers to the number of members in a reference state.

Results and Discussion

Configurational Space Sampled. In order to demonstrate the sampled configuration space in the REMD simulation,

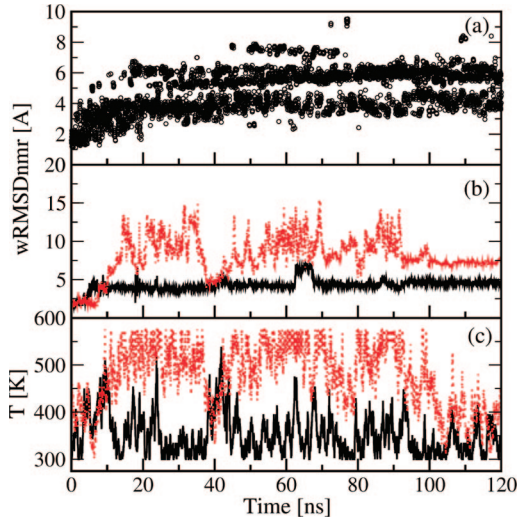

Figure 1. (a) wRMSDnmr evolution of two ensemble trajectories (300 K, black line; 344.6 K, red dotted line). (b) wRMSDnmr evolution of three replica trajectories (replica 1 in black and replica 21 in red). (c) Temperature evolution of the same replica trajectories (replicas 1 and 21).

Figure 1a shows the wRMSDnmr of ensemble trajectories at lowest temperatures (300 K). At the beginning of the simulation the wRMSDnmrs are around 2 Å. After 20 ns, most of the structures have wRMSDnmr of 4 Å. Meanwhile, a group of structures with wRMSDnmr of 6 Å is accumulating. From 40 ns on, structures with wRMSDnmr more than 7 Å enter the low-temperature ensembles with small population.

Figure 1b,c shows the wRMSDnmr and temperature evolution of two replica trajectories with replica 1 (solid black line) and replica 21 (dashed red line). Replica 21 experiences unfolding quickly after the simulation begins. Its wRMSDnmr changes from 2 to 12 Å during the first 20 ns simulation. Around $t = 40$ ns it refolds with wRMSDnmr decreased below 5 Å. Then it unfolds again. Its temperature changes from low values (300 K) to high values (around 550 K) when it unfolds and decreases to low values (350 K) when it refolds. Such unfolding/refolding events happen in other replica trajectories as well.

There are a few replica trajectories whose wRMSDnmr maintains below 5 Å during the whole simulation such as replica 1 (solid line in Figure 1b). Unlike the wRMSDnmr value, its temperature undergoes frequent changes (solid line in Figure 1c) from 300 to 450 K. The invariance of wRMSDnmr against temperature indicates the stability of the configuration in the temperature range.

Figure 2 is the pseudo-free-energy surface as a function of wRMSDnmr and temperature to illustrate the sampled conformation during simulation. There are two local minima at low temperature range ($T < 400$ K). One of the local minima is located at wRMSDnmr < 5 Å centered at wRMSDnmr = 3.5 Å, corresponding to the ensemble of native folded structures and the wRMSDnmr of the other minimum is around 5.7 Å, which is a kind of intermediate state. In the high-temperature region ($T > 450$ K) there is a broad valley on the surface, which represents a heterogeneous ensemble of unfolded structures (wRMSDnmr > 7 Å). The inset in Figure 2 plots the average wRMSDnmr as a function

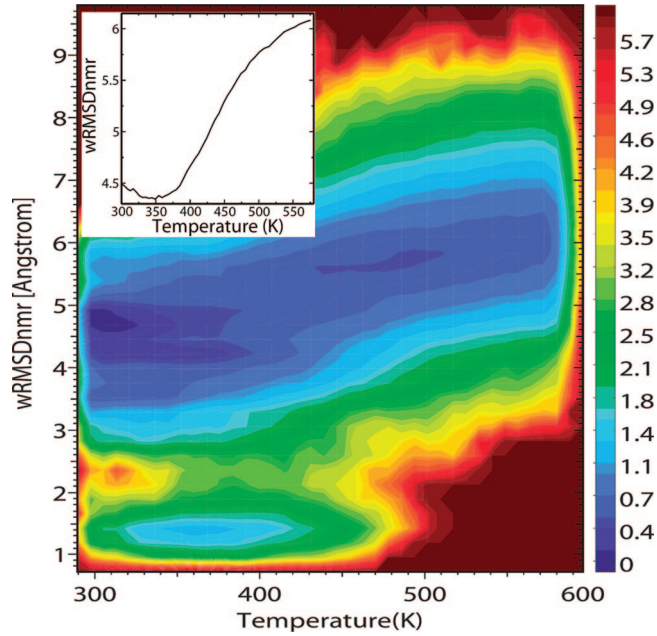

Figure 2. Free energy of sampled conformations as a function of wRMSDnmr and temperature. (Inset) Average wRMSDnmr as a function of temperature.

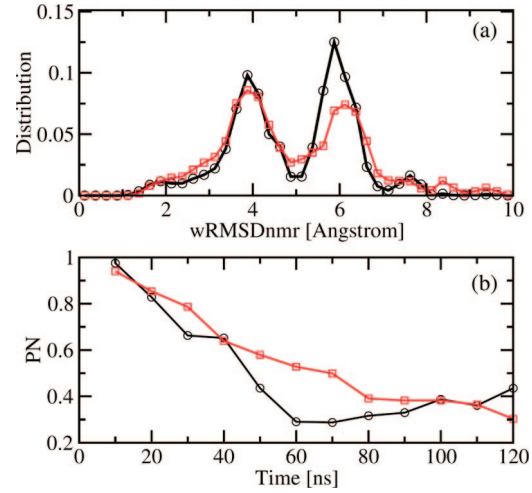

Figure 3. (a) Distribution of wRMSDnmr at $T = 300$ K (black line and circles) and $T = 350$ K (red line and squares). (b) Evolution of the population of near-native state as a function of simulation time; the population is calculated in an interval of 10 ns.

as temperature. The average wRMSDnmr in the temperature range of 300∼350 K is around 5 Å, and the value of wRMSDnmr quickly increases as the temperature rises.

Figure 3a shows the distribution of wRMSDnmr at two temperatures, $T = 300$ K (black circles) and $T = 350$ K (red squares). From these wRMSDnmr distributions it is clearly seen that the structural ensembles at these temperatures can be classified into two states, one with wRMSDnmr smaller than 5 Å, which is called native/near-native state, and the other with wRMSDnmr larger than 5 Å, which is denatured state. To further check the convergence of the simulation, the population of near-native state (PN) as a function of simulation time is monitored and shown in Figure 3b. The near-native state is defined by wRMSDnmr ≤ 5 Å. The PN is calculated in an interval of 10 ns at two temperature, $T =$

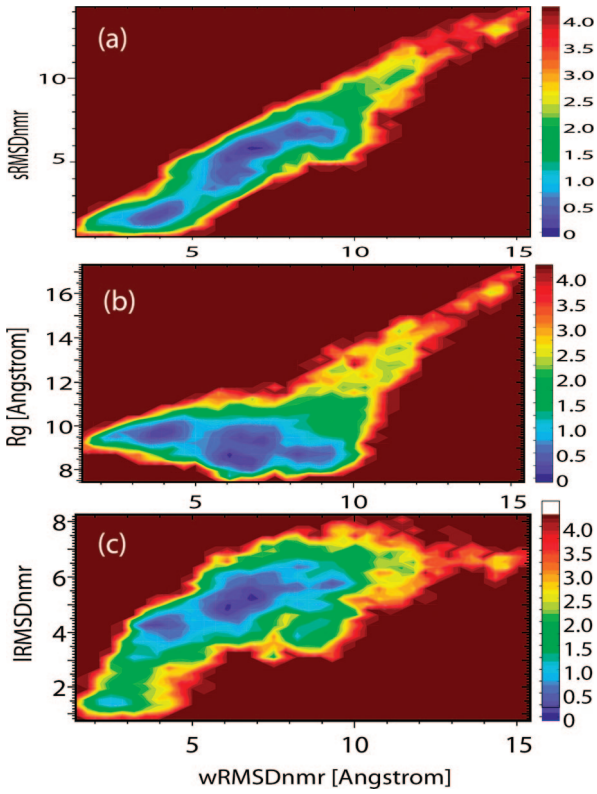

Figure 4. Free energy surfaces at 418 K as functions of (a) sRMSDnmr and wRMSDnmr, (b) R_g and wRMSDnmr, and (c) lRMSDnmr and wRMSDnmr.

300 K (black circles) and $T = 350$ K (red squares). Because the initial configurations are native, PN is close to 1 at the beginning of simulation. PN decreases as the simulation goes on until $t = 60$ ns when PN drops to 0.3 at $T = 300$ K, which indicates a general unfolding behavior during the first 60 ns. After that, the PN value is maintained between 0.3 and 0.4 during the simulation at $T = 300$K. Thus a rough equilibrium between unfolding and refolding processes is being established during the last 60 ns simulation.

Folding/Unfolding of GCAA Tetraloop. Simulation of the folding and unfolding of biomolecules has been one of the major computational challenges of molecular biology.[23] REMD simulations have been successfully applied in folding and unfolding study for small nucleic acids.[22,26] Conformational dynamic transitions related to unfolding and refolding in the GCAA tetraloop were also sampled in the current REMD simulation.

Four parameters were employed here to monitor the structural transitions: wRMSDnmr, stem rmsd (sRMSDnmr, rmsd calculated only for stem residues G1, G2, G3, C4, G9, C10, C11, and U12), loop rmsd (lRMSDnmr, rmsd calculated only for loop residues C4, G5, C6, A7, A8, and G9), and radius of gyration of the whole RNA, R_g. Figure 4 shows the free energy surfaces as a function of (a) wRMSDnmr and sRMSDnmr, (b) wRMSDnmr and R_g, and (c) wRMSDnmr and lRMSDnmr at 418 K. The reason to choose 418 K is that around this temperature the folded and unfolded conformations have nearly equal populations. Figure 4a displays high correlation between sRMSDnmr and wRMSDnmr, which indicates that the folding/unfolding of the tetraloop RNA is mainly determined by the formation/disturbance of the stem part. This observation is consistent with a recent MD study on short RNA loop sequences.[24] On the contrary, the loop dynamics seems uncoupled from the whole RNA (Figure 4c): when wRMSDnmr decreases from 10 to 5 Å, the lRMSDnmr changes only from 6 to 5 Å; in the native basin where wRMSDnmr < 5 Å, there is still a large amount of loop dynamics happening with lRMSDnmr changes between 5 and 1 Å and such loop dynamics in the native basin is the main focus of the next section. The free energy surface of wRMSDnmr and R_g (Figure 4b) clearly indicates that a structural collapse happens at the very early stage of folding and some intermediate states with wRMSDnmr around 7 Å are more compact than native structures.

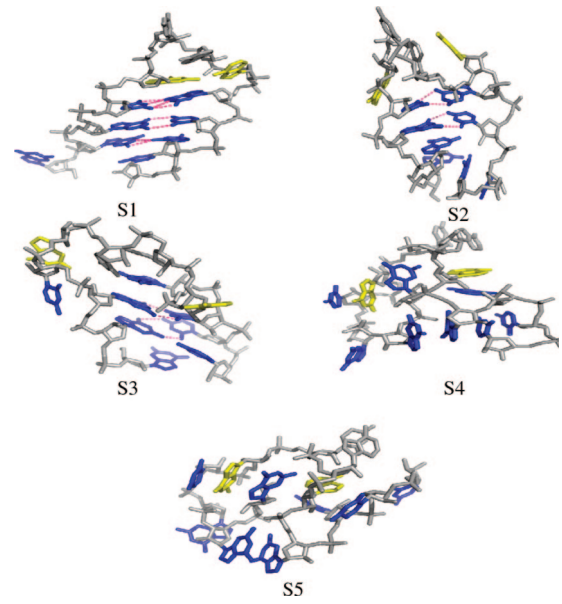

Figure 5. Three-dimensional conformations of the five representative structures (the eight bases of the stem are shown in blue, the G5 and A8 bases of the loop are shown in yellow, and the polar contacts between base pairs are shown in pink).

Based on the information provided by the three free energy surfaces, five representative structures (denoted as S1−S5) corresponding to the minima on the surfaces were selected and are shown in Figure 5. Their structural characterization is summarized in Table 1. In Figure 5 the eight bases of the stem are shown in blue, the G5 and A8 bases of the loop are shown in yellow, and the polar contacts between base pairs are indicated with pink dotted lines. S1 represents the folded conformation with $R_g = 9.6$ Å, wRMSDnmr = 4.1 Å, sRMSDnmr = 2.0 Å, and lRMSDnmr = 4.3 Å. It contains three hydrogen-bonded stem base pairs (C4-G9, G3-C10, and G2-C11) and the bases are stacking properly in the stem. S2 and S3 have two stem paired bases with wRMSDnmr larger than 6 Å, which represent the intermediate states. Both S4 and S5 do not have paired stem residues and the base stacking pattern in the stem region is lost, which represent the unfolded conformations with small R_g and large wRMSDnmr values.

From the free energy surfaces and the representative structures, some conclusions about the folding/unfolding of RNA GCAA tetraloop can be drawn. First, an obvious

Table 1. Structural Characteristics of Representative Structures (Denoted as S1−S5) Sampled in the RNA GCAA Tetraloop at 418 K

structure (rmsd for total, stem, loop, and R_g; Å)	stem base pairs	base stacking patterns in stem
S1 (4.1, 2.0, 4.3, 9.6)	C4-G9 G3-C10 G2-C11	C4/G3/G2/U12 G5/G9/C10/C11
S2 (6.1, 5.0, 4.7, 8.8)	C4-G9 G3-C10	C4/G3/G2/G1 G9/C10 C11/U12
S3 (7.1, 5.9, 5.2, 9.4)	G3-C10 G2-C11	G9/G3/G2
S4 (8.2, 6.9, 5.6, 8.7)		G1/G5/C4 A8/C10 G2/G9/U12/C11
S5 (9.4, 6.7, 5.8, 8.9)		G1/G5/C4 G2/G9

multiple-state (including folded, intermediate, and unfolded states) folding landscape of the RNA GCAA tetraloop is disclosed, which is in good agreement with the previous RNA simulations.[17,21] Second, the folded-to-unfolded conformational transitions happen beginning with breaking of the terminal stem base pairs and decreasing of R_g. The decrease of R_g is mainly related to the loss of stacking pattern of bases on both strands of the stem. This is well consistent with the previous simulations,[17] which demonstrated that the lost of terminal base pair is the first step of unfolding mechanism in the GNRA tetraloop and proposed that a folding pathway includes the collapse of the unfolded state. Third, some intermediate conformations are observed with the central stem base pairs (G3-C10, G2-C11) intact and with wRMSDnmr of 6−7 Å.

Loop Dynamics near the Native Basin. As mentioned in the Introduction, fluorescence spectroscopic measurements indicated that ample conformational transitions of the loop residues exist within the native state.[14,15] In order to study the loop dynamics in more detail, an extensive clustering was performed based on the ensembles; in total 2 880 000 structural snapshots from the last 60 ns simulation. First 72 000 structural snapshots were chosen by taking one structure out of every 40. A clustering analysis was performed on the 72 000 structures with pairwise loop RMSDs (lRMSDp) cutoff of 1.5 Å. The first largest 100 clusters were chosen. The center of each cluster identified by clustering analysis tool was taken as the representative structure. Then the lRMSDp of all 2 880 000 structures with respect to the 100 representative structures was calculated. Each structure was assigned a cluster label if the lRMSDp with respect to the cluster center is smaller than 1.3 Å. Structures whose lRMSDps with respect to the 100 cluster centers are larger than 1.3 Å are called outliers, labeled as 0.

To check the near-native nature of the representative structures that are related to the cluster centers, Figure 6a shows the wRMSDnmr of the cluster center of the largest 34 clusters. Clusters 1, 4, 7, and 26 represents the native folded structure with wRMSDnmr ∼3 Å, and the other clusters correspond to the near-native ensemble of structures with wRMSDnmr ≤ 5 Å, with the exception of clusters 14 and 22 whose wRMSDnmrs are larger than 7 Å. It is not surprising to find that most clusters with many members belong to near-native ensembles because the structural heterogeneity of the unfolded ensembles is greater than that of near-native ones.

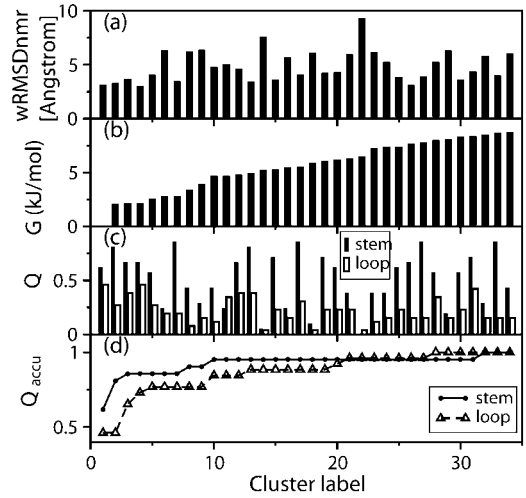

Figure 6. (a) Global wRMSDnmr of the largest 34 clusters with respect to NMR structure. The clustering is based on loop C(GCAA)G structure. (b) Relative free energy of the 34 clusters. (c) Degree of NOE constraint satisfaction, Q, for each cluster. (d) Accumulated Q values (Q_{accu}) as a function of n largest clusters

Figure 6b shows the free energy of different structural clusters relative to class 1 at a simulation temperature of 300 K. The free energy differences range from 0 to 8 kJ/mol. These relatively small free energy differences demonstrate that the structures of GCAA tetraloop are quite flexible and multiple structural ensembles coexist with moderate free energy difference. Our finding is quite consistent with the previous experimental data which indicated the flexibility of the tetraloop.[4,14,16]

NOE Distances Comparison. NOE constraints provide direct structural information obtained from NMR measurement and can be used to gauge the simulated results directly. In Figure 6c, the degree of NOE constraint satisfaction, Q, for each cluster is shown. On average the Q value is less than 0.5, which means in each individual structural cluster less than half of the NOE constraints are satisfied simultaneously. For clusters 1 and 4, which have the lowest wRMSDnmr values, Q values turn out to be larger than 0.5. Generally the Q values are larger for stem than for loop. The relatively low value of Q for each structural cluster indicates that, due to the structural heterogeneity of the RNA tetraloop, it is not the case that an individual structural snapshot may satisfy all of the NOE constraints, which should be an ensemble property intrinsic to the NMR measurement.[44]

To test the ensemble properties of NOE constraints, the accumulated Q values (Q_{accu}) were applied. In calculation of Q_{accu}, the interhydrogen distance was not averaged within each structural cluster. More and more clusters were included to evaluate the Q value instead. Thus Q_{accu} values as a function of n largest clusters included were obtained and are shown in Figure 6d. Q_{accu} values for both stem and loop residues increase quickly as more clusters are included. When

Table 2. Base Stacking Patterns for Nine Groups of Conformations in RNA G1C2A3A4 Tetraloop[a]

conformation type	base stacking patterns in G1C2A3A4 loop[b]
A	G1×C2/A3/A4
B	G1×C2×A3/A4 (C2 out of loop)
C	G1×C2/A3×A4, G1/A3
D	G1×C2×A3×A4, G1/A3
E	G1/C2/A3×A4
F	G1/C2×A3×A4
G	G1/C2×A3/A4
H	G1×C2/A3×A4
I	G1×C2×A3/A4, G1/A3

[a] Based on the distance distribution, the cutoff values are 5.1, 5.6, 6.7, 5.6, and 6.1 Å for the maximum distances between bases 1 and 2, 1 and 3, 2 and 3, 2 and 4, and 3 and 4, respectively. [b] × refers to unstacking; / refers to stacking.

the first five clusters are included in the calculation, the value of Q_{accu} for loop is 75% and that for stem is 85%. When the first 13 clusters are taken as an ensemble, both Q_{accu} values approach 0.90.

Combing Q and Q_{accu} values, our simulation results indicate the heterogeneity of the individual configuration sampled, and on the other hand the NMR NOE constrains are able to be satisfied as an ensemble.

Base Stacking Pattern Identification. In order to have a direct comparison of loop dynamics found in the simulation with those indicated by fluorescence measurements,[14,16] the structures sampled by the REMD simulation were grouped according to base stacking pattern. Two bases in the loop were set to be stacked only when the *maximum* distance between six heavy atoms of a six-membered ring on the two bases is smaller than a cutoff value, which is determined on the basis of the distance distribution. Due to the distinct stacking patterns, nine groups with different loop structure were identified (labeled as A−I); their loop base stacking patterns are explained in Table 2. Six out of these nine structure groups (A−F) were found to be analogues of the experimental model.[16] Three-dimensional representative structures of the nine conformations are shown in Figure 7. The four bases in the loop part, G1C2A3A4, are shown in yellow.

Distinct Loop Stacking Patterns Found in the Simulation. From Figure 7 and Table 2, it is found that group A represents the 3′-stacked structure, in which the last three bases are stacked on the 3′ side. This kind of structure has been revealed to be the main conformation both for the isolated tetraloop and for the tetraloop−receptor complexes.[4−6,16,45] In group B, A3 stacks on A4 on the 3′ side and C2 is looped out. Such a conformation has been illustrated by NMR experiment.[4] Group C has the base stacking pattern of G1, C2, and A3 stacking on the 5′ side. In group D, bases A3 and G1 are stacking on the 5′ side. Group E is a typical 5′-stacking conformation, with the first three bases stacking on the 5′ side. The conformations found in the simulation support the earlier proposal that a 5′-stacking form coexists with a 3′-stacking form in the GNRA tetraloop.[14,16] Group F has the base stacking pattern of C2 on G1 in the 5′ stack. In group G, the stacking pattern is C2, G1 stacking on the 5′ side and A3, A4 on the 3′ side.

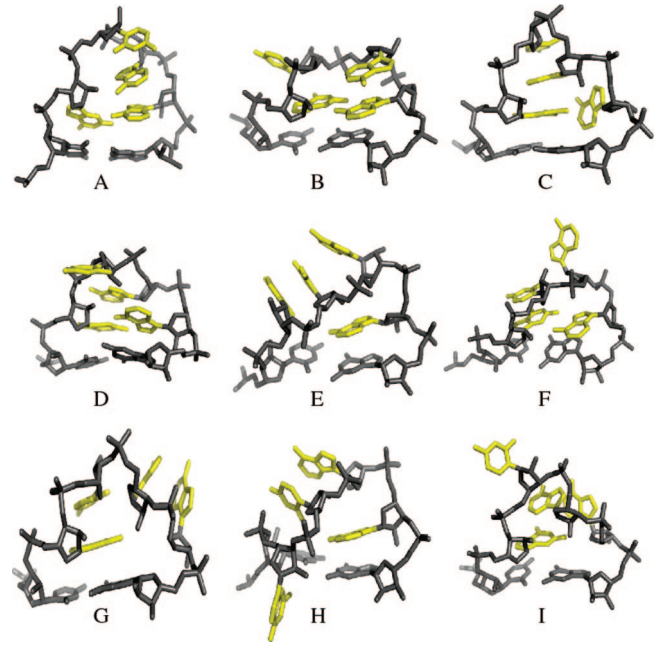

Figure 7. Representative structures of nine structural groups of G(GCAA)C loop, with the four bases of the GCAA tetraloop shown in yellow.

Group H has the base stacking pattern of C2 on A3, and these two bases are in a looped-out configuration. In group I, A3 stacks on both A4 and G1.

Stacking Patterns in NMR Structures. Table 3 shows stacking patterns resolved in NMR-determined structures of GCAA tetraloop as well as of other tetraloops (including GNRA, UNCG and RNYA, where Y = pyrimidine).[46] In the canonical conformation of GNRA tetraloop, PDB entry 1hmh,[47] the last three bases are stacked on the 3′ side, corresponding to group A. For other GNRA loop conformations, PDB entries 1cn8,[48] 1etf, [49] and 1f1t[50] show that the second base N is looped out and the last two bases are stacked on the 3′ side, similar to group B. In the standard conformation of UNCG tetraloop, PDB entry 1dk1,[51] the first and third bases are posed in the 5′ stack and the second base N is looped out, similar to group D. In other structures, PDB entries 1bgz,[7] 1d6k,[52] and 1tlr,[53] the second and third bases are looped out, corresponding to group H. In one conformation of RNYA tetraloop, PDB entry 5msf,[54] the first and third bases come close on the 5′ side and the second base is looped out, similar to group D. In another structure of RNYA tetraloops, PDB entry 1tfn,[55] the second and third bases are looped out, corresponding to group H. In other structures of RNYA tetraloops, from PDB entries 1d0t and 1d0u,[56] the first two bases are in the 5′ stacking and the third is looped out, similar to group F.

The loop stacking patterns in groups A, B, D, F, and H can find their analogues in the NMR-determined structures. Such matching is an encouraging sign, which indicates that sampling results from the REMD simulation are testable by the experimental models.

Structure Transition Map. Combined with the "kinetic" information available from continuous replica trajectories, a structural transition map for the GCAA tetraloop between distinct groups was constructed, which is shown in Figure

Table 3. Comparison of Base Stacking Patterns of GCAA Tetraloops Sampled in Our Simulation with NMR Models (Including GNRA, UNCG, and RNYA)

tetraloop	PDB entry	12[a]	23[a]	34[a]	13[a]	conformation
GNRA	1hmh		3′ stack	3′ stack		A
GNRA	1cn8, 1etf, 1f1t	loop-out of N2		3′ stack		B
UNCG	1dk1	loop-out of N2			5′ stack	D
UNCG	1bgz, 1d6k, 1tlr		loop-out of N2 and C3			H
RNYA	5msf	loop-out of N2		loop-out of A4	5′ stack	D
RNYA	1tfn		loop-out of N2 and C3			H
RNYA	1d0t, 1d0u	5′ stack	loop-out of Y3			F

[a] Numbers 1, 2, 3, and 4 refer to the first, second, third, and last base in the tetraloop, respectively.

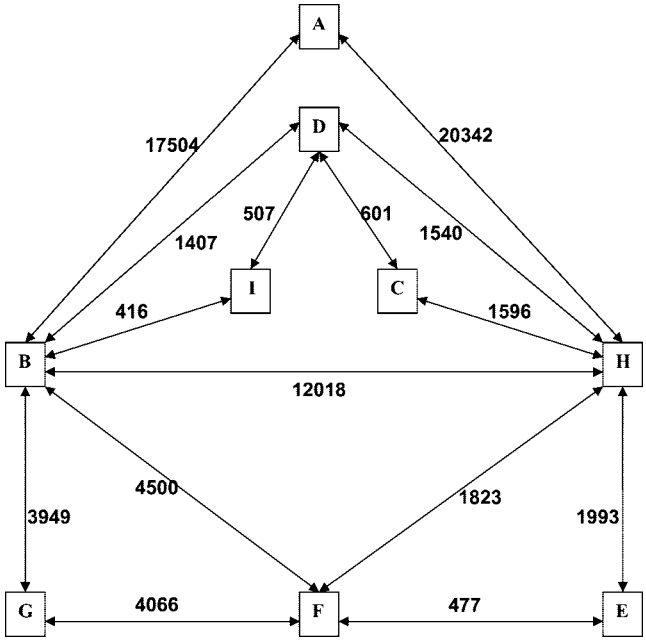

Figure 8. Conformational transition map for the GCAA tetraloop, where A−I are nine groups of conformations that have distinct base stacking patterns. Arrows between groups indicates conformational transitions, with the number of transitions nearby.

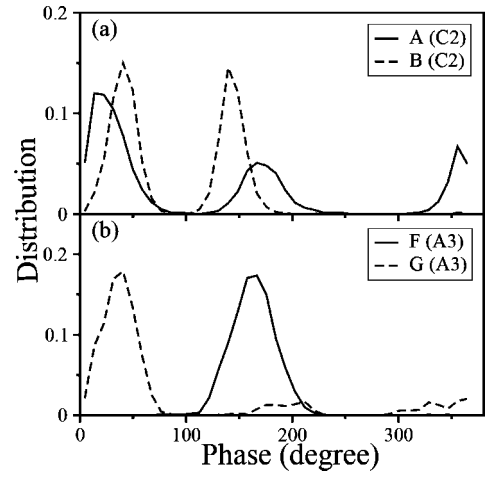

Figure 9. Distributions of the pucker phase: (a) C2 in groups A and B; (b) A3 in groups F and G.

8. Such a transition map can be directly compared with recent fluorescence measurements in which a detailed dynamic multiconformation model is suggested.[16] Encouragingly, the transition map shown in Figure 8 supports the multiconformation model, and moreover, detailed transition pathways are consistent with each other.

The A−B−F−E transition pathway is in good agreement with the experimental model,[16] which proposed an A−B−D−F−E transition pathway and predicted that the equilibrium between groups A and B exists in GNRA tetraloops and could be an important pathway for transition from group A to other conformations.

The transition between B and D groups is also consistent with the proposal of the experiment.[16] Such a transition indicates that the third base R3 can slide over the G1-A4 sheared base pair, switching from stacking on A4 to stacking on G1 and vice versa.

Interestingly, a new transition pathway linking groups A and E through group H is found, which has not been resolved by experimental measurement. The structural characteristic of group H is that the middle two bases (2 and 3) are stacking with each other, however, in a looped-out configuration. Although group H has not been found in NMR structure models of GCAA, for other kinds of tetraloop RNA (UNCG and RNYA), NMR structural models do show configurations similar to group H.[7,55]

The transitions between looped-in and looped-out base conformations may generally occur cooperatively with transitions of puckering of furanose rings from 3′-endo to 2′-endo in the RNA GCAA tetraloop.[17] Experimental support came from the Raman spectroscopy study by Leulliot et al.[57] In their study a 2′-endo shoulder was seen in the UUCG tetraloop spectrum, which was assigned to the second base U2 within a looped-out conformation. The sugar pucker phase was calculated here to investigate the pucker mode of the residues in different structural groups. Distributions of pucker phase angles are shown in Figure 9. Distributions of the pucker phase of C2 for groups A and B (shown in Figure 9a) demonstrate that the occupancy located at ∼150° (corresponding to 2′-endo pucker) increases from structure group A to B. The pucker phase of A3 shows a similar trend (Figure 9b): when it is in the looped-out configuration (structure group F), A3 takes the 2′-endo conformation predominantly. From the structural point of view, the 2′-endo pucker mode expands the backbone of the nucleotide.[58] Our simulation confirms that when the nucleotide takes the looped-out conformation, its sugar pucker phase has more probability to be in the 2′-endo state.

The results of our simulation show that the GCAA tetraloop is not rigid and may undergo multiple conformational transitions, which provide theoretical support of observations of previous fluorescence studies.[4,14,16] And these structural fluctuations may lead to a variable set of hydrogen bonds.[4] These heterogeneous hydrogen bonds can signifi-

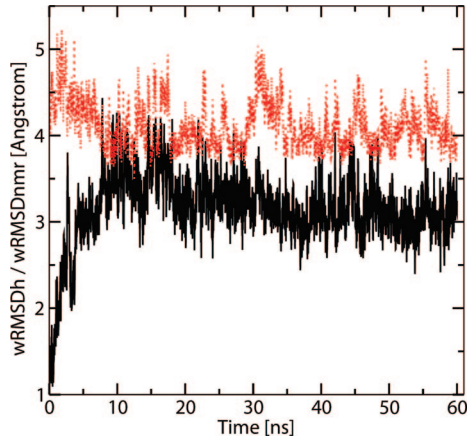

Figure 10. Evolution of rmsd values simulated by use of the new Amber force field parmbsc0, initiated from a loop configuration of H type with respect to initial structure (black solid line) and NMR structure (red dotted line).

cantly stabilize these multiple conformations. This may be one of the possible explanations for the multiple conformational transitions in the RNA GCAA tetraloop. A recent NMR ^{13}C relaxation study on the same GCAA tetraloop also revealed from the fast dynamics that this tetraloop has a rather rigid stem and a significantly more flexible loop.[13]

New Amber parmbsc0 Force Field. All the simulations so far were run with the force field Amber parm98. Recently a new modification of Amber force field was proposed that corrected the fault of artificial α/γ crankshaft motion of the nucleic acid backbone.[38] To test to what extent our simulation results depend on the force field, a test simulation was performed. An initial structure with loop pattern of H type (only bases C2 and A3 are stacked in the loop) was chosen. A 60 ns simulation with the new parmbsc0 force field was performed at 300 K. The reason that the H-type configuration was tested is that this configuration is the prediction of the current study that was not mentioned in earlier experimental interpretations. The rmsd values for the whole hairpin with respect to the initial H-type configuration (wRMSDh) and with respect to the NMR structural model (wRMSDnmr) are monitored as shown in Figure 10. During the last 40 ns of the simulation, wRMSDh fluctuates between 2.5 and 4 Å (black solid line) and wRMSDnmr fluctuates between 3.5 and 5 Å (red dotted line). Three dominant loop stacking patterns, B, H, and A type, were found with populations of 42%, 12%, and 6%, respectively. Frequent transitions between these three loop stacking patterns were observed, which is consistent with the transition map shown in Figure 8.

The detailed differences between the parm98 and parmbsc0 simulations are disclosed in the distributions of the backbone dihedral angles, α and γ, on which the force field parameters have been refined in parmbsc0. Both simulations produce similar α and γ distributions for stem residues; for example, see the distributions of α and γ for residue 3 in Figure 11. For residues on the loop, the parm98 simulation gives a broader distribution, probably due to the REMD simulation protocol, which can generate enhanced sampling: for example, the α and γ dihedral angles of residue 7, which is the third residue in the loop, are mainly located around

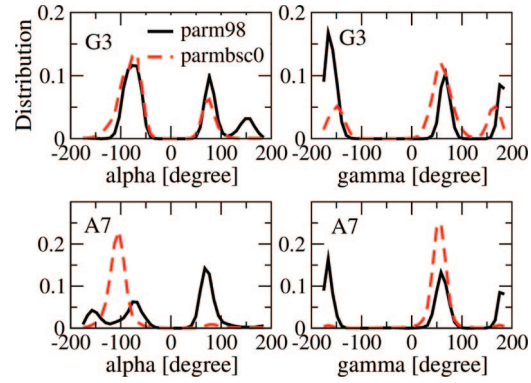

Figure 11. Distributions of backbone dihedral angles, α and γ, sampled with Amber parm98 force field (black solid line) in comparison with those sampled with the new force field parmbsc0 (red dashed line) for residues 3 and 7 of the tetraloop RNA.

$-100°$ and 60°, respectively, in the parmbsc0 simulation; in the parm98 REMD simulation, the distributions of both α and γ angles are multiple-peaked with one of the maxima positions coinciding with or close to the maximum position found in the parmbsc0 simulation. Thus we think that the main results of our simulation do not depend on the force field in a sensitive way.

Summary

A REMD simulation in explicit solvent was performed to probe the multiple conformations coexisting in RNA GCAA tetraloop. An obvious multiple-state (including folded, intermediate, and unfolded states) folding landscape of the RNA GCAA tetraloop is disclosed, which is in good agreement with previous RNA simulations.[17,21] On the basis of extensive cluster analysis of ample simulation trajectories, a dynamic structure transition map for the GCAA tetraloop is constructed, which is well consistent with the model from fluorescence measurements. The structure transition map of the GCAA tetraloop presented here should lead to a deeper understanding of the dynamic transition mechanism of the GNRA tetraloop family.

Acknowledgment. This work was supported by the University Research Committee, URC RG65/06, grant and academic research fund AcRF Tier 2 by the MOE (T206B3210RS), which are gratefully acknowledged. Financial support from the China Scholarship Council is gratefully acknowledged by Y.Z.

Supporting Information Available: Complete atom pairs and distances for NOE calculations. This material is available free of charge via the Internet at http://pubs.acs.org.

References

(1) Uhlenbeck, O. C. *Nature (London)* **1990**, *346*, 613.

(2) Cheong, C. J.; Varani, G.; Tinoco, I. *Nature (London)* **1990**, *346*, 680.

(3) Wolters, J. *Nucleic Acids Res.* **1992**, *20*, 1843.

(4) Jucker, F. M.; Heus, H. A.; Yip, P. F.; Moors, E. H. M.; Pardi, A. *J. Mol. Biol.* **1996**, *264*, 968.

(5) Heus, H. A.; Pardi, A. *Science* **1991**, *253*, 191.

(6) Cate, J. H.; Gooding, A. R.; Podell, E.; Zhou, K. H.; Golden, B. L.; Kundrot, C. E.; Cech, T. R.; Doudna, J. A. *Science* **1996**, *273*, 1678.

(7) Kalurachchi, K.; Nikonowicz, E. P. *J. Mol. Biol.* **1998**, *280*, 639.

(8) Zhang, Q.; Al-Hashimi, H. M. *Nat. Methods* **2008**, *5*, 243.

(9) Hodak, J. H.; Fiore, J. L.; Nesbitt, D. J.; Downey, C. D.; Pardi, A. *Proc. Natl. Acad. Sci. U.S.A.* **2005**, *102*, 10505.

(10) Furtig, B.; Richter, C.; Wohnert, J.; Schwalbe, H. *ChemBioChem* **2003**, *4*, 936.

(11) Legault, P.; Hoogstraten, C. G.; Metlitzky, E.; Pardi, A. *J. Mol. Biol.* **1998**, *284*, 325.

(12) Hoogstraten, C. G.; Wank, J. R.; Pardi, A. *Biochemistry* **2000**, *39*, 9951.

(13) Trantirek, L.; Caha, E.; Kaderavek, P.; Fiala, R. *J. Biomol. Struct. Dyn.* **2007**, *25*, 243.

(14) Menger, M.; Eckstein, F.; Porschke, D. *Biochemistry* **2000**, *39*, 4500.

(15) Rist, M. J.; Marino, J. P. *Curr. Org. Chem.* **2002**, *6*, 775.

(16) Zhao, L.; Xia, T. B. *J. Am. Chem. Soc.* **2007**, *129*, 4118.

(17) Sorin, E. J.; Engelhardt, M. A.; Herschlag, D.; Pande, V. S. *J. Mol. Biol.* **2002**, *317*, 493.

(18) Nivon, L. G.; Shakhnovich, E. I. *J. Mol. Biol.* **2004**, *344*, 29.

(19) Koplin, J.; Mu, Y.; Richter, C.; Schwalbe, H.; Stock, G. *Structure* **2005**, *13*, 1255.

(20) Hyeon, C.; Thirumalai, D. *Biophys. J.* **2006**, *90*, 3410.

(21) Ma, H.; Proctor, D. J.; Kierzek, E.; Kierzek, R.; Bevilacqua, P. C.; Gruebele, M. *J. Am. Chem. Soc.* **2006**, *128*, 1523.

(22) Kannan, S.; Zacharias, M. *Biophys. J.* **2007**, *93*, 3218.

(23) McDowell, S. E.; Spackova, N.; Sponer, J.; Walter, N. G. *Biopolymers* **2007**, *85*, 169.

(24) Nystrom, B.; Nilsson, L. *J. Biomol. Struct. Dyn.* **2007**, *24*, 525.

(25) Zhuang, L.; Jaeger, L.; Shea, J.-E. *Nucleic Acids Res.* **2007**, *35*, 6995.

(26) Garcia, A. E.; Paschek, D. *J. Am. Chem. Soc.* **2008**, *130*, 815.

(27) Villa, A.; Widjajakusuma, E.; Stock, G. *J. Phys. Chem. B* **2008**, *112*, 134.

(28) Sarzynska, J.; Nilsson, L.; Kulinski, T. *Biophys. J.* **2003**, *85*, 3445.

(29) Sarzynska, J.; Kulinski, T. *J. Biomol. Struct. Dyn.* **2005**, *22*, 425.

(30) Sanbonmatsu, K. Y.; Garcıa, A. E. *Proteins: Struct., Funct., Genet.* **2002**, *46*, 225.

(31) Mitsutake, A.; Sugita, Y.; Okamoto, Y. *Biopolymers* **2001**, *60*, 96.

(32) Zhou, R. H. *J. Mol. Graph.* **2004**, *22*, 451.

(33) Mu, Y.; Nordenskiold, L.; Tam, J. P. *Biophys. J.* **2006**, *90*, 3983.

(34) Sugita, Y.; Okamoto, Y. *Chem. Phys. Lett.* **1999**, *314*, 141.

(35) Zhang, J.; Qin, M.; Wang, W. *Proteins: Struct., Funct., Genet.* **2006**, *62*, 672.

(36) Berendsen, H. J. C.; Vanderspoel, D.; Vandrunen, R. *Comput. Phys. Commun.* **1995**, *91*, 43.

(37) Cheatham, T. E.; Cieplak, P.; Kollman, P. A. *J. Biomol. Struct. Dyn.* **1999**, *16*, 845.

(38) Perez, A.; Marchan, I.; Svozil, D.; Sponer, J.; Cheatham, T. E., III; Laughton, C. A.; Orozco, M. *Biophys. J.* **2007**, *92*, 3817.

(39) Hess, B.; Bekker, H.; Berendsen, H. J. C.; Fraaije, J *J. Comput. Chem.* **1997**, *18*, 1463.

(40) Daura, X.; van Gunsteren, W. F.; Rigo, D.; Jaun, B.; Seebach, D. *Chem.—Eur. J.* **1997**, *3*, 1410.

(41) Jorgensen, W. L.; Chandrasekhar, J.; Madura, J. D.; Impey, R. W.; Klein, M. L. *J. Chem. Phys.* **1983**, *79*, 926.

(42) Daura, X.; Gademann, K.; Jaun, B.; Seebach, D.; van Gunsteren, W. F.; Mark, A. E. *Angew. Chem., Int. Ed.* **1999**, *38*, 236.

(43) Lavery, R.; Sklenar, H. *J. Biomol. Struct. Dyn.* **1988**, *6*, 63.

(44) Daura, X.; Antes, I.; van Gunsteren, W. F.; Thiel, W.; Mark, A. E. *Proteins: Struct., Funct., Genet.* **1999**, *36*, 542.

(45) Davis, J. H.; Tonelli, M.; Scott, L. G.; Jaeger, L.; Williamson, J. R.; Butcher, S. E. *J. Mol. Biol.* **2005**, *351*, 371.

(46) Klosterman, P. S.; Hendrix, D. K.; Tamura, M.; Holbrook, S. R.; Brenner, S. E. *Nucleic Acids Res.* **2004**, *32*, 2342.

(47) Pley, H. W.; Flaherty, K. M.; McKay, D. B. *Nature (London)* **1994**, *372*, 111.

(48) Mao, H. Y.; White, S. A.; Williamson, J. R. *Nat. Struct. Biol.* **1999**, *6*, 1139.

(49) Battiste, J. L.; Mao, H. Y.; Rao, N. S.; Tan, R. Y.; Muhandiram, D. R.; Kay, L. E.; Frankel, A. D.; Williamson, J. R. *Science* **1996**, *273*, 1547.

(50) Baugh, C.; Grate, D.; Wilson, C. *J. Mol. Biol.* **2000**, *301*, 117.

(51) Nikulin, A.; Serganov, A.; Ennifar, E.; Tishchenko, S.; Nevskaya, N.; Shepard, W.; Portier, C.; Garber, M.; Ehresmann, B.; Ehresmann, C.; Nikonov, S.; Dumas, P. *Nat. Struct. Biol.* **2000**, *7*, 273.

(52) Stoldt, M.; Wohnert, J.; Ohlenschlager, O.; Gorlach, M.; Brown, L. R. *EMBO J.* **1999**, *18*, 6508.

(53) Butcher, S. E.; Dieckmann, T.; Feigon, J. *EMBO J.* **1997**, *16*, 7490.

(54) Rowsell, S.; Stonehouse, N. J.; Convery, M. A.; Adams, C. J.; Ellington, A. D.; Hirao, I.; Peabody, D. S.; Stockley, P. G.; Phillips, S. E. V. *Nat. Struct. Biol.* **1998**, *5*, 970.

(55) Kerwood, D. J.; Borer, P. N. *Magn. Reson. Chem.* **1996**, *34*, S136.

(56) Smith, J. S.; Nikonowicz, E. P. *Biochemistry* **2000**, *39*, 5642.

(57) Leulliot, N.; Baumruk, V.; Abdelkafi, M.; Turpin, P. Y.; Namane, A.; Gouyette, C.; Huynh-Dinh, T.; Ghomi, M. *Nucleic Acids Res.* **1999**, *27*, 1398.

(58) Saenger, W. *Principles of Nucleic Acid Structure*; Springer-Verlag: New York, 1984.

CT8004276

JCTC Journal of Chemical Theory and Computation

High-Level ab Initio Calculations To Improve Protein Backbone Dihedral Parameters

Hideaki Fujitani,* Azuma Matsuura, Sino Sakai, Hiroyuki Sato, and Yoshiaki Tanida

Fujitsu Laboratories Ltd., 10-1 Morinosato-Wakamiya, Atsugi 243-0197, Japan

Received December 8, 2008

Abstract: We present new molecular mechanical dihedral parameters for the Ramachandran angles ϕ and ψ of a protein backbone based on high-level ab initio molecular orbital calculations for hydrogen-blocked or methyl-blocked glycine and alanine dipeptides. Fully relaxed 15° (ϕ, ψ) contour maps were calculated at the MP2/6-31G(d) level of theory. Finding out the lowest energy path for ϕ (or ψ) to change from −180° to 180° in the contour map, we performed a DF-LCCSD(T0)/Aug-cc-pVTZ//DF-LMP2/Aug-cc-pVTZ level calculation to get the torsional energy profiles of ϕ (or ψ). Molecular mechanical torsion profiles with AMBER force field variants significantly differed from the ab initio profiles, so we derived new molecular mechanical dihedral parameters of a protein backbone to fit the ab initio profiles.

1. Introduction

Structural, dynamical, and equilibrium thermodynamic properties of biological macromolecules such as proteins and nucleic acids are commonly studied by molecular mechanics and molecular dynamics simulations. But their usefulness depends critically on the adequacy of the empirical force field parameters such as atomic charges, van der Waals parameters, and bond parameters. In the 1990s, Kollman's group developed a second generation of the Assisted Model Building with Energy Refinement (AMBER) force field for the simulation of proteins, nucleic acids, and organic molecules in condensed phases.[1] In addition to improvements in the parameters, they tried to explicitly describe the algorithm by which those parameters were derived, so that consistent extensions could be made to molecules other than proteins.

The peptides *N*-acetyl-*N*′-methylglycinamide and *N*-acetyl-*N*′-methylalaninamide have been widely studied. As they show conformational variations similar to proteins, they are considered model peptides for studying the character of Ramachandran angles ϕ and ψ (Figure 1). They are referred to as glycine dipeptide (GD) and alanine dipeptide (AD), respectively. Molecules such as α-(formylamino)ethanamide and (*S*)-α-(formylamino)propanamide have also been studied since they are formed from GD and AD by replacing the terminal methyl groups with hydrogen atoms. They are referred to as glycine dipeptide analogue (GDA) and alanine dipeptide analogue (ADA), respectively.

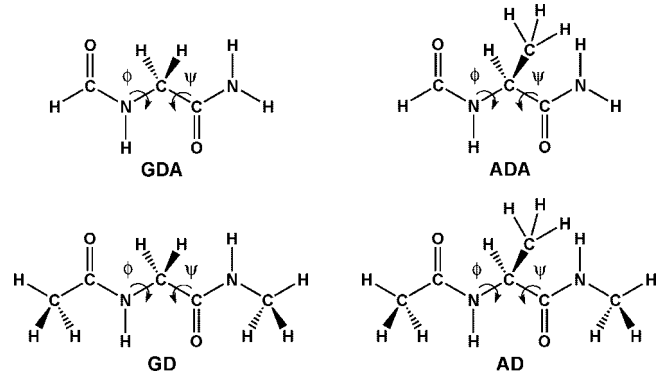

Figure 1. The structures of α-(formylamino)ethanamide (GDA), *N*-acetyl-*N*′-methylglycinamide (GD), (*S*)-α-(formylamino)propanamide (ADA), and *N*-acetyl-*N*′-methylalaninamide (AD). The dihedral angles, ϕ and ψ, are defined as C(O)−N−C^{α}−C(O) and N−C^{α}−C(O)−N, respectively.

Various quantum mechanical studies on these molecules were performed using Hartree−Fock (HF), density functional theory (DFT), Møller−Plesset (MP2, MP4), and coupled-cluster singles and doubles (CCSD, CCSD(T)) including the local electron correlation methods, because their conformation structure and energy in global or local minimum depend on the level of theory.[2−21] In 1982 Schäfer et al. calculated

* To whom correspondence should be addressed. E-mail: fjtani@labs.fujitsu.com.

10.1021/ct8005437 CCC: $40.75
Published on Web 03/24/2009

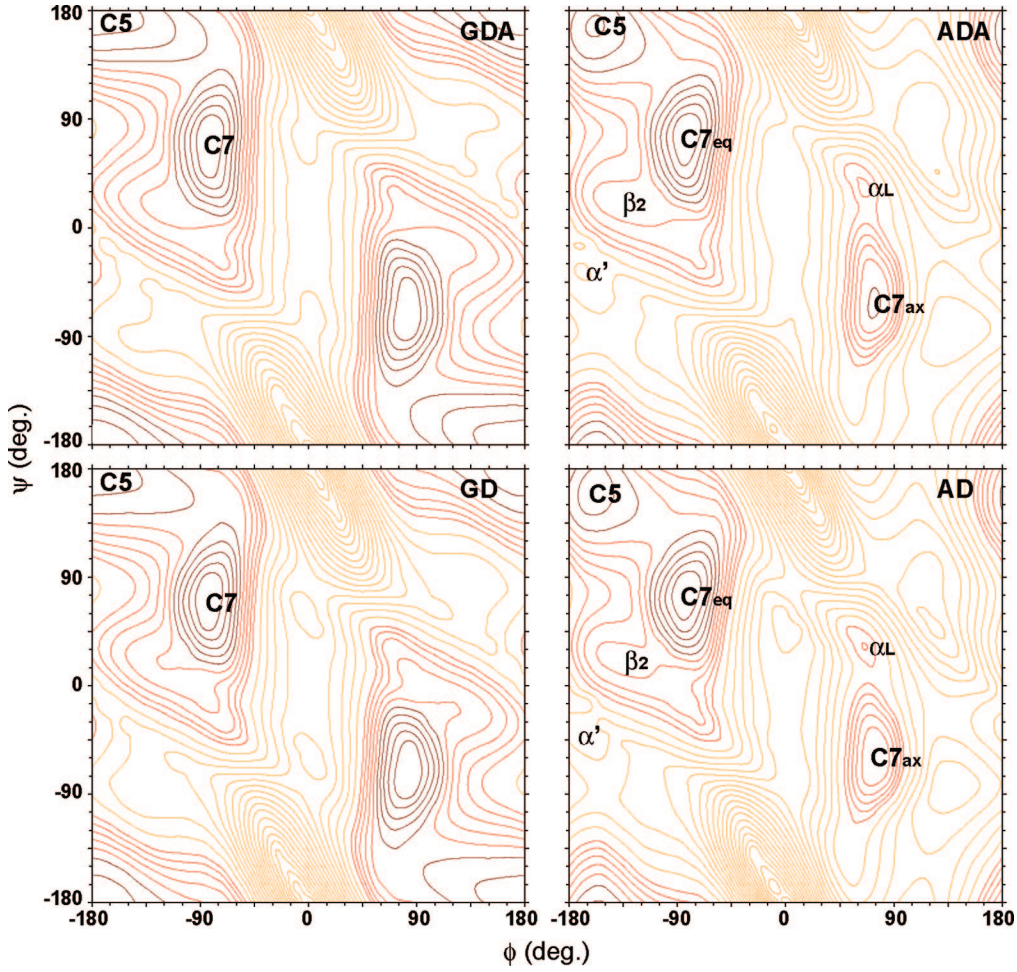

Figure 2. The (ϕ, ψ) maps of GDA, GD, ADA, and AD at the MP2/6-31G(d) level of theory. The maroon contours are drawn every 0.5 kcal/mol from the zero energy to 2.5 kcal/mol. The red contours are drawn every 0.5 kcal/mol from 3 to 5 kcal/mol. The orange contours are drawn every 1 kcal/mol above 6 kcal/mol. The figures were drawn using xfarbe version 2.6c.[34]

low-lying conformers of GD at the HF/4-21 level and concluded that the global minimum was C7 and the second lowest minimum was C5.[3] Using the analogues of GDA and ADA, Head-Gordon et al. obtained the fully relaxed 15° (ϕ, ψ) maps at the HF/3-21G level and then calculated the energies of some stationary points at higher levels of theory.[4] They found that (a) several local minima of GDA and ADA at HF/3-21G disappeared at higher levels, (b) the global minimum of GDA was the C7 conformer at HF/3-21G and MP2/6-31+G(d,p)//HF/6-31+G(d) levels whereas it was the C5 conformer at HF/6-31+G(d), (c) the third lowest local minimum of ADA was the $C7_{ax}$ conformer at HF/3-21G and MP2/6-31+G(d,p)//HF/6-31+G(d) levels whereas it was the β_2 conformer at HF/6-31+G(d). Gould et al. found that the global minimum of GD was C7 at MP2/TZVP//HF/6-31G(d,p) whereas it was C5 at HF/6-31G(d,p) and that the third lowest local minimum of AD was $C7_{ax}$ at MP2/TZVP//HF/6-31G(d,p) whereas it was β_2 at HF/6-31G(d,p).[6]

After these works, higher-level calculations were applied for AD and all gave the same order of the low-lying conformers as $C7_{eq} < C5 < C7_{ax} < \beta_2$.[7,9,12,15,20] Although the relative order of stability was the same at higher level calculations, their structures are significantly different. For example, the equilibrium (ϕ, ψ) angles of the β_2 conformer was (−135.9°, 23.4°) at B3LYP/6-31G(d),[7] but it was (−82.3°, −9.5°) at MP2(Full)/Aug-cc-pVDZ.[12] The hydrogen bond length of N−H···O of the β_2 conformer was 3.51 Å at BLYP/TZVP+ whereas it was 2.95 Å at MP2(Full)/Aug-cc-pVDZ.[12] The first reason for the difficulty to get precise results is the shallow minima and very flat regions of potential energy surfaces with respect to ϕ and ψ. The second is intramolecular hydrogen bonds, and the third is intramolecular dispersive interactions. In addition to these reasons, the artificial energy by intramolecular basis set superposition error (BSSE) makes it more difficult to choose an appropriate level of theory.[11,20,22−25]

In this work, we clarify the accuracy of various levels of quantum mechanical theory by comparing the precise conformation structures and energies of the global and local minima. Because of the accuracy and computational efficiency to calculate rotational energy profiles of ϕ and ψ, we use the density-fitting local coupled-cluster singles and doubles[26,27] with perturbative noniterative local triples[28] at the density-fitting local MP2[26,29,30] geometries with the Aug-cc-pVTZ basis set:[31] DF-LCCSD(T0)/Aug-cc-pVTZ//DF-LMP2/Aug-cc-pVTZ. We compare the ab initio rotational energy profiles with molecular mechanical profiles calculated with AMBER force field variants. Since there are significant

deviations, we optimize the molecular mechanical dihedral parameters of ϕ and ψ to fit the ab initio profiles. Calculations with a local correlation, density-fitting, and CCSD were performed using the MOLPRO package.[32] The other molecular orbital calculations were performed using Gaussian 98.[33] Vibrational frequency analyses at energy minima were performed using both MOLPRO and Gaussian 98. We adopted a frozen core approximation in all molecular orbital calculations.

2. MP2/6-31G(d) Contour Map of (ϕ, ψ)

We first generated the fully relaxed 15° (ϕ,ψ) energy maps of the GDA, GD, ADA, and AD molecules at the MP2/6-31G(d) level of theory in order to clarify the whole energy landscape and obtain the relaxed atomic structure at each (ϕ, ψ) grid point. Figure 2 shows the (ϕ, ψ) maps for GDA, GD, ADA, and AD, which were drawn using xfarbe version 2.6c.[34] For ADA and AD we optimized the molecular structure at the 576 (24 × 24) grid points. For GDA we used the symmetry (ϕ, ψ) =($-\phi$, $-\psi$) and thus 312 GDA structures were optimized. For GD we performed the structure optimization at (ϕ, ψ) and ($-\phi$, $-\psi$) and then symmetrized the (ϕ, ψ) map using the lower energy of the two. These calculations were performed using Gaussian 98 with the default convergence criteria. For each energy minimum conformer we performed vibrational analysis to check the absence of imaginary frequencies at MP2/6-311++G(d,p) for GDA, at MP2/6-31+G(d) for ADA and GD, and at MP2/6-31G(d) for AD.

The contour maps for GD and AD reported by Mackerell et al. are almost the same as ours, except in the vicinity of the α′ conformer of AD.[15] We performed vibrational analysis of the α′ conformer at (−166.1°, −37.2°) to confirm the absence of imaginary frequencies, which is evidence of a local minimum.

Global and local minima are clarified by the (ϕ, ψ) contour maps obtained at the MP2/6-31G(d) level, but their precise energies and structures depend on the level of theory. We first apply various levels of theory to the smallest molecule of GDA to examine the accuracy of the method, including MP2, MP4, CCSD with or without the local correlation method, and the density fitting approximation (DF). We use not only Pople basis sets like 6-311++G(d,p) but also augmented correlation consistent Dunning basis sets like Aug-cc-pVnZ (n = D, T, Q). DF reduces the calculation cost of two-electron-four-index integrals by several times.

3. Comparison of Levels of Theory

When optimizing the geometries of conformers, i.e., local minima, using MOLPRO and Gaussian 98, we adopted a tight convergence criteria in that the maximum force is 1.5 × 10^{-5}, the rms force is 1 × 10^{-5}, the maximum displacement is 6 × 10^{-5}, and the rms displacement is 4 × 10^{-5} atomic units. This corresponds to the "Opt=Tight" keyword of Gaussian 98.

For MOLPRO, we tightened the SCF convergence criterion on density matrix to 10^{-8} by specifying "accu=16". In the local calculation, the two most diffuse functions of each angular momentum functions were ignored in the localization to yield better-localized orbitals; unless otherwise noted, completion criterion of 0.99 was used for the orbital domain selection by specifying "PMDEL=2" and "THRBP=0.99", respectively. When computing the extrapolation to the complete basis set (CBS) limit, we employed the $E_X = E_{CBS} + AX^{-3}$ formula[35] using the Aug-cc-pVTZ and Aug-cc-pVQZ basis sets.

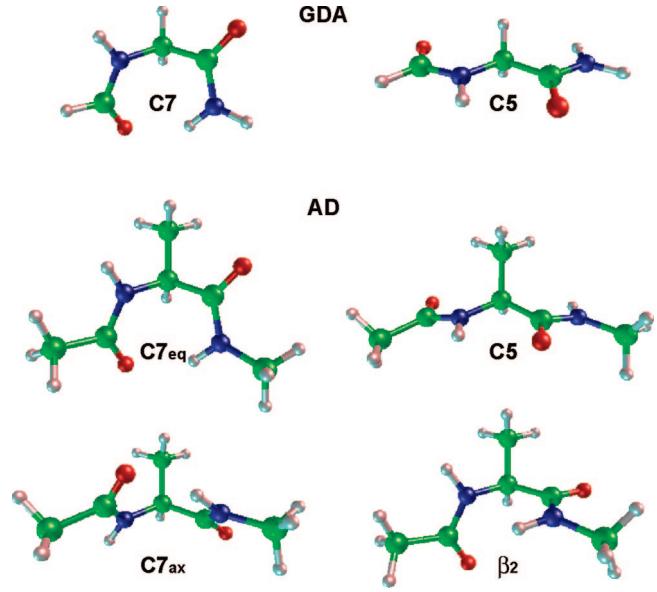

Figure 3. Graphical representations of low-lying conformers for GDA and AD optimized at the DF-LMP2/Aug-cc-pVTZ level of theory. The figures were drawn using xmo V4.0.[36]

Table 1. Torsional Angles ϕ and ψ and N−H···O Hydrogen Bond Length r of C7 and C5 Conformers of GDA Calculated at Different Levels of Theory[a]

	C7			C5		
theory	ϕ	ψ	r	ϕ	ψ	r
HF/6-31G(d)	−84.9	68.1	2.22	180.0	180.0	2.21
HF/6-31+G(d)[b]	−85.3	67.3	2.24	180.0	180.0	2.22
MP2/6-31G(d)	−82.5	74.2	2.08	175.7	179.5	2.17
MP2/6-31+G(d)	−82.5	74.7	2.10	169.3	173.7	2.20
MP2/6-31++G(d,p)	−82.8	72.4	2.09	162.4	177.7	2.20
MP2/6-311++G(d,p)	−82.1	76.7	2.10	165.8	171.6	2.21
MP2/AVDZ	−82.4	68.0	2.06	180.0	180.0	2.20
MP2/AVTZ	−82.6	67.4	2.04	180.0	180.0	2.18
LMP2/AVTZ	−82.8	68.5	2.08	180.0	180.0	2.19
DF-LMP2/AVTZ	−82.8	68.5	2.08	180.0	180.0	2.19

[a] Angles are in degrees, and hydrogen bond length is in angstroms. [b] The (ϕ, ψ) is (−85.2, 67.4) for C7 conformer and (180.0, 180.0) for C5 conformer in ref 4 which does not report the hydrogen bond lengths.

Figure 3 shows low-lying conformers of GDA and AD molecules which were drawn using the xmo V4.0 MO visualizer.[36]

GDA. We examined the precise structures of the C7 and C5 conformers of GDA at different levels of theory. The C7 and C5 conformers have different N−H···O hydrogen bonds (Figure 3). Their bond length and torsional angles of ϕ and ψ are listed in Table 1. We abbreviate the basis sets of Aug-cc-pVDZ, Aug-cc-pVTZ, and Aug-cc-pVQZ as AVDZ, AVTZ, and AVQZ, respectively. The ϕ and ψ of

Table 2. Relative Energies (kcal/mol) of C7 and C5 Conformers of GDA Calculated at Different Levels of Theory

theory	C7	C5
HF/6-31G(d)	0.45	0.00
HF/6-31+G(d)[a]	0.58	0.00
MP2/6-31G(d)	0.00	1.23
MP2/6-31+G(d)	0.00	1.37
MP2/6-31++G(d,p)	0.00	1.35
MP2/6-311++G(d,p)	0.00	1.08
MP4/6-311G(d,p)//MP2/6-31G(d)	0.00	1.52
MP4/6-311+G(d,p)//MP2/6-31G(d)	0.00	1.53
MP4/6-311++G(d,p)//MP2/6-31G(d)	0.00	1.56
MP4/6-311+G(d,p)//MP2/6-31+G(d)	0.00	1.29
MP4/6-311++G(d,p)//MP2/6-31++G(d,p)	0.00	1.24
MP2/AVDZ	0.00	1.03
MP2/AVTZ//MP2/AVDZ	0.00	0.75
MP2/AVTZ	0.00	0.74
MP2/AVTZ//LMP2/AVTZ	0.00	0.73
DF-MP2/AVTZ//DF-LMP2/AVTZ	0.00	0.73
LMP2/AVTZ	0.00	0.51
DF-LMP2/AVTZ	0.00	0.51
LMP4/AVTZ//LMP2/AVTZ	0.00	0.44
DF-LMP4/AVTZ//DF-LMP2/AVTZ	0.00	0.44
CCSD(T)/AVTZ//MP2/AVTZ	0.00	0.78
CCSD(T)/AVTZ//LMP2/AVTZ	0.00	0.77
LCCSD(T0)/AVTZ//LMP2/AVTZ	0.00	0.44
DF-LCCSD(T0)/AVTZ//DF-LMP2/AVTZ	0.00	0.44

[a] The value is the same as in ref 4.

the C5 conformer are all 180° at the MP2, LMP2, and DF-LMP2 levels with Dunning basis set, but they deviate from 180° at MP2 with Pople basis sets. The deviation of ϕ is about 18° at MP2/6-31++G(d,p), about 14° at MP2/6-311++G(d,p), and about 4° at MP2/6-31G(d). Larger Pople basis sets gave larger deviation in Table 1. Similar deviations are observed in the ψ values of the C7 conformer while the deviations are smaller.

The intermolecular BSSE effects on geometry and interaction energy can be accounted for by using the counterpoise procedure. Schütz et al. reported that the interaction energy and O−O distance of water dimer at the MP2/AVTZ level were −5.18 kcal/mol and 2.907 Å, that the counterpoise corrected values were −4.72 kcal/mol and 2.932 Å, and those at DF-LMP2/AVTZ were −4.67 kcal/mol and 2.935 Å, respectively.[29] Although there is no straightforward way to correct for intramolecular BSSE, it is well-known that the local correlation method reduces the intramolecular BSSE.[25]

Since the N−H···O hydrogen bond of the C7 conformer is stronger than that of the C5 conformer, the hydrogen bond length of the C7 conformer ranges from 2.04 to 2.24 Å depending on the basis set, while that of the C5 conformer ranges from 2.17 Å to 2.22 Å. The HF calculation gave a little longer hydrogen bond lengths for both C5 and C7 conformers, as it does not take into account both dispersion and electron correlation. The hydrogen bond length at MP2/AVTZ is the shortest of all and is 0.04 Å shorter than that at DF-LMP2/AVTZ. This is consistent with the BSSE correction which slightly extended the O−O distance of water dimer.

Table 2 lists the relative energies of the C7 and C5 conformers of GDA at various levels of theory. All the relative energies at the MP2 and MP4 levels with Pople basis sets are larger than those with Dunning basis sets. Pople basis sets cannot give precise structures and relative energies of the C7 and C5 conformers and they are not suitable for investigating precise energy profiles of the protein model system. Within Dunning basis sets, the relative energy varies more than 0.5 kcal/mol depending on the level of theory. Canonical MP2 and CCSD(T) give slightly larger relative energies than those at the local correlation methods of LMP2 and LCCSD(T0), because the canonical methods give BSSE excessive lower energies to the hydrogen bond of the C7 conformer. There is no difference in structure between DF-LMP2/AVTZ and LMP2/AVTZ in Table 1, and there is no difference in relative energy in Table 2 by the density fitting approximation (DF). We did not observe any deviation owing to DF in our calculations. DF is very useful for reducing the calculation cost.

Table 3. The Relative Energies (kcal/mol) of C5 Conformer to C7 Conformer of GDA Calculated at the DF-LMP2/AVTZ and MP2/AVTZ Geometries

	geometry	
energy	DF-LMP2/AVTZ	MP2/AVTZ
MP2/AVTZ	0.73	0.74
DF-MP2/AVTZ	0.73	–
DF-MP2/AVQZ	0.64	–
DF-MP2/CBS	0.59	–
DF-LMP2/AVTZ	0.51	0.50
DF-LMP2/AVQZ[a]	0.54	–
DF-LMP2/CBS	0.56	–
DF-LMP4/AVTZ	0.44	0.42
CCSD(T)/AVTZ	0.77	0.78
DF-LCCSD(T0)/AVTZ	0.44	0.41
DF-LCCSD(T0)/AVQZ[a]	0.46	–
DF-LCCSD(T0)/CBS	0.48	–

[a] THRBP = 0.993 for C7 conformer, and THRBP = 0.992 for C5 conformer.

We examined the basis set truncation error (BSTE) by enlarging the basis set. Table 3 lists the relative energies of the C5 conformer to the C7 conformer calculated at the DF-LMP2/AVTZ and MP2/AVTZ geometries. The relative energies only depend on the level of theory used in the energy calculation, and the differences between them when comparing the DF-LMP2 and MP2 geometries are negligible. When the basis set is enlarged from AVTZ to CBS, the relative energy at the canonical DF-MP2 decreases while one at the local correlation DF-LMP2 increases, because the former contains both BSTE and BSSE while the latter contains only BSTE. We evaluate the BSSE at DF-MP2/AVTZ as 0.19 = (0.73 − 0.59) − (0.51 − 0.56) in kcal/mol. It decreases when the basis set is enlarged. On the reasonable assumption that DF-LCCSD(T0)/AVTZ//DF-LMP2/AVTZ is essentially free from BSSE, we calculate the BSTE in the relative energy between the C5 and C7 conformers as being 0.04 kcal/mol.

AD. AD is the largest molecule in this study. Table 4 lists the torsional angles, ϕ and ψ, and the hydrogen bond lengths of N−H···O for the $C7_{eq}$, C5, $C7_{ax}$, and β_2 conformers of AD at different levels of theory including several reported values.[7,9,12,15] The graphical representations for these conformers at DF-LMP2/AVTZ are shown in Figure 3. The structures of the $C7_{eq}$, C5, and $C7_{ax}$ conformers are not sensitive to the level of theory, but the β_2 conformer is

Table 4. The Torsional Angles, ϕ and ψ, and the Hydrogen Bond Lengths r of N−H···O for $C7_{eq}$, C5, $C7_{ax}$, and β_2 Conformers of AD at Different Levels of Theory[a]

	$C7_{eq}$			C5			$C7_{ax}$			β_2		
theory	ϕ	ψ	r	ϕ	ψ	r	ϕ	ψ	r	ϕ	ψ	r
HF/6-31G(d)	−85.4	79.3	2.23	−157.3	158.8	2.22	75.9	−55.7	2.04	−132.6	22.4	3.66
HF/6-31+G(d)	−86.4	79.4	2.26	−153.8	151.9	2.24	75.9	−56.4	2.05	−102.7	4.1	3.28
HF/VDZ	−84.7	81.0	2.23	−155.6	162.7	2.20	75.7	−66.9	2.04	−138.1	25.0	3.72
HF/AVDZ	−86.1	80.9	2.26	−155.6	156.5	2.25	75.8	−53.8	2.04	−99.4	1.8	3.21
B3LYP/6-31G(d)	−82.9	72.9	2.04	−158.1	164.1	2.15	73.6	−57.7	1.92	−126.7	20.9	3.56
B3LYP/6-31G(d)	−81.9	72.3	−	−157.3	165.3	−	73.8	−60.0	−	−135.9	23.4	−
B3LYP/6-31+G(d)	−83.1	74.8	2.08	−155.2	159.1	2.21	73.1	−55.5	1.94	−113.4	12.6	3.40
MP2/6-31G(d)	−83.1	77.8	2.06	−158.4	161.3	2.17	74.4	−64.1	1.93	−137.9	22.9	3.71
MP2/6-31+G(d)	−82.2	79.7	2.09	−153.8	151.9	2.26	74.5	−55.9	1.93	−89.0	−5.3	3.04
MP2/6-31++G(d,p)	−82.4	80.4	2.09	−152.9	151.5	2.27	74.7	−55.9	1.92	−91.8	−3.6	3.08
MP2/6-311++G(d,p)[e]	−81.9	81.6	2.09	−158.4	151.6	2.28	74.3	−57.4	1.91	−90.7	−7.8	3.12
MP2(Full)/AVDZ	−82.6	75.8	2.02	−161.1	155.5	2.23	73.7	−53.7	1.88	−82.3	−9.5	2.95
DF-LMP2/AVTZ	−83.1	75.0	2.05	−159.1	161.7	2.19	73.7	−53.2	1.90	−88.1	−4.6	3.02

[a] Angles are in degrees, and hydrogen bond lengths are in angstroms. [b] Total energies in hartree: $C7_{eq}$ = −495.855 139 7, C5 = −495.852 890 7, $C7_{ax}$ = −495.850 994 3, β_2 = −495.850 199 2. [c] Hydrogen bond lengths are not reported in ref 7. [d] Calculated angles in refs 9 and 15, and this work agrees within a 0.3° range. Hydrogen bond lengths are not reported in the references. [e] Calculated angles in ref 15, and this work agrees within a 0.1° range. Hydrogen bond lengths are not reported in the references. [f] Reference 12.

Table 5. Relative Energies (kcal/mol) of $C7_{eq}$, C5, $C7_{ax}$, and β_2 Conformers of AD Calculated at Different Levels of Theory

theory	$C7_{eq}$	C5	$C7_{ax}$	β_2
HF/6-31G(d)	0.0	0.41	2.82	2.58
HF/6-31+G(d)	0.0	0.30	2.87	2.42
HF/VDZ	0.0	0.54	3.07	2.35
HF/AVDZ	0.0	0.21	2.93	2.55
B3LYP/6-31G(d)	0.0	1.41	2.60	3.10
B3LYP/6-31G(d)[a]	0.0	1.43	2.61	3.18
B3LYP/6-31+G(d)	0.0	1.09	2.49	2.74
MP2/6-31G(d)[b]	0.0	1.73	2.54	3.30
MP2/6-31+G(d)	0.0	1.79	2.42	2.98
MP2/6-31++G(d,p)	0.0	1.68	2.18	2.91
MP2/6-311++G(d,p)[c]	0.0	1.66	2.33	2.83
MP2(Full)/AVDZ[d]	0.0	1.91	2.28	3.11
MP2(Full)/CBS//MP2(Full)/AVDZ[d]	0.0	1.39	2.66	3.35
LMP2/VQZ(-g)//MP2/6-311++G(d,p)[e]	0.0	0.91	2.06	2.51
MP4/6-311G(d,p)//MP2/6-31G(d)	0.0	1.88	2.68	2.87
MP4-BSSE/VTZ(-f)//MP2/6-31G(d)[f]	0.0	0.89	2.55	2.56
CCSD(T)/CBS-MP2//MP2/AVDZ[g]	0.0	1.43	2.41	3.23
DF-MP2/AVTZ//DF-LMP2/AVTZ	0.0	1.46	2.29	3.04
DF-MP2/AVQZ//DF-LMP2/AVTZ	0.0	1.36	2.36	3.08
DF-MP2/CBS//DF-LMP2/AVTZ	0.0	1.32	2.39	3.12
DF-LMP2/AVTZ	0.0	1.22	2.41	2.86
DF-LMP2/AVQZ//DF-LMP2/AVTZ[h]	0.0	1.24	2.44	2.99
DF-LMP2/CBS//DF-LMP2/AVTZ	0.0	1.28	2.44	3.09
DF-LMP4/AVTZ//DF-LMP2/AVTZ	0.0	1.16	2.43	2.65
DF-LCCSD(T0)/AVTZ//DF-LMP2/AVTZ	0.0	1.14	2.38	2.71
DF-LCCSD(T0)/AVQZ//DF-LMP2/AVTZ[h]	0.0	1.19	2.41	2.87
DF-LCCSD(T0)/CBS//DF-LMP2/AVTZ	0.0	1.24	2.42	3.00

[a] Reference 7. [b] Calculated relative energies in ref 15, and this work agrees within a 0.02 kcal/mol range. [c] Calculated relative energies in this work are identical with those in ref 15. [d] Reference 12. [e] Reference 15. [f] Reference 9. [g] Reference 20. [h] THRBP = 0.992.

sensitive because it is located in the very flat region of the potential energy surface.[12]

Table 5 lists the relative energies for the $C7_{eq}$, C5, $C7_{ax}$, and β_2 conformers of AD at different levels of theory including several reported values.[7,9,12,15,20] There are the same features as those of GDA. The results at the HF levels are qualitatively inconsistent with those at higher levels of theory. All the energies of the C5 conformer at the MP2 levels with Pople basis sets are larger than those with Dunning basis sets. Because of BSSE, the canonical DF-MP2 calculations give larger energies for the C5 conformer than the local correlation DF-LMP2 calculations. Enlarging the basis sets from AVTZ to CBS, the DF-MP2 energy of the C5 conformer decreases while its DF-LMP2 energy increases.

For DF-LCCSD(T0), the energy differences between AVTZ and CBS are less than 0.3 kcal/mol for all the low-lying conformers. Taking into account computational cost and accuracy of the theory, DF-LCCSD(T0)/AVTZ//DF-LMP2/AVTZ is the best choice for calculating the torsional energy profiles of ϕ and ψ.

Low-Lying Conformation. Table 6 lists the structures and relative energies of the low-lying conformers of GDA, GD, ADA, and AD at DF-LCCSD(T0)/AVTZ//DF-LMP2/AVTZ. Kaminský and Jensen calculated the conformation structures and relative energies of some peptides, including GD and AD, at their CCSD(T)/CBS-MP2//MP2/AVDZ method which extrapolates the energy to the complete basis set limit with the HF/cc-pVXZ, MP2/cc-pVXZ (X = D, T, and Q), and the CCSD(T)/cc-pVDZ energies, and then compared them with molecular mechanical energies using various force fields.[20] As they pointed out, there are some discrepancies between the ab initio results and molecular mechanics results. We try to improve the molecular mechanical force field parameters by comparing the torsional energy profiles of ϕ and ψ.

4. Torsional Energy Profiles

4.1. Quantum Mechanical Torsional Profile. First we looked for the lowest energy path for ϕ (or ψ) to change from −180° to 180° in the contour map (Figure 2). Using the lowest mesh point structure as an initial structure, we fully optimized the molecular structure by the MP2/6-31G(d) calculation with fixed ϕ (or ψ) at the 15° step mesh value and then performed the MP4/6-311G(d,p) energy calculation to get a rotational energy profile of ϕ (or ψ). The torsional

Table 6. Structures and Relative Energies of Low-Lying Conformers of GDA, GD, ADA, and AD Calculated at the DF-LCCSD(T0)/Aug-cc-pVTZ//DF-LMP2/Aug-cc-pVTZ Level[a]

	C7/C7$_{eq}$				C5				C7$_{ax}$				β_2			
	ϕ	ψ	r	E	ϕ	ψ	r	E	ϕ	ψ	r	E	ϕ	ψ	r	E
GDA	−82.8	68.5	2.08	0.0	180.0	180.0	2.19	0.44								
GD	−82.8	70.6	2.05	0.0	180.0	180.0	2.18	0.91[b]								
ADA	−83.2	73.5	2.08	0.0	−159.8	165.1	2.19	0.85	73.5	−52.5	1.95	2.16	−90.0	−2.2	3.06	2.65
AD	−83.1	75.0	2.05	0.0	−159.1	161.7	2.19	1.14	73.7	−53.2	1.90	2.38	−88.1	−4.6	3.02	2.71

[a] Angles are in degrees and hydrogen bond lengths (N−H···O) are in angstroms. Relative energy with respect to C7 or C7$_{eq}$ in kcal/mol. C7 or C7$_{eq}$ energies of GDA, GD, ADA, and AD are −377.358 480 3, −455.842 733 4, −416.604 581 2, and −495.088 760 7 hartree, respectively. [b] Relative energy at CCSD(T)/CBS-MP2//MP2/Aug-cc-pVDZ is 0.98 kcal/mol.[20]

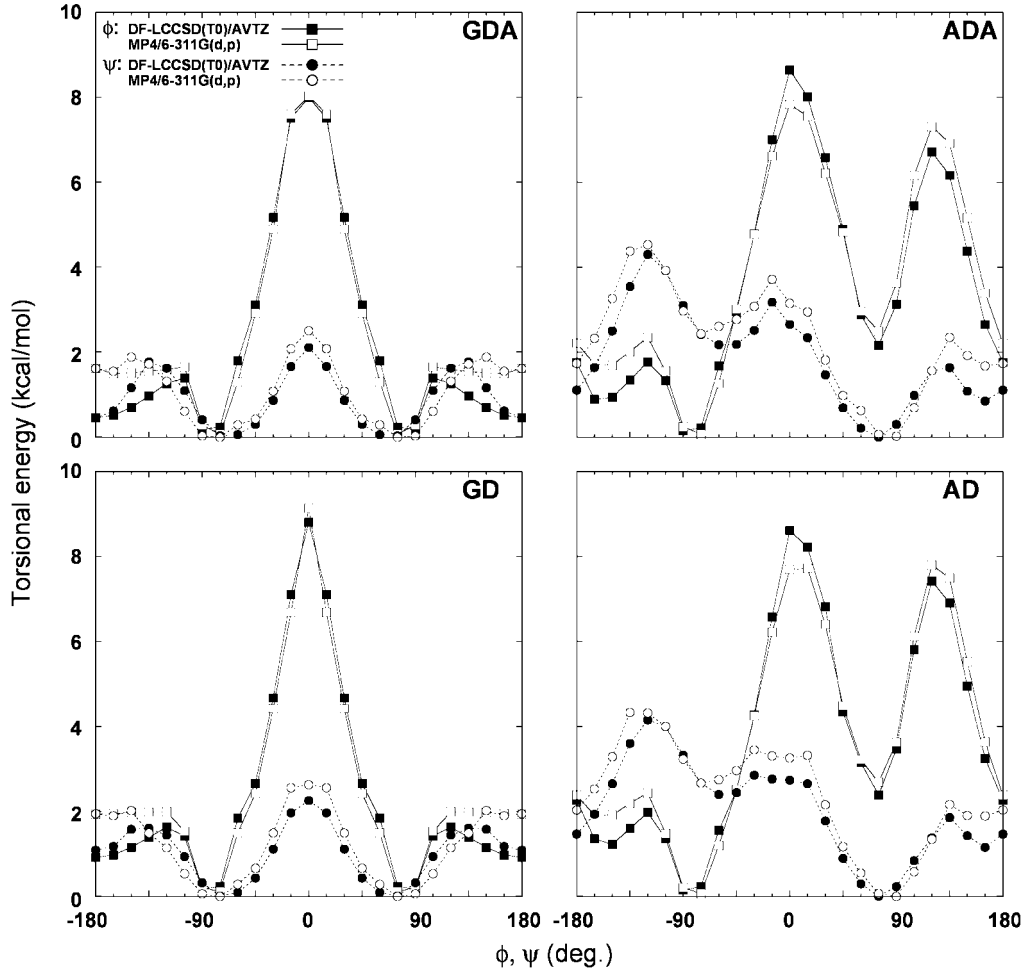

Figure 4. The torsional energy profiles of ϕ and ψ of GDA, GD, ADA, and AD. The solid lines are the ϕ profiles and the dashed lines are the ψ profiles. The filled squares and filled circles are at the DF-LCCSD(T0)/Aug-cc-pVTZ//DF-LMP2/Aug-cc-pVTZ level and the open squares and open circles are at the MP4/6-311G(d,p)//MP2/6-31G(d) level.

energy profile at the MP4/6-311G(d,p)//MP2/6-31G(d) level was used in the development of general AMBER force field (GAFF).[37]

Starting from the optimized MP2/6-31G(d) structure at the 15° step, we fully optimized the molecular structure by DF-LMP2/AVTZ with the fixed ϕ (or ψ) value using the default convergence criteria of structure optimization by MOLPRO and then calculated more accurate energy at the DF-LCCSD(T0)/AVTZ level to get a rotational energy profile of ϕ (or ψ) at DF-LCCSD(T0)/AVTZ//DF-LMP2/AVTZ. In the previous section we note the differences between MP2/6-31G(d) and DF-LMP2/AVTZ in the molecular structures and energies of the low-lying conformers, but they are smaller differences from the viewpoint of the whole (ϕ, ψ) contour maps. In addition, we performed the vibrational analysis for the low-lying conformers at the DF-LMP2/AVTZ level of theory to confirm the absence of imaginary frequencies. Therefore, it can be safely assumed that the energy minimum character is preserved in the torsional energy profiles at DF-LCCSD(T0)/AVTZ//DF-LMP2/AVTZ.

Figure 4 shows the torsional energy profiles for GDA, GD, ADA, and AD. For GDA and GD, the profiles of both ϕ and ψ from 105° to 180° disagree between DF-LCCSD(T0) and MP4. Especially there are significant differences in the vicinity of 180°, which is close to the C5 conformer. The profiles at DF-LCCSD(T0) indicate that a local minimum is

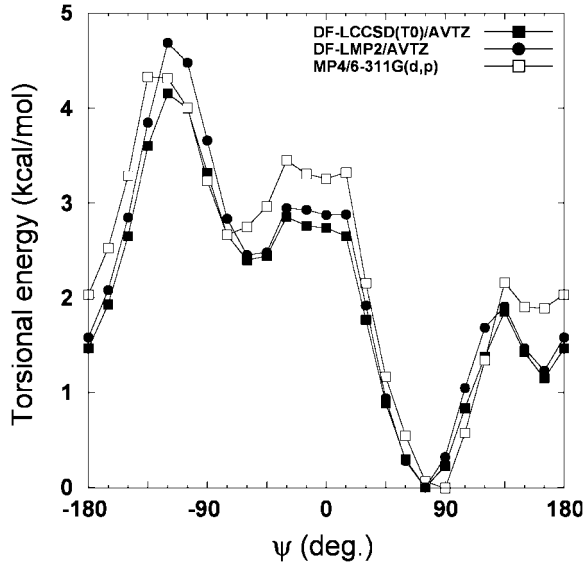

Figure 5. The torsional energy profiles of ψ of AD. The filled squares are at DF-LCCSD(T0)/Aug-cc-pVTZ, and the filled circles are at DF-LMP2/Aug-cc-pVTZ with the same geometries at DF-LMP2/Aug-cc-pVTZ. The open squares are at MP4/6-311G(d,p)//MP2/6-31G(d).

at 180° unlike those at MP4. The MP4 torsional energy at 180° is almost twice that at DF-LCCSD(T0) for GD, and it is three times larger for GDA. For ADA and AD, not only the energy value but also the position of a local minimum or maximum differ between DF-LCCSD(T0) and MP4, like in the vicinity of $\psi = -60°$ and $-135°$.

Figure 5 shows that the torsional energy profile of ψ of AD at the DF-LCCSD(T0)/AVTZ and DF-LMP2/AVTZ levels of theory with the same geometry at DF-LMP2/AVTZ, together with the profile at MP4/6-311G(d,p)//MP2/6-31G(d). There is a significant difference between DF-LCCSD(T0) and DF-LMP2 around $-120°$. This difference is more than 0.5 kcal/mol. Similar differences between DF-LCCSD(T0) and DF-LMP2 were also observed in other torsional profiles. Although the DF-LMP2 profile better agrees with the DF-LCCSD(T0) profile than the MP4/6-311G(d,p) profile, the higher-order correlation beyond MP2 is significant for some conformers with higher energies.

4.2. Molecular Mechanical Torsional Profile. The total energy in the AMBER force field model is given by[1]

$$E_{\text{total}} = \sum_{\text{bonds}} K_r(r_{ij} - r_{\text{eq}})^2 + \sum_{\text{angles}} K_\theta(\theta_{ijk} - \theta_{\text{eq}})^2 + \sum_{\text{dihedrals}} \sum_n \frac{V_n}{2}[1 + \cos(n\varphi_{ijkl} - \gamma_n)] + \sum_{i<j} \left[4\varepsilon_{ij}\left(\left(\frac{\sigma_{ij}}{r_{ij}}\right)^{12} - \left(\frac{\sigma_{ij}}{r_{ij}}\right)^{6}\right) + \frac{q_i q_j}{r_{ij}} \right] \quad (1)$$

Here, r_{eq} and θ_{eq} are equilibrium structural parameters; K_r, K_θ, V_n are force constants; n is multiplicity, and γ_n is the phase angle for the torsional angle parameters. ε_{ij} and σ_{ij} are van der Waals parameters, and q_i is the partial charge.

We compare the torsional energy profiles of ϕ and ψ between the DF-LCCSD(T0)/AVTZ//DF-LMP2/AVTZ level of theory and molecular mechanics with AMBER force field variants. In order to derive the molecular mechanical torsional profiles, we used version 3.3.3 of the GROMACS molecular dynamics suite[38] and the AMBER force field variants ported to GROMACS by Sorin and Pande.[39] As the initial structure for the molecular mechanical calculation, we used the 15° step structure optimized by DF-LMP2/AVTZ and performed an energy minimization by GROMACS with the fixed ϕ (or ψ) value to get a torsional energy profile.

Figure 6 shows the molecular mechanical profiles with the ab initio profiles. In the GD profiles, the potential barrier from the C7 conformer to the C5 conformer is too large in all molecular mechanical force fields. The lowest energy structure in AMBER99 (f99) is the C5 conformer, not the C7 conformer, and the molecular mechanical ψ values of the C7 conformer largely deviate from the ab initio value (Table 6). For AD, the peak around $-120°$ in the ψ profile is too large in all the molecular mechanical force fields and AMBER99SB (f99sb)[40] has a too large barrier around 120° in the ϕ profile. We suppose these deviations are one of the reasons why the molecular dynamics simulation with AMBER force fields did not have a good agreement with the experiments.[39]

A force field formulator for organic molecules (FF-FOM) was developed to assign force field parameters to arbitrary organic molecules in a unified manner including proteins and nucleic acids.[41] FF-FOM uses the GAFF bond parameters which have much improved characters after the experience of the AMBER99 force field parametrization.[42] The GROMACS input files of the unified force field for all amino acids and nucleic acids including GD and AD are available as a Supporting Information of ref 41. It uses the AMBER restrained electrostatic potential charges (RESP) and van der Waals potential parameters,[1] and the GAFF bond, angle, and dihedral parameters.[37]

Since GAFF has the same dihedral parameters for protein backbone torsions as AMBER99, we optimized the backbone dihedral parameters in order to get a better agreement with the ab initio profiles using the unified force field for GD and AD. Without any modification of other force field parameters, we first optimized the dihedral parameters of C−N−C$^\alpha$−C (ϕ) and N−C$^\alpha$−C−N (ψ) comparing the ab initio and molecular mechanical torsional profiles of GD. Then, using the obtained dihedral parameters of ϕ and ψ, we optimized the side-chain-related dihedral parameters of C−N−C$^\alpha$−C$^\beta$ (ϕ') and N−C−C$^\alpha$−C$^\beta$ (ψ'), comparing the torsional profiles of AD. In the optimization, we performed an exhaustive grid search in the parameter space of four amplitudes (V_1, V_2, V_3, V_4) and four phases (γ_1, γ_2, γ_3, γ_4) using the maximum absolute error function defined as

$$\text{MAE} = \max_{i<j} |E^i_{\text{QM}}(j) - E^i_{\text{MM}}(j)| \quad (2)$$

where $E^i_{\text{QM}}(j)$ is the ab initio energy of conformer j with conformer i as a reference, and $E^i_{\text{MM}}(j)$ is the molecular mechanical energy of conformer j with conformer i as a reference.[40] Amplitudes were checked from 0 to 3 kcal/mol, and phases were set to either 0 or π radians.

Table 7 lists the optimized dihedral parameters, and Figure 7 compares the optimized molecular mechanical profiles with

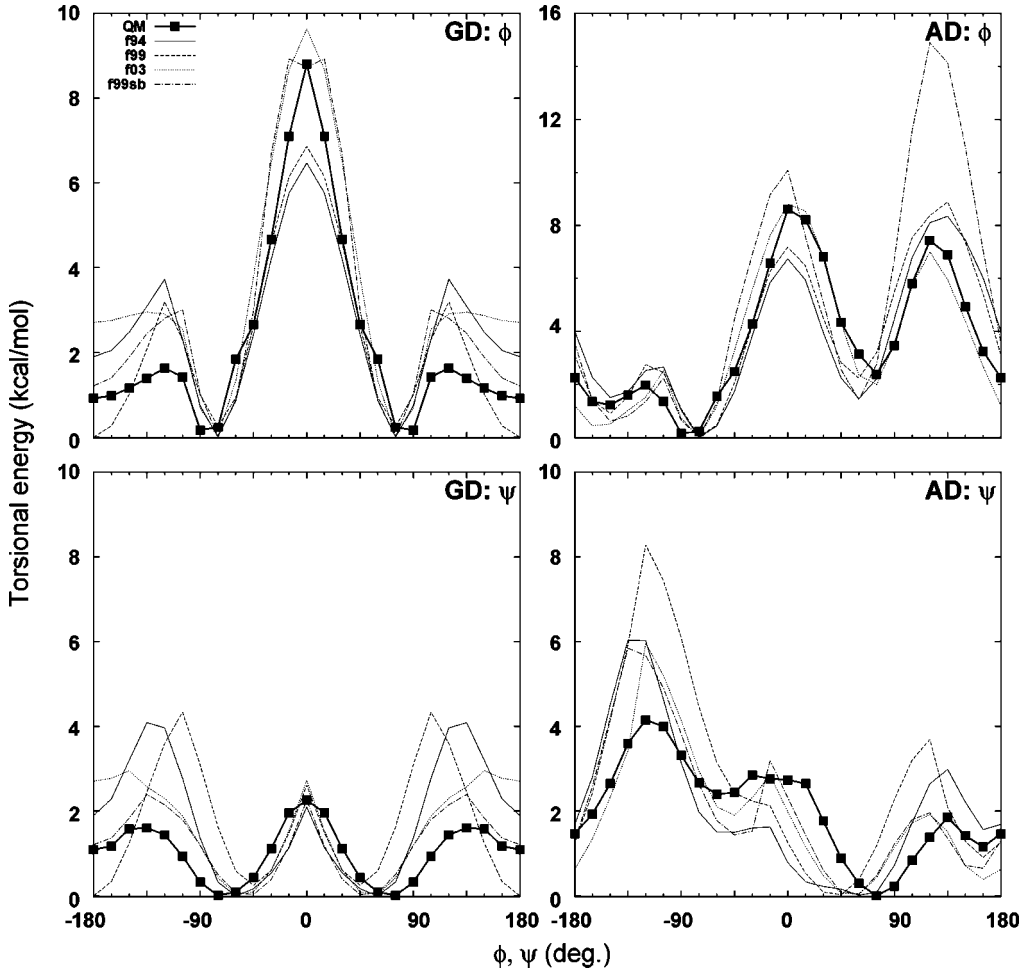

Figure 6. The torsional energy profiles of ϕ and ψ calculated with four AMBER force field variants (f94, f99, f03, f99sb) for GD and AD. The filled squares with a solid line show the torsional energy profile of ϕ and ψ at the DF-LCCSD(T0)/Aug-cc-pVTZ//DF-LMP2/Aug-cc-pVTZ level.

Table 7. Optimized Molecular Mechanical Dihedral Parameters for the Protein Backbone Torsions[a]

		V_1	γ_1	V_2	γ_2	V_3	γ_3	V_4	γ_4
ϕ	C−N−C$^\alpha$−C	0.17	0	0.21	0	0.07	π	0.10	0
ψ	N−C$^\alpha$−C−N	0.15	0	0.93	π	0.77	π	0.39	π
ϕ'	C−N−C$^\alpha$−C$^\beta$	0.25	π	0.19	π	0.13	π	0.14	π
ψ'	N−C−C$^\alpha$−C$^\beta$	0.48	π	0.39	π	0.30	0	0.33	π

[a] Phases are in radians, and amplitudes are in kcal/mol.

the ab initio profiles. We optimized only the dihedral parameters of the four torsions without any modification of other parameters. Our optimized profiles agree with the ab initio profiles much better than with the AMBER force field variants, but there are small deviations caused by other (general) AMBER parameters. Figure 8 compares the molecular structure of the $C7_{eq}$ conformer of AD between the DF-LMP2/AVTZ and molecular mechanical calculations. The molecular mechanical (MM) structure reasonably agrees with the ab initio (QM) structure, but the hydrogen bonds in the terminal methyl have slightly different orientations. The same deviation was observed in the GD and AD structures with the AMBER force field variants. This is an example of a remaining issue that needs to be overcome to improve the "minimalist model" of eq 1, although the protein does not have a methyl at either terminal in a standard condition. Our optimized dihedral parameters for the protein backbone torsions significantly differ from those of the AMBER force field variants. We hope the new dihedral parameters will improve the accuracy of molecular dynamics simulations for protein folding and absolute binding free energies.

5. Conclusion

In order to determine the starting geometry to get the fully relaxed torsional energy profiles of ϕ and ψ, we first generated the fully relaxed 15° (ϕ, ψ) maps of GDA, GD, ADA, and AD at the MP2/6-31G(d) level of theory. Global and local minimum conformers were clarified from the (ϕ, ψ) contour maps, but their precise energies and structures depend on the level of theory. Comparing low-lying conformers of GDA and AD at different levels of theory, we concluded that DF-LCCSD(T0)/Aug-cc-pVTZ//DF-LMP2/Aug-cc-pVTZ is the best choice for calculating the torsional energy profiles. It excludes the intramolecular BSSE and gives accurate energies with BSTE less than 0.3 kcal/mol.

Finding out the lowest energy path for ϕ (or ψ) to change from −180 to 180 degrees in the contour map, we performed

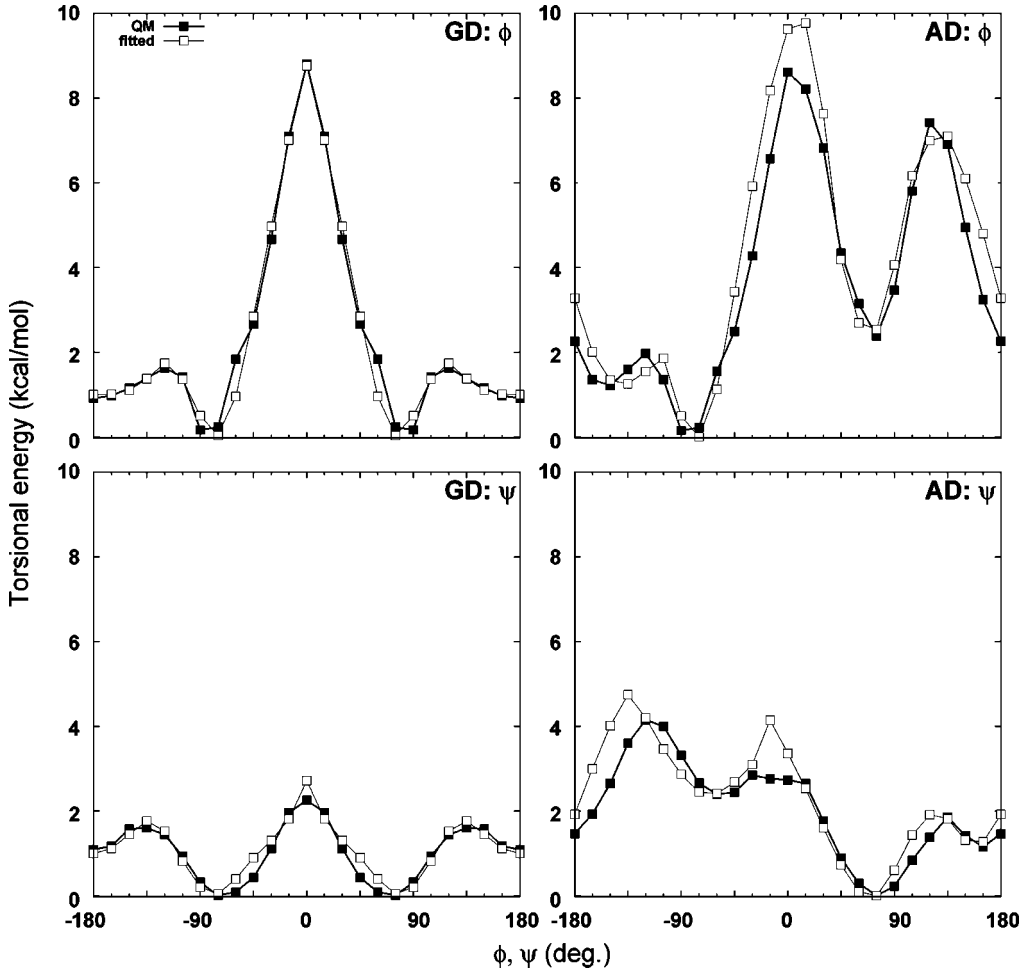

Figure 7. The molecular mechanical torsional energy profiles of GD and AD calculated with the optimized dihedral parameters. The filled squares show the torsional energy profile at the DF-LCCSD(T0)/Aug-cc-pVTZ//DF-LMP2/Aug-cc-pVTZ level, and the open squares show the optimized molecular mechanical profile.

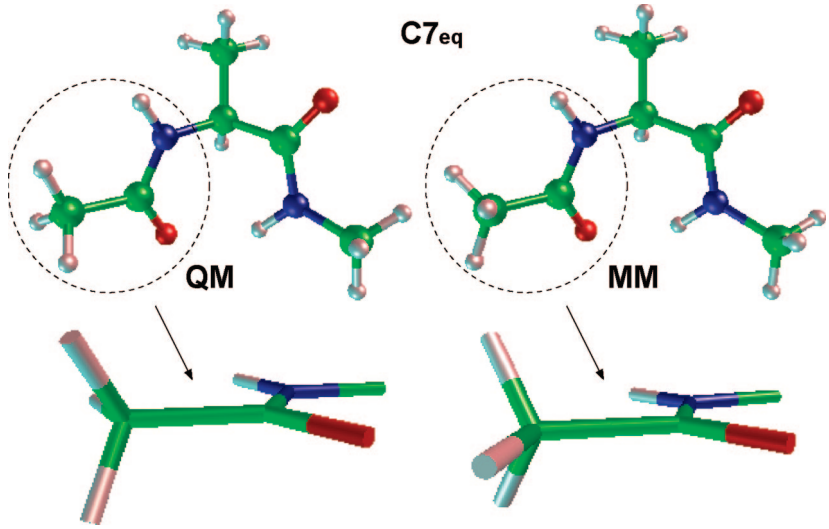

Figure 8. Molecular structures of the $C7_{eq}$ conformer of AD. The QM structure was obtained by the DF-LMP2/Aug-cc-pVTZ level of theory and the MM structure was obtained by the molecular mechanical calculation with our optimized dihedral parameters. The figures were drawn using xmo V4.0.[36]

a DF-LCCSD(T0)/Aug-cc-pVTZ//DF-LMP2/Aug-cc-pVTZ level calculation to get the torsional energy profiles of ϕ and ψ. Molecular mechanics with the AMBER force field variants gave significantly different torsional profiles, so we optimized the molecular mechanical dihedral parameters of the protein backbone to fit the ab initio torsional profiles. We hope the optimized dihedral parameters will improve the accuracy of molecular dynamics simulations.

Supporting Information Available: Optimized geometries and total energies at the DF-LCCSD(T0)/Aug-cc-pVTZ//DF-LMP2/Aug-cc-pVTZ level in the torsional energy profiles of ϕ and ψ are available free of charge via the Internet at http://pubs.acs.org.

References

(1) Cornell, W. D.; Cieplak, P.; Bayly, C. I.; Gould, I. R.; Merz, K. M., Jr.; Ferguson, D. M.; Spellmeyer, D. C.; Fox, T.; Caldwell, J. W.; Kollman, P. A. *J. Am. Chem. Soc.* **1995**, *117*, 5179–5197.

(2) Pullman, B.; Pullman, A. *Adv. Protein Chem.* **1974**, *28*, 347–526.

(3) Schäfer, L.; van Alsenoy, C.; Scarsdale, J. N. *J. Chem. Phys.* **1982**, *76*, 1439–1444.

(4) Head-Gordon, T.; Head-Gordon, M.; Frisch, M. J.; Brooks, C. L., III; Pople, J. A. *J. Am. Chem. Soc.* **1991**, *113*, 5989–5997.

(5) Shang, H. S.; Head-Gordon, T. *J. Am. Chem. Soc.* **1994**, *116*, 1528–1532.

(6) Gould, I. R.; Cornell, W. D.; Hiller, I. H. *J. Am. Chem. Soc.* **1994**, *116*, 9250–9256.

(7) Jalkanen, K. J.; Suhai, S. *Chem. Phys.* **1996**, *208*, 81–116.

(8) Cornell, W. D.; Gould, I. R.; Kollman, P. A. *J. Mol. Struct. (THEOCHEM)* **1997**, *392*, 101–109.

(9) Beachy, M. D.; Chasman, D.; Murphy, R. B.; Halgren, T. A.; Friesner, R. A. *J. Am. Chem. Soc.* **1997**, *119*, 5908–5920.

(10) Rodríguez, A. M.; Baldoni, H. A.; Suvire, F.; Vázquez, R. N.; Zamarbide, G.; Enriz, R. D.; Farkas, Ö.; Perczel, A.; McAllister, M. A.; Torday, L. L.; Papp, J. G.; Csizmadia, I. G. *J. Mol. Struct. (THEOCHEM)* **1998**, *455*, 275–301.

(11) Yu, C.-H.; Norman, M. A.; Schäfer, L.; Ramek, M.; Peeters, A.; van Alsenoy, C. *J. Mol. Struct.* **2001**, *567−568*, 361–374.

(12) Vargas, R.; Garza, J.; Hay, B. P.; Dixon, D. A. *J. Phys. Chem. A* **2002**, *106*, 3213–3218.

(13) Perczel, A.; Farkas, Ö.; Jákli, I.; Topol, I. A.; Csizmadia, I. G. *J. Comput. Chem.* **2003**, *24*, 1026–1042.

(14) Duan, Y.; Wu, C.; Chowdhury, S.; Lee, M. C.; Xiong, G.; Zhang, W.; Yang, R.; Cieplak, P.; Luo, R.; Lee, T.; Caldwell, J.; Wang, J.; Kollman, P. *J. Comput. Chem.* **2003**, *24*, 1999–2012.

(15) Mackerell, A. D., Jr.; Feig, M.; Brooks, C. L., III. *J. Comput. Chem.* **2004**, *25*, 1400–1415.

(16) Papamokos, G. V.; Demetropoulos, I. N. *J. Phys. Chem. A* **2004**, *108*, 7291–7300.

(17) Johnson, E. R.; Becke, A. D. *Chem. Phys. Lett.* **2006**, *432*, 600–603.

(18) Subotnik, J. E.; Sodt, A.; Head-Gordon, M. *J. Chem. Phys.* **2006**, *125*, 074116/1–12.

(19) Echenique, P.; Calvo, I.; Alonso, J. L. *J. Comput. Chem.* **2006**, *27*, 1733–1747.

(20) Kaminský, J.; Jensen, F. *J. Chem. Theory Comput.* **2007**, *3*, 1774–1788.

(21) Echenique, P.; Alonso, J. L. *J. Comput. Chem.* **2008**, *29*, 1408–1422.

(22) Gresh, N.; Kafafi, S. A.; Truchon, J.-F.; Salahub, D. R. *J. Comput. Chem.* **2004**, *25*, 823–834.

(23) DiStasio, R. A., Jr.; Jung, Y.; Head-Gordon, M. *J. Chem. Theory Comput.* **2005**, *1*, 862–876.

(24) DiStasio, R. A., Jr.; Steele, R. P.; Rhee, Y. M.; Shao, Y.; Head-Gordon, M. *J. Comput. Chem.* **2007**, *28*, 839–856.

(25) (a) Holroyd, L. F.; van Mourik, T. *Chem. Phys. Lett.* **2007**, *442*, 42–46. (b) Shields, A. E.; van Mourik, T. *J. Phys. Chem. A* **2007**, *111*, 13272–13277.

(26) Polly, R.; Werner, H.-J.; Manby, F. R.; Knowles, P. J. *Mol. Phys.* **2004**, *102*, 2311–2321.

(27) (a) Hampel, C.; Werner, H.-J. *J. Chem. Phys.* **1996**, *104*, 6286–6297. (b) Schütz, M.; Werner, H.-J. *J. Chem. Phys.* **2001**, *114*, 661–681. (c) Schütz, M. *Phys. Chem. Chem. Phys.* **2002**, *4*, 3941–3947. (d) Schütz, M.; Manby, F. R. *Phys. Chem. Chem. Phys.* **2003**, *5*, 3349–3358.

(28) (a) Schütz, M.; Werner, H.-J. *Chem. Phys. Lett.* **2000**, *318*, 370–378. (b) Schütz, M. *J. Chem. Phys.* **2000**, *113*, 9986–10001.

(29) Schütz, M.; Werner, H.-J.; Lindh, R.; Manby, F. R. *J. Chem. Phys.* **2004**, *121*, 737–750.

(30) (a) Hetzer, G.; Pulay, P.; Werner, H.-J. *Chem. Phys. Lett.* **1998**, *290*, 143–149. (b) Schütz, M.; Hetzer, G.; Werner, H.-J. *J. Chem. Phys.* **1999**, *111*, 5691–5705. (c) Hetzer, G.; Schütz, M.; Stoll, H.; Werner, H.-J. *J. Chem. Phys.* **2000**, *113*, 9443–9455. (d) Werner, H.-J.; Manby, F. R.; Knowles, P. J. *J. Chem. Phys.* **2003**, *118*, 8149–8160.

(31) (a) Dunning, T. H., Jr. *J. Chem. Phys.* **1989**, *90*, 1007–1023. (b) Kendall, R. A.; Dunning, T. H., Jr.; Harrison, R. J. *J. Chem. Phys.* **1992**, *96*, 6796–6806.

(32) Werner, H.-J.; Knowles, P. J.; Lindh, R.; Manby, F. R.; Schütz, M.; Celani, P.; Korona, T.; Mitrushenkov, A.; Rauhut, G.; Adler, T. B.; Amos, R. D.; Bernhardsson, A.; Berning, A.; Cooper, D. L.; Deegan, M. J. O.; Dobbyn, A. J.; Eckert, F.; Goll, E.; Hampel, C.; Hetzer, G.; Hrenar, T.; Knizia, G.; Köppl, C.; Liu, Y.; Lloyd, A. W.; Mata, R. A.; May, A. J.; McNicholas, S. J.; Meyer, W.; Mura, M. E.; Nicklass, A.; Palmieri, P.; Pflüger, K.; Pitzer, R.; Reiher, M.; Schumann, U.; Stoll, H.; Stone, A. J.; Tarroni, R.; Thorsteinsson, T.; Wang, M.; Wolf, A. MOLPRO, version 2006. 4; Cardiff School of Chemistry, Cardiff University, Cardiff, UK, 2006.

(33) Frisch, M. J.; Trucks, G. W.; Schlegel, H. B.; Scuseria, G. E.; Robb, M. A.; Cheeseman, J. R.; Zakrzewski, V. G.; Montgomery, J. A., Jr.; Stratmann, R. E.; Burant, J. C.; Dapprich, S.; Millam, J. M.; Daniels, A. D.; Kudin, K. N.; Strain, M. C.; Farkas, O.; Tomasi, J.; Barone, V.; Cossi, M.; Cammi, R.; Mennucci, B.; Pomelli, C.; Adamo, C.; Clifford, S.; Ochterski, J.; Petersson, G. A.; Ayala, P. Y.; Cui, Q.; Morokuma, K.; Malick, D. K.; Rabuck, A. D.; Raghavachari, K.; Foresman, J. B.; Cioslowski, J.; Ortiz, J. V.; Baboul, A. G.; Stefanov, B. B.; Liu, G.; Liashenko, A.; Piskorz, P.; Komaromi, I.; Gomperts, R.; Martin, R. L.; Fox, D. J.; Keith, T.; Al-Laham, M. A.; Peng, C. Y.; Nanayakkara, A.; Gonzalez, C.; Challacombe, M.; Gill, P. M. W.; Johnson, B.; Chen, W.; Wong, M. W.; Andres, J. L.; Gonzalez, C.; Head-Gordon, M.; Replogle, E. S.; Pople, J. A. Gaussian 98, Revision A.7; Gaussian, Inc., Pittsburgh, PA, 1998.

(34) Preusser, A. *ACM Trans. Math. Software* **1989**, *15*, 79–89.

(35) (a) Helgaker, T.; Klopper, W.; Koch, H.; Noga, J. *J. Chem. Phys.* **1997**, *106*, 9639–9646. (b) Halkier, A.; Helgaker, T.; Jørgensen, P.; Klopper, W.; Koch, H.; Olsen, J.; Wilson, A. K. *Chem. Phys. Lett.* **1998**, *286*, 243–252.

(36) Hayano, T. xmo, V 4.0 (MOPAC2002 V1); Fujitsu Ltd., Tokyo, Japan, 2001.

(37) Wang, J.; Wolf, R. M.; Caldwell, J. W.; Kollman, P. A.; Case, D. A. *J. Comput. Chem.* **2004**, *25*, 1157–1174.

(38) (a) Berendsen, H. J. C.; van der Spoel, D.; van Drunen, R. *Comput. Phys. Commun.* **1995**, *91*, 43–56. (b) Lindahl, E.; Hess, B.; van der Spoel, D. *J. Mol. Model.* **2001**, *7*, 306–317. (c) van der Spoel, D.; Lindahl, E.; Hess, B.; Groenhof, G.; Mark, A. E.; Berendsen, H. J. C. *J. Comput. Chem.* **2005**, *26*, 1701–1718.

(39) Sorin, E. J.; Pande, V. S. *Biophys. J.* **2005**, *88*, 2472–2493.

(40) Hornak, V.; Abel, R.; Okur, A.; Strockbine, B.; Roitberg, A.; Simmerling, C. *Proteins: Struct. Funct. Bioinf.* **2006**, *65*, 712–725.

(41) Fujitani, H.; Tanida, Y.; Matsuura, A. Phys. Rev. E 2009, *79*, 021914.

(42) Wang, J.; Cieplak, P.; Kollman, P. A. *J. Comput. Chem.* **2000**, *21*, 1049–1074.

CT8005437

JCTC Journal of Chemical Theory and Computation

Reference Quantum Chemical Calculations on RNA Base Pairs Directly Involving the 2′-OH Group of Ribose

Jiří Šponer,*[,†] Marie Zgarbová,[‡] Petr Jurečka,*[,†,‡] Kevin E. Riley,[§,||] Judit E. Šponer,[†,⊥] and Pavel Hobza[§]

Institute of Biophysics, Academy of Sciences of the Czech Republic, Královopolská 135, 612 65 Brno, Czech Republic, Department of Physical Chemistry, Palacky University, tr. Svobody 26, 771 46 Olomouc, Czech Republic, Institute of Organic Chemistry and Biochemistry, Academy of Sciences of the Czech Republic and Center of Biomolecules and Complex Molecular Systems, Flemingovo náměstí 2, 166 10 Prague 6, Czech Republic, Department of Chemistry, P.O. Box 23346, University of Puerto Rico, Rio Piedras, Puerto Rico 00931, and National Center for Biomolecular Research, Faculty of Science, Masaryk University, Brno, Czech Republic

Received December 10, 2008

Abstract: The folded structures of RNA molecules and large ribonucleoprotein particles are stabilized by a wide range of base pairs that actively utilize the 2′-OH groups of ribose for base pairing. Such base pairing does not occur in DNA and is essential for functional RNAs. We report reference quantum chemical calculations of base pairing energies for a representative selection of 25 RNA base pairs utilizing the ribose moiety for base pairing, including structures with amino acceptor interactions. All base pairs are evaluated at the MP2 level with extrapolation to the complete basis set (CBS) of atomic orbitals. CCSD(T) correction terms were obtained for four base pairs. In addition, the base pairing is evaluated using the DFT-SAPT perturbational procedure along with the aug-cc-pVDZ basis set, which allows for the decomposition of the interaction energies into separate, physically meaningful, components. These calculations confirm that, compared to canonical base pairs, many RNA base pairs exhibit a modestly increased role of dispersion attraction compared to canonical base pairs. However, the effect is smaller than one would assume based on assessment of the ratio of HF and correlation components of the interaction energies. Interaction energies are further calculated using the SCS(MI)-MP2 and DFT-D methods. Finally, we estimate the effect of aqueous solvent screening on the base pairing stability using the continuum solvent approach.

Introduction

The principles of RNA base pairing differ strikingly from those of DNA due to the presence of the 2′-hydroxyl group of ribose. Thus, besides the common canonical base pairs, functional RNAs utilize a very wide range of non-Watson−Crick (non-WC) base pairing patterns[1−21] (Figure 1). The most important non-WC RNA base pairs directly involve the ribose 2′-OH groups as either donors or acceptors of H-bonds. These "sugar-edge" base pairs are absolutely essential for building up complex three-dimensional (3D) RNA architectures. They include the leading RNA tertiary interactions, such as the A-minor [10−12] and packing interactions,[13,14] and many important base pairs in the internal RNA loops.[15−19] Some RNA base pairs lack base-base H-bonds,[8,9] many are intrinsically nonplanar,[8,9,22−25] and the conformational space of RNA base pairs can consist

* Corresponding author e-mail: sponer@ncbr.chemi.muni.cz (J.S.),petr.jurecka@upol.cz (P.J.).

† Institute of Biophysics, Academy of Sciences of the Czech Republic.

‡ Palacky University.

§ Institute of Organic Chemistry and Biochemistry, Academy of Sciences of the Czech Republic and Center of Biomolecules and Complex Molecular Systems.

|| University of Puerto Rico.

⊥ Masaryk University.

10.1021/ct800547k CCC: $40.75
Published on Web 02/25/2009

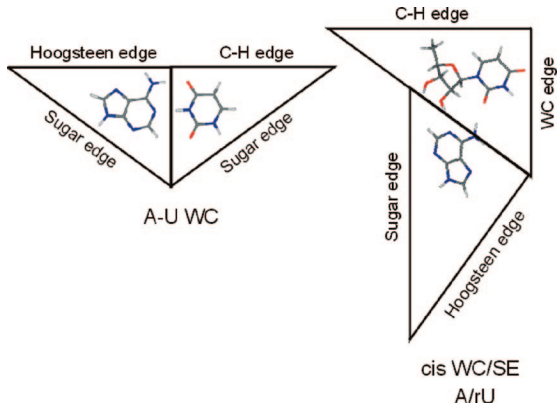

Figure 1. RNA nucleotides create base pairs in a systematic manner using three edges: Watson Crick, Sugar, and Hoogsteen (or C−H for pyrimidines).[9,21]

of several substates including water-inserted structures.[14,19] While many RNA base pairs are strong, with clear minima on the gas phase potential energy surfaces, others are weakly bound and are evidently held together by the overall RNA architecture.[22−26] Even these weak interactions, however, have biochemical relevance.

RNA base pairs have been classified by Leontis and Westhof according to their 3D shapes, considering the span of the base pair and orientation of the attached sugar phosphate backbone as the main structural determinants.[8,9,18] There are rare instances where this classification scheme fails to unambiguously describe an RNA base pair.[19]

The classification describes twelve principal base pair families as well as additional intermediate (bifurcated) families. The families are further divided into isosteric subgroups.[8,9] Each isosteric subgroup can be primarily characterized by the distance between the C1′ atoms and the mutual orientation of the corresponding vectors between C1′ and the glycosidic N (N1 in pyrimidines and N9 in purines). Isosteric base pairs can substitute for each other without affecting the RNA 3D structure. Since the RNA function depends chiefly on the 3D structure, isosteric substitutions are presumed to have a minimal effect on function, i.e., can be considered as functionally neutral substitutions.[8,9,15,16] This is known as the RNA isostericity principle. The isostericity principle is very robust, although it is based exclusively on structures and does not take into account the energetics of base pairing. The RNA 2D structures are considerably less conserved compared with the 3D structures, reflecting the fact that the 3D structure is the primary target of evolutionary constraints.[16] Nevertheless, the basic isostericity principle can be modulated by other factors. In such a case only a subset of possible isosteric substitutions is realized during evolution, or the frequency of occurrence (in the aligned sequences) differs for otherwise isosteric base pairs. A textbook example is the P-interaction tertiary quartet, where a G/U wobble base pair interacts with the C=G Watson Crick base pair while it cannot be substituted with the isosteric A/C base pair. The reason is an unfavorable electrostatic interaction between the A/C and C=G base pairs.[14] (In this paper, the "/" mark indicates non-WC base pairs, while G=C and A-U marks are used for the standard base pairs). The phylogenetic preference to utilize the G=C base pairs as receptors rather than the A-U ones in A-minor tertiary interactions could also be caused by the strength of the interactions, although available biochemical experiments did not indicate any large free energy differences.[20] Similarly, the otherwise isosteric cis-Watson−Crick/Watson−Crick A/G and G/A base pairs do not covary when the amino group of guanine is involved in out-of-plane or tertiary interactions utilizing the unpaired nonplanar guanine amino group.[22]

Despite their biological importance, computational and physical chemistry literature on the RNA base pairing is sparse,[14,19,23−37] contrasting the abundance of studies on simple Watson Crick base pairs. Computations provide a useful complement to experimental techniques and bioinformatics, as they can capture certain physical chemistry features of the RNA base pairing that cannot be directly visualized by experiment. The leading structural methods (X-ray crystallography,[1−7] structural bioinformatics,[8,9,16−18] and cryoelectron microscopy[38,39]) show basically static averaged RNA structures with some resolution limits. They thus provide only limited insights into the dynamics of the molecular interactions. NMR can provide more data on structural dynamics of RNA, but this method has significant resolution limits for RNA.[40−43] These techniques do not reveal the magnitude and nature of the intermolecular forces between the interacting groups and nucleotides. Insights into energetics of molecular interactions in RNA can be obtained by thermodynamics studies, which, however, do not allow an unambiguous analysis of the individual energy contributions.[44,45] Computational methods (molecular dynamics simulations and quantum chemistry) can complement the information available in atomic resolution structures by providing energetics of molecular interactions and structural dynamics.

Recently, we have carried out studies to complement the structural and bioinformatics classification of RNA base pairs using advanced quantum chemical calculations. These studies were specifically aimed at the characterization of RNA base pair families directly utilizing the sugar edges.[23−27] The structures of these complexes were relaxed using the density functional theory method, often with constraints to keep the base pairs in biologically relevant geometries. The interaction energies were derived at the MP2 level with the aug-cc-pVDZ basis set of atomic orbitals, which is sufficient for semiquantitative accuracy.[46] The results were compared with those obtained using the leading molecular modeling force field, AMBER.[47] The force field provides reasonably accurate results for these types of interactions, which is also reflected by its, generally very good, behavior in treating these base pairs in explicit solvent simulations.[19,34−37]

In the present study, we selected a set of 25 RNA base pairs on which to perform reference QM calculations and to obtain better insights into the balance of forces in various types of RNA base pairs. These 25 base pairs were chosen from five key families in which the sugar interaction is important or dominant, to cover as broad a spectrum as possible of RNA interactions. The gas phase interaction energies (see below) of these base pair interactions range from −10 to −31 kcal/mol. Our set also contains alternative substates in which some of the nucleobase amino groups are in amino-acceptor positions with respect to the 2′-OH group

of ribose. Due to the medium to low resolution of RNA X-ray structures, the amino-acceptor interactions would be difficult to prove by experiment, but their presence in RNAs cannot be ruled out.[22]

Most reference data reported in this paper were obtained using the MP2 method with binding energy results extrapolated to the complete basis set limit using the aug-cc-pVDZ and aug-cc-pVTZ basis sets of atomic orbitals (MP2/CBS level, see Methods below). For four base pairs we report the CBS(T) data, i.e., MP2/CBS calculations corrected for the higher electron correlation effects using the CCSD(T) method with a smaller basis set of atomic orbitals (see Methods below). In contrast to our preceding reference study on pure "base to base" nucleic acids base pairs,[48] in this study we were not able to carry out the CBS(T) calculations systematically due to the size of the RNA base pairs with one or two riboses directly involved in the interactions. Nevertheless, the MP2/CBS method is a viable benchmark, as the CCSD(T) corrections for H-bonded base pairs are only modest.

The studied base pairs were further evaluated using the perturbational DFT-SAPT technique,[49−52] which, with large basis sets, should yield results similar to those of the CCSD(T) method. The present SAPT calculations were carried out with the medium aug-cc-pVDZ basis set (see Methods below). The SAPT procedure allows decomposition of the interaction energies into well-defined components, corresponding to physical phenomena such as dispersion and induction. Although energy decompositions should not be overinterpreted, they provide new insights into the complexity of the RNA and DNA[53−59] base pair interactions.

Additional interaction energy computations on these base pairs were carried out with the SCS(MI)-MP2[60] and DFT-D[61,62] methods. The SCS(MI)-MP2 method is a recently proposed semiempirical MP2 technique providing a balanced description of stacked and H-bonded molecular clusters. The DFT-D is a fast method that includes the dispersion forces via a damped empirical correction. Finally, we carried out solvation calculations, which should give us an estimate of the stability of the base pairs studied in solution and provide an alternative energy ordering of the individual structures.

Methods

Geometry Optimizations. Geometry optimizations were carried out at the DFT (Density Functional Theory) level of theory using the Gaussian03 program package. The density functional was built up by Becke's three-parameter exchange and Lee−Yang−Parr's correlation functional (abbreviated as B3LYP). The 6−31G** basis set was used for all geometry optimizations. The B3LYP/6−31G**-optimized structures compare quite well with reference RIMP2/cc-pVTZ data and are entirely sufficient for the subsequent high-quality interaction energy calculations.[48] For many RNA base pairs we had to apply specific constraints to impose the target geometry, as unconstrained optimization would result in a different base pair type or a substantially perturbed geometry. Considering this fact, the flexibility of RNA pairing and the limited accuracy (resolution) of X-ray structures of complex RNAs, such geometry optimization procedure is entirely appropriate for our purpose. Where relevant, the geometries were taken from our preceding studies where more details about the geometries can be obtained.[23−26] All computed structures can be found in the Supporting Information.

Interaction Energies. Total interaction energy of a dimer [AB] ΔE^{AB} is defined as

$$\Delta E^{AB} = E^{AB} - E^{A} - E^{B} \quad (1)$$

where E^{AB} stands for the electronic energy of the whole system in the optimized geometry, and E^{A} and E^{B} are the electronic energies of the isolated subsystems A and B in the dimer geometry. In a few cases (base pairs with water insertion) we evaluated trimers; the extension of eq 1 for trimers is straightforward.[63]

The interaction energy (ΔE) of the standard electron correlation calculations (MP2 and CCSD(T)) has two components: the Hartree−Fock (HF) term (ΔE^{HF}) and the electron correlation term (ΔE^{cor}).

$$\Delta E = \Delta E^{HF} + \Delta E^{corr} \quad (2)$$

The main quantities described by the ΔE^{HF} term are the electrostatic interaction energy, short-range exchange repulsion, and polarization/charge transfer contributions to the total interaction energy. The ΔE^{corr} term is dominated by the dispersion attraction and also includes the electron correlation corrections to the other contributions. The correlation correction to electrostatics is usually repulsive since the electron correlation reduces the dipole moments of the monomers and thus also the electrostatic attraction.

All variational interaction energies are corrected for the basis set superposition error (BSSE) using the standard counterpoise procedure but do not include the deformation energies. The deformation energies are disregarded due to substantial structural alterations of the sugar-base segment upon base pairing in many RNA base pairs. Such rearrangements do not reflect the direct (electronic) forces between the interacting monomers. Thus a direct inclusion of monomer deformations into the interaction energies would bias the results. For a detailed discussion regarding the role of the deformation energies in base pairing calculations see refs 23−25 and 48 where we explain why a formal inclusion of deformation energies into the BSSE correction is inappropriate except when dealing with the simplest H-bonded systems.

The interaction energies were evaluated by the following methods:

Reference Interaction Energies. The MP2 calculations were performed with aug-cc-pVDZ (aDZ) and aug-cc-pVTZ (aTZ) basis sets and extrapolated to the complete basis set (MP2/CBS) using the technique of Helgaker and co-workers (eq 3).[64,65]

$$E_X^{HF} = E^{HF}_{CBS} + Ae^{-\alpha X} \text{ and } E_X^{corr} = E^{corr}_{CBS} + BX^{-3} \quad (3)$$

E_X and E_{CBS} are energies for the basis set with the largest angular momentum X and for the complete basis set, respectively, and α is a parameter fitted by the authors.[64,65]

In four cases (cWS C/rG, cWS C/rC, tWS A/rA, and tWS A/rG; see below for the abbreviation) the MP2/CBS energies were further corrected for the higher order correlation effects by adding a ΔCCSD(T) correction to the MP2/CBS energy. The ΔCCSD(T) correction is the difference between the CCSD(T) and MP2 interaction energies ($\Delta E^{CCSD(T)} - \Delta E^{MP2}$) calculated in a small basis set (eq 4).

$$\Delta E_{CBS(T)} = \Delta E_{CBS}{}^{MP2} + (\Delta E^{CCSD(T)} - \Delta E^{MP2})_{6\text{-}31+G^*} \quad (4)$$

For more details see elsewhere.[48,66]

All MP2 calculations were performed in TurboMole 5.10 program[67,68] with RI approximation (RI-MP2[68]) and CCSD(T) calculations in the Molpro package.[69] The frozen-core approximation was used throughout the study.

Decomposition of Interaction Energies via DFT-SAPT. The symmetry adapted perturbation theory method[70] allows for decomposition of the total interaction energies into physically meaningful components. Recently a computationally less demanding approach, in which the monomer is described by DFT and intermolecular interactions by SAPT, became available.[49−52,71] Here we chose the DFT-SAPT method implemented in the Molpro program package.[69] The total interaction energy is usually calculated as a sum of the following terms (eq 5):

$$E^{SAPT} = E_{el}{}^{(1)} + E_{exch}{}^{(1)} + E_{ind}{}^{(2)} + E_{exch\text{-}ind}{}^{(2)} + E_{disp}{}^{(2)} + E_{exch\text{-}disp}{}^{(2)} + \delta(HF) \quad (5)$$

The individual terms correspond to the electrostatic ($E_{el}{}^{(1)}$), exchange repulsion ($E_{exch}{}^{(1)}$), induction including charge transfer ($E_{ind}{}^{(2)}$) and dispersion ($E_{disp}{}^{(2)}$) contributions and their mixing terms ($E_{exch\text{-}ind}{}^{(2)}$ and $E_{exch\text{-}disp}{}^{(2)}$). δ(HF) is a correction term for the most important higher order contributions (for details see e.g. refs 64−66). In the following we will add the mixing terms $E_{exch\text{-}ind}{}^{(2)}$ and $E_{exch\text{-}disp}{}^{(2)}$ to their corresponding second order components denoting them as E_{ind} ($= E_{ind}{}^{(2)} + E_{exch\text{-}ind}{}^{(2)}$) and E_{disp} ($= E_{disp}{}^{(2)} + E_{exch\text{-}disp}{}^{(2)}$). All calculations are performed with density fitting, asymptotically corrected exchange-correlation density functional PBE0AC recommended by the authors[50] and the aug-cc-pVDZ basis set.

DFT Calculations with Empirical Dispersion Correction. DFT-D combines a standard DFT calculation with an empirical correction for long-range correlation, also called dispersion or van der Waals interaction.[61,62] At the typical van der Waals distances the empirical dispersion of the form $-C_6/r^6$ is dampened by a damping function, which corrects for the nonphysical divergence and correlation double counting in the overlap region.[62] Here we used a combination of the TPSS density functional, 6−311++G(3df,3pd) basis set and dispersion parametrization based on radii scaling as described in ref 62. DFT interaction energies were not corrected for the basis set superposition error, and dispersion parameters corresponding to BSSE uncorrected calculation were chosen (by adjusting the dispersion to the BSSE uncorrected DFT energies, the BSSE error is partially mitigated). DFT calculations were performed with the TurboMole 5.10[67,68] program, and dispersion was calculated using our own Fortran code.

SCS(MI)-MP2 Calculations. The spin component scaled second order Møller−Plesset perturbation method (SCS-MP2) scales the relative contributions of singlet and triplet states to the correlation energy.[60] In principle any scaling factors can be used, and the SCS-MP2 method can be parametrized against a particular training set in order to obtain accurate results for some given property. The molecular interactions variant of the SCS-MP2 method, SCS(MI)-MP2, was parametrized against the S22 test set of molecular complexes which includes a balanced mixture of hydrogen bonded, dispersion bound and mixed structures.[72,73] This method, when used along with the cc-pVTZ basis set, has shown promise in terms of its ability to accurately describe noncovalent interactions at a relatively low computational cost, including potential energy curves for the hydrogen bonded and stacked uracil dimer.[74]

Desolvation Energies. To calculate the desolvation energy upon complex formation, i. e., the energy difference between the solvated monomers and solvated complex, we used the IEFPCM model implemented in program Gaussian 03[75] with UAKS radii, PBE functional, 6−311G** basis set and default parameters for water. Resulting dehydration energies, which are computed as Gibbs energies, were then added to the MP2/CBS interaction energies to obtain an estimate of the base pair stability in water solution. The limitations of this approach are discussed below.

Abbreviations. We use standard abbreviation for the base pairs, where "t" and "c" stand for trans and cis, and "W", "H", and "S" stand for Watson Crick, Hoogsteen, and Sugar edges, respectively. When ribose is included in the QM calculations (we included the ribose for those base pairs where it directly participates in the interaction), it is denoted by a preceding "r". Thus, tHS A/rG means trans-Hoogsteen Sugar Edge base pair where adenine interacts with its Hoogsteen edge with guanosine sugar edge. Amino acceptor variants of the base pairs are indicated as "aa". G=C and A-U stand for the canonical base pairs.

Results and Discussion

Table 1 summarizes the calculated interaction energies, while Figure 2 summarizes the structures. The first three columns give the MP2/aug-cc-pVDZ, MP2/aug-cc-pVTZ, and MP2/CBS data (shown in bold). The numbers in parentheses in the third column are the CBS(T) values. The next three columns give SCS(MI)-MP2, SAPT, and DFT-D data. Finally, the last two columns list estimates of the solvation energies.

The first 22 rows in the Table 1 (rows cWS A/rG to tHS G/G) summarize data for 18 base pairs including four alternative structures with amino acceptor interactions (see above for abbreviations). The next row corresponds to the rC/rU base pair taken from the fully optimized GC/UG P-interaction; the rC/rU base pair is the key interaction in this important RNA tertiary quartet.[14,26] The subsequent six rows list pairwise interaction energies calculated for two systems that were formally optimized as trimers. The first one is the A-minor I triad, where the minor groove side of canonical rG=rC base pair acts as a receptor for adenosine through two SE/SE interactions.[10−12,26] A-minor I is the most common RNA tertiary interaction. The second trimer is a water mediated cSS rU/rC base pair. Finally,

Table 1. Total Interaction Energies and Solvation Energies (kcal/mol) Calculated by Different Methods for RNA Base Pairs (Figure *2*)

base pair	MP2/aDZ	MP2/aTZ	MP2/CBS (CBS(T))	SCS(MI)-MP2	DFT-SAPT aDZ	DFT-D TPSS/LP[c]	ΔG_{Solv}	MP2/CBS + ΔG_{Solv}
cWS A/rG	−16.00	−17.27	**−17.78**	−16.90	−14.62	−17.99	16.38	−1.40
cWS C/rG	−16.99	−18.24	**−18.74** (−17.74)	−18.10	−15.76	−18.87	17.70	−1.04
cWS C/rC	−21.84	−23.16	**−23.68** (−22.95)	−23.70	−21.23	−23.56	18.78	−4.90
tWS A/rA	−9.96	−10.70	**−11.01** (−10.62)	−10.10	−9.01	−10.95	10.30	−0.71
tWS A/rG	−16.51	−17.84	**−18.38** (−17.60)	−17.40	−14.92	−18.81	15.54	−2.84
tWS G/rC	−28.47	−29.97	**−30.58**	−31.60	−27.92	−30.87	25.14	−5.44
cSS rA/rA	−18.54	−20.18	**−20.84**	−20.00	−17.32	−21.81	18.36	−2.48
cSS rA/rC	−19.02	−20.53	**−21.15**	−20.70	−17.67	−21.46	20.64	−0.51
cSS rC/rA	−20.00	−22.15	**−23.02**	−22.10	−18.17	−23.88	19.91	−3.11
cSS rC/rU	−17.23	−18.85	**−19.49**	−18.80	−15.73	−19.05	19.24	−0.25
cSS rA/rG[d]	−23.63	−25.55	**−26.34**	−25.10	-	−27.32	24.24	−2.10
tSS rA/rG	−21.49	−23.41	**−24.20**	−22.40	−19.25	−24.22	21.71	−2.49
tSS rG/rC	−13.52	−14.13	**−14.38**	−14.50	−13.27	−14.10	14.69	0.31
tSS rG/rC aa[a]	−20.92	−22.69	**−23.41**	−22.40	−19.27	−23.53	21.88	−1.53
tWS C/rC	−9.72	−10.19	**−10.39**	−9.90	−9.33	−9.81	8.46	−1.93
tWS C/rC aa[a]	−14.46	−15.58	**−16.03**	−15.70	−13.48	−15.65	16.31	0.28
tWS U/rC	−15.90	−17.03	**−17.48**	−17.70	−15.16	−17.28	14.65	−2.83
tHS A/rA	−10.23	−11.00	**−11.33**	−10.40	−9.26	−11.13	10.60	−0.73
tHS A/rA aa[a]	−9.96	−10.97	**−11.39**	−10.60	−8.82	−11.17	12.79	1.40
tHS A/rG	−15.16	−16.34	**−16.82**	−15.80	−13.64	−17.22	15.69	−1.13
tHS A/rG aa[a]	−15.65	−16.86	**−17.36**	−16.60	−14.00	−17.94	16.70	−0.66
tHS G/G	−9.27	−9.76	**−9.96**	−10.00	−9.14	−9.95	9.35	−0.61
rU/rC pair of the P-motif	−16.98	−18.30	**−18.82**	−18.60	−15.79	−18.99	18.36	−0.46
rG/rA of A_minor I[d]	−15.22	−16.52	**−17.06**	−15.60	-	−17.22	18.98	1.92
rG=rC of A_minor I	−29.05	−30.64	**−31.29**	−31.70	−28.38	−31.72	25.08	−6.21
rA/rC of A_minor I	−17.02	−18.50	**−19.10**	−18.70	−15.69	−19.17	16.66	−2.44
cSS rU/rC WM[b]	−15.39	−16.81	**−17.38**	−17.00	−14.32	−15.91	17.27	−0.11
rU_wat WM[b]	−3.50	−3.83	**−3.96**	−3.68	−3.42	−4.29	3.84	−0.12
rC_wat WM[b]	−9.04	−10.02	**−10.42**	−10.19	−8.71	−11.14	9.44	−0.98
U-A	−15.30	−16.52	**−17.02**	−16.64	−14.52	−17.49	14.01	−3.01
C=G	−29.47	−31.21	**−31.91**	−32.42	−28.75	−32.37	24.64	−7.27
				wrt MP2/CBS	wrt MP2/aDZ	wrt MP2/CBS		
mean signed error				0.51	1.04	−0.13		
rmsd				0.78	1.16	0.51		

[a] aa: amino-acceptor. [b] WM: water mediated. [c] For the basis set description see Methods. [d] SAPT calculation failed.

the last two rows in Table 1 show data for canonical A-U and G=C pairs calculated with the same methods.

Nature and Magnitude of the Interaction Energies in Vacuum. Variations in total interaction energies in vacuum should be governed mainly by the number of common hydrogen bonds, their strength, and the overall complementarity of the electrostatic potentials. The MP2/CBS data support this view. The complexes with the largest interaction energies are characterized by multiple hydrogen bonds and often by strong hydrogen bonds including two oxygen atoms (OH...O) or an oxygen atom as the donor (OH...N) see, e.g., structures of G=C (−32.0 kcal/mol), tWS G/rC (−30.6 kcal/mol), cSS rA/rG (−26.3 kcal/mol), and tSS rA/rG (−24.2 kcal/mol) base pairs. On the other hand, the least stable structure, tHS G/G (−10.0 kcal/mol), contains just one NH...O bond. Thus, the base pairing strength seems to be roughly correlated with the number and character of the hydrogen bonds.

SAPT Energy Decomposition and the Role of Dispersion Energy. In our preceding studies we have suggested that the contribution of dispersion to the stabilities of many of the "SE" RNA base pairs is greater than its contribution to the overall stabilities of canonical base pairs.[23−26] This tentative idea was indirectly derived from the large values of the correlation components of the computed MP2/aug-cc-pVDZ interaction energies. The correlation component contains the dispersion energy (intermolecular correlation interaction energy) as the dominant contribution. However, such calculations do not allow an unambiguous decomposition because the correlation component also contains other terms, most notably the correlation correction of the electrostatic term. In addition, the balance of the HF and electron correlation components is sensitive to the intermonomer separation. Thus, in the present study we analyzed this issue using a rigorous evaluation of the dispersion energy by the SAPT procedure (Table 2). Note that the analysis is complicated by the fact that the individual energy terms are very sensitive to the intermonomer separations. The complex RNA base pairs obviously may have locally compressed or extended intermolecular contacts as the result of the overall structure balancing. This complexity will be demonstrated below on selected examples. Therefore, in order to obtain a correct picture, it is vital to analyze the relation of the dispersion, electrostatic, and induction term to the other energy terms. We suggest that the best measure of the relative role of, e.g., dispersion could be the % contribution of the dispersion energy to the overall attractive interaction (i.e., the sum of all attractive terms). This will be marked as Disp/Stab ratio in the following text and

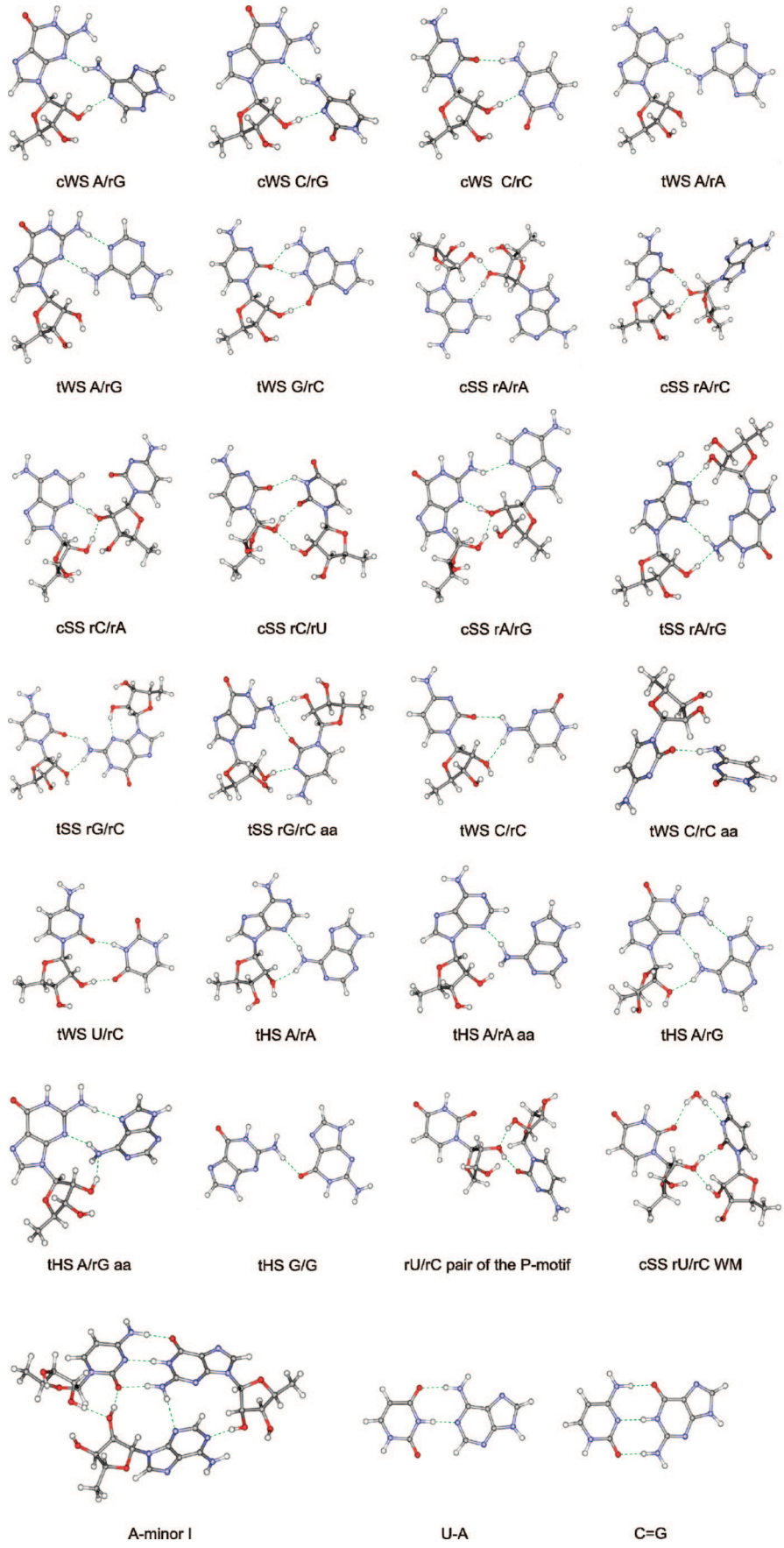

Figure 2. Structures of the calculated base pairs. Outmoded nucleotide order from reference 9 is used for tSS pairs.

analogically for electrostatics and induction Elst/Stab and Ind/Stab, respectively.

The Elst/Stab ratios for the canonical G=C and A-U base pairs are 58.0% and 56.7%. This actually is quite a small

Table 2. Decomposition of the Gas Phase Interaction Energies in RNA Base Pairs (kcal/mol)

	E_{el}[c]	E_{exch}[c]	E_{ind}[c]	E_{disp}[c]	δ(HF)[c]	E^{SAPT}	% E_{disp}[d]	ΔE^{HF}_{CBS}	$\Delta E^{corr}_{MP2/CBS}$	DFT[e]	DISP[f]
cWS A/rG	−26.4	32.9	−5.8	−11.0	−4.4	−14.6	23.2	−8.1	−9.7	−13.3	−4.7
cWS C/rG	−25.8	31.3	−6.0	−11.0	−4.3	−15.8	23.4	−9.3	−9.5	−14.0	−4.9
cWS C/rC	−30.6	33.8	−8.0	−10.8	−5.6	−21.2	19.6	−16.4	−7.3	−19.7	−3.9
tWS A/rA	−14.7	18.0	−2.5	−7.8	−2.0	−9.0	28.8	−4.4	−6.6	−6.9	−4.0
tWS A/rG	−27.2	33.5	−5.6	−11.2	−4.5	−14.9	23.1	−9.0	−9.4	−13.7	−5.1
tWS G/rC	−39.6	40.6	−10.4	−11.9	−6.7	−27.9	17.3	−24.5	−6.0	−27.0	−3.9
cSS rA/rA	−32.8	44.7	−8.8	−14.1	−6.4	−17.3	22.7	−9.2	−11.6	−15.5	−6.3
cSS rA/rC	−29.5	36.7	−7.1	−13.0	−4.8	−17.7	23.9	−11.1	−10.0	−15.1	−6.4
cSS rC/rA	−42.3	59.9	−10.9	−17.3	−7.6	−18.2	22.2	−9.6	−13.4	−16.9	−7.0
cSS rC/rU	−28.2	37.9	−7.3	−13.1	−5.0	−15.7	24.4	−9.3	−10.2	−13.6	−5.4
cSS rA/rG[g]	-	-	-	-	-	-	-	−11.4	−15.0	−18.7	−8.6
tSS rA/rG	−38.4	51.3	−8.4	−17.5	−6.3	−19.2	24.8	−8.0	−16.2	−16.4	−7.8
tSS rG/rC	−16.3	13.9	−3.2	−6.0	−1.7	−13.3	22.0	−11.0	−3.3	−11.4	−2.7
tSS rG/rC aa[a]	−33.4	42.8	−8.2	−14.9	−5.7	−19.3	23.9	−11.2	−12.2	−17.2	−6.3
tWS C/rC	−11.5	10.4	−2.1	−5.0	−1.1	−9.3	25.5	−6.6	−3.7	−7.4	−2.4
tWS C/rC aa[a]	−20.8	25.6	−4.9	−9.9	−3.5	−13.5	25.2	−8.5	−7.6	−11.3	−4.3
tWS U/rC	−24.2	28.8	−6.4	−8.6	−4.7	−15.2	19.7	−12.2	−5.2	−14.7	−2.6
tHS A/rA	−15.0	18.1	−2.4	−8.0	−1.9	−9.3	29.3	−4.6	−6.7	−7.1	−4.0
tHS A/rA aa[a]	−17.2	23.5	−3.3	−9.3	−2.5	−8.8	28.7	−3.4	−8.0	−6.9	−4.3
tHS A/rG	−23.2	28.0	−4.5	−10.4	−3.5	−13.6	24.9	−8.0	−8.8	−12.2	−5.0
tHS A/rG aa[a]	−24.5	30.7	−5.1	−11.3	−3.8	−14.0	25.3	−7.5	−9.9	−12.4	−5.6
tHS G/G	−11.7	10.9	−2.3	−4.7	−1.5	−9.1	23.3	−7.1	−2.9	−7.9	−2.0
rU/rC pair of the P-motif	−25.2	31.8	−6.8	−11.1	−4.4	−15.8	23.4	−10.8	−8.0	−13.9	−5.1
rG/rA of A_minor I[g]	-	-	-	-	-	-	-	−4.9	−12.1	−10.7	−6.5
rG=rC of A_minor I	−41.5	43.3	−10.5	−12.0	−7.7	−28.4	16.7	−25.4	−5.9	−27.9	−3.8
rA/rC of A_minor I	−29.2	36.3	−6.9	−11.4	−4.5	−15.7	21.9	−10.7	−8.4	−14.7	−4.4
cSS rU/rC WM[b]	−24.6	34.0	−7.3	−11.2	−5.2	−14.3	23.2	−8.5	−8.9	−12.9	−3.1
rU_wat WM[b]	−6.2	7.0	−1.2	−2.3	−0.7	−3.4	22.4	−2.7	−1.3	−3.5	−0.8
rC_wat WM[b]	−20.8	24.5	−4.0	−5.8	−2.6	−8.7	17.4	−6.4	−4.0	−9.7	−1.5
U-A	−28.1	35.0	−6.5	−9.5	−5.5	−14.5	19.1	−10.6	−6.4	−14.4	−3.1
C=G	−44.2	47.5	−11.3	−12.2	−8.5	−28.8	16.1	−25.8	−6.1	−28.8	−3.5

[a] aa: amino-acceptor. [b] WM: water mediated. [c] E_{el}: electrostatic component; E_{exch}: exchange repulsion; E_{ind}: induction (sum of E_{ind} and $E_{exch\text{-}ind}$); E_{disp}: dispersion (sum of E_{disp} and $E_{exch\text{-}disp}$); δ(HF): delta HF correction for higher order induction terms (see eq 5). [d] Percent of the dispersion attraction with respect to the total attraction ($100*E_{disp}/(E_{disp} + E_{ind} + E_{el} + \delta(HF))$). [e] DFT term from the DFT-D TPSS/LP calculations. [f] Dispersion term from the DFT-D TPSS/LP calculations. [g] SAPT calculation failed.

difference, taking into account that the A-U base pair is assumed to be less polar than the G=C one due to the considerably smaller polarity of the interacting monomers.[76] When considering all studied interactions, the Elst/Stab ratio ranges from 50% (rU...rC dimer from the corresponding water mediated structure) to 63% (rC interaction with water from the same structure). However, the later two structures are obvious outliers. Waters typically bridge the most polar sites of the base pairs, and then the direct nucleoside-nucleoside contacts in such water mediated structures are less electrostatic.

For the noncanonical RNA base pairs with conventional H-bonding (disregarding the alternative amino acceptor geometries), the Elst/Stab ratio is in the range of 52.6 to 59.9%. Comparing with the data for canonical base pairs this appears to be a significant variability. For most of the base pairs this ratio is smaller than 56%, indicating a weaker relative contribution of the electrostatics compared to the canonical base pairs.

The complexity of the SAPT analysis can be demonstrated for the amino-acceptor geometries of the base pairs. For example, the conventional binding of the tSS rG/rC base pair is associated with the small electrostatic term of −16.3 kcal/mol, which, at first sight, could indicate weak electrostatics. However, the Elst/Stab ratio is 59.9% which is the largest value among all base pairs. Then, the amino-acceptor variant of this base pair has an electrostatic term of −33.4 kcal/mol. This, at first sight, indicates an increase of the electrostatic nature of the base pair. This is obviously counterintuitive, as replacing one standard H-bond by an amino-acceptor interaction should reduce the electrostatic contribution to the total interaction. Indeed, for the amino-acceptor geometry all terms (in absolute value) increase, while the Elst/Stab ratio drops to 53.7%. These numbers nicely illustrate that, due to the sensitivity of the individual SAPT terms to interatomic distances, the decomposition is not straightforward and can be easily misinterpreted. As such, the literature interpretations of these values should be treated with great care.

The induction component (sum of the E_{ind} and δ(HF) terms, Ind/Stab) contributes between 16% for the tHS A/rA base pair and 26% for the rU/C interaction from the water mediated complex. It parallels the trends in the overall strengths (statistically, $R^2 = 0.59$). The induction correlates very nicely with the electrostatics ($R^2 = 0.96$), which in part explains the success of the pair additive empirical force fields, which use systematically overestimated charges (dipoles) to substitute for the missing polarization term.

The dispersion contribution to the sum of all attractive terms, Disp/Stab ($100*E_{disp}/(E_{disp} + E_{ind} + E_{el} + \delta(HF))$), varies between 16% in the G=C base pair and 29% in the tHS A/rA base pair (see Table 2). The relative dispersion contribution is smallest in the strongest complex and largest in one of the weakest complexes, but this is rather accidental, because the strength of the complex does not correlate with its dispersion contribution. In absolute values the dispersion

is largest in the extended complexes in which the aliphatic sugar hydrogen appears close to the interacting molecule, i.e., mostly in the SS rX/rY base pairs.

Closer inspection of the data, nevertheless, reveals a change in the balance between dispersion and electrostatic energies in many RNA base pairs, when these base pairs are compared with the reference canonical A-U and G=C base pairs. While the G=C base pair is known to be a strong electrostatic pair formed by two bases with large dipole moments, the A-U base pair has weaker electrostatics. Thus, we can consider properties of the A-U and G=C base pairs as demarcating the conventional range of the balance of forces in nucleic acids base pairs. To get the full picture, we consider not only the overall trends and correlations but also the individual cases and outliers, since the diversity of molecular interactions provides the variability of RNA molecular structures. RNA base pairs play numerous roles in nature, and trying to characterize them only by "average" base pairing properties and overall correlations could be like mixing apples and oranges.

The SAPT dispersion components of the A-U and G=C base pairs are −9.5 and −12.2 kcal/mol, respectively. The dispersion components in RNA base pairs (considering the first 23 rows of Table 1) vary between −4.7 and −17.5 kcal/mol, with the largest dispersion component in the cSS rC/rA (−17.3 kcal/mol) and tSS rA/rG (−17.5 kcal/mol) base pairs. This is also confirmed by the Disp/Stab ratio, which is 19 and 16% for the A-U and G=C base pairs, but in the range of 20−29% for the vast majority of RNA base pairs. The dispersion vs electrostatics ratio is 0.34:1 and 0.28:1 in the A-U and G=C base pairs and increases to 0.46:1 in the tSS rA/rG base pair and 0.43:1 in the rU/rC dimer from the P-interaction. The tSS rA/rG base pair is the key interaction stabilizing the A-minor I tertiary interaction. The differences are also visualized by the ratio between the dispersion energy and the total SAPT interaction energy, which is 0.42:1, 0.66:1, 0.70:1, and 0.91:1 in G=C, A-U, rC/rU P-interaction, and tSS rA/rG base pairs, respectively. This value is 0.75:1 in cWS A/rG base pair, etc. Therefore, although the data confirm that the RNA base pairs generally exhibit behavior typical of H-bonded systems, some of them clearly profit from an increased role of dispersion energy compared to canonical base pairs. Although the differences appear modest in the gas phase, they might be important in a natural RNA environment, where the primary H-bonds of the base pairs always compete with binding of water molecules. The increased dispersion is likely important mainly for the tertiary interactions which are exposed to solvent much more than Watson−Crick base pairs that are sheltered and stacked inside double helices.

Let us now comment on other options to separate the dispersion energy from the other contributions. A crude estimate is based on the evaluation of the MP2 (correlation) contribution to the intermolecular energy, i.e., the difference between the MP2 and HF interaction energies. Although this difference is often dominated by dispersion, it contains also the MP2 corrections to the electrostatics and induction, which cannot be separated. The data in Table 2 reveal that the MP2 intermolecular contribution is about 2.6 kcal/mol lower than that of the SAPT dispersion term, but it correlates with the DFT-SAPT dispersion values fairly well, with $R^2 = 0.83$. Because these lower dispersion values can be partly explained by the, typically repulsive, MP2 correction to electrostatics, it seems that the main contribution to the MP2 correction indeed comes from dispersion. Note that these conclusions are valid for hydrogen bonded complexes and should not be generalized to other types of bonding interactions without further justification. The studied base pairs show a large degree of variability in the ratio between HF and correlation contributions to the interaction energies. This ratio is 4.2:1 and 1.7:1 for the G=C and A-U base pairs, contrasting the values of 0.7:1 and 0.49:1 obtained for cSS rC/rA and tSS rA/rG RNA base pairs, i.e., for those RNA base pairs with the largest dispersion energy. However, closer inspection of the available data reveals that the actual differences in binding are not as dramatic. The difference between the A-U and G=C base pairs is not surprising, as the strong electrostatics of the G=C base pair is well-known. However, a substantial part of the difference in the ratios of HF and correlation components for these two base pairs is due to the correlation correction of the electrostatic term, caused by intramolecular electron correlation reduction of the dipoles of guanine and cytosine. It reduces mainly the correlation interaction energy of the G=C base pair and is not related to the dispersion energy which is due to intermolecular electron correlation contributions. This effect for the A-U base pair is considerably smaller as their smaller dipoles are much less affected by the electron correlation. Furthermore, close inspection of the SAPT data for the two RNA base pairs reveals that their large dispersion (the largest among systems studied here) and electron correlation energies are associated with the largest exchange repulsion terms of 59.9 and 51.3 kcal/mol. This evidently contributes to the large change in the HF vs correlation interaction energy ratio, especially for the cSS rC/rA base pair. Thus, the increased correlation interaction energy component rather reflects the larger compactness of the base pairs, which (in absolute values) increases magnitude of all the energy components. In other words, although we see that in some H-bonded RNA base pairs the role of dispersion energy is somewhat increased, this effect is smaller than one would guess from the ratio of HF and correlation components of the interaction energies.

Another way to approximate the dispersion contribution is based on empirical formulas, such as those used, along with an appropriate damping function, in the DFT-D method.[62] Table 2 shows that the empirical dispersion is far smaller in magnitude than the DFT-SAPT reference (on average by more than 6 kcal/mol). This is in agreement with our earlier study of DNA bases,[55] in which the undamped empirical dispersion was in fairly good agreement with the DFT-SAPT reference, but damping significantly reduced the magnitude of dispersion, especially in the hydrogen bonded complexes (by about 80%). In other orientations of bases, for instance in stacks, dispersion is damped much less (often by only about 20%). In this respect, the damped empirical dispersion should be understood as a complement to a given DFT functional rather than as an estimate of the dispersion

contribution, and therefore care is needed when assessing the importance of dispersion from the DFT-D data. Still, within a group of similar complexes (hydrogen bonded complexes here), relative dispersion contribution is informative, and the empirical dispersion correlates fairly well with the DFT-SAPT values here. As pointed out in ref 62, damping is in DFT-D used mainly to correct for double counting of the interaction energy at short distances, and it has little physical meaning. Damping is necessary, because current density functionals seemingly cover some portion of the correlation attraction at short distances. However, this attraction is largely spurious as it comes in part from the physically incorrect behavior of the exchange functional (for more details see ref 62). In this respect, decomposing the (supermolecular) DFT interaction energy is dubious. The perturbative (as opposed to supermolecular) DFT-SAPT values are much more meaningful, and they are necessary to obtain a rigorous estimate of the dispersion contribution to intermolecular interactions.

We have also tested whether the strength of the dispersion interaction can be related to the contact area between the bases, estimated as a half of the difference between the surface of the base pair and the surfaces of the isolated bases. The surfaces of the monomers and dimers were taken from the Gaussian 03 solvation calculations with standard UAKS radii of the atoms and default cavity construction algorithm. The contact area indeed correlates with the dispersion component of the interaction obtained by the SAPT method with $R^2 = 0.81$ (intercept forced to 0) and also with the damped dispersion from DFT-D ($R^2 = 0.78$). The average surface dispersion energy is -0.52 kcal mol^{-1} Å^{-2} for SAPT and -0.22 kcal mol^{-1} Å^{-2} for DFT-D. Although this correlation is statistically significant, dispersion prediction based on the contact area would be rather inaccurate. Also, our set of complexes is fairly homogeneous, and if another type of interaction was included, the correlation would likely be worse.

Correction for the Higher Order Electron Correlation Effects. In the four complexes for which we were able to calculate the ΔCCSD(T) correction (cWS C/rG, cWS C/rC, tWS A/rA, and tWS A/rG), the value of this term was smaller than 1 kcal/mol (see Table 1). For purely hydrogen bonded complexes this correction is usually very close to zero, and the value of roughly 1 kcal/mol may be related to the somewhat larger dispersion contribution in the present systems (as indicated by DFT-SAPT analysis). Due to the fact that the systems studied here interact in similar manners, the CCSD(T) corrections of approximately the same magnitude can also be expected for the remaining complexes in the present set. When we take into account the expected underestimation of the MP2/CBS limit by the aDZ/aTZ extrapolation, which should partially cancel out the missing CCSD(T) correction term, the value of approximately ±1 kcal/mol can be viewed as a reasonable estimate of the maximum error in present MP2/CBS interaction energies.

Comparison of Different QM Methods. Table 1 also compares the performance of different methods used to calculate interaction energies in vacuum. Comparisons are made with respect to the MP2/CBS energies. For the sake of consistency MP2/CBS energies were used as the reference even for structures where the ΔCCSD(T) correction terms are available.

The partly semiepirical SCS(MI)-MP2 by Distasio and Head-Gordon[72] paired with the cc-pVTZ basis set (column 5 in Table 1) compares fairly well with the MP2/CBS results with an average signed error of 0.51 kcal/mol and a root-mean-square deviation (rmsd) of 0.78 kcal/mol. An average underestimation of 0.51 kcal/mol is a good result, because the reference MP2 values likely on average overestimate the real value, as indicated by the available ΔCCSD(T) corrections. The SCS(MI)-MP2 − MP2/CBS differences cover a range from ∼−1 kcal/mol to +2.2 kcal/mol.

The DFT-D calculations with the TPSS functional and 6−311++G(3df,3pd) (LP) basis set demonstrate the high quality of the DFT-D relative energies (rmsd only 0.51 kcal/mol) and also yield small average errors (−0.13 kcal/mol). If we take into account the above-mentioned MP2 overestimation of the binding energies, it seems that the DFT-D method probably also slightly overestimates the interaction strengths, which is attributable to the well-known overestimation of hydrogen bonding stabilities in DFT-D.[62] Because of its speed/accuracy ratio the DFT-D method seems to be an excellent compromise. In addition, all these discussed differences are so subtle that they are expected to be insignificant in most applications. The DFT-D − MP2/CBS differences cover a range from ∼−1.0 kcal/mol to +1.5 kcal/mol.

The DFT-SAPT/aDZ calculations were compared with the MP2/aDZ results rather than with the MP2/CBS for the sake of basis set consistency. DFT-SAPT interaction energies are on average about 1 kcal/mol smaller (in absolute value), which is partly because MP2 overestimates dispersion and in part because of different basis set convergence behavior of the DFT-SAPT and MP2 methods. rmsd is rather large here, but standard deviation, which is a better measure of accuracy in the case of large systematic error, is quite small (0.53 kcal/mol). Because DFT-SAPT is often considered a more accurate method than MP2 this increases our confidence in the MP2/CBS data as a reference. The largest difference between DFT-SAPT and MP2/aDZ (2.24 kcal/mol) is found for the tSS rA/rG base pair.

Many-Body Terms. In the clusters containing three or more molecules the total interaction energy is not simply a sum of all the pair interaction energies. The difference between the pairwise sum and the total interaction energy - the nonadditivity - consists of the sum of the many-body terms. Two of our model complexes consist of three molecules (the A-minor I and the water mediated complex) where the 3-body terms arise. We calculated the 3-body term at the MP2/aug-cc-pVDZ level, and it amounts to −0.37 kcal/mol for the water mediated rU...rC pair and 0.84 kcal/mol for the A-minor I trimer. These terms are rather small, and it is unlikely that omitting them would affect any conclusion derived in this article. Inclusion of many body terms would be needed for quantitative analyses of larger clusters. This result is entirely consistent with calculations of base trimers.[77] Note that the MP2 method does not include eventual dispersion nonadditivity.

Inclusion of Solvent Effects. Within an aqueous environment, the electrostatic interaction loses much of its strength, which is reflected in the positive solvation Gibbs energies (column 8 of Table 1). Taken together with the gas phase interaction energies the resulting stabilizations in water (the last column of Table 1) are in line with our expectations for hydrogen bonded complexes. The calculated free energies of A-U and G=C base pairs are −3 and −7 kcal/mol, respectively. It is roughly in agreement with a contribution of −2 to −3 kcal/mol per H-bond suggested by force field calculations;[78] note, however, that these force field calculations include only the solvation effect on the electrostatic interactions.

The corresponding experimental estimates of base pair stability of −1 to −2 kcal/mol[79−81] per base pair are smaller in absolute value than our calculated values. The experiments, however, also include the destabilizing contribution of the configuration entropy including the cost of bringing the monomers together. In addition, the experimental data are derived for base pairs embedded within nucleic acids. It is not straightforward to subtract the net base pair stability from the overall free energy data. Data for H-bonded base pairs in water are in fact not available since base stacking is preferred over H-bonding in water; the free energy of stacking association in water is 0 to −1 kcal/mol, and the base pairing should thus be even less stable.[82−85]

Considering all these data, our calculations most likely exaggerate stabilities of canonical base pairs in water and also the difference in stability of A-U and G=C base pairs. We do not know, however, how much of this exaggeration is due to neglect of the configuration entropy changes. The paucity and complexity of the experimental data do not allow us to make any unambiguous conclusion.

Available theoretical data are also mutually inconsistent. Using MD free energy simulations with the AMBER force field, Stofer et al.[86] predicted values of −4.3 and −5.8 kcal/mol for A-T and G=C base pairs. A Langevine Dipole (LD) study by Florian et al.[87] predicted values of −0.8 and −1.8, apparently being much closer to the range expected based on the experimental data. The LD method was adjusted to reproduce the available experimental values of stacking free energies in water.

The G=C base pair is predicted to be the most stable one among all studied base pairs by our calculations, which is probably a correct result, taking into consideration the key role of this base pair in RNA thermodynamics. The calculations indicate that, among the noncanonical RNA base pairs, the most stable complexes in water are the tWS G/rC and cWS C/rC ones. The least stable RNA base pair is the tSS rG/rC one, when considering conventional binding only and disregarding the trimers. rG/rA of A-minor I and tHS A/rA amino-acceptor structures are predicted to be even less stable. Perhaps surprisingly, the tSS rA/rG base pair, which has the largest dispersion contribution, possesses only medium stability upon inclusion of continuum solvent effects. As noted above, however, we have to keep in mind that the calculated Gibbs solvation energies are of significantly lower accuracy than the gas phase interaction energies due to many approximations in the continuum model calculations. Also, the dehydration energy can be significantly different when a chosen motif is immersed in a certain RNA environment (the present calculations assume that both the pair and the isolated monomers are fully hydrated). Although water is probably a good average representation of the highly hydrated RNA structure, local interactions can significantly influence the stability of a given motif, both through modified solvation exposure and through interplay with additional interactions. Another factor, which is not included in our calculations, is the change of the configuration entropy of the solute (we add Gibbs solvation energies to interaction energies). Configuration entropy is very hard to estimate and depends critically on the local structure through flexibility. Our stabilization energies in the water environment should thus be viewed only as very rough estimates. We presently do not see any straightforward way how to improve the reliability of the RNA base pair solvation calculations or to independently verify them.

The solvent calculations can be perhaps used to get relative stability ranking of the RNA base pairs. However, even here some caution is needed. As the base pairs have quite variable shapes and thus solvent exposures, their stability evaluation can be biased by variable sensitivity to approximations of the solvent calculations. It is known from thermodynamics experiments that non-WC base pairs typically destabilize A-RNA helices; however, these effects are known to be context-dependent. In addition, it is known that double-helices are optimally sterically suited for canonical base pairs. In fact, the base pairing stabilization effects may be much more complicated than usually assumed. The stabilization or destabilization associated with a given base pair may very much depend on its context, on its complementarity to all the other interactions around, including specific water and ion binding. Thus, a given base pair may have very different influence on stabilization depending on where is the base pair inserted. Understanding of this "promiscuity" of molecular interactions would be a major step forward in studies of RNA structure and folding and, in our opinion, is one of the main challenges for computational chemistry of nucleic acids.

Conclusions

We have carried out reference quantum chemical calculations of base pairing energies for a representative selection of 25 diverse RNA base pairs utilizing the ribose moiety through the 2′-OH group, including structures with amino acceptor interactions. Such extended RNA base pairs are of primary importance for building up the complex three-dimensional structures of RNA molecules, which, thus far, have been largely ignored in the quantum chemical and physical chemistry literature. Since the RNA base pairs bring new interactions not present in standard base pairing, we suggest that some of our complexes should be added to the portfolio of structures considered in parametrization of computational methods that are designed to study RNA.

The base pairs were evaluated at the MP2 level with extrapolation to the complete basis set limit (CBS) of atomic orbitals. CCSD(T) correction terms were obtained for four base pairs. The interaction energy decomposition has been

performed using the DFT-SAPT perturbational procedure with the aug-cc-pVDZ basis set. Many RNA base pairs have a modestly increased role of dispersion attraction compared to canonical base pairs. However, the effect is smaller than one would assume based on assessment of the ratio of HF and correlation components of the interaction energies. The increased role of dispersion energy is nevertheless assumed to be important for stabilization of RNA tertiary interactions. Complexity of the interpretation of the SAPT energy decomposition is discussed.

SCS(MI)-MP2 and DFT-D methods have exhibited very good performance for RNA base pairs involving the ribose 2′-OH interactions as well as amino acceptor interactions. The differences between these methods and the reference data are nevertheless visibly larger than those achieved for canonical base pairs, with uncertainty in the calculated relative energies of ∼3 kcal/mol. The DFT-D method produces results that are generally closer to the reference data. We also roughly estimate the effect of aqueous solvent screening on the base pairing stability using continuum solvent approach.

The RNA base pairs are very diverse molecular interactions which offer a range of structures with different shapes, stabilities, and balance of interaction energy contributions.

Acknowledgment. This contribution was supported by the Grant Agency of the Academy of Sciences of the Czech Republic, grants No. IAA400040802 and IAA400550701; the Ministry of Education of the Czech Republic, grants LC06030, LC512, MSM0021622413, and MSM6198959216 (P.J.); and by the Academy of Sciences of the Czech Republic, grants no. AV0Z50040507, AV0Z50040702, and Z40550506. P.H. acknowledges the support from Praemium Academiae, Academy of Sciences of the Czech Republic, dedicated to P.H. in 2007. K.R. gratefully acknowledges the support of the NSF EPSCOR program (EPS-0701525). We thank Zdenek Salvet for kind help with the computer facilities in Brno.

Supporting Information Available: Structures of studied base pairs. This material is available free of charge via the Internet at http://pubs.acs.org.

References

(1) Cate, J. H.; Gooding, A. R.; Podell, E.; Zhou, K.; Golden, B. L.; Kundrot, C. E.; Cech, T. R.; Doudna, J. A. Crystal Structure of a Group I Ribozyme Domain: Principles of RNA Packing. *Science* **1996**, *273*, 1678–1685.

(2) Ban, N.; Nissen, P.; Hansen, J.; Moore, P. B.; Steitz, T. A. The Complete Atomic Structure of the Large Ribosomal Subunit at 2.4 A Resolution. *Science* **2000**, *289*, 905–920.

(3) Wimberly, B. T.; Brodersen, D. E.; Clemons, W. M., Jr.; Morgan-Warren, R. J.; Carter, A. P.; Vonrhein, C.; Hartsch, T.; Ramakrishnan, V. Structure of the 30S Ribosomal Subunit. *Nature* **2000**, *407*, 327–339.

(4) Moore, P. B.; Steitz, T. A. The Structural Basis of Large Ribosomal Subunit Function. *Annu. Rev. Biochem.* **2003**, *72*, 813–850.

(5) Schuwirth, B. S.; Borovinskaya, M. A.; Hau, C. W.; Zhang, W.; Vila-Sanjurjo, A.; Holton, J. M.; Cate, J. H. Structures of the Bacterial Ribosome at 3.5 A Resolution. *Science* **2005**, *310*, 827–834.

(6) Korostelev, A.; Trakhanov, S.; Laurberg, M.; Noller, H. F. Crystal Structure of a 70S Ribosome-tRNA Complex Reveals Functional Interactions and Rearrangements. *Cell* **2006**, *126*, 1065–1077.

(7) Selmer, M.; Dunham, C. M.; Murphy, F.; Weixlbaumer, A.; Petry, S.; Kelley, A. C.; Weir, J. R.; Ramakrishnan, V. Structure of the 70S Ribosome Complexed with mRNA and tRNA. *Science* **2006**, *313*, 1935–1942.

(8) Leontis, N. B.; Westhof, E. Conserved Geometrical Base-Pairing Patterns in RNA. *Q. Rev. Biophys.* **1998**, *31*, 399–455.

(9) Leontis, N. B.; Stombaugh, J.; Westhof, E. The Non-Watson-Crick Base Pairs and Their Associated Isostericity Matrices. *Nucleic Acids Res.* **2002**, *30*, 3497–3531.

(10) Nissen, P.; Ippolito, J. A.; Ban, N.; Moore, P. B.; Steitz, T. A. RNA Tertiary Interactions in the Large Ribosomal Subunit: the A-Minor Motif. *Proc. Natl. Acad. Sci. U.S.A.* **2001**, *98*, 4899–4903.

(11) Tamura, M.; Holbrook, S. R. Sequence and Structural Conservation in RNA Ribose Zippers. *J. Mol. Biol.* **2002**, *320*, 455–474.

(12) Lescoute, A.; Westhof, E. The A-Minor Motifs in the Decoding Recognition Process. *Biochimie* **2006**, *88*, 993–999.

(13) Gagnon, M. G.; Steinberg, S. V. GU Receptors of Double Helices Mediate tRNA Movement in the Ribosome. *RNA* **2002**, *8*, 873–877.

(14) Mokdad, A.; Krasovska, M. V.; Šponer, J.; Leontis, N. B. Structural and Evolutionary Classification of G/U Wobble Basepairs in the Ribosome. *Nucleic Acids Res.* **2006**, *34*, 1326–1341.

(15) Leontis, N. B.; Westhof, E. The 5S rRNA Loop E: Chemical Probing and Phylogenetic Data Versus Crystal Structure. *RNA* **1998**, *4*, 1134–1153.

(16) Lescoute, A.; Leontis, N. B.; Massire, C.; Westhof, E. Recurrent Structural RNA Motifs, Isostericity Matrices and Sequence Alignments. *Nucleic Acids Res.* **2005**, *33*, 2395–2409.

(17) Mokdad, A.; Frankel, A. D. ISFOLD: Structure Prediction of Base Pairs in Non-Helical RNA Motifs from Isostericity Signatures in Their Sequence Alignments. *J. Biomol. Struct. Dyn.* **2008**, *25*, 467–472.

(18) Sarver, M.; Zirbel, C. L.; Stombaugh, J.; Mokdad, A.; Leontis, N. B. FR3D: Finding Local and Composite Recurrent Structural Motifs in RNA 3D Structures. *J. Math. Biol.* **2008**, *56*, 215–252.

(19) Razga, F.; Koča, J.; Mokdad, A.; Šponer, J. Elastic Properties of Ribosomal RNA Building Blocks: Molecular Dynamics of the GTPase-Associated Center rRNA. *Nucleic Acids Res.* **2007**, *35*, 4007–4017.

(20) Battle, D. J.; Doudna, J. A. Specificity of RNA-RNA Helix Recognition. *Proc. Natl. Acad. Sci. U.S.A.* **2002**, *99*, 11676–11681.

(21) Nasalean, L.; Stombaugh, J.; Zirbel, C. L.; Leontis, N. B. RNA 3D Structural Motifs: Definition, Identification, Annotation, and Database Searching. In *Non-Protein Coding RNAs*, Walter, N. G., Woodson, S. A., Batey, R. T., Eds.; Springer: Berlin, 2009; Vol. 13, pp 1−26.

(22) Šponer, J.; Mokdad, A.; Šponer, J. E.; Špačková, N.; Leszczynski, J.; Leontis, N. B. Unique Tertiary and Neighbor Interactions Determine Conservation Patterns of

cis Watson-Crick A/G Base-pairs. *J. Mol. Biol.* **2003**, *330*, 967–978.

(23) Šponer, J. E.; Špačková, N.; Kulhánek, P.; Leszczynski, J.; Šponer, J. Non-Watson-Crick Base Pairing in RNA Quantum Chemical Analysis of the cis Watson-Crick/Sugar Edge Base Pair Family. *J. Phys. Chem. A* **2005**, *109*, 2292–2301.

(24) Šponer, J. E.; Špačková, N.; Leszczynski, J.; Šponer, J. Principles of RNA Base Pairing: Structures and Energies of the trans Watson-Crick/Sugar Edge Base Pairs. *J. Phys. Chem. B* **2005**, *109*, 11399–11410.

(25) Šponer, J. E.; Leszczynski, J.; Sychrovský, V.; Šponer, J. Sugar Edge/Sugar Edge Base Pairs in RNA: Stabilities and Structures from Quantum Chemical Calculations. *J. Phys. Chem. B* **2005**, *109*, 18680–18689.

(26) Šponer, J. E.; Réblová, K.; Mokdad, A.; Sychrovský, V.; Leszczynski, J.; Šponer, J. Leading RNA Tertiary Interactions: Structures, Energies, and Water Insertion of A-Minor and P-Interactions. A Quantum Chemical View. *J. Phys. Chem. B* **2007**, *111*, 9153–9164.

(27) Vokáčová, Z.; Šponer, J.; Šponer, J. E.; Sychrovský, V. Theoretical Study of the Scalar Coupling Constants across the Noncovalent Contacts in RNA Base Pairs: the cis- and trans-Watson-Crick/Sugar Edge Base Pair Family. *J. Phys. Chem. B* **2007**, *111*, 10813–10824.

(28) Roy, A.; Panigrahi, S.; Bhattacharyya, M.; Bhattacharyya, D. Structure, Stability, and Dynamics of Canonical and Noncanonical Base Pairs: Quantum Chemical Studies. *J. Phys. Chem. B* **2008**, *112*, 3786–3796.

(29) Bhattacharyya, D.; Koripella, S. C.; Mitra, A.; Rajendran, V. B.; Sinha, B. Theoretical Analysis of Noncanonical Base Pairing Interactions in RNA Molecules. *J. Biosci.* **2007**, *32*, 809–825.

(30) Brandl, M.; Meyer, M.; Sühnel, J. Water-Mediated Base Pairs in RNA: A Quantum-Chemical Study. *J. Phys. Chem. A* **2000**, *104*, 11177–11187.

(31) Oliva, R.; Tramontano, A.; Cavallo, L. Mg^{2+} Binding and Archaeosine Modification Stabilize the G15 C48 Levitt Base Pair in tRNAs. *RNA* **2007**, *13*, 1427–1436.

(32) Oliva, R.; Cavallo, L.; Tramontano, A. Accurate Energies of Hydrogen Bonded Nucleic Acid Base Pairs and Triplets in tRNA Tertiary Interactions. *Nucleic Acids Res.* **2006**, *34*, 865–879.

(33) Schneider, C.; Brandl, M.; Sühnel, J. Molecular Dynamics Simulation Reveals Conformational Switching of Water-Mediated Uracil-Cytosine Base-Pairs in an RNA Duplex. *J. Mol. Biol.* **2001**, *305*, 659–667.

(34) Réblová, K.; Špačková, N.; Štefl, R.; Csaszar, K.; Koča, J.; Leontis, N. B.; Šponer, J. Non-Watson-Crick Basepairing and Hydration in RNA Motifs: Molecular Dynamics of 5S rRNA Loop E. *Biophys. J.* **2003**, *84*, 3564–3582.

(35) Razga, F.; Koča, J.; Šponer, J.; Leontis, N. B. Hinge-Like Motions in RNA Kink-Turns: the Role of the Second A-Minor Motif and Nominally Unpaired Bases. *Biophys. J.* **2005**, *88*, 3466–3485.

(36) Krasovska, M. V.; Sefcikova, J.; Réblová, K.; Schneider, B.; Walter, N. G.; Šponer, J. Cations and Hydration in Catalytic RNA: Molecular Dynamics of the Hepatitis Delta Virus Ribozyme. *Biophys. J.* **2006**, *91*, 626–638.

(37) Špačková, N.; Šponer, J. Molecular Dynamics Simulations of Sarcin-Ricin rRNA Motif. *Nucleic Acids Res.* **2006**, *34*, 697–708.

(38) Frank, J.; Spahn, C. M. T. The Ribosome and the Mechanism of Protein Synthesis. *Rep. Prog. Phys.* **2006**, *69*, 1383–1417.

(39) Mitra, K.; Frank, J. Ribosome Dynamics: Insights from Atomic Structure Modeling into Cryo-Electron Microscopy Maps. *Annu. Rev. Biophys. Biomol. Struct.* **2006**, *35*, 299–317.

(40) Ferner, J.; Villa, A.; Duchardt, E.; Widjajakusuma, E.; Wöhnert, J.; Stock, G.; Schwalbe, H. NMR and MD Studies of the Temperature-Dependent Dynamics of RNA YNMG-Tetraloops. *Nucleic Acids Res.* **2008**, *36*, 1928–1940.

(41) Musselman, C.; Al-Hashimi, H. M.; Andricioaei, I. iRED Analysis of TAR RNA Reveals Motional Coupling, Long-Range Correlations, and a Dynamical Hinge. *Biophys. J.* **2007**, *93*, 411–422.

(42) Réblová, K.; Fadrná, E.; Sarzynska, J.; Kulinski, T.; Kulhánek, P.; Ennifar, E.; Koča, J.; Šponer, J. Conformations of Flanking Bases in HIV-1 RNA DIS Kissing Complexes Studied by Molecular Dynamics. *Biophys. J.* **2007**, *93*, 3932–3949.

(43) Shankar, N.; Xia, T.; Kennedy, S. D.; Krugh, T. R.; Mathews, D. H.; Turner, D. H. NMR Reveals the Absence of Hydrogen Bonding in Adjacent UU and AG Mismatches in an Isolated Internal Loop from Ribosomal RNA. *Biochemistry* **2007**, *46*, 12665–12678.

(44) Chen, G.; Kierzek, R.; Yildirim, I.; Krugh, T. R.; Turner, D. H.; Kennedy, S. D. Stacking Effects on Local Structure in RNA: Changes in the Structure of Tandem GA Pairs when Flanking GC Pairs are Replaced by isoG-isoC Pairs. *J. Phys. Chem. B* **2007**, *111*, 6718–6727.

(45) Mathews, D. H.; Sabina, J.; Zuker, M.; Turner, D. H. Expanded Sequence Dependence of Thermodynamic Parameters Improves Prediction of RNA Secondary Structure. *J. Mol. Biol.* **1999**, *288*, 911–940.

(46) Riley, K. E.; Hobza, P. Assessment of the MP2 Method, along with Several Basis Sets, for the Computation of Interaction Energies of Biologically Relevant Hydrogen Bonded and Dispersion Bound Complexes. *J. Phys. Chem. A* **2007**, *111*, 8257–8263.

(47) Cornell, W. D.; Cieplak, P.; Bayly, C. I.; Gould, I. R.; Merz, K. M.; Ferguson, D. M.; Spellmeyer, D. C.; Fox, T.; Caldwell, J. W.; Kollman, P. A. A 2nd Generation Force Field for the Simulation of Proteins, Nucleic Acids, and Organic Molecules. *J. Am. Chem. Soc.* **1995**, *117*, 5179–5197.

(48) Šponer, J.; Jurečka, P.; Hobza, P. Accurate Interaction Energies of Hydrogen-Bonded Nucleic Acid Base Pairs. *J. Am. Chem. Soc.* **2004**, *126*, 10142–10151.

(49) Hesselmann, A.; Jansen, G.; Schütz, M. Density-Functional Theory-Symmetry-Adapted Intermolecular Perturbation Theory with Density Fitting: A New Efficient Method to Study Intermolecular Interaction Energies. *J. Chem. Phys.* **2005**, *122*, 14103.

(50) Hesselmann, A.; Jansen, G. First-Order Intermolecular Interaction Energies from Kohn-Sham Orbitals. *Chem. Phys. Lett.* **2002**, *357*, 464–470.

(51) Hesselmann, A.; Jansen, G. Intermolecular Induction and Exchange-Induction Energies from Coupled-Perturbed Kohn-Sham Density Functional Theory. *Chem. Phys. Lett.* **2002**, *362*, 319–325.

(52) Hesselmann, A.; Jansen, G. Intermolecular Dispersion Energies from Time-Dependent Density Functional Theory. *Chem. Phys. Lett.* **2003**, *367*, 778–784.

(53) Toczylowski, R. R.; Cybulski, S. M. An Analysis of the Interactions between Nucleic Acid Bases: Hydrogen-Bonded Base Pairs. *J. Phys. Chem. A* **2003**, *107*, 418–426.

(54) Hesselmann, A.; Jansen, G.; Schütz, M. Interaction Energy Contributions of H-Bonded and Stacked Structures of the AT and GC DNA Base Pairs from the Combined Density Functional Theory and Intermolecular Perturbation Theory Approach. *J. Am. Chem. Soc.* **2006**, *128*, 11730–11731.

(55) Sedlák, R.; Jurečka, P.; Hobza, P. Density Functional Theory-Symmetry Adapted Perturbation Treatment Energy Decomposition of Nucleic Acid Base Pairs Taken from DNA Crystal Geometry. *J. Chem. Phys.* **2007**, *127*, 075104.

(56) Langner, K. M.; Sokalski, W. A.; Leszczynski, J. Intriguing Relations of Interaction Energy Components in Stacked Nucleic Acids. *J. Chem. Phys.* **2007**, *127*, 111102.

(57) Cybulski, H.; Sadlej, J. Symmetry-Adapted Perturbation-Theory Interaction-Energy Decomposition for Hydrogen-Bonded and Stacking Structures. *J. Chem. Theory Comput.* **2008**, *4*, 892–897.

(58) Guerra, C. F.; Bickelhaupt, F. M.; Snijders, J. G.; Baerends, E. J. The Nature of the Hydrogen Bond in DNA Base Pairs: The Role of Charge Transfer and Resonance Assistance. *Chem.-Eur. J.* **1999**, *5*, 3581–3594.

(59) Mo, Y. R. Probing the Nature of Hydrogen Bonds in DNA Base Pairs. *J. Mol. Model.* **2006**, *12*, 665–672.

(60) Grimme, S. Improved Second-Order Møller-Plesset Perturbation Theory by Separate Scaling of Parallel- and Antiparallel-Spin Pair Correlation Energies. *J. Chem. Phys.* **2003**, *118*, 9095–9102.

(61) Grimme, S. Accurate Description of van der Waals Complexes by Density Functional Theory Including Empirical Corrections. *J. Comput. Chem.* **2004**, *25*, 1463–1473.

(62) Jurečka, P.; Černý, J.; Hobza, P.; Salahub, D. R. Density Functional Theory Augmented with an Empirical Dispersion Term. Interaction Energies and Geometries of 80 Noncovalent Complexes Compared with Ab Initio Quantum Mechanics Calculations. *J. Comput. Chem.* **2007**, *28*, 555–569.

(63) Burda, J. V.; Šponer, J.; Leszczynski, J.; Hobza, P. Interaction of DNA Base Pairs with Various Metal Cations (Mg^{2+}, Ca^{2+}, Sr^{2+}, Ba^{2+}, Cu^{+}, Ag^{+}, Au^{+}, Zn^{2+}, Cd^{2+}, and Hg^{2+}): Nonempirical Ab Initio Calculations on Structures, Energies, and Nonadditivity of the Interaction. *J. Phys. Chem. B* **1997**, *101*, 9670–9677.

(64) Halkier, A.; Helgaker, T.; Jørgensen, P.; Klopper, W.; Olsen, J. Basis-Set Convergence of the Energy in Molecular Hartree-Fock Calculations. *Chem. Phys. Lett.* **1999**, *302*, 437–446.

(65) Halkier, A.; Helgaker, T.; Jørgensen, P.; Klopper, W.; Koch, H.; Olsen, J.; Wilson, A. K. Basis-Set Convergence in Correlated Calculations on Ne, N-2, and H2O. *Chem. Phys. Lett.* **1998**, *286*, 243–252.

(66) Jurečka, P.; Hobza, P. True Stabilization Energies for the Optimal Planar Hydrogen-Bonded and Stacked Structures of Guanine. .Cytosine, Adenine. .Thymine, and Their 9- and 1-Methyl Derivatives: Complete Basis Set Calculations at the MP2 and CCSD(T) Levels and Comparison with Experiment. *J. Am. Chem. Soc.* **2003**, *125*, 15608–15613.

(67) Ahlrichs, R.; Bär, M.; Häser, M.; Horn, H.; Kölmel, C. Electronic-Structure Calculations on Workstation Computers - the Program System Turbomole. *Chem. Phys. Lett.* **1989**, *162*, 165–169.

(68) Weigend, F.; Häser, M. RI-MP2: First Derivatives and Global Consistency. *Theor. Chem. Acc.* **1997**, *97*, 331–340.

(69) Werner, H.-J.; Knowles, P. J.; Lindh, R.; Manby, F. R.; Schütz, M.; Celani, P.; Korona, T.; Rauhut, G.; Amos, R. D.; Bernhardsson, A.; Berning, A.; Cooper, D. L.; Deegan, M. J. O.; Dobbyn, A. J.; Eckert, F.; Hampel, C.; Hetzer, G.; Lloyd, A. W.; McNicholas, S. J.; Meyer, W.; Mura, M. E.; Nicklass, A.; Palmieri, P.; Pitzer, R.; Schumann, U.; Stoll, H.; Stone, A. J.; Tarroni, R.; Thorsteinsson, T. *Molpro version 2006.1*; a Package of Ab Initio Programs, 2006. See http://www.molpro.net (accessed month year).

(70) Jeziorski, B.; Moszynski, R.; Szalewicz, K. Perturbation Theory Approach to Intermolecular Potential Energy Surfaces of van der Waals Complexes. *Chem. Rev.* **1994**, *94*, 1887–1930.

(71) Misquitta, A. J.; Podeszwa, R.; Jeziorski, B.; Szalewicz, K. Intermolecular Potentials Based on Symmetry-Adapted Perturbation Theory with Dispersion Energies from Time-Dependent Density-Functional Calculations. *J. Chem. Phys.* **2005**, *123*, 214103.

(72) Distasio, R. A.; Head-Gordon, M. Optimized Spin-Component Scaled Second-Order Møller-Plesset Perturbation Theory for Intermolecular Interaction Energies. *Mol. Phys.* **2007**, *105*, 1073–1083.

(73) Jurečka, P.; Šponer, J.; Černý, J.; Hobza, P. Benchmark Database of Accurate (MP2 and CCSD(T) Complete Basis Set Limit) Interaction Energies of Small Model Complexes, DNA Base Pairs, and Amino Acid Pairs. *Phys. Chem. Chem. Phys.* **2006**, *8*, 1985–1993.

(74) Pitoňák, M.; Riley, K. E.; Neogrady, P.; Hobza, P. Highly Accurate CCSD(T) and DFT-SAPT Stabilization Energies of H-Bonded and Stacked Structures of the Uracil Dimer. *ChemPhysChem* **2008**, *9*, 1636–1644.

(75) Frisch, M. J. ; Trucks, G. W.; Schlegel, H. B.; Scuseria, G. E.; Robb, M. A.; Cheeseman, J. R.; Montgomery, J. A., Jr.; Vreven, T.; Kudin, K. N.; Burant, J. C.; Millam, J. M.; Iyengar, S. S.; Tomasi, J.; Barone, V.; Mennucci, B.; Cossi, M.; Scalmani, G.; Rega, N.; Petersson, G. A.; Nakatsuji, H.; Hada, M.; Ehara, M.; Toyota, K.; Fukuda, R.; Hasegawa, J.; Ishida, M.; Nakajima, T.; Honda, Y.; Kitao, O.; Nakai, H.; Klene, M.; Li, X.; Knox, J. E.; Hratchian, H. P.; Cross, J. B.; Bakken, V.; Adamo, C.; Jaramillo, J.; Gomperts, R.; Stratmann, R. E.; Yazyev, O.; Austin, A. J.; Cammi, R.; Pomelli, C.; Ochterski, J. W.; Ayala, P. Y.; Morokuma, K.; Voth, G. A.; Salvador, P.; Dannenberg, J. J.; Zakrzewski, V. G.; Dapprich, S.; Daniels, A. D.; Strain, M. C.; Farkas, O.; Malick, D. K.; Rabuck, A. D.; Raghavachari, K.; Foresman, J. B.; Ortiz, J. V.; Cui, Q.; Baboul, A. G.; Clifford, S.; Cioslowski, J.; Stefanov, B. B.; Liu, G.; Liashenko, A.; Piskorz, P.; Komaromi, I.; Martin, R. L.; Fox, D. J.; Keith, T.; Al-Laham, M. A.; Peng, C. Y.; Nanayakkara, A.; Challacombe, M.; Gill, P. M. W.; Johnson, B.; Chen, W.; Wong, M. W.; Gonzalez, C.; Pople, J. A. *Gaussian 03; revision C.02*; Gaussian Inc.: Wallingford, CT, 2004.

(76) Šponer, J.; Leszczynski, J.; Hobza, P. Structures and Energies of Hydrogen-Bonded DNA Base Pairs. A Nonempirical Study with Inclusion of Electron Correlation. *J. Phys. Chem.* **1996**, *100*, 1965–1974.

(77) Šponer, J.; Burda, J. V.; Mejzlík, P.; Leszczynski, J.; Hobza, P. Hydrogen-Bonded Trimers of DNA Bases and Their Interaction with Metal Cations: Ab Initio Quantum-Chemical and Empirical Potential Study. *J. Biomol. Struct. Dyn.* **1997**, *14*, 613–628.

(78) Arora, N.; Jayaram, B. Energetics of Base Pairs in B-DNA in Solution: An Appraisal of Potential Functions and Dielectric Treatments. *J. Phys. Chem. B* **1998**, *102*, 6139–6144.

(79) Freier, S. M.; Sugimoto, N.; Sinclair, A.; Alkema, D.; Neilson, T.; Kierzek, R.; Caruthers, M. H.; Turner, D. H. Stability of XGCGCp, GCGCYp, and XGCGCYp Helixes: an Empirical Estimate of the Energetics of Hydrogen Bonds in Nucleic Acids. *Biochemistry* **1986**, *25*, 3214–3219.

(80) Turner, D. H.; Sugimoto, N.; Kierzek, R.; Dreiker, S. D. Free Energy Increments for Hydrogen Bonds in Nucleic Acid Base Pairs. *J. Am. Chem. Soc.* **1987**, *109*, 3783–3785.

(81) Tanner, N. K.; Cech, T. R. Guanosine Binding Required for Cyclization of the Self-Splicing Intervening Sequence Ribonucleic Acid from Tetrahymena Thermophila. *Biochemistry* **1987**, *26*, 3330–3340.

(82) Nakano, N. I.; Igarashi, S. J. Molecular Interactions of Pyrimidines, Purines, and Some Other Heteroaromatic Compounds in Aqueous Media. *Biochemistry* **1970**, *9*, 577–583.

(83) Ts'o, P. O. P.; Melvin, I. S.; Olson, A. C. Interaction and Association of Bases and Nucleosides in Aqueous Solutions. *J. Am. Chem. Soc.* **1963**, *85*, 1289–1296.

(84) van Holde, K. E.; Rossetti, G. P. A Sedimentation Equilibrium Study of the Association of Purine in Aqueous Solutions. *Biochemistry* **1967**, *6*, 2189–2194.

(85) Solie, T. N.; Schellman, J. A. The Interaction of Nucleosides in Aqueous Solution. *J. Mol. Biol.* **1968**, *33*, 61–77.

(86) Stofer, E.; Chipot, C.; Lavery, R. Free Energy Calculations of Watson-Crick Base Pairing in Aqueous Solution. *J. Am. Chem. Soc.* **1999**, *121*, 9503–9508.

(87) Florián, J.; Šponer, J.; Warshel, A. Thermodynamic Parameters for Stacking and Hydrogen Bonding of Nucleic Acid Bases in Aqueous Solution: Ab Initio/Langevin Dipoles Study. *J. Phys. Chem. B* **1999**, *103*, 884–892.

CT800547K

JCTC Journal of Chemical Theory and Computation

On the Nature of Bonding in Lone Pair···π-Electron Complexes: CCSD(T)/Complete Basis Set Limit Calculations

Jiong Ran[†] and Pavel Hobza*[,†,‡]

Institute of Organic Chemistry and Biochemistry, Academy of Sciences of the Czech Republic and Center for Biomolecules and Complex Molecular Systems, Flemingovo náměstí 2, 166 10 Prague 6, Czech Republic, and Department of Physical Chemistry, Palacký University, 771 46 Olomouc, Czech Republic

Received January 19, 2009

Abstract: The nature of the stabilization in lone pair···π-electron complexes was investigated using the highly accurate CCSD(T) method based on the complete basis set limit, as well as the DFT-SAPT perturabative method. Specifically, we studied various structures of benzene···water, benzene···dimethylether, and 1,2,4,5-tetracyanobenzene···water complexes. The lone pair···π-electron interactions between an unsubstituted aromatic ring and a water molecule are repulsive in the whole range of vertical distances. Partial stabilization results by rotating the water molecule by 90° (with the water and aromatic ring being localized in parallel planes) or by decreasing the negative charge at oxygen and simultaneously increasing the polarizability of the system, which provides stabilization even for genuine lone pair···π-electron interactions. In these cases, a substantial part of the stabilization stems from dispersion energy. Substituting an aromatic ring by electron-withdrawing cyano groups represents the most powerful way to achieve a substantial stabilization of genuine lone pair···π-electron interactions. This stabilization is comparable to quite strong H-bonding, originating in electrostatic and, to a slightly lesser degree, dispersion energies.

Introduction

The world of noncovalent interactions has become much broader in recent years, and new types of noncovalent bonding have appeared. In addition to classical (red-shifted) H-bonding, also improper blue-shifted H-bonding has been described, and the family of H-bonding interactions has been further extended by dihydrogen bonds.[1] Dihydrogen bonding (attractive interactions between two hydrogen atoms, one bearing positive and one bearing negative charge) was first detected in crystalline structures, and the same is true of other interactions between halogens and electronegative elements that also initially seemed very strange. The latter interaction was later called halogen bonding[2] and was explained as an interaction between the positive σ-hole at the top of negatively charged halogens and negatively charged electronegative elements. Again, from the crystalline structures, two other very unusual interaction types have appeared recently, namely, lone pair···π and anion···π interactions. Anion···π interactions were recently investigated by Kim et al.[3] In both cases, negatively charged elements are found at the top of the aromatic system, and thus, a water···benzene complex becomes the prototype of the lone pair···π interaction. Lone pair···π interactions have been found in different protein crystalline structures,[4−6] and despite the fact that the exact position of the hydrogens is not known, it is expected that lone pair···π and not X—H···π interactions are present.

Confirming the presence of lone pair···π interactions is thus an important task, which the analysis of crystalline structures, however, evidently cannot achieve. On the other hand, quantum chemical calculations could prove favorable because they not

* To whom correspondence should be addressed. E-mail: pavel.hobza@uochb.cas.cz.

[†] Academy of Sciences of the Czech Republic and Center for Biomolecules and Complex Molecular Systems.

[‡] Palacký University.

10.1021/ct900036y CCC: $40.75
Published on Web 03/23/2009

only provide sufficiently accurate energies and structures but also can shed light on the nature of the respective interactions. To investigate the nature of the bonding in lone pair···π complexes, it is necessary to determine the interaction energy as accurately as possible. Accurate stabilization energies of various types of noncovalent complexes, including the present ones, can be obtained only at the CCSD(T) level using the complete basis set (CBS) limit.[7] The MP2 method, even if performed at the CBS limit, cannot be used here, as it is known to overestimate the dispersion energy,[7] which might be critical for the complexes under consideration. The application of other recently introduced methods such as SCS-MP2[8] and its variants including SCS (MI)-MP2[9] or various DFT-D[10,11] approaches is limited in this case, because their good performances are based on parametrization toward a suitable data set of accurate energies (e.g., ref 12), which, however, does not contain the present stabilization motif. CCSD(T)/CBS values represent the benchmark data with a high accuracy, expected to be higher than 5% from the unknown exact values.[1] To understand the nature of the bonding of lone pair···π interactions, we need to know their energy components as well as their accurate stabilization energies. These values can be determined on the basis of perturbative SAPT[13] calculations.

To explain the stabilization in lone pair···π complexes, we decided to investigate water···benzene, dimethylether···benzene, and water···1,2,4,5-tetracyanobenzene complexes.

Methods

The structures of water, dimethylether, benzene, and 1,2,4,5-tetracyanobenzene were optimized without any constraints at the MP2 level using the cc-pVTZ basis set. This level provides accurate geometries of isolated systems.[14]

To understand the nature of lone pair···π interactions, we investigated different arrangements of benzene···water, benzene···dimethylether, and 1,2,4,5-tetracyanobenzene···water complexes (cf. Figure 1). In structures **1**, **4**, and **5**, the π-aromatic rings of benzene and 1,2,4,5-tetracyanobenzene interact exclusively with the lone electron pairs of water or dimethylether, whereas in structures **3** and **7**, the dominant stabilization feature is the O−H···π H-bond. In the cases of structures **2** and **6**, the π-aromatic rings interact with both the lone electron pairs and protons of water. The vertical distance (from O to the center of the aromatic ring) in all of the complexes investigated was optimized by the step-by-step method using the CCSD(T)/CBS energies. Gradient optimization at this level is impractical, and if based on another computational method, it can yield completely misleading structures.

The CCSD(T)/CBS binding energies were determined as a sum of the MP2/CBS energies and a CCSD(T) correction term.[15] This method takes advantage of the fact that the CCSD(T) and MP2 methods exhibit approximately the same basis set dependence.[16] The extrapolations based on the aug-cc-pVDZ and aug-cc-pVTZ basis sets were performed using the method of Halkier et al.[17] Because of the different dependences on the basis set, the Hartree−Fock energies and MP2 correlation energies were extrapolated separately. The CCSD(T) correction term [ΔCCSD(T)], defined as

$$\Delta\mathrm{CCSD(T)} = (\Delta E_{\mathrm{CCSD(T)}} - \Delta E_{\mathrm{MP2}})|_{\mathrm{basis}} \quad (1)$$

was then added to the MP2/CBS interaction energy. The correction term is generally obtained with a relatively small or medium-sized basis set, and in this case, we used the aug-cc-pVDZ basis set. One of the reasons for the success of this technique is the fact that the ΔCCSD(T) correction term converges much more quickly, as a function of the basis set size, than the CCSD(T) or MP2 interaction energies themselves.

All interaction energies were corrected for the basis set superposition error using the counterpoise method of Boys and Bernardi,[18] and the frozen-core approximation was systematically used throughout this work.

The CCSD(T)/CBS energies represent benchmark data but do not provide any information about the energy components that can be used to analyze the nature of the stabilization. Therefore, we also used the DFT-SAPT calculations[19,20] performed with the aug-cc-pVDZ basis set. This method allows for the separation of interaction energies into physically well-defined components, such as those arising from the electrostatic, induction, dispersion, and exchange terms. The DFT-SAPT interaction energy (E^{int}) is given by the equation

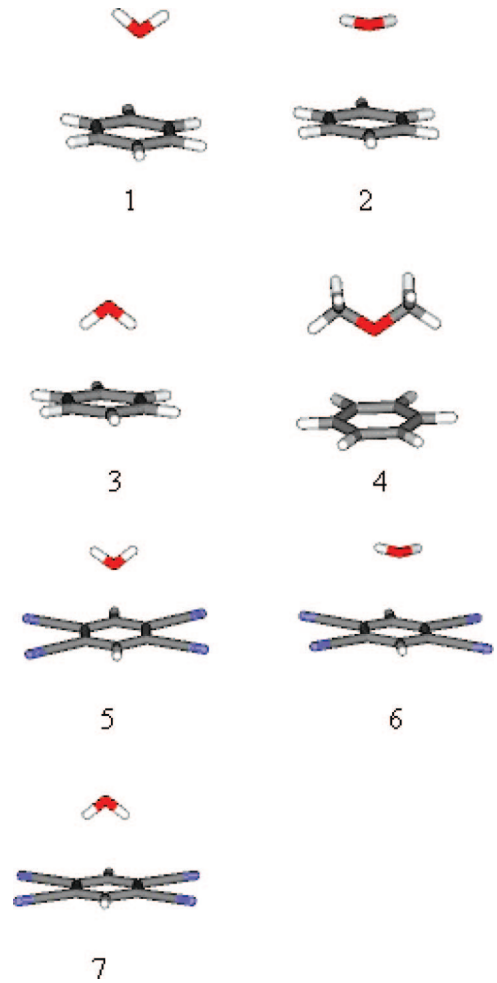

Figure 1. Various structures of the benzene···water (**1**−**3**), benzene···dimethylether (**4**), and 1,2,4,5-tetracyanobenzene···water (**5**−**7**) complexes.

$$E^{\text{int}} = E^{(1)}_{\text{el}} + E^{(1)}_{\text{ex}} + E^{(2)}_{\text{ind}} + E^{(2)}_{\text{ex-ind}} + E^{(2)}_{\text{disp}} + E^{(2)}_{\text{ex-disp}} + \delta(\text{HF}) \quad (2)$$

where the individual terms describe the electrostatic, exchange-repulsion, induction, exchange-induction, dispersion, and exchange-dispersion terms. The last term is a Hartree−Fock correction for higher-order contributions to the interaction energy. Throughout the study, the exchange-induction and exchange-dispersion terms will be included in the parent induction and dispersion terms. The DFT-SAPT interaction energies calculated with the aug-cc-pVDZ basis sets are known to be slightly underestimated with respect to mainly the dispersion energy.[19] The SAPT/aug-cc-pVTZ energy was estimated by enlarging the dispersion energy by 15% while keeping the other terms at the aug-cc-pVDZ values. Finally, Halkier et al.'s extrapolation scheme[17] was used to extrapolate the DFT-SAPT CBS energy from calculated aug-cc-pVDY and estimated aug-cc-pVTY values. All calculations were performed with the Gaussian 03[21] and MOLPRO[22] programs.

Results and Discussion

Table 1 lists the interaction energies of structures **2**−**6** (cf. Figure 1) at their minimum distances using various methods. Structures **1** and **7** are not included because no energy minima were detected in their potential energy curves. Table 2 lists the CCSD(T)/CBS interaction energies for all structures for selected distances from 2.2 to 15 Å. Table 3 reports the DFT-SAPT energies for structures **2**−**6** (structures **1** and **7** are omitted for the same reason as in Table 1). Tables S1 and S2 in the Supporting Information include all interaction energies determined by various methods for all structures considered and the Cartesian coordinates of complexes **1**−**7** at the MP2/cc-pVTZ level, respectively.

Overall, the CCSD(T)/CBS energies are consistent with the DFT-SAPT/CBS results. The energy differences are less than 5%. The only exception is structure **4**, where the energy difference is higher (17%) and can be explained by the much higher positive CCSD(T) correction term.

Benzene···Water Complexes. First, the genuine lone pair···π interactions (structure **1**) in the title complex were investigated. Figure 2 and Tables 2 and S1 (Supporting Information) show the dependence of the CCSD(T)/CBS and various MP2 interaction energies on the vertical distance. Evidently, neither of the curves exhibits an energy minimum (at negative energies), and only repulsion results. As the distance increases, the interaction energy becomes less repulsive, and with the exception of long distances, the CCSD(T) correction term is also repulsive. These results tell us clearly that there is no stabilization between the lone electron pairs and the aromatic ring. We do not know how to explain the existence of a small repulsion peak around 4.0−4.5 Å. It might be due to the extrapolation procedure or to the interaction of higher multipoles.

The only way to gain some stabilization in this complex is to change the orientation of the lone pair donor, specifically for which structures **2** and **3** were studied. In addition to the lone pair···π interaction, structure **2** is also expected to be stabilized by O−H···π H-bonding, which is of electrostatic origin. The respective energy curve (cf. Figure 2) exhibits a non-negligible minimum of 0.64 kcal/mol at a vertical separation of 3.4 Å. The MP2/CBS interaction energy is stabilizing, and the CCSD(T) correction term is small and repulsive. Note the significant basis set dependence of the MP2 interaction energy. Analyzing the energy components (cf. Table 3), we found that stabilization in this structure originates predominantly in dispersion energy, with the induction term being less important. Here, the slightly repulsive electrostatic term should be noted. All of these data confirm the fact that the stabilization of this lone pair···π interaction originates from dispersion and only to a lesser degree from induction and charge transfer, which is included in the induction energy term. Repulsive electrostatic energy showed no evidence of H-bonding.

Further rotation of the water molecule leads to a H-bonded structure (structure **3**) that is characterized by a large stabilization of more than 3 kcal/mol. The energy minimum is localized at 3.3 Å, and also here, the MP2 interaction energy is stabilizing, and the CCSD(T) correction term is repulsive. This structure contains two O−H···π H-bonds, and there is no evidence of a lone pair···π interaction. These findings are confirmed by the DFT-SAPT calculations. Table 3 shows a large attractive electrostatic term, a rather small induction term, and a surprisingly large dispersion energy.

Table 1. Calculated Intermolecular Distances (R in Å) and Interaction Energies (kcal/mol) for the Energy Minima of the Different Lone Pair···π Complexes[a]

complex	R	MP2/a VDZ	MP2/a VTZ	MP2/CBS	ΔCCSD (T)	CCSD (T)/CBS
2	3.4	−0.375	−0.601	−0.696	0.060	−0.636
3	3.3	−2.837	−3.218	−3.378	0.129	−3.249
4	3.2	−0.873	−1.086	−1.176	0.354	−0.822
5	3.0	−4.853	−5.015	−5.083	0.171	−4.912
6	3.3	−2.453	−2.585	−2.641	0.009	−2.632

[a] Compare Figure 1; structures **1** and **7** have no energy minima.

Table 2. Calculated Interaction Energies (kcal/mol) at Various Distances (R in Å) for Various Structures of the Lone Pair···π Complexes at the CCSD(T)/CBS Level

	complexes						
R	**1**[a]	**2**	**3**	**4**	**5**	**6**	**7**
2.20	16.400	21.386	36.706	15.472	7.693	18.064	43.173
2.50	5.729	6.756	9.833	3.633	−1.755	3.846	15.691
2.80	1.829	0.791	−0.053	0.073	−4.574	−1.244	5.029
2.90	1.237	0.542	−1.486	−0.400	−4.883	−1.960	3.334
3.00	0.845	0.010	−2.392	−0.667	−4.912	−2.271	2.174
3.10	0.591	−0.320	−2.911	−0.791	−4.866	−2.514	1.402
3.20	0.436	−0.512	−3.171	−0.822	−4.696	−2.618	0.914
3.30	0.346	−0.606	−3.249	−0.794	−4.558	−2.632	0.509
3.40	0.300	−0.636	−3.208	−0.729	−4.307	−2.577	0.370
3.50	0.283	−0.626	−3.087	−0.645	−4.121	−2.483	0.317
3.60	0.284	−0.587	−2.924	−0.551	−3.888	−2.364	0.242
3.70	0.296	−0.525	−2.732	−0.456	−3.662	−2.228	0.278
3.80	0.312	−0.477	−2.586	−0.367	−3.440	−2.089	0.294
4.00	0.343	−0.355	−2.142	−0.207	−3.031	−1.814	0.303
4.50	0.371	−0.136	−1.390	0.043	−2.215	−1.243	0.395
5.00	0.337	0.010	−0.909	0.131	−1.609	−0.862	0.500
6.00	0.236	0.029	−0.430	0.140	−0.969	−0.509	0.333
8.00	0.103	0.020	−0.138	0.092	−0.417	−0.179	0.096
10.00	0.048	0.008	−0.058	0.036	−0.226	−0.111	−0.081
15.00	0.011	0.001	−0.012	0.008	−0.057	−0.154	−0.147

[a] Compare Figure 1.

Table 3. Calculated[a] DFT-SAPT Interaction Energies (kcal/mol) for the Lone Pair···π Complexes at Each Minimum Distance

structure[b]	$E^{(1)}_{el}$	$E^{(1)}_{ex}$	$E^{(1)}$	$E^{(2)}_{ind}$	$E^{(2)}_{disp}$ [c]	$E^{(2)}$ [c]	δ(HF)	E (kcal/mol)[c,d]
2	0.033	1.758	1.791	−0.229	−1.753 (−2.015)	−1.981 (−2.244)	−0.046	−0.237 (−0.499, −0.609)
3	−3.080	3.980	0.900	−0.507	−2.868 (−3.298)	−3.375 (−3.805)	−0.304	−2.779 (−3.209, −3.390)
4	0.637	2.727	3.364	−0.275	−3.277 (−3.768)	−3.552 (−4.043)	−0.113	−0.301 (−0.792, −0.999)
5	−4.417	3.541	−0.876	−0.566	−2.883 (−3.315)	−3.449 (−3.881)	−0.195	−4.520 (−4.952, −5.134)
6	−1.656	2.152	0.496	−0.365	−2.218 (−2.551)	−2.583 (−2.916)	−0.064	−2.151 (−2.484, −2.624)

[a] DFT-SAPT (PBE0AC/aug-cc-pVDZ basis set). [b] Compare Figure 1; structures **1** and **7** have no energy minima. [c] Values in parentheses were estimated using the aug-cc-pVTZ basis set. [d] Second values in parentheses were extrapolated from energies calculated using the aug-cc-pVDZ basis set and energies estimated using the aug-cc-pVTZ basis set.

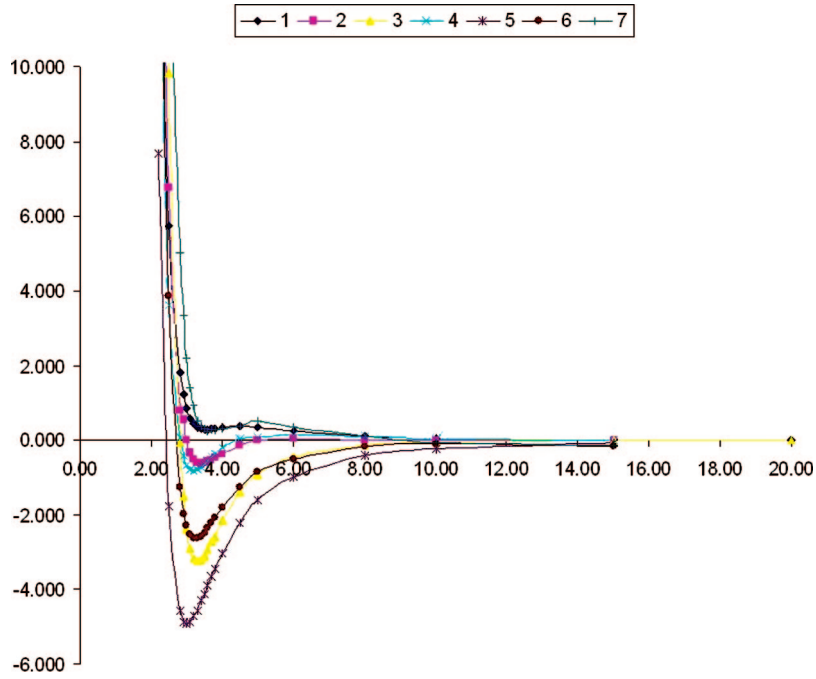

Figure 2. Calculated potential energy plot for the various lone pair···π complexes (see Figure 1 for compound numbers) at the CCSD(T)/CBS level. The *X* and *Y* axes show distance (Å) and the interaction energy (kcal/mol), respectively.

The latter term is almost as attractive as the electrostatic energy, and if we consider the estimated aug-cc-pVTZ value, it is even larger. It must be mentioned that this structure is different from the standard H-bonded structure, where just one hydrogen interacts with the aromatic ring. Consequently, the distance between the centers of mass of the two subsystems is smaller in the present structure, which makes the dispersion energy larger. Nevertheless, in all H-bonded complexes of the aromatic system with water, the dispersion energy should be of comparable importance to the electrostatic energy.

Benzene···Dimethylether Complex. We have seen that the approach of water and benzene (structure **1**) is connected with repulsion only. By substituting hydrogens in water with methyl groups (passing from water to dimethylether), the situation is changed. Analyzing the charge at oxygen, we found that it is less negative in dimethylether than in water, which indicates that the electrostatic repulsion term might be smaller in the dimethylether···benzene complex than in the water···benzene complex. Further, the polarizability of dimethylether is higher than that of water, which implies a larger dispersion energy stabilization in the dimethylether··· benzene complex. Tables 1, 2, and S1 (Supporting Information) and Figure 2 suggest the existence of a rather deep minimum (0.82 kcal/mol) localized at 3.2 Å. In this case, the MP2 interaction energy is attractive, and the CCSD(T) correction term repulsive. In contrast to the previous cases, the latter term is considerably larger. The DFT-SAPT analysis (Table 3) undoubtedly clarifies the origin of stabilization. As in the previous cases, it is the dispersion energy that is almost completely responsible for the stabilization of the complex. The induction energy, which includes charge transfer, is more than 1 order of magnitude smaller than the dispersion energy. The negligible role of charge transfer is also reflected in the rather small value of the δ(HF) term (see Table 3). In agreement with the above-mentioned facts, the electrostatic energy is repulsive.

We can summarize that, when polarizability of the lone pair acceptor is increased and its negative partial charge on the interacting site is decreased, the lone pair···π interactions become attractive. Evidently, upon larger substitution, the attraction can be substantially larger. The attraction originates, however, unambiguously from the London dispersion energy.

1,2,4,5-Tetracyanobenzene···Water Complexes. Upon substitution of the hydrogens at positions 1, 2, 4, and 5 of benzene with electron-withdrawing cyano groups, the π-electron clouds above the ring become less negative. The elec-

trostatic potentials of benzene and 1,2,4,5-tetracyanobenzene are entirely different (not shown). Whereas the former contains a significant negative region above the ring, the latter does not have any negative region but has only a positive one. Consequently, interactions with proton donors (H-bonding) should be suppressed, whereas interactions with proton acceptors (electron donors) should be magnified. In both cases, we considered the stacking approach, which was fully confirmed in Tables 1, 2, and S1 (Supporting Information) and Figure 2. Structure **5** exhibits a very deep energy minimum of about 5 kcal/mol at a rather short distance of 3.0 Å. Notice the relatively large (positive) value of the CCSD(T) correction term. Rotating the water molecule by 180°, i.e., when water approaches benzene by its hydrogens (structure **7**), the situation is reversed, and practically no minimum in the potential energy curve is detected. We do not know how to explain the small attraction beyond 10 Å. This might be due to the extrapolation method used or to interactions of higher multipoles. The approach of water and 1,2,4,5-tetracyanobenzene localized in parallel planes (structure **6**) is characterized by a relatively deep energy minimum of 2.63 kcal/mol at a rather large vertical separation of 3.3 Å. The DFT-SAPT analysis shows a very large attractive electrostatic energy for structure **5**. This energy is considerably less attractive for structure **6**. Induction energy is largest for structure **5**, and the same is true for dispersion energy. The largest values of dispersion and induction energies for structure **5** are certainly also related to its very short vertical distance (3.0 and 3.3 Å in structures **5** and **6**, respectively). The electrostatic and dispersion energies in complex **5** are similar, which resembles the situation in complex **3** (see above).

Substituting benzene with electron-withdrawing groups evidently represents the most powerful way to stabilize the lone pair$\cdots\pi$-electron complexes. The respective stabilization can be substantial, even comparable to a rather strong H-bonding.

Conclusions

(i) The lone pair$\cdots\pi$-electron interactions between an unsubstituted aromatic ring and a water molecule are repulsive for the whole range of vertical distances. Partial stabilization results when the water molecule is rotated by 90° (with the water and the aromatic ring located in parallel planes). In this structural arrangement, there is no H-bonding, and the dominant stabilization comes from dispersion energy.

(ii) Decreasing the negative charge at oxygen and increasing the polarizability of the system provides stabilization even for genuine lone pair$\cdots\pi$ electron interactions. Also in this case, the substantial part of the stabilization stems from dispersion energy.

(iii) Substituting an aromatic ring by electron-withdrawing groups represents the most powerful way to achieve a substantial stabilization of genuine lone pair$\cdots\pi$-electron interactions. This stabilization, which is comparable to a rather strong H-bonding, originates in electrostatic and, to a slightly lesser degree, dispersion energy.

Acknowledgment. This work was part of Research Project Z4 055 0506 of Institute of Organic Chemistry and Biochemistry, Academy of Sciences of the Czech Republic, and was supported by grants from the Ministry of Education of the Czech Republic (Center for Biomolecules and Complex Molecular Systems, LC512 and MSM6198959216) and Grant Agency of the Academy of Sciences of the Czech Republic (A400550510). The authors acknowledge the support of Praemium Academiae of the Academy of Sciences of the Czech Republic, awarded to P.H. in 2007.

Supporting Information Available: Intermolecular distances (R in Å) and interaction energies (kcal/mol) for the lone pair$\cdots\pi$ complexes obtained with various methods (Table S1), as well as Cartesian coordinates of complexes 1−7 (monomers optimized at the MP2/cc-pVTZ level) (Table S2) are available free of charge via the Internet at http://pubs.acs.org.

References

(1) (a) Crabtree, R. H.; Siegbahn, P. E. M.; Eisenstein, O.; Rheingold, A. L.; Koetzle, T. F. *Acc. Chem. Res.* **1996**, *29*, 348. (b) Hobza, P.; Havlas, Z. *Chem. Rev.* **2000**, *100*, 4253. (c) Hobza, P.; Müller-Dethlefs, K. *Chem. Rev.* **2000**, *100*, 143. (d) Hobza, P.; Zahradník, R.; Müller-Dethlefs, K. *Collect. Czech. Chem. Commun.* **2006**, *71*, 443.

(2) Aufinger, P.; Hays, F. A.; Westhof, E.; Ho, P. S. *Proc. Natl. Acad. Sci. U.S.A.* **2004**, *101*, 16789.

(3) Kim, D. Y.; Singh, N. J.; Kim, K. S. *J. Chem. Theory Comput.* **2008**, *4*, 1401.

(4) Steiner, T. *Biophys. Chem.* **2002**, *95*, 195.

(5) Sarkhel, S.; Rich, A.; Egli, M. *J. Am. Chem. Soc.* **2003**, *125*, 8998.

(6) Egli, M.; Sarkhel, S. *Acc. Chem. Res.* **2007**, *40*, 197.

(7) Jurečka, P.; Šponer, J.; Černý, J.; Hobza, P. *Phys. Chem. Chem. Phys.* **2006**, *8*, 1985.

(8) Grimme, S. *J. Chem. Phys.* **2003**, *118*, 141102.

(9) Distasio, R. A.; Head-Gordon, M. *Mol. Phys.* **2007**, *105*, 1073.

(10) Grimme, S. *J. Comput. Chem.* **2004**, *25*, 1463.

(11) Jurečka, P.; Černý, J.; Hobza, P.; Salahub, D. *J. Comput. Chem.* **2007**, *28*, 555.

(12) Řezáč, J.; Jurečka, P.; Riley, K. E.; Černý, J.; Valdes, H.; Pluháčková, K.; Berka, K.; Řezáč, T.; Pitoňák, M.; Vondrášek, J.; Hobza, P. *Collect. Czech. Chem. Commun.* **2008**, *73*, 1261.

(13) Jeziorski, B.; Moszynski, R.; Szalewicz, K. *Chem. Rev.* **1994**, *94*, 1887.

(14) Dabkowska, I.; Jurečka, P.; Hobza, P. *J. Chem. Phys.* **2005**, *122*, 204322.

(15) Jurečka, P.; Hobza, P. *J. Am. Chem. Soc.* **2003**, *125*, 15608.

(16) Jurečka, P.; Hobza, P. *Chem. Phys. Lett.* **2002**, *365*, 89.

(17) Halkier, A.; Helgaker, T.; Jorgensen, P.; Klopper, W.; Koch, H.; Olsen, J.; Wilson, A. K. *Chem. Phys. Lett.* **1998**, *286*, 243.

(18) Boys, S. F.; Bernardi, F. *Mol. Phys.* **1970**, *19*, 553.

(19) Hesselman, A.; Jansen, G.; Schutz, M. *J. Chem. Phys.* **2005**, *122*, 14103.

(20) Hesselman, A.; Jansen, G.; Schutz, M. *J. Am. Chem. Soc.* **2006**, *128*, 11730.

(21) Frisch, M. J.; Trucks, G. W.; Schlegel, H. B.; Scuseria, G. E.; Robb, M. A.; Cheeseman, J. R.; Montgomery, J. A., Jr.; Vreven, T.; Kudin, K. N.; Burant, J. C.; Millam, J. M.; Iyengar, S. S.; Tomasi, J.; Barone, V.; Mennucci, B.; Cossi, M.; Scalmani, G.; Rega, N.; Petersson, G. A.; Nakatsuji, H.; Hada, M.; Ehara, M.; Toyota, K.; Fukuda, R.; Hasegawa, J.; Ishida, M.; Nakajima, T.; Honda, Y.; Kitao, O.; Nakai, H.; Klene, M.; Li, X.; Knox, J. E.; Hratchian, H. P.; Cross, J. B.; Bakken, V.; Adamo, C.; Jaramillo, J.; Gomperts, R.; Stratmann, R. E.; Yazyev, O.; Austin, A. J.; Cammi, R.; Pomelli, C.; Ochterski, J. W.; Ayala, P. Y.; Morokuma, K.; Voth, G. A.; Salvador, P.; Dannenberg, J. J.; Zakrzewski, V. G.; Dapprich, S.; Daniels, A. D.; Strain, M. C.; Farkas, O.; Malick, D. K.; Rabuck, A. D.; Raghavachari, K.; Foresman, J. B.; Ortiz, J. V.; Cui, Q.; Baboul, A. G.; Clifford, S.; Cioslowski, J.; Stefanov, B. B.; Liu, G.; Liashenko, A.; Piskorz, P.; Komaromi, I.; Martin, R. L.; Fox, D. J.; Keith, T.; Al.Laham, M. A.; Peng, C. Y.; Nanayakkara, A.; Challacombe, M.; Gill, P. M. W.; Johnson, B.; Chen, W.; Wong, M. W.; Gonzalez, C.; Pople, J. A. *Gaussian 03*; Revision C.02. Gaussian, Inc.: Wallingford CT, 2004.

(22) Werner, H.-J.; Knowles, P. J.; Lindh, R.; Manby, F. R.; Schütz, M.; Celani, P.; Korona, T.; Rauhut, G.; Amos, R. D.; Bernhardsson, A.; Berning, A.; Cooper, D. L.; Deegan, M. J. O.; Dobbyn, A. J.; Eckert, F.; Hampel, C.; Hetzer, G.; Lloyd, A. W.; McNicholas, S. J.; Meyer, W.; Mura, M. E.; Nicklass, A.; Palmieri, P.; Pitzer, R.; Schumann, U.; Stoll, H.; Stone, A. J.; Tarroni, R.; Thorsteinsson, T. *MOLPRO*, version 2006.1; University College Cardiff Consultants Limited: Cardiff, U.K., 2006.

CT900036Y

JCTC Journal of Chemical Theory and Computation

Simultaneous Interaction of Tetrafluoroethene with Anions and Hydrogen-Bond Donors: A Cooperativity Study

Ibon Alkorta,* Fernando Blanco, and José Elguero

Instituto de Química Médica, Consejo Superior de Investigaciones Científicas, Juan de la Cierva 3, E-28006 Madrid, Spain

Carolina Estarellas, Antonio Frontera,* David Quiñonero, and Pere M. Deyà

Department of Chemistry, Universitat de les Illes Balears, Carretera de Valldemossa km 7.5, E-07122 Palma de Mallorca, Spain

Received November 24, 2008

Abstract: A computational study of the complexes formed by tetrafluoroethylene, C_2F_4, with anions has been carried out by means of density functional theory (DFT) and second-order Möller−Plesset (MP2) computational methods, up to MP2/aug-cc-pVTZ level. In addition, the possibility of cooperativity in the interaction of anions and hydrogen-bond donors (FH, ClH, and H_2O) when interacting with different faces of the C_2F_4 molecule has been explored. Electron density of the complexes has been analyzed by means of atoms in molecules (AIM) methodology, while natural bond orbital (NBO) methodology has been used to characterize the orbital interaction. In addition, natural energy decomposition analysis (NEDA) has been applied to analyze the source of the interaction. The energetic results indicate that C_2F_4 is a weaker anion receptor than C_6F_6, but in combination with the anions, it became a stronger hydrogen acceptor than C_2H_4. Cooperativity effects are observed in $YH\cdot C_2F_4\cdot X^-$ clusters. In $C_2F_4\cdot X^-$ complexes the dominant attractive terms are the electrostatic and polarization ones, while in $YH\cdot C_2F_4\cdot X^-$ complexes the charge transfer increases significantly, becoming the most important term for most of the FH and ClH complexes studied here.

Introduction

Noncovalent interactions play a crucial role in many areas of modern chemistry. They are important in deciding the conformation of many molecules.[1] They are also relevant in chemical reactions, molecular recognition, and regulation of biochemical processes.[2] These chemical processes are accomplished with specificity and efficiency by means of intricate combinations of weak intermolecular interactions of various sorts. Noncovalent interactions such as hydrogen bonding, anion−π, cation−π, and π−π interactions, and other weak forces govern the organization of multicomponent supramolecular assemblies.[3] A deep understanding of these interactions is of outstanding importance for the rationalization of effects observed in several fields, such as biochemistry and materials science. A quantitative description of these interactions can be performed by taking advantage of quantum chemical calculations on small model systems.[4] In complex biological systems and in the solid state a multitude of these noncovalent interactions may operate simultaneously, giving rise to interesting cooperativity effects. For instance, it is well-known that hydrogen bonding shows highly cooperative behavior. The cumulative strength of networks of hydrogen bonds is larger than the sum of the individual bond strengths when they work simultaneously.[5] Similar observations have been made for the interplay between stacking and hydrogen-bonding interactions. This

* Corresponding authors. (I.A.) E-mail: ibon@iqm.csic.es; fax: (+34) 915644853. (A.F.) E-mail: toni.frontera@uib.es; fax: (+34) 971173426.

10.1021/ct800444e CCC: $40.75
Published on Web 03/24/2009

combination is of great importance for the structural control in oligonucleotides.[6] In addition, it has been recently demonstrated that there is interplay between ion−π and either $\pi-\pi$ or hydrogen-bonding interactions, which can lead to strong cooperativity effects.[7]

In recent years, a number of reports have described an increasing variety of groups that can be involved in hydrogen-bond (HB) interactions.[8] Among them, π-systems are able to act as hydrogen-bonding acceptors. In addition to pioneering works dealing with the complexation properties of benzene and hydrogen fluoride, water, and ammonia,[9] several more recent studies have shed light on this topic from both theoretical and experimental views.[10] Simultaneously, a large set of articles has shown the possibility of favorable interactions between electron-rich groups and π-deficient systems.[11] Among them, anion−π interactions[12] have attracted considerable attention in the last 5 years.[13] There is a great deal of experimental[14] and theoretical[15] work that shows that anion−π interactions play a prominent role in several areas of chemistry, such as molecular recognition[16] and transmembrane anion transport.[17] Anion coordination is an important and challenging aspect of contemporary supramolecular chemistry. Recent investigations provided experimental evidence for the usefulness of anion−π interaction in a structurally directing role.[18]

Besides hydrogen bonds, the interactions between anions and π-systems are among the strongest noncovalent interactions in absolute terms. Obviously this depends on just how electron-deficient the π-system is. In the present paper we examine how these two interactions influence each other, using several criteria, that is, energetic and geometric features, an atoms-in-molecules (AIM) analysis, and a natural bond orbital (NBO) study. We describe the possible formation of anion−π complexes with a simple π-deficient system, C_2F_4. In addition, the interesting possibility of formation of ternary complexes produced by the combination of several anions, C_2F_4, and protic hydrogen-bonding donors has been explored.

Methods

The geometry of the systems has been initially optimized at the MP2/6-311++G(d,p)[19,20] computational level. Frequency calculations at this computational level have been performed to confirm that the structures obtained correspond to energetic minima. Further optimization has been performed with the M05-2x/6-311++G(d,p)[21] and MP2/aug-cc-pVTZ,[22] computational methods. All these calculations have been carried out within the Gaussian-03 package.[23]

The interaction energy has been calculated as the difference between the total energy of the complexes minus the sum of the energies of the isolated monomers. The basis sets used in this work are of sufficient quality that basis set superposition errors (BSSEs) should be rather small.[24] Moreover, it has been shown that uncorrected MP2/aug-cc-pVTZ binding energies lie between corrected and uncorrected MP2/aug-cc-pVQZ energies.[25] BSSE corrections may not always improve binding energies of weakly bonded complexes, since in the counterpoise method[26] a monomer may utilize the valence and core functions of its partner, which are not available to the monomer in the complex.

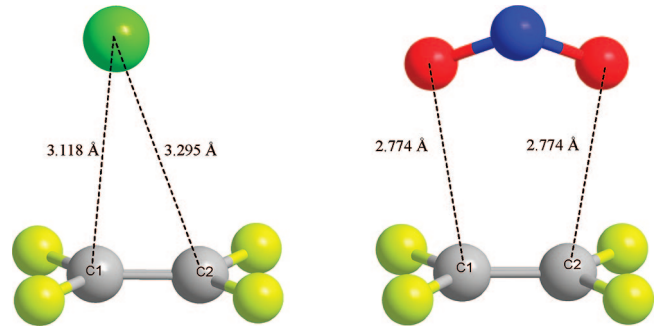

Figure 1. Optimized geometry of $C_2F_4 \cdot Cl^-$ and $C_2F_4 \cdot NO_2^-$ complexes at the MP2/6-311++G(d,p) computational level.

Electron density topology and atomic properties have been evaluated within the AIM methodology[27] with AIMPAC,[28] Morphy98,[29] and AIMAll programs[30] using the M05-2x/6-311++G(d,p) wave function. Calculation of the atomic properties has been carried out by integration within the atomic basins by use of the default parameters except in those cases where the integrated Laplacian was larger than 1×10^{-3}, where more tight conditions have been used. Previous reports have shown small errors in energy and charge for systems where all values of the integrated Laplacian were smaller than the mentioned value.[31]

Orbital interactions have been analyzed within the NBO[32] framework and the NBO 5.0G program[33] at the M05-2x/6-311++G(d,p) computational level. This method allows analyses of the interaction between filled and empty orbitals and associates them with charge-transfer processes. In addition, natural energy decomposition analysis (NEDA)[34,35] has been carried out to obtain insights into the source of the interactions. These calculations have been performed within the Gamess program.[36]

Results and Discussion

C_2F_4·Anion Complexes. Geometrical characteristics of the obtained minimum-energy complexes are shown in Figure 1 and Table 1. For other anions, such as F^- and OH^-, a spontaneous attack of these systems on the C_2F_4 molecules is obtained with formation of covalent bond and will not be considered here. In general, the interacting atom of the anionic system is closer to one of the carbon atoms of C_2F_4 than the other. However, in the complexes with Br^-, NNN^-, HCO_2^-, and NO_2^-, the interaction with the two carbon atoms of C_2F_4 is the same, presenting C_{2v} symmetry in the first three cases and C_s symmetry in the last one. The distances obtained are very similar for the two computational methods used here; the longest distance is for the $C_2F_4 \cdot Br^-$ complex (3.34 Å at MP2/aug-cc-pVTZ computational level) and the shortest is that for C2F4·O_2^- (2.50 Å), followed by those of the $C_2F_4 \cdot NCO$, $C_2F_4 \cdot HCO_2^-$, and $C_2F_4 \cdot NO_2^-$ complexes (2.71, 2.77, and 2.73 Å, respectively).

Interaction energies have been gathered in Table 2. The values range from −62.6 kJ mol^{-1} for the $C_2F_4 \cdot O_2^-$ complex to −32.4 kJ mol^{-1} for the $C_2F_4 \cdot CN^-$ one obtained at the MP2/aug-cc-pVTZ computational level. The interaction

Table 1. Interatomic Distances between the Closest Atom of the Anion and the Two Carbon Atoms of C_2F_4[a]

	MP2/6-311++G(d,p)		M05-2x/6-311++G(d,p)		MP2/aug-cc-pvtz	
complex	X−C1	X−C2	X−C1	X−C2	X−C1	X−C2
$C_2F_4 \cdot Cl^-$	3.118	3.295	3.130	3.336	3.118	3.294
$C_2F_4 \cdot Br^-$	3.415	3.415	3.429	3.429	3.340	3.340
$C_2F_4 \cdot CN^-$ [b]	3.011	3.381	2.912	3.395	2.921	3.357
$C_2F_4 \cdot NC^-$ [b]	2.851	3.124	2.707	3.203	2.804	3.098
$C_2F_4 \cdot NNN^-$	2.847	2.847	2.873	2.873	2.824	2.824
$C_2F_4 \cdot NO_2^-$	2.774	2.774	2.733	2.733	2.732	2.732
$C_2F_4 \cdot HCO_2^-$	2.779	2.779	2.726	2.726	2.772	2.772
$C_2F_4 \cdot CCH^-$	2.988	3.124	2.845	3.175	2.884	3.103
$C_2F_4 \cdot OCN^-$ [b,c]	2.875	3.046	2.838	3.043	2.856	3.012
$C_2F_4 \cdot NCO^-$ [b]	2.774	3.154	2.684	3.187	2.709	3.152
$C_2F_4 \cdot O_2^-$	2.481	2.481	2.524	2.524	2.497	2.497

[a] All distances are given in angstroms. [b] The first atom after C_2F_4 indicates the one pointing toward this molecule. [c] The oxygen is closer to C1, while the nitrogen is closer to C2.

Table 2. Interaction Energies of Calculated Complexes

	E_i (kJ mol^{-1})		
complex	MP2/ 6-311++G(d,p)	M05-2x/ 6-311++G(d,p)	MP2/ aug-cc-pvtz
$C_2F_4 \cdot Cl^-$	−39.01	−35.92	−35.16
$C_2F_4 \cdot Br^-$	−34.76	−30.65	−34.18
$C_2F_4 \cdot CN^-$ [a]	−31.34	−32.71	−32.42
$C_2F_4 \cdot NC^-$ [a]	−36.00	−36.05	−35.69
$C_2F_4 \cdot NNN^-$	−46.02	−40.82	−45.34
$C_2F_4 \cdot NO_2^-$	−43.77	−47.44	−42.93
$C_2F_4 \cdot HCO_2^-$	−48.49	−50.90	−46.76
$C_2F_4 \cdot CCH^-$	−40.99	−39.04	−39.55
$C_2F_4 \cdot OCN^-$ [a]	−40.39	−37.17	−38.93
$C_2F_4 \cdot NCO^-$ [a]	−36.74	−37.86	−37.33
$C_2F_4 \cdot O_2^-$	−62.37	−70.87	−62.55

[a] The first atom after C_2F_4 indicates the one pointing toward this molecule.

energies are smaller than those reported for complexes of the same anions with hexafluorobenzene[12b] [for instance, interaction energies of $C_6F_6 \cdot Cl^-$ and $C_6F_6 \cdot CN^-$ complexes at MP2/6-311++G(d,p) computational level are −51.0 and −52.2 kJ mol^{-1}, respectively] and are similar to those complexes with triazine.[12a] Thus, it can be considered that the C_2F_4 molecule is a weak anion acceptor. The interaction energies computed at the M05-2x/6-311++G** level of theory are in good agreement with those computed at the MP2/aug-cc-pVTZ level. The largest differences are observed in the strongest complex (8.32 kJ mol^{-1}), $C_2F_4 \cdot O_2^-$, followed by $C_2F_4 \cdot Br^-$ (4.53 kJ mol^{-1}) and $C_2F_4 \cdot NNN^-$ (4.52 kJ mol^{-1}).

Topological analysis of the electron density shows three different patterns (Figure 2): (i) For those cases where one of the atoms of the anion is closer to C1 than C2, a unique bond critical point (bcp) is found between the anion and C1, with the exception of the $C_2F_4 \cdot OCN^-$ complex. (ii) For $C_2F_4 \cdot Br^-$, a bifurcated bond path is found connecting the bromine atom to the center of the CC bond, similar to the one found in the hydrogen-bonded $C_2H_4 \cdot HF$ complex.[37] (iii) For $C_2F_4 \cdot HCO_2^-$, $C_2F_4 \cdot NO_2^-$, $C_2F_4 \cdot OCN^-$, and $C_2F_4 \cdot O_2^-$, two bond critical points between the C1 and C2 atoms and the anions are found. The bcp's present small values of the electron density, ρ, between 0.029 and 0.010 au and small and positive values of the Laplacian, $\nabla^2\rho$, between 0.083 and 0.029 au, which corresponds to a closed-shell interaction similar to those found in other weak interactions such as hydrogen bonds.[38]

A summary of the calculated properties obtained by integration within the atomic basins has been gathered in Table 3. A charge transfer from the anion to the C_2F_4 is observed, up to 0.138 e for the $C_2F_4 \cdot O_2^-$ complex. A representation of the electron shift (Figure 3) shows that the charge gained by the C_2F_4 molecule is concentrated in the face opposite the position of the anion, increasing the nucleophilic character of the C_2F_4 molecule in this region.

The calculated energy of the anions within the complex with AIM methodology indicates an energy destabilization for all the anions except Cl^-, Br^-, NO_2^-, and O_2^-. In closely related systems, a linear relationship has been observed between these two parameters but in the present case, the diverse nature of the anions prevents observation of a similar relationship.[39]

NBO analysis shows an interaction of the lone pair of the anion with the antibonding C−C orbital (Table 4) with the corresponding charge transfer between them. The stabilization provided for this interaction ranges from 2.1 kJ mol^{-1} for the $C_2F_4 \cdot Br^-$ complex to 19.4 kJ mol^{-1} in the case of the two interactions obtained for the $C_2F_4 \cdot HCO_2^-$ cluster.

Natural energy decomposition analysis (NEDA) is a method for partitioning molecular interaction energies including charge transfer (CT), electrostatic (ES), polarization (POL), exchange (XC), and core repulsion contributions (DEF). The charge transfer term is based on the interaction of filled orbitals, donor, with empty ones, acceptor, of the species involved. For the complexes studied here, the electrostatic and polarization terms are the most important ones in all cases. For the complexes where a nitrogen atom is directly interacting with the C_2F_4 molecule ($C_2F_4 \cdot NC^-$, $C_2F_4 \cdot NNN^-$, and $C_2F_4 \cdot NCO^-$), the polarization term is the dominant one, while in those cases where a carbon or a halogen is interacting with C_2F_4, the electrostatic term is the largest one. In the complexes where oxygen is involved in the interaction, the electrostatic term is the dominant one in the three cases where a double interaction is observed ($C_2F_4 \cdot HCO_2^-$, $C_2F_4 \cdot NO_2^-$, and $C_2F_4 \cdot O_2^-$) while the polarization term is more important in the $C_2F_4 \cdot OCN^-$case. In addition, the charge transfer and exchange terms have large values. In fact, several complexes can each contribute up to 20% of the total stabilization energy.

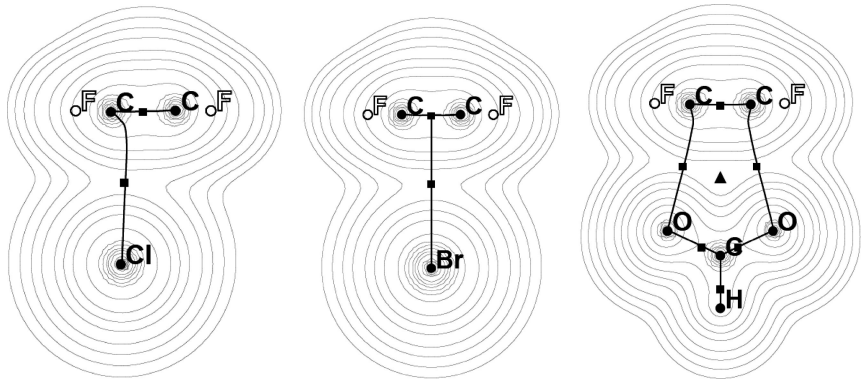

Figure 2. Electron density maps of $C_2F_4 \cdot Cl^-$, $C_2F_4 \cdot Br^-$, and $C_2F_4 \cdot HCO_2^-$ complexes. The outer contour line corresponds to 0.001 au and the next ones correspond to values increasing according to the pattern 2×10^n, 4×10^n, and 8×10^n, where n varies from −3 to 2. (■) Bond critical points (bcp); (▲) ring critical points. Lines connecting the atoms correspond to bond paths. Atoms in the represented plane are shown in black, and those out of the plane are in white.

Table 3. Properties of Intermolecular Bond Critical Points and Variation of Integrated Charge and Energy of Anions[a]

	ρ (au)	$\nabla^2\rho$ (au)	charge transfer (e)	energy variation (kJ mol^{-1})
$C_2F_4 \cdot Cl^-$	0.013	0.038	0.057	−109.8
$C_2F_4 \cdot Br^-$	0.010	0.029	0.052	−1261.6
$C_2F_4 \cdot CN^-$	0.015	0.038	0.060	94.2
$C_2F_4 \cdot NC^-$	0.017	0.056	0.043	86.9
$C_2F_4 \cdot NNN^-$ [b]	0.014	0.040	0.074	77.0
$C_2F_4 \cdot NO_2^-$ [b]	0.016	0.050	0.051	−62.9
$C_2F_4 \cdot HCO_2^-$ [b]	0.016	0.050	0.054	51.3
$C_2F_4 \cdot CCH^-$	0.016	0.040	0.076	154.8
$C_2F_4 \cdot OCN^-$	0.013[c]	0.042	0.047	95.6
$C_2F_4 \cdot OCN^-$	0.012[d]	0.039		
$C_2F_4 \cdot NCO^-$	0.018	0.059	0.043	97.7
$C_2F_4 \cdot O_2^-$ [b]	0.029	0.083	0.138	−176.3

[a] Obtained by use of the M05-2x/6-311++G(d,p) wavefunction. [b] Two identical bcp's are found in these complexes. [c] Values of O···C interaction. [d] Values of N···C interaction.

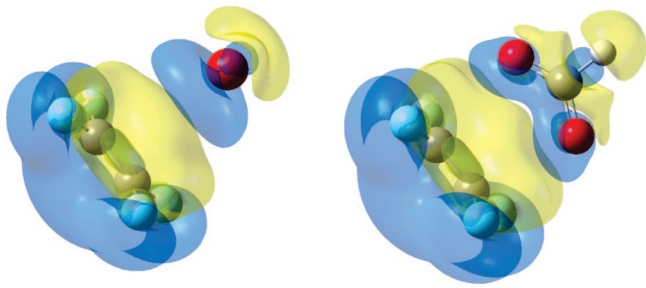

Figure 3. Electron density difference maps of $C_2F_4 \cdot Br^-$ and $C_2F_4 \cdot HCO_2^-$ complexes. Blue and yellow isosurfaces represent gain and loss of electron density upon complex formation, relative to the isolated subunits. Contours shown are ±0.0002 e/au^3 calculated at the M05-2x/6-311++G(d,p) level.

Anion·C_2F_4·HY Complexes. The isolated C_2F_4 system is not able to form a stable complex with hydrogen-bond donors, such as FH, ClH, and H_2O, while interacting with the π-cloud of the former. However, the presence of electron donors in one face of the C_2F_4 molecule has been shown to allow its interaction with electron-deficient groups acting as hydrogen-bond acceptor.[40] In this section the cluster formed by an anion interacting with C_2F_4 on one face and a hydrogen-bond donor on the opposite will be discussed.

Interactions between FH and all the complexes studied in the previous section have been considered, while only four cases have been chosen for the complexes with ClH and H_2O. In the case of the $FH \cdot C_2F_4 \cdot CCH^-$ system, the CCH^- and O_2^- anions spontaneously tend to form a covalent bond with one of the carbon atoms of the C_2F_4 molecule. $FH \cdot C_2F_4 \cdot CN^-$ and $FH \cdot C_2F_4 \cdot NC^-$ became the same, being better described as the latter one (Figure 4). In the rest of the cases, stable clusters are obtained. The same symmetries obtained for the corresponding $C_2F_4 \cdot X^-$ complexes are observed for $FH \cdot C_2F_4 \cdot X^-$ and $ClH \cdot C_2F_4 \cdot X^-$, except for the $FH \cdot C_2F_4 \cdot Br^-$ case, which now adopts C_s symmetry. The complexes studied with H_2O adopt C_s symmetry in all cases.

The intermolecular distances are gathered in Table 5. The X···C1 distances obtained in these clusters are in all the cases shorter than the corresponding ones of the $C_2F_4 \cdot X^-$ complexes. For a given cation, in general, the longest distance is obtained in the complexes with H_2O. Of the four anions considered for all the hydrogen bond donors, two of the complexes present the shortest distance with ClH and another two with FH at MP2/aug-cc-pVTZ computational level. These results indicate that another effect in addition to the expected amount of positive charge of the interacting hydrogen at the hydrogen bond donors (FH > ClH > H_2O), can be important for the final geometry of the complex. The individual larger difference in the X···C1 distance between the $C_2F_4 \cdot X^-$ complexes and the corresponding $YH \cdot C_2F_4 \cdot X^-$ ones is obtained in the $ClH \cdot C_2F_4 \cdot Cl^-$case where the difference at the MP2/aug-cc-pVTZ computational level is 0.24 Å.

With respect to FH and ClH molecules acting as hydrogen-bond donors, in those cases where they are not symmetrically oriented with respect to C1 and C2, they tend to be closer to C2 than to C1, except in the $FH \cdot C_2F_4 \cdot OCN^-$ complex. In any case, the difference between these distances is always smaller than 0.22 Å. Intermolecular distances obtained for the FH complexes (between 2.11 and 2.33 Å) are in general shorter than those obtained for the $FH \cdot C_2H_4$ complex calculated at the MP2/6-311++G(d,p) computational level (FH···C1/C2 distance of 2.30 Å).[37] In complexes with H_2O, in general, the interacting hydrogen is closer to C1 than C2 with the exception of the $H_2O \cdot C_2F_4 \cdot NC^-$ complex, probably

Table 4. Orbital Interaction Energies and Natural Energy Decomposition Analysis[a]

		NEDA					
complex	lp (X^-) → σ^* CC	CT	ES	POL	XC	DEF (C_2F_4)	DEF (X^-)
$C_2F_4 \cdot Cl^-$	4.4	−13.4	−52.8	−42.5	−30.7	65.0	39.8
$C_2F_4 \cdot Br^-$	2.1	−10.1	−44.2	−35.5	−27.2	57.2	29.9
$C_2F_4 \cdot CN^-$	10.2	−32.3	−57.7	−50.2	−31.6	60.5	79.0
$C_2F_4 \cdot NC^-$	11.0	−39.6	−52.8	−85.9	−40.9	92.4	91.6
$C_2F_4 \cdot NNN^-$	23.0	−53.3	−58.5	−61.6	−46.7	81.9	96.9
$C_2F_4 \cdot NO_2^-$	2 × 3.8	−46.7	−73.1	−54.1	−44.0	66.3	108.4
$C_2F_4 \cdot HCO_2^-$	2 × 9.7	−45.1	−76.7	−71.0	−49.2	82.8	111.3
$C_2F_4 \cdot CCH^-$	10.8	−37.8	−71.3	−55.6	−42.2	87.6	80.4
$C_2F_4 \cdot OCN^-$	10.3	−38.4	−48.5	−57.7	−41.0	77.2	72.5
$C_2F_4 \cdot NCO^-$	10.8	−35.6	−53.1	−71.8	−36.4	72.7	87.3
$C_2F_4 \cdot O_2^-$	2 × 14.3	−109.9	−133.9	−91.0	−66.4	114.1	215.1

[a] Calculated at the M05-2x/6-311++G(d,p) computational level. All energies are given in kilojoules per mole.

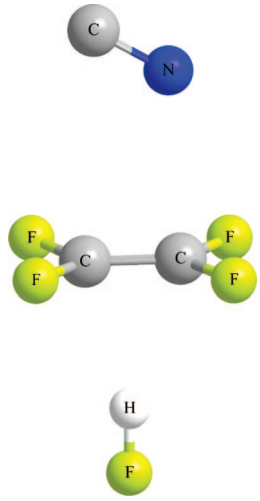

Figure 4. Optimized geometry of $FH \cdot C_2F_4 \cdot NC^-$ complex at the MP2/6-311++G(d,p) computational level.

due to secondary interactions of the additional hydrogen of this molecule with the fluorine atoms of C_2F_4.

Calculated interaction energies of the cluster (Table 6) range between −54.5 kJ mol^{-1} for the weakest complex, $H_2O \cdot C_2F_4 \cdot Br^-$, and −80.3 kJ/mol for the strongest one, $FH \cdot C_2F_4 \cdot HCO_2^-$, at the MP2/aug-cc-pVTZ computational level. For a given cation, the strongest complex is the one formed with FH, followed by ClH, being andthose obtained with H_2O are the weakest ones. This order follows the expected charge of hydrogen atoms involved in the interaction (FH > ClH > H_2O). In general, a similar stabilization order to that obtained for the $C_2F_4 \cdot X^-$ complexes is obtained here, showing square correlation coefficients with the data reported in Table 2 of 0.95, 0.995, and 0.997 for FH, ClH, and H_2O complexes obtained at the MP2/aug-cc-pVTZ computational level.

In order to evaluate the possible existence of cooperativity in these complexes, the attractive interaction between FH and the anions in the disposition of the cluster has been evaluated. Thus, the cooperativity has been calculated by use of eq 1:

$$\text{coop} = E_i(YH \cdot C_2F_4 \cdot X^-) - E_i(C_2F_4 \cdot X^-) - E_i(YH \cdot X^-) \quad (1)$$

where $E_i(YH \cdot C_2F_4 \cdot X^-)$ and $E_i(C_2F_4 \cdot X^-)$ correspond to interaction energies of the corresponding minima structures, which are gathered in Tables 6 and 2, respectively. $E_i(YH \cdot X^-)$ is the attractive interaction of these two molecules as they stand in the $YH \cdot C_2F_4 \cdot X^-$ cluster. As indicated previously, the $YH \cdot C_2F_4$ complex where YH points toward the π-cloud of C_2F_4 system is not attractive, and thus it has not been considered to calculate the cooperativity. The values found for this parameter are always negative, as indicative of true cooperativity. The cooperativity values obtained are much larger at the MP2/aug-cc-pVTZ computational level (between −15.2 and −5.4 kJ mol^{-1}) than those obtained with the 6-311++G(d,p) basis set at MP2 or M05-2x levels (between −9.6 and −3.0 kJ mol^{-1}). These results are due to a slightly larger interaction energy obtained at the MP2/aug-cc-pVTZ computational level in the trimers and a smaller stabilization in the $YH \cdot X^-$ pair that favor, in both, cases larger cooperativities. With respect to the HB donors, larger cooperativities are obtained in the ClH complexes than in the FH ones, with the smallest values in the H_2O cases for a given anion. This tendency can be associated with the strength of the interaction in the first place and with the polarization of the HB donor in the second.

Electron density maps show that while the anions tend to form a bond path with C1, the FH and ClH molecules do so with C2 and H_2O with C1, in agreement with the closer proximity of these molecules to the corresponding carbon atoms of C_2F_4 (Figure 5). Values of the electron density and Laplacian at the X···C bcp (Table 7) are larger than those found in the corresponding $C_2F_4 \cdot X^-$, as expected due to the shorter interatomic distance found in these complexes.[41,42]

Integrated electron density within the atomic basins shows that in FH and ClH most of the charge lost by the anionic systems goes to the YH molecule, while the electronic gain of the C_2F_4 molecule is here smaller than in the $C_2F_4 \cdot X$ complexes. In contrast, in the H_2O complexes the electronic gain of this molecule is very small due to the long interatomic distances obtained between this molecule and the C_2F_4 one. The electron density difference for two $FH \cdot C_2F_4 \cdot X^-$ complexes (Figure 6) clearly shows, again, how the electron gain tends to be shifted further away from the position of the anion.

The calculated energy variation per molecule shows different patterns depending on the hydrogen-bond donor and anionic systems studied. As in the case of the $C_2F_4 \cdot X^-$ complexes, those complexes with Cl^-, Br^-, and NO_2^- present

Table 5. Intermolecular Distances from Anions and Hydrogen-Bond Donor Molecules to C_2F_4[a]

	MP2/6-311++G(d,p)				M05-2x/6-311++G(d,p)				MP2/aug-cc-pVTZ			
	X···C1	X···C2	YH···C1	YH···C2	X···C1	X···C2	YH···C1	YH···C2	X···C1	X···C2	YH···C1	YH···C2
$FH\cdot C_2F_4\cdot Cl^-$	2.810	3.267	2.329	2.110	2.859	3.275	2.305	2.145	2.894	3.236	2.274	2.138
$FH\cdot C_2F_4\cdot Br^-$	3.282	3.287	2.259	2.259	3.260	3.267	2.253	2.251	3.215	3.220	2.219	2.217
$FH\cdot C_2F_4\cdot NC^-$	2.734	2.996	2.275	2.219	2.574	3.034	2.296	2.167	2.668	2.993	2.245	2.168
$FH\cdot C_2F_4\cdot HCO_2^-$	2.685	2.685	2.219	2.219	2.628	2.628	2.199	2.199	2.663	2.663	2.195	2.195
$FH\cdot C_2F_4\cdot NNN^-$	2.765	2.765	2.253	2.253	2.764	2.764	2.248	2.248	2.739	2.739	2.215	2.215
$FH\cdot C_2F_4\cdot NO_2^-$	2.685	2.685	2.226	2.226	2.658	2.658	2.216	2.216	2.649	2.649	2.202	2.202
$FH\cdot C_2F_4\cdot OCN^-$	2.801	2.939	2.251	2.264	2.751	2.956	2.235	2.247	2.794	2.898	2.212	2.237
$FH\cdot C_2F_4\cdot NCO^-$	2.253	3.047	2.323	2.172	2.549	3.047	2.302	2.160	2.541	3.046	2.286	2.123
$ClH\cdot C_2F_4\cdot Cl^-$	2.831	3.293	2.172	2.388	2.955	3.280	2.427	2.301	2.875	3.255	2.288	2.119
$ClH\cdot C_2F_4\cdot Br^-$	3.305	3.305	2.353	2.353	3.293	3.293	2.409	2.409	3.227	3.227	2.234	2.234
$ClH\cdot C_2F_4\cdot NC^-$	2.741	3.027	2.369	2.299	2.599	3.065	2.425	2.304	2.650	3.009	2.270	2.183
$ClH\cdot C_2F_4\cdot HCO_2^-$	2.674	2.674	2.267	2.267	2.632	2.632	2.275	2.275	2.687	2.687	2.267	2.267
$HOH\cdot C_2F_4\cdot Cl^-$	2.951	3.339	2.754	3.054	2.990	3.348	2.661	2.963	2.956	3.317	2.470	2.562
$HOH\cdot C_2F_4\cdot Br^-$	3.299	3.389	2.462	2.624	3.238	3.441	2.647	3.022	3.146	3.407	2.455	2.592
$HOH\cdot C_2F_4\cdot NC^-$	2.816	3.046	3.126	2.718	2.734	3.065	3.072	2.605	2.759	3.016	2.649	2.441
$HOH\cdot C_2F_4\cdot HCO_2^-$	2.707	2.740	2.653	2.983	2.665	2.684	2.590	2.914	2.678	2.731	2.444	2.674

[a] Intermolecular distances are given in angstroms.

Table 6. Total Interaction Energy, Attractive Energy between FH and X^-, and Cooperativity[a]

	MP2/6-311++G(d,p)			M05-2x/6−311++G(d,p)			MP2/aug-cc-pvtz		
	E_i	$YH\cdot X^-$ [b]	coop	E_i	$YH\cdot X^-$ [b]	coop	E_i	$YH\cdot X^-$ [b]	coop
$FH\cdot C_2F_4\cdot Cl^-$	−66.30	−20.11	−7.18	−63.00	−20.20	−6.89	−66.13	−18.75	−12.22
$FH\cdot C_2F_4\cdot Br^-$	−58.61	−18.19	−5.66	−55.23	−18.56	−6.02	−63.67	−17.89	−11.60
$FH\cdot C_2F_4\cdot NC^-$	−61.06	−18.80	−6.26	−62.68	−19.24	−7.40	−65.44	−18.11	−11.64
$FH\cdot C_2F_4\cdot HCO_2^-$	−77.56	−21.69	−7.38	−82.99	−22.61	−9.47	−80.32	−20.74	−12.83
$FH\cdot C_2F_4\cdot NNN^-$	−71.32	−18.01	−7.29	−66.14	−18.27	−7.04	−74.27	−17.30	−11.63
$FH\cdot C_2F_4\cdot NO_2^-$	−70.99	−20.77	−6.46	−77.89	−22.01	−8.43	−74.04	−19.57	−11.54
$FH\cdot C_2F_4\cdot OCN^-$	−64.18	−17.84	−5.36	−61.64	−18.17	−4.44	−66.99	−17.13	−10.31
$FH\cdot C_2F_4\cdot NCO^-$	−61.83	−18.23	−3.20	−64.59	−18.56	−8.86	−66.41	−17.38	−10.10
$ClH\cdot C_2F_4\cdot Cl^-$	−62.91	−15.43	−8.47	−56.79	−15.00	−5.87	−63.21	−13.85	−14.20
$ClH\cdot C_2F_4\cdot Br^-$	−55.89	−13.83	−7.29	−49.46	−13.77	−5.03	−60.93	−13.29	−13.45
$ClH\cdot C_2F_4\cdot NC^-$	−58.21	−14.28	−7.93	−56.45	−14.35	−6.05	−62.56	−13.31	−13.56
$ClH\cdot C_2F_4\cdot HCO_2^-$	−74.80	−16.71	−9.61	−76.36	−17.31	−8.15	−77.54	−15.60	−15.19
$HOH\cdot C_2F_4\cdot Cl^-$	−59.86	−17.27	−3.58	−56.47	−17.58	−2.98	−55.11	−14.58	−5.36
$HOH\cdot C_2F_4\cdot Br^-$	−51.71	−13.85	−3.09	−49.93	−15.94	−3.34	−54.52	−13.76	−6.57
$HOH\cdot C_2F_4\cdot NC^-$	−55.18	−15.20	−3.98	−55.50	−15.43	−4.02	−55.49	−13.22	−6.58
$HOH\cdot C_2F_4\cdot HCO_2^-$	−70.64	−17.84	−4.31	−74.69	−18.77	−5.02	−69.42	−15.88	−6.78

[a] All values are given in kilojoules per mole. [b] In the geometrical disposition of the $FH\cdot C_2F_4\cdot X^-$ cluster.

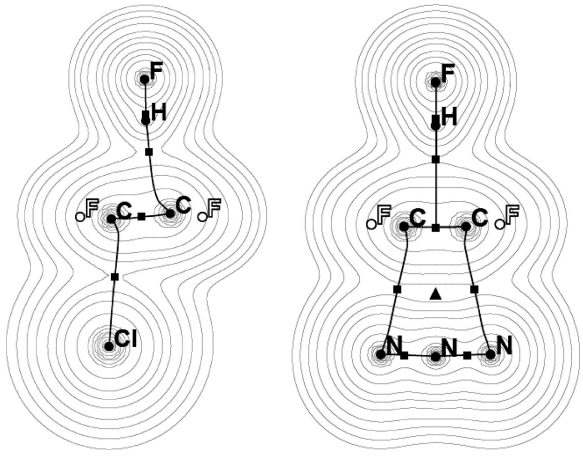

Figure 5. Electron density maps of $FH\cdot C_2F_4\cdot Cl^-$ and $FH\cdot C_2F_4\cdot NNN^-$ clusters. Contour levels, symbols, and atoms are represented as in Figure 2.

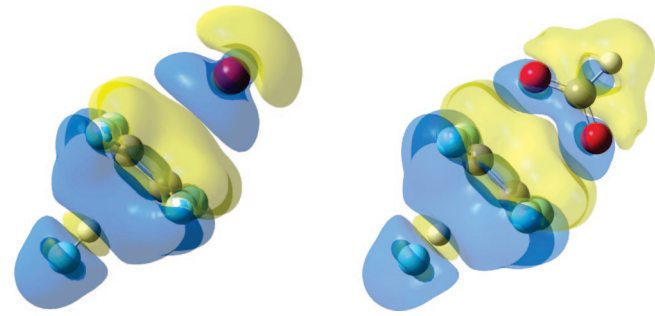

Figure 6. Electron density difference maps of $FH\cdot C_2F_4\cdot Br^-$ and $FH\cdot C_2F_4\cdot HCO_2^-$ complexes. Blue and yellow isosurfaces represent gain and loss of electron density upon complex formation, relative to the isolated subunits. The contours shown are ±0.0002 e/au^3 calculated at the M05-2x/6-311++G(d,p) level.

important destabilization of the C_2F_4 molecule. For the rest of the anions, in the complexes with FH, a gain of electronic charge is associated with an energy stabilization of the C_2F_4 and FH molecules similar in value. In the complexes with ClH, this molecule is stabilized while the C_2F_4 one is destabilized. Finally, the H_2O molecule, which shows a small gain of electron density, presents an energy destabilization due to complex formation, while the C_2F_4 present significant stabilization energies.

Table 7. Properties of Intermolecular Bond Critical Points and Variation of Integrated Charge and Energy of C_2F_4 and Hydrogen-Bond Donor Molecules upon Complexation

	X···C		YH···C		charge		Δ energy	
complex	ρ (au)	$\nabla^2\rho$ (au)	ρ (au)	$\nabla^2\rho$ (au)	C_2F_4 (e)	YH (e)	C_2F_4 (kJ mol^{-1})	YH (kJ mol^{-1})
FH·C_2F_4·Cl^-	0.0205	0.0524	0.0226	0.0538	−0.045	−0.054	104.9	−29.4
FH·C_2F_4·Br^-	0.0138	0.0393	0.0199	0.0510	−0.027	−0.049	1201.0	205.3
FH·C_2F_4·NC^-	0.0224	0.0696	0.0218	0.0534	−0.012	−0.051	−63.6	−67.8
FH·C_2F_4·NNN^- [a]	0.0173	0.0482	0.0193	0.0527	−0.061	−0.039	−63.4	−64.4
FH·C_2F_4·NO_2^- [a]	0.0183	0.0574	0.0220	0.0535	−0.017	−0.054	43.6	−43.5
FH·C_2F_4·HCO_2^- [a]	0.0191	0.0601	0.0228	0.0552	−0.018	−0.055	−52.0	−66.5
FH·C_2F_4·OCN^-	0.0150[b], 0.0139[c]	0.0492, 0.0450	0.0199	0.0531	−0.019	−0.042	−76.7	−69.8
FH·C_2F_4·NCO^-	0.0229	0.0744	0.0220	0.0536	−0.010	−0.051	−78.5	−72.0
ClH·C_2F_4·Cl^-	0.0173	0.0471	0.0182	0.0417	−0.040	−0.042	124.37	−81.70
ClH·C_2F_4·Br^-	0.0131	0.0372	0.0159	0.0378	−0.034	−0.037	1095.12	−3085.97
ClH·C_2F_4·NC^-	0.0213	0.0666	0.0181	0.0419	−0.018	−0.040	33.83	−184.41
ClH·C_2F_4·HCO_2^-	0.0191	0.0597	0.0216	0.0479	−0.020	−0.051	43.75	−198.14
HOH·C_2F_4·Cl^-	0.0261	0.0442	0.0080	0.0233	−0.068	−0.006	36.12	66.94
HOH·C_2F_4·Br^-	0.0129	0.0347	0.0079	0.0236	−0.061	−0.005	1179.60	250.42
HOH·C_2F_4·NC^-	0.0166	0.0542	0.0085	0.0253	−0.044	−0.004	−165.57	32.67
HOH·C_2F_4·HCO_2^-	0.0179	0.0562	0.0092	0.0261	−0.056	−0.008	−135.29	35.18

[a] Two identical X···C bcp's are found in these complexes. [b] Values of O···C1 interaction. [c] Values of N···C1 interaction.

Table 8. Intermolecular Orbital Interaction Energies and Natural Energy Decomposition Analysis[a]

			NEDA						
complex	X lp → σ^*CC	πCC → σ^*HF	CT	ES	POL	XC	DEF (C_2F_4)	DEF (X^-)	DEF (HF)
FH·C_2F_4·Cl^-	24.6	33.3	−94.0	−94.6	−48.9	−55.4	118.6	81.5	28.0
FH·C_2F_4·Br^-	4.1	27.9	−67.6	−73.0	−39.0	−46.3	98.7	49.7	24.9
FH·C_2F_4·NC^-	17.5	32.5	−108.4	−83.6	−98.1	−63.0	142.0	121.0	28.9
FH·C_2F_4·HCO_2^-	2 × 14.3	34.6	−117.3	−110.9	−85.4	−73.9	126.1	153.4	30.5
FH·C_2F_4·NNN^-	36.0	24.5	−112.3	−85.4	−84.2	−70.8	126.9	133.8	26.9
FH·C_2F_4·NO_2^-	2 × 8.0	32.8	−114.3	−108.8	−58.4	−65.0	100.9	145.6	29.5
FH·C_2F_4·OCN^-	14.1	26.8	−92.6	−70.3	−72.2	−61.5	115.7	96.2	26.5
FH·C_2F_4·NCO^-	19.8	32.4	−106.7	−83.6	−90.3	−58.7	119.9	126.9	29.1
ClH·C_2F_4·Cl^-	0.7	31.4	−71.80	−81.13	−51.71	−53.56	114.52	58.70	25.19
ClH·C_2F_4·Br^-	3.6	25.8	−54.77	−67.40	−45.15	−47.36	101.71	21.55	44.89
ClH·C_2F_4·NC^-	15.7	31.1	−95.40	−78.12	−99.33	−63.64	142.34	113.14	27.03
ClH·C_2F_4·HCO_2^-	2 × 14.0	41.7	−116.11	−109.70	−88.99	−78.70	137.36	151.84	33.51
HOH·C_2F_4·Cl^-	12.6	2.0	−41.13	−76.57	−56.44	−46.82	90.42	57.40	19.71
HOH·C_2F_4·Br^-	4.6	1.8	−33.10	−65.73	−49.79	−42.59	82.89	42.76	19.46
HOH·C_2F_4·NC^-	6.7	2.4	−50.79	−66.90	−84.64	−51.71	105.23	77.24	20.54
HOH·C_2F_4·HCO_2^-	13.0/11.4	2.9	−71.92	−100.29	−90.75	−66.40	108.32	130.88	21.55

[a] Calculated at the M05-2x/6-311++G(d,p) computational level. All energies are given in kilojoules per mole.

Analysis of the orbital interaction in the FH and ClH complexes shows a strong interaction between the π-electrons of C_2F_4 and the σ antibonding orbital of the YH molecule (Table 8). The value of this interaction is able to account for the difference in stability between C_2F_4·X^- and YH·C_2F_4·X^- complexess. In addition, reinforcement of the interaction between the anion lone pair and the antibonding CC orbital is found in the trimeric structures when compared to the dimeric ones. In the NEDA analysis, a significant increment of the charge-transfer term due to the presence of the HB with the π-systems is observed. These results are in agreement with previous reports that have indicated the preponderance of charge transfer in HB complexes.

In contrast, in the H_2O complexes, a small interaction is observed between π-electrons of C_2F_4 and the OH antibonding orbital. These results are in agreement with the long distances of the hydrogen bonds formed in these cases. Due to this effect, the NEDA analysis indicates that in these complexes the electrostatic and polarization terms are the most important stabilization forces.

Conclusion

A theoretical study of the complexes formed by tetrafluoroethylene (C_2F_4) with anions has been carried out by means of ab initio, MP2, and DFT, M05-2x, methods. In several complexes obtained, the position of the anions avoids the center of the C═C bond. However, several complexes are symmetric around the CC middle point, providing a similar environment to both carbon atoms of C_2F_4. The interaction energy of the complexes indicates that C_2F_4 is a weaker acceptor of anions than C_6F_6. Natural energy decomposition analysis shows that electrostatic and polarization terms are the most important attractive forces in these complexes.

In addition, possible cooperativity in the interaction of anions and hydrogen-bond donors (FH, ClH, and H_2O) in opposite faces of C_2F_4 has been explored. The minima complexes obtained show a shortening of the intermolecular distance between the anions and C_2F_4. In addition, the FH

molecule is located, in general, at shorter distances than in the $FH \cdot C_2H_4$ complex, indicating that the $C_2F_4 \cdot X^-$ is a more effective hydrogen-bond acceptor than C_2H_4. Cooperativity values between −15.2 and −5.4 kJ mol^{-1} have been obtained for all the systems studied here. Finally, the presence of hydrogen bonding increases significantly the charge-transfer attractive term in the NEDA analysis for the FH and ClH complexes, becoming the most important term in most cases.

Acknowledgment. This work was carried out with financial support from the Ministerio de Educación y Ciencia (Projects CTQ2007-61901/BQU and CTQ2005-08989-01), Comunidad Autónoma de Madrid (Project MADRISOLAR, ref S-0505/PPQ/0225) and Govern Balear (project PROGECIB-33A). We thank the CTI (CSIC) for computational facilities.

Supporting Information Available: Optimized geometries of the complexes at the MP2/6-311++G(d,p) computational level. This information is available free of charge via the Internet at http://pubs.acs.org.

References

(1) Hunter, C. A.; Sanders, J. K. M. *J. Am. Chem. Soc.* **1990**, *112*, 5525.

(2) Meyer, E. A.; Castellano, R. K.; Diederich, F. *Angew. Chem., Int. Ed.* **2003**, *42*, 1210.

(3) (a) Dougherty, D. A. *Science* **1996**, *271*, 163. (b) Kim, K. S.; Tarakeshwar, P.; Lee, J. Y. *Chem. Rev.* **2000**, *100*, 4145. (c) Lee, E. C.; Kim, D.; Jureèka, P.; Tarakeshwar, P.; Hobza, P.; Kim, K. S. *J. Phys. Chem. A* **2007**, *111*, 3446. (d) Reddy, A. S.; Sastry, G. N. *J. Phys. Chem. A* **2005**, *109*, 8893. (e) Èernỳ, J.; Hobza, P. *Phys. Chem. Chem. Phys.* **2007**, *9*, 5291.

(4) (a) Rappè, A. K.; Bernstein, E. R. *J. Phys. Chem. A* **2000**, *104*, 6117. (b) Hesselmann, A.; Jansen, G.; Schutz, M. *J. Am. Chem. Soc.* **2006**, *128*, 11730. (c) Piacenza, M.; Grimme, S. *Chem. Phys. Chem.* **2005**, *6*, 1554.

(5) (a) Parthasarathi, R.; Subramanian, V.; Sathyamurthy, N. *J. Phys. Chem. A* **2005**, *109*, 843. (b) Ludwig, R. *Angew. Chem., Int. Ed.* **2001**, *40*, 1808.

(6) (a) Mignon, P.; Loverix, S.; Steyaert, J.; Geerlings, P. *Nucleic Acids Res.* **2005**, *33*, 1779. (b) Vanommeslaeghe, K.; Mignon, P.; Loverix, S.; Tourwè, D.; Geerlings, P. *J. Chem. Theory Comput.* **2006**, *2*, 1444. (c) Leist, R.; Frey, J. A.; Ottiger, P.; Frey, H.-M.; Leutwyler, S.; Bachorz, R. A.; Klopper, W. *Angew. Chem., Int. Ed.* **2007**, *46*, 7449.

(7) (a) Reddy, A. S.; Vijay, D.; Sastry, G. M.; Sastry, G. N. *J. Phys. Chem. B* **2006**, *110*, 2479. (b) Reddy, A. S.; Vijay, D.; Sastry, G. M.; Sastry, G. N. *J. Phys. Chem. B* **2006**, *110*, 10206. (c) Escudero, D.; Frontera, A.; Quiñonero, D.; Deyà, P. M. *Chem. Phys. Lett.* **2008**, *456*, 257. (d) Vijay, D.; Zipse, H.; Sastry, G. N *J. Phys. Chem. B,* **2008**, *112*, 8863. (e) Garcia-Raso, A.; Alberti, F. M.; Fiol, J. J.; Tasada, A.; Barceló-Oliver, M.; Molins, E.; Escudero, D.; Frontera, A.; Quiñonero, D.; Deyà, P. M. *Inorg. Chem.* **2007**, *46*, 10724. (f) Frontera, A.; Quiñonero, D.; Costa, A.; Ballester, P.; Deyà, P. M. *New J. Chem.* **2007**, *31*, 556. (g) Quiñonero, D.; Frontera, A.; Garau, C.; Ballester, P.; Costa, A.; Deyà, P. M. *Chem. Phys. Chem.* **2006**, *7*, 2487. (h) Zaccheddu, M.; Filippi, C.; Buda, F. *J. Phys. Chem. A* **2008**, *112*, 1627. (i) Quiñonero, D.; Frontera, A.; Escudero, D.; Costa, A.; Ballester, P.; Deyà, P. M. *Theor. Chem. Acc.* **2008**, *120*, 385. (j) Mignon, P.; Loverix, S.; De Proft, F.; Geerlings, P. *J. Phys. Chem. A* **2004**, *108*, 6043.

(8) (a) Alkorta, I.; Rozas, I.; Elguero, J. *Chem. Soc. Rev.* **1998**, *27*, 163. (b) Desiraju, G. R.; Steiner, T. *The weak hydrogen bond*; Oxford University Press: Oxford, 1999.

(9) (a) Baiocchi, F. A.; Williams, J. H.; Klemperer, W. *J. Phys. Chem.* **1983**, *87*, 2079. (b) Rodham, D. A.; Suzuki, S.; Suenram, R. D.; Lovas, F. J.; Dasgupta, S.; Goddard, W. A.; Blake, G. A. *Nature* **1993**, *362*, 735. (c) Suzuki, S.; Green, P. G.; Bumgarner, R. E.; Dasgupta, S.; Goddard, W. A.; Blake, G. A. *Science* **1992**, *257*, 942.

(10) (a) Rozas, I.; Alkorta, I.; Elguero, J. *J Phys Chem A* **1998**, *102*, 2398. (b) Rozas, I.; Alkorta, I.; Elguero, J. *J Phys Chem A* **1997**, *101*, 9457. (c) Alkorta, I.; Elguero, J. *Chem. Phys. Lett.* **2003**, *381*, 505. (d) Prieto, P.; de la Hoz, A.; Alkorta, I.; Rozas, I.; Elguero, J. *Chem. Phys. Lett.* **2001**, *350*, 325. (e) Rozas, I. *Phys. Chem. Chem. Phys.* **2007**, *9*, 2782. (f) Kawahara, S.; Tsuzuki, S.; Uchimaru, T. *Chem.-Eur. J.* **2005**, *11*, 4458. (g) Grabowski, S. J.; Sokalski, W. A.; Leszczynski, J. *J. Phys. Chem. A* **2004**, *108*, 1806. (h) Scheiner, S.; Grabowski, S. J. *J. Mol. Struct.* **2002**, *615*, 209. (i) Wojtulewski, S.; Grabowski, S. J. *J. Mol. Struct.* **2002**, *605*, 235. (j) Takahashi, H.; Tsuboyama, S.; Umezawa, Y.; Honda, K.; Nishio, M. *Tetrahedron* **2000**, *56*, 6185.

(11) (a) Alkorta, I.; Rozas, I.; Elguero, J. *J. Fluorine Chem.* **2000**, *101*, 233. (b) Alkorta, I.; Rozas, I.; Jimeno, M. L.; Elguero, J. *Struct. Chem.* **2001**, *12*, 459. (c) Alkorta, I.; Elguero, J. *J. Phys. Chem. A* **2003**, *107*, 9428. (d) Alkorta, I.; Rozas, I.; Elguero, J. *J. Org. Chem.* **1997**, *62*, 4687. (e) Alkorta, I.; Quiñonero, D.; Garau, C.; Frontera, A.; Elguero, J.; Deyà, P. M. *J. Phys. Chem. A* **2007**, *111*, 3137. (f) Alkorta, I.; Blanco, F.; Elguero, J. *J. Phys. Chem. A* **2008**, *112*, 1817. (g) Schottel, B. L.; Chifotides, H. T.; Dunbar, K. R. *Chem. Soc. Rev.* **2008**, *37*, 68. (h) Garau, C.; Quiñonero, D.; Frontera, A.; Ballester, P.; Costa, A.; Deyà, P. M. *New. J. Chem* **2003**, *27*, 211. (k) Schneider, H.; Vogelhuber, K. M.; Schinle, F.; Weber, J. M. *J. Am. Chem. Soc.* **2007**, *129*, 13022.

(12) (a) Mascal, M.; Armstrong, A.; Bartberger, M. *J. Am. Chem. Soc.* **2002**, *124*, 6274. (b) Alkorta, I.; Rozas, I.; Elguero, J. *J. Am. Chem. Soc.* **2002**, *124*, 8593. (c) Quiñonero, D.; Garau, C.; Rotger, C.; Frontera, A.; Ballester, P.; Costa, A.; Deyà, P. M. *Angew. Chem., Int. Ed.* **2002**, *41*, 3389.

(13) Gamez, P.; Mooibroek, T. J.; Teat, S. J.; Reedijk, J. *Acc. Chem. Res.* **2007**, *40*, 435.

(14) (a) Demeshko, S.; Dechert, S.; Meyer, F. *J. Am. Chem. Soc.* **2004**, *126*, 4508. (b) Schottel, B. L.; Bacsa, J.; Dunbar, K. R. *Chem. Commun.* **2005**, 46. (c) Rosokha, Y. S.; Lindeman, S. V.; Rosokha, S. V.; Kochi, J. K. *Angew. Chem., Int. Ed.* **2004**, *43*, 4650. (d) de Hoog, P.; Gamez, P.; Mutikainen, I.; Turpeinen, U.; Reedijk, J. *Angew. Chem., Int. Ed.* **2004**, *43*, 5815. (e) Frontera, A.; Saczewski, F.; Gdaniec, M.; Dziemidowicz-Borys, E.; Kurland, A.; Deyà, P. M.; Quiñonero, D.; Garau, C. *Chem.—Eur. J.* **2005**, *11*, 6560.

(15) (a) Berryman, O. B.; Bryantsev, V. S.; Stay, D. P.; Johnson, D. W.; Hay, B. P. *J. Am. Chem. Soc.* **2007**, *129*, 48. (b) Mascal, M. *Angew. Chem., Int. Ed.* **2006**, *45*, 2890.

(16) Mascal, M.; Yakovlev, I.; Nikitin, E. B.; Fettinger, J. C. *Angew. Chem., Int. Ed.* **2007**, *46*, 8782.

(17) (a) Gorteau, V.; Bollot, G.; Mareda, J.; Perez-Velasco, A.; Matile, S. *J. Am. Chem. Soc.* **2006**, *128*, 14788. (b) Gorteau, V.; Bollot, G.; Mareda, J.; Matile, S. *Org. Biomol. Chem.* **2007**, *5*, 3000.

(18) (a) Schottel, B. L.; Chifotides, H. T.; Shatruk, M.; Chouai, A.; Perez, L. M.; Bacsa, J.; Dunbar, K. R. *J. Am. Chem. Soc.* **2006**, *128*, 5895. (b) Reger, D. L.; Wayson, R. P.; Smith, M. D. *Inorg. Chem.* **2006**, *45*, 10077. (c) Zhou, X.-P.; Zhang, X.; Lin, S.-H.; Li, D. *Cryst. Growth Des.* **2007**, *7*, 485. (d) Steel, J.; Sumbly, C. J. *Dalton Trans.* **2003**, 4505. (e) Domasevitch, K. V.; Solntsev, P. V.; Gural'skiy, I. A.; Krautscheid, H.; Rusanov, E. B.; Chernega, A. N.; Howard, J. A. K. *Dalton Trans.* **2007**, 3893. (f) Black, C. A.; Hanton, L. R; Spicer, M. D. *Chem. Commun.* **2007**, 3171.

(19) Møller, C.; Plesset, M. S. *Phys. Rev.* **1934**, *46*, 618.

(20) Frisch, M. J.; Pople, J. A.; Binkley, J. S. *J. Chem. Phys.* **1984**, *80*, 3265.

(21) Zhao, Y.; Schultz, N. E.; Truhlar, D. G. *J. Chem. Theory Comput.* **2006**, *2*, 364.

(22) Dunning, T. H. *J. Chem. Phys.* **1989**, *90*, 1007.

(23) Frisch, M. J.; Trucks, G. W.; Schlegel, H. B.; Scuseria, G. E.; Robb, M. A.; Cheeseman, J. R.; Montgomery, J. A., Jr.; Vreven, T.; Kudin, K. N.; Burant, J. C.; Millam, J. M.; Iyengar, S. S.; Tomasi, J.; Barone, V.; Mennucci, B.; Cossi, M.; Scalmani, G.; Rega, N.; Petersson, G. A.; Nakatsuji, H.; Hada, M.; Ehara, M.; Toyota, K.; Fukuda, R.; Hasegawa, J.; Ishida, M.; Nakajima, T.; Honda, Y.; Kitao, O.; Nakai, H.; Klene, M.; Li, X.; Knox, J. E.; Hratchian, H. P.; Cross, J. B.; Bakken, V.; Adamo, C.; Jaramillo, J.; Gomperts, R.; Stratmann, R. E.; Yazyev, O.; Austin, A. J.; Cammi, R.; Pomelli, C.; Ochterski, J. W.; Ayala, P. Y.; Morokuma, K.; Voth, G. A.; Salvador, P.; Dannenberg, J. J.; Zakrzewski, V. G.; Dapprich, S.; Daniels, A. D.; Strain, M. C.; Farkas, O.; Malick, D. K.; Rabuck, A. D.; Raghavachari, K.; Foresman, J. B.; Ortiz, J. V.; Cui, Q.; Baboul, A. G.; Clifford, S.; Cioslowski, J.; Stefanov, B. B.; Liu, G.; Liashenko, A.; Piskorz, P.; Komaromi, I.; Martin, R. L.; Fox, D. J.; Keith, T.; Al-Laham, M. A.; Peng, C. Y.; Nanayakkara, A.; Challacombe, M.; Gill, P. M. W.; Johnson, B.; Chen, W.; Wong, M. W.; Gonzalez, C.; Pople, J. A. *Gaussian-03*; Gaussian, Inc.: Wallingford, CT, 2003.

(24) Dunning, T. H. *J. Phys. Chem. A* **2000**, *104*, 9062.

(25) Bene, J. E. D. ; Shavitt, I. In *Molecular Interactions: From Van der Waals to Strongly Bound Complexes*; Scheiner, S., Ed.; Wiley: Sussex, U.K., 1997; p 157.

(26) Boys, S. F.; Bernardi, F. *Mol. Phys.* **1970**, *19*, 553.

(27) Bader, R. F. W. *Atoms in Molecules: A Quantum Theory*; Clarendon Press: Oxford, U.K., 1990.

(28) Biegler-König, F. W.; Bader, R. F. W.; Tang, T. H. *J. Comput. Chem.* **1982**, *3*, 317.

(29) Popelier, P. L. A., with a contribution from Bone, R. G. A. MORPHY98, a topological analysis program; 0.2 ed.; UMIST, U.K., 1999.

(30) Keith, T. A. AIMAll (version 08.11.29), 2008; aim.tkgristmill.com.

(31) Alkorta, I.; Picazo, O. *Arkivoc* **2005**, *ix*, 305.

(32) Weinhold, F.; Landis, C. R. *Valency and Bonding. A Natural Bond Orbital Donor-Acceptor Perspective*; Cambridge Press: Cambridge, U.K., 2005.

(33) Glendening E. D.; Badenhoop, J. K., Reed, A. E.; Carpenter, J. E.; Bohmann, J. A.; Morales, C. M.; Weinhold, F. NBO 5.G; Theoretical Chemistry Institute, University of Wisconsin, Madison, WI, 2004.

(34) Glendening, E. D. *J. Am. Chem. Soc.* **1996**, *118*, 2473.

(35) Glendening, E. D. *J. Phys. Chem. A* **2005**, *109*, 11936.

(36) Schmidt, M. W.; Baldridge, K. K.; Boatz, J. A.; Elbert, S. T.; Gordon, M. S.; Jensen, J. H.; Koseki, J.; Matsunaga, N.; Nguyen, K. A.; Su, S. J.; Windus, T. L.; Dupuis, M.; Montgomery, J. A. Gamess version 11. *J. Comput. Chem.* **1993**, *14*, 1347–1363.

(37) Rozas, I.; Alkorta, I.; Elguero, J. *J. Phys. Chem. A* **1997**, *101*, 9457.

(38) Koch, U.; Popelier, P. *J. Phys. Chem.* **1995**, *99*, 9747.

(39) Alkorta, I.; Elguero, J. *J. Phys. Chem. A* **2006**, *110*, 2259.

(40) Alkorta, I.; Blanco, F.; Elguero, J. *J. Phys. Chem. A* **2008**, *112*, 6753.

(41) Alkorta, I.; Barrios, L.; Rozas, I.; Elguero, J. *THEOCHEM* **2000**, *496*, 131.

(42) Mata, I.; Alkorta, I.; Espinosa, E.; Molins, E.; Elguero, J. In *The Quantum Theory of Atoms in Molecules: From Solid State to DNA and Drug Design*; Matta, C. F., Russell, R. J., Eds.; Wiley: New York, 2007; pp 425452.

CT800444E

JCTC Journal of Chemical Theory and Computation

Molecular Modeling of Geometries, Charge Distributions, and Binding Energies of Small, Druglike Molecules Containing Nitrogen Heterocycles and Exocyclic Amino Groups in the Gas Phase and Aqueous Solution. [*J. Chem. Theory Comput. 4,,* 1718–1732 (2008)]. By Brian R. White, Carston R. Wagner, Donald G. Truhlar, and Elizabeth A. Amin*.

Page 1730. The following statement should have been included in the Acknowledgment of the article: Partial funding for this project is gratefully acknowledged from NIH grants CA120116 (C.R.W.) and CA125360 (C.R.W.).

CT9000944

10.1021/ct9000944
Published on Web 03/10/2009

Published on Web 03/10/2009